

# AGARD

ADVISORY GROUP FOR AEROSPACE RESEARCH & DEVELOPMENT

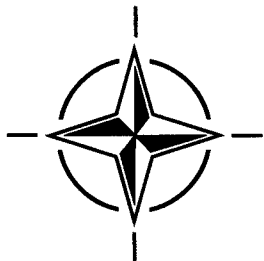
7 RUE ANCELLE, 92200 NEUILLY-SUR-SEINE, FRANCE

## AGARD REPORT 813

### Aerothermodynamics and Propulsion Integration for Hypersonic Vehicles

(l'Intégration de la propulsion et de l'aérodynamique pour les véhicules hypersoniques)

*This publication was prepared at the request of the Fluid Dynamics Panel. Papers were presented at a Special Course on "Aerothermodynamics and Propulsion Integration for Hypersonic Vehicles", held at the von Kármán Institute for Fluid Dynamics (VKI) in Rhode-Saint-Genèse, Belgium, 15-19 April 1996.*



## NORTH ATLANTIC TREATY ORGANIZATION

### DISTRIBUTION STATEMENT A

Approved for public release;  
Distribution Unlimited

Published October 1996

Distribution and Availability on Back Cover

DTIC QUALITY ASSURANCE

# AGARD

ADVISORY GROUP FOR AEROSPACE RESEARCH & DEVELOPMENT

7 RUE ANCELLE, 92200 NEUILLY-SUR-SEINE, FRANCE

## AGARD REPORT 813

### **Aerothermodynamics and Propulsion Integration for Hypersonic Vehicles**

(l'Intégration de la propulsion et de l'aérodynamique pour les véhicules hypersoniques)

This publication was prepared at the request of the Fluid Dynamics Panel. Papers were presented at a Special Course on "Aerothermodynamics and Propulsion Integration for Hypersonic Vehicles", held at the von Kármán Institute for Fluid Dynamics (VKI) in Rhode-Saint-Genèse, Belgium, 15-19 April 1996.



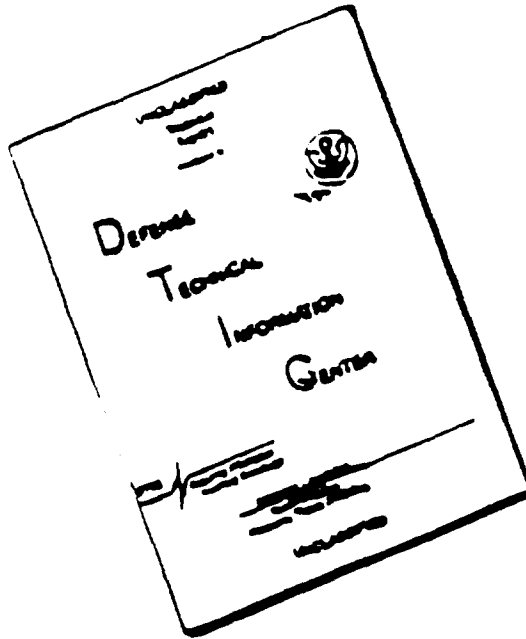
North Atlantic Treaty Organization  
*Organisation du Traité de l'Atlantique Nord*

**DISTRIBUTION STATEMENT A**

Approved for public release;  
Distribution Unlimited

19961220 099

# DISCLAIMER NOTICE



THIS DOCUMENT IS BEST  
QUALITY AVAILABLE. THE COPY  
FURNISHED TO DTIC CONTAINED  
A SIGNIFICANT NUMBER OF  
PAGES WHICH DO NOT  
REPRODUCE LEGIBLY.

# The Mission of AGARD

According to its Charter, the mission of AGARD is to bring together the leading personalities of the NATO nations in the fields of science and technology relating to aerospace for the following purposes:

- Recommending effective ways for the member nations to use their research and development capabilities for the common benefit of the NATO community;
- Providing scientific and technical advice and assistance to the Military Committee in the field of aerospace research and development (with particular regard to its military application);
- Continuously stimulating advances in the aerospace sciences relevant to strengthening the common defence posture;
- Improving the co-operation among member nations in aerospace research and development;
- Exchange of scientific and technical information;
- Providing assistance to member nations for the purpose of increasing their scientific and technical potential;
- Rendering scientific and technical assistance, as requested, to other NATO bodies and to member nations in connection with research and development problems in the aerospace field.

The highest authority within AGARD is the National Delegates Board consisting of officially appointed senior representatives from each member nation. The mission of AGARD is carried out through the Panels which are composed of experts appointed by the National Delegates, the Consultant and Exchange Programme and the Aerospace Applications Studies Programme. The results of AGARD work are reported to the member nations and the NATO Authorities through the AGARD series of publications of which this is one.

Participation in AGARD activities is by invitation only and is normally limited to citizens of the NATO nations.

The content of this publication has been reproduced  
directly from material supplied by AGARD or the authors.

Published October 1996

Copyright © AGARD 1996  
All Rights Reserved

ISBN 92-836-1041-5



*Printed by Canada Communication Group  
45 Sacré-Cœur Blvd., Hull (Québec), Canada K1A 0S7*



# **Aerothermodynamics and Propulsion Integration for Hypersonic Vehicles**

**(AGARD R-813)**

## **Executive Summary**

This report is a compilation of the edited proceedings of the "Aerothermodynamics and Propulsion Integration for Hypersonic Vehicles" course held at the von Kármán Institute for Fluid Dynamics (VKI) in Rhode-Saint-Genèse, Belgium 15-19 April 1996.

The integration of the airframe, fuselage, and propulsion system is a formidable problem and this is particularly the case for Hypersonic Vehicles. Therefore, it is important to keep the Aerothermodynamics and Propulsion Integration Technology associated with the design of these vehicles up to date.

This series of lectures, supported by the AGARD Fluid Dynamics Panel and the von Kármán Institute for Fluid Dynamics, covered the following topics: Aerothermodynamics of radiation-cooled surfaces, Real-gas and strong interaction phenomena, Hypersonic laminar turbulent transition and turbulence modeling, Configurational aerothermodynamics of reentry vehicles (winged and capsule) as well as RAM and SCRAM propelled vehicles, RAM and SCRAM inlet and propulsion integration, and the subjects of hypersonic missile aerothermodynamics, and stage separation for two-stage launch configurations. In addition, the Hypersonic Experimental and Computational Research program at VKI was presented.

# **L'intégration de la propulsion et de l'aérodynamique pour les véhicules hypersoniques**

**(AGARD R-813)**

## **Synthèse**

Ce rapport est une compilation des documents édités pendant le cours sur "l'Intégration de la Propulsion et de l'Aérodynamique pour les Véhicules Hypersoniques" qui s'est tenu à l'Institut von Kármán pour la Dynamique des fluides (VKI) de Rhode-Saint-Genèse, en Belgique, du 15 au 19 avril 1996.

L'intégration de la cellule, du fuselage et du système de propulsion est un énorme problème et tout particulièrement pour les Véhicules Hypersoniques. Cependant, il est primordial de conserver au gout du jour la technologie de l'Intégration de la Propulsion et de l'Aérodynamique en liaison avec l'évolution du concept de ces véhicules.

Ces séries de conférences, supportées par la Commission de la Dynamique des Fluides Dynamiques d'AGARD et l'Institut von Kármán pour la Dynamique des Fluides, couvrent les domaines suivants: l'Aérodynamique des surfaces refroidies par radiation, le Gaz réel et le phénomène d'interaction puissant, la Transition laminaire turbulente en mode hypersonique et le gabarit de la turbulence, la Configuration aérodynamique de la rentrée dans l'atmosphère des véhicules (capsules et ailés) à propulsion type RAMJET ou RAMJET à combustion supersonique (SCRAMJET), l'Intégration de la propulsion et de l'admission de type RAMJET et SCRAMJET, les sujets de l'aérodynamique des missiles hypersoniques, et la séparation des étages pour des configurations d'engins à deux étages. De plus, le Programme de Recherche Expérimental de Calcul dans le Domaine Hypersonique à VKI a été présenté.

# Contents

	Page
<b>Executive Summary</b>	iii
<b>Synthèse</b>	iv
<b>Recent Publications of the Fluid Dynamics Panel</b>	vi
<b>Special Course Staff</b>	viii
	Reference
<b>Introduction to the AGARD-FDP-VKI Special Course on Aerothermodynamics and Propulsion Integration for Hypersonic Vehicles</b> by E.H. Hirschel	1
<b>Hypersonic Experimental and Computational Research at VKI</b>	
<b>Part A: Hypersonic Aerothermodynamics</b> by M. Carbonaro, J.-M. Charbonnier and H. Deconinck	2A
<b>Part B: A Parallel Implicit Multidimensional Upwind Cell Vertex Navier-Stokes Solver for Hypersonic Applications</b> by E. van der Weide, E. Issman, H. Deconinck and G. Degrez	2B
<b>Aerothermodynamics of Radiation-Cooled Surfaces</b> by E.H. Hirschel	3
<b>Viscous/Inviscid and Real-Gas Effects Associated with Hypersonic Vehicles</b> by M.S. Holden	4
<b>Hypersonic Laminar-Turbulent Transition and its Implications for Winged Configurations</b> by D.I.A. Poll	5
<b>Configuration Aerothermodynamics of Entry Vehicles</b> by D.A. Throckmorton	6
<b>Configurational Aerothermodynamics of RAM and SCRAM Propelled Vehicles</b> by P. Perrier and J.C. Courty	7
<b>Inlet and Propulsion Integration of RAM Propelled Vehicles</b> by N.C. Bissinger	8
<b>Inlet and Propulsion Integration of SCRAM Propelled Vehicles</b> by L.A. Povinelli	9
<b>Missile Aerothermodynamics and Propulsion Integration</b> by D. Pagan and R.-G. Lacau	10
<b>Stage Separation Aerothermodynamics</b> by C. Weiland	11
<b>The Technology Development and Verification Concept of the German Hypersonics Technology Programme</b> by E.H. Hirschel	12

# Recent Publications of the Fluid Dynamics Panel

## **AGARDOGRAPHS (AG)**

### **Turbulent Boundary Layers in Subsonic and Supersonic Flow**

AGARD AG-335 July 1996

### **Computational Aerodynamics Based on the Euler Equations**

AGARD AG-325, September 1994

### **Scale Effects on Aircraft and Weapon Aerodynamics**

AGARD AG-323, July 1994

### **Design and Testing of High-Performance Parachutes**

AGARD AG-319, November 1991

### **Experimental Techniques in the Field of Low Density Aerodynamics**

AGARD AG-318 (E), April 1991

### **Techniques Expérimentales Liées à l'Aérodynamique à Basse Densité**

AGARD AG-318 (FR), April 1990

### **A Survey of Measurements and Measuring Techniques in Rapidly Distorted Compressible Turbulent Boundary Layers**

AGARD AG-315, May 1989

### **Reynolds Number Effects in Transonic Flows**

AGARD AG-303, December 1988

## **REPORTS (R)**

### **Hypersonic Experimental and Computational Capability, Improvement and Validation**

AGARD AR-319, Vol. I, Report of WG 18, May 1996

### **Parallel Computing in CFD**

AGARD R-807, Special Course Notes, October 1995

### **Optimum Design Methods for Aerodynamics**

AGARD R-803, Special Course Notes, November 1994

### **Missile Aerodynamics**

AGARD R-804, Special Course Notes, May 1994

### **Progress in Transition Modelling**

AGARD R-793, Special Course Notes, April 1994

### **Shock-Wave/Boundary-Layer Interactions in Supersonic and Hypersonic Flows**

AGARD R-792, Special Course Notes, August 1993

### **Unstructured Grid Methods for Advection Dominated Flows**

AGARD R-787, Special Course Notes, May 1992

### **Skin Friction Drag Reduction**

AGARD R-786, Special Course Notes, March 1992

### **Engineering Methods in Aerodynamic Analysis and Design of Aircraft**

AGARD R-783, Special Course Notes, January 1992

### **Aircraft Dynamics at High Angles of Attack: Experiments and Modelling**

AGARD R-776, Special Course Notes, March 1991

## **ADVISORY REPORTS (AR)**

### **Cooperative Programme on Dynamic Wind Tunnel Experiments for Manoeuvring Aircraft**

AGARD AR-305, Report of WG 16, to be published in Fall 1996

### **Aerodynamics of 3-D Aircraft Afterbodies**

AGARD AR-318, Report of WG 17, September 1995

### **A Selection of Experimental Test Cases for the Validation of CFD Codes**

AGARD AR-303, Vols. I and II, Report of WG 14, August 1994

### **Quality Assessment for Wind Tunnel Testing**

AGARD AR-304, Report of WG 15, July 1994

### **Air Intakes of High Speed Vehicles**

AGARD AR-270, Report of WG 13, September 1991

### **Appraisal of the Suitability of Turbulence Models in Flow Calculations**

AGARD AR-291, Technical Status Review, July 1991

**Rotary-Balance Testing for Aircraft Dynamics**

AGARD AR-265, Report of WG11, December 1990

**Calculation of 3D Separated Turbulent Flows in Boundary Layer Limit**

AGARD AR-255, Report of WG10, May 1990

**Adaptive Wind Tunnel Walls: Technology and Applications**

AGARD AR-269, Report of WG12, April 1990

**CONFERENCE PROCEEDINGS (CP)**

**Aerodynamics of Store Integration and Separation**

AGARD CP-570, February 1996

**Aerodynamics and Aeroacoustics of Rotorcraft**

AGARD CP-552, August 1995

**Application of Direct and Large Eddy Simulation to Transition and Turbulence**

AGARD CP-551, December 1994

**Wall Interference, Support Interference, and Flow Field Measurements**

AGARD CP-535, July 1994

**Computational and Experimental Assessment of Jets in Cross Flow**

AGARD CP-534, November 1993

**High-Lift System Aerodynamics**

AGARD CP-515, September 1993

**Theoretical and Experimental Methods in Hypersonic Flows**

AGARD CP-514, April 1993

**Aerodynamic Engine/Airframe Integration for High Performance Aircraft and Missiles**

AGARD CP-498, September 1992

**Effects of Adverse Weather on Aerodynamics**

AGARD CP-496, December 1991

**Manoeuvring Aerodynamics**

AGARD CP-497, November 1991

**Vortex Flow Aerodynamics**

AGARD CP-494, July 1991

**Missile Aerodynamics**

AGARD CP-493, October 1990

**Aerodynamics of Combat Aircraft Controls and of Ground Effects**

AGARD CP-465, April 1990

**Computational Methods for Aerodynamic Design (Inverse) and Optimization**

AGARD CP-463, March 1990

**Applications of Mesh Generation to Complex 3-D Configurations**

AGARD CP-464, March 1990

**Fluid Dynamics of Three-Dimensional Turbulent Shear Flows and Transition**

AGARD CP-438, April 1989

**Validation of Computational Fluid Dynamics**

AGARD CP-437, December 1988

**Aerodynamic Data Accuracy and Quality: Requirements and Capabilities in Wind Tunnel Testing**

AGARD CP-429, July 1988

**Aerodynamics of Hypersonic Lifting Vehicles**

AGARD CP-428, November 1987

**Aerodynamic and Related Hydrodynamic Studies Using Water Facilities**

AGARD CP-413, June 1987

**Applications of Computational Fluid Dynamics in Aeronautics**

AGARD CP-412, November 1986

# Special Course Staff

## SPECIAL COURSE DIRECTOR

E.H. Hirschel  
Daimler-Benz Aerospace AG  
81663 München  
Germany

## LECTURERS

H. Deconinck  
von Kármán Institute  
Chausée de Waterloo, 72  
1640 Rhode-Saint-Genèse  
Belgium

J.M. Charbonnier  
von Kármán Institute  
Chausée de Waterloo, 72  
1640 Rhode-Saint-Genèse  
Belgium

M.S. Holden  
Calspan-University at Buffalo  
Buffalo, New York  
14225

D.I.A. Poll  
College of Aeronautics  
Cranfield University  
Cranfield, Bedford  
MK43 OAL  
United Kingdom

D.A. Throckmorton  
NASA Langley Research Center  
Hampton, Virginia  
23681-0001  
United States

P. Perrier  
Dassault Aviation  
78, Quai Marcel Dassault  
92214 Saint-Cloud  
France

N.C. Bissinger  
Daimler-Benz Aerospace  
München, Germany

L.A. Povinelli  
NASA Lewis Research Center  
Cleveland, Ohio  
44135-3191  
United States

R.G. Lacau  
Aerospatiale Missiles  
2 rue Béranger  
92322 Châtillon Cedex  
France

C. Weiland  
Daimler-Benz Aerospace AG  
München, Germany

## NATIONAL COORDINATORS

M. Carbonaro  
von Kármán Institute  
Chausée de Waterloo, 72  
1640 Rhode-Saint-Genèse  
Belgium

## PANEL EXECUTIVE

J.K. Molloy

**Mail from Europe:**  
AGARD/OTAN  
Attn. FDP Executive  
92200 Neuilly-sur-Seine  
France

**Mail from US and Canada:**  
Attn. FDP Executive  
PSC 116  
AGARD/NATO  
APO AE 09777

# Introduction to the AGARD-FDP-VKI Special Course Aerothermodynamics and Propulsion Integration for Hypersonic Vehicles

E.H. Hirschel  
Daimler-Benz Aerospace AG  
Militarflugzeuge  
Postfach 80 11 60  
81663 München  
Germany

## SUMMARY

After a short general introduction to the topic the objectives of the course are presented. The background in form of technology programmes, development projects and operational vehicles is sketched, distinguishing four classes of hypersonic vehicles ranging from aeroassisted(winged)reentry vehicles over air-breathing and rocket-propelled space transportation systems to missiles. The different roles of aerothermodynamics and propulsion integration in vehicle definition and development work are identified as well as the evolution needs of these key technologies. A short discussion of the structure of the course and the background of the lecturers closes this introduction to the course.

## 1. OBJECTIVES OF THE COURSE

Hypersonic flight with manned, aeroassisted, rocket-propelled and/or airbreathing vehicles is since several decades the topic of technology work all over the world. So far it has led to only one truly operational vehicle, the US Space Shuttle as a space transportation system. Unmanned aeroassisted hypersonic vehicles are in operation in the military missile realm, they begin also to enter the space-transportation scene.

Aerothermodynamics and propulsion integration are key technologies needed for the definition and development of hypersonic vehicles. The term "hypersonic vehicle" is used here in the widest sense. The major characteristic of these vehicles is that they are aeroassisted, i.e. winged vehicles, although modern reentry capsule designs also exhibit elements of aeroassistance.

Hypersonic vehicles, as elements of space transportation systems, as high-speed earth transportation means and as military defense, reconnaissance or weapon delivery systems are, with few exceptions, more or less at the begin of their careers. Because recently all over the world several large technology programmes and development projects were performed and finished (only a few of them are still continuing), and on the other hand new efforts are only slowly taking off, it was thought to be timely to organize this special course.

The objectives of this special course are

- Review of recent research and industrial work in aerothermodynamics and propulsion integration.

- Consolidation and dissemination of newly gained knowledge, experience and techniques.

- Identification of new development and evolution needs in the field.

## 2. THE BACKGROUND: TECHNOLOGY PROGRAMMES, DEVELOPMENT PROJECTS, OPERATIONAL VEHICLES

In the following a short general overview is given over the background of the course. No in-depth review is intended of the many programmes, projects and (the few) operational systems, where aerothermodynamics and propulsion integration are involved. For this overview four major classes of hypersonic vehicles are distinguished, not with the design problems in mind, rather with regard to their operation modes.

### 1. Aeroassisted (winged) reentry vehicles

These vehicles are typically launched with rockets and rocket boosters, and make a controlled, non-propelled aerodynamic reentry flight and land horizontally. The only truly operational vehicle in this class is the US Space Shuttle. The Russian BURAN has flown only once. The European HERMES development was terminated early. The Japanese HOPE plans are further pursued. Much experience was gained in the development projects and related technology programmes. Flight experience with regard to aerothermodynamics was gained with several American and Russian experimental vehicles and with the Space Shuttle, especially during its first four flights.

### 2. Airbreathing aeroassisted space transportation systems

This class encompasses two-stage-to-orbit (TSTO) and single-stage-to-orbit (SSTO) airbreathing, fully reusable systems. RAM and/or SCRAM propulsion, augmented by rocket propulsion - the upper stages of TSTO systems only with rocket propulsion - are the typical propulsion modes in this class. Consequently, the vehicles, which are true space planes, start and land horizontally. American, European, Japanese and

Russian technology programmes, partly with very large funding, brought a large amount of results in propulsion technology, aerothermodynamics, materials and structures, and guidance, control and sub-systems. Although several experimental vehicles were envisaged at times, no hardware was build and flown.

### 3. Rocket-propelled aeroassisted space transportation systems

To this class, which came into being after a certain disillusionment happened with airbreathing technologies, belong fully reusable SSTO and TSTO systems, which may take off horizontally or vertically, but land horizontally in any case. Efforts are underway especially in the USA and in Europe (FESTIP) to establish the enabling technologies for this vehicle class.

### 4. Missiles

This class of hypersonic vehicles, which is also in the background of this course, encompasses military systems, which are aeroassisted systems with rocket or airbreathing propulsion. Here operational and near-operational systems exist, at the same time extended technology development is underway.

## 3. AEROTHERMODYNAMICS AND PROPULSION INTEGRATION AS KEY TECHNOLOGIES

Aerothermodynamics and propulsion integration have several roles in the design of hypersonic vehicles. The primary role of aerothermodynamics is - like that of aerodynamics in aircraft design - the definition of the outer shape of the flight vehicle, which holds for every vehicle class, even for advanced capsules, which are not in the center of attention of this course. This definition work, which is made in concert with the work of the other involved disciplines, has the objective to form the shape of the vehicle in such a way, that the necessary aerodynamic performance is ensured, and that the vehicle is flyable and controllable on all trajectory elements, with the associated (very large) Mach number span.

Aerothermodynamic propulsion integration shapes part of the outer flow path of the airbreathing vehicle (forebody), and the inner flow path through the inlet and through the external nozzle/afterbody. The engine and its nozzle are usually considered as extra items. However the larger the flight speed is, the more integrated are the lift system (outer flow path) and the propulsion system (inner flow path) of the vehicle, so that the paradigms of classical aircraft design must give way to new ones. Aerothermodynamic integration of the airframe and the propulsion system poses the largest challenge in the design of hypersonic airbreathing vehicles.

Aeroassisted two-stage-to-orbit space transportation systems face the problem of aerothermodynamic upper stage integration and separation. The latter usually is to happen at hypersonic Mach numbers at altitudes, where aerodynamic forces still are of large magnitude and the system flight still is aeroassisted. The separation process is a complicated process with strongly

non-linear and highly dynamical phenomena, which aerothermodynamics as a discipline together with the other involved disciplines must form and prescribe.

The determination of the aerothermodynamic loads on the vehicle is of utmost importance, too. The mechanical loads - surface pressure and skin friction - and the thermal loads - temperature level and heat flux into the structure - determine the structural concept. Cold primary (load bearing) structures, so far typical for aeroassisted reentry vehicles, must be protected by a thermal protection system. Hot primary structures, studied especially for airbreathing vehicles, face special problems with aerothermoelasticity, temperature gradients and internal heat protection. The demand of extreme light-weight structures for single-stage-to-orbit systems with either rocket or airbreathing propulsion puts heavy burdens on exact and reliable predictions of aerothermodynamic loads.

Finally the surface properties of hypersonic vehicles are considered. Surface radiation cooling is the primary cooling means for such vehicles. The surface coating must combine large radiation emissivity, low catalyticity (if thermochemical effects are present in the surface-near flow) and, if necessary, anti-oxidation properties in an flow environment with high mechanical and heat loads. If the vehicle is drag sensitive, which is typical for airbreathing systems, surface roughness, waviness, etc. are of large importance. At flight at altitudes, where the flow is turbulent on large parts of the vehicle surface, large drag increments, and heat loads increments, would result, if the surface quality is not sufficiently good. On the other hand, very small structural tolerances of the vehicle surface would drive up manufacturing costs very strongly. Aerothermodynamics therefore increasingly becomes instrumental in the determination of the surface properties, either necessary ones, like radiation emissivity, or permissible ones, like catalyticity, roughness, waviness, gaps etc..

In view of the performance demands especially of novel space transportation systems (reduction of specific transportation costs by up to one order of magnitude) aerothermodynamics and propulsion integration are by no means technologies without evolution needs. The further evolution of these technologies is of deciding importance, if hypersonic flight is to become a routine business. The most important of the evolution needs are listed in the following:

- o Understanding of flow and thermochemical phenomena and their implications for vehicle design.
- o Experimental techniques for ground-facility simulation and flight testing.
- o Tools of computational simulation and optimization, and the exploitation of the challenges and potentials of high-performance computing.
- o Flow-physics (laminar-turbulent transition and turbulence), and thermo-chemical modelling for computational simulation and optimization.
- o Multidisciplinary computational simulation and optimization (flow-structure couplings, TPS design, etc.).
- o Integration of computational simulation, ground-facility



simulation and in-flight simulation into Transfer Models.

- o Embedding of aerothermodynamics and propulsion integration into formalized and computerized vehicle definition and development processes, which will become, due to the recent advances of the information technologies, the - since a long time urgently needed - tools of concurrent engineering.

#### 4. THE STRUCTURE OF THE COURSE

The structure of the course is shown in Fig. 1. After the introduction to the course the activities of the hosting VKI in aerothermodynamics are presented. It follows an introduction to the aerothermodynamics of radiation-cooled surfaces, which is a rather novel subject. Basics of aerothermodynamics are addressed in the two lectures on real-gas and strong interaction phenomena, and on hypersonic laminar-turbulent transition and turbulence modelling. Following are two lectures on configurational aerothermodynamics of reentry vehicles, and of RAM and SCRAM propelled vehicles. Inlet and propulsion integration are treated then, first of RAM propelled vehicles, and after that of SCRAM propelled vehicles. One lecture each is devoted to missile aerothermodynamics and to stage separation aerothermodynamics. Finally some results from the technology development and verification concept study of the German Hypersonics Technology Programme are presented.

The lecturers of the course are senior engineers and researchers from industry, research establishments and universities with a wide background in technology and project work. All major topics of aerothermodynamics and propulsion integration are covered and treated in depth.

#### 5. CLOSING REMARKS

Aerothermodynamics and propulsion integration are key technologies, which enable the design and development of reusable aeroassisted space transportation systems, hypersonic vehicles and missiles. Performance demands on future systems are large, hence a further evolution of these technologies is necessary. Developments in information technologies give new impetus to the field, and pose in turn new and large challenges in understanding and modelling of physics. The course will review, consolidate and disseminate knowledge, experience and techniques, which have been gathered in the past decades in the field.

The sponsoring of the course by the Fluid Dynamics Panel of AGARD through the AGARD Consultant and Exchange Programme and by the von Karman Institute for Fluid Dynamics is gratefully acknowledged. The same holds for the large efforts by Prof. Carbonaro and the VKI staff, who organized the course locally. Last not least, thanks are due to the lecturers, who spent much time and effort in order to prepare the material for this course.

Day 1	Day 2	Day 3	Day 4	Day 5
<b>Introduction</b> <i>E.H. Hirschel, Daimler-Benz Aerospace, Germany</i>  <b>Hypersonic aerothermodynamics at VKI</b> <i>M. Carbonaro, J.-M. Charbonnier, H. Deconinck, VKI, Belgium</i>  <b>Aerothermodynamics of radiation-cooled surfaces</b> <i>E.H. Hirschel</i>	<b>Hypersonic laminar-turbulent transition and turbulence modelling</b> <i>D.I.A. Poll, University of Manchester, United Kingdom</i>	<b>Configurational aerothermodynamics of RAM and SCRAM propelled vehicles</b> <i>P. Perrier, J.C. Courty, Dassault DGT/DEA, France</i>	<b>Inlet and propulsion integration of SCRAM propelled vehicles</b> <i>L.A. Povinelli, NASA Lewis Research Center, U.S.A.</i>	<b>Stage integration and separation aerothermodynamics</b> <i>C. Weiland, Daimler-Benz Aerospace, Germany</i>  <b>Technology development and verification</b> <i>E.H. Hirschel</i>
<b>Real-gas and strong interaction phenomena</b> <i>M.S. Holden, Calspan Advanced Technology Center, U.S.A.</i>	<b>Configurational aerothermodynamics of reentry vehicles</b> <i>D.A. Throckmorton, NASA, Langley, U.S.A.</i>	<b>Inlet and propulsion integration of RAM propelled vehicles</b> <i>N.C. Bissinger, Daimler-Benz Aerospace, Germany</i>	<b>Missile aerothermodynamics</b> <i>D. Pagan, R.-G. Lacau, Aerospatiale, France</i>	

Fig. 1 The structure of the course

AGARD-R-813, 1996

(AGARD-FDP-VKI Special Course on Aerothermodynamics and Propulsion Integration, Rhode-Saint-Gen  se, April 15-19, 1996)

# Hypersonic Aerothermodynamics at VKI

M. Carbonaro, J.-M. Charbonnier, H. Deconinck  
 von Karman Institute for Fluid Dynamics  
 Aeronautics / Aerospace Department  
 Chaussée de Waterloo, 72  
 B-1640 Rhode-Saint-Genèse  
 Belgium

## 1. Introduction

The Aeronautics / Aerospace Department of the von Karman Institute has been involved in research activities in the hypersonic regime since the 1960's with the installation of the hypersonic free piston tunnel Longshot which allows to simulate high Reynolds number hypersonic flows. Since then, a Mach 6 blow down facility H3 is also operational and at present time an induction heating facility called Plasmatron is being developed under supervision of the European Space Agency. Simultaneously to the development of experimental techniques, Computational Fluid Dynamics was initiated and in-house made codes are operational to simulate hypersonic flows without chemistry and in thermal equilibrium.

The objective of the present paper is to briefly describe the research topics which have been addressed the past years and the current activities at the VKI in the hypersonic aerothermodynamics area. Basic research topics will be first presented and then applications to hypersonic vehicles and development of facilities will be discussed.

## 2. Basic Research

The von Karman Institute is involved in basic research areas in the field of hypersonic and aerothermodynamics almost since its creation. Research is carried out by Faculty members, PhD candidates, members of the Advanced Program in Basic Research and members of the Diploma Course Program.

Two main areas have been investigated during the past years: boundary layer transition and shock wave - boundary layer interactions. In the next sections, some of the major findings and the current state of the research are presented.

## 2.1 Boundary layer transition

In hypersonic, boundary layer transition is of major importance because of the impact it has on the heat load imposed to the vehicle. In the next section, investigations carried out at Mach 6 on smooth and roughened surfaces are presented.

### 2.1.1 Boundary layer transition on smooth surfaces (H.L. Boerigter, J.-M. Charbonnier)

#### 2.1.1.1 Introduction

The H-3 blowdown wind tunnel has a contoured axisymmetric nozzle, providing a Mach 6 free jet with 0.12 m diameter (Fig. 2.1.1.1) [1, 2]. Typical unit Reynolds numbers vary from 8 to 25 million per meter, using stagnation pressures ranging from 7 to 35 bar and stagnation temperatures up to 580 Kelvin. The tunnel is equipped with a three degrees of freedom traversing mechanism for model support, including a variable incidence mechanism. A mechanism for rapid model injection is used. Instrumentation includes shadowgraph and schlieren systems, a three-component strain gauge balance, fast pressure response transducers, scanivalves and an electronic pressure measurement system, and equipment for heat transfer measurements including an infrared camera. Currently a microphone measurement system is being implemented.

One of the main topics of research in this tunnel is concerned with the heating of reentry vehicles during their return into the atmosphere. Typical points of interest are the nose region, wing and fin leading edges where high total temperatures are reached, but also the windward side where the aerodynamic heating is caused by friction and depends on the laminar or turbulent state of the boundary layer. Research has been focused on this particular case, and in particular on the

effects of a local surface roughness on transition [3]. During this research it was found that not only the model roughness has a large influence on transition, but also the flowfield non- uniformity.

### **2.1.1.2 Determination of the boundary layer transition location on standard models**

One of the problems of boundary layer research in this hypersonic wind tunnel are the typical dimensions. The uniform part of the free jet has a maximum diameter of about 12 cm, and a length of about 25 cm. This means that models have to be rather small. As a result, a typical boundary layer thickness is of the order of 1 mm. To study transition without having to make intrusive measurements in this thin boundary layer, it was decided to look at the influence which transition has on the heat transfer coefficient which can then be related to the skin friction coefficient.

The models tested are basically flat plates and cones. The heat transfer is determined using the so-called semi infinite slab method where the surface temperature is measured during the test by an infrared scanner [2]. The experimental results are compared to theoretical predictions based on the fact that the heat transfer distribution along a flat plate in incompressible flow can be applied to the case of compressible flow, if the flow properties are evaluated at a reference temperature [2,4]. In both the laminar and the turbulent case, the so-called Reynolds analogy is used to calculate the heat transfer coefficient from the skin friction coefficient.

When the skin friction distribution over the surface is known, the momentum integral relation can be used to derive the momentum thickness distribution over the surface. Assuming that there is no pressure gradient over the flat plate, the momentum integral relation can be written as:

$$\theta(x) = 1/2 \int_0^x C_f(x) dx$$

The laminar and turbulent theories provide a direct relationship between  $x$  and  $C_f$  so that the value of  $\theta$  can be calculated directly. In order to determine the virtual origin of the turbulent boundary layer, the curves for the turbulent momentum thickness can be shifted until they fit the measurement. Due to the integration process the measured momentum thickness has a low noise level, so this fitting can be done with more accuracy than for the skin friction curve. This means that not only the absolute value of  $\theta$  can be matched, but also the slope of the curve. Doing this, it was found that the theory for turbulent boundary layer

provided by McLaughlin fit best to the measurements as observed in figure 2.1.1.2 [5].

If the values of the momentum thickness deduced from the measurements are compared to those predicted by the Blasius solution, it can easily be calculated where the predicted laminar momentum thickness reaches below 99% of the measured value, defining this point as the beginning of transition. This process can be automated and is repeatable, contrary to the extrapolation procedure by fairing a straight line through the transition region. Following the same reasoning, the end of transition can be defined to be at the point where the predicted turbulent momentum thickness reaches 99% of the measured value.

### **2.1.1.3 Effect of the model leading edge**

Analyzing the heat transfer results it appeared that the heat transfer distribution and thus the transition position on the plate was not uniform in spanwise direction, even though a seemingly uniform flat plate was used. Figure 2.1.1.3 shows the heat transfer coefficient or the Stanton number distribution on two lines, on coordinates  $y = 35$  mm and  $y = 65$  mm.

It is clear that on both lines the measurement follows the laminar curve at first, but then transition occurs on one, while the other remains laminar for some 20-30 mm more. This results in local differences in heat transfer coefficient of a factor of two on lines only 30 mm apart, and also in the momentum thickness (fig. 2.1.1.4).

Figure 2.1.1.5 shows the heat transfer coefficient on a vertical line parallel to the leading edge, at a distance of about 130 mm from the leading edge, where one curve has just reached the end of transition. In the same graph is shown the thickness distribution of the leading edge as measured using a microscope.

The correlation between the two curves is obvious. Where the leading edge is locally thin the heat transfer coefficient is high and vice versa. The variation in Stanton number is a factor 2 over a spanwise distance of about 30 mm. So it seems that where the leading edge is locally thin, transition downstream occurs closer to that leading edge.

To see whether the correlation between leading edge thickness and transition position also applies to uniform leading edges, it was decided to manually improve an existing, fairly blunt leading edge. Using a grinding stone the thickness was first made uniform at  $b=154$   $\mu$ m and then gradually reduced until at  $b=14$   $\mu$ m it was impossible to reduce the thickness any more while keeping it uniform. It is found that for leading edges with average thickness  $b=154$   $\mu$ m and  $b=96$   $\mu$ m

the boundary layer remains laminar over the full length of the plate. For the high unit Reynolds number tests this implies a Reynolds number at the beginning of transition which is larger than 4 million. When the leading edge thickness was reduced to  $b=54\text{ }\mu\text{m}$ , for the three standard unit Reynolds numbers transition occurs on the plate, albeit close to the trailing edge. For the two smaller thicknesses tested,  $b=34\text{ }\mu\text{m}$  and  $b=14\text{ }\mu\text{m}$ , transition shifts upstream. The smallest Reynolds number at the beginning of transition is 1.3 million for thickness  $b=14\text{ }\mu\text{m}$ , more than three times smaller than for the thicker leading edge.

When the obtained transition Reynolds numbers are depicted vs the unit Reynolds number with the thickness as an extra parameter, a trend shows in figure 2.1.1.6.

The transition Reynolds number increases linearly with the unit Reynolds number, and it also increases with the thickness. Extrapolating the unit Reynolds number to zero, the transition Reynolds number for all thicknesses seems to go to 0.2 million, this is called the apparent origin of transition.

The triangular marks with an arrow indicate that in this particular case transition does not occur on the flat plate and that the transition Reynolds number should be higher than the value indicated by the triangle. A so-called distance parameter can be found. It has been mentioned before that there is a limit equal to 0.2 million. When this so-called distance parameter  $(Re_x - 0.2 \cdot 10^6) / Re_u$  is displayed vs the average thickness, all data points fall on one curve (fig. 2.1.1.7).

The value of the Reynolds number at the beginning of transition on a flat plate at Mach 6 in the VKI-H3 tunnel is thus given by:

$$Re_x = 2 \cdot 10^5 + 0.124 \cdot Re_u + 105 \cdot 10^5 \cdot b^2 \cdot Re_u$$

( $b$  in meters and  $Re_u$  in 1/m)

#### 2.1.1.4 Effect of the wind tunnel flow field

Even using a uniform leading edge there still remains a non-uniformity of the heat transfer distribution. These heat transfer variations are smaller than those in figure 2.1.1.5, and they also seem to be more or less symmetric on the plate. Moreover, when moving the model sideways in the tunnel, the shape of the heat transfer distribution remains fixed in the tunnel and moves over the model. This indicates that the observed variations are not caused by the plate but by the flowfield. To possibly explain these remaining non-uniformities, a detailed calibration of the wind tunnel flow field is carried out using Pitot pressure and static

pressure measurements [6]. Simultaneously, computations of the nozzle flow are performed with the VKI-MB Navier Stokes code [7,8] for both laminar and turbulent nozzle wall boundary layers.

As expected, the nozzle wall boundary layers are turbulent and the best fit with the experiments is obtained when the transition is placed immediately after the nozzle throat. In these computations, not only the nozzle flow is calculated but also the free jet flow in the test chamber as indicated by the grid displayed in figure 2.1.1.8.

As most of the contoured nozzle of hypersonic facilities, it can be seen in figure 2.1.1.9 that the Mach number at the nozzle exit is not uniform because of weak compression waves originating from the incorrect modeling of the boundary layer thickness during the design phase of the nozzle. Moreover, the free jet itself is affected by the pressure level in the test chamber (taken equal to the measured one) which is likely to produce a slightly under or over expanded jet.

A typical example of the Mach number on the centerline of the tunnel measured at three stagnation pressure levels is given in figure 2.1.1.10 and compared to computational results for the lowest stagnation pressure. The computation reproduces rather well the Mach number measured even at 200 mm from the nozzle exit which would indicate that the computation of the free jet is relevant. These computations are still in progress for the other standard flow conditions and will be used as input conditions to the computations of the flow field over the flat plate tested in the wind tunnel.

The other well known effect of the wind tunnel on transition is associated to the so-called wind tunnel noise. In hypersonic wind tunnels, noise radiated from the nozzle wall boundary layers is believed to be a major cause of early transition. With a typical nozzle wall boundary layer thickness of about 10 mm and a typical speed of 1000 m/s, this gives frequencies up to 100 kHz. However, the pressure transducers used in the Pitot tubes have a resonance frequency of about 140 kHz and a flat response up to about 30 kHz. In order to push further the limits of use of the transducers, special calibrations with respect to a reference microphone (fig. 2.1.1.11) are performed which allow to extend the usable frequency domain up to about 100 kHz.

Moreover, these transducers will experience very high temperatures (up to 550 K) and therefore the measurements have to be made in very short time to avoid burning the transducers. Even though they are compensated for temperature effects, the transducers experience transients in temperature which are not correctly compensated and which require a special correction. These unsteady total pressure and static pressure measurements are presently in progress.

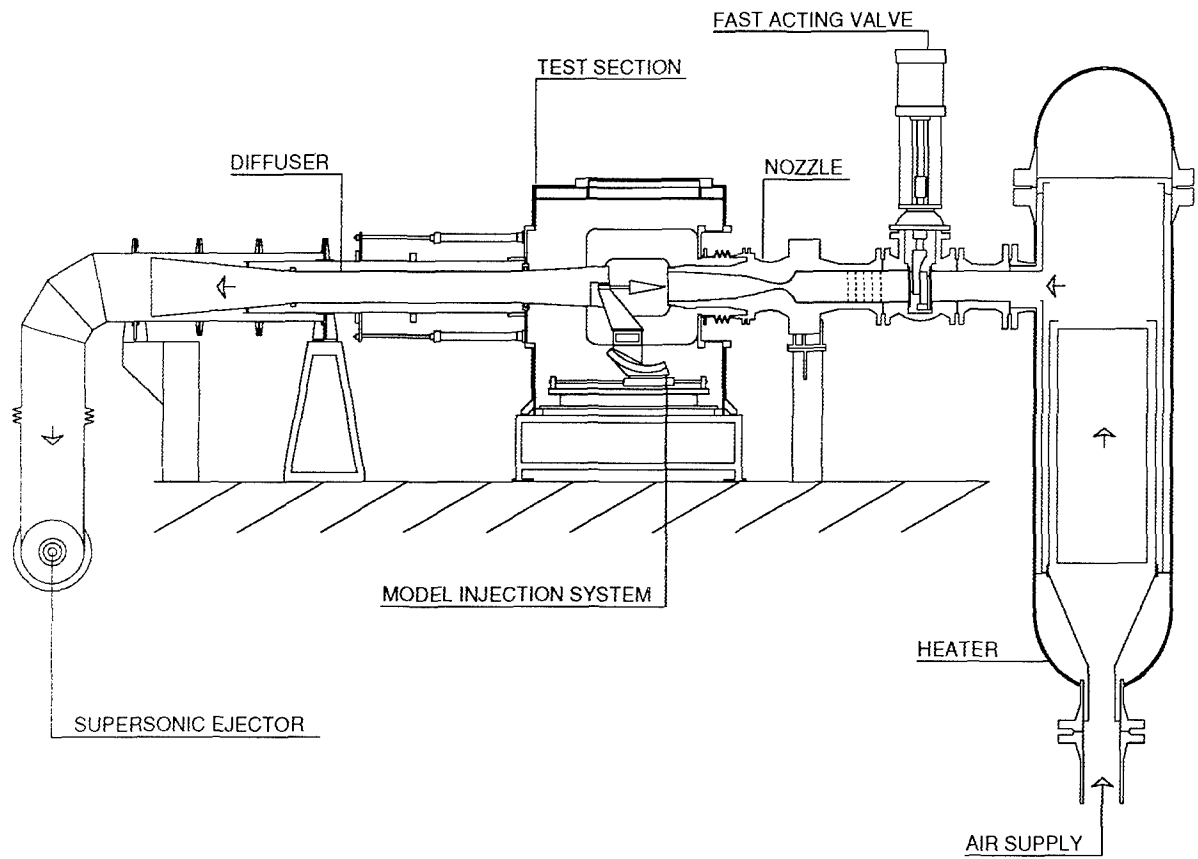
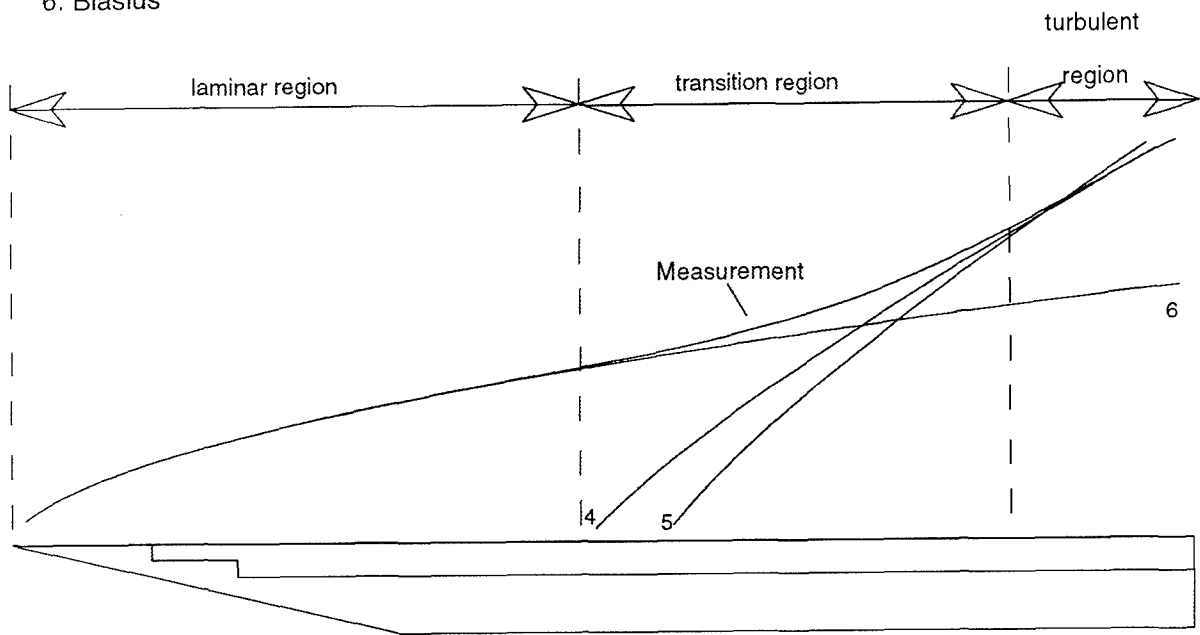


Fig. 2.1.1.1: H-3 blowdown wind tunnel.

- 4: McLaughlin
- 5: Ludwig-Tillmann
- 6: Blasius



(Momentum thickness not to scale)

Fig. 2.1.1.2: Predicted momentum thicknesses compared to a measured result

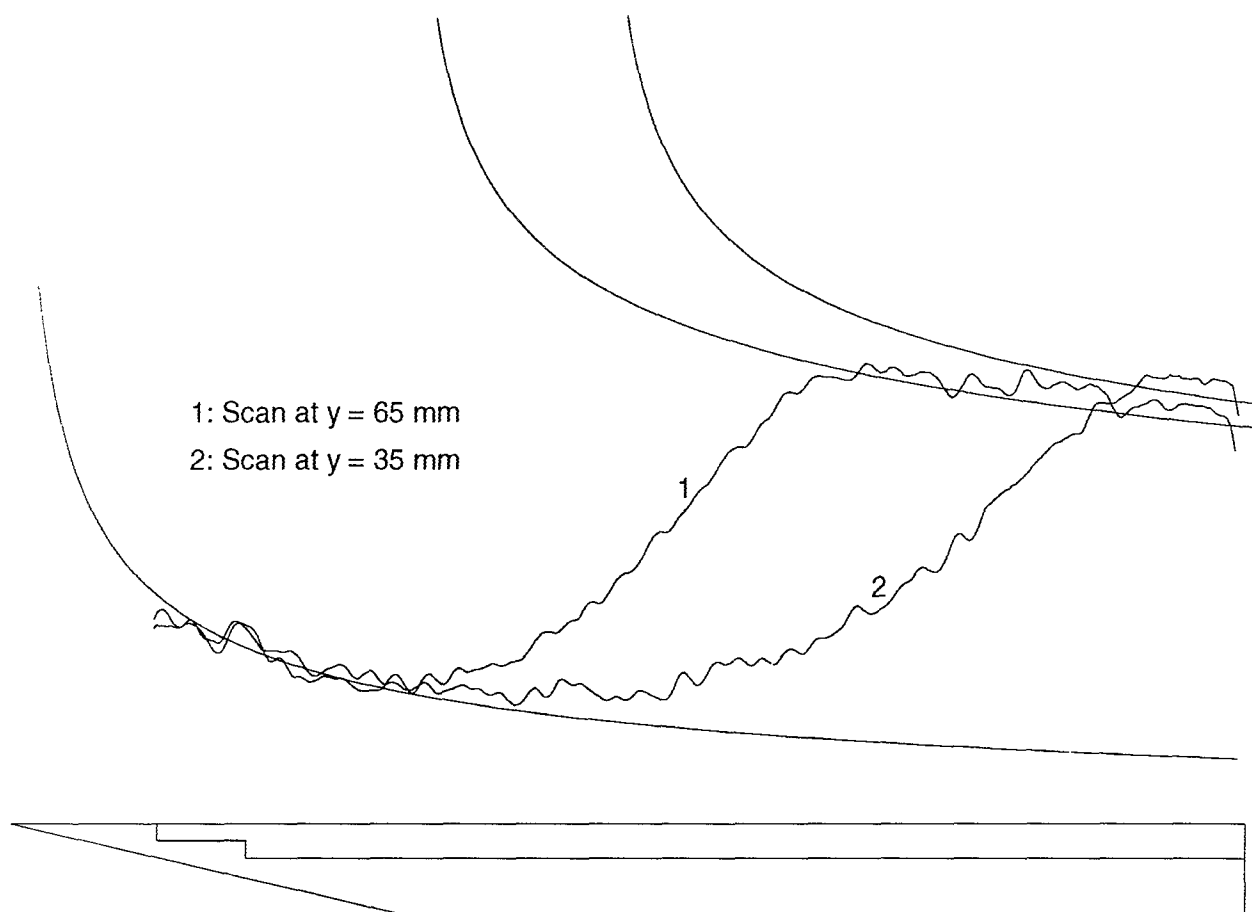


Fig. 2.1.1.3: Stanton number distribution on two horizontal lines

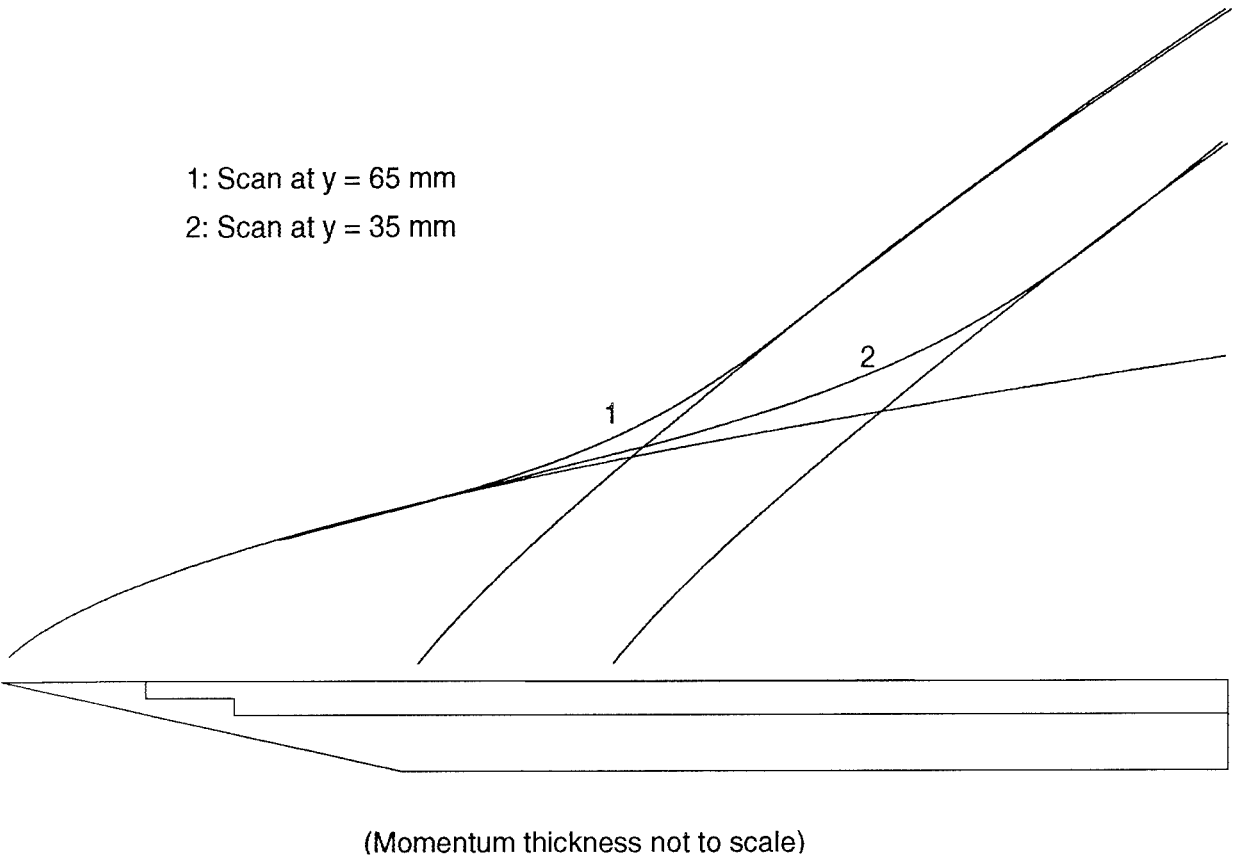


Fig. 2.1.1.4: Momentum thickness development on two horizontal lines

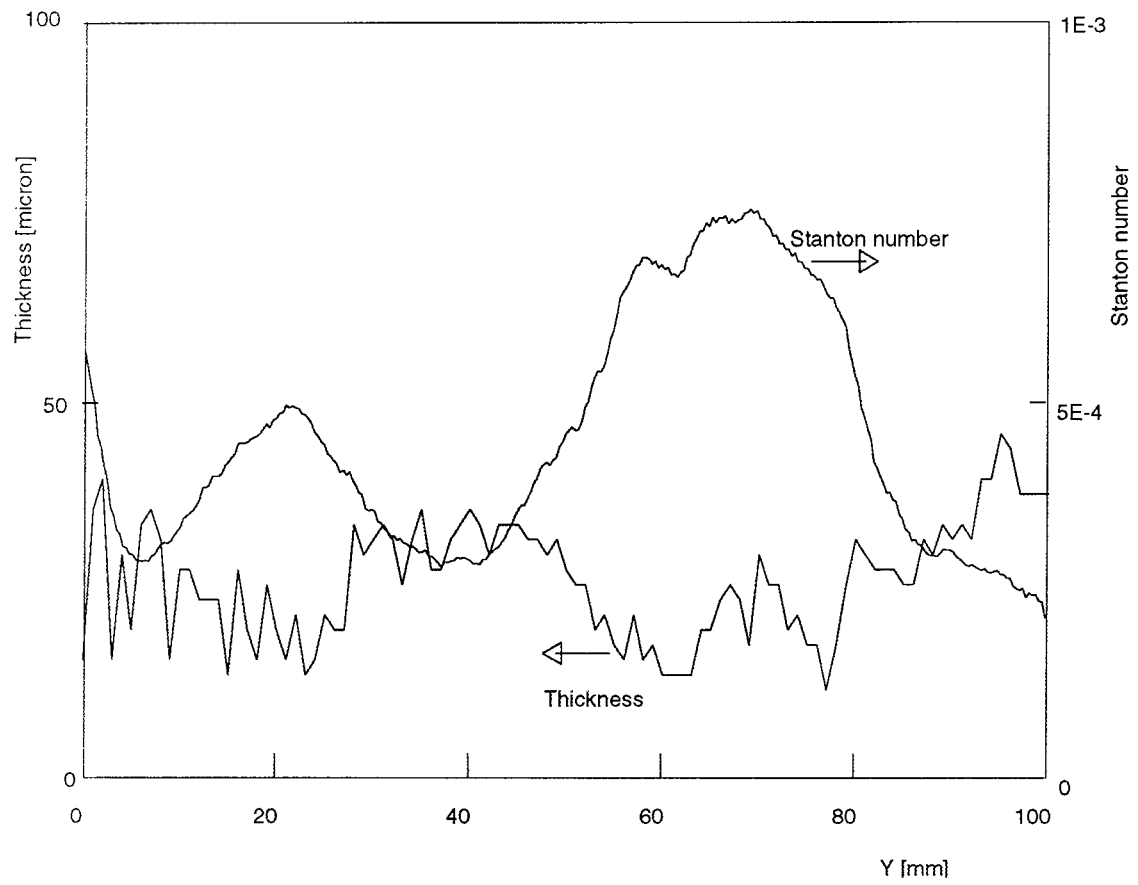


Fig. 2.1.1.5: Spanwise Stanton number distribution and the local leading edge thickness



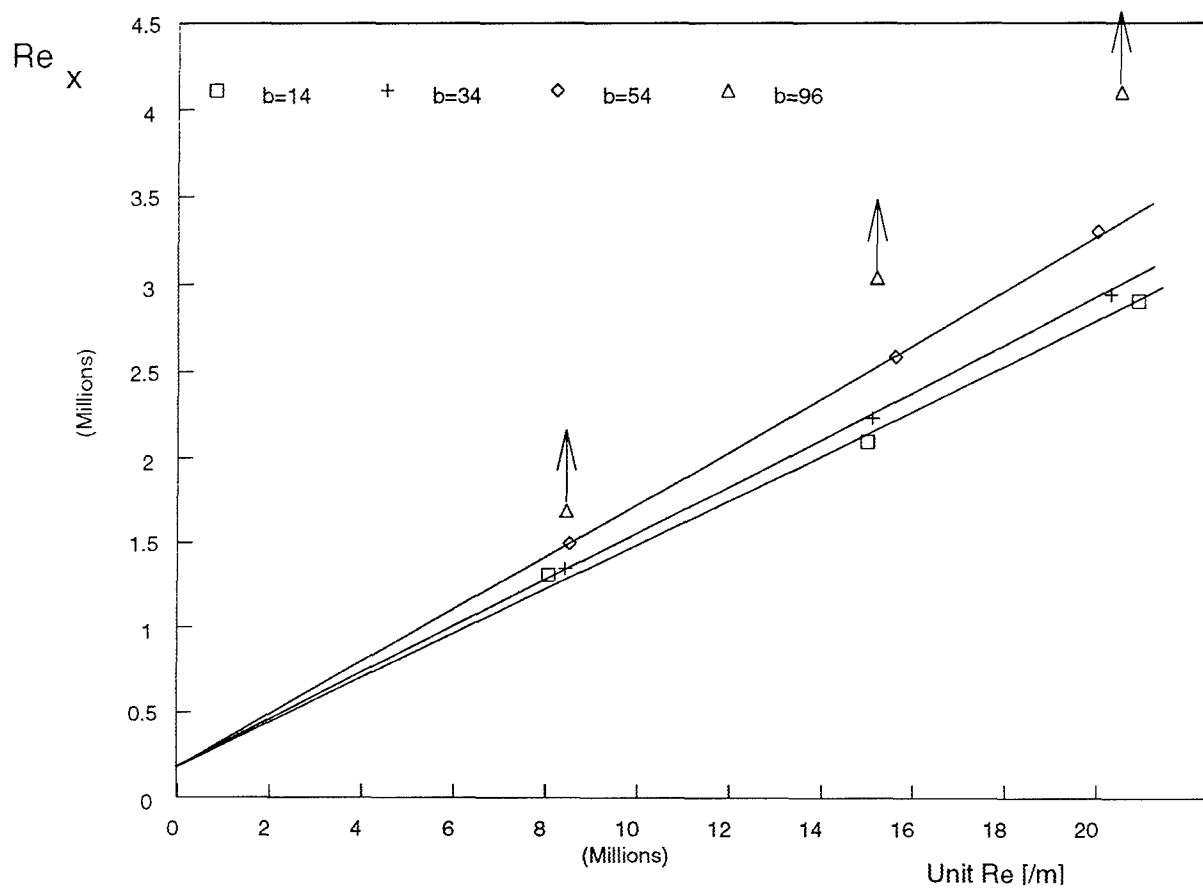


Fig. 2.1.1.6: Transition versus unit Reynolds number

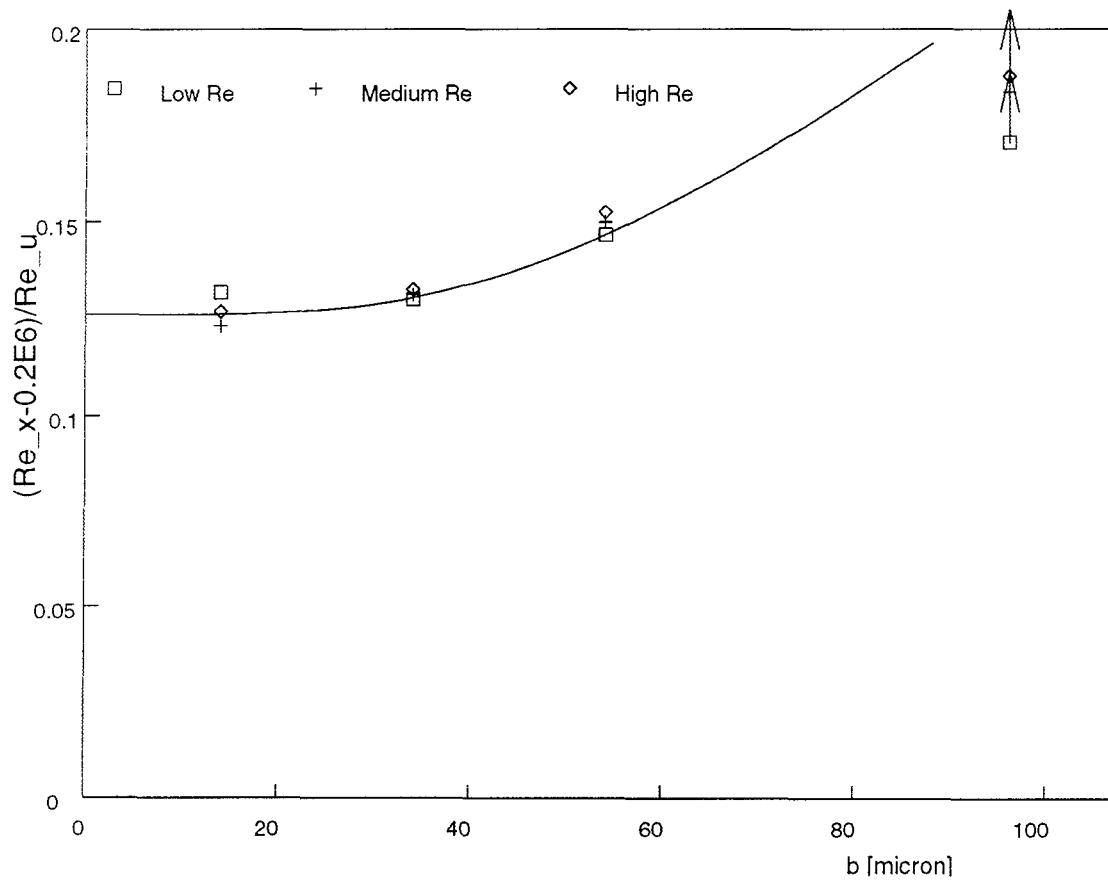


Fig. 2.1.1.7: Distance parameter

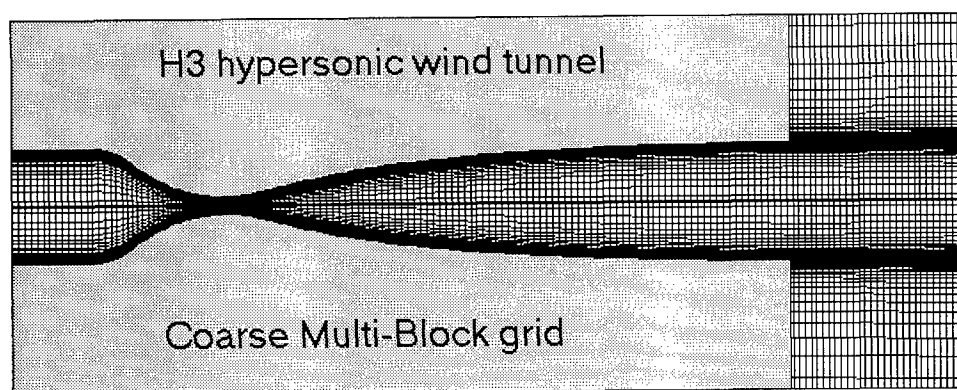


Fig. 2.1.1.8: Computational grids for the H3 wind tunnel

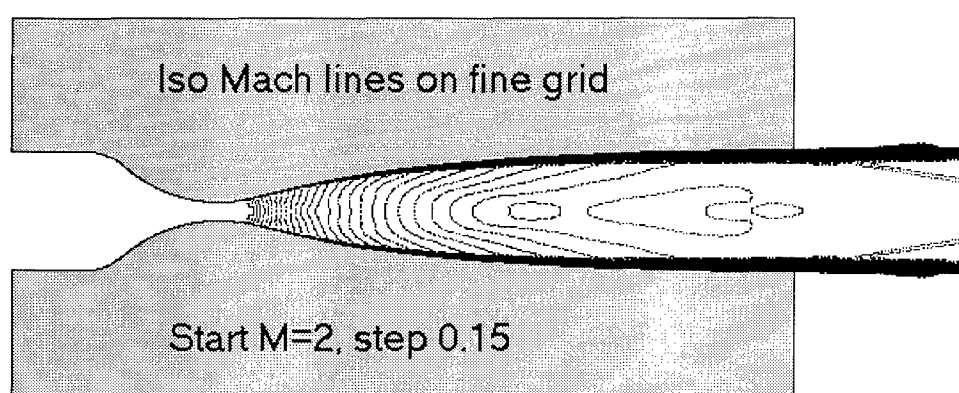


Fig. 2.1.1.9: Computed iso-Mach lines in the H3 wind tunnel

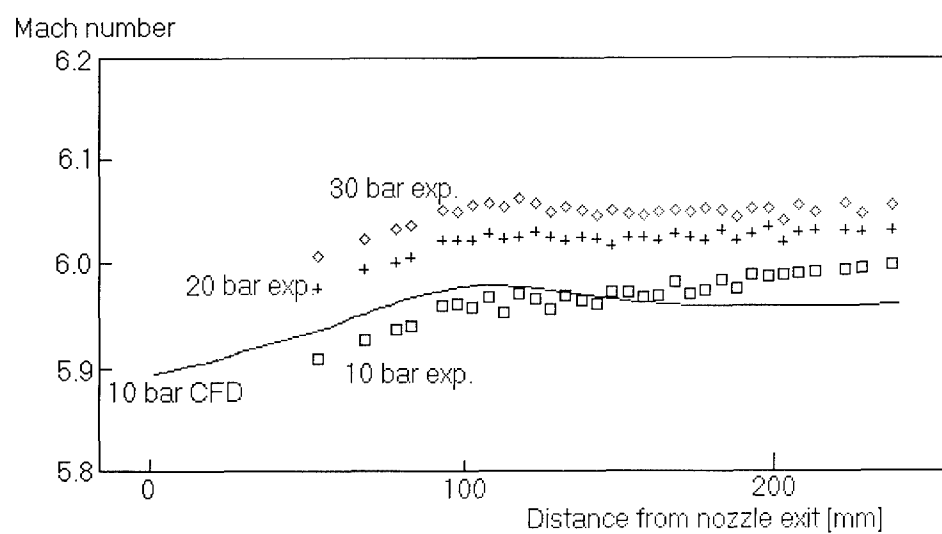


Fig. 2.1.1.10: Measured and computed Mach number in the H3 wind tunnel

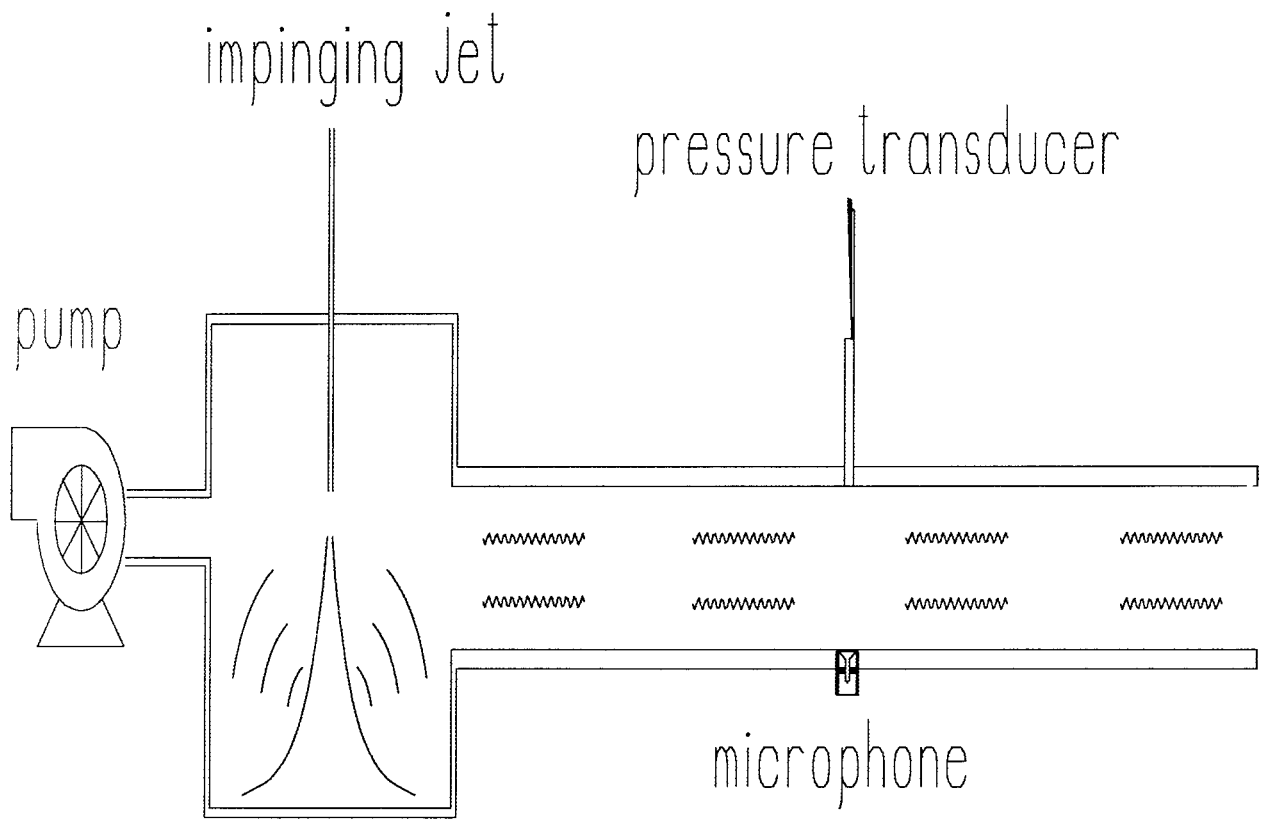


Fig. 2.1.1.11: Wave guide calibrator device

## 2.1.2 Roughness induced transition

(H. L. Boerrigter, J.-M. Charbonnier)

### 2.1.2.1 Introduction

As mentioned before, for reentry of hypersonic vehicle in general, boundary layer transition is a key issue. In addition to the natural transition discussed previously, it is important for a practical vehicle design to quantify the admissible wall roughness with a good accuracy in order to guarantee a safe operation of the vehicle while keeping the fabrication constraints to the minimum level.

In this section, the research carried out at the VKI during this past decade in the field of roughness induced transition is briefly exposed and some of the current activities are mentioned.

### 2.1.2.2 Roughness induced transition for attached flows

The VKI has been involved in the study of roughness induced transition since 1988 in the framework of the Hermes program [3,9,10]. This work has led to the establishment of criteria which predict the change in the transition position when the roughness height is increased. A large number of roughness geometries were tested (2D gap/step, 3D perturbation, spheres, ...) on flat plates and cones with sharp leading edges in the H3 Mach 6 facility of the VKI. Recently, these data were compared with data published by Bertin [12], obtained on an Orbiter model at angle of attack placed in a Mach 8 wind tunnel [9].

As seen in figure 2.1.2.1, the very good agreement between the Orbiter data and the data obtained at VKI shows that the transition criteria established on simple geometries with rather sharp leading edges can be used for a blunt body as the Orbiter. This is true provided the actual boundary layer properties (momentum thickness) are used to evaluate the Reynolds numbers which are entered in the transition criteria. However, it was found that the criteria presented by Bertin in [11,12], using the Reynolds number based on the roughness height and the boundary layer edge conditions do not agree with the measurements made at the VKI as can be seen from the differences in figures 2.1.2.2 and 2.1.2.3.

It appears that the ratio  $R_{\theta}/M$  which is already used for transition on smooth bodies [5] is also a good candidate when using the ratio of the values taken at the transition location for the rough and for the smooth cases as seen in fig. 2.1.2.1, 2.1.2.2 and 2.1.2.3. On the contrary, the Reynolds number based on the roughness height does not allow to correlate the transition data obtained on different geometries as indicated by the

order of magnitude difference between the Orbiter data and VKI data. Therefore, it seems that the criteria using  $h/\delta^*$  is a better candidate to predict the critical roughness height (fig. 2.1.2.1). When coupled with a boundary layer calculation on the body it should provide the admissible roughness heights as function of the flow conditions. For the extrapolation to flight of this criteria, one has to consider the ratio of the wall temperature to the stagnation temperature. Since the displacement thickness accounts for the effect of wall temperature, the extrapolation to flight can be achieved through these criteria as indicated by Bertin et al in [13] who found for the Orbiter windward tiles reasonable admissible roughness heights up to 2 mm for different trajectory points.

However in some cases like for instance for strongly accelerated flow over cooled surfaces, the boundary layer displacement thickness may become negative and the criteria based on the relative height of the roughness to the boundary layer displacement thickness fail. For such a reason, Bertin et al [11] proposed to use a Reynolds number based on the roughness height instead of the ratio  $h/\delta^*$ . However as indicated by the comparison of figures 2.1.2.2 and 2.1.2.3, these criteria are geometry dependent which is not the case of the  $h/\delta^*$  criteria. Moreover, as noticed by Boudreau in [14], it is unlikely that such a simple  $h/\delta^*$  criteria be universal because it does not account for pressure gradients whose effects are, when favorable, to "laminarize" the boundary layer. Actually two effects may play a role on the transition when induced by roughness: the entropy layer and pressure gradients. For the former, there are already some indications (as discussed above) that the effects of the entropy layer can be accounted for by using the local edge condition of the boundary layer to compute the flow parameters. For the latter, there is no evidence of their influence in the experiments conducted so far at the VKI and also on the Orbiter where the roughness elements were placed in a region of weak gradients. However as noted by Boudreau [14], when one wants to trigger the boundary layer transition on a blunt cone without creating large disturbances in the flowfield, the position of the distributed roughness with respect to the sonic line and to the minimum pressure level is of major importance. This particular situation was investigated on an axisymmetric model defined based on the wind direction and on windward side of the ARD capsule at 23° incidence [15]. Figure 2.1.2.5 shows the model with spherical roughness glued on the conical afterbody.

It has been demonstrated that in the conditions of the

H3 wind tunnel at Mach 6, transition can not be triggered by roughness elements placed on the front part of the model. When placing roughness elements at the beginning of the conical region, transition can be triggered with an arrangement of spheres of about 5 times the boundary layer displacement thickness which can not be considered anymore as small roughness (Fig. 2.1.2.6). These investigations, which are still under progress, confirm that the transposition of the roughness induced transition criteria from simple geometries to cases with strong entropy layers and pressure gradients is not straightforward.

Surface waviness is also responsible for earlier transition as demonstrated by the studies carried out at Mach 3.5 in the NASA quiet tunnel [16] on sharp cones with different wave lengths  $L$  and amplitudes  $H$ . The conclusions of this study are that "no lower critical wave size was reached" i.e. "no waves were found which did not affect transition" and that waves have "less effect than trip wire of same height". The ratio  $H/L$  was found to correlate the data i.e. at same  $H/L$ , the same change in transition is observed. Finally an important remark, already reached by Goodrich et al in [17], is made as far as the relevance of transition studies in wind tunnels are concerned by comparing results obtained in the quiet and noisy Mach 3.5 tunnel: "a given wave caused the same percentage change in transition Reynolds numbers in quiet and noisy flows". These particular roughnesses are presently studied in the VKI-H3 wind tunnel at Mach 6 on sharp cone models.

#### ***2.1.2.3 Roughness induced transition in presence of separated flow***

Even though the roughness does not trigger transition, it may have an influence on the re-attaching flow over a deflected surface. This was for instance observed in [18] when small roughness elements were deposited on the blunt leading edge of a flat plate/compression ramp model. The leading edge perturbations were creating striations on the flat plate part but were not triggering the boundary layer to transition. On the contrary, at re-attachment on the ramp, the perturbations were promoting transition of the boundary layer on the whole ramp. The same observation was made on the blunted cone/flare configuration tested also at Mach 6 [19]. With a 3.5 mm radius nose, the whole interaction is laminar for a unit Reynolds number of 8 millions per meter. When four 1 mm spheres (every 90 degrees azimuth) are placed at 20 mm from the stagnation point, it does not trigger transition of the cone but it is sufficient to trigger transition at re-attachment on the flare as shown by the sublimation test given in figure 2.1.2.7.

This aspect of roughness induced transition is coupled with the amplification mechanisms which take place over the separated region resulting from the shock wave boundary layer interaction.

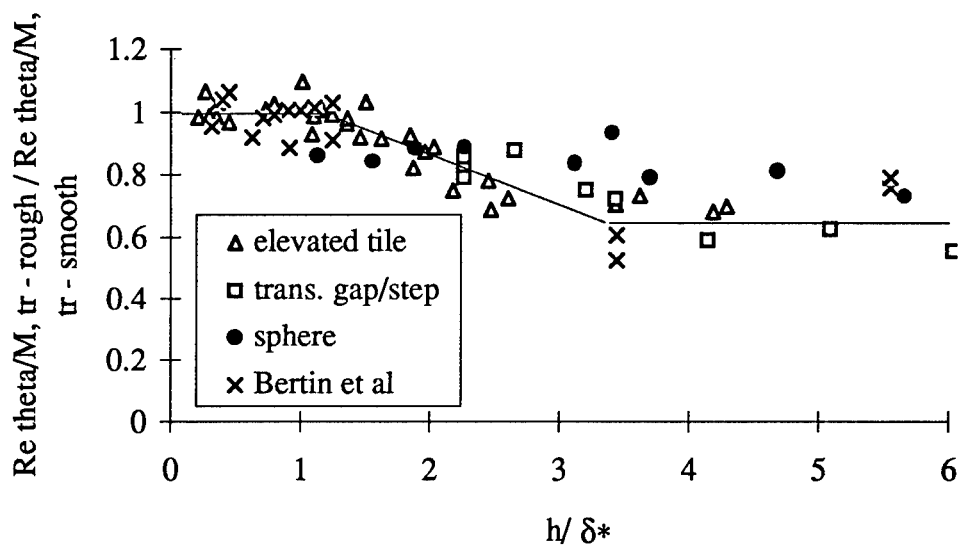


Fig. 2.1.2.1: Correlation between the ratio of Reynolds numbers based on the boundary layer momentum thickness and the normalized perturbation height

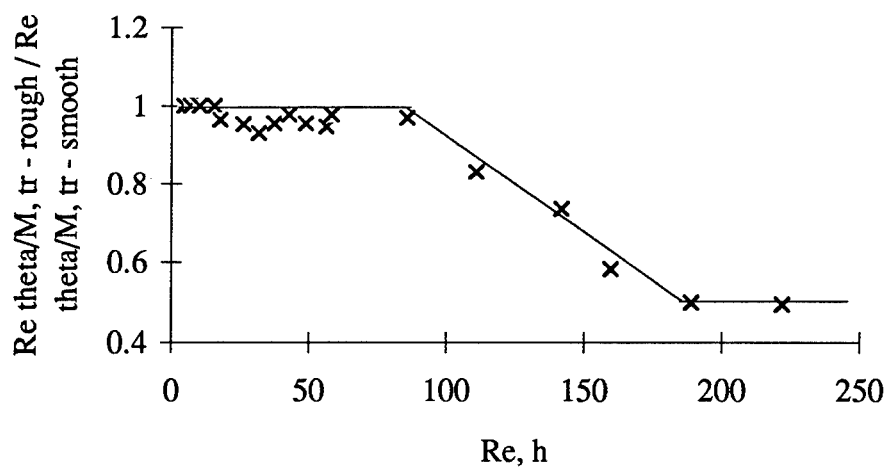


Fig. 2.1.2.2 : Transition data from the Orbiter by Bertin et al [12]

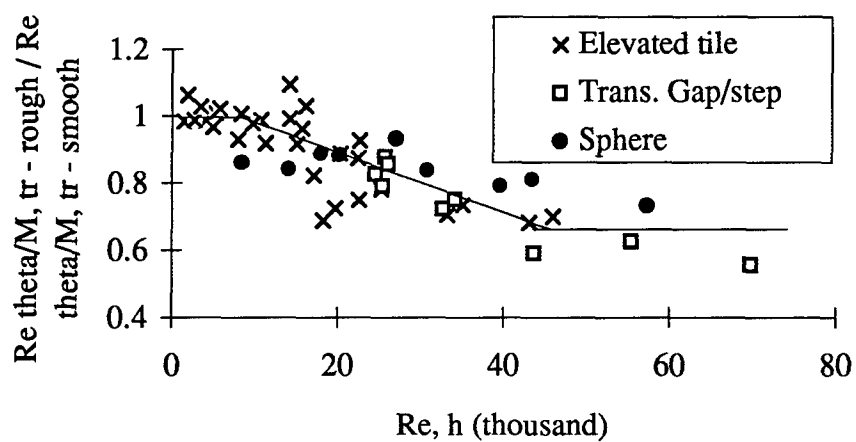


Fig. 2.1.2.3 : Transition data from VKI for the different perturbations studied.

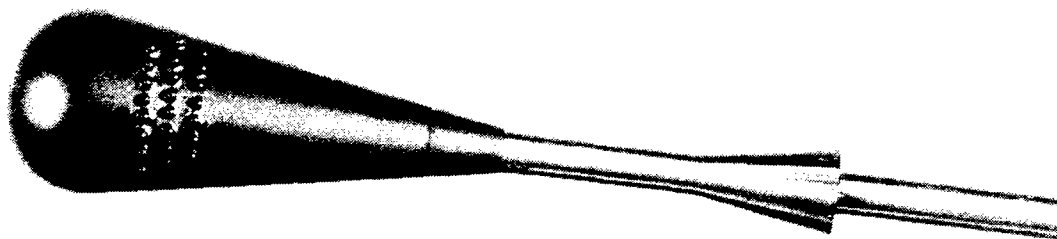


Fig. 2.1.2.5: Modified ARD model with spherical roughness elements



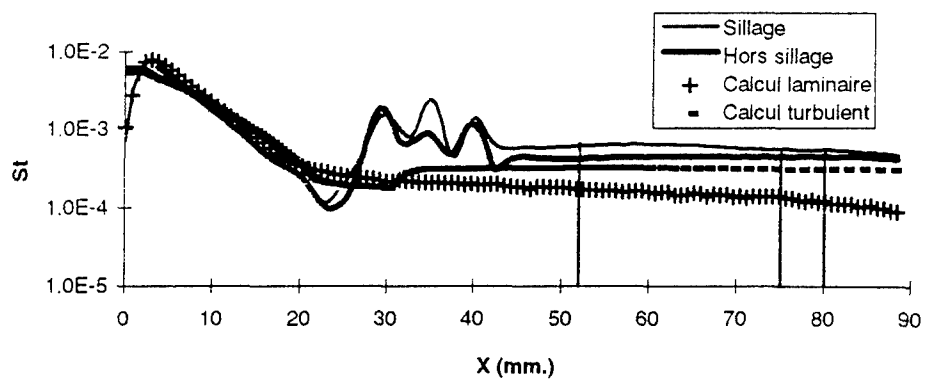


Fig. 2.1.2.6: Experimental and numerical Stanton number distributions on the modified ARD model with spherical roughness elements in the VKI-H3 high Reynolds condition

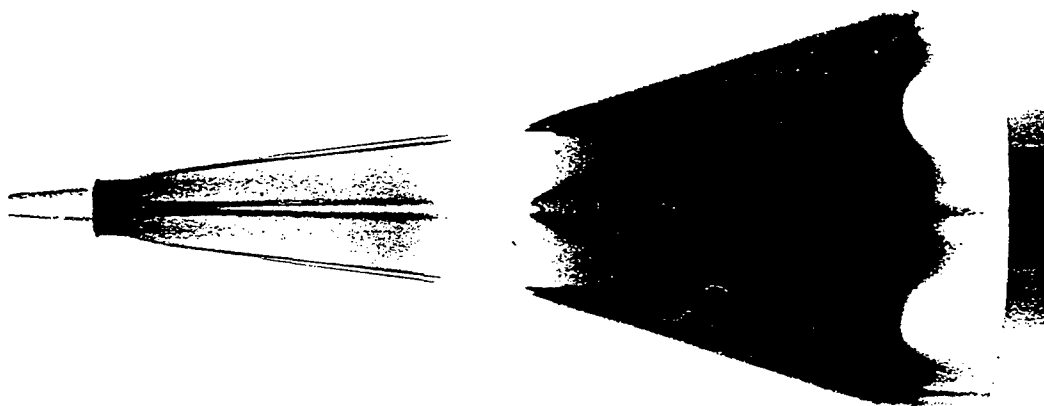


Fig. 2.1.2.7: Sublimation test on a blunted cone/flare model at Mach 6 with 4 spheres placed at 20 mm from the stagnation point.

## 2.2 Shock wave - boundary layer interaction

The phenomenon of shock wave - boundary layer interaction has been extensively studied at the VKI in the supersonic and hypersonic regimes. In the following sections, the experimental and numerical investigations carried out on 2D and axisymmetric configurations are presented.

### 2.2.1 Flat plate-ramp

(G.A. Simeonides, J.Ph. Vermeulen)

#### 2.2.1.1 Introduction

Shock wave boundary layer interaction phenomena have been investigated at the VKI since the late 1960's, starting with experimental studies involving two-dimensional flat plate ramp configurations [20,21]. This simple configuration has been further investigated in recent years in the two hypersonic wind tunnels of the Institute, namely the Mach 6 H-3 and the Mach 14 Longshot facilities, and has also served as an initiation test case for the computational (CFD) analysis of shock wave boundary layer interaction phenomena [22,26].

The subsequent discussion on two-dimensional shock wave boundary layer interactions over flat plate ramp configurations focuses on heat transfer distributions and interaction-induced peak heating and, in particular, on the following three major aspects of the work performed at the VKI:

- comparison of measured heat transfer distributions and reference enthalpy predictions
- Goertler instability in the flow reattachment region, striation heating and promotion of laminar-turbulent transition

peak heating correlation and transition criterion for shock wave boundary layer interactions

Details of the associated computational work may be found in [24,26].

#### 2.2.1.2 Comparison of measured heat transfer distributions and reference enthalpy predictions

Heat transfer distributions measured over flat plate ramp configurations in the H-3 and Longshot hypersonic wind tunnels of the VKI have been extensively compared to reference enthalpy predictions. This prediction methodology is based on the extension of incompressible boundary layer results (i.e. Blasius for laminar flow) to the compressible flow regime by means of Eckert's reference enthalpy concept; it is recalled in detail in [22].

Typical comparisons between measurements and reference enthalpy predictions are shown, after [22,23], in Figs. 2.2.1.1 and 2.2.1.2 for Mach 6 and Mach 14

flow conditions, respectively. Very good agreement between measurements and predictions is noted in all cases over the attached flow regions both upstream and downstream of the interaction, particularly when the actual pressure distribution is accounted for rather than assuming the inviscid pressure field for the predictions. Moreover, a shift of the virtual origin of the reattaching boundary layer to the near vicinity of reattachment has been found necessary, in order to account for the thinning of the boundary layer through the interaction<sup>1</sup>. It is noted that, in the cases of Figs. 2.2.1.1 and 2.2.1.2, the measured data upstream of the interaction agree with laminar reference enthalpy predictions, but downstream of the interaction they agree with turbulent flow predictions. This is already an indication of laminar-turbulent transition promotion by shock wave boundary layer interactions and, noting, the decrease in heat transfer over the separated flow region (which is characteristic for laminar flow and not for turbulent flow), it is an indication of transition promotion in the close vicinity of flow reattachment. Supporting macroscopic indications of transition promotion in the close vicinity of reattachment have been provided through the examination of schlieren photographs and unfiltered high frequency response surface temperature time traces obtained in Longshot short duration experiments [22,28].

Lastly, it is noted that a fully laminar shock wave boundary layer interaction over a (nominally) sharp flat plate ramp configuration has been achieved only at the minimum Reynolds number attained in the Longshot facility at the time [22]. The result is shown in Fig. 2.2.1.3 where it is seen that, although the flow reattaches as fully laminar, transition does eventually occur in the attached flow region over the ramp only a modest distance downstream of reattachment.

#### 2.2.1.3 Flow instability in reattachment regions, striation heating and promotion of laminar-turbulent transition

A number of investigations, including the work of Ginoux [20] at VKI, have revealed the formation of short wavelength streaky structures in reattaching flows under supersonic and hypersonic flow conditions. This so-called striation phenomenon is attributed to the formation of Goertler-type vortices supported by the concave flow curvature in the reattachment region; it is a form of instability and is closely related to the

<sup>1</sup> More recently, this shift in the virtual origin of the reattaching boundary layer has been approximated in a more formalistic manner by imposing a balance of the boundary layer momentum deficit at conditions upstream and downstream of the interaction [8].

occurrence / promotion of laminar-turbulent transition in the close vicinity of reattachment.

Because of the significant spanwise (short wavelength) heat transfer variations that may result from the formation of striations over, say, deflected control surfaces, the phenomenon has received further attention at the VKI under the framework of the Hermes spaceplane program [22,23,25,26]. In particular, high resolution heat transfer measurements over flat plate ramp configurations in the Mach 6 H-3 wind tunnel by means of infrared thermography have revealed some of the characteristics of this instability.

At low Reynolds numbers and with low-strength interactions (i.e. small ramp deflection angles), an irregular striation pattern is first observed over a significant distance downstream of reattachment on the deflected ramp. This irregular striation pattern and the resulting spanwise heat transfer distribution has been qualitatively correlated to the distribution of initial disturbances (in this case, irregularities along the nominally sharp model leading edge), as illustrated in Fig. 2.2.1.4. With increasing Reynolds number and/or interaction strength, the striation pattern becomes more regular (i.e. the signature of the initial disturbances is progressively overridden by the strength of destabilizing factors), periodic striations appear with decreasing streamwise extent and, eventually, they disappear again as fully turbulent flow is attained over the entire ramp shortly downstream of reattachment.

To quantify the influence of this localized three-dimensional phenomenon on the heat transfer evolution over deflected control surface configurations, bands between the minimum and maximum streamwise heat transfer distributions measured over the model span are plotted in Fig. 2.2.1.5 for a given nominally sharp (but irregular) model leading edge and various Reynolds number and ramp deflection angles. Evidently, significant spanwise heat transfer variations commence only in the close vicinity of reattachment, which is the most unstable region of the flow due to the adverse pressure gradient and flow concavity. Their streamwise extent is decreasing with increasing Reynolds number and/or interaction strength and, at sufficiently high values of one or both, they disappear altogether. The amplitude of these spanwise heat transfer variations may be in excess of  $\pm 50\%$  but is always closely bounded on the upper limit by the local turbulent heating level; this amplitude reduces to zero as the spanwise mean heat transfer rises to the local turbulent level and fully turbulent flow is attained over the whole ramp.

In effect, flow reattachment regions are the most unstable regions in this type of flow situation. At Reynolds numbers which are significantly lower than the values necessary to promote laminar-turbulent

transition, initial disturbances may be amplified through the destabilizing mechanisms of adverse pressure gradient and flow concavity that characterize reattaching flows. Initially, the instability takes the form of Goertler-type vortices and with increasing disturbance environment and destabilizing factors eventually leads to a very efficient transition to turbulence restricted in the close vicinity of reattachment.

#### ***2.2.1.4 Peak heating correlation and transition criterion for shock wave boundary layer interactions***

Having noted the success of the reference enthalpy method, discussed in section 2.2.1.1, in the prediction of heat transfer distributions over attached flow regions, the method has been employed at the VKI [22,23] to improve previous correlations for the peak heating downstream of shock wave boundary layer interactions that were based solely on the pressure interaction concept. Of particular importance was the determination of the virtual origin and effective growth length of the reattaching boundary layer: in the earlier versions of the peak heating correlation of [22,23], the virtual origin was taken in the close vicinity of reattachment; more recently, the momentum deficit balance approach was adopted to better formalize the determination of this parameter [27].

Without entering into the details of the proposed peak heating correlation, which may be found in [22,23,25-27], a large number of data (in excess of 200 data points) have been correlated covering a Mach number range between 5 and 19, a Reynolds number range of five orders of magnitude and, more recently, including axisymmetric configurations in the high enthalpy regime. The correlation, using laminar reference values at freestream conditions as normalizing parameters is shown in Fig. 2.2.1.6. The data corresponding to fully laminar interactions (laminar peak heating) exhibit a constant value of the ordinate equal to unity (within the  $\pm 20\%$  scatter), independent of Reynolds number. On the contrary, turbulent peak heating data (normalized by laminar reference values) exhibit a well defined Reynolds number dependence.

In addition to the success of the proposed correlation, providing peak heating estimates within 20%, the crossover between the laminar and the turbulent peak heating correlation curves, occurring at a Reynolds number (based on Eckert's reference enthalpy conditions upstream of the interaction) of approximately 6000, gives a minimum critical Reynolds number criterion at which a shock wave boundary layer interaction may promote laminar-turbulent transition provided, of course, that the

combination of initial disturbances and interaction strength is adequate. Notably, In quiet flow conditions, fully laminar interactions may persist up to reference Reynolds numbers of the order of 100,000. In general, however, these critical Reynolds are significantly lower than those necessary to promote laminar-turbulent transition in the absence of an interaction.

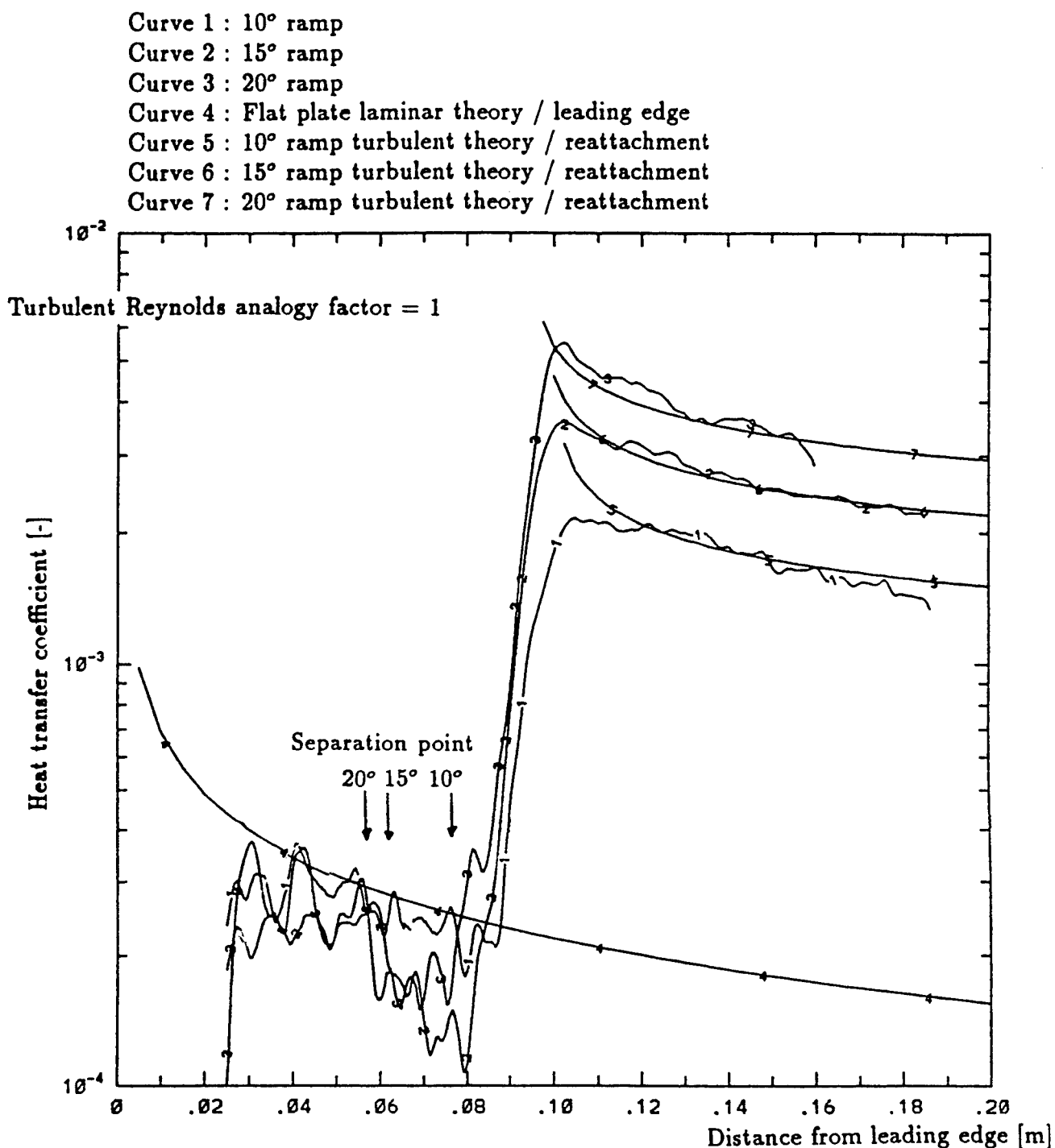


Fig. 2.2.1.1: Heat transfer distribution on flap-plate compression ramps in the VKI-H3 Mach 6 wind tunnel. Comparison with the reference enthalpy method predictions

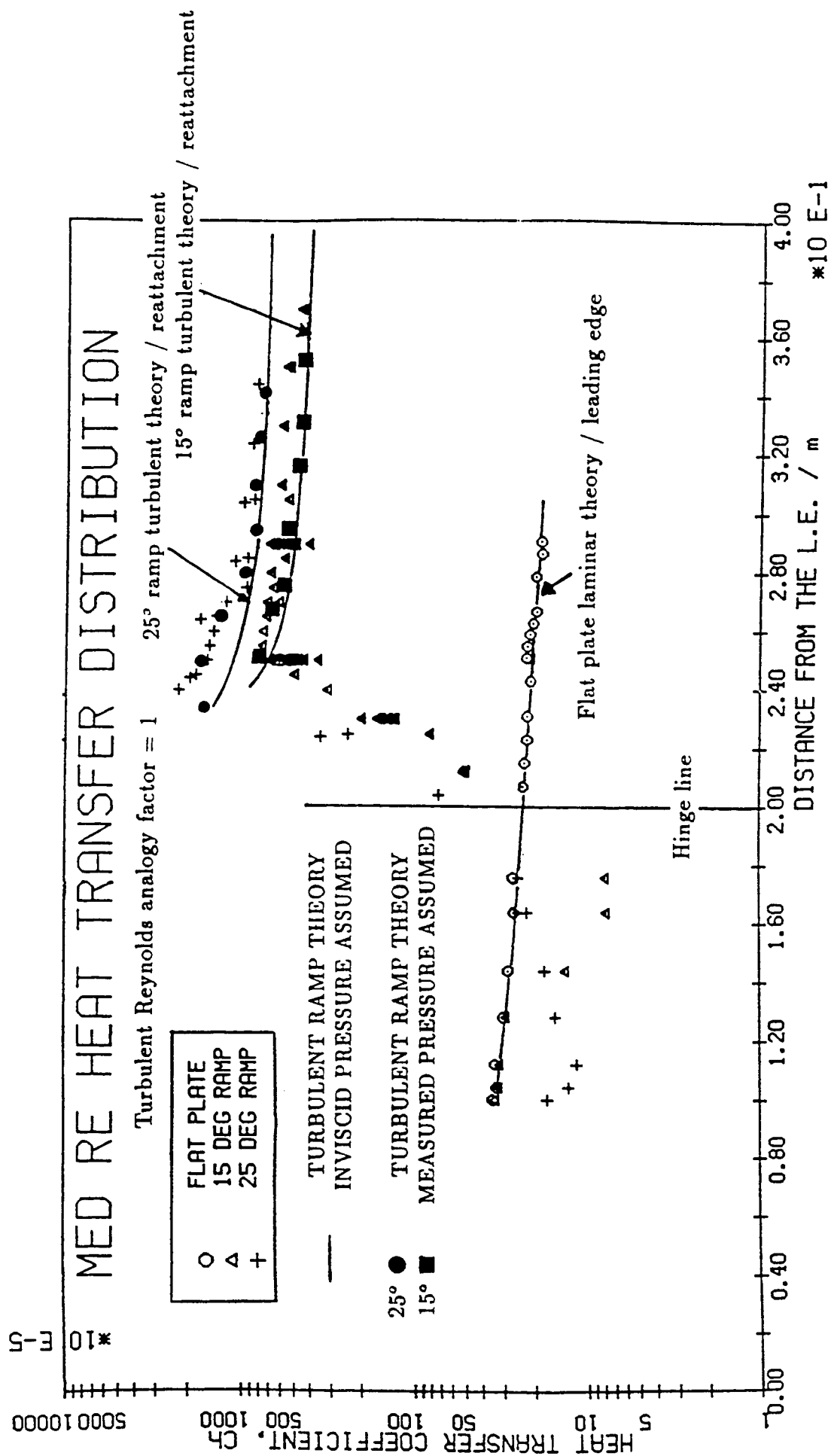


Fig. 2.2.1.2: Heat transfer distribution on flap-plate compression ramps in the VKI-Longshot Mach 14.2 wind tunnel. Comparison with the reference enthalpy method predictions

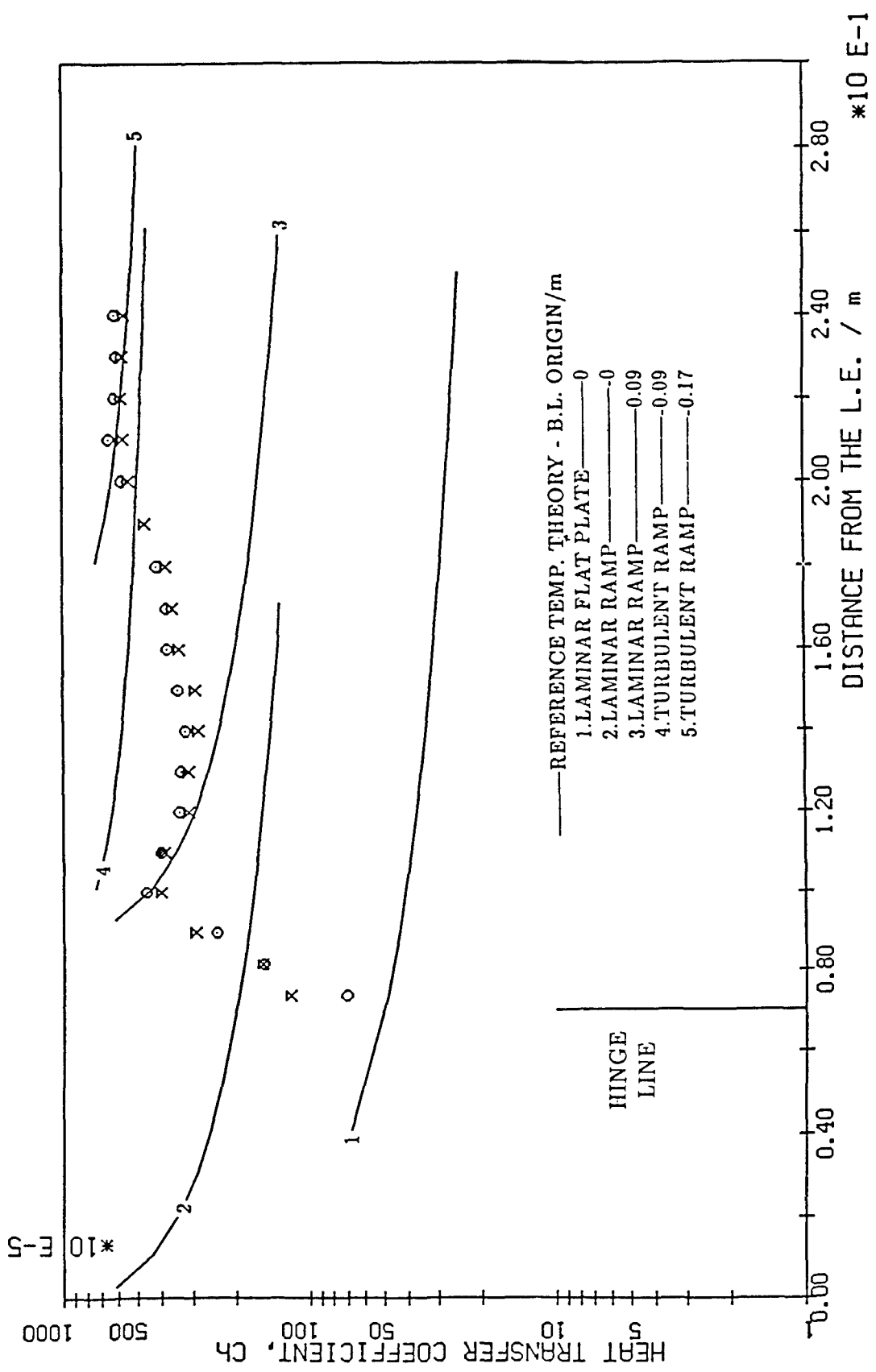


Fig. 2.2.1.3: Heat transfer distribution on flap-plate compression ramps in the VKI-Longshot Mach 14.2 wind tunnel. Comparison with the reference enthalpy method predictions in case of laminar interaction

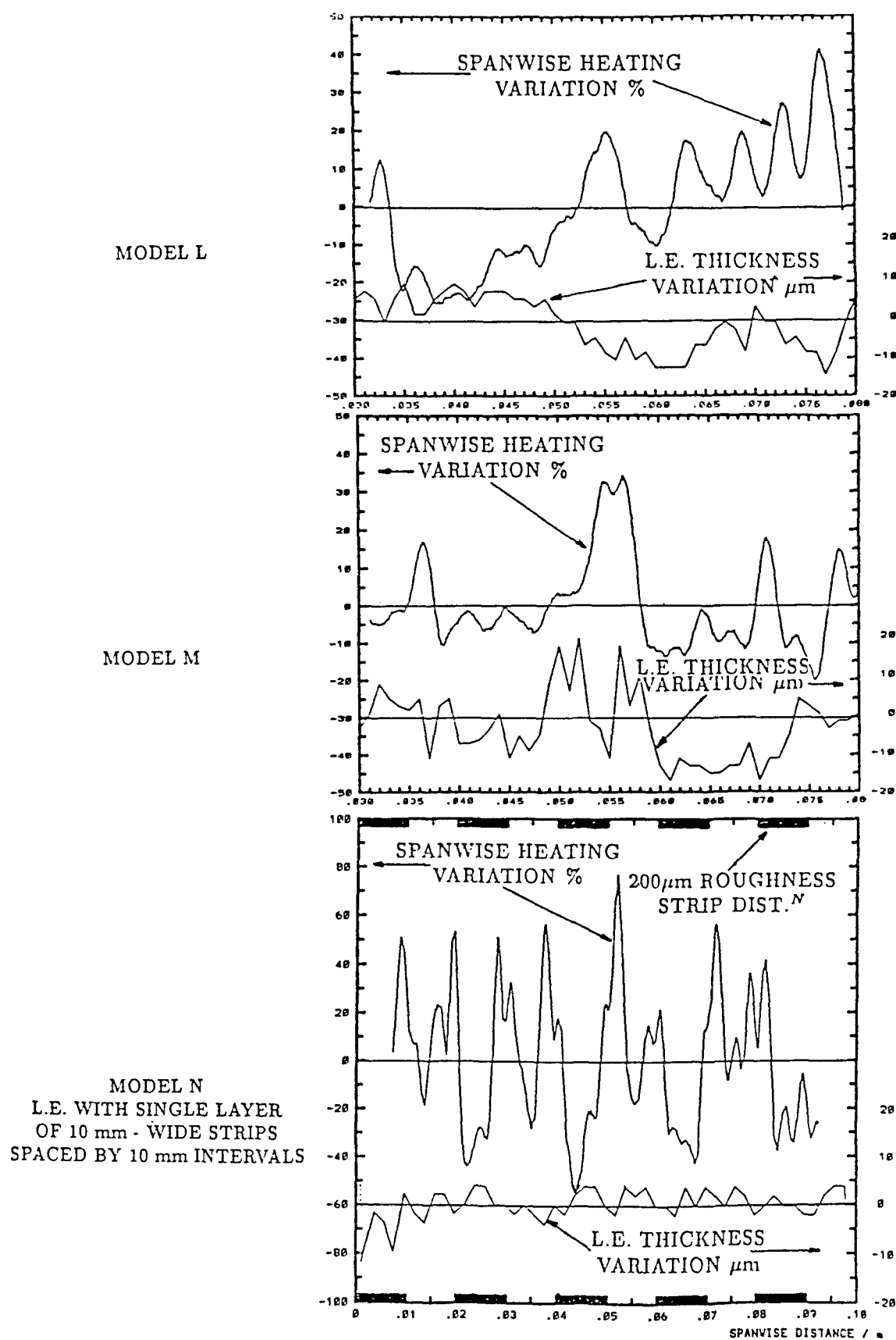


Fig. 2.2.1.4: Spanwise heat transfer distribution on flap-plate compression ramps in the VKI-H3 Mach 6 wind tunnel. Effect of the model leading edge disturbances



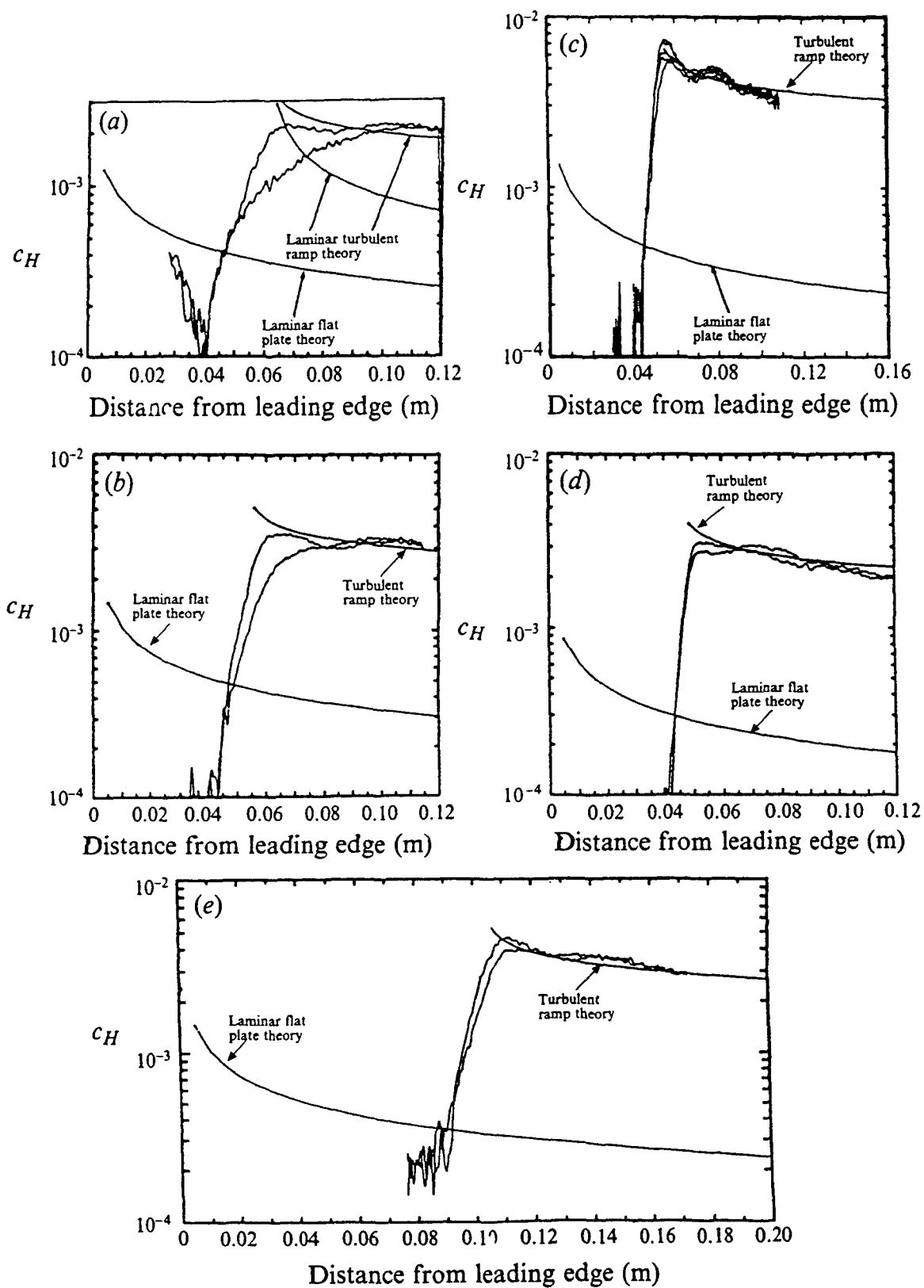


Fig. 2.2.1.5: Bands of maximum - minimum streamwise heat transfer distribution on flap-plate compression ramps in the VKI-H3 Mach 6 wind tunnel.

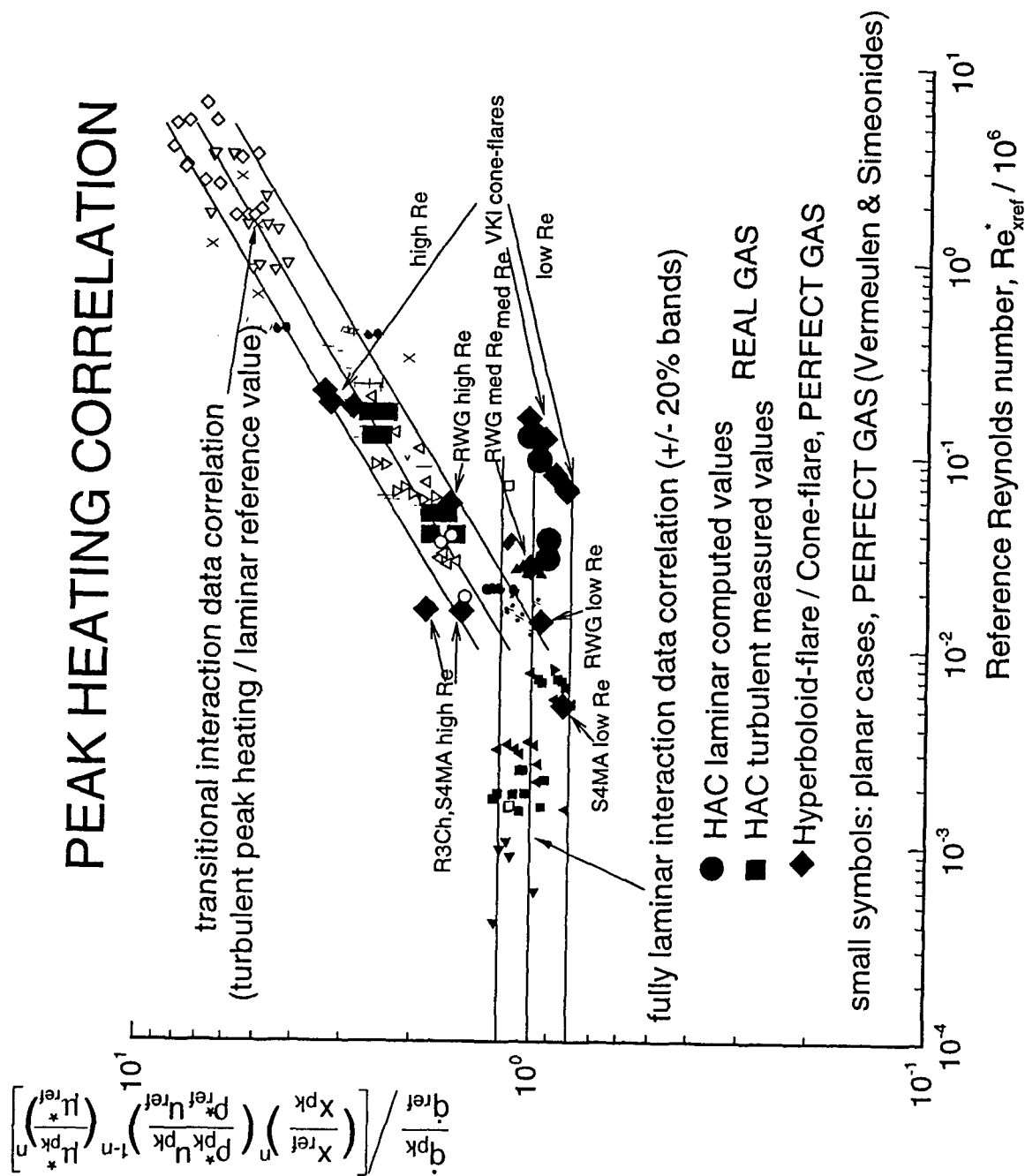


Fig. 2.2.1.6: Peak heating correlation for shock wave boundary layer interactions

## 2.2.2 Cone-flare

(W. Dieudonné, J.-M. Charbonnier)

### 2.2.2.1 Introduction

In order to eliminate the uncertainties associated with the assumption of two dimensional flows when investigating flat plate - ramp models, it was decided to use axisymmetric configurations. The cone-flare model has the advantage with respect to the hollow-cylinder-flare to minimize the blockage in the wind tunnel. When compared to the hyperboloid-flare model, it does not exhibit this expansion in the region of the boundary layer separation and therefore it provides an intermediate level in the process of assessment of the physical modeling of shock wave - boundary layer interaction phenomenon.

### 2.2.2.2 Assessment of the experimental configuration

A set of experiments were carried out in the VKI-H3 Mach 6 wind tunnel on a  $7.5^\circ$  cone with a  $10^\circ$  flare for sharp and spherically blunted noses [19]. Figure 2.2.2.1 shows the Stanton number measured on the model with the sharp nose for the three standard unit Reynolds number of the tunnel (8, 15 and  $20 \cdot 10^6$  /m). As indicated by the Stanton number levels, the re-attachment on the flare is laminar at low Reynolds number, transitional at medium and presumably turbulent for the high Reynolds number case.

In a first step, in order to remove the transition modeling uncertainties from the comparison between experiments and computations, a 3.5 mm diameter spherically blunted nose model was tested under the same flow conditions (Fig. 2.2.2.2). In this case, although for the high Reynolds number case, the re-attachment remains turbulent, for the two other flow conditions, a fully laminar interaction is observed.

This last geometry was kept as a standard model and tested in detail for the low Reynolds number flow condition [29]. Pressure coefficients are measured by means of electronic pressure scanners and heat transfer coefficients are obtained using the recently acquired new infrared scanner. The experimental study has shown that the flow over the model is very sensitive to the angle of attack. For instance, an incidence of  $0.25^\circ$  is sufficient to move significantly the separation location and even to trigger the boundary layer transition on the flare as demonstrated in figure 2.2.2.3. It is therefore essential to assess the axisymmetry of the flow over the model and the level of repeatability of the experiments before drawing any conclusions.

### 2.2.2.3 Re-building of the experiment

In parallel to the experimental work, a numerical study is carried out using the VKI-MB Navier Stokes code [7,30]. Attention is focused on grid convergence and it appears that the separation area where the experimental data differ from the numerical results, is not totally grid converged. For instance, the  $C_p$  distribution in figure 2.2.2.4 shows that the separation location is not well predicted which induces differences in the re-attachment region. However, the grid convergence can not explain the differences in Stanton number observed on the front part of the model in figure 2.2.2.5. This offset is likely to be due to the input conditions (or boundary conditions) used in the computations which are not properly representing the actual flow in the free jet of the wind tunnel. This assumption is supported by the fact that the flow over the model is very sensitive to the angle of attack. In order to confirm this explanation, the flow over the model is presently being computed using as input conditions the flow computed in the H3 nozzle as shown in figure 2.2.2.6

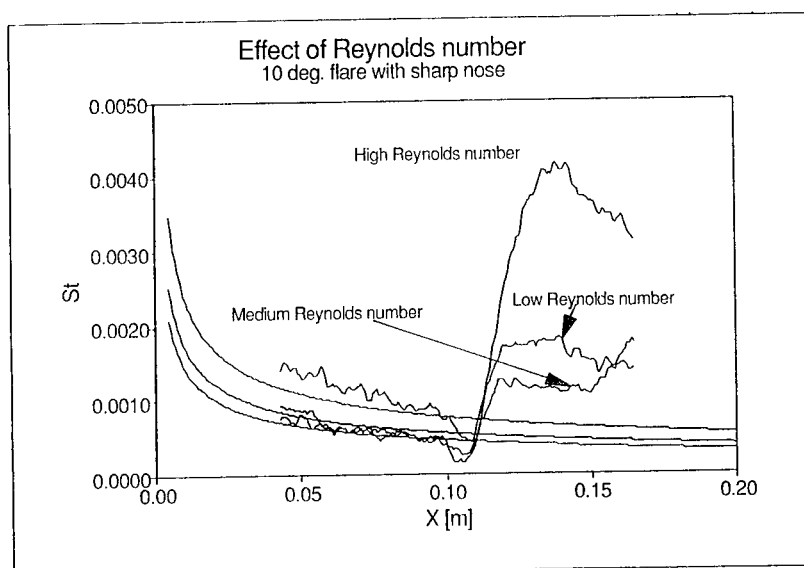


Fig. 2.2.2.1: Reynolds number effect on a cone-flare model with sharp nose

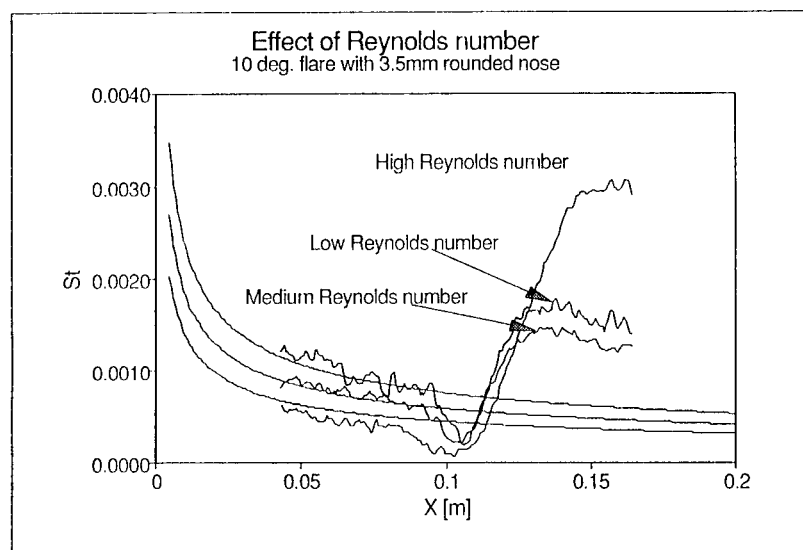


Fig. 2.2.2.2: Reynolds number effect on a cone-flare model with a 3.5 mm spherically blunted nose

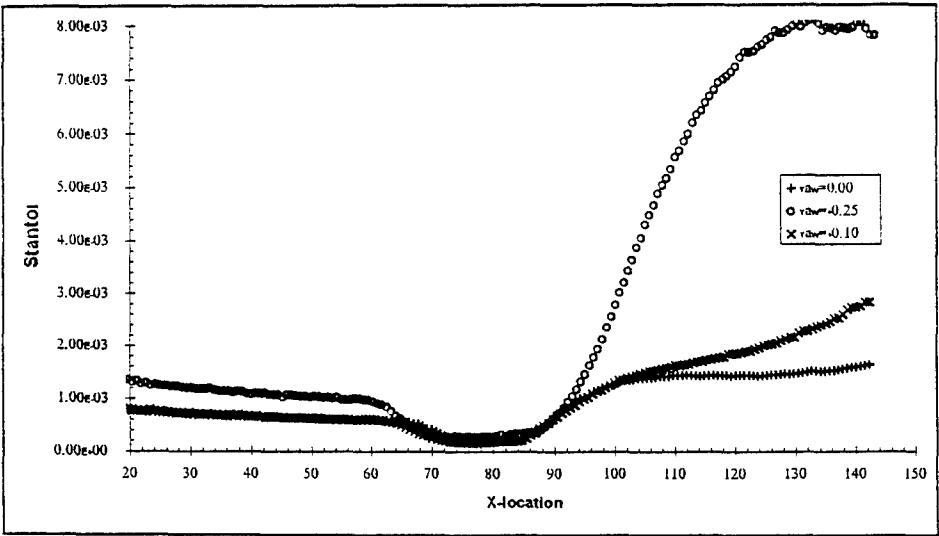


Fig. 2.2.2.3: Angle of attack effect on a cone-flare model with a 3.5 mm spherically blunted nose

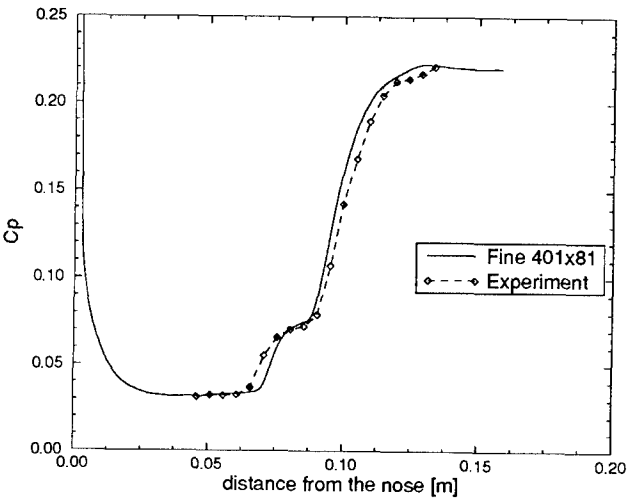


Fig. 2.2.2.4: Experimental and computed pressure coefficients on a cone-flare model with 3.5 mm spherically blunted nose in the VKI-H3 tunnel at low Reynolds number

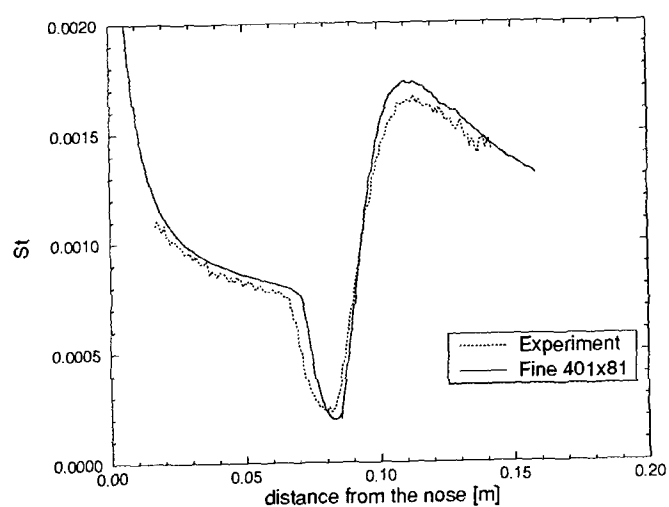


Fig. 2.2.2.5: Experimental and computed heat transfer coefficients on a cone-flare model with 3.5 mm spherically blunted nose in the VKI-H3 tunnel at low Reynolds number

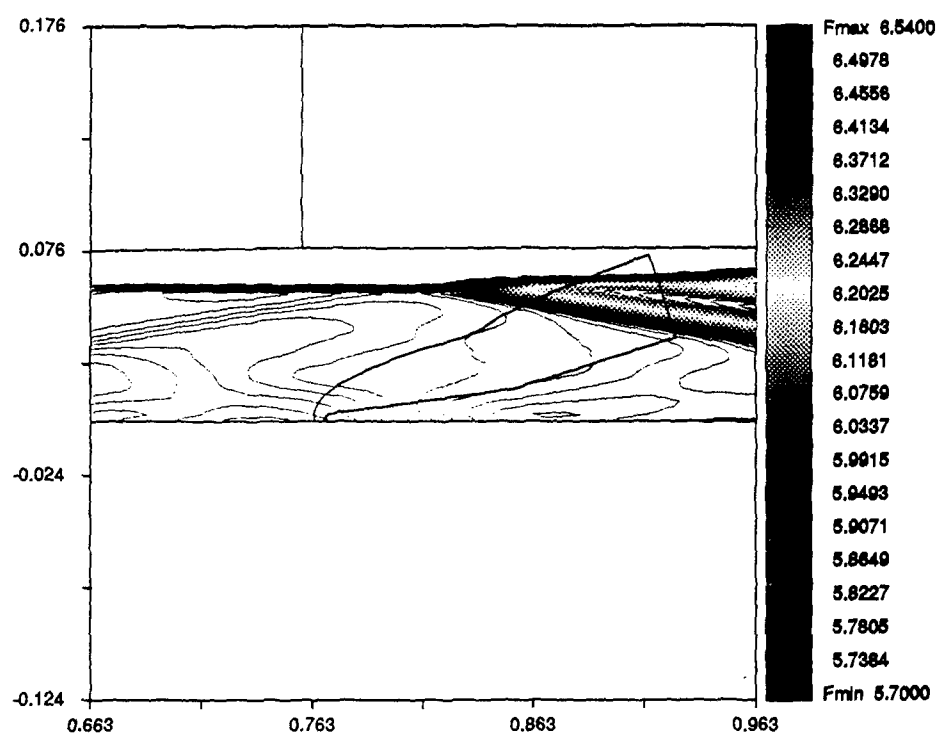


Fig. 2.2.2.6: Iso-Mach lines of the flow in the H3 tunnel at the location of the cone-flare model

### 2.2.3 Hyperboloid-flare

(W. Dieudonné, J.-M. Charbonnier, H. Deconinck, S. Paris)

#### 2.2.3.1 Introduction

In the frame work of the ESA/Manned Space Transportation Program the flow over an hyperboloid flare geometry tested in the DLR-RWG wind tunnel at Mach 6 was computed as contribution to the Workshops organized at ESA/ESTEC in 1994 [31] and 1996 [30]. The code used is the VKI-MB which is a multidomain finite volume cell centered code based on an upwind numerical scheme and with a spatial discretization based on quadrilaterals [7,32]. The one equation Spalart- Allmaras turbulent model has been implemented and validated for the 2D and axisymmetric versions of the code [8].

#### 2.2.3.2 The ESA/ESTEC Workshop testcase in DLR-RWG conditions

Because of the flare, a complex flow structure exists over the body, such as a shock wave - boundary layer interaction and recirculatory flow. For the last workshop in March 96, two configurations are considered: the Low Reynolds Number (LRC) case ( $3.5 \cdot 10^6$  /m) and the High Reynolds Number (HRC) case ( $14.8 \cdot 10^6$  /m) [30]. The former is expected to show a fully laminar interaction whereas for the latter boundary layer transition is expected to take place on the flare at re-attachment of the boundary layer. Figure 2.2.3.1 shows the computed iso-Mach lines on the hyperboloid/flare geometry for the LRC case.

The influence of grid refinement in the x and y directions was investigated separately and it is demonstrated that the separation point is sensitive to the grid refinement along the y direction normal to the wall whereas the capture of the re-attachment very much depends on the grid refinement in the x direction along the wall. Comparison with experimental data confirms that the flow is fully laminar for this case as indicated in figure 2.2.3.2 by the Stanton number distribution.

For the HRC case, the laminar computation clearly shows that the boundary layer at re-attachment on the flare is not laminar. The effect of the location of transition with respect to the separation and reattachment point is also investigated using the Spalart Allmaras turbulence model [8]. In figure 2.2.3.3, the best agreement with the experimental data is obtained when the boundary layer transition is fixed at the re-attachment point on the flare which seems to indicate that transition takes place in the shear layer over the separated zone.

#### 2.2.3.3 The hyperboloid-flare in the VKI-Longshot tunnel

The standard hyperboloid/flare model is also tested and computed for the flow condition LSCN1 of the VKI-Longshot wind tunnel [33]. A Schlieren photograph of the flow over the model in the Longshot tunnel is reproduced in figure 2.2.3.4 where can the location of the boundary layer separation with respect to the region of expansion due to the model wall curvature can be seen.

The measurements and the associated computations for the re-building of the flow over the model are under process for the four new operating conditions of the Longshot with N<sub>2</sub> and CO<sub>2</sub> used as test gases. So far the first measurements carried out in the Longshot are aimed at qualifying the tests in terms of reproducibility and positioning of the model in the test section. Figures 2.2.3.5 and 2.2.3.6 quantify the influence of 0.5 degrees angle of attack on the pressure and heat transfer distributions for the condition LSCN1.

It is observed that both the separation point location and the re-attachment region are sensitive to the incidence. At re-attachment the model incidence modifies significantly the Stanton number distribution on the flare after re-attachment when compared to the tests performed without incidence.

This study is in progress with the completion of the tests for the other flow conditions and the analysis of the results with respect to the influence of the rarefaction parameter and of the specific heat ratio of the Longshot operating conditions.

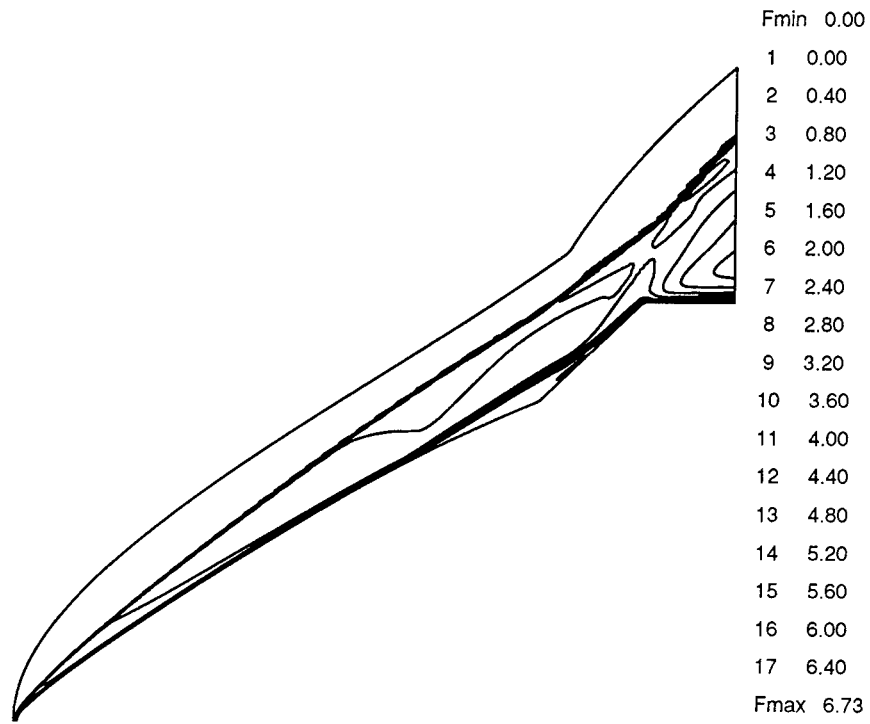


Fig. 2.2.3.1: Iso-Mach lines for the LRC conditions

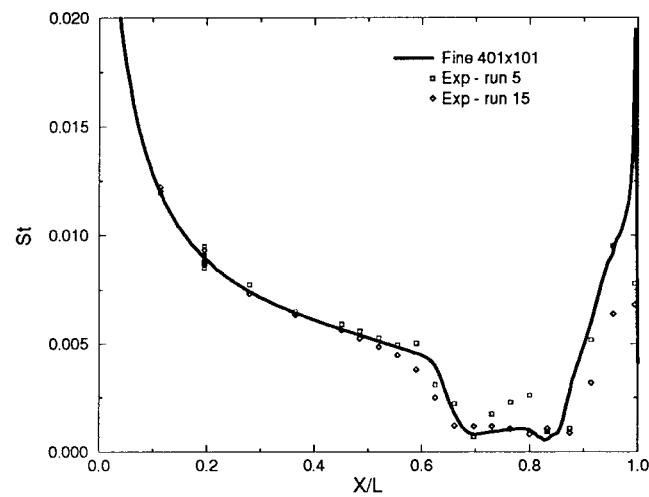


Fig. 2.2.3.2: Experimental and computed Stanton number for the LRC



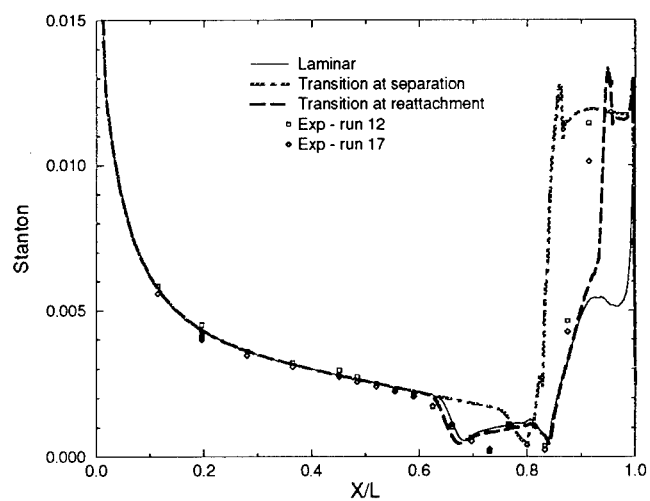


Fig. 2.2.3.3: Experimental and computed Stanton number for the HRC

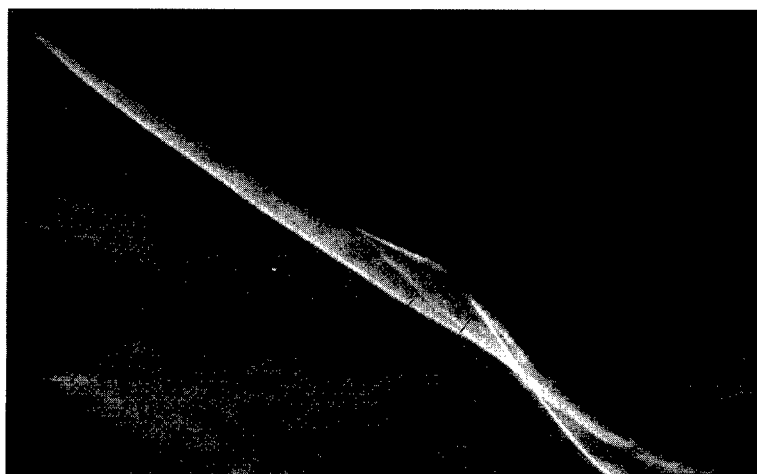


Fig. 2.2.3.4: Schlieren photograph of the hyperboloid/flare model in the Longshot for the flow condition LSCN1

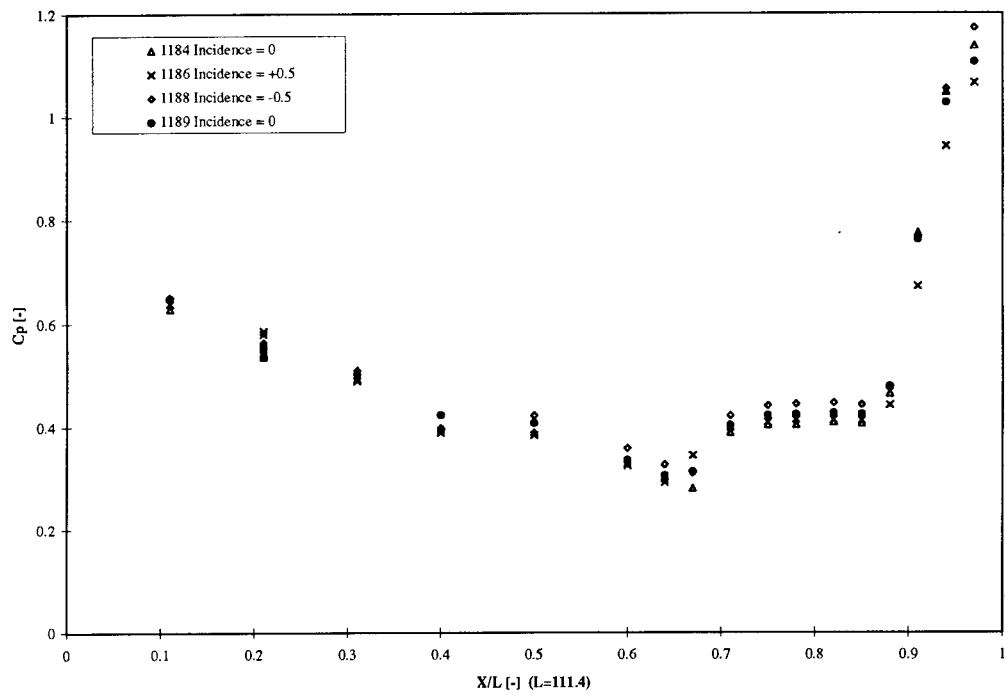


Fig. 2.2.3.5: Effect of 0.5 degrees incidence on  $C_p$  distribution on the hyperboloid/flare for condition LSCN1

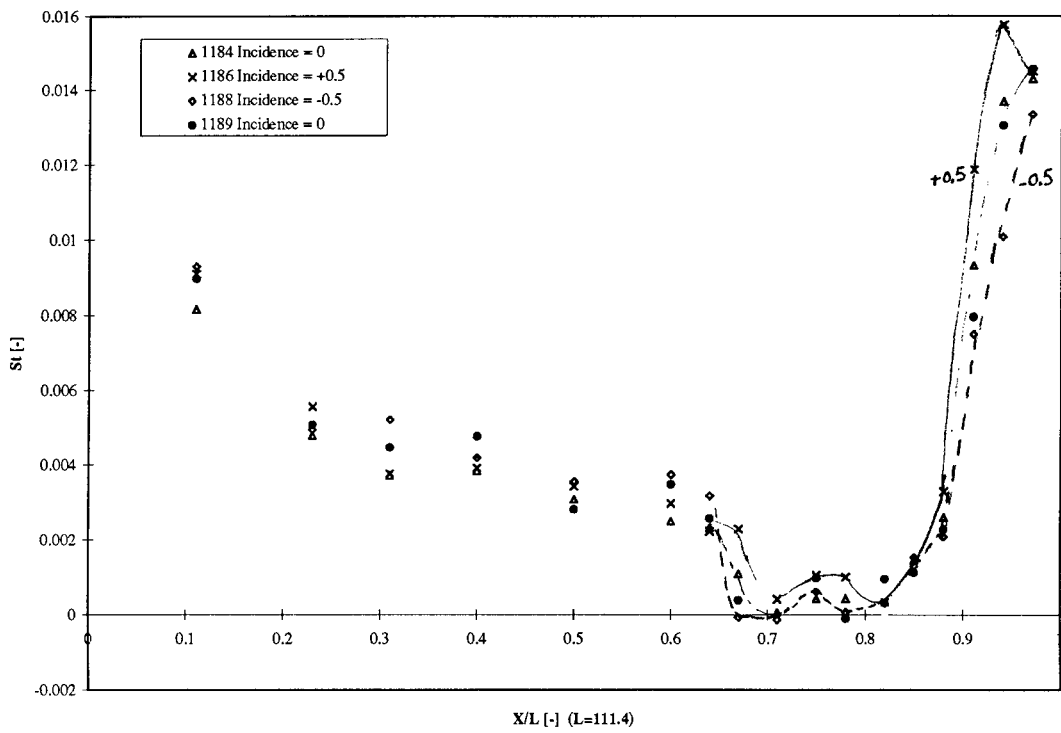


Fig. 2.2.3.6: Effect of 0.5 degrees incidence on  $St$  number distribution on the hyperboloid/flare for condition LSCN1

## 2.3 Fin induced vortex boundary layer interactions (S. Zemsch, G. Degrez)

### 2.3.1 Introduction

This study addresses the vortical flow downstream of blunt fins under large angles of attack and its interference with a laminar flat plate boundary layer. The used geometry models the junction between the wing and the fuselage of a hypersonic spacecraft. Fig. 2.3.1 shows a schematic of this flow.

A leading edge vortex forms leeward of the wing whose position and extension strongly depends on the flow- and geometrical parameters. For a certain combination of these parameters, streamwise striations are observed downstream of a conical flow attachment line on the flat plate as shown on the sublimation picture of Fig. 2.3.2 that shows the top view of the flat plate/wing model.

These striations are vortical structures, embedded in the flat plate boundary layer, that influence the surface mass- and heat transfer. Such striations were observed on the side fuselage of a space shuttle model under similar conditions[34]. The exact knowledge of the local value of the heat transfer is important for the efficient design of a thermal protection system.

The objective of this joint experimental and numerical study is to determine the conditions for which striations exist, the correlation of their existence to the topology of the flow, the evaluation of local peak heating and the influence of striations on surface heating.

A schematic of the wind tunnel model is shown in Fig. 2.3.3. It consisted of a conical blunt wing with leading edge sweepback angle,  $\lambda = 75^\circ$ , mounted under  $\alpha = 40^\circ$  incidence at different distances  $x_{LE} = 0$  and  $40 \text{ mm}$  from the flat plate sharp leading edge.

Due to experimental difficulties in accessing in detail the three-dimensional vortical hypersonic flow field, a joint numerical and experimental program was set up where experiments were used to validate computations. Initial calculations demonstrated a strong dependence of the numerical solution on the used mesh requiring very fine mesh sizes to obtain a grid-independent solution. Hence, computations in three dimensions were not feasible due to the high requirements in computational power and memory. Since surface flow visualization indicated some conical flow symmetry (see Fig. 2.3.2), a conical Navier-Stokes solver was selected for the flow analysis. The tests were conducted for the freestream Mach numbers 2 and 6 and Reynolds numbers in the range of 0.1 to 2.1 million.

### 2.3.2 Results

The reliability of the numerical results is demonstrated by a detailed validation with experiments: Consequently, flow field data are compared with LDV measurements taken on traverses through the primary vortex at several downstream locations at a freestream Mach number of 2. Furthermore, surface pressure- and heat transfer data were acquired downstream of the wing on the flat plate for a Mach 6 flow. All these data were compared to the computed values. Surface flow visualizations supplemented the validation.

Initial computations of the complete geometry including the compression side flow demonstrated that there is basically no influence of the compression side flow on the expansion side interaction[35]. In the following, only the expansion side was numerically modeled which allowed for important savings in computational time and memory.

#### 2.3.2.1 Validation of flow field - Mach 2

Single component LDV measurements of the streamwise velocity component,  $v_x$ , at different streamwise locations on the same conical ray were compared to computed flow and particle velocities. Fig. 2.3.4 shows such data for the two streamwise positions A and C (see Fig. 2.3.3). General features of such a flow field traverse are an indication of the position of the bow shock, here at about of  $y_c = 0.8$ , causing a strong deceleration of the flow and an following acceleration of the flow when the vortex core is approached.

In the following, the different sets of data will be compared: The close overall agreement of the inviscid and viscous computations show the little effect viscosity has on the flow field. Only a small region close to the flat plate surface (small  $y_c$  values) is influenced by the presence of a boundary layer. However, measurements and computations reveal significant differences for the location of the bow shock and velocity values of the accelerated flow indicating velocity lag of the particles. Consequently, the dynamics of the particles was computed by means of solving the particle equations of motion for the computed flow field (for more details see ref.[35]). Good agreement was found between numerical and experimental particle velocities, at least for the accelerated flow part. (Large displacements (large  $y_c$ -values) suffered from a critical uncertainty of the position of the probe volume due to a deformation

of the employed traversing bench). Test 14 and 16 (see Fig. 2.3.4) were acquired on the same conical ray and should be identical for a perfectly conical flow. Differences in regions of strong velocity gradients between these two sets of data could very well be reproduced by the numerical particle model identifying them as particle lag.

In conclusion of the Mach 2 flow field survey it can be said that the LDV measurement suffer from particle lag in regions of strong flow gradients. Using the computed velocity distribution and modeling the particle behavior numerically this particle lag can be reproduced. This is a strong indication for the conicity of the flow field.

### 2.3.2.2 Validation of surface flow data - Mach 6

Different surface flow visualization techniques were used for the analysis of the surface flow pattern. Fig. 2.3.2 and Fig. 2.3.5 present a sublimation and oil flow photograph, respectively, which were taken from the flat plate after a test. As seen for both visualization techniques, the expansion side surface pattern is dominated by a conical singular line indicating flow attachment. The striation pattern emanates from this line and convects far down stream.

Surface pressure measurements at the streamwise position C are shown in Fig. 2.3.6 for three experimental Reynolds numbers ( $Re_{low} = 0.31$  million,  $Re_{med} = 0.57$  million,  $Re_{high} = 0.85$  million). Each data point presents an average value computed from 11 individual tests. The uncertainty band therefore includes the measurement uncertainty as well as the test repeatability. Grid-resolved Euler and Navier-Stokes results are also included.

For all Reynolds number cases, the wing lee side pressure distribution is marked by a peak in pressure ( $0.28 < x_c < 0.4$ ), which corresponds to an angle of  $16^\circ < \text{atan}(x_c) < 22^\circ$ . Referring to the visualization pictures (Fig. 2.3.2 and Fig. 2.3.5), this angle correlates well with the location of the attachment line. Low pressure values close to the wing (small  $x_c$ -values) indicate an accelerated flow situated under the primary vortex. For decreasing Reynolds numbers, the point of flow attachment moves away from the wing while the peak value remains little affected.

The Navier-Stokes computation agrees well with the overall pressure distribution and predicted pressure levels. Only a shift in the exact position of the pressure peak indicates the problems of the conical computation to correctly predict the flow, which was demonstrated to be influenced by the Reynolds number.

The same comparison is done for the heat transfer and is shown in Fig. 2.3.7 in the form of the heat transfer coefficient,  $c_h$ , versus the conical coordinate  $x_c$ .

A very good correlation for the measured location of the peaks between the pressure and the heat transfer data is obtained which confirms the existence of the attaching flow. The magnitude of the peak was found to be only little affected by the Reynolds number. As for the pressure data, the effect of the Reynolds number on the position of the attachment line as well as the shift between computational and experimental results is observed. Outboard of the location of flow attachment the effect of striations on the heat transfer coefficient is seen as oscillation of the data around the undisturbed flat plate level.

The observed discrepancy in the position of flow attachment between experimental and numerical data is by far larger than the uncertainty on the measurement. In fact, if we recognize the effect of the Reynolds number on the lee side flow field, it is not surprising that the conical viscous computation shows difficulties in precisely predicting the surface interaction. Numerically predicted peak locations seem to indicate a computational Reynolds number, which is larger than that of the experiment. Indeed, the conical flow assumption predicts a boundary layer which is significantly thinner than the parabolic one for the same flow situation. Thus, the computation was performed for an effective freestream Reynolds number which was too large. This explains the displacement of the computational data in the direction of larger Reynolds numbers. However, for a detailed understanding of the flow structure an absolute quantitative agreement is not required as long as the flow topology is preserved throughout the computations.

### 2.3.2.3 Concluding Remarks - Validation

LDV, pressure and heat transfer data together with surface flow visualizations were compared to conical inviscid and viscous computations. Concerning the validation of the flow field, encountered problems with particle lag could be overcome by numerical modeling of the particle behavior. The position of the primary vortex and the streamwise velocity component were validated. An effect of the freestream Reynolds number on the lee side flow field was discussed for the hypersonic flow. The existence of a flow attachment line was evenly confirmed by visualizations, pressure and heat transfer data. A good agreement in the overall pressure and heat transfer distributions confirm the

conicity of the hypersonic interaction. Consequently, the use of conical viscous computations is justified for the analyses of the blunt wing-induced vortex boundary-layer interaction.

### 2.3.3 Flow field structure

In the following chapter, a description of the supersonic flow field will be given: After passing through the bow shock, the flow expands around the leading edge. There, it separates to form a free shear layer that divides an outer- from an inner-, vortical region (see Fig. 2.3.8a). The expansion terminates by a cross-flow shock, which turns the flow towards the wing surface. Close to the flat plate / wing junction as well as towards the wing leading edge, boundary layer separation is observed. The vortex is seen to scrap along the flat plate surface leading to increased skin friction (see Fig. 2.3.8b). The free shear layer stretches down to the flat plate where it interferes with the boundary layer.

Since free shear layers are known to be susceptible to vortical instabilities (vortex-cell instability[36]), the interaction of the shear layer can introduce vortical structures in the flat plate boundary layer.

Based on these observations a flow model is suggested and displayed in Fig. 2.3.9. It shows a perspective view of the attaching shear layer including the embedded helical substructures. For this presentation the viscous region close to the wing apex is ignored.

The striations develop in the free shear layer from the line of separation at the wing leading edge. High velocities in the outer region and smaller velocities in the inner region cause a co-rotation of these vortical substructures in the same sense as the primary vortex. A line of flow attachment on the flat plate is necessary to allow for further development in the flat plate boundary layer. (For a more detailed description, the reader is referred to ref.[35].)

### 2.3.4 Conclusions

The supersonic/hypersonic flow about a highly swept conical blunt wing/flat plate junction under large angle of attack was investigated experimentally and numerically. The study concentrated on the lee side flow structure and the formation of striations. It could be shown that major parts of the flow field are correctly captured by the inviscid flow analysis. Good agreement with the experimental data in all cases demonstrated that the applied conical flow solver is an appropriate tool for the exact prediction of the flow field topology of conical wing/fuselage junctions.

The critical flow field structure, which leads to the formation of striations, was identified: Wing leading edge separation connected to the formation of a free

shear layer. This shear layer, susceptible to vortical structures, interferes with the boundary layer on the flat plate. Under these conditions, a flow attachment line on the flat plate exists downstream of which periodic striations develop.

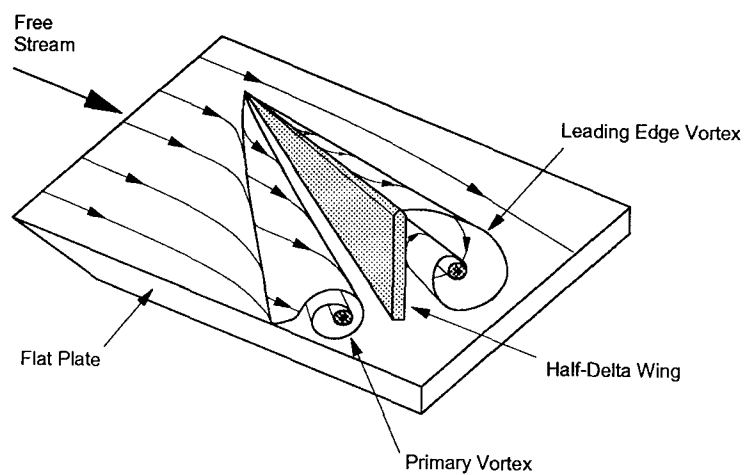


Fig.2.3.1: Schematic of flow interaction.



Fig. 2.3.2: Sublimation visualization, Blunt wing / flat plate interaction,  
 $M_{\infty} = 6$ ,  $\alpha = 40^{\circ}$ ,  $\lambda = 75^{\circ}$

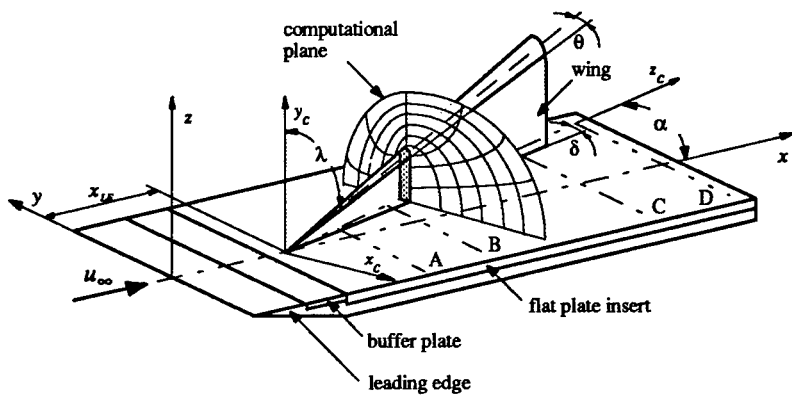


Fig. 2.3.3: Schematic diagram of conical wing/flat plate configuration

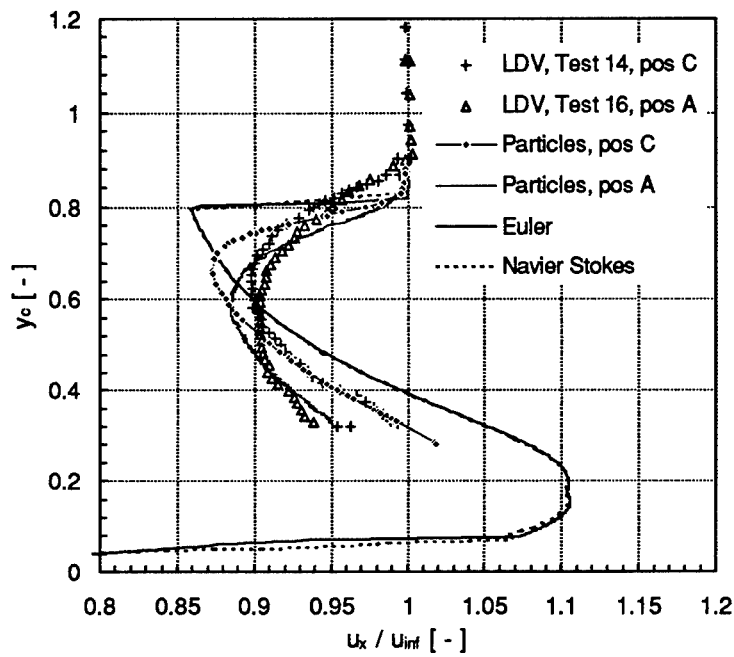


Fig. 2.3.4: Streamwise velocity component on conical ray  $x_c = 0.25$ .

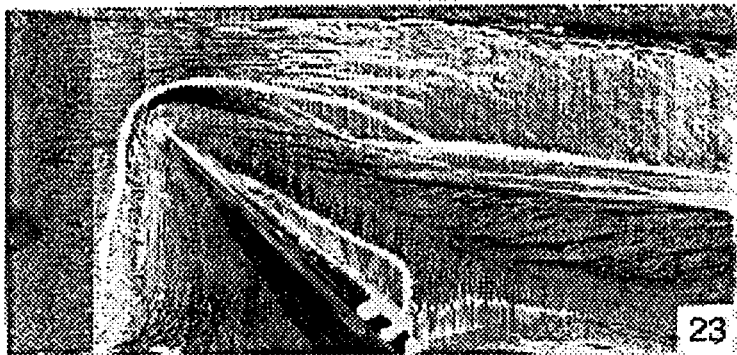


Fig. 2.3.5: Flat plate surface oil flow visualization,  
 $M_\infty = 6$ ,  $\alpha = 40^\circ$ ,  $\lambda = 75^\circ$ .

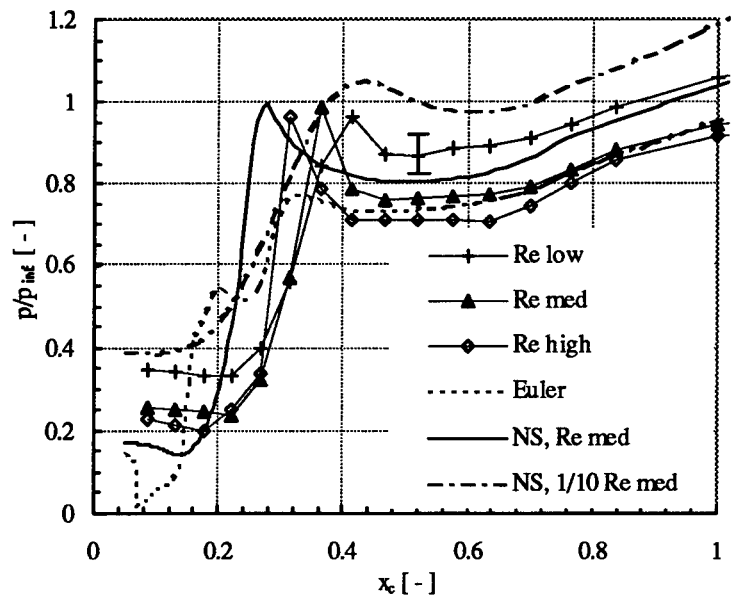


Fig. 2.3.6: Flat plate static pressure distribution downstream of wing, pos. C,  $M_\infty = 6$ ,  $\alpha = 40^\circ$ ,  $\lambda = 75^\circ$ .

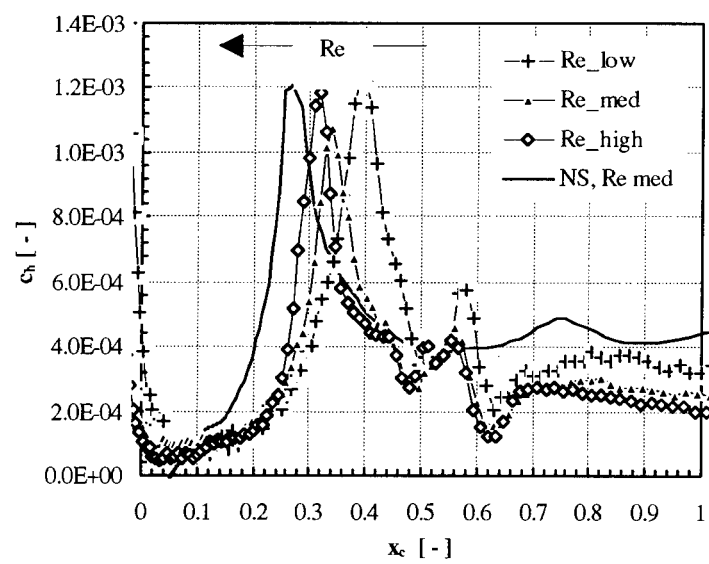


Fig. 2.3.7: Flat plate heat transfer distribution downstream of wing, pos. C,  $M_\infty = 6$ ,  $\alpha = 40^\circ$ ,  $\lambda = 75^\circ$



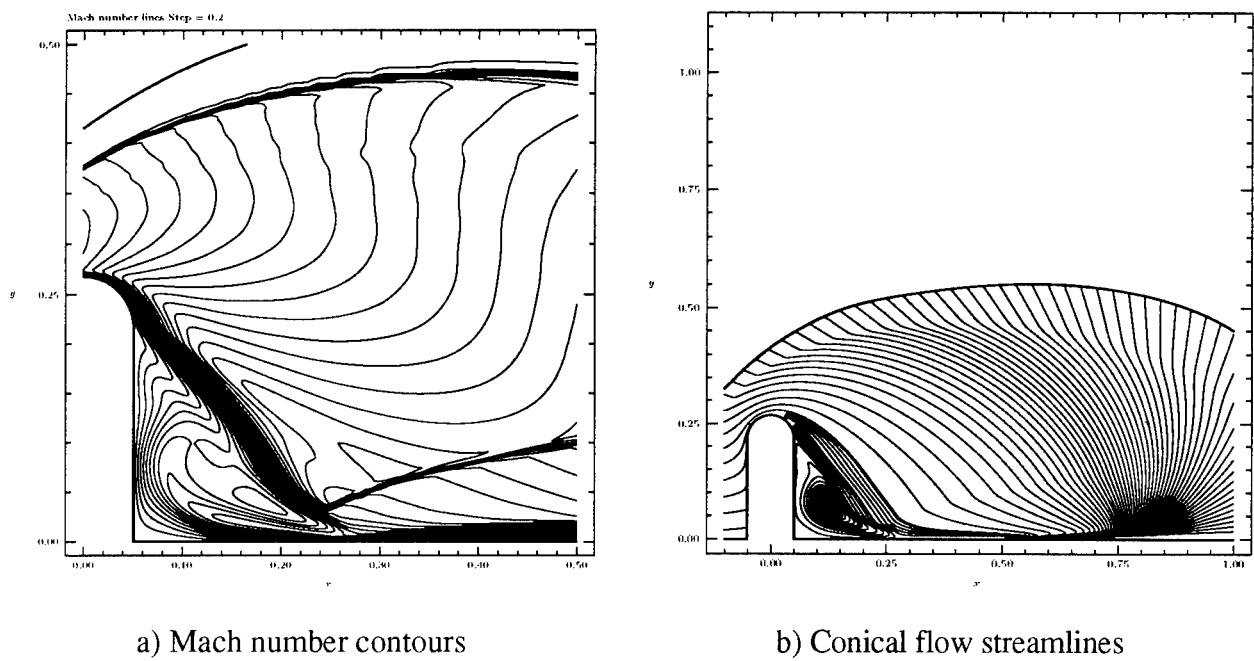


Fig. 2.3.8: Conical flow computations (detailed view of lee side flow),  
 $M_\infty = 6$ ,  $Re_\infty = 0.57$  million,

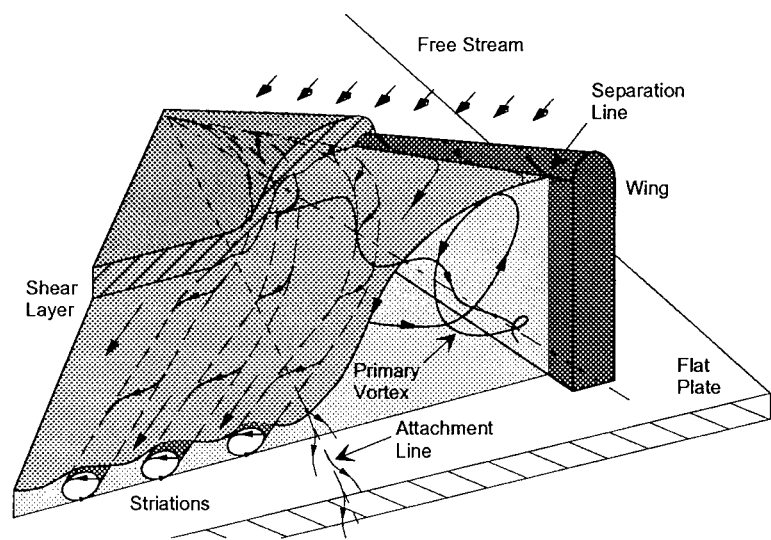


Fig. 2.3.9: Suggested flow field model for Mach 6 interaction

### 3. Applied Research

During the years, the VKI has been involved in wind tunnel testing for aerospace programs in the hypersonic facilities of the Institute. In the next section, the extension of the operating domain of the Longshot tunnel is discussed and typical aerothermodynamic studies carried out in this facilities are presented. Finally, the present development of a Plasmatron facility at the VKI is discussed.

#### 3.1 Extension of the operating domain of the VKI-Longshot free piston tunnel

(J.-M. Charbonnier, W. Dieudonné, S. Paris)

##### 3.1.1 Introduction

Due to the very high level of stagnation temperatures, the chemistry taking place downstream of the bow shock of a hypersonic vehicle will produce atomic oxygen and nitrogen and eventually will ionize the atoms. If one considers the mixture created as a combination of perfect gases, it is possible to determine an equivalent specific heat ratio which value is lower than the value for air. Of course during their passage around the model, the chemical components may react together and consequently, the composition of the mixture will change around the body.

In order to simulate these phenomena, the natural tendency is to try to reproduce in wind tunnel the flight conditions. This implies that the reservoir temperature of the wind tunnel should be very high and consequently, the experimentalists are facing the problem that the test gas will react in the reservoir and will not recombine to a composition equivalent to the stagnant air of the atmosphere when it arrives onto the model. It is the situation that takes place in the so-called high enthalpy facilities which were recently developed in Europe. In such a case, the analysis of the data collected on the model is rather difficult to achieve because the gas which flows on the model is not correctly characterized. Therefore these facilities do not duplicate flight conditions but rather provide an additional set of conditions which of course introduces high temperature gas effects but which has the disadvantage of not being well characterized.

In order to assess the influence of high temperature gas effects, a simpler approach consists in using a test gas which has a specific heat ratio  $\gamma$  lower than the value for air at ambient conditions. This simulation corresponds to the case of a frozen composition for the mixture of components created downstream of the shock which would pass around the body.

##### 3.1.2 The VKI-Longshot facility

The VKI-Longshot is a free piston wind tunnel which uses a piston to compress the test gas (fig. 3.1.1) [1]. It can provide very high pressure levels (up to 4000 bars) for moderate temperatures (up to 2500K) so that the vibrational mode of the test gas molecule is only moderately excited. The facility is classified as a cold hypersonic facility because the test case can still be considered as a perfect gas. Due to the very high pressure levels achieved into the reservoir, the Reynolds numbers simulated are very high (up to 10 millions per meter). The Mach number of the flow in the test chamber can be changed from 14 to 20. This facility is particularly well suited for the study of boundary layer transition at high Mach and Reynolds number and provides a good duplication of spacecraft reentry trajectories with respect to these two non dimensional parameters as seen in figure 3.1.2.

To operate with different gases (N<sub>2</sub> and CO<sub>2</sub>), the contoured nozzle designed for nitrogen was replaced by a conical nozzle with a removable throat block in order to accommodate the throat diameter to the desired nozzle exit Mach number. The nozzle wall is equipped with heat transfer gauges and pressure gauges starting at 0.3 m from the nozzle throat to the end of the nozzle (1.7 m) [37]. In the test chamber, the free jet created at the nozzle exit is characterized by a calibration rake equipped with 21 Pitot pressure tubes and 8 hemispherical probes providing the heat transfer level at the stagnation point (fig. 3.1.3). A modeling of the compression phase is developed for the two testing gases based on the operating parameters. Then a simple one dimensional computation of the flow expansion in the nozzle associated with a correlation to account for the boundary layer displacement thickness provides the flow properties in the test section [38].

##### 3.1.3 Determination and calibration of the new operating conditions

The objective in the definition of four operating conditions is to vary the specific heat ratio  $\gamma$  of the test gas while keeping constant a parameter relevant for the measurement of heat transfer and aerodynamic coefficients on a hypersonic vehicle. This parameter is known as the rarefaction parameter  $\bar{V}^*$  and is a combination of the Mach and Reynolds numbers. Two values of the rarefaction parameter relevant for hypersonic flight are selected providing a variation of  $\gamma$  at iso-value of  $\bar{V}^*$ . The new operating condition parameters are summarized in table 3.1.1 [39].

Measurements of pressure and heat transfer are made in the nozzle flow and in the free jet for the four operating conditions [33].

In order to enhance the experimental data, a parallel study is performed using the VKI-MB Navier Stokes solver [7,8] where the nozzle flow is computed for both laminar and turbulent nozzle wall boundary layers. The purpose of these computations is to validate the code and assess the future comparison between the measurements made on models in the tunnel using the four operating conditions. Actually a complete re-building of the flow over the models will allow to isolate the differences in the measurements due to the changes in  $\gamma$  or  $\overline{V^*}$  from the influences resulting from incoming flow non uniformities.

Figure 3.1.4 shows an example of the Pitot pressures measured in the free jet in two sections downstream of the nozzle exit compared to the results of a laminar and a fully turbulent computations for the operating condition LSCN1. It can be observed that the computations frame the experimental data indicating that the nozzle wall boundary layer transition takes place somewhere after the throat. Therefore a sensitivity study of the results to the position of the transition is performed where the transition point is placed at 0.15 m and 0.3 m from the throat. Figures 3.1.5 and 3.1.6 show that the comparison of the measured and computed wall quantities in the nozzle are in good agreement when the transition location is placed at 0.15 m from the throat. In figure 3.1.7, the normalized Pitot pressures measured are compared to the computations assuming either fully laminar flow, or a turbulent boundary layer starting at 0.3 m or at 0.15 m from the throat. Actually the case with transition fixed at 0.15 m gives the best agreement with the experimental data both in terms of pressure level in the potential core and in terms of boundary layer thickness [40].

This approach is extended to the 3 other flow conditions newly defined in the Longshot with N2 and CO2. The numerical results will provide a complementary qualification of the flow in the Longshot nozzle with respect to the experimental calibration and also inlet conditions for the re-building of the flow over standard geometries such as the hyperboloid-flare and the Electre models.

Cond. #	Test Gas	$\gamma$	Mach #	Reynolds #	Treservoir	Preservoir	$\overline{V^*}$
		[-]	[-]	$[10^6 / \text{m}]$	[K]	$[10^5 \text{ Pa}]$	[-]
LSCN1	N2	1.4	15	7.5	2000	950	0.013
LSCN2	CO2	1.3	11.2	6.7	2000	1300	0.013
LSCN3	N2	1.4	14.8	4.2	1900	500	0.018
LSCN4	CO2	1.4	13.3	4.6	2250	2250	0.018

Table 3.1.1: New operating condition for the Longshot equipped with the conical nozzle

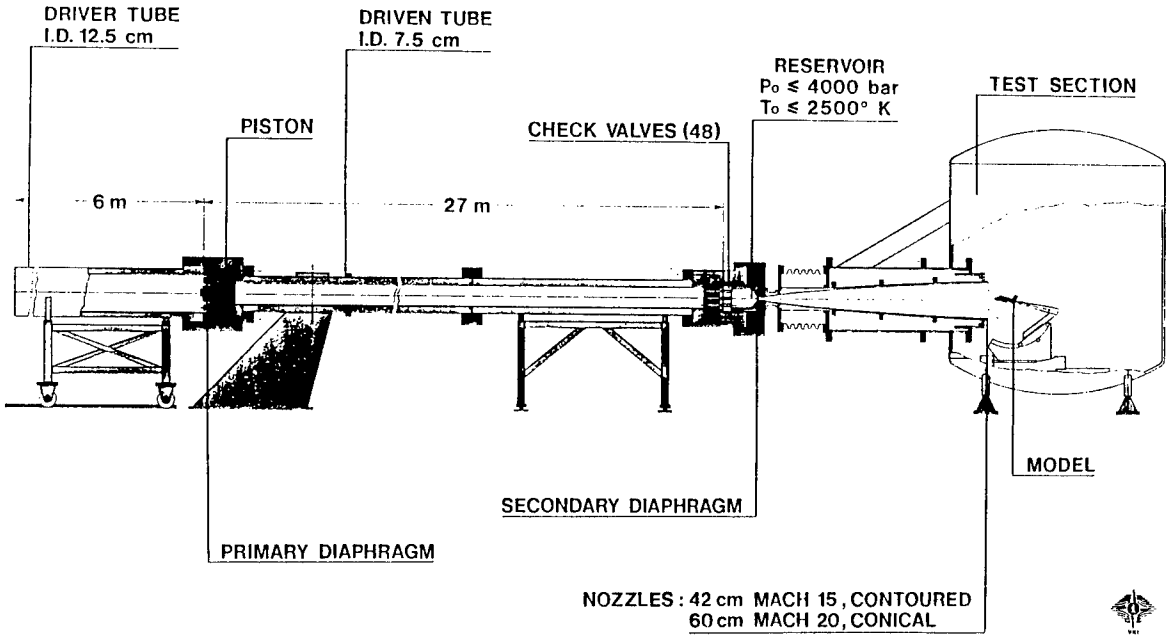


Fig. 3.1.1: Schematic of the VKI-Longshot wind tunnel

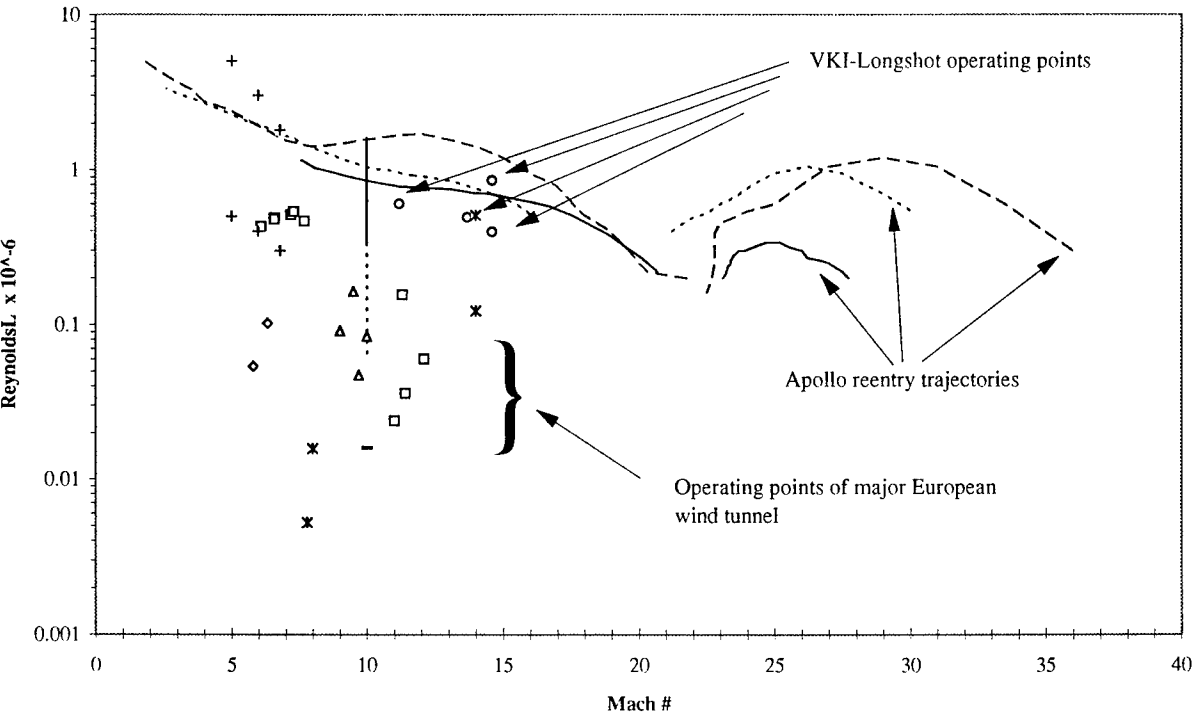


Fig. 3.1.2: The VKI-Longshot wind tunnel operating points vs Apollo reentry trajectories

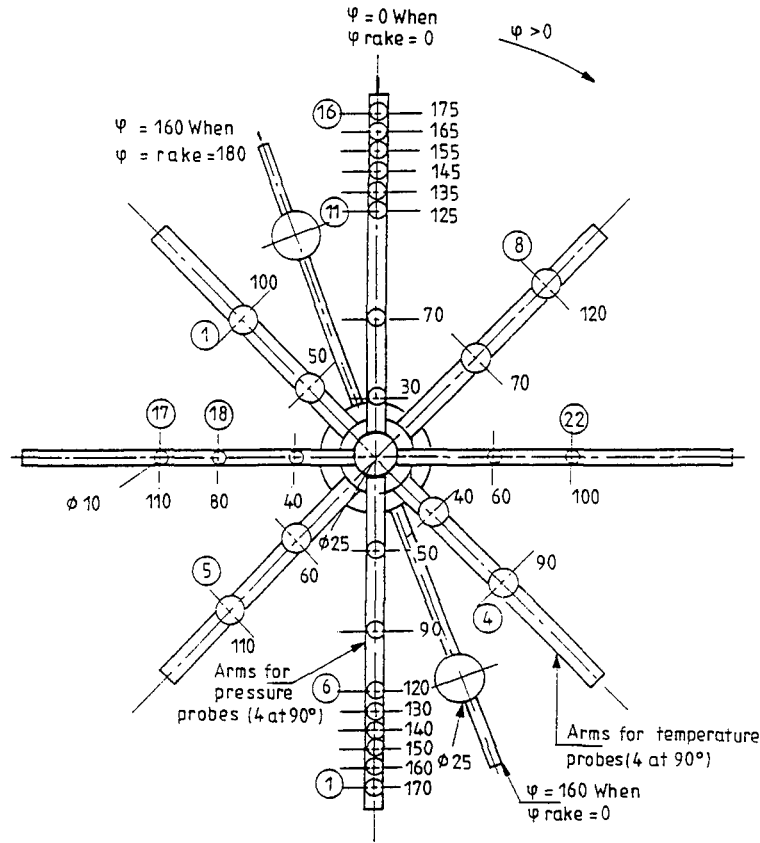


Fig. 3.1.3: Schematic of the calibration rake

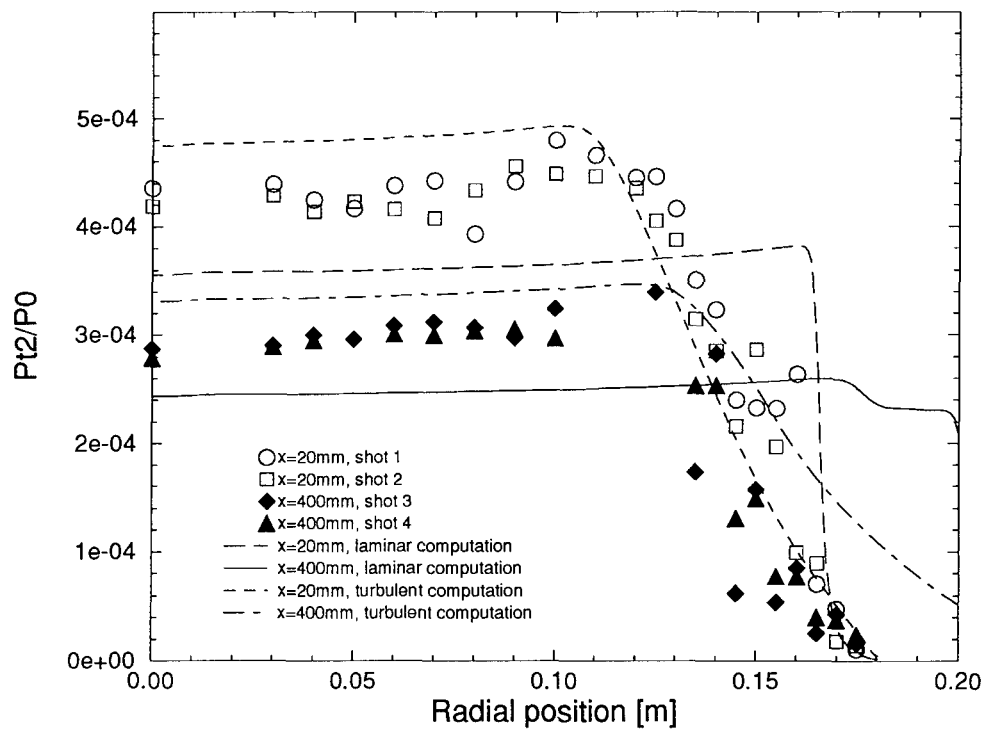


Fig. 3.1.4: Comparison of measured and computed Pitot pressure profiles in the test section at two streamwise positions for the condition LSCN1

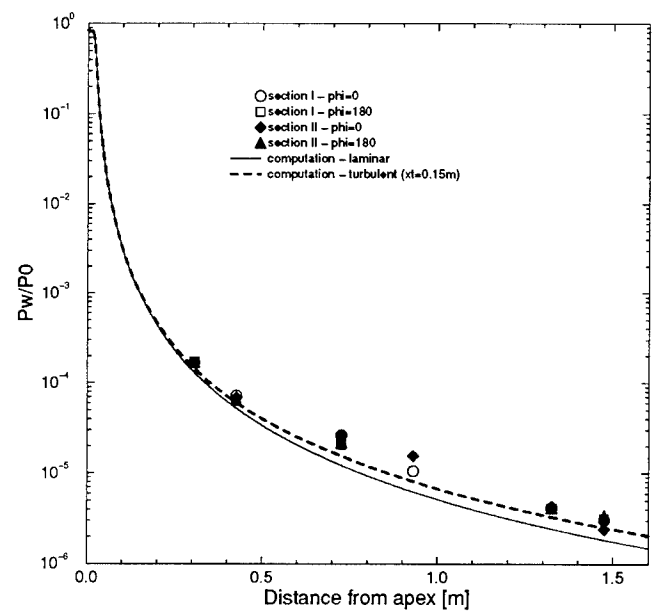


Fig. 3.1.5: Comparison of measured and computed nozzle wall pressure for the condition LSCN1

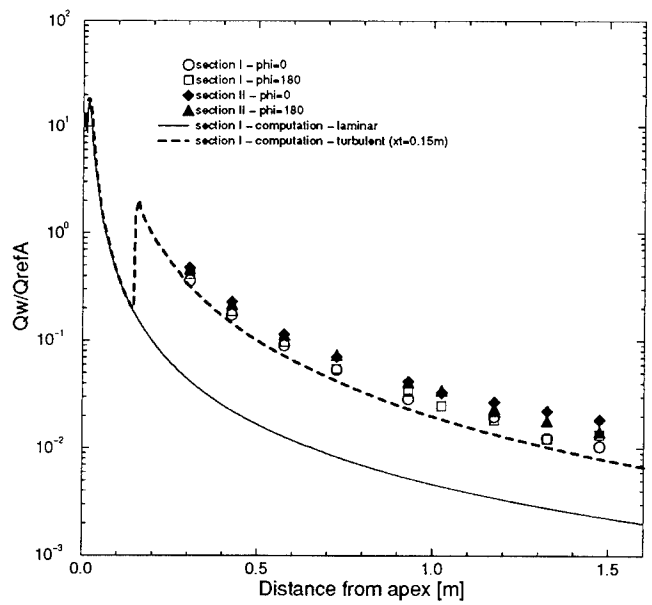


Fig. 3.1.6: Comparison of measured and computed nozzle wall heat flux for the condition LSCN1

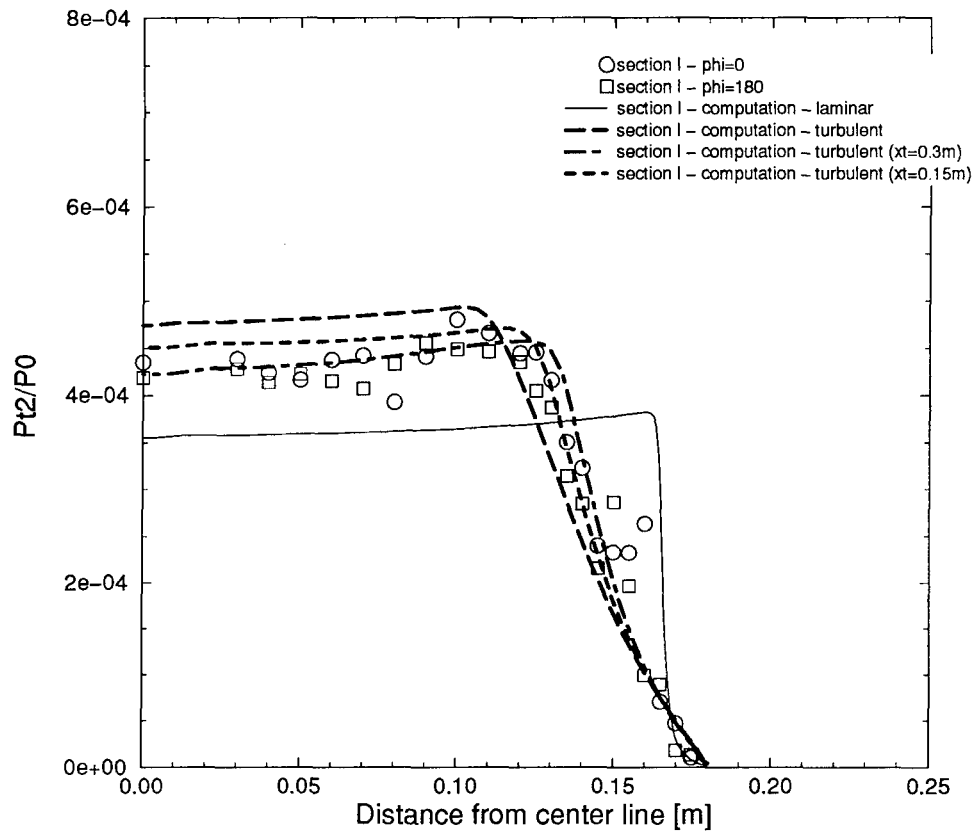


Fig. 3.1.7: Comparison of measured and computed normalized Pitot pressures for the condition LSCN1 at 20 mm downstream of the nozzle exit



### 3.2 Aerothermodynamics of reentry vehicles (J.-M. Charbonnier, S. Paris)

#### 3.2.1 Introduction

In the frame of the Hermes and Atmospheric Reentry Demonstrator programs, the VKI has been involved in the aerothermodynamic characterization of reentry vehicles. In the following sections, typical heat transfer and pressure measurements carried out in the VKI-Longshot wind tunnel are briefly presented. Then the method used to compensate the inertial forces during the measurement of aerodynamic coefficients are recalled and the present developments are discussed.

#### 3.2.2 Pressure and heat transfer measurements

In the past years, the VKI was involved in the characterization of the aerothermodynamics of the Hermes spacecraft. In this program, various configurations of Hermes were tested to evaluate pressure and heat transfer distribution in the condition of the Longshot wind tunnel at Mach 14 [41,42,43]. Figure 3.2.2.1 shows an example of Hermes model equipped with thin films gauges.

In the frame of the Atmospheric Reentry Demonstrator, the VKI is manufacturing an ARD capsule model equipped with pressure transducers and temperature gauges which will be tested in the Longshot with the new operating conditions. This model is devoted to the study of the boundary layer transition and has several inserts with roughness elements. As already mentioned in Sec. 2.1.2, it is not straightforward to find a good criterion for roughness induced transition on blunt body with very high pressure gradients such as in the case of the windward side of the ARD capsule

#### 3.2.3 Measurement of aerodynamic loads

A method for the measurement of aerodynamic forces and moments was developed to compensate for the inertial forces which are always perturbing the measurements in short duration facilities. The principle of these inertial force corrections is based on the experimental determination of the model accelerations along and around its axis using measurements of acceleration at selected locations in the model. Figure 3.2.2 presents the implementation of the accelerometers in a Hermes model as tested in [44,45,46]. In order to evaluate the importance of the inertial forces, figure 3.2.3 shows the comparison between the raw normal force as measured by the strain gauge balance and the aerodynamic force after correction on a Hermes model

in the Longshot. It is clear that inertial compensation is needed in order to get usable measurements.

The method used at the VKI is described in [47] and [48] and was recently compared to the so-called LRBA method which is based on the same principle but which is easier to apply since it does not require the knowledge of the characteristics of the oscillating body. Actually one of the difficulties in applying the method developed at VKI is that the oscillating part must be defined with its center of gravity and moments of inertia. This oscillating part is taken to be the model plus the front part of the strain gauge balance; however there is always an uncertainty associated to the fact that the part of the balance that has to be considered is not well defined. The modified method proposed at the LRBA Vernon (F) overcomes the problem by leaving the mass and inertia of the oscillating body as unknowns. Since the basic equations are the same, the way to find these new unknowns is to solve the system for several instants during the running time by a least square technique instead of solving the equations at each instant. The two techniques applied to a simple geometry such as a blunt cone give the same results [49]; however when the model geometry becomes more complicated, the modified method may be more easy to apply.

The drawback of both techniques is the need to place accelerometers in the model and therefore to make a special design of the model which usually ends up with more complicated and costly models. In order to overcome this problem, the University of Aachen (RWTH) has developed a strain gauge balance on which accelerometers are mounted. This balance will be tested in the Longshot on an Apollo capsule shape which will also be equipped with accelerometers as shown in figure 3.2.4 in order to evaluate the capability of the method developed in Aachen compared to the traditional compensation technique.

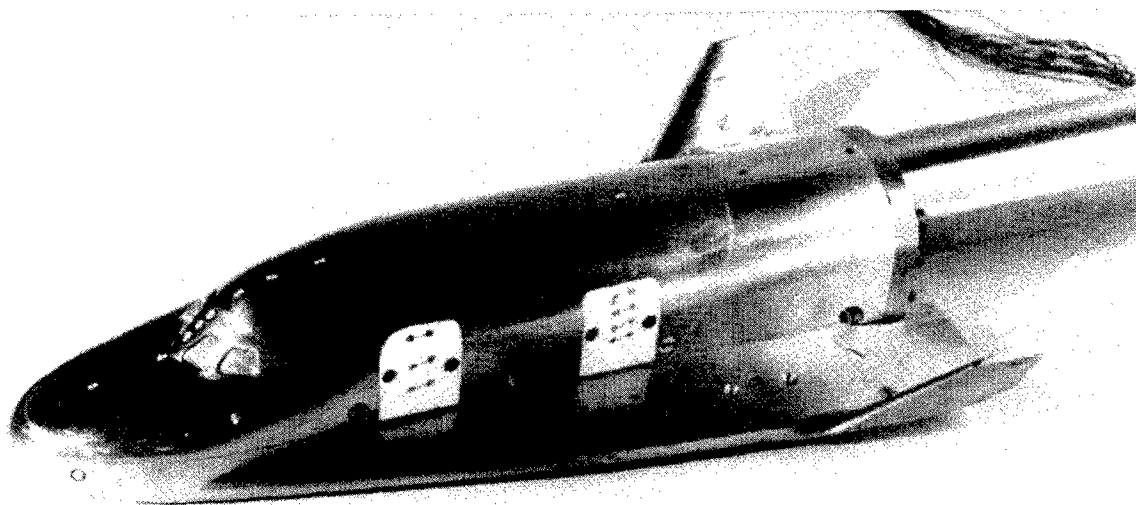


Fig. 3.2.2.1: Hermes model equipped with thin film gauges for heat transfer measurements in the VKI-Longshot (courtesy Dassault-Aviation)

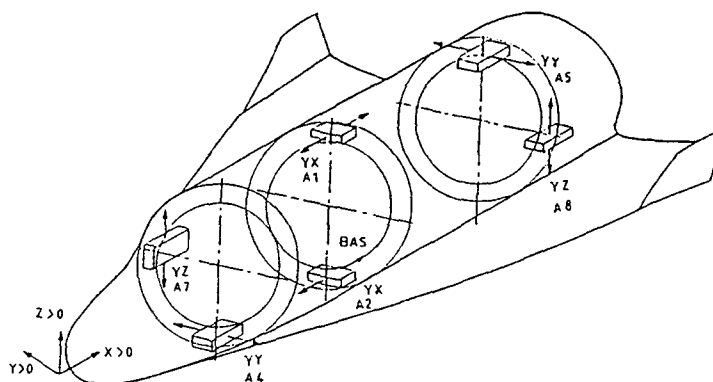


Fig. 3.2.2: Schematic of the implementation of the accelerometers in a Hermes model

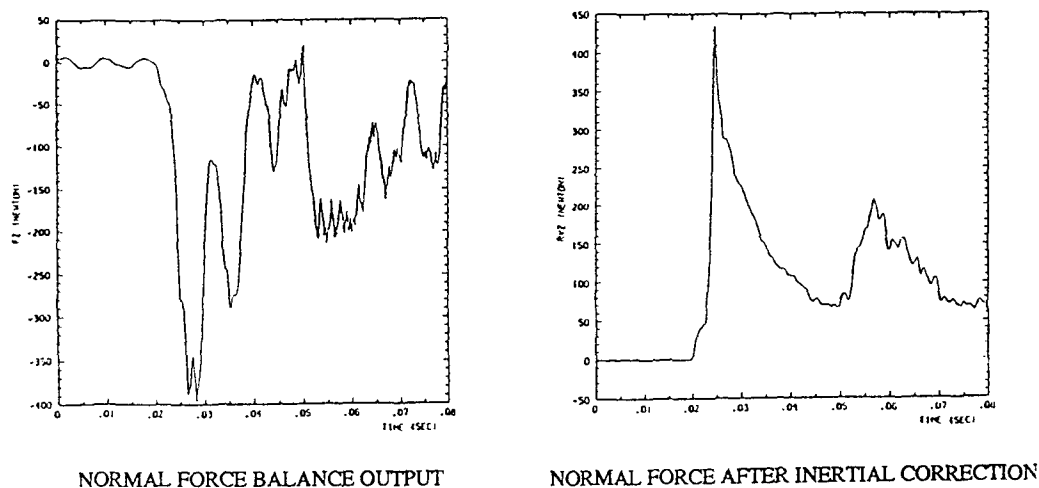


Fig. 3.2.3: Raw and aerodynamic normal forces on an Hermes model in the Longshot

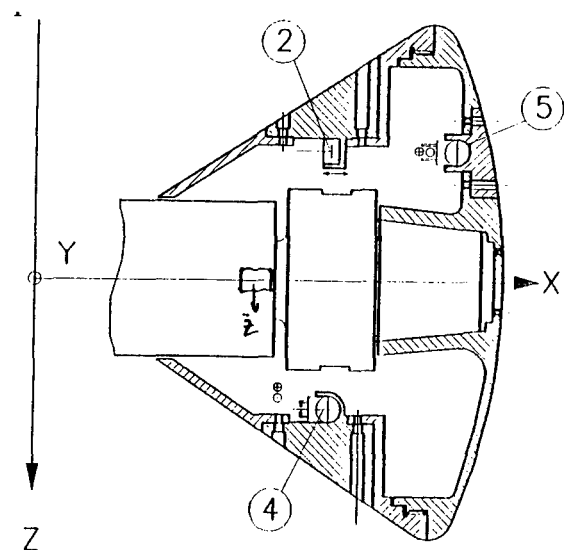


Fig. 3.2.4: Schematic of the implementation of the accelerometers in the RWTH capsule model

### 3.3 Development of the Plasmatron facility

(B. Bottin, M. Carbonaro, M. Decré)

#### 3.3.1 Introduction

A Plasmatron is an induction plasma wind tunnel, where a jet of air, heated at extremely high temperatures (from around 6000 K to 10000 K) to a plasma state, is directed onto a target, primarily for the purpose of testing the resistance of thermal protection systems (TPS) for space re-entry vehicles, combustion chambers, turbine blades or ceramic coatings exposed to severe heat loads.

In 1992, facilities of this kind were found to exist in Russia, where they have been extensively used for the testing and optimization of the ceramic composites used as thermal protection tiles for space-re-entry objects, like the soviet capsules and the shuttle Buran.

The European Space Agency, recognizing the advantages offered by such facilities, in terms of chemical purity of plasma compared to the arc-jet facilities traditionally used in the western world for the same purpose, decided, as an aid to European space programs, to sponsor together with the Belgian Federal Office for Scientific, Technical and Cultural Affairs, the construction of a 1 MW Plasmatron at the von Karman Institute. The planned completion date of this work is October 1997.

TPS materials samples will be tested in subsonic and supersonic high-enthalpy flows with stagnation pressures of 5 to 175 hPa and cold wall stagnation convective heat fluxes of 350 to 1200 kW/m<sup>2</sup>. It is intended in a late stage of facility realization to have an automated standard operation of the whole facility.

#### 3.3.2 Principle of operation

The concept behind plasma generation by induction is sketched on figure 3.3.1. A coil surrounds a quartz tube in which cold air is injected. This coil is connected to a high-frequency generator and is traversed by high-voltage, high-frequency current (a few thousand volts with frequencies from 400 kHz to several MHz). Due to these conditions, an induced magnetic field exists in the center of the quartz tube, with induction lines parallel to the axis, as in a classical solenoid.

The time variation of the induction creates circular, oscillating electric fields in planes perpendicular to the tube axis. Considering that air has been ionized, these fields can move the free electrons, creating current loops heating the gas by Joule effect. Once the gas heats up, it dissociates and ionizes into a plasma. Conceptually, the torch is actually a transformer, of which the primary is the coil and the secondaries the induced current loops in the gas.

The first free electrons can be obtained by introducing an electrode into the plasma torch or, preferably, by reducing the pressure under 0.1 mbar and applying voltage on the coil. Electric field gradients appearing in the vicinity of the coil (between turns) are strong enough to cause a local ionization of the gas in the tube. Once these first free electrons have appeared, the whole gas is rapidly heated by Joule effect. In order to facilitate the initial electric discharge, one can use argon, which has a much lower ionization potential than air.

By these means plasma can be generated from low to atmospheric pressures with temperatures of the order of 6000 K to 10000 K.

#### 3.3.3 Differences between inductively-heated and arc-heated facilities

Another mean of plasma generation is an electric arc. The principle has been widely and successfully used in many arcjet wind tunnels. Nevertheless, inductively-heated plasma sources have several advantages over arc-heated sources.

In arcjets, the discharge is produced between electrodes, which constantly erode during operation. This results in copper pollution of the flow, which depends on the pressure as well as on the heater design. The contamination can range from 50 ppm[50] up to about 1% of relative copper vapor content when no special care is applied. While this does not seem to pose problems for aerodynamic studies under high temperatures, it can significantly influence heat flux studies. TPS materials tested under moderate stagnation temperatures will be covered by copper condensing on the surface, with the result that the initially non-catalytic surface will gradually become catalytic, increasing the convective heat transfer because of recombination processes[51]. The electrodeless heating of inductive torches suppresses all risks of flow contamination. This makes inductively-heated plasmas very attractive for materials catalytic and heat resistance studies, plasma diagnostic techniques development (especially the modern, non-intrusive techniques like emission spectroscopy and laser-induced fluorescence) and new trends in industrial processes, such as purification or synthesis of materials and spectroscopic analysis.

In most cases, once the plasma has been ignited, the discharge remains very stable, confined in the torch by electromagnetic forces. The flow is therefore very stable, much more than in conventional arcjet facilities, where arc oscillations produce flow fluctuations. One needs a carefully designed arc generator (such as segmented arc heaters) to overcome this problem.

It must be additionally mentioned that inductively-heated tunnels can operate in subsonic and supersonic modes, whereas most arcjets mainly work in the supersonic regime. This duality allows to have stagnation-point flows with or without shocks. Subsonic operation also features flows with a greater degree of equilibrium, much farther from the frozen state. This greater diversity is ideal for the validation of high-temperature CFD codes.

It must however be mentioned that the overall efficiency of an inductively-heated facility is lower than in the case of arc-heated facilities. Furthermore, the operation at low pressures and low velocities, while seemingly attractive for code validation, has the important drawback of low Reynolds numbers (about 6000 per meter) that totally preclude any use of such facilities for aerodynamic testing with Reynolds number similarity.

The main characteristics of some plasmatrons are summarized in table 3.3.1.

### 3.3.4 Description of the VKI Plasmatron

The European Space Agency has set several technical requirements concerning the facility

It has to achieve values of total pressure and catalytic cold wall convective stagnation heat flux indicated on figure 3.3.2, on material samples of 2.5 cm diameter mounted on a 5 cm diameter sample holder. It must be capable to function in subsonic and supersonic modes with good flow homogeneity in continuous operation during 25-minute periods at pressures lower than 75 mbar and 5-minute periods at pressures higher than 75 mbar.

The main elements of the Plasmatron facility are schematically drawn on figure 3.3.3. The heart of the Plasmatron is the torch that creates high-enthalpy plasma by induction heating of the supplied working gas. The plasma flows into the test enclosure, where the TPS model is located. The rear of the enclosure contains a diffuser to collect the flow. It is water-cooled to reduce the temperature of the flow. Further cooling is achieved through a heat exchanger that reduces the flow temperature to below 50°C, the maximal entrance temperature to the vacuum pumps system. This vacuum system is composed of three volumetric vacuum pumps providing the required underpressure and maintaining the necessary mass flow rate through the whole system. The gas is discharged into the exhaust stack of VKI. The torch must be fed with precisely controlled mass flow rates of various gases, both argon for start-up and others for testing. A specific gas supply system collects gas from carboys and/or air from the compressed air network of VKI or from the Plasmatron laboratory (ambient air). The facility receives 1600 kVA at 11 kV

from the electricity network, in a transformer that provides 1400 kVA (204 V) to the high-frequency generator and 200 kVA (380 V) to the auxiliary systems.

The high-frequency generator is a solid-state technology ("statitron") HF inverter composed of two cabinets: one DC unit and one HF unit. It provides the torch with the high-frequency (400 kHz) current necessary to create and maintain the discharge. The whole facility has to be cooled by de-ionized water. Each system (torch, test enclosure, model support, heat exchanger, vacuum pumps, HF generator) has its separate cooling line, the whole circuit being driven by a pump. The water used in the circuit is cooled in three dry air coolers located on the roof of the building. Finally, the control system is capable of conducting tests under constant or varying conditions while monitoring all alarms and warnings from the subsystems to insure a safe operation. In addition, the facility is equipped with an 80-channel data acquisition system and intrusive and non-intrusive test instrumentation, the latter requiring the use of an excimer laser for certain specific applications such as laser-induced fluorescence (LIF).

In order to cover the whole specification matrix (figure 3.3.2), two torches are needed. The test conditions at low pressures and high heat fluxes require low plasma powers. They will be obtained by using the low power range of the HF generator (15-150 kW) coupled to a small, 80 mm diameter torch. Points at higher pressures will be obtained with the high-power range output of the HF generator (100-1000 kW) and a big, 160 mm diameter, torch. Each torch is mounted in a separate casing, the diameter of which is compatible with the openings of the test enclosure (figure 3.3.4).

The successful ignition of the plasma requires the inside of the torch to be at a low pressure, in order to reduce the ionization potential of the gas. However, the outside of the torch has to be kept at a higher pressure, otherwise there is a risk that the initial discharge will occur between two successive turns of the coil rather than in the torch. This is why the inner and outer parts have to be tightly separated by the quartz tube, which also works as the plasma container.

For moderate to high plasma powers, a water-cooled segmented copper cage will be placed inside the quartz tube to prevent melting. Water supply will be through the back of the casing, separate cooling lines serving the cold cage, the end plate (in contact with radiation from the enclosure as well as convective transfer at the outlet), the gas injectors (in contact with radiation from within the torch) and the coil (heated by Joule effect as any conductor).

There are two separate gas injectors: the peripheral injection insures a protecting layer of cool gas along the

walls of the torch, while the central injection provides most of the working gas.

The setup as described is valid only for subsonic flows. In order to reach sonic and supersonic conditions, convergent and convergent-divergent nozzles matching the cold cage internal diameter will be fixed on the end plate. A set of five nozzles is presently envisaged: a converging nozzle for each torch diameter, for sonic operation and supersonic acceleration through underexpansion, a converging-diverging (conical) nozzle for each torch diameter, for supersonic flow, and finally a converging-diverging contoured nozzle for one of the two torches, at a reference flow condition, for flow homogeneity purposes. Typical Mach numbers presently envisaged are of the order of 1.2 to 2.

place	facility	power	frequency	jet diameter
IPM	IPG-3	700 kW (coil)	1.76 MHz	200 mm
IPM	IPG-4	100 kW (anode)	1.76 MHz	80 mm
TsAGI	VTS	600 kW (coil)	440 kHz	300 mm core
TsAGI	VAT-104	160 kW (coil)	1.76 MHz	50 mm core
TsNIIMASH	Y-13-PHF	1000 kW (gen.)	440 kHz	200 mm
IRS	PWK 3	150 kW (gen.)	650 kHz	100 mm
CORIA	(?)	200 kW (gen.)	1.7 MHz	80 mm
VKI	PTRON (?)	1200 kW (gen.)	400 kHz	160 mm

Table 3.3.1: summary of plasmatron characteristics

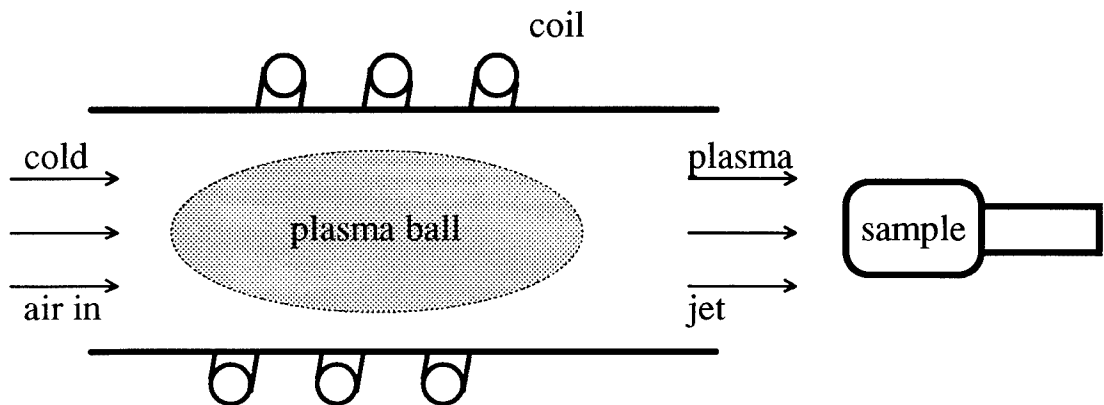


Figure 3.3.1: inductive plasma torch concept

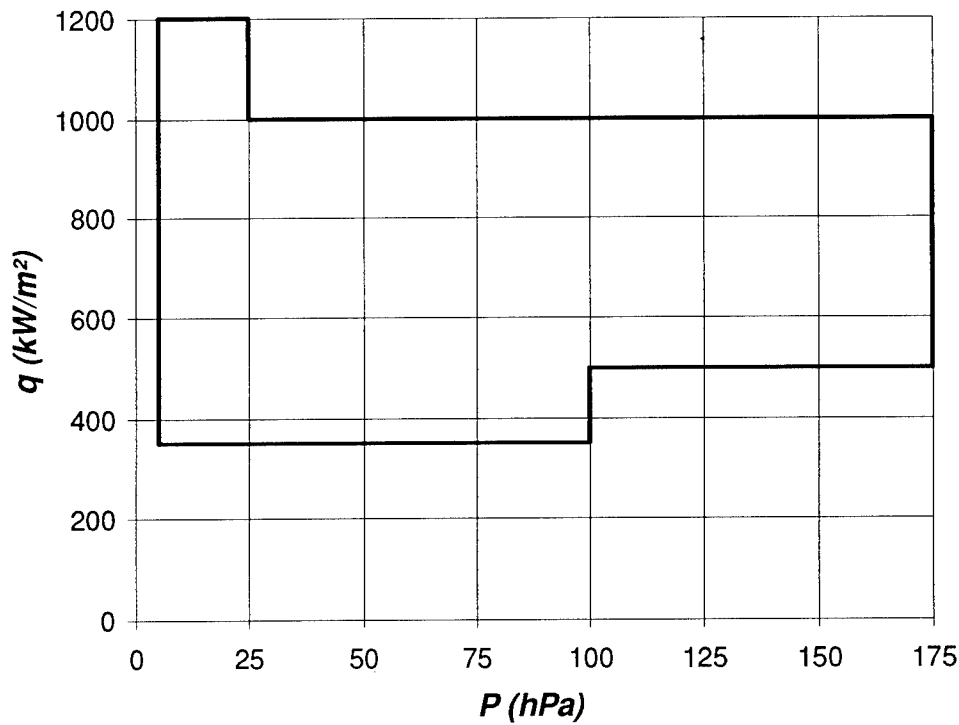


Figure 3.3.2: ESA requirements matrix

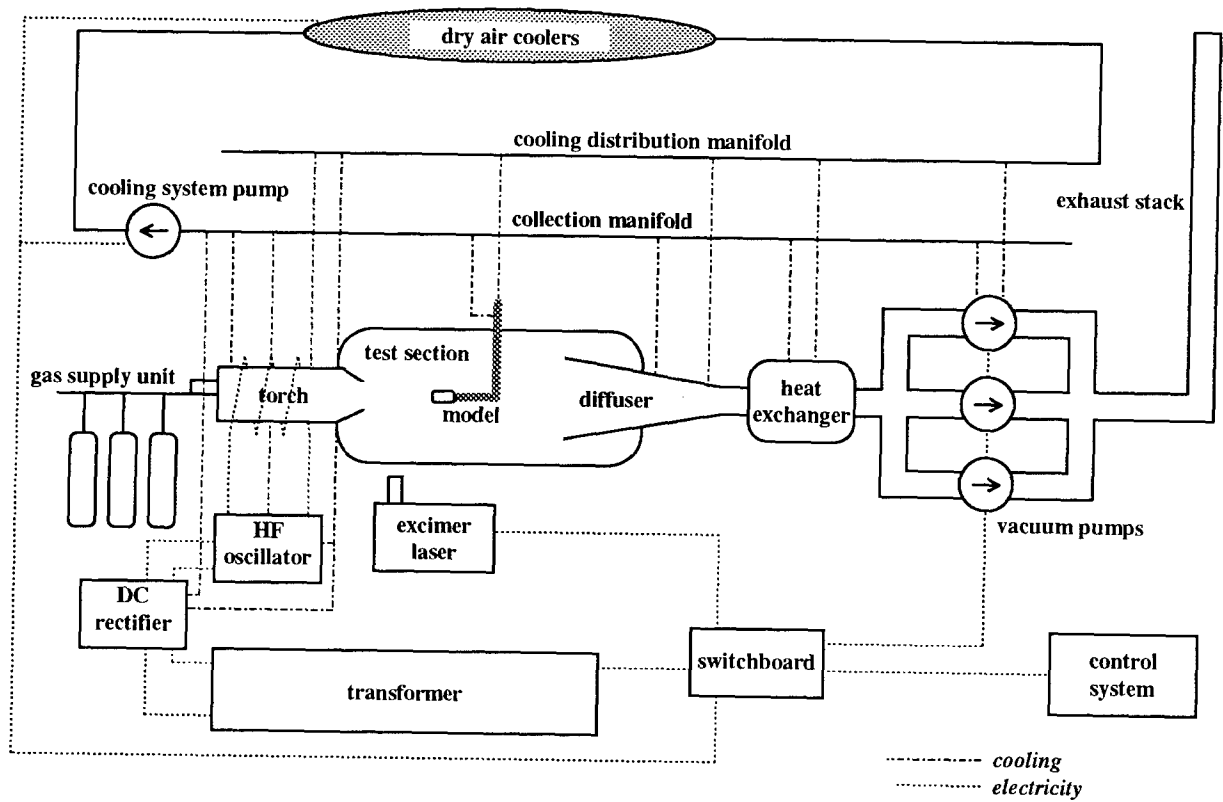


Figure 3.3.3: Plasmatron facility schematic diagram

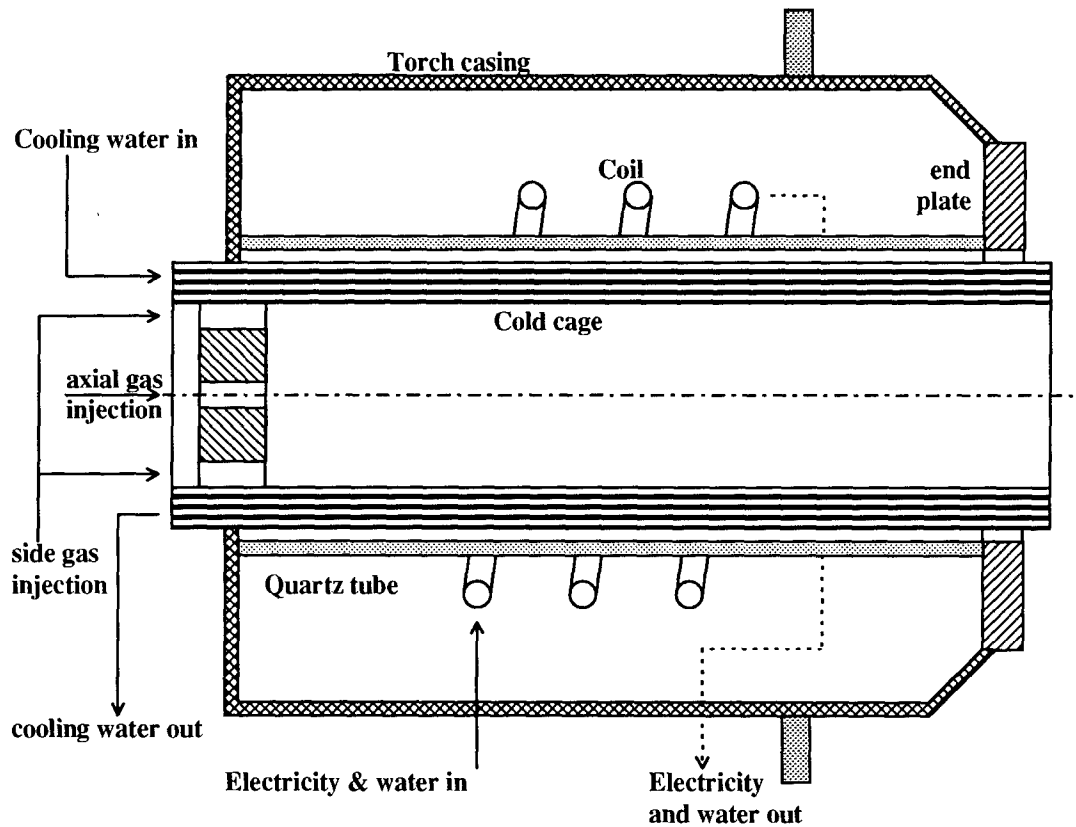


Figure 3.3.4: plasmatron torch and torch casing



## References

1. Simeonides, G.A., The VKI hypersonic facilities and associated measurement techniques, TM 46, von Karman Institute for Fluid Dynamics, November 1990.
2. Simeonides, G.A., Vermeulen, J.-Ph., Boerrigter H.L., & Wendt, J.F., Quantitative heat transfer measurements in hypersonic wind tunnels by means of infrared thermography. IEEE Transactions on aerospace and electronic systems, Volume 29 #3, July 1993, pp.878-893.
3. Charbonnier, J.-M. & Boerrigter, H.L., Contribution to the study of gap induced boundary layer transition in hypersonic flow. AIAA Paper93-5111, 5th International Aerospace Planes and Hypersonics Technologies Conference, Munich Germany, Nov.30 - Dec.3, 1993.
4. Michel. Caractéristiques des couches limites en hypersonique. Progress in Aeronautical Sciences Vol 9, 1968.
5. Boerrigter, H.L., Charbonnier, J.-M., On the effect of flowfield non-uniformities on boundary layer transition in hypersonic flow, Euromech 330 Laminar/turbulent transition of boundary layer influenced by free-stream disturbances, Prague, von Karman Institute for Fluid Dynamics Preprint 1995-19, April 1995.
6. Boerrigter, H.L., Calibration of the H3 wind tunnel using Pitot probes, Internal Note 94, von Karman Institute for Fluid Dynamics, December 1993.
7. Broglia, R.; Manna, M.; Deconinck, H.; Degrez, G., Development and Validation of an Axisymmetric Navier-Stokes Solver for Hypersonic Flows, Technical Note 188, von Karman Institute for Fluid Dynamics, May 1995.
8. Paciorri, R., Implementation and validation of the Spalart-Allmaras turbulence model for application in hypersonic flows, Technical 190, von Karman Institute for Fluid Dynamics, January 1996.
9. Boerrigter, H.L., Charbonnier, J.-M., Braem, S., Boundary Layer Transition Induced by Roughness in Hypersonic, proceedings of the 2nd International Conference on Experimental Fluid Dynamics, ICEFM 94, Torino, Italy, July 1994.
10. Boerrigter, H.L., Charbonnier, J.-M., Elbay, M.K., Quantitative Boundary Layer Transition Measurements on Flat Plates and Cones in Hypersonic Flow, Euromech 312 on Turbulence and Vortices in Hypersonic Flows, Gottingen, Oct. 1993.
11. Bertin, J.J., Hayden, T. E., Goodrich, W.D., Shuttle boundary layer transition due to distributed roughness and surface cooling, J. Spacecraft, Vol. 19, # 5, Sept. -Oct. 1982, pp. 389-396.
12. Bertin, J.J., Hypersonic Aerothermodynamics, AIAA Education Series, 1994.
13. Bertin, J.J., Idar III, E.S., Goodrich, W.D., Effect of surface cooling and roughness on transition for the Shuttle Orbiter, J. Spacecraft, Vol. 15, # 2, March-April 1978, pp. 113-119.
14. Boudreau, A.H., Artificially induced boundary layer transition on blunt slender cones at hypersonic speeds, J. Spacecraft, Vol. 16, # 4, July-August 1979, pp. 245-251.
15. Coudroy, L., Etude expérimentale et numérique de la transition de la couche limite sur des capsules de rentrée, Mémoire de Fin d'Etude, Université Libre de Bruxelles, Institut von Karman de Dynamique des Fluides, Avril 1996.
16. Morrisette, E.L., Creel, T.R., Chen, F.J., Effects of cone surface waviness on transition in quiet and noisy supersonic freestreams, AIAA/ASME 4th Fluid Mechanics, Plasma Dynamics and Laser Conference, Atlanta, AIAA Paper 86-1086, May 1986.
17. Goodrich, W.D., Derry, S.M., Bertin, J.J., Shuttle Orbiter boundary layer transition at flight and wind tunnel conditions, NASA Conference Publication 2283, Part 2, March 1983.
18. Lapostolle, S., 2D compression corners at Mach 6 with emphasis on detection of Gortler vortices, von Karman Institute for Fluid Dynamics, Project Report 1994-19, June 1994.
19. Elbay, M.K., Axisymmetric shock wave - boundary layer interaction over conical flared bodies in hypersonic flows, von Karman Institute for Fluid Dynamics, Project Report 1993-20, June 1993.
20. Ginoux, J.J.: On some properties of reattaching laminar and transitional high speed flows. von Karman Institute TN53, September 1969.
21. Gautier, B.: Etude théorique et expérimentale des effets du refroidissement pariétal sur l'interaction onde de choc - couche limite en écoulement laminaire plan hypersonique, Thèse de Doctorat en Sciences Appliquées de l'Université Libre de Bruxelles / Institut von Karman de Dynamique des Fluides, Avril 1972.
22. Simeonides, G.: Hypersonic shock wave boundary layer interactions over compression corners. Ph.D. thesis, von Karman Institute / University of Bristol, April 1992.
23. Vermeulen, J.P. & Simeonides, G.: Parametric studies of shock wave boundary layer interactions over 2D compression corners at Mach 6. von Karman Institute TN 181, September 1992.
24. Simeonides, G., Haase, W. & Manna, M.: Experimental, analytical and computational methods applied to hypersonic compression ramp flows. AIAA J., Vol. 32, No.2, February 1994.

25. Simeonides, G.: Hypersonic shock wave boundary layer interactions over simplified deflected control surface configurations. AGARD Report 792, August 1993.
26. Simeonides, G. & Haase, W.: Experimental and computational investigations of hypersonic flow about compression corners. *J. Fluid Mechanics*, Vol. 283, 1995, pp17-42.
27. Simeonides, G.: Simple formulations for convective heat transfer prediction over generic aerodynamic configurations and scaling of radiation-equilibrium wall temperature. ESA/ESTEC EWP-1860, October 1995.
28. Simeonides, G.: Laminar-turbulent transition promotion in regions of shock wave boundary layer interaction. Paper presented at ESA/MSTP CFD Code Validation Workshop, ESA/ESTEC, Noordwijk, March 1996.
29. Dieudonné, W., Hypersonic flow over axisymmetric bodies, von Karman Institute for Fluid Dynamics, Project Report 1995-18, June 1995.
30. Dieudonné, W.; Charbonnier, J.-M.; Deconinck, H., Test Case III.b: Hyperboloid-Flare Standard Model at RWG Reference Calibration Point, ESA/MSTP Workshop 1996 on Reentry Aerothermodynamics and Ground-to-Flight Extrapolation, Technical Note HT-TN-E34-621-VKIN, von Karman Institute for Fluid Dynamics, April 1996.
31. Broglia, R.; Manna, M.; Deconinck, H.; Degrez, G., Axisymmetric Navier-Stokes computations of two hyperboloid flares in reentry configuration, 4th European High Velocity Database Workshop ESA/ESTEC, Preprint 1995-09, von Karman Institute for Fluid Dynamics, Nov. 1994.
32. Mensink, C., A 2-D Parallel MultiBlock Method for Viscous and Inviscid Compressible Flow, PhD Thesis VKI/U. Twente, December 1992.
33. Charbonnier, J.-M. ; Paris, S., Calibration of the Longshot tunnel operated with variable  $\gamma$  testing gases, Technical Note HT-TN-E34-241-VKIN, von Karman Institute for Fluid Dynamics, to appear.
34. Kipp, H.W. and Helms, V.T., Some Observations on the Occurrence of Striation Heating, AIAA Paper 85-0324, 1985.
35. Zemsch, S., Fin-Induced Vortex Boundary-Layer Interactions in High Speed Flow, Ph.D thesis, Rheinisch-Westfälische Technische Hochschule, Aachen, Germany, Oct. 1995.
36. Nelson, R.C., Unsteady Aerodynamics of Slender Wings, In Special Course on Aircraft Dynamics at High Angles of Attack: Experiments and Modeling, AGARD-R-776, 1991.
37. Charbonnier, J.-M., Conniasselle, R., Paris, S., Adaptation of the Longshot tunnel hardware for variable  $\gamma$  testing, Technical Note HT-TN-E34-731-VKIN, Aug. 1995.
38. Charbonnier, J.-M., Quiodbach, D., Paris, S., Predicted operating conditions for the Longshot tunnel operated with variable  $\gamma$  testing gases, Technical Note HT-TN-E34-211-VKIN, von Karman Institute for Fluid Dynamics, Sept. 1995.
39. Charbonnier, J.-M., Paris, S., The Longshot tunnel operated with variable  $\gamma$  testing gases. Definition of standard operating conditions, Technical Note HT-TN-E34-221-VKIN, von Karman Institute for Fluid Dynamics, March. 1996.
40. Dieudonné, W.; Charbonnier, J.-M.; Deconinck, H., Nozzle flow sensitivity analysis and wind tunnel operating envelope; Part III Turbulent case - Final computations, Technical Note HT-TN-E34-551-VKIN, von Karman Institute for Fluid Dynamics, to appear.
41. Vanmol, D., Résultats du programme d'essai en soufflerie 2232. Mesure de flux de chaleur sur les drapeaux de winglets de l'avion Hermes, forme 00, à Mach 14. Programme Hermes HPE-1-1132-AMD, Report CR 1990-28/AR, von Karman Institute for Fluid Dynamics, August 1990.
42. Vanmol, D., Résultats du programme d'essai en soufflerie 2085. Mesure de flux de chaleur et de pression sur l'avion Hermes, forme 00, à Mach 14, Report CR 1990-29/AR, von Karman Institute for Fluid Dynamics, August 1990.
43. Vanmol, D., Résultats du programme d'essai en soufflerie 1859-C. Mesure de flux de chaleur sur l'avion Hermes, forme R, à Mach 15. Programme Hermes 4C., Report CR 1990-30/AR, von Karman Institute for Fluid Dynamics, August 1990.
44. Vanmol, D., Carbonaro, M., Résultats du programme d'essai en soufflerie n° 1882. Mesure d'efforts aérodynamiques à Mach 15 sur la maquette 9R de l'avion Hermes, Report CR 1989-27/AR, von Karman Institute for Fluid Dynamics, June 1989.
45. Vanmol, D., Carbonaro, M., Measurements of aerodynamic loads at Mach 14 on the Hermes shape 00, model n° 3014. Results of wind tunnel test program n° 2110-a, Report CR 1990-25/AR, von Karman Institute for Fluid Dynamics, August 1990.
46. Charbonnier, J.-M., Carbonaro, M., Measurements of aerodynamic loads at Mach 14 on the Hermes shape 1.0, model n° 3040. Results of wind tunnel test program n° 2273, Report CR 1993-15/AR, von Karman Institute for Fluid Dynamics, May 1993.
47. Carbonaro, M., Aerodynamic force measurements in the VKI-Longshot hypersonic facility, NATO Advanced Workshop on 'New trends in instrumentation for hypersonic research', ONERA

- Le Fauga - Mauzac April 1992, published in NATO ASI series 224, Kulwer Academic Publishers, 1993.
48. Carbonaro, M., Charbonnier, J.-M., Aerodynamic force measurements in the VKI-Longshot hypersonic facility, 80th STA meeting Köln, Preprint 1994-07, von Karman Institute for Fluid Dynamics, Oct. 1993.
  49. Vaisman, B., Di Micco, A., Evaluation of methods for the determination of aerodynamic coefficients in short duration facilities, SR 1995-01, von Karman Institute for Fluid Dynamics, Oct. 1994.
  50. Babikian, D.S. & Palumbo, G.: Measured and calculated spectral radiation from a blunt body shock layer in an arc-jet wind tunnel. AIAA 94-0086, 1994.
  51. Anfimov, N. TSNIIMASH: Capabilities for aerogasdynamical and thermal testing of hypersonic vehicles. AIAA 92-3962, 1992.

# A Parallel Implicit Multidimensional Upwind Cell Vertex Navier-Stokes Solver for Hypersonic Applications

E. van der Weide

E. Issman

H. Deconinck

G. Degrez

CFD-Group, von Karman Institute for Fluid Dynamics

Waterloosesteenweg 72

B-1640 Sint-Genesius-Rode

Belgium

## 1 SUMMARY

A parallel perfect gas flow solver for axisymmetric applications is described, which has the following characteristics: For the spatial discretization of the convective fluxes it uses a multi-dimensional upwind, monotonic shock capturing, matrix distribution scheme on a compact stencil (at most the points used by the Galerkin finite element discretization) in an unstructured grid, and the Galerkin finite element method for the viscous part.

For fast convergence towards steady state a fully parallel implicit Newton algorithm has been implemented, where the resulting linear systems are solved by subdomain block ILU(0) preconditioned GMRES. A vertex oriented domain decomposition is used, allowing an efficient parallel preconditioner for the GMRES. As the linear systems themselves are solved on the complete grid, the convergence is practically independent of the way the grid is decomposed into subdomains. The message passing library MPI was used for the communication to make the code as portable as possible.

Applications are shown for a hypersonic cone-flare configuration at different Mach and Reynolds numbers and a detailed comparison is made with a structured grid standard Finite Volume solver (the VKI-MB code). Results have been obtained on a four and eight processors SP2, demonstrating the robustness and efficiency of the new flow solver.

## 2 INTRODUCTION

The majority of present CFD codes for hypersonic applications are cell centered upwind finite volume methods based on the solution of one dimensional Riemann problems in the direction of the cell faces. A typical example of such a code is the VKI Multiblock code (VKI-MB) extensively tested in the past ESA workshops on hypersonic flow [1, 2].

Although very successful, the splitting of the multi-dimensional problem into a set of one-dimensional subproblems is not optimal in the sense that for the scalar advection equation the amount of cross-wind diffusion (dissipation) is much higher than for the optimal multi-dimensional scheme of Rice and Schnipke [3]. Indeed the accuracy of state-of-the-art solvers degrades considerably when jets or shear layers are not aligned with the mesh. This happens inevitably when the flow separates, or in strong shock-shock interactions. Therefore, the need for high quality grids is a matter of strong concern, especially in complex three dimensional flow configurations,

requiring large human efforts for the grid generation.

One possible way to help overcome these problems is to use truly multi-dimensional upwinding instead of the dimensionally split approach. For scalar advection these optimal schemes already exist for some years, both in two and three space dimensions, on structured quadrilateral (hexahedral) and on unstructured triangular (tetrahedral) grids, see [3, 4, 5]. However, the extension to non-commuting hyperbolic systems is far more difficult than in the standard dimension by dimension approach.

Within this generalization to non-diagonalizable systems two points of view can be distinguished :

(1) transform the equations in a form which minimizes the coupling terms and treat them as a set of scalar convection laws with (minimized) source terms and

(2) extend the scalar upwind schemes to matrix upwind schemes.

The first approach has been studied extensively in the past and good results have been obtained for transonic problems, see [6, 7, 8, 9, 10, 11]. However, for hypersonic blunt body flows the presence of the coupling terms, which have to be distributed with a non-positive scheme, causes severe non-monotonicity and consequently instability problems.

Therefore, approach (2) has been adopted in this work, as described in detail in section 3. The resulting space discretization is more accurate than the standard finite volume method, especially in capturing shear layers. Further, the stencil is more compact (at most the Galerkin stencil), which is very beneficial for implicit time integration and parallelization.

To accelerate the convergence to steady state, a parallel implicit time integrator has been developed. The Jacobian matrix is computed numerically at the cost of only 12 cell residual evaluations, due to the compact stencil of the spatial discretization. The domain decomposition strategy is the vertex oriented decomposition (VOD) with effectively half a layer of ghost cells, which is more economical than the one or two layers used in standard Finite Volume schemes. The parallel temporal discretization is given in section 4.

The combination of the compact space discretization and the parallel implicit time integration leads to a robust and efficient solver. The test cases presented in section 5 demonstrate that typical hypersonic flow computations (proposed at ESA workshops in 1994 and 1996) on a mesh of 40 000 meshpoints can be made in 2 to 2.5 CPU hours on a 4-processor IBM SP2.

### 3 THE SPATIAL DISCRETIZATION

The axisymmetric Navier-Stokes equations, describing conservation of mass, momentum and energy, in cylindrical coordinates are given by:

$$\frac{\partial U}{\partial t} + \frac{\partial F^c}{\partial x} + \frac{\partial G^c}{\partial r} = \frac{\partial F^d}{\partial x} + \frac{\partial G^d}{\partial r} + S^c + S^d \quad (1)$$

where  $x$  and  $r$  are the axial and radial coordinate respectively.  $U = (\rho, \rho u, \rho v, \rho E)^T$  is the vector of conservative variables,  $F^c$ ,  $F^d$  and  $G^c$ ,  $G^d$  are the convective and diffusive flux vectors in  $x$  and  $r$  direction and  $S^c$  and  $S^d$  are the convective and diffusive source term vectors. The following expressions hold for the convective fluxes:

$$F^c = \begin{pmatrix} \rho u \\ \rho u^2 + p \\ \rho uv \\ \rho uH \end{pmatrix} \quad G^c = \begin{pmatrix} \rho v \\ \rho uv \\ \rho v^2 + p \\ \rho vH \end{pmatrix} \quad (2)$$

while the diffusive fluxes are given by:

$$F^d = \begin{pmatrix} 0 \\ \tau_{xx} \\ \tau_{xr} \\ -q_x + \tau_{xx}u + \tau_{xr}v \end{pmatrix}, \quad G^d = \begin{pmatrix} 0 \\ \tau_{rx} \\ \tau_{rr} \\ -q_r + \tau_{rx}u + \tau_{rr}v \end{pmatrix} \quad (3)$$

and the source term vectors by:

$$S^c = \frac{-1}{r} \begin{pmatrix} \rho v \\ \rho uv \\ \rho v^2 \\ \rho vH \end{pmatrix}, \quad S^d = \frac{1}{r} \begin{pmatrix} 0 \\ \tau_{rx} \\ \tau_{rr} - \tau_{\Theta\Theta} \\ -q_r + \tau_{rx}u + \tau_{rr}v \end{pmatrix}. \quad (4)$$

In these expressions the symbols ( $\rho$ ,  $u$ ,  $v$ ,  $p$ ,  $\tau$  etc.) have their usual meaning and  $\Theta$  is the circumferential coordinate. The total enthalpy is given by  $H = E + p/\rho$  and the pressure by the perfect gas law:

$$p = \rho RT = (\gamma - 1) \rho \left[ E - \frac{1}{2} (u^2 + v^2) \right] \quad (5)$$

where  $\gamma$ , the specific heat ratio, is assumed to be constant and equal to 1.4 in this work. The expressions for the viscous stresses are standard, with the viscosity  $\mu$  given by Sutherland's law:

$$\mu = 1.458 \cdot 10^{-6} \frac{T^{\frac{3}{2}}}{T + 110.4}. \quad (6)$$

The heat flux is modeled according to Fourier's law:

$$q_x = -k \frac{\partial T}{\partial x} = -\frac{\mu}{Pr(\gamma - 1)} \frac{\partial a^2}{\partial x} \quad (7)$$

$$q_r = -k \frac{\partial T}{\partial r} = -\frac{\mu}{Pr(\gamma - 1)} \frac{\partial a^2}{\partial r}$$

where  $k = \mu \frac{c_p}{Pr}$  is the thermal conductivity,  $Pr$  the Prandtl number (taken constant and equal to 0.72),  $c_p$  the specific heat at constant pressure and  $a$  the speed of sound.

As discussed below, the convective part of the spatial operator,  $F^c$ ,  $G^c$  and  $S^c$ , is discretized using a compact multidimensional upwind discretization, while for the diffusive part,  $F^d$ ,  $G^d$  and  $S^d$ , the standard Galerkin Finite Element method is applied.

#### 3.1 Discretization of the Convective Terms

The quasilinear form of the convective part of equation (1) is given by

$$\frac{\partial U}{\partial t} + A_U \frac{\partial U}{\partial x} + B_U \frac{\partial U}{\partial r} = S^c. \quad (8)$$

Here  $A = \frac{\partial F^c}{\partial U}$  and  $B = \frac{\partial G^c}{\partial U}$  are the Jacobian matrices in  $x$  and  $r$  direction respectively. As the eigenvalues of  $A \cos \theta + B \sin \theta$ ,  $0 \leq \theta \leq 2\pi$ , are real, system (8) is hyperbolic and can have discontinuous solutions. To capture these discontinuities monotonically, a positive discretization technique for coupled hyperbolic systems must be developed. This is first explained for the scalar case and then for the system.

##### 3.1.1 Scalar Advection Equation

The governing equation for the scalar schemes is the two-dimensional linear advection equation

$$\frac{\partial u}{\partial t} + \vec{\lambda} \cdot \nabla u = 0 \quad (9)$$

with constant advection vector  $\vec{\lambda}$ . The discretization technique uses the integral form of equation (9) which is

$$\Phi = \iint_T \frac{\partial u}{\partial t} d\Omega = \oint_{\Gamma} u \vec{\lambda} \cdot \vec{n} d\Gamma, \quad (10)$$

where  $\Phi$  is called the cell residual,  $T$  is the triangular control volume,  $\Gamma$  the boundary of  $T$  and  $\vec{n}$  the inward normal. In principle, equation (10) is valid for any control volume, but from now on attention will be restricted to triangles, because only for these control volumes system schemes have been developed. Scalar multidimensional upwind schemes for quadrilaterals are discussed in [12, 7, 13]. As the unknowns are stored in the vertices of the triangle, see figure 1, the contour integral in the RHS of equation (10) can easily be approximated with the trapezium rule. The result after some manipu-

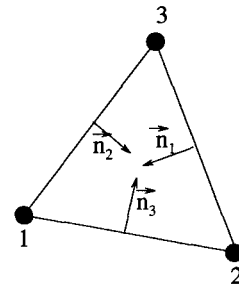


Fig. 1 : A generic triangle with its inner scaled normals

$$\Phi = - \sum_{i=1}^3 k_i u_i, \quad k_i = \frac{1}{2} \vec{\lambda} \cdot \vec{n}_i, \quad (11)$$

where  $\vec{n}_i$  are the inward scaled normals of the triangle, see figure 1. In a residual distribution scheme, fractions of the cell residual  $\Phi$  are sent to the cell vertices, which after assembling contributions from all cells leads to the nodal update, i.e.:

$$\frac{du_i}{dt} S_i = \sum_{k=1}^{\# \text{ cells}} \beta_k^i \Phi_k = \sum_{k=1}^{\# \text{ cells}} \Phi_k^i. \quad (12)$$

Here  $S_i$  is the area of the median dual cell around node  $i$  and  $\beta_k^i$  is the distribution coefficient of cell  $k$  to node  $i$ . The different schemes are distinguished in the way these distribution coefficients are determined. Below, three important schemes are discussed, the N-scheme, the LDA-scheme and the PSI-scheme.

**N-scheme :** The Narrow scheme (N-scheme, Roe, 1986) is the most optimal first order scheme in terms of cross wind diffusion. It is based on the quadrilateral finite difference scheme of Rice and Schnipke [3] and is derived in [4]. For the scalar case two possible configurations can be distinguished, the one-target case and the two-target case.

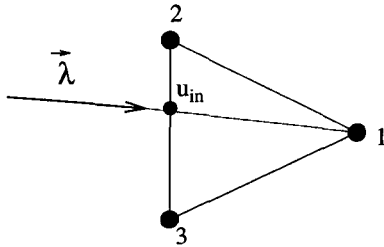


Fig. 2 : One-target case:  $\Phi_1^N = \Phi_T$ ,  $\Phi_2^N = \Phi_3^N = 0$

In the one-target case, see figure 2, only one of the parameters  $k_i$ , see equation (11), is positive and the whole cell residual is sent to this particular node. In the two-target case, see figure 3, two  $k_i$ 's are positive. The advection vector  $\vec{\lambda}$  is split into two components along the cell faces, see figure 3. The subresiduals sent to the two downstream nodes are then computed using the component of  $\vec{\lambda}$  which points towards the particular node.

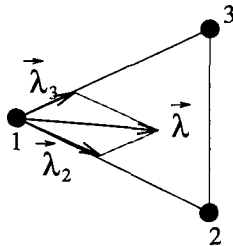


Fig. 3 : Two-target case:  $\Phi_1^N = 0$ ,  $\Phi_2^N = k_2(u_1 - u_2)$ ,  $\Phi_3^N = k_3(u_1 - u_3)$

Both situations can be caught in one general formula:

$$\Phi_i^N = \beta_i^N \Phi_T = k_i^+(u_{in} - u_i), \quad u_{in} = \frac{\sum k_i^- u_i}{\sum k_i^-} \quad (13)$$

where

$$k_i = \frac{1}{2} \vec{\lambda} \cdot \vec{n}_i, \quad k_i^+ = \max(0, k_i), \quad k_i^- = \min(0, k_i). \quad (14)$$

If the expression for  $u_{in}$  is plugged into equation (13) the result is:

$$\Phi_i^N = \sum_j \frac{k_i^+ k_j^-}{\sum_k \underbrace{k_k^-}_{\alpha_{ij}}} (u_j - u_i). \quad (15)$$

This is exactly the form which Jameson [14] uses for defining his Local Extremum Diminishing (LED) property. He

proves that for a positive scheme the coefficients  $\alpha_{ij}$  have to be non-negative. From the definitions (14) it is obvious that the coefficients  $\alpha_{ij}$  are non-negative, so the N-scheme is a positive scheme. From equation (13) and (15) it is clear that the N-scheme is also a linear scheme and therefore only first order accurate.

**LDA-scheme :** The Low Diffusion A (LDA) scheme is a linear second order scheme and consequently not positive. The distribution to the three nodes of the triangle is given by:

$$\Phi_i^{LDA} = \beta_i^{LDA} \Phi_T = \frac{k_i^+}{\sum_j k_j^+} \Phi_T \quad (16)$$

For problems without discontinuities this scheme can be used, giving very accurate results. However for the applications in this work it is absolutely inappropriate for the discretization of the hyperbolic part, because of the presence of strong shocks. It will be used for the discretization of the axisymmetric source term, see section 3.2.

**PSI- or Limited N-scheme :** To combine monotonic discontinuity capturing and second order accuracy the discretization must be non-linear, even for linear problems. One of the earlier attempts is the Positive Streamwise Invariant (PSI) scheme, for which the following formula holds:

$$\Phi_i^{PSI} = \beta_i^{PSI} \Phi_T = \frac{\max(0, \Phi_i^N \Phi_T)}{\sum_j \max(0, \Phi_j^N \Phi_T)} \Phi_T. \quad (17)$$

More recently Sidilkover and Roe [15] observed that a non-linear positive scheme can be obtained from the N-scheme by applying a limiter function to the distribution coefficients  $\beta_i^N$ , i.e.:

$$\beta_i^{\lim} = \Psi(\beta_i^N), \quad (18)$$

where  $\Psi$  is a limiter function with the following properties

- $\Psi(r) + \Psi(1-r) = 1$
- $\frac{\Psi(r)}{r} \geq 0$
- $\Psi(r) \leq M$ ,  $r \rightarrow \infty$ ,  $M$  bounded

If the minmod limiter is chosen,  $\Psi(r) = \max(0, \min(r, 1))$ , the result is exactly the same as the PSI-scheme (17). In case there are more than two targets the expression for the minmod limiter generalizes to

$$\beta_i^{\lim} = \frac{\max(0, \beta_i^N)}{\sum_j \max(0, \beta_j^N)}. \quad (19)$$

This generalization is needed for scalar advection problems in three space dimensions and also for the non-linear system schemes.

### 3.1.2 Coupled Hyperbolic System

The key to a robust discretization for hypersonic problems developed in this project, was the extension of the scalar schemes to hyperbolic systems with non-commuting Jacobians [16]. Consider the system of equations in two space dimensions given by

$$\frac{\partial W}{\partial t} + A_W \frac{\partial W}{\partial x} + B_W \frac{\partial W}{\partial y} = 0, \quad (20)$$

where  $A_W$  and  $B_W$  are the Jacobian matrices in  $x$ - and  $y$ -direction respectively. The extension of the scalar parameters  $k_i$  are the matrices  $K_i$ :

$$K_i = \frac{1}{2} (A_W \tilde{l}_x + B_W \tilde{l}_y) \cdot \tilde{n}_i = R_i \Lambda_i L_i, \quad (21)$$

where the columns of  $R_i$  contain the right eigenvectors,  $\Lambda_i$  is a diagonal matrix of the eigenvalues and  $L_i = R_i^{-1}$ . As system (20) is hyperbolic, the matrices  $R_i$ ,  $\Lambda_i$  and  $L_i$  will be real. In analogy to the scalar case, the matrices  $K_i^+$  and  $K_i^-$  have been defined. They are given by

$$K_i^+ = R_i \Lambda_i^+ L_i, \quad K_i^- = R_i \Lambda_i^- L_i. \quad (22)$$

Here  $\Lambda_i^+$  contains the positive and  $\Lambda_i^-$  the negative eigenvalues,  $\Lambda^\pm = \frac{\Lambda \pm |\Lambda|}{2}$ . With these definitions the linear scalar schemes, N-scheme and LDA-scheme, can easily be extended to systems. For the non-linear PSI-scheme there are several possibilities, but unfortunately none of them works satisfactory yet.

**System N-scheme :** The residual vector sent to node  $i$  for the system N-scheme is given by

$$\Phi_i^N = \beta_i^N \Phi_T = K_i^+ (W_{in} - W_i), \quad (23)$$

where  $\beta_i^N$  is now a matrix and the state  $W_{in}$  is defined as

$$W_{in} = \left( \sum_j K_j^- \right)^{-1} \sum_j K_j^- W_j. \quad (24)$$

It can be shown [17] that this scheme is positive and energy stable.

**System LDA-scheme :** The distribution to the nodes of the system LDA-scheme is

$$\Phi_i^{LDA} = \beta_i^{LDA} \Phi_T = K_i^+ \left( \sum_j K_j^+ \right)^{-1} \Phi_T. \quad (25)$$

Again this is a linear second order scheme, so it is not positive.

**System PSI-scheme :** The general scalar limiting formula (19) can be extended to matrices. The result is:

$$\beta_i^{\text{lim}} = \left( \sum_j \beta_j^{N+} \right)^{-1} \beta_i^{N+}, \quad (26)$$

where  $\beta_i^{N+}$  is the matrix with only the positive eigenvalues of  $\beta_i^N$ . The problem is that  $\beta_i^N$  is not uniquely defined, because for a system with  $n$  coupled equations equation (23) only gives  $n$  equations for  $n^2$  elements of  $\beta_i^N$ . A first attempt is a diagonal matrix, but it can be shown that this expression is not correct in the one-dimensional limit. Therefore the following is done. If it is possible to decouple system (20), i.e. the matrices  $R_i$  are all the same, the expression for the  $\beta_i^N$  is easily determined from a transformation to characteristic variables and back. The result is:

$$\beta_i^N = R_i D_i L_i, \quad D_i = \text{diag}(d_{i1}, d_{i2}, \dots, d_{in}), \quad (27)$$

where the diagonal elements  $d_{ik}$  of  $D_i$  are given by:

$$d_{ik} = \frac{l_{ik} \cdot \Phi_i^N}{l_{ik} \cdot \Phi_T}. \quad (28)$$

Here  $l_{ik}$  is the  $k^{\text{th}}$  row of  $L_i$ . For a general non-commuting system equations (27) and (28) can be applied as well, but the  $\beta_i^N$ 's do not sum up to  $I$  any more. This can be overcome by introducing the following form for  $\beta_i^N$ :

$$\beta_i^N = R_i D_i L_i + \beta_i^{\text{corr}}. \quad (29)$$

The  $\beta_i^{\text{corr}}$  must satisfy the following requirements:

- $\beta_i^{\text{corr}} \Phi_T = 0, i = 1, 2, 3$
- $\sum_j \beta_j^{\text{corr}} = I - \sum_j R_j D_j L_j$

These equations are not sufficient to determine  $\beta_i^{\text{corr}}$  completely, but they are used as constraints in a minimization problem for the  $L2$  norm of the elements of  $\beta_i^{\text{corr}}$ . Because of symmetry reasons the solution of this problem is very simple. The results is:

$$\beta_i^N = R_i D_i L_i + \frac{1}{3} \left( I - \sum_j R_j D_j L_j \right) \quad (30)$$

It can be proven that if the system (20) is symmetrizable (as is the case for the Euler equations), the eigenvalues of  $\beta_i^N$  are real. The form (30) obeys the one-dimensional limit, it returns to the scalar scheme if the system is (partially) decoupled, it gives the correct expression if a system is diagonalizable and it is continuous. In practice however, it suffers from severe convergence problems, although the results are monotonic. Furthermore the eigenvalues and eigenvectors of  $\beta_i^N$  are needed to apply the limiter formula (26). As this eigenvector decomposition cannot be done analytically, it is done numerically with the EISPACK routine rg. This is a very stable, but also expensive routine, which makes the scheme quite costly. The convergence problems with the limited matrix scheme (see section 5) show that the optimal form of  $\beta_i^N$  has not been found yet and this is a topic of current research.

### 3.2 Discretization of the Source Term

In the quasi-linear form of the axisymmetric Euler equations (8) there is the source term  $S^c$  which must be distributed. As the method described in the previous section uses the integral form of the equations,  $S^c$  is integrated over a triangle with a numerical integration rule and distributed to the nodes. To avoid the singularity at  $r = 0$ , see equation (4), a one point integration rule in the centroid is applied and the system LDA-scheme is used for the distribution. So the overall discretization becomes:

$$\Phi_i = \Phi_{\text{convective}} + K_i^+ \left( \sum_j K_j^+ \right)^{-1} \Omega_T \bar{S}^c, \quad (31)$$

where  $\Phi_{\text{convective}}$  is the discretization of  $A_U \frac{\partial U}{\partial x} + B_U \frac{\partial U}{\partial r}$ ,  $\Omega_T$  is the area of the triangle and  $\bar{S}^c$  is computed in the centroid using linear variation of the Roe parameter vector  $Z$ , see section 3.3. Although the source term is distributed with a non-monotonic scheme this does not change the monotonicity of the overall discretization, for  $S^c$  does not contain any derivatives.

### 3.3 Conservative Linearization

The distribution schemes are based on the quasi-linear form of the equations. To capture the discontinuities with the correct jump relations the conservative form must be

solved. The link between the two formulations is the conservative linearization and a detailed description can be found in [18]. A more general approach, with the same result for triangles and tetrahedra, is given here. If the convective fluxes of the conservative form (1) and the corresponding terms of the quasi-linear form (8) are integrated over a control volume, with the assumption of constant Jacobian matrices  $A_V$  and  $B_V$  per cell, and both expressions are required to be equal, the following conservation constraint is obtained:

$$\oint_{\Gamma} (F^c \bar{l}_x + G^c \bar{l}_r) \cdot \bar{n} d\Gamma \equiv \oint_{\Gamma} (A_V(\bar{V}) \bar{l}_x + B_V(\bar{V}) \bar{l}_r) \cdot \bar{n} d\Gamma. \quad (32)$$

Here  $V$  is an arbitrary set of independent variables,  $\bar{V}$  a cell averaged state of  $V$ ,  $\Gamma$  the edge of the control volume and  $\bar{n}$  the unit inward or outward normal. The Jacobian matrices  $A_V$  and  $B_V$  are given by:

$$A_V = \frac{\partial F^c}{\partial V}, \quad B_V = \frac{\partial G^c}{\partial V}. \quad (33)$$

The degrees of freedom are the choice of the set of variables  $V$  and the integration rule of the fluxes in the LHS of equation (32). Because of the distribution schemes, the contour integral in the RHS of this equation must be integrated with the trapezium rule. This approximation is the same as assuming that the set of variables  $V$  varies linearly along the edges of the control volume.

For the Euler equations the Roe parameter vector  $Z$  turns out to be a good choice for the variables  $V$ . For 2D and axisymmetric problems  $Z$  is defined as

$$Z = \begin{pmatrix} \sqrt{\rho} \\ \sqrt{\rho} u \\ \sqrt{\rho} v \\ \sqrt{\rho} H \end{pmatrix}. \quad (34)$$

Because of this particular choice the fluxes  $F^c$  and  $G^c$  are quadratic expressions in  $Z$  and therefore the Jacobian matrices  $A_Z$  and  $B_Z$  are linear in the elements of  $Z$ . It is this property that makes the linearization

$$\bar{Z} = \frac{1}{3} (Z_1 + Z_2 + Z_3), \quad (35)$$

where the subscripts refer to the numbers of the vertices, conservative for triangles in combination with the Simpson integration rule for the fluxes. It should be noted that for a general conservation law it might be difficult to find a simple expression for the cell averaged state.

### 3.4 Discretization of the Diffusive Terms

For the discretization of the diffusive terms two approaches can be considered [10]: (1) a central (Galerkin) discretization and (2) a residual-based approach. The latter is more consistent with the discretization of the convective terms, but it requires a larger stencil than the former, which uses the same stencil as the convective part. As the narrowness of the stencil is very important for both the implicit and parallel algorithm, the standard Galerkin Finite Element discretization for second order diffusive terms was used in this work.

## 4 THE PARALLEL IMPLICIT TEMPORAL DISCRETIZATION

In this section a parallel implicit algorithm is explained for the integration in time of the ordinary set of differential equations

$$\frac{dU}{dt} = RES(U), \quad (36)$$

which results from the spatial discretization. In equation (36) the mass matrix is lumped and therefore only first order accuracy in time can be achieved, even with higher order methods. For our purposes this is no problem, because we are only interested in steady state problems. If time accurate problems are considered this mass matrix should be taken into account, which gives rise to a linear system of equations even for an explicit time integrator. First the sequential algorithm will be explained, section 4.1, then the parallelization technique will be discussed in section 4.2.

### 4.1 The Sequential Algorithm

As time accuracy is not important, the backward Euler method is used to integrate equation (36). This results in the non-linear system for the state on time  $t = t^{n+1}$

$$\frac{U^{n+1} - U^n}{\Delta t} = RES(U^{n+1}), \quad (37)$$

where  $\Delta t$  indicates the local time step. The RHS of equation (37) is approximated using a Newton linearization, which leads to the following linear system for the update  $\Delta U = U^{n+1} - U^n$ :

$$\underbrace{\left[ \frac{I}{\Delta t} - \frac{\partial RES(U^n)}{\partial U^n} \right]}_{J_F} \Delta U = RES(U^n). \quad (38)$$

Here  $J_F$  is the augmented Jacobian. This loop is repeated in time until convergence. For a computationally complex residual expression, as is the case for the spatial discretization technique of section 3, computing the Jacobian matrix  $\frac{\partial RES}{\partial U}$  analytically becomes untractable. An alternative to the analytic computation is a numerical evaluation of the Jacobian. Truncating the Taylor expansion of  $RES_i(U_j + \epsilon_m l_m)$  (the nodal residual at node  $i$  with the  $m^{\text{th}}$  component of  $U$  at node  $j$  perturbed by a small quantity  $\epsilon_m$ ) to the first order terms, one has:

$$\left[ \frac{\partial RES_i(U)}{\partial U_j} \right]_m \simeq \frac{RES_i(U_j + \epsilon_m l_m) - RES_i(U_j)}{\epsilon_m}. \quad (39)$$

Because of the compact stencil of the discretization, this numerical computation of the Jacobian requires only 12 additional evaluations of the cell residuals [19]. The convergence depends on the value of  $\epsilon_m$  and the following expression has been used for the derivative with respect to the  $m^{\text{th}}$  component of  $U$ :

$$\epsilon_m = \epsilon \text{sign}(U_m) \max(|U_m|, 10^{-3}), \quad (40)$$

where  $\text{sign}(U_m)$  is 1 for positive and -1 for negative  $U_m$ . The constant  $\epsilon$  is a user specified value and is of the order  $10^{-8}$  to  $10^{-10}$ . Because of these small values of the disturbances it is important that all computations are done in double precision. It was also found necessary to use the dimensionless form of the equations to minimize errors caused by finite arithmetic.

The linear system (38) is iteratively solved with GMRES [20] with left preconditioning:

$$\tilde{J}_F^{-1} J_F \Delta U = \tilde{J}_F^{-1} RES(U^n) \quad (41)$$

where  $\tilde{J}_F$  is the preconditioning matrix. All the obtained results have been computed using a block incomplete factorization of  $J_F$  with zero fill in (ILU(0)) as preconditioner (with block size  $4 \times 4$ ).



## 4.2 The Parallel Algorithm

The parallel implicit algorithm consists of three parts: (1) domain decomposition, (2) parallel preconditioners to solve the linear system (41), and (3) the handling of the communication, section 4.2.3.

### 4.2.1 Domain Decomposition

As we are dealing with unstructured grids, the grid is decomposed in as many subdomains as there are processors. At the moment Chaco<sup>1</sup> [21] is used for this purpose (with the limitation that the number of subdomains must be  $2^n$ ). It uses a connected graph made of vertices to be spread over a set of separated subdomains. In the vertex oriented decomposition (VOD) case, see figure 4, the vertices of the graph are the vertices of the grid. As a result,

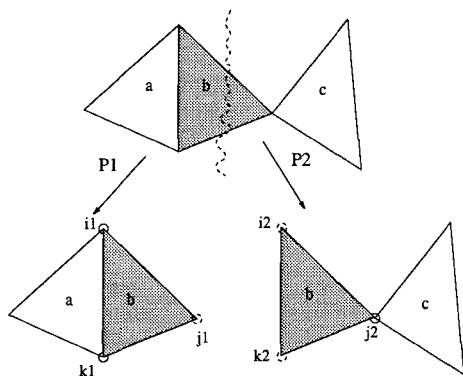


Fig. 4 : VOD, Close-up of the overlapping stripe and respective mapping onto processors, internal (solid circles) and external (dashed circles) nodes.

the separation between neighbouring partitions occurs at the edge-level. If overlapping of neighbouring partitions is performed (effectively half a layer of ghost cells, for cell  $b$  is stored on two processors), any computational task can be carried out in the same way as in the sequential code, provided that nodes on the outer boundaries of each domain have been properly updated.

A closer look at the three cells  $a$ ,  $b$  and  $c$  of figure 4 shows two different types of vertices in the overlapped stripe of cells:

Nodes  $i_1$ ,  $k_1$  in partition 1 and node  $j_2$  in partition 2 are internal nodes. Since they are surrounded, in each of their partition, by their complete set of triangles, the nodal residual as well as all entries of the Jacobian matrix are correctly computed. This means that the matrix vector operations, needed in the GMRES part, will be consistent in these nodes.

Node  $j_1$  in partition 1 and nodes  $i_2$ ,  $k_2$  in partition 2 are external nodes. Since their set of surrounding triangles is incomplete (with respect to the original grid), the nodal residuals and the Jacobian matrix are incorrect. Therefore after every iteration the state vector in these nodes are overwritten by the values of their corresponding counterparts on a different processor. This of course requires communication between the processors.

### 4.2.2 Parallel Preconditioners

Most of the operations in the spatial and temporal discretization (residual and Jacobian evaluations, matrix vector operations in GMRES) require a compact computational molecule and lend themselves for parallelization.

<sup>1</sup> with spectral partitioning (Lanczos method with selective orthogonalization at left end only), no local refinement.

Only the inversion of the ILU(0) preconditioner  $\tilde{J}_F$  is an inherently recursive and thus a sequential operation (a lower and an upper sweep across the vertices). However this preconditioner is only used in equation (41) to speed up the convergence of the GMRES and it is allowed to use different preconditioners. One of the advantages of the VOD partitioning over the element oriented decomposition (EOD), separation between subdomains occurs at the node-level) lies in the construction of a parallel preconditioner. This can be obtained by first ignoring the interdomain connections and then performing an ILU(0) factorization of each submatrix corresponding to a subdomain. By neglecting the interdomain connections the efficiency of the preconditioner is expected to decrease as the number of processors (subdomains) increases. However the linear system (41) itself is solved over the entire domain and the convergence in number of Newton iterations is independent of the number of processors if this system is solved to machine accuracy (which takes more GMRES iterations for an increasing number of subdomains). However in practice equation (41) is not solved to machine accuracy and the parallel convergence histories will (only slightly) differ from the sequential one.

### 4.2.3 Communications

The message passing library MPI [22] is used to handle the communications. As this library runs on most of the parallel machines available, the code is highly portable, e.g. it has been used on a Cray T3D of the University of Edinburgh [23], on a DEC- $\alpha$  cluster of the VKI and on the IBM SP2 of the University of Leuven. The underlying data structure information consists of the arrays `Comm_Send` and `Comm_Recv`. The first array lists the (local) internal node numbers whose values have to be sent to other partitions while the second one lists the (local) external nodes whose values must be overwritten. For as long as the array `Comm_send(P,i)` in partition  $Q$  mirrors exactly (as for the ordering (i)) the array `Comm_Recv(Q,i)` in partition  $P$ , and conversely, there is no need to keep track of mapping information from/to local numbering in a partition to/from global ordering in the original mesh. Communication is achieved through non-blocking send primitives `MPI_Isend()` and blocking receive primitives `MPI_Recv()`.

## 5 NUMERICAL RESULTS

In this section results are presented for the flow around a hyperboloid flare under three different free stream conditions. These testcases are the RWG condition 1 case, the H2K case and the LTB case, proposed on the occasion of two recent ESA workshops on hypersonic flow computation, see [24, 25].

Detailed comparisons of the solutions with a reference standard finite volume solver on quadrilateral grids (the VKI Multiblock code VKI-MB) are given. The results with the reference solver VKI-MB were thoroughly compared with other solvers during the ESA workshops and turned out to be of very high quality [1, 2]. Therefore the new code can be considered to be well validated.

Convergence histories and CPU times on four and eight processors are shown. Newton convergence is obtained for the first order scheme, while robustness problems exist with the second order scheme (as with the standard solver), giving a reduction of the residual of about two orders starting from the first order solution. Speedups are given for the first order scheme, as it is the worst case for speedups: the communication is the same as for the second order scheme, while the computation time is

$M_\infty$	6.73
$T_\infty$	59.65 K
$T_w$	310 K
$Re_\infty/m$	$3.50 \cdot 10^6/m$
$L$	0.05924 m

Table 1 : Flow conditions for the RWG condition 1 test case

lower.

In all cases the grid is a  $400 \times 100$  triangulated structured grid, taken from [2]. The stretching in the boundary layer of the H2K grid is lower than for the other two cases, which use the same grid. A coarsened version is shown in figure 5. In the decomposition of the grid into 4 and 8 subdomains, figures 6 and 7, it is seen that CHACO partially cuts parallel to the solid wall in the boundary layer. This might cause problems if interdomain connections are neglected, but for the solver presented in this work this is not the case, because these connections are only neglected in the preconditioner.

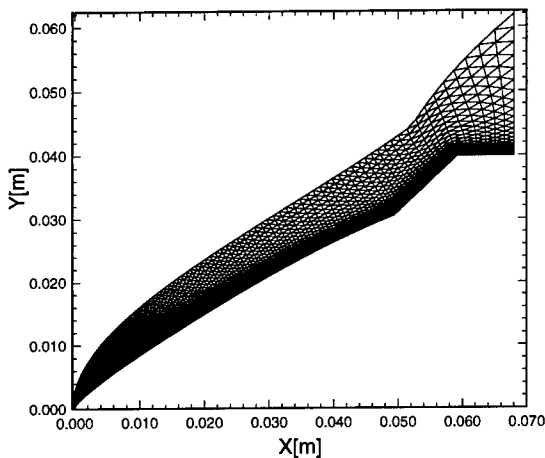


Fig. 5 : Triangulated  $100 \times 25$  grid (Real grid is  $400 \times 100$ ).



Fig. 6 : Decomposition in four subdomains ( $400 \times 100$  meshpoints).

### 5.1 RWG Condition 1 Test Case

This test case is the low Reynolds number case for the hyperboloid flare of the MSTP Workshop 1996 [25]. The flow conditions are given in table 1. A robust procedure for doing the computation is the following : First, an

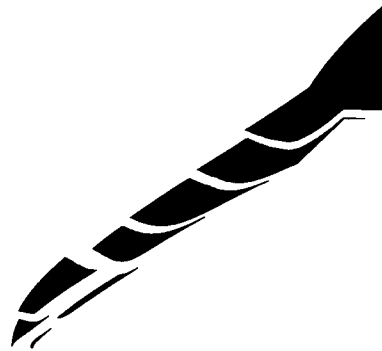


Fig. 7 : Decomposition in eight subdomains ( $400 \times 100$  meshpoints).

initial solution using grid sequencing is created : starting from free stream values imposed on all meshpoints on the  $200 \times 50$  mesh, 1500 to 2500 (depending on the testcase) forward Euler explicit time steps with a CFL number of 0.7 are carried out, such that the bow shock is in position, but the solution is far from converged. Then the implicit solver is started with an increasing CFL number per iteration and the solution is interpolated to the fine mesh ( $400 \times 100$ ). From the converged first order solution on the finest mesh (obtained with the implicit solver), the second order implicit solver is started, again with an increasing CFL strategy. The CFL strategy is defined as follows :

$$CFL^{n+1} = \max(\alpha CFL^n, CFL_{\max}). \quad (42)$$

The values of  $CFL^1$ ,  $CFL_{\max}$  and  $\alpha$  are parameters which must be selected by the user. In all cases we used:  $CFL^1 = 1$ ,  $CFL_{\max} = 10^6$  and  $\alpha = 2$  for the first order scheme and  $CFL^1 = 1$ ,  $CFL_{\max} = 1000$  and  $\alpha = 1.2$  for the second order scheme. Furthermore the Jacobians of the first order scheme are used for the second order scheme, because these are much better conditioned (and much cheaper to compute). The stopping criterion for the GMRES solver was either a residual drop of six orders of magnitude, or the maximum Krylov subspace dimension (set to 30 in all calculations), whichever occurred first. The Mach number isolines and  $C_p$  isolines of the second order PSI scheme can be found in the figures 8 to 9. It is clear that the Mach number is smooth, but the pressure solution shows some wiggles. The probable cause of this is the distribution of the axis-symmetric source terms. A comparison of the first order N- and second order PSI-scheme with the standard Finite Volume solver (the VKI-MB code, based on Coquel and Liou's Hybrid solver in combination with the Minmod limiter) on the quadrilateral grid is given in the figures 10 and 11, both for the skin friction coefficient and the Stanton number distribution along the body as a function of the axial coordinate. The solutions of the second order PSI scheme compare very well with the ones of the standard solver, but the first order N scheme underpredicts the separation region (which could be expected of course).

The convergence history for the first order scheme on four and eight processors is shown in figure 12 both in terms of number of iterations and CPU-time. It is clear that full Newton convergence is reached after an initial phase of 15 iterations (20 iterations in total), and that the convergence behaviour is virtually independent (at least for four and eight processors) of the number of subdomains. A speed up of about 1.95 for the computation on eight processors is obtained compared to the computation on four processors. The ideal speed up of 2 is not reached be-

cause of the relative increase in communication time for an increasing number of processors and load imbalance: Although the subdomains have almost the same number of cells, the treatment of the boundary conditions is not taken into account in the decomposition. As the centerline boundary with its layer of ghost cells is computationally more expensive than the other boundary conditions, the subdomain which shares the centerline has more work to do per iteration than the other subdomains. The percentage of this extra work increases when the number of processors increases (size of the subdomains decrease) if the centerline boundary is still in one subdomain as in our case. The convergence history for the second order scheme (on four processors, with first order Jacobians and the first order solution as initial solution, with the increasing CFL strategy) is very irregular and stalls after two orders of magnitude, figure 13 .. Note that the number of iterations (100) is about five times as high as for the first order scheme, before the plateau is reached. Figure 13 shows the total CPU-time on 4 processors, needed to obtain the second order solution starting from a uniform flowfield on the  $200 \times 50$  mesh. This CPU time is about 2.5 hours.

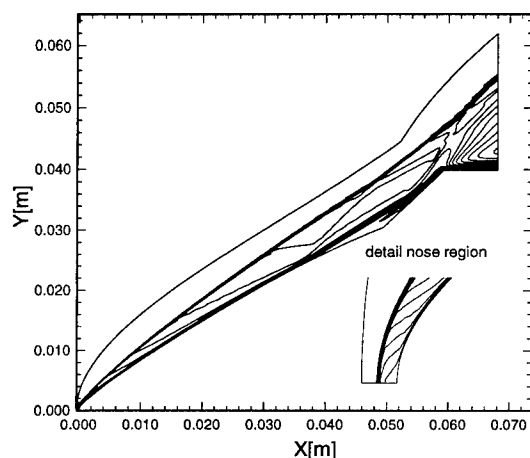


Fig. 8 : Mach number isolines for the RWG condition 1 test case for the second order PSI-scheme. Min. = 0.0, Max. = 6.73, Step = 0.2

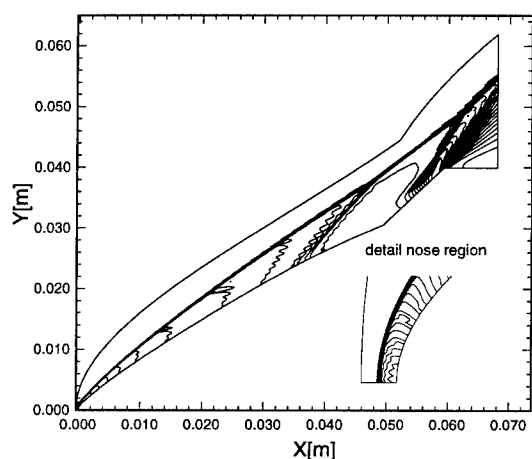


Fig. 9 :  $C_p$  isolines for the RWG condition 1 test case for the second order PSI-scheme. Min. = 0.0, Max. = 1.79, Step = 0.05

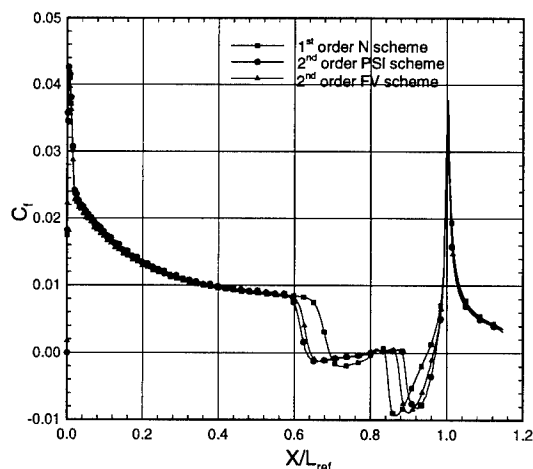


Fig. 10 : Skin friction coefficients for the RWG condition 1 test case for 3 different solutions

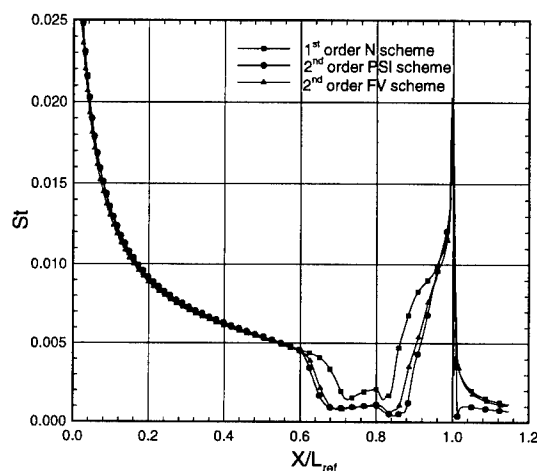


Fig. 11 : Stanton numbers for the RWG condition 1 test case for 3 different solutions

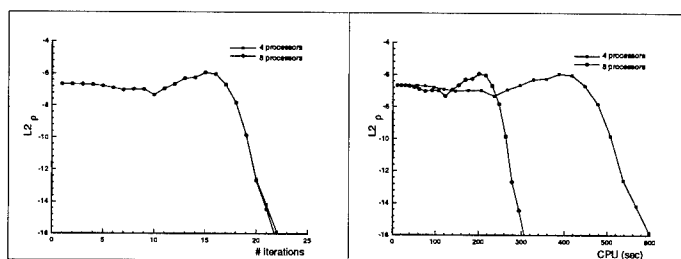


Fig. 12 :  $L_2$  norm of the density residual of the first order N scheme as a function of the number of iterations and the CPU time on four and eight processors for the RWG condition 1 test case

## 5.2 H2K Test Case

The H2K test case is the low Reynolds number condition of the 3<sup>rd</sup> test case of the 4<sup>th</sup> EHVD workshop [24]. The flow conditions are given in table 2. The creation of the initial solution, the CFL strategy and the parameters for the GMRES are exactly the same as for the previous test case, showing the robustness of the approach. The results can be found in the figures 14 to 21. Due to the lower Reynolds number the bow shock is smeared over 8 cells, figure 14 and 15, and the pressure isolines for

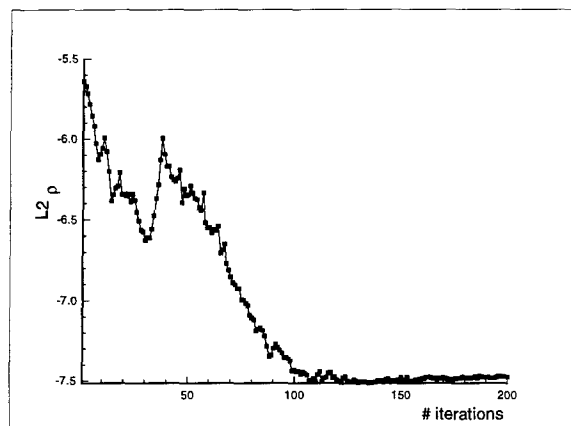


Fig. 13 : L2 norm of the density residual of the second order PSI scheme as a function of the number of iterations on four processors for the RWG condition 1 test case

$M_\infty$	8.70
$T_\infty$	72.69 K
$T_w$	310 K
$Re_\infty/m$	$6.25 \cdot 10^5/m$
$L$	0.05924 m

Table 2 : Flow conditions for the H2K test case

the second order scheme, figure 17, are much smoother than in the previous case. Only in the nose region some wiggles can be seen.

Comparison of the skin friction coefficient, figure 18, and Stanton number, figure 19, with a standard solver on quadrilaterals again show that the solutions of both second order schemes are almost identical. The solution of the first order N scheme is much closer to the second order solutions than for the other two cases.

The speed up of the computation on eight processors compared to four is again about 1.95, figure 20a, as explained before (the decompositions of the grids are identical). The convergence of the second order scheme is seen in figure 21 and a comparison with the convergence histories of the second order scheme of the previous and next test case, figures 13 and 26, shows that this test case is much easier to converge than the other two: only 60 iterations are needed to reach the plateau (compared to 100 in the previous test case). The reason for this is the much lower Reynolds number in the H2K conditions. The total CPU time for this computation is less than 2 hours on the 4 processor SP2, figure 20b.

### 5.3 LTB Test Case

The LTB test case is the high Reynolds number condition of the 3<sup>rd</sup> test case of the 4<sup>th</sup> EHVDB workshop [24]. The free stream conditions can be found in table 3. Again the initial solution was created in the same way as before and nothing was changed for the CFL strategy and GMRES parameters.

Mach number isolines for the second order solution are plotted in figure 22. Skin friction coefficients, figure 23, and Stanton numbers, figure 24, compare well, the convergence in number of iterations is almost the same for four and eight processors, figure 25, the speed up is again about 1.95, figure 25, and the second order scheme (with first order Jacobians) converges 2 orders of magnitude

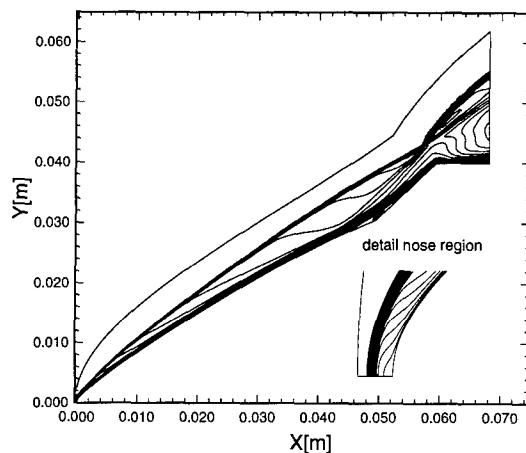


Fig. 14 : Mach number isolines for the H2K test case for the first order N scheme.  
Min. = 0.0, Max. = 8.70, Step = 0.2

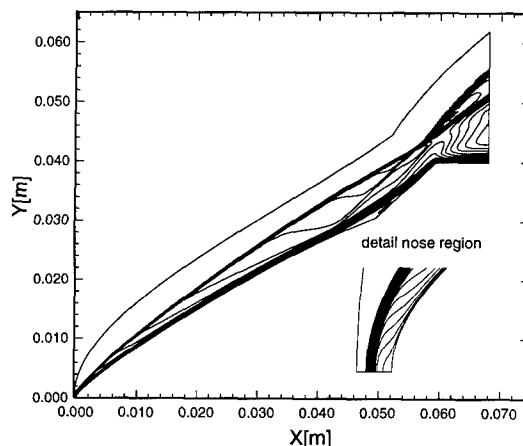


Fig. 15 : Mach number isolines for the H2K test case for the second order PSI scheme. Min. = 0.0, Max. = 8.70, Step = 0.2

from the restart of the first order solution, see figure 26. This time, about 200 iterations are needed to reach the plateau at 2 orders of residual reduction. The total CPU time on 4 processors was about 2.5 hours, figure 25b.

## 6 CONCLUSIONS AND FUTURE WORK

An efficient and robust parallel flow solver for axisymmetric hypersonic flows has been developed, capable of producing accurate results for typical configurations in about 1 to 1.5 hours CPU time on an 8-processor IBM SP2, a commonly available departmental computer. The spatial discretization uses newly developed multidimensional monotonic matrix distribution schemes on a triangular grid for the inviscid part of the equations and the Galerkin finite element method for the viscous fluxes. This leads to a non-linear set of algebraic equations which is iteratively solved by means of a backward Euler time integration method in combination with block-ILU preconditioned GMRES for the linear systems. Because of the complexity of the spatial discretization the neces-

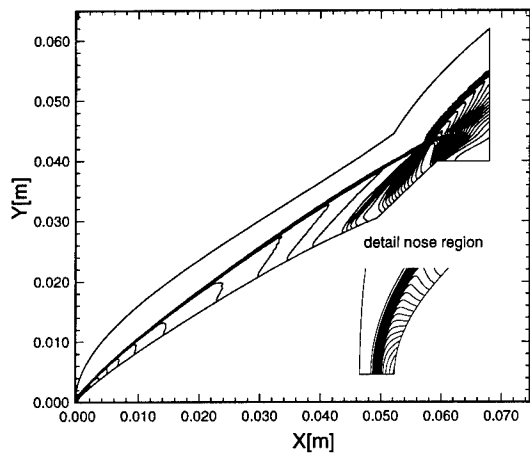


Fig. 16 : Cp isolines for the H2K test case for the first order N scheme. Min. = 0.0, Max. = 1.83, Step = 0.05

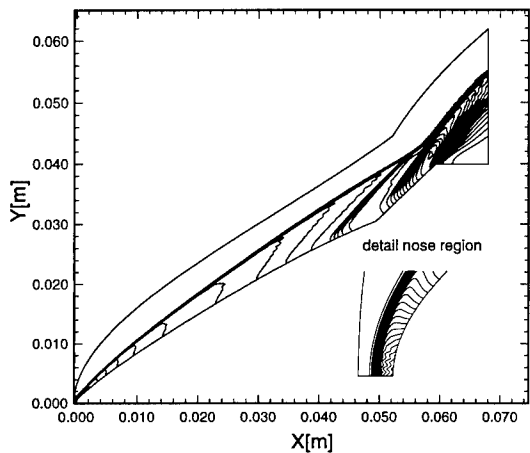


Fig. 17 : Cp isolines for the H2K test case for the second order PSI scheme. Min. = 0.0, Max. = 1.84, Step = 0.05

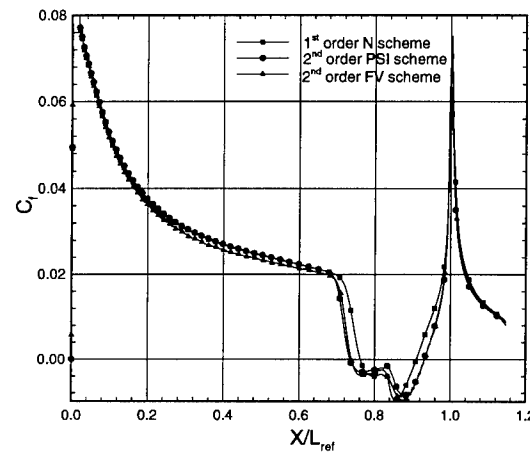


Fig. 18 : Skin friction coefficients for the H2K test case for 3 different solutions

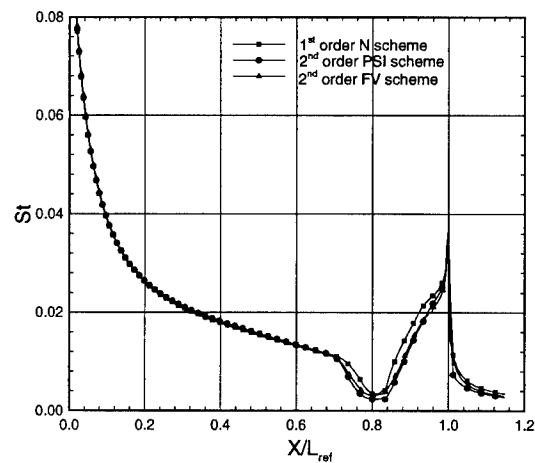


Fig. 19 : Stanton numbers for the H2K test case for 3 different solutions

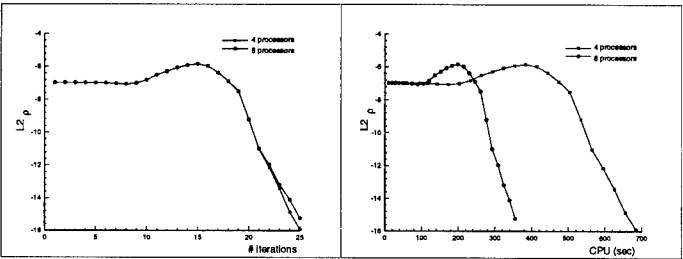


Fig. 20 : L2 norm of the density residual of the first order N scheme as a function of the number of iterations and the CPU time on four and eight processors for the H2K test case

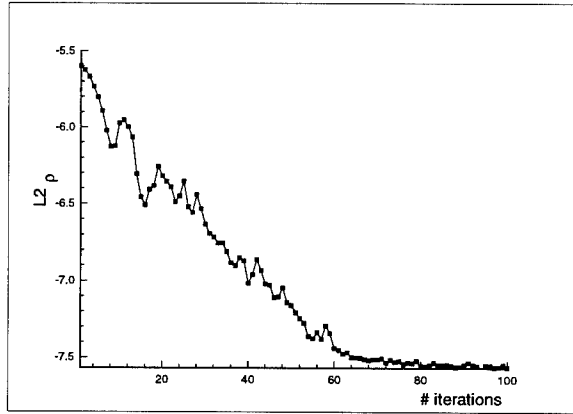


Fig. 21 : L2 norm of the density residual of the second order PSI scheme as a function of the number of iterations on four processors for the H2K test case

sary Jacobian matrix is computed by a finite difference method at the cost of 12 cell-residual evaluations, due to the compactness of the spatial discretization. In order to achieve parallelization, the computational domain is divided into a set of subdomains, mapped onto the processors. The problem is still solved across all partitions and irrespective of the number of subdomains, the solution is exactly the same as the one of the sequential algorithm. Vertex-oriented decomposition (VOD) naturally leads to a parallel preconditioner, where interdo-

$M_\infty$	6.83
$T_\infty$	67.765 K
$T_w$	310 K
$Re_\infty/m$	$7.0 \cdot 10^6/m$
$L$	0.05924 m

Table 3 : Flow conditions for the LTB test case

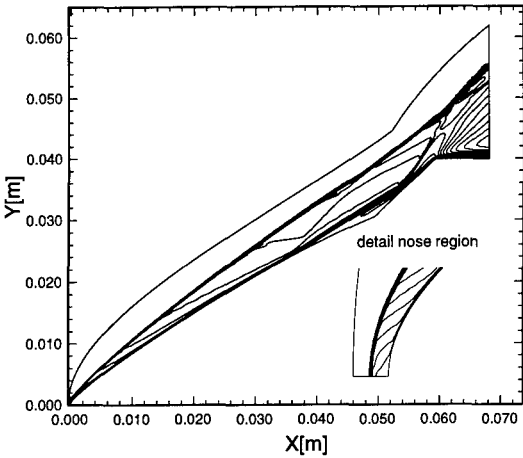


Fig. 22 : Mach number isolines for the LTB test case for the second order PSI scheme. Min. = 0.0, Max. = 6.83, Step = 0.2

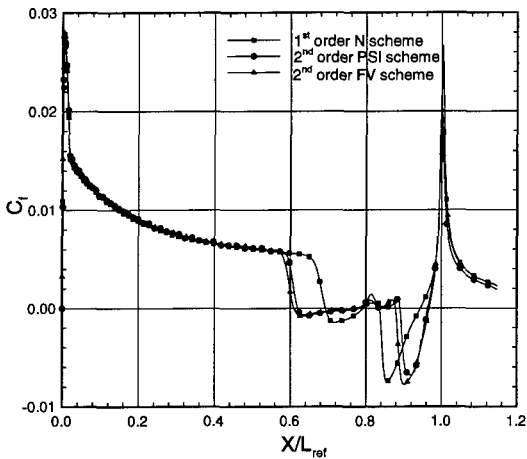


Fig. 23 : Skin friction coefficients for the LTB test case for 3 different solutions

main connections are ignored. However it requires for computational efficiency an effective overlap of half a cell with neighbouring domains. As the number of subdomains increases, the preconditioner deteriorates, because of the neglect of the interdomain connections and it can be expected that the convergence degrades with increasing number of processors. However, in the results presented in this work this has not been observed, but only a maximum of eight processors have been used. The results of the first order scheme are better than standard dimensionally split upwind finite volume schemes on quadrilaterals. The results of the second order scheme are comparable, although it is clear that the optimal formulation of the non-linear matrix scheme has not been found yet. The one used in this work suffers from robust-

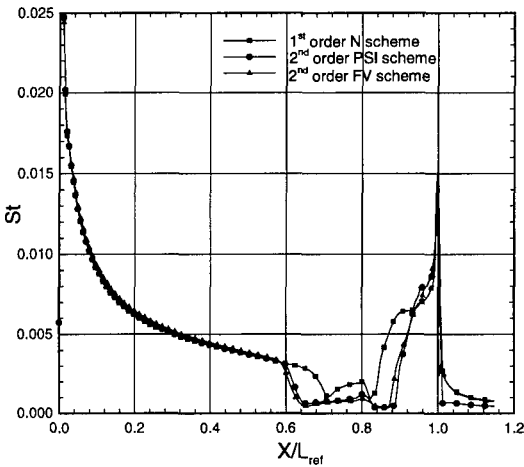


Fig. 24 : Stanton numbers for the LTB test case for 3 different solutions

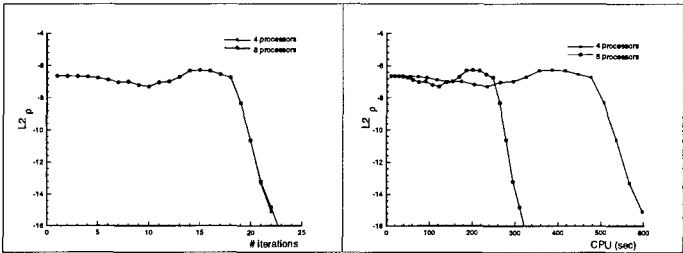


Fig. 25 : L2 norm of the density residual of the first order N scheme as a function of the number of iterations and the CPU time on four and eight processors for the LTB test case

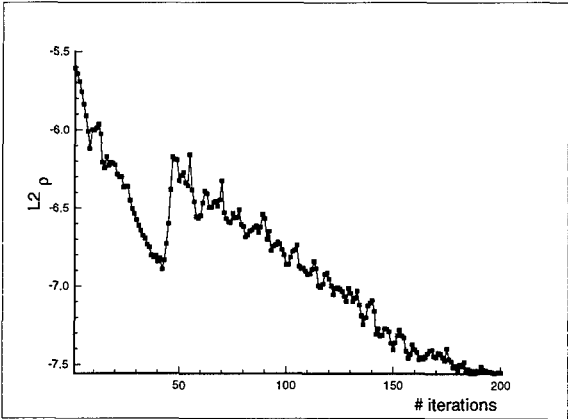


Fig. 26 : L2 norm of the density residual of the second order PSI scheme as a function of the number of iterations on four processors for the LTB test case

ness problems and only converges two orders of magnitude from a restart from the first order solution. Also the corresponding Jacobian matrix is ill-conditioned and consequently the Jacobian of the first order scheme had to be used in the implicit time integrator. This inconsistency does not allow Newton convergence for the second order scheme. Also the relatively simple CFL strategy used in this work is capable of improvement, e.g. one could think of relating it to the norm of the residuals or to the change in number of supersonic nodes (triggering the CFL number as soon as the bowshock is in position).

The extension of the present algorithms to three-dimensional grids composed of tetrahedra is straightforward and requires no theoretical developments. Also the implicit solution method can be used in 3D, although one could run into memory problems, because of the storage of the full Jacobian matrix and the GMRES solver.

## ACKNOWLEDGEMENT

This research was supported by ESA contract No 9363/91/NL/FG/CCN2, monitored by Dr. R. Schwane. The authors would like to thank Hugo Embrechts of the Computing Centre of the University of Leuven for his support concerning the computations on the SP2.

## REFERENCES

- [1] R. Broglia, M. Manna, G. Degrez, and H. Deconinck. Axisymmetric Navier-Stokes Computation of Two Hyperboloid Flares in Reentry Configuration. in *Proceedings 4th European High Velocity Database Workshop, ESTEC, Noordwijk*, 1994.
- [2] W. Dieudonné, J.M. Charbonnier, and H. Deconinck. ESA/MSTP Workshop 96: Testcase III.B. Hyperboloid-Flare Standard Model at RWG Reference Calibration Points. in *Proceedings ESA MSTP Workshop 96, ESTEC, Noordwijk, NL, March 25-27*, 1996.
- [3] J. Rice and R. Schnipke. A Monotone Streamline Upwind Method for Convection-dominated Problems. *Computer Methods in Applied Mechanics and Engineering*, 48:313-327, 1985.
- [4] R. Struijs, H. Deconinck, and P.L. Roe. Fluctuation Splitting Schemes for Multidimensional Convection Problems: an alternative to finite volume and finite element methods. *VKI LS 1990-04, Computational Fluid Dynamics*, 1990.
- [5] H. Deconinck, R. Struijs, G. Bourgois, and P.L. Roe. Compact Advection Schemes on Unstructured Grids. *VKI LS 1993-04, Computational Fluid Dynamics*, 1993.
- [6] H. Paillère, J.-C. Carette, and H. Deconinck. Multidimensional Upwind and SUPG methods for the Solution of the Compressible Flow Equations on Unstructured Grids. *VKI LS 1994-05, Computational Fluid Dynamics*, 1994.
- [7] H. Paillère, E. van der Weide, and H. Deconinck. Multidimensional Upwind Methods for Inviscid and Viscous Compressible Flows. *VKI LS 1995-02, Computational Fluid Dynamics*, 1995.
- [8] L.M. Mesaros and P.L. Roe. Multidimensional Fluctuation Splitting Schemes Based on Decomposition Methods. *AIAA Paper 95-1699, AIAA 12th CFD Conference, San Diego, CA*, 1995.
- [9] H. Paillère, H. Deconinck, and P.L. Roe. Conservative Upwind Residual-Distribution Schemes Based on the Steady Characteristics of the Euler Equations. *AIAA Paper 95-1700, AIAA 12th CFD Conference, San Diego, CA*, 1995.
- [10] H. Paillère. Multidimensional Upwind Residual Distribution Schemes for the Euler and Navier-Stokes Equations on Unstructured Grids. *PhD thesis, Université Libre de Bruxelles*, 1995.
- [11] L. Mesaros. Multi-dimensional Fluctuation Splitting Schemes for the Euler Equations on Unstructured Grids. *PhD thesis, The University of Michigan*, 1995.
- [12] E. van der Weide and H. Deconinck. Fluctuation Splitting Schemes for the Euler Equations on Quadrilateral Grids. *ICDF'95, Conference on Numerical Methods for Fluid Dynamics, Oxford*, 1995.
- [13] E. van der Weide and H. Deconinck. Study Note: Algorithmic Development for Improving Efficiency and Accuracy of FORTRAN 3D Navier-Stokes Code. *ESA Project No 9363/91/NL/FG/CCN no.2 report Work Package 3*, 1995.
- [14] A. Jameson. Artificial Diffusion, Upwind Biasing, Limiters and their Effect on Accuracy and Multigrid Convergence in Transonic and Hypersonic Flows. *AIAA Paper 93-3359, AIAA 11th CFD Conference, Orlando, FL*, 1993.
- [15] D. Sidilkover and P.L. Roe. Unification of Some Advection Schemes in Two Dimensions. *Technical Report 95-10, ICASE*, 1995.
- [16] E. van der Weide and H. Deconinck. Positive Matrix Distribution Schemes for Hyperbolic Systems, with application to the Euler Equations. *paper presented at the 3rd Eccomas Conference*, 1996.
- [17] T.J. Barth, E. van der Weide, H. Deconinck, and R. Abgrall. Matrix Distribution Schemes and Energy-Stability for Hyperbolic Systems, with Application to Compressible Flows. in *Proc. 6th International Conference on Hyperbolic Problems, Honkong*, 1996.
- [18] H. Deconinck, H. Paillère, R. Struijs, and P.L. Roe. A Multi-dimensional Generalization of Roe's Flux Difference Splitter for the Euler Equations. *Journal of Computers and Fluids*, 22(2/3):215-222, 1993.
- [19] E. Issman, G. Degrez, and H. Deconinck. Implicit Iterative Methods for a Multidimensional Upwind Euler/Navier-Stokes solver on Unstructured Meshes. *AIAA Paper 95-163, AIAA 12th CFD Conference, San Diego, CA*, 1995.
- [20] H.H. Schultz and Y. Saad. Gmres: A Generalized Minimal Residual Algorithm for solving Nonsymmetric Linear Systems. *SIAM, J. Sci. Stat. Comput.*, 7(3):pp 856-869, 1986.
- [21] B. Hendrickson and R. Leland. The Chaco User's Guide, version 2.0. *Sandia National Laboratories, Albuquerque, NM 87185*, 1994.
- [22] J. Dongarra. MPI: A Message-passing Interface Standard. *Technical report, University of Tennessee*, 1995.
- [23] E. Issman and G. Degrez. A Parallel Implicit Compressible Multidimensional Upwind Euler/Navier-Stokes solver on Unstructured Grids. *HPCN96 Conference, Brussel*, 1996.
- [24] R. Schwane and J. Muylaert. Description of the Testcases: Fourth European High Velocity Database Workshop. *Noordwijk, NL, November 24-25*, 1994.
- [25] R. Schwane. Description of the Testcases: MSTP workshop 1996. Reentry Aerothermodynamics and Ground-to-Flight Extrapolation. *ESA ESTEC Doc. YPA/1889/RS, Noordwijk, NL*, 1996.

# Aerothermodynamics of Radiation-Cooled Surfaces

E.H. Hirschel

Daimler-Benz Aerospace AG  
Militärflugzeuge  
Postfach 80 11 60  
81663 München  
Germany

## 1. SUMMARY

This lecture introduces to the aerothermodynamics of radiation-cooled surfaces of high-speed flight vehicles operating in the earth atmosphere at speeds below approximately 8 km/s. After a discussion of the technical background of heat loads at hypersonic flight, a simple analysis shows how the radiation-adiabatic temperature qualitatively depends on the local boundary-layer properties. Computed examples illustrate the findings and show the implications of radiation cooling for the vehicle design. Scaling laws and non-convex effects are treated, and the influence of radiation cooling on several surface phenomena is considered. Finally the need of a hot experimental technique is discussed and a possible integrated aerothermodynamic design approach is sketched.

## 2. INTRODUCTION

Surface radiation cooling can be considered as the basic cooling mode of high-speed vehicles operating in the earth atmosphere at speeds below approximately 8 km/s (Ref. 1). At this condition, typical, for instance, of reentry flight from a low earth orbit, emission and absorption processes in the air stream can be neglected. If, for whatsoever reason, radiation cooling is not sufficient, other (additional) cooling means, for instance ablation cooling, regenerative cooling etc. must be employed. Usually this results in extra weight, enlarged systems complexity, or non-reusability.

Surface radiation cooling up to now did not receive very much attention during the aerodynamic design of winged reentry vehicles, because such vehicles in general are not drag critical. It was more or less only a concern of the structural design. However, the study of airbreathing launch vehicles has shown important couplings between the radiation-cooled surface, the flow field, heat loads and the viscous drag, especially if the surface-near flow is turbulent. Of course, also all thermochemical processes in the wall-near flow are affected.

Any future aero-assisted launch and/or reentry vehicle demands very good aerodynamic performance, and very accurate mechanical (pressure, skin friction) and heat loads predictions in order to reduce the launch costs to a substantial degree. Therefore it is necessary to understand, predict and verify heat loads, especially the radiation-adiabatic temperature, to a high degree of accuracy.

The term "heat loads" is used here in a very general way. It covers

- temperatures:  $T$  [K],
- heat fluxes: heat transported through an unit area per unit time:  $q$  [ $J/sm^2 = W/m^2$ ],
- amounts of heat:  $H$  [J].

The heat transported per unit area and unit time towards a flight vehicle is

$$Q = \rho_{\infty} v_{\infty} \left( h_{\infty} + \frac{v_{\infty}^2}{2} \right) \quad [J/sm^2 = W/m^2], \quad (1)$$

with  $\rho_{\infty}$  and  $v_{\infty}$  the free-stream density and speed, respectively, and  $h_{\infty}$  the enthalpy of the free stream. The term in brackets is called the total enthalpy, which is composed of the enthalpy of the undisturbed atmosphere and the kinetic energy of the vehicle. At hypersonic speed the total enthalpy is more or less proportional to the flight velocity squared.

A considerable part of the heat transported towards the vehicle is finally transported by diffusion mechanisms towards the vehicle surface (Stanton number as a local measure). Depending on the heat amount penetrating the surface and the heat capacity of the structure below it, the surface will be heated up. The surface temperature will be always that of the gas at the surface (apart from possible low density effects). If enough heat has entered the structure (function of flight time), the surface will reach an upper temperature limit (finite heat capacity assumed), the recovery (adiabatic) temperature. The surface is then called an adiabatic surface. The recovery temperature is somewhat smaller than the total temperature, but always of the same order of magnitude. It serves as a conservatively estimated wall-material temperature in the initial considerations of the materials and structure concept.

Another conservatively estimated wall temperature is the radiation-adiabatic temperature, if radiation-cooling is employed. This is the topic of this lecture. Depending somewhat on the employed structures and materials concept, either cold primary structure with thermal protection system (TPS), or hot primary structure, the actual wall temperature during flight is always near (below) the radiation-adiabatic temperature. In Fig. 1 all these aspects of heat loads are put together schematically.

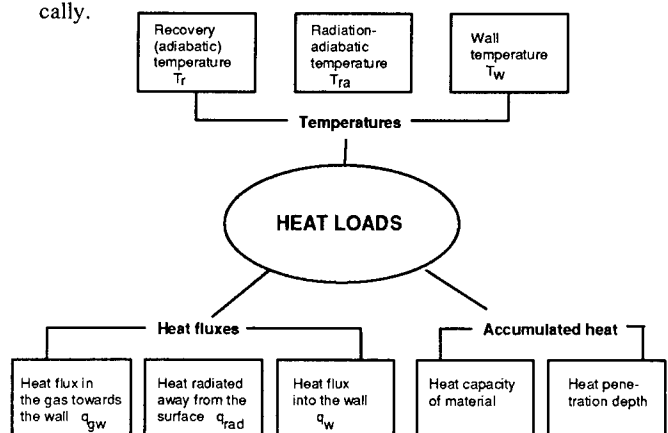


Fig. 1 Definition of heat loads



## 2. SURFACE RADIATION COOLING AS PRE-REQUISITE FOR HYPERSONIC FLIGHT

It was already mentioned that the total enthalpy at hypersonic flight is proportional to the flight velocity squared. This holds also for the total temperature in a certain speed regime. If perfect gas behaviour can be assumed ( $v_\infty < 1$  km/s), the total temperature  $T_o$  is a function of only the total enthalpy, which can be expressed as function of the flight Mach number:

$$T_o = T_\infty \left( 1 + \frac{\gamma-1}{2} M_\infty^2 \right), \quad (2)$$

The recovery temperature  $T_r$  is then

$$T_r = T_\infty \left( 1 + r \frac{\gamma-1}{2} M_\infty^2 \right), \quad (3)$$

with  $r$  ( $0.8 < r < 1$ ) the recovery factor,  $\gamma (= c_p/c_v)$  the ratio of the specific heats, and  $M_\infty$  the free-stream Mach number. At velocities larger than 1 km/s real-gas effects play a role. The temperature in thermal and chemical equilibrium becomes a function of two variables, for instance of the enthalpy and of the density. At velocities larger than 5 km/s non-equilibrium effects play a role, complicating very much all considerations, and leading even to other definitions of the temperature. For deeper discussions the reader is referred to Ref. 2. For applications in the equilibrium range he finds for instance in Ref. 3 state-surface approximations, which allow a fast estimation of thermodynamic and transport properties.

Fig. 2 shows for illustration purposes the equilibrium total temperature as function of flight velocity and altitude, Ref. 4. Indicated are the nominal flight points of the lower stage of the reference concept SÄNGER, of the X-30 (cruise) and the Concorde. Also indicated is the lower flight regime of typical reentry vehicles.

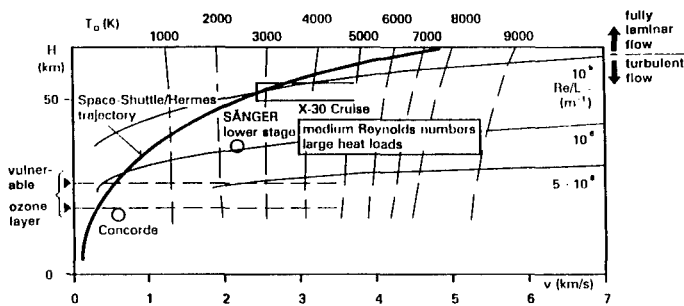


Fig. 2 Total temperatures (and unit Reynolds numbers) as overall heat-loads measure as function of speed and altitude for different vehicle classes (Ref. 4)

If now material properties, in this case the specific tensile strength, are considered, Fig. 3, it is seen at once, that even with the most advanced carbon materials hypersonic flight would not be possible above speeds of  $v_\infty \approx 2$  km/s ( $M_\infty \approx 6$ ). The vehicle designer thus has to solve the problem of heat loads at hypersonic flight first of all by reducing them.

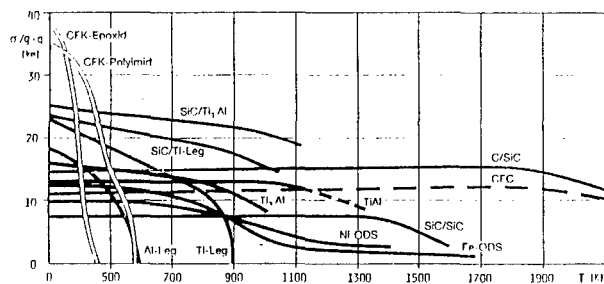


Fig. 3 Materials and the temperature dependence of their specific tensile strength (with permission of Dornier Luftfahrt)

That indeed is accomplished by surface radiation cooling. Surface radiation cooling is the most effective, and the most often employed means to reduce heat loads at high-speed flight. Of course it can be used only at outer surface portions, and not in inlets, ducts, engines, nozzles, etc. If outer surface portions look at each other, the cooling effect is reduced (non-convex effects). Radiation cooling permits fully reusable structures and heat-protection systems with low-orbit reentry vehicles, and with sustained hypersonic flight vehicles, depending on the structure and materials concept, up to possibly  $v_\infty = 3$  to 4 km/s ( $M_\infty = 10$  to 12).

The effect of radiation cooling during reentry is shown in Fig. 4 for the HERMES vehicle. The computations were made with a coupled Euler/second-order boundary-layer code, Ref. 5 (note that for both the recovery temperature and the radiation-adiabatic temperature a maximum of the wall temperature exists at  $H \approx 65$  km due to the density dependence of the temperature mentioned in the introduction). Fig. 4 demonstrates that radiation cooling reduces the wall temperature by such a degree that present-day materials can cope with it. The U.S. Space Shuttle and BURAN have cold primary structures (for instance on an aluminium base), and fully reusable ceramic protection systems (tiles). This was planned also for the upper stage of SÄNGER and for HERMES. For HERMES a CFC-nose cone as hot primary structure (up to  $x = 1.4$  m) was foreseen.

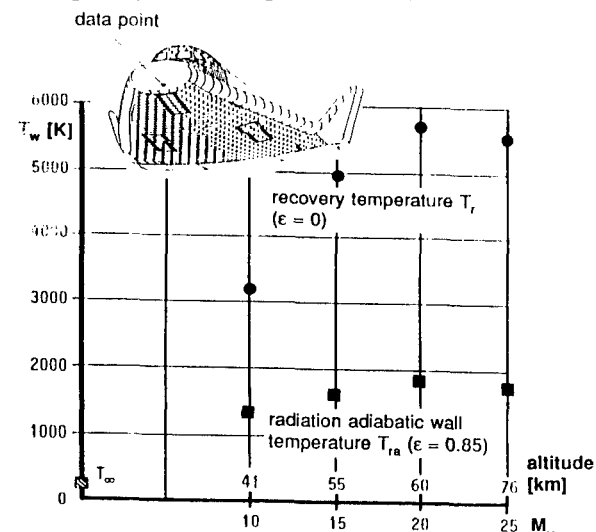


Fig. 4 Effect of radiation cooling at a given point on the lower symmetry line of HERMES ( $x = 1$  m,  $\alpha = 40^\circ$ ), laminar flow, equilibrium real-gas model, at different trajectory points ( $M_\infty$ , altitude  $H$ ), Ref. 6

### 3. LOCAL ANALYSIS

For the following analysis (Refs. 7, 8, 9) it is assumed that the continuum approach is valid, albeit wall slip effects may occur at high altitudes. Real gas effects of any kind are not particularly regarded. The boundary-layer flow is considered to be laminar, which is taken into account by the simplest possible model. A steady state is assumed throughout.

With regard to the surface heat radiation it is strictly assumed that no absorption or emission of the radiation energy takes place in the gas flow past the surface under consideration. The heat is simply radiated away from the vehicle surface to infinity. This neglect of absorption and emission is justified at velocities smaller than approximately 8 km/s, that is at LEO-reentry missions or atmospheric flight missions, Ref. 10. In addition it is assumed that no opposite surface portions of the vehicle radiate or reflect radiation (non-convex effects), and that other external heat radiation sources, like the sun, can be neglected.

Another basic assumption is that locally one-dimensional considerations can be made. This implies neglect of changes of the thermal state of the gas flow and the vehicle surface in directions tangential to the vehicle surface at the location under consideration. It implies further that the heat radiation is directed away locally normal to the vehicle surface.

Three basic thermal situations at a vehicle surface can be distinguished, Fig. 5:

- $T_w$  is prescribed: the wall-heat flux  $q_w$  is the consequence of the balance of the flux in the gas towards the wall  $q_{gw}$  and the radiation flux  $q_{rad}$ .
- $q_w$  is prescribed. The wall temperature  $T_w$  is the consequence of the flux balance,
- $q_w = 0$  is prescribed: with  $q_{rad} = 0$ , the recovery temperature  $T_w = T_r$  is defined; with finite  $q_{rad}$ , the radiation-adiabatic wall temperature  $T_w = T_{ra}$  is the consequence of the flux balance.

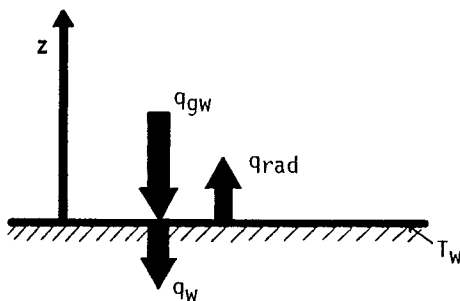


Fig. 5 Schematic of heat fluxes at a radiation cooled wall, Ref. 8,  $z$  is the direction normal to the wall

In design work the engineer is interested for instance in case a), where a material temperature constraint tells him the cooling requirements. On the other hand case c) gives the maximum (conservative) temperature to be expected locally. Without radiation this is the recovery temperature, with finite radiation it is the radiation-adiabatic temperature, which is considered here.

For the local analysis of the latter the simplest case without real-gas effects etc. is considered:

$$\begin{aligned} q_w &= q_{gw} + q_{rad} = 0 = \\ &= -k \frac{\partial T}{\partial z} \Big|_w + \epsilon \sigma T_w^4 \end{aligned} \quad (4)$$

where  $k$  is the heat conductivity,  $\epsilon$  the emissivity coefficient,  $\sigma$  the Stefan-Boltzmann constant ( $\sigma = 5.6697 \pm 0.0029 \cdot 10^{-8} \text{ W/m}^2\text{K}^4$ ), and  $z$  the direction normal to the surface, Fig. 5.

A finite difference is introduced for the derivative of  $T$ , with  $\Delta$  being a characteristic length, and  $T_r$  the recovery temperature of the problem:

$$T_{ra}^4 \approx \frac{k}{\epsilon \sigma} \frac{T_r - T_{ra}}{\Delta} = \frac{k}{\epsilon \sigma} \frac{T_r}{\Delta} \left(1 - \frac{T_{ra}}{T_r}\right). \quad (5)$$

Assuming  $\Delta$  to be the thickness of the thermal boundary layer  $\delta_T$ , and  $T_{ra}$  sufficiently small compared to  $T_r$ , yields that (the fourth power of) the radiation-adiabatic wall temperature is, to begin with, inversely proportional to the (thermal) boundary-layer thickness.

For the thermal boundary-layer thickness the lowest-order ansatz (flat plate boundary layer, no dependency of  $\delta_T$  (and  $\delta$ ) on  $T_w$ ) is made:

$$\frac{\delta_T}{x} \sim \frac{1}{Pe_x^{0.5}} = \frac{1}{(Pr Re_x)^{0.5}}, \quad (6)$$

where  $Pe_x$ ,  $Pr$ ,  $Re_x$  are the Peclet number, the Prandtl number and the Reynolds number, respectively.

Note, that for laminar flow the influence of  $T_w$  and  $\delta$  or  $\delta_T$  can be taken into account by assuming

$$\rho_w/\mu_w \sim \rho_\infty/\mu_\infty (T_\infty/T_w)^2$$

in the Reynolds number. For the adiabatic wall ( $T_w = T_r$ ) and large Mach numbers, this leads to (see for instance Ref. 11):

$$\frac{\delta}{x} \sim \frac{M_\infty^2}{Re_x^{0.5}}. \quad (7)$$

Relation (6) could be refined in this way, however, for the present analysis it is kept for the sake of clarity, and introduced for  $\Delta$  into eq. (5):

$$T_{ra}^4 \sim \frac{k}{\epsilon \sigma} Pr^{0.5} \frac{Re_L^{0.5}}{(x/L)^{0.5}} \frac{1}{L} T_r \left(1 - \frac{T_{ra}}{T_r}\right), \quad (8)$$

with  $L$  the body length, and  $Re_L = \rho_\infty v_\infty L / \mu_\infty$ .

Discussing eq. (8) in the extremes yields:

$$\begin{aligned} \epsilon \rightarrow 0 &: T_{ra} \rightarrow T_r, \\ Re_L \rightarrow 0 &: T_{ra} \rightarrow 0, \\ Re_L \rightarrow \infty &: T_{ra} \rightarrow T_r, \\ L \rightarrow 0 &: T_{ra} \rightarrow T_r, \\ L \rightarrow \infty &: T_{ra} \rightarrow 0, \\ x/L \rightarrow 0 &: T_{ra} \rightarrow T_r, \\ T_r \rightarrow 0 &: T_{ra} \rightarrow 0. \end{aligned}$$

(9)

Assuming again  $T_{ra}$  to be small compared to  $T_r$ , relation (8) is changed to:

$$T_{ra}^4 \sim \frac{k}{\epsilon \sigma} Pr^{0.5} \frac{Re_L^{0.5}}{(x/L)^{0.5}} \frac{1}{L} T_r.$$

(10)

The qualitative result of the analysis then is that the fourth power of the radiation-adiabatic wall temperature with laminar flow

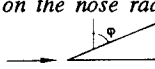
- is inversely proportional to some characteristic boundary-layer length (boundary-layer thickness),
- is proportional to the recovery (total) temperature  $T_r$ ,
- is proportional to  $Re_L^{0.5}$  (note that the recovery temperature does not directly depend on the Reynolds number),
- is inversely proportional to the body length,
- falls with increasing running length of the boundary layer  $(x/L)^{-0.5}$ ,
- is proportional to the heat conductivity at the wall, which, however could with  $k \sim T_{ra}$  be regarded in the above relations.

For two-dimensional flow and for not too strongly three-dimensional flow good correlations of the radiation-adiabatic temperature are possible for laminar flow (see. Chapter 6).

In vehicle design it is of course not only of interest how the radiation-adiabatic temperature behaves on more or less flat surface portions. The behaviour at the vehicle nose and the leading edges is of particular interest, because on the one hand at a stagnation point and along attachment lines the boundary layer is very thin, and on the other hand nose and leading-edge radii and leading-edge sweep govern the wave drag of the configuration.

Assuming  $T_{ra}^4 \sim 1/\delta$ , and that  $\delta$  is inversely proportional to the square root of the flow acceleration ( $\delta \sim 1/\sqrt{du/dx}$ ,  $x$  along surface), and this in turn is inversely proportional to the nose or leading edge radius, gives the general trends shown in Table 1.

Table 1 Trends of the dependency of  $T_{ra}^4$  on the nose radii and leading-edge sweep



	$\delta$	$T_{ra}^4$
axisymmetric stagnation point (spherical nose)	$\sim \sqrt{R}$	$\sim 1 / \sqrt{R}$
2-D stagnation point (cylinder)	$\sim \sqrt{2} \sqrt{R}$	$\sim 1 / \sqrt{2} \sqrt{R}$
swept stagnation line (laminar) swept cylinder	$\sim \sqrt{2} \sqrt{R} / \sqrt{\cos \varphi}$	$\sim \sqrt{\cos \varphi} / \sqrt{2} \sqrt{R}$

Not surprisingly the fourth power of the radiation-adiabatic temperature is like the cold-wall heat flux, Ref. 12, inversely proportional to the square root of the radius and decreases at a leading edge with increasing sweep angle.

A closer examination of the situation at attachment lines shows that there due to the diverging flow pattern the boundary layer is thin compared to the boundary-layers in the vicinity, Fig. 6. At separation lines the flow has a converging pattern and hence the tendency is the other way around, Fig. 7.

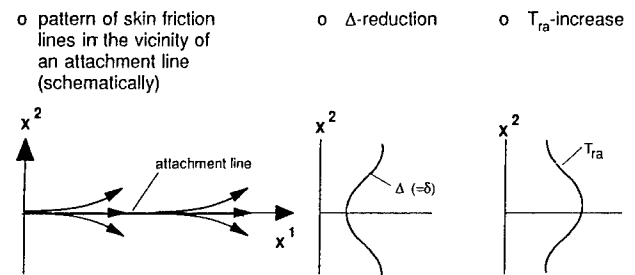


Fig. 6 Pattern of skin-friction lines in the vicinity of an attachment line,  $\Delta$ -reduction,  $T_{ra}$ -increase (all schematically)

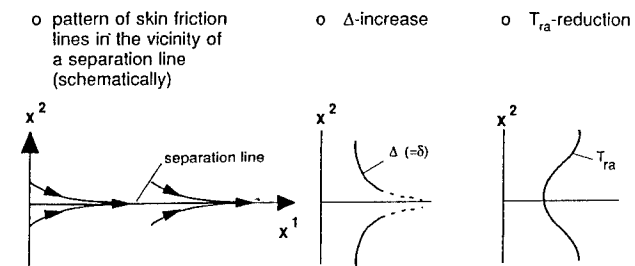


Fig. 7 Pattern of skin-friction lines in the vicinity of a separation line,  $\Delta$ -increase,  $T_{ra}$ -reduction (all schematically)

Consequently, the characteristic boundary-layer length  $\Delta$  is reduced at attachment lines, and one has to expect a rise of the radiation-adiabatic temperature compared to that in the vicinity. Indeed, as will be shown in Chapter 4, a hot-spot situation arises at attachment lines, whereas at separation lines the opposites happens, i.e. a cold-spot situation ensues. The  $\Delta$  behaviour can be observed in boundary-layer calculations, Ref. 13. The mathematical proof, however, is lengthy and is not given here, neither in Ref. 13.

With turbulent flow the radiation-adiabatic temperature behaves qualitatively in the same way as with laminar flow. In Ref. 14 the following general relation is proposed for flat surfaces and cones (compared to eq. (8) it takes the dependencies on the local surface and boundary-layer edge data into account):

$$T_{ra}^A = A \frac{k_\infty}{\epsilon \sigma} Pr^{1/3} \left( \frac{T_\infty}{T^*} \right)^{1-n} \left( \frac{\mu^*}{\mu_\infty} \right)^n \quad (11)$$

$$\cdot \frac{Re_L^{1-n}}{L} \frac{1}{(x/L)^n} \left( \frac{p_\infty \mu_\infty}{p_\infty \mu_\infty} \right)^{1-n} T_r \left( 1 - \frac{T_{ra}}{T_r} \right).$$

Here the subscript "e" stands for "boundary-layer edge",  $T^*$  and  $\mu^*$  are functions of Eckert's reference enthalpy  $h^* = 0.28 h_e + 0.5 h_w + 0.22 h_\infty$ . The constants are  $n = 0.5$  for laminar flow,  $n = 0.2$  for turbulent flow,  $A = 0.332$  ( $0.332 \sqrt{3}$ ) for laminar planar (conical) and  $A = 0.0296$  ( $0.0296 (9/4)^{0.2}$ ) for turbulent planar (conical) flow. This relation and the relations for stagnation-point regimes and (infinitely) swept leading edges are presently in a verification process by means of numerical investigations.

Finally the reader is warned that relation (8) cannot be used to actually determine the radiation-adiabatic temperature. It shows qualitatively dependencies and trends, which is important in design work. It helps to explain phenomena seen in results of computations and in flight data, Chapter 4. It leads to scaling laws, Chapter 6, which so far at least for laminar flow have shown to be simple and robust tools for the use in design work and for general considerations.

The discussed dependencies and trends are similar to those which can be observed with cold-surface model tests in wind tunnels. A relation similar to eqs. (5) and (8) (for laminar flow) describes the situation there:

$$q_w \approx \frac{k}{\Delta} T_r \left( 1 - \frac{T_w}{T_r} \right) \sim$$

$$\sim k Pr^{0.5} \frac{Re_L^{0.5}}{(x/L)^{0.5}} \frac{1}{L} T_r \left( 1 - \frac{T_w}{T_r} \right). \quad (12)$$

The general behaviour is the same, however, with the important difference, that  $T_w$  is given, whereas in eq. (8) it is  $T_w = T_{ra}$ , which is the unknown.

For both the cold surface and the radiation cooled surface the state of the boundary layer - laminar or turbulent - will make a big difference in  $q_w$  and  $T_{ra}$ , respectively. This is due to the fact, that with large temperature gradients changes in the heat conductivity of the boundary layer fluid - laminar or turbulent - will have a large effect, even if at the wall the heat conductivity is only the laminar one. At the adiabatic wall however, the temperature gradient goes to zero at the wall, hence the state of the boundary will not affect strongly the recovery temperature, see Fig. 13 in Chapter 4.

Last not least it is noted, that the radiation-adiabatic temperature cannot be determined from measured cold-surface heat fluxes or Stanton numbers. This is due to the highly non-linear coupling of it to the boundary-layer thickness, which itself depends on the wall temperature, see relation (11).

#### 4. COMPUTED EXAMPLES

In the following several numerical examples are discussed and analysed. First the effect of radiation cooling is demonstrated.

Fig. 8 shows the effect at a given point on the configuration of a hypersonic vehicle as function of the Mach number and the flight altitude, Ref. 4. The emissivity coefficient of the surface was assumed to be  $\epsilon = 0.85$ . The data were computed with an approximate method, Ref. 15. The radiation-adiabatic wall temperature  $T_{ra}$  is found with  $q_w = 0$ . At Mach numbers below  $M_\infty = 2$  the radiation-cooling effect is small, because the Reynolds numbers there are large and therefore the boundary layers thin. With rising Mach number (and altitude) it becomes larger. At  $M_\infty = 5.6$  the cooling effect amounts to nearly 350 K compared to the recovery temperature, and nearly 450 K compared to the total temperature. If for instance at  $M_\infty = 5.6$  a wall temperature of 900 K is to be maintained, it can be achieved by radiation cooling. Without radiation cooling, however, a heat flux into the surface of  $q_w \approx 30 \text{ KW/m}^2$  would be necessary.

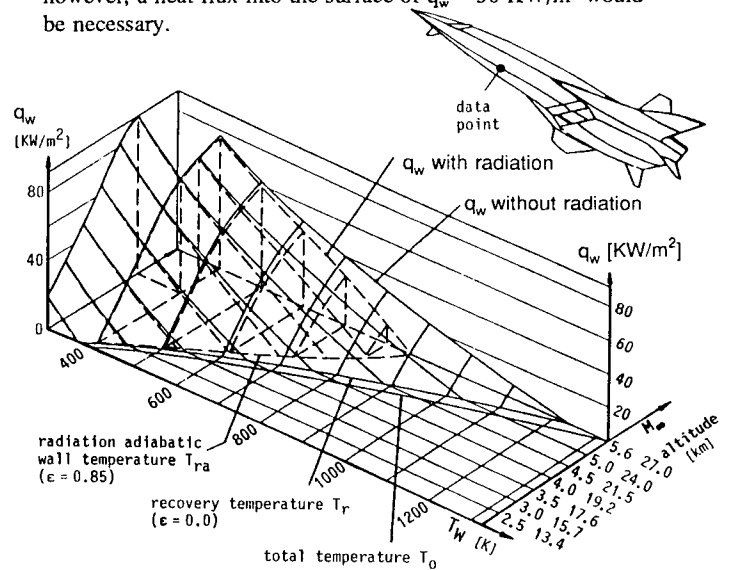


Fig. 8 Heat loads alleviation by radiation cooling ( $\epsilon = 0.85$ ), Ref. 4, hypersonic aircraft (HYTEX 2-91), lower symmetry line of the forebody ( $x = 5 \text{ m}$ ,  $\alpha = 5^\circ$ , turbulent flow, vibration excitation, approximative method), at different trajectory points ( $M_\infty$ , altitude),  $q_w$  is the heat flux into the wall (see Fig. 5)

In Chapter 3 the qualitative behaviour of the radiation-adiabatic temperature in the vicinity of attachment and separation lines was discussed. On a delta wing, like shown in Fig. 9, an additional effect occurs. The wall-near flow past surfaces with heat transfer into the body, or away from it by radiation, is non-isoenthalpic. At such attachment lines, however, flow with the original total enthalpy is transported from the free-stream towards the surface, Fig. 9.

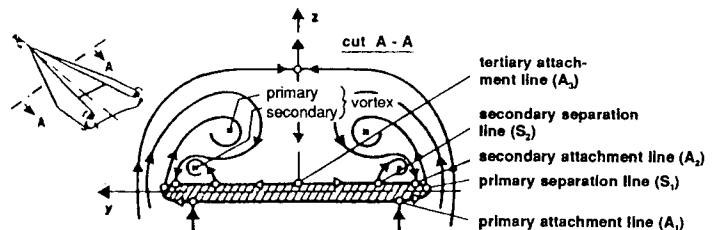


Fig. 9 Topological structure (schematically) of delta wing flow (A: attachment line, S: separation line): attachment flow transports original enthalpy towards surface at  $A_1$ ,  $A_2$ ,  $A_3$ .

Therefore along an attachment line, which in the limit may resemble that on an infinitely swept wing, due to the diverging flow pattern **and** the original total enthalpy, large radiation-adiabatic wall temperatures compared to that of the adjacent boundary layers will prevail. In the adjacent boundary layers this temperature falls anyway with increasing running length, eq. (5). This of course also affects the situation at separation lines, where the temperature in main flow direction becomes smaller, than in the adjacent boundary layers (Chaper 3).

Fig. 10 shows results from a solution of the Navier-Stokes equations for laminar flow past a delta wing with leeside separation at  $M_\infty = 7.15$ , Refs. 16 and 17. All the features discussed in Chapter 3 and above are present. Note especially the skin-friction line topology at the windward side, where between the two primary attachment lines the flow is nearly two-dimensional. On the leeside the secondary attachment line tapers off down-stream. The tertiary attachment line (schematic see Fig. 9) of course also is a hot-spot line. The presence of a fuselage, however, would change the leeside flow topology.

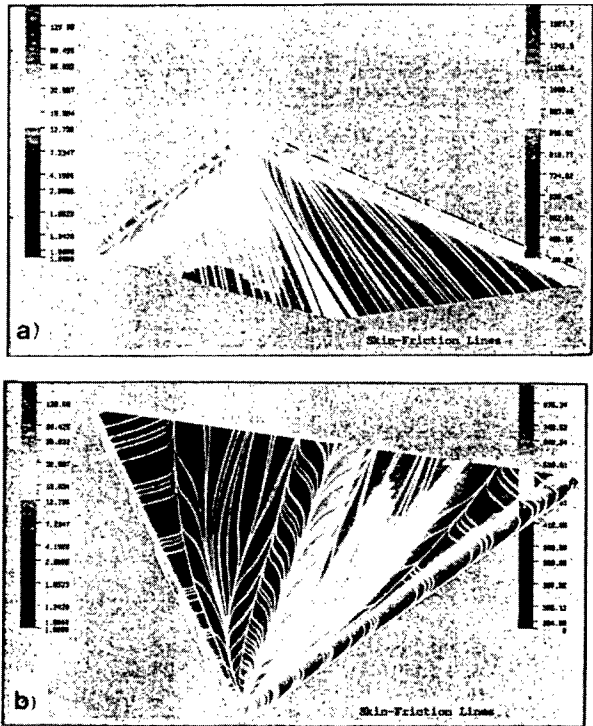


Fig. 10 Hot-spot phenomena at attachment lines of a delta wing with surface radiation cooling, a) windward side, b) leeward side, Refs. 16 and 17,  $M_\infty = 7.15$ ,  $Re = 5 \cdot 10^5$ ,  $L = 13$  m,  $\alpha = 15^\circ$ ,  $\epsilon = 0.85$  (right-hand sides: wall temperatures (cold areas are dark), left-hand sides: radiation heat fluxes)

On the leeward side of a spaceplane at large angle of attack the boundary layer is thick and therefore radiation cooling is very effective, leading to rather small wall temperatures. However, one must avoid situations like that shown from a Navier-Stokes study, in Fig. 11 (see Ref. 18 for details). If an attachment line lies on the canopy window, locally temperatures will become very large. Fig. 11 indicates that either configurational, or angle of attack changes or even active cooling efforts, would be necessary, if in such a situation the permissible wall tempera-

ture is exceeded (which in this case is not critical).

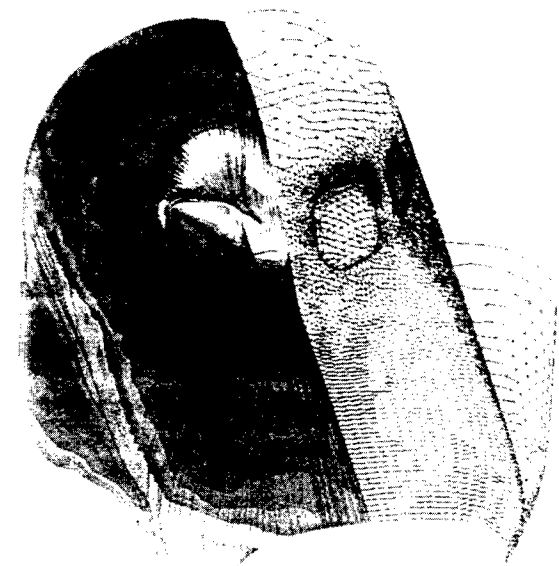


Fig. 11 Skin-friction lines and radiation heat fluxes on the HERMES canopy,  $M_\infty = 10$ ,  $\alpha = 30^\circ$ ,  $Re_\infty^* = 1355000$  m<sup>-1</sup>,  $\epsilon = 0.85$ , Navier-Stokes Solution, laminar flow (see Ref.18 for details)

Even at rather small flight Mach numbers the skin-friction line pattern on a capsule can well be matched to the radiation-adiabatic temperature, Fig. 12, Ref. 19. The rather complicated topology is not reconstructed completely. Only some major attachment and separation lines are indicated. Because of the low Reynolds number ( $Re_\infty = 4.5 \cdot 10^5$ ), the radiation cooling is very effective. At the separation lines ①  $T_{ra} \approx 350$  K, and at the attachment line ②  $T_{ra} \approx 450$  K result, compared to the total temperature  $T_o \approx 745$  K.

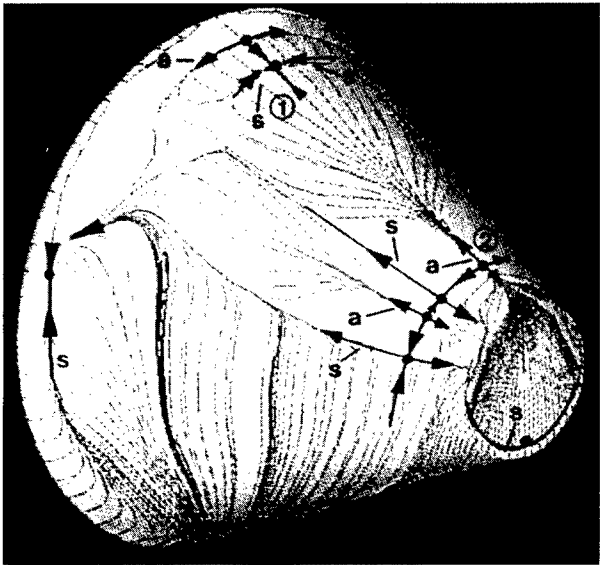


Fig. 12a Navier-Stokes solution for the Viking shape ( $\Theta_c = 25^\circ$ ) with  $M_\infty = 3$ ,  $\alpha = 25^\circ$ ,  $A = 35$  km,  $\epsilon = 0.85$ , Ref. 19, skin-friction lines (a = attachment line, s = separation line)

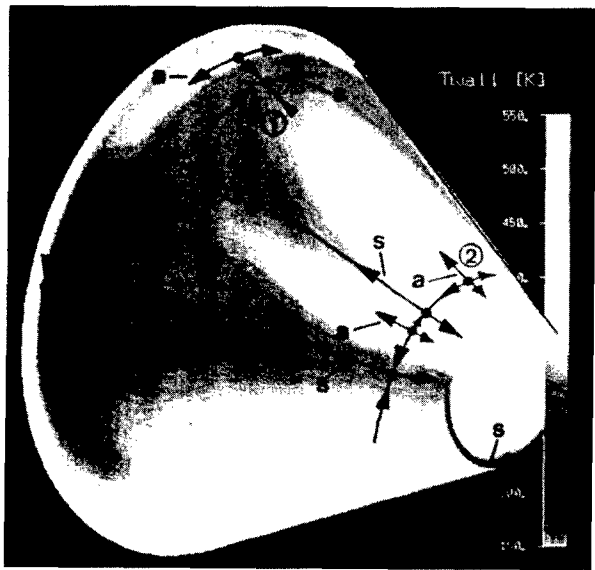


Fig. 12b Navier-Stokes solution for the Viking shape ( $\Theta_e = 25^\circ$ ) with  $M_\infty = 3$ ,  $\alpha = 25^\circ$ ,  $A = 35$  km,  $\epsilon = 0.85$ , Ref. 19, radiation-adiabatic temperature ( $a$  = attachment line,  $s$  = separation line)

Finally a Navier-Stokes solution for the SÄNGER forebody, Ref. 20, shows that radiation cooling enhances very strongly the influence of the boundary-layer state on the wall temperature and the skin friction, Fig. 13. Without radiation cooling the wall temperature (recovery temperature) is some thirty to forty degrees larger for turbulent flow than for laminar flow, Fig. 13a. The transition location was chosen arbitrarily to lie at  $x/L = 0.1$ . With radiation cooling the difference is about ten times larger (see discussion at the end of Chapter 3) and hence the location of transition laminar-turbulent becomes much more important. Note that real-gas effects at that Mach number also play a role, at least in the case of no radiation cooling. Note further that it is not known how reliable present-day turbulence models are in such cases. The figure shows well that the radiation-adiabatic temperature decreases with  $x/L$  for the laminar as well as for the turbulent case in contrast to the recovery temperature.

Fig. 13b shows the influence of surface radiation cooling on the skin friction, which is low for the laminar case, but is large for the turbulent case. In this case, a skin-friction estimation based on the recovery temperature would give values about 30 per cent too low. This shows also that for drag minimization the surface should be as hot as possible.

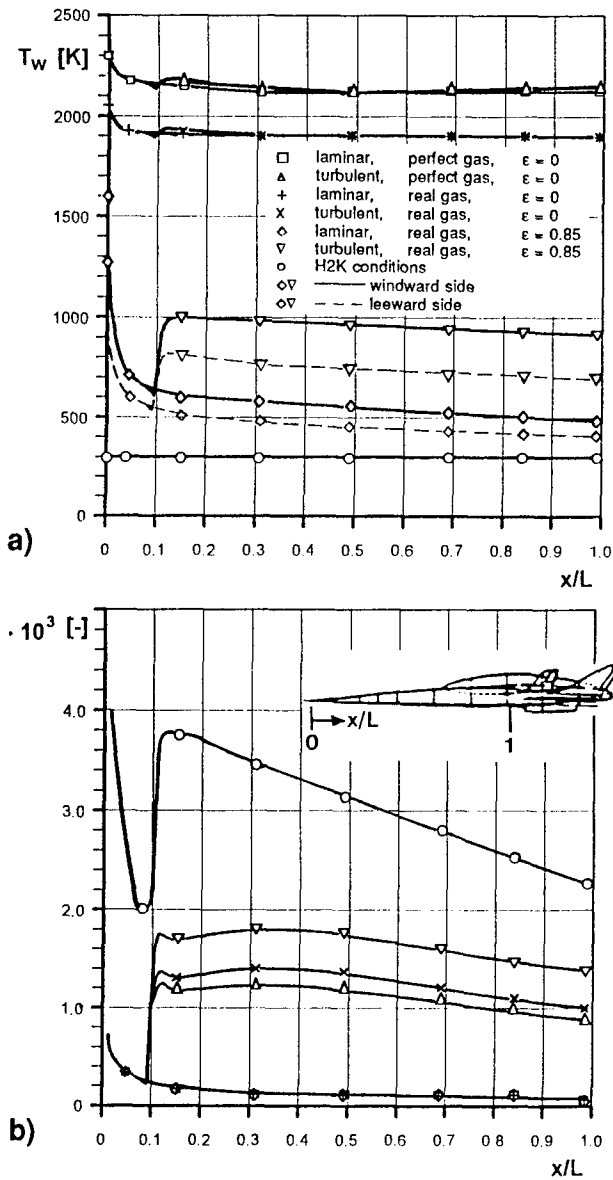


Fig. 13 Influence of the state of the boundary layer (laminar/turbulent, real-gas effects, and radiation cooling on a) wall temperature, b) skin friction. Lower symmetry line of SÄNGER forebody,  $M_\infty = 6.8$ ,  $Re = 1.22 \cdot 10^6$ ,  $L = 55$  m,  $\alpha = 6^\circ$ , Ref. 20

In Fig. 13a also the computed radiation-adiabatic temperatures for the leeward side are indicated. The temperature for the turbulent case is approximately 270 K, and that for the laminar case approximately 90 K lower than on the windward side. This will be discussed further in Chapter 6.

For a typical cold hypersonic wind-tunnel situation, that in the H2K at the DLR Köln-Porz, a computation has been performed for the present case, Ref. 21. With the tunnel data at  $M_\infty = 6.8$ :  $Re = 3 \cdot 10^6$ ,  $T_\infty = 61$  K and  $T_w = 300$  K (Fig. 13a) the turbulent skin-friction shown in Fig. 13b is two times larger than that for the radiation-cooled flight case, with a much steeper slope, which partly is due to the smaller Reynolds number.

The large influence of the state of the boundary layer - laminar or turbulent - on the wall temperature and on the skin friction for the radiation-cooled wall, compared to that in the case of the adiabatic wall poses very large problems in vehicle design. The transition location is very important in view of the thermal loads, especially if a hot primary structure is foreseen. On the other hand the prediction and verification of the viscous drag is affected strongly, if the vehicle, typically for airbreathers, is drag critical. Fig. 13b demonstrates that with presentday wind-tunnel techniques the skin friction cannot be found with the needed degree of reliability and accuracy.

That the spreading of the radiation-adiabatic temperature with transition laminar-turbulent in reality happens, can be seen from Space Shuttle data, Fig. 14, Ref. 22.

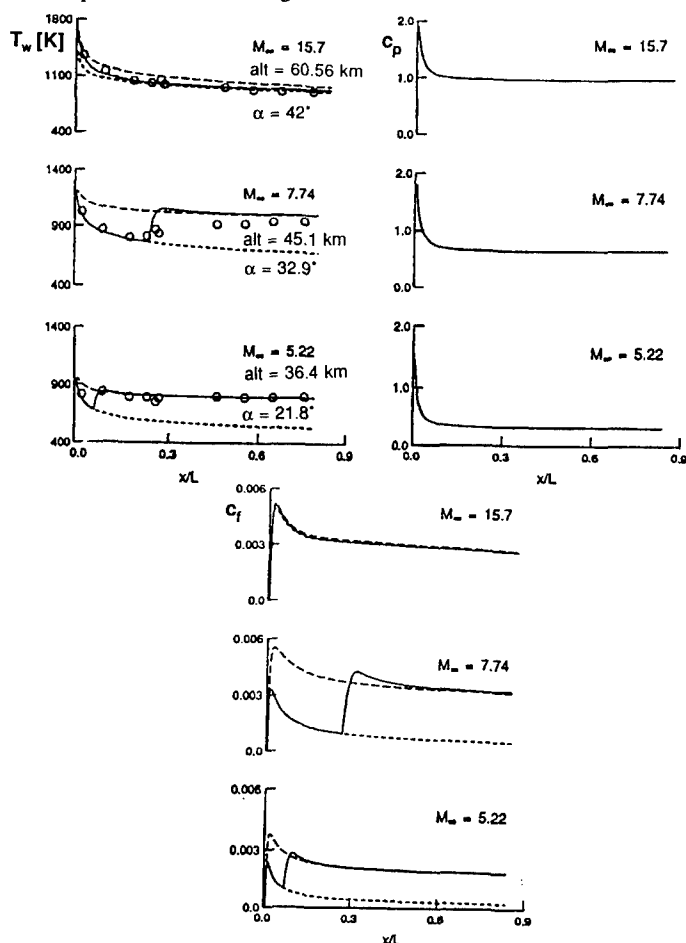


Fig. 14 US Space Shuttle flight STS-2, computed data, Ref. 22, and flight data, Refs. 23, 24: a) radiation-adiabatic wall temperature, b) pressure coefficient, c) skin-friction coefficient, transition location from flight data,  $\epsilon = 0.85$ ;  $M_\infty = 15.7$ : ---- fully catalytic wall, ---- non-catalytic wall, --- partially catalytic wall;  $M_\infty = 7.14$  and  $5.22$ : ---- fully turbulent, ---- fully laminar, --- with transition;  $\circ$  flight data

In Fig. 14a, despite the scatter of the flight data for  $M_\infty = 7.14$ , the same behaviour of the radiation-adiabatic wall temperature, measured and computed, is present as in Fig. 13a (the laminar  $M_\infty = 15.7$  data are included for comparison). Fig. 14c shows the spreading in the skin friction, whereas the surface pressure coefficient, Fig. 14b, is not affected. Unfortunately flight data are not available to compare with these results. For a detailed discussion see Ref. 22.

## 5. NON-CONVEX EFFECTS

Up to now radiation cooling on completely convex surfaces was considered. On real configurations surfaces may look partly at each other, which reduces the cooling effect. In the extreme, in an inlet, a RAM combustor etc., no radiation cooling is possible at all. In the following the reduction of radiation cooling due to non-convex effects, which appear at wing roots, fin roots and the like, is treated following Ref. 25.

Consider the situation shown in Fig. 15.

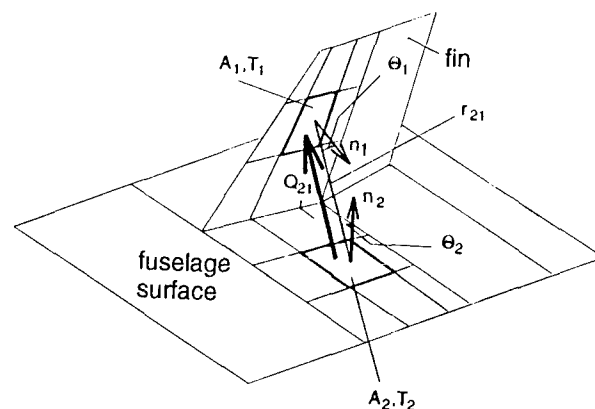


Fig. 15 Schematic of non-convex effects in radiation cooling at a generic fin configuration, after Ref. 25

The rate of energy  $Q_{21}$  radiated from  $A_2$  and acting on  $A_1$  is

$$Q_{21} = \frac{\epsilon \sigma}{\pi} \iint \frac{T_2^4 \cos \theta_1 \cos \theta_2}{r_{21}^2} dA_1 dA_2 \quad (13)$$

The surface element  $A_1$  absorbs the heat flux

$$q_{1,ab} = -\epsilon Q_{21}/A_1 \quad (14)$$

Note that the absorption coefficient is equal to the emission coefficient.

With the heat flux emitted from  $A_1$

$$q_{1,em} = \epsilon \sigma T_1^4 \quad (15)$$

a balance can be made for  $A_1$ :

$$\Delta q_1 = q_{1,em} + q_{1,ab} = \epsilon (\sigma T_1^4 - Q_{21}/A_1) \quad (16)$$

With this a fictitious emission coefficient  $\epsilon_f$  is defined:

$$\epsilon_f = \Delta q_1 / (\sigma T_1^4) \quad (17)$$

To apply it, an influence matrix for the whole discretized configuration surface has to be computed, taking into account the sight lines between the individual surface elements. Because the radiation-cooling effect depends (locally) on the boundary-layer thickness, and this in turn on the temperature of the wall and the wall-near flow, the fictitious emission coefficient must

be determined iteratively. This can easily be done in Navier-Stokes methods. With approximative methods or boundary-layer methods, special iteration approaches are necessary. The authors of Ref. 25 have devised a General Thermal Radiation (GETHRA) module, which can be incorporated into any computation scheme.

A computation result from Ref. 26, typical for non-convex effects, is seen in Fig. 16. At the lower wing root of the HYTEX R-A<sub>3</sub> vehicle, which was investigated in the German Hypersonics Technology Programme, means of heat loads alleviation by introducing a fillet were studied. The introduction of non-

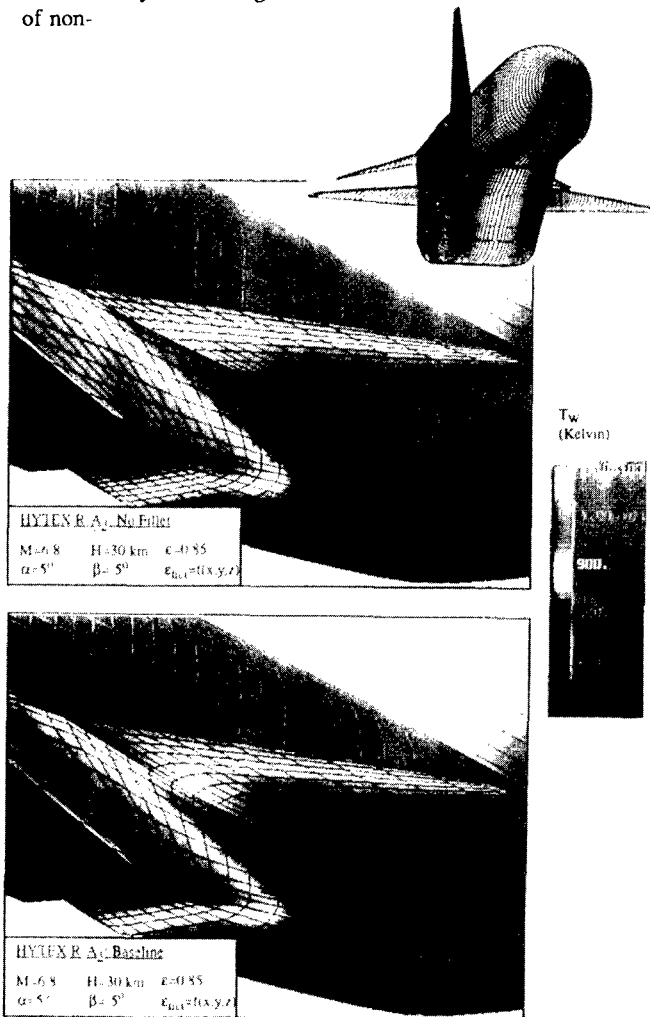


Fig. 16 Heat loads alleviation at the wing root of a HYTEX vehicle, Ref. 26,  $M_\infty = 6.8$ ,  $A = 30$  km,  $\alpha = 5^\circ$ ,  $\beta = 5^\circ$ ,  $\epsilon_{nom} = 0.85$ , approximative method, turbulent flow; radiation-adiabatic temperature: a) without fillet, b) with fillet

convex effects in the computation for the non-fillet case resulted in a temperature rise of 50 K to 100 K. The wing surface in the root region was less strongly affected compared to the propulsion unit surface there. This is due to the fact, that the boundary layer is thicker on the latter. Note that the classical viscous corner-flow effects were not prescribed with the employed approximative methods. The introduction of the fillet, which anyway would reduce the viscous corner-flow effects, resulted as expected, in a reduction of the radiation-adiabatic temperature by about 50 K towards the end of the wing root. Unexpectedly the temperature rose at the leading

edge by up to 30 K. A closer examination showed, that this was due to the compression of the flow, which was induced by the fillet. The resulting local rise of the unit Reynolds number then decreased the boundary-layer thickness, and the temperature rose, which can be understood in light of the results of the local analysis in Chapter 3.

Although the non-convex effects were not large in this case, the results of the investigation show clearly the influence of non-convex effects on the radiation-adiabatic temperature. Remembering that the viscous drag is affected too, non-convex effects must, like local strong-interaction effects, be monitored and quantified if necessary, in the design of hypersonic vehicles.

## 6. SCALING LAWS

Other than the recovery temperature, the radiation-adiabatic temperature is Reynolds number and scale dependent, eqs. (8) and (11). Therefore data from different cases, even with the same total enthalpy, cannot directly be compared. The radiation-adiabatic wall temperature on a small body (wind-tunnel model) would be much larger than that on a large one (real configuration), if all flow parameters are the same, which makes a full simulation in a hypothetical ideal wind tunnel impossible, unless the model can be actively, and very strongly, cooled. This holds also for an experimental vehicle, which is a scaled-down version of a reference concept. The relations from Chapter 3 allow a quick scaling of the radiation-adiabatic temperature for general considerations, and especially for design work (configuration finding process).

At flat surface portions with laminar flow, provided the flow is two-dimensional or not too strongly three-dimensional, relation (8) can be used to scale the radiation-adiabatic wall temperature (note that in eq. (8) the dependency of the boundary-layer thickness on  $T_w$  has been omitted). It is, however, mandatory that the flow topology remains qualitatively and quantitatively the same in both cases (geometrical affinity, the same angles of attack and yaw), and that real-gas effects are similar. If the two different cases 1 and 2 are considered, the following relation can be obtained:

$$\frac{T_{ra1}}{T_{ra2}} \approx \left( \frac{\epsilon_2}{\epsilon_1} \frac{k_1}{k_2} \frac{Pr_1^{0.5}}{Pr_2^{0.5}} \frac{Re_{L_1}^{0.5}}{Re_{L_2}^{0.5}} \frac{L_2}{L_1} \frac{T_{r1}}{T_{r2}} \frac{1 - \frac{T_{ra1}}{T_{r1}}}{1 - \frac{T_{ra2}}{T_{r2}}} \right)^{1/4}, \quad (18)$$

which does not depend on  $x/L$ .

If  $T_{ra}$  is small compared to  $T_r$  in both cases, and if  $Pr_1 \approx Pr_2$ , eq. (18) can be reduced to

$$\frac{T_{ra1}}{T_{ra2}} \approx \left( \frac{\epsilon_2}{\epsilon_1} \frac{k_1}{k_2} \frac{Re_{L_1}^{0.5}}{Re_{L_2}^{0.5}} \frac{L_2}{L_1} \frac{T_{r1}}{T_{r2}} \right)^{1/4}. \quad (19)$$

This relation is very intriguing, because it shows that a wide range of parameters can be covered in the scaling process. Special cases with equal lengths or unit Reynolds numbers have



been discussed in Ref. 7. The parameter variation range has sofar been tested only in some few cases. In the following two of them are shortly discussed.

Fig. 17 shows comparisons of the radiation-adiabatic wall temperatures at the surface of the HERMES configuration for laminar flow, Ref. 7. Three cases were studied at the windward side of the HERMES vehicle. The results were found with the coupled Euler/2nd order boundary-layer method approach described in Ref. 5. Case 1 compares HERMES with the original lenth  $L_a$  with a HERMES configuration enlarged linearly to the length  $L_b$  of the

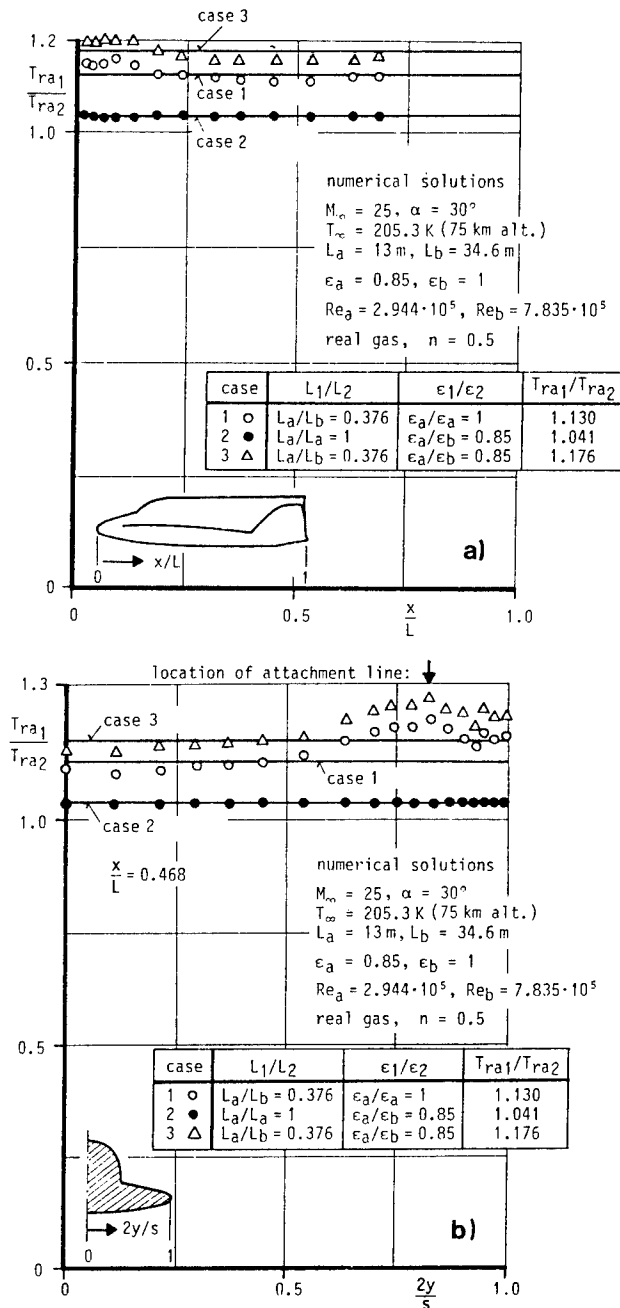


Fig. 17 Comparison of numerical (symbols) and scaled (full lines) radiation-adiabatic wall temperatures for the HERMES configuration, Ref. 7, a) in lower symmetry line, b) at lower side cross-section  $x/L = 0.468$

US Space Shuttle. In case 2 for the original configuration two different emissivity coefficients were assumed,  $\epsilon_a = 0.85, \epsilon_b = 1$ . In case 3 finally case 1 and case 2 are combined. It is seen that with eq. (19) a fair correlation is possible except for the vicinity of the windward attachment lines, where due to the strong divergence of the flow the temperature is higher (see discussion in Chapter 4), and obviously the simple (Blasius)  $n = 0.5$  dependency does not hold.

Equation (18) has been used to compare the radiation-adiabatic wall temperatures - found with a Navier-Stokes solver on the delta wing - from Fig. 10 for two different lengths  $L = 13 \text{ m}$  (case 2) and  $L = 4.67 \text{ m}$  (case 1), Refs. 16, 17. Fig. 18 shows in two cuts the Navier-Stokes results and the result of the scaling case 2 to case 1 with eq. (18) reduced to

$$\frac{T_{ra1}}{T_{ra2}} \approx \left( \frac{k_1}{k_2} \frac{Re_{L_1}^{0.5}}{Re_{L_2}^{0.5}} \frac{L_2}{L_1} \frac{1 - \frac{T_{ra1}}{T_{r1}}}{1 - \frac{T_{ra2}}{T_{r2}}} \right)^{1/4} \quad (20)$$

The data compare better, if in addition  $k_1 \approx k_2$  is assumed. At the attachment and separation lines, where larger three-dimensional effects are present, deviations up to 100 K can be observed. However, the hot-spot situations at the attachment lines are in general well scaled.

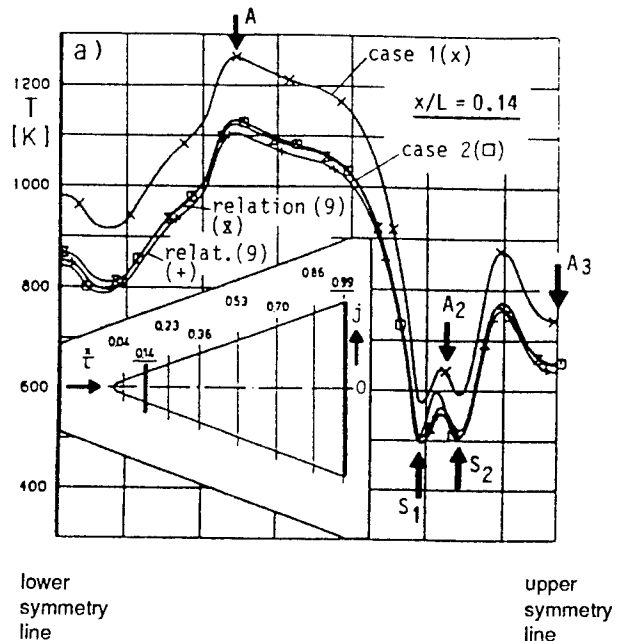


Fig. 18a Comparison of numerical (x, □) and scaled (+; relation (20); X: relation (20) with  $k_1 = k_2$ ) radiation-adiabatic wall temperatures, Refs. 16, 17, for the delta wing of Fig. 10; indicated are the locations of attachment and separation lines (schematic see Fig. 9), cross-section at 14 per cent body length

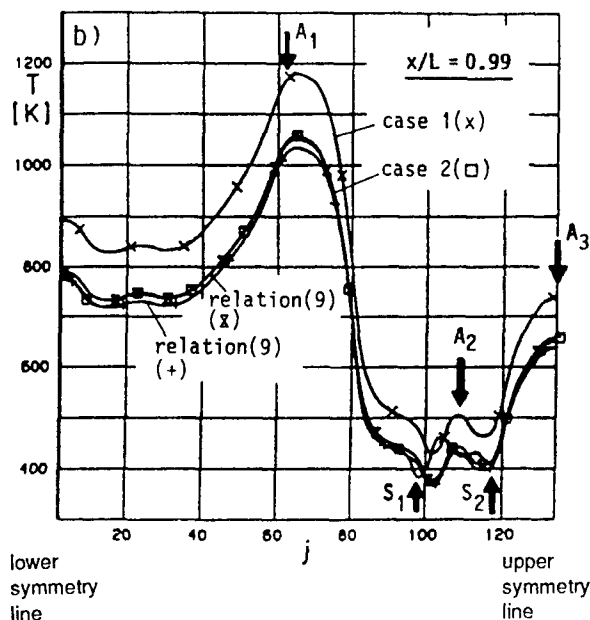


Fig. 18b Comparison of numerical ( $x$ ,  $\square$ ) and scaled ( $+$ : relation (20);  $\times$ : relation (20) with  $k_1 = k_2$ ) radiation-adiabatic wall temperatures, Refs. 16, 17, for the delta wing of Fig. 10; indicated are the locations of attachment and separation lines (schematic see Fig. 9), cross section at 99 per cent body length

For turbulent flows, scaling laws are proposed in Ref. 14. They base on eq. (11), and similar relations for noses and swept leading edges. They include the laminar cases and the  $\delta$ -dependency on  $T_w$ . They too are presently investigated by means of numerical solutions.

In Chapter 4 it was seen, Fig. 13 (also Fig. 18 of this chapter), that on the leeside of hypersonic vehicles at angle of attack the radiation-adiabatic temperature is markedly smaller than on the windward side (the leeside of a winged reentry vehicle (see the US Space Shuttle) must not be black!). This can be explained with help of Fig. 19. There an infinitely thin flat plate at angle of attack is considered as

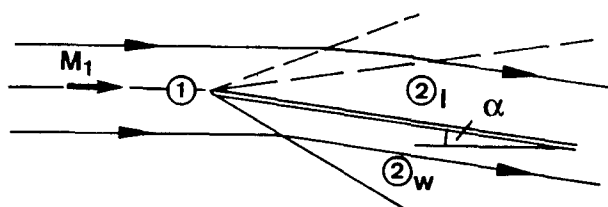


Fig. 19 Hypersonic flow past a flat plate at angle of attack as limiting case of a hypersonic vehicle at angle of attack

limiting case of a hypersonic vehicle at angle of attack. It is obvious, that on the windward side the stream tube is compressed by the wedge shock, whereas on the leeside it is expanded by the Prandtl-Meyer expansion. Consequently the unit Reynolds number must rise on the windward side, and drop on the leeside. By interpreting the Reynolds number in eq. (8) as a local Reynolds number (see also eq. (11)), it becomes clear, that indeed the radiation-adiabatic temperature will be larger on the windward side than on the leeside. This is a

qualitative explanation. The flat plate analogy must not be over-interpreted, especially when a blunt body at large angle of attack, with a large subsonic region on the windward side, is considered.

Fig. 20 gives for the windward side and the leeside of the flat plate at angle of attack (wedge angle)  $\alpha = 5^\circ$  the quantitative behaviour of the reduced unit Reynolds number as function of the Mach number. It has been found with the perfect gas relations from Ref. 27.

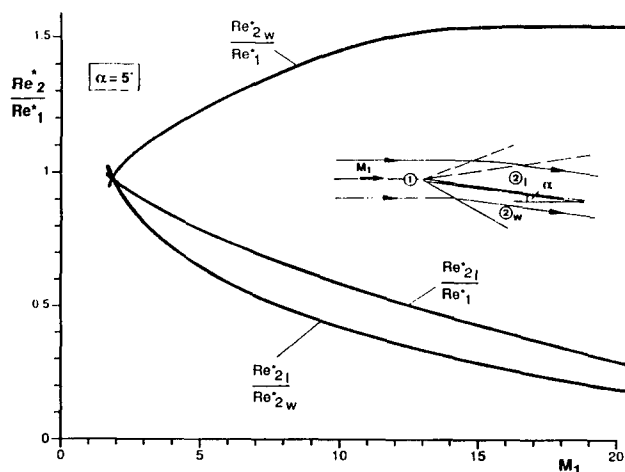


Fig. 20 The reduced unit Reynolds number  $Re^*$  on the windward side ( $w$ ), and the leeside ( $l$ ) of a flat plate at angle of attack  $\alpha = 5^\circ$  as function of the free-stream Mach number

On the windward side the reduced unit Reynolds number

$$Re^* = \frac{\rho v}{T} \quad (21)$$

at the plate (2), compared to that of the freestream (1), rises for all free-stream Mach numbers larger than  $M_\infty = \sqrt{2}$ . On the leeside it falls for all Mach numbers. Accordingly the ratio of the unit Reynolds number at the leeside to that at the windward side drops. Note that in relation (21) for the viscosity ( $\mu \sim T^\omega$ )  $\omega = 1$  was assumed. A closer examination reveals that upper and lower bounds for  $\omega$  exist, for which the result in Fig. 20 holds. These bounds are comfortably wide for perfect gas flow.

Fig. 21 shows for the fixed free-stream Mach number  $M_\infty = 6$  the change of the unit Reynolds number ratio on the windward side with the angle of attack. Surprisingly it exhibits a maximum at  $\alpha \approx 12.5^\circ$  and then a steep drop towards  $\alpha \approx 42.5^\circ$ , where the wedge shock lifts off. The value for the isolated normal shock is indicated, too.

In general it can be observed that the heat loads at the windward side, for instance of a reentry vehicle, rise in level with increasing angle of attack (the drop from the nose to the rear is not affected). However, Fig. 21

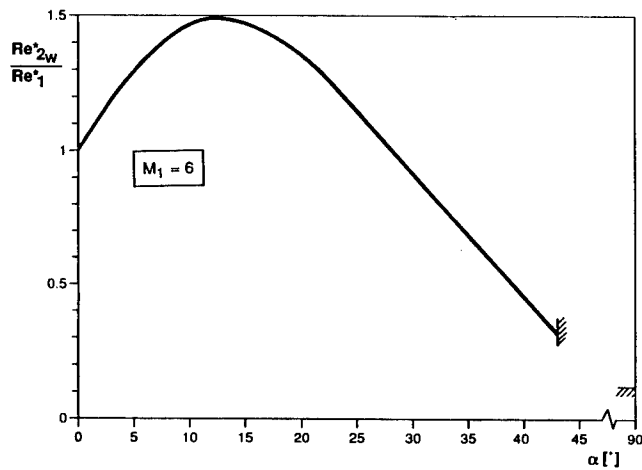


Fig. 21 The reduced unit Reynolds number  $Re^*$  on the windward side of a flat plate at  $M_\infty = 6$  as function of the angle of attack

shows, that the flat-plate analogy needs to be exploited further. Fig. 21 could be a hint towards the possibility that heat loads at a vehicle, or a control surface have a maximum for a certain deflection angle, and then decrease with increasing angle. However, the effects present in reality, real-gas and non-convex effects, separation and attachment, must be regarded in such speculations.

In any case, the discussion reveals also, why at the ramps of an inlet the radiation-adiabatic temperature increases with every deflection, Fig. 22, Ref. 28. The Mach number is reduced over the (oblique) wedge shocks and accordingly the unit Reynolds number rises, Fig. 22a. With that the boundary-layer thickness decreases, and hence the radiation-adiabatic temperature rises with each ramp stepwise by almost 200 K to a higher level, Fig. 22b, and then always decreases slightly with the boundary-layer running length, as was discussed in Chapter 4.

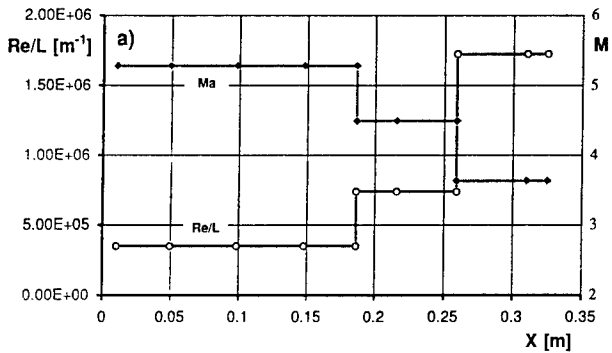


Fig. 22a Generic intake model (3 outer ramps) at  $M_\infty = 7$ ,  $A = 35$  km,  $\epsilon = 0.85$ , turbulent boundary layer, approximate method, Ref. 28, unit Reynolds numbers and Mach numbers on the ramps

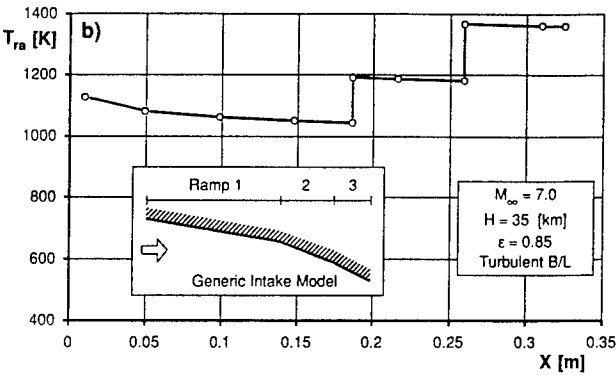


Fig. 22b Generic intake model (3 outer ramps) at  $M_\infty = 7$ ,  $A = 35$  km,  $\epsilon = 0.85$ , turbulent boundary layer, approximate method, Ref. 28, radiation-adiabatic temperatures

7. IMPLICATIONS FOR SURFACE PHENOMENA

The discussion sofar has shown, that radiation cooling influences strongly heat loads, viscous drag - if the flow is turbulent - and that the state of the boundary layer - laminar or turbulent - plays a large role. It has also been shown that hot-spot situations at attachment lines occur, and that in general some characteristic boundary-layer thickness plays a role, which itself depends on the wall temperature. Consequently one has to ask whether and how transition and turbulence themselves, thermochemical effects (catalytic surface recombination), and strong viscous interaction phenomena are affected by, or interrelated with the thermal state of the vehicle surface, i.e. with the radiation-adiabatic temperature. In the following some considerations are given in this regard.

The influence of the surface temperature and the surface-near temperature gradient on the properties of turbulent flow is not well known. The turbulent heat transfer, as well as the turbulent (diffusive) mass transfer (important also in turbulent mixing processes) is regarded in computations by choosing, more or less without any reasonable justification, a constant turbulent Prandtl number or Schmidt number.

The situation is different with regard to the instability and transition behaviour of boundary layers. It is long known from inviscid stability theory (Rayleigh equation and the resulting point-of-inflexion criterion), that heat transfer out of the flow at the wall (cooling) stabilizes the flow, while heat transfer into the flow (heating) destabilizes it (this hold for air, generally for gases, only). If higher instability modes (Mack modes) are present, which is typical for boundary-layer edge Mach numbers larger  $M_e = 3$  to 4, this behaviour is reversed. Hypersonic boundary-layer instability and transition is affected accordingly (generalized point-of-inflexion criterion). Hence the radiation-adiabatic temperature, or with active cooling, the effective surface temperature, with the resulting steep temperature gradients has a large influence, and has to be regarded in design work, when transition locations and patterns have to be determined.

Thermochemical effects rise with the total enthalpy of the flow, which rises with the flight speed squared. If thermal and/or chemical non-equilibrium is present in the flow, especially in

the wall-near flow, the wall temperature and possible catalytic surface recombination, as well as the mass-diffusion phenomena in the boundary layer are coupled to a high degree. Again, the surface temperature to be regarded in the aerothermodynamic design is the radiation-adiabatic temperature, or, with active cooling, the effective surface temperature.

Finally, it can be shown, see e.g. Ref. 8, that strong shock/boundary-layer interaction phenomena are governed by the momentum flux of the boundary layer approaching the interaction region (shock/boundary-layer interactions at control devices, leading edges, etc.). This momentum flux depends on the density distribution across the boundary layer, which in turn depends on the temperature distribution: cold surfaces hence lead to larger momentum fluxes, and hot surfaces to smaller ones. The situation is somewhat different with viscous hypersonic interaction, the other strong viscous-interaction phenomenon. Here the boundary-layer thickness is the governing item, and accordingly the interaction is stronger on hot surfaces than on cold ones (important for mechanical loads and pitching moments of slender forebodies of airbreathers). In the design of both airbreathers and reentry vehicles strong interaction effects must be regarded, because they can be very important with regard to mechanical and heat loads, and component efficiencies (control surfaces, inlets, etc.).

## 8. NEED OF HOT EXPERIMENTAL TECHNIQUE

The preceding chapters have shown, that at this time quite some knowledge is available about the phenomena on, and the problems connected with radiation-cooled surfaces. There is, however, a major problem. All the knowledge about radiation-cooling effects, which is available today, has been derived from computations. This concerns the mechanisms and dependencies, including scaling laws, which are an important tool in design work. Completely missing is the experimental verification and validation, except for some flight data, Chapter 4. Both are essential, especially if the configuration under consideration is drag critical and/or weight critical. Moreover, the uncertainties in transition and turbulence modelling, as well as the modelling of catalytic surface recombination, must be taken into account.

The experimental problem is not only to be seen with regard to the general simulation (similarity) problem, but especially with regard to the fact that both radiation cooling and catalytic surface recombination depend on the absolute temperature, which cannot simply be scaled up or down like the wall temperature in classical aerodynamic wind-tunnel simulations.

In addition they depend on the Reynolds number (boundary-layer thickness) and the Mach number, at high total enthalpy flow also on the Damköhler numbers. A full ground test simulation of the flight situation thus is not possible, see Chapter 6, and e.g. Ref. 29, and the Transfer Model approach discussed in Ref. 30, or building block approaches as discussed in Ref. 31 are necessary, if the design sensitivities demand large prediction accuracies.

In experimental work the radiation-adiabatic temperature for a given configuration at given flight conditions, non-withstanding the scaling problem, has not simply to be duplicated (this would imply that it is known already to the needed degree of accuracy), but has to be determined, i.e. any theoretically found data has to be validated, like the understanding of the involved and coupled phenomena.

In view of this discussion the most pressing problem is to build the experimental capabilities (model techniques, measurement techniques, Refs. 32, 33) in order, initially, not to aim for a solution of the design simulation problems, but to investigate the effects seen in computations, to quantify them, to study the influence on, and the influence by transition and turbulence phenomena, to study thermochemical effects, strong interaction effects and so on. These will then be building blocks of the transfer models, which are essentially numerical computation methods and/or scaling laws.

A suitable hot experimental technique should have the following characteristics (see e.g. Ref. 32):

- o duplication or near-duplication of free flight Mach number, Reynolds number and total enthalpy,
- o model surface in radiation-adiabatic equilibrium or near-equilibrium.

The Hot Experimental technique would have four major constituent parts:

- o hot-surface model techniques,
- o suitable measurement techniques,
- o the wind tunnel with the flow properties mentioned above,
- o effective scaling laws.

The wind tunnel must be a quiet tunnel, if transition laminar-turbulent is to be simulated. For very high total enthalpies the question of freezing of internal degrees of freedom and of dissociation must be considered. In any case the tunnel walls itself must not radiate heat towards the wind-tunnel model (short measurement times, cooling of tunnel walls).

The surface of the model must attain radiation-adiabatic equilibrium or near-equilibrium during the running time of the wind tunnel. A controlled heat flux into the surface could be tolerated depending on the test objective. The model surface must have a controlled emissivity near to the real one. For very high total enthalpies a hot surface model would allow in principle also a proper simulation of catalytic surface recombination, if realistic surface materials/coatings are employed.

The measurement technique should encompass non-intrusive field measurement methods as well as force measurement methods, again depending on the test objectives. For the scaling laws see Chapter 6.

Work on aspects of the hot experimental techniques has been performed recently. Simple configurations (flat plate and wedge) were designed and partly also tested by Dasa, Refs. 34, 35, and the DLR Köln-Porz. Wind-tunnel testing with insulated HERMES models, Refs. 33, 36, was performed, Ref. 37. Major problems are seen in the model philosophy: either self-heating models, or pre-heated models, which come close, also in short-time test facilities, to the radiation-adiabatic temperature, Ref. 32. The other problem is measurement techniques: any insert into the surface (temperature and heat flux measurement gauges, pressure measurement gauges, wall shear-stress measurement gauges) falsifies in principle the surface properties (emissivity, catalyticity), and the material-in-depth heat transmission and capacity properties. Any heat loads-related measurements then represent the situation in the insert, and not the actual situation, if the insert can bear the heat loads at all. Hence the above quest for non-intrusive measurement methods.

### 9. TOWARDS THE INTEGRATED AERO-THERMODYNAMIC DESIGN

In the following an - idealized - integrated aerothermodynamic design approach, Ref. 38, is sketched, which makes use of the insights into the implications of surface radiation cooling, which were discussed in the preceeding chapters. Of course, the present aerodynamic configuration definition of hypersonic vehicles also regards heat-loads aspects. However, the definition and development (engineering) processes are not yet refined in the above sense, the tools are not yet fully ready and integrated, and the general experience has still to be build.

The major elements of the integrated aerothermodynamics design are shown schematically in Fig. 23. They hold for any high-speed vehicle, however, elements of propulsion integration are not included. Assume that

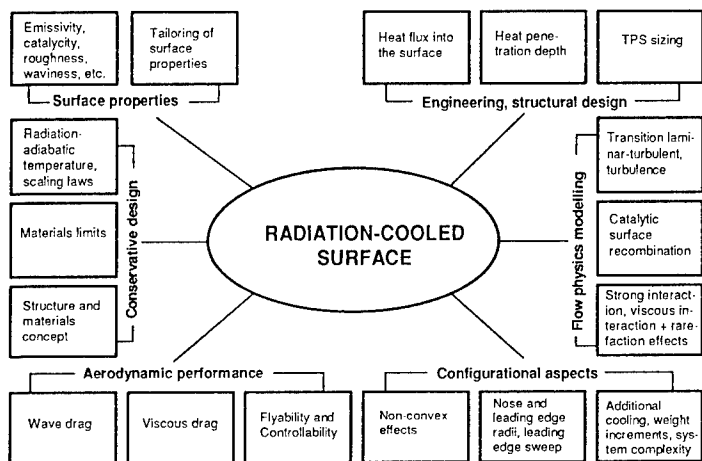


Fig. 23 Elements of the integrated aerothermodynamic design and their interrelation with radiation-cooled surfaces (TPS: thermal protection system)

an initial configuration is defined, and that the governing flight situation (speed, altitude, vehicle attitude) is specified. With a chosen nominal surface emissivity and catalyticity (**surface properties**) the radiation-adiabatic temperature as conservative heat-load estimation can be computed with either approximate or numerical method (this gives also the data base for scalings). With this the materials limits (structure and materials concept) can be fixed for (discrete) parts of the configuration (**conservative design**). The viscous drag of the configuration with its strong dependency on the surface temperature, if the flow is turbulent, is then determined, together with the wave drag, which depends on the nose radius, and on the radii and sweep of all leading edge. Flyability and controllability are investigated (**aerodynamic performance**). If the latter demand configurations changes, if wave drag considerations demand smaller radii and/or larger sweep angles, the changes are made accordingly. With the scaling laws immediately the influence on the radiation-adiabatic surface temperature can be checked. Non-convex must be quantified, if they become critical. Finally, if the materials limits are exceeded by the surface temperature, for instance at the nose, and the radius must remain small for wave-drag reasons, active cooling must be considered, with its weight increments and possible increase of systems complexity (**configurational aspects**).

If the design is critical with regard, for example, to structural weight (mechanical loads and heat loads) and/or viscous drag, the transition location must be determined with high accuracy, catalytic surface recombination must be considered in detail, strong interaction and rarefaction effects (mechanical and heat loads) must be localized (especially the former) and quantified (**flow physics modelling**). This would demand in general the use of sophisticated numerical methods.

After the design is frozen and verified as far as possible in ground-simulation facilities (for the simulation problems and shortcomings see e.g. Refs. 30, 39) etc., the dimensioning loads cases for the structural design must be determined on the nominal flight trajectory, including possible emergency trajectories. The time-dependent heat flux into hot primary structures, stresses and deformations, heat penetration depths in outer or inner thermal protection systems, etc. are to be estimated with sufficient accuracy (**engineering, structural design**), which demands more and more sophisticated tools with exotic materials and weight-saving demands.

Finally permissible surface roughness, waviness etc. must be determined, if the viscous drag and heat loads especially in flight regimes, where the boundary layers are turbulent, are critical. Surface roughness and waviness should be permitted to be as large as possible, i.e. just subcritical, because small tolerances would lead to excessive manufacturing costs for the airframe, or a thermal protection system. Of course, where the surface temperature is low compared to the materials limits temperature, the surface emissivity can be reduced. With turbulent flow, the surface temperature should be as large as possible, because this reduces the viscous drag (**surface properties**).

This very schematically and with large abstractions discussed approach becomes nevertheless more and more desirable to be established. The general demands on new space transportation systems to reduce the transportation costs strongly (by one order of magnitude as often is claimed), makes highly integrated design and optimization processes necessary. This holds especially for possible airbreathing systems. Fig. 24 finally summarizes the tools necessary for such an integrated approach.

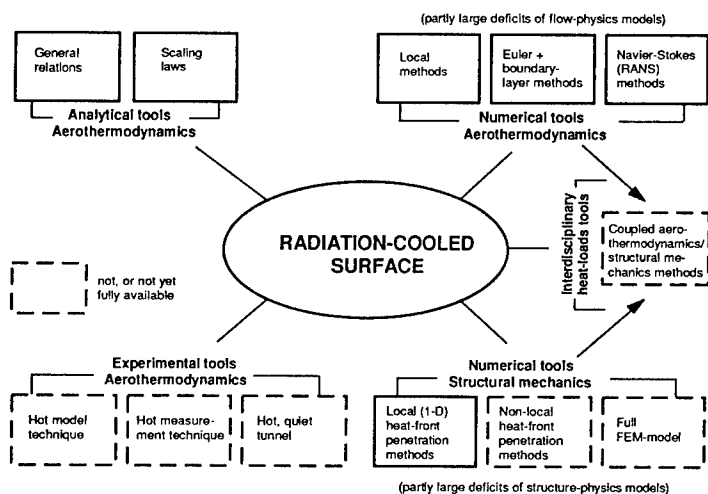


Fig. 24 Tools of the integrated aerothermodynamic design and their availability in design work

Again, this is a very schematical look at the situation. Some of the tools dubbed to be not available or not yet fully available, do already exist in the scientific community. In order to be suitable for design work, they must be robust, verified and reliable tools, and if they are computational tools, they must be compatible with the computing means (and their costs) usually available in design work. Of course, computing costs are decreasing rapidly, and the advent of parallel architectures with teraflops performance will change the design processes lastingly.

# 10. CONCLUSION

Radiation cooling of the surface of hypersonic vehicles involves very interesting fluid mechanical problems with strong implications for the design of such vehicles. It was shown that the radiation-adiabatic temperature, like the recovery temperature a conservatively estimated surface temperature, depends, other than the recovery temperature, on the Reynolds number, on a length scale, etc. This was demonstrated with numerical examples, which show the very strong influence of the boundary-layer state (laminar or turbulent), and also that at attachment lines hot-spot situations exist, which was explained in detail. Because of the different dependencies a scaling approach can be formulated, when comparing data on bodies of different size (e.g. wind-tunnel model/real-size configuration). Similar flow topologies in both cases permit a sufficiently good scaling of the radiation-adiabatic temperature. An experimental validation of the findings is not possible with the presently employed cold-surface wind-tunnel models. A Hot Experimental Technique must be developed, if an accurate and reliable prediction and validation is desired. Such a possible technique was discussed. Finally the structure of a possible integrated aerothermodynamic design approach, with the radiation-cooled surface in the center, was sketched. It certainly is a very demanding, but at the same time also necessary approach, which must be realized in one or the other form in the future.

# 11 REFERENCES

- Hirschel, E.H., "Heat Loads as Key Problem of Hypersonic Flight", *Zeitschrift für Flugwissenschaften und Weltraumforschung (ZfW)*, Vol. 16, No. 6, 1992, pp 349-350.
- Bertin, J.J., Glowinski, R., Periaux, J., (eds), "Hypersonics", Volume I, "Defining the Hypersonic Environment", Birkhäuser, Boston, 1989.
- Mundt, Ch., Keraus, R., Fischer, J., "New, Accurate, Vectorized Approximations of State Surfaces for the Thermodynamic and Transport Properties of Equilibrium Air." *Z. Flugwiss. Weltraumforsch.*, Vol. 15, No. 3, 1991, pp 179-184.
- Hirschel, E.H., "Aerothermodynamic Phenomena and the Design of Atmospheric Hypersonic Airplanes", in "Advances in Hypersonics II", Vol. I, "Defining the Hypersonic Environment" (J.J. Bertin, J. Periaux, J. Ballmann, eds.), Birkhäuser, Boston, 1993, pp 1-39.
- Monnoyer, F., Mundt, Ch., Pfitzner, M., "Calculation of the Hypersonic Viscous Flow Past Reentry Vehicles with an Euler/Boundary-Layer Coupling Method", *AIAA-Paper 90-0417*, 1990.
- Monnoyer, F., "Personal communication", 1992.
- Hirschel, E.H., Mundt, Ch., Monnoyer, F., Schmatz, M.A., "Reynolds-Number Dependency of Radiation-Adiabatic Wall Temperature", *MBB-FE122-AERO-MT-872*, 1990.
- Hirschel, E.H., "Viscous Effects", *Space Course Aachen 1991*, Paper No. 12, also *MBB/FE202/S/PUB/441*, 1991.
- Hirschel, E.H., Koç, A., Riedelbauch, S., "Hypersonic Flow Past Radiation-Cooled Surfaces", *AIAA-Paper 91-5031*, 1991.
- Höld, R., "Die Berechnung dreidimensionaler Hyperschallströmungen mit Hilfe der Viscous-Shock-Layer Gleichungen", *Doctoral Theses, University of the Armed Forces München*, 1989, *Fortschrittsberichte VDI, Reihe 7, Nr. 171*, Düsseldorf, VDI-Verlag, 1990.
- Anderson, J.D., "Hypersonic and High Temperature Gas Dynamics", McGraw-Hill, New York, 1989.
- Fay, J.A., Riddell, F.R., "Theory of Stagnation Point Heat Transfer in Dissociated Air", *J. of Aeronautical Science*, Vol. 25, No. 2, 1958, pp 73-85.
- Hirschel, E.H., "Evaluation of Results of Boundary-Layer Calculations with Regard to Design Aerodynamics", *AGARD-R-741*, 1986, pp 6-1 to 6-29.
- Simeonides, G., "Simple Formulations for Convective Heat Transfer Prediction Over General Aerodynamic Configurations and Scaling of Radiation-Equilibrium Wall Temperature", *ESA EWP-1860*, 1995.
- Koç, A., "Aerodynamische Aufheizung des Demonstrators", *MBB/FE122/HYPAC/TN/ 0130*, 1990.
- Riedelbauch, S., "Aerothermodynamische Eigenschaften von Hyperschallströmungen über strahlungsadiabate Oberflächen", *Doctoral Thesis, Technical University München*, 1991.
- Riedelbauch, S., Hirschel, E.H., "Aerothermodynamic Properties of Hypersonic Flow Over Radiation-Adiabatic Surfaces", *Journal of Aircraft*, Vol. 30, No. 6, 1993, pp 840-846.
- Hagmeijer, R., Oskam, B., de Cock, K.M.J., Perrier, P., Rostand, P., Hashholder, J.M., "Validation of the Computational Methods used for the Design of the Canopy of the HERMES Spaceplane", *AIAA-paper 94-1865*, 1994.

19. Weiland, C., "External Shape Definition and Aerodynamic Data Set of CRV/CTV Shapes", CRV/CTV-Report HV-TN-2100-01-Dasa, 1995.
20. Schmatz, M.A., Höld, R.K., Monnoyer, F., Mundt, Ch., Rieger, H., Wanie, K.M., "Numerical Methods for Aerodynamic Design II", Space Course Aachen, 1991, Paper No. 62, also MBB/FE211/ S/PUB/442, 1991.
21. Radespiel, R., personal communication, 1994.
22. Wüthrich, S., Sawley, M.L., Perruchoud, G., "The Coupled Euler/Boundary-Layer Method as a Design Tool for Hypersonic Re-Entry Vehicles", Z. Flugwiss. Weltraumforsch., Vol. 20, No. 3, 1996.
23. Williams, S.D., "Columbia, the First Five Flights Entry Heating Data Series, Volume 1: an Overview", NASA CR-171 820, 1984.
24. Williams, S.D., "Columbia, the First Five Flights Entry Heating Data Series, Volume 3: the Lower Windward Surface Center Line", NASA CR-171 665, 1983.
25. Höld, R.K., Fornasier, L., "Investigation of Thermal Loads of Hypersonic Vehicles with Emphasis on Surface Radiation Effects", ICAS-Paper 94-4.4.1, 1994.
26. Åslund, H., "Configurational Heat Loads Calculations on the Hypersonic Flight Test Vehicle HYTEX R-A<sub>3</sub>", SAAB TM L-0-1 B 789, 1994.
27. N.N., "Equations, Tables, and Charts for Compressible Flow", NACA R-1135, 1953.
28. Georg, H.-U., personal communication, 1996.
29. Henckels, A., Maurer, F., "Hypersonic Wind-Tunnel Testing with Simulation of Local Hot Wall Boundary Layer and Radiation Cooling", Z. Flugwiss. Weltraumforsch., Vol. 18, No. 3, 1994, pp 160-166.
30. Hirschel, E.H., "The Hypersonics Technology Development and Verification Concept of the German Hypersonics Technology Programme", AIAA-Paper 93-5072, 1993.
31. Perrier, P., Rostand, P., "Hypersonic Airbreathing Aircraft Integration Through CFD: Global Simulations for Global Thinking", AIAA-Paper 94-3090, 1994.
32. Hirschel, E.H., "Hot experimental Technique: a New Requirement of Aerothermodynamics", in "New Trends in Instrumentation for Hypersonic Research" (A. Boutier, ed.), Kluwer Academic Publ., Dordrecht, 1992, pp 23-39.
33. Visintini, L., Couedor, C., "Design and Production of Insulated Models of the HERMES Shuttle for Heat-Transfer Measurements at Hypersonic Speeds", AGARD CP514, 1993, pp 10-1 to 10-9.
34. Schulze, B., Hakenesch, P. "Rapid Skin Development". Phase 1/Model 4006, Final Report, H-NT-1-0351-Dasa, 1993.
35. Schulze, B., Hakenesch, P. "Rapid Skin Development". Phase 2/Model 4006, Final Report, H-NT-1-0350-Dasa, 1993.
36. Le Bozec, A., Rapuc, M., Guillemet, V., Krek, R., Eitelberg, G., "Heat Flux and Pressure Measurements on Hermes at High Enthalpy Conditions in HEG", Second European Symposium on Aerothermodynamics for Space Vehicles, ESTEC SP-367, 1994, pp 215-219.
37. Wolfrum, G., "Industrial Report of Test Program No. 2504 - Industrial Technology Conservation on Aero-controlled Reusable Reentry Vehicles Hypersonic Wind-Tunnel Testing", HT-N-E33.3-022-DASA, 1995.
38. Hirschel, E.H., Heindl, H.A., "Aerothermodynamics Analysis Tools and Strategy for the Design of Reusable Launch Vehicles", Dasa/LME12/S/STY/188/B, 1996.
39. Hirschel, E.H., "Hypersonic Aerodynamics", Contribution to the Space Course 1993. München, October 11-22, 1993, 2nd Space Course on Low Earth Orbit Transportation, München, 1993, Vol. 1, pp 2-1 to 2-17.

AGARD-R-813, 1996

(AGARD-FDP-VKI Special Course on Aerothermodynamics and Propulsion Integration, Rhode-Saint-Genèse, April 15-19, 1996)

# VISCOUS/INVISCID AND REAL-GAS EFFECTS ASSOCIATED WITH HYPERSONIC VEHICLES

Michael S. Holden

Research Fellow, Physics & Chem. Sciences Dept.  
Calspan-University at Buffalo Research Center  
4455 Genesee Street, P.O. Box 400  
Buffalo, New York 14225

## 1. SUMMARY

In this segment of the lecture series, we discussed some of the important effects of viscous/inviscid interaction and real gas phenomena on the design and performance of hypersonic vehicles. Following a general review of the importance of such effects on vehicle design and performance, we discuss the effects of non-equilibrium and real-gas flows with emphasis on their importance to the accurate simulation of hypervelocity flows in ground test facilities. Because boundary layer transition exerts a dominant influence on vehicle performance in a hypersonic flow regime, we briefly review some of the key phenomena which control boundary layer transition in regions of adverse pressure gradient, crossflow and along the attachment line of swept leading edges. For it is such phenomena, where it is currently believed that experimental measurements in hypersonic ground test facilities are of relevance. The key phenomena associated with shockwave/boundary layer interaction for both laminar and turbulent, two- and three-dimensional flows are briefly reviewed and compared with the most recent prediction techniques. The aerothermal loads and flowfield phenomena associated with regions of shock/shock interaction are then discussed with particular emphasis on the effects of boundary layer transition and low-density flows on the magnitude of the peak heating in regions of Type III and IV interactions. Film and transpiration cooling must be employed to cool the internal components of high performance scramjet engines. Correlations are presented to show the effectiveness and relative effectiveness of film and transpiration cooling both with and in the absence of shockwave/boundary layer interaction. The aerothermal and aero-optical performance of seekerheads for hypersonic interceptors represents currently one of the most key areas in hypersonic technology. The techniques that are being employed to obtain measurements of the aerothermal and aero-optical performance in the LENS facility are briefly reviewed. Finally, we present information on the "CUBDAT" database of hypersonic measurements which have been assembled from fundamental studies of the phenomena discussed in this segment of the lecture series.

## 2. INTRODUCTION

With the development of powerful high-speed computers and robust efficient numerical techniques to solve the Navier-Stokes equations, the prediction of simple flows over configurations such as the Space Shuttle and the Hope Spacecraft have become a practical reality. However, even in the analysis of such simple configurations, we are faced with modeling the effect of chemical nonequilibrium, boundary-layer transition, surface roughness and laminar, transitional and turbulent leeside wakes and regions of shockwave/boundary layer interaction over the control surfaces and in the interactions generated by attitude control thrusters. Such problems are significantly multiplied when the design of an air-breathing vehicle designed to fly into orbit is considered. Here the effects of nonequilibrium must be combined with those associated with mixing and combustion, as well as techniques to cool regions associated with hot spots in the flow such as those generated in the shock/shock interaction regions on the inlets and the three-dimensional interactions which are generated on and downstream of the fuel injector systems. Again, chemical nonequilibrium is combined with reacting gas phenomena and boundary layer relaminarization in the nozzle section of the hypersonic vehicle.

Although there are major problems associated with the construction of models of turbulence and chemical kinetics for boundary layers and free shear layers subjected to strong pressure gradients and influenced by chemical non-equilibrium and combustion, there are a number of key problem areas in which modeling must be addressed if we are to predict the overall vehicle performance over the complete flow regime. In the high-Mach-number, high-temperature, low-density regime, there are important modeling problems associated with the catalytic surface/reacting gas interaction. Whereas research in low-density flows has continued at a steady pace in low-enthalpy flows, there has been almost no experimental research during the past two decades in hypervelocity ( $V > 10,000$  fps or  $3.05$  km/s) flows. One of the areas of interest for small re-entry vehicles such as the Japanese Hope is the transitional flow regime between free-molecular and continuum flow. Here, flow computation using combined Navier-Stokes and DSMC codes must incorporate models of real gas chemistry and gas/surface interaction which must be validated by experiment. The short-duration facility, in one of its various modes of operation, has been used successfully to generate the high-purity hypervelocity flows necessary to study such phenomena. Flowfield and surface diagnostics have been developed to



obtain measurements in short-duration flows ( $\sim 1$  ms), typically generated in these facilities when operated at high-temperature conditions. Thus, there are the tools available for experimental studies to contribute significantly to an increased understanding in this flow regime.

One of the most important areas for research in hypersonic laminar boundary-layer flows is associated with the understanding of chemical nonequilibrium and combustion effects on the size and characteristics of separated flows developed in regions of shockwave/boundary-layer interaction, shock/shock interaction and wakes. Whereas solutions to the full Navier-Stokes equations have been shown to successfully describe separated regions in non-reacting hypersonic flows, nonequilibrium air chemistry or combustion in the recirculation regions provides problems that can be resolved only with combined experimental and numerical studies. In such separated flows, free shear layer transition can occur at Reynolds numbers between  $10^3$  and  $10^4$  or close to the boundaries of continuum and non-continuum flow. The influence of nonequilibrium chemistry on hypersonic ramjet performance in laminar flows is an area for which experimental research is essential to provide the answers to critical questions. Likewise, one can have little confidence in numerical solutions to laminar combusting hypersonic flows without experimental verification. In the experimental study of such separated flows, flow duration becomes an important parameter, and test times of one or more milliseconds may be required for establishment of complex interaction flows. For this application, larger reflected shock tunnels are currently in existence that would be acceptable facilities to use, which are capable of generating test times of up to 5 ms.

Predicting boundary-layer transition to turbulent flow and the characteristics of transitional flows presents one of the formidable and key problems in hypersonic flows. Whereas such flows are difficult to predict at any Mach number, at hypersonic speeds, they are so extensive and have such large effects on aerothermal loads that they must be adequately described. Since the basic mechanisms of transition are not understood, only a careful combination of measurements in ground and flight tests will provide the insight required to validate the modeling of these flows. Semi-empirical transition prediction techniques such as the  $(Re)^N$  method and more sophisticated techniques such as those developed by Herbert require validation on both the fundamental and correlational level. Measurements are required to define the basic instability modes associated with transition in hypersonic flow, and the mechanism involved with the gross breakdown of the laminar flow and the transition to fully developed turbulent flow and to quantify the level of background disturbances. Extensive regions of transitional and low Reynolds-number turbulent flows in and downstream of the transition can dominate the aerothermal characteristics of hypersonic vehicles

and the performance of air-breathing engines in the transitional flow regime.

The structure of turbulent boundary layers in regions of shockwave/turbulent boundary-layer interaction, and shear-layer mixing regions in hypersonic flows are strongly influenced by compressibility effects. How compressibility influences shock/turbulence interaction, flow unsteadiness and eddy shocklets, and flow structure remains to be determined. However, it is clear that accurately predicting the size and structure of turbulent flows in strong pressure gradients will require detailed insight from experimental research. The shear-layer development in mixing regions between dissimilar gases, in regions of jet injection, and also film or transpiration cooling at hypersonic speeds require extensive experimental research. Clearly, adding nonequilibrium flow chemistry and combustion to the problem, as they occur in a scramjet engine, presents a situation well beyond the current state of the art in understanding and computation.

Because of the intrinsic integrated structure of the airframe and engine for a hypersonic air-breathing vehicle, all of the problems mentioned previously are important in the design of the engine of an air-breathing vehicle. The nonequilibrium flow developed in the leading-edge flowfield will influence the flow development on the compression ramps and possibly into the inlet. Earlier experimental studies have shown that strong distortions to the inlet flows results from boundary layer transition and viscous/inviscid interaction and crossflow over compression ramps. Flow distortions can arise from the compression ramp and cowl shocks separating the sidewall and cowl boundary layer. The sidewall boundary layer will be intrinsically transitional in nature, and predicting the flows in the presence of interacting shock waves and flow separation will be extremely difficult. Regions of shock/shock interaction on the cowl lip and leading-edge of the sidewalls will induce large leading edge heating rates as well as significant flow disturbances inside the engine. The blunt leading edges of the sidewalls and cowl will induce flow chemistry that may exert significant effects on combustion chemistry and the regions of shockwave/boundary layer interaction inside the engine. Two- and three-dimensional separated flows may be induced on the floor, the sidewalls, and the cowl of the engine. The characteristics of these flows must be carefully simulated in experiment and/or predicted in numerical computations. It is in these flows that there are currently no successful turbulence models. Unquestionably, various forms of film and transpiration cooling must be employed to maintain the engine integrity. Fuel injection from the engine walls and possibly struts will generate complex interacting flowfields, which again must be carefully simulated numerically and experimentally. Here combustion and nonequilibrium turbulence and flow chemistry are all important. Without experimental verification, current models of turbulent mixing in these flows are seriously in question.

Again, flow chemistry and viscous/inviscid flow interaction control the flow in, and hence the performance of, the nozzle. In these flows, relaminarization may also play an important, but poorly understood, role, which must be explored in experimental simulations.

3. REAL-GAS EFFECTS ASSOCIATED WITH AEROTHERMODYNAMIC AND PROPULSION TESTING IN HYPERVELOCITY FACILITIES

3.1 Real-Gas Effects Associated With Non-Equilibrium Flows and Scramjet Combustion Testing

The stagnation enthalpies encountered in flight at hypersonic speeds result in flowfield temperatures high enough to dissociate the chemical species in air (see Figure 3.1). To generate high velocities in ground test facilities, the reservoir states must be at comparable enthalpies and so, in the reservoir, the test gas is also dissociated. During the expansion to hypersonic speeds in the test section, the flow can depart from thermal and chemical equilibrium, and the conditions of the gas in the freestream flow in the test section can differ from those of the freestream gas under flight conditions. The static pressures and temperatures may differ, and the air may contain oxygen atoms and nitric oxide molecules. The latter species is relatively easily ionized, and so electrons are also present. At enthalpies corresponding to flight velocities above 5km/sec, nitrogen would also dissociate, and other ionized species would appear in significant concentration.

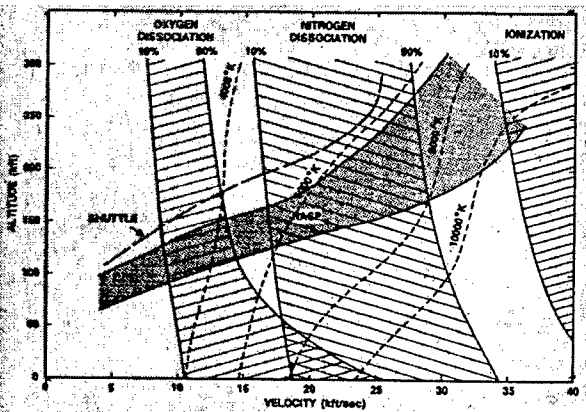


Figure 3.1 Illustrative Dissociation Fractions for Equilibrium Air Behind a Normal Shockwave

Because the level of chemical non-equilibrium in the freestream is strongly linked to reservoir pressure conditions, extremely high reservoir pressures are needed to closely replicate hypervelocity flows. Thus, developing high reservoir pressures represents an important factor as total enthalpy in developing high-temperature flows with low levels of freestream dissociation. The lack of duplication of flight conditions due to facility limitations is coupled to any lack of duplication due to nonequilibrium effects, simply because the degree of nonequilibrium varies with reservoir conditions and rate of expansion of gas into the test section. In this section, the impact of nonequilibrium on the lack of full simulation is emphasized, but both factors are addressed.

The velocity/altitude requirements for a number of vehicles of current interest are shown in Figure 3.2. This figure shows the requirements for duplicating flows over the Space Shuttle, airbreathing re-entry vehicles and a number of interceptor configurations which are currently being developed.

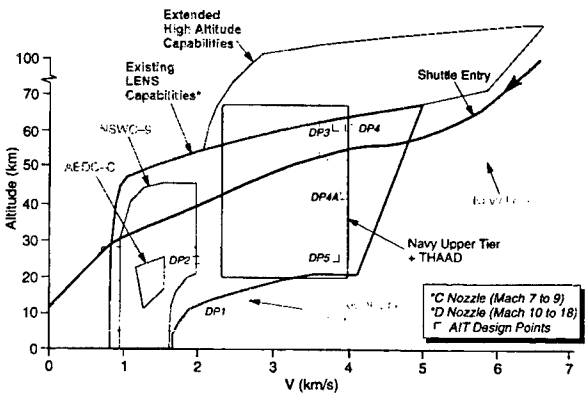


Figure 3.2 Velocity/Altitude Performance of LENS Facility

The thermodynamic state of the atmosphere at any altitude and the desired flow velocity, can be used to define the reservoir conditions from which expansion would produce a test flow duplicating the selected flight conditions. The equilibrium reservoir conditions corresponding to a portion of the flight regime of interest are shown in Figure 3.3. There the temperatures and pressures are shown for a stagnated, equilibrium reservoir condition for each altitude and velocity.

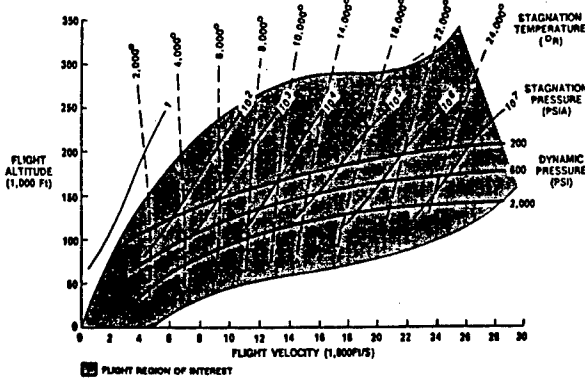


Figure 3.3 Reservoir Conditions for Ground Test Flight Duplication

Figure 3.3 also shows the extension of the full flow duplication region that is possible by using a nonreflected shock tunnel, i.e., by not stagnating the test gas. It should be noted that such operation entails a significant decrease in test time, which is already very limited at these high flow enthalpies. For aerothermal studies, often the flight Mach number and Reynolds number is duplicated in hypersonic flows by expanding the test gas to lower

velocity and static temperature. For density/velocity duplication, the flow can be expanded from an equilibrium reservoir to the desired velocity and the density corresponding to a given altitude, but with the static temperature at a level higher than that which will be obtained for a fully duplicated condition. The plots for density-altitude duplication are also shown in Figure 3.3.

Velocity and density-altitude duplication preserve the match in the total enthalpy and dynamic pressure, therefore, in the stagnation region of blunt body flows, the real-gas flowfields can be simulated to a good approximation. This is because the pressures and temperatures in the shock layer of such blunt body flows are relatively independent of the level of freestream dissociation. For slender bodies with thickness ratio  $\tau$ , the hypersonic similarity parameter  $M\tau$  can be duplicated under some circumstances. While for blunted slender configurations the situation is more complex, it is still possible to develop conditions such as to match the density and velocity inside the shock layer. The issues of test flow nonequilibrium effects on simulation of the flows about such vehicles were addressed recently in Reference 3-1.

The departure from chemical equilibrium in hypersonic expansions of air results in a test gas that is composed not only of molecular oxygen and nitrogen, but also of atomic oxygen and nitrogen as well as nitric oxide (NO), as discussed in References 40 through 42.  $N_2$  is basically equilibrated in nozzle expansions, and even though the N concentration is negligible in the element balance, it must be included in the chemical model because of its role in the shuffle reactions, which control the NO concentration:



Over the same range of flow velocities,  $NO^+$  is the dominant source of electrons in air.

The results of a sample calculation of the quasi-one-dimensional expansion of air are shown in Figure 3.4. Figure 3.4a illustrates the static temperature and static pressure, whereas Figure 3.4b shows the species concentrations for an expansion in the "D" nozzle of Calspan's 96-inch shock-tunnel. The reservoir or reflected shock conditions for this example are a temperature of 6000°K and a pressure of 500 atm, which produce a test flow velocity at high expansion ratios of approximately 14,000 fps. From the figure, the expected lag can be seen in the decrease in the static temperature due to the chemical energy not returned to the nonequilibrium flow. The static pressure also falls below the value for an equilibrium expansion; the density is affected very little by the nonequilibrium effects.

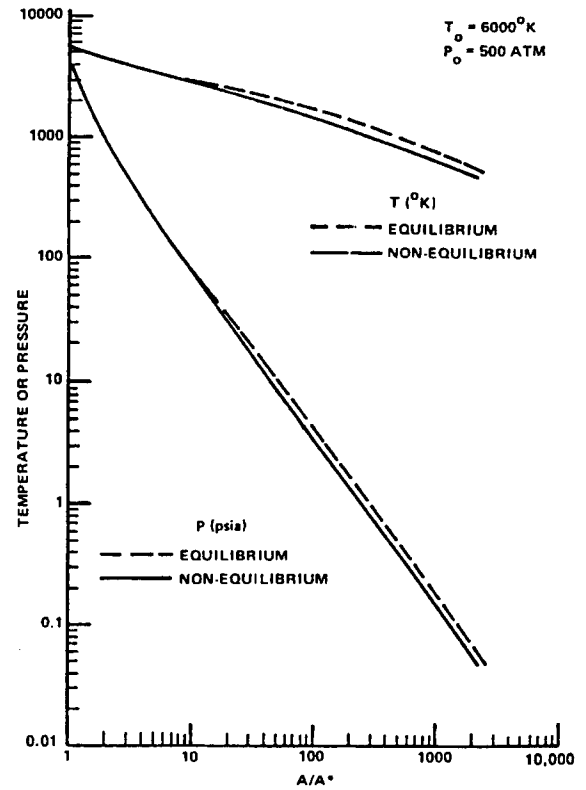


Figure 3.4a Nozzle Flow Gas Dynamic Properties

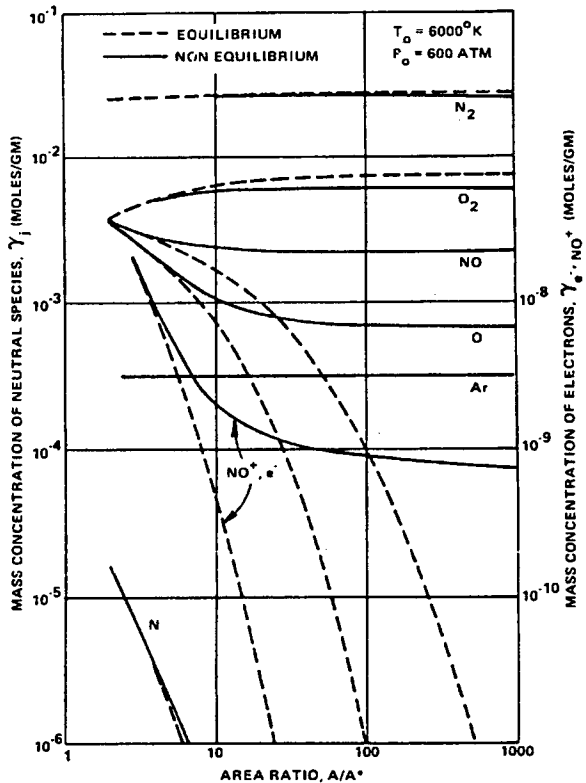


Figure 3.4b Nozzle Flow Species Concentration

The species concentrations are shown in mass concentrations units (moles/g). This removes the density dependence from the distributions and highlights the freezing process, i.e., when frozen,  $\gamma_j = \text{constant}$ . For this case, the NO concentration is about 5% of the total and exceeds the "frozen" O-atom concentration. The results of calculations similar to this example are used to examine the effects of test flow nonequilibrium on the interpretation of experiments in hypersonic facilities. In the remainder of this section, some generally useful results in correlating nonequilibrium effects are briefly reviewed.

Lordi and Mates (see Reference 3-2), performed a number of nonequilibrium nozzle flow calculations for expansions of air from reservoir temperatures up to 15,000°K and densities up to 100 amagats (standard atmosphere densities,  $\rho/\rho_0$ ). Based on the sudden freezing approximations for hypersonic expansion of simpler gases, it was found that the frozen enthalpy in nonequilibrium expansions of air could be correlated with the reservoir entropy. When the frozen enthalpy determined from the above computations for air was plotted against reservoir entropy, the results collapse to a single curve, as shown in Figure 3.5. The correlation with reservoir entropy is a consequence of the small entropy production due to chemical nonequilibrium effects. The limiting cases of frozen and equilibrium flows are both isentropic. The entropy values in the correlation can then be associated with that for the reservoir conditions and can be obtained from an equilibrium computation of the reservoir entropy or a Mollier diagram for air. The frozen species concentrations in hypersonic expansions of air also correlate with reservoir entropy. Figure 3.6, which is reported in Reference 3-3, is based on the solutions reported in References 3-4 and 3-2. The correlation with reservoir entropy is valid only for a specific nozzle geometry. However, the behavior of the results for the hyperbolic nozzle are representative and so are useful in defining the expected trends in the results for other facilities.

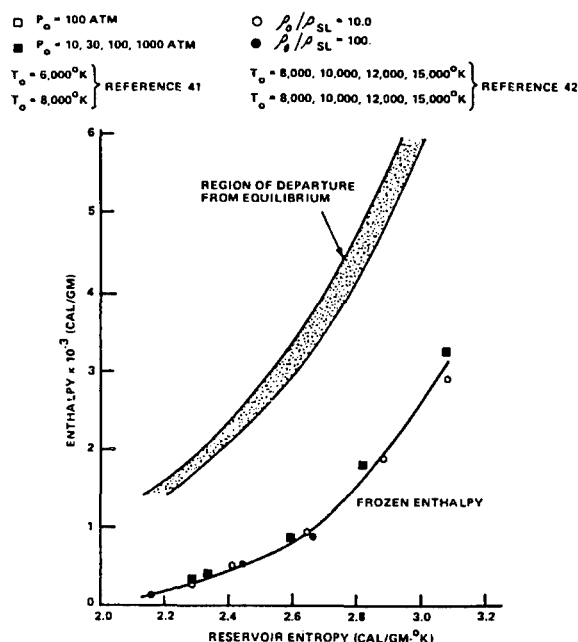


Figure 3.5 Correlation of Frozen Enthalpy Data for Nonequilibrium Nozzle Flow Solutions

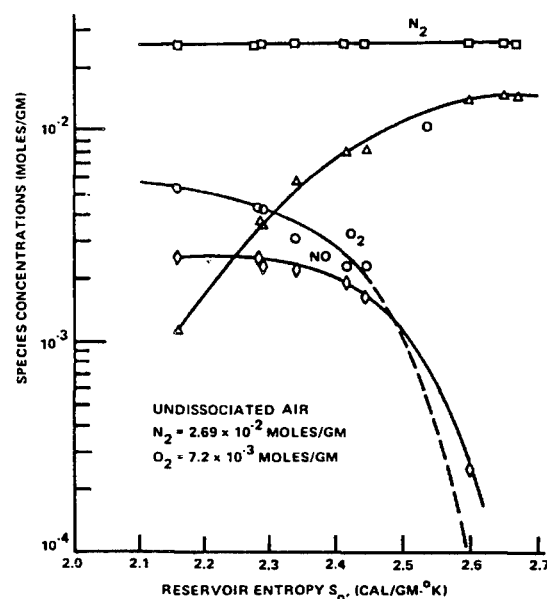


Figure 3.6 Correlations of Nozzle Flow Results for Frozen Species Concentrations

The nonequilibrium effect on velocity at high area ratios ( $>1000$ ) can be related to the frozen enthalpy by

$$U_{neq} / U_{eq} = (1 - H_f / H_0)^{0.5}$$

With the preceding correlations and the facility performance assumed in defining the full flight

duplication region of Figure 3.3, it was concluded<sup>39</sup> that nonequilibrium effects on flow velocity and concentration are negligible outside that region of facility performance. Whereas the simplification that nonequilibrium effects are confined to the velocity-altitude region in which full duplication of flight conditions would otherwise be possible is convenient, that situation may be optimistic because of the performance of advanced facilities considered in Reference 3-5. In some cases, special similitudes like binary scaling (see Reference 3-6) may be employed to achieve some flexibility in facility requirements and model scale. However, in other instances, it is possible to operate the test facility at high enough enthalpy and pressure levels to produce the physical phenomena being studied and to use a judicious combination of measurements and computations that contain the key physics to interpret the experiment.<sup>17</sup>

### 3.2 Test Flow Non-Equilibrium and Facility Limitations on the Simulation of Hypervelocity Flowfields

In discussions of hypersonic facilities, nonequilibrium effects are often cited as limiting the ability to define the test flow conditions. However, at these reservoir density levels, intermolecular forces can be even more important in the initial part of the nozzle expansion and are seldom mentioned. The effect of intermolecular forces on the compressibility in the reservoir is about 10%, whereas the dissociation effects on this quantity are only about 1%. The properties of a chemical equilibrium expansion for the case  $T_0 = 4000^\circ\text{K}$  and  $p_0 = 1000$  atm are tabulated in Table 1. These values were computed using the tables of equilibrium properties of air presented in Reference 3-7. The compressibility factors in the equation of state, as defined in Reference 3-7, are  $Z$  and  $Z^*$ , where

$$P = Z_p \frac{R0}{M} T = ZZ^* \rho \frac{R0}{M_0} T$$

where  $p$ ,  $\rho$ , and  $T$  are the mixture pressure, density and temperature, respectively,  $M_0$  is the undissociated molecular weight, and  $M$  is the molecular weight of the dissociated mixture. Thus,  $Z$  represents the contribution of the intermolecular force effects to the compressibility and  $Z^*$  the contribution of dissociation effects. Before the flow has expanded to an area ratio of 10 in the supersonic section of the nozzle, both contributions to the compressibility have decreased to less than 1%. Consequently, the dominant real-gas effects present in the reservoir and the initial portion of the nozzle expansion are the intermolecular force effects on the equations of state for air.

Table 1 Properties of equilibrium expansion of air ( $T_0 = 4000^\circ\text{K}$ ,  $p_0 = 1000$  atm)

	Reservoir	Throat	$A/A^* = 10$	$A/A^* = 100$	$A/A^* = 1000$
$T$ , K	4000.0	3591.9	1808.3	734.3	247.3
$p$ , atm	976.8	835.8	10.08	0.4715	0.0165
$p$ , kg/cm <sup>2</sup>	76.59	49.51	2.197	0.2131	0.0195
$\rho$	1.0938	1.0900	1.0023	1.0002	1.0000
$z^*$	1.0048	1.0051	1.0000	1.0000	1.0000
$u$ , ft/s	—	3895	8855	10020	10498
$x_{\text{NO}}$	0.0988	0.0782	0.0022	—	—
$x_{\text{O}}$	0.0181	0.0109	0.0000	—	—
$x_{\text{O}_2}$	0.1461	0.1630	0.2014	—	—
$x_{\text{H}_2}$	0.7241	0.7373	0.7795	—	—
$(\sum v)_{\text{H}_2}/\text{H}_0$	0.0981	0.0852	0.0196	—	—

a Conditions at sonic throat

For the total or reservoir temperatures in the range that can be obtained in current hypervelocity facilities, the dominant internal modes of excitation and chemical composition effects include: vibrational excitation of nitrogen molecules ( $\text{N}_2$ ) and the formation of oxygen atoms ( $\text{O}$ ) and nitric oxide ( $\text{NO}$ ) from the dissociation of  $\text{N}_2$  and  $\text{O}_2$ . In hypersonic nozzle expansions from the reservoir conditions being considered here, these quantities remain very close to their equilibrium values into the supersonic portion of the nozzle flow.

The potential effects of nozzle nonequilibrium on hypersonic testing have been the subject of extensive earlier studies and were reviewed in a recent paper (Reference 3-1 and 3-8). The shuffle reactions (Equations 1 and 2) are a key control on the generation of  $\text{NO}$  in expanding flows. These reactions have much larger rates than the net production of  $\text{NO}$ . Reaction (3) tends to be dominated by the reverse rate and Reaction (4) by the forward rate, so that  $\text{NO}$  is consumed by Reaction (3) and produced by Reaction (4), resulting in nearly a stationary state or constant concentration as shown by the equations below:



While nitrogen is a trace species at stagnation temperatures typical of flight below 5 km/sec, it is consumed by both reactions, thereby decreasing the  $\text{N}$  concentration even further. The  $\text{O}$  atoms are produced by both reactions but are consumed by the three-body recombination process until collisional freezing occurs.

The results of the nozzle calculations for the reservoir conditions of  $3500^\circ\text{K}$ , 1000 atm indicate that the freestream conditions are essentially ideal-gas, undissociated air in the shock-tunnel test section. The neutral species concentration variations along the nozzle expansion are plotted in Figures 3.7a and 3.7b. There, the behavior of the neutral species chemistry is graphically illustrated, with the  $\text{NO}$  concentration reaching a nearly constant, stationary-state value not far below the reservoir concentration. The computed concentration of  $\text{NO}$  in the test section is small, being less than 5 mole %. As illustrated on

Figure 3.7b, the frozen O-atom concentration is much lower than the NO concentration which, with the N-atom concentration (which is extremely small to begin with), is consumed very rapidly in the expansion at almost the rate corresponding to chemical equilibrium. At the 4000°K reservoir condition, the test section NO concentration is somewhat lower than that for the 3500°K case, being about 2.5%.

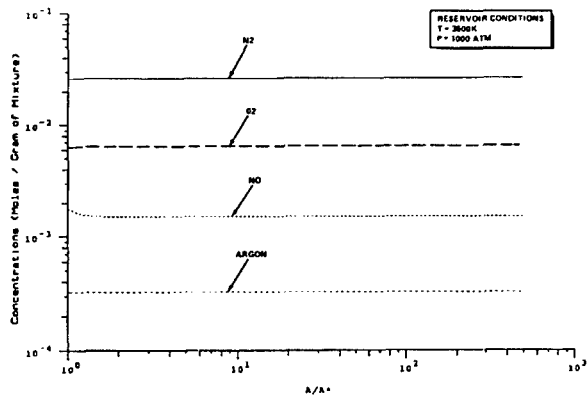


Figure 3.7a Nozzle Species Concentrations Versus Area Ratio

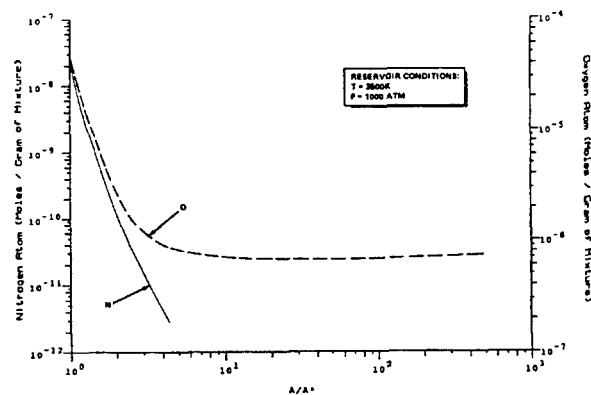
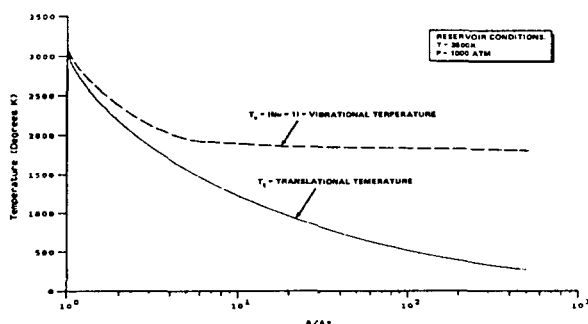


Figure 3.7b Nozzle Species Concentrations Versus Area Ratio

The N<sub>2</sub> vibrational temperature defined by the ratio of the first vibrational level is plotted, along with the translational/rotational temperature in Figure 3.8. The lower vibrational levels are essentially in a Boltzmann distribution at the frozen vibrational temperature of 1800°K indicated in the figure. This vibrational temperature value is well above the translational temperature, but the fraction of flow enthalpy tied up in this internal degree of freedom is only about 2% at this stage in the expansion.



**Figure 3.8** Nozzle Temperature Distribution Versus Area Ratio

Unless vehicle scale and all the freestream properties are duplicated, then the flowfield about complex configurations will differ to some degree from the flight flowfields. The discussions here demonstrate that facility limitations and nonequilibrium effects prevent full duplication. However, meaningful measurements can still be made that provide validation data for CFD codes and that can guide the design and reduce the risk of flight experiments. The approach taken here is that, if carefully designed, ground-test experiments can simulate some of the major physical effects of nonequilibrium hypersonic flowfields. Such experiments require predictive techniques to design the experiments and specific flowfield measurements to verify that the design conditions of the experiment have been met. Measurements of freestream conditions, including the nonequilibrium vibrational temperatures and species concentrations, should also be part of such measurements.

## REFERENCES

- 3-1. Lordi, J.A., Boyer, D.W., Dunn, M.G., Smolarek, K.K., and Wittliff, C.E., "Description of Nonequilibrium Effects on Simulation of Flows About Hypersonic Vehicles," AIAA Paper 88-0476, 1988.
- 3-2. Lordi, J.A. and Mates, R.E., "Nonequilibrium Expansions of High-Enthalpy Airflows," AIAA Journal, Vol. 3, Oct. 1965, pp. 1972-1974.
- 3-3. Harris, C.J., "Nonequilibrium Effects on High-Enthalpy Expansion of Air," AIAA Journal, Vol. 4, June 1966, pp. 1148-1149.
- 3-4. Eschenroeder, A.Q., Boyer, D.B., and Hall, J.G., "Exact Solutions for Nonequilibrium Expansions of Air with Coupled Chemical Reactions," Cornell Univ., Ithaca, NY, Cornell Aeronautical Laboratory Rep. AF-1413-A-1, May 1961.
- 3-5. Wittliff, E.C., Dundaram, T.R., Rae, W.J. and Lordi, J.A., "Study of High Density Hypervelocity Flows and Similitudes," AEDC TR-67-72, April 1967.
- 3-6. Gibson, W.E., and Marrone, P.V., "A Similitude for Nonequilibrium Phenomena in Hypersonic Flight," The High Temperature Aspects of Hypersonic Flow, edited by W.C. Nelson, AGARDograph 68, Macmillan, New York, 1964, pp. 105-132.
- 3-7. Hilsenrath, J., and Klein, M., "Tables of Thermodynamic Properties of Air in Chemical Equilibrium Including Second Virial Corrections from 1,500K to 15,000K," AEDC-TR-65-58, March 1965.
- 3-8. Dunn, M.G., Lordi, J.A., Wittliff, C.E., and Holden, M.S., "Facility Requirements for Hypersonic Propulsion System Testing," reprint from High-Speed Flight Propulsion Systems, Vol. 137 of *Progress in Astronautics and Aeronautics*, 1991.



#### 4. KEY BOUNDARY LAYER TRANSITION PHENOMENA FOR HYPERSONIC VEHICLE DESIGN

##### 4.1 Introduction

While boundary layer transition is one of the most important parameters in the design of hypersonic vehicles, there remains a considerable gap between "engineering" efforts to correlate the occurrence of transition and fundamental theoretical studies. The engineering studies have concentrated on correlating experimental measurements of transition obtained in flight tests, ballistic ranges, and wind tunnels against almost every conceivable parameter, while the fundamental studies have been aimed principally at exploring the modes of instability of the laminar boundary. The basic problem is that boundary layer transition is controlled by the detailed aerodynamic environment as well as the Reynolds number as demonstrated by Osborn Reynolds<sup>4-1</sup> in his classic studies.

##### 4.2 Observations of Turbulent Instabilities in Constant Pressure Laminar Hypersonic Boundary Layers

Shown in Figures 4.1 and 4.2 are schlieren photographs of the boundary layer transition region over a sharp, slender cone at Mach 13 and zero angle of attack. The first evidence of transition is given by the appearance of regular instabilities in the boundary layer. These eventually break down into a random structure as transition proceeds. Transition is observed as a growth of the boundary layer in the schlieren photographs as the position of maximum density gradient changes. Additionally, the heat transfer measurements in the transition region exhibit an intermittent character, which first appears as "spikes" in the heat transfer data measured near the beginning of the transition region. The magnitude and frequency of these spikes increase with downstream distance until the end of the transition process, when the spikes coalesce to give a higher heating rate with less intermittence. Spatial and temporal correlations of these measurements suggest that, close to their point of origin, the disturbances are convected downstream at approximately half the freestream velocity, while, toward the end of transition, the convection velocity has risen to approximately 85% of the freestream velocity. Closer examination of the photographs, as well as the heat transfer data, suggests that the instabilities leading to transition in the zero-angle-of-attack case

originate near the edge of the boundary layer and are three-dimensional in nature.

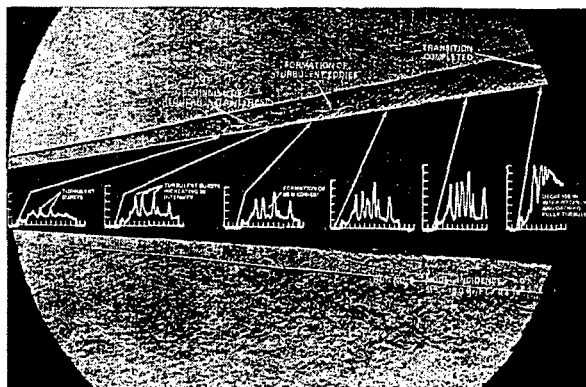


**Figure 4.1** Schlieren Photograph Showing Development of Transition of a Conical Boundary Layer in Hypersonic Flow

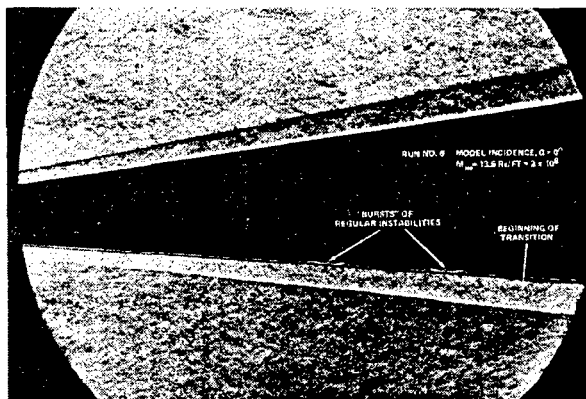


**Figure 4.2** Schlieren Photograph Showing Regular Bursting that Precedes Nonlinear Breakdown into Turbulence

These results, as well as the nature of the regular instabilities observed in the schlieren photographs, indicate that the dominant mode leading to transition in this case is not the axisymmetric second-mode disturbance, but a helical mode in the same frequency range as the axisymmetric range, and propagating at an oblique angle to the freestream. Recent computational studies (Bestek et al.<sup>4-2</sup>, Chang and Malik<sup>4-3</sup>) have found that the more relevant transition mechanism in high-speed boundary layers is the oblique-mode breakdown. Most notably, Chang and Malik<sup>4-4</sup> examined the non-linear interaction of a pair of oblique helical second-mode disturbances in a boundary layer over a sharp slender cone at Mach 8; they found that it is possible for the dominant transition mechanism to be the oblique-mode

breakdown when the freestream temperature fluctuation is greater than 1% and the freestream pressure fluctuation is not at the range of frequencies related to the second mode. As stated previously, it is expected that the dominant freestream disturbance in the Calspan shock tunnel is a temperature fluctuation, which presumably would cause the dominance of the oblique helical second-mode transition mechanism, which eventually breaks up into random motion as transition develops.

#### 4.3 Boundary Layer Transition in Regions of Adverse Pressure Gradient

In the design of hypersonic air-breathing vehicles, the prediction of transition and transitional regions in regions of adverse pressure gradient represents a key factor in the design and performance of the integrated vehicle and propulsion system configuration. In order to examine the performance of contemporary prediction techniques, such as the GASP code where it is possible to obtain predictions of the distribution of heat transfer through regions of boundary layer transition, a series of experiments were performed with a curved compression ramp similar to that which might be used as an inlet for vehicles traveling up to Mach 12. In the series of experiments discussed here, freestream Mach numbers of 10, 11, and 12 were selected so that the unit Reynolds number of the freestream could be varied at each Mach number to move the onset of transition from the beginning of the curved section of the model, at the largest Reynolds number, to the trailing edge of the curved section at the lowest Reynolds number. We examined both the shape of the mean distribution of heat transfer as well as the fluctuations in the output of the thin-film heat transfer gages to determine the beginning and end of the transition region. While appearance of spikes in the heat transfer record provided a clear indication of transition onset, the end of transition, as marked by a decrease in the intermittency, is a less-definitive quantity. The situation is further complicated, because the position of the beginning of transition fluctuates with time. The distributions of heating reported here are time-averaged measurements over a 5-ms period of the run time.

To provide further insight into the laminar and turbulent nature of these flows and to examine the performance of one of the standard Navier-Stokes codes, we ran comparisons between the experimental measurements and the GASP code for a number of selected test conditions at each Mach number. In

general, three comparisons were made, one with transition as far forward as possible, one with transition at the farthest downstream station, and a third between these cases. The computer solutions were obtained either for fully laminar flow or for turbulent flow employing either a Baldwin-Lomax or  $k-\epsilon$  model of turbulence. Predictions were also made for a hybrid case where the code was switched from laminar to turbulent at an axial station prescribed by the operator. This position was generally selected to coincide with the beginning of transition as determined from the experiment.

Comparisons between the experimental measurements and computations employing the GASP code were made for the Mach 10 condition at three unit Reynolds number conditions covering the unit Reynolds number range employed in the experiments. In each case, the flow was assumed to be laminar or turbulent from the leading edge; for the turbulent flow, Baldwin-Lomax and  $k-\epsilon$  models were used in the computation. An additional set of calculations was made by switching from the laminar solution to a turbulent calculation employing the Baldwin-Lomax model at a prescribed axial location. In these latter calculations, there was no attempt to employ a model of the transition region. Figure 4.3 shows comparisons between the computations and the heat

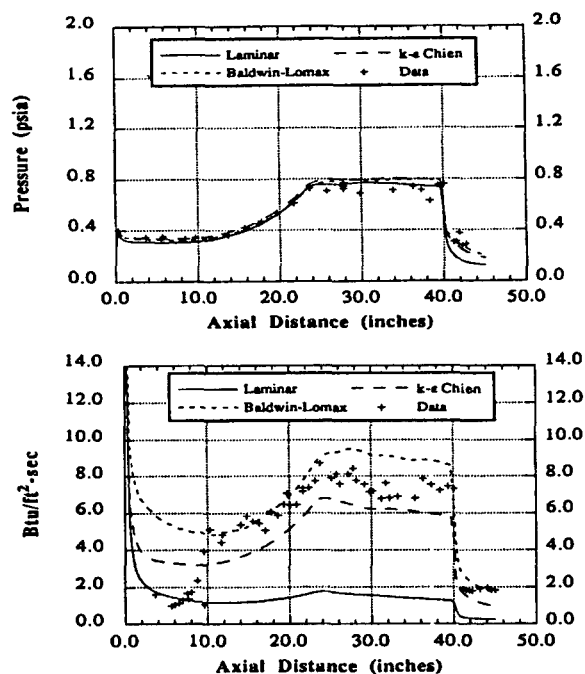


Figure 4.3 Surface Pressure and Heat Transfer Measurements and Predictions for Run 5

transfer and pressure measurements. The comparisons between measurements of pressure and the theoretical predictions show that the boundary layer model exhibits little influence on the pressure distribution, and that the theory is in good agreement with the experimental measurements. Conversely, errors in the selection of the condition of the boundary layer or the turbulent model can result in orders-of-magnitude errors in the prediction of the heating level. Assumption of a laminar boundary layer over the complete configuration would result in underestimating the heat load to the major segment of the compression surface by a factor of eight. Assuming the flow to be turbulent from the leading edge would result in underpredicting the heating load with the  $k-\epsilon$  model and over-predicting with the algebraic model. Clearly, the position of transition and the development of the boundary layer downstream of this point must be carefully modeled. If the solution is switched to laminar from turbulent close to the point that transition was observed experimentally, we obtain a closer agreement between theory and experiment, as shown in Figure 4.4. One could conjecture that the theory could be brought into closer agreement to the experiment if a model of the transition region were incorporated into the prediction method. Figure 4.5 shows the comparison between predictions and experiment for an intermediate Reynolds number condition. Comparisons between theory and experiment at the lowest Reynolds number at which the Mach 10 studies were conducted are shown in Figure 4.6. Again, the pressure is in good agreement with the experiment. For this condition, where transition occurs well downstream of the leading edge, theory is in good agreement with the measurements in the laminar flow, and, although the heating in the transition region is poorly predicted, the final heating levels on the ramp are predicted with reasonable accuracy by the Baldwin-Lomax method. Surprisingly, the  $k-\epsilon$  method gives a very poor prediction. Figure 4.7 shows the comparison between the measured heat transfer and the computation in which the solution is switched from laminar to turbulent at the 23-inch station. The predictions for this case are in relatively good agreement with the experimental data in the laminar zone and on the second straight compression ramp. Finally, at the intermediate Reynolds number condition shown in Figure 4.8, we see that the predictions of heat transfer with the assumption of laminar or turbulent heating from the leading edge are in poor agreement with the data, whereas assuming transition in the prediction method at

approximately 12 inches results in surprisingly good agreement between theory and experiment, as shown in Figure 4.9.

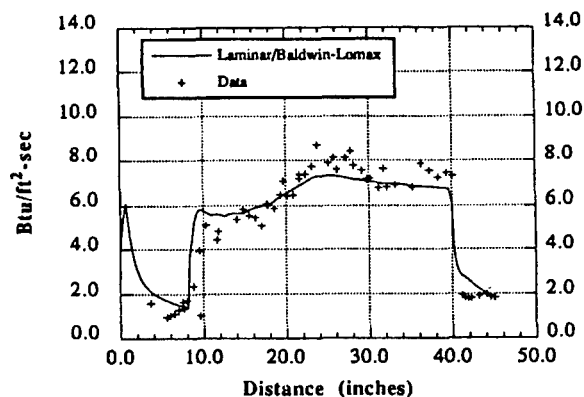


Figure 4.4 Heat Transfer Measurements and Predictions with Transition for Run 5

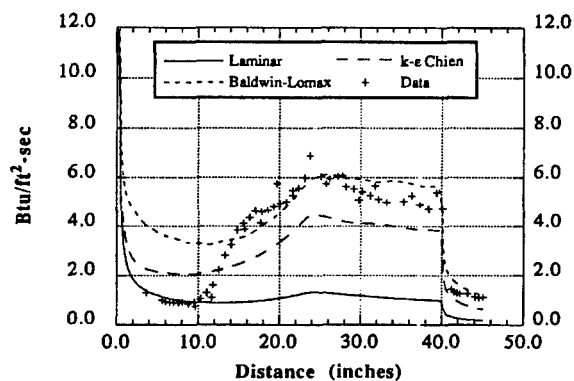
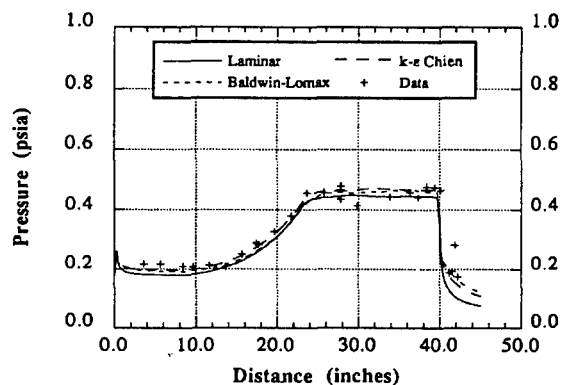


Figure 4.5 Surface Pressure and Heat Transfer Measurements and Predictions for Run 9

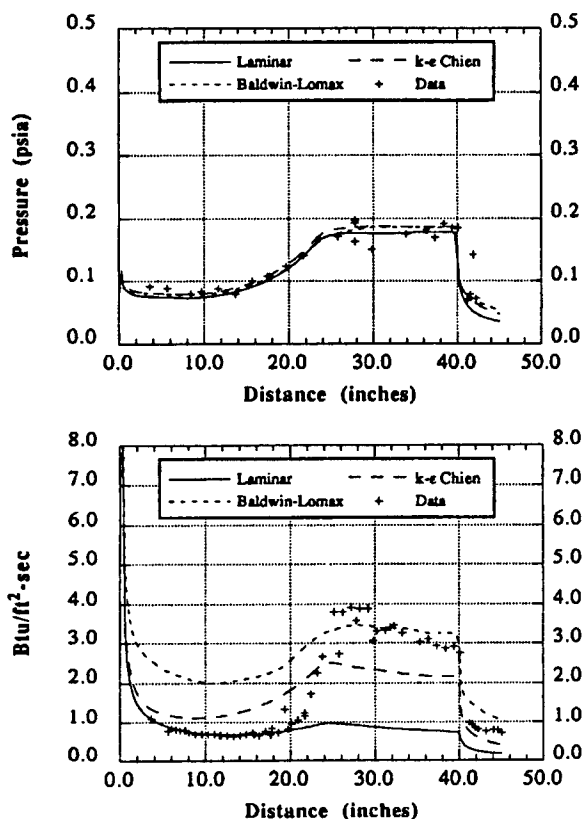


Figure 4.6 Surface Pressure and Heat Transfer Measurements and Predictions for Run 14

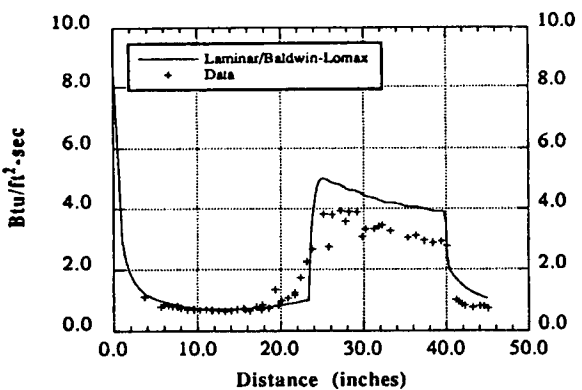


Figure 4.7 Heat Transfer Measurements and Predictions with Transition for Run 14

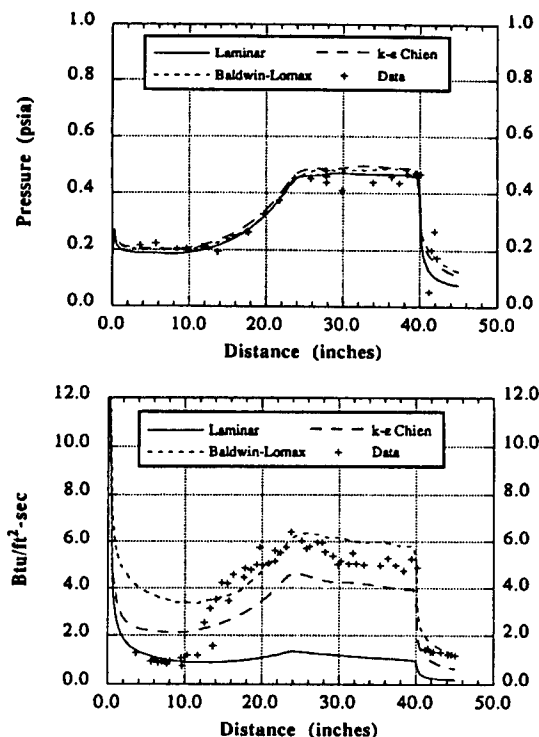


Figure 4.8 Surface Pressure and Heat Transfer Measurements and Predictions for Run 20

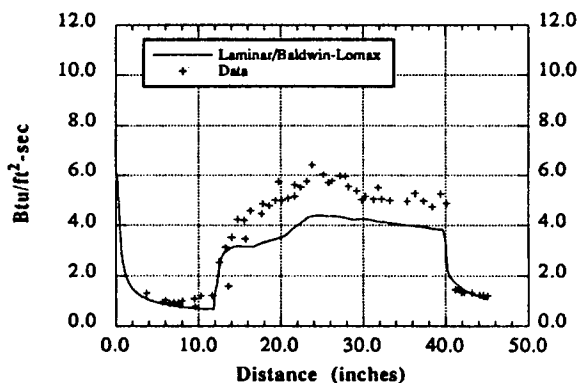
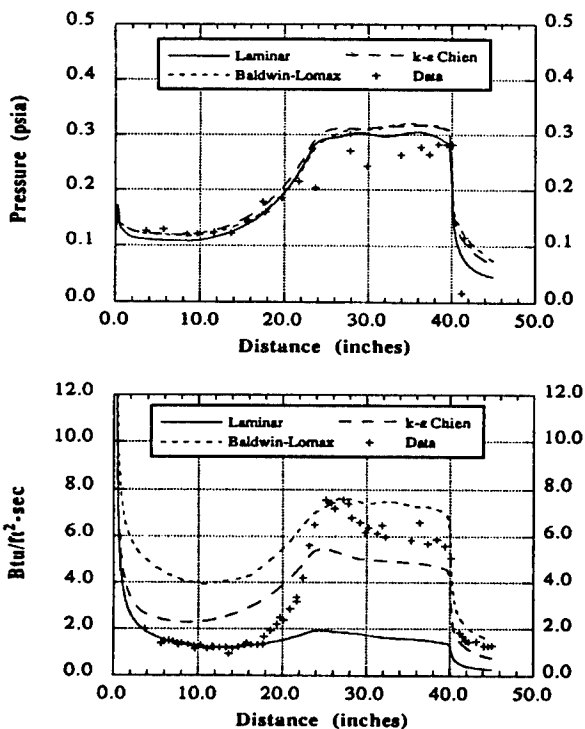


Figure 4.9 Heat Transfer Measurements and Predictions with Transition for Run 20

Comparisons between the GASP code predictions and the experimental measurements at Mach 12 were made for two conditions spanning the range of unit Reynolds numbers employed in the experiment. Comparisons between theory and experiment at the largest unit Reynolds number are shown in Figure 4.10. For these flows, where transition occurs well downstream on the curved compression surface, the theory is in good agreement in the laminar

segment of the flow, and in good agreement with the Baldwin-Lomax turbulence model for heat transfer levels over the latter half of the second straight compression ramp. Again, the more complex  $k-\epsilon$  model does not result in good agreement in the fully turbulent flow over the second straight ramp section. Switching the solution from laminar to one with the Baldwin-Lomax model close to the point where transition is experimentally observed results in a prediction (see Figure 4.11) that is in relatively good agreement with the experimental measurements. At the lowest Reynolds number at which this segment of the study was conducted, there is an extensive laminar region over the straight initial section and curved compression ramp, and the laminar theory is in good agreement with the heat transfer measurements, as shown in Figure 4.12. The heat transfer along the second straight section is poorly predicted, even if the position of transition is inputted from experimental measurements, as shown in Figure 4.13. Finally, the code predictions are compared with the data at Mach 12 from the intermediate Reynolds number condition in Figure 4.14. Again, the laminar predictions are in good agreement with the measurements, and the Baldwin-Lomax model provides the most accurate predictions in fully turbulent flow.



**Figure 4.10** Surface Pressure and Heat Transfer Measurements and Predictions for Run 22

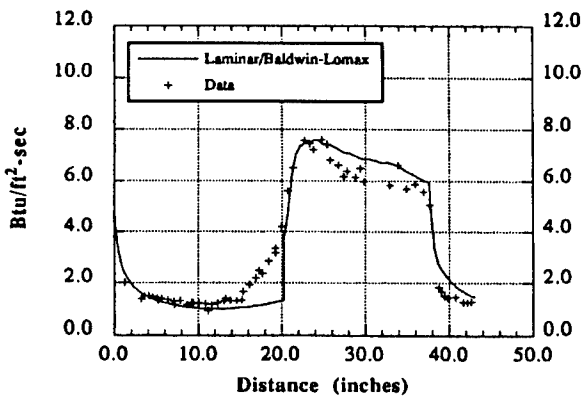


**Figure 4.11** Heat Transfer Measurements and Predictions with Transition for Run 22

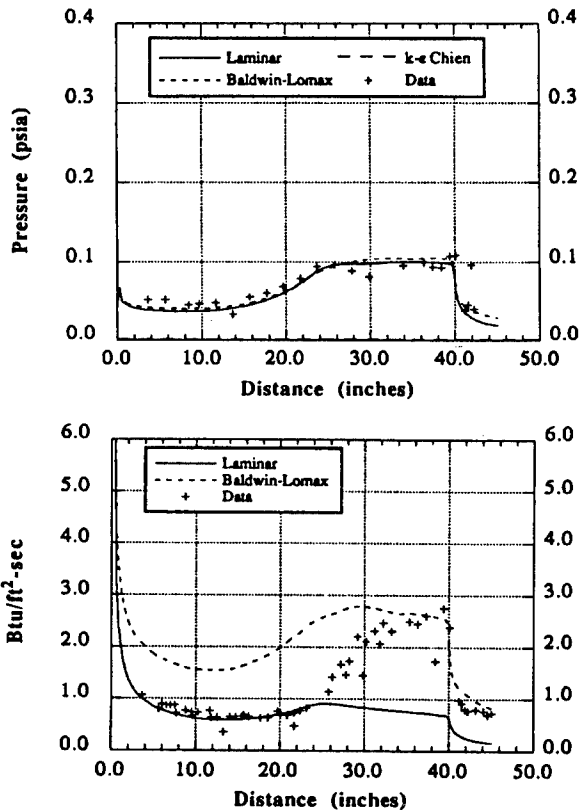


**Figure 4.12** Surface Pressure and Heat Transfer Measurements and Predictions for Run 39

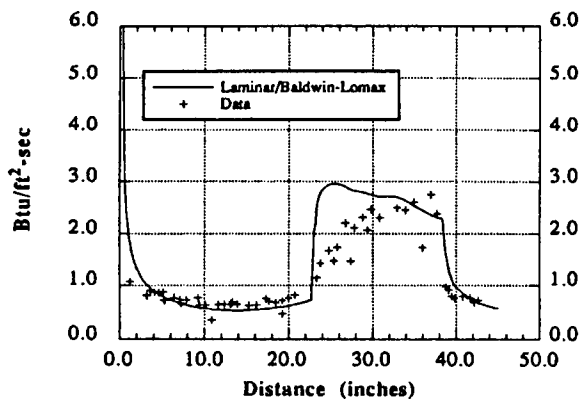


**Figure 4.13** Heat Transfer Measurements and Predictions with Transition for Run 39

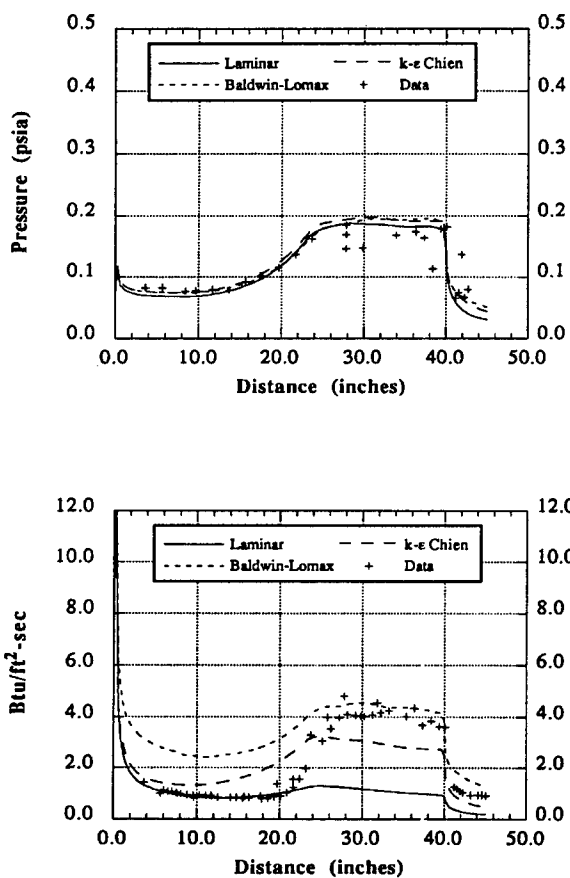


**Figure 4.14** Surface Pressure and Heat Transfer Measurements and Predictions for Run 26

### 4.3 Attachment Line Transition on Swept Leading Edges

#### 4.3.1 Introduction

The occurrence of boundary layer transition on the attachment line of highly swept leading edges is an important design consideration factor, not only because it influences leading-edge heating, but also because disturbances generated in this region of the flow can exert the dominant effect on transition on the three-dimensional afterbody. For example, disturbances generated on the leading edge of the Space Shuttle have been linked by Poll (Reference 4-5) to the occurrence of transition on the main body of the Shuttle's wing. Introducing a disturbance on the attachment line with surface discontinuities or roughness, or a wing-body junction, can result in transition Reynolds numbers that are consistently lower than those for the smooth configuration. In fact, the relatively low Reynolds numbers at which the stagnation-line heating becomes turbulent on swept wings or fins, because of disturbances introduced at the wing root, can become a major low-altitude performance limitation for finned hypersonic vehicles. Studies in supersonic flow by Bushnell<sup>4-6</sup> and Poll<sup>4-7</sup> have suggested that, for highly swept fins, freestream Reynolds numbers of just over  $10^5$  based on leading-edge diameter are required to induce transition downstream of a wing/body junction. For this configuration, Poll<sup>4-7</sup> suggests the transition criteria  $\overline{Re}_* = 245$ , where

$$\overline{Re}_* = \left( \overline{Re}_{D_\infty} \frac{\mu_\infty}{\mu_*} \frac{\rho_*}{\rho_\infty} \frac{\sin \lambda \cdot \tan \lambda}{U_1} \right) = 245 \quad (1)$$

for high Mach number flows, the boundary layer properties are evaluated at the reference temperature  $T^* = T_A + 0.10 (T_W - T_A) + 0.60 (T_{aw} - T_A)$ . The correlation developed earlier by Poll is shown in Figure 4.15. For swept leading edges without disturbances introduced at the wing root or surface discontinuities on the attachment line, measurements by Creel<sup>4-8</sup> at  $M=3.5$  suggest an  $Re_D = 7 \times 10^5$  for a freestream Reynolds number for transition onset for highly swept leading edges. A survey of the published results of attachment line transition studies<sup>4-9</sup> thru <sup>4-22</sup> indicates that transition measurements have not been reported above Mach 8. Recently, Holden and Kolly<sup>4-23</sup> have extended the

range of measurements from Mach 8 to 12 and the results of these studies are presented here.

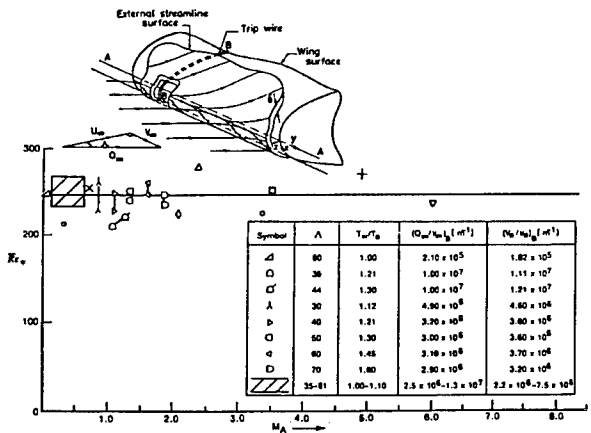


Figure 4.15 The Variation of  $\overline{Re}^*$  at the Onset of Transition with Edge Mach Number and Wall Temperature

4.3.2 Correlation of Attachment-Line Heating

There are two flow configurations of interest, (1) the smooth swept cylinder, where attachment line transition is influenced by the attachment line Reynolds number and disturbance in the freestream, and (2) the swept cylinder with attachment line contamination, where transition onset is controlled principally by the attachment line Reynolds number and the magnitude of the surface roughness or disturbance introduced at the tip. Studies in subsonic and supersonic flows have established that the major parameter controlling laminar and turbulent heating along the attachment line, as well as transition onset, is the attachment line Reynolds number, ( $\overline{Re}$ ), which is defined as

$$\overline{Re} = \frac{V_A \cdot \eta}{\nu_A}$$
 evaluated on attachment line (See Figure 4.16)

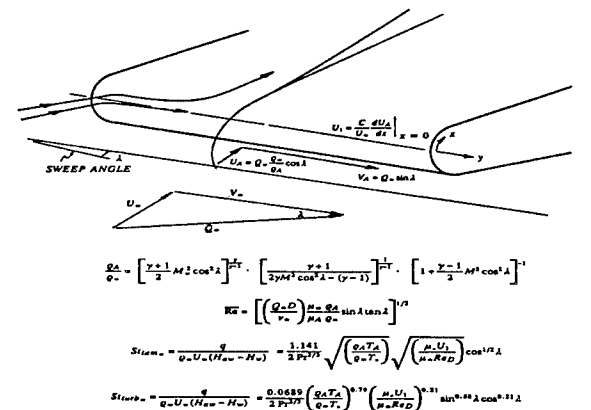


Figure 4.16 Flowfield and Attachment Line Equations

where  $\eta$  is a characteristic dimension of this viscous flow and has been defined by the expression

$$\eta = \left[ \nu_A \left( \frac{dU_A}{dx} \right)_{x=0} \right]^{1/2} \quad (2)$$

then 
$$\overline{Re} = \left[ \frac{V_A^2}{\nu_A} \cdot \left( \frac{dU_A}{dx} \right)_{x=0}^{-1} \right]^{1/2} \quad (3)$$

or 
$$\overline{Re} = \left[ V_A^2 \cdot C \cdot / (\nu_A U_\infty U_1) \right]^{1/2} \quad (4)$$

where 
$$U_1 = \left[ \frac{C}{U_\infty} \left( \frac{dU_A}{dx} \right)_{x=0} \right] \quad (5)$$

Introducing trips on the attachment line introduces a characteristic roughness ratio  $k/\eta^*$ , which has been shown by Poll to control the Reynolds number for transition onset for  $\overline{Re}$  less than 800. Figure 4.17 shows Poll's correlation of transition onset obtained on cylinders in compressible flows. The key conclusion from this figure is that, for values of  $k/\eta > 2$ , the attachment line Reynolds number for transition onset was independent of internal or external disturbances. A correlation of transition onset on very rough long swept cylinders is shown in Figure 4.15 and suggests the attachment line transition number  $\overline{Re}^* = 245$ . Here, the "star" denotes conditions evaluated at a reference temperature  $T^*$ , defined by Poll as

$$T^* = T_e + 0.10 (T_w - T_e) + 0.60 (T_R - T_e) \quad (6)$$

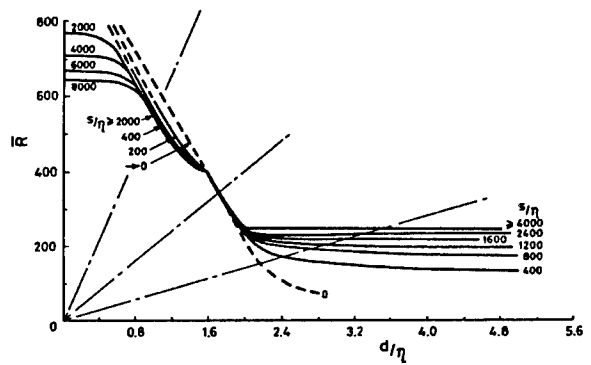


Figure 4.17 Correlation of Attachment Line Transition Onset with Surface Roughness Height

Poll, in a similar somewhat arbitrary manner, suggests that compressibility effects could be incorporated into the roughness-effects correlation by replacing  $\overline{Re}$  by  $\overline{Re}^*$  and  $\eta$  by  $\eta^*$ .

For incompressible laminar flow, it can be shown that the heating rate to the attachment line is given by

$$St_A = 0.571 / (\overline{Re}) \cdot 1/Pr^{2/3} \quad (7)$$

For incompressible turbulent flows, the attachment line heating can be expressed as

$$St_A = \frac{0.0689}{2Pr^{2/3}} \frac{1}{(\overline{Re})^{0.42}} \quad (8)$$

To account for compressibility effects, employing a reference temperature at which the properties of the flow are evaluated has been used successfully for flat-plate and cone flows. Poll<sup>4,7</sup> has suggested that, for the attachment line, a reference temperature defined by the relationship

$$T^* = 0.1T_w + 0.60T_{aw} + 0.3T_{aw} \quad (9)$$

is the most appropriate for attachment line flows.

The expressions for laminar and turbulent attachment line heating in compressible flow, employing the above expression together with the relationships from Figure 4.16, then become

$$(10) \quad St_A = \frac{q}{\rho_\infty U_\infty (H_{aw} - H_w)} = \frac{1.141}{2Pr^{2/3}} \sqrt{\left(\frac{\rho_A T_A}{\rho_\infty T^*}\right)} \sqrt{\left(\frac{\mu_\infty U_\infty}{\mu_A Re_D}\right)} \cos^{1/2} \lambda$$

for laminar flows and

$$(11) \quad St_A = \frac{q}{\rho_\infty U_\infty (H_{aw} - H_w)} = \frac{0.0689}{2Pr^{2/3}} \left(\frac{\rho_A T_A}{\rho_\infty T^*}\right)^{0.79} \left(\frac{\mu_\infty U_\infty}{\mu_A Re_D}\right)^{0.21} \sin^{0.58} \lambda \cos^{0.21} \lambda$$

for turbulent flows where

$$Re_D = Q_\infty D / \nu_\infty \quad (12)$$

Comparisons between the attachment line heat transfer measurements and predictions employing Poll's reference temperature are presented in

Figure 4.18 for the measurement made in the current program. On the basis of analysis of the measurements made in an earlier study, Holden suggests a new reference condition defined by

$$T^* = 0.3T_w + 0.5T_{aw} + 0.28T_A \quad (13)$$

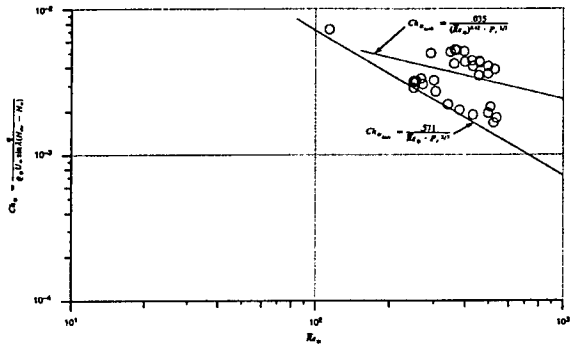


**Figure 4.18** Correlation of Attachment Line Heating (Poll Reference Temperature)

Correlations of the attachment line heating measurements in terms of this parameter are shown in Figure 4.19.

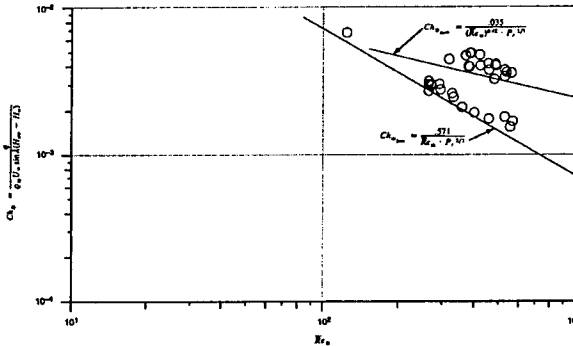


**Figure 4.19** Correlation of Attachment Line Heating (Holden Reference Temperature)

The measurements of laminar heating rates along the attachment line of smooth cylinder configurations are in good agreement with the prediction and indicate that flow can remain laminar for attachment line Reynolds numbers of up to 600 before transition is observed on the attachment line, and a Reynolds number of 800 before the flow in the attachment line boundary layer is fully turbulent. The measurements of turbulent heating rates are greater than the predicted levels, particularly for the boundary layers



tripped by the 0.030-inch roughness. Here, we believe that we are observing the combined effects of the enhanced mixing downstream of the roughness, coupled within the characteristic heating "overshoot" that is similar to that observed just downstream of these transitions on flat plates and cones. Again, effects are more pronounced and persist over greater downstream distances in high Mach number, low Reynolds number flows. Despite the use of trips with  $k/\eta^*$  well above 2, we begin to observe turbulent heating levels only after generating attachment line Reynolds numbers above 300, as shown in Figure 4.19.

#### 4.3.3 Correlation of Attachment Line Transition Onset

Flight and ground test studies of the swept leading edge of delta wings found that transition on the attachment line occurred at attachment line Reynolds numbers of approximately 250. These relatively low values were traced to the presence of large disturbances introduced by boundary layer fences, streamwise end plates, and the wing/fuselage junction. Studies by Cumpsty and Head, and subsequently by Poll, suggested that transition onset on long swept leading edges can be evaluated in four flow regimes in terms of the parameters  $\overline{Re}$  and  $k/\eta$ , as discussed. For values of  $k/\eta$  less than 0.5, attachment line contamination effects are small, and values of  $\overline{Re}$  greater than 600 are required for transition, depending on the level of disturbance in the freestream. For values of  $k/\eta > 0.8$ , transition is controlled by the disturbances introduced by the trips, and  $\overline{Re}$  for transition onset is strongly dependent on  $k/\eta$ . In the third region ( $1 < k/\eta < 1.5$ ), the transition is induced close to the trip, but attachment line transition Reynolds number is still dependent on trip size. Finally, for  $k/\eta > 2.5$ , the transition Reynolds number appears to be independent on the trip size at a value of close to 250. Although these observations were assembled from incompressible-flow data, Poll has suggested that a modified attachment line Reynolds number  $\overline{Re}^*$  based on a reference condition be employed to correlate measurements in supersonic and hypersonic flows.

Further, Poll suggests that  $\eta$  be replaced by  $\eta^*$  when computing the disturbance levels ( $k/\eta^*$ ) in compressible flows. Neither assumption is strongly grounded. However, Poll was able to correlate attachment line transition measurements for strongly

tripped conditions in supersonic flows as shown in Figure 4.20, resulting in the equivalent transition criteria  $\overline{Re}^* = 250$ . In recent experimental studies (see Reference 4-23), we have varied  $\overline{Re}^*$  from 200 to 600 and  $k/\eta^*$  from 0.8 to 2.4, which covers the range from smooth to fully rough on Poll's correlation. Here, it should be noted that the  $\overline{Re}$  based on inviscid flow conditions over the attachment line varies from 500 to 1200, and that employing reference conditions for  $\eta$  and  $\overline{Re}$  has yet to be validated. For the smooth configuration, turbulent bursts were observed for Runs 18 and 20, which are at  $\overline{Re}^*$  of 550, and laminar boundary layers were observed at larger values. This value corresponds to a freestream Reynolds number based on cylinder diameter of  $8 \times 10^5$ . The effects of the alignment of the nosetip may be critical in controlling transition on the attachment line of the smooth cylinder. For the fully tripped configuration employing the 0.030-inch trips, we found that the minimum attachment line Reynolds number to induce transition was 330, rather than the 245 found in earlier studies by Poll. For roughness ratios between 2 and 0.8, we observed a trend similar to that observed in incompressible flows, although, clearly, the data interpretation for this plot is difficult. Plotting the transition Reynolds number for the fully rough limit on Poll's transition correlation in Figure 4.20, it can be seen that we find that, at local Mach numbers of 8, the onset of transition occurs at 330, rather than at Poll's value of 245, obtained at the lower Mach numbers.

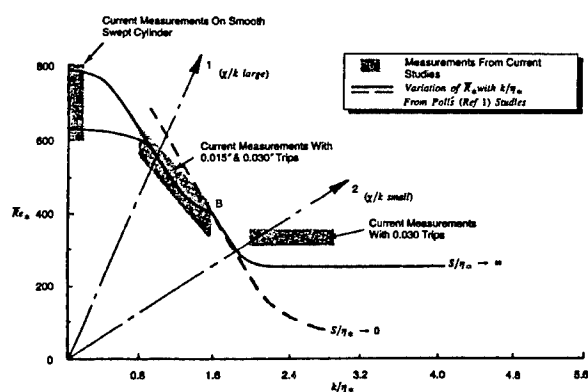


Figure 4.20 Comparison of Present Study Transition Onset Data with Poll's Correlation of Attachment Line Transition with Surface Roughness Height

## 4.4 Crossflow Transition

### 4.4.1 Introduction

Recently, concerted efforts have been made to extend this understanding to the three-dimensional boundary layer, where crossflow effects can become a dominant influence on transition. Three-dimensional flowfields exist along the swept leading edge of high-speed vehicles, as well as any flows having curved streamlines/transverse pressure gradients. Some notable studies of the leading-edge and three-dimensional transition phenomenon include Poll<sup>4-24</sup>, Chapman<sup>4-22</sup>, and Balakumar<sup>4-25</sup>. Because transition is first observed on vehicles at incidence, an understanding of transition in a three-dimensional boundary layer is vital in the design of a high-speed vehicle, since 3-D transition may be the dominant transition process over most of the vehicle.

In three-dimensional flow, the combination of pressure gradient and sweep deflects the inviscid streamlines. Since the fluid near the wall has a lower momentum, this deflection is larger in the boundary layer and causes a crossflow, as depicted in Figure 4.21, i.e., a velocity component within the boundary layer that is perpendicular to the local mean inviscid-flow velocity vector. To match the boundary conditions at the wall and in the freestream, the crossflow velocity profile is zero at these points and attains a maximum at some point in the boundary layer. This crossflow acts to transfer momentum; for example, on a cone at angle of attack, momentum is transferred from the windward side to the leeward side, resulting in a decrease of momentum thickness on the windward side and in an increase of it on the leeward side. The crossflow velocity profile has an inflection point, which causes it to be dynamically unstable. The crossflow instability produces crossflow vortices, approximately aligned in the local inviscid-flow direction. It is this crossflow instability that dominates the transition process at angle of attack. The paper by Reed and Saric<sup>4-26</sup> provide an excellent review of this subject. This instability is fundamentally different than the two-dimensional, axisymmetric second-mode and oblique Tollmein-Schlichting<sup>4-27</sup> (TS) instabilities that lead to transition in the hypersonic zero-angle-of-attack case. As angle of attack increases, the dominant instability changes from the second-D mode and/or TS instabilities to a combination of second-mode, TS, and crossflow instabilities; eventually, the crossflow instability is dominant.

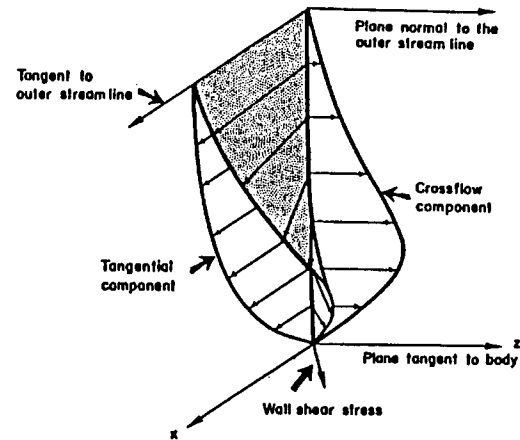


Figure 4.21 Three-Dimensional Profiles in a Crossflow Boundary Layer

There have been numerous experiments to investigate the movement of the point of transition as a function of angle of attack. Experiments performed by Stetson<sup>4-28,4-29</sup>, Krogmann<sup>4-30</sup>, Reda<sup>4-31</sup>, and DiCristina<sup>4-32</sup> have all consistently found the expected rearward movement of the transition region on the windward side, and forward movement on the leeward side. However, of particular importance is that part of the transition zone where crossflow is at a maximum, i.e., on the sides (90° and 270° relative to windward) of slender cones at angle of attack. Transition data in this region has been obtained by relatively few researchers (e.g., Stetson<sup>4-29</sup>, Holden<sup>4-33</sup>).

### 4.4.2 Influence of Angle of Attack and Bluntness on Transition

There have been several investigations to examine the movement of transition with angle of attack. Results have consistently found a rearward movement of transition location on the windward side, and forward movement on the leeward side. This effect is largely due to the effect of crossflow, which transfers momentum from the windward side to the leeward side, thickening the boundary layer on the leeward side and, therefore, affecting local Mach number and Reynolds number. Experimental studies by Reda<sup>4-31</sup>, Krogmann<sup>4-30</sup>, and Stetson and Rushton<sup>4-28</sup> have all shown transition delayed on the windward side, and the corresponding movement forward of transition location on the leeward side. Stability studies, such as those by Stetson et al.<sup>4-34</sup>, Simon and Dallman<sup>4-35</sup>, and Hanifi and Dahlkild<sup>4-36</sup>, have demonstrated the increase of growth rate of the

dominant instabilities on the windward rays, and opposite behavior on the leeward rays. However, of importance in understanding crossflow transition is the transition location in the region of highest crossflow, which occurs on the sides of the cone relative to the freestream direction.

Measurements of heat transfer and corresponding circumferential transition locus were made for various freestream flow conditions. Shown in Figure 4.22 are distributions of transition fronts on the sharp 6-degree cone at various angles of attack, together with previous measurements on similar cones, but at lower Mach number. As in previous studies, the measurements show the transition point moving forward with increasing angle of attack on the leeward side, and the transition point moving towards the base of the cone on the windward side. A unique feature of the shape of the transition front determined in the present study is that the positions of the most aft transition points occurred on the 90\_ and 270\_ rays, rather than on the windward rays as observed in the earlier studies at lower Mach numbers. This feature of further reduction in transition Reynolds number on the sides of the cone is evident at all angles of attack in this study, and has an increasing effect not only with azimuthal angle, but also with angle of attack, as shown in Figure 4.22. Recall that the sides of the cone are the regions of highest crossflow, and it is these regions where the crossflow instability first becomes the dominant instability as angle of attack increases. As shown in this plot, the stabilizing influence of crossflow becomes more apparent as angle of attack increases.

Source	Sym.	Technique	Facility	$\Theta_c$	$\alpha/\Theta_c$	$M_\infty$	$T_w/T_\infty$	$Re/\ell$
Reda (Ref. 13)	◊	Spark Shadowgraph	Range	5.°	.35-.45	4.5	.22-.48	12.5 -31.9 X 10 <sup>6</sup>
Krogmann (Ref. 12)	△	Single Line Oil Flow	Tunnel	7.5°	.40	5.0	-1.0	7.58 X 10 <sup>6</sup>
Sutton (Ref. 11)	○	Heat Transfer	Tunnel	8.°	.25-.50	5.9	.52-.58	9.70 X 10 <sup>6</sup>
Present Study	+	Heat Transfer & Schlieren	Shock Tunnel	6.°	.1667-.333	13.5	.143	3.00 X 10 <sup>6</sup>
	*	Photographs			.5			

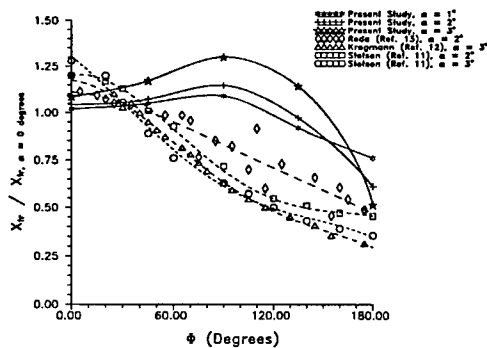
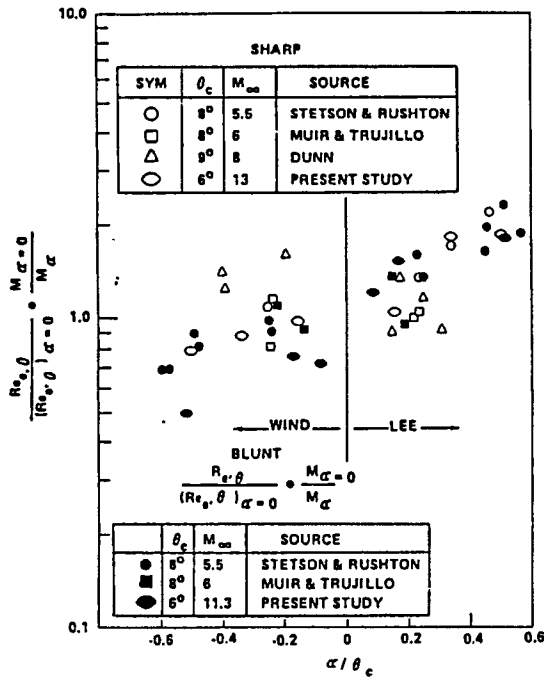


Figure 4.22 Transition-Front Asymmetry, Sharp Cone

This stabilizing effect is clearly not evident in the results obtained by Reda<sup>4-31</sup>, Krogmann<sup>4-30</sup>, and Potter<sup>4-37</sup> at lower Mach numbers, which implies that the interaction of the crossflow instability in these cases exhibits a destabilizing influence. This effect is further evidenced by the reduction in transition location with increase in angle of attack in the curves reported by Potter, based on wind tunnel results of Ward<sup>4-38</sup>, DiCristina<sup>4-32</sup> and Mateer<sup>4-39</sup>. The destabilizing effect of crossflow is also demonstrated in the calculations of Balakumar and Reed<sup>4-25</sup>, who found a strong destabilizing effect of crossflow on the oblique first-mode and 2-D second-mode disturbances, which diminished as Mach number increased.

In the analysis of transition measure obtained on sharp flat plates and cones, we found that the Reynolds number based on the local momentum thickness ( $Re_\theta$ ) provided the best correlation of both wind tunnel and flight measurements in hypersonic flow over highly cooled walls. Thus, following Finson<sup>4-40</sup>, we have plotted the measurements made in the present studies together with those from earlier work in terms of the Reynolds number local momentum thickness and the local Mach number for both sharp and blunt bodies (see Figure 4.23). It can be seen that for both sharp and blunt configurations, that  $(Re_x/Re_{x_0}) \frac{M_0}{M}$  is relatively independent of angle of attack. Thus, for sharp cones, it may be observed that transition moves forward on the leeside ray, principally because of the large increase in the momentum thickness; on the windward ray, the effects of crossflow and higher unit Reynolds number combine to cause a decrease in the momentum thickness. In the situation with relatively large bluntness, the entropy layer is swallowed more rapidly on the windward ray than on the leeward, which acts to increase the momentum thickness on the windward ray. This counteracts the action of crossflow to bleed some momentum from the windward ray to the leeside, and acts to further destabilize the windward side relative to the zero-angle-of-attack case.



**Figure 4.23** Correlation of Transition Front Locations on Sharp and Blunt Slender Cones at Angle of Attack

#### 4.4.3 Correlation of Transition-Front Location Using Compressible Crossflow Transition Reynolds Number

A low-speed crossflow Reynolds number transition criterion was introduced by Owen and Randall<sup>4-41</sup>, given by  $\frac{W_{\max} \delta}{V_e}$ , that correlates well with low-speed data. However, extending this correlation to the high-speed range has met with limited success. Chapman<sup>4-22</sup> extended this approach into the supersonic and low-hypersonic range; however, these results have been criticized by Poll<sup>4-24</sup>, claiming that contamination of the attachment line affected the boundary layer in the crossflow region. King's<sup>4-42</sup> results also found no correlation with the traditional crossflow Reynolds number.

Since the traditional crossflow Reynolds number is used successfully at subsonic speeds, Reed and Haynes developed additional factors in the definition of crossflow Reynolds number to compensate for the effects of compressibility and to compensate for heat transfer to the surface. Their definition is

$$R_{CF(new)} = HL \frac{W_{\max} \delta_{10}}{V_e}$$

where

$$\delta_{10} = \text{point in boundary layer above } W_{\max} \text{ where } \frac{W}{W_{\max}} = 10\%$$

$$H = \eta(\delta_{10}) / \int_0^{\eta(\delta_{10})} (T/T_e) d\eta$$

$$L = \sqrt{C^*/C_{ad}^*} (3.279 + 1.721 \frac{T_w}{T_{ad}} (1 + A) + 0.664A)/(5 + 2.385A)$$

$$A = \sqrt{Pr} \frac{(\gamma-1)}{2} Me^2$$

$$C^* = \sqrt{\frac{T^*}{T_e}} \frac{(1 + 110.4/T_e)}{(\frac{T^*}{T_e} + 110.4/T_e)}$$

$$C_{ad}^* = \sqrt{\frac{T_{ad}^*}{T_e}} \frac{(1 + 110.4/T_e)}{(\frac{T_{ad}^*}{T_e} + 110.4/T_e)}$$

$$\frac{T^*}{T_e} = 0.5 + 0.5 \frac{T_w}{T_e} + A/6$$

$$\frac{T_{ad}^*}{T_e} = 0.5 + 0.5 (1+A) + A/6$$

$\eta$  is a typical similarity variable, and  $\eta(\delta_{10})$  is the value of  $\eta$  at  $\delta_{10}$ . The factor  $H$  compensates for compressibility, and the factor  $L$  compensates for heat transfer. Note that, since  $H$  is basically a ratio of two distances normal to the wall,  $H$  can be calculated regardless of how  $\eta$  is defined. For an incompressible, adiabatic-wall flow,  $R_{CF(new)}$  is reduced to the traditional crossflow Reynolds number.

In their study, Reed and Haynes calculated  $R_{CF(new)}$  for the experimental data of Stetson<sup>4-43</sup> at  $M_\infty=6$ , and King<sup>4-42</sup> at  $M_\infty=3.5$  in both noisy and quiet freestream environments. The authors suggested a correlation between the crossflow Reynolds number and the maximum crossflow velocity. However, separate correlations were developed for the noisy and quiet data. Results for

the sharp cone at  $M_\infty=13$  in the present study are shown in Figure 4.24, with the noisy and quiet correlations of Reed and Haynes. Most notable is that the present results follow the quiet correlation, especially as the level of crossflow ( $W_{\max}/U_e$ ) increases. The reduction in scatter as crossflow increases is expected, since, as Reed and Haynes point out, the lower end of the curve and data are somewhat suspect. At low levels of crossflow ( $W_{\max}/U_e < 2\%$ ), the crossflow instabilities interact with the other more dominant instabilities (T-S, 2nd mode, helical, etc.) generated in the windward and leeside regions. The additional problem arises in the low-crossflow situation in that defining a precise  $\delta_{10}$  point in the boundary layer for RCF calculation becomes increasingly difficult. Nonetheless, the trend shown in Figure 4.25 further demonstrates the contentions that crossflow instabilities are not greatly influenced by any freestream acoustic disturbances, and that the dominant transition mechanisms in the present study are not largely influenced by freestream disturbances.

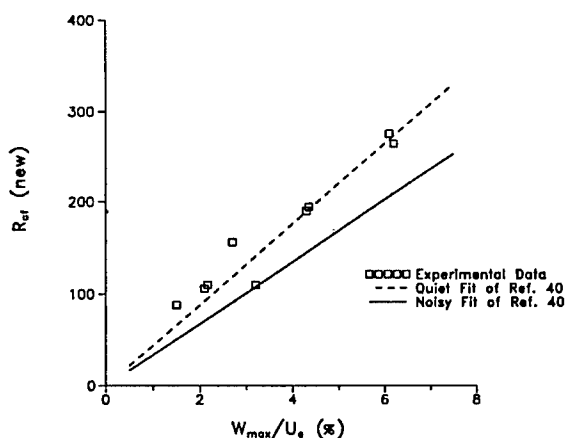


**Figure 4.24** Correlation of Transition Front Location in Regions of Crossflow with "New" Crossflow Reynolds Number,  $M_\infty=13$ ,  $Re_\infty/Ft=3.0 \times 10^6$

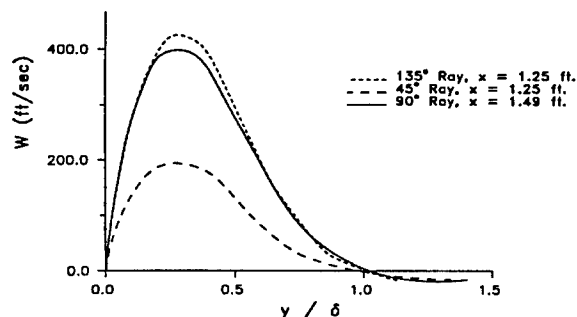


**Figure 4.25** Crossflow Velocity Component at Transition Onset,  $M_\infty=13$ ,  $\alpha=3^\circ$ ,  $Re_\infty/Ft=3.0 \times 10^6$

## REFERENCES

- 4-1. Reynolds, O., "An Experimental Investigation of the Circumstances Which Determine Whether the Motion of Water Shall Be Direct or Sinuous and of the Law of Resistance in Parallel Channels," Trans. Roy. Soc. (London) A174, 1883, pp. 935-982, Sci Papers 2:51.
- 4-2. Bestek, H., Thumm, A., and Fasel, H., "Direct Numerical Simulation of Three-Dimensional Breakdown to Turbulence in Compressible Boundary Layers," The 13th International Conference of Numerical Methods for Fluid Dynamics, Rome, Italy, July 6-10, 1992.
- 4-3. Chang, C.L., and Malik, M.R., "Oblique Mode Breakdown in a Supersonic Boundary Layer Using Nonlinear PSE," Instability, Transition and Turbulence, Edited by Hussani, M.Y., Kumar, A., and Strett, C.L., Springer-Verlag, 1992, pp. 231-241.
- 4-4. Chang, C.L., and Malik, M.R., "Non-Parallel Stability of Compressible Boundary Layers," AIAA Paper No. 93-2912, July 1993.
- 4-5. Poll, D.I.A., "Boundary Layer Transition on the Windward Face of Space Shuttle During Re-Entry," AIAA Paper Number 85-0899, Presented at the AIAA 20th Thermophysics Conference, Williamsburg, Virginia, June 19-21, 1985.
- 4-6. Bushnell, D.M., "Interference Heating on a Swept Cylinder in Region of Intersection with a Wedge at Mach 8," NASA TN-D-3094, December 1965.

- 4-7. Poll, D.I.A., "The Development of Intermittent Turbulence on a Swept Attachment-Line Including the Effects of Compressibility," *The Aeronautical Quarterly*, Vol. XXXIV, February 1983, pp. 1-23.
- 4-8. Creel, T.R., "Transition on Swept Cylinders in the Langley Supersonic Low Disturbance Tunnel," 4th NASP Transition Workshop, NASA-LaRC, December 4, 1990.
- 4-9. Reshotko, E. and Beckwith, I.E., "Compressible Laminar Boundary Layer Over a Yawed Infinite Cylinder with Heat Transfer and Arbitrary Prandtl Number," NACA Report 1379, 1958.
- 4-10. Beckwith, I.E., "Similar Solutions for the Compressible Boundary Layer on a Yawed Cylinder with Transpiration Cooling," NASA TRR-42, 1959.
- 4-11. Beckwith, I.E., and Gallagher, J.J., "Local Heat Transfer and Recovery Temperatures on a Yawed Cylinder at a Mach Number of 4.15 and High Reynolds Numbers," NASA TR R-104, 1961.
- 4-12. Bertran, M.H. and Everhart, P.E., "An Experimental Study of the Pressure and Heat Transfer Distribution on a 70° Sweep Slab Delta Wing in Hypersonic Flow," NASA TR R-153, December 1963.
- 4-13. Beckwith, I.E., "Experimental Investigation of Heat Transfer and Pressures on a Swept Cylinder in the Vicinity of Its Intersection With a Wedge and Flat Plate at Mach Number 4.15 and High Reynolds Numbers," NASA TN D-2020, July 1964.
- 4-14. Cumpsty, N.A., and Head, M.R., "The Calculation of Three-Dimensional Boundary Layers, Part II-Attachment Line Flow on an Infinite Swept Wing," *The Aeronautical Quarterly*, Vol. XVIII, pp. 150-164, May 1967.
- 4-15. Bushnell, D.M. and Huffman, J.K., "Investigation of Heat Transfer to Leading Edge of a 76° Swept Fin With and Without Chordwise Slots and Correlations of Swept Leading-Edge Transition Data for Mach 2 to 8," NASATM-X-1475, 1967.
- 4-16. Hunt, J.L., Bushness, D.M., and Beckwith, I.E., "The Compressible Turbulent Boundary Layer on a Blunt Swept Slab With and Without Leading Edge Blowing," NASA TN D-6203, March 1971.
- 4-17. Poll, D.I.A., "Transition in the Infinite Swept Attachment Line Boundary Layer," *The Aeronautical Quarterly*, Vol. XXX, pp. 607629, November 1979.
- 4-18. Poll, D.I.A., "Skin Friction and Heat Transfer at an Infinite Swept AttachmentLine," *The Aeronautical Quarterly*, Vol. XXXII, November 1981, pp. 299-318.
- 4-19. Topham, D.R., "A Correlation of Leading Edge Transition and Heat Transfer on Swept Cylinders in Supersonic Flow," *Journal of the Royal Aeronautical Society*, Vol. 69, pp. 4952, January 1965.
- 4-20. Scott-Wilson, J.B. AND Capps, D.S., "Wind Tunnel Observations of Boundary Layer Transition On Two Sweptback Wings at a Mach Number of 1.61," R.A.E., TN Aero 2347, December 1954.
- 4-21. Dunning, R.A. AND Ulmann, E.F., "Effects of Sweep and Angle of Attack on Boundary Layer Transition on Wings at Mach Number 4.04," NACA TN 3473, March 1955.
- 4-22. Chapman, G.T., "Some Effects of Leading Edge Sweep on Boundary Layer Transition at Supersonic Speeds," NASA TN D-1075, 1961.
- 4-23. Holden, M.S. and Kolly J., "Attachment Line Transition Studies on Swept Cylindrical Leading Edges at Mach Numbers from 10 to 12, AIAA 95-2279, 26th AIAA Fluid Dynamics Conference, San Diego, CA, June 19-22, 1995.
- 4-24. Poll, D.I.A., "Transition Description and Prediction in Three-Dimensional Flows," Special Course: Stability and Transition of Laminar Flows, AGARD-R-709, March 1984.
- 4-25. Balakumar, P. and Reed, H.L., "Stability of Three-Dimensional Supersonic Boundary Layers," *Physics of Fluids A*, Vol. 3, No. 4, 1991, pp. 617-632.

- 4-26. Reed, H.L. and Saric, W.S., "Stability of Three-Dimensional Boundary Layers," Annual Review of Fluid Mechanics, Vol. 21, Jan. 1989, pp. 235-284.
- 4-27. Schlichting, H., Boundary-Layer Theory, 4th Edition, McGraw-Hill Book Co., New York, NY 1960.
- 4-28. Stetson, K.F. and Rushton, G.H., "Shock Tunnel Investigation of Boundary Layer Transition at  $M=5.5$ ," *AIAA Journal*, Vol. 5, No. 5, May 1967, pp. 899-906.
- 4-29. Stetson, K.F., "Hypersonic Laminar Boundary Layer Transition, Part II: Mach 6 Experiments of Transition on a Cone at Angle of Attack," AFWAL-TR-3089, December 1986.
- 4-30. Krogmann, P., "An Experimental Study of Boundary Layer Transition on a Slender Cone at Mach 5," AGARD-CPP 224, AGARD Symposium on Laminar-Turbulent Transition, Copenhagen, Denmark, 1977.
- 4-31. Reda, D.C., "Boundary Layer Transition Experiments on Sharp, Slender Cones in Supersonic Free Flight," AIAA Paper No 78-1129, July 1978.
- 4-32. Di Cristina, V., "Three-Dimensional Laminar Boundary Layer Transition on a Sharp 8-Degree Cone at Mach 10," *AIAA Journal*, Vol. 8, No. 5, May 1970, pp. 852-856.
- 4-33. Holden, M.S., "Experimental Studies of the Effects of Asymmetric Transition on the Aerothermal Characteristics of Hypersonic Blunted Slender Cones," AIAA Paper 85-0325, January, 1985.
- 4-34. Stetson, K.F., Thompson, E.R., Donaldson, J.C., and Siler, L.G., "Laminar Boundary Layer Stability Experiments on a Cone at Mach 8, Part 3: Sharp Cone at Angle of Attack," AIAA Paper No. 85-0492, January 1985.
- 4-35. Simon, M. and Dallman, U., "On the Instability of Hypersonic Flow Past a Pointed Cone - Comparison of Theoretical and Experimental Results at Mach 8," Deutscher Luft - und Raumfahrtkongress/DGLR - Jahrestagung, 1992.
- 4-36. Hanifi, A. and Dahlkild, A.A., "Some Stability Characteristics of the Boundary Layer on a Yawed Cone," AIAA Paper No. 93-3048, July 1993.
- 4-37. Potter, J.L., "Boundary Layer Transition on Supersonic Cones in an Aeroballistic Range," *AIAA Journal*, Vol. 13, No. 3, March 1975, pp. 270-277.
- 4-38. Ward, L.K., "Influence of Boundary Layer Transition on Dynamic Stability at Hypersonic Speeds," Transactions of the Second Technical Workshop on Dynamic Stability Testing, Vol. II, AEDC, Tullahoma, TN, April 1965.
- 4-39. Mateer, G.C., "Effects of Wall Cooling and Angle of Attack on Boundary Layer Transition on Sharp Cones at  $M = 7.4$ ," NASA TN D-6908, August 1972.
- 4-40. Finson, M. "Frustum Transition Modeling," Proceedings of the ABRES Accuracy Review, Vol. 8, No. 9, November 1977.
- 4-41. Owen, R.R., and RANDALL, D.J., "Boundary Layer Transition on the Swept Wing," *RAE TM Aero 277*, 1952.
- 4-42. King, R. A., "Mach 3.5 Boundary Layer Transition on a Cone at Angle of Attack," AIAA Paper 91-1804, June 1991.
- 4-43. Stetson, K.F., "Mach 6 Experiments of Transition on a Cone at Angle of Attack," *Journal of Spacecraft*, Vol. 19, No. 5, 1982, p. 397.

## 5. SHOCKWAVE/BOUNDARY LAYER INTERACTION IN LAMINAR AND TURBULENT HYPERSONIC FLOWS

### 5.1 Introduction

### 5.2 Laminar Boundary Layer Separation in Planar and Axisymmetric Flows

In high Mach number, low Reynolds number flows, the interaction between the growth of the laminar boundary layer and the outer inviscid flow over the nosetip or leading edge and subsequent interaction over control surfaces or inlets can play an important role in determining the aero-thermodynamic performance of a high flying hypersonic vehicle. Also because most practical vehicle designs employ blunt leading surfaces, the entropy layer can have a strong influence on the structure of the boundary layer upstream of the interaction and on the pressures and heating rates on the compression surfaces. As illustrated in the Schlieren photographs shown in Figures 5.1 and 5.2 for flow over flat plate/wedge and curved compression surface, at high Mach numbers it is difficult to distinguish between the separation shock and the edge of the viscous layer while in supersonic flow these features are distinct. An important feature of the structure of a hypersonic laminar boundary layer over a cooled wall is that most of the mass and momentum is contained at the outer edge of the boundary layer thus making it difficult to employ boundary layer control.

The importance of viscous interaction and leading edge bluntness on the flow over a two-dimensional compression corner are illustrated by the measurements of heat transfer, skin friction and pressure shown in Figure 5.2. Here on the configuration with the sharp leading edge, the viscous interaction extends 20 boundary layer thicknesses downstream of the corner at which point the pressure has risen two orders of magnitude to the inviscid wedge value. In contrast, the flap pressure (and heat transfer) on the configuration with the blunt leading edge are dominated by entropy swallowing effects and rise to no more than five times the values just upstream of the corner interaction. In this study it was found that while bluntness was found to decrease the size of the reverse flow embedded within the interaction region, flow separation occurred at approximately the same wedge angle. In a subsequent

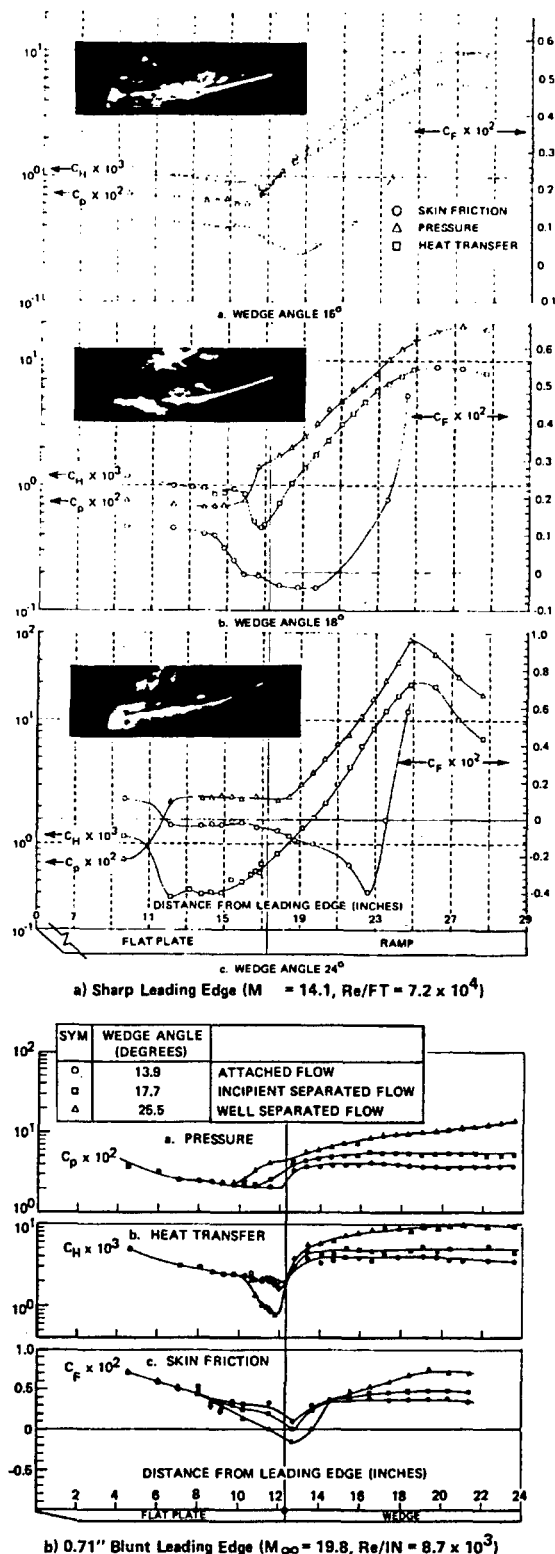
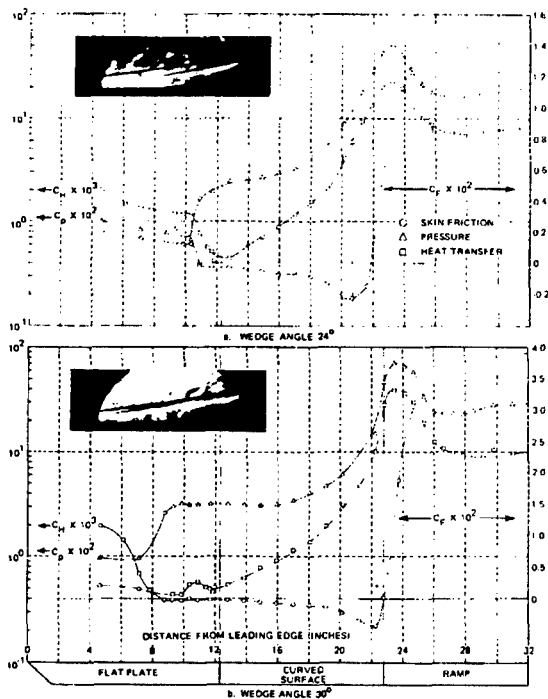


Figure 5.1 Skin Friction, Heat Transfer, and Pressure Distributions on the Flat Plate-Wedge Models





**Figure 5.2** Skin Friction, Heat Transfer and Pressure Distributions on the Flat Plate - 20'' R Cylindrical Arc-Wedge Models (Ref.11)  
( $M_\infty=14.0$ ,  $Re/Ft=7.2 \times 10^4$ )

study, it was also shown that in contrast with turbulent flows the angle through which the flow could be turned without inducing separation could not be changed by radiusing the corner until the corner radius approached at least 15 initial boundary thicknesses. While, as discussed below, Holden<sup>5-1</sup> was able to obtain predictions in reasonable agreement with measurements made in these studies employing boundary layer equations modified to incorporate the normal pressure gradient, it is clear that such predictions are now best obtained with numerical solutions to the full Navier-Stokes equations.

#### Laminar Two-Dimensional Viscous Interaction

The increased stability of the laminar boundary at high Mach numbers, and the ease with which laminar boundary layers separate, coupled with interest in high altitude hypersonic flight, has made laminar flow separation in two- and three-dimensional interacting flows of considerable practical importance. Experimental studies and flight tests show that the very large heat transfer rates and gradients generated in the reattachment regions of laminar separated flows in high-speed flight are of

considerable importance to the heat shield designer. The simple viscous interaction flow models that have been developed to describe laminar two-dimensional separated regions have their origins in the earlier studies of Howarth<sup>5-2</sup> Lighthill<sup>5-3</sup> and Oswatitsch and Wiegardt<sup>5-4</sup> who proposed models for the mechanism of upstream influence and boundary layer separation. It was then shown that upstream influence and flow separation could be described with good accuracy by a model in which the viscous layer grew by mutual interaction with the outer inviscid flow. At high Mach numbers, Holden<sup>5-1</sup> showed that the normal pressure gradients must be included in the description of hypersonic interaction regions to describe such flows correctly.

While Carter<sup>5-5</sup> obtained one of the first solutions to the Navier-Stokes equations for separated flows, the technique developed by Hung and MacCormack<sup>5-6</sup> represents the first relatively efficient method devised to predict the characteristics of laminar separated flows. Using the Navier-Stokes code developed by Hung and MacCormack, laminar solutions were obtained for comparison with the experimental measurements at Mach 16. Comparisons between the Navier-Stokes solutions and measurements in attached incipient separated flows are shown in Figures 5.3a and b. For attached and separated flow over the flat-plate wedge configuration, the theoretical predictions are in excellent agreement with the experimental data. In particular, the form of the heat transfer and skin friction in the region of minimum heat transfer is well reflected by the theoretical predictions. Both theory and experiment display a minimum skin friction downstream of the corner or the wedge.

#### Laminar Three-Dimensional Interactions

Most studies of three-dimensional interaction have been conducted to examine flow in the corner of two intersecting wedges with sharp leading edges aligned at an angle of 90 degrees with each other. Stainback<sup>5-7, 5-8</sup> made detailed heat transfer and pressure measurements in laminar flow over such a configuration at Mach 5, and later at Mach 8, for a range of Reynolds numbers to identify transition. These experiments led Stainback to distinguish between two flow regions: the near corner with which most previous theoretical work had been concerned and the far corner which had been studied experimentally (see Figure 5.4). The near corner was a region of mutual interaction of two boundary layers and resulted in lower heating. The far corner was the region of mutual interaction of the two inviscid

flowfields caused by the intersection of the two flat plates forming the corner. In subsequent studies, Stainback and Weinstein<sup>5-9</sup> further observed that interaction between the mutual boundary layers in the corner results in a decrease in heat transfer in the very near corner. Away from the corner, the vortex system and reattachment of the boundary layer downstream of the shock induced separation (see Figure 5.4) results in an increase of heat transfer outboard of the near corner region. The basic structure of laminar interacting flows was defined in studies by Charwat and Redekopp<sup>5-10</sup> at Mach 2 to 4. Studies in hypersonic flow by Watson and Weinstein<sup>5-11</sup> demonstrated similar features.

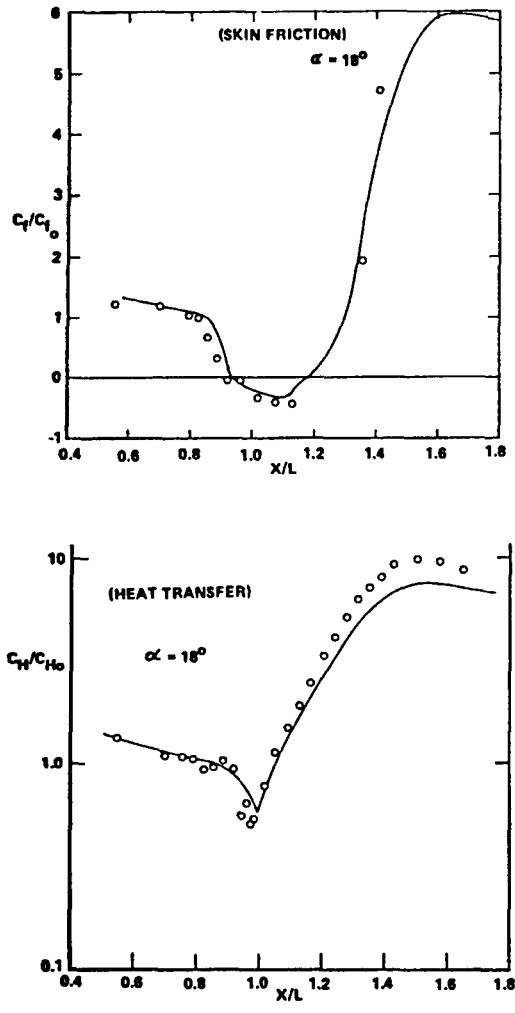


**Figure 5.3a** Comparison Between Experimental and Navier Stokes Solution for a Mildly Separated Flow (Reference 11)

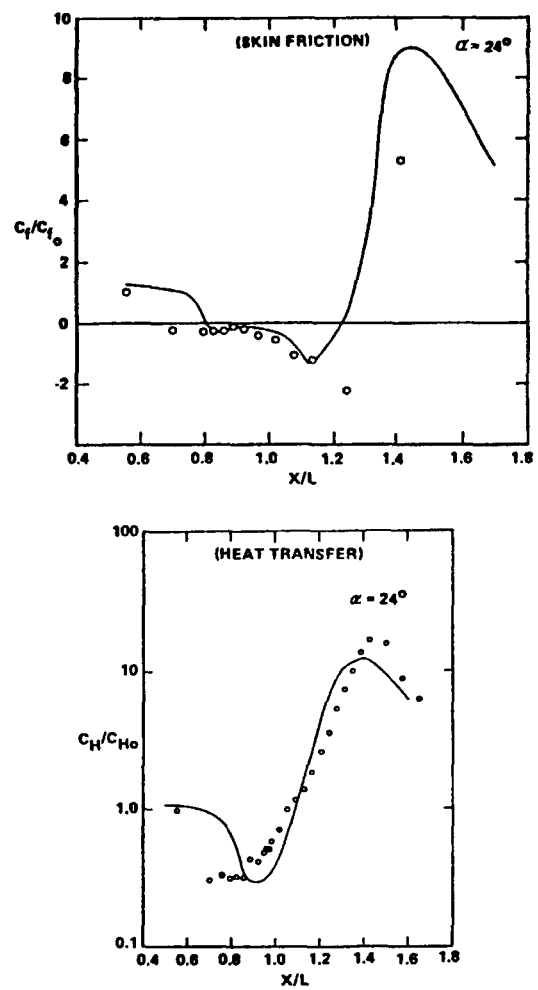


**Figure 5.3b** Comparison Between Experimental Measurements and Navier Stokes Solution for a Well-Separated Flow

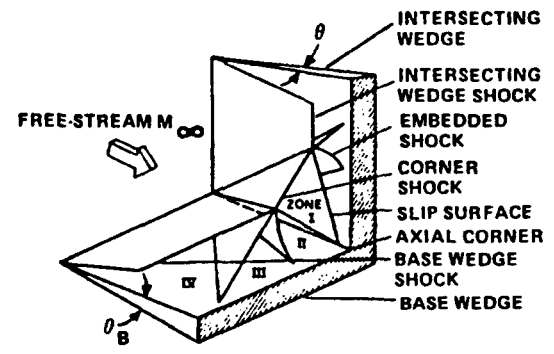


**Figure 5.4** Schematic Representative of Model with Crossflow in Swept-Shock Laminar Boundary-Layer Interaction

Figure 5.5 shows the flow structure established from pitot pressure and flow visualization measurements. The shockwaves generated by each wedge are joined by a third shockwave, bordering Zone I and the freestream flow. Slip surfaces pass from the ends of this third shock towards the corner. Shock legs extend to the surface -- a curved shock between Zones II and III and a spread of the corner disturbance outside of the inner shocks. Kutler et al.,<sup>5-12</sup> have shown that shock capturing techniques describe the inviscid flow with good accuracy; however, viscous characteristics, particularly with laminar flows, where viscous interaction is important, are predicted with significantly less accuracy.

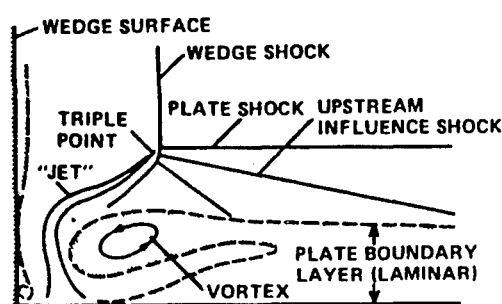


**Figure 5.5** Shock-Wave Structure in Axial Corner Comprised of Two Intersecting Wedges

### 5.3 Turbulent Boundary Layer Separation in Two- and Three-Dimensional Flows

The development of two-dimensional turbulent separated regions, induced in a compression corner, and at the base of an incident shock, with increase in interaction strength in hypersonic flow as obtained by Holden,<sup>5-13</sup> are illustrated in Figures 5.6 and 5.7. Separation is first observed in the laminar sublayer and a well-defined separation bubble is clearly visible in Figure 5.6. The initial development of the separation region takes place by an elongation into the laminar sublayer, with the separation and reattachment shocks combining within the boundary layer to form a single shock. Only when the separation point has fed well forward of the junction is a well-defined plateau region formed. Then, in contrast to laminar interaction regions, the separation shock originates at the bottom of the boundary layer and is contained within the boundary layer until it coalesces with the reattachment compression process. In separated regions induced by an externally generated shock, separation first takes place in the

region where the incident shock strikes the laminar sublayer, see Figure 5.7b. The separation point moves forward with increasing strength of the incident shock until the separation shock becomes visible in the inviscid flow downstream of the incident shock; as yet, separation is still downstream of the point where the incident shock passes through the edge of the boundary layer. For large incident shocks, boundary thickening occurs ahead of the incident shock in an analogous fashion to laminar flow separation. However, as in wedge-induced separated regions, viscous/inviscid interaction takes place almost entirely within the original boundary layer. The structure wedge and shock-induced turbulent interaction regions at Mach 13 are very similar to those at Mach 8; however, as we might anticipate, the viscous interaction region and the associated shocks are even more firmly embedded within the original boundary layer.

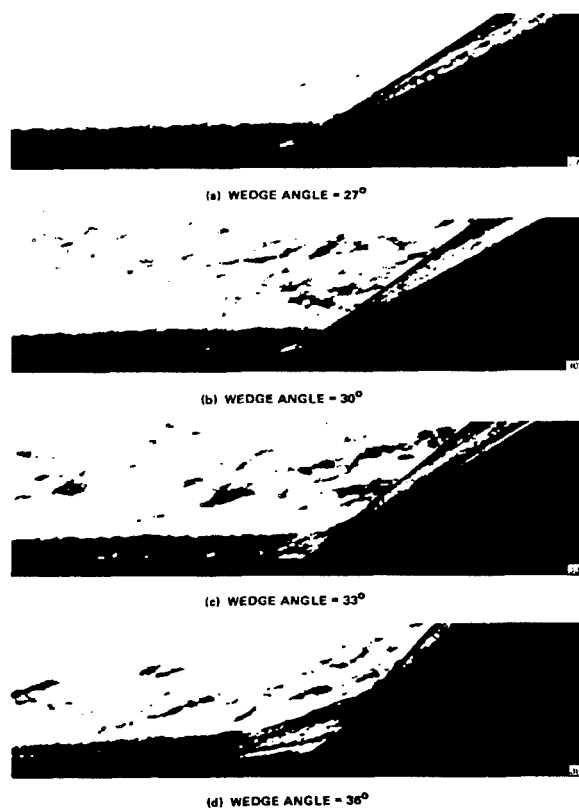


**Figure 5.6** The Development of a Wedge-Induced Separated Flow ( $M_\infty=8.6$ ,  $Re_L=22.5 \times 10^6$ )

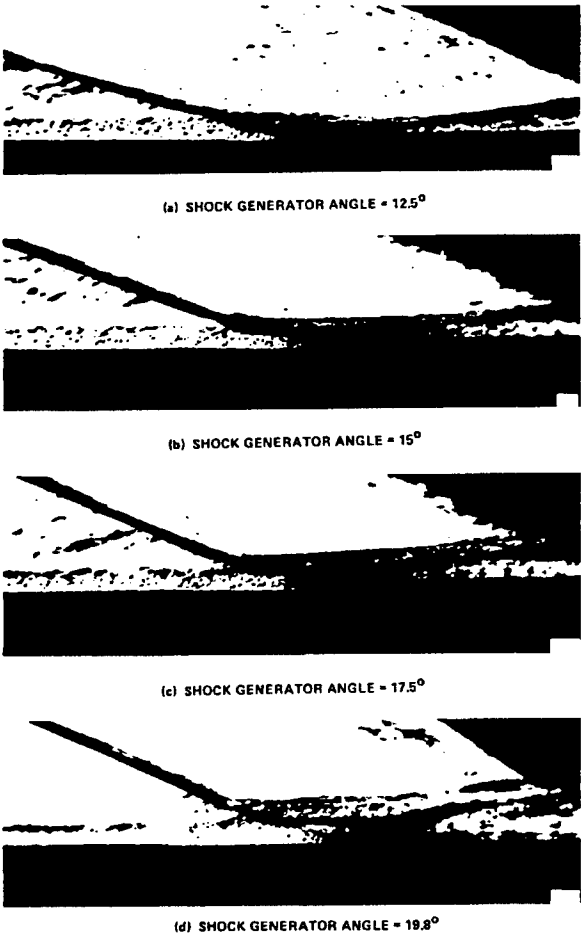


**Figure 5.7** The Development of a Shock-Induced Separated Flow ( $M_\infty=8.6$ ,  $Re_L=22.5 \times 10^6$ )

Surface measurements with high frequency instrumentation indicated that turbulent separated regions were highly unsteady, and typically the separation point would oscillate in a streamwise direction with an amplitude of approximately one-quarter to one-third of the local boundary layer thickness, at frequencies in the range from 1 to 10 kHz. The unsteady character of the records from transducers in the recirculation region indicated it could be unrealistic to assume that a laminar sublayer model, in the conventional sense, could be used to describe the lower part of the recirculating region as is done in some of the triple deck calculations. The mean distribution of skin friction, heat transfer and pressure to the walls bounding, both shock- and wedge-induced interaction region were similar for well-separated flows with identical total pressure rises. Both the pressures and heat transfer distributions are characterized by well-defined plateaus in the recirculation region and large

gradients in the separation and reattachment regions. The maximum heat transfer rates generated in the reattachment regions of these flows is, of course, of considerable importance. Holden<sup>5-14</sup> found that for separated interaction regions the maximum pressure and heat transfer measurements over the Mach number range from 2 to 13 could be correlated in the form shown in Figure 5.8a.

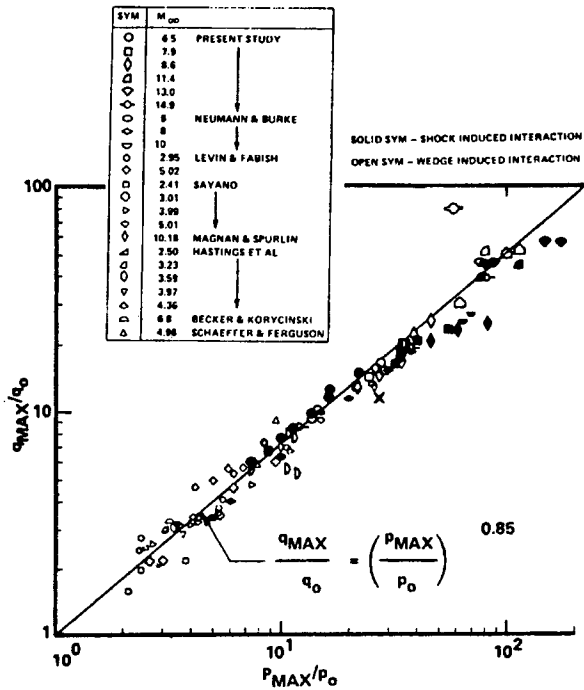


**Figure 5.8a** Correlation of Maximum Heating Rate in Wedge- and Externally-Generated Shock-Induced Turbulent Separated Flows

The influence of Reynolds number on the size of two-dimensional separated regions remains unresolved. Most of the early studies of shockwave-turbulent boundary layer interaction were made in the turbulent boundary layer over a tunnel wall. Major discrepancies were found between experimental facilities; for example, the measurements of Bogdonoff and Kepler<sup>5-15</sup> differed considerably from those of Gadd<sup>5-16</sup> for identical freestream Mach numbers and interaction strength when both experimenters had indicated that there was little effect of freestream Reynolds number on the length of the separated region. However, the measurements of Green<sup>5-17</sup>, Roshko and Thomke,<sup>5-18</sup> Law,<sup>5-19</sup> Settles, Bogdonoff and Vas,<sup>5-20</sup> and Appels,<sup>5-21</sup> all made under adiabatic wall conditions, indicate that increasing

Reynolds number decreases the size of a turbulent separated region. In contrast, the studies of Chapman, Kuehn and Larson<sup>5-22</sup> Kuehn,<sup>5-23</sup> and Holden,<sup>5-13</sup> Elfstrom<sup>5-24</sup> and Appels<sup>5-25</sup> at hypersonic speeds, all conducted on highly cooled models mounted in the test section, have shown the opposite trend. As in the case of incipient separation, the answer may lie in changes in the equilibrium structure of a turbulent boundary layer with Reynolds number. This hypothesis is supported by present measurements of shock- and wedge-induced separated flows at Reynolds numbers of up to  $3 \times 10^7$  by Holden.<sup>5-14</sup>

The plateau pressure of a turbulent separated region is an important characteristic, which from free interaction theory should not depend upon the way in which separation is promoted. The correlation of experimental measurements shown in Figure 4.8b suggest that this case, and the method of Reshotko and Tucker<sup>5-26</sup> presents a simple way of calculating this quantity.

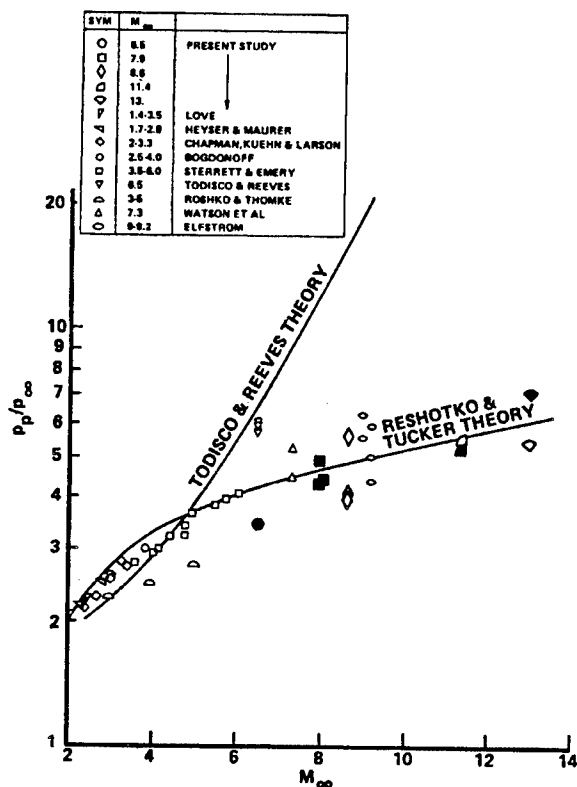


**Figure 5.8b** Correlation of Plateau Pressure Measurements in Wedge- and Shock-Induced Turbulent Separated Region

Comparisons with Navier-Stokes Solutions

The complexity of the flowfield in regions of shockwave/turbulent boundary layer interaction is such that it is unrealistic to expect to describe such regions in any detail within the framework of the boundary layer equations. Indeed there are some who would question whether the time or mass averaged Navier-Stokes equations capture the basic fluid mechanics associated with the intrinsically unsteady nature of separated regions. In hypersonic flows the effects of compressibility on the structure and development of turbulence must also be considered.

While there have been strenuous efforts to obtain predictions of 2D and 3D turbulent interaction regions, it is currently recognized that successes with Navier-Stokes code in describing some 3D turbulent interactions regions is a result of the dominance of the pressure and inertial terms in these flows. In these latter comparisons (References 5-27 and 5-28) it was found that the modeling of turbulence could be changed without significantly changing the numerical solution. For 2D interactions it appears the modeling of turbulence is more critical. To obtain good agreement for these latter flows, some very gross assumptions must be made in the turbulence model. Shang and Hankey,<sup>5-29</sup> for example chose to apply an empirical relationship (selected by matching the length of the separated region) to rapidly decrease the turbulent scale size through the interaction region as shown in Figure 5.9. Horstmann,<sup>5-30</sup> however, found the best agreement with Settles<sup>5-31</sup> measurements in wedge-induced separated regions using a two equation model for turbulence scale size and vorticity, as shown in Figure 5.10. Figure 5.10b shows a correlation of incipient separation conditions determined in the studies at hypersonic speeds together with the measurements on adiabatic walls at supersonic speeds. Working with this same turbulence model, however, Horstmann<sup>5-30</sup> was unable to predict the occurrence of separation on two incident shock/turbulent boundary layer configurations studied by Holden<sup>5-32</sup> at Mach 11.2. As shown in Figures 5.11 and 5.12 both these flowfields are clearly separated and yet the numerical solution fails to predict the characteristic plateaus in either the heat transfer or pressure distributions. The modeling of turbulence in separated interaction regions at hypersonic Mach numbers should account for the effects of compressibility and the generation of turbulence by the unsteady movement of the incident and induced shocks as they traverse and interact with a major region of the turbulent boundary layer. Clearly further detailed

experimental work and insightful theoretical modeling are required to develop numerical prediction techniques which are capable of describing turbulent interaction regions in detail.

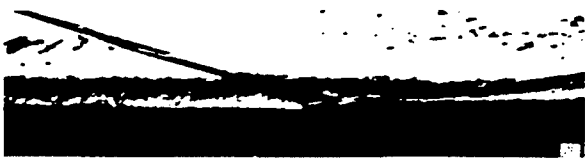


Figure 5.9 Incipient Separation at Mach 6.5 and  $Re_L=27 \times 10^6$

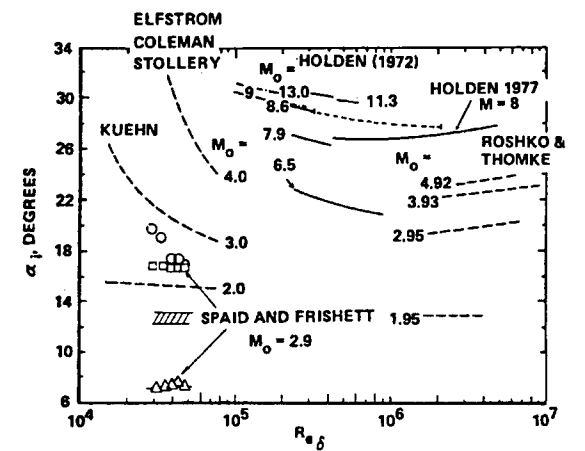


Figure 5.10a Wedge Angle to Induce Incipient Separation

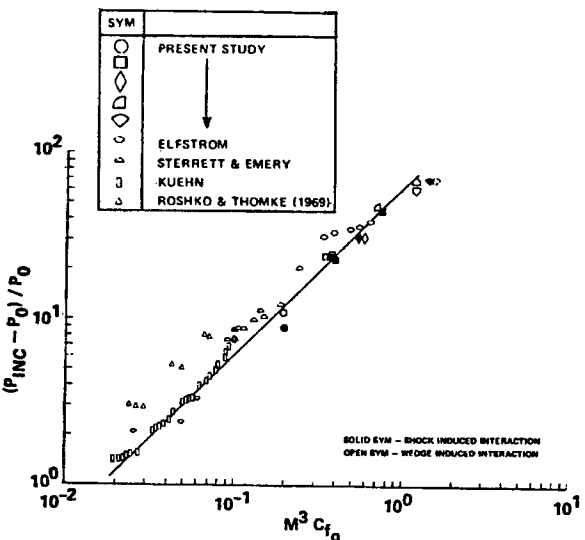


Figure 5.10b Correlation of Incipient Separation Conditions for Wedge- and Shock-Induced Turbulent Interaction Regions

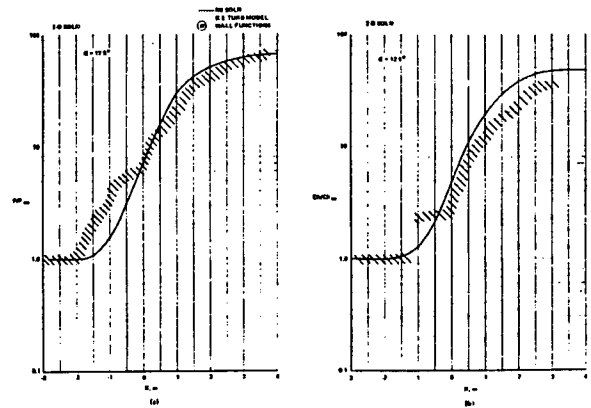


Figure 5.11 Comparison Between Navier-Stokes Solution and Experiment for a Mildly Separated Flow

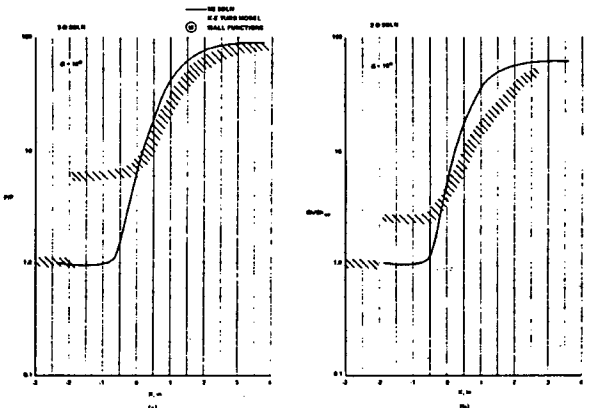


Figure 5.12 Comparison Between Navier-Stokes Solution and Experiment for a Well-Separated Flow

### Three-Dimensional Shock Wave/Turbulent Boundary Layer Interaction

Many of the conceptual problems associated with the use of the boundary layer equations to describe separated regions induced by shockwave/turbulent boundary layer interaction are circumvented by the direct solution of the Navier-Stokes equations. However, in their place we find the equally thorny problem of specifying a detailed model of turbulence for flows with exceedingly large streamwise pressure gradients. Despite the lack of success in developing credible turbulence models for two-dimensional interaction regions, or perhaps because of it, three-dimensional turbulent interaction regions have become the focus of attention of the Navier-Stokes solvers.

### a. Corner Interaction Studies

The axial corner flow or swept-shock interaction has been one of the principal configurations selected to investigate three-dimensional regions of shockwave boundary layer interaction. The swept-shock, which is generated by a wedge or fin mounted perpendicular to a flat plate, impinges normally onto the flat plate boundary layer. The initial studies in this area by Stalker<sup>5-33</sup> and Stanbrook<sup>5-34</sup> were followed by the more detailed investigations of McCabe,<sup>5-35</sup> Peake and Rainbird,<sup>5-36</sup> Oskam et al.,<sup>5-37</sup> Cousteix and Houdeville,<sup>5-38</sup> Dolling and Bogdonoff,<sup>5-39, 5-40</sup> Dolling and Murphy,<sup>5-41</sup> and Dolling.<sup>5-42</sup> The latter extensive series of studies was conducted at Mach 3 under adiabatic wall conditions. While incipient separation is relatively easy to define for two-dimensional turbulent interactions, this concept has generated considerable controversy in three-dimensional flows. While McCabe<sup>5-35</sup> suggests that separation should be defined on the basis of converging streamlines, Stanbrook<sup>5-34</sup> and others have used criteria based on the inflection points in the pressure distribution. The occurrence of separation was correlated in simple terms by Korkegi,<sup>5-43</sup> who found that in low Mach number flow, deflection angle  $\Theta_{wi}$  for incipient separation varies as the inverse of the upstream Mach number, i.e.,  $\Theta_{wi} = 0.3M_o$ , while for  $2 < M < 3.4$  Korkegi suggests that  $\pi/p$  is independent of Mach number. Goldberg's<sup>5-44</sup> and Holden's<sup>5-45</sup> measurements at Mach 6 and 11 respectively do not agree with the Korkegi correlation.

Studies with the emphasis on the heating in swept-shock interaction regions have been conducted by Neumann and Burke,<sup>5-46</sup> Law,<sup>5-47</sup> Token,<sup>5-48</sup> and Scuderi<sup>5-49</sup> and Holden.<sup>5-50</sup> Figure 5.13 shows typical distributions of heat transfer and pressure along a streamwise cut through the interaction region together with nomenclature which is in conventional use. While the heat transfer and pressure distributions exhibit a uniform and monotonic increase through attached interaction regions, when the flow separates, distinctive plateau regions are formed in the heat transfer and pressure distributions, as depicted in Figure 5.13. As noted above, at low Mach numbers ( $M = 2 \rightarrow 4$ ) and for adiabatic surfaces, a large body of data exists on the mean characteristics of swept-shock interactions. Strangely, this body of 3D data has been found to be in better overall agreement with the Hung and McCormack,<sup>5-51</sup> Horstmann,<sup>5-30</sup> Shang and Hankey,<sup>5-29</sup> Settles and Horstmann<sup>5-31</sup> solutions to the Navier-Stokes equations than the relatively less complex

two-dimensional flow separation over a flat plate/wedge. These results are not as sensitive to the turbulence model and suggest that the gross features of the flows are controlled principally by inviscid effects.

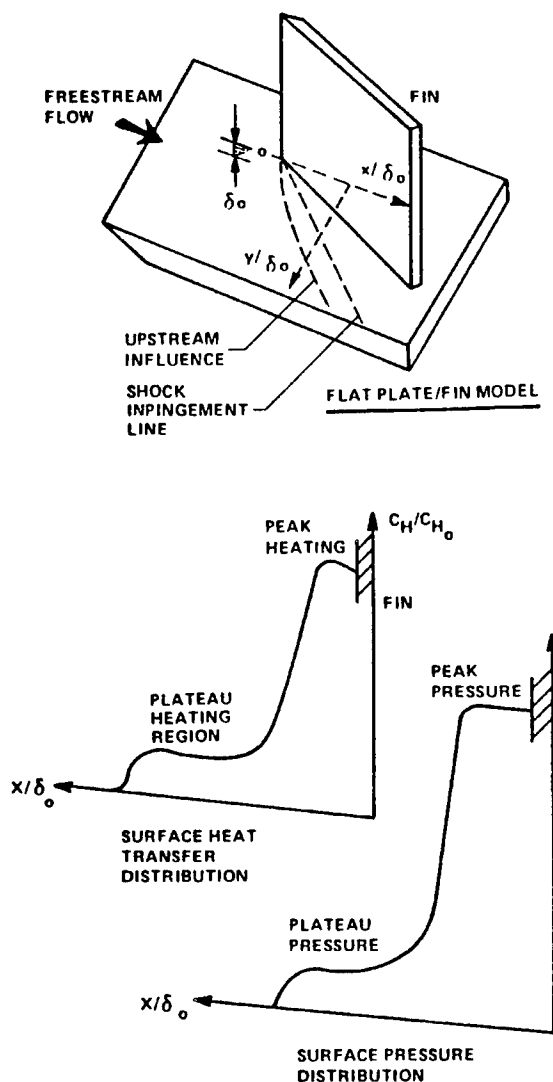


**Figure 5.13** Typical Surface Heating and Surface Pressure Distributions Through Swept Shock/Turbulent Boundary Layer Interaction

In a corner flow, the swept-shock generated by the inclined fin impinges on the turbulent boundary layer in a plane perpendicular to the flat plate. The basic mechanism of pressure rise through the interaction is therefore controlled principally by the component of freestream Mach number normal to this shock ( $M_o \sin \Theta$ ). A highly simplified visualization of the viscous/inviscid interaction with flow separation is sketched in Figure 5.14. Here, we consider the flow

in the plane normal to the plane of the shock to be similar to that in transonic flow. When flow separation occurs, a three-dimensional vortex is formed, the pressure in which is relatively constant at the “two-dimensional” plateau level, as we will show later. The streamwise distribution of heat transfer in this region is also found to be relatively constant, and indeed we and others using skin friction and oil flow measurements have correlated the first appearance of a plateau region in the heat transfer with a significant change in the flow structure which is linked with flow separation. In fact, Token<sup>5-48</sup> has shown that the McCabe<sup>5-35</sup> criteria, based on an examination of surface oil streaks in the neighborhood of flow separation, are less sensitive methods for detecting flow separation than observations based on changes in the heat transfer distribution with increased interaction strength. In a recent experimental study at Mach 11, Holden<sup>5-50</sup> used the incipient formation of a plateau in the heat transfer distribution, together with a marked increase in the fluctuation levels in the output of the thin film instrumentation, as marking the onset of flow separation. As shown in Figure 5.15 Holden’s measurements indicated that in hypersonic flow over highly-cooled surfaces the turbulent boundary is more tenacious in resisting boundary layer separation than predicted by the methods derived by McCabe<sup>5-35</sup> and Korkegi<sup>5-43</sup>. Holden’s measurements of the peak pressure ratio through the interaction and the plateau pressure rise are in better agreement with calculations based on an inviscid flow model in the 2D theory of Reshotko and Tucker<sup>5-26</sup> than the correlations of Scuderi<sup>5-49</sup> as shown in Figure 5.16. Holden found that, as in the studies of two-dimensional separated interaction regions, the peak heating can be related to the overall pressure rise by a simple power law relationship as shown in Figure 5.17. Figure 5.18 shows that the maximum pressure rise through the interaction region can be calculated with good accuracy from inviscid flow relationships. While there appears to be merit for the development of simple prediction methods in describing the flow in terms of the normal flow Mach number, this is clearly a gross oversimplification and it should be noted that the plateau pressure measurements obtained in the current study were relatively independent of  $M_o \sin \Theta$ .

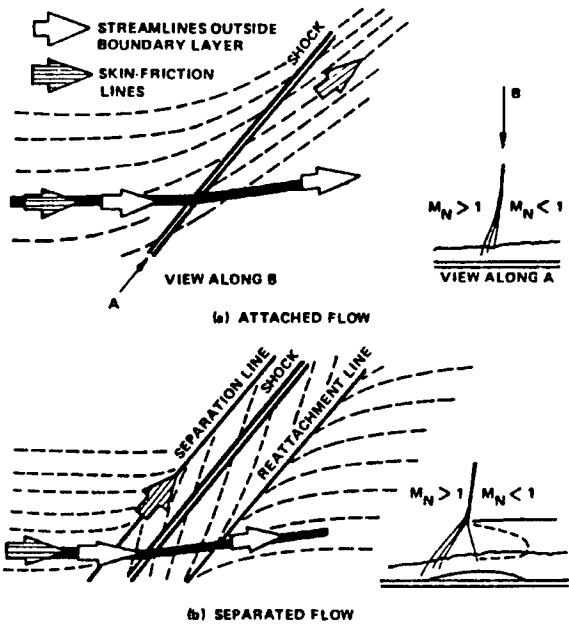


Figure 5.14 Schematic Representation of Attached and Separated Regions in Swept-Shock/Boundary Layer Interactions

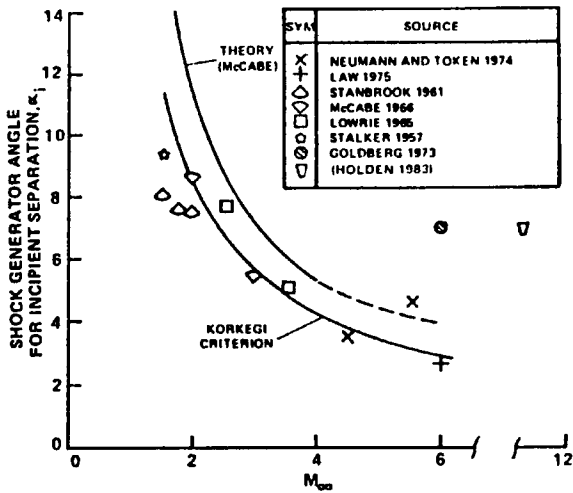


Figure 5.15 Variation of Shock Generator Angle to Induce Incipient Separation with Mach Number



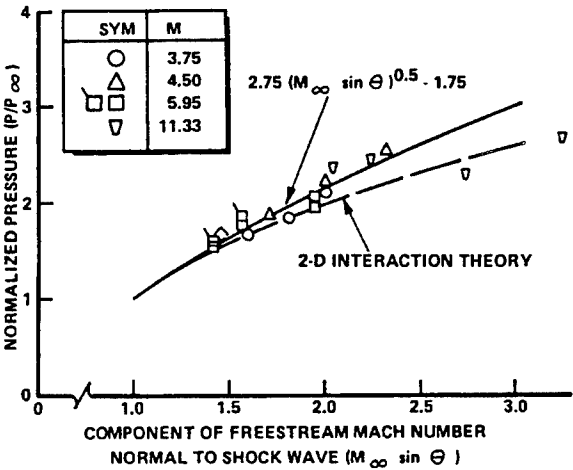


Figure 5.16 Correlation of Plateau Pressure Measurement From Swept-Shock Interaction Studies

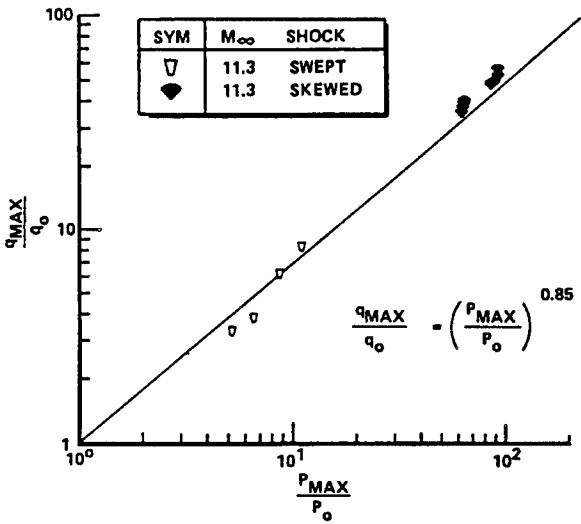


Figure 5.17 Correlation of Peak Heating Rates in Skewed- and Swept-Shock Interaction Regions

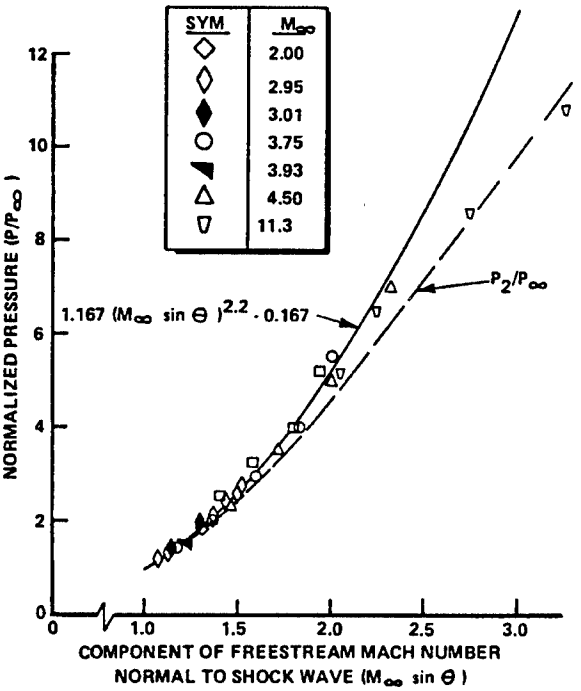


Figure 5.18 Correlation of Maximum Pressures Recorded in Swept-Shock Interaction Regions

b. Skewed Shock/Boundary Layer Interaction

Another approach to exploring flow separation in regions of three-dimensional shockwave/boundary layer interaction is to begin with a two-dimensional or axisymmetric interaction and sweep this interaction (or introduce angle of attack for the axisymmetric case) to progressively introduce crossflow into the interaction region. Experimental studies of this type have been conducted by Ericsson, Reding and Guenther<sup>5-52</sup> Settles and Perkins,<sup>5-53</sup> and Settles and Teng.<sup>5-54</sup> Settles, who studied the interaction region over swept and unswept flat plate/wedge configurations in an adiabatic Mach 3 airflow, found that introducing crossflow increased the scale of the separated interaction region. Considerable effort was expended in this latter study to determine the Reynolds number scaling, and the length from the upstream tip of the wedge for the flow to become quasi-two-dimensional. However, the effect of changing the overall spanwise scale of the model on the scale of the interaction was not examined explicitly. The measurements of surface and pitot pressure through the interaction regions were in good agreement with solutions to the Navier-Stokes equations obtained by Horstman<sup>5-30</sup>; however, some key features of the flow were poorly predicted. It is known that agreement with pressure data is not

the most definitive of tests. More recently Holden<sup>5-45</sup> performed studies of crossflow effects on the size and properties of the interaction region induced by a swept-oblique-shock incident on a turbulent boundary layer over a flat plate at Mach 11 and  $Re = 30 \times 10^6$ . Experiments were conducted for two strengths of incident shock, the first ( $\Theta_{SG} = 12.5^\circ$ ) to generate a separated condition close to incipient separation, and the second ( $\Theta_{SG} = 15^\circ$ ) to generate a well-separated flow. Distributions of heat transfer and pressure as well as Schlieren photographs of the unswept or two-dimensional flow condition and the 30 degree swept condition are shown in Figures 5.19 and 5.20. It is clear from the well-defined plateau regions in the distributions of pressure and heat transfer, as well as the well-defined separation shock in the Schlieren photograph, that a well separated region, extending two inches in length, is induced beneath the stronger incident shock. The measurements made of the distribution of heat transfer and pressure beneath the well separated flow induced by both the 12.5 degree and the 15 degree shock generators swept at angles of 0 and 30 (shown in Figures 5.19 and 5.20) indicated that the induced crossflow has little effect on the size and characteristics of the interaction regions. If there is a perceptible effect, it is a decrease in the length of the separated region with increased crossflow. The significant differences between Holden's and Settles<sup>5-31</sup> measurements of the variation of interaction length with sweep angle and those obtained in these studies are shown in Figure 5.21. While Settles finds an almost threefold increase in separation length at sweep angles of 40 degrees, Holden found 10 percent reduction in this length. Further studies are required to resolve this issue.

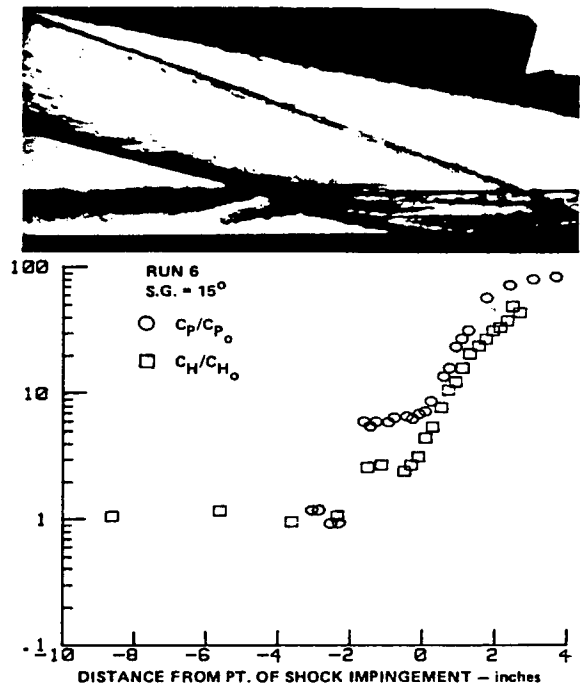


Figure 5.19 Streamwise Distributions of Heat Transfer and Pressure Through Skewed-Oblique-Shock Boundary Layer Interaction ( $\Theta=15^\circ$ ,  $\psi=0^\circ$ )

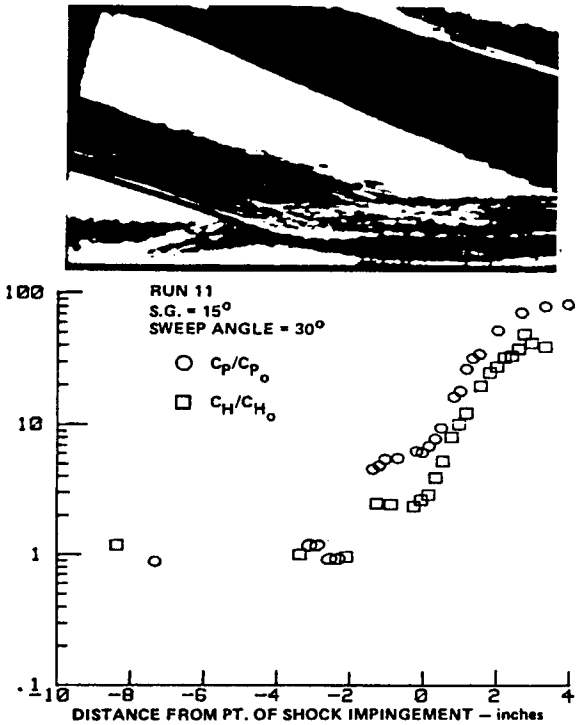
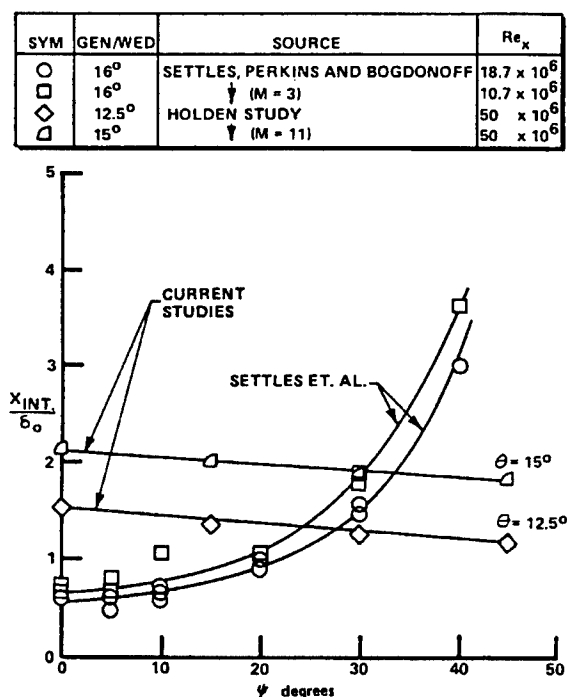


Figure 5.20 Streamwise Distributions of Heat Transfer and Pressure Through Skewed-Oblique-Shock Boundary Layer Interaction ( $\Theta=15^\circ$ ,  $\psi=30^\circ$ )



**Figure 5.21** Variation of Streamwise Extent of Interaction Ahead of Shock Impingement (or Corner) with Sweep Angle

## REFERENCES

- 5-1. Holden, M.S. "Theoretical and Experimental Studies of the Shock Wave-Boundary Layer Interaction on Curved Compression Surfaces," Paper presented at the ARL Symposium on "Viscous Interaction Phenomena in Supersonic and Hypersonic Flow," WBAFB, OH May 7-8, 1969.
- 5-2. Howarth, L., "The Propagation of Steady Disturbances in a Supersonic Stream Bounded on One Side by a Parallel Subsonic Stream," Proc. Camb. Phi. Soc. 1947, p. 44, Part 3.
- 5-3. Lighthill, M.J., "On Boundary-Layers and Upstream Influence. Part II. Supersonic Flows Without Separation," P.R.S.A., 1953, pp. 217 and 478.
- 5-4. Oswatitsch, K. and Wiegardt, K., "Theoretical Analysis of Stationary Potential Flows and Boundary-Layers at High-Speed, German Wartime Report, 1941," Translated as NACA TM 1189.
- 5-5. Carter, J.E., "Numerical Solution of the Supersonic Laminar Flow Over a Two-Dimensional Compression Corner," Lecture Notes in Physics, Col. 19 Springer-Verlag, New York, 1973, p. 69.
- 5-6. Hung, C.M. and MacCormack, R.W., "Numerical Solutions of Supersonic and Hypersonic Laminar Flows Over a Two-Dimensional Compression Corner," AIAA Paper 75-2, January 1975.
- 5-7. Stainbeck, P.C., "An Experimental Investigation at a Mach Number of 4.95 of Flow in the Vicinity of a 90° Interior Corner Aligned with the Freestream Velocity," Feb. 1960, NASA TN D-184 231 524.
- 5-8. Stainback, P.C., "Heat Transfer Measurements at a Mach Number of 8 in the Vicinity of a 90° Interior Corner Aligned with the Free-stream Velocity," Aug. 1964, NASA TN D 2417.
- 5-9. Stainback, P.C., "Weinstein, L.M., "Aerodynamic Heating in the Vicinity of Corners at Hypersonic Speeds," Nov. 1967, NASA TN D-4130.
- 5-10. Charwat, A.F. and Redekopp, L.G., "Supersonic Interference Flow Along the Corner of Intersecting Wedges," AIAA J., Vol. 5, No. 3, March 1967.
- 5-11. Watson, R.D. and Weinstein, L.M., "A Study of Hypersonic Corner Flow Interactions," AIAA Paper 70-227, 1970.
- 5-12. Kutler, P., Shankar, V., Anderson, D.A., and Sorenson, R.L., "Internal and External Axial Corner Flows for Integrated Ram/Scramjet Nacelles, Part I," NASA SP-347, March 1975.
- 5-13. Holden, M.S., "Shock Wave-Turbulent Boundary Layer Interaction in Hypersonic Flow," AIAA 10th Aerospace Sciences Meeting, San Diego, California, January 17-19, 1972, AIAA-72-74.
- 5-14. Holden, M.S., "Shock Wave-Turbulent Boundary Layer Interaction in Hypersonic Flow," AIAA 77-45.
- 5-15. Bogdonoff, S.M. and Kepler, C.E., "Separation of a Supersonic Turbulent

- Boundary Layer," J. Aero. Sci., 22, pp. 441-424 (1955).
- 5-16. Gadd, G.E., "Interactions Between Wholly Laminar or Wholly Turbulent Boundary Layers and Shock Waves Enough to Cause Separation," J. Aeronautical Sciences, Vol. 20, pp. 729-739, November 1953.
  - 5-17. Green, J.E., "Interactions Between Shock Waves and Turbulent Boundary Layers," Progress in Aerospace Sciences, Vol. 11, pp. 235-340, Pergamon Press, Oxford, 1970.
  - 5-18. Roshko, A. and Thomke, G. J., "Flare-Induced Separation Lengths in Supersonic, Turbulent Boundary Layers," AIAA Aerospace Sciences Meeting, Paper No. 75-6, 1975.
  - 5-19. Law, C.H., "Supersonic Turbulent Boundary Layer Separation Measurements at Reynolds Numbers of 10107 and 108", AIAA Journal, Vol. 12, No. 6, June 1974, pp. 794-797.
  - 5-20. Settles, G.S., Bogdonoff, S.M., and Vas, I.E., "Incipient Separation of a Supersonic Turbulent Boundary Layer at Moderate to High Reynolds Numbers," AIAA Paper 75-7, 1975.
  - 5-21. Appels, C., "Incipient Separation of a Compressible Turbulent Boundary Layer," von Karman Institute Technical, Note 99, April 1974.
  - 5-22. Chapman, D.R., Kuehn, D.M., and Larson, H.G., "The Investigation of Separated Flows in Supersonic and Subsonic Streams with Emphasis on the Effects of Transition," NACA Report No. 1355, 1958.
  - 5-23. Kuehn, D.M., "Experimental Investigation of the Pressure Rise Required for the Incipient Separation of Turbulent Boundary Layers in Two-Dimensional Supersonic Flow," NASA Memo 1-21-59A, Feb. 1959.
  - 5-24. Elfstrom, G.M., Coleman, G.T., and Stollery, J.L., "Turbulent Boundary Layer Studies in a Hypersonic Gun Tunnel," 8th Annual International Shock Tube Symposium, London, England, Jul. 1971.
  - 5-25. Appels, C. and Richards, B.E., "Incipient Separation of a Compressible Turbulent Boundary Layer," AGARD Conference Preprint No. 168 on Flow Separation.
  - 5-26. Reshotko, E., and Tucker, M., "Effects of a Discontinuity on Turbulent Boundary Layer Thickness Parameters With Applications to Shock Induced Separation," NACA, TN 3435, 1955.
  - 5-27. Knight, D.D., "Problems in Reconciling Computation and Experiment," 1985 Princeton University Workshop on the Structure of High-Speed Turbulent Boundary Layers.
  - 5-28. Knight, D., Horstman, C.C., Shapey, B., and Bogdonoff, S., "The Flowfield Structure of the 3-D Shock Wave Boundary Layer Interaction Generated by a 20 degree Sharp F in at Mach 3" AIAA-86-343.
  - 5-29. Shang, J.S., Hankey, W.L., and Petty, J.S., "Three-Dimensional Supersonic Interacting Turbulent Flow Along a Corner," AIAA Paper 78-1210, July 1978; also AIAA Journal, Vol. 17, No. 7, July 1979, pp. 706-713.
  - 5-30. Horstmann, C.C. and Hung, C.M., "Computations of Three-Dimensional Turbulent Separated Flows at Supersonic Speeds," AIAA Paper 79-2, January 1979.
  - 5-31. Settles, G.S. and Horstmann, C.C., "Flowfield Scaling of a Swept Compression Corner Interaction--A Comparison of Experiment and Computation," AIAA-84-0096, 22nd Aerospace Sciences Meeting, January 9-12, 1984.
  - 5-32. Holden, M.S., "Experimental Studies of Quasi-Two-Dimensional and Three-Dimensional Viscous Interaction Regions Induced by Skewed-Shock and Swept-Shock Boundary Layer Interaction" Paper presented at the AIAA 19th Thermophysics Conference Snowmass, Colorado 25-27 June 1984, AIAA Paper AIAA-84-1677.
  - 5-33. Stalker, R.J., "The Pressure Rise at Shock-Induced Turbulent Boundary Layer Separation in Three-Dimensional Supersonic Flow," J.

- Aeronautical Science, Vol. 24, No. 7, July 1951, pp. 547.
- 5-34. Stanbrook, A., "An Experimental Study of the Glancing Interaction Between a Shock Wave and a Turbulent Boundary Layer," ARC CP 555, 1961.
  - 5-35. McCabe, A., "The Three-Dimensional Interaction of a Shock Wave with a Turbulent Boundary Layer," Aeronautical Quarterly Vol. XVII, August 1966, pp. 231-252.
  - 5-36. Peake, D.J. and Rainbird, W.J., "The Three-Dimensional Separation of a Turbulent Boundary Layer by a Skewed Shock Wave and Its Control by the Use of Tangential Air Injection," AGARD CP-168, May 1975.
  - 5-37. Oskam, B., Vas, I.E., and Bogdonoff, S.M., "Oblique Shock Wave/Turbulent Boundary Layer Interactions in Three-Dimensions at Mach 3, Part 1," AFFDL-TR-76-48, June 1976.
  - 5-38. Cousteix, J.A. and Houdeville, R., "Epaississement et Separation d'une Couche Limite Turbulente Sournise en Interaction avec un Choc Oblique," La Recherche Aerospatiale, No. 1, Jan./Feh. 1976, pp. 1-11.
  - 5-39. Dolling, D.S. and Bogdonoff, S.M., "An Experimental Investigation of the Unsteady Behavior of Blunt Fin-Induced Shock Wave Turbulent Boundary Layer Interactions," AIAA-81-12S7, 14th Fluid and Plasma Dynamics Conference, June 23-25, 1981.
  - 5-40. Dolling, D.S. and Bogdonoff, S.M., "Upstream Influence Scaling of Sharp Fin-Induced Shock Wave Turbulent Boundary Layer-Interactions," AIAA Paper 81-0336, AIAA 19th Aerospace Sciences Meeting, January 1981.
  - 5-41. Dolling D.S. and Murphy, M., "Wall Pressure Fluctuations in a Supersonic Separated Compression Ramp Flowfield," AIAA-82-0986, AIAA/ASME 3rd Joint Thermophysics, Fluids, Plasma and Heat Transfer Conference, June 7-11, 1982.
  - 5-42. Dolling, D.S., "Effects of Mach Number in Sharp Fin-Induced Shock Wave Turbulent Boundary Layer Interaction," AIAA-84-0095, 22nd Aerospace Sciences Meeting, Jan. 9-12, 1984.
  - 5-43. Korkegi, R.H., "A Simple Correlation for Incipient Turbulent Boundary-Layer Separation Due to a Skewed Shock Wave," AIAA Journal, Vol. 11, No. 11, November 1973, pp. 1578-1579.
  - 5-44. Goldberg, T.J., "Three-dimensional Separation for Interaction of Shock Waves with Turbulent Boundary Layers," AIAA Journal, Vol. 11, No. 11, November 1973, pp. 1573-1575.
  - 5-45. Holden, M.S. "Experimental Studies of Quasi-Two-Dimensional and Three-Dimensional Viscous Interaction Regions Induced by Skewed-Shock and Swept-Shock Boundary Layer Interaction" Paper presented at the AIAA 19th Thermophysics Conference Snowmass, Colorado 25-27 June 1984, AIAA Paper AIAA-84-1677.
  - 5-46. Newmann, R.D. and Burke, G., "The Influence of Shock Wave-Boundary Layer Effects on the Design of Hypersonic Aircraft," AFFDL-TR-68-152, IJSAF Flight Dynamics Laboratory, 196S.
  - 5-47. Law, H.C., "Three-Dhnensional Shock Wave Turbulent Boundary Layer Interactions at Mach 6," ARL TR-75-0191, June 1975.
  - 5-48. Token, K.H., "Heat Transfer Due to Shock Wave Turbulent Boundary Layer Interactions on High-Speed Weapon Systems," AFFDL-TR-74-77, April 1974.
  - 5-49. Scuderi, L.F., "Expressions for Predicting 3D Shock Wave-Turbulent Boundary Layer Interaction Pressures and Heating Rates," AIAA Paper 78-162, January 1978.
  - 5-50. Holden, M.S. "Experimental Studies of Quasi-Two-Dimensional and Three-Dimensional Viscous Interaction Regions Induced by Skewed-Shock and Swept-Shock Boundary Layer Interactions" Calspan Report No. 7018-A-2 Report Covering Period 15 January 1982 - 31 July 1984 July 1984.

- 5-51. Hung, C.M., and MacCormack, R.W., "Numerical Solutions of Supersonic and Hypersonic Laminar Flows Over a Two-Dimensional Compression Corner," AIAA Paper 75-2, January, 1975.
- 5-52. Ericsson, L.E., Reding, J.P., and Guenther, R.A., "Effects of Shock-Induced Separation," Lockheed Missiles and Space Co., Sunnyvale, CA, L-87-691, July 1969.
- 5-53. Settles, G.S., and Perkins, J.J., "Upstream Influence Scaling of 2D & 3D Shock/Turbulent Boundary Layer Interactions at Compression Corners," AIAA- 81-0334, 19th Aerospace Sciences Meeting, January 12-15, 1981.
- 5-54. Settles, G.S. and Teng, H.Y., "Flow Visualization of Separated 3D Shock Wave/Turbulent Boundary Layer Interactions," AIAA-82-0229, 20th Aerospace Sciences Meeting, January 11-14, 1982.

## 6.0 FLOWFIELD AND AEROTHERMAL EFFECTS ASSOCIATED WITH SHOCK/SHOCK INTERACTION PHENOMENA

### 6.1 Introduction

The heating rates generated in two and three-dimensional interaction regions by shock-shock interaction can pose serious problems for the designer of TPS. Heating levels up to two orders of magnitude larger than the stagnation point value can be generated at hypersonic speeds by shock-shock interaction over the leading edge of fins, inlets and structures connecting two vehicles. These regions of sharply peaked heating levels are accompanied by high pressures, and unlike the stagnation point their position cannot be defined with ease. Perhaps the most dramatic example of damage resulting from shock impingement heating was that recorded on the ventral fin supporting a ramjet model on the X-15. At Mach 6.7, the heating resulting from shock-shock interaction caused a burn-through in the fin, as shown in Figure 6.1, which also graphically demonstrates the high gradients generated in such flows.<sup>6-1</sup>



**Figure 6.1** Damage Resulting from Shock Impingement on Vertical Support

During the past two decades, a significant number of studies have been conducted to investigate the aerothermal loads generated in regions of shock/shock interaction. A detailed review of these studies, as well as an extensive set of heat transfer and pressure measurements in regions of shock/shock interaction at Mach numbers from 6 to 18, is presented by Holden et al. in Reference 6-2. Comparisons between the peak heat transfer and pressure measurements on cylindrical leading edges made in these studies with the simple prediction techniques devised by Edney (Reference 6-3) and Keyes and Hains (Reference 6-4) showed general agreement. However, these studies suggest that it is

necessary to understand the role of the disturbances generated by shear-layer turbulence, and the influence of viscous effects on jet structure, to better predict these flows. The heating levels predicted by these semiempirical techniques are capable of bounding the levels of heating generated by laminar and turbulent Type III interactions. However, for flows where the viscous region occupies an extensive part of the shock layer, the compression and heating mechanisms may be significantly modified. Within the past several years, both Navier-Stokes equations and Direct-Simulation Monte Carlo (DSMC) methods have been used to calculate regions of shock/shock interaction. An adequate solution for these types of flows requires a careful and detailed gridding of the flowfield in the jet or shear-layer region between the shock intersection point and the body. Once again, an accurate solution for flows with shear-layer transition depends on correctly describing the transitional and turbulent flow structures of the shear layer and the radiated noise effects on Type IV heating, or on reattachment characteristics for Type III flows. Consequently, in predicting the heating loads in these flows, it is essential to establish a transition criterion of the type shown in Figure 6.2 (Reference 6-2), where the Reynolds number based on the shear-layer length and adjacent flow properties is plotted versus effective shear-layer Mach number. Generally, for shear-layer Reynolds numbers below  $5 \times 10^4$ , the shear layer should remain laminar; for shear layer Reynolds numbers above  $5 \times 10^5$ , a turbulent flow may be expected. The exact Reynolds number at which shear-layer transition will occur will, of course, also depend upon the disturbances that are radiated from upstream surfaces of the vehicle and those present in the freestream. Other experiments were conducted in a free piston shock tunnel to determine the effects of thermochemistry associated with shock/shock interactions at high-enthalpy.<sup>6-5</sup>

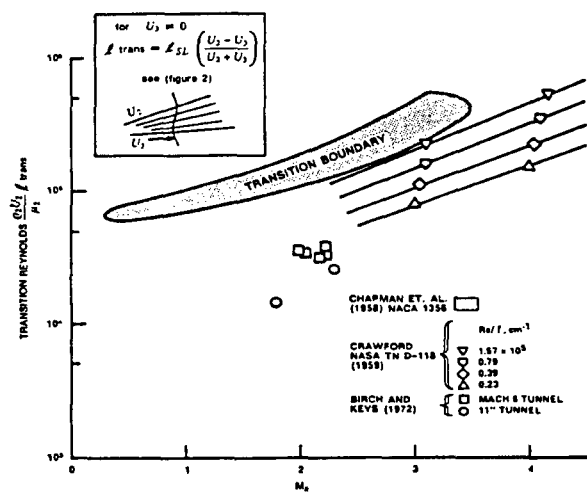


Figure 6.2 Variation of Transition Reynolds Number with Convective Mach Number

6.2 Shock/Shock Interaction Effects for Two- and Three-Dimensional Configurations

In a recent study (Reference 6-6), measurements were made to examine the variation in the magnitude and the distribution of heating rate generated in regions of shock/shock interaction with changes in the Reynolds number and Mach number of the flow to determine the magnitude of changes that occur in the peak heating from turbulent to laminar interactions and then from laminar to non-continuum flows. The Reynolds number were varied by changing both the size of the cylinder and the unit Reynolds number of the freestream. Data sets were also obtained at freestream Mach numbers from 8 to 18. In Figures 6.3 to 6.6, we show a set of measurements made on the 3-inch-diameter cylinder to obtain the heat transfer distributions for a low Reynolds number flow. In Figures 6.3 and 6.4, we show the data used to select the peak values in heat transfer and pressure shown in Figure 6.5 and 6.6. An equivalent set of measurements for a high Reynolds number turbulent flow is shown in Figures 6.7 through 6.10. Again, we employed the information contained in Figures 6.7 and 6.8 to select the data shown in Figures 6.9 and 6.10. In Figure 6.11, we show the variation of peak heating with angular position at a common Mach number and Reynolds number condition for the three different cylinders. Here, we see that, with decreasing size, there is a decrease in the peak heating level independent of the angular position of the interaction. Again, we obtained overlapping sets of measurements from runs with a different mean position of the interaction region. It can be seen that,

while, for the 3-inch cylinder, we obtain amplification factors of 15 to 20, for the 1/4-inch cylinder, the amplification factors are reduced to less than 5 in a shock layer dominated by viscous effects. The effects of the variation of unit Reynolds number for a given leading-edge diameter are shown for the 3-inch nose diameter in Figure 6.12. Here, again, we see a similar trend, where there is a reduction in heating enhancement with unit Reynolds number as the flow changes from turbulent to laminar and from an inviscid to a viscous-dominated shock layer. In all these flows, we do not observe a strong change in the heating levels for interaction positions from 20 to 35 degrees, despite potential changes from Type III to Type IV interactions. Finally, in Figures 6.13 and 6.14, we show a composite of the measurements where we have plotted amplification factors as a function of the shear layer Reynolds number and the rarefaction parameter  $M_\infty/\sqrt{Re_D}$ . Here, we see that typical values of the enhancement factor for turbulent interactions vary from 35 to 18, those in laminar flows are between 18 and 12, and, for viscous-dominated flows, the enhancement factors have dropped to levels of 5 or below.

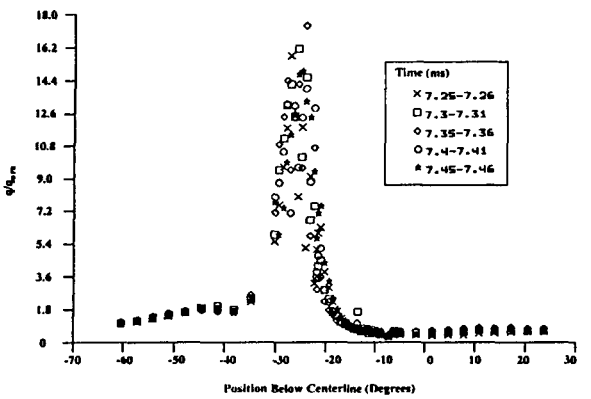


Figure 6.3 Surface Heat Transfer Rates of Sequential Time Steps

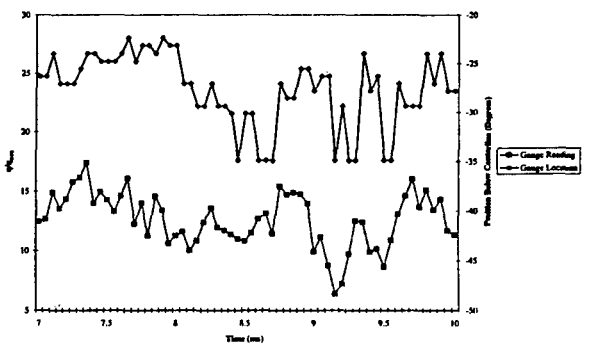


Figure 6.4 Time History of Heating Rates



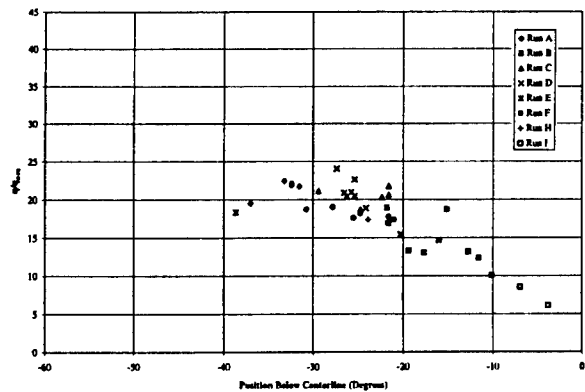


Figure 6.5 Heat Transfer Distribution

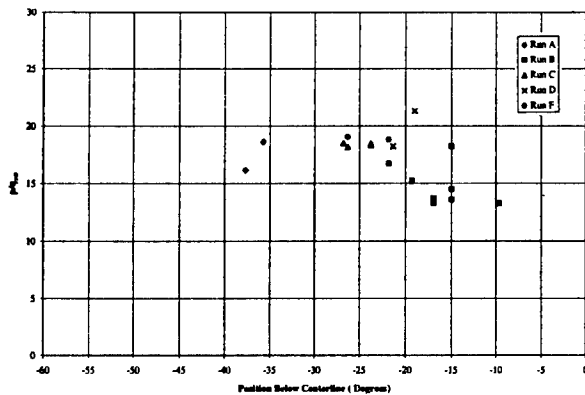


Figure 6.6 Pressure Distribution

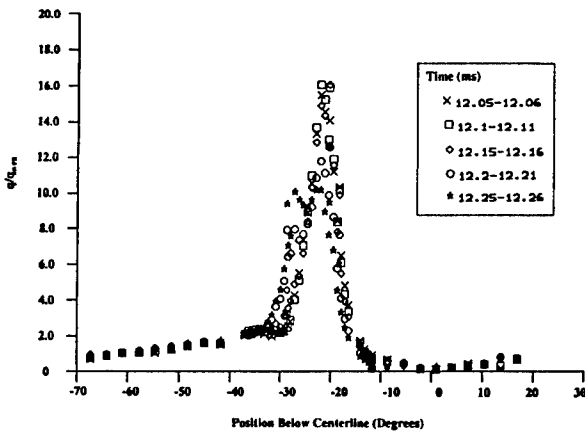


Figure 6.7 Surface Heat Transfer Rates of Sequential Time Steps

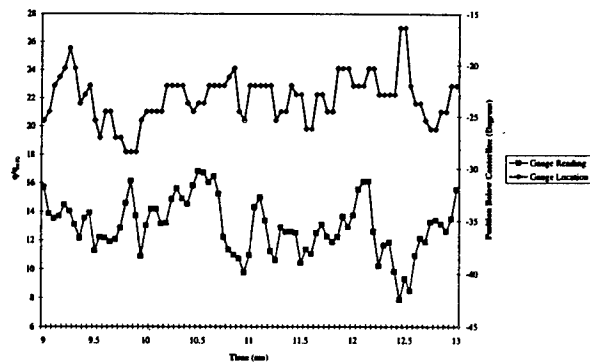


Figure 6.8 Time History of Heating Rates

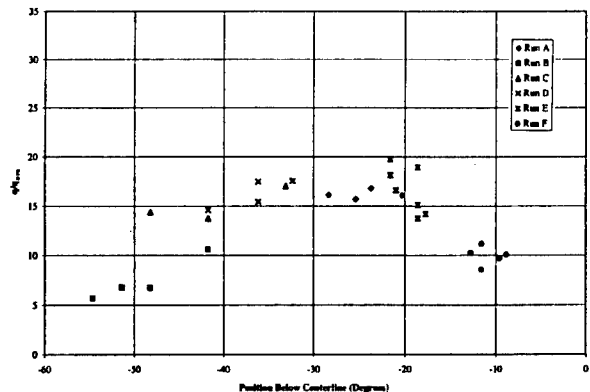


Figure 6.9 Heat Transfer Distribution

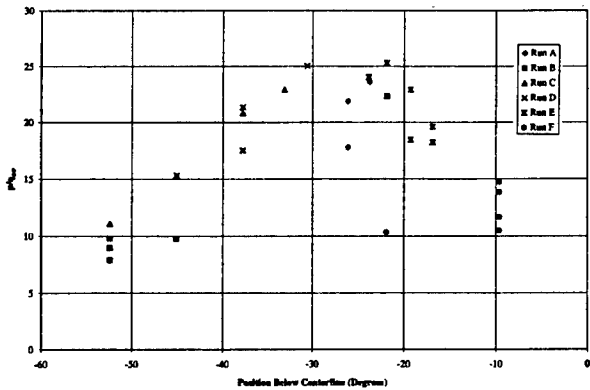
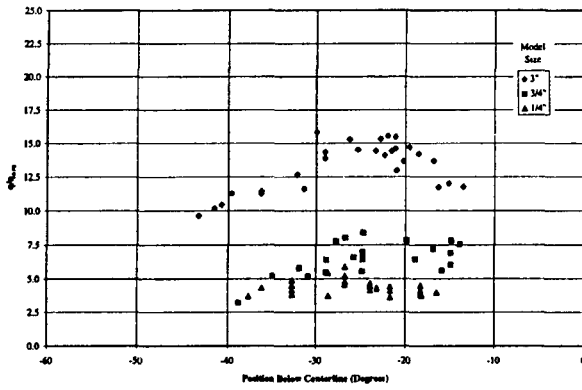
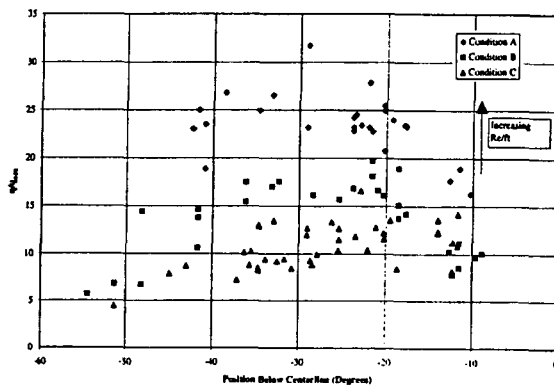


Figure 6.10 Pressure Distribution



**Figure 6.11** Condition 6AA, Heat Transfer Data All Models



**Figure 6.12** Heat Transfer Distributions at Various Reynolds Numbers, 3" Cylinder Model

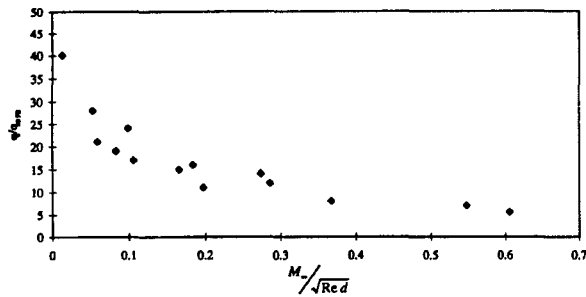


**Figure 6.13** Rarefaction Effects on Peak Heat Transfer Measurements

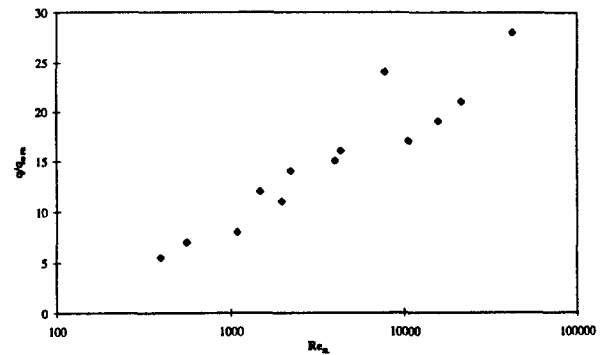


**Figure 6.14** Shear Layer Reynolds Number Effects on Peak Heat Transfer Measurements

### 6.3 Alleviation of Peak Heating Loads from Shock/Shock Interaction with Surface Blowing

#### 6.3.1 Introduction

An experimental program was reported by Holden, Rodriguez and Nowak (see Reference 6-7) to assess the effectiveness of transpiration cooling in reducing the large heat transfer loads generated in regions of shock/shock interaction. While a cylindrical configuration is more representative of the practical problems on the cowl lip, it proved more expedient to employ the existing transpiration-cooled hemisphere (Reference 6-8) in this initial investigation.

#### 6.3.2 Studies on the Transpiration Model Without Blowing

This set of measurements was made to provide the base against which to evaluate the effectiveness of transpiration cooling. Also, by comparing these measurements with the equivalent set on the smooth model (Figures 6.15a through 6.15c), the effects of the intrinsic roughness of the model on interaction heating can be determined. Examples of the distribution of heating on the transpiration model without blowing are shown in Figures 6.16a through 6.16c. When the interaction is placed close to the axis of the hemisphere (Figure 6.16a), there is relatively little enhancement. However, as observed on the smooth hemisphere (Figure 6.15a), heating-enhancement factors of close to 20 are generated (Figure 6.16b) when the type IV jet is incident close to 20° from the axis of the model. In slight contrast, the rough-wall heating enhancement ratio remains relatively high until the impingement point drops below 40°. Possibly, the surface roughness has induced transition on the model's surface. Comparing the sets of measurements shown in Figure 6.15c with those in Figure 6.16c, it is clear that the

peak heating for type IV interaction is relatively uninfluenced by surface roughness, while heating-enhancement factors for the type III interaction are increased by roughness, possibly as a result of transition.

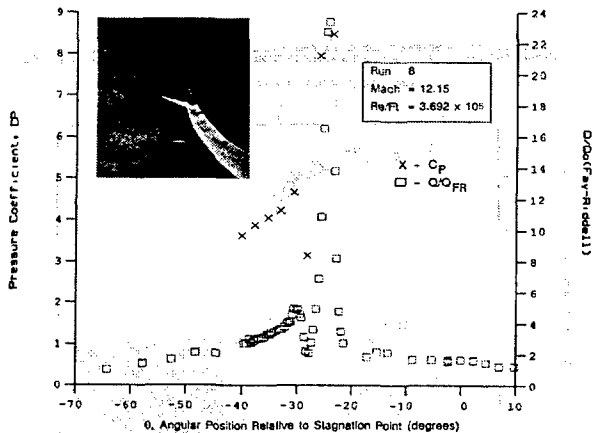


**Figure 6.15a** Heat and Pressure Distributions in Shock/Shock-Interaction Regions Induced by a 10° Shock Generator Over a Smooth 12-Inch Diameter Hemisphere at Mach 12.15 for Run 8

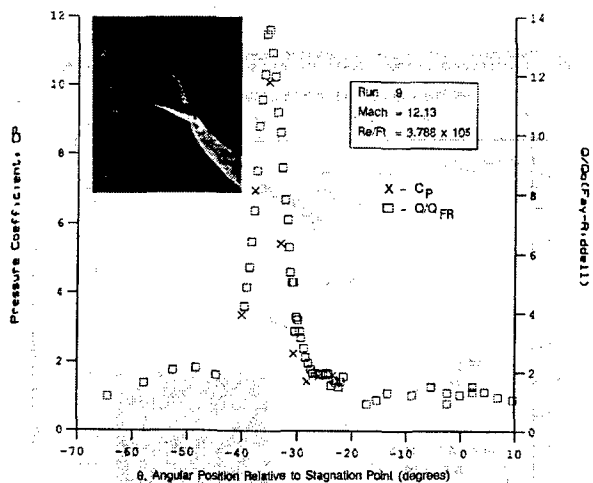


**Figure 6.15b** Heat and Pressure Distributions in Shock/Shock-Interaction Regions Induced by a 10° Shock Generator Over a Smooth 12-Inch Diameter Hemisphere at Mach 12.13 for Run 9

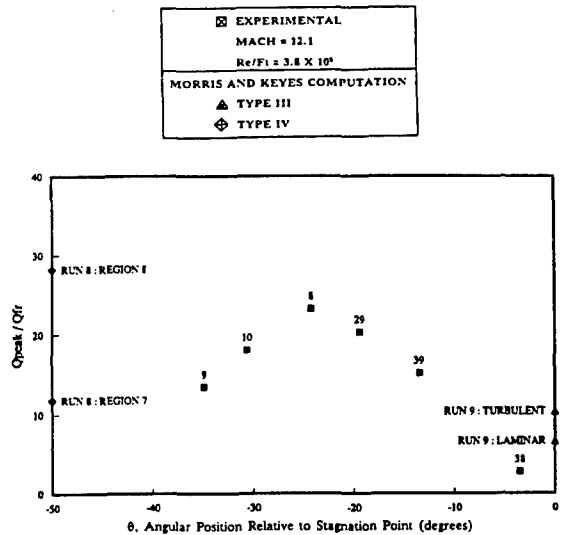


**Figure 6.15c** Variations of Peak Heating with Angular Position of the Interaction Region for Mach 12.1 and  $Re/Ft=3.8 \times 10^5$

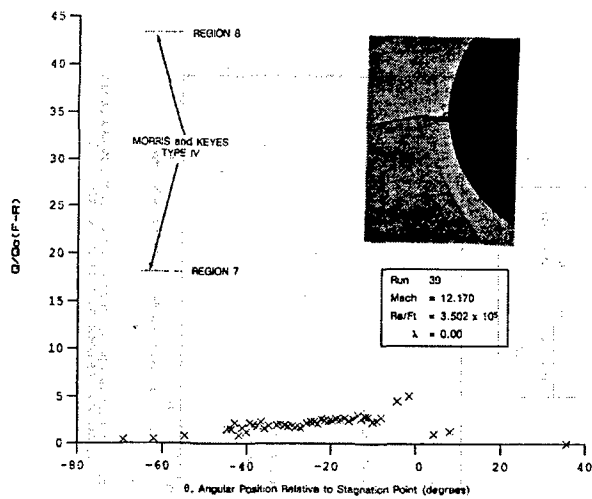


**Figure 6.16a** Heat Transfer Distribution in Shock/Shock-Interaction Regions Induced by a 10° Shock Generator Over a Transpiration-Cooled Hemisphere Without Blowing at Mach 12 for Run 39

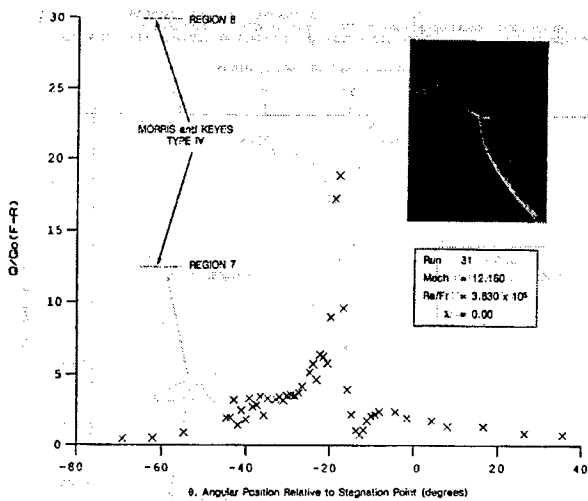


**Figure 6.16b** Heat Transfer Distribution in Shock/Shock-Interaction Regions Induced by a 10° Shock Generator Over a Transpiration-Cooled Hemisphere Without Blowing at Mach 12 for Run 31

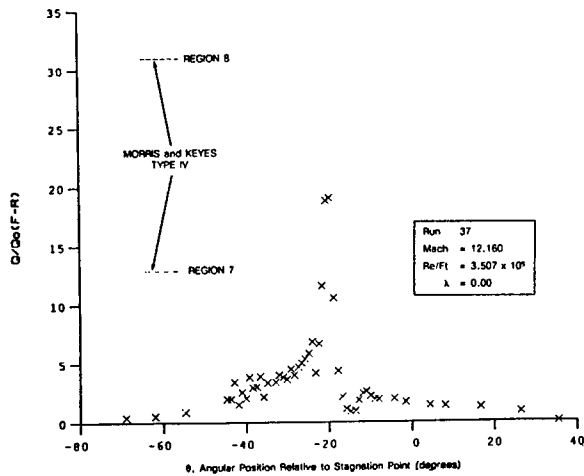


**Figure 6.16c** Heat Transfer Distribution in Shock/Shock-Interaction Regions Induced by a 10° Shock Generator Over a Transpiration-Cooled Hemisphere Without Blowing at Mach 12 for Run 37

**6.3.3 Studies of Surface Blowing Effects on Shock/Shock-Interaction Heating**

The effects of surface blowing on interaction heating are demonstrated first by presenting sets of measurements for a range of blowing rates with a fixed shock-generator geometry. We then present the

measurements obtained at a fixed blowing rate for a range of model geometries.

Positioning the interaction at 20° below the axis of the model without blowing, we see in Figures 6.17a through 6.17c that the effect of blowing is basically to move the interaction downward from the model axis—an effect that results from the displacement of the bow shock away from the hemisphere in response to an increased volume of gas in the shock layer. As was observed in the zero-blowing studies, the impingement heating does not decrease appreciably until the interaction drops 40° below the axis. If the interaction is positioned on the axis of the model without blowing, the effect of blowing is still to move the interaction downward, as illustrated in Figures 6.18a through 6.18c. Comparing the measurements in Figures 6.16, 6.17, and 6.18, it can be seen that the peak heating for the type IV interaction is not significantly reduced by surface blowing; however, there is a small reduction for the type III interaction, which is well below the centerline. It is noted here that, for values of the blowing-rate parameter ( $\lambda$ ) close to or greater than 0.3, the shock layer is unsteady, and it is difficult to select a representative distribution of heating.

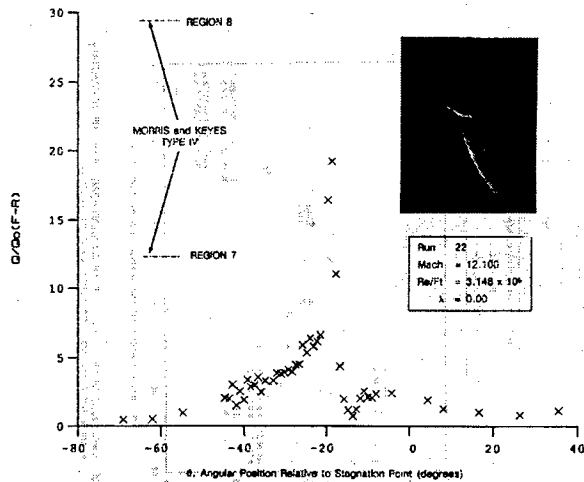


**Figure 6.17a** Heat Transfer Distribution in Shock/Shock-Interaction Regions Induced by a 10° Shock Generator Over a Transpiration-Cooled Hemisphere With  $\lambda = 0$  at Mach 12 for Run 22

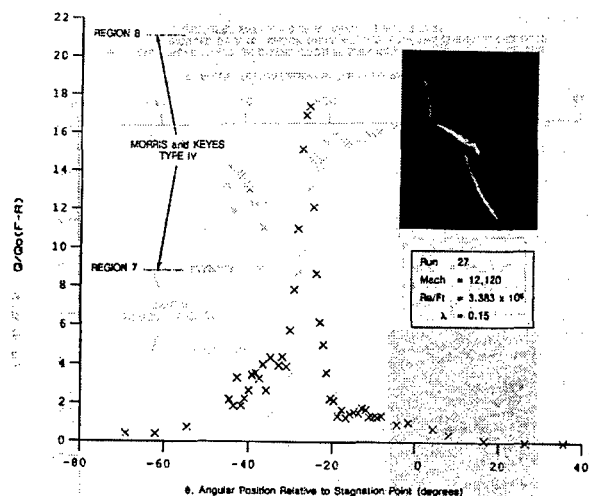


**Figure 6.17b** Heat Transfer Distribution in Shock/Shock-Interaction Regions Induced by a 10° Shock Generator Over a Transpiration-Cooled Hemisphere With  $\lambda = 0.15$  at Mach 12 for Run 27

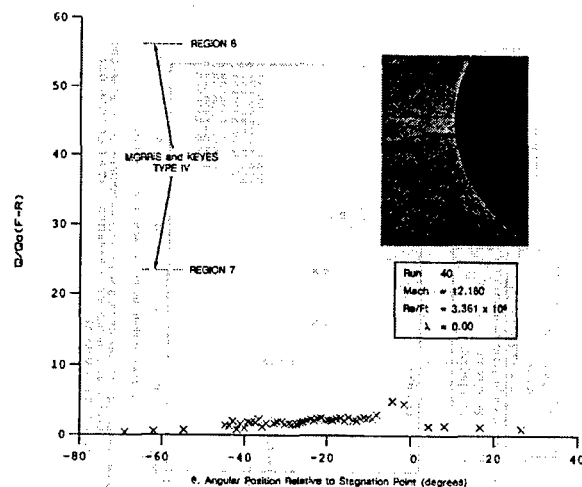


**Figure 6.18a** Heat Transfer Distribution in Shock/Shock-Interaction Regions Induced by a 10° Shock Generator Over a Transpiration-Cooled Hemisphere With  $\lambda = 0$  at Mach 12 for Run 40

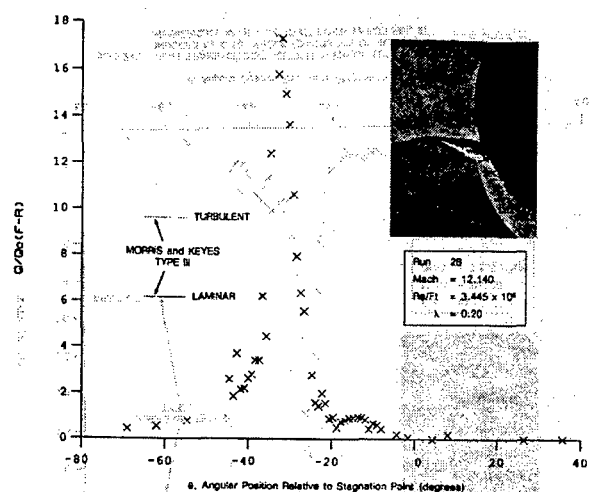


**Figure 6.17c** Heat Transfer Distribution in Shock/Shock-Interaction Regions Induced by a 10° Shock Generator Over a Transpiration-Cooled Hemisphere With  $\lambda = 0.20$  at Mach 12 for Run 28

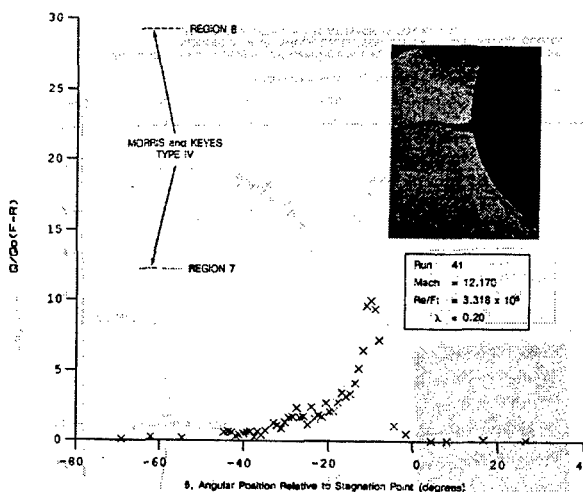


**Figure 6.18b** Heat Transfer Distribution in Shock/Shock-Interaction Regions Induced by a 10° Shock Generator Over a Transpiration-Cooled Hemisphere With  $\lambda = 0.20$  at Mach 12 for Run 41

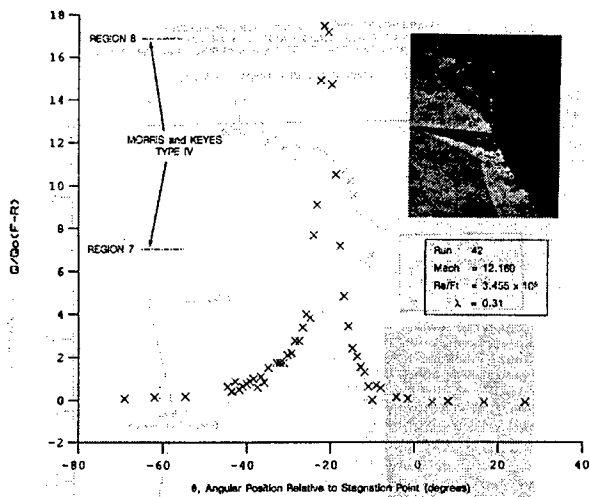


**Figure 6.18c** Heat Transfer Distribution in Shock/Shock-Interaction Regions Induced by a 10° Shock Generator Over a Transpiration-Cooled Hemisphere With  $\lambda = 0.31$  at Mach 12 for Run 42

These measurements are plotted together with those for the other blowing rates in Figure 6.19, which again emphasizes that neither the magnitude nor the shape of the locus of the heating-enhancement factor is significantly influenced by transpiration cooling.

These measurements are plotted together with those for the other blowing rates in Figure 6.19, which again emphasizes that neither the magnitude nor the shape of the locus of the heating-enhancement factor is significantly influenced by transpiration cooling.

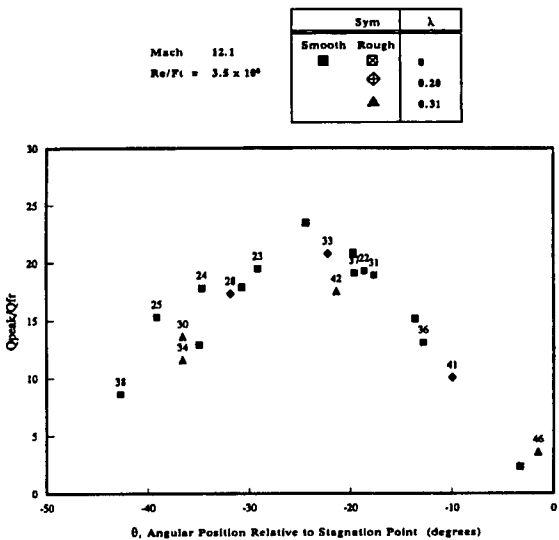


**Figure 6.19** Variations of Peak Heating With Angular Position of the Interaction Region for Various Blowing Parameters,  $\lambda$ , at Mach 12

REFERENCES

6-1. Watts, J.D., "Flight Experience with Shock Impingement and Interference Heating on the X-15-2 Research Airplane," NASA TM X-1669, 1968.

6-2. Holden, M.S., Moselle, J.R., Lee, J., Weiting, A.R., and Glass, C., "Studies of Aerothermal Loads Generated in Regions of Shock/Shock Interaction in Hypersonic Flow," NAS1-17721, April 1991.

6-3. Edney, B., "Anomalous Heat Transfer and Pressure Distributions on Blunt Bodies at Hypersonic Speeds in the Presence of an Impinging Shock," FFA Report 115, Aeronautical Research Institute of Sweden, 1968.

6-4. Keyes, J.W. and Hains, F.D., "Analytical and Experimental Studies of Shock Interference Heating in Hypersonic Flow," NASA Report TN D-7139, May 1973.

6-5. Sanderson, S.R., "Shock Wave Interaction in Hypervelocity Flow," Graduate Aeronautical Laboratories California Institute of Technology, 1995.

- 6-6. Holden, M.S. and Kolly, J.M., "Measurements of Heating in Regions of Shock/Shock Interaction in Hypersonic Flow," AIAA 95-0640, 33rd Aerospace Sciences Meeting, Reno, NV, January 9-12, 1995.
  
- 6-7. Holden, M.S., Rodriguez, K.M., and Nowak, R.J., "Studies of Shock/Shock Interaction on Smooth and Transpiration-Cooled Hemispherical Nosetips in Hypersonic Flow," AIAA 91-1765, presented at 22nd Fluid Dynamics Conference, Honolulu, Hawaii, June 24-26, 1991.
  
- 6-8. Holden, M.S., "An Experimental Study of Massive Blowing from a Nosetip During Jovian Entry," AIAA Paper 81-1070, June 1981.

## 7. WALL-JET AND TRANSPIRATION COOLING FOR FLOWS WITH SHOCK INTERACTION AND SURFACE ROUGHNESS

### 7.1 Introduction

A key aspect of the design of scramjet propulsion systems is the development of an active wall-cooling system for the combustor region of the engine. Transpiration cooling and film cooling are two techniques that have been proposed to reduce the large heating loads on the walls of a supersonic-combustion (scramjet) combustor. The relative merits of film and transpiration cooling must be evaluated against complications associated with the fluid mechanical design of these systems, the sensitivity of each technique to combustion of the coolant, causing wall heating, and the sensitivity of such flows to shock impingement. Film-cooling techniques have also been used to reduce the aerothermal loads on the optical windows of hypersonic seeker heads, and to alleviate the heating levels in the combustor flows downstream of the injectors in scramjet engines. For the specific application to scramjet combustors, employing film cooling is attractive, because the injectant momentum contributes directly to thrust, and the mechanical construction is intrinsically simple. However, recent studies (References 7-1 through 7-3) have demonstrated that relatively large levels of mass addition are required to maintain a cooling film over the length of the combustor. Also, if shocks generated in the inlet section and the combustion region of an engine impinge on the film-cooled surface, they can easily return the heating levels to uncooled values. Transpiration-cooling techniques have been used successfully to reduce the heating and skin friction levels on the nosetips and frusta of conical hypersonic reentry vehicles (References 7-4 through 7-6). Transpiration cooling is also advantageous in that it can significantly reduce the wall skin friction (which is a major component of the engine drag). However, the resulting low-momentum region adjacent to the wall can potentially be easily separated by a shock system impinging on the wall. The sensitivity to flow separation on a transpiration-cooled surface was demonstrated in studies (Reference 7-7) of transpiration-cooled maneuvering reentry vehicles (MRVs), where flap effectiveness was significantly reduced by the introduction of a low-momentum layer adjacent to the surface upstream of the flaps. However, recent studies (Reference 7-8) have indicated that transpiration-cooled surfaces are not as

sensitive to shock interaction as one might have deduced from the results of wedge-induced separated regions.

### 7.2 Film and Transpiration Cooling in the Absence of Surface Roughness and Shock Interaction

#### 7.2.1 Film-Cooling Studies

In the film-cooling studies without incident shocks, measurements of heat transfer and pressure were made downstream of the 0.080- and 0.120-inch cooling slots for non-dimensional blowing rates  $\lambda_c$  from 0.0 to 0.28. Figure 7.1 shows the heating distribution for a range of blowing rates from the 0.080-inch slot, while Figure 7.2 shows a similar set of measurements with the 0.120-inch slot. For the cases without film cooling where a strong recompression shock was generated downstream of the step, a local peak in the heating rate was observed, followed by a gradual return to the flat-plate heating level. For the matched-pressure condition, there was a very weak wave at the top of the nozzles and the initial turbulent boundary layer moved smoothly from the step. In contrast, for the highest blowing rates where the flow was underexpanded, strong shocks were generated above and behind the nozzle exit, which may lead to enhanced mixing. It is clear from Figure 7.2 that the greatest rate of heating reduction occurred for the largest cooling rates. However, beyond a certain coolant mass-flow rate, there was relatively little change in the heat transfer to the plate with increased coolant flow rate. Close to the matched-blowing condition the measurements from the two slot heights scale relatively well in terms of non-dimensional slot height. This can be seen by plotting the measurements in terms of cooling effectiveness (as shown in Figure 7.3 and 7.4). Cooling effectiveness ( $\eta$ ) is defined as

$$\eta = \frac{T_{awc} - T_{T\infty}}{T_{TC} - T_{T\infty}}$$

taking the reference value from the no-cooling run, we have

$$h_r = q_{hc}/(T_{aw} - T_w);$$

$$\text{for coolant flow } T_{awc} = \frac{q}{h_r} + T_w$$

$$\text{thus, } \eta = (q/h_r + T_w - T_{T\infty})/(T_{TC} - T_{T\infty})$$



(1)

$$\therefore \eta = \left[ 1 - \frac{q}{q_{ic}} \frac{(T_{aw} - T_w)}{T_\infty - T_c} \right]$$

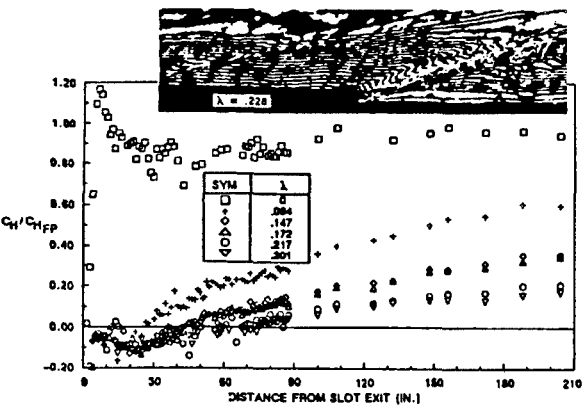


Figure 7.1 Heat Transfer Variation with Mass Addition for 0.080-Inch Slot

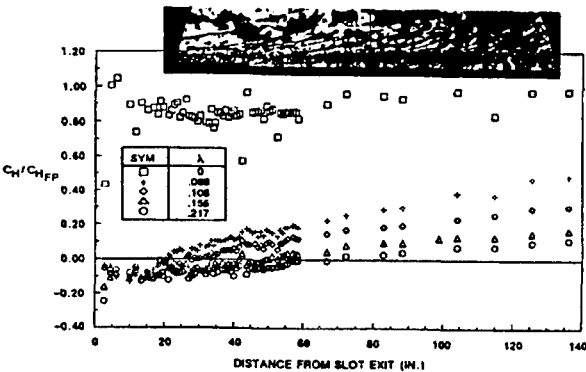


Figure 7.2 Heat Transfer Variation with Mass Addition for 0.120-Inch Slot

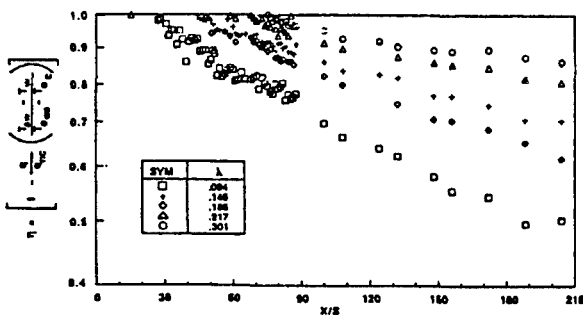


Figure 7.3 "Effective Efficiency" of Film Cooling for 0.080-Inch Slot

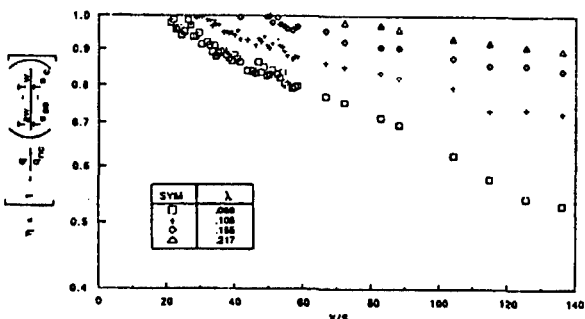


Figure 7.4 "Effective Efficiency" of Film Cooling for 0.120-Inch Slot

These measurements made in the film-cooling studies correlated well when plotting  $\eta$  in terms of the scaled slot-height parameter  $(X/S)/\lambda^{0.8}$  as shown in Figure 7.5. Here, following accepted practice, the measurements are plotted for  $\eta$  of 1 or less. Also shown in Figure 7.5 are high Mach number measurements from Reference 7-1 for a nitrogen coolant, demonstrating the superior cooling properties of helium. The measurements made in these studies for a specific slot height, in fact, scale better in terms of  $\lambda^{-1}$ , as shown in Figure 7.6. To account for the effects of the molecular weight and specific heat of the coolant and the specific injection Mach number of the coolant, we have employed a modified cooling-length parameter

$$\frac{X}{s\lambda} \left( \frac{R_{ec} \mu_c}{\mu_e} \right)^{-0.25} \left( \frac{\rho_c}{\rho_e} \right)^{0.4} \left( \frac{\mu_e}{\mu_c} \right)^{0.75} \left[ 1 + \frac{\gamma - 1}{2} M_c^2 \right]^{-0.5} \left( \frac{C_{pe}}{C_{pc}} \right)^{0.8} \quad (2)$$

in the correlation shown in Figure 7.7. Employing this parameter appears to correlate the existing measurements for the two slot heights, and those compiled earlier by Majeski and Weatherford<sup>7-3</sup> suggest a break point of close to two.

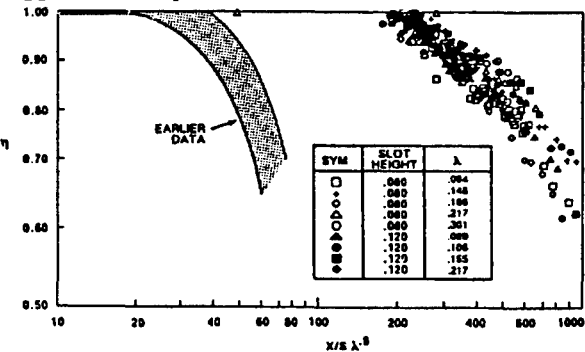


Figure 7.5 Correlation of Film-Cooling Effective Efficiency with Simple Scaling Parameters

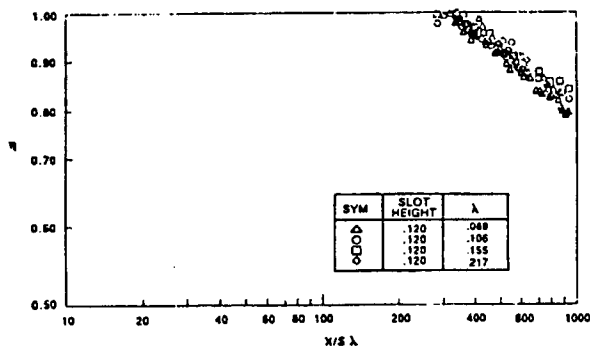


Figure 7.6 Correlation of Film-Cooling Effective Efficiency with Simple Scaling Parameters

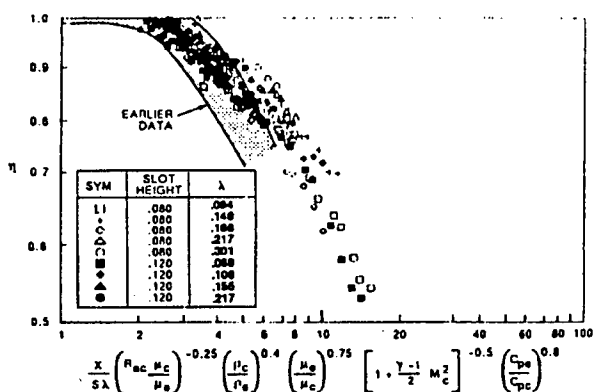


Figure 7.7 Correlations of Effective Efficiency of Film Cooling

7.2.2 Transpiration-Cooling Studies

In the transpiration-cooling studies, measurements were made at Mach numbers of 6 and 8 for nitrogen and helium coolants. At each of the freestream correlation and coolant, measurements of heat transfer and pressure were made for a series of coolant rates through the transpiration sections of the model. The effects of blowing rate on the heat transfer and pressure in the transpiration-cooled region are shown for the Mach 6 condition with nitrogen and helium coolants in Figure 7.8 and Figure 7.9, respectively. For the nitrogen coolant, a mass-addition level of 1.5% resulted in a 50% reduction in the heating rate; employing a helium coolant accomplished this reduction with one-third of the mass-flow rate. The measurements made with nitrogen coolants suggest that beyond a certain level for blowing rate (for blowing rates to achieve a 70% reduction in heating), to further reduce the heating level required significantly more coolant. For helium, this "knee" occurred at approximately a 90%

heating reduction. The effectiveness of transpiration cooling was not strongly influenced by Mach number. Correlations of the heating reduction for the nitrogen and helium coolants are shown in Figures 7.10 and 7.11, respectively. The two sets of measurements are plotted together in Figure 7.12, demonstrating the superior characteristics of helium as a coolant. To account for the effects of the molecular weight and specific heat of the coolant gases, we have correlated the measurements in terms of a modified blowing parameter

$$B' = \dot{m} / (\rho_s U_s C_{H_s}) (\tilde{M}_{fs} / \tilde{M}_{inj})$$

or

$$B' = \dot{m} / (\rho_s U_s C_{H_s}) (C_{pinf} / C_{pfs})^{0.7} (\tilde{M}_{fs} / \tilde{M}_{inj})^{0.5} \quad (3)$$

which was deduced in earlier studies (see Reference 7-5). As shown in Figure 7.13, the measurements for both the helium and nitrogen coolants as well as the Mach 6 and 8 data can be correlated well with these parameters. Also shown is the empirical relationship

$$\frac{CH_c - CH_s}{CH_o} = 0.92 (1 - e^{-B'/4}) \quad (4)$$

which provides an analytical expression for predicting heating reductions in transpiration-cooled flows.

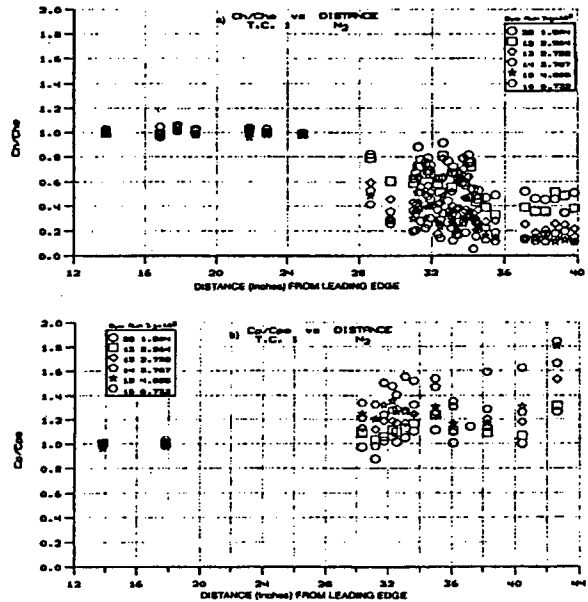


Figure 7.8 Heat Transfer and Pressure Distributions Along Flat Plate-Transpiration Surface for Nitrogen Coolant at Mach 6

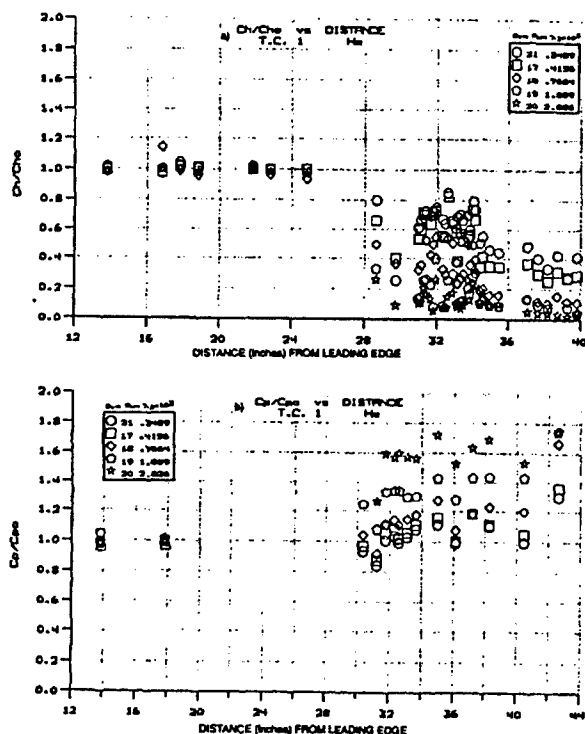


Figure 7.9 Heat Transfer and Pressure Distributions Along Flat Plate-Transpiration Surface for Helium Coolant at Mach 6

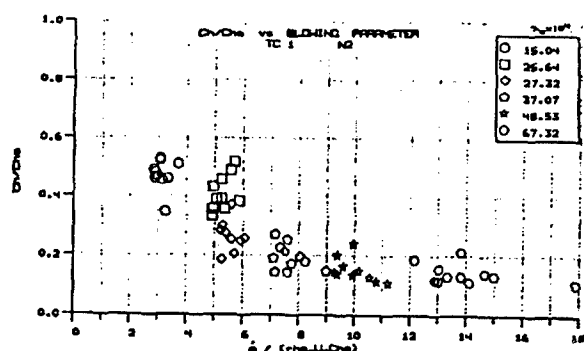


Figure 7.10 Correlation of Heat Transfer Measurements with Transpiration Cooling in Terms of Simple Blowing Parameter for Nitrogen Coolant at Mach 6

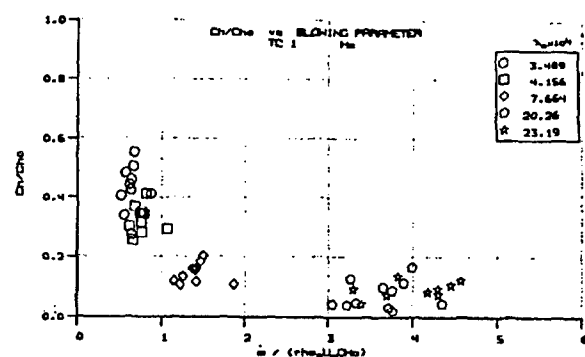


Figure 7.11 Correlation of Heat Transfer Measurements with Transpiration Cooling in Terms of Simple Blowing Parameter for Helium Coolant at Mach 6

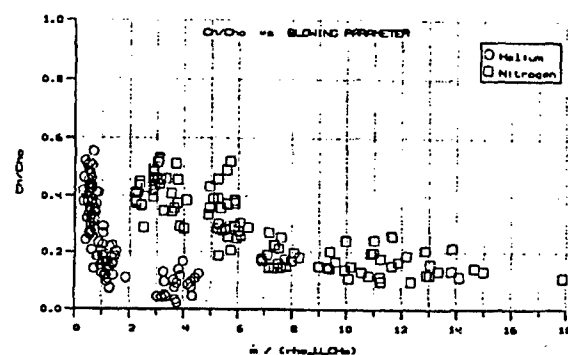


Figure 7.12 Correlation of Heat Transfer Measurements for Nitrogen and Helium Coolants with Simple Blowing Parameter

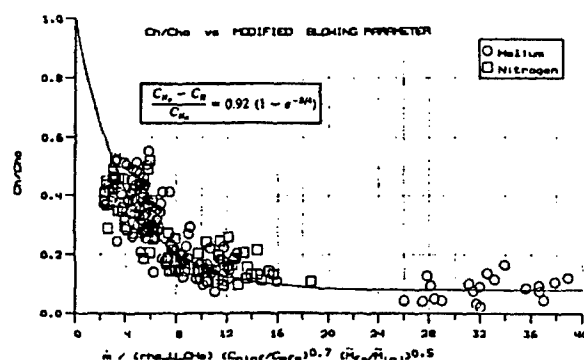


Figure 7.13 Correlation of all Transpiration-Cooling Heat Transfer Measurements with Modified Blowing Parameter

7.2.3 Comparison and Correlation of Measurements With Shock Impingement

A qualitative comparison of the film cooling versus the transpiration cooling is straightforward and is presented here. Quantitative comparisons or correlations are more difficult. In the case of film cooling data is strongly correlated by  $X/S$  which is essentially the number of slot heights downstream. For transpiration cooling, this parameter has no meaning and therein lies the difficulty of obtaining a correlation between the two cooling techniques. However, there is some common conditions between the two sets of data that can be compared. Presented here is a comparison based on mass flow rate of coolant over equivalent wall surface area. Essentially, the cooling effectiveness for a given mass flow rate from the slot injector is compared with the cooling effectiveness for the same mass flow from the transpiration surface for an equal amount of wall surface area. The cooling length was selected by choosing a representative ratio of cooled length to slot height.

In order to compare the effectiveness of the two techniques with the data from these experiments, two sets of measurements have been selected for illustrating the heat transfer measurements obtained for cases without shock interaction. Figure 7.14 shows the heat transfer variation for two transpiration cooled tests and two film cooled tests with the 0.08 inch slot.<sup>7-9</sup> Figure 7.15 presents similar results for the 0.120 inch slot.<sup>7-9</sup> The freestream conditions are essentially the same between the film and transpiration-cooled experiments. Nominally, the freestream Mach number is 6.4 with Reynolds number at  $8 \times 10^7$  per foot and the length of the model preceding cooling is the same. In all cases, helium is the cooling gas. It is clear from these comparisons that for a given mass injection rate of coolant over a fixed surface area that initially the cooling effectiveness of the slot/film technique is superior. Although, as would be expected, the further downstream from the slot injector as the film is dispersed, the less efficient the film technique becomes. On the other hand, after an initial establishment length, the transpiration cooling reaches a near constant level. In the cases shown, the transpiration cooling effectiveness becomes slightly better than the film technique. It should be noted however, that for additional cooling downstream of what is depicted in the figures, additional mass injection would be required in the transpiration case, whereas a slowly degrading level of cooling is

obtained from the current mass flow from the film technique. It is not known, however, how quickly the cooling effectiveness will degrade without additional transpiration-cooling mass addition. It would appear that for the cases selected that the film technique would be the better technique, because at nearly equivalent cooling levels between the two techniques, an additional benefit of thrust can be obtained. Two points should be noted, however. First, there would be a benefit from a reduction in skin friction from the transpiration cooling, and second, the cases with film cooling are for a matched pressure and velocity condition which tends to benefit the cooling effectiveness by keeping the film intact for longer periods. As will be shown in a later section, this conclusion is not made when shock interactions are present. Two major questions remain if hydrogen is used as the coolant. Would burning occur at the wall for film cooling as air is entrained into the base of the boundary layer, and would transpiration cooling inhibit wall burning by maintaining a purely hydrogen layer next to the surface?

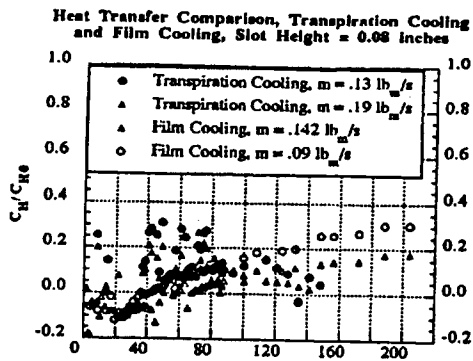


Figure 7.14 Distance (Slot Heights) From Slot Exit/Transpiration Leading Edge

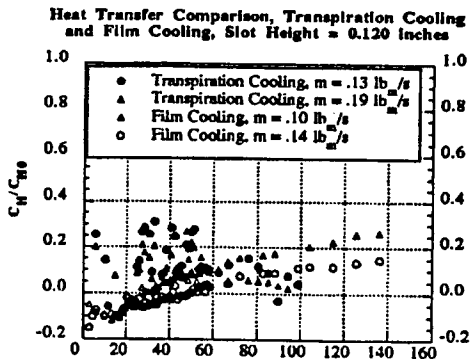


Figure 7.15 Distance (Slot Heights) From Slot Exit/Transpiration Leading Edge

### 7.3 Studies of Shockwave/Coolant-Layer Interaction

#### 7.3.1 Film-Cooling Studies

Figure 7.16a and b illustrates the major features of the viscous/inviscid interaction regions in regions of shock-wave/film-cooling interactions. Shown schematically in Figure 7.16a is a shock/film-cooling interaction for a large blowing rate at an incident shock strength of  $5.5^\circ$ . The shocks generated by the underexpanded nozzle flow interacting with the freestream are clearly visible at the injector station. However, both the injector shock and the film shock were relatively weak and did not significantly alter the strength of the incident shock. As the incident shock impinged on the boundary layer/coolant film, the flow at the edge of the viscous layer was turned toward the flat plate, as illustrated in Figure 7.16a. As the flow returned parallel to the flat plate, a recompression shock was formed and the boundary/coolant layer thinned dramatically through this recompression process. In Figure 7.16a, we have shown a case where the flow remains attached and the coolant layer was not dispersed by the interaction region. In Figure 7.16b, we show a flow where the coolant layer was separated in the interaction region. Again, the flow was for a large cooling rate; however, the shock from a  $10.5^\circ$  shock generator created a large separation region as it impinged on the boundary layer. The two nozzle shocks are, again, clearly evident; however, just upstream of the point that the incident shock struck the boundary layer, a third shock, the separation shock, was induced upstream of the point of shock impingement as the boundary layer separated. A separation region was formed in which the heat transfer and pressure were relatively constant - the plateau region. As the flow turned parallel to the surface, the separated shear layer reattached, and a recompression shock was formed. In these turbulent flows, the separated region extended from the beginning of the heat transfer rise to the end of the plateau region. For the separated region shown in Figure 7.16b, the coolant layer was rapidly dispersed in the separation and the reattachment regions, resulting in heating levels downstream of the incident shock that were not reduced by film cooling.

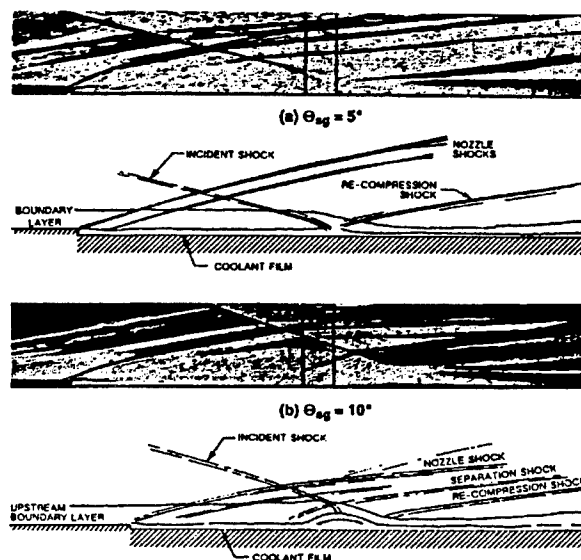


Figure 30 SEPARATED SHOCK-WAVE/COOLING-FILM INTERACTION

Figure 7.16 Separated Shock-Wave/Cooling-Film Interaction

Typical measurements showing the heat transfer and pressure characteristics of a shock-coolant-layer interaction are shown in Figures 7.17 and 7.18 for a slot height of 0.120 inch and a shock-generator angle of  $8^\circ$ . The Schlieren photographs shown in Figure 7.19 indicate that the flow, which was attached without blowing, was fully separated for the two blowing conditions. As can be seen in Figure 7.17, the heating rate at the end of the recompression process was not reduced by film cooling. Also, a twofold increase in the blowing rate from the matched-flow conditions did not significantly increase the cooling capability downstream of the incident shock. A similar set of heat transfer and pressure measurements for the  $5.5^\circ$  shock generator is shown in Figure 7.20 and 7.21. Figure 7.22 shows the Schlieren photographs for this case. For the  $8^\circ$  shock generator, a large separated region was formed ( $l_{sep}/\delta_{FP=5}$ ) that decreased only slightly as the blowing rate was doubled. For the  $5.5^\circ$  shock generator, the small separated region that was formed in the matched-blowing case was swept away when the blowing rate was doubled. As illustrated in Figure 7.20, the coolant film remained intact and caused a reduction in the peak heating of 90% to 50%, depending on the position downstream of the cooling slot. However, in general, a film cooled layer can easily be dispersed by a plain incident shock.

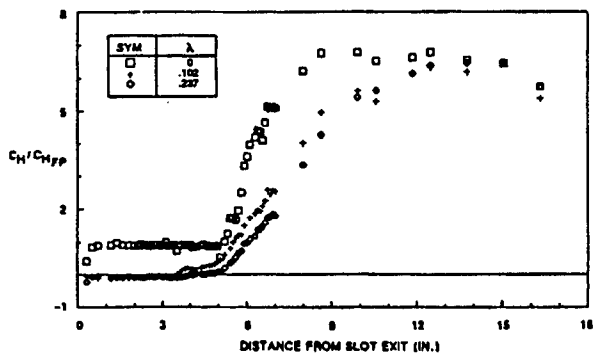


Figure 7.17 Heat Transfer Distribution in Regions of Incident Shock/Wall-Jet Interaction (Θsg=8.0 Degrees, Slot Height=0.120 Inch)

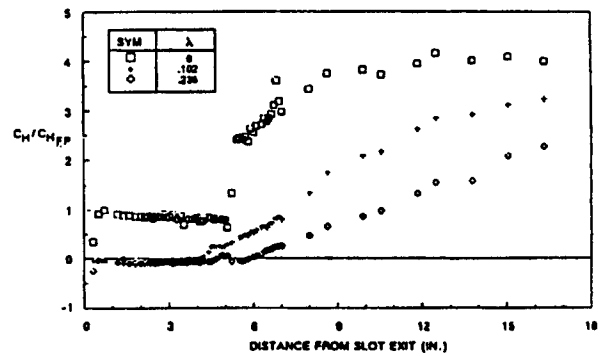


Figure 7.20 Heat Transfer Distribution in Regions of Incident-Shock/Wall-Jet Interaction (Θsg=5.5 Degrees, Slot Height=0.120 Inch)

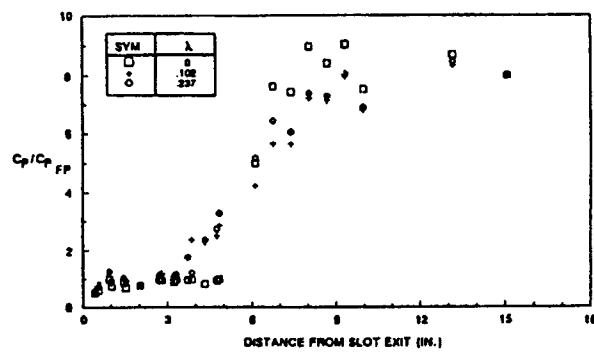


Figure 7.18 Pressure Distribution in Regions of Incident Shock/Wall-Jet Interaction (Θsg=8.0 Degrees, Slot Height=0.120 Inch)

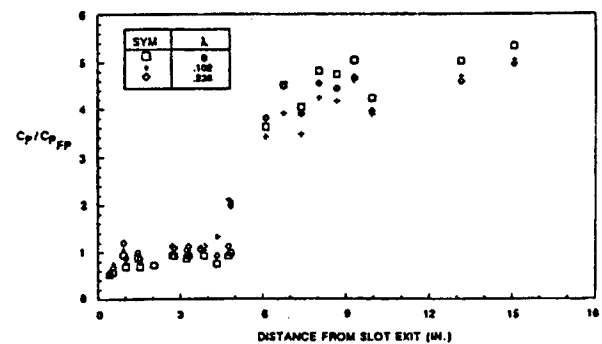


Figure 7.21 Pressure Distribution in Regions of Incident-Shock/Wall-Jet Interaction (Θsg=5.5 Degrees, Slot Height=0.120 Inch)

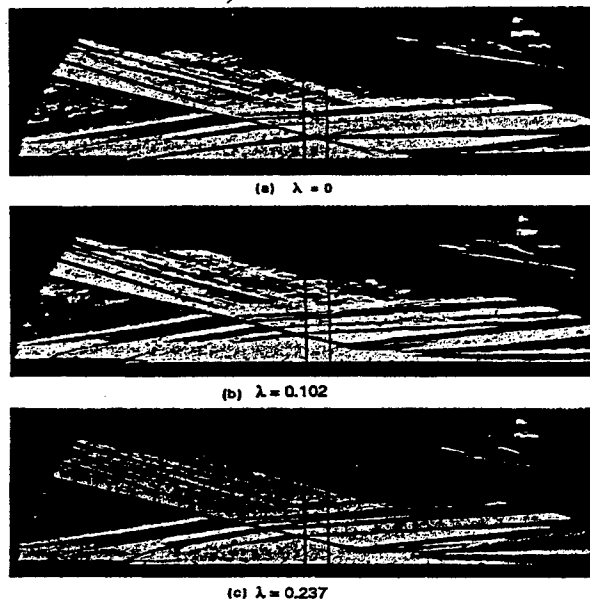
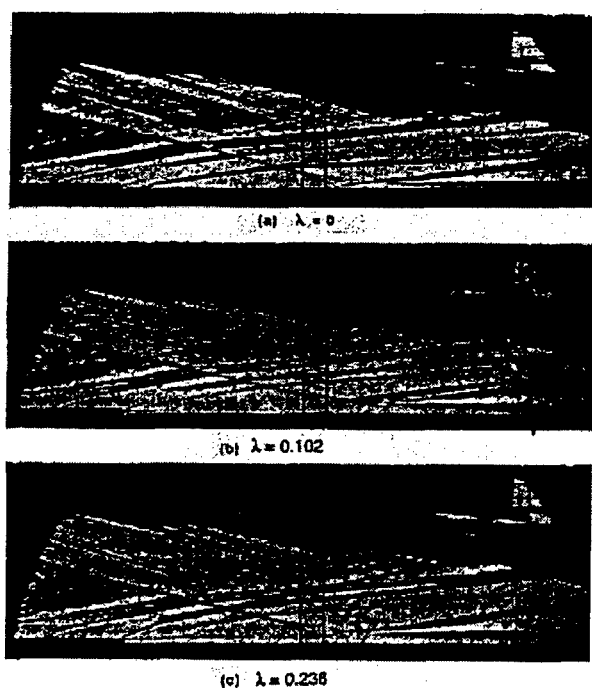


Figure 7.19 Schlieren Photographs for Incident-Shock/Wall-Jet Interactions (Θsg=8.0 Degrees, Slot Height=0.120 Inch)



**Figure 7.22** Schlieren Photographs for Incident-Shock/Wall-Jet Interactions ( $\Theta_{sg}=5.5$  Degrees, Slot Height=0.120 Inch)

### 7.3.2 Transpiration-Cooling Studies

The studies conducted at Mach 6 of transpiration-cooling effectiveness in the presence of shock impingement were conducted for shock-generator angles of  $5^\circ$ ,  $7.5^\circ$ , and  $10^\circ$  for a range of blowing rates with nitrogen and helium coolants. Figures 7.23 and 7.24 show the distribution of heat transfer and pressure in regions of shock/coolant-layer interaction for a  $5.3^\circ$  shock generator and nitrogen and helium coolants. For the non-blowing case, the shock interaction caused a pressure increase that was fed upstream of shock impingement through the transpiration-cooled surface, introducing air into the sublayer upstream of shock impingement. The heat transfer rate in this region was dramatically reduced, even in the absence of coolant addition. However, it can be seen from the pressure distribution in Figure 7.23b that the pressure upstream of shock impingement was not significantly modified by this influx of gas into the base of the boundary layer. It is observed that introducing a nitrogen coolant rate of less than 5% or a helium coolant rate of one-third this value is required to reduce the heating level downstream of shock impingement to less than that upstream of the shock on the smooth plate. It can be seen from Figure 7.24b that the pressures upstream of shock impingement were not significantly modified by

introduction of gas through the transpiration-cooled surface. The heat transfer and pressure distributions for the interaction strength generated by the  $7.5^\circ$  shock generator are shown in Figures 7.25 and 7.26. It can be seen that even with this increase in shock strength, there was, little upstream influence of the shock, both in the presence and in the absence of transpiration cooling. Again, we observed a decrease in heat transfer upstream of the incident shock resulting from flow under the porous surface for the non-blowing case. Introducing coolant induced a small upstream influence as a result of flow separation, which is clearly evident from what appears in the plateau in the pressure distribution (see Figures 7.25 and 7.26). However, as observed earlier, there was a significant decrease in heat transfer in this region. Schlieren photographs of these flows indicate that transpiration cooling does not induce strong distortions in the inviscid flow, and that the pressure levels and distribution downstream of shock impingement were basically uninfluenced by the introduction of coolant. The heat transfer downstream of the incident shock can be reduced to the initial flat-plate levels by the introduction of 2% of the freestream mass-flow rate of helium downstream of the incident shock. Measurements with heat transfer and pressure with the  $10.5^\circ$  shock generator are similar in nature to those obtained with the weaker shock strength. However, at the highest blowing rates, we began to observe flow distortions in the freestream downstream of the incident shock. In general, however, it was observed that transpiration cooling is an effective way of controlling peak heating in regions of shock-wave/boundary layer interaction. From these studies we were able to develop a simple relationship for predicting the cooling requirements in regions of shock-wave/transpiration-cooling interaction. By employing correlations based on the heat transfer coefficients and blowing parameters determined from the local inviscid conditions downstream of the reflected shock, we were able to collapse the data sets from the different interaction strengths and test conditions into a single correlation shown in Figure 7.27. The form of this correlation

$$\frac{C_{H_0} - C_{H_s}}{C_{H_0}} = 0.92 (1 - e^{-B/4}) \quad (5)$$

is similar to that for the constant-pressure flat-plate data. Employing this correlation together with simple calculations to determine the local inviscid flow conditions, it is possible to provide good

estimates for the levels of mass addition required to control the peak heating levels downstream of shock impingement.

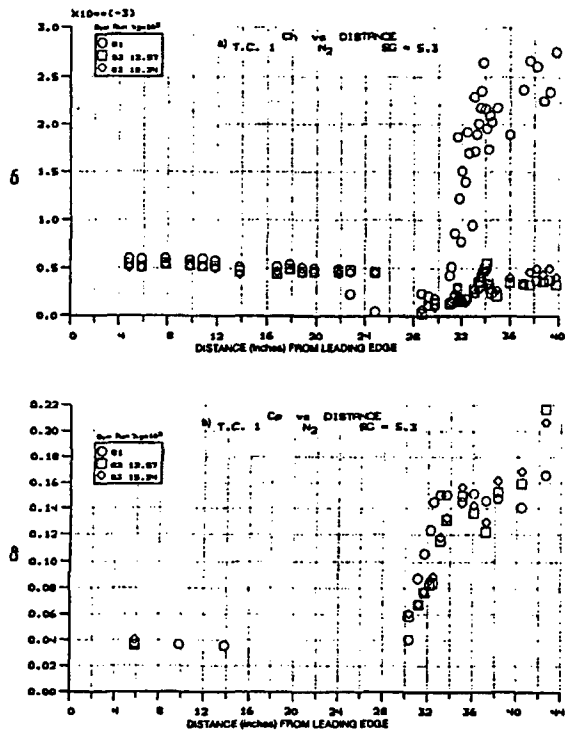


Figure 7.23 Heat Transfer and Pressure Measurements at Mach 6 on Nitrogen-Cooled Transpiration Surface with Shock Interaction from  $5.3^\circ$  Shock Generator

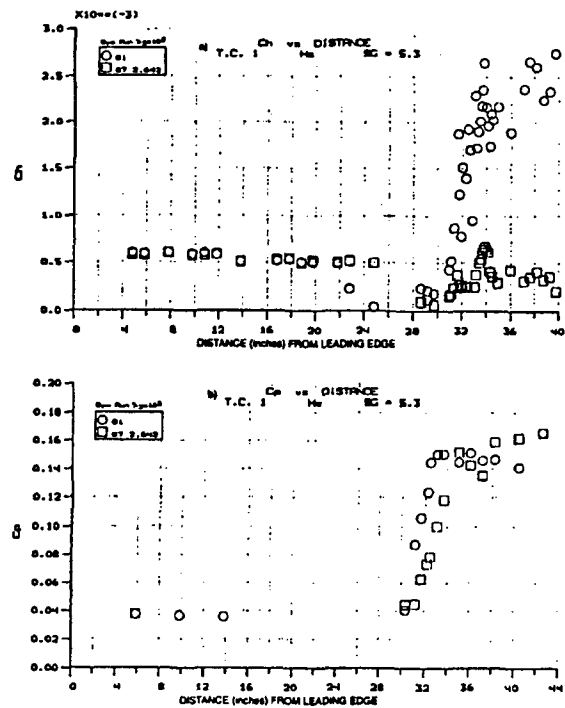


Figure 7.24 Heat Transfer and Pressure Measurements at Mach 6 on Helium-Cooled Transpiration Surface with Shock Interaction from  $5.3^\circ$  Shock Generator

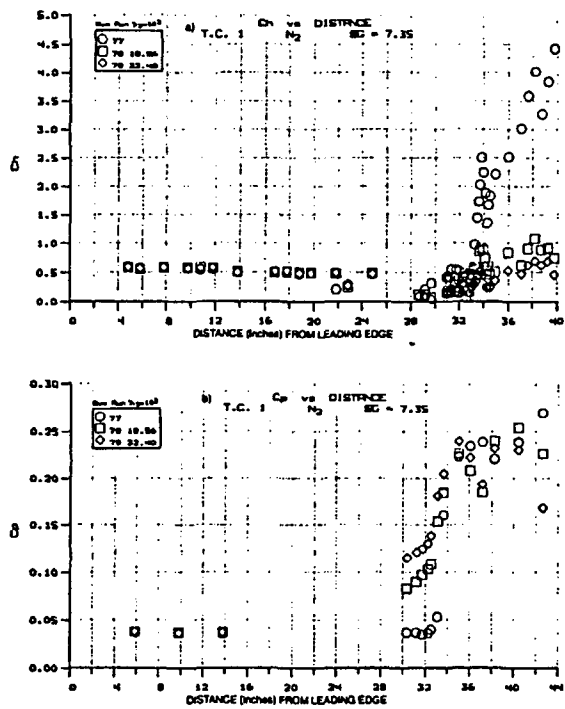


Figure 7.25 Heat Transfer and Pressure Measurements at Mach 6 on Nitrogen-Cooled Transpiration



Surface with Shock Interaction from  
7.35° Shock Generator

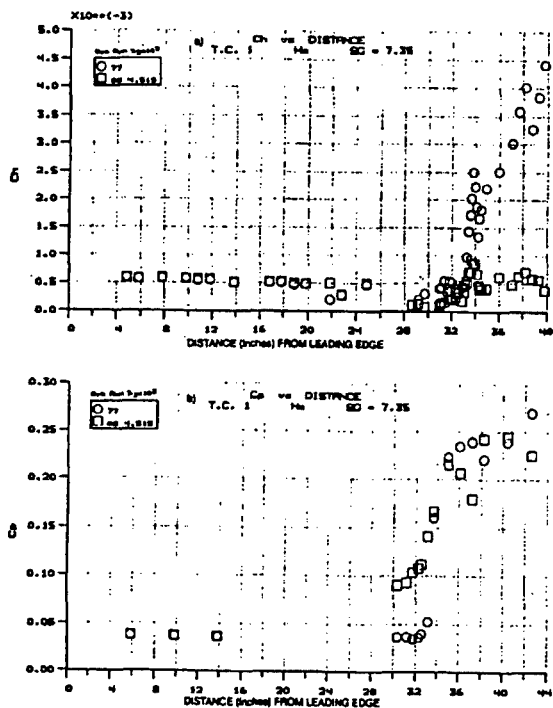


Figure 7.26 Heat Transfer and Pressure Measurements at Mach 6 on Helium-Cooled Transpiration Surface with Shock Interaction from 7.35° Shock Generator

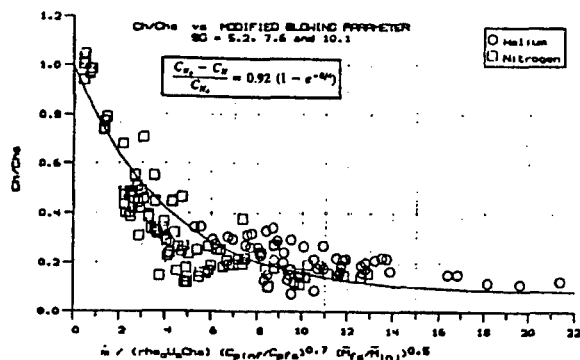


Figure 7.27 Correlation of Heating Reduction Ratio with Modified Blowing Parameter  $m(\rho_s U_s C_{hs}) (C_{pinf}/C_{pfs})^{0.7} (M_{sf}/M_{inj})^{0.5}$  for Shock-Generator Angles of 5°, 7.5°, and 10° and Both Nitrogen and Helium Coolants

7.3.3 Comparison Between Film and Transpiration-Cooling Techniques with Shock Interaction

A comparison of the results for film cooling versus transpiration cooling are presented in a similar manner as the non-shock interaction results. That is, for a given cooling surface area, the cooling effectiveness is compared for the two techniques based on mass flow rates of the cooling injectant; in this case, the cooling injectant is helium and the freestream conditions are nominally Mach 6.4 with  $Re/ft = 8 \times (10^7)$  and the boundary layer upstream of cooling is identical. The measurements from four illustrative cases have been selected for comparison. Figures 7.28 and 7.29 show the results for the 5.5° incident shock generator cases for transpiration cooling as compared to the 0.08" and 0.120" slot cases. Figures 7.30 and 7.31 depict similar results for the 8° shock generator results. There is a dramatic difference in the cooling effectiveness of the two techniques downstream of the shock interaction region. For the 5.5° case, (Figures 7.28 and 7.29) increasing the mass flow rate does reduce the heating levels downstream of the interaction region. For the two cases shown, by nearly doubling the injectant mass flow, the heating load is approximately reduced by a factor of two. However, the effectiveness of the film cooling is continuously degrading in the downstream direction. In each of the two figures (Figures 7.28 and 7.29) downstream of the interaction regions are lines which represent approximate heating values for the equivalent mass addition rate as the depicted transpiration cooling case. These were obtained by simply interpolating between the two sets of measured data. There is a significant improvement in the cooling levels of the transpiration case over that of the interpolated film cooling result. In fact, the heating level is reduced by over a factor of two for both comparisons shown. Moreover, the transpiration cooling is more effective than the film cooling case with 50% more mass addition in (Figure 7.28) and is as effective as the case with twice the mass addition as shown in Figure 7.29.

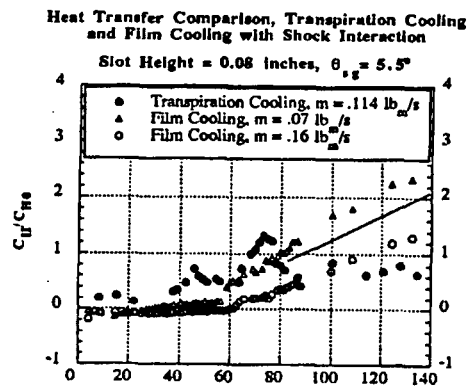


Figure 7.28 Distance (Slot Heights) From Slot Exit/Transpiration Leading Edge

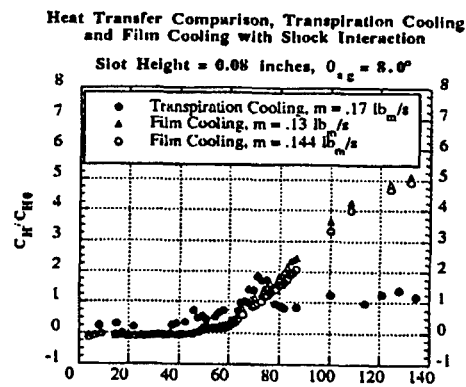


Figure 7.31 Distance (Slot Heights) From Slot Exit/Transpiration Leading Edge

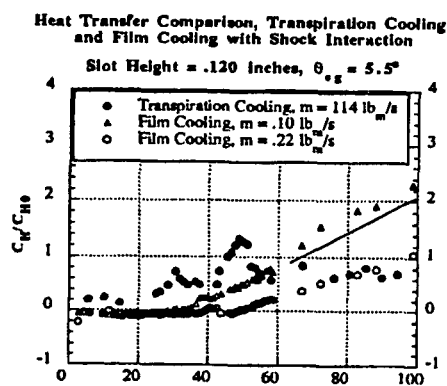


Figure 7.29 Distance (Slot Heights) From Slot Exit/Transpiration Leading Edge

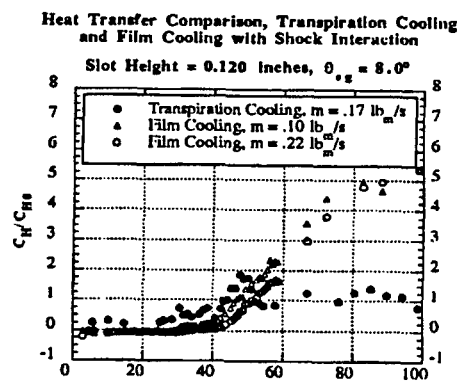


Figure 7.30 Distance (Slot Heights) From Slot Exit/Transpiration Leading Edge

Figures 7.30 and 7.31 depict similar trends for the  $8^\circ$  shock generator cases. It is interesting to note that increasing the mass addition rates of the coolant in these cases makes little difference in the downstream heating levels. In Figure 7.30, the mass addition rate for the transpiration cooling data is somewhat higher ( $\sim 15\%$ ) than the highest rate for the film cooling results. It appears, however, that extrapolating the film cooling result up to this mass addition level would not significantly alter the cooling effectiveness for this case. In Figure 7.31, the transpiration cooling mass addition rate falls between the two film cooling levels. Again, it appears that at these film coolant mass addition levels and at this shock strength, increasing the mass flow does not significantly improve the cooling effectiveness. Additionally, the film cooling levels at the furthest downstream positions shown in Figures 7.30 and 7.31 indicate only a slight improvement over no film cooling at all (see Figures 7.32a and 7.32b). As indicated in the figures, there can be as much as five times less wall heat transfer for the transpiration cooling cases as compared to the film cooling cases at comparable coolant mass addition levels. In any case, the cooling ability of the transpiration technique is much better at reducing the downstream levels. Furthermore, the transpiration cooling holds the heating loads to approximately that of the upstream uncooled results.

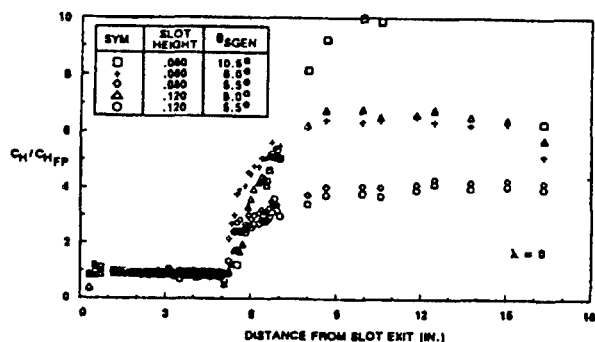


Figure 7.31a Heat Transfer Measurements in Shock-Interaction Region, without Film Cooling

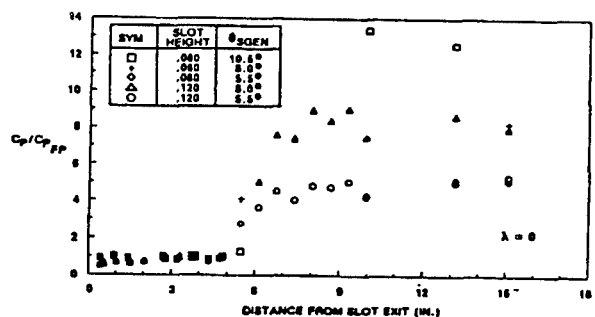


Figure 7.31b Pressure Measurements in Shock-Interaction Region, Without Film Cooling

At these conditions, it is clear that downstream of the shock interaction region transpiration cooling is more effective in reducing the wall heat transfer. Although, this technique does not have the added benefit of increasing momentum in the main stream direction, it can reduce the skin friction. Furthermore, for a given mass flow rate, the transpiration cooling is much more effective at reducing the wall heating downstream of the shock interaction region without having to overcool the upstream region of the shock interaction zone.

#### 7.4. Flow With Surface Roughness and Blowing

The accuracy of codes designed to predict the aerothermal characteristics of passively and actively cooled hypersonic vehicles at lower altitude are dependent on both the algorithms to describe the combined effects of surface roughness and blowing, and the way in which the semi-empirical constants used in the codes have been deduced from flight and ground test data. Although the studies of Voisinet<sup>7-10</sup> and Holden<sup>7-11</sup> have shown that the effects of surface roughness and blowing are not additive, in most codes the magnitude of rough-wall heating and

surface blowing are calculated by essentially superimposing calculations based on models of these two effects considered separately. In these codes the assumption that surface roughness plays the primary role in controlling heating augmentation may be significantly in error when applied to highly ablating surfaces. If, as we deduce from the experimental studies, surface blowing effectively smooths the rough surfaces, then selection of an effective roughness height as the single correlating parameter connecting flight measurements with code predictions may be in error. Since most predictive techniques employ an effective sand-grain roughness as the single length scale characterizing roughness size, there continues to remain a key problem in defining the surface topography of a rough hypersonic vehicle. The experimental studies of Nikuradse<sup>7-12</sup> and Schlichting<sup>7-13</sup>, both hydraulic pipe flow studies, were principally responsible for the selection of sand-grain roughness as the standard against which to measure relative effects of other types of roughness. Although this standard has been frequently employed, the topographical characteristics of a sand-grain surface have yet to be defined. The Schlichting studies, conducted with roughness of well-defined geometric shapes, provided the first set of measurements which could be reproduced in both experimental and theoretical studies. The results from these studies, together with those from a number of subsequent investigations in subsonic adiabatic flows, were correlated by researchers to yield relationships between an "effective sand-grain height" and parameters which describe the geometric features of the surface--a step which further perpetuated the use of sand-grain roughness as a standard. The Dirling correlation, see (Figures 7.32 and 7.33) is one such plot, from which an effective sandgrain roughness height can be determined from knowledge of peak-to-valley roughness height together with the shape and spacing of the roughness elements. The roughness Reynolds number  $\tilde{Re}_k(U_\infty K / \nu_w)$  originally used by Nikuradse, and the non-dimensional roughness heights  $K/\delta^*$ ,  $K/\Theta_m$ , and  $K/\Theta_r$  (where  $\delta^*$ ,  $\Theta_m$ , and  $\Theta_r$  are the displacement, momentum, and thermal energy thickness respectively), have all been used to correlate the aerothermal effects associated with boundary layers over rough re-entry vehicles. To date, however, no single parameter or combinations of parameters (e.g.,  $\tilde{Re}_k, k/\Theta$ ) has been used with any great success to describe the general similitude of turbulent boundary layers in supersonic and hypersonic flows over rough, highly cooled walls.

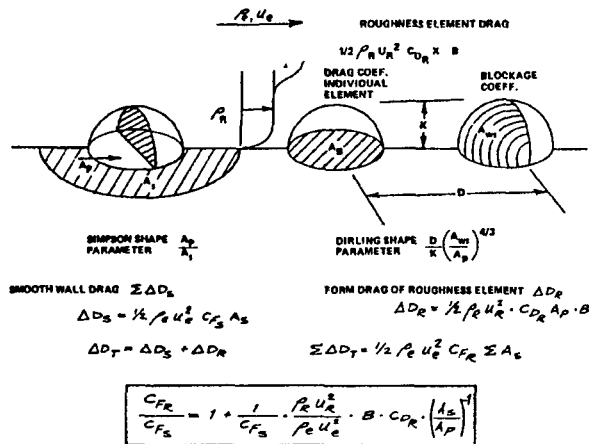


Figure 7.32 Simplified Drag Model for Rough-Wall Skin Friction

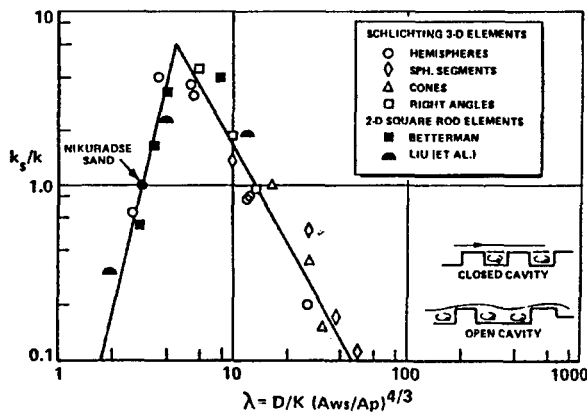


Figure 7.33 "Effective" Roughness Correlations for Differing Roughness Geometries and Spacings

The studies of Dvorak<sup>7-14</sup>, Bettermann<sup>7-15</sup>, Lewis<sup>7-16</sup>, Simpson<sup>7-17</sup> and more recently Lin<sup>7-18</sup> and Finson<sup>7-19</sup> have provided further insight into the basic effects of roughness shape and spacing on the characteristics of the rough wall boundary layer and skin friction and heating to a rough surface. Dvorak combined the effects of roughness shape and spacing into a single parameter  $A$  (the roughness density), defined as shown in Figure 7.33. He linked the downward shift in the velocity profile  $\Delta U/U_i$  to a combination of roughness Reynolds number  $\tilde{Re}_K(U_i K/\nu_w)$  and  $\lambda$  through the relationship

$$\frac{U}{U_i} = \frac{1}{x} \ln \left( \frac{y U_i}{\nu} \right) + A - \frac{\Delta U}{U_i} \frac{K U_i}{\nu}, \lambda$$

In incompressible flows the smooth regime, where the surface shear is entirely due to viscous shear is defined by  $K U_i / \nu < 5$ . At larger  $\tilde{Re}_K$ , ( $5 < \tilde{Re}_K < 70$ ) the surface shear is composed of form drag on the roughness elements combined with viscous shear. For  $K \frac{U_i}{\nu} > 70$ , the surface shear results principally from drag, and viscosity is no longer a factor in controlling the velocity profile.

Finson's engineering model based on the early concepts of Liepmann and Goddard<sup>7-20</sup> and his (Finson's) detailed numerical calculations provides a good basis for interpreting the physical phenomena of key importance in rough wall heating, as well as a relatively simple prediction technique. The shear on a rough wall can be expressed as the sum of the viscous and form drag of the rough surface:

$$C_F = C_{F_{BASE}} + \int_B^T \frac{\rho u^2}{\rho_e u_e^2} C_{D_B}(y) \cdot \frac{d^2(y)}{D^2} dy$$

where  $B(y)$  is the blockage factor, and  $d(y)$  and  $D$  are the diameter of the roughness element and the spacing between elements, respectively. From his detailed numerical solutions, Finson showed that  $p$  and  $u$  were relatively constant between the base and top of the roughness element at values  $P_R$ ,  $U_R$  close to the top of the roughness, and this equation becomes

$$C_F = C_{F_B} + \frac{\rho_R U_R^2}{\rho_e U_e^2} C_{D_B} \left( \frac{K}{2} \right) \frac{A_p}{A_s}$$

where  $A_p/A_s$  is the ratio of projected area of the roughness element in the direction of the flow to total area of the flow on which they stand, and  $B\left(\frac{K}{2}\right)$  is the average value of  $B(y)$ .

For compressible flows Finson found that

$$U_R/U_e = 0.247 + .234 \log \frac{\rho_r A_s}{\rho_e A_p}$$

Therefore, assuming  $C_{FB}$  is the smooth wall heating level, it is possible to relate the rough wall skin friction to the smooth wall value in the generalized form

$$\frac{C_{F\text{ROUGH}}}{C_{F\text{SMOOTH}}} = 1 + F_1\left(M_e, T_w, \frac{K}{\Theta}\right) * F_2\left(\Lambda, B, \left(\frac{K}{D}\right), C_D\right)$$

and the relationship for heat transfer is assumed of the same form.

$$\frac{C_{H\text{ROUGH}}}{C_{H\text{SMOOTH}}} = F_1\left(M_e, \frac{T_w}{T_e}, \frac{K}{\Theta}\right) * F_2\left(\Lambda, B, \left(\frac{K}{D}\right), C_D\right)$$

If we assume that the product of the blockage factor and CD are invariant with roughness shape and space, then for constant local free stream condition, we get the Dvorak-Simpson Parameter:

$$\frac{C_{H\text{ROUGH}}}{C_{H\text{SMOOTH}}} = F\left(\frac{A_p}{A_s}\right)$$

A slightly different form can be obtained by the subsonic blunt body approximation

$$C_D = C_{D\text{REF}}\left(A_p / A_{ws}\right)$$

and using D/K rather than  $A_s/A_p$  to obtain the correlation in terms of the Dirling<sup>7-21</sup> parameter,

$$\frac{C_{H\text{ROUGH}}}{C_{H\text{SMOOTH}}} = F\left(\frac{D}{K} \cdot \left(\frac{A_{ws}}{A_p}\right)^{4/3}\right)$$

where the various areas are illustrated in Figure 7.32.

In recent studies of effects of roughness, shape and spacing on the heat transfer and skin friction to the roughness, nosetips, frusta and flaps of a typical MRV configuration, Holden<sup>7-11</sup> used both the Dvorak/Simpson parameter  $A_s/A_p$  and the Dirling

parameter/ $\frac{D}{K}\left(\frac{A_p}{A_{ws}}\right)^{4/3}$ , and achieved reasonable

success in correlations. In these studies, the effects of roughness shape and spacing on the heat transfer and skin friction both for surfaces with sand-grain roughness and those constructed with geometrically well-defined hemispherical and conical roughness elements were examined. Also, heat transfer, skin-friction, and pressure-distribution measurements were obtained on spherical and ablated noseshapes, conical frusta, and the control surfaces of MRV vehicles in hypersonic flow. Typical measurements and correlations are shown in Figures 7.34, 7.35 and 7.36.

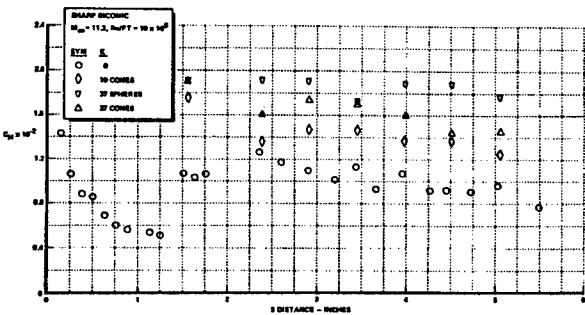


Figure 7.34 Heat Transfer Measurements on the Sharp Biconic Configuration Showing the Importance of Roughness Shape and Spacing Effects on Roughness-Induced Augmentation Heating (Ref. 7-10)

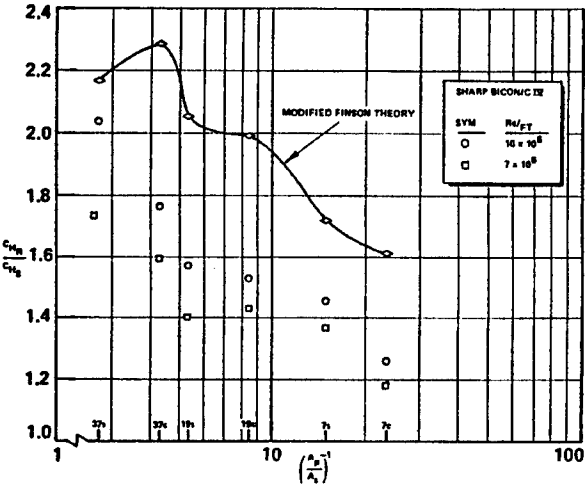
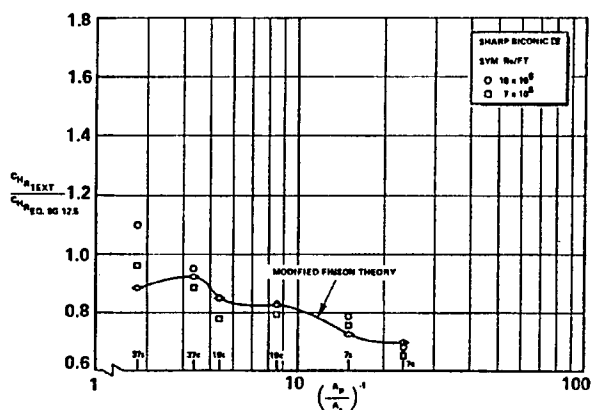


Figure 7.35 Correlation of Patterned Roughness Heating on Sharp Biconic Nosetips in Terms of Effective Windward Area ( $A_p/A_s$ )



**Figure 7.36** Correlation of Effective Roughness Heating Parameter For Sharp Biconic Nosetips in Terms of the Effective Windward Area Parameter ( $A_p/A_s$ )

The results of this work have demonstrated that the low-speed measurements of Nikuradse<sup>7-12</sup>, Schlichting<sup>7-13</sup>, and others, and the correlations of Dirling<sup>7-21</sup>/Simpson<sup>7-17</sup>, cannot be used directly to predict rough-wall heating and skin friction in supersonic and hypersonic flows over nonadiabatic surfaces. Even the more solidly founded prediction scheme developed by Finson<sup>7-18</sup>, which is based upon his detailed numerical solutions, consistently overpredicts the roughness-enhanced heating levels in high-speed flows.

Voisinnet's<sup>7-10</sup> studies of the combined effects of roughness and blowing were conducted at Mach 6 under adiabatic wall conditions. The measurements made in these studies have clearly demonstrated that the combined effects of blowing and roughness on skin friction cannot be described in a simple manner. The effects of surface roughness alone on skin friction were shown to be correlated in terms of the roughness Reynolds numbers; a result consistent with earlier measurements on adiabatic walls by Goddard<sup>7-20</sup> and Reda<sup>7-22</sup>. In contrast, measurements on models placed in the flow involving significant levels of heating ( $H_w/H_o = 0.5$ ) have in general correlated better with parameters like  $K/\delta$ ,  $K/\Theta$  or  $K/\delta_T$  which, as shown by the theoretical studies of Dvorak and Finson, should have greater relevance to roughness effects on re-entry vehicles. Voisinnet's studies demonstrated that the effects of surface roughness and blowing on skin friction cannot be deduced from simple expressions derived from the measurements made of each of the separate effects.

The measurements made in studies with a transpiration cooled model with and without blowing are shown in Figure 7.37 together with measurements of the heating rates to rough and smooth non-porous hemispherical models at the same condition. The measurements on the model with zero blowing, shown in Figure 7.37, clearly show that the intrinsic roughness of the surface causes heating enhancement factors of over 1.7. In fact, it can be seen by comparing Figures 7.37 and 7.38 that the heat transfer measurements on the rough hemisphere are in good agreement with those obtained on the non-blowing transpiration-cooled nosetip model such that they would be biased toward the larger heating. When a small amount of blowing ( $\dot{m}/\rho u_c = 0.032$ ) was introduced, the heating rates over a major part of the transpiration-cooled model dropped to levels close to those recorded on the smooth model, as shown in Figure 7.37. It could be postulated, on the basis of these measurements, that the initial effect of mass addition from a rough ablating nosetip is to modify the flow around the roughness elements, by eliminating the cavity flows, in such a way that the momentum defect introduced by the roughness is small as illustrated in Figure 7.39. Holden's studies of roughness shape and spacing effects on non-ablating configurations suggest that not only are the subsonic studies inapplicable to the heating of heat shields in hypersonic flow, but further that the basic modeling of the roughness drag and mechanisms of heating in the theoretical models is highly questionable. In these studies it was shown that even in mildly supersonic flow, shocklets are clearly evident (see Figure 7.40) around each roughness element. Thus not only is the model of drag incorrect, the entropy layer associated with each shocklet contributes to a higher temperature/lower momentum flow around the roughness elements than described in the current roughness models.

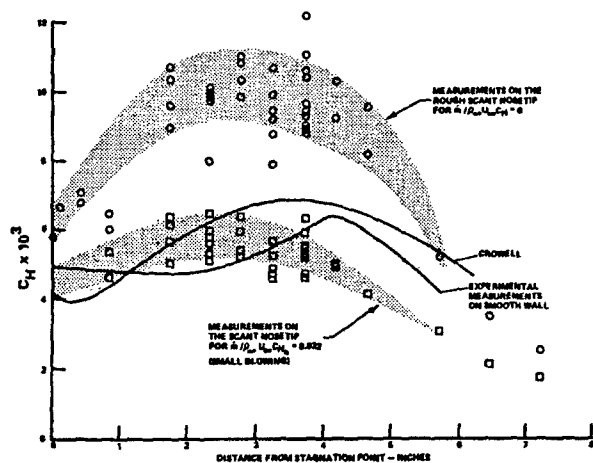


**Figure 7.37** Heat Transfer Measurements on Scant and Smooth Hemispherical Nosetip Showing How Small Blowing Brings Down Heating Levels to Smooth-Wall Values

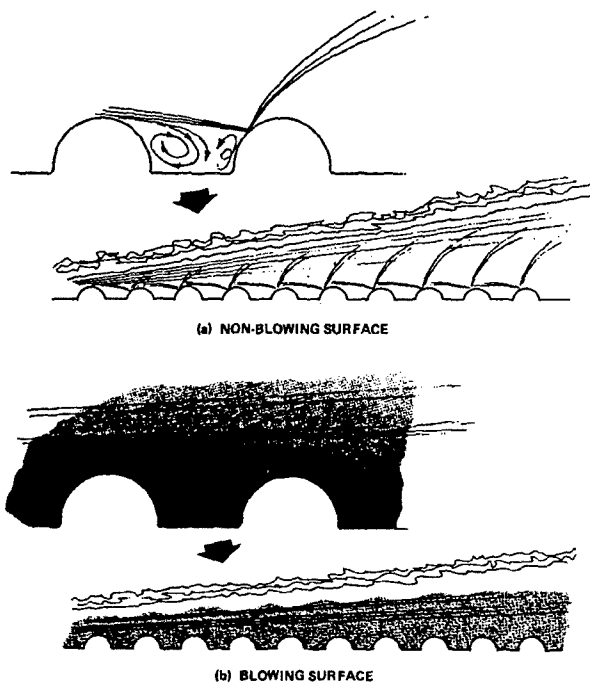


**Figure 7.38** Schematic Diagrams of the Flow Structure Between and Above the Roughness Elements on Blowing and Non-Blowing Surfaces

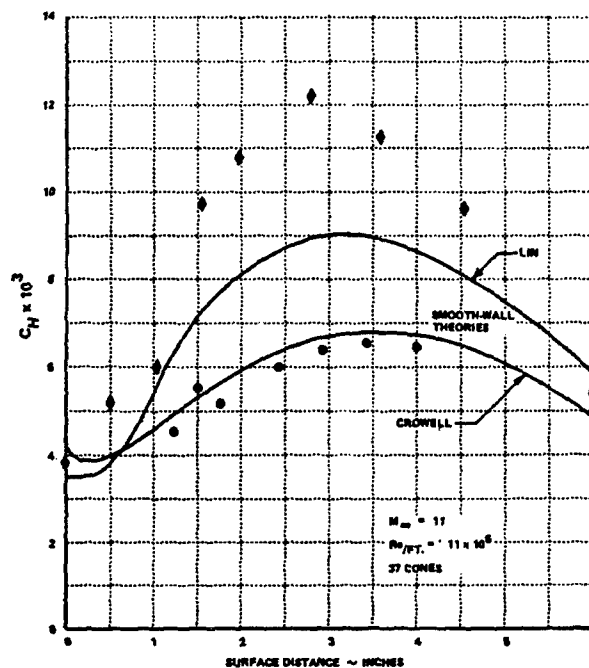


**Figure 7.39** Comparison Between the Turbulent Theories of Lin & Crowell for Smooth-Wall and Rough-Wall Measurements of Holden on 12" Diameter Hemisphere ( $M=11.2$ ,  $ReD=11 \times 10^6$ ,  $K=12.5$ )

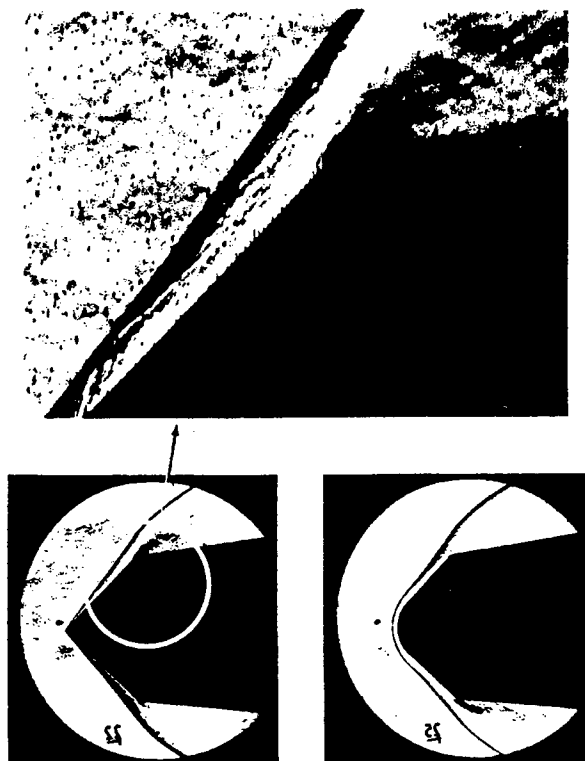


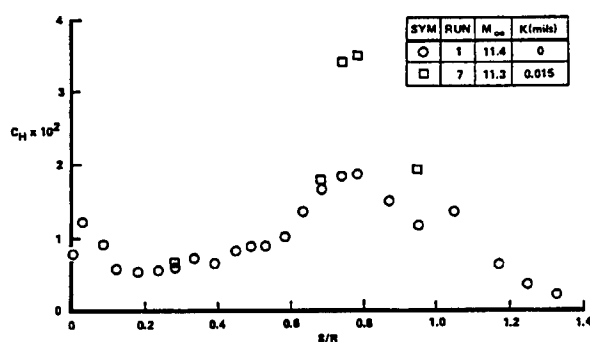
**Figure 7.40** Schlieren Photographs of the Flow Over the Sharp Biconic Nosetip Showing the Individual Shocks for the Roughness Elements (Ref. 7-11)

#### Surface Roughness and Shock/Boundary Layer Interactions on Indented Nosetips

Measurements made in full-scale flight tests and ground test facilities with ablating nosetips have demonstrated that under many re-entry conditions, concave or indented noseshapes can be developed<sup>7-23</sup> as nosetip ablates. The increased heating resulting from boundary layer transition coupled with increased surface roughness close to the sonic region is responsible for the initial development of the indentation. Subsequently, the large heating rates which are developed in the recompression region resulting from shock-boundary layer interaction at the base of the indentation can cause grossly indented noseshapes. While it is possible to predict the initial indenting using relatively simple shape change codes, when significant ablation occurs the computation of heating over the rough surface for flows with embedded regions of shock wave-boundary layer interaction are subject to considerable uncertainties. Although there have been a number of experimental studies<sup>(7-24, 7-25, 7-26)</sup> to examine the distribution of heating to non-indenting nose-shapes and investigations with a major emphasis on examining

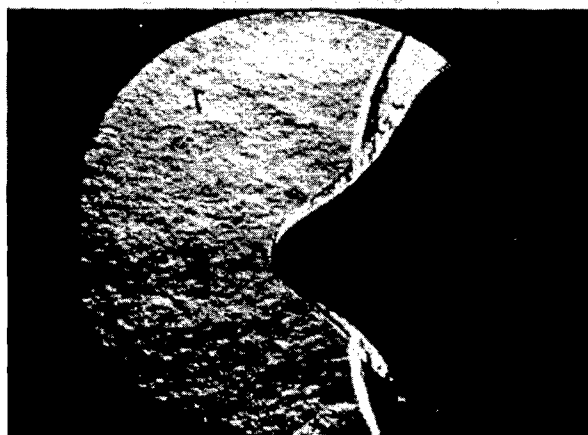
the gross stability of flows over highly indented noseshapes, little detailed information is available for rough indented nosetips where attached or slightly separated regions of shock wave-turbulent interactions occur.

Typical flow fields and distributions of heat transfer over an axisymmetric indented nosetip configuration are shown in Figures 7.41 and 7.42 for smooth and rough surface conditions. Here it can be seen that surface roughness causes a significant increase in the size of the separated interaction region as well as in the heat transfer in the reattachment compression region. It has also been observed that introducing surface roughness increased the size of interaction region on flat plate/wedge compression surfaces as graphically illustrated in Figure 7.43. One might also speculate on the basis of these observations that surface blowing would have an even larger effect on the occurrence of flow separation and the characteristics of separated interaction regions.

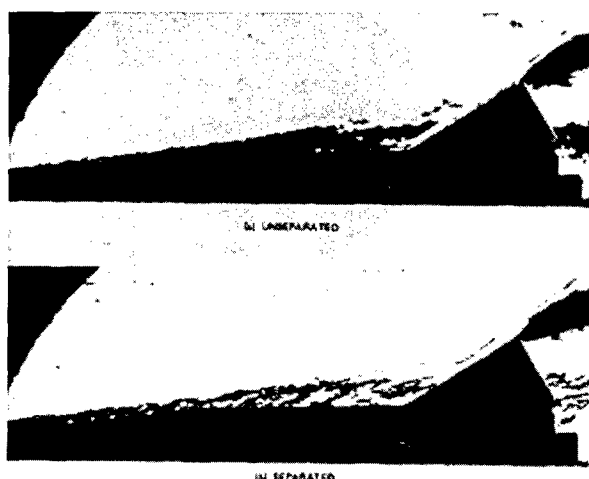


**Figure 7.41** Influence of Surface Roughness on the Heating Distribution ( $M=11.4$   $Re_D=12 \times 10^6$ )



(a)  $K = 0$ (b)  $K = 15 \text{ MILS}$ 

**Figure 7.42** Influence of Surface Roughness on the Flow Field on Indented Nosetips (Ref. 7-11)



IN SEPARATED

**Figure 7.43** Flow Over the Rough MRV Configuration With a 30° Flap Detection

The Nose Tip Recovery Vehicle (NRV) nosetip is one of the few nosetips which has been recovered from flight during re-entry<sup>7-27</sup>. The nosetip is of particular interest because it was "caught" during the portion of the trajectory where transition was spreading over the nosetip, and a non-similar shape change was occurring. An enlarged model of the nosetip, shown in Figure 7.44, displays two characteristics which are of interest to the nosetip designer. The first is that the nosetip is indented to the point where three-dimensional separated regions of significant proportions must have been formed. The second feature is the distinctive three-dimensional grooved shape of the NRV nosetip, a shape which could not have been predicted from shape change codes. It could be speculated that because of the intrinsically three-dimensional characteristics of boundary layer transition, an intrinsically three-dimensional nosetip similar to the NRV is formed on ablating nosetips whenever the transition moves onto the nosetip. If such nose shaping occurs, it will not only be difficult to predict but also induce nosetip forces which can change rapidly with small changes in nose shape or angle of attack.



**Figure 7.44** Installation of NRV Heat Transfer and Pressure Model in 96" Shock Tunnel

A Schlieren photograph of the flow over the NRV model is shown in Figure 7.45. This photograph

illustrates the two classes of flow with embedded shocks which are typical of the flow over indented nose shapes. The flow over the top of the model separates as it expands downstream of the spherical cap and a small three-dimensional separated region is formed in the cavity formed by the grooves. The compression waves generated in the reattachment region coalesce to form a single shock -- the re-compression shock. The bow shock and re-compression shock interact with the formation of a single shock and a shear layer.



**Figure 7.45** Schlieren Photograph of the Flow Over the NRV Heat Transfer and Pressure Model ( $M=11.3$ ,  $Re/FT=10 \times 10^6$ )

A typical heat transfer distribution for freestream conditions closest to those encountered in flight is shown in Figure 7.46, indicating that the boundary layer remains laminar over the spherical cap of the model, with transition occurring in the free shear layer downstream of the shoulder expansion. While the heat transfer rates drop below the stagnation point value in the separated regions just downstream of the shoulder, heat transfer rates in the reattachment and recompression regions over the model can rise to close to three times the stagnation point value.

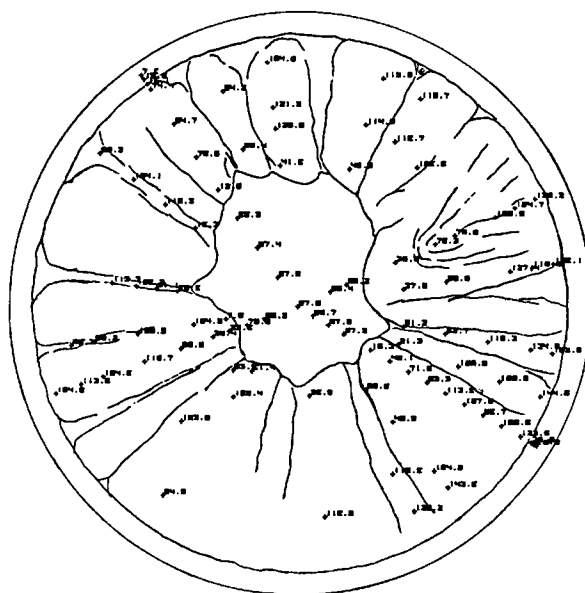


**Figure 7.46** Heat Transfer Distribution Over the NRV Configuration -  $M=11$ ,  $Re/FT=10 \times 10^6$ ,  $\alpha=0^\circ$  (Ref. 7-25)

## REFERENCES

- 7-1. Holden, M.S., and Rodriquez, K., "Experimental Studies of Shock-Wave/Wall-Jet Interaction in Hypersonic Flow," NASA Final Report Part A, Grant No. NAG1-790, May 1994.
- 7-2. Baker, N.R., Kamath, P.S., McClinton, C.R., and Olsen, G.C., "A Film Cooling Parametric Study for NASP Engine Applications Using the 'SHIP' Code," Paper No. 40, Presented at the Fifth National AeroSpace Plane Technology Symposium, October 1988.
- 7-3. Majeski, J.A. and Weatherford, R.H., "Development of an Empirical Correlation for Film-Cooling Effectiveness," AIAA Paper 88-2624, June 1988.
- 7-4. Holden, M.S., "An Experimental Simulation of Massive Blowing from a Nostip During Jovian Entry," in *Thermophysics of Atmospheric Entry*, Vol. 82, *Progress in Astronautics and Aeronautics*, Edited by T.E. Horton, Dept. Mech. Eng., The University of Mississippi, Published by AIAA, 1982.

- 7-5. Holden, M.S., Rodriguez, K.M., and Nowak, R.J., "Studies of Shock/Shock Interaction on Smooth and Transpiration-Cooled Hemispherical Nosedtips in Hypersonic Flow," AIAA Paper 91-1765, presented at the AIAA 22nd Fluid Dynamics, Plasma Dynamics and Lasers Conference, Honolulu, Hawaii, 24-26 June 1991.
- 7-6. Holden, M.S., "Studies of Surface Roughness and Blowing Effects on Hypersonic Turbulent Boundary Layers Over Slender Cones," AIAA Paper 89-0458, presented at the AIAA 27th Aerospace Sciences Meeting, Reno, Nevada, 9-12 January 1989.
- 7-7. Holden, M.S., Neumann, R.D., Burke, J., and Rodriguez, K.M., "An Experimental Study of the Effects of Injectant Properties on the Aerothermal Characteristics of Transpiration-Cooled Cones in Hypersonic Flow," AIAA Paper 90-1487, presented at the AIAA 21st Fluid Dynamics, Plasma Dynamics and Lasers Conference, Seattle, Washington, 18-20 June 1990.
- 7-8. Holden, M. S., "Experimental Studies of Transpiration Cooling with Shock Interaction in Hypersonic Flow," NASA Final Report Part B, Grant No. NAGI-790, May 1994.
- 7-9. Holden, M.S., and Chadwick, K.M., "Studies of Film and Transpiration Cooled Flows in Regions of Shock Interaction," AIAA Paper 94-2306, Presented at the AIAA 25<sup>th</sup> Fluid Dynamics Conference, Colorado Springs, CO, June 20-23, 1994.
- 7-10. Voisin, R.L.P., "Influence of Roughness and Blowing on Compressible Turbulent Boundary Layer Flow," Naval Surface Weapons Center, NSWC TR-79-153, June 1979.
- 7-11. Holden, M.S., "Studies of Surface Roughness Effects in Hypersonic Flow," Final Report, AFOSR, F49620-82-C-0026, October 1983.
- 7-12. Nikuradse, J., "Stromungsgeretze en rauken Rohren," VDI Forshungsheft No. 361, 1933, Translated as NACA TM 1292, 1950.
- 7-13. Schlichting, H., "Boundary Layer Theory," 4th Edition, McGraw Hill Book Co., New York, 1960.
- 7-14. Dvorak, F.A., "Calculation of Turbulent Boundary Layers with Roughness and Heat Transfer," AIAA Journal, 10, pp. 1447-1451, 1969.
- 7-15. Betterman, D., "Contribution a L'etude de la Couche Limite Turbulente le Long Plagnes Rugueuses," Rapport 65-5, Centre National de la Recherche Scientifique, Paris, France, 1965.
- 7-16. Lewis, M.J., "An Elementary Analysis for Predicting the Momentum - and Heat-Transfer Characteristics of a Hydraulically Rough Surface," J. Heat Transfer, 97, pp. 249-254, 1975.
- 7-17. Simpson, R.L., "A Generalized Correlation of Roughness Density Effects on the Turbulent Boundary Layer," AIAA Journal, Vol. 11, No. 2, pp. 242-244, 1973.
- 7-18. Lin, T.C. and Bywater, R.J., "The Evaluation of Selected Turbulence Models for High-Speed Rough-Wall Boundary Layer Calculation," AIAA Paper 80-0132, Pasadena, CA, 1980.
- 7-19. Finson, M.L. and Wu, P.K.S., "Analysis of Roughwall Turbulent Heating with Application to Blunted Flight Vehicles," AIAA Paper No. 79-0008, 17th Aerospace Sciences Meeting, 1979.
- 7-20. Goddard, F.E., Jr., "Effect of Uniformly Distributed Roughness on Turbulent Skin-Friction Drag at Supersonic Speeds," Journal of Aerospace Sciences, 26, pp. 1-15, 1959.
- 7-21. Dirling, R.B., Jr., "A Method for Computing Rough Wall Heat Transfer Rates on Reentry Nosedtips," MDAC Paper WD 1778, AIAA 8th Thermophysics Conference, Palm Springs, 1973.
- 7-22. Reda, D.C., "Compressible Turbulent Skin Friction on Rough and Rough/Wavy Walls in Adiabatic Flow," Naval Ordnance Laboratory, Report No. NOLTR 74-34, Silver Spring, MD, 1974.
- 7-23. Welsh, W.E., "Shape and Surface Roughness Effects on Turbulent Nose Tip Ablation", AIAA Journal Vol. 8 No. 11, November 1970, pp. 1983-1989.

- 7-24. Abott, J.J., et al., "Unsteady Flow on Ablated Nosetip Shapes--PANT Series G Test and Analysis Report" Aerotherm Report 73-87, Project 7040, December 1973.
- 7-25. Holden, M.S., "Studies of the Effects of Transitional and Turbulent Boundary Layers on the Aerodynamic Performance of Hypersonic Re-Entry Vehicles in High Reynolds Number Flow," Calspan Report No. AB-5834-A-2.
- 7-26. Holden, M.S., "Studies of Transitional Flow, Unsteady Separation Phenomena and Particle Induced Augmentation Heating on Ablated Nose Tips," AFOSR TR 76-1066, October 1975.
- 7-27. English, E.A., "Nosetip Recovery Vehicle Postflight Development Report," SAND75-8059, Sandia Laboratories, Livermore, CA, January 1976.

## 8. AEROTHERMAL AND AERO-OPTICAL EFFECTS ASSOCIATED WITH THE DESIGN OF SEEKERHEADS FOR HYPERVELOCITY INTERCEPTORS

### 8.1 Introduction

During the past year, the LENS facility and the associated instrumentation suites have been completed with extensive modifications including those to use hydrogen as a driver gas at pressures of up to 30,000 psi, and the assembly of the complete instrumentation suite of refractive and radiative instrumentation. In order to obtain accurate measurements of the aerothermal and aero-optic environment around film and internally-cooled window configurations, it is essential that the velocity and density fields around the seeker head be duplicated to obtain the correct refractive and radiative fields associated with coolant-mixing and high-temperature non-equilibrium flow chemistry. To obtain the correct turbulent mixing environment, Reynolds numbers of over  $1 \times 10^6$  must be obtained for shock layer temperatures where vibrational and dissociational as well as chemical non-equilibrium effects are correctly duplicated. To achieve these conditions at velocities from 1 to 5 km/sec, a ground test facility must operate at pressure levels of up to 30,000 psi at stagnation temperatures of up to 15,000 °R. At these conditions, the chemical structure of the shock layer must differ little from the environment generated in flight, therefore levels of freestream dissociation should be small.

A major design feature of a facility constructed to make accurate aero-optic measurements is the virtual elimination of the vibration of the model and the optical bench system supporting the refractive and radiative measurement instrumentation. An additional inertial isolation system has been constructed to support the optical bench system. As a part of the completion of the LENS facility, a new visible/MWIR wavelength aero-optical instrumentation system has been developed for the evaluation of seeker heads in the LENS facility. In addition, a radiative instrumentation package including an IR spectrometer and radiometer has been added to the instrumentation which has been previously described in Reference 8-1. These systems were statically calibrated and their performance was then validated, prior to the evaluation programs for McDonnell Douglas and Lockheed seeker head configurations, in the testing described in Section 4.

### 8.2. Aerothermal and Aero-Optical Studies on 3-D Seekerhead Configuration

The principal objective of this experimental program was to obtain both aerothermal and aero-optical measurements on a triconic seeker head configuration. The studies were conducted at two basic test points. The first was at a velocity of just under 3 km/sec and an altitude of 23,000 ft, a condition typical of boost-phase intercept operation, while the second condition was selected to duplicate a velocity of 4 km/sec at an altitude of 45 km, as shown in Figure 8.1. The three-dimensional triconic seeker head configuration which was used in these studies is shown in Figure 8.2. This model has a flush-mounted window containing aerothermal instrumentation on one side and a recessed film-cooled optical window on the opposite side of the model.

Nonequilibrium Test Conditions - Run # 6	
Mi	= 5.2730
Po	= 2.4577E+04 psia
Ho	= 4.2436E+07 (ft/sec)**2
To	= 5.8710E+03 degrees R
Minf	= 9.5402
Uinf	= 8.9695E+03 ft/sec
Tinf	= 3.5576E+02 degrees R
Pinf	= 4.6956E-01 psia
Qinf	= 2.9904E+01 psia
Rhoinf	= 1.0705E-04 slugs/ft3
Muinf	= 2.7492E-07 slugs/ft-sec
Re	= 3.4932E+06 1/R
Gamma	= 1.4000
Vbarinf	= 3.6603E-03
Pitot <sub>st</sub>	= 5.5019E+01 psia
Qo(F-R) <sub>(162)</sub>	= 4.1937E+02 BTU/Ft2-sec
Twall	= 5.3770E+02 degrees R
Flow Rate	= 1.0193E+01 slugs/sec

Nonequilibrium Test Conditions - Run # 7	
Mi	= 8.1650
Po	= 2.2903E+04 psia
Ho	= 9.3404E+07 (ft/sec)**2
To	= 1.0393E+04 degrees R
Minf	= 7.9294
Uinf	= 1.2984E+04 ft/sec
Tinf	= 1.1371E+03 degrees R
Pinf	= 7.0144E-01 psia
Qinf	= 3.0248E+01 psia
Rhoinf	= 5.1672E-05 slugs/ft3
Muinf	= 6.5163E-07 slugs/ft-sec
Re	= 1.0298E+06 1/R
Gamma	= 1.3722
Vbarinf	= 5.6748E-03
Pitot <sub>st</sub>	= 5.6045E+01 psia
Qo(F-R) <sub>(162)</sub>	= 9.8706E+02 BTU/Ft2-sec
Twall	= 5.3810E+02 degrees R
Flow Rate	= 6.9322E+00 slugs/sec

Molecular weight of Freestream Air = 28.0140  
 Species Mole Fraction  
 N2 1.000E+00  
 N 6.952E-07  
 Upstream Start  
 Pure Nitrogen  
 Chi tests specified for reactions = 0.90

Molecular weight of Freestream Air = 28.9342  
 Species Mole Fraction  
 N2 7.497E-01  
 O2 1.782E-01  
 AR 9.315E-03  
 N 7.220E-17  
 O 1.882E-03  
 NO 6.090E-02

Figure 8.1 Test Conditions at 3 and 4 km/sec



**Figure 8.2** CUBRC 3-D Triconic Seekerhead Model

### 8.3 Aerothermal Measurements and Comparison with Predictions

Schlieren photographs of the flow over the seeker head configuration without window cooling and for a match pressure helium condition are shown in Figures 8.3 and 8.4. Here it can be seen that cooling causes slight distortions in the shock layer. However, there is little difference between the flows with and without cooling. The distribution of heat transfer and pressure over the flush window for the 3 km/sec test condition are shown in Figures 8.5a and 8.5b. From the heat transfer distribution it can be seen that transition began 2.5 inches from the stagnation point and the boundary is fully turbulent over the window section of the model. Comparisons between the theoretical predictions of the GASP code and the heat transfer measurements are shown in Figure 8.6. It

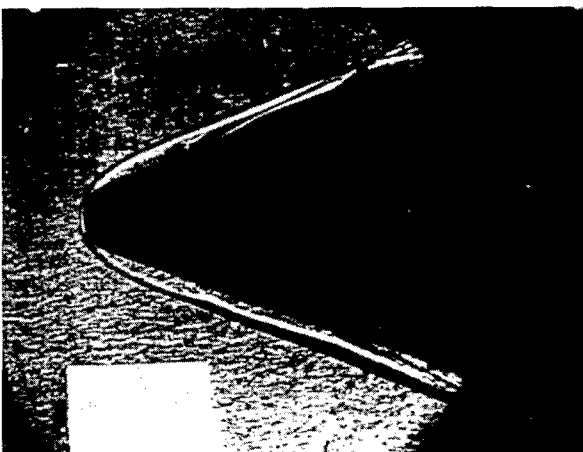


**Figure 8.3** Schlieren Photo of Flow Over Model Without Coolant



**Figure 8.4** Schlieren Photo of Flow Over Model With Matched Pressure Helium Coolant

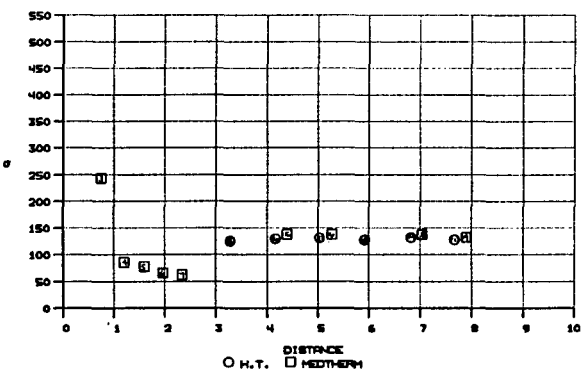


**Figure 8.5a** Distribution of Heat Transfer Over Flush Window at 3 km/sec Test Point

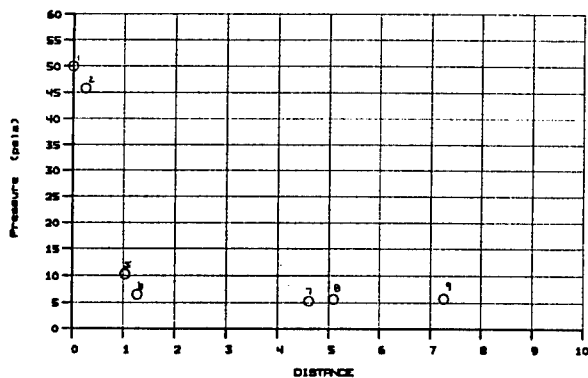


**Figure 8.5b** Distribution of Pressure Over Flush Window at 3 km/sec Test Point

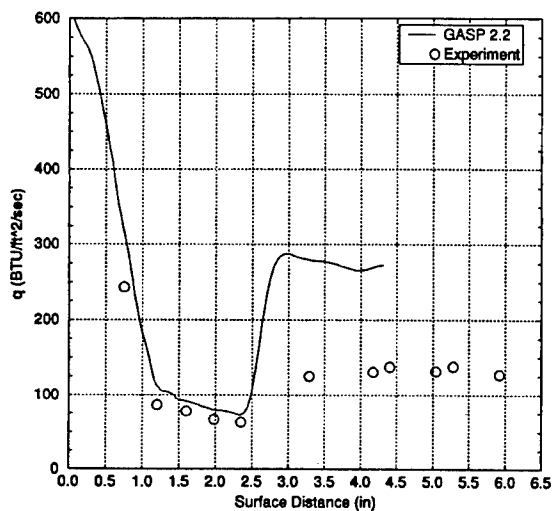


**Figure 8.6** Navier-Stokes Prediction Compared with Data Over Flush Window at 3km/sec Test Point

can be seen that the turbulent heating levels are in good agreement with the GASP code predictions if transition is positioned close to the stagnation region. However placing transition in the experimentally determined transition region results in a significant over prediction of the heating levels. The heat transfer and pressure measurements made at the 4 km condition are shown in Figures 8.7a and 8.7b. The heat transfer measurements indicate that the flow over the major part of the seeker head is laminar with transition beginning toward the base of the model. Again the pressure measurements indicate that the pressure is basically constant along the window section of the model.

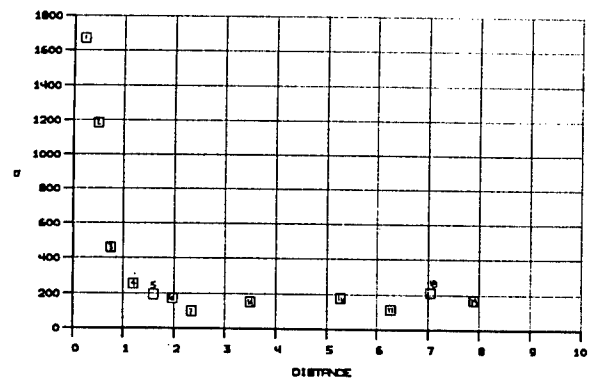


**Figure 8.7a** Heat Transfer Distribution Over Flush Window at 4km/sec Test Point

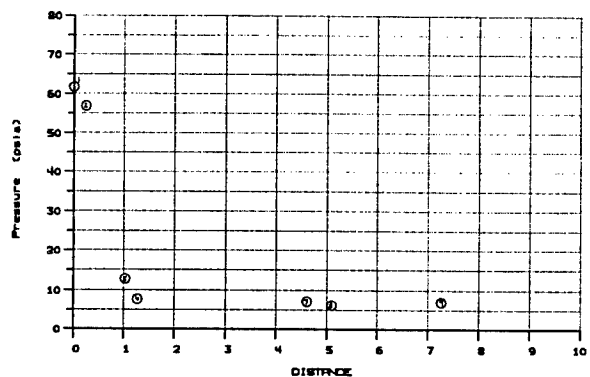


**Figure 8.7b** Pressure Distribution Over Flush Window at 4 km/sec Test Point

#### 8.4 Aero-Optic Measurements

A new, visible/MWIR-wavelength aero-optic instrument has been developed for seeker-aperture evaluation in the LENS facility. The instrument has been installed and integrated with the facility. A test program was performed with the instrument to evaluate the film-cooled aperture of a 3D model. The facility was designed to utilize visible and infrared (IR) light sources, a wide-band optical bus, and refractive and radiative sensors. The wide-band optical bus, shown in Figure 8.8, was developed to couple visible and MWIR optical signals into the aero-optical experiment. The visible and MWIR refractive instruments include pulsed laser holographic interferometry, laser point-source imagery and line-of-sight, and point thermal-source imagery. The radiative instruments include a variable-band radiometer and a multiple-band spectro-radiometer. These instruments are coupled into the experiment through the optical bus. An aero-optics software analysis system provides a comprehensive optical evaluation of visible and IR data sets, as illustrated in Figure 8.9. The aero-optic

evaluation capability uses interferograms from the holography device, point spread functions from the visible and IR imagery, and line-of-sight signals from the boresight error (BSE) sensor and results in wavefront maps, encircled-energy functions, and BSE levels, respectively. These optical evaluations are available in wavebands defined by the user, for example, visible, SWIR, or MWIR.

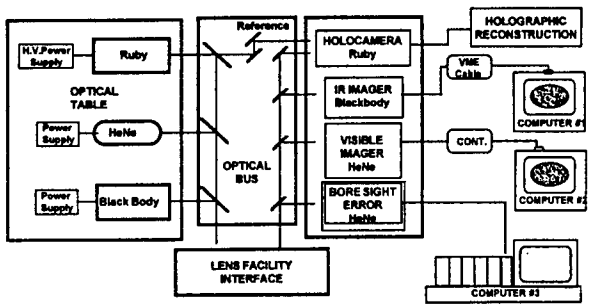


Figure 8.8 The Wideband Optical Bus Couples the Visible and Infrared Optical Signals into the Aero-Optical Experiments

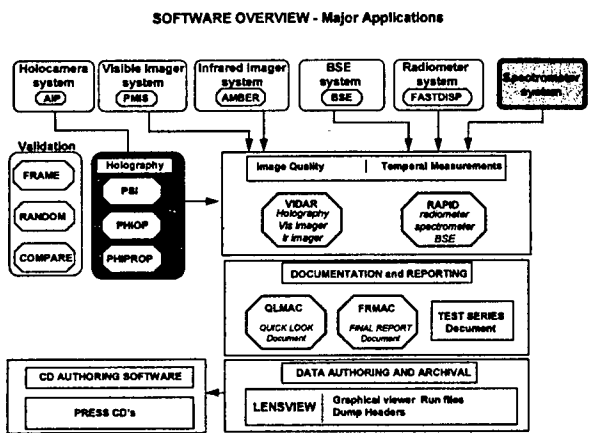
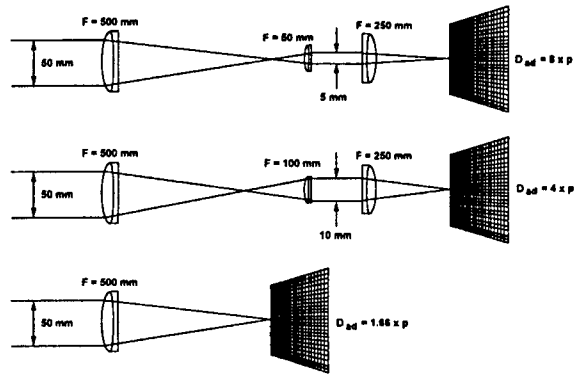


Figure 8.9 The Aero-Optic Software System Provides Comprehensive Optical Evaluation Based on Visible, Infrared and Holography Data

The 6-pulse holographic interferometry system records at 100-microsecond intervals and features 1/100-waves accuracy and 200-micron spatial resolution. The rapidly scanned, visible-band, point-source imaging system features computer-programmable scanning of 16 images onto a single 512 x 512 pixel FPA and long-duration exposure. The cooled visible CCD provides an intensity-measurement dynamic range of 65,000:1. The

boresight sensor has a noise level of 4  $\mu$ radians and a dynamic range of  $\pm 480$   $\mu$ radians. The IR imager features an InSb focal plane array, FPA, with 128 x 128 pixels and 12 bit digitizing at 1 kHz. The 1.25 meter telescope achieves an angular resolution of 40  $\mu$ radians per pixel, 50  $\mu$ m pixel spacing. The IR imager looks through the optical bus at a sub resolved pinhole, which is back lit with a blackbody at high temperature. The specifications and optical configuration of the IR imager are shown in Figure 8.10.



Object Space Parameters:						
Wavelength	.833 microns					
Pupil Diameter	50 mm					
Collimator Focal Length	500mm					
Collimator f#	f10					
Image Space Parameters:						
Effective Focal Length	8000mm	5000mm	2000mm	1350mm	890mm	500mm
Image Space f#	f2.8	f2.8	f4.18	f7	f5.6	f2.8
Any Dia Diameter	247 $\mu$ m	154 $\mu$ m	81.8 $\mu$ m	41.6 $\mu$ m	20.9 $\mu$ m	15.4 $\mu$ m
Pupil Parameter, m-DAOP	9.15	8.7	2.28	1.54	0.774	0.57
Field of View	3.73mR	4.8mR	2.7mR	13.5mR	13.5	13.5
Strehl Ratio (Zernike)	68 to 75					
% Transmission	8%					
Peak to Valley Wavefront Error	8.84 waves					
Sensor Parameters						
Minimum Stray Ratio	4.1					
Pixel	512x512					
Pixel Size	27x27 microns					
Digitization	16 bit					
Noise Electrons per Pixel	9					
Saturation, Electrons per Pixel	500,000					
Dynamic Range	62,500					
Quantum Efficiency	0.3					
Operational Temperature	-45 to -50, Cel					
Readout Rate in Pixels/Second	40,000					

Figure 8.10 The Infrared Imager Features an InSb Focal Plane Array with 128 x 128 Pixels and 12 Bit Digitizing

### 8.4.1 Holography Measurements

The holographic interferograms from the runs with nitrogen and helium coolants were compared through interferometry analysis and wavefront reconstruction, which results in a phase map of the optical wavefront as it exists in the seeker aperture. This is a convenient result, because it can be used to determine the point spread function on the focal-plane array (FPA) through Fourier optics. The phase map is resolved on all pixels within the interferogram, providing a continuous phase function within the seeker aperture. The phase maps are processed to remove both angular-tilt components and the mean



value. The standard deviation, or RMS value from a plane wave is determined from the wavefront in this form. The RMS value is a measure representative of wavefront distortion, which is typically quoted in units of waves. Distortions of one tenth waves or less produce only small effects on the image at the FPA. For larger distortions, the image is measurably degraded in peak intensity and sharpness.

The holographic interferograms for the nitrogen and helium coolant runs depict vastly different distortions, as shown in Figure 8.11. The fringe distortions in the nitrogen case represent a high-spatial-frequency distortion appearing essentially uniformly throughout the aperture. The fringe distortions for the helium case are much weaker and are slightly higher than the noise level of the interferometer or  $\lambda/20$ , waves for visible wavelength light,  $0.69 \mu\text{m}$ .

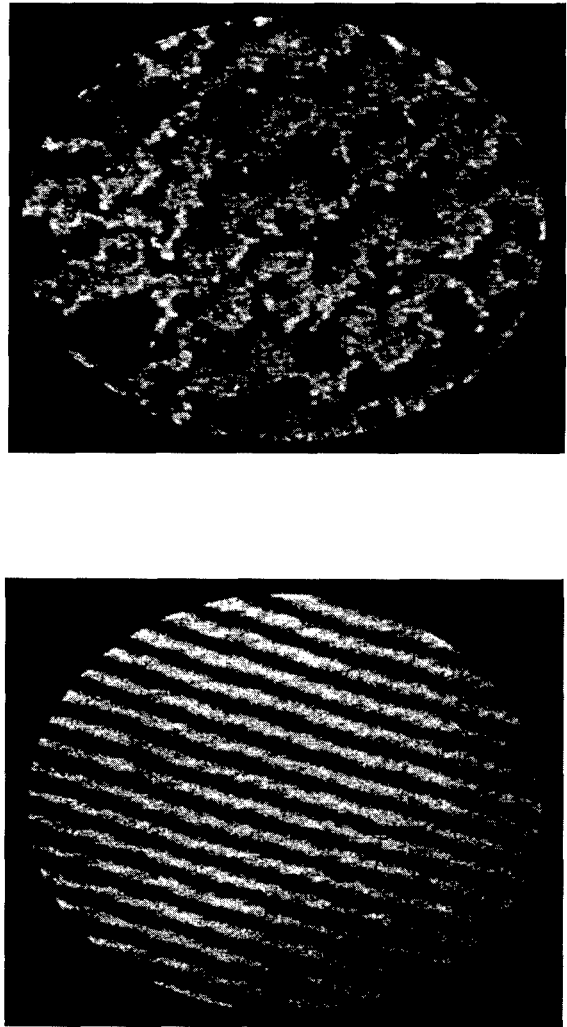
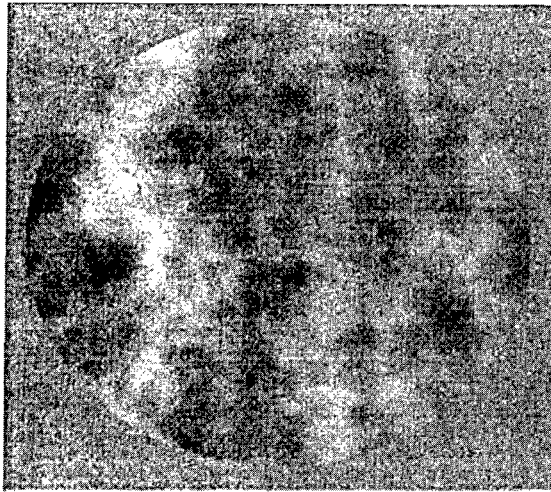
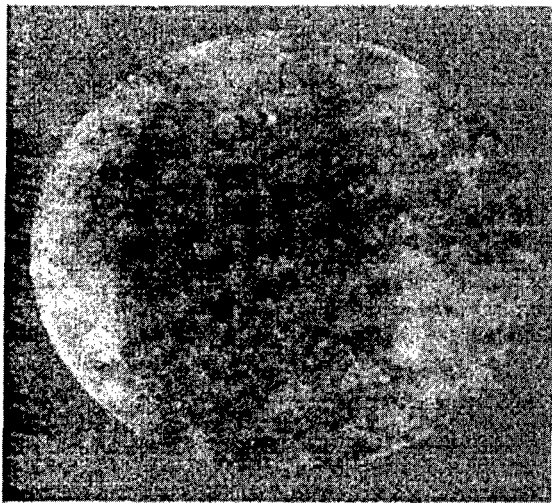


**Figure 8.11** Interferograms for Run 6 and Run 8 are Compared. Note Larger Distortion for Run 8 Which Used the Nitrogen Coolant

The wavefront reconstructions, i.e., phase maps, are rendered by gray-scale and wire-grid plots in Figures 8.12 and 8.13, respectively. The gray-scale plots exhibit the general features observed in the interferograms, while the wire-grid plots reveal a more quantitative result. The wavefront distortions for the nitrogen and helium cases are 0.288 and 0.051 waves, respectively. The wavelength of the interferometer is equal to the wavelength of the ruby laser, 0.69 microns. This wavelength is about a factor of five shorter than a typical MWIR wavelength of 3.5 microns. Hence, the accuracy of the visible wavelength interferometer is enhanced by a factor of five when the evaluation is performed in the MWIR.

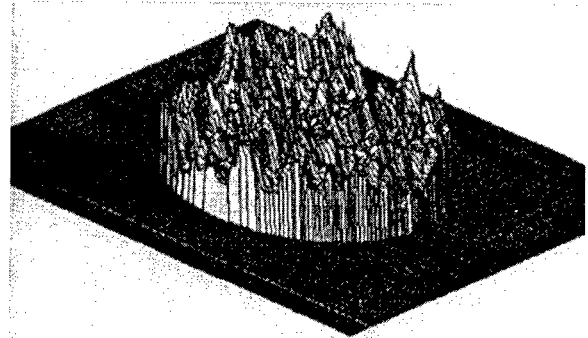


Run 8 Phase Map

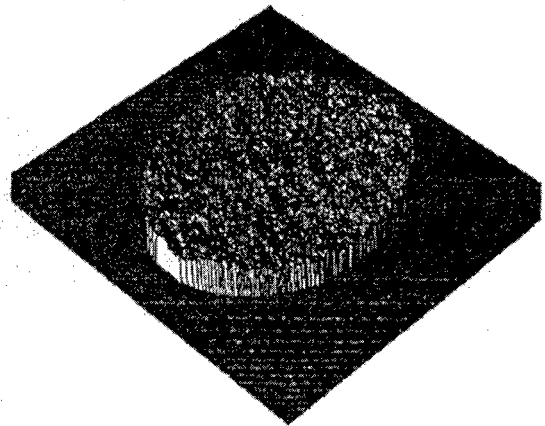


Run 6 Phase Map

**Figure 8.12** Gray Scale Plots of the Computed Phase Maps for Runs 6 and 8



Run 8 Phase Map. RMS = 0.288 waves



Run 6 Phase Map. RMS = 0.051 waves

**Figure 8.13** Phase Maps for Runs 6 and 8

#### 8.4.2 Point-Source Imagery Measurements

The imagery measurements were obtained for the nitrogen-coolant run. The tare (without-flow) and flow images for Run 8 (nitrogen coolant) are shown in **Figure 8.14** for both the visible and infrared imagers. The visible tare image is the best-focus image obtained; however it is not diffraction-limited, (DL), image. Its actual image size is about two times DL. The peak intensities of the visible tare and flow images are 17673 and 492 counts, respectively, in arbitrary units, and the Strehl ratio is 0.028. The flow image is characterized by a large number of low-intensity peaks that are distributed across a large portion of the FPA. The infrared point source imagery is much higher quality with tare and flow peak intensities of 33538 and 27433, for a Strehl ratio of 0.82.

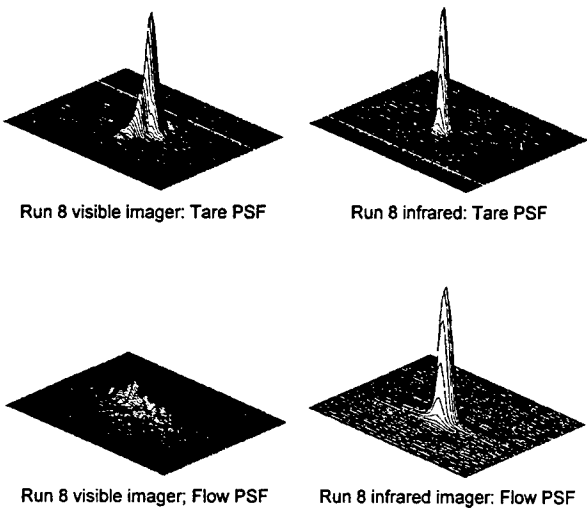


**Figure 8.14** The Measured Point Spread Functions for the Visible and Infrared Imager Systems are Shown for the Tare and Flow Cases. Image 1 (of 4) is Displayed

The encircled-energy (EE), function exhibits, in one dimension, how the image brightness is distributed on the FPA for both the visible and infrared imager, as shown in Figure 8.15. The EE of the visible tare image reaches the 83 percent point of the collected energy at an angular dimension of 84  $\mu$ radian. The first Airy ring of a perfect image would reach this point at an angle of 47  $\mu$ rad, given the characteristics of the telescope. The focal length is 4.8 meters, the aperture is 30 mm and the wavelength is 0.63 microns. The EE of the visible flow image rises much more slowly, depicting its significant distortion. The blur observed in the flow image is about 5 times larger than the tare image at the 30-percent collected-energy point

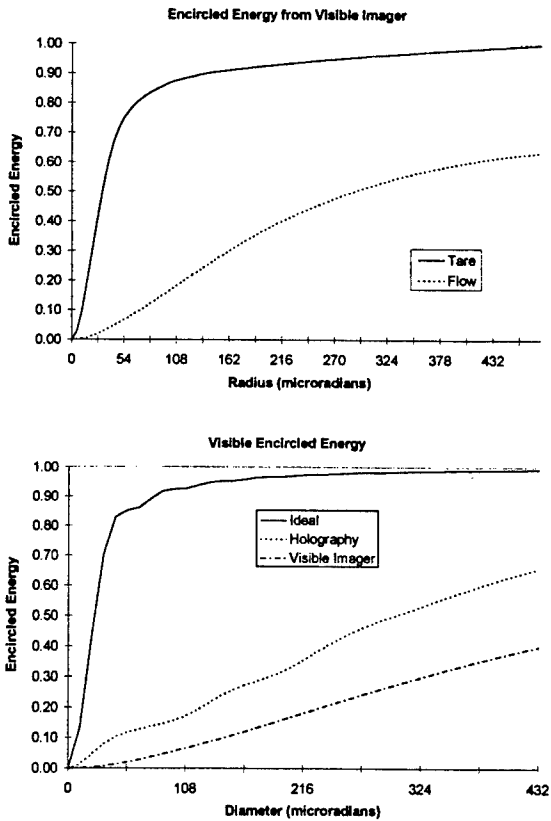


**Figure 8.15** The Tare Encircled Energy Curve is Compared to the Flow Encircled Energy Curve for the Visible and Infrared Imager Data from Run 8

The encircled energy curve for the infrared imager in the MWIR region rises much more quickly than the curves for the visible imager. An ideal infrared Airy distribution contains 83% of the encircled energy at an angular diameter of 240  $\mu$ rad. The infrared imager reaches the 83% point at 915  $\mu$ rad. Thus, the blur observed in the infrared image is approximately 4 times diffraction limited, a factor of 2 improvement over the visible imager.

**8.4.3 Line-of-Sight Sensor Measurements**

The line-of-sight (LOS) sensor measurements for Run 503 (without-coolant) and Run 6 (helium coolant) are shown in Figure 8.16. The vertical angular deflection is plotted for approximately 5 msec prior to and during the established flow. The mean and RMS values are determined both prior to and during the flow. The instrument was modified after Run 6 to increase its sensitivity, and as a result the absolute noise level in angular units was reduced from about ten to one  $\mu$ radian.

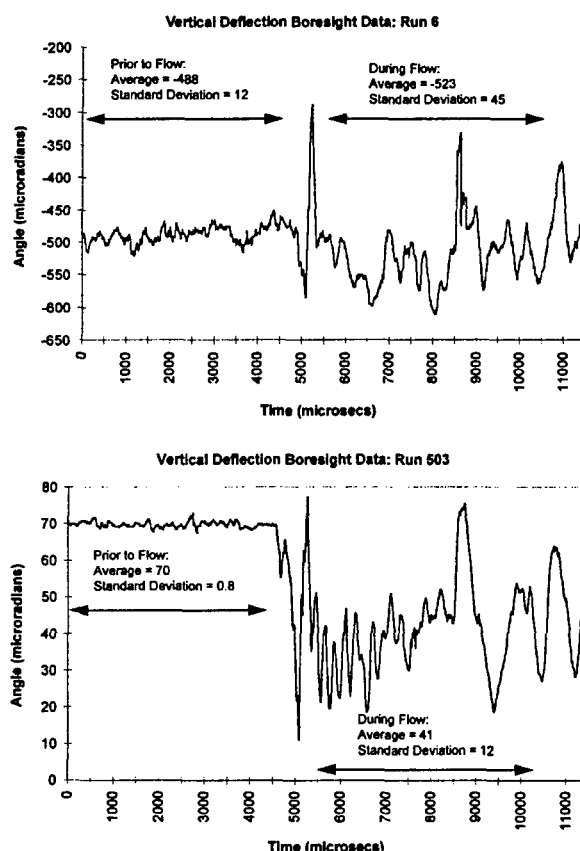


**Figure 8.16** Bore sight Error Signals for Run 6 (top) and the No Coolant Run (bottom)

Run 6 shows an absolute LOS level of  $-488 \mu\text{radian}$  with a STD level prior to flow. The initiation of flow is depicted by a brief period of oscillation in LOS, which persists for about 1 millisecond. The following period contains the established flow and lasts for over 4 milliseconds. The absolute LOS is  $-523 \mu\text{radian}$  with a STD of  $45 \mu\text{radian}$  during the period of established flow. The net LOS shift is  $35 \mu\text{radian}$  with an uncertainty of  $12 \mu\text{radian}$ . The instrumentation modification after Run 6 resulted in a reduction in the LOS uncertainty to less than one  $\mu\text{radian}$ .

The first 4 milliseconds of Run 503 illustrate the high level of stability of the bore sight sensor in the absence of flow. The absolute LOS level was  $70 \mu\text{radians}$  while the STD level was less than  $1 \mu\text{radian}$ . During the flow, the absolute LOS level shifted to  $41 \mu\text{radians}$  and the STD increased to  $12 \mu\text{radians}$ . Thus the net LOS shift produced by flow was  $39 \mu\text{radians}$ .

#### 8.4.4 Results from Aero-Optic Studies

##### Platform Stability

For the uncooled Run 503, the uncertainty in the LOS changes from about  $0.8 \mu\text{radian}$  prior to flow, to about  $12 \mu\text{radian}$  during flow. This shows the absolute mechanical stability is at most  $12 \mu\text{radian}$  and potentially as low as  $0.8 \mu\text{radian}$ . This stability is about 10 to 20 percent of a typical FPA pixel, and therefore long exposure images formed during the established flow period will contain aberration indicative of those induced by flow and not be contaminated by mechanical vibrations.

##### Validity of Pseudo Imagery versus Point-Source Imagery

The wavefront phase maps obtained from the holographic interferometer are used to compute the corresponding PSF in the visible. Also, since the magnitude of the wavefront phase map can be scaled to the MWIR, the image performance can also be obtained for longer wavelengths. These pseudo PSFs are suitable for comparison to the PSFs measured directly with a CCD in the visible or with the InSb FPA in the MWIR. The comparison in the visible and MWIR bands is pursued to examine the validity of the scaling.

Initially, a plane wavefront is propagated to obtain an ideal image, Figure 8.17, which provides the on-axis intensity for the Strehl ratio and provides an angular calibration of the numerical sampling of the PSF. The angular calibration is achieved by selecting an aperture, in pixels, which produces an image size at the FPA equal to the diffraction limit of the aperture. For the visible, the aperture required to match the image size in pixels to the diffraction limit of the aperture is  $16 \text{ mm}$  to achieve a 10 pixel image size. For the infrared, the aperture is  $23 \text{ mm}$  to achieve a 7 pixel image size. The wavefront phase map from the nitrogen-coolant run (Run 8) is used to obtain the degraded PSF, which is then scaled into absolute magnitudes, i.e., intensities and angular dimensions, by using the ideal image obtained by propagation of a plane wave. This pseudo image, when appropriately scaled, is compared to the "real" image obtained with the point source imager, i.e., the CCD in the visible and the FPA in the IR band. This comparison of the pseudo and real PSFs is shown in Figure 8.18. Qualitatively, the visible PSFs exhibit similar features--that is, dramatically reduced peak intensities from ideal and a significant reduction in image sharpness. Quantitatively, the pseudo and real visible PSFs have Strehl ratios of  $0.104$  and  $0.028$ ,

respectively. The pseudo image is representative of a very-short-exposure image, since the wavefront is assumed frozen. For that reason the pseudo image should be brighter and sharper than the real image, with its comparatively longer exposure, 300 $\mu$ s. The Run 8 infrared images exhibit a much lower level of distortion with Strehl ratios of 0.819 for the pseudo PSF and 0.896 for the PSF measured directly with the FPA.

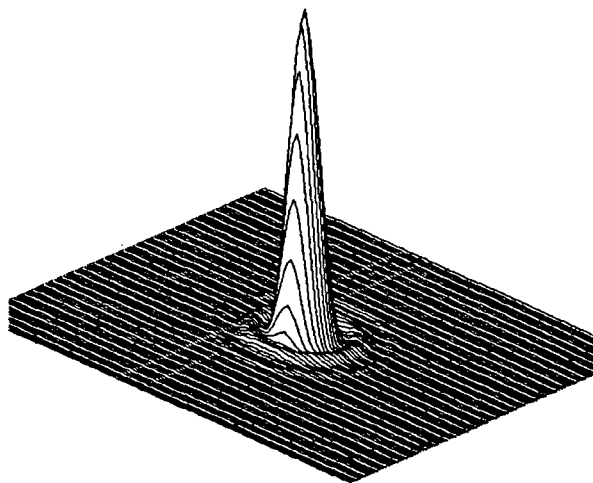


**Figure 8.17** Plane Wave Propagation Yields an Ideal Point Spread Function as Shown

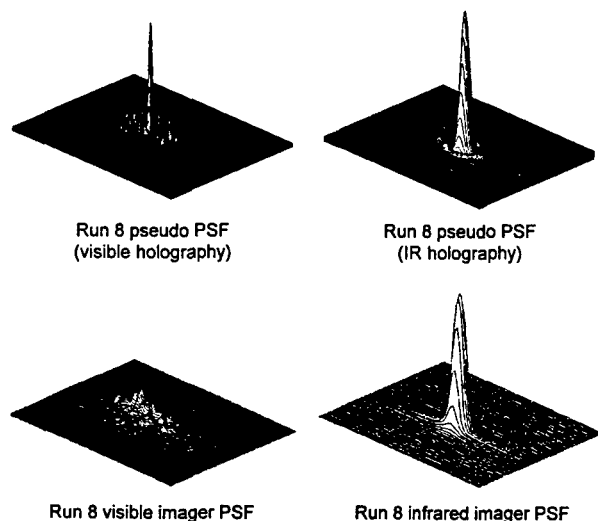


**Figure 8.18** Run 8 Comparison of the Pseudo PSFs from Holography and the Measured PSFs from the Visible and Infrared Imager Systems

The encircled-energy functions of both pseudo and real images are shown in Figure 8.19. The

holographic analysis results in a brighter PSF compared to the visible-image analysis. For the pseudo-PSF, approximately 24% of the total encircled energy is recovered at the fourth ring of the ideal Airy distribution, compared to 95% for the ideal case. The encircled energy curve from the visible imager recovered only 10% of the total encircled energy at the same diameter. This powerful pseudo imagery analysis will allow for the longer exposure imagery by incorporating multiple wavefronts into the analysis and averaging the PSF's on the FPA.

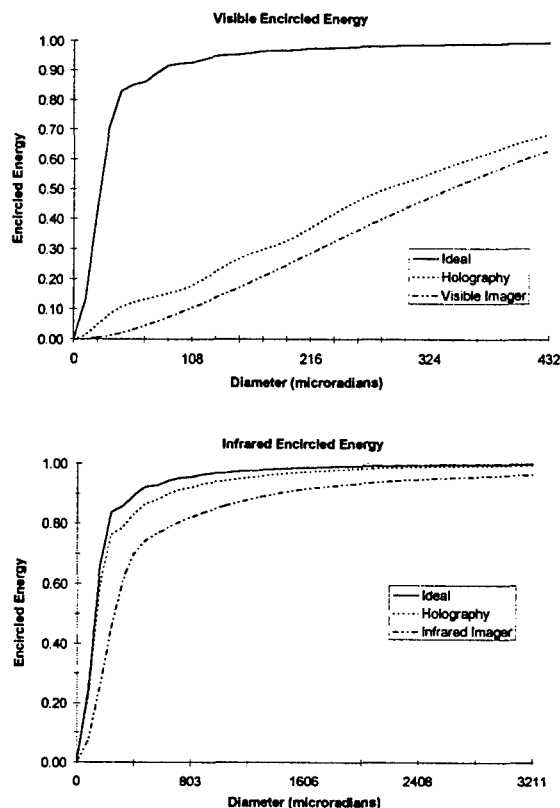


**Figure 8.19** The Encircled Energy Curves for the Run 8 Flow Case for the Visible and Infrared Imager Systems are Compared to the Holography Analysis

#### Aero-Optical Evaluation of Nitrogen and Helium Coolants

The wavefront phase maps for the nitrogen and helium coolant cases are used to obtain the corresponding PSFs in the visible (0.69 micron) and in the MWIR (3.5 micron) regions. The visible images are shown in Figure 8.20. The image with nitrogen coolant is significantly more degraded, as the on-axis intensity is lower and the sharpness is reduced, when compared to the image with helium

coolant. The Strehl ratios for the nitrogen and helium coolant images are 0.104 and 0.923, respectively. Hence, the helium image exhibits approximately 10 times the brightness of the nitrogen image.

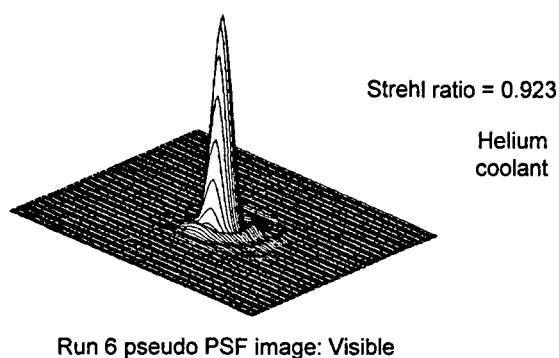
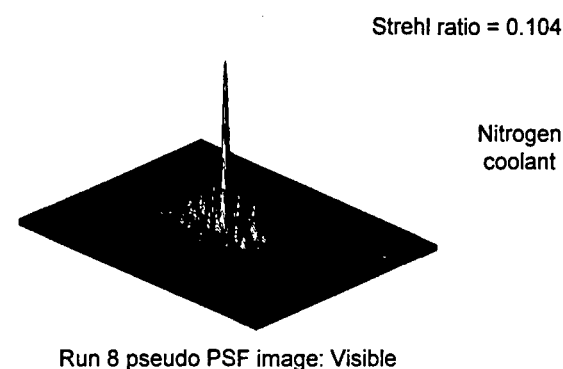


**Figure 8.20** Pseudo PSFs at Visible Wavelength from the Holography Analysis are Compared with Runs 6 and 8

A similar analysis has been obtained for MWIR wavelengths. The PSFs are shown in Figure 8.21. The nitrogen-coolant image in the MWIR is still degraded, with a Strehl ratio of 0.896, compared to the value of 0.997 for the image obtained with the helium coolant. The nitrogen coolant run exhibits some intensity outside of the main peak. The helium image in the MWIR is essentially at the diffraction limit of the aperture with a Strehl ratio of one.

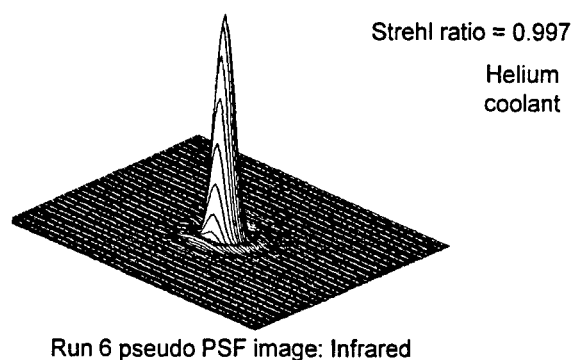
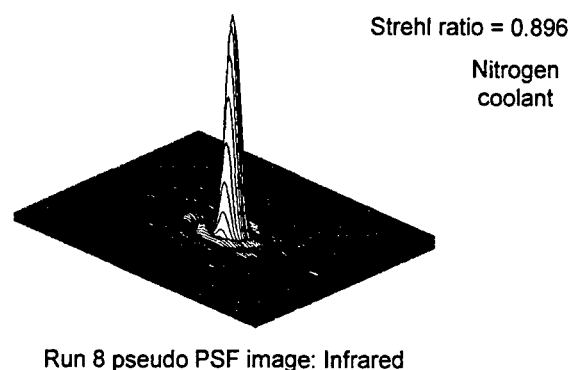


**Figure 8.21** Pseudo PSFs at Infrared Wavelength from the Holography Analysis are Compared for Runs 6 and 8

## REFERENCES

- 8-1. Holden, M.S., Craig, J.E., Parker, R.A., and Kolly, J.M., "Aerothermal and Aero-Optical Seeker-Head Studies in the LENS Facility at Velocities Up to 3.5 km/sec," Paper presented at the 3rd Annual AIAA/BMDO Interceptor Technology Conference, San Diego, CA, July 11-14, 1994.

## 9. CUBDAT DATABASE OF MEASUREMENTS IN HYPERSONIC FLOW

### 9.1 Introduction

The experimental studies entered in this database were selected from studies conducted in hypersonic flows in Calspan's 48-inch, 96-inch, 6-foot shock tunnels and the LENS facility, during the past 30 years. The measurements selected for this database were assembled from a far larger data set by choosing only the measurements in laminar, transitional, and turbulent flows, which we believe are of the greatest value for code validation. A special computer program, "CUBDAT," was constructed to provide easy access to the measurements in the database as well as the means to plot the measurements and compare them with imported data. The database contains tabulations of model configurations; freestream conditions; and measurements of heat transfer, pressure, and skin friction for each of the studies selected for inclusion. The measurements tabulated in this database are divided into seven main areas. The first segment contains measurements in laminar flow emphasizing shockwave-boundary layer interaction. In the second segment, we present measurements in transitional flows over flat plates and cones. The third segment comprises measurements in regions of shockwave/turbulent boundary layer interactions. Studies of the effects of surface roughness of nosetips and conical afterbodies are presented in the fourth segment of the database. Detailed measurements in regions of shock/shock boundary layer interaction are contained in the fifth segment. Measurements in regions of wall jet and transpiration cooling are presented in the final two segments. Finally, we include measurements for the recently conducted studies with the Planetary Probe configuration taken in the LENS facility.

To adequately specify the boundary conditions, in addition to accurate specification of model configuration and freestream properties, we must include measurements to define the length and characteristics of the laminar, transitional, and turbulent flow on the body. Because of the small thickness (typically .05 inches) and intrinsically full structure of the turbulent boundary layers developed on the models, it is virtually impossible to make flowfield surveys of a definitive nature. We believe that it is more useful to present data which will enable the code validator to make "tip to tail" calculations starting in laminar flows and preceeding

through transition through a turbulent boundary structure. Therefore, in the database we have presented heat transfer and pressure measurements which span the laminar to turbulent regions to enable the analyst to validate the modeling of the transitional process. A summary of the studies presented in the database are listed in Table I.

### 9.2 Review of Database

CUBDAT is a program that provides access to reduced data from a number of experimental studies conducted in Calspan's shock tunnels from 1964 to present. Data from each study are stored in ASCII files that are compatible for use with LOTUS 1-2-3. The sequence number, n, of each run performed is part of its associated filename, which is of the form "RUNn.LTS." The use of appropriately named subdirectories provides the ability to discriminate data from different experimental series. A file named "CONFIGUR" must also be present in each subdirectory. It defines the single character abbreviations used in place of lengthy descriptions for model parameters related to the experiments. For instance, the phrase "Distance from the Leading Edge" might be represented by the letter "A" in the data files.

Although CUBDAT provides the user with a number of options for the plotting and tabulation of the information within the ASCII files, the ability to use the data in other contexts is essential. Toward this end, added information is provided in the form of:

1. Brief description of file organization;
2. Sample RUNn.LTS file;
3. Sample CONFIGUR file;
4. Plots derived from data in Item 2.

CUBDAT is available to qualified users, and details of its distribution are provided in the Appendix. It can only be used on PCs or compatibles, and there are no plans to convert it to other operating environments. Primary user interaction with CUBDAT is through the Main Menu, whose content is presented below.

- |   |  |
|---|--|
| # | Choices (Active Values in Parentheses)           |
| 0 | Place program usage overview on the screen       |
| 1 | Set default drive and directory (d: & directory) |
| 2 | Select a different run for processing (0)        |
| 3 | Display test conditdons                          |
| 4 | Draw plots (Grid is Off)                         |
| 5 | Present data in tabular form                     |
| 6 | Display model parameters                         |

- 7 List information in the summary file
  - 8 Change Qo(F-R) parameters (Nd=.25 ft, Shape=Cylin., Twall=530.00 degR)
- Enter # of choice or G to toggle Grid (Q to Quit)-->

The user responds by entering his/her choice to produce a result or another level of queries. For example, if item 7 were chosen, a second menu would appear offering the choice of any of the 30 studies for which data are available. Once a study has been selected, information pertinent to the study is displayed. If test matrix data are present, a yes/no query is offered to the user for a response. Figure 9.1 combines information from the displays produced when study 14 [SHK-SHK] and its corresponding test matrix data were opted.

Capsule: Shock - Shock Interaction  
Runs: 9-22,24,26-44,59-64,66-95,98-104,106-110,112-116/  
Title: "Studies of Aerothermal Loads Generated in Regions of Shock/Shock Interaction in Hypersonic Flow"  
Author: M.S.Holden, A.R.Welting, J.R.Moselle, C.Glass  
Date: 8/86 - 9/87  
W/A: 25-576  
Report#: AIAA paper No. 88-0477 (Jan 1988)

SHK-SHK Test Matrix									
----- MODEL PARAMETERS -----									
CLEARANCES ANGLE LENGTH SWEEP RAMP PARAMETERS									
RUN	MACH	RE/FT	STAG GAGE	V (in)	H (in)	C (deg)	P (in)	ANGLE (deg)	DIST (in)
9	6.35	4.50	P18	N/A	N/A	N/A	26.5	0.00	N/A
10	6.35	4.40	P18	3.20	0.09	10.0	26.5	0.00	N/A
11	6.35	4.40	P18	3.50	0.05	10.0	26.5	0.00	N/A
12	6.35	4.30	P21	3.34	0.06	10.0	26.5	0.00	N/A
13	6.35	4.40	P18	3.34	0.06	10.0	26.5	0.00	N/A
14	6.36	4.70	P23	3.55	0.09	10.0	26.5	0.00	N/A
15	6.33	2.40	P23	3.55	0.09	10.0	26.5	0.00	N/A
16	8.02	1.40	P23	2.95	0.06	10.0	26.5	0.00	N/A
17	8.06	1.50	P23	2.95	0.06	10.0	26.5	0.00	N/A
18	8.03	1.50	P21	2.86	0.50	10.0	26.5	0.00	N/A
19	8.03	1.50	P21	2.78	0.50	10.0	26.5	0.00	N/A
20	7.94	0.76	P21	2.78	0.50	10.0	26.5	0.00	N/A
21	8.03	1.60	P21	2.89	0.59	12.5	26.5	0.00	N/A
22	7.95	0.77	P21	2.89	0.59	12.5	26.5	0.00	N/A
23	7.95	0.77	P21	2.89	0.59	12.5	26.5	0.00	N/A
24	8.14	3.80	P21	2.89	0.59	12.5	26.5	0.00	N/A
25	8.03	1.50	HT39	3.36	0.63	12.5	26.5	0.00	N/A
26	8.03	1.50	P21	2.95	0.31	15.0	26.5	0.00	N/A
27	7.93	0.72	P21	2.95	0.31	15.0	26.5	0.00	N/A
28	8.03	1.50	P23	3.19	0.31	15.0	26.5	0.00	N/A
29	8.15	1.80	P11	2.31	0.75	15.0	26.5	0.00	N/A
30	8.03	1.50	P18	N/A	N/A	N/A	N/A	0.00	N/A
31	8.03	1.50	P18	N/A	N/A	N/A	N/A	0.00	N/A
32	6.38	5.00	P18	N/A	N/A	N/A	N/A	0.00	N/A
33	11.00	4.30	P21	2.00	0.44	10.0	26.5	0.00	N/A
34	11.01	4.40	P21	2.25	0.44	10.0	26.5	0.00	N/A
35	11.02	4.50	P21	2.72	1.81	10.0	26.5	0.00	N/A
36	11.01	4.30	P21	2.41	1.50	10.0	26.5	0.00	N/A
37	11.00	4.20	P21	2.41	2.10	10.0	26.5	0.00	N/A
38	11.00	4.30	P18	N/A	N/A	N/A	N/A	0.00	N/A
39	12.97	4.70	P18	N/A	N/A	N/A	N/A	0.00	N/A
40	16.50	1.20	P18	N/A	N/A	N/A	N/A	0.00	N/A
41	19.14	0.37	P18	N/A	N/A	N/A	N/A	0.00	N/A
42	16.31	1.00	P21	2.94	0.16	10.0	48.0	0.00	N/A
43	16.33	1.00	P23	3.63	0.09	10.0	48.0	0.00	N/A
44	16.27	0.94	P25	3.94	-0.25	10.0	48.0	0.00	N/A
59	8.04	1.40	P21	2.83	2.76	12.5	26.5	0.00	N/A
60	8.04	1.40	P21	3.19	1.81	12.5	26.5	0.00	N/A
61	8.05	1.50	P23	3.08	0.35	12.5	26.5	0.00	N/A
62	8.05	0.73	P24	3.08	0.35	12.5	26.5	0.00	N/A
63	7.75	0.37	P24	3.08	0.35	12.5	26.5	0.00	N/A

Figure 9.1 Format of Source Capsule and Test Matrix for Shock/Shock Interaction Database Available in CUBDAT

The most useful feature available in CUBDAT is the ability to produce graphic information. Option 4 provides this capability only if there is an active run number (i.e., nonzero) in the parentheses for option 2. An error message will be flashed if zero is indicated. This is also true for options 3, 5, and 6. Figure 9.2 provides a representative plot of combined pressure and heat transfer data once option 4 has been selected.

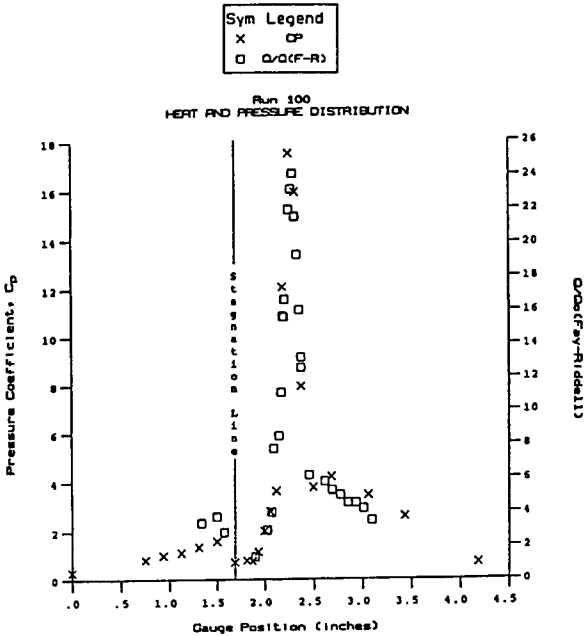


Figure 9.2 Typical Plots of the Heat Transfer and Pressure Distribution in Regions of Shock/Shock Interaction Which Can Be Obtained Directly from the CUBDAT Database



# Hypersonic Laminar-Turbulent Transition and its Implications for Winged Configurations

D.I.A. Poll  
College of Aeronautics  
Cranfield University  
Cranfield, Bedford MK43 0AL, U.K.

## 1. Summary

The problem of laminar-turbulent transition on swept back wings travelling at hypersonic speeds is one of great practical significance. Swept back wings support three-dimensional boundary layer flows and, in consequence, two mechanisms for transition are admitted which do not occur in two-dimensional situations. These are attachment-line contamination and cross-flow instability. Both these are known to be very important in the generation of turbulent flow in low-speed flows. It is argued that these phenomena are also important in high speed conditions. Available evidence is reviewed and, when possible, estimates are made of the conditions necessary for transition onset.

## 2. Introduction

Vehicles, or devices, which are required to travel at hypersonic speeds often incorporate surfaces for the generation of lift, stabilizing or control forces. The requirement for good aerodynamic efficiency invariably leads to the use of thin aerofoil sections and planforms with highly swept leading edges. However, since there will also be a considerable heat loading at the high Mach number phases of flight, it will be necessary to introduce blunting in order to reduce the very large surface heating rates which occur at the leading edge. The degree of blunting will have to be chosen very carefully since, whilst alleviating the very serious heating problem, it introduces two undesirable effects. Firstly, the aerodynamic efficiency is reduced because blunting increases the pressure drag of the wing. Secondly, and possibly more importantly, the combination of blunting and leading edge sweep may cause transition to turbulence in the boundary layer close to the leading edge. This will cause both increased drag, through increased surface shear, and increased heating rates close to, or even at, the leading edge. It is this boundary layer transition which is our primary concern and, for the transition in the leading edge region, the following parameters are of primary importance.

1. leading edge sweep angle
2. leading edge blunting - i.e. nose shape
3. aerofoil thickness
4. aerofoil incidence.

A generic aerofoil section is sketched in figure 1 which gives an indication of the main features.

For typical wings the sweep angles are unlikely to exceed  $80^\circ$  and so, for free stream Mach numbers in excess of 6 (i.e. hypersonic flow), the component of the free stream Mach number in a plane drawn normal to the leading edge will be in excess of unity. This being the case the general characteristics of the flow will be as indicated in figure 2. i.e. there will be a strong detached shock wave wrapped around the leading edge. Moreover, away from the apex of the wing the leading edge region will be unaware of the delta wing plan form i.e. the flow will be locally "infinite swept".

By referring to figure 3 it may be shown that for the general delta wing with leading edge sweep angle,  $\Lambda$ , at an angle of incidence,  $\alpha$  to a free stream with a Mach number,  $M_\infty$ , the components of the free stream Mach number parallel to, and normal to, the leading edge are

$$M_{t_\infty} = M_\infty \sin \Lambda \cos \alpha \quad (1)$$

$$\text{and} \quad M_{N_\infty} = M_\infty (1 - \sin^2 \Lambda \cos^2 \alpha)^{1/2} \quad (2)$$

respectively. From which it follows that the effective sweep angle  $\Lambda'$  is given by

$$\Lambda' = \tan^{-1} \left\{ \frac{\sin \Lambda \cos \alpha}{(1 - \sin^2 \Lambda \cos^2 \alpha)^{1/2}} \right\} \quad (3)$$

Moreover, the incidence of the flow in a plane drawn normal to the leading edge is given by

$$\alpha_N = \cos^{-1} \left\{ \frac{\cos \Lambda \cos \alpha}{(1 - \sin^2 \Lambda \cos^2 \alpha)^{1/2}} \right\} \quad (4)$$

It is important to note that the flow close to the leading edge depends upon  $\alpha_N$  and that, for a highly

swept wing, small values of planform incidence,  $\alpha$ , can lead to large values of  $\alpha_N$  e.g. if  $\Lambda$  is  $80^\circ$  and  $\alpha$  is  $2^\circ$  then  $\alpha_N$  is  $11.4^\circ$ . Therefore, care must be taken when small angle approximations are being made. It follows that, provided the "infinite swept" assumption is valid, the flow in the immediate vicinity of the leading edge is completely specified by the following parameters.

1. the spanwise component of the free stream Mach number  $M_{T_\infty}$  (equation 1)
  2. the normal to leading edge component of the free stream Mach number  $M_{N_\infty}$  (equation 2)
  3. the incidence in the plane normal to the leading edge  $\alpha_N$  (equation 4)
  4. the leading edge thickness  $t$  (figure 2)
  5. the leading edge geometry (figure 2)
  6. the "wedge" angle  $\beta$  (figure 2)
- and
7. the ratio of the wall temperature to the free stream total temperature  $T_w/T_{o_\infty}$

### 3. Pressure Distribution

When considering the pressure field generated by the wing leading edge it is convenient, in the first instance, to consider two extreme cases. The first occurs when the leading edge is blunt and the free stream unit Reynolds number is high. In this case the pressure field is determined purely by the leading edge geometry. The local surface pressure is highest at the point of flow attachment and drops to a local minimum value at the point where the blunt nose meets the flat surface (this location is sometimes referred to as the "shoulder"). Downstream of the shoulder the pressure rises to reach a local maximum (the value here being much less than at the point of attachment). Thereafter the pressure relaxes slowly towards an asymptotic value which is determined by the local wedge angle  $\beta$ . A typical example of this behaviour is given in figure 4. In this case, the wing is a cylindrically blunted slab ( $\beta = 0$ ) at zero angle of attack. The three regions i.e.

- a) cylindrical (attachment to shoulder)
  - b) blending
- and
- c) relaxation

are clearly visible. From the point of view of the analyses which follow, it is useful to note that regions (a) and (c) exhibit a special kind of "similarity" which can be useful in the analysis of complex situations. Since the normal to leading edge Mach number is supersonic, the pressure distribution over the cylindrical portion is independent of the

shape of the wing downstream of the shoulder. Consequently, the pressure distribution in region (a) depends only upon  $M_{N_\infty}$  and the nose geometry. To a first approximation the pressure distribution is given by the modified Newtonian form i.e.

$$C_p = C_{p_0} \cos^2 \left( \frac{2x}{t} \right)$$

In the relaxation region (c) there is a similarity which results from the analogy between the two-dimensional pressure field developing downstream of the shoulder and the one-dimensional unsteady flow resulting from an explosion (rapid energy release along a line). This is the so called "blast-wave" analogy which is described in most textbooks on hypersonic aerodynamics - see for example Anderson<sup>1</sup>. By making use of the analogy, it can be argued that the pressure variation in the relaxation region is such that

$$\frac{p}{p_\infty} = K M_{N_\infty}^2 \left[ \frac{C_d}{x/t} \right]^{2/3}$$

where  $C_d$  is the drag coefficient of the nose and  $K$  is a constant. Analysis of experimental data reveals that to a good approximation the pressure distribution is given by

$$\frac{p}{p_\infty} = 0.121 M_{N_\infty}^2 \left[ \frac{C_d}{x/t} \right]^{2/3} + 0.56$$

This form guarantees that the correct pressure level is reached for downstream of the nose. However, when the normal to leading edge Mach number is high, the pressure field close to the nose is given by

$$\frac{p}{p_\infty} \approx 0.12 M_{N_\infty}^2 \left[ \frac{C_d}{x/t} \right]^{2/3}$$

Unfortunately, there appears to be no simple form for the pressure distribution in the blending region (b). The second limiting case occurs when the leading edge is sharp and the free stream unit Reynolds number is low. In this case, the streamwise growth of the boundary layer is sufficiently large to modify the position and strength of the shock wave with consequential changes to the pressure distribution over the surface. If we consider the special case of the perfectly sharp leading edge and a plate at zero angle of attack, then, if the boundary layer is thin, there will be no shock wave at the leading edge and no variation of surface pressure along the plate. However, when the free stream unit Reynolds number is low, a thick boundary layer will be formed

which will displace the streamlines of the inviscid flow away from the surface. This produces a shock wave at the leading edge, giving an initial surface pressure which is much higher than the static pressure in the undisturbed free stream ahead of the plate. Away from the leading edge, the surface pressure decreases monotonically - approaching the undisturbed free stream value asymptotically - see figure 5. In this case the important parameter is  $\Omega_N$

$$\text{where } \Omega_N = M_{N_\infty}^{1/2} M_\infty^2 \left( \frac{\mu_\infty}{a_\infty \rho_\infty x} \right)^{1/2} \quad (7)$$

and  $a_\infty$  is the speed of sound in the undisturbed free stream. This parameter depends upon both normal to leading edge conditions and undisturbed free stream conditions. Near the leading edge the induced pressure field is given (approximately) by

$$\frac{p_e}{p_\infty} = \frac{3}{4}(\gamma-1) \left[ \frac{\gamma(\gamma+1)}{2} \right]^{1/2} I_1 \Omega_N$$

where  $I_1$  is a coefficient of order unity and very weakly dependent upon the sweep angle. Therefore, close to the leading edge -

$$\frac{p_e}{p_\infty} \approx 0.3 \Omega_N = 0.3 \frac{M_{N_\infty}^{2.5}}{\cos^2 \Lambda} \left( \frac{\mu_\infty}{a_\infty \rho_\infty x} \right)^{1/2}$$

Downstream the induced pressure distribution tends to

$$\frac{p_e}{p_\infty} \approx 1 + \frac{\gamma}{2} \left( \frac{\gamma-1}{2} \right) (0.664) \left( 1 + 2.6 \frac{T_w}{T_\infty} \right) \chi_N$$

and, for air, this is

$$\frac{p_e}{p_\infty} \approx 1 + \frac{0.2 M_{N_\infty}^{2.5}}{\cos^2 \Lambda} \left( \frac{\mu_\infty}{a_\infty \rho_\infty x} \right)^{1/2}$$

In both cases the pressure perturbations are proportional to  $\cos^{1/2} \Lambda$ .

These simple expressions also allow a comparison of the effects of viscous-inviscid interaction and leading edge bluntness. Close to the leading edge, where  $x/t$  is of order unity, the ratio of the two effects is

$$\frac{(p_e/p_\infty)_V}{(p_e/p_\infty)_B} \approx 3 \frac{M_\infty}{\cos^{1.5} \Lambda} \left( \frac{\mu_\infty}{Q_\infty \rho_\infty t} \right)^{1/2}$$

whilst for downstream

$$\frac{(p_e/p_\infty - 1)_V}{(p_e/p_\infty - 1)_B} \approx 3 \frac{M_\infty}{\cos^{1.5} \Lambda} \left( \frac{\mu_\infty}{Q_\infty \rho_\infty t} \right)^{1/2} \left( \frac{x}{t} \right)^{1/6}$$

These results clearly show that, whilst sweep back reduces the pressure perturbations due to both effects, the relative importance of viscous-inviscid interaction increases rapidly as the sweep angle is increased. If the pressure distribution produced by the viscous-inviscid interaction is to be negligibly small compared to the bluntness induced pressure (say  $> 1/10$ th) then

$$R_{t_\infty} = \left( \frac{Q_\infty \rho_\infty t}{\mu_\infty} \right) > \frac{1000 M_\infty^2}{\cos^3 \Lambda}$$

Conversely, the viscous induced pressure disturbance will be much greater than the bluntness induced pressure distribution (say 10 times) when

$$R_{t_\infty} < \frac{1}{10} \frac{M_\infty^2}{\cos^3 \Lambda}$$

Therefore when

$$0.10 < \frac{R_{t_\infty} \cos^3 \Lambda}{M_\infty^2} < 1000$$

both viscous induced and bluntness induced pressure perturbations are significant close to the leading edge.

For the far downstream pressure distribution, if the viscous induced perturbation is to be less than 1/10th of the bluntness induced value then

$$R_{t_\infty} > 1000 \frac{M_\infty^2}{\cos^3 \Lambda} \left( \frac{x}{t} \right)^{1/3}$$

and, if the effect of viscosity is to be 10 times that of bluntness,

$$R_{t_\infty} < \frac{1}{10} \frac{M_\infty^2}{\cos^3 \Lambda} \left( \frac{x}{t} \right)^{1/3}$$

Therefore for

$$0.10 < \frac{R_{t_\infty} \cos^3 \Lambda}{M_\infty^2} \left( \frac{t}{x} \right)^{1/3} < 1000$$

both viscous interaction and bluntness are significant.

#### 4. Attachment-line transition

For the infinite swept wing, the attachment line is the projection onto the wing surface of the limiting streamline of the external (inviscid) flow which separates the upper surface flow from that over the lower surface - see figure 6. When the leading edge is at zero sweep the attachment line becomes the locus of the two-dimensional stagnation points i.e. the local velocity there is zero. However, when the leading edge is swept, there is a velocity along the attachment line which, for an infinite swept wing, is equal to the spanwise component of the free stream velocity. In this case, a boundary layer forms along the attachment line and this may be laminar, transitional or turbulent depending upon conditions. If the attachment-line flow is turbulent, then, unless there is relaminarisation in regions of strong favourable pressure gradient, the flow over both the upper and lower surfaces will be turbulent. It should be noted that, as yet, off attachment-line relaminarisation has not been observed experimentally under hypersonic conditions and, consequently, attachment line transition must be considered to be a very important issue for wing design.

The properties of the flow at the attachment line are governed by the following local parameters - a characteristic Reynolds number  $\bar{R}$  where

$$\bar{R} = \left\{ \frac{V_{\infty}^2}{v_e (dU_e/dx)_{x=0}} \right\}^{1/2} \quad (8)$$

the Mach number at the edge of the boundary layer,  $Me$ , and the ratio of the wall to flow total temperature,  $T_w/T_o$  - see reference 2. When transition is being considered, a roughness height,  $k$ , and the spanwise distance,  $s$ , (measured along the attachment line) between the trip location and the transition location also need to be specified. The complete transition picture is then given in terms of

$$\bar{R}, M_e, T_w/T_o, k/\eta \text{ and } s/\eta$$

where  $\eta$  is a characteristic length of the boundary layer

$$\eta = \left( \frac{\eta_e}{(dU_e/dx)_{x=0}} \right)^{1/2}$$

For two-dimensional and three-dimensional trips in an incompressible attachment line flow the transition picture is completely mapped out - see references 3 and 4 but, when the flow is compressible, our current knowledge of the critical conditions for transition is

incomplete. However, in the limiting case of "large" roughness elements and "large" values of the spanwise separation  $s$ , it has been demonstrated that the conditions necessary for the onset of transition correspond to

$$\bar{R}_* = \left( \frac{V_{\infty}^2}{v_e (dU_e/dx)_{x=0}} \right)^{1/2} = 245 \quad (9)$$

where

$$\frac{T_*}{T_e} = 1 + 0.10 \left( \frac{T_w}{T_e} - 1 \right) + 0.60 \left( \frac{T_r}{T_e} - 1 \right)$$

- see references 2, 5, 6 and 7. In the case of "smooth wall" transition, it may be expected that stability theory could be used to predict the conditions necessary for transition since, in the limit of very small forcing disturbances, a linear instability of the flow should be precursor to transition. Once again, for incompressible flow, this has been shown to be the case - reference 8. Stability theory predicts that the flow is unstable to small disturbance when  $\bar{R}$  exceeds 583 and this is borne out by experiments. However, when the flow is compressible, the situation is not so clear, since experiment and theory are not in agreement - see reference 5. At present, it is not possible to identify the reason for the discrepancy. However, we note that from the experimental data available the conditions for smooth surface transition are correlated (approximately) by a relation similar to that given in equation 9, i.e.

$$\bar{R}_* \approx 600 \quad (10)$$

Whilst this is in good agreement with the predictions of stability theory for incompressible flow, it suggests that transition behaviour is not modified by compressibility and surface heat transfer in the way predicted by linear stability theory.

To summarise the current position we may make the following statements. Firstly, a clearly defined lower boundary exists for the generation of turbulent flow by large sources of disturbance ( $\bar{R}_* = 245$ ). This limit has been verified by a large number of wind tunnel tests. Transition occurs at Reynolds numbers which are much lower than the theoretically determined minimum critical Reynolds numbers for the existence of amplified linear disturbances. Consequently this bound cannot be predicted with linear stability theory and it is appropriately described as a "bypass" mechanism (bypassing classical stability theory). Secondly, Using

observations made in both conventional supersonic wind tunnels and the NASA Langley Mach 3.5 "Quiet Tunnel", an experimentally determined upper bound for smooth surface, attachment line transition occurs when  $\bar{R}_* \approx 600$ . This does not correspond to any known limit based upon stability theory - except under incompressible conditions.

In view of the apparent success the "reference temperature" based modification to the incompressible result, it is tempting to ask whether the hypothesis is capable of producing a complete picture of the transition process for flows with compressibility and heat transfer. The success of this approach may be judged by examination of figure 7 which comes from reference 5. It is clear that there is some merit in the idea and it is probably accurate enough for the estimation of the critical roughness heights. In view of this, we may identify two particular conditions for the roughness height

- a) Effective roughness height - this is defined as the smallest height which first affects the attachment line transition. From the figure,  $\bar{R}_*$  for transition is less than 600 for values of  $k \geq \eta_*$ , i.e. the critical height occurs when

$$k/\eta_* = 1.0$$

and

- b) Fully effective roughness height - this is defined as the smallest height of roughness which will cause transition at the lowest possible Reynolds number i.e.  $\bar{R}_* = 245$ . This occurs when  $k/\eta_* \geq 2.0$ . Hence the critical value is

$$k/\eta_* = 2.0$$

In order to appreciate the consequences of the various criteria, it is appropriate to express them in terms of free-stream parameters and sweep angle. For an attachment line which is

- infinite swept
- $M_\infty \cos \Lambda \geq 2$

and c)  $T_w/T_o < 0.3$

$$\left. \frac{dU_e}{dx} \right|_{x=0} \approx \left[ \frac{7.20}{\gamma} \right]^{1/2} \frac{a_e}{d} \quad (\text{see reference 9})$$

from which it follows that -

$$\bar{R}_* \approx \left[ \left( \frac{\gamma+1}{2} \right)^{\frac{\gamma}{\gamma-1}} \left( \frac{\gamma+1}{2\gamma} \right)^{\frac{1}{\gamma-1}} \left( \frac{\gamma}{7.2} \right)^{1/2} \right]^{1/2} \left[ \frac{\rho_\infty d \tan^2 \Lambda}{\Omega} \right]^{1/2} \left[ \frac{M_\infty^2 \cos^2 \Lambda}{1 + \left( \frac{\gamma-1}{2} \right) M_\infty^2 \cos^2 \Lambda} \right]^{1/2} \times \left[ \frac{1 + \left( \frac{\gamma-1}{2} \right) M_\infty^2 \cos^2 \Lambda}{0.90 + \left( \frac{\gamma-1}{2} \right) M_\infty^2 \cos^2 \Lambda (0.90 + 0.54 \tan^2 \Lambda)} \right]^{5/4} \times \left[ \frac{(0.90 + 110/T_\infty) + \left( \frac{\gamma-1}{2} \right) M_\infty^2 \cos^2 \Lambda (0.90 + 0.54 \tan^2 \Lambda)}{1 + \left( \frac{\gamma-1}{2} \right) M_\infty^2 \cos^2 \Lambda} \right]^{1/2}$$

where  $\Omega$  is the atmospheric constant which equals  $7.273 \times 10^{-8} \text{ kg/m}^2$ .

By using this expression, the "critical" points on any particular trajectory can be located. For example, taking the variation of Mach number with altitude for a given trajectory, it is possible to determine the values of leading edge diameter which correspond to  $\bar{R}_*$  of 245 and 600. Moreover, it is also possible to determine the size of the smallest roughness element which will induce transition at  $\bar{R}_* = 245$ , since at this condition -

$$\frac{k}{d} = \frac{2.0}{245} \left[ \frac{\gamma}{7.20} \right]^{1/2} \tan \Lambda \left[ \frac{M_\infty^2 \cos^2 \Lambda}{1 + \left( \frac{\gamma-1}{2} \right) M_\infty^2 \cos^2 \Lambda} \right]^{1/2}$$

Similarly, the largest tolerable roughness height for transition to occur at an  $\bar{R}_*$  of 600 is given by

$$\frac{k}{d} = \frac{1.0}{600} \left[ \frac{\gamma}{7.20} \right]^{1/2} \tan \Lambda \left[ \frac{M_\infty^2 \cos^2 \Lambda}{1 + \left( \frac{\gamma-1}{2} \right) M_\infty^2 \cos^2 \Lambda} \right]^{1/2}$$

Sample results are given in the following table where a typical transmospheric ascent trajectory has been assumed and the leading edge sweep of the wing is taken to be  $70^\circ$  -

Altitude    Mach number     $\bar{R}_* = 245$

$\bar{R}_* = 600$

(km)	( $M_\infty$ )	$d(m)$	$k(mm)$	$d(m)$	$k(mm)$
24.6	6	0.020	0.299	0.122	0.372
28.0	8	0.026	0.445	0.158	0.551
31.4	10	0.037	0.685	0.223	0.844
33.8	12	0.049	0.952	0.292	1.159

It is immediately apparent that, the larger the leading edge radius, the higher the altitude at which the attachment line flow reverts to the laminar state - whether there is roughness on the surface or not. Moreover, it is clear that the roughness heights being considered are directly proportional to the leading edge diameter and that the values required to promote transition are very small. This result clearly indicates the importance of roughness on the leading edge and the value of the leading edge diameter.

Finally, it is interesting to note the values of the free stream Reynolds number,  $Q_\infty d/v_\infty$ , at which the two critical conditions are reached. These are given in the following table, for the same trajectory.

	$\bar{R}_* = 245$	$\bar{R}_* = 600$
$M_\infty$	$Q_\infty d/v_\infty$	$Q_\infty d/v_\infty$
6	$1.04 \times 10^5$	$6.35 \times 10^5$
8	$1.01 \times 10^5$	$6.15 \times 10^5$
10	$1.13 \times 10^5$	$6.78 \times 10^5$
12	$1.21 \times 10^5$	$7.19 \times 10^5$

The two Reynolds numbers are approximately constant over a very wide range of Mach number and altitude. Similarly, the critical roughness heights exhibit the following behaviour

	$\bar{R}_* = 245$	$\bar{R}_* = 600$
$M_\infty$	$k/d(\%)$	$k/d(\%)$
6	1.5	0.30
8	1.7	0.35
10	1.9	0.38
12	1.9	0.40

These results also have only a weak variation with Mach number and altitude. However, it should be noted that there is an effect of sweep angle.

5. Cross-flow transition

In general, a three-dimensional boundary-layer flow is characterised by curvature of the streamlines in planes drawn parallel to the surface. Referring to figure 6, it is clear that, for  $x$  greater than zero, the streamlines at the edge of the boundary layer are highly curved. If the velocity variation within the viscous layer is resolved in the direction parallel to the external streamline the resulting profile is similar to the conventional two-dimensional form - see figure 8. However, unlike the two-dimensional situation, there is also a profile obtained when the resolution is carried out in a direction normal to the external streamline. This "cross-flow" profile exists since, in accordance with the boundary layer approximations, the static pressure is invariant with the normal to surface coordinate,  $z$ . Consequently, whereas at the edge of the layer the pressure gradient and the centrifugal acceleration are in balance, as the wall is approached the pressure gradient remains the same but the velocity is reduced. In order to maintain the local force balance, the curvature of the streamlines must change and this leads to the appearance of the cross-flow component of velocity. All cross-flow velocity profiles have zero velocity at the wall and zero velocity at the viscous layer edge. Within the layer, the profiles may take a variety of shapes depending upon the variation of the surface pressure - see figure 9. However, in the vicinity of a swept leading-edge the cross-flow profile has the "C" form with a single maximum - as indicated in figure 8.

In general, it is rather difficult to formulate a characteristic Reynolds number and over the years authors have suggested a variety of forms - none of which is entirely satisfactory. If the maximum value of the cross-flow velocity is denoted by  $C_{max}$  then the cross-flow Reynolds number  $\chi$  may be defined as

$$\chi_1 = \frac{C_{max} \delta_{0.1} C_{max}}{v_e} \text{ (Pfenninger reference 10)}$$

or 
$$\chi_2 = \frac{C_{max} \delta_{0.01} C_{max}}{v_e} \text{ (Poll reference 11)}$$

Alternatively, an integral form may be used e.g.

$$\chi = \frac{\rho_e C_{max}}{\mu_e} \int_0^\infty \frac{\rho c}{\rho_e C_{max}} dz$$

$$\text{i.e. } \chi = \frac{1}{\mu_e} \int_0^{\infty} \rho c \, dz$$

This latter form can be described as a Reynolds number based upon the cross-flow "displacement" thickness. However, it should be noted that, in this context the "displacement" is not related to the actual displacement of the inviscid flow, nor does the definition uniquely characterise the velocity profile. Nevertheless, this integral definition will be used in the context of the present work.

It is clear from the above that for a swept-back wing cross-flow profiles will develop wherever there is a pressure gradient. Therefore, referring to figure 4, a strong cross-flow will be generated initially in region (a). This will be moderated in region (b) and, finally, reinforced in region (c). It follows that cross-flow instability is likely to be particularly important in regions (a) and (c). Furthermore, from figure 5, it is also apparent that cross-flow instability may play a role when the pressure field is induced by viscous-inviscid interaction.

For incompressible flow on the windward face of a swept cylinder, transition due to cross-flow instability takes place when  $\chi$  is of order 100. However, as shown in reference 11, a single value of  $\chi$  is insufficient to adequately describe the conditions necessary for transition. In fact, for transition very close to the leading edge of an infinite swept wing in incompressible flow two independent parameters are needed. Figure 10 shows that, in this case,  $\chi$  and the streamwise flow shape factor  $H_{11}$  are a suitable combination.

In the general area of compressible flow with heat transfer, an extensive literature search has revealed that only a small number of experimental investigations have been carried out into the problem of transition via cross-flow instability when the free stream Mach number is supersonic. Most significantly, no example has been found in which cross-flow induced transition has occurred on the windward face of a swept circular cylinder.

Although in several cases, e.g. Creel, Beckwith and Chen<sup>12</sup>, there is clear evidence of the presence of streamwise vortices in the laminar layer. These vortices are characteristic of cross-flow instability. However in reference 13, Stainback presents heat transfer data taken on a slab delta wing with cylindrically blunted leading edges. The leading edge swept back is 60°, the free stream Mach number

is 4.95 and the wall-to-total temperature ratio is 0.60. Figure 11 shows results for Stainback's plain delta model at zero angle of attack. It is apparent that the attachment line is laminar as is the entire cylindrical portion of the leading edge. However, at the highest free stream unit Reynolds number ( $12.24 \times 10^6/\text{ft}$ ), transition occurs on the flat part of the wing very close to the shoulder. Under these conditions, the value of  $\bar{R}_\tau$  on the attachment-line is 530 and, since the delta wing has a smooth surface with no obvious source of attachment-line contamination, the observation of laminar flow is consistent with our current expectations (see the previous section).

Figure 12 shows the development of the cross-flow Reynolds number  $\chi$  (integral definition) as a function of the surface distance measured from the attachment line. The variation exhibits all the characteristic features for flow close to a swept leading edge. At the attachment line ( $x = 0$ ),  $\chi$  is zero. Over the cylindrical leading edge,  $\chi$  increases very rapidly reaching a maximum at the "shoulder" ( $x = 1.571R$ ). Beyond the shoulder there is a modest reduction of  $\chi$  leading to a local minimum when  $x/R$  is approximately 4.5. Thereafter, as the local surface pressure reduces with increasing distance from the leading edge (following the "blast wave" trend),  $\chi$  increases slowly, but monotonically. The point of transition onset is marked on the figure showing that, in this case, transition is occurring when  $\chi$  is 400. However, it is immediately apparent that there are several problems

1. The variation of  $\chi$  with  $x$  is multivalued. There are three values of  $x$  at which  $\chi$  is equal to 400!
  2. The value of 400 for transition onset is three times the value for transition onset in incompressible flow
- and
3. Further increases in free-stream Reynolds number could well produce transition on the attachment line since  $\bar{R}_\tau$  is close to 600 i.e. it may be impossible to bring transition onto the cylindrical leading edge through the mechanism of cross flow instability.

A second important experimental study of transition on swept wings is that conducted by Jillie and Hopkins<sup>14</sup>. In this case, a flat plate with varying degrees of small, leading-edge blunting was tested at different sweep angles for free-stream Mach numbers ranging from 2.5 to 4.0. A typical configuration is shown in figure 13 which illustrates the type of results obtained with their surface

sublimation technique (naphthalene and petroleum ether). The transition front is clearly indicated - as is the streak pattern in the laminar region, which is characteristic of the presence of cross-flow instability. When the plate leading edge was swept, the streamwise Reynolds number for transition was reduced relative to the unswept value and a typical example of the behaviour is given in figure 14. As sweep angle was increased the transition Reynolds number ratio decreased monotonically. Moreover, as is also clear from the figure, increasing the leading edge bluntness also reduced the transition Reynolds number ratio.

There is an important difference between the Jillie and Hopkins experiment and that of Stainback. In the latter case transition occurred very close to the leading edge whilst in the former transition is occurring some distance back along the chord e.g. in figure 13 transition is at  $x/d$  of 16. The consequence of transition being a large distance from the leading edge is that the pressure field is of the blast wave type and entropy swallowing may become an issue. If it is assumed that the flow at the edge of the boundary layer has been processed by the plane part of the leading-edge, bow shock, then, as the sweep is increased at fixed free-stream conditions, the local value of the Reynolds number is increased. Provided the local value of the Reynolds number at transition remained constant, the effect of sweep would be to move the transition front forward. The dashed line drawn on figure 14 indicates how the free-stream streamwise transition Reynolds number would vary in response to sweep changes if the local streamwise transition Reynolds number was constant. It is clear that, whilst the general shape of the curves is rather similar to the dashed line, the results do not support the concept of a fixed transition Reynolds number. This means that the sweep must be modifying the value of the local transition Reynolds number i.e. this is evidence of the existence of cross-flow instability. It is also clear that increasing the leading edge bluntness reduces the transition Reynolds number and it is conjectured that this is due to the consequential change in the pressure distribution.

A sample computation of the cross-flow Reynolds number,  $\chi$ , has been carried out for the case in which the leading edge radius was 0.5 mm ( $R_d = 0.5 \times 10^5$ ). The distribution of  $\chi$  is given in figure 15 for a range of sweep angles. The calculations show that the cross-flow Reynolds number reaches a maximum at sweep angles between 60 and 70°. This corresponds to the conditions which give the minimum values of

the transition Reynolds number. Moreover, the experimentally observed transition locations for 60° and 68° of sweep correspond to a constant value of  $\chi$ . The critical value of  $\chi$  is approximately 140. This value is very different from that found in Stainback experiment but it is typical of the values found in incompressible flow.

The work of Jillie and Hopkins has been complemented by a similar study performed by Pate and Groth<sup>15</sup>. In this case a swept, slightly blunt plate was tested over a range of free-stream unit Reynolds numbers. The results for a single value of leading edge bluntness ( $t \approx 0.15$  mm) are given in figure 16. These show that increasing the sweep reduces the free stream transition Reynolds number substantially. Moreover, there is a variation with the free stream unit Reynolds number. However, the data clearly show that, as sweep angle is increased, the influence of unit Reynolds number is substantially reduced. This is demonstrated in figure 17 where a coefficient  $N$  has been determined from the relation

$$R_{e_t} = A(\text{Unit } R_e)^N$$

$N$  is found to decrease in proportion to  $\cos^2 \Lambda$ . The reduced dependence of transition Reynolds number upon free stream Reynolds number has also been observed by King<sup>16</sup> who studied transition on a circular cone at incidence in the Mach 3.5 Quiet Tunnel at NASA Langley. It is tempting to conclude from this that useful work on transition for three-dimensional shapes may be performed in conventional wind tunnels. In order to reinforce this point, it is possible to compare the data of Jillie and Hopkins and Pate and Groth for a free stream Mach number of 3, with similar leading edge bluntness but with a factor of three difference in the free stream unit Reynolds numbers. These results are presented in figure 18, where it can be seen that the agreement is quite good. Of particular interest is the way in which the role of leading edge bluntness changes with sweep angle. At the lower sweep angles, increasing the leading edge bluntness increases the free-stream transition Reynolds number i.e. at a fixed free-stream unit Reynolds number the transition location moves back along the chord. However, at a sweep angle of about 25°, this effect is reversed i.e. increasing the bluntness causes transition to move forward. The clear implication is that sweep angle variations are producing a fundamental change in the underlying instability mechanism which is causing the transition. Finally figure 19 shows good agreement between the two data sets when the ratio



of the swept to unswept transition Reynolds numbers is plotted against sweep angle. Once again there is no indication of a strong unit Reynolds number effect.

Under high Mach number conditions it is well known that there is an interaction between the viscous, near surface, flow and the inviscid outer flow. The consequence of this is that, even for a sharp edged flat plate at zero angle of attack, a shock wave will be formed at the leading edge and a surface pressure field will be established - see figure 5. If the plate is yawed the strength of the leading edge shock wave will be reduced and a cross flow will be established in the viscous layer. This may affect the location of transition. Strong evidence that the swept interaction can cause major changes to the location of transition is provided by East and Baxter<sup>17</sup>. Using the thermochromic liquid crystal technique, they were able to show that the effect of sweeping the wing was to bring boundary layer transition forward to a position close to, and parallel to, the leading edge. By quantitative analysis of the colour changes in the crystals, East and Baxter were also able to demonstrate that, when transition takes place, the local heating rate rises very rapidly as indicated in figure 20. This demonstrates the importance of understanding the transition when designing a vehicle which will travel at hypersonic speed.

As previously noted, the parameter which characterises the flow modifications due to the interaction is  $\Omega_N$  where

$$\Omega_N = \cos^4 \Lambda M_\infty^3 \left( \frac{\mu_\infty}{a_\infty \rho_\infty x} \right)^{1/4}$$

In the interacting flow, a pressure distribution is established and, when the leading edge is swept, a cross-flow develops in the viscous layer. For an infinite-swept, leading edge, the cross-flow Reynolds number  $\chi$  is such that

$$\chi = \chi(\Lambda, M_\infty, \Omega_N, T_w/T_o)$$

By way of an illustrative example, the development of  $\chi$  has been computed for flow with a Mach number of 9 over a plate with a range of leading edge sweep back angles. The resulting variation of  $\chi$  with chordwise position,  $x$ , is shown in figure 21. There are a number of features which should be noted.

a) Initially,  $\chi$  rises rapidly with  $x$ . However, as  $x$

increases the rate of rise reduces.

- b) At large values of  $x$ ,  $\chi$  has an asymptotic value i.e. once the cross-flow Reynolds number has been established it remains in the flow and
- c) The maximum cross-flow Reynolds number increases rapidly with increasing sweep angle - up to angles of at least 80°.

An initial analysis of this problem has been carried out by Poll<sup>18</sup>. This has revealed that the maximum value of  $\chi$  occurs close to the leading edge (as in figure 21) and that

$$\chi_{\max} \propto M_\infty^3 \tan \Lambda$$

where the constant of proportionality is a weak function of sweep, Mach number and wall-to-total temperature ratio. Particularly noteworthy is the fact that the magnitude of  $\chi$  depends upon  $M_\infty^3$  and not upon the value of the free-stream unit Reynolds number! As the flight Mach number increases towards the levels necessary for orbital insertion, very large cross-flow Reynolds numbers may be generated. This could constitute a transition mechanism which can operate at very high altitudes and very low Reynolds numbers!

## 6. Conclusions

Based upon a preliminary assessment of current knowledge of transition near the leading edge of a swept back wing, the following conclusions may be drawn.

- a) Attachment-line transition is very important at hypersonic speeds. It is also the best understood of the three-dimensional mechanisms. However, this understanding rests upon firmly established empirical correlations. At present, there are no theoretical verifications for any of the criteria.
- b) In the absence of attachment-line contamination, transition can be brought close to the leading edge by the combined effects of nose bluntness and sweep. At zero sweep, increasing the nose radius can delay transition onset up to a maximum value of  $x$ . This is due, to some extent, to the fact that the generation of a strong bow-shock produces a consequential reduction in the local unit Reynolds number in the region close to the leading edge. Sweeping the leading edge weakens the bow shock. This causes the local unit Reynolds number at the edge of the viscous layer to rise and, for fixed free-stream conditions, the transition should move forward.

This effect is clearly limited in its extent. However, the available experimental data indicate that, for sweep angles greater than  $30^\circ$ , the forward movement of transition with increasing leading edge radius continues without limit. It is postulated that this is the result of cross flow instability within the viscous layer.

and

- c) When the leading edge is perfectly sharp, viscous-inviscid interaction leads to the generation of a shock wave which modifies the local conditions at the edge of the viscous layer. The induced shock wave is strongest at zero sweep. Consequently, the application of sweep back, at fixed free-stream conditions, should cause transition to move forward. This is borne out by experimental observation. However, the sweeping of the leading edge also introduces cross flow. The maximum, cross-flow Reynolds number occurs in the region of "weak" interaction. It increases as  $M_\infty^3$  and does not depend upon the free-stream unit Reynolds number.

#### References

1. Anderson, J.D. Hypersonic and High Temperature Gas Dynamics, McGraw Hill, 1989.
2. Poll, D.I.A. The development of intermittent-turbulence on an infinite swept attachment line including the effect of compressibility. The Aeronautical Quarterly Vol. XXXIV, Part 1, Feb. 1983.
3. Poll, D.I.A. Transition in the infinite swept attachment line boundary layer. The Aeronautical Quarterly Vol. XXX, Nov. 1979.
4. Poll, D.I.A. The effect of isolated roughness elements on transition in attachment-line flows. Third IUTAM Symposium of Laminar-Turbulent Transition, Springer Verlag, 1989.
5. Arnal, D., Juillen, J.C., Jallade, S. Recherches sur la transition aux vitesses élevées. Rapport No. 27/5005.15 DY, DERAT, CERT-ONERA, March 1989.
6. Creel, T.R., Beckwith, I.E., Chen, F.J. Transition on swept leading edges at Mach 3.5. Journal of Aircraft Vol. 25, No. 10, Oct. 1987.
7. Skuratov, A.S. and Fedorov, A.V. Supersonic boundary layer induced by roughness on the attachment line of a yawed cylinder. Izvestiya Akademii Nauk SSSR, Mekhanika Zhidkosti i Gaza No. 6, pp 28-35, Nov-Dec. 1991.
8. Hall, P., Malik, M.R. and Poll, D.I.A. On the stability of an infinite swept attachment line. Proceedings of the Royal Society, Series A, Volume 395, Oct. 1984.
9. Poll, D.I.A. 3-D transition to turbulence by contamination. Part II Accurate determination of the attachment-line chordwise velocity gradient. Department of Engineering, University of Manchester, March 1993.
10. Pfenninger, W. Laminar Flow Control - Laminarization. AGARD-R-654, April 1977.
11. Poll, D.I.A. Some observations of the transition process on the windward face of a long yawed cylinder. Journal of Fluid Mechanics, Vol. 150, pp 329-356, January 1985.
12. Creel, T.R., Beckwith, I.E. and Chen, F.J. Transition on swept leading edges at Mach 3.5. Journal of the Aircraft, Vol. 25, No. 10, October 1987.
13. Stainback, P.C. Heat transfer measurement at a Mach number of 4.95 on two  $60^\circ$  swept delta wings with blunt leading edges and dihedral angles of  $0^\circ$  and  $45^\circ$ . NASA TN-D 549, January 1961.
14. Jillic, D.W. and Hopkins, E.J. Effects of Mach number, leading-edge bluntness and sweep on boundary layer transition on a flat plate. NASA TN D-1071, September 1961.
15. Pate, S.R. and Groth, E.E. Boundary-layer transition measurements on swept wings with supersonic leading edges. AIAA Journal, Vol. 4, No. 4, pp 737-738, April 1966.
16. King, R.A. Three-dimensional boundary-layer transition on a cone at Mach 3.5. Experiments in Fluids, 13, pp 305-314, 1992.
17. East, R.A. and Baxter, D.R.J. Comparative heat transfer measurements on caret and flat compression surfaces for hypersonic intakes. First International Hypersonic Waverider Symposium, October 1990, University of Maryland, USA.
18. Poll, D.I.A. Role of viscous-inviscid interaction on transition near a swept leading edge in hypersonic flow. 1993 Hypersonics Symposium, Wright-Patterson Airforce Base, Ohio, USA, May 1993.

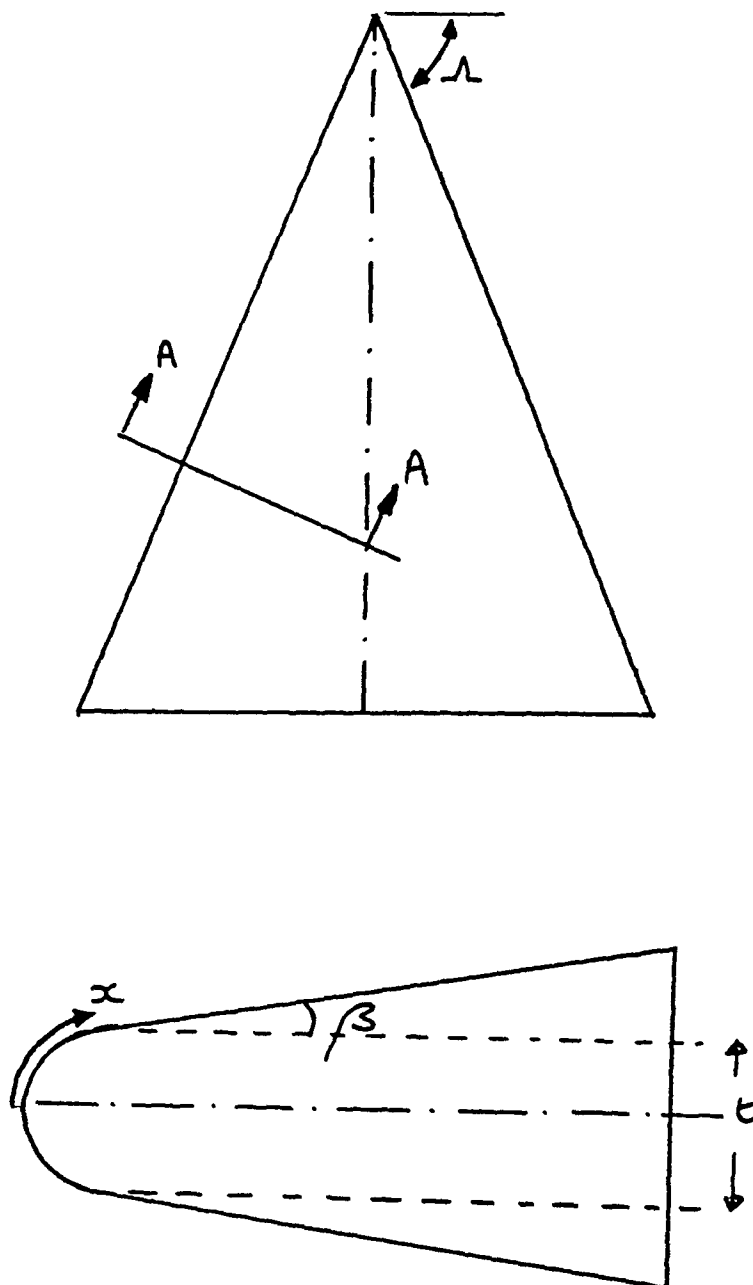


Figure 1 Typical plan form and normal to leading edge section details

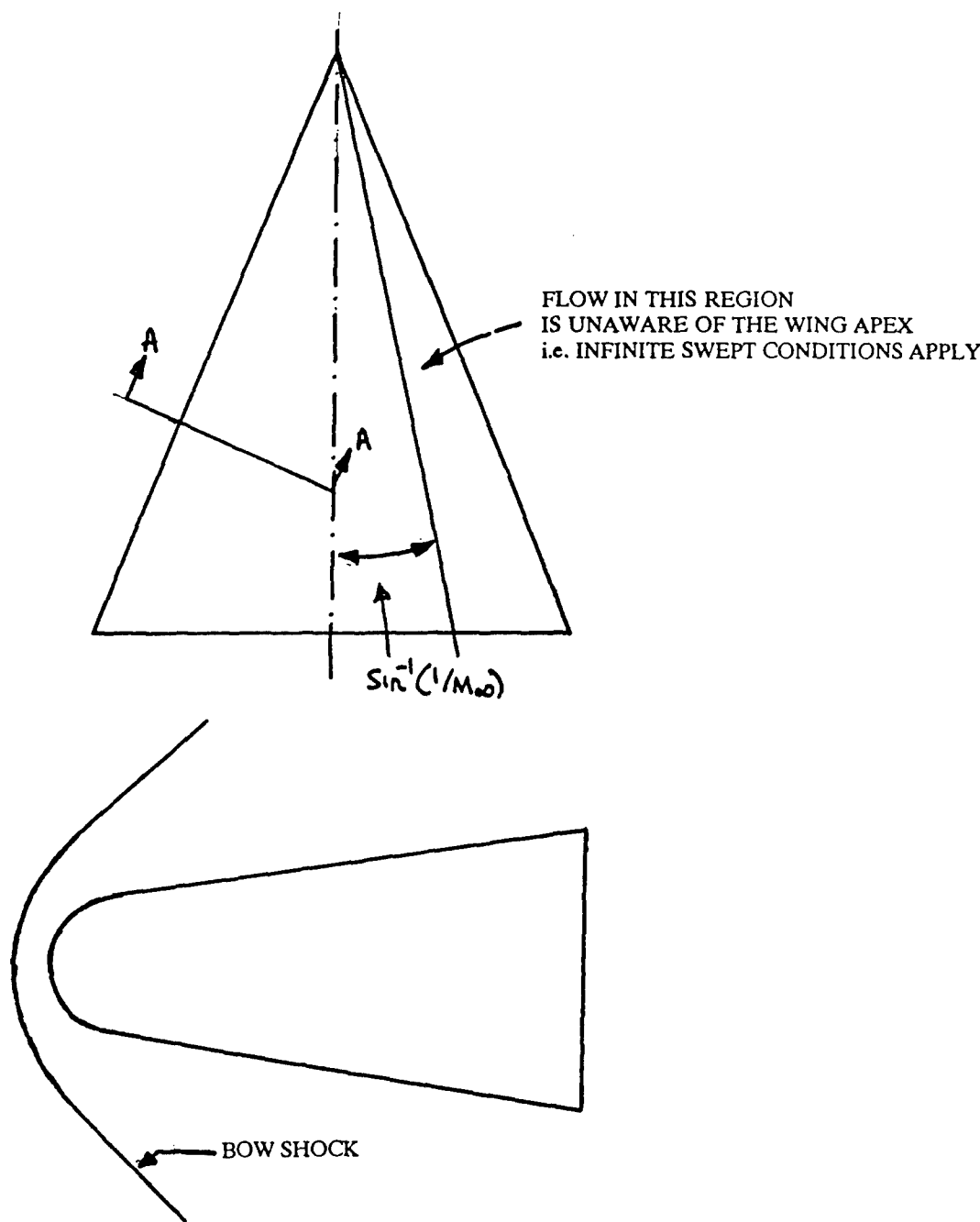


Figure 2      General characteristics of the inviscid flow for a delta wing at high Mach number

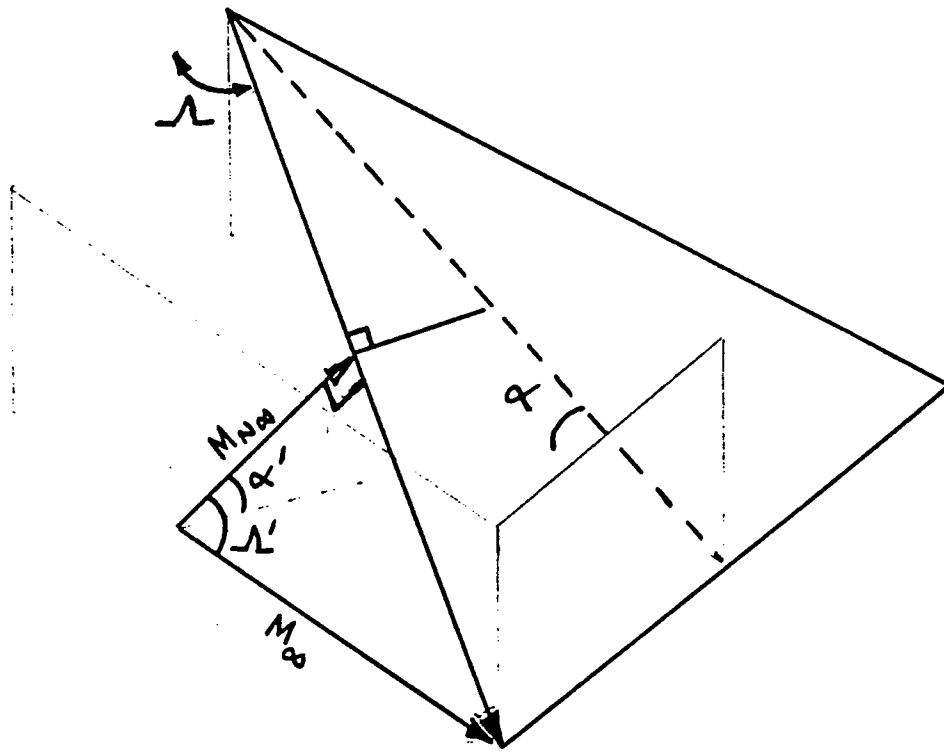


Figure 3      Relationship between streamwise flow components and those normal to the wing leading edge

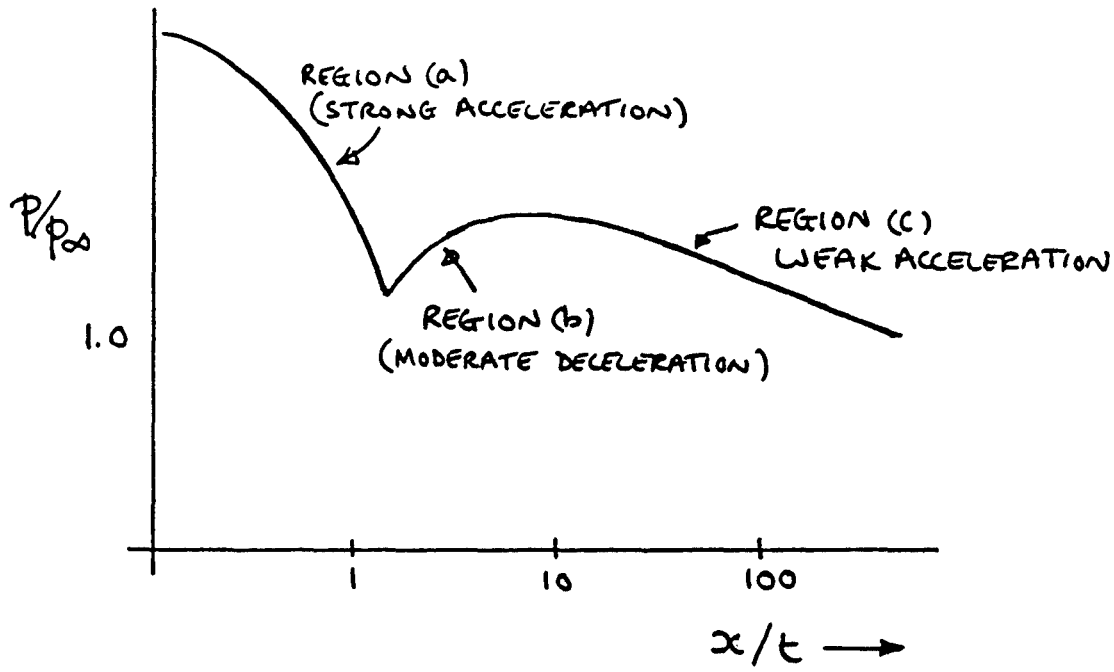


Figure 4 Typical pressure distribution near the leading edge of a blunt swept wing

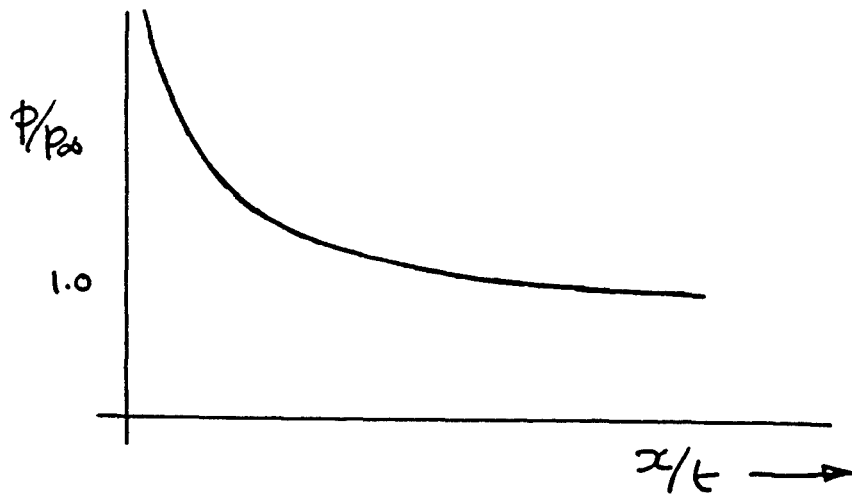


Figure 5 Form of the pressure distribution induced by viscous-inviscid interaction

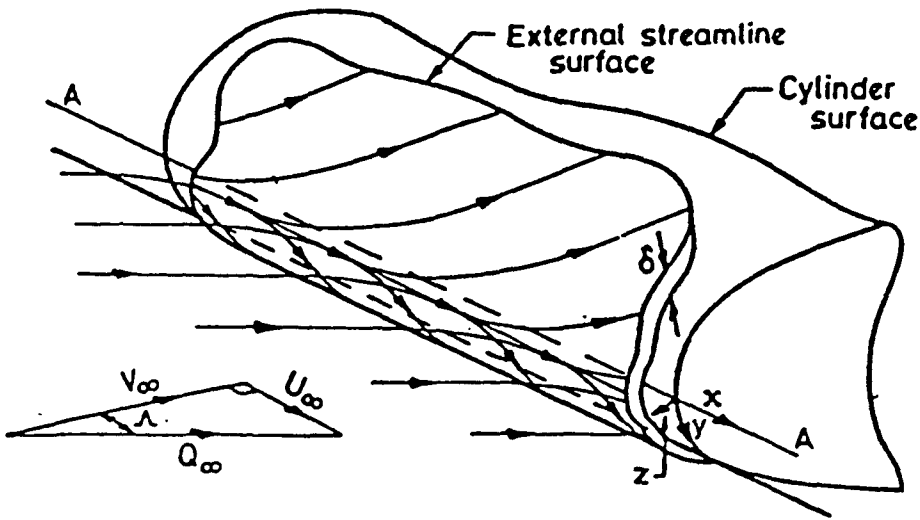


Figure 6      Standard attachment line picture

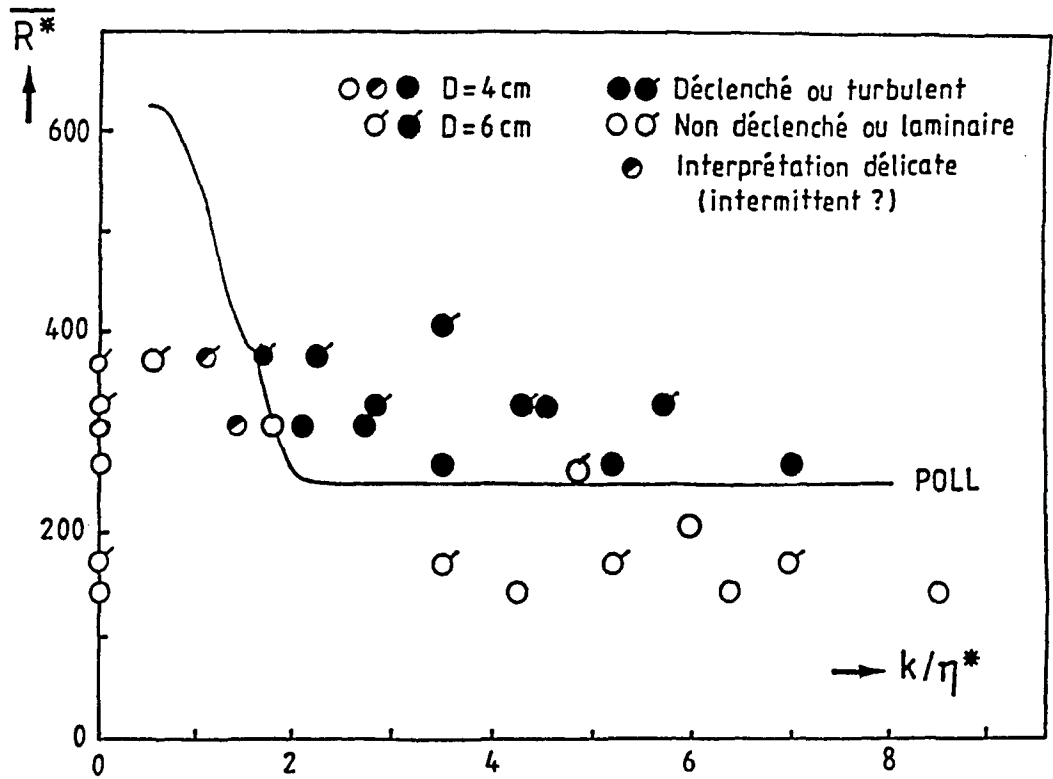


Figure 7      The variation of critical Reynolds Number with roughness height for the onset of attachment line

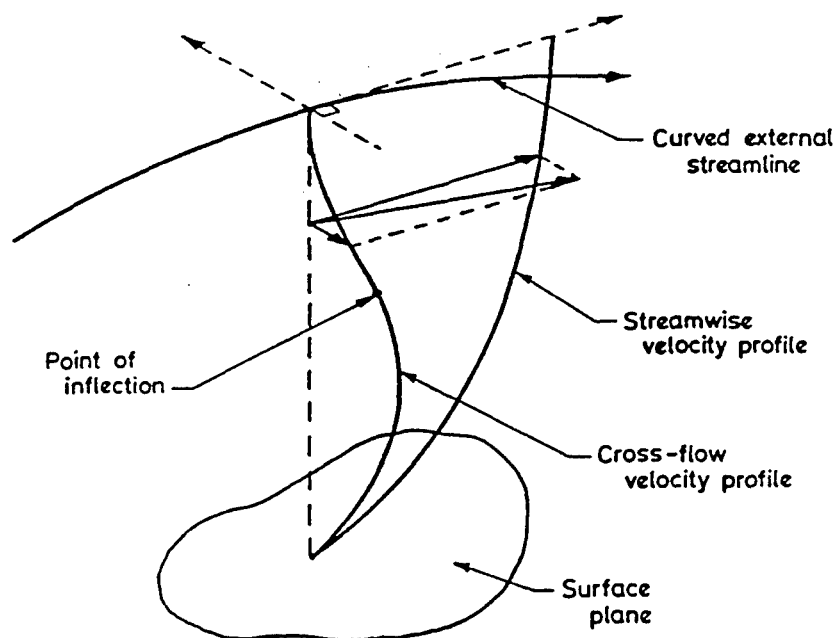


Figure 8 Typical boundary layer velocity distribution near the leading edge of a yawed cylinder

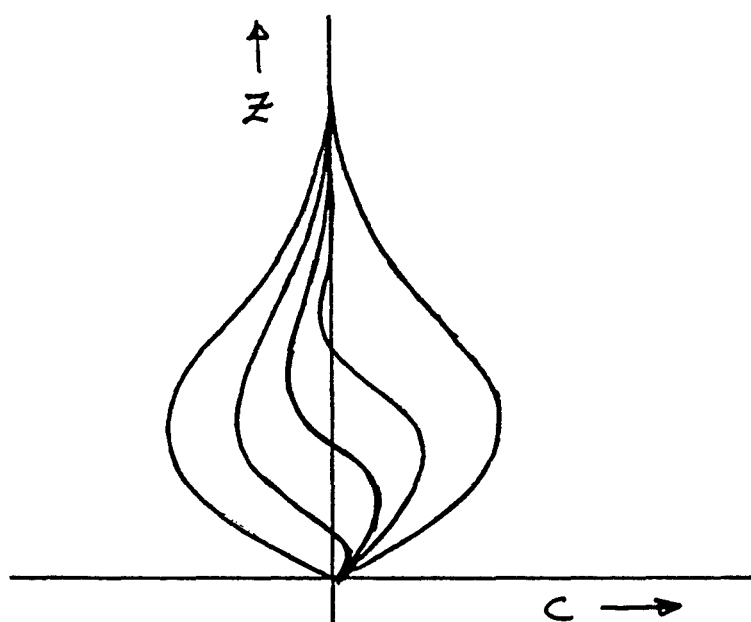


Figure 9 Various possible forms of the cross flow velocity profile



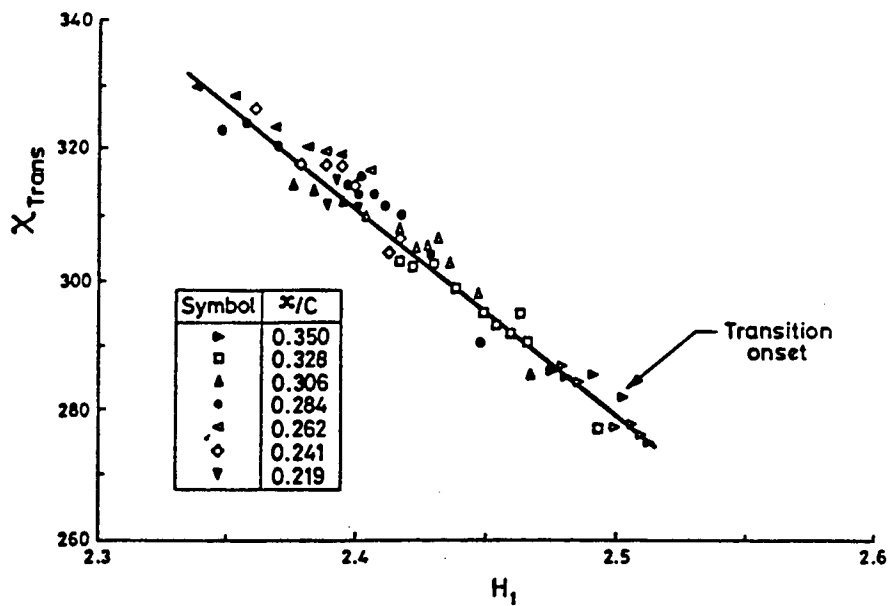


Figure 10 The variation of cross-flow Reynolds number with streamwise shape factor for transition on a yawed cylinder in low-speed flow

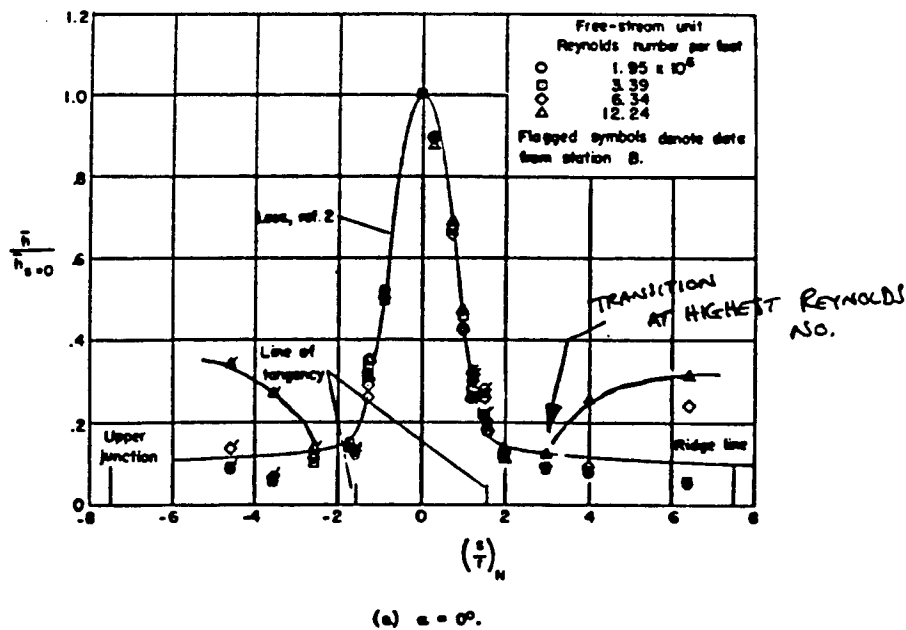


Figure 11 Chordwise distribution of heat transfer for a  $60^\circ$  swept cylindrically blunted slab wing at Mach number 4.95 and  $0^\circ$  angle of attack

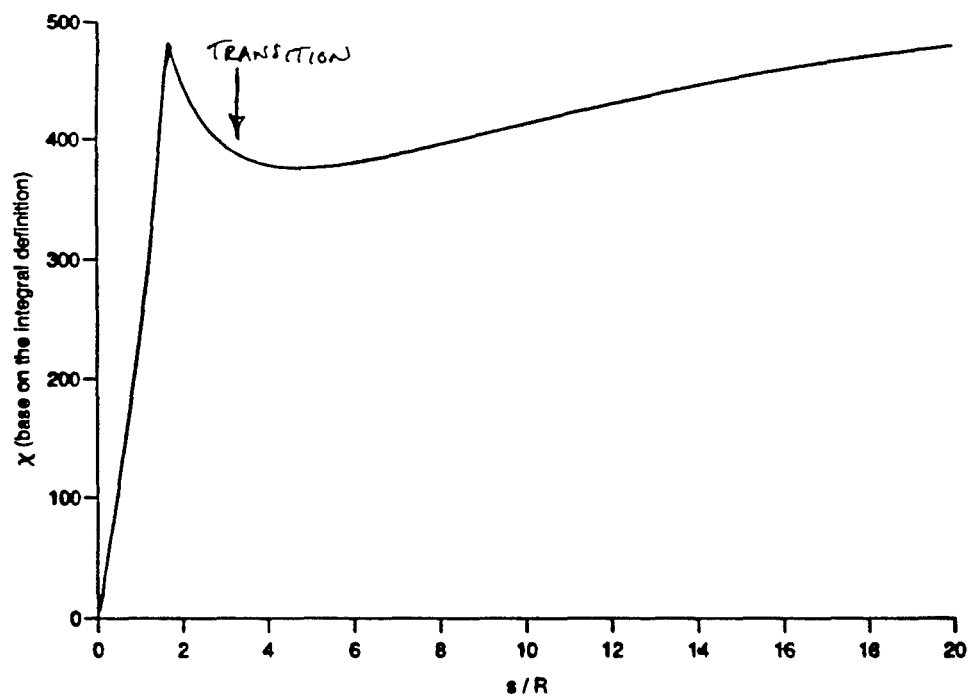


Figure 12 Chordwise variation of crossflow Reynolds number for Stainback's delta wing

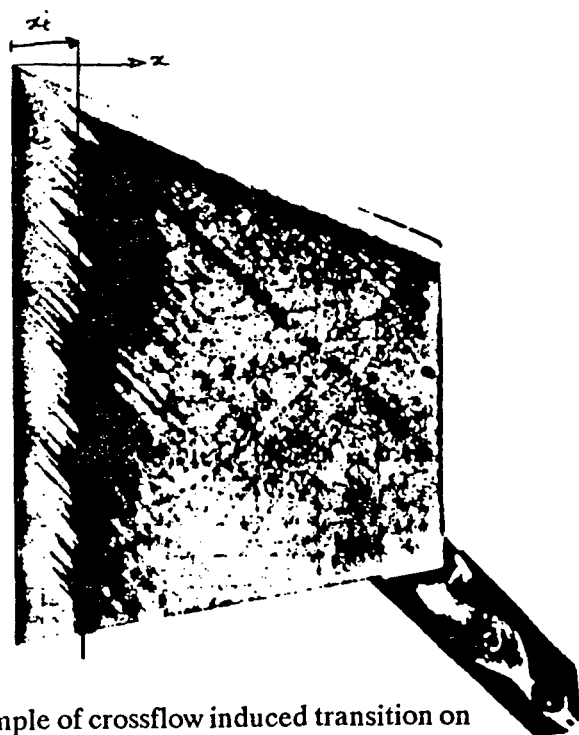


Figure 13 An example of crossflow induced transition on a wing swept at  $45^\circ$  with a leading edge radius of .02" in a Mach 4 flow (after Jillie and Hopkins reference 14)

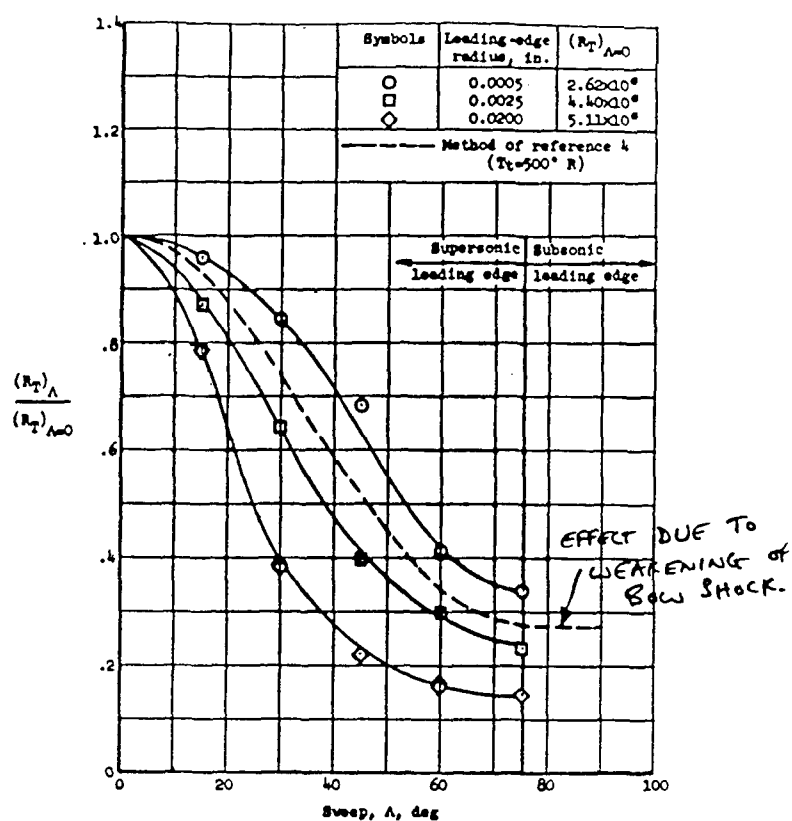


Figure 14 Variation of streamwise transition Reynolds number with sweep and bluntness at Mach 4 (after Jillie and Hopkins reference 14)

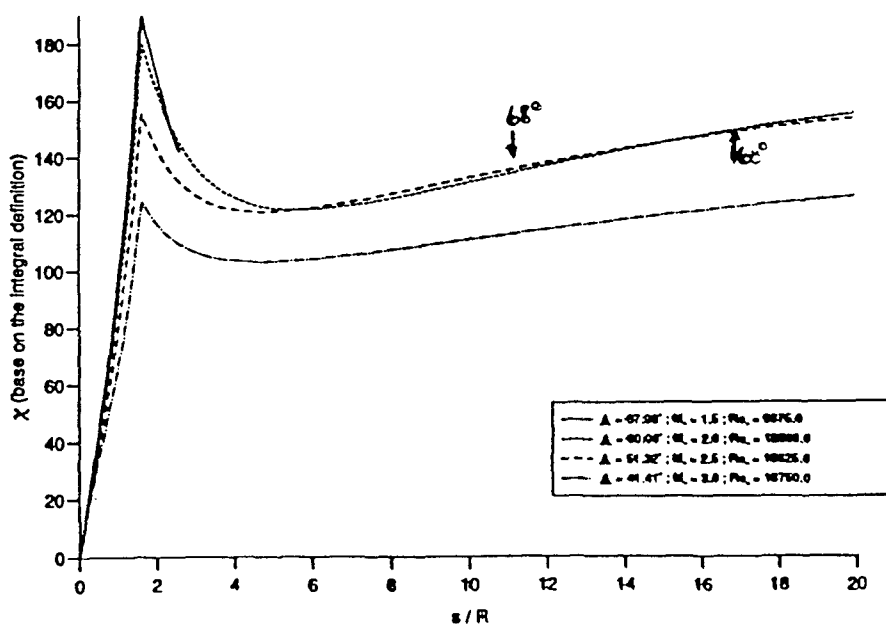


Figure 15 Variation of cross-flow Reynolds number with surface position and sweep angle for the Jillie and Hopkins experiment

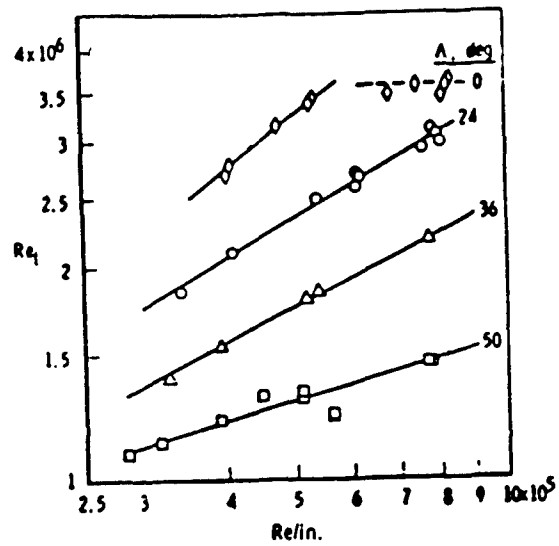


Figure 16 Variation of streamwise transition Reynolds number with freestream unit Reynolds number and sweep angle for a flat plate at Mach 3 (after Pate and Groth reference 15)

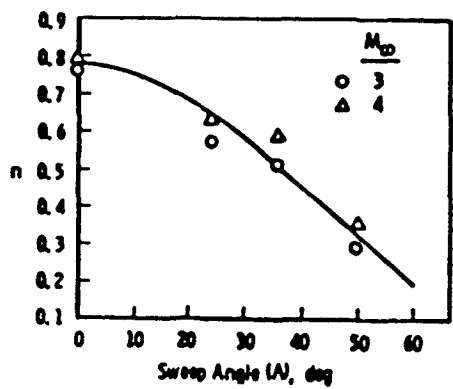


Figure 17 Dependence of the unit Reynolds number exponent upon sweep angle for the Pate and Groth data

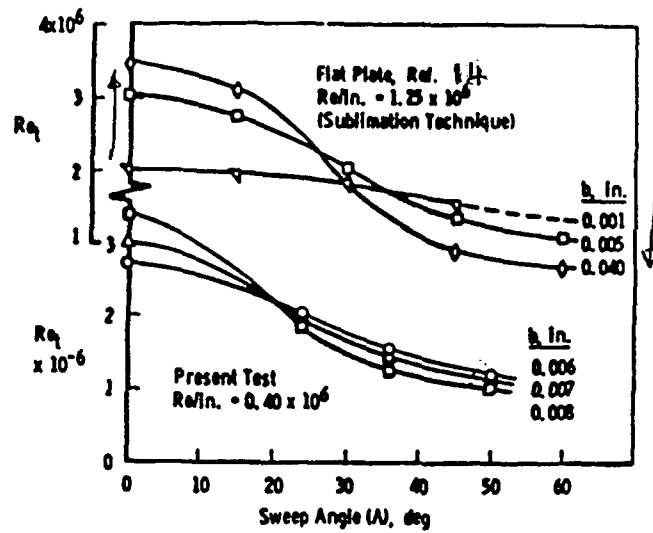


Figure 18 Effect of leading edge bluntness and sweep angle upon the streamwise transition Reynolds number for a flat plate (after Pate and Groth)

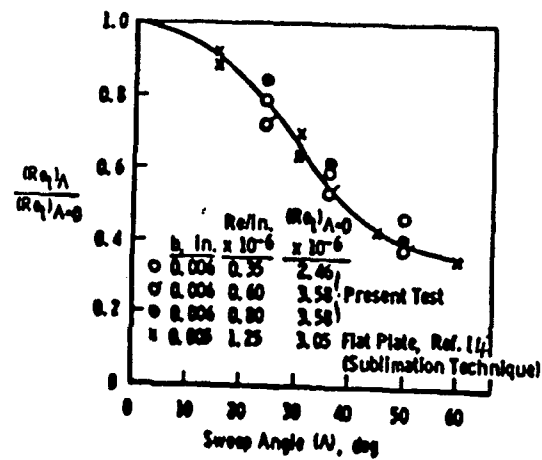


Figure 19 Normalised transition Reynolds number as a function of sweep angle for fixed nose bluntness and varying free stream unit Reynolds number

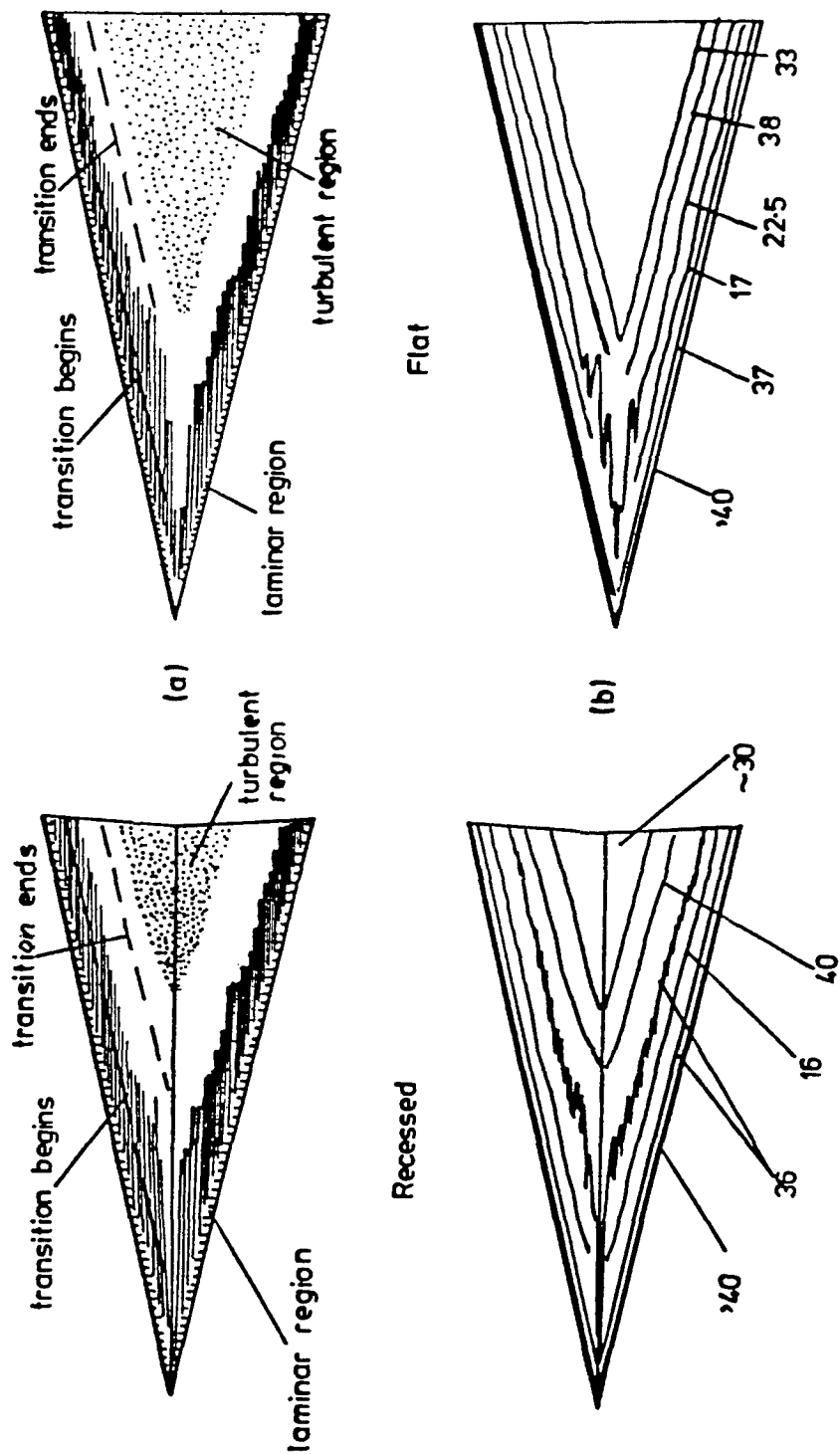


Figure 20 General features and heat transfer contours for delta wings in hypersonic flow (East and Baxter )

$M_\infty=8.80$ ,  $Re = 3.773 \times 10^6$ ,  $T_w=300K$ ,  $T_\infty=64.3K$ .

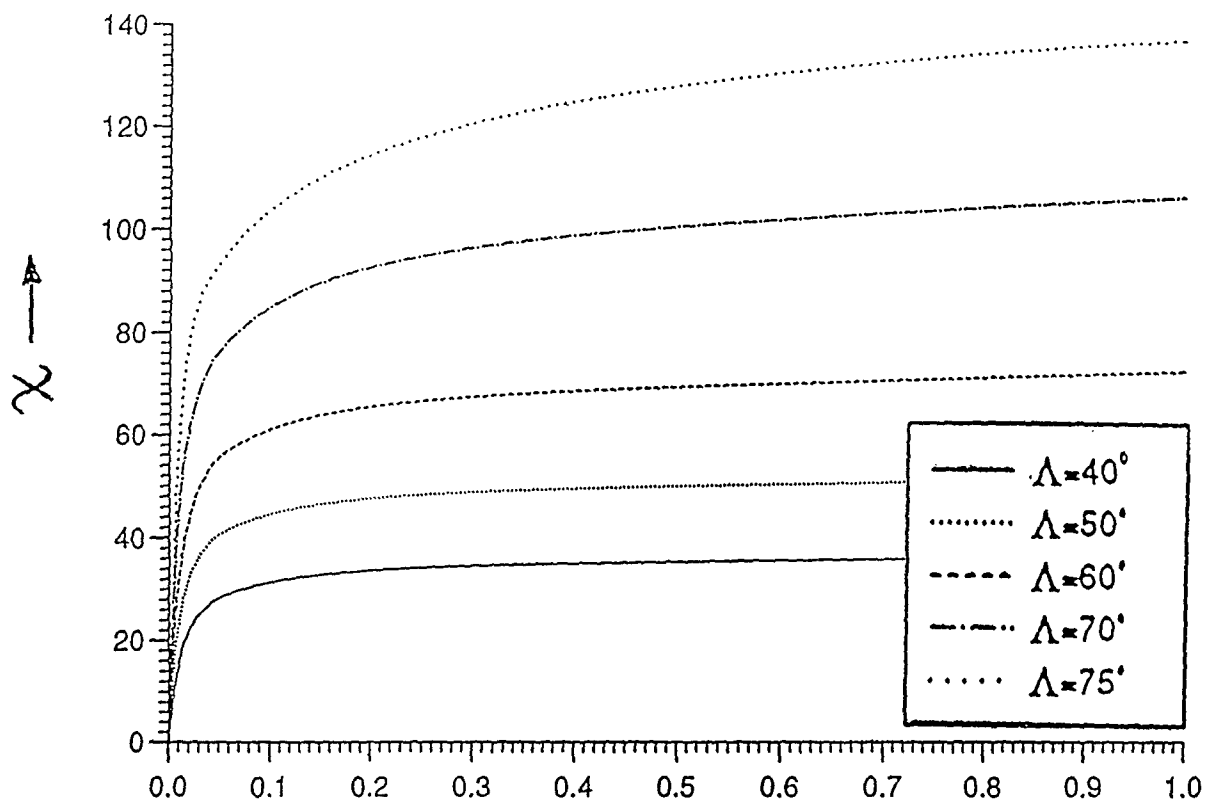


Figure 21 Variation of cross-flow Reynolds number with chordwise position for a swept flat plate with a sharp leading edge.

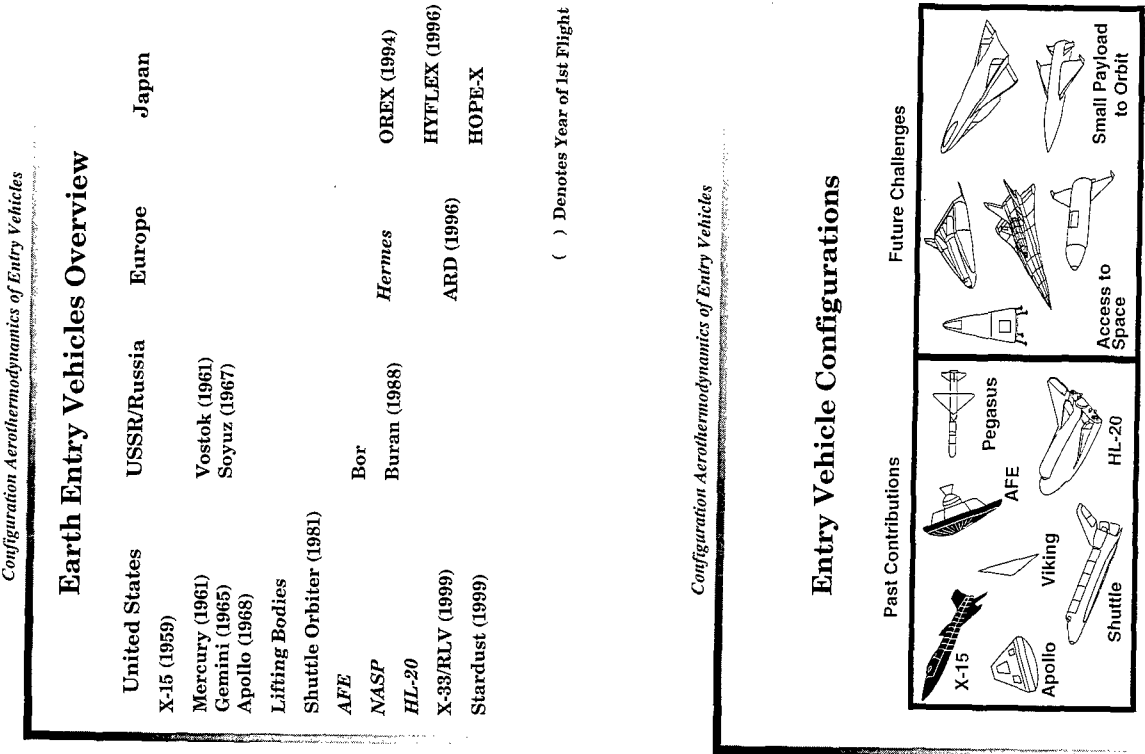
Configuration Aerothermodynamics  
of Entry Vehicles

David A. Throckmorton  
NASA Langley Research Center  
Space Transportation Office  
Mail Stop 367  
Hampton, VA 23681, USA

Part 1

Design Issues and Methods

“AGARD regrets that it is possible to print only the viewgraphs and not the text of this lecture, since the author was a last-minute replacement for another who was unable to take part, and thanks the author for doing so at very short notice.”





# Planetary Entry Vehicles Overview

United States	USSR/Russia	Europe
Viking (1975)	Venera (1965-75)	
Pioneer Venus (1978)	Mars (1971)	
Galileo (1989)	Vega (1984)	
Magellan (1989)		
Mars Pathfinder (1996)		
Mars Global Surveyor (1996)		
Mars 98 (1999)		Huygens
Mars MicroProbe (1999)		

( ) Denotes Year of 1st Launch

# Configuration Aerothermodynamics of Entry Vehicles

## Primary Aeroheating Design Issues

## Real-Gas Chemistry Effects on Aerodynamic Heat Transfer

TPS Surface / Gas Chemistry Interaction (Catalycity)

## Leaside Heat Transfer

## Boundary Layer Transition

### Configuration Aerothermodynamics of Entry Vehicles

## Primary Aerodynamic Design Issues

# Aerodynamic Performance, Stability and Control

## Hypersonic

## Supersonic

## Subsonic

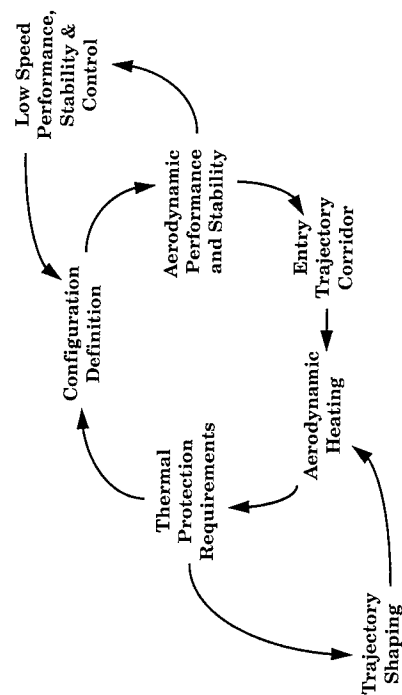
## Hypersonic Real-Gas Chemistry Effects

## Pitch Trim

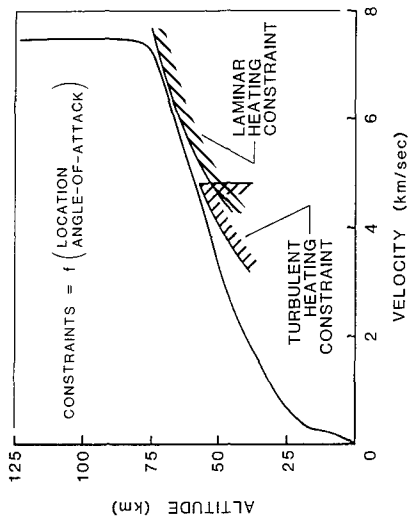
## Control Surface Effectiveness

Reaction Control System / Aerodynamic Flowfield Interactions

# Entry Vehicle Aerothermodynamic Design Process



### Entry Trajectory Shaping



### Aerothermodynamic Flowfield Concepts

#### Gas Fluid State

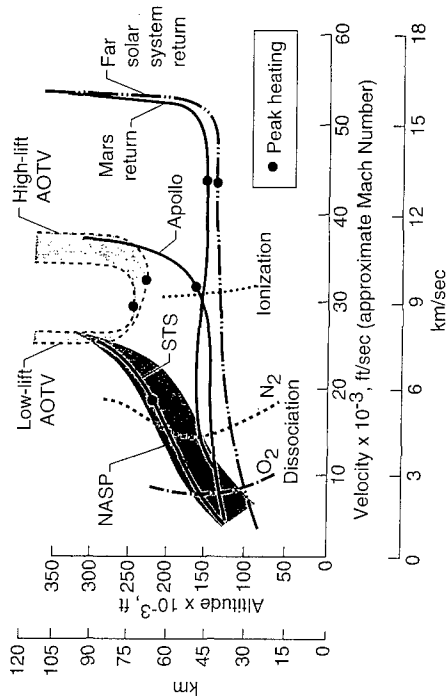
- Free-Molecular
- Transitional
- Continuum

### Aerothermodynamic Flowfield Concepts

#### Gas Chemistry State

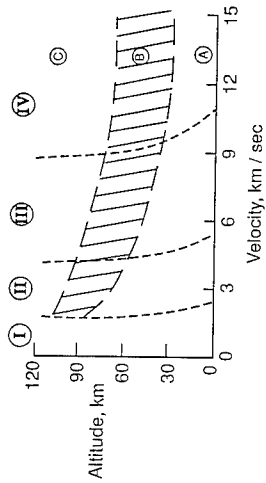
- Perfect Gas
- Equilibrium
- Finite-Rate Reacting (Nonequilibrium)
- Chemical Nonequilibrium
- Thermal Nonequilibrium
- Radiating

### Earth Atmospheric Flight Regimes



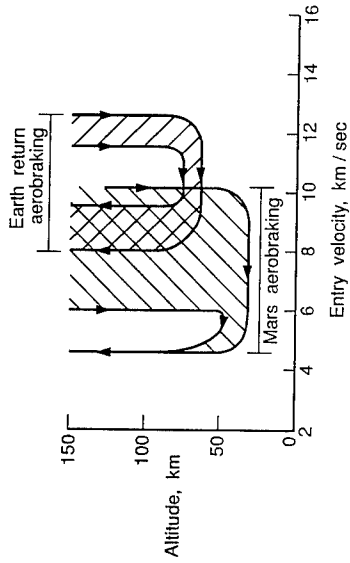
### Gas Fluid and Chemical State Regimes (Stagnation Region, 0.3-m Radius Sphere)

Regions with Chemical Thermal Nonequilibrium		Chemical Species in High Temperature Air	
Region	Aerothermal Equilibrium	Region	Chemical Model
(A)	Chemical and thermal equilibrium	(I)	2 species
(B)	Chemical nonequilibrium with thermal equilibrium	(II)	5 species
(C)	Chemical and thermal nonequilibrium	(III)	7 species
		(IV)	11 species



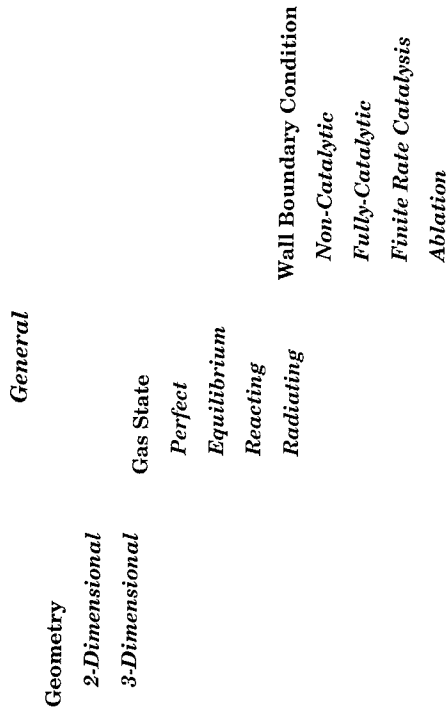
REF: Matheis, R. A. and Gault, P. A., "Thermochemical Nonequilibrium in the Stagnation Region of Mars Mission Vehicles," *Journal of Spacecraft and Rockets*, vol. 28, no. 3, September-October 1991.

### Typical Mars Mission Flight Trajectories

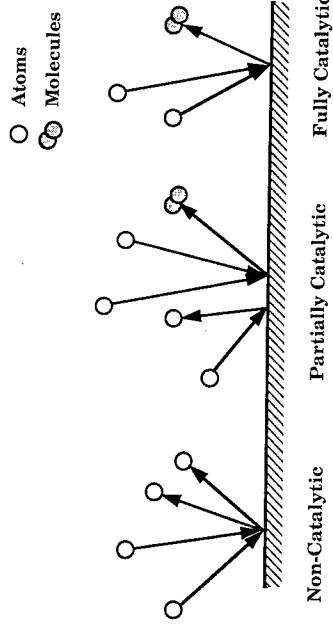


REF: Matheis, R. A. and Gault, P. A., "Thermochemical Nonequilibrium in the Stagnation Region of Mars Mission Vehicles," *Journal of Spacecraft and Rockets*, vol. 28, no. 3, September-October 1991.

### Aerothermodynamic Design/Analysis Influences



### Surface Catalytic Recombination



Configuration Aerothermodynamics of Entry Vehicles

## Aerothermodynamic Design/Analysis Influences

### Specific

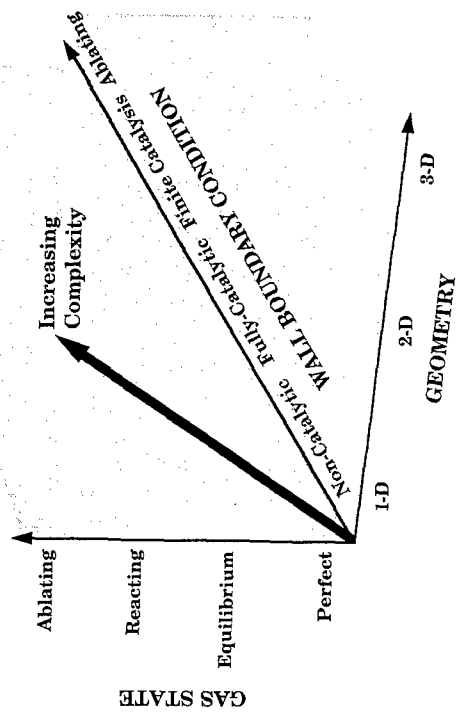
- Reaction Control System/Aerodynamic Flowfield Interactions
- Control Surface Effectiveness
- Separation and Reattachment
- Laminar-to-Turbulent Transition
- Roughness (Steps, Gaps, and Protuberances)
- Shock/Shock and Shock/Boundary-Layer Interactions
- Vortex Scrubbing and Impingement
- Dissimilar Materials

Configuration Aerothermodynamics of Entry Vehicles

## Computational Aerothermodynamics

Configuration Aerothermodynamics of Entry Vehicles

## Aerothermodynamic Simulation Complexity

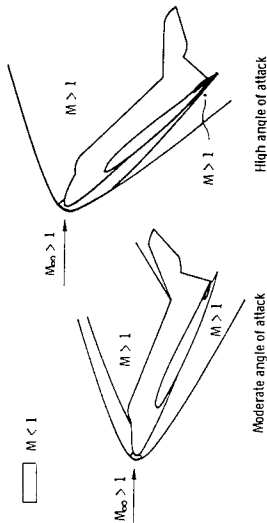


Configuration Aerothermodynamics of Entry Vehicles

## Computational Aerothermodynamic Methods

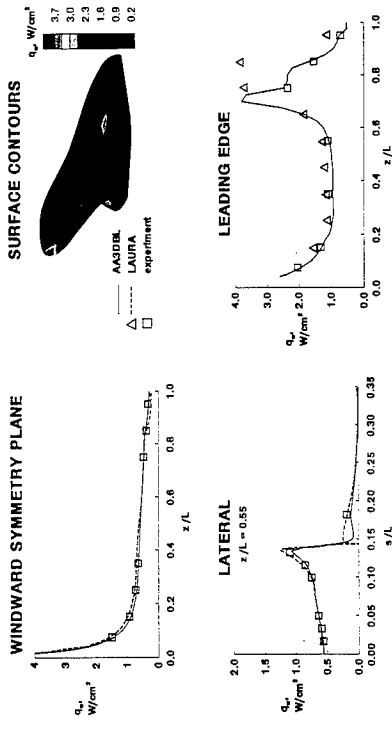
- Engineering Techniques
- Inviscid (Euler)  
w/ Boundary Layer (for Aeroheating)
- Viscous Shock Layer
- Full Navier-Stokes
- Direct Simulation Monte Carlo (DSMC)

# Hypersonic Flowfield Characteristics as a Function of Angle-of-Attack



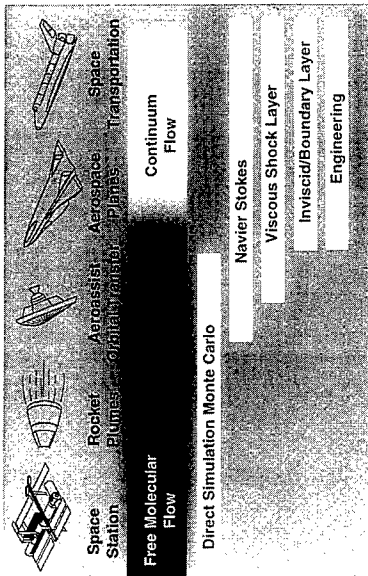
REF: Williamson, K. J., and Gault, R. A., "Solutions for the Three-Dimensional Configuration at Hypersonic Speeds," *Journal of Propulsion and Power*, vol. 10, no. 4, July-August 1994.

# Aeroheating to Modified Orbiter Configuration (M = 6, $\alpha = 30$ deg)

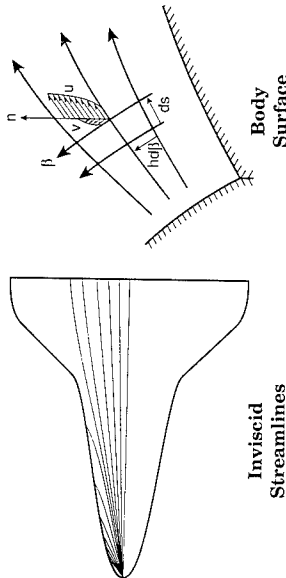


REF: Hattaway, H. H., H. G. Green, J. A., and Williamson, K. J., "Comparison of Heating Calculations with Experimental Data for a Modified Orbiter Configuration," *Journal of Propulsion and Power*, vol. 2, March-April 1992.

# Computational Aerothermodynamic Methods

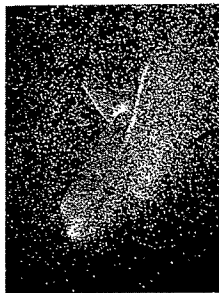


# Axisymmetric-Analog Boundary Layer Computation

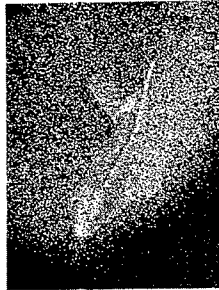


REF: Hattaway, H. H., H. G. Green, J. A., and Williamson, K. J., "Approximate Solution for Computing Heating Rates on Free-Form Bodies," *Journal of Propulsion and Power*, vol. 3, no. 3, May-June 1991.

## DSMC Simulation of Shuttle Orbiter Flowfield



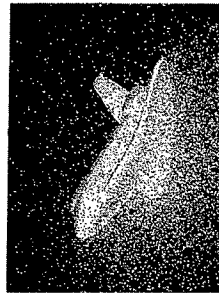
Alt = 120 km



Alt = 100 km

BLUE = Molecules unaffected by vehicle  
 RED = Molecules that have struck the surface  
 YELLOW = Blue in collision with red or yellow

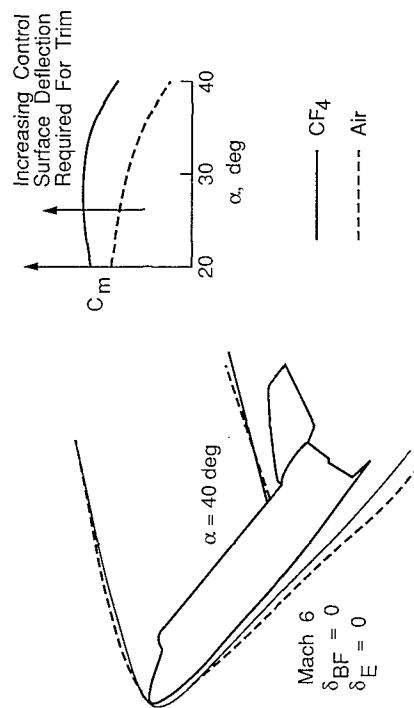
Alt = 170 km



ACF: Best G.A. "Application of the New Code to the Full Shock Geometry" AIAA Paper 96-002

## Experimental Aerothermodynamics

## Experimental Testing in CF4 Enables Simulation of Real Gas Effects in Air



## Experimental Facilities

Conventional Wind Tunnels

Air

Simulant Gases

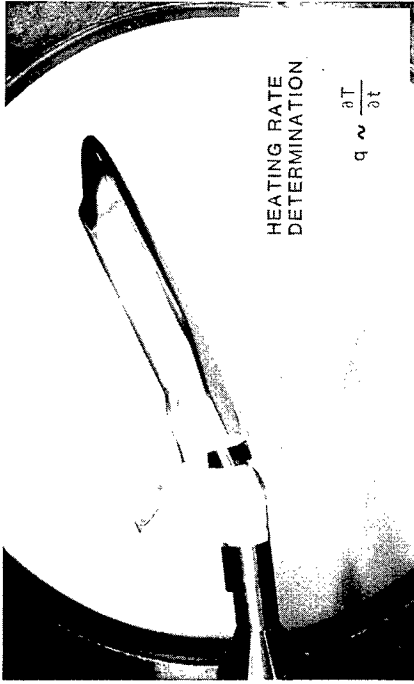
Impulse Facilities

Ballistic Ranges

## Experimental Methods

- Aerodynamics
  - Force and Moment Balance
  - Free-Flight
- Aeroheating
  - Thin Skin Calorimetry
  - Phase Change Paint
  - Thin Film Calorimetry
  - Phosphor Thermography

## Thin Skin Calorimetry



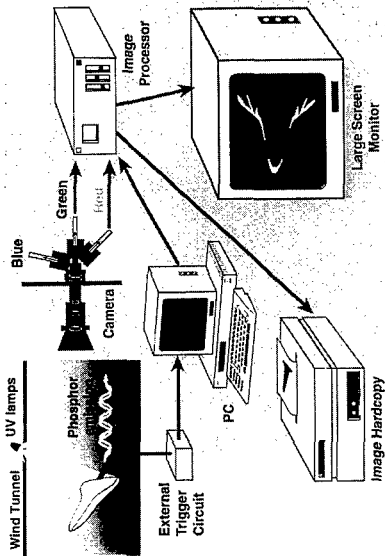
## Phase Change Paint



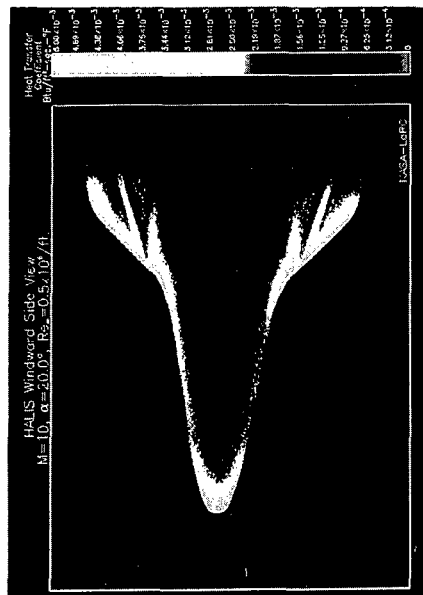
## Thin Film Calorimetry



### Phospher Thermography

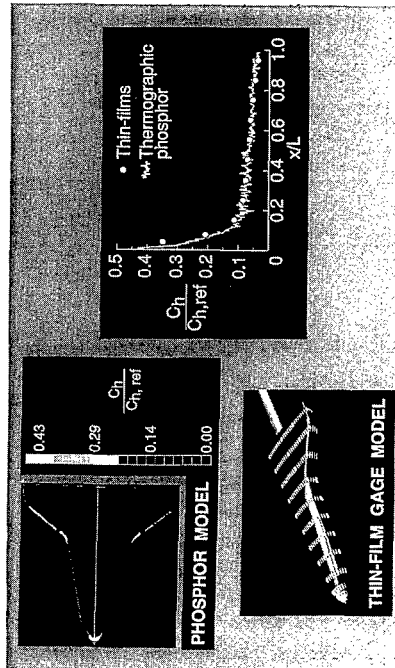


### Typical Phospher Thermography Data Image



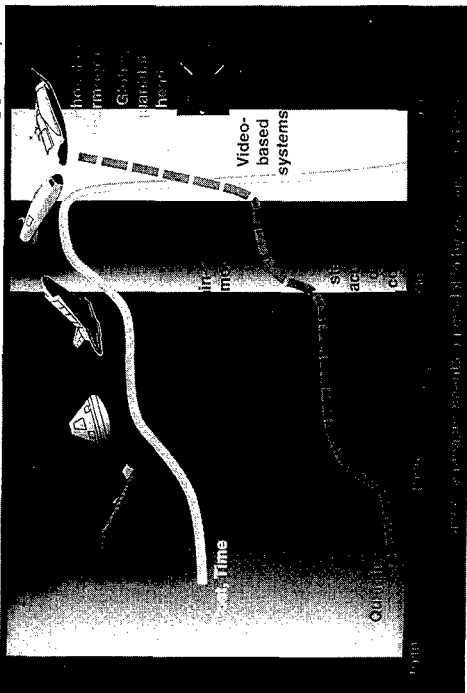
REF: Michel, J. R., "Aerothermodynamic Measurements and Predictions for Modified Orion at Mach 6 and 10," *Journal of Spacecraft and Rockets*, Vol. 1, No. 3, September-October 1965.

### Thin Film Gage / Thermographic Phospher Data Comparison



REF: Michel, J. R., "Aerothermodynamic Measurements and Predictions for Modified Orion at Mach 6 and 10," *Journal of Spacecraft and Rockets*, Vol. 1, No. 3, September-October 1965.

### Aeroheating Measurement Technology





**Configuration Aerothermodynamics  
of Entry Vehicles**

**David A. Throckmorton**  
NASA Langley Research Center

**Part 2**

*“Real-World” Experiences and  
Current Challenges*

*Configuration Aerothermodynamics of Entry Vehicles*

**Primary Aerodynamic Design Issues**

Aerodynamic Performance, Stability and Control

Hypersonic

Supersonic

Subsonic

Hypersonic Real-Gas Chemistry Effects

Pitch Trim

Control Surface Effectiveness

Reaction Control System / Aerodynamic Flowfield Interactions

*Configuration Aerothermodynamics of Entry Vehicles*

**Primary Aeroheating Design Issues**

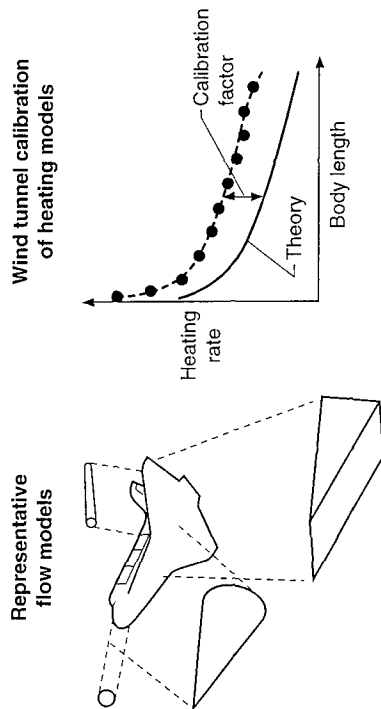
Real-Gas Chemistry Effects on Aerodynamic Heat Transfer

TPS Surface / Gas Chemistry Interaction (Catalycity)

Leeside Heat Transfer

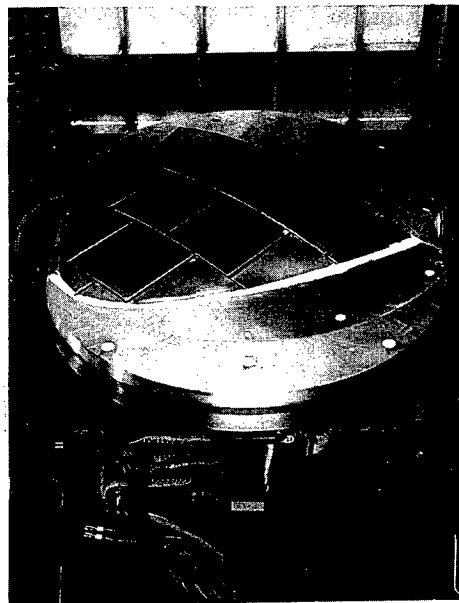
Boundary Layer Transition

# Shuttle Orbiter Design Heating Methodology



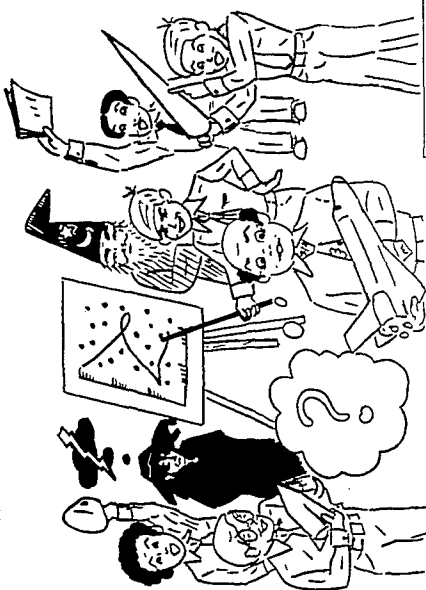
RDT, Reid, R. C. "Orbiter Entry Aerothermodynamics." Space Shuttle Technical Conference. NASA CP 2402, 1983.

# Orbiter Tile-Gap Heating Assessment



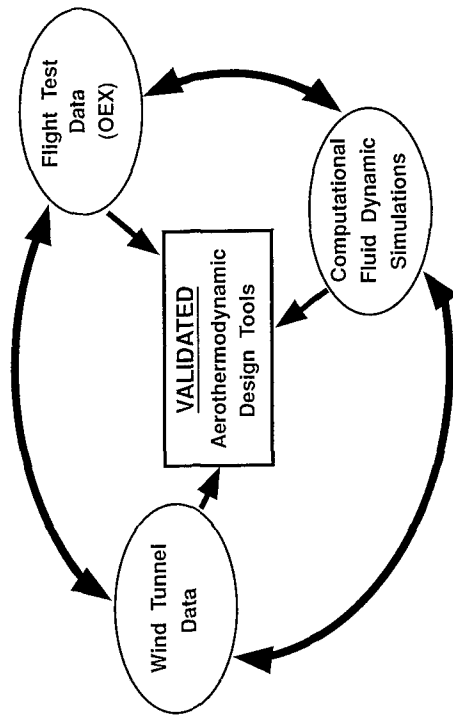
RCE, "Thermal Analysis of the Shuttle Orbiter." NASA Technical Report, NASA SP-700, August 1965.

# Boundary-Layer Transition Prediction State-of-the-Art -- Circa 1975



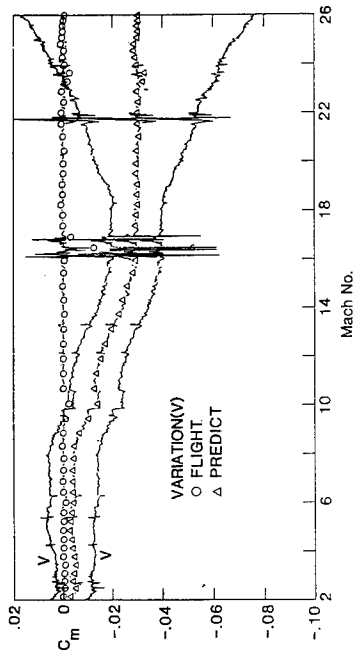
RDT, Reid, R. C. "Orbiter Entry Aerothermodynamics." Space Shuttle Technical Conference. NASA CP 2402, 1983.

# Aerothermodynamic Design Tool Validation



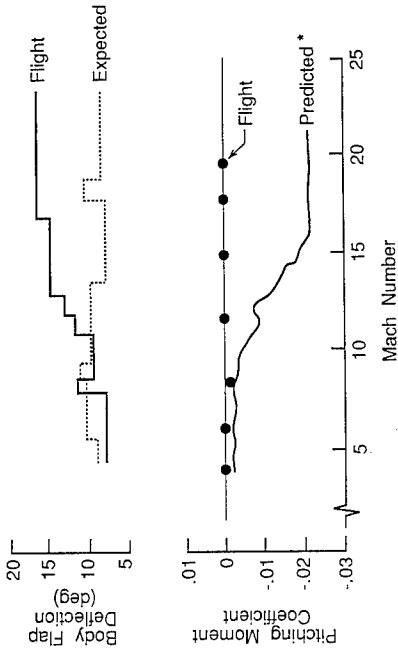
Shuttle Orbiter Pitching Moment Anomaly  
and  
Other "Real-Gas" Effects

Typical Shuttle Orbiter Pitching Moment Data  
(STS-5)



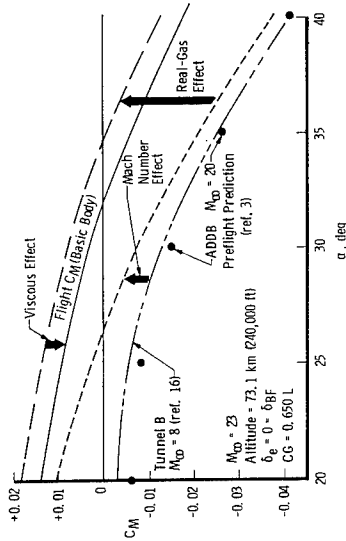
REF: Gentry, R. L., et al., "Shuttle Orbiter Pitching Moment Anomaly Investigation," NASA CR 2283, 1984.

STS-1 Shuttle Hypersonic Pitch Trim Anomaly



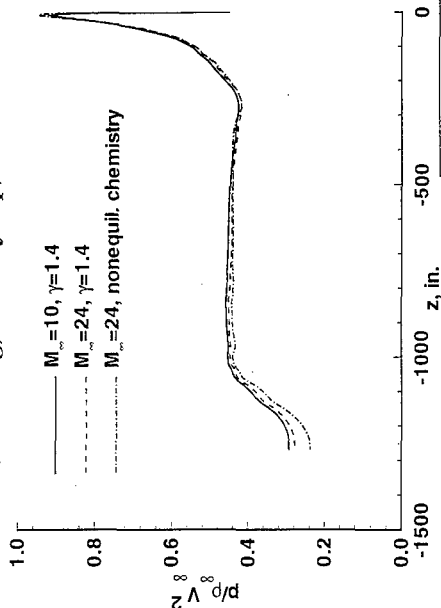
\* Wind Tunnel Aerodynamics at Flight Body Flap Deflection

Pitching Moment Incremental "Build-up"



REF: Gentry, R. L., et al., "Shuttle Orbiter Pitching Moment Anomaly Investigation," NASA CR 2283, 1984.

### Orbiter Windward Centerline Pressures ( $\alpha = 40$ deg, No Bodyflap)



REF: Williamson, R. L., Griffin, R. A., and Greene, J. A., "Orbiter Windward Centerline Pressures and Heating Rates for the Orion and Lifting Body," *Journal of Spacecraft and Rockets*, vol. 21, no. 5, September 1984, pp. 1000-1005.

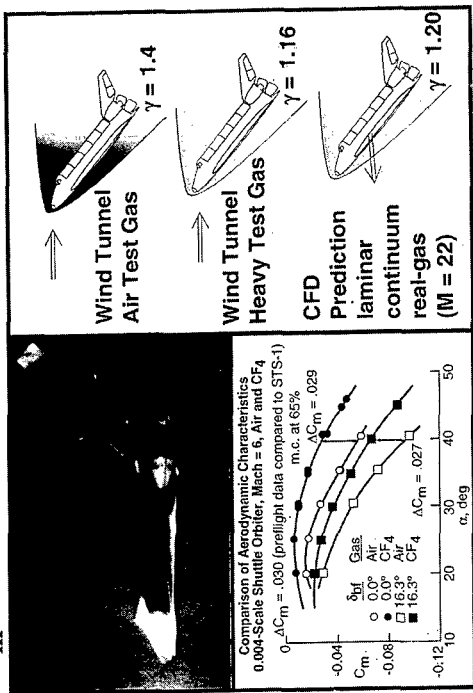
### HL-20 Lifting Body Wind Tunnel Model

31 INCH MACH 10 TUNNEL  
EXPERIMENTAL AERODYNAMICS BRANCH  
SPACE SYSTEMS DIVISION  
NASA LANGLEY RESEARCH CENTER



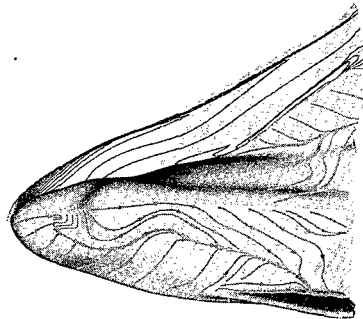
REF: Williamson, R. L., and Griffin, R. A., "HL-20 Computational and Experimental Aerodynamic Data," *Journal of Spacecraft and Rockets*, vol. 21, no. 5, September 1984, pp. 1006-1011.

### $C_m$ Increments Assessed by Testing in CF4

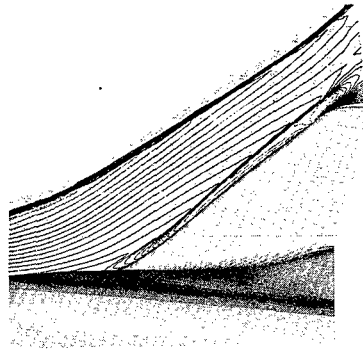


REF: Williamson, R. L., Griffin, R. A., and Greene, J. A., "Orbiter Windward Centerline Pressures and Heating Rates for the Orion and Lifting Body," *Journal of Spacecraft and Rockets*, vol. 21, no. 5, September 1984, pp. 1000-1005.

### HL-20 Flowfield at Wind Tunnel Conditions (Perfect Gas, $M = 5.9$ , $\alpha = 25$ deg)



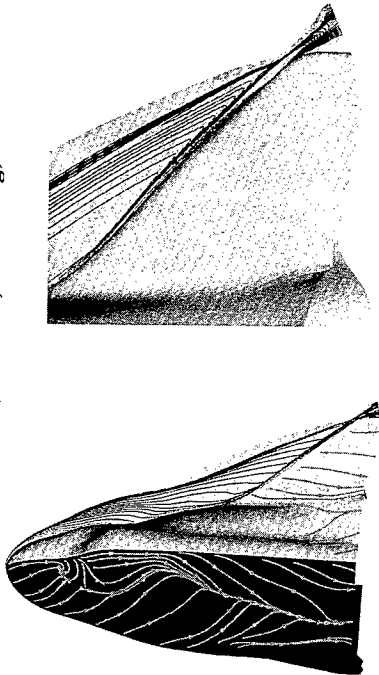
Temperature Contours



Density Contours

REF: Williamson, R. L., and Griffin, R. A., "HL-20 Computational and Experimental Aerodynamic Data," *Journal of Spacecraft and Rockets*, vol. 21, no. 5, September 1984, pp. 1006-1011.

HL-20 Flowfield at Flight Conditions  
(Equilibrium Air,  $M = 15.8$ ,  $\alpha = 25$  deg)

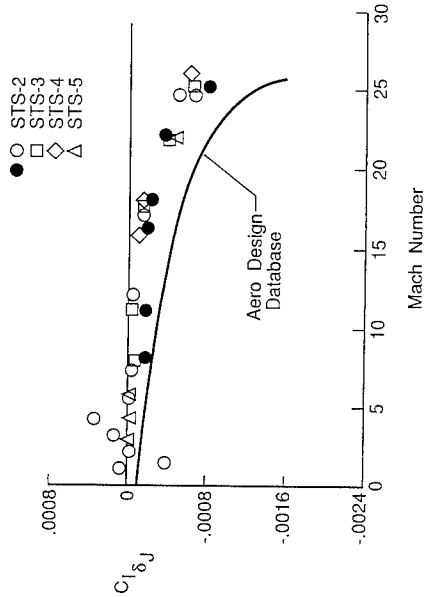


Temperature Contours

Density Contours

CHURCH, E. A. Glenn NACA Langley Research Center

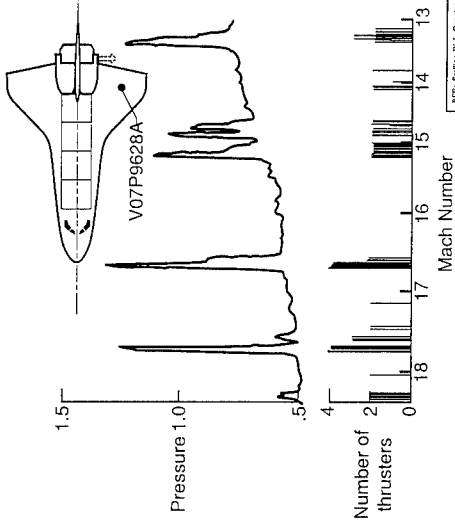
RCS / Aerodynamic Rolling Moment Interaction



REF: Sullivan, W. L., Cooper, H. B., Shi, W. T., French, J. W., Bhatnagar, T. A., and Bhatnagar, H. L., "Four-Channel Thrust Light (FTLS-3) Entry RCS Analysis," AIAA Paper 84-0116, January 1984.

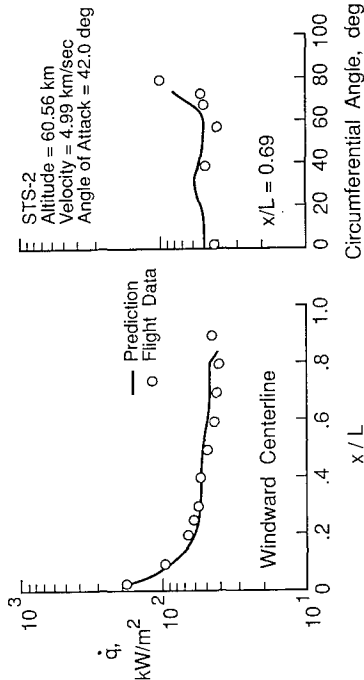
Reaction Control / Aerodynamic Flowfield  
Interactions

Wing Pressure Response to RCS Jet Firings



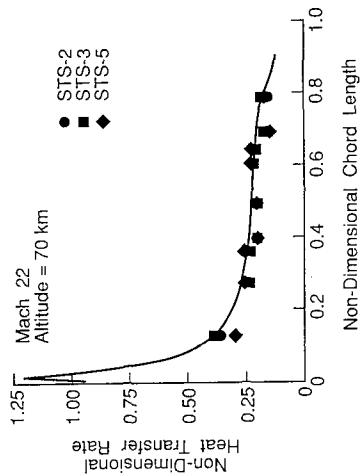
REF: Sullivan, W. L., Cooper, H. B., Shi, W. T., French, J. W., Bhatnagar, T. A., and Bhatnagar, H. L., "Four-Channel Thrust Light (FTLS-3) Entry RCS Analysis," AIAA Paper 84-0116, January 1984.

### Orbiter Flight Heat Transfer Data Compared With 3-D Viscous-Shock-Layer Solution



REF: Thompson, R. A., "Comparison of Three-Dimensional Viscous Shock-Layer Solution with Shuttle Heating Measurements," *Journal of Spacecraft and Rockets*, vol. 1, no. 2, April 1964.

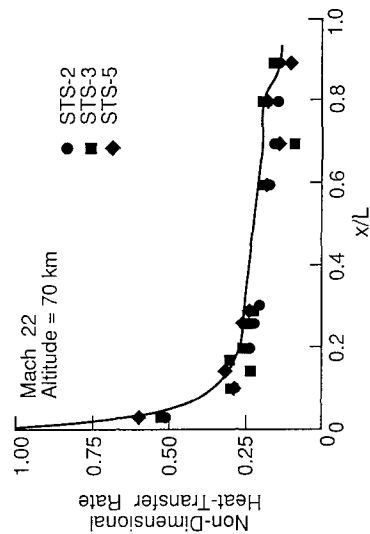
### Orbiter Flight Heat Transfer Data Compared With 3-D Navier-Stokes Solution (Wing 50-Percent Semispan)



REF: Williamson, R. J. and Gentry, P. A., "Shuttle Heating Data Compared with Three-Dimensional Navier-Stokes Solution," *Journal of Spacecraft and Rockets*, vol. 20, no. 4, July-August 1983.

### Orbiter Aerodynamic Heating Comparisons

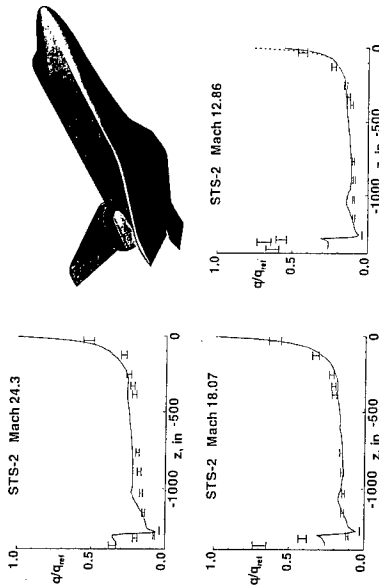
### Orbiter Flight Heat Transfer Data Compared With 3-D Navier-Stokes Solution (Windward Surface Centerline)



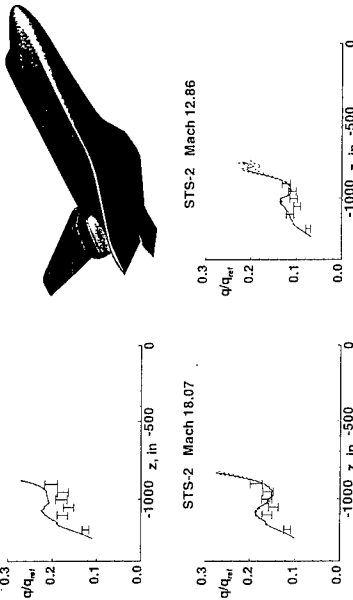
REF: Williamson, R. J. and Gentry, P. A., "Shuttle Heating Data Compared with Three-Dimensional Navier-Stokes Solution," *Journal of Spacecraft and Rockets*, vol. 20, no. 4, July-August 1983.

Configuration Aerothermodynamics of Entry Vehicles

Orbiter Flight Heat Transfer Data Compared With Nonequilibrium Navier-Stokes Solution (Windward Centerline)



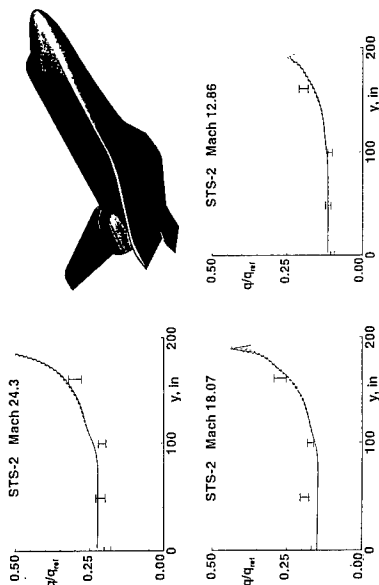
RTF: Gertler, P. A., Whittemore, K. L., and Allen, S. J., "Handbook Analysis for Shuttle Orbiter Re-entry Heating from Mach 24 to Mach 12," *Journal of Spacecraft and Rockets*, vol. 31, no. 3, May-June 1994.



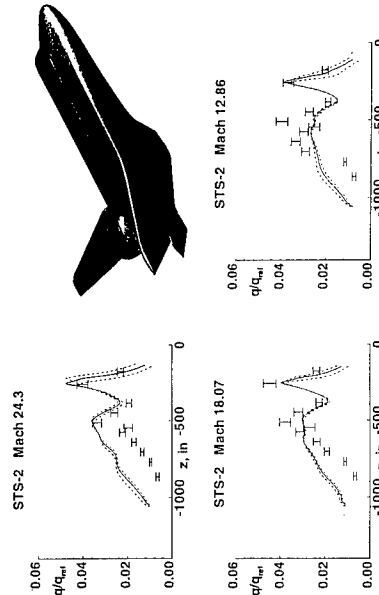
RTF: Gertler, P. A., Whittemore, K. L., and Allen, S. J., "Handbook Analysis for Shuttle Orbiter Re-entry Heating from Mach 24 to Mach 12," *Journal of Spacecraft and Rockets*, vol. 31, no. 3, May-June 1994.

Configuration Aerothermodynamics of Entry Vehicles

Orbiter Flight Heat Transfer Data Compared With Nonequilibrium Navier-Stokes Solution (Lower Surface - Transverse at 60-Percent Vehicle Length)



RTF: Gertler, P. A., Whittemore, K. L., and Allen, S. J., "Handbook Analysis for Shuttle Orbiter Re-entry Heating from Mach 24 to Mach 12," *Journal of Spacecraft and Rockets*, vol. 31, no. 3, May-June 1994.

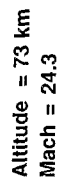


RTF: Gertler, P. A., Whittemore, K. L., and Allen, S. J., "Handbook Analysis for Shuttle Orbiter Re-entry Heating from Mach 24 to Mach 12," *Journal of Spacecraft and Rockets*, vol. 31, no. 3, May-June 1994.

Configuration Aerothermodynamics of Entry Vehicles

Orbiter Flight Heat Transfer Data Compared With Nonequilibrium Navier-Stokes Solution (Fuselage Side - Cargo Bay Door Hinge Line)

## Predicted and Flight-Measured Surface Temperature Data



## Navier-Stokes Solution

Increasing Temperature

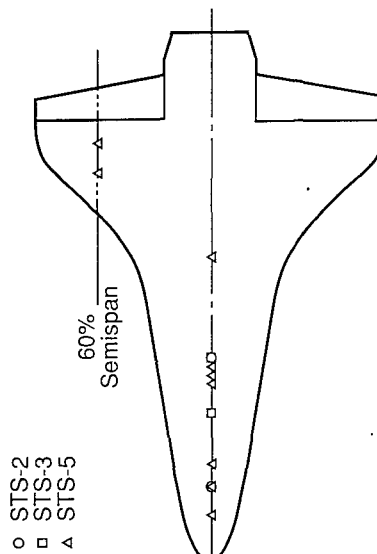
# SILTS STS-32 Flight Data

KUO, Kueh, W. L., and Weissenberg, K. J.: "Characteristics of the Shallow Oblique Laminar Flow During a Re-Entry Condition." *Journal of Spacecraft and Rockets*, vol. 31, no. 1, January-February 1994.

REF: Kiehl, W. L., and Weinman, K. J.: "Characteristics of the Shuttle Orbiter Laminar Flow During a Re-Entry Condition." *Journal of Spacecraft and Rockets*, vol. 31, no. 1, January-February 1994.

### Configuration Aerothermodynamics of Entry Vehicles

## Catalytic Surface Effects Experiment Measurement Locations

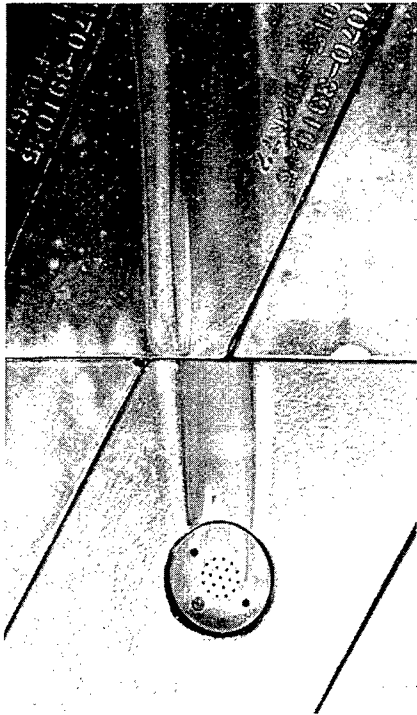


RIF: Theodoresco, D. A. "Shuttle Entry Aerothermodynamic Flight Research: The Odessa Experiment Program." *Journal of Spacecraft and Rockets*, vol. 35, no. 4, July-August 1991.

## Heating to Catalytic Surfaces

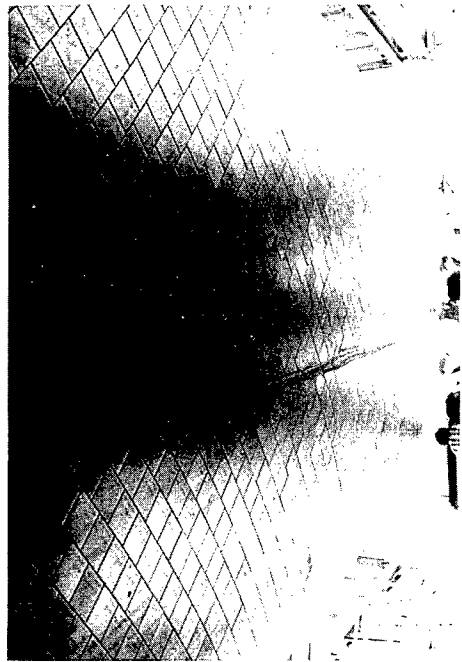


### Orbiter STS-1 TPS Surface Contamination Acoustic Sensor at 10-Percent Vehicle Length



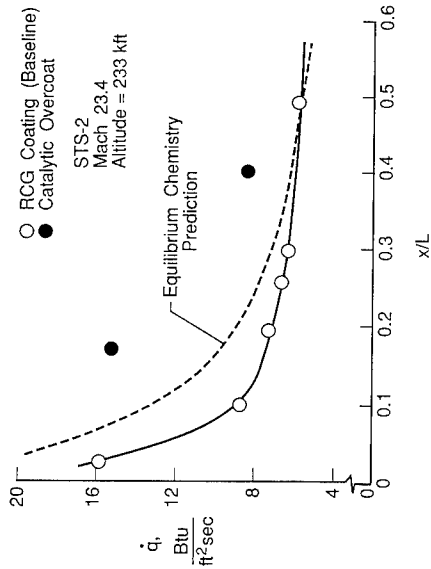
REF: Thompson, D. A., Zoby, E. V., and Hamilton, H. H. "Orbiter Catalytic Coating Heat Transfer and Evidence for Having as a Catalyst for the Reaction of the Reaction Products." *Journal of Spacecraft and Rockets*, Vol. 20, No. 4, July-August 1983.

### Orbiter STS-1 TPS Surface Contamination



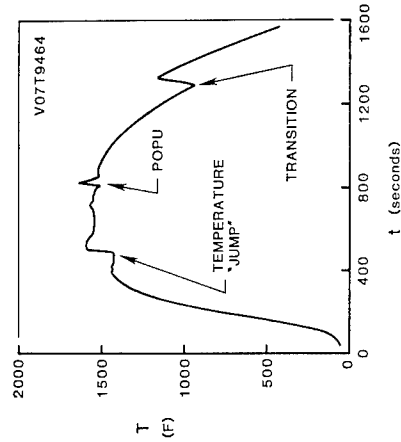
REF: Thompson, D. A., Zoby, E. V., and Hamilton, H. H. "Orbiter Catalytic Coating Heat Transfer and Evidence for Having as a Catalyst for the Reaction of the Reaction Products." *Journal of Spacecraft and Rockets*, Vol. 20, No. 4, July-August 1983.

### Catalytic Surface Effects Experiment Results



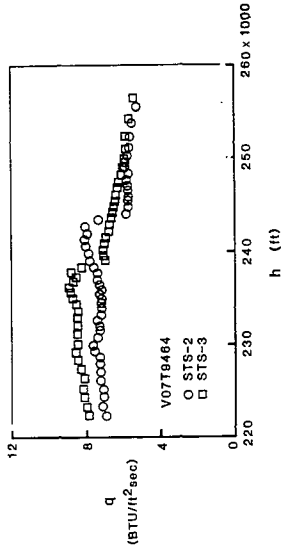
REF: Thompson, D. A. "Space Ship Aerothermodynamics: The Catalytic Surface Effects Experiment Program." *Journal of Spacecraft and Rockets*, Vol. 20, No. 4, July-August 1983.

### STS-2 Surface Temperature Response as a Result of Contamination



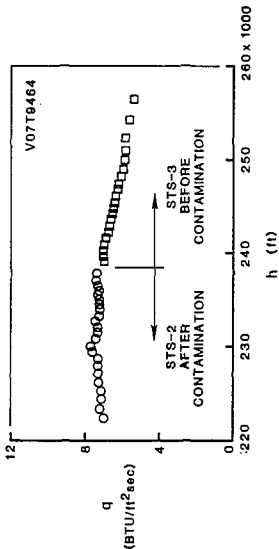
REF: Thompson, D. A., Zoby, E. V., and Hamilton, H. H. "Orbiter Catalytic Coating Heat Transfer and Evidence for Having as a Catalyst for the Reaction of the Reaction Products." *Journal of Spacecraft and Rockets*, Vol. 20, No. 4, July-August 1983.

Heat Transfer to Contaminated Tile



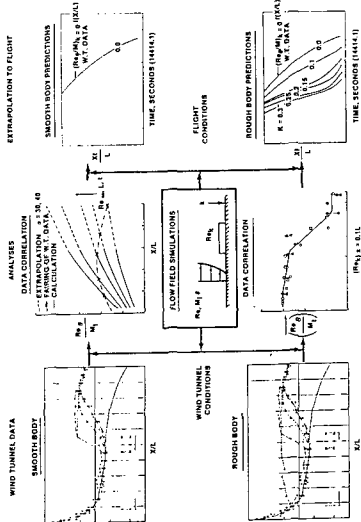
REF: Thompson, D. A., Zuber, E. V., and Hamilton, J. B. II. "Orbit-Dependent Contaminated Heat Transfer to Entry Vehicle Tiles." *Orbit-Dependent Contaminated Heat Transfer to Entry Vehicle Tiles*. NASA CP-2263, 1983.

Heat Transfer to Contaminated Tile



REF: Thompson, D. A., Zuber, E. V., and Hamilton, J. B. II. "Orbit-Dependent Contaminated Heat Transfer to Entry Vehicle Tiles." *Orbit-Dependent Contaminated Heat Transfer to Entry Vehicle Tiles*. NASA CP-2263, 1983.

Orbiter Transition Prediction Methodology



REF: Burt, R. C. "Orbiter Entry Aerothermodynamic." *Space Shuttle*. NASA CP-2263, 1983.

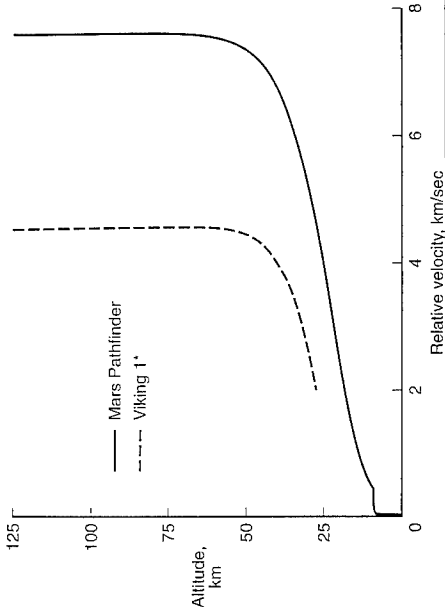
Shuttle Orbiter Boundary Layer Transition





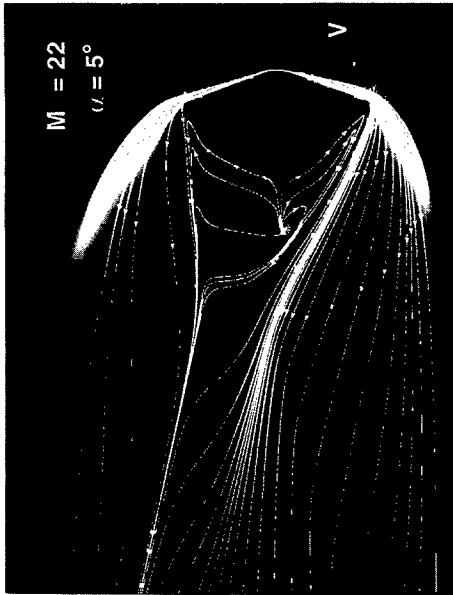
Configuration Aerothermodynamics of Entry Vehicles

Mars Pathfinder and Viking Entry Trajectories



REF: Basso, R. D., Powell, R. W., Eggen, W. C., Gault, P. A., and Gault, P. A., "Entry Trajectories of Mars Pathfinder and Viking 1\*," *Journal of Spacecraft and Rockets*, vol. 32, no. 5, November-December 1995.

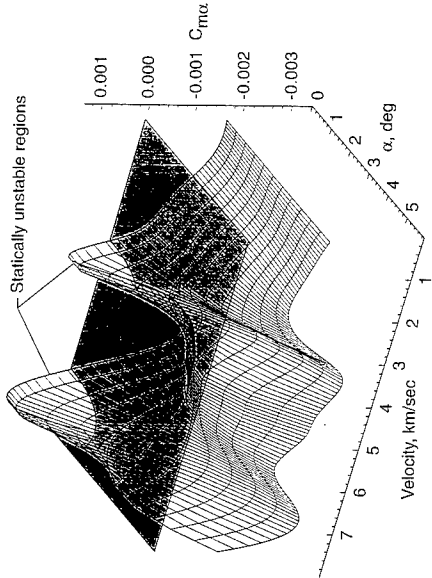
Mars Pathfinder Flowfield Pressures



CREDIT: P. A. Gault, NASA Langley Research Center

Configuration Aerothermodynamics of Entry Vehicles

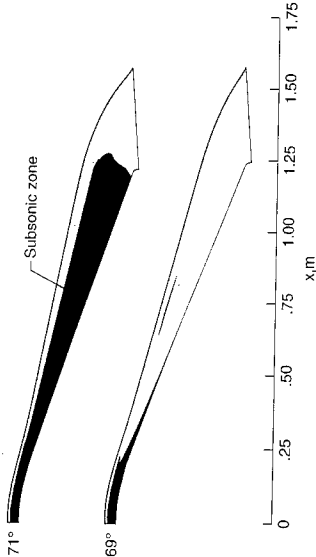
Mars Pathfinder Static Stability



REF: Basso, R. D., Powell, R. W., Eggen, W. C., Gault, P. A., and Gault, P. A., "Entry Trajectories of Mars Pathfinder and Viking 1\*," *Journal of Spacecraft and Rockets*, vol. 32, no. 5, November-December 1995.

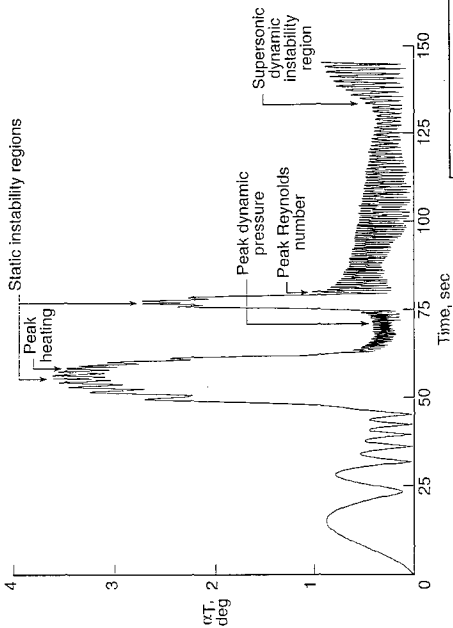
Configuration Aerothermodynamics of Entry Vehicles

Flowfield Sensitivity to Cone Half-Angle  
(Mars Entry, Vel=5.82 km/s, Alt=37.9 km)



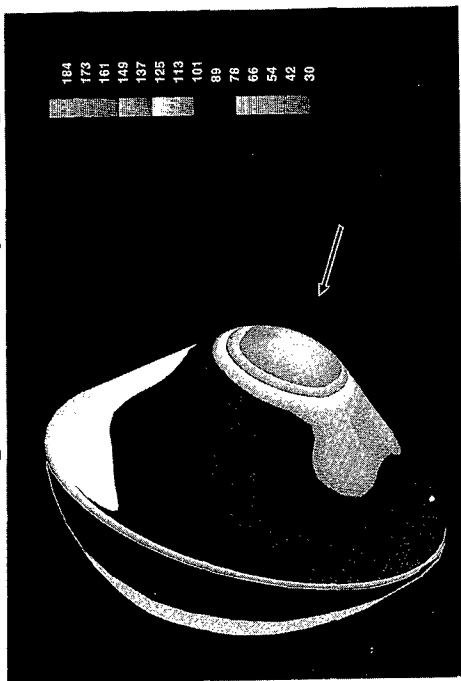
REF: Munk, R. A., "Numerical Solution of the Flowfield around a Cone at a Half-Angle of 71°," *Journal of Spacecraft and Rockets*, vol. 3, no. 3, May-June 1966.

## Mars Pathfinder Entry Attitude Profile



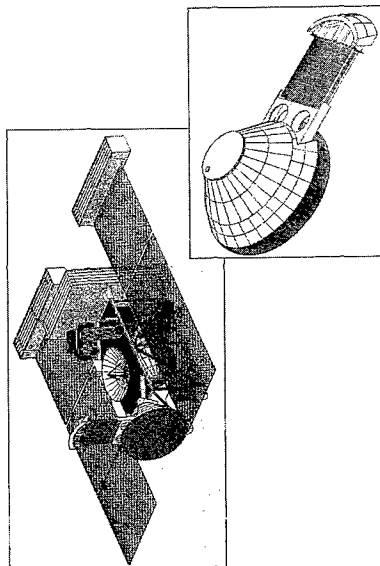
RTTC, Brown, R. D., Powell, R. W., Crawford, W. C., Gault, P. A.,  
Widomay, R. J., and Johnson, J. A. "Mars Pathfinder's Entry  
Attitude Profile." *Journal of Spacecraft and Rockets*, Vol. 32, No. 4, November/December 1995.

## Mars Microprobe Forebody Heating



CREDIT: R. A. Murchison, NASA Langley Research Center

## Stardust



## Glossary

ADDB	Aerodynamic Design Data Book
AFE	Aeroassist Flight Experiment
AOTV	Aeroassisted Orbital Transfer Vehicle
ARD	Atmospheric Reentry Demonstrator
CFD	Computational Fluid Dynamics
DSMC	Direct Simulation Monte Carlo
HOPE-X	H-II Orbiting Plane - Experimental
HYFLEX	Hypersonic Flight Experiment
LAURA	Langley Aerothermodynamic Upwind Relaxation Algorithm
NASP	National Aero-Space Plane
OEX	Orbiter Experiments
OREX	Orbital Reentry Experiment
RCG	Reaction Cured Glass
RCS	Reaction Control System
RLV	Reusable Launch Vehicle
SILTS	Shuttle Infrared Leeside Temperature Sensing

# Configurational aerothermodynamics of RAM and SCRAM propelled vehicles.

P. Perrier and J.C. Courty  
Dassault Aviation  
78, Quai Marcel Dassault  
92214 Saint-Cloud  
France

## 0. INTRODUCTION

A lot of complexity is added to any flying vehicle by the propulsion integration. However it is clear that in subsonic the presence of inlets and exits have a vanishing effect with distance, so that the integration of propulsion is a local problem except for very high deflection of flow as in the V.T.O.L. vehicles. In transonic and supersonic regime the integration is more complex as induced by the extent of interactions downstream along the characteristics or in throat areas in transonic. The development of supersonic fighters and of Concorde has promoted the understanding of shock-waves interactions in a near 2-D or axisymmetric flow on the 3-D edges of supersonic inlets and exits, and of shock wave-boundary layer interaction in the boundary layer diverters, or in local impingement of normal shocks in ducts. Some major interactive effects were appearing on the longitudinal and lateral stability at the unstart of intake and exit, but generally the integration was not requiring complete redesign of conventional wing-fuselage layout. Some designs were keeping nacelle or pod engine installation (B.58 hustler, Concorde, B.1, SST projects, Russian projects...) and all others relying on fuselage engine installation with lateral air intakes (Mirage, US fighters, Russian Binder,...) taking opportunity of jet exits in the base for a streamlined design with long internal ducts.

One major characteristic of hypersonic propulsion is the reduced amount of thrust by unit area of air intake or exit nozzle. Such effect comes from high level of contraction needed for comparatively low Mach number in combustion chamber compared to high Mach number in external flow and in nozzle flow; additive effect comes from the reduction of net drag for a given gross thrust: the velocity at the exit of nozzle is limited by maximum enthalpy of flow after combustion of hydrocarbon fuel and hydrogen. So that the variation of momentum of one square meter of incoming air captured by air intake and heated in combustion process is decreasing rapidly with Mach Number leading to larger air intake, versus combustion chamber, as maximum Mach Number of flight is increasing: a similar trend occurs in nozzle area. At very high Mach Number or near the limit in speed of combustion products, the thrust minus drag may be so low that only very thin vehicles can accelerate or sustain flight and impossible constraints on heat fluxes on thin lips or leading edges are appearing. Moreover this implies the extension to the complete vehicle of parts of design devoted to interaction between propulsion and elements contributing to flight performance and control: it mixes all the design constraints of a flying vehicle with the design constraints of a propulsion engine, the problems of control of the trajectory and of the internal or external flows with combustion (Fig. 0-1).

One major constraint in hypersonic is the heat fluxes generated in boundary layers of the air intake as pressure increases. If the friction temperature is almost the same on all the surface in contact with free air without combustion, the fluxes are very high where high pressure are generated. Similarly the fluxes are very high in the highest pressure and temperature near the combustion chamber. It can be deduced that long ducts of compressed air are to be avoided at the intake and even more for the exit. It induced the elimination of all the typical design retained in supersonic with nacelle under wing because they will be larger than fuselage itself, and long fuselage with long ducts at the entrance and exit of combustion chamber (air intake ducts and afterburner pipes), taking into account the suppression of any compressor-turbine groups in the duct as natural compression of hypersonic flow is sufficiently high by itself in hypersonics.

In conclusion it is clear that integrated management of heat and pressure is the major focus in design of hypersonic vehicles with RAM and SCRAM jet.

However it is possible to summarise the aerothermodynamics of the RAM jet propelled vehicles by consideration of the loss in entropy and the gain in total temperature. The systems of shock waves are producing losses in entropy so that the integral of the losses will give the drag and local overheating gives thrust. Due to high sweep angle of the shock waves the deflection of flow by shocks allow the rebuilding of lift. So the analysis of the wake (Fig. 0-2) let the designer optimize the configuration as a whole, whereas the detailed geometry of the flow field near the body is the key of local problems analysis and the data needed for any measure of the quality of global optimisation with heat fluxes constraints appearing on the body (as induced e.g. by interaction of boundary layer with shear layer identified in the flowfield). We will cover in this paper the analytical and global (functional) approaches.

## 1. AEROTHERMAL ANALYTICAL PROBLEMS DUE TO COMPLEXITY OF CONFIGURATION

1.0 We will cover first the general configuration of vehicle as generating interaction of bow shock wave with air intake, then the interaction of fuselage wing flow field with afterbody requirement and coupling of front and rear part of the vehicle.

1.1 Interaction of bow shock forebody and air intake

Basically any vehicle will give birth, while travelling hypersonically in an incoming flow, to a bow shock wave of high intensity.

Tailoring the forebody shape must solve the following problems:

- the forebody shape must lead to allowable heat fluxes at the nose and to sufficient windward slope for a correct compression , must allow to manage the bow shock shape for an efficient shielding of the air intake, must lead to a correct entropy homogeneity and sufficient flow captation ability in front of the air intake and to a spanwise homogeneous laminar stable flow as much as possible (this last point being addressed in § 2.2.1) ; moreover all these requirements must be compatible with a minimum forebody drag
- the air intake configuration must lead to a sufficient mass flow rate , with minimum efficiency loss (no boundary layer separation) , to non critical overheating in case of bow shock interaction, and to stable flow (no buffeting induced by shock-wave boundary layer interaction or at least damped buffeting by specific control)

1.1.1 Forebody shape configuration

One major constraint will come from heat flux at nose where Reynolds number is low. Thus the sharp cone cannot be a realistic configuration and rounded nose is mandatory; it gives an entropy layer near the wall which may be included in the boundary layers after some meters of fuselage length. Besides entropy swallowing effect so generated by rounded nose, major interest in reduction of heat fluxes is identified as coming from the concept of « shielding shock » (see Fig. 1.1-1). It is clear that such requirement of non-intersection of bow shock with air intake put a coupling process between nose of vehicle and air intake, coupling increasing with Mach Number as air intake increases in size. There are two extreme designs to solve the problem of front fuselage, one with pointed quasi axisymmetric nose leading to highly curved convex air intake, or one with concave nose leading to embedded round air intake - Middle design is with flat lower surface of front body (Fig. 1.1-8 and 1.1-9)

Coming back to the forebody shape influence , let us consider two forebody geometries - one with a circular section and another one with an elliptical section (Fig. 1.1-2)- and five different noses - spatula (b), blunt spheroid (c), blunt ellipsoid (d), blunt prolate spheroid (e) and blunt prolate ellipsoid (f)- (Fig. 1.1-3). By combining these elements we consider five forebody configurations: a spatula elliptical F1 , a blunt spheroid circular F2, a blunt ellipsoid elliptical F3 , a blunt prolate spheroid circular F4 and a blunt prolate ellipsoid elliptical F5 configuration (Fig. 1.1-4).

1.1.1.1 Influence on drag

On Figure 1.1-5 we compare the pressure drag coefficient  $C_x$  obtained by inviscid Euler computation ( $Mach=8$   $\alpha=0^\circ$ ) for the five configurations. If we consider the noses alone it appears that the blunt spheroid and ellipsoid noses are the most penalised , but after the nose , if we consider the slope of the  $C_x$  curves , the elliptical forebodies have higher drag than circular ones.

The nose drag represents an important part of the forebody drag (85% of the drag for a blunt spheroid mounted on circular cross sectionnal forebody.). Among the five configurations the best one in term of drag is F5 ( blunt prolate ellipsoid nose mounted on an elliptical cross sectionnal forebody) and the worst is F2 (blunt spheroid nose mounted on a circular cross sectionnal forebody).

1.1.1.2 Influence on forebody compression

One of the forebody missions is to compress the flow in order to slow down it for a good working of the inlet. This compression must be sought with the other important objective to obtain the more homogeneous flow as possible.

For a given freestream Mach number of 8 ,the minimum wall Mach numbers  $Me$  computed at a given section ( $X=19m$  for instance) are summarized in the following table:

Forebody Configuration		Me
prolate ellipsoid elliptical	F5	4.6
prolate spheroid circular	F4	4.4
spatula elliptical	F1	3.9
blunt spheroid circular	F2	3.8
blunt ellipsoid elliptical	F3	3.6

As foreseen , blunt noses lead to lower Mach number than prolate ones; moreover ,the influence of the section type, circular or elliptical, has not so much importance.

Concerning the Mach number homogeneity (see Fig 1.1-6), the elliptical cross sectionnal forebodies (F1,F3,F5) are characterized by a small region of low mach number on the windward side near the center line; this region is lower for prolate noses than for blunt ones. The same trend is observed on circular cross section forebody when considering the width of the iso Mach number crown.

The spatula elliptical forebody is located in the mean value. On Fig. 1.1-7 are shown the iso Mach number maps in the symmetry plane.

1.1.1.3 Influence on shielding

In addition to a correct flow in front of the air intake , the forebody design must allow to make easy the air intake integration. In this respect the forebody shape must induce a bow shock which is sufficiently far from the windward side, and which do not intersect the air intake.

The distances  $H$  between the wall and the shock for the different forebody shapes are presented in the following table:

Forebody configurations		Distance $H$ (meter)
blunt ellipsoid elliptical	F3	2.06
prolate ellipsoid elliptical	F5	1.03
spatula elliptical	F1	1.03
blunt spheroid circular	F2	0.82
prolate spheroid circular	F4	0.62

In order to obtain a shock far from the wall , it appears that it is preferable to consider an elliptical cross section forebody with a blunt nose.

Once again the spatula elliptical forebody is located in the mean.



#### 1.1.1.4 « Optimal » forebody

From the above studies we can summarize the main trends:

for a weak drag	a prolate ellipsoid nose a circular cross section forebody
for a good compression	a blunt nose
for a good integration	a blunt nose an elliptic cross section forebody

It can be seen that it is hard to find a forebody which meets all the requirements. Consequently the best trade off seems to be a kind of spatula nose on an elliptical forebody. Nevertheless one evident solution for getting a spanwise Mach number homogeneity is to have a flat windward side. Taking into account all these various but not always compatible constraints, a forebody shape can be proposed as the one shown on Fig. 1.1-8 and 1.1-9. The chosen windward slope is here of 4°.

If we examine the flow field in such flat configuration, it is obvious that the best reduced height of entropy swallowing (leading to distortion of recovery pressure) is obtained by elliptic nose. We know that the maximum heat flux is proportional to the square root of the curvature at the nose or to the square root of a mean value evaluated from the two curvatures  $C1$  and  $C2$  for 3D nose. Reduction of entropy layer thickness and simultaneously of nose heat fluxes led to flat nose position. If we examine the flow field on a derived mixed 3D - 2D shape with flat windward fuselage (Fig. 1.1-10) at Mach 6  $\alpha=0^\circ$ , in a plane just upstream the air intake, we notice that a convergence effect of streamlines (Fig. 1.1-18) gives birth to an accumulation of high entropy streamlines, low Mach number, on the plane of symmetry very detrimental to any efficient air intake. At an angle of attack  $\alpha=5^\circ$  (Fig. 1.1-11) this bulge of entropy is always present but has decreased in size. The same trends exist for a higher mach number  $M=12$  and the same angles of attack (Fig. 1.1-12 and 1.1-13).

#### Camber effect

A slightly modified shape, with a windward slope evolving in streamwise direction from 2.5° to 4.5° (Fig. 1.1-14) lead to the same flow characteristics. Nevertheless if we consider mean quantities in the captation surface, like mach number, efficiency and mass flow rate, respectively on Fig. 1.1-15, 1.1-16 and 1.1-17, we can see that the windward forebody with an evolving ramp, compared with the reference one, keeps the mach number in front of the air intake relatively identical but leads to a significant increase in efficiency and above all to an increase in the inlet flow rate (12% increase).

#### Viscous effects

In the preliminary design loop the viscous effects can be assessed at low cost with a boundary layer code. Turbulent boundary layer mean thicknesses  $\delta$  and displacement thicknesses  $\delta_1$  on the windward side in front of the air intake (at  $X=40m$  in the present case) for two freestream Mach number 6 and 12 and two angles of attack 0° and 5°, are presented in the following table:

Mach	$\alpha(^{\circ})$	$\delta$ (m)	$\delta_1$ (m)
6	0	0.21	0.06
6	5	0.18	0.04
12	0	0.30	0.09
12	5	0.25	0.07

The relative important height of the viscous layer as compared to the captation height (1.35 m in the present case) implies that viscous effects must be taken into account at the very beginning of the design, since the air intake efficiency and flow mass rate will be strongly dependant on them.

A comparison between Euler and Euler+Boundary Layer computations on a similar forebody at Mach number 6.4 for three angles of attack 0°, 5° and 10° allows to analyze the effects on the mass flow rate ( $Q$ ) captured by the air intake and on the total pressure efficiency ( $\eta$ ). The results are presented in the following table:

$\alpha$	Euler			Euler+B.L.			
	$Q\ m^2$	$\eta$	M	$Q\ m^2$	$\eta$	M	$Scxm^2$
0°	26	0.82	5.9	25	0.54	5.4	1.9
5°	38	0.90	5.5	36	0.76	5.3	2.4
10°	52	0.75	4.8	50	0.68	4.8	5.7

We can see that viscous effects on local Mach number are more important at lower incidence. The total pressure efficiency exhibits a maximum value between 0° and 10°: at low incidence the bulge of entropy and the boundary layers lead to more important losses, when at higher incidence the bow shock strengthens and lead to increasing losses. The efficiency is maximum when these two tendencies compensate.

The mass flow rate and the drag are rapidly increasing with angle of attack; an optimal angle of attack concerning the trade off between drag and mass flow rate must be sought, and this angle is not necessary the same as the one leading to the best efficiency.

Another important viscous effect on performances already mentioned is the transition position. We present hereafter some computations on a 40 meter length forebody concerning the drag  $Scx$ , the captured mass flow rate  $Q$  and the total pressure efficiency  $\eta$ , for inviscid, laminar and turbulent flow hypotheses.

	$Scx\ m^2$	$Q\ m^2$	$\eta$
Euler	1.8	38	0.89
Laminar	2.1	37	0.83
Turbulent	2.4	36	0.76

We can see that the losses due to turbulent boundary layers are twice the ones for laminar boundary layers.

Transition prediction is therefore very important and needs sophisticated tools as addressed in § 2.2.1.

#### Flow three dimensionnality effects

The three dimensionnality of the flow on the windward side of the forebody is characterized by streamlines convergence in the centerline region and by streamlines divergence in the outer spanwise region (Fig. 1.1-18).

This divergence of the flow can lead to higher heat transfer rates if the wall curvature is important, and to a thinning of

the boundary layer which is favorable for a good working of the air intake.

The streamlines divergence will also lead to oblique shock waves on the lateral part of the air intake whose induced recompression will increase the boundary layer thickness in the corners, which in turn is not favorable for a good efficiency of the air intake.

Another important unfavorable effect is a loss of flow mass rate in the inlet which is very penalizing especially in the SCRAM mode for which the mass flow rate captation is the most influential parameter on the propulsive system performance.

Such important three dimensionnal effects must also be taken into account very soon in the design process for a correct forebody performance assessment.

#### 1.1.1.5 Conclusions on forebody configurations

We have seen that the forebody conception must be performed taking into account several aerodynamics parameters, the most important for a SCRAMjet vehicle being the completion of an objective of the flow mass rate which can be captured by the air intake. The others criteria to be fulfilled are a prescribed compression ratio, the drag for this compression ratio, the mean total pressure of the flow to be captured, its homogeneity, the wall heat transfer rates; others criteria are linked to the integration in the vehicle (lift,...).

The main aerodynamic phenomenon is the bow shock which influences at the same time, the captation of mass flow rate (its distance from the forebody conditioning the maximum air intake height), the total pressure losses and the compression rate.

Even if they have a less important effect than for the internal flow, the thick boundary layers which develop along the forebody have a significant influence on the performances. Particularly they modify the total pressure efficiency and greatly contribute to the flow heterogeneity; they can also influence the mass flow rate captation.

The forebody friction drag is an important contributor to the thrust minus drag budget of the vehicle, and is strongly varying with the transition onset (laminar/turbulent) position. The flow quality entering the air intake is also strongly dependant on the transition position.

One specific design will be required for thinning such bulge of high entropy near the wall, with increased divergence of streamlines generated by locally conical convex shape; another way is, on the contrary to generate conical concave shape on the external part. In both cases it is necessary to have better knowledge on interaction of shock wave and such highly three dimensional thick boundary layer: such knowledge remains to be identified by Navier Stokes computation and mainly by experiments.

#### 1.1.2 Air intake configuration

Another important issue is the interaction of walls of inlet with forebody. If one tries to determine the boundaries of acceptable angles of attack or Mach number, the interaction of bow shock with the lips is to be determined and evaluated in its criticality. Well known phenomena of dangerous type IV interaction will occur in the symmetry plane where plan tangent to the shock will also be tangent to the lip curve at

the entrance of inlets. More complex 3D inlets can reduce the criticality of such peak of overheating. (Fig. 1.1-19).

On the sides of air intake, non integrated shapes will give birth to corner flows with a lot of complex behaviour due to accumulation of low energy air in the corner and interaction with boundary layer thickening (Fig. 1.1-20).

Inside the air intake, the same problems are present but are generators of more detrimental effect on the flow in the duct at the position where high shock-waves are present (normal shock-waves in subsonic combustion RAMjet and oblique shock-waves for SCRAM). Best medicine is by suction of low pressure sublayers. Present knowledge of hypersonic turbulence neither allows precise knowledge of suction level, nor better the shape of holes for suction with regard to the local overheating induced in the perforated wall. Probably any blowing will be better if it mixes cooling effect and reenergization of boundary layers. Only Large Eddy Simulation seems able to help experimentally developed apparatus for stabilisation and/or suppression of separated areas of the wall flow.

Nevertheless we remind hereafter some general features for the definition and optimization of an air intake, and then we will present an example of a generic concept.

##### 1.1.2.1 Criteria for definition and optimization

A strong integration of propulsion with the aircraft is mandatory for an hypersonic airplane because of the important contributions of the forebody and afterbody to the thrust. At hypersonic speeds the mass flow rate required by the engine is so important that a pre-compression of the flow by the forebody is mandatory. It's the reason why it is difficult to consider separately the respective effects of the different components and particularly the forebody and the air intake. Nevertheless, in the present case, the air intake will be defined between the plane 0 at forebody end and plane 2 corresponding to the engine inlet (see Fig. 1.1-21).

Given the air intake size relatively to the other parts, the different interactions will be important, like viscous interactions, internal flow distortion or corner flows. Specially, as discussed in § 1.1.1.4, the relative boundary layer thickness generated by the forebody is an unfavorable feature which must be considered in the air intake design.

We will define a simplified air intake geometry, taking into account the forebody and the inlet engine conditions, in order to allow the evaluations of its working in the 6 to 12 Mach number range. But we must keep in mind that we need to know the afterbody configuration if we want to know the amount of thrust and drag losses.

The engine inlet conditions which must be insured by the air intake are the pressure level, the Mach number and some geometrical specifications like contraction rate for a good mixing between air and hydrogen.

The performance parameters to be fulfilled are the optimal compression efficiency, the flow mass rate and drag characteristics and the start-unstart characteristics.

The air intake design must insure a trade-off between, a sufficient captation for the Mach number range in order to obtain a good level of thrust and specific impulse, and minimum drag.

### 1.1.2.2 Geometrical definition of a generic hypersonic air intake

The choice of a SCRAMjet air intake concept will be linked, at least concerning the captation section shape, to the integration on the forebody and the vehicle. For instance, given the windward forebody shape of the generic vehicle defined in the previous paragrapha and the chamber geometry, the choice can be made for a rectangular air intake with compressions performed by planes. These recompressions can be made by two faces (bidimensionnal concept) or by the four faces (three dimensionnal concept).

In order to define such an air intake many geometrical parameters are to be considered:

- the deflection angles of the different compression plans. From these angles are dependant the air intake geometry (length, height), its efficiency and its behaviour with boundary layers. The compression angles can be external (generated by ramps at the forebody end, or internal (generated by lateral plans and/or in continuity with the external ramps). The struts for hydrogen injection in the chamber can also contribute to the compression.

The choice of the angles and of the number of compression plans will result from a trade-off between important deflections leading to stagnation pressure losses and increasing the probability of separation, and small deflections leading to long air intakes. Lateral walls will contribute to compression in a different way than the ramps (because of boundary layers)

- the internal contraction rate which depends upon the internal compression, and which is conditioning the air intake characteristics at start-unstart and at the engine inlet. An air intake with high internal compression presents a high contraction rate and a small drag; but in counterpart adjustment problems are increased (boundary layer separation and start-unstart limit)

- the struts position relatively to the air intake lips which influences the start-unstart limit and the compression

- a variable geometry for correct efficiency and engine inlet conditions on the whole Mach number range. The studies already performed have not demonstrated this necessity, a fixed geometry being a good trade-off between performances and complexity reduction

- the captation section geometry for structural and start-unstart limits

### 1.1.2.3 Examples of air intake generic concepts

We consider three geometrical angles that we can combine in order to study four air intakes AI1 to AI4. The first angle is the angle between the lateral walls, the sidewall angle; the second is the angle of the upper wall, the ramp angle; the third is the sweep angle of the lateral walls. The generic values considered for these angles are respectively 6°, 5° and 45°.

The first air intake AI1 is a two dimensionnal one with only a lateral compression; the second one AI2 is AI1 plus a

swweep angle for the lateral wall; the third one AI3 is AI1 plus a ramp angle for the upper wall; the fourth one AI4 combines the three kinds of compression by sidewall, ramp angle and sweep angle.

Their characteristics can be summarized in the following table:

	AI1	AI2	AI3	AI4
Sidewall angle	X	X	X	X
Sweep angle		X		X
Ramp angle			X	X

These configurations are respectively shown in figures 1.1-22 to 1.1-25, with iso-Mach number countours.

Given the Mach number 5.8 at the air inlet, the results concerning mean values for the Mach number  $M$ , the pressure  $P$  (in bars) and the efficiency  $\eta$  in the engine inlet plan are summarized in the following table:

	AI1	AI2	AI3	AI4
Mmin	2.97	2.62	2.86	2.50
Mmax	3.04	3.50	3.24	3.65
M	3.00	3.22	3.05	3.08
Pmin	1.25	0.65	0.84	0.48
Pmax	1.30	2.38	1.54	2.90
P	1.27	1.28	1.23	1.40
$\eta$	0.71	0.78	0.72	0.73

It can be seen that for a same contraction rate, the mean values for Mach number, pressure and efficiency are not greatly influenced by the recompression type. But concerning the difference between min and max value, it can be seen that important inhomogeneities of the flow are expected according to the different configurations.

A more realistic configuration is presented on figure 1.1-26 from [16] with the presence of injection struts which contribute to the contraction rate. An example of a Dassault Aviation Navier-Stokes computation on a 2D air intake with struts is shown in figures 1.1-27 (unstructured mesh) and 1.1-28, in order to highlight the automatic mesh refinement in regions of strong gradient.

## 1.2. Interaction with afterbody

We will divide following remarks between the two main concepts of internal and external combustion.

The main problem with external combustion arises from the generation of large oblique shock-waves for overheating at the level of temperature needed for sustained combustion of propellant with heated incoming air. The calculation of compression effect built by source term in combustion need to have precise kinetics of the always complex chemistry (except hydrogen propellant) and of the ignition time related to equilibrium chemistry. Major problems of heating of the wall are related to the process of diffusion of the propellant injected upstream by wake of injectors as by boundary layer. The propulsive effect is generated on the afterbody and, except for an axisymmetric vehicle, is highly

dissymmetric. Present knowledge of hydrocarbon combustion is not sufficient for benefiting of optimisation that could be done by CFD. Interaction of boundary layer, wake and shock-wave with combustion process put such concept in the grade « poor », being difficult to ascertain in the next years, but it remains basically easier to integrate, particularly for aerothermal problems : the radiative cooling of the skin near combustion areas is possible and effective if insulation is sufficient under the skin.

When there is « contained » combustion, in a combustion chamber, only external skin can emit radiation, and specific cooling is needed in the internal side of combustion chamber in interface with the core structure of the vehicle. High temperature insulation is done by multilayer reflective insulation; it is mandatory due to the difficulty to have large amount of cooled airflow for aerodynamic cooling.

Major losses of thrust- minus-drag of an external expansion on the rear of a fuselage are coming from the poor efficiency of nozzle. Aerodynamic problem underlined by such losses of efficiency are present with axisymmetric nozzle and come from difficulty to convert enthalpy in kinetic energy due to freezing of internal degrees of freedom of the molecules of air resulting in nozzle frozen conditions just after the throat of the nozzle. Similarly the decrease in pressure can lead to over expansion of jet at moderate altitude and to internal separation after a normal shock wave of compatibility with external higher pressure. Such phenomena are difficult to simulate at small scale due to laminarization of the boundary layers in the nozzle and the corresponding large separated areas induced by laminar shock wave interaction. Another source of losses is generated by the open nozzle generally put on flight vehicles because of the constraint of room for a large rate of expansion complete nozzle. Such source of losses is particularly large on 2D open-nozzle if the lateral deflection is induced by expansion of flow at the end of splitter plate (Fig. 1.2-1).

The use of variable flaps for reducing the losses in variable pressure ratio behaviour needs a careful estimation of thin layer effect for avoiding extralosses in shock waves or separated areas (Fig. 1.2-2). Again the shock wave interaction with boundary layer is a prominent factor particularly with overexpansion of the flow. The prediction of heat fluxes at the throat of the nozzle is an essential element of design of high temperature parts of any vehicle. Good prediction will be possible only if the incoming boundary layer is known with sufficient accuracy. For practical conditions, some relaminarization effect can also be present which is difficult to predict with a poor knowledge of the effect of external turbulence, as present in any combustion process.

### 1.2.1 Methodology for afterbody concepts analysis

These questions are analyzed in more details in the following paragraph.

We will concentrate mainly on the SCRAMjet mode; nevertheless § 1.2.6 will be devoted to overexpanded nozzle flow for lower Mach number regime.

The analysis will be performed around a generic afterbody configuration based on the Single Expansion Ramp Nozzle concept which is a good candidate as regard to the mass saving associated with a single ramp, to the easier

integration in the vehicle (as compared to a complete nozzle), and to a lower drag for the RAM jet regime.

A systematic study of the main dimensionning parameters influence on the afterbody performances is also presented hereafter.

The afterbody is a key element of the vehicle, not only because of its influence on the performances but also because of its important size (about 1/3 of the vehicle length) which makes it difficult to integrate in the vehicle. Afterbody conception cannot be made independantly from the conception of the other parts of the vehicle. A generic configuration of the vehicle (Fig. 1.2-3 and 1.2-4) has been chosen as a reference and afterbody variants are modifications of the rear part of the reference vehicle. These variants must take into account the layout constraints of the generic vehicle.

The afterbody must give thrust, lift and a pitch up moment in order to trim the vehicle. The objectives and rate of exchange between these features can be obtained only for a complete study of the whole vehicle. Nevertheless some tendencies can be drawn by considering a first quality criterion for the afterbody:  $F_x + 0.23 F_z$ ,  $F_x$  being the afterbody thrust and  $F_z$  its lift.

This criterion is only indicative, but it is used here to take into account the lift and not only the thrust when comparing different concepts. This lift is mandatory to trim the vehicle at high Mach number, and must not be neglected in the afterbody optimization process.

In order to compare different concepts the same computation tool has to be used, an Euler code for instance for sake of less CPU time requirements, at least for preliminary analysis. Nevertheless the whole vehicle with various afterbodies is computed in order to have a more realistic simulation of flow confluence than for an isolated afterbody.

The performances are computed for two flight conditions (Mach=6 and Mach=10,  $\alpha = 4^\circ$ ) and compared relatively to the thrust and lift of the whole vehicle, of the afterbody alone (pressure integration on the rear part of the vehicle,  $X > 45m$ , cf Fig. 1.2-4), of the nozzle alone (pressure integration on the expansion ramp and the internal part of the flap), and of for the external part of the afterbody (pressure integration downstream the nozzle sidewalls, for  $X > 55m$ , cf Fig. 1.2-4); this allows to decompose the influences and to translate them in terms of global performances of the vehicle.

### 1.2.2 Analysis of a generic configuration

A 65m long configuration is shown on Fig. 1.2-3 and 1.2-4.

This aircraft is a generic airbreathing SSTD launcher. Performances are sought for the airbreathing part of the trajectory; in this phase the aircraft is propelled successively by an ejector rocket, a RAMjet and a SCRAMjet, which are all fitted in a single propulsive stream.

This aircraft shape is by no means optimized, and should not be taken as a candidate design; however it is used as a test case for the design tools and analysis.

The net thrust ( $D-T = \text{drag} - \text{thrust}$ ), lift  $C_z$  and pitching moment  $C_m$  (pitch up for  $C_m > 0$ ) for the two flight conditions are listed below in the following tables and

compared to the corresponding values of an ideal nozzle (adapted and without any losses). These values are multiplied by 100.

Mach=10  $\alpha=4^\circ$

	Whole vehicle	Afterbody (X>45m)	Nozzle (ramp + flap)	External afterbody (X>55m)	Ideal nozzle
D-T	-1.	-1.35	-1.5	-0.3	-2.5
Cz	4.7	2.8	1.5	1.3	0.
Cm	0.09	-0.29	-0.21	-0.24	0.

Mach=6  $\alpha=4^\circ$

	Whole vehicle	Afterbody (X>45m)	Nozzle (ramp + flap)	External afterbody (X>55m)	Ideal nozzle
D-T	-3.	-2.3	-2.5	-0.5	-3.2
Cz	5.3	2.7	1.6	1.3	0.
Cm	0.25	-0.4	-0.27	-0.36	0.

These values of efforts must be considered as examples; they vary with the flight Mach number, the angle of attack, the combustor outlet conditions,.... Nevertheless their order of magnitude are characteristic and allow a certain number of remarks.

- The afterbody efficiency on thrust is weak at high mach number (60% efficiency when compared to the ideal nozzle). At Mach 6 the efficiency is better but of only 75%. The major part of this loss is due to the under expansion of the engine jet.

- There is a sensible difference in Afterbody and Nozzle performances (about 15% of D-T at Mach=10); this difference is partly due to the cowl drag and partly due to the jet bursting and thus to the induced increase of pressure on the fuselage;

- The afterbody influence on the trim is very important and beneficial, but not enough to trim the generic vehicle configuration

- The external afterbody contribution to the thrust, if weak as compared to the afterbody contribution, can represent 30% of the vehicle D-T. Moreover its contribution to the lift and moment coefficient is a major one.

The losses in performances (when compared to the ideal nozzle) have several origins:

- Losses due to the under expansion of the Single Expansion Ramp Nozzle; but it must be stressed that an ideal nozzle would be about 5 times longer, therefore inducing a mass penalty and a huge friction drag.

- Losses due to a flow spillage induced by the lateral expansion downstream the sidewalls; possible remedies are greater sidewalls and/or a transverse concave ramp in order to better contain the spillage (as analyzed in the next paragraph)

- Losses due to friction on the ramp, the flap and the sidewalls

- Losses due to shockwave boundary layer interactions

- Losses due non complete recombination of combustion products at the combustor outlet leading to a decrease of static pressures and thus a decrease in thrust.

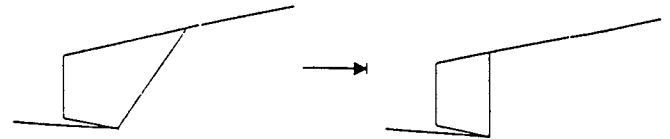
- Losses due to inhomogeneous flow at the outlet combustor

### 1.2.3 Analysis of variations around the generic configuration

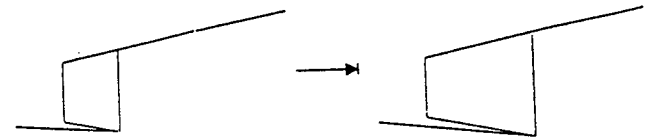
The variants are presented below and the corresponding shapes are shown on Figures 1.2-5 to 1.2-10

- « concave ramp »: in order to fight against the lateral spillage a concave shape is given to the expansion ramp in a plane normal to the longitudinal axis

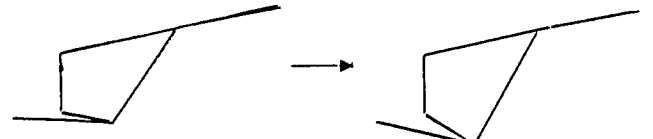
- « short sidewalls »: in order to quantify the sidewalls effect on the spillage, a variant leading to more spillage is proposed by shortening the sidewalls



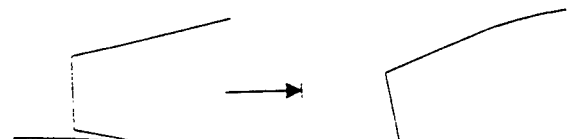
- « long flap »: in order to reduce the losses due to the single expansion ramp nozzle, a longer flap is proposed. A double positive effect is expected: an increase of the flap thrust and a reduction of the spillage. As a counterpart an increase in friction drag and a decrease in lift are expected



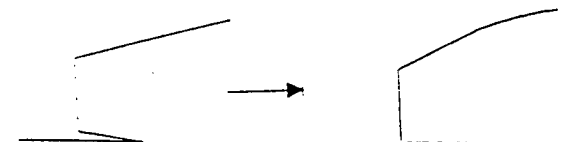
- « deflected flap »: in order to help in the trim of the vehicle, a variant with a 5° deflection angle is assessed



- « engine axis +5° »: the nozzle and the combustion chamber are together tilted up with an angle of 5°



- « nozzle axis +5° »: the nozzle alone is tilted up with an angle of 5°



These variants have been computed for Mach=6 and 10 for  $\alpha=4^\circ$ . The effect of each variants on the afterbody performances is presented in the following tables, where results are given in percentage relatively to the generic configuration ,except for the « long flap » variant where the reference is the « short sidewalls » configuration.

Mach=10  $\alpha=4^\circ$

Variant	Afterbody				Nozzle		Afterbody (X>55m)	
	-Cx	Cz	Fx+23Fz	CP	-Cx	Cz	-Cx	Cz
Convex ramp	0.4 %	5.1 %	1.8 %	0.9 %	0.3 %	9 %	9 %	9 %
Short sidewall	-1.7 %	-4 %	-2.5 %	-0.6 %	-2 %	-10 %	-7 %	-6 %
Long flap	15 %	-21 %	3.3 %	-2.6 %	23 %	-86 %	8 %	7 %
Deflect flap	-17 %	39 %	1.6 %	3.3 %	-3.1 %	37 %	-8 %	-7 %
Engine axis +5°	13 %	-41 %	-4.4 %		1.3 %	-30 %	-41 %	130 %
Nozzle axis +5°	-1.4 %	-41 %	-14 %	4 %	-11 %	-30 %	-52 %	105 %

Where CP is the center of pressure and its movement is positive in the downstream direction given in % of the total length (65m in the present case)

Mach=6  $\alpha=4^\circ$

Variant	Afterbody				Nozzle		Afterbody (X>55m)	
	-Cx	Cz	Fx+23Fz	CP	-Cx	Cz	-Cx	Cz
Convex ramp	0.6 %	7 %	1.8 %	1.4 %	0.6 %	11 %	14 %	14 %
Short sidewall	-1.8 %	-7 %	-3 %	-1.2 %	-2.3 %	-15 %	-12 %	-12 %
Long flap	12 %	-18 %	5.3 %	-2 %	16 %	-63 %	20 %	18 %
Deflect flap	-7.2 %	22 %	-0.5 %	0.6 %	-1.6 %	16 %	-30 %	-30 %
Engine axis +5°	7 %	-25 %	-0.3 %		1.4 %	-10 %	-34 %	93 %
Nozzle axis +5°	5.4 %	-29 %	-2.6 %	4.7 %	-0.3 %	-18 %	-21 %	106 %

These results lead to the following remarks.

- « convex ramp » : the gain on the efforts on the external afterbody is 9% at Mach 10 and 14% at Mach 6, which represents half the spillage effect. The efficiency is better at the lower Mach number since the spillage effect is more important But the gain in thrust on the whole afterbody is weak: yet, the gain in lift is significant with an increase of  $Fx+0.23Fz$  of about 2% which represents 4% of the vehicle thrust - minus- drag at Mach 10. Moreover the center of pressure has a favorable rearward movement of 1%.
- «short sidewalls »: considering the effect of increasing the sidewalls (short sidewalls configuration towards the reference configuration , the gains on  $Fx+0.23Fz$  and on the

center of pressure is similar to those of the convex ramp configuration. These two variants can be combined with benefit.

- «long flap »: the gain in thrust is very important but so much important is the loss in lift. Nevertheless the gain in  $Fx+0.23Fz$  is significant, representing 7% of the vehicle thrust-minus-drag at Mach 10. The effect on the center of pressure is unfavorable.

- «deflected flap »: there is a loss in thrust and a gain in lift leading to a slight increase of  $Fx+0.23Fz$  at Mach 10 and a slight decrease at Mach 6. The flap efficiency in term of center of pressure is strongly variable with Mach number (3% at M=10 and 0.6% at M=6). In fact at Mach 6 the flap deflection induces a strong decrease in pressure level on the external afterbody(due to the expansion impact generated by the flap trailing edge), which leads to a pitch up moment in opposition with the pitch down moment generated by the deflected flap.

- « engine axis +5° »: this configuration leads to an important gain in thrust and an important decrease in lift, with a  $Fx+0.23Fz$  decrease.

- « nozzle axis +5° »: this configuration is slightly favorable for the thrust (mainly due to a cowl drag reduction), but here again there is an important loss of lift with a decrease for  $Fx+0.23Fz$ . Nevertheless we notice a very favorable movement of the center of pressure(8%) .Therefore ,this configuration could be used with a less tilt angle to solve trimming problems.

In conclusion ,the above variants had the objectives of limiting the losses due to the single expansion ramp nozzle concept as well as the losses due to the spillage of flow. For the first kind of losses ,as expected, the longer flap solution can answer favorably even if partially. For the second kind of losses ,the concave ramp allows to reduce the losses by a factor of two and can be used as alternate or complementary with the sidewalls.

It is clear that an analysis focused on the afterbody can afford informations of interest on the aerodynamic viewpoint, but generally does not allow to conclude on the best afterbody concept; an integrated study of the global configuration is mandatory for this purpose ,as discussed in § 1.3.

Moreover, the above analysis has been performed with an inviscid Euler code for sake of rapidity and low cost, but the viscous and chemical effects must be assessed

1.2.4 Viscous effects

Even if the efforts due to pressure are the most important, thus justifying an inviscid analysis for preliminary studies of the design loop, the friction drag is not negligible and the viscous interactions can lead to significant modifications of the pressure field. Moreover the prediction of the wall heat transfer rates which can be high in the nozzle, need viscous computations

These viscous computations can be performed at lower cost by use of boundary layer codes for obtaining boundary layer thicknesses (see Fig. 1.2-11, and 1.2-12) and wall heat fluxes (see Fig. 1.2-13). The turbulent boundary layer thicknesses are relatively small as compared to the nozzle

size:the displacement thickness represents 2% of the inlet nozzle height and 4% of the outlet height. Therefore,no major pressure field modification is expected (which is not the case in the air intake). Concerning heat fluxes, a maximum value of about 1MW/m<sup>2</sup> is obtained at the nozzle inlet and then decreases rapidly on the ramp due to the strong expansion: on the flap they are relatively higher. It must be stressed that these figures may be lower if possible relaminarization occurs on the ramp.

When important viscous interactions take place the best way of doing is to use Navier-Stokes code (Fig. 1.2-14 and 1.2-15), particularly when recirculating zones are present(see Fig. 1.2-16 for separation on the windward side of the flap trailing edge).

1.2.5 Chemistry kinetics effects

In the combustor outlet the combustion products are at such a high temperature that the H<sub>2</sub>O molecules are partly dissociated and the internal energy contained by the vibration modes is important. During the expansion in the nozzle the dissociation and vibration rates decrease and the majority of the internal energy is contained in the translation and rotation modes, thus contributing to the pressure.

This recombination process has a finite reaction speed and if the expansion is too fast it can be uncomplete (frozen state). Therefore a certain amount of allowable energy is locked under dissociation/vibration energy and does not contribute to the pressure, leading to a loss of thrust.

Some Euler computations with a kinetic model for seven species (H,H<sub>2</sub>,O,O<sub>2</sub>,OH,H<sub>2</sub>O,N<sub>2</sub>) for two hypotheses, thermochemical equilibrium and frozen state, have shown that an unacceptable degradation of about 30% of D-T could be induced by a frozen state, state which seems unlikely but need to be confirmed. by further investigations.

1.2.6 Performances at low expansion ratio

During the initial phase of the launch trajectory,the nozzle, designed in order to insure a required thrust level at high Mach number, is overexpanded. For Mach numbers less than about 3, a low pressure region on the expansion ramp and even on the internal nozzle, is observed..

This low pressure region is followed by a system of oblique shock waves issued from the flap and sidewalls trailing edges,leading to higher pressures. These shocks can induce boundary layer separation,wich is favorable since it reduces the low pressure extent and thus the drag.

This drag increase is mainly dependant on the afterbody configurations and on their ability to adapt themselves(flap deflection,secondary flow injection).

In order to assess the losses due to this overexpansion some Euler computations have been made for the performances of a few afterbody variants studied in § 1.2.3, for two flight conditions: Mach=1.5 corresponding to the ejector rocket mode and Mach=2.5 corresponding to a RAMjet mode. The results of 100\*C<sub>x</sub> (<0 for thrust) and 100\*C<sub>z</sub> for the X>45m afterbody are summarized in the following tables:

Mach=1.5    α=0°

Afterbody shape	100*C <sub>x</sub>	100*C <sub>z</sub>
generic	1.78	-5.42
concave ramp	1.86	-6.28
short sidewalls	1.67	-5.64
long flap	2.12	-4.86

Mach=2.5    α=0°

Afterbody shape	100*C <sub>x</sub>	100*C <sub>z</sub>
generic	0.51	-1.68
concave ramp	0.55	-1.84
short sidewalls	0.49	-1.67
long flap	0.67	-1.55

We notice that the afterbody contribution to the thrust is negative for all the variants, and much more pronounced at Mach=1.5.If at Mach 1.5 the propulsive system (rocket) is not too much penalized by this drag excess, at Mach 2.5 the drag excess represents 70% of the RAMjet thrust.

The performances of the different concepts are of the same order of magnitude but with a classification inverse to that at high Mach numbers.

In conclusion we observe an important afterbody drag which seems hard to reduce in a significant way, unless if we use a variable geometry or a secondary flow injection in the nozzle. During the design phase of an airbreathing vehicle with a SCRAMjet propulsion, it will be mandatory to find the best tradeoff between this kind of disposals (with a weight penalty) and the use of complementary engines with sufficient thrust.

1.2.7 Conclusion

The afterbody design is well understood and masterized when working with the inviscid approximation; by comparison to an ideal nozzle it is possible to analyze the causes of performance losses and the three dimensionnal effects, and to propose solutions in order to minimize them.

Nevertheless for a more precise evaluation of performances a viscous approach is needed which can modify also the afterbody design.

The studies which are focused on the afterbody, if they afford very useful informations on the aerodynamic viewpoint, does not allow to conclude on the design of even a part of the vehicle; an integrated study of the global configuration is mandatory for that purpose.

1.3 Aerothermodynamics of the global configuration

Some scientists or engineers have tried to have a general evaluation of the performance of a vehicle built around an hypersonic RAM or SCRAM jet by using a thermodynamic global approach. Such an approach is to be related to the analogous effort in the field of engine design; it can help to delineate the significant parameters to be put as variables in a preliminary study or a global study with the aim of improving the global performance. Such studies recommend selection of cold sources and use of high pressure cycle or high temperature reversible heat exchange; all recommendations that are competing with thermal and aerodynamics possibilities. So we consider that it is more profitable to have a much more complex simulation tool, able to rebuild the 3D flow in details or, at least, to give realistic value, in conjunction with elementary experiments,

for the global uncertainties and the local origin of the uncertainties.

In addition to global performance evaluation, the aim of such modelisation is to furnish major derivatives that help the designer to focus research on the more sensitive parameters or constraints, and on the problems of physics that are present behind, and are not well understood or modelled.

The entropy distribution concerning flow and wake surveys related to cold air deflected by body and hot air generated by combustion of incoming flow in air intake, gives the visible indicator of the problems, their difficulties and their localisation, knowing that computation has to be validated areas by areas with the identical phenomena rebuilt in laboratory experiments.

### 1.3.1 Methodology

The methodology proposed by Dassault Aviation can be found in [2] and [3] and is briefly recalled hereafter. It relies on the fact that the design of an hypersonic aircraft propelled by an airbreathing engine is a very integrated process, for many reasons. One is the geometrical imbrication of all the components: the forebody is a part of the air intake, the afterbody is a part of the nozzle, the fuselage is a combustion chamber wall, so that the aircraft can be described as a « flying engine », or alternatively as a « propelling airframe ».

Another reason is the difficulty of this design process: difficulty because success is by no means assured; the feasibility is not proven and performances are expected to be at best marginal, so that no provision can be made for improper interfaces between components; difficulty also because of the accuracy needed in the analysis: the aerodynamic forces sustained by the different elements can be an order of magnitude larger than the resulting effort on the aircraft, so that the former must be accounted for with minimal errors if the latter is to be known with any accuracy.

The contribution of all the aircraft components to each of the aircraft's aerodynamic properties is yet another reason for integrated design: the nozzle contributes not only to thrust, but also to lift and to pitch, the combustion chamber contributes to pitch, to longitudinal and lateral stability, etc..., so that optimization of one of these properties can only be made on the complete aircraft.

For all these reasons, the design of an hypersonic airbreather can only be made globally; this is especially true in the preliminary stages, during which the aircraft shape can be changed drastically. Conception is usually made iteratively: one or more shapes are proposed, their performances, in terms of aerothermodynamics and of mass are predicted, and compared both to those of previous proposals and to the objectives: an analysis is made of the remaining defects and possible solutions are investigated, before new shape candidates can be derived.

In order to perform this design from an aerothermodynamic point of view, the chosen methodology is based on global CFD simulations of the flowfield around and through the vehicle considered, using a multidomain method.

Such numerical tools must be capable of nose to tail predictions, so that computational cost is a major difficulty; however they must also be sufficiently accurate to give reliable informations to the designer. The solution chosen by Dassault Aviation relies on a multizone / multimodel strategy, which allows the user to specify in each zone the degree of complexity he wants to take into account, based on required accuracy and available funding. The multizone code incorporates elementary methods of widely varying complexity, ranging from empirical "behaviour laws" (e.g. correlated mixing distances, induction times, etc...) to three dimensional nonequilibrium turbulent Navier Stokes solvers.

The elementary numerical tools composing the global numerical tool must be well validated for reliable analysis of the flow in each of the components of the aircraft, such as done in § 1.1 and 1.2. A detailed description of these elementary solvers can be found in [2] to [6] and validation efforts in [7] to [10].

The interfaces between the zones must be carefully specified, more so when different computational methods are used in different regions. This is especially true if the simulation of the different zones is undertaken by different teams; it is necessary to specify not only the nominal physical quantities at the interface, but also uncertainties on these quantities.

Interfaces can have a varying degree of complexity, depending on the configurations. The easiest case is the parabolic one, where there is no upstream influence. The interface is then passive, in the sense that the interfacing method has minor influence on the results, and introduces no new uncertainty. The more difficult situation occurs when the interface has an active influence on both the upstream and the downstream component; this is for example the case when simulating a scramjet with injection and combustion at Mach numbers only slightly greater than one: the interface between the inlet and the combustor plays a very active role in the prediction of the stability of the whole system, and the global simulation must be very integrated, with permanent data exchange between the zones.

### 1.3.2 Example of results

An example of application of the principles and methods mentioned above is described here. More details can be found in [2]. The aircraft studied is the generic airbreathing SSTO launcher already presented in figures 1.2-3 and 1.2-4. Performances are sought for the airbreathing part of the trajectory; in this phase the aircraft is propelled successively by an ejector rocket, a ramjet and a scramjet, which are all fitted in a single propulsive stream. The current aircraft shape is by no means optimized, and should not be taken as a candidate design; however it is used as a test case for the design tools which are being developed.

To compute the performances of the aircraft, a decomposition is made between the flow through the combustor and the rest of the flowfield. The latter is computed in the Euler and boundary layer approximation, using a single unstructured mesh (figure 1.3-1). A model of the flow through the combustor is provided by engine manufacturers; it outputs average flow quantities at the



combustor exit as a function of the average flow quantities at the entrance.

Examples of the results of the flow simulations are given in figures 1.3-2 to 1.3-7. Around twenty computations have been performed to cover the trajectory corridor, in terms of Mach number and angle of attack. Each of those takes three to five hours of cpu time on an IBM RS 6000 workstation, so that the complete set can be obtained overnight on a seven nodes cluster, or in a couple of hours on a multiprocessor supercomputer.

The unstructured mesh is adapted to represent a variable geometry aircraft. In the present simulations, it has been modified around the inlet to account for the moving lip. Such a modification is straightforward with unstructured, tetrahedric meshes, and can easily be automated.

The aerodynamic coefficients (Lift, pitch, "drag minus thrust", effect of sideslip on yaw and roll moments, control surface efficiencies, ...) are a direct result of the simulations. They are stored in a computerized database, to be used by trajectory simulators. The evolution of the coefficients with Mach number and angle of attack is usually represented graphically as "carpet plots", figure 1.3-8, which allow interpolation of the results to any trajectory point.

Figure 1.3-9 shows the integration of drag along the aircraft, from nose to tail, for different Mach numbers in scramjet mode, at a given angle of attack. It is seen that the largest effect of Mach number is in the combustion chamber, due to the higher losses in high speed combustion.

Figure 1.3-10 show the effect of angle of attack on the drag. This representation emphasises how integrated this effect is: the increase of the angle of attack increases the air capture and decreases the Mach number at the combustor entrance, both of which increase the thrust, however not all this thrust is recovered because higher pressures lead to lower nozzle efficiencies. The increase of angle of attack also increases the induced drag of the front part of the aircraft; altogether the drag is decreased when angle of attack is increased within the range studied. However the rate of this evolution is very dependant on the trajectory point (figure 1.3-9).

The effect of angle of attack and of Mach number on the lift and pitch are shown on figures 1.3-11 to 1.3-13. It is seen again that the global effects are the sum of large and opposing local ones, so that only an integrated simulation can predict them correctly. For example the inlet causes a large loss of lift, which increases with angle of attack; in parallel the lift of the forebody increases, and that of the rearbody also because the engine pressure increases. Altogether the lift increases with the angle of attack, but only a global simulation can predict the rate of this evolution.

The same is true of the effect on pitch: only a simulation accounting for all elements of the aircraft, including propulsion, can predict correctly longitudinal stability. It is seen on figure 1.3-12 that the generic configuration studied is severely unstable.

### 1.3.3 Influence of the modelisation hypothesis

The results presented in the previous paragraph have been obtained with a fully three dimensional method, except for the combustion chamber. It is felt that no results useful for design, i.e. no quantitative results, can be obtained with one or two dimensional methods, even for so called "2D shapes". Also, and perhaps more critical, planar simulations tend to restrict the designer to these 2D shapes, which are very probably not the optimal ones ([2]), and so should be avoided if at all possible.

However a number of approximations have been made in these simulations, based on cost limitation considerations. The major ones are the following:

1. The flow field everywhere but in the combustion chamber has been calculated using the Euler plus boundary layer approximation, neglecting viscous / inviscid interactions.
2. The flow computation has been coupled with the engine model in an ad-hoc, zero dimensional manner. Also the eight side by side scramjet modules have been treated as one "average" entity, neglecting the effect of distorsion.
3. The combustion products in the nozzle and rear body have been treated as a fixed composition gas, with no accounting of kinetic effects (freezing of recombinations).
4. The location of transition to turbulent flow on the forebody has been fixed arbitrarily, introducing an uncertainty in the prediction of friction drag.

The objective of the study for which preliminary results are presented here is to quantify the effect of these approximations, in order to support future decisions on the level of modelization necessary for actual design cycles, based on a cost versus accuracy trade-of.

In the two following paragraphs we present the first sensitivity studies which have been performed, all of them concerning the scramjet mode of propulsion. The effect of the first two approximations mentioned above is analysed. In part 1.3.3.1 we investigate the effect of some of the approximations in the coupling between the combustion chamber model and the flow field computation, in scramjet mode. In part 1.3.3.2 we present a first estimation of the effect of losses due to viscous interactions on global performances.

#### 1.3.3.1 Degree of integration of the combustor simulation in the overall calculation

The conception of an hypersonic, ram / scramjet propelled vehicle is necessarily a collaborative effort between an aircraft and an engine manufacturer. The former however needs to be able to predict the global performances of the vehicle, and so will use a modelization of the flow in the combustor, provided by the engine designers.

This modelization, for the case of a supersonic ramjet, is necessarily a transfer operator: it provides flow properties at the rear end of the combustor as a function of those it receives at the front one. Upstream coupling can be necessary in a number of situations ([2], [3], [12]), for

instance when combustion generated shock trains propagate in the air intake, however it has not been considered here.

This transfer operator can be based on different principles: it can be a CFD solver, either one, two or three dimensional, with different possible levels of modelization. The flow at the downstream end of the air intake is then used as boundary conditions for this solver, which in turn gives the fluid state at the downstream end of the combustor. This is probably the best solution; however it requires the integration of a reliable and efficient combustion solver in the global simulation software, which will require further efforts and has not been accomplished yet.

Alternatively the transfer operator can be a model based on the transposition of existing performance data for the combustor, coming either from CFD simulations or from wind tunnel experiments. Because these simulations or experiments have been performed in conditions different from those actually encountered, a transposition is necessary:

In the PREPHA program only limited performance data for scramjet combustors in flight conditions is available; it has been generated using simple zero or one dimensional simulations, with entrance conditions in the combustor obtained using assumed performances of the forebody and inlet.

However, for the purpose of estimating in principle the uncertainties introduced by using the second method to establish the combustor transfer operator (transposition), a comparison has been made between global performance numbers obtained with a transfer operator relying on a transposition of preexisting combustor results, and those obtained by repeating the one dimensional combustor calculation using the actual flow properties at the air intake exit.

The results are the following:

Recomp. / Transp.	Aircraft T-D	Combustor thrust	Lift	C.P. loc.
Mach=6	- 2 %	- 2 %	- 3 %	-0.9%
Mach=10	+ 9 %	+ 4 %	- 0.5%	- 0.3 %

Table 1: Effect of the re-computation of the combustor properties using the actual entrance conditions, compared to a transposition of preexisting results, on aircraft thrust minus drag, lift and center of pressure location, and on combustor "conventional" thrust.

The effect obtained on global performances can be considered as acceptable for early studies, so that the transposition of predetermined performances can be used if necessary. Such a transposition can be particularly useful if the combustor performances are determined experimentally.

Another approximation often introduced in the coupling between combustor model and flow computations, in multi engine aircrafts, is the accounting for only one "average" engine. For example the generic "2D" design considered here has eight side by side identical engines; however in the computations described in paragraph 2 inflow conditions averaged over the eight engines have been fed to the transfer operator, and uniform properties downstream of the

combustor are used as boundary conditions in the global computation.

This approximation has been removed partially by treating separately the two extreme lateral engines. The difference in inflow conditions is the following, for a Mach=10 flight point:

	Mach	Stag. pres.	Mass flow / area
Average	3.7	1100	575
Central engines	3.8	1150	550
Lateral engines	3.6	1050	655

Table 2: Difference in inflow conditions between the lateral and central engines.

The effect on the global performances of the aircraft is the following:

	Aircraft T-D	Combustor thrust	Lift	C.P. loc.
Mach=10	- 4 %	+7%(lateral) -7 % (central) - 3% average	0	+ 0.2 %

Table 3: Effect of the accounting of the actual inflow properties of the different engines, on aircraft thrust minus drag, lift and center of pressure location, and on combustor "conventional" thrust.

Because the lateral engines receive a larger air flow, they have higher thrust. The overall effect of the distorsion is negative however, but not very much so.

From this simple estimation, it appears that the effect of distorsions is significant on individual engines, but that the overall effect on aircraft performance is smaller than the sum of these elementary influences, because they induce flow changes in other parts of the aircraft, and in particular in the nozzle.

The dispersion on global performances induced by the inlet distorsion is predicted here by the comparison of global simulations with and without taking them into account, and so includes all correlations between the dispersions in individual elements. Consequently an estimation of the uncertainties based on their analysis would intrinsiquely account for all correlations and so be minimal.

1.3.3.2 Representation of viscous losses

In all the computations mentionned above, the flow in the air intake is calculated with an Euler and boundary layer approximation, which does not account for the viscous interactions. This introduces a large uncertainty especially on total pressure losses; however a scramjet is primarily

sensitive to air flow capture, so that the uncertainty on global performances is probably not so large.

To obtain an order of magnitude of this effect, a subdomain was introduced in the global computations to represent the inlet, where the Navier Stokes equations are solved (figure 1.3-14). As a first step, an assumption of two dimensional flow has been made, so that only an order of magnitude of the viscous effect is obtained here. In particular, the probably very important corner effects are neglected. Nevertheless from the comparison of viscous and inviscid two dimensional inlet simulations we derived an approximate "viscous correction" to the combustor inflow conditions, and to the inlet drag.

Computations were performed for flight Mach numbers of 6 and 10. The results are shown in figures 1.3-15 to 1.3-19. The inviscid simulation of the inlet flow at Mach=6 (figure 1.3-15) illustrates the manner in which the inlet was conceived, in order to obtain "shock on lip" at this Mach number. However the viscous calculation (figure 1.3-16) shows that the shock / boundary layer interaction leads to inlet unstart for this generic design at this Mach number.

The results for Mach=10 are presented in figures 1.3-17 to 1.3-19. The shock boundary layer interaction causes a large increase in static pressure (figure 1.3-19), however not sufficient to cause boundary layer separation.

In terms of global performances the influence of viscous interactions is the following:

Aircft. T-D	Combor. Thrust	Inlet Drag	Lift	C.P. loc.
- 5 %	- 20 %	+ 15 %	+ 1 %	- 0.5 %

Table 4: Effect of viscous interactions on aircraft thrust minus drag, lift and center of pressure location, on inlet drag, and on combustor "conventional" thrust, for a Mach=10 flight point.

The effect is largely negative on inlet and combustor performances; however the higher (static) pressure levels lead to higher nozzle thrust, so that altogether the global performances are degraded far less than would be guessed from the effect on inlet-only.

Again the effect of viscous interactions is estimated through the comparison of two global simulation results, so that all correlations are accounted for and the dispersion is minimal. It appears that the effect is significant but not major on aircraft thrust minus drag: it is however crucial on the prediction of the stability of the flowfield, and so either on the Mach range where scramjet operation is possible for a given design, or on the sizing of the inlet if scramjet operation is required at Mach=6. Such sizing is a general design issue, and the results shown here illustrate the necessity to take into account the thick boundary layers and their stability in the global conception of the aircraft.

1.3.4 Conclusion

A methodology for the integrated design of hypersonic airbreathers has been presented in its current status and the planned improvements have been discussed. The basic tool

for this design method is a global, 3D CFD code, incorporating a domain decomposition method which allows the choice of the most adapted method locally, based on a trade-off between cost and accuracy. The domain decomposition allows cooperation between industrial teams specializing on different elements of the aircraft without compromising the globality of the simulation.

An application to a generic design has been presented; the results confirm the occurrence of large three dimensional effects even on such "2D" shapes, they also highlight the close integration of all the aircraft elements: each of them influences most of the aerodynamic properties of the aircraft, often in large and opposite ways, so that only a global simulation, which guarantees that the contribution of the different elements is evaluated taking into account the effect of others, can give an accurate prediction of the overall properties.

The cost of the simulations is of the order of three to five hours on a workstation, or less than fifteen minutes on a supercomputer. Such cpu consumption and turnover times are clearly acceptable for design utilisation.

2. FUNCTIONAL APPROACH

2.0 Another way of surveying the aerothermodynamic problems of RAM and SCRAM vehicles is to consider the functions and their relation to the problems. We can separate the function of sustentation, of propulsion, of control, of structural resistance under the constraint of reusability or structural integrity. However it is no gain to do such separation except to consider other functions than has been surveyed in the previous part where connexion between lift thrust and drag was clearly large. We will turn better to the problem of control and of compatibility with low-speed requirements. However the structural resistance is a major functional need that cover mainly the resistance to high pressure in air intake and combustion chamber and resistance to thermal stresses in transient and stabilized regime of flight. The increase of pressure in air intake is the true limitation to maximum indicated airspeed of hypersonic vehicle, and so to the capabilities of acceleration coming from proportionality of thrust minus drag to dynamic pressure. Figures 1.3-10 and 1.3-11 gives typical distribution of integral forces from the nose to x position with and without internal flows. Integrating these forces will give drag with and without internal flow.

2.1 Problems of stability and control of hypersonic vehicle

The destabilizing effect of the air intake is proportional to its size, that we have identify as increasing with Mach Number. Roughly it can be said that destabilizing effect is proportional to the momentum of captured air in air intake and to  $\beta$ ,  $\beta$  being the sideslip angle. So it precludes any forward air intake and favour air intakes in rearward position relative to center of gravity. For pitch movement the things are much more complex due to non-linear variation of pressure with angle of attack not only on forebody but on the afterbody with nonlinear coupling

through the combustion process. So the longitudinal stability has to be correlated with computation and computation with experiments : the experiments are covering the derivative pitching moment with angle of attack in the case of flow-through geometry, or with real gases expansion but not generally with both phenomena. The computation has its own uncertainties but is alone able to give a « lift breakdown » curve, as seen in § 1.3.2 figure 1.3-11). For example in the figure 2.1-1, such curves are given for two angles of attack versus longitudinal coordinate, allowing to analyse the contribution of all major elements of the vehicle to the lift and consequently to the pitching moment. Optimisation of the design can only be realistic with constant lift and pitching moment, so the derivatives with respect to angle of attack are to balance with other derivatives and the deflection of controls. Similarly it is mandatory in design balance to have the color image of heat fluxes or better of integrated heat conduction/radiation (at least by local integration of heat transfer equation) for keeping also the constraint of temperature boundaries in the loop.

Not of least importance are the derivatives for angular velocity of pitch that help to reduce the complexity of control systems by avoiding too large unstable behaviour leading to large control surfaces and rate of deflection. Such derivatives are also directly connected to lift variation along x coordinate.

For lateral control the same analysis can be done in yaw and roll with curves of contribution along x coordinate and y coordinate of the different parts of the vehicle (Fig. 2.1-2). But it is of relevant importance to carefully analyse the yaw stability with combustion because there is a balance of nose destabilizing effect and of rearward stabilizing effect due to derivative of jet induced pressure in sideslip on the edge of nozzle, if it is, as usually, not completely axisymmetric and with separation due to under or over expansion. The quality of modelling such derivatives of separated or wash-out areas in 3D is actually poor and request special interest by ad-hoc experiments and numerical workshops.

## 2.2. Problems of stability and control of the flow field

### 2.2.1. Stability of laminar boundary layer.

The first problem for aerothermal design is the delimitation of transition from laminar to turbulent flows. Large increase in the knowledge of the process of transition by amplification of unstable viscous modes has helped to have some codes for evaluation of the most amplified mode and crude rule for transition positioning e.g. value of  $N$  associated to  $e^N$  linear amplification. Some non linear effects are necessary to be accounted for in hypersonic, in the frame of amplification of incoming flow fluctuations. However if we consider corner flows or internal flows the noise radiated by upstream turbulent flows may force to transition neighbouring areas so that the importance of keeping laminar the forebody has not to be underestimate and can contribute significantly to total drag. Air intake by its interaction with forebody boundary layers will anyway give transition through shock impingements.

Moreover the laminar flow on the first centimeter of leading edges of body, air intake, fins will contribute

significantly to maintain low Stanton number and help to reduce critical temperature at least in nominal flight.

Contrary to the problem of the transition prediction for reentry vehicles, where transition onset is mainly due to wall roughness induced by ablative erosion and/or discontinuities between the different pieces or tiles of the Thermal Protection System, the problem of transition prediction during the launch phase for RAM and SCRAM propelled vehicles is mainly posed by natural transition if we consider a relatively smooth forebody.

Besides the interest in lower heat loads, when transition to turbulent state is delayed, a major advantage is a thinner boundary layer thickness in front of the inlet, leading to a better efficiency of this latter. For instance, for a nominal flight condition, the turbulent boundary layer thickness at the end of the very long forebody can be about 1/3 to 1/4 of the inlet height, and it can be lowered by a factor of 4 to 5 if the boundary layer remains laminar.

Moreover the control of the spanwise homogeneity of the boundary layer thickness is directly related to the transition onset homogeneity which can be controlled by a suited shape design of the forebody. And this design activity is very dependant on the accuracy of the boundary layer stability tools, since the three dimensionnal flow can give rise to a rather complex map of transition. Such situation is illustrated by Fig. 2.2-1 to 2.2-4 from ONERA/DERAT computations. These figures show the intermittency factor  $\gamma$  and the boundary layer thickness for a generic forebody shape and two flight conditions:

Mach=6  $\alpha=0^\circ$  and Mach=12  $\alpha=5^\circ$

The transition onset has been obtained with the linear stability analysis code CASTET from ONERA/DERAT, which gives the most unstable waves and their direction, giving insight in the type of instability (Tollmien-Schlichting or Cross Flow), coupled with the  $e^N$  envelop method and a given value of  $N$  at transition of 10.

Such a code is very useful in the design process since it allows to understand where the shape must be modified and tailored in order to postpone transition

### 2.2.2 Control of separated flows.

Of same importance is the control of separated flows. Generally it comes from interaction of shock waves and boundary layer but of greater importance is the wake-shock interaction at the rear of the configuration. The shock-B.L. interaction is generally with high sweep due to high Mach number so the separated areas are well organized in stable patterns of conical vortical flows; exception is for low Mach Number or normal shock-wave before subsonic combustion where the classical control are well known (but not so easy to implement). The major concern is on the upstream lambda shock-wave boundary layer-wake interaction because it appears at the rear of the configuration and is sensitive to the pressure ratio of nozzle, to the mixing process and to the temperature of the wall by the thickness of the subsonic sublayer. Stabilizing process by passive means or by active control would be of considerable interest.

### 2.3 Problems of compatibility with low-speed

A lot of subsonic problems are generated by the unusual aerodynamic shape imposed by hypersonic requirements. Generally very slender configurations need to have good handling in high angle of attack because of the necessity of such high angle due to very low lift generated at low incidences. Major problems are coming from vortex bursting location near the control surfaces at the rear and so to non-linear behaviour in lateral characteristics of such vehicles. If it is a long iteration process to carefully design the shape of leading edges and their camber compatible with aerothermal requirements of high speed, it is of high value to avoid solving the problems by large (for high angle of attack) tails or fins that gives birth to difficult thermal problems in hypersonic outside of very large leading edge radius for the low sweep angle giving efficiency in low-speed lateral behaviour.

## 3. DEMONSTRATION - QUALIFICATION OF RAM-SCRAM VEHICLES

**3.0.** The major problem with such vehicles comes from the cost of flight if they need boosters or aircraft to deliver in the point of the self sustained flight envelope where acceleration can take place. One good solution, if possible, is to drop such vehicles in supersonic Mach number when supersonic inlet can be started in supercritical regime - roughly  $M \geq 1.8$ . Moreover the instrumentation to be put on such vehicle can be costly due to local high temperature, and generally rebuilding of performance of combustion and local losses are done indirectly outside of limited number of pressure and temperature measurement. So it is of utmost importance to have comprehensive ground tests for helping to have experimental data for supporting analysis and research of improved design - or problem - free design. So there is a well balanced strategy of ground experiments - computations - flight experiments to build with rationale methodology.

Moreover the main problem will be, after solving problem phasis, to recover the uncertainties to be transformed in margins not too large, otherwise there is no attractive product, and not too small otherwise there is no end to the refinements in design.

### 3.1 Design tools necessary for success in design

Outside of test and error preliminary demonstrators of hopes and problems, where usefulness or cost are not major requirements, it is clear that all the advanced way of design is mandatory for an efficient design. Of particular importance are the flexibility of design and the detailed CFD and thermal solvers. Without such tools no convergence towards a good design is possible. It means :

- features modeling in CAO
- unstructured fluid dynamics and thermal solvers with automatic mesh refinement on shocks and viscous layers
- visualization of data.

The use of basic fluid dynamics reference tests for validation of codes, of dedicated material tests in realistic temperature environment, of aerodynamics tests with and without combustion are the necessary complement to a systematic numerical simulation approach. Difficult

problems encountered in solving complex chemistry and turbulence modeling equations encourage to have alternate approach with different codes: giving alternate answer and so error chasing process it supports an uncertainty assessment process as in the hypersonic Hermes program.

### 3.2 Integration Validation Object Methodology

For being sufficiently confident in CFD, it is needed to have reference tests used in comparative self-substantiation between experiments and computation. For that the best methodology is the I.V.O. methodology as developed in the French PREPHA program by Dassault Aviation. Such methodology asks for a comprehensive demonstration of codes capabilities that led to improvement of complete code at the level just needed for optimization work in the design phase and then to flight - simulation self substantiation of performance.

I.V.O. for Integration Validation Object is a vehicle design not to be flyable but to contain all the basic fluid dynamic phenomena, all the difficulty of the flow solver and of the geometry of real vehicle but favoring the quality of measurement in experiments. For example, the thickness of the lip will be larger to help to measure easily and accurately its effect on Stanton number and distortion of flow, the divergence or convergence of flow will be larger than necessary to exemplify the convergence - divergence effect on flow field, etc... Roughly it is a not so slender but realistic design, easier to be instrumented in tests. Such « object » is not at the level of a workshop because it is at the level of complexity of real vehicle and clearly announce that the « true » design being evolutive in the design phasis, it will remain as a reference not far but not exactly real : between real industrial and analytic test it has the characteristic of being a « virtual object » for the designer and a good tool for experimentalist.

One main objective of such Integration Validation Object is to test that the quality of codes is sufficient for really designing an integrated vehicle and not only reference objects use in research centers with the true weighting of problems of elementary accuracy leading to global uncertainties. For example, the models of turbulence and combustion to be used really in the design has to be at the good level for a thrust minus drag data without too large scatter compared to alternate code ; such verification can be done globally on I.V.O and elementary by comparison to more detailed experiments and computations with more complex modeling of thermochemistry.

Comparison between experimental and numerical data on this I.V.O. configuration will highlight possible defects in the integrated simulation method , and reveal the « hard points » in the correct predictions of overall performance data.

The first definition of such an I.V.O. ,based on an experiment performed by ITAM (Russian Academy of Sciences), and a preliminary analysis of its adequation to the objective of integration validation ,can be found in [1]. Results of related results of experimental investigations may be found in [14] and [15].

### 3.3 Problems of stability of flow and control

For effective design of RAM and SCRAM jet propelled vehicles with internal or external combustion we need to add to the steady experiments and computation, unsteady problems solving procedure. First is the start-unstart of air intake flow, and start-unstart of combustion process. A lot of work remains to be done before efficient design tools can take into account such transient phenomena that will give confidence in any future design. But the increase in power of computer (teraflops challenge to be practically fulfilled at the end of the century) and of solvers (multiscale - multiphysics solvers) let us hope a near future first level capability in that field.

Second is the unstable flow field oscillations to be damped by passive design or active control. Such active control will be mandatory for increasing stability of flow with combustion and will appear in the loop of transient flow computation and experiments in the future. We have to be ready for such effort.

### 4. CONCLUSIONS

Numerical and experimental (IVO, tests) tools are available for effective design of realistic RAM and SCRAM propelled vehicles.

However flight conditions are not really duplicated in wind tunnel for high enthalpy flow.

So the design to be checked by experiments is to be well managed at the level of predicted performances by computation.

Basic knowledge is available, codes are efficient so that a design freezing is possible if an efficient multidisciplinary approach is done in a major industrial design office able to take into account all the constraints coming from aerothermal and aerodynamic critical design points.

#### Aknowledgments:

Most of these studies have been funded by DGA, CNES and MENESR, in particular in the framework of the PREPHA program.

The work presented here could not have been performed without the help of a number of Dassault Aviation staff members; we are in particular grateful to P. Rostand, J.M. Hasholder, M.P. Leclercq, M. Ravachol, M. Mallet, F. Chalot

#### REFERENCES:

- [1] P. Perrier, B. Stoufflet, P. Rostand, V.K. Baev, A.F. Latypov, V.V. Shumsky, M.I. Yaroslavtsev, « *Integration of an hypersonic airbreathing vehicle : assessment of overall aerodynamic performances and of uncertainties* », AIAA 95-6100, Sixth international aerospace planes and hypersonics technologies conference, 3-7 April 1995, Chattanooga, TN
- [2] Perrier, P. Rostand, « *Hypersonic airbreathing aircraft integration through CFD: Global simulations for global thinking* », AIAA 94-3090, 30th Joint AIAA/SAE/ASME/ASEE Propulsion Conference and Exhibit, Indianapolis, 1994
- [3] P. Perrier, P. Rostand, B. Stoufflet, « *Integration of an air-breathing hypersonic airplane* », AIAA 93-5032, Fifth NASP conference, Munich, 1993
- [4] M.P. Leclercq, B. Mantel, J. Périaux, P. Perrier, B. Stoufflet, "On recent 3-D Euler computations around a complete aircraft using adaptive unstructured mesh refinements", in proceedings of Second World Congress on Computational Mechanics, Stuttgart (Germany), August 27-31, 1990.
- [5] F. Chalot, J.M. Hasholder, M. Mallet, A. Naim, J.A. Nicolai, J. Périaux, P. Perrier, P. Rostand, B. Stoufflet: "Finite element methods for the compressible Euler and Navier Stokes equations with chemistry. Applications to aerospace engineering.", IUTAM SYMPOSIUM - Marseille, France - September, 1-4, 1992.
- [6] F. Chalot, Z. Johan, M. Mallet, M. Ravachol and G. Rogé, "Development of a finite element Navier Stokes solver with applications to turbulent and hypersonic flows", AIAA 92-0670.
- [7] M. Mallet, J. Périaux, P. Rostand and B. Stoufflet, "Validation on aerodynamic simulation methods for Hermès spaceplane and future hypersonic vehicles", AIAA / NASP conference, Orlando, 1992.
- [8] J.P. Rosenblum, "Afterbody conception for hypersonic vehicles", AIAA 93-5031, Fifth NASP conference, Munich, 1993.
- [9] European Hypersonic Data Base, Workshop on hypersonic flows for reentry problems, CICA Sophia Antipolis, France, January 27-29, 1993.
- [10] F. Chalot, S. Guillemot, J.M. Hasholder, M.P. Leclercq, M. Mallet, A. Naim, M. Ravachol, J.P. Rosenblum, P. Rostand, B. Stoufflet, E. Teupootahiti, "Validation et utilisation industrielle d'un code résolvant les équations de la mécanique des fluides compressibles", 30th A3AF Conference (23), Nantes, France, October 1993.
- [11] P. Perrier, "Problèmes Mathématiques posés par l'estimation des incertitudes des simulations numériques", Masson, 1993.

- [12] E.S. Billig, S. Corda, R.D. Stockbridge, "Combustor - inlet interactions in scramjet engines", APL technical review, vol 2, n°1, pp 118-126, November 1990.
- [13] M. Pierce and W. Ely, "A computational exploration of the importance of three dimensionality, boundary layer development, and flow chemistry to the prediction of scramjet nozzle forces and moments", AIAA 91-5059.
- [14] V.K.Baev, V.V.Shumsky, M.I.Yaroslavl'tsev. "The Study of a Two-Mode Combustion Chamber Operation at Subsonic Heat Supply". In: "Flow Gasdynamics in Nozzles and Diffusers", Novosibirsk, 1982.
- [15] V.K.Baev, V.V.Shumsky, M.I.Yaroslavl'tsev. "Study of Combustion and Heat Exchange Processes in High-Enthalpy Short-Duration Facilities". High-Speed Flight Propulsion Systems, Chapter 8, Progress in Astronautics and Aeronautics, Vol.137, Edited by S.N.B.Murthy, E.T.Curran, Washington, USA, 1991.
- [16] Carl A. Trexler and Sue W. Souders. « Design and performance at a local Mach number of 6 of an inlet for an integrated scramjet concept ». NASA-TN D-7944-August 1975

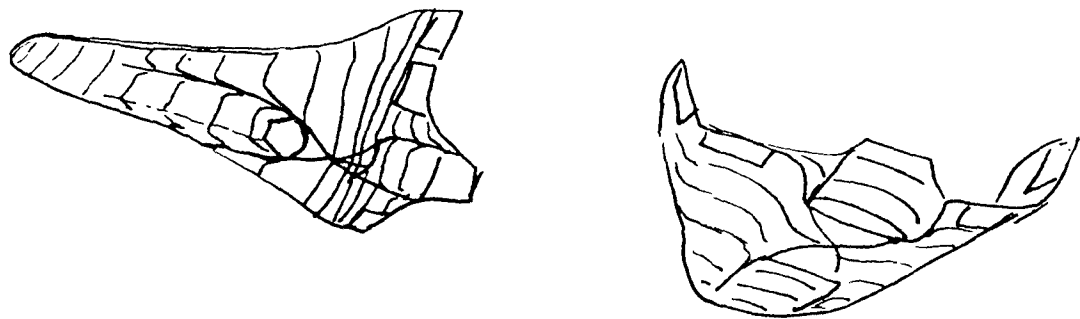


Figure 0.1: Schematics of the strong integration of air intake in a vehicle

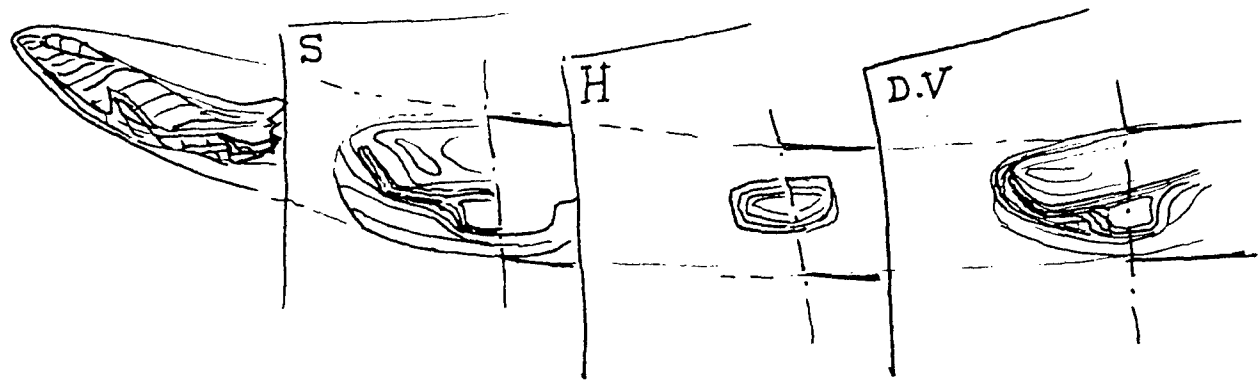


Figure 0-2: Wake survey analysis in entropy,enthalpy and momentum



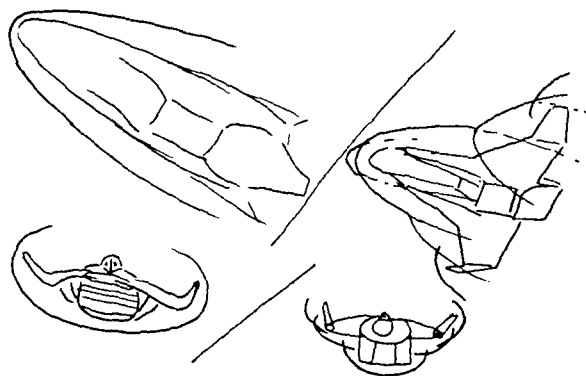


Figure 1.1-1: Shielding shock

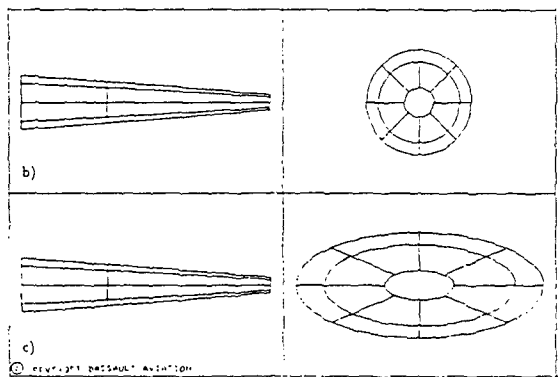


Figure 1.1-2: Different forebody shapes without nose

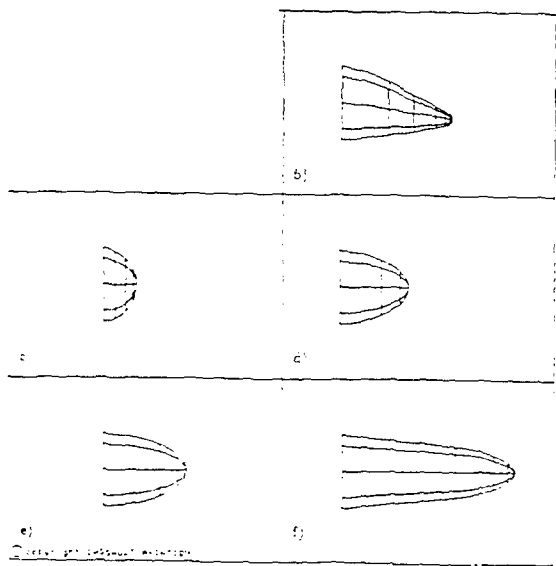


Figure 1.1-3: Different noses considered

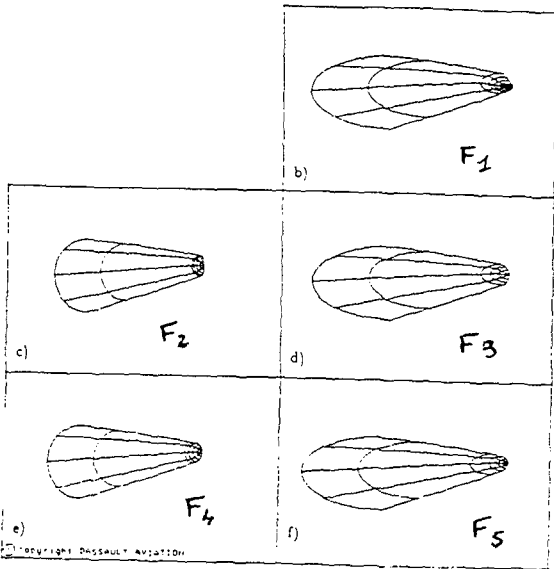


Figure 1.1-4: Different forebody configurations

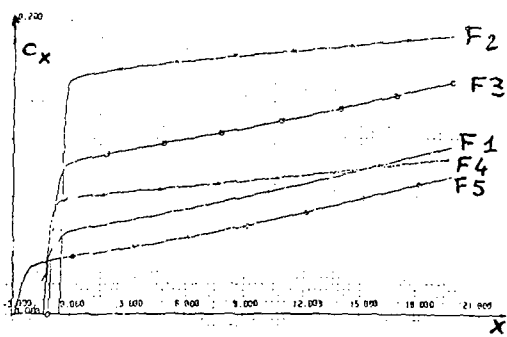


Figure 1.1-5: Drag coefficients for the different configurations

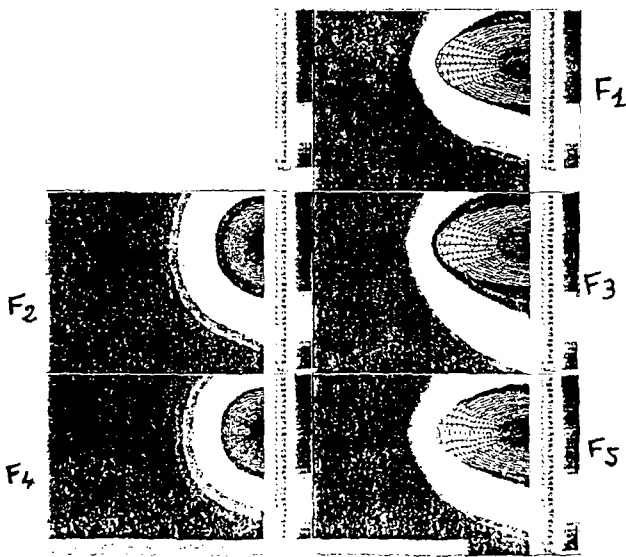


Figure 1.1-6: Iso-Mach maps for the different configurations (X=19m )

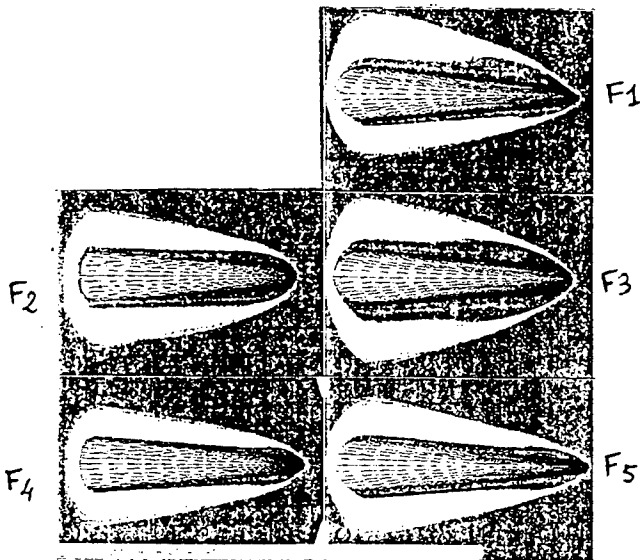


Figure 1.1-7: Iso-Mach maps in the symmetry plan for the different configurations

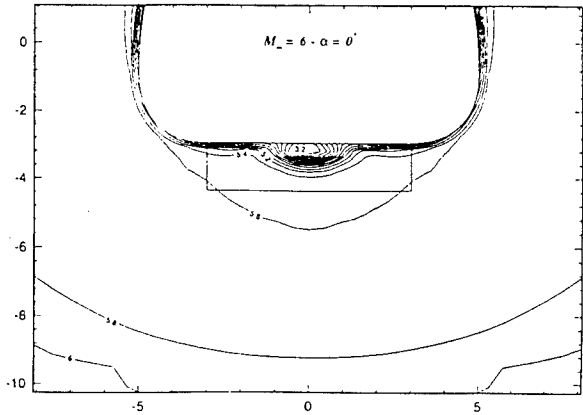


Figure 1.1-10: Generic forebody;  $M=6$   $\alpha=0^\circ$  Iso-Mach line in front of the air intake

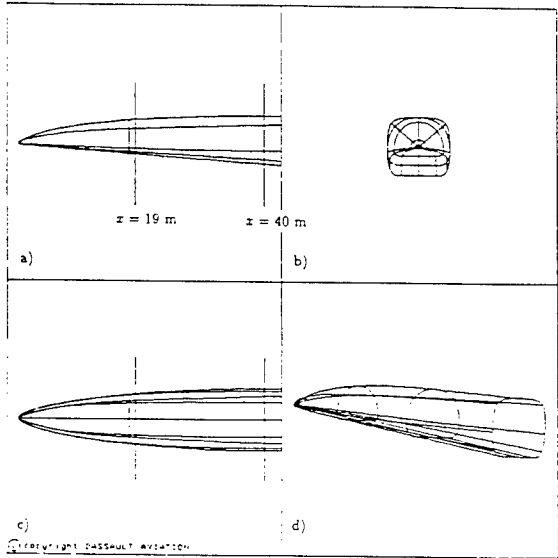


Figure 1.1-8: Modified generic forebody

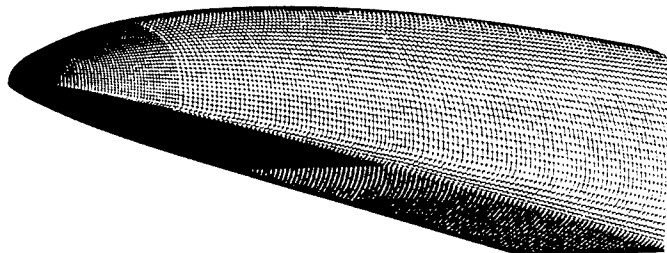


Figure 1.1-9: Mesh of the generic forebody

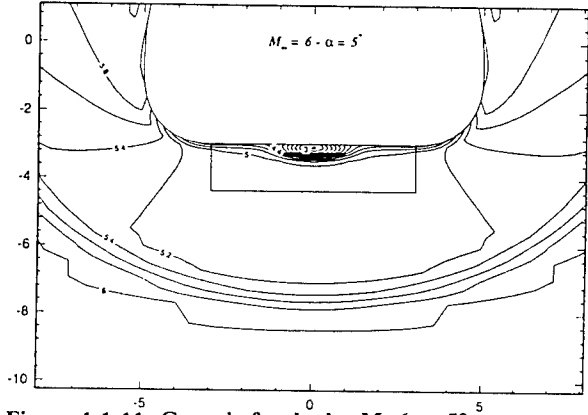


Figure 1.1-11: Generic forebody;  $M=6$   $\alpha=5^\circ$  Iso-Mach line in front of the air intake

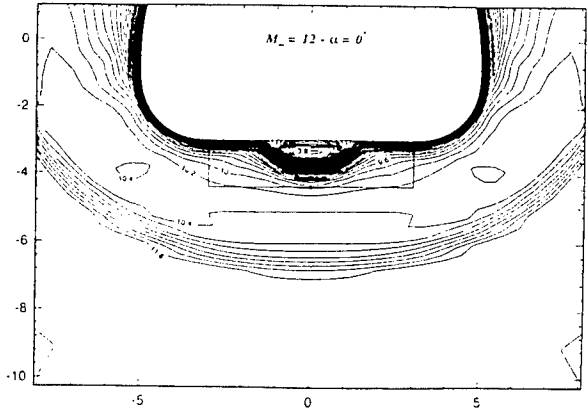


Figure 1.1-12: Generic forebody;  $M=12$   $\alpha=0^\circ$  Iso-Mach line in front of the air intake

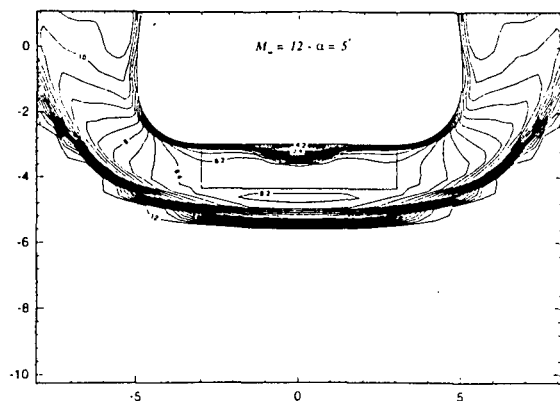


Figure 1.1-13: Generic forebody;  $M=12$   $\alpha=5^\circ$   
Iso-Mach line in front of the air intake

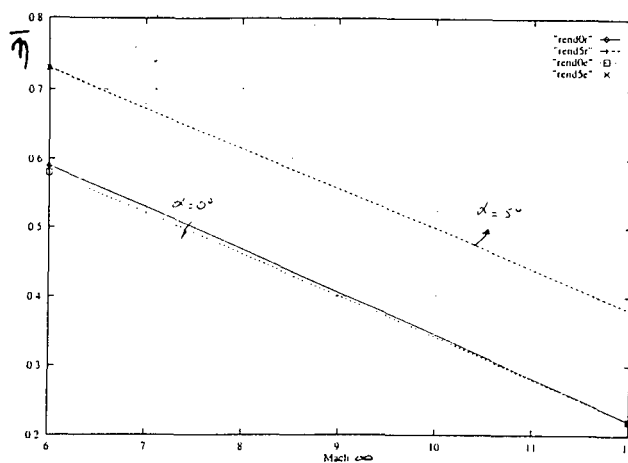


Figure 1.1-16: Mean efficiency in the captation section: generic--->evolutive forebody

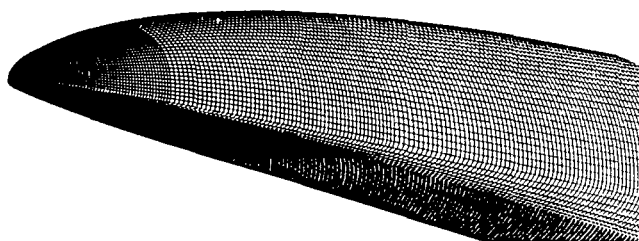


Figure 1.1-14: Mesh of the evolutive generic forebody

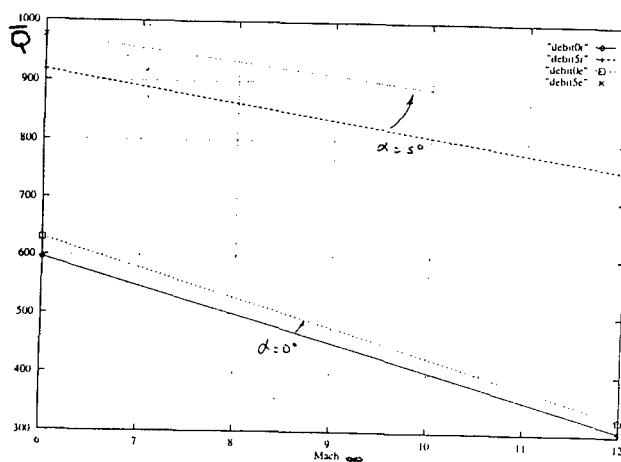


Figure 1.1-17: Mean mass flow rate in the captation section: generic--->evolutive forebody

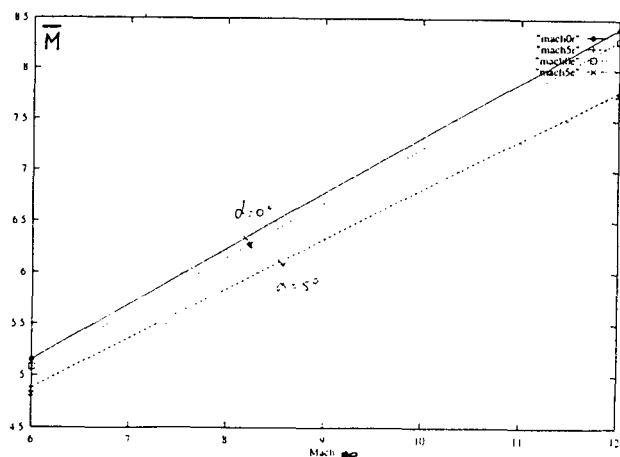


Figure 1.1-15: Mean Mach number in the captation section: generic--->evolutive forebody

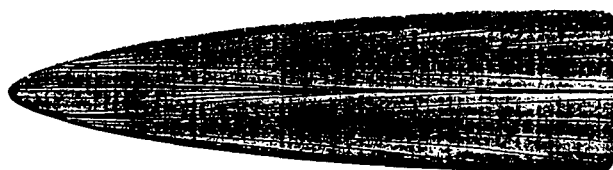


Figure 1.1-18: Evolutive forebody;  $M=12$   $\alpha=5^\circ$ ;  
wall streamlines

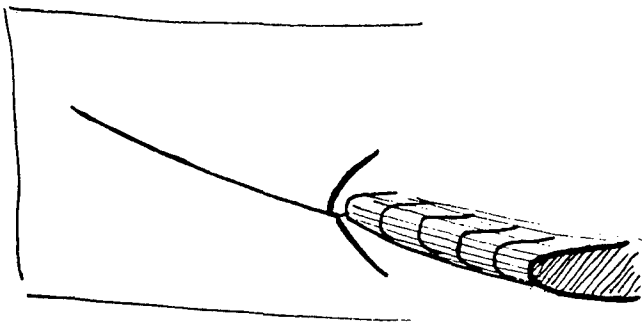


Figure 1.1-19: Overheating due to shock-shock interaction

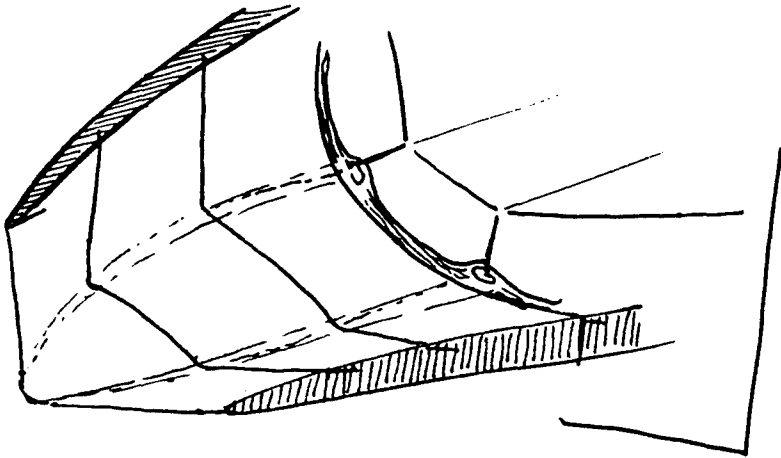


Figure 1.1-20: Shock boundary layer interaction in a corner

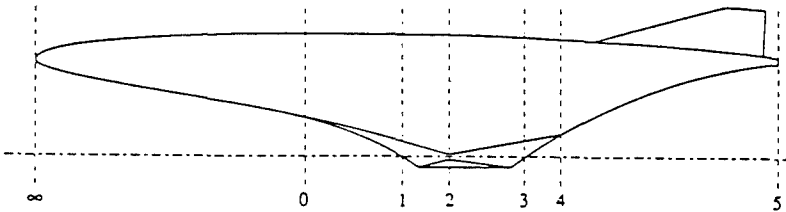


Figure 1.1-21: Reference positions on a generic configuration

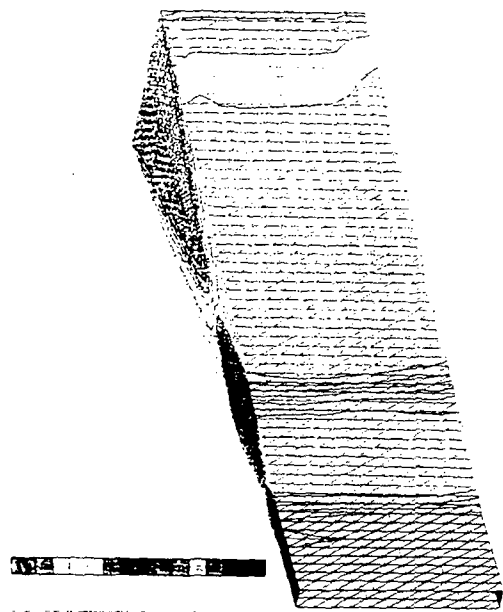


Figure 1.1-22: Generic air intake AI1

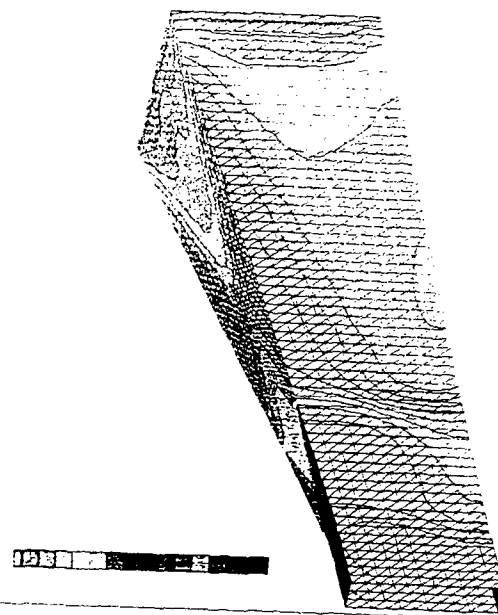


Figure 1.1-24: Generic air intake AI3

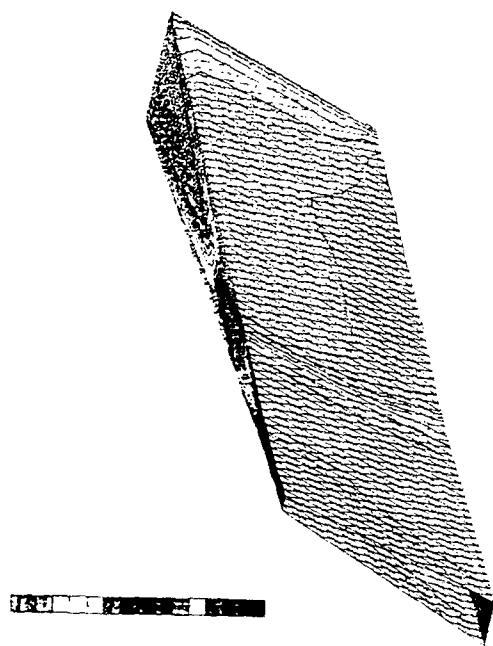


Figure 1.1-23: Generic air intake AI2

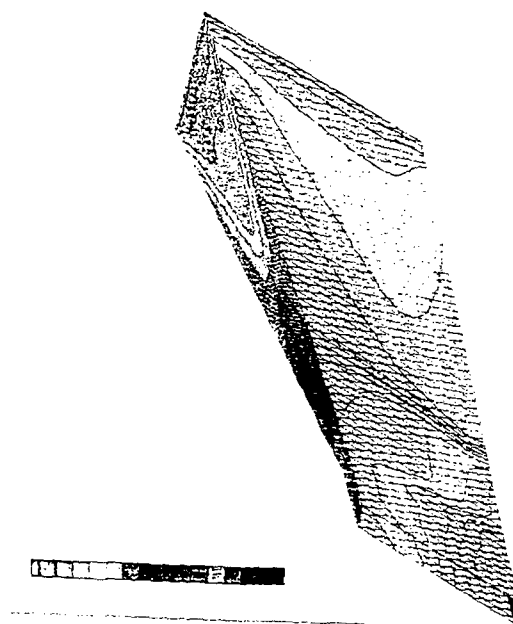


Figure 1.1-25: Generic air intake AI4

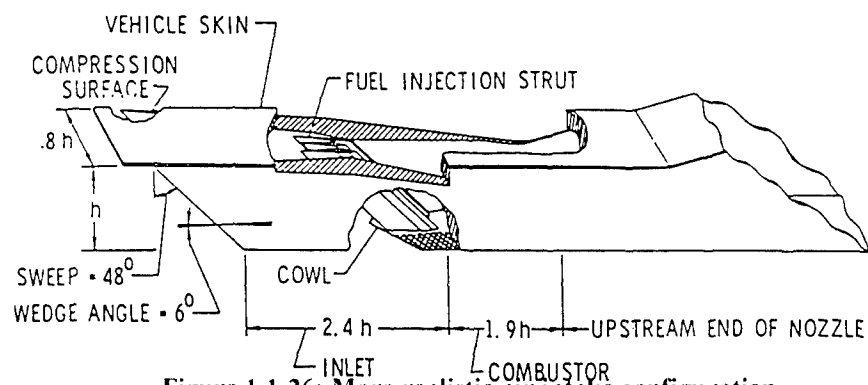


Figure 1.1-26: More realistic air intake configuration

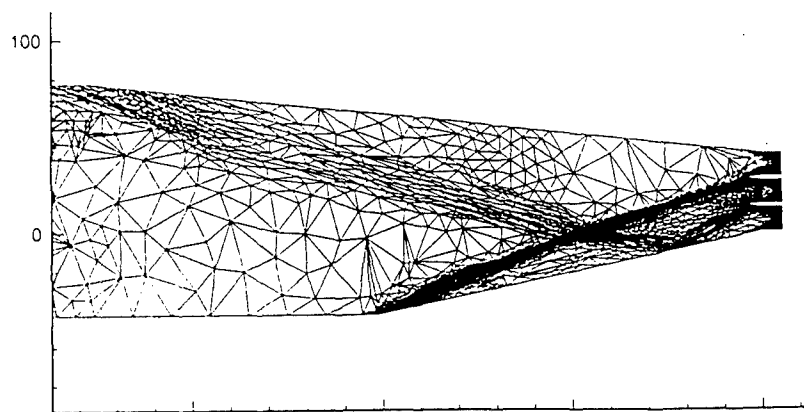


Figure 1.1-27: Unstructured mesh of a 2D air intake with struts

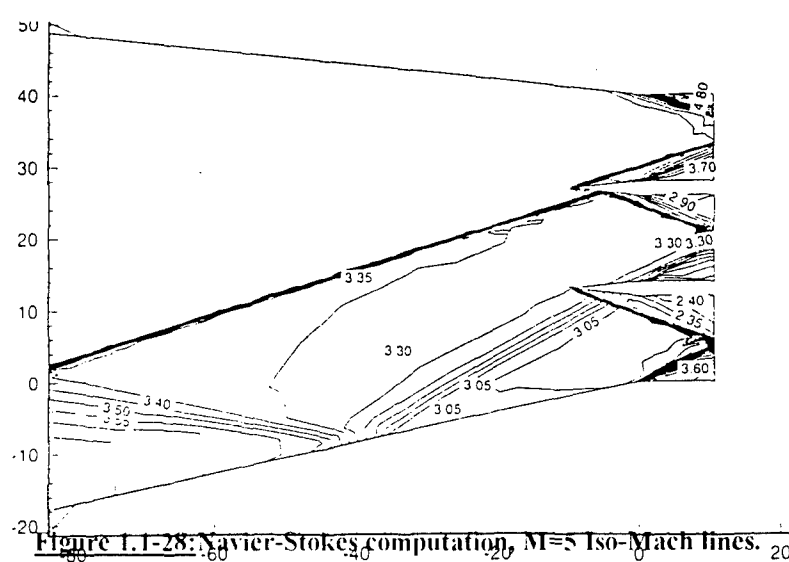
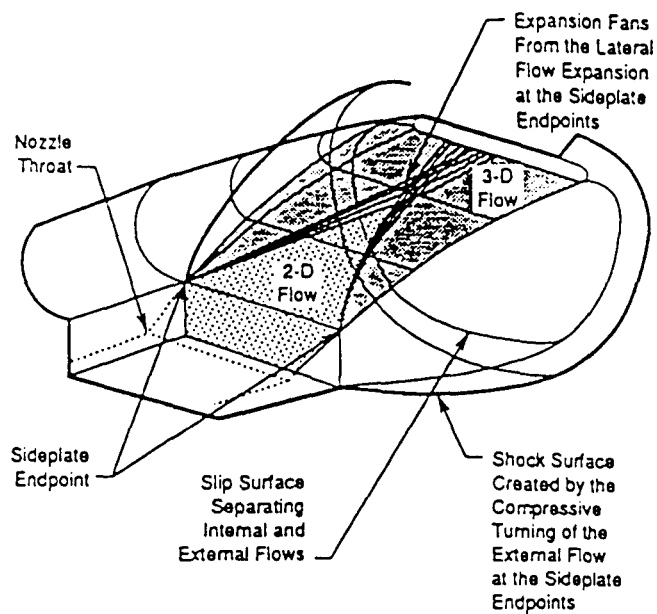
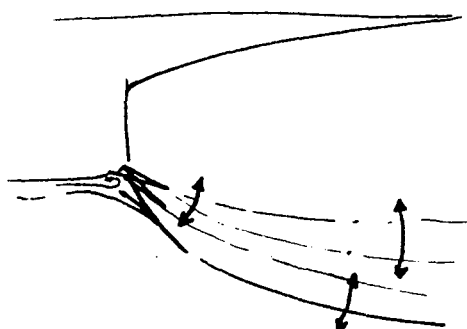


Figure 1.1-28: Navier-Stokes computation,  $M=5$  Iso-Mach lines.



**Figure 1.2-1:** Schematics of the flow on a SERN nozzle. Three dimensional effects occur due to the pressure waves initiated at the lower surface trailing edge and on the sides. From [13].



**Figure 1.2-2:** Schematics of variable flap concept

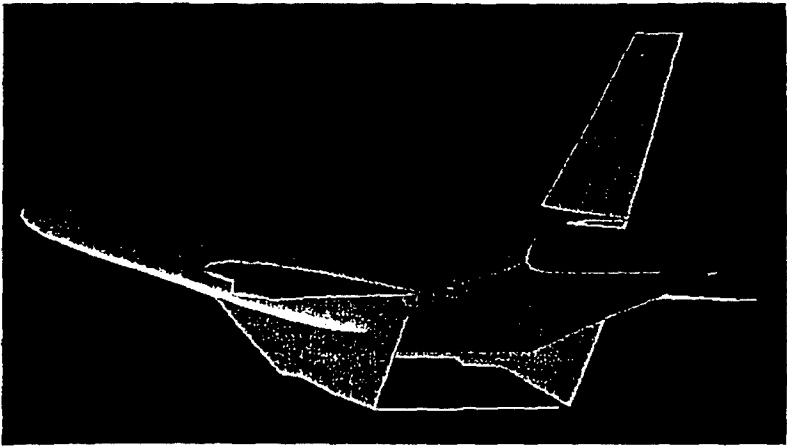


Figure 1.2-3: Reference generic vehicle. Rear view

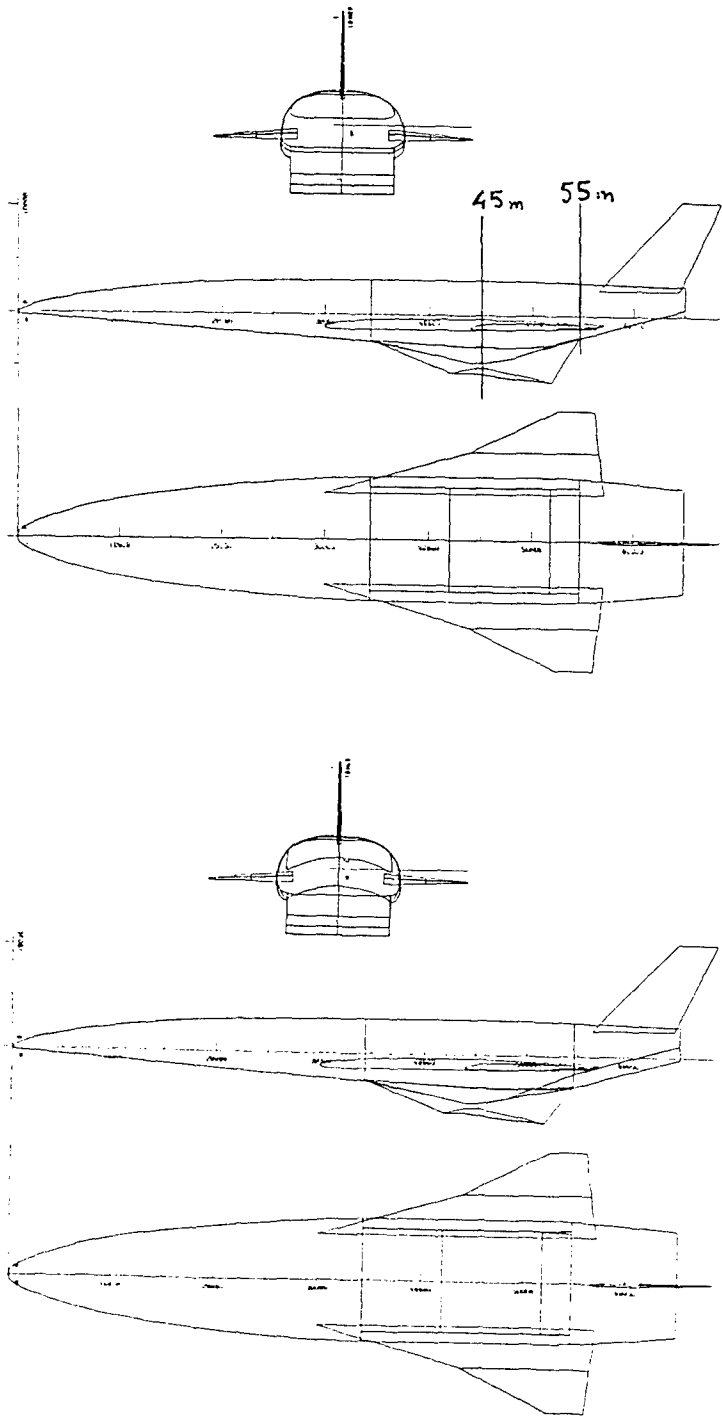
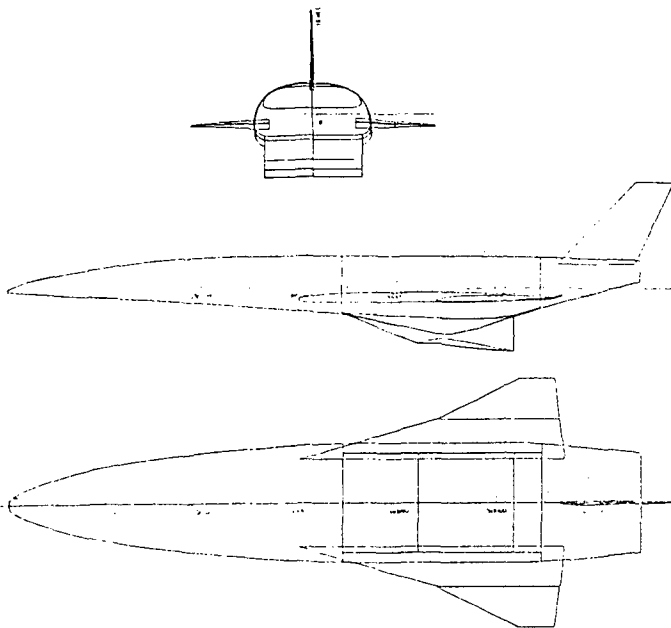


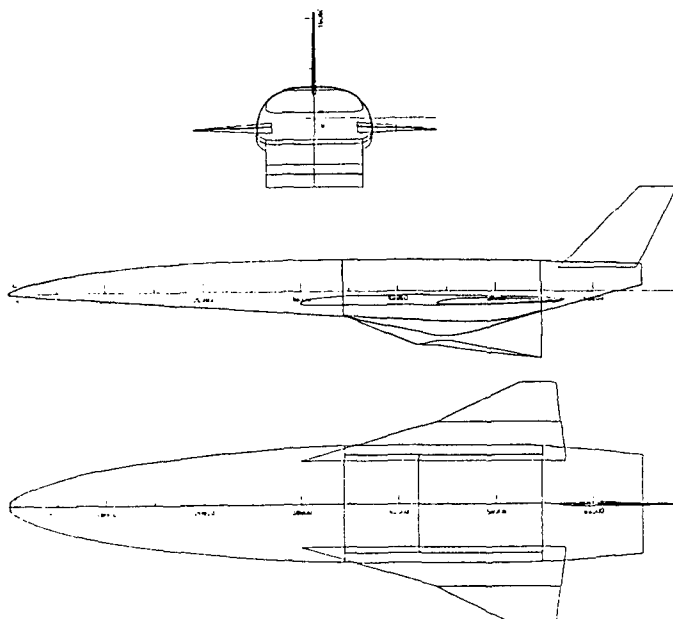
Figure 1.2-4: Reference generic vehicle

Figure 1.2-5: « concave ramp » variant of the generic configuration





**Figure 1.2-6:** « short sidewall » variant of the generic configuration



**Figure 1.2-7:** « long flap » variant of the generic configuration

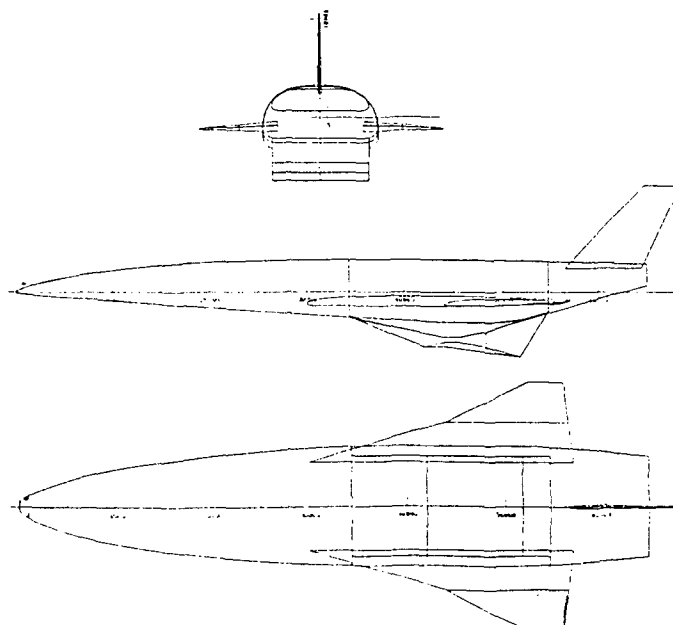


**Figure 1.2-8:** « deflected flap » variant of the generic configuration

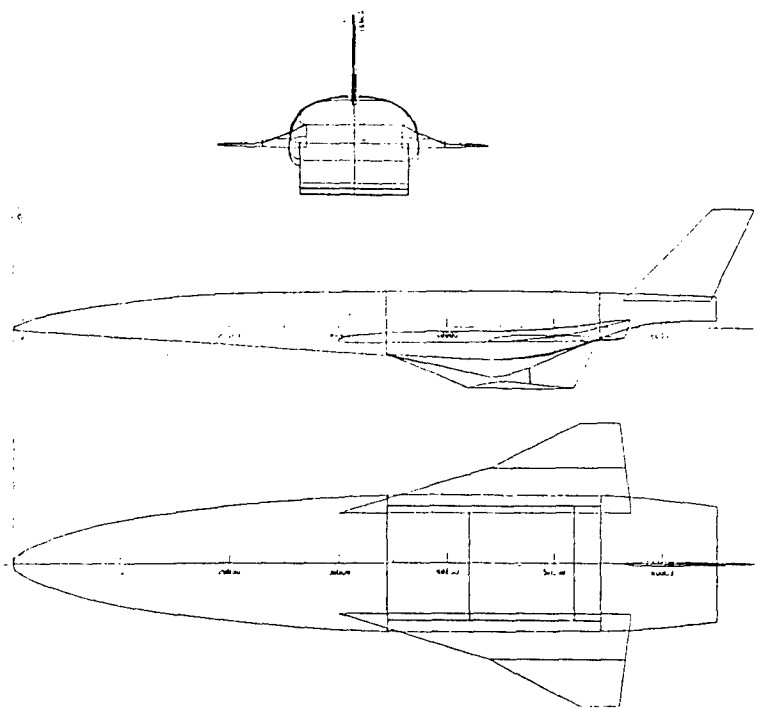


**Figure 1.2-9:** « engine axis +5° » variant of the gneric configuration

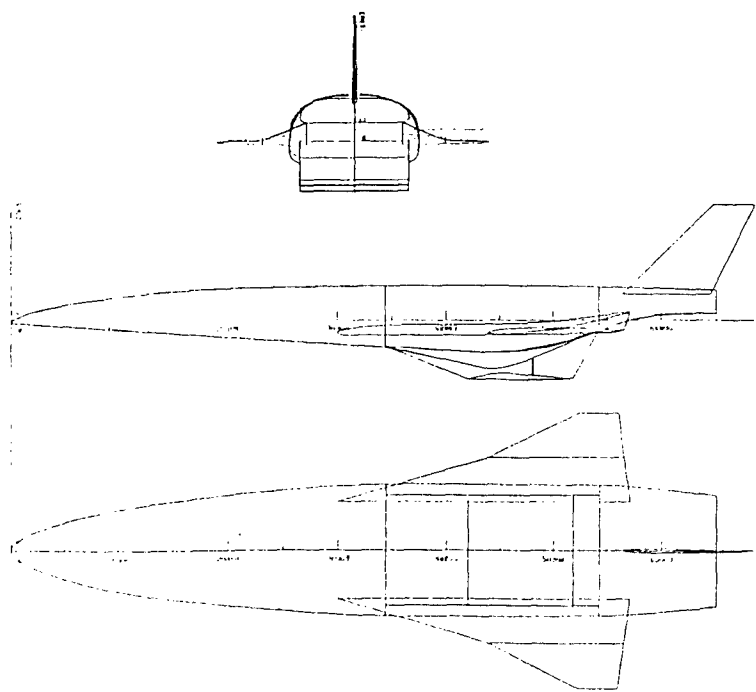


**Figure 1.2-10:** « nozzle axis +5° » variant of the generic configuration

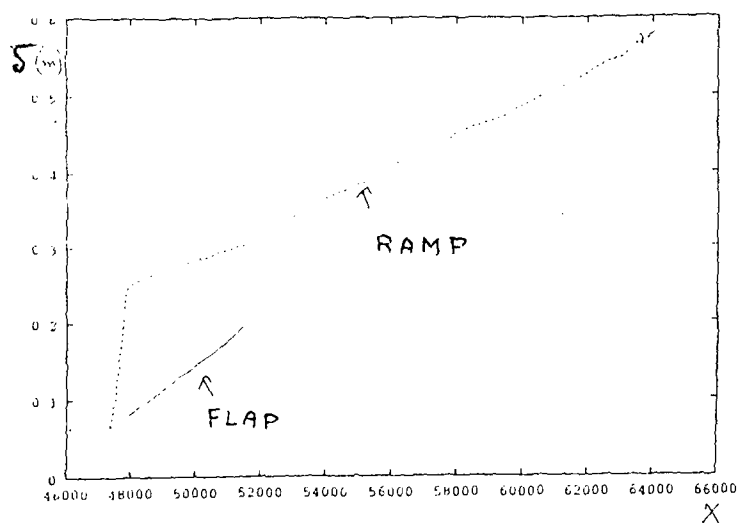


Figure 1.2-11: Boundary layer thickness.  $M_\infty=10$

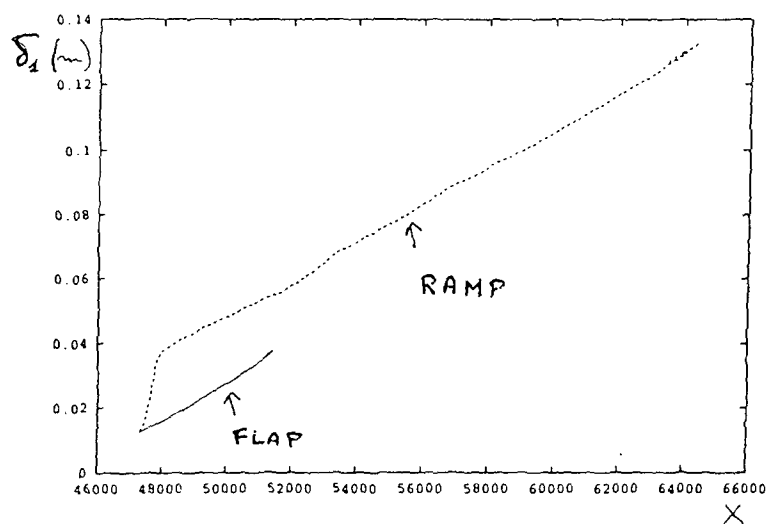


Figure 1.2-12: Boundary layer displacement thickness.  $M_\infty=10$

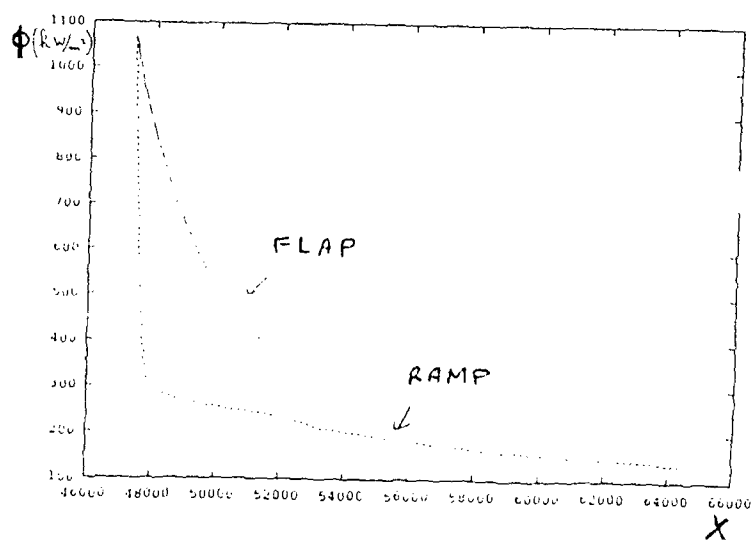


Figure 1.2-13: Wall heat flux.  $M_\infty=10$

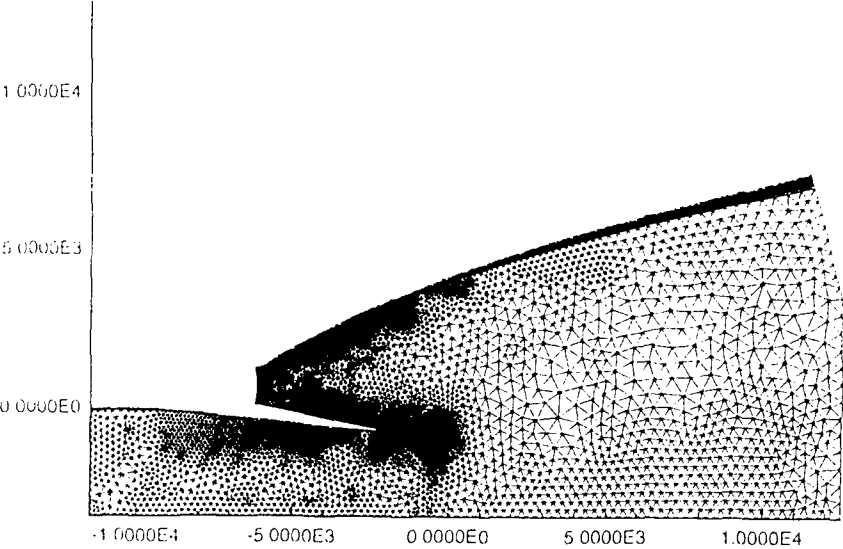


Figure 1.2-14: 2D unstructured mesh of the afterbody

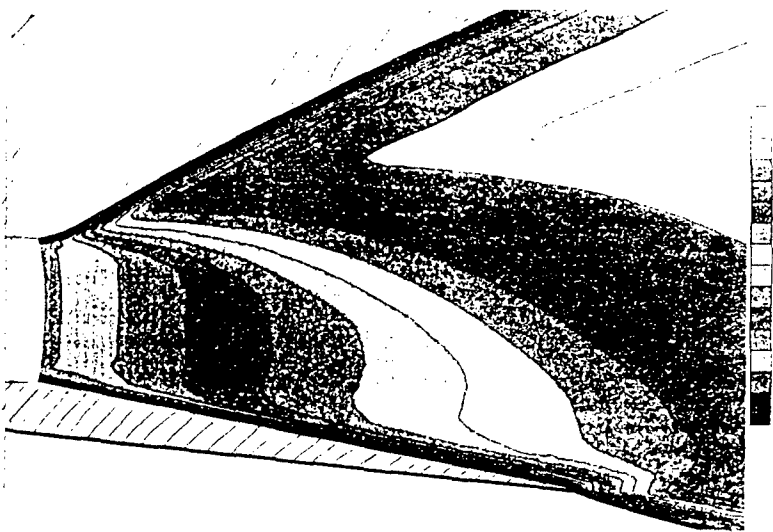


Figure 1.2-15: Iso-Mach map showing the viscous regions.  $M_{\infty}=10$

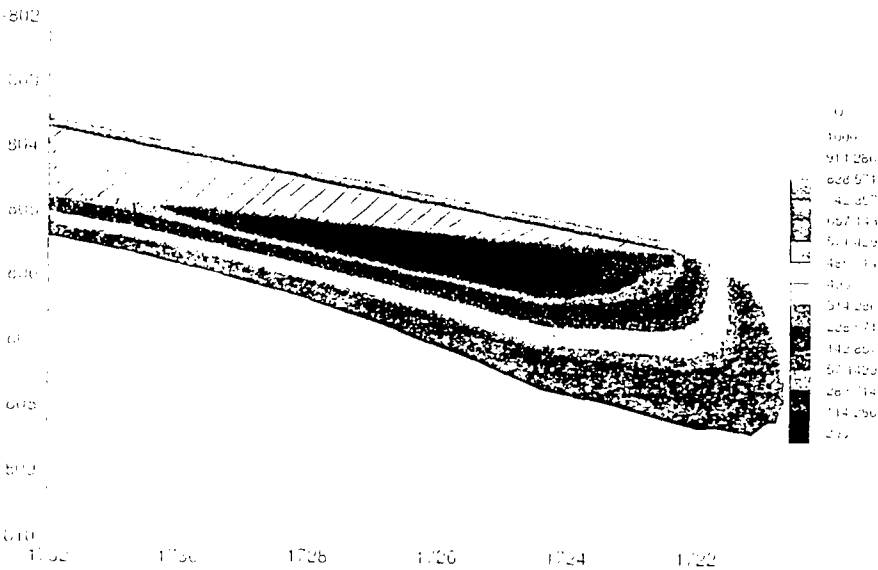


Figure 1.2-16: Local velocity field on the flap windward side showing the separated zone.  $M_{\infty}=10$

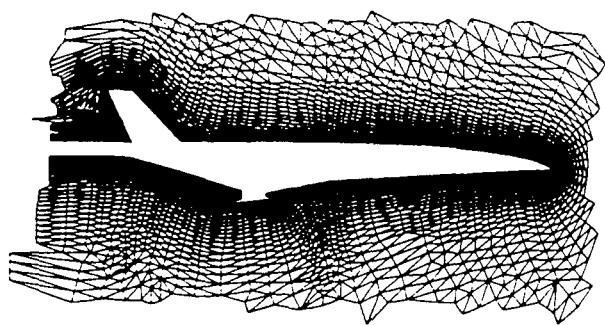


Figure 1.3-1: Cut in the unstructured mesh, in the symmetry plane of the aircraft

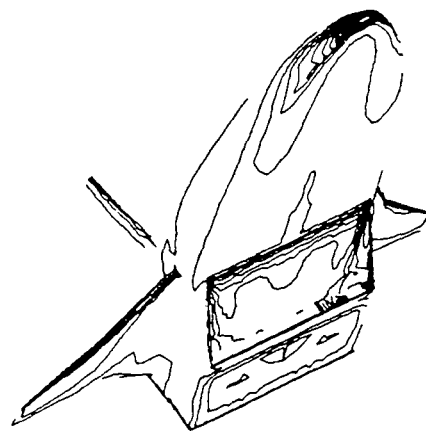


Figure 1.3-4: Pressure coefficient on the body surface,  $M=10$   $\alpha=4^\circ$ , scramjet mode.

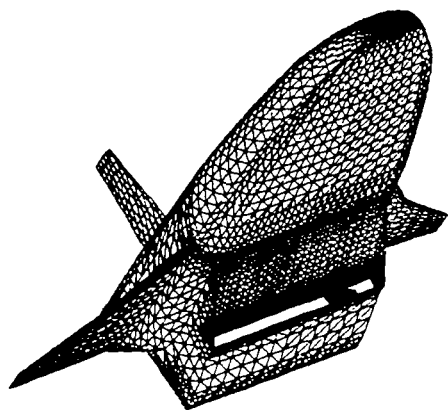


Figure 1.3-2: Surface mesh.

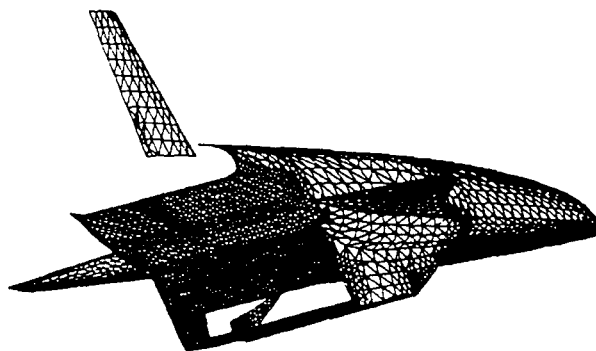


Figure 1.3-5: Skin mesh, view from the rear

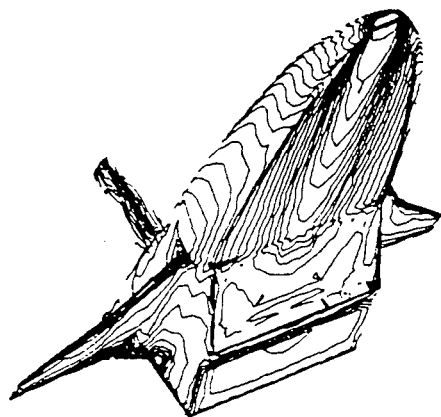


Figure 1.3-3: Mach number on the surface, for  $M=10$   $\alpha=4^\circ$ , scramjet mode. The normal bow shock causes higher pressure losses in the forebody center line.

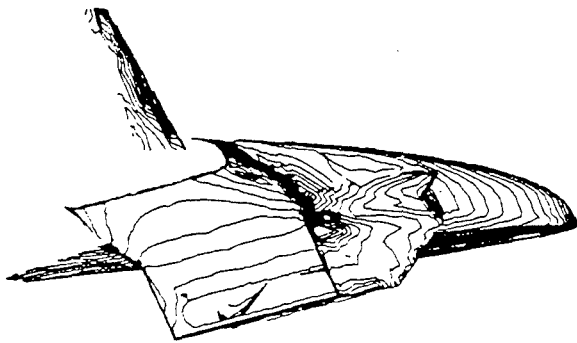


Figure 1.3-6: Mach number on the surface  $M=10$   
 $\alpha=4^\circ$ , scramjet mode.

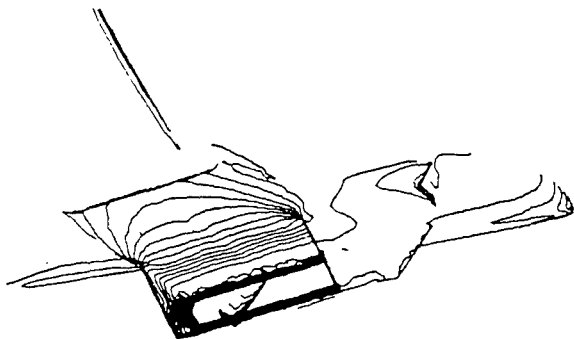


Figure 1.3-7: Pressure on the surface  $M=10$   
 $\alpha=4^\circ$ , scramjet mode.

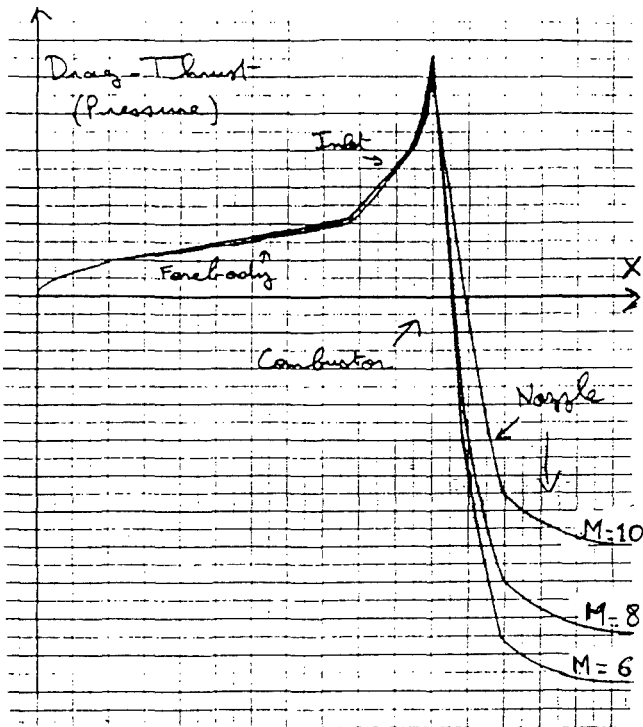


Figure 1.3-10: Integrated evolution of drag along the vehicle, for  $\alpha=4^\circ$ , scramjet mode.

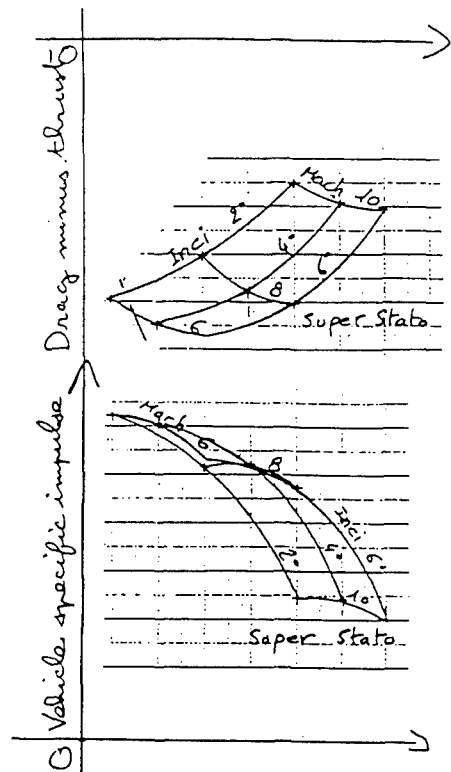


Figure 1.3-8: «Carpet plot» of the evolution of thrust minus drag and vehicle specific impulse with Mach number and angle of attack.

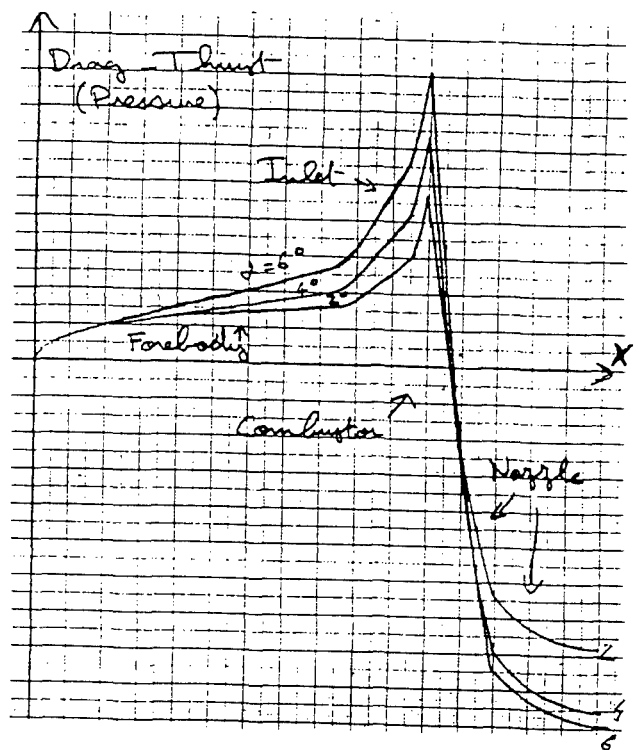


Figure 1.3-9: Integrated evolution of drag along the vehicle, for  $M=8$ , scramjet mode

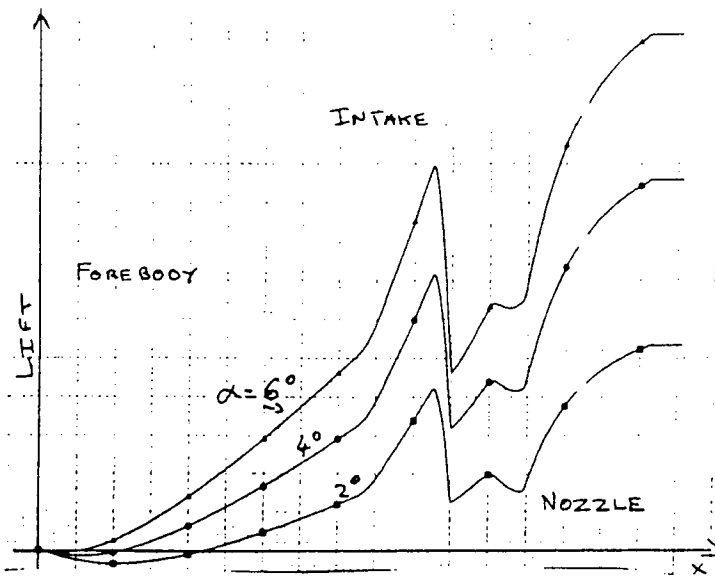


Figure 1.3-11: Integrated evolution of lift along the vehicle. Effect of angle of attack (scramjet mode).

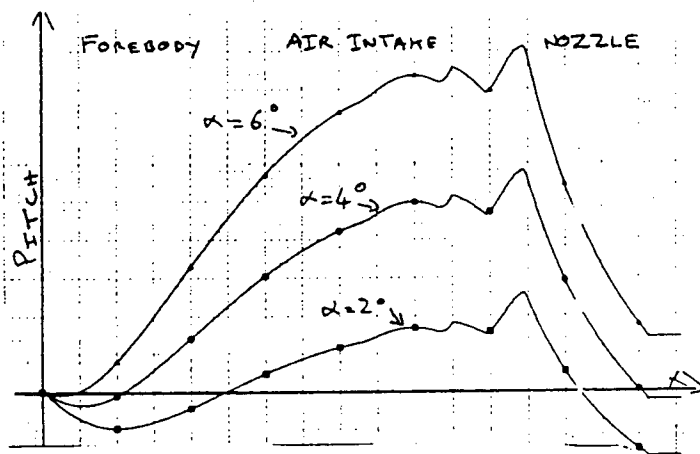


Figure 1.3-12: Integrated evolution of pitch along the vehicle. Effect of angle of attack (scramjet mode).

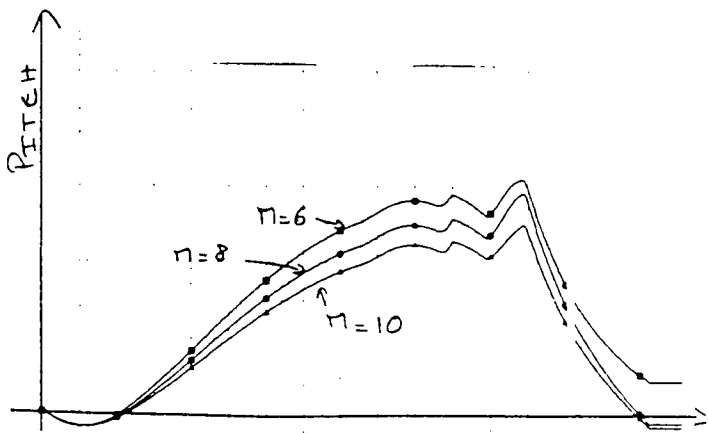
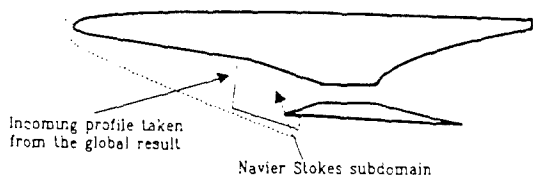
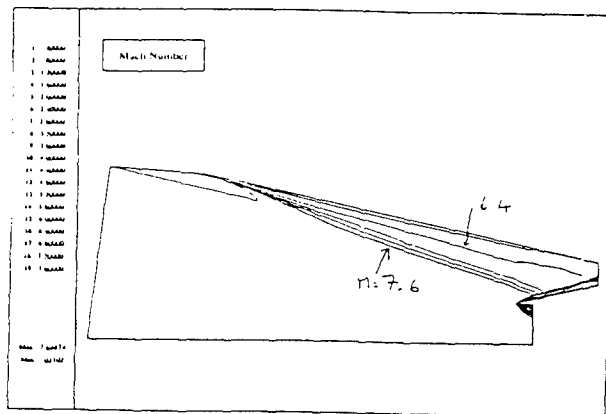


Figure 1.3-13: Integrated evolution of pitch along the vehicle. Effect of Mach number (scramjet mode).



**Figure 1.3-14:** Domain decomposition between areas where the Navier-Stokes equations are solved and areas where the Euler and Boundary layer equations are solved.



**Figure 1.3-17:** Inviscid calculation of the flow in the air intake, for Mach=10

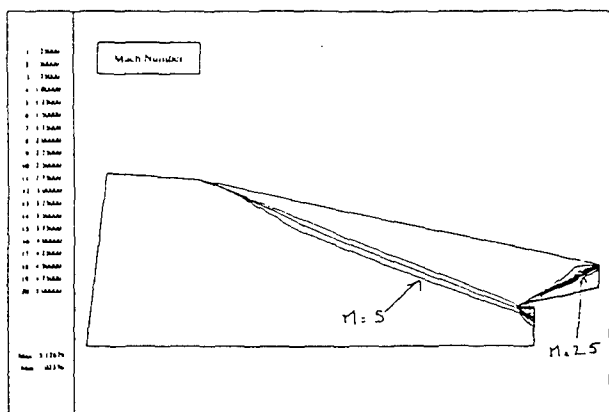


**Figure 1.3-15:** Inviscid calculation of the flow in the air intake, for Mach=6. Note the shock on lip adaptation.

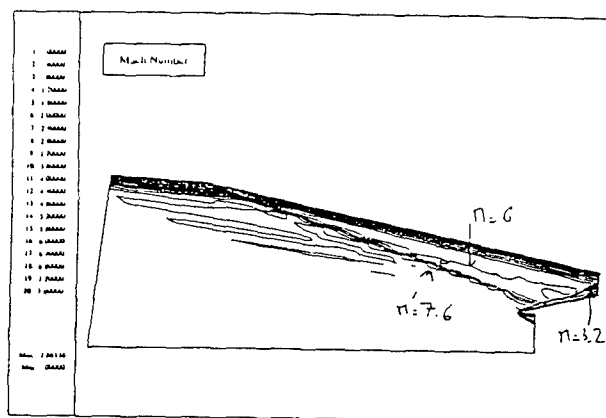


**Figure 1.3-18:** Viscous calculation of the flow in the air intake for Mach=10

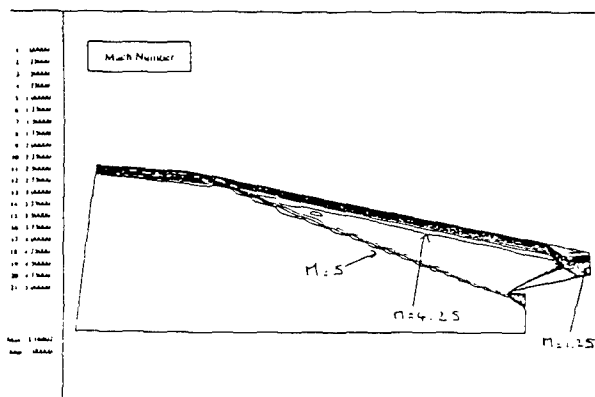


**Figure 1.3-16:** Viscous calculation of the flow in the air intake for Mach=6. The shock/boundary layer leads to inlet unstart.

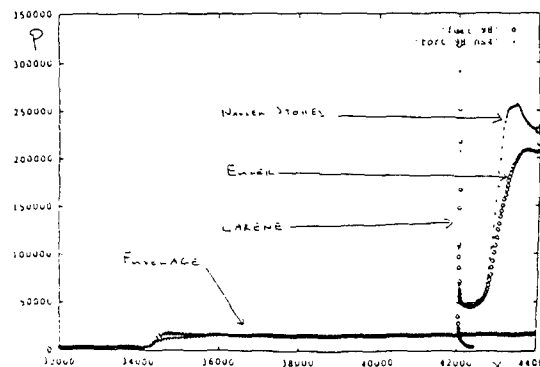


**Figure 1.3-19:** Comparison of wall pressures for inviscid and viscous calculations, for Mach=10



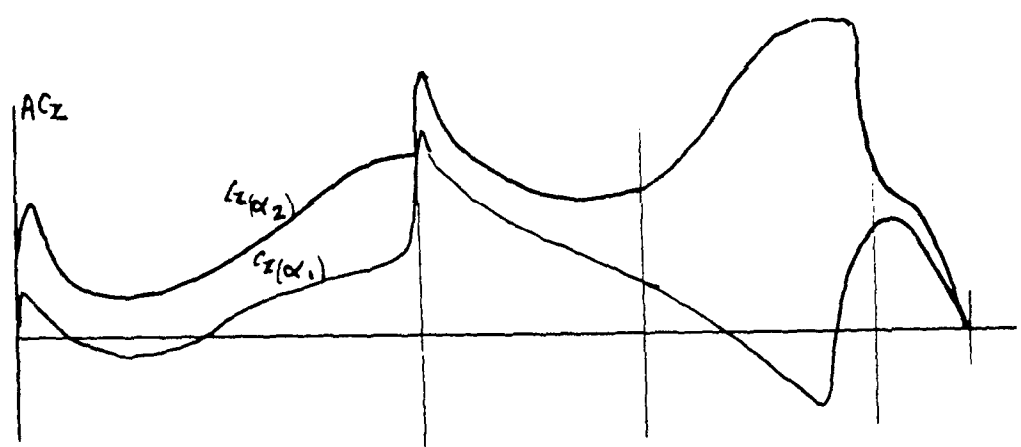


Figure 2.1-1: Schematics of the integration of the lift along X axis for two incidences

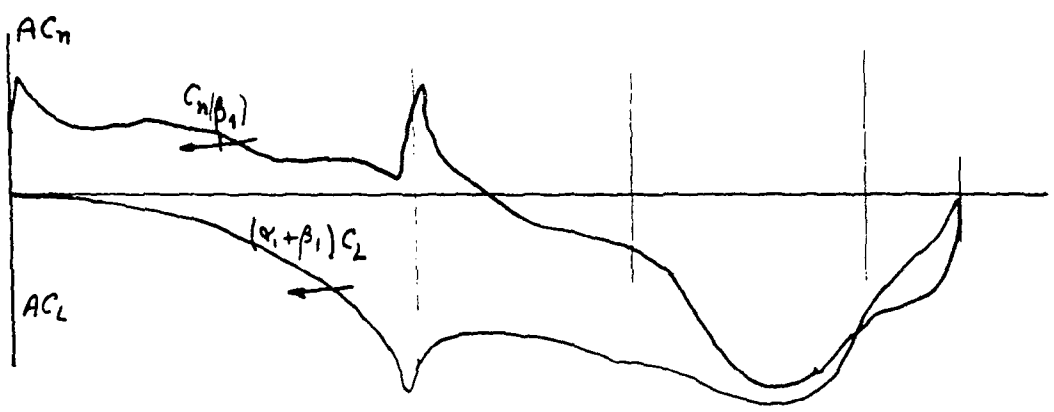


Figure 2.1-2: Schematics of the integration of yaw (Cn) and roll (Cl) along the X axis

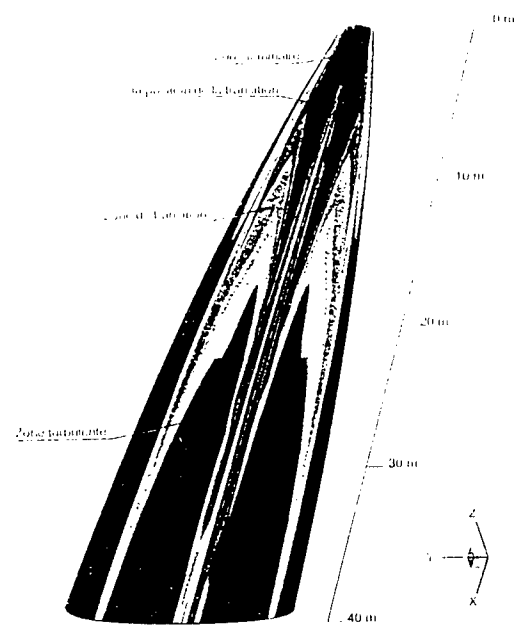


Figure 2.2-1: Generic forebody windward side,  $M=6$   $\alpha=0^\circ$ . Intermittency function. Laminar and turbulent zones. (ONERA computation)

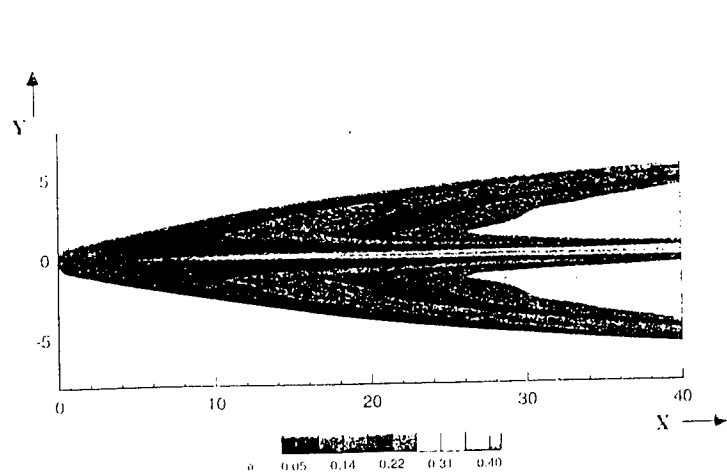


Figure 2.2-2: Generic forebody windward side,  $M=6$   $\alpha=0^\circ$ . Boundary layer thickness. (ONERA computation)

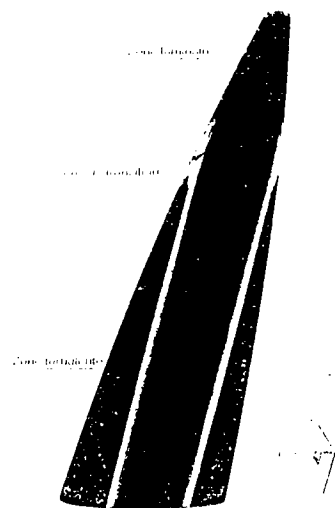


Figure 2.2-3: Generic forebody windward side,  $M=12$   $\alpha=5^\circ$ . Intermittency function. Laminar and turbulent zones. (ONERA computation)

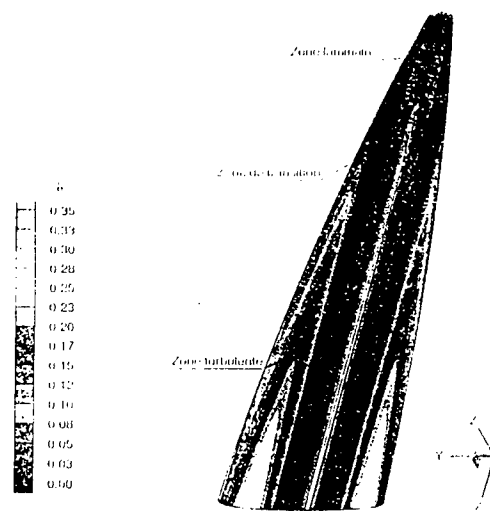


Figure 2.2-4: Generic forebody windward side,  $M=12$   $\alpha=5^\circ$ . Boundary layer thickness. (ONERA computation)

## Inlet and Propulsion Integration of RAM Propelled Vehicles

N.C. Bissinger  
Daimler-Benz Aerospace  
Military Aircraft, FE 122  
Postfach 80 11 60  
81663 Munich, Germany

### Summary

The design of intakes and afterbodies for hypersonic vehicles with RAM air breathing propulsion systems is described. The aerodynamic aspects of the integration of the forebody with the intake and the afterbody with the nozzle are outlined. The potentials and deficits of today's available tools are demonstrated and a strategy for the design of the propulsion system for a hypersonic vehicle is proposed.

### 1. Introduction

Integration of a propulsion system into a flight vehicle has always been a task of the intake and afterbody specialists. E.g. in fighters the intake and the nozzle were integrated such that an optimum on performance for a given engine could be achieved. Of special importance was the adaptation of the intake geometry to the on-set flow produced by the forebody and the shaping of the afterbody such that separations, shocks and unsteady flow phenomena could be avoided. Besides the major problem of finding the "proper aerodynamics" it has always been necessary to also consider boundary conditions like weight, complexity, fuel consumption etc. of the found solutions.

In order to reduce the size, i.e. improve the overall performance, of a hypersonic flight vehicle parts of the aerodynamic tasks of the intake and nozzle are transferred to the forebody and afterbody. The forebody is supposed to produce part of the compression of the intake air, the afterbody is used as a part of the expansion surface of the nozzle. This way the aerodynamic vehicle performance and the propulsion performance become closely coupled via the integration of the intake with the forebody and the afterbody with the nozzle. Both have to be optimized together in order to achieve the mission requirements with a minimum of vehicle size and costs and a maximum payload (fig.1-1).

The strategy of component integration can only work if it can be assured that it does not lead to major aerodynamic problems with unwanted drag increases or thrust reductions. In the contrary it is hoped that it might produce drag reductions or thrust increases, hopefully both.

Aerodynamics/Aerothermodynamics is a major design driver for a hypersonic vehicle. However other important boundary conditions cannot be disregarded: type of propulsion, structures and weight, systems and control necessary, complexity and reliability,

development and life cycle costs are some of the more important ones (fig.1-2).

This presentation will concentrate on the aerodynamic/aerothermodynamic aspects of the integration of a flight vehicle with its propulsion. These can best be comprehended by looking into the aerodynamic design and its problems of both forebody/intake and nozzle/afterbody (fig.1-3). The state of the art of the development and verification tools is discussed. One possible strategy for the development of a hypersonic vehicle is presented.

### 2. Intake Design

#### 2.1 The RAM Compression Process

The thermodynamic cycle for a RAMjet propulsion is shown in Figure 2.1-1. Nearly all of the kinetic energy of the free-stream flow is converted by the intake into pressure energy (points 2t, 3t). The combustion takes place at nearly constant pressure and the combustion products are accelerated by the nozzle from station 7 and expand to the external static pressure  $p_0$  at station 9. The compression taking place in the intake is called a RAM compression in which the flow is decelerated to low subsonic Mach numbers. The process inside the intake is the same regardless in which way the energy is added behind it. This could be inside a combustion chamber as in the case for a RAMjet or inside a Turbo-engine. This RAM compression takes even place inside the intake of a LACE engine (liquid air collection). There the air is cooled and compressed before being used in a rocket chamber.

The Mach number range for both the Turbojet and RAMjet are indicated in Figure 2.1-2. As can be seen in Figure 2.1-3 at higher Mach numbers the total temperatures exceed 2000K and dissociation begins to degrade the performance of the RAMjet engine drastically. The maximum Mach number for a RAMjet Propulsion is between  $Ma = 6.0$  and  $7.0$ .

#### 2.2 The Task of the Intake

The intake is the most critical part of a supersonic/hypersonic airbreathing propulsion system. It must deliver air to the engine or combustion chamber for all flight Mach numbers at a desired rate (mass flow) and flow conditions (pressure recovery and distortion). This delivery must be accomplished by as little losses and drag as possible. The intake weight and complexity should not be excessive. Many non-aerodynamic factors are influencing the selection and

design of an intake. Examples are vehicle configuration and its overall performance.

Aerodynamically the intake is converting the kinetic energy of the flow into pressure energy (fig.2.2-1). This compression can take place either in front of the intake (e.g. precompression due to a forebody) or inside the intake. At Mach numbers larger than one the compression with minimum losses would be an isentropic compression. However, the geometry of an intake with such a property can only be a point design for one specific Mach number. Instead, the supersonic compression is being accomplished by a succession of shocks. The higher the number of shocks the closer will be the compression process to the isentropic one. The supersonic compression is ended by a nearly normal shock after which the flow is completely subsonic. There is further compression inside the subsonic diffuser by area variation.

### 2.3 Intake Types

Intakes are characterized by the way and where the supersonic and subsonic compression takes place. The pitot intake (fig.2.3-1) can be optimized for subsonic flight vehicles. At supersonic Mach numbers a normal shock forms ahead of the intake. The external ramps (i.e. external of the intake duct) of the external compression intake are responsible for the supersonic compression. The final shock stays ahead of the intake lip. The duct flow is purely subsonic. The compression shocks of the internal compression intake are located inside the intake duct. This type of an intake with purely internal compression is used very seldom. The more common form is the mixed compression intake which is a combination of an external and an internal compression intake.

The flight Mach numbers of these intake types can be quite different. Figure 2.3-2 depicts the attempt to identify their Mach number range and the maximum flight Mach numbers achievable.

This figure indicates that the pitot intake is of no interest for hypersonic vehicles although aircraft like the F16 can reach Mach numbers close to  $Ma=2$  with such an intake.

The external compression intake is typical of aircraft like the Tornado or F14 and F15.  $Ma=3.0^+$  is probably the highest Mach number reachable with such an intake.

The mixed compression intake has been proposed for the supersonic commercial transport aircraft of the 1970's. Their design Mach number has been  $Ma=3^+$ . Recent proposals like the Beta II airplane (Ref.2.12) claim to be able to reach  $Ma=6.5$  with this intake design although integration of the propulsion system with the aircraft is not very close. Mach numbers of  $Ma=3.5$  have been flown by the SR71.

For the intake of the Sanger first stage the fuselage precompression will help to down-size the mixed compression intake. The highest flight Mach number envisioned is  $Ma=6.8$ .

The fact that for the highly integrated mixed compression intake there is no upper Mach number limit given does not mean that no limit will be reached. There is just no information on operational intakes above  $Ma\sim 8$  available in the open literature. In addition these will be purely SCRAM intakes not to be covered here.

All this intake types can be realized by an axisymmetric, two-dimensional or even three-dimensional design.

The axisymmetric intake consist of a translating conical centerbody inside a circular cowl (Fig.2.3-3). This design is not very flexible in the variation of the throat area. Today research is still going on to design and manufacture a variable-diameter centerbody without structure and leakage problems (Fig.2.3-4).

The two-dimensional intake accomplishes the compression by a succession of plane shocks created at flat ramps and inside a rectangular intake duct (Fig.2.3-5). It is superior to the axisymmetric intake with respect to its good adaptation to the required mass flow variation inside the flight envelope.

Three-dimensional intakes are very difficult (and probably expensive) to design and develop that so far only few projects have become known. In Ref. 2.7 a very interesting study is presented for a 3D fixed geometry mixed compression SCRAM intake (Fig.2.3-6).

### 2.4 Basic Intake Parameters

This section can just give a very short overview. More details can be found in the excellent Reference 2.1.

#### 2.4.1 Efficiency

The efficiency of the compression process inside and ahead of the intake for todays aircraft is described by the ratio of the mean total pressure  $p_{t2}$  at the engine face to the free stream total pressure  $p_{t0}$  (fig.2.4.1-1). The total pressure at the engine face plane is measured in model tests by pitot rakes. The individual pitot pressures are area weighted to form the mean value. Another way to define the efficiency of the compression is by the kinetic energy efficiency  $\eta_{kin}$ . In contrast to the total pressure recovery this parameter cannot be measured directly with a windtunnel model. For ideal gas flows both the pressure recovery and the kinetic energy efficiency are connected by the equation in Figure 2.4.1-1. As can be seen for high Mach numbers  $\eta_{kin}$  is very close to one and can be very misleading.

In case that there is heat removal, e.g. due to cooling of the forebody wall, the exergy efficiency might be a good way to characterize the compression process (Ref.2.8).

At higher Mach numbers the temperatures in the intake flow become so high that the ideal gas model no longer applies. The measurement and derivation of the efficiency parameters is then no longer straightforward.

Figure 2.4.1-2 gives the calculated values the oblique shocks, the boundary layers, the normal shock and the subsonic diffuser contribute to the overall losses of fixed and variable intake models. At the design Mach number  $Ma = 8.0$  the fixed intake shows a lower pressure recovery than the variable intake. This could be due to the higher internal compression of the fixed intake. This illustrates the fact that good efficiency is also connected with the "correct" ratio of external to internal compression. The kinetic energy efficiency of all the models is of the order of  $\eta_{kin} = 0.92$ . Calculations of the specific Impulse of a RAMjet indicate that an  $\eta_{kin}$  of 0.90 to 0.92 should be sufficient for nearly optimum performance (fig.2.4.1-3).

#### 2.4.2 Distortion and Swirl

For the Turbo engine the flow at the entry must be as uniform as possible because flow distortion and swirl can degrade performance and reduce the surge margin of the compressor drastically. The combustion chamber of a RAMjet seems not to be so sensitive because it is possible to stage the injection of fuel such that it fits to the flow coming from the intake. What happens if the location of the low pressure area(s) and of the center of the swirl varies with mass flow, i.e. power setting, is still an open question. Figure 2.4.2-1 gives the example of the distortion and swirl produced by an S-shaped diffuser and the definition of a distortion parameter defined by a turbo engine manufacturer.

#### 2.4.3 Intake Airflow Characteristics

The mass-flow characteristic of an intake is expressed in terms of its capture area-ratio  $A_0/A_C$  (Fig.2.4.3-1 and 2.4.3-2). Both total pressure recovery and intake drag are a function of this mass flow ratio. At supersonic flight the mass flow entering the intake depends largely on the geometry of the compression surfaces ahead of the intake and the shocks created by these surfaces. The mixed compression intake shows the best performance when the terminal shock is located just downstream of the throat and when the throat Mach number is nearly one. Increasing the downstream pressure (e.g. by fuel injection or closing of the nozzle) pushes the terminal shock out of the intake. This event is called "unstart" (of the internal compression) which produces very large and unsteady structural loads. Ideal would be the highest pressure recovery  $\eta$  in connection with an  $A_0/A_C = 1.0$ . In reality there will always be a compromise between pressure recovery and mass flow.

Best performance would be reached when intake and engine mass flows would match at all flight conditions. However, an intake sized for the mass flow of the engine at the highest supersonic Mach number delivers too much air at transonic flight (Fig.2.4.3-3). If no bypass for excess air is available spillage around the intake lip (and sidewalls) of external compression intakes takes place. In mixed compression intakes dump doors and/or the variable geometry must provide the spillage necessary. In any case increased total pressure losses and additional drag are the consequences. A variable capture area of the intake could also relieve the situation to some extent. However, the price for the possibly reduced drag is a higher complexity.

#### 2.4.4 Intake Drag

Intake drag is defined as the drag difference between the flow with  $A_0/A_C = 1.0$  and  $A_0/A_C < 1.0$ . Considered are the components in flight direction of the forces on the free surfaces of the streamtube entering the intake (F1 and F2 in Figure 2.4.4-1). Because the pressure on the intake cowl depends also on the intake mass flow, i.e. spillage, its change of its drag component is usually added. Depending on the configuration additional drag components can derive from a bypass/bleed system and a diverter.

### 2.5 Design Considerations

#### 2.5.1 Intake Selection

The selection of the intake depends on several factors between which it is not easy to find a good compromise.

From Figure 2.5.1-1 it is clear that at hypersonic Mach numbers only the mixed compression intake will deliver the pressure recovery necessary. A good compromise would be to design a variable intake that operates with external compression in the lower Mach number regime and with mixed compression at the highest Mach numbers. For the Mach regime  $3.5 < Ma < 6.0$  a typical sensitivity of net thrust on intake pressure recovery is given. Compared to the nozzle gross thrust sensitivity this is not very large. The net thrust is much more sensitive to changes in intake mass flow (Ref.2.14).

Next the ratio between external and internal compression of the intake must be determined. Figure 2.5.1-2 gives some Pros and Cons for an increase of the internal compression. Depending on the actual vehicle configuration some of the arguments can be more or less important. A good and large data base on intake flows is needed to find a reasonable decision. It does not matter whether this data base was generated by windtunnel testing or by CFD.

Compared with a two-dimensional intake one can expect higher pressure recoveries for the axisymmetric mixed compression intake (fig.2.5.1-3). The reason lies in the reduced viscous losses inside the intake and the

lower shock losses of cone shocks. In addition the inevitable leakage rates of the axisymmetric intake will be smaller than the ones of the two-dimensional intake.

Figure 2.5.1-4 gives the qualitative results of the selection process for different intake types for a hypersonic vehicle like Snger. As can be seen there are various aspects that can influence the selection of an intake for a specific vehicle and its mission.

### 2.5.2 Forebodies

For the intake engineer everything in front of the first intake ramp is forebody. Its shape must be such that the intake is downstream of the forebody shock(s) for all Mach numbers and angles of attack (fig.2.5.2-1). The geometry of the forebody defines the conditions with which the air enters the intake. Nose bluntness and angle of the lower forebody surface influence the shock strength and losses. Boundary layer transition, real gas effects and radiation are other factors responsible for the energy losses of the intake on-set flow.

The shape of the forebody also influences the flow angularity and uniformity at the intake station. Figure 2.5.2-2 demonstrates the ability of different forebody shapes to compress the air and therefore deliver different amounts of air.

The geometry of the fuselage bottom and side walls have a strong influence on the boundary layer development of the forebody. (Other important factors are Mach number and angle of attack.) Figure 2.5.2-3 clearly shows that the boundary layer thickness on the centerline is more than twice as thick than at the position of the intake sidewalls. Similar effects have been found in other references, e.g. Ref.2.19. The knowledge of the boundary layer thickness is needed for the determination of the diverter height.

How much the Mach number in front of the intake can be reduced and therefore the mass flow be increased for a specific forebody configuration is depicted in Figure2.5.2-4. Because of the reduced Mach number the compression of the intake and shock strengths can be reduced. Losses due to shock/boundary layer interactions decrease. The increased mass flow ratio makes a reduction in intake size or a thrust increase possible.

### 2.5.3 Definition of the Intake Geometry

After the specification of the mission and the general configurational layout of the vehicle (including the location of the intake(s)) the design of the intake can start. The flow conditions at the begin of the intake must be determined. This may be done by three-dimensional CFD calculations covering the whole of the flight envelope. Design points along the flight corridor must be specified. Usually the highest Mach number defines the capture area of the intake. However, requirements at lower Mach numbers can force the

intake engineer to look for difficult compromises in the intake design. For example, the demand for high total pressure recovery during the turbo propulsion mode can make the use of boundary layer bleed mandatory which during the RAM mode (at higher Ma) is not necessary or even unwanted because of the mass flow sensitivity mentioned above.

In the following chapters the topics intake capture area, the external compression, the supersonic diffuser, the internal cowl lip angle, the throat area and the subsonic diffuser of a two-dimensional mixed compression intake will be looked at (fig. 2.5.3-1).

#### 2.5.3.1 Intake Capture Area

The intake capture area is defined by the mass flow demand of the engine at the highest flight Mach number. At this condition the intake is run at full flow, i.e.  $A_0 = A_C$ , and with the external compression shocks coalescing at or close to the lip of the cowl. Spillage is minimum, its magnitude depends mainly on the geometry of the intake sidewalls.

#### 2.5.3.2 External Compression Ramps

The length of the external ramps are defined by the shock on lip condition at the highest flight Mach number and the specified capture area  $A_C$ . The number of ramps depends on the external compression that is to be achieved. Small total pressure losses and simplicity of the design are main goals in the selection process. Ideally, the ramp angles are selected such that the shocks are of equal strength thus producing optimum pressure recovery (Ref. 2.21). At the same time the lip area  $A_{lip}$  must be large enough for the mass flow demand of the engine. If the intake is to be used in the lower Mach number range as an external compression intake together with a turbo propulsion unit the number of oblique shocks and their ramp angles must be large enough to reduce the flow Mach number ahead of the normal shock at the intake lip to about  $Ma \sim 1.2$ . Otherwise the normal shock losses may become too large and/or a large amount of bleed is necessary to stabilize the normal shock. It is obvious that only a variable intake can have a flow that comes close to the wanted one. To find the optimum control laws for the external ramps is a very difficult task and requires several iteration cycles until the intake performance achieved gives optimum propulsion and vehicle performance.

Aerodynamically there are two limits for the ramp angles that can be selected. If the ramp angles become too large the shocks detach producing large losses. They can even become unstable. Before the limiting ramp angle for shock detachment is reached the pressure jump across a shock can become so large that it produces a separation. Bleed or blowing is the means to remedy such a situation if the shock strengths cannot be reduced by reducing the ramp angles. Reduced ramp

angles mean less compression and more entering mass flow.

With the three-dimensional effects of viscous shock/boundary layer interactions unknown experience shows that it is a good approximation to use inviscid shock tables (Ref. 2.22) for the location and the determination of the flow changes across the external shocks. The effects of varying ratio of specific heats can be included if necessary. The boundary layers on the ramps will make the shocks steeper, i.e. they move upstream, away from the lip. This small effect usually is considered as a safety margin for the shock on lip design point. So the shocks are not directly focused on the lip but just in front of it. This way excessive heating of the cowl can be prevented.

### 2.5.3.3 Throat Area

In the external compression mode (e.g. turbo propulsion) the throat is located close to the lip plane. The Mach number in the throat is subsonic and of the order of about  $Ma \sim 0.6 \div 0.8$ . The external ramps must be positioned such that the correct throat area is formed. At the same time the shocks of the external ramps should have the same strength for optimum pressure recovery and they should pass the lip as close as possible for minimum spillage.

In the mixed compression mode the throat is inside the intake (internal compression). The Mach number at the throat should be close to  $Ma = 1.0$ . For safety reasons (e.g. for small variations in the flight conditions) the throat Mach number is fixed at  $Ma = 1.2$ . This defines a minimum area ratio  $A_{throat}/A_{lip}$ . The actual value of this ratio depends on the Mach number at the lip and the losses in the flow between the lip and the throat. For an isentropic supersonic compression an analytical expression for this area ratio can be derived (Ref. 2.1). This expression is plotted in Figure 2.5.3.3-1. It is called "unstart limit" there. If the area ratio is smaller than defined by this curve the internal compression breaks down. Its final shock pops out of the intake to start an external compression mode with high losses and possible instabilities. This graph also shows the "starting limit" of an isentropic supersonic compression. In order to start the internal compression again the area ratio  $A_{throat}/A_{lip}$  has to exceed the values defined by this limit. After the start of the internal compression the area ratio can be reduced again for higher total pressure recovery until it reaches values in the shaded area called "operational intakes", see Figure 2.5.3.3-1.

In an actual intake design the determination of the throat area is very critical and difficult. Many factors can influence its value that cannot be specified at the beginning of the design process. For example the thickness of the boundary layers, the amount of bleed mass flow and the number of shock reflections of the internal compression play an important role. The estimation of the throat area can be based on available

data either from model tests or CFD calculations. As a first estimate the kinetic energy efficiency and thus the total pressure recovery for similar intakes can be taken from the literature (fig. 2.5.3.3-2). Subtracting the total pressure recovery across the external shocks gives the total pressure recovery for the supersonic diffuser. With the known total pressure ratio inside the supersonic diffuser a simple mass balance consideration does produce the wanted area ratio  $A_{lip}/A_{throat}$  where  $A/A^*$  is a function of Mach number only (fig. 2.5.3.3-2).

### 2.5.3.4 Lip Angle

Aerodynamically the geometric lip angle  $\delta_{lip}$  is of no interest. What is important is the flow turning angle at the lip ( $\delta_{Ramp} - \delta_{Lip}$ ). The turning angle defines how much internal compression can follow after a given external compression or how much external compression can precede a given internal compression.

There are several important aspects for the selection of  $\delta_{Lip}$  (fig. 2.5.3.4-1):

- In general  $\delta_{Lip}$  should be small in order to keep the frontal area and the external axial forces (e.g. on the cowl) of the intake small.
- During the external compression mode the subsonic diffuser should start as close as possible to the lip. Therefore,  $\delta_{Lip}$  should be equal or bigger than  $\delta_{Ramp}$ . Its value depends on the highest Mach number reached with external compression. For this compression mode  $\delta_{Ramp}$  is largest at the highest Mach number.
- During the mixed compression mode the lip flow turning angle must be selected such that a lip shock of sufficient strength is created. For a turbo propulsion that requires high total pressure recoveries the lip shock and its reflections should have the same strength (according to Oswatitsch, Ref. 2.21) as the external compression shocks. This requirement usually is somewhat relaxed at the highest flight Mach number. Here RAM propulsion is used and total pressure recovery is less important than mass flow.  $\delta_{Ramp}$  assumes its maximum value. This can result in an appreciable magnitude for  $\delta_{Lip}$ .

As with the external compression shocks the flow turning angle at the lip should not exceed its detachment limit. The lip shock should also not separate the boundary layer. This danger is relatively small at the lip. However, at the shock reflection point on the ramp side the pressure jump can be large enough to separate the boundary layer. This danger of separation is even higher if on the ramp side a thick fuselage boundary layer is swallowed by the intake. There is a conflicting requirement for a lip shock strength high enough to give good total pressure recovery and low enough to not separate the intake boundary layers which could unstart the intake. If bleed can be utilized (up to Mach numbers of  $Ma \sim 4.5$ ) this

problem can be solved although it involves additional drag. For Mach numbers above  $Ma \sim 4.5$  without bleed quite a lot of development work will be needed including flight test vehicle investigations.

### 2.5.3.5 Supersonic Diffusor

With the internal lip angle and the lip and throat area determined the next step is to find the geometry of the supersonic diffusor. Its task is not only to compress the air and to reduce its Mach number but also to reverse the flow turning of the external compression surfaces. This requires local curvature of the walls. Therefore, the flow and its shocks can no longer be treated with simple methods like inviscid shock tables. Here Euler and Navier-Stokes methods are of great help to the intake designer. At least for two-dimensional intakes the 2D flow can be calculated for quite a large number of different and alternative geometries within a reasonable time. The Euler results need some empirical information about shock/boundary layer interactions as a function of say pressure gradients or jumps. The Navier-Stokes calculations will clearly reveal all separations and even unstart problems.

In 1972/1973 Boeing and NASA (Refs. 2.24, 2.25, 2.26) developed simpler methods which were based on the patching of the solutions of the calculation of rotational inviscid flow and boundary layers. A special treatment for the shock/boundary layer interaction was needed (fig. 2.5.3.5-1). Even extensions to three dimensions have been developed (Ref. 2.27). The efforts to produce fast and robust methods to find the global flow conditions during the intake design process have been continued until today (Refs. 2.28 and 2.29). Figure 2.5.3.5-2 shows the difference between the geometric and the effective (inviscid) intake contour from the lip station to the throat. It can clearly be seen that the boundary layer on the ramp side is relatively thick compared to the cowl boundary layer. The ramp boundary layer thinnens at  $X \sim 45$  in.. This is the position where the lip shock is reflected on the ramp.

### 2.5.3.6 Throat Length and Subsonic Diffusor

The shape of the terminal shock of the internal compression can be quite different. Depending on the Mach number in front of this shock and the boundary layer thickness on the throat walls it can consist of a single shock ( $Ma \sim 1.0$ ) or a succession of shocks (called shock train) for higher Mach numbers, see sketch in Figure 2.5.3.6-1. Within this shock system a turbulent mixing process takes place that must be completed within a constant area section otherwise losses in total pressure will result. The shock train length is given in Figure 2.5.3.6-1 as a function of boundary layer thickness and upstream Mach number. In addition total pressure losses due to insufficient constant area section length are also specified. As can be seen the total pressure losses are much larger in case the throat section is too short. A throat section of 6 to 10 times the duct height can contribute considerably to the length

and weight of the intake. Because a lowering the total pressure reduces the static pressure loads of the intake here again a compromise between performance and weight has to be found.

The task of the subsonic diffusor is the maintenance or establishment of uniform flow. A well behaved diffusor depicts only small total pressure losses (3 to 6 %). However, in case the throat section is not long enough, separation at the entrance of the subsonic diffusor can occur that can become unstable. In Ref. 2.30 the length of this separation reached about 6 times the throat height (fig. 2.5.3.6-2) at the highest shock Mach number connected with a highly curved shock. At intermediated Mach numbers the flow transitioned intermittently between a fully attached and a fully separated flow situation (fig. 2.5.3.6-3). The steep increase in unsteady top wall static pressures indicates the unsteadiness of the separated subsonic diffusor flow. The shock motion is predominantly of a low frequency ( $< 100\text{Hz}$  for full-scale intakes, Ref. 2.32). The mechanisms of these separated flow oscillations are not yet fully understood. Attempts to calculate the dynamic effects were not satisfactory (Ref. 2.31). So there remains an uncertainty for the intake designer whether or not for his specific design and its entrance flow conditions unsteady behaviour and unexpected losses might occur.

### 2.5.3.7 Bleed

Control of the boundary layer growth and separations inside the intake can be accomplished by bleeding. Also by removing low momentum portions of the boundary layer shocks can be stabilized. Because this removal is connected with losses (mass flow deficit and momentum) bleed should be applied as little as possible. The bleed ducts necessary also add to the intake weight. Partial recovery of the bleed air moment is not an easy task.

The mass flow that can be removed by a bleed hole of a given diameter depends on the inclination of the hole, the pressure ratio between intake and bleed plenum and the local Mach number (Fig. 2.5.3.7-1). Inclination of the hole gives minimum losses. For the stabilization of the terminal (normal) shock of the internal compression bleed holes normal to the intake wall must be applied. The total amount of bleed mass flow is a function of the effective area of all bleed holes on an intake surface. However, there is not always the area available that would be needed. Also a large number of bleed holes can lead to structural problems and weight increases.

Figure 2.5.3.7-2 lists some of the aspects connected with bleed for the Sanger project.

### 2.5.3.8 Intake Control

Intake control is highly configuration-specific. Therefore only general ideas (for a two-dimensional intake like that for Sanger) can be presented here.



Control of the external compression mode requires that the external ramps are positioned such that the shock losses and the spillage are not larger than anticipated and the lip area is large enough to swallow the mass flow demanded by the engine. The internal ramps have to be positioned such that the intake throat is at the intake lip and the intake duct forms a subsonic diffuser with small losses. Control systems for this mode are well known from the development of fighter aircraft.

In the mixed compression mode not only the correct ramp positions and lip area have to be arranged but also the throat height that optimizes the internal compression without unstart (fig. 2.5.3.8-1). In addition the position of the terminal shock has to be controlled to assure pressure recovery and prevent unstart. The position of the terminal shock (for a given intake geometry) is defined by the back-pressure of the intake diffuser. This pressure can be varied by the amount of fuel injection and/or the size of the nozzle throat area. Therefore the control of the intake is highly connected to the control of the rest of the propulsion system. In addition the intake control has to establish the internal compression system and to initiate the restarting procedure in case of an unstart.

Several systems have been proposed in the open literature (Refs. 2.32, 2.33). They all must fulfill the requirements of simplicity, reliability and accuracy under very severe working conditions of high temperatures, high pressures and high levels of noise and vibrations. Static wall pressures and/or total pressures in the flow are in general used as control variables. Final calibration of such a system can probably not be done in a windtunnel. So preliminary scale-model data will have to be validated during flight testing.

### 2.5.3.9 Sidewalls

Sidewalls are usually selected based on experience. Reducing sidewalls decreases friction drag, boundary layer build-up, boundary layer/shock interactions and weight. However, due to the pressure difference between the external ramp shocks and the freestream side-spillage will be increased. Again a compromise between performance, mass flow and weight has to be found. A sidewall from the hinge-point of the second ramp to the leading edge of the cowl from the aerodynamic stand-point seems to be close to an optimum solution.

## 2.6 Some Selected Topics

### 2.6.1 Aerodynamic Phenomena Affecting Intake Performance

**Forebody flow:** Figure 2.6.1-1 gives some of the aerothermodynamic phenomena one is confronted with during the hypersonic intake design. Starting on the top left the aerothermodynamics of the forebody has already

be touched in chapter 2.5.2. The effects of energy losses due to radiation and cooling on the intake flow can only be estimated in the mean. The usual assumption of constant total temperature in the intake flow becomes more and more unrealistic with increasing Mach number.

**Shock/boundary layer interactions:** Ramp shock and reflected shock/boundary layer interactions are the next phenomena bothering the intake designer. There exist several criteria for incipient shock induced boundary layer separations. The more simpler ones are functions of local Mach number and turning angle only. They are supported by test data up to  $Ma \equiv 4.0$ . More sophisticated ones include the flow conditions of the boundary layers. However, especially during the design phase the state of the boundary layers are never known. So the engineer has to rely on the simpler and not so accurate ones. It is interesting to note that for incipient separation the pressure rise across a ramp shock and across a shock reflection are equivalent (Ref. 2.34). Thus, the shock reflection is more prone to separation due to its larger pressure jump which is twice the pressure jump of the single shock.

Cooling of the wall delays separation because of the larger momentum fluxes in the boundary layer (Ref. 2.35). According to Ref. 2.36 shock separated flows can be classified as pure laminar, transitional or turbulent. Pure laminar separations are steady in a supersonic stream and depict only a small Reynolds number dependency (these become more likely with increasing Mach numbers). Transitional separations are generally unsteady and exhibit a marked Reynolds number dependency. Turbulent separations are relatively steady compared with transitional separations and depend only weakly on Reynolds number. If separations cannot be prevented transitional separations conceal the biggest uncertainties for a successful intake design because they can hardly be modelled neither in the windtunnel nor in CFD.

The question whether or not "just a little" separation is permissible for the optimization of the intake (i.e. optimization of the vehicle) cannot be answered because there is no way in quantifying the losses due to shock boundary layer interactions and separations. So it is most likely that an intake design is too conservative or that it is not conservative enough and does not work. Final proof of concept is only possible during flight testing of the vehicle.

**Corner flows/glancing shock:** Corners are predominant in two-dimensional intakes. However, even in axisymmetric intakes corners can be found at the struts that hold the center-body. These strut-corners are usually located in the subsonic flow behind the terminal shock of the internal shock system. So with sufficient rounding of the strut leading edges and the corners losses can be kept small.

The corner flows in two-dimensional intakes are supersonic and are usually modelled as flows around fins on a flat plate or a ramp (e.g. Refs. 2.37 to 2.39). They are closely connected to the glancing shock problem. 3D separations both on the ramp and on the sidewall lead to the formation of vortices which transport boundary layer and high energy core air into the corner. This flow produces peak heating values similar to shock reflection flows.

In an intake this type of a flow occurs either between the first ramp and the intake sidewalls or between the cowl and the sidewalls. On the first ramp the sidewall boundary layer is either very thin due to its short length, or, if e.g. fuselage boundary layer is swallowed by the intake the ramp (fin) boundary layer is much thicker than that on the sidewall. The corner flow on all following ramps will differ from this model due to additional shocks and pressure jumps. Only the calculation of the complete duct flow could give a complete description of the flow physics inside the intake.

For the cowl side the boundary layers of these modelling tests are closer to reality. However, the cowl is not a plane but a curved surface. Therefore, there will be pressure gradients in flow direction. Also the flow along the cowl is not an external flow. It takes place inside an intake duct, i.e. it is a confined flow. The pressure gradient along the cowl is influenced by the flow on the opposing ramp side. So far no investigations concerning blowing at the corner came to the attention of the author. With such an investigation one could model intentional leakage flow between the ramps and the sidewalls. Using cold gases for this leakage flow could ease the heating problem of the ramp seals.

### 2.6.2 Confined Flows

In intakes shock boundary layer interactions cannot be considered as two-dimensional flow effects. They depend on the confinement parameter  $\delta/w$ , i.e. the ratio of the boundary layer thickness to the duct width (Ref. 2.40). For large values, i.e. for thick boundary layers, the separation on the bottom of the duct becomes highly three-dimensional (fig. 2.6.2-1) whereas for smaller values at least part of the separation is nearly two-dimensional. The separation is accompanied by longitudinal vortices. The introduction of an additional important parameter makes the prediction of the danger of separations and the quantification of their losses even more complicated.

### 2.6.3 Optimization

Always looking for new topics to work on the CFD community started to implement optimization methods. The first step in this direction are still somewhat limited (fig. 2.6.3-1). However, there is a potential that should be used if it offers the possibility to reduce the efforts of designing the optimum intake for a hypersonic vehicle.

The optimization is done by minimizing an objective function. The flow codes used in references 2.41 and 2.42 have been an Euler and a laminar PNS code. Performing a three-dimensional viscous optimization (today) seems to be an extremely costly adventure but even the optimization of detail aspects of a hypersonic intake (e.g. the ratio of the (inviscid) external to internal compression) could help the designer considerably.

### 2.6.4 Structural Aspects

To demonstrate the magnitude of temperature and pressure loads inside the intake values are given in Figure 2.6.4-1 for HYTEX. Temperatures as high as 1800 °C and pressures of  $\approx 6$  bars can be present in the subsonic diffuser. A structure that can withstand such high loads without too much deformations and with minimum weight must carefully be selected. For the pressure relief of the ramps the ramp cavity must be pressurized. The pressure difference on the cowl tip can become large. Because at the higher flight Mach numbers the external ramp shocks are very close to or at the cowl the cowl tip is very critical concerning deformations. Ramp actuators available today must be cooled or insulated.

Other aspects applicable for Sanger are collected in Figure 2.6.4-2. Although no strong temporal temperature gradients are to be expected the local temperature gradients can be quite high. Deformations of the flat surfaces can alter the intake flow and critically influence the capture and throat area. Gaps and steps in the intake skin are dangerous because of confined flow effects (shock reflections). The effect of forebody deformation on pre-compression must be known and included in the intake control laws. In addition to have a clearly defined intake on-set flow the intake should be rigidly attached to the forebody.

A light-weight flight structure will not be able to sustain intake unstart loads. So the control system must be designed such that no unstart will occur. How atmospheric disturbances that could lead to intake unstart will be discovered and quantified is a still open problem.

## 3. Afterbody design

The "ideal" afterbody would be just a thrust producing nozzle. The process of expansion in such a nozzle is shown in figure 2.1-1. Because the combustion takes place at nearly constant pressure the maximum nozzle pressure ratio (from station 7t to 9) is determined by the pressure ratio realized by the intake.

The flow at station 7 is subsonic for a propulsion system with an intake of the RAM type. It can be produced by the combustion chamber of a RAMjet or a turbojet with or without an afterburner. The task of the nozzle is to expand this flow (i.e. accelerate it) as

efficiently as possible to the conditions given at station 9.

The flow conditions at station 9 are defined by the actual nozzle and afterbody flow, i.e. they can deviate from the free stream flow conditions (station 0). Therefore, for the understanding of the integration problems of the afterbody/nozzle configuration of a hypersonic vehicle it is necessary to look into the nozzle design problem which has the afterbody flow as boundary conditions.

### 3.1 Nozzles for supersonic Mach numbers

The Laval nozzle in Figure 3.1-1 accelerates the flow to supersonic Mach numbers if the exit pressure  $p_E$  is low enough. Between the flow conditions d and f indicated in the left half of the figure there are flow conditions with separations inside the nozzle connected with oblique shocks (shown on the right of the figure). These separations could be beneficial (compared with the non-separated flow the oblique shocks exhibit increased pressures) if the mixing losses do not become too large (Ref. 1.5) However, the stability of the shock/boundary layer/separation interactions cannot be guaranteed.

Nozzles of this type with a convergent/divergent area distribution are in use in many aircraft flying supersonically. Figure 3.1-2 gives several axisymmetric examples of which three vary the nozzle area by moving parts of the nozzle surface whereas in one example the area variation is accomplished by moving a plug in axial direction.

### 3.2 Basic Nozzle Parameters and Nozzle Performance

The thrust coefficient  $C_{FG}$  is a measure of the nozzle efficiency (Fig. 3.2-1). It is the ratio of the thrust achieved to the thrust that could be produced by an isentropic expansion from the same flow conditions at station 7 to  $p_\infty$ . This coefficient includes all losses because of friction, angularity, expansion and mass flow leakage. When such a nozzle is installed into a flight vehicle the drag on the external nozzle walls depends on the nozzle expansion ratio  $A_9/A_8$ . This drag is usually included into the engine performance. Traditionally the engine manufacturer quotes the difference between this installed thrust and the Ram drag (implications due to book-keeping are disregarded here for simplicity).

The internal nozzle performance for a convergent/divergent axisymmetric nozzle is recapitulated in Figure 3.2-2. For a given expansion ratio  $A_9/A_8$  nozzle thrust coefficient  $C_{FG}$  has a maximum at that nozzle pressure ratio  $p_{T7}/p_0$  for which  $p_9 = p_0$  ( $C_{FGpeak}$ ). At this condition the losses are mainly angularity and friction losses and depend on the nozzle geometry only. For pressure ratios less or larger than this optimum one overexpansion or underexpansion losses occur respectively. The pressure ratio  $p_{T7}/p_0$  for the peak

coefficient  $C_{FG}$  increases whereas the magnitude of peak  $C_{FG}$  decreases with increasing  $A_9/A_8$ . For a given operating condition the optimum nozzle performance occurs at an area ratio that is smaller than that one for the peak thrust coefficient. Factors that influence the nozzle efficiency are summarized in Figure 3.2-3.

Subtracting external boattail drag produces another nozzle area ratio for maximum installed performance (Fig. 3.2-4). The external drag is increasing with decreasing nozzle area ratio because for a fixed  $A_8$  the boattail angle  $\beta$  is increasing. So, in general nozzles are operating slightly underexpanded.

According to Ref. 1.4 (and as shown in Figure 3.1-1) it is possible that during overexpanded operation the nozzle flow adjusts itself to the ambient pressure by compression that can lead to oblique shocks and separations. This results in an increased static pressure compared to the unseparated nozzle flow. Depending on the actual nozzle design this can raise the nozzle thrust coefficient (Fig. 3.2-5). Usually nozzles are not designed for conditions like this. Therefore there is little or no experience that would help answering the questions about the stability and the predictability of such flows. Engineers coping with nozzle flows try to avoid separations and shocks.

### 3.3 Nozzles for high Mach numbers

The nozzles shown so far have been designed for subsonic and supersonic flight Mach numbers. If the flight Mach number is extended over today's range the nozzle pressure ratio and therefore the desired nozzle area ratio increase drastically (fig. 3.3-1). Because of the additional low Mach number requirements this means large, heavy, complicated variable nozzles. In Figure 3.3-1 the area variation for both the exit and the throat of a hypersonic nozzle is given. In this typical example the exit area of a fully expanding nozzle must be variable between half and six times the intake capture area. Compared with current nozzle designs both the pressure and temperature loads are increased. Two conclusions can be drawn from the data presented in the figure. Axisymmetric nozzles can no longer be realized for Mach numbers beyond  $Ma = 4.0$ . For weight and size (drag) reasons fully expanding nozzles are not practical at high Mach numbers.

### 3.4 SERN Nozzles

In order to save weight and frontal area parts of the "ideal" axisymmetric (or in two-dimensions symmetric) nozzle are cut-off. Resulting losses are taken into account. The resulting nozzles are called SERN (single expansion ramp nozzle). Two candidates are depicted in Figure 3.4-1. One is a two-dimensional solution utilizing flat ramps to vary the throat and expansion area. The other uses an axis-symmetric plug nozzle that is also followed by a two-dimensional expansion ramp. In the following only the two-dimensional SERN

nozzle is considered which is the baseline nozzle of Sanger.

### 3.5 Design of Minimum Length SERN

Because flow losses are minimum in an isentropic flow it is obvious to design a nozzle such that its flow is as close to this ideal situation as possible. Also, the method of characteristics (MOC) can be utilized during the design of the SERN nozzle (Refs. 3.3, 3.26, 3.27). The method to find the minimum length and the geometry for such a nozzle can best be explained with the help of the upper sketch in Figure 3.5-1. For a given sonic on-set flow under arbitrary flow angle and sharp corners at points a and d the shape of the nozzle has to be found such that the outflow of the nozzle is horizontal and at points f and c the pressure in the jet is equal to the free-stream pressure at that stations. The upper sketch in Figure 3.5-1 shows the characteristics of the general case. The shortest nozzle is found when the geometry of the upper and lower nozzle walls are such that point e and f collapse and the jet pressure is equal to the free-stream pressure. Then the geometry would reach from point a to c and from point d to e/f.

This design procedure has to be run through for many operating conditions along the flight path of the hypersonic vehicle. Then a decision has to be made which design point will determine the actual nozzle geometry and how the variability of the nozzle has to be accomplished such that at other operating points the nozzle performance is still near optimum. This selection procedure for the nozzle ramps is similar to the one for the geometry of the supersonic diffuser for the intake (see chapter 2.5.3.5) except that for the intake shocks are created by purpose whereas in the nozzle shocks are tried to be prevented as good as possible.

Because in an actual SERN design the nozzle length (weight) or the nozzle height can still be too large it would be of interest to further shorten this minimum length nozzle. That this is possible can be recognized in Figure 3.5-2. There it is shown that this specific nozzle can be shortened to a quarter of its length without sacrificing too much axial gross thrust. However, the net installed thrust is very sensitive to thrust coefficient changes. Fig. 3.5-3 makes it clear that at  $Ma \approx 7.0$  a 1 % change in thrust coefficient can result in about 4% net installed thrust. This is somewhat larger than the change in net installed thrust due to a change of intake mass flow by 1% (e.g. by bleed).

The inviscid design of the SERN has to be corrected for all losses not considered, e.g. also friction and leakage losses. These losses are difficult to estimate and are usually found by experiment. So far only generic type SERN nozzle tests are reported on in the open literature (e.g. Ref. 3.31)

### 3.6 Operation Problems Connected with SERN

In Figure 3.6-1 the thrust coefficient and the thrust vector angle is given as a function of Mach number. Whereas at high Mach numbers the performance is quite good and the thrust vector angle is relatively small at  $Ma \approx 1.2$  there is a sharp decrease in thrust connected with large negative thrust vector angles that produce nose-up moments for the vehicle.

To understand this effect it is best to look into some CFD results. In Figure 3.6-2 the Mach number distribution calculated with a 2D Euler method for  $Ma = 5.6$  is represented in colours. The pressure distribution along the nozzle walls (ramp and cowl side) is plotted in Figure 3.6-3. As can be seen the pressures inside the nozzle are not too much different on both sides. The pressure coefficient on the expansion ramp is nearly zero and positive. Considering for the determination of the thrust vector and its direction a control volume at the throat and from there along the expansion ramp and the cowl flap one has to assume that the direction of the thrust force is defined solely by the flow direction in the throat. Even adding the pressures on the external cowl (installed thrust by book-keeping definition) changes the magnitude and direction of the thrust vector only slightly (fig. 3.6-4). Both vectors pass the vehicle's center of gravity by a small distance thus producing a very small nose-down moment that has to be balanced by the external aerodynamics.

At  $Ma = 1.2$  the nozzle geometry is chosen such that it operates in an overexpanded mode (fig. 3.6-5). There is a shock starting at the trailing edge of the cowl flap. This shock does not touch the expansion ramp. At the expansion ramp the nozzle flow is continually accelerated with pressures reducing. At the end of the expansion ramp two shocks, one in the jet and one in the free-stream, are formed because both flows have to turn into the free-stream flow direction. The pressure distribution along the nozzle walls are plotted in Figure 3.6-6. Shortly downstream of the throat both the pressure coefficients of the ramp and cowl side become negative. The pressure forces on the lower and upper nozzle contours again nearly cancel each other. But, on the expansion ramp there are pressures acting which produce nose-up moments. The thrust vectors (installed and uninstalled) and their relative position to the vehicle's center of gravity are depicted in Figure 3.6-7. The large nose-up moments can clearly be visualized.

The nozzle could have been operated in an underexpanded mode too. In order to obtain this mode the expansion ratio has to be reduced by turning the cowl flap towards the expansion ramp. As a by-product one ends up with a nearly blunt external cowl (fig. 3.6-8). The expansion in the jet flow at the trailing edge of the cowl flap can clearly be seen in the Euler result. This expansion reduces the pressure on the expansion ramp. The negative pressure coefficient values towards the end of the expansion ramp (fig

3.6-9) are not as large in magnitude than those of Figure 3.6-6. The thrust vector angle of this nozzle/afterbody configuration (fig. 3.6-10) is only by about 1.5 degrees more positive than that one of figure 3.6-7. The angle of the installed thrust vector is even more negative. The main difference between these two solutions is the turning of the flow in the throat of the underexpanded case which the overexpanded case does not have. In addition to the turning of the throat flow which counter balances the increased pressures on the expansion ramp (compared to the overexpanded case) the negative pressure coefficients on the blunt external cowl flap reduce the thrust and push the thrust vector to larger negative values. From this it follows that the transonic pitch problem of the SERN cannot be solved by geometry variation alone.

### 3.7 Proposals for the Solution of the Transonic Pitch Problem

There are ways around the problem of the SERN nozzle at transonic Mach numbers. However all methods available in the open literature are more or less still in the research stage. Final proof of reliable application and the production of a necessary data base have not been accomplished.

The method that suggests itself would be the use of reversed bleed. In Ref. 3.10 such a method has been proposed. By the use of active and/or passive bleed a separation is induced at the rear end of the expansion ramp (fig. 3.7-1). In some cases the separation leads to vortices which reduce the favorable pressure on the expansion ramp again. Depending on the shape of the sidewalls a strong influence of the external flow seems to exist. A short and a scarfed sidewall have been investigated although the test conditions have not been representative. The flow on the expansion ramp is very similar to the flow with separations in overexpanded axi-symmetric nozzles (see chapter 3.2 and Figure 3.2-5). A bleeding system including compressors for the necessary bleed air has been designed.

The second method comprises the injection of air through a slot downstream of the nozzle throat. The air to be used is intake bleed and fuselage boundary layer air from the intake diverter. As can be seen in Figure 3.7-2 this air is injected with subsonic Mach numbers and is accelerated by the jet flow to just supersonic Mach number at the rear of the expansion ramp. The change in thrust vector angle of the afterbody of Figure 3.6-8 due to this method can be derived by comparing the data with and without injection. There is an improvement at  $Ma = 1.2$  but for  $Ma > 2.0$  the thrust vector angle is increasing to +10 degrees. Both results do not seem to be satisfactory.

Different results have been produced for the overexpanded nozzle of Figure 3.6-5. In the upper half of Figure 3.7-3 the secondary air is injected with subsonic Mach number and a pressure higher than the jet pressure. The jet is deflected due to this high

pressure injection and an oblique shock is formed in the jet. The subsonic injection flow is further decelerated due to the increasing area between expansion ramp and jet which results in even higher pressures along the expansion ramp. This way the total thrust vector angle is reduced from nearly -24 (fig. 3.6-7) to about zero degrees.

In the lower half of Figure 3.7-3 the secondary air is injected supersonically at a pressure that is lower than the jet pressure at the injection station. The jet expands locally thus reducing the area of the injection stream which is decelerated until it goes subsonic through a normal shock. Again the pressures on the expansion ramp are higher with than without injection. The total thrust vector angle reduces to -7.5 degrees. The position of the normal shock in the injection stream is highly depending on the pressure at the upper end of the boattail. This pressure is a function of the external flow turning imposed by the jet. Thus it varies with angle of attack (fig. 3.7-4). For a large angle of attack this pressure is high and the position of the normal shock is close to the injection location. For smaller angles of attack the pressure is lower and the position of the normal shock is somewhat more downstream. The resulting thrust vectors are also shown in Figure 3.7-4.

A third method tries to remove the influence of the blunt external cowl flap (fig. 3.6-8) on the thrust vector and its angle. Due to the expansion of the external flow the pressures on this external surface are very low. They depend on the Mach number and the turning angle. Because of separation they are limited in magnitude. The plot in Figure 3.7-5 reveals that the pressures are lowest for  $Ma = 1.2/1.5$ .

It has been proposed to increase these low pressures so much that their negative contributions to the thrust vector and angle are diminished. Because the pressure on the external cowl flap determines the operating mode of the nozzle an additional optimization is necessary. If the pressure becomes too high the nozzle flow is overexpanded with oblique shocks in the jet. For an underexpanded operation the jet pressure has to be larger than the pressure on the external ramp. So with increasing external cowl pressures the expansion ratio of the nozzle has to be decreased with further losses. In the case of underexpanded flow the Mach line from the trailing edge of the cowl determines whether external combustion will influence parts of the expansion ramp or the external cowl surface only (fig. 3.7-6).

Figure 3.7-7 shows the calculated particle traces and center-line pressure distributions for an external hydrogen burning experiment. Particle traces on the surface and Mach contours in the exit cross-section demonstrate the flow redistribution due to the hydrogen combustion (fig. 3.7-8).

Figure 3.7-9 presents the results of a rough estimation of the effect of external hydrogen combustion on the

Sänger afterbody. No optimization has been accomplished yet.

### 3.8 The Plug SERN

This type of afterbody configuration has been looked into during work for the experimental vehicle HYTEX. This a two engine vehicle therefore larger three-dimensional flow effects were to be expected. One possible geometry of this afterbody is drawn in Figure 3.8-1. With some imagination one can see that due to the circular exit of the closed part of the plug nozzle additional base areas are formed (connected with drag and heat loads) that have to be faired into the shape of the expansion ramp. This makes the definition of an expansion ramp shape without inflection points and/or corners a rather difficult task. The expansion ramp has been cut-off on the sides in order to save weight.

Two-dimensional and three-dimensional Euler calculations have been performed the results of which are plotted in Figures 3.8-2 and 3.8-3. As can be seen there are shocks on the plug occurring in the underexpanded example at  $Ma = 1.2$  and in the overexpanded example at  $Ma = 3.5$  (fig. 3.8-2). The three-dimensional underexpanded calculation at  $Ma = 5.6$  reveals the shock which is due to the interaction of the axi-symmetric flows of the two engines (fig. 3.8-3).

Compared to the two-dimensional configuration the plug nozzle should offer the advantage of reduced weight and probably less leakage. However, only extensive structural and experimental/numerical flow investigations could make the trades e.g. between weight and performance reliable enough for the selection of one of these configurations.

### 3.9 Three-dimensional Afterbody Effects

The propulsion system integrated into the Sänger fuselage is shown in Figure 3.9-1. The overall width of the 5 expansion ramps is about 12 meters. This gives an impression of the size of the vehicle.

Clearly it cannot be expected that there is a constant pressure at the trailing edges of the lower cowl flap, the expansion ramp and the sidewalls. The downwash of the wing, the flow due to wing flap settings and even to the stabilizer will change the flow boundary conditions for the jet flow. On the sidewalls and on the top surface of the fuselage there will be a thick turbulent boundary layer whereas on the bottom the boundary layer will not be as thick due to its shorter length. However, on the bottom a separation on the blunt external cowl flap occurs.

On the top of the fuselage the second stage is sitting. The base area of this stage will need a cover (which is not shown here) until stage separation in order to reduce drag. An optimum boattail angle for the stage would be about 3 degrees. The pressure drag of the

cover is not very sensitive to the length of it (fig. 3.9-2). Therefore the length can be selected by weight considerations. There will be an interaction between the wake flow of the remaining base and the thick fuselage boundary layer. This will make the flow at the end of the expansion ramp highly non-uniform.

Between the 5 engines 4 partition walls will be needed. These walls will have a finite thickness and therefore expansions and shocks will occur at the trailing edges of these walls. These shocks will interact with the expansion ramp boundary layer and could lead to separations. The measured lines of constant pitot pressures from a model test simulating 4 engines in Figure 3.9-3 clearly depict these crossing shocks ("B").

The effect of sidewalls can best be appreciated by visualizing the differences between an afterbody without and with sidewalls. In Figure 3.9-4 a three-dimensional sketch of the afterbody flow features and a cross-section through the jet plume are reproduced. The nozzle flow is underexpanded. As can be seen in the 3D figure there is an area where the jet flow is completely two-dimensional up to the first Mach line of the expansion fan originating at the endpoints of the sidewalls of the closed nozzle. The location of this Mach line is a function of Mach number only. The expansion fan starts a strong outward curving of the flow (fig. 3.9-5). The flow is no longer 2D but 3-dimensional. A shock is created ("Internal shock") when the jet flow is turned back by the free-stream flow. There is another shock in the free-stream flow ("Jet shock") created by the turning of the free-stream due to the underexpanded jet. Between the two shocks the shear layer between jet and free-stream is located. The internal shock which is "sitting" on the expansion ramp is producing a cross-flow separation there whereas the jet shock separates the external (fuselage) model boundary layer. This afterbody flow is accompanied by at least two vortices on each side (like in fig. 3.9-6). From these flow features it is clear that thrust and thrust vector angles can only approximately be estimated with two-dimensional methods.

Adding sidewalls like on Sänger the situation changes the underexpanded flow somewhat. The limiting Mach line which bounds the two-dimensional flow area on the expansion ramp now starts at the trailing edge of the cowl flap, runs along the sidewall and then along the expansion ramp (fig. 3.9-7). Compared with the case without sidewalls the two-dimensional flow area is enlarged its higher pressures delivering more thrust (and nose-down moments). The three-dimensional flow can become rather complex depending on the nozzle pressure ratio and the external flow conditions. Cross-flow shocks at the rear ends of the sidewalls and expansion ramp can start separations and vortical flows. It cannot be predicted without experiment or CFD whether the thrust or thrust angle will be increased or decreased by these flows. In the unseparated flow situation the internal shock is no longer resting on the expansion ramp surface but starts

just downstream of the trailing edge of the sidewalls. The jet shock most likely does separate the fuselage boundary layer on all sides.

#### 4. Integration Aspects

Figure 4-1 gives an example what consequences the close integration of the intake with the forebody does have. Here an intake has been designed for the short blunt forebody shown. Because a higher propulsion performance was wanted it was decided to increase the precompression of the forebody by turning it by about 5 degrees. For drag reasons the forebody was made more slender too. Now, if one would just turn the existing intake by also 5 degrees the bottom of the intake lip would move down so much that the maximum cross-section of the vehicle would increase by about a quarter of its original value. Most likely this would not improve the performance of the vehicle. However, an intake especially designed for the decreased Mach number of the new forebody would not only swallow more mass flow through the same capture area during the shock-on-lip operation but would also swallow more mass flow during the off-design operation due to the reduced turning of the external ramps. The consequence out of this is that for every change of a component of the vehicle design changes for other components can ensue. This makes the design of highly integrated vehicles so tedious (and expensive).

One of the most important things before the design of a propulsion system should start is the definition of a book-keeping system. This is necessary to make sure that all forces acting on the vehicle are accounted for only once. Also, with a book-keeping system the responsibilities for the design and performance estimations of the components are fixed. In Figure 4-2 one possible candidate for a book-keeping system is defined. (Others can be found in the literature, e.g. Refs. 3.29 and 3.30). Here all the forces acting on the hatched and cross-hatched stream-tube including the forces on the intake cowl and afterbody flap are accounted for in the propulsion deck. All the other forces acting on the vehicle are accounted for in the aerodynamic deck. This book-keeping method has the advantage that all forces which are thrust depending are separated from the aerodynamic forces which do not depend on thrust. One important aspect that makes some difficulties at hypersonic Mach numbers is the fact that the book-keeping must also be defined such that all forces can be measured separately in different models, i.e. five component aerodynamic model, intake model, afterbody model. E.g., one difficulty with the aerodynamic model is the correct representation of the intake flow and its measurement because of the generally small size of the model which is due to the windtunnels available.

Considering the complete propulsion performance Figure 4-3 gives an impression of the relative magnitude of different propulsion components. As can be seen the drag of a blunt external cowl flap (called

nozzle/afterbody in the figure) is not negligible. Also, the Ram drag, that is the free-stream momentum of the intake air stream tube, is growing considerably with increasing Mach number. So the installed net thrust becomes a small difference between two large numbers, i.e. the ideal nozzle gross thrust and the ram drag. At the high flight Mach numbers small estimation errors in these two variables can make large differences in the installed net thrust.

In chapter 2 moments due to the intake have not been considered whereas in chapter 3 moments have been an important aspect of the SERN nozzle operation. Figure 4-4 gives the explanation for this. In this figure the forces according to the book-keeping are given for the intake and the afterbody at possible flight conditions at  $Ma = 1.2$  and  $Ma = 5.6$ . (The center fuselage has been omitted in the figure.) As can be seen the intake force has nearly no moment with respect to the center of gravity for  $Ma = 1.2$  whereas the afterbody force does have a large moment. At  $Ma = 5.6$  the moments of the intake and afterbody nearly cancel each other. The combined moments of the propulsion system are plotted in Figure 4-5 together with the moments of the airframe. The moments of the vehicle indicate large nose-down moments at around  $Ma \approx 1.0$  that have to be balanced by trimming.

#### 5. Development and Verification

For the development and the design verification of an air-breathing propulsion there are three tools that are indispensable: the windtunnel, numerical fluid dynamics (CFD) and flight testing of experimental vehicles. The strategy for the development and verification of a hypersonic vehicle will be covered in a separate paper. Here only some aspects will be touched.

##### 5.1 Windtunnel testing

In Germany we did intake and afterbody model testing in the TMK at the DLR in Cologne. Its test range is given in Figure 5.1-1. The tunnel can run without heating the air up to  $Ma = 4.5$ . With heating we did testing up to  $Ma = 5.2$ . Because of the limited test section size testing of small-scale models is possible only. However, the small scale and the cold windtunnel air flow allow to test at nearly exact Reynolds numbers. This is especially important where turbulent flows have to be modeled.

The generic afterbody model of Figure 5.1-2 has been tested in this windtunnel up to Mach numbers of  $Ma = 4.5$ . The tests have been conducted for various combinations of primary and secondary nozzle pressure ratios and angles of attack. Figure 5.1-3 shows a comparison for this generic afterbody model between a 2D Euler result and the Schlieren photo of the test in the TMK. The Mach number has been  $Ma = 3.5$  for this testpoint. The wall pressure distributions of both the tests and the calculations agreed quite well. In the figure it can be seen that the calculation captures all



important flow features that can be recognized in the Schlieren picture.

The intake model ETM3M in Figure 5.1-4 has been tested not only in the TMK but also in the SVS2 windtunnel at TsAGI, Moscow. This is a small-scale model of the intake for a hydrogen RAMjet propulsion unit that has been designed within the German Hypersonic Technology Programm. The design for this intake was based on the development work for hypersonic intakes accomplished at Dasa and at the DLR in Cologne. For the definition of the intake geometry extensive 2D Navier-Stokes calculations have been conducted to investigate the separation behaviour of different supersonic diffuser geometries. These calculations also verified that the internal compression of the intake would start with the final design geometry and at the actual windtunnel flow conditions. The testing of the isolated intake model was very successful. The performance predicted was exceeded. The highest test Mach number at the DLR has been  $Ma = 5.2$  and  $Ma = 6.0$  at TsAGI.

For the testing of larger intakes or even of complete propulsion units combustion-heated windtunnels are available, e.g. the APTU facility of the AEDC in Tullahoma in Tennessee, USA (fig. 5.1-5). In these windtunnels high enthalpy flows are produced by the combustion of butane, methane or hydrogen. The burned oxygen has to be added after the combustion. These facilities allow free-jet testing inside evacuated test cabins. This way the low static pressures at high altitudes can be simulated. The size of the models that can be tested depends on the size of the Mach rhombus of the windtunnel nozzle. The maximum Mach number generally is  $Ma \leq 8.0$ . In the APTU the maximum total temperature is  $T_t \approx 1100K$ . Because of the combustion products the test conditions may be limited by the formation of water or ice.

An intake of a capture area  $48 \times 48$  cm has been designed by Dasa for testing inside the APTU. These tests were to model the flow conditions of an experimental hypersonic vehicle as close as possible. The highest Mach number would have been  $Ma = 5.8$ . Figure 5.1-6 shows a three-dimensional view of the intake inside the test section of the APTU. On the left one can see the windtunnel nozzle and on the right the diffuser which produces the high altitude conditions. In the side view of Figure 5.1-7 the complete RAMjet propulsion unit consisting of intake combustion chamber and SERN nozzle can be recognized. The hydrogen combustion chamber together with the SERN nozzle have been tested successfully in the connected pipe test facility at Dasa-RI in Ottbrunn. The design of the full-scale intake is nearly completed. Its performance has been verified by the model tests described above. It would be very easy and only of low risk to continue the original plans and conduct the planned hydrogen RAMjet testing.

Larger propulsion units cannot be tested at hypersonic Mach numbers today. Also testing of forebody/intake or complete afterbody models is limited to extremely small models if it is possible at all. The problems and limitations of windtunnel testing both for Sänger and an experimental vehicle are roughly sketched in Figure 5.1-8. Windtunnel testing for Sänger will be restricted to small scale-testing of components. These tests must be supplemented by CFD and flight testing of experimental vehicles as necessary.

## 5.2 Computational Fluid Dynamics

CFD results have been extensively used in this paper to visualize the flows. Very often inviscid methods have to be applied due to the high costs of Navier-Stokes methods. This can only be done in situations when viscosity is not dominant in the flow. The example of an afterbody with secondary injection at a Mach number of  $Ma = 1.2$  in Figure 5.2-1 demonstrates the influence viscosity can have. In this figure an Euler and a Navier-Stokes solution are presented for the same geometry and flow conditions. The Euler solution produces all flow features like expansion fans, shear layers and shocks as does the Navier-Stokes solution. The main difference is in the interaction effects between the shocks and the boundary layers. E.g., both the shocks on the trailing edges of the expansion ramp and the external cowl flap respectively move up-stream due to this interaction in the Navier-Stokes solution. Because the boundary layers are very thin inside the nozzle the flow there is not so much different in the two CFD solutions.

In intake calculations it is still not possible to receive absolute performance data from CFD calculations. The state-of-the-art has been demonstrated in AGARD working group 13 (Ref. 2.43). From that work one result is presented in Figure 5.2-2. It shows the pitot pressure distribution in a cross-section of the P8 intake which is a two-dimensional NASA intake that has been tested at  $Ma = 7.4$ . The results clearly demonstrate quite a difference between the many CFD methods. Especially the shock of the internal compression is not as sharp as it should be. It seems that besides the numerical problems small differences in modeling geometry details can make large differences in the results. This test case revealed another problem of the validation procedure for numerical methods. The CFD pitot pressures are consistently larger than the measured data. This is due to inaccuracies of the test conditions.

Figure 5.2-3 gives a summary of what calculations have been conducted at Dasa in the German Hypersonic Technology Programm. For the determination of the precompression of forebodies Euler, Euler plus boundary layer and Navier-Stokes methods have been applied. Intake flows have been calculated by two- and three-dimensional Euler methods (Refs. 2.44, 2.45, 2.46). The afterbody flows were modeled by a two-dimensional Euler method only. The next necessary



step would have been to perform and verify three-dimensional Euler and Navier-Stokes calculations of forebody/intake and complete afterbody flows.

The potentials and deficits of CFD as presented in Figure 5.2-4 do not need to be explained here. In summary it can be said that CFD is - applied reasonably - the best analysis and diagnostic tool available. It is very much needed in the hands of the designer and should not be restricted to application within research institutions only.

## 6. Concluding Remarks

Because of the high integration a hypersonic vehicle has to be optimized in a close cooperation of propulsion and aircraft engineers (fig. 6-1). The integration problems to be solved during this optimization are not new. They are different and more complex because of the large Mach number range of a hypersonic vehicle.

Aerothermodynamics is one of the important design drivers for a hypersonic vehicle. Because the aerodynamic tools available, e.g. windtunnel testing, have limitations a strategy that combines windtunnel testing, CFD and flight testing of experimental vehicles promises success in the design of hypersonic aircraft like Sanger.

## 7. Acknowledgement

Hypersonics is bound to be team work. I myself feel as a member of that team. Therefore I acknowledge the support and the many fruitful discussions with all the colleagues at Dasa-LM, Dasa-RI, Dasa MTU, DLR, TsAGI and at the universities. I have learned a lot by working with them.

I feel also indebted to those who published their knowledge in the literature and thus made it possible to discover new solutions or problems.

The work within the German Hypersonic Technology Programm has been supported by the german ministry BMBF.

## References:

- 1.1 H.W. Liepmann; A. Roshko  
Elements of Gasdynamics  
Galcit Aeronautical Series, John Wiley& Sons, Inc., 1957
- 1.2 H.G. Munzberg  
Flugantriebe  
Springer-Verlag, Berlin, 1972  
ISBN 0-540-05626-2
- 1.3 W.H. Heiser; D.T. Pratt  
Hypersonic Airbreathing Propulsion  
AIAA Education Series, 1994  
ISBN 1-56347-035-7
- 1.4 G.C. Oates  
Aircraft Propulsion Systems Technology and Design  
AIAA Education Series, ISBN 0-930403-24-X
- 1.5 J.V. Foa  
Elements of Flight Propulsion  
John Wiley&Sons, Inc., 1960
- 2.1 J. Seddon, E.L. Goldsmith  
Intake Aerodynamics  
W. Collins Sons&Co. Ltd, London, 1985  
ISBN 0-00-383048-9
- 2.2 J. J. Mahoney  
Inlets for Supersonic Missiles  
AIAA Education Series, 1990  
ISBN 0-930403-79-7
- 2.3 W. Koschel  
Luftatmende Hyperschallantriebe  
3. Space Course, Stuttgart, 1993  
MTUM-B93EP-0002
- 2.4 D.L. Kors  
Design Considerations for Combined Air Breathing-Rocket Propulsion Systems  
AGARD-DP-479, paper 12
- 2.5 E. Tjonneland  
The Design, Development and Testing of a Supersonic Transport Intake System  
The Boeing Company, Seattle, USA  
AGARD-CP-91, 1971
- 2.6 Aviation Week&Space Technology  
Sept.13, 1993
- 2.7 A.M. Agnone  
Analytical and Experimental Investigation of a Swept 3-D Fixed Geometry Mixed Compression Hypersonic Inlet  
AIAA-87-0159
- 2.8 V. Selmin  
Numerical Simulation of the Flow Through a Scramjet Engine  
Alenia Aeronautica D.V.D., AGARD-CP-
- 2.9 G. H. McLafferty  
Hypersonic Inlet Studies at UAC Research Laboratories  
4th AGARD Coloquium on combustion and propulsion, Milan, April 1960
- 2.10 J. F. Connors, L. J. Obery  
Some Considerations of Hypersonic Inlets  
NASA Lewis Research Center, Cleveland, Ohio  
4th AGARD Coloquium on combustion and propulsion, Milan, April 1960
- 2.11 J.L.Benson; L.D. Miller  
Mach 5 Turbo-Ramjet Inlet Design and Performance  
ISABE 91-7079, 1991
- 2.12 L. Burkardt; R. Norris  
The Design and Evolution of the Beta Two-Stage-to-Orbit Horizontal Takeoff and Landing Launch System  
AIAA 4th International Aerospace Planes Conference, AIAA-92-5080, 1992

- 2.13 D.J. Dusa  
High Mach Propulsion System Installation and Exhaust System Design Considerations  
AIAA 87-2941
- 2.14 E. Krause  
Entwurfsprobleme supersonischer Einlaufdiffusoren  
DVL Bericht Nr. 198, 1962
- 2.15 N.C. Bissinger; H. Weinreich  
Gestaltung und Leistung von Hyperschall-Lufteinläufen  
DGLR-Fachausschußsitzung 21./22.11.1991
- 2.16 F. Monnoyer  
Hypersonic Configuration Optimization with an Euler/Boundary Layer Coupling Technique  
AIAA-93-3116 (and unpublished internal Dasa report)
- 2.17 J.L. Hunt; P.J. Johnston; G.D. Riebe  
Flow Fields and Aerodynamic Characteristics for Hypersonic Missiles with Mid-Fuselage Inlets  
AIAA 83-0542
- 2.18 J. Keller  
HYTEX 02/91  
Vorkörpergrenzschichtabschätzung mit DOBLAA  
Unpublished internal Dasa report, 1993
- 2.19 J. Wilson; W.H. Davis  
Hypersonic Forebody Performance Sensitivities Based on 3-D Equilibrium Navier-Stokes Calculations  
AIAA 88-0370
- 2.20 J. Keller  
HYTEX 02/91 Vorkompressionsdatensatz und Grenzschichtabschätzung  
Unpublished internal Dasa report, 1992
- 2.21 K.L. Oswatitsch  
Der Druckrückgewinn bei Geschossen mit Rückstoßantrieb bei hohen Überschall geschwindigkeiten  
Forschung und Entwicklungen des Heereswaffenamtes,  
Bericht No. 1005, Göttingen, 1944
- 2.22 Equations, Tables, and Charts for Compressible Flow  
NACA Report 1135
- 2.23 P.J. Waltrup; F.S. Billig; R.D. Stockbridge  
Engine Sizing and Integration Requirements for Hypersonic Airbreathing Missile Applications  
AGARD CP-365
- 2.24 T.A. Reyhner; T.E. Hickcox  
Combined Viscous-Inviscid Analysis of Supersonic Inlet Flowfields  
J. Aircraft, Vol. 9, No. 8, August 1972
- 2.25 A.V. Gnos; E.C. Watson; W.R. Seebaugh; R.J. Sanator  
Investigation of Flow Fields within Large-Scale Hypersonic Inlet Models  
NASA TN D-7150, April 1973
- 2.26 J.L. Benson; L.D. Miller  
Mach 5 Turbo-Ramjet Inlet Design and Performance  
ISABE 91-7079
- 2.27 J. Vadyak; J.D. Hoffmann  
Three-Dimensional Flow Simulations for Supersonic Mixed-Compression Inlets at Incidence  
AIAA Journal, Vol. 22, No. 7, July 1984
- 2.28 D. Darling; B. Sakowski  
Interface of an Uncoupled Boundary Layer Algorithm with an Inviscid Core Flow Algorithm for Unsteady Supersonic Engine Inlets  
AIAA 92-3083, 1992
- 2.29 O. Penanhoat; D. Darracq  
Simplified Model and Navier-Stokes Calculations for Optimization and Prediction of an Hypersonic Air Intake  
AIAA-95-6016
- 2.30 T.J. Bogar; M. Sajben; J.C. Krouti  
Characteristic Frequency and Length Scales in Transonic Diffusor Flow Oscillations  
AIAA 81-1291
- 2.31 J.T. Salmon; T.J. Bogar; M. Sajben  
Laser Velocimeter Measurements in Unsteady, Separated, Transonic Diffusor Flows  
AIAA 81-1197
- 2.32 M. Sajben; J. Donovan; M. Morris  
Experimental Investigation of Terminal Shock Sensors in Mixed-Compression Inlets  
AIAA-90-1931
- 2.33 Ref. 4.21 K.S. Chun; R.H. Burr  
A Control System Concept for an Axisymmetric Supersonic Inlet  
AIAA-68-581
- 2.34 J.M. Delery  
Shock Interference Phenomena in Hypersonic Flows  
The 3rd Joint Europe/US Short Course in Hypersonics at the RWTH Aachen, 1990
- 2.35 L.H. Back; R.F. Cuffel  
Shock Wave / Turbulent Boundary-Layer Interactions with and without Surface Cooling  
AIAA Journal, Vol. 14, No. 4, April 1976
- 2.36 D.R. Chapman; D.M. Kuehn; H.K. Larson  
Investigation of Separated Flows in Supersonic and Subsonic Streams with Emphases on the Effect of Transition  
National Advisory Committee for Aeronautics, Report 1356
- 2.37 F.S. Alvi; G.S. Settles  
Structure of Swept Shock Wave/Boundary Layer Interactions using Conical Shadowgraphy  
AIAA 90-1644
- 2.38 H. Kubota; J.L. Stollery  
An Experimental Study of the Interaction between a Glancing Shock Wave and a Turbulent Boundary Layer  
J. Fluid Mechanics 116, 431-458
- 2.39 A.G. Panaras  
Numerical Investigation of the High-Speed Conical Flow past a Sharp Fin  
J. Fluid Mech. (1992), Vol. 236, pp 607-633

- 2.40 W. Yang, I. Greber  
Turbulent Boundary Layer Interaction in a Duct  
AIAA-93-3127
- 2.41 J.J. Korte, A.H. Auslender  
Optimization of Contoured Hypersonic Scramjet  
Inlets with a Least-Squares Parabolized Navier-  
Stokes Procedure  
Computing Systems in Engineering, Vol.4,  
No.1, 1993
- 2.42 R. Munipalli, G. Wadawadigi, D.A. Anderson,  
D.R. Wilson  
Application of Optimization Techniques to Inlet  
Design  
AIAA-95-1824
- 2.43 AGARD-AR-270  
Air Intakes for High Speed Vehicles  
AGARD FDP Working Group 13, 1991
- 2.44 A. Eberle, M.A. Schmatz, N.C. Bissinger  
Generalized Flux Vectors for Hypersonic  
Shock-Capturing  
AIAA-90-0390
- 2.45 N.C. Bissinger, A. Eberle  
CFD Contributions during Hypersonic Airplane  
Intake Design  
AGARD-CP-510, paper 26, 1992
- 2.46 N.C. Bissinger, D.M. Schmitz  
Design and Wind Tunnel Testing of Intakes for  
Hypersonic Vehicles  
AIAA-93-5042
- 3.1 D.J. Dusa  
Exhaust Nozzle System Design Considerations  
ISABE 89-7077
- 3.2 H. Hermann; H. Rick  
Propulsion Aspects of Hypersonic Turbo-Ramjet-  
Engines with Special Emphasis on  
Nozzle/Aftbody Integration  
ASME-91-GT-395, 1991
- 3.3 M. Göing  
Nozzle Design Optimization by Method-of-  
Characteristics  
AIAA-90-2024
- 3.4 R.R. Schwab; F. Aulehla; M. Göing;  
H.-L. Weinreich  
Einige Gesichtspunkte zur Auslegung eines  
Hyperschall-Antriebssystems im Hinblick auf die  
Abstimmung von Einlauf und Heck mit dem  
Triebwerk  
DGLR Jahrestagung 1988, Vortrag 88-040
- 3.5 E. Eckert; M. Göing; H. Scheitle  
Optimization of Hypersonic Thrust Nozzles  
ISABE 91-7117
- 3.6 T. Berens  
Berechnung des Strömungsfeldes einer  
Rechteckdüse mit Expansionsrampe für  
Hyperschallflugzeuge bei Mach 1.2 (mit  
Einblasung der Vorderrumpfgrenzschicht) und  
Mach 5.6  
Unpublished internal MBB report 204, 28.6.91
- 3.7 T. Berens  
Thrust Vector Optimization for Hypersonic  
Vehicles in the Transonic Mach Number Regime  
AIAA 93-5060
- 3.8 T. Gronland; T. Berens  
Nozzle/Afterbody Integration for Hypersonic  
Vehicles by Means of Secondary Air Injection  
AIAA 95-6050
- 3.9 T. Berens  
Berechnung des Strömungsfeldes und  
Ermittlung des Bruttoschubvektors der HYTEX-  
Düse bei Mach 1.2  
Unpublished internal MBB report 202, 26.06.91
- 3.10 M. Zeutzius; A.E. Beylich; S. Matsuo;  
T. Setoguchi  
Vector Control for Hypersonic Space Planes  
JSME Paper No. 95-4024
- 3.11 T. Berens  
Eulerrechnungen zur  
Vorderrumpfgrenzschichteinblasung in  
die Düsenströmung bei Hyperschallflugzeugen  
Unpublished internal Dasa report 286, 1993
- 3.12 R. Lederer; J. Hertel  
Exhaust System Technology  
Space Course 1993, TU München, October 11-  
22, 1993
- 3.13 T. Berens  
Numerical Investigation of Thrust Vectoring by  
Injection of Secondary Air into Nozzle Flows  
AGARD-CP-534, 1993, paper 11
- 3.14 G. Besigk  
HYTEX - Abschätzung der Druckbeiwerte auf  
der Außenseite der unteren Düsenklappen  
Unpublished internal MBB note 123, 1990
- 3.15 M. Zeutzius; A.E. Beylich  
Experimental Investigation of Asymmetric  
Nozzles for Advanced Hypersonic Space Planes -  
Structure of Nozzle Jets and Thrust Vector  
Control  
Z. Flugwiss. Weltraumforsch. 17, pp.311-322,  
Springer-Verlag, 1993
- 3.16 C. Weiland; G. Hartmann; S. Menne  
Aerothermodynamics of Nozzle Flows for  
Advanced Hypersonic Propulsion Systems  
AGARD CP-510, 1992
- 3.17 W. Koschel, W. Rick  
Design Considerations for Nozzles of  
Hypersonic Airbreathing Propulsion  
AIAA-91-5019
- 3.18 A. Eberle  
Recent CFD Enhancements for Structured Mesh  
Navier-Stokes and Euler Solvers  
AIAA 93-5068
- 3.19 H.T. Lai  
Computation of H<sub>2</sub>/Air Reacting Flowfields in  
Drag-Reduction External Combustion  
AIAA-92-3672
- 3.20 F.W. Spaid; E.R. Keener  
Experimental Results for a Hypersonic  
Nozzle/Afterbody Flow Field  
AIAA-92-3915
- 3.21 S.M. Ruffin; E. Venkatapathy; S.H. Lee;  
E.R. Keener; F.W. Spaid  
Single Expansion Ramp Nozzle Simulations  
AIAA-92-0387

- 3.22 G. Besigk  
Sänger-Oberstufe / Druckwiderstand von  
konisch eingezogenen Düsenverkleidungen mit  
näherungsweise halbkreisförmigen  
Querschnitten  
Unpublished internal Dasa report 308, 1993
- 3.23 T. Berens  
Experimental and Numerical Analysis of a Two-  
Duct Nozzle/Afterbody Model at Supersonic  
Mach Numbers  
AIAA 95-6085
- 3.24 T. Berens  
Auswertung der Windkanalmessung mit dem  
Sänger-Strahleinflußmodell  
Unpublished internal Dasa report 295, 1993
- 3.25 G. Karadimas  
On the use of supercomputers to control flows  
and turbulence in the propulsion system  
development  
ECCOMAS 94, 2nd European Computational  
Fluid Dynamics Conference, Stuttgart, Germany
- 3.26 G.R. Nickerson; S.S. Dunn; D. Migdal  
Optimized Supersonic Exhaust Nozzles for  
Hypersonic Propulsion  
AIAA 88-3161
- 3.27 A.P. Kuchar; J.P. Wolf  
Preliminary Assessment of Exhaust Systems for  
High Mach (4 to 6) Fighter Aircraft  
AIAA 89-2356
- 3.28 M. Pierce; W. Ely  
A Computational Exploration of the Importance  
of Three-Dimensionality, Boundary Layer  
Development, and Flow Chemistry to the  
Prediction of Scramjet Nozzle Forces and  
Moments  
AIAA 91-5059
- 3.29 K. Numbers  
Hypersonic Propulsion System Force Accounting  
AIAA 91-0228, 1991
- 3.30 R.P.C. Lehrach  
Thrust/Drag Accounting for Aerospace Plane  
Vehicles  
AIAA-87-1966
- 3.31 N.A. Dubov, A.P. Mazurov, E.V. Pavlyukov  
Investigation of Hypersonic Plane Exhausted  
Nozzle Performance at Transonic Speed  
ISABE-95-7038, pages 427-437
- 4.1 Miki, Eguchi, Yamanaka  
SCRAM-LACE Propulsion System  
IAF-91-272
- 4.2 R. Hardy, L. Eldrenkamp, D. Ruzicka  
The Boeing TSTO  
AIAA-93-5167
- 4.3 A. Wagner, A. Dufour  
A Generic Fast Airbreathing First Stage TSTO  
Vehicle: RADIANCE  
AIAA-92-5084
- 4.4 A. Wagner; J.P. Bombled  
ORIFLAMME: A Reference Airbreathing  
Launcher to Highlight Areas that are  
Technological Drivers for Hypersonic Vehicles  
IAF 91-207, Canada
- 4.5 F. Falempin; M. Forrat; J. Baldeck; E. Hermat  
Flight Test Vehicles: A Mandatory Step in  
Scramjet Development  
AIAA 4th International Aerospace Planes  
Conference, 1-4 December 1992, Florida
- 4.6 N. Tanatsugu et al.  
Development Study on Atrex Engine  
45th Congress of the International Astronautical  
Federation, Oct. 94, Jerusalem
- 4.7 F. Heitmeir; R. Lederer; O. Herrmann  
German Hypersonic Technology Programme  
Airbreathing Propulsion Activities  
4th International Aerospace Planes Conference,  
Dec. 92, Orlando, USA  
AIAA-92-5057

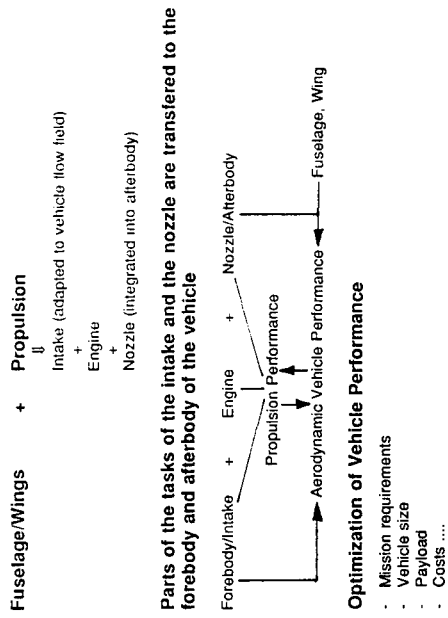
#### Copyright Statement

For some of the figures used in this paper copyright has  
been requested from and granted by

AIAA  
ISABE  
John Wiley & Sons Ltd.  
McDonnell Douglas Corporation  
Northrop Grumman Corporation  
Pergamon Press Ltd./Elsevier Science Ltd.  
ZFW

The sources of these figures can be identified by the  
reference numbers given. All rights reserved under the  
copyright laws.

Traditionally:  
(e.g. fighter)



Hypersonic Vehicle:

### Aerodynamics of Intake/Forebody and Afterbody/Nozzle

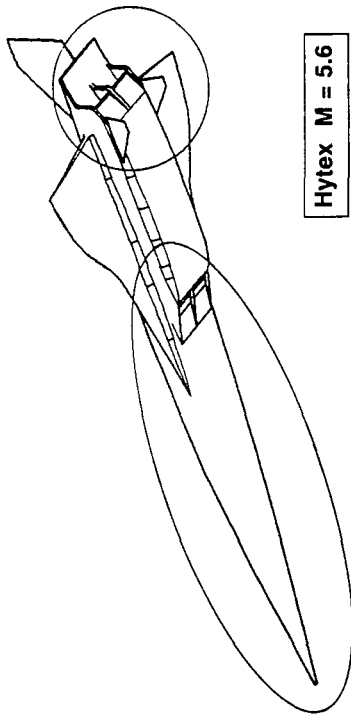


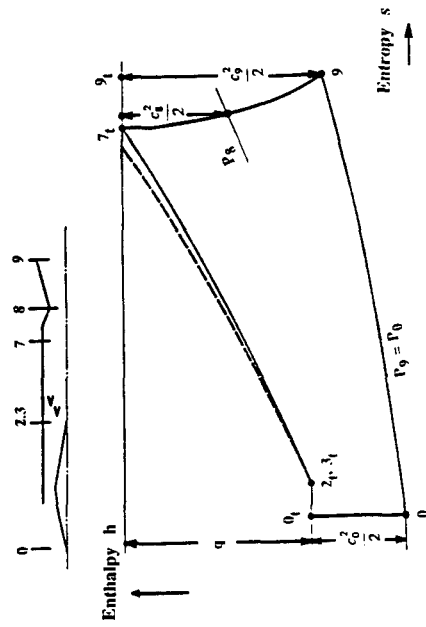
Fig. 1-3

NCB-VKI 96/130

Fig. 1-1

NCB-VKI 96/60

### Aerodynamic Vehicle Integration



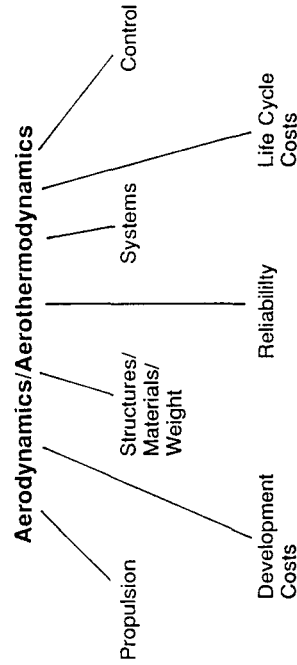
h-s Diagram for RAM Propulsion

Ref. 2.3

NCB-VKI 96/1

Fig. 2.1-1

### Some Important Boundary Conditions for the Design of Hypersonic Vehicle



NCB-VKI 96/60

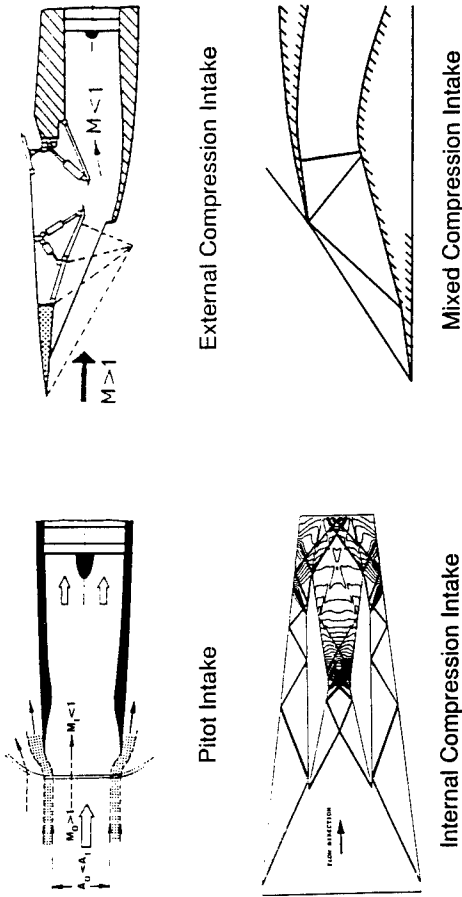
Fig. 1-2

- Deliver air to the engine (combustion chamber) for all flight Mach numbers at a desired rate (mass flow) and flow conditions (Mach number, pressure recovery and distortion)
- Small losses, drag, weight and complexity
- Conversion of kinetic energy into pressure energy (compression)
- Subsonic compression by area variation
- Supersonic compression by "isentropic" shapes or by shocks

Task of Intake

Fig. 2.2-1

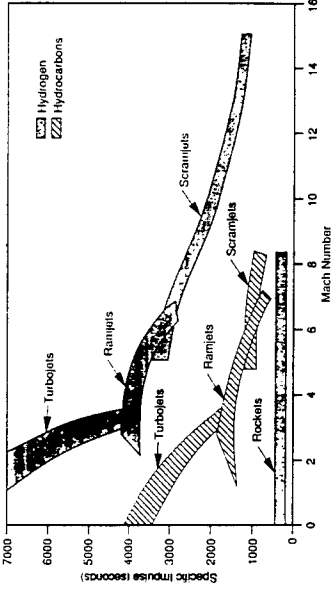
NCB VKI 9665



Intake Types

Fig. 2.3-1

NCB VKI 9665

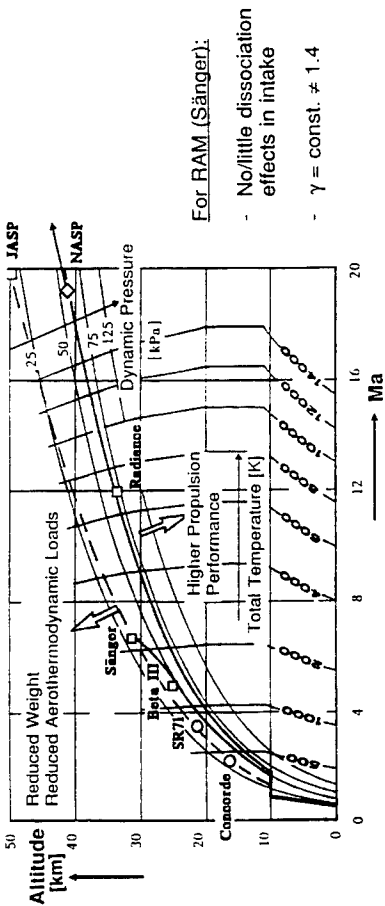


**RAM:**  
Air entering the intake is decelerated to subsonic Mach numbers ( $M \sim 0.1 - 0.3$ )  
⇒ Turbojet Engine  
Ramjet Combustion Chamber  
LACE

Fig. 2.1-2

Ref. 2.4  
NCB VKI 9662

Definition of RAM



Flight Envelope of Air-Breathing Hypersonic Vehicles

Fig. 2.1-3

Ref. 2.3  
NCB VKI 9664

Fig. 2.3-2

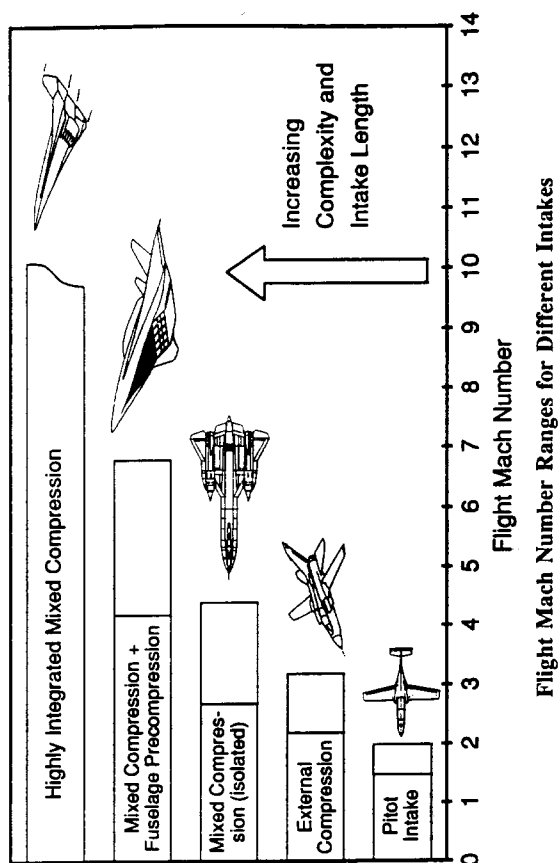


Fig. 2.3-2

NCB VKI 96/67

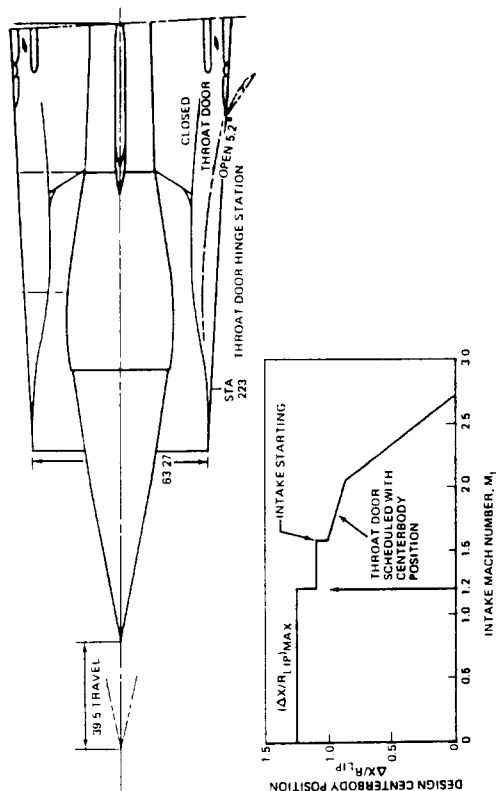


Fig. 2.3-3

Ref. 2.5

NCB VKI 96/68

Fig. 2.3-5



North American Supersonic Bomber XB-70A "Valkyrie" - Flight Mach Number Ma = 3.0

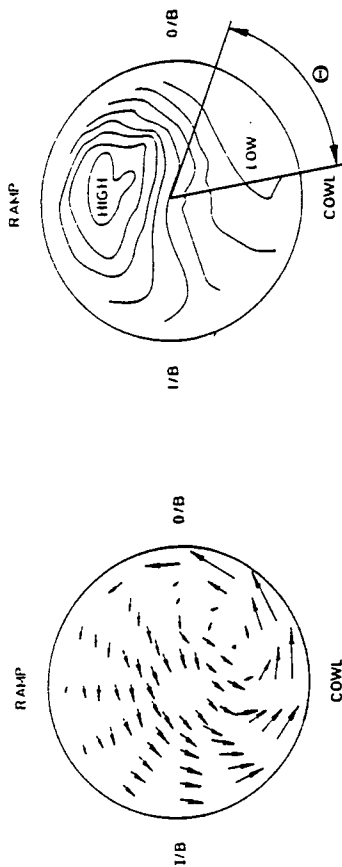
Two Dimensional Intake

NCB VKI 96/70

No permission for publication has been granted.  
For figure see page 47 of reference 2.6







Flow angles at engine/intake interface

Isobars at engine/intake interface

Definition:  $DC_\theta = \frac{\bar{p}_{t2} - \bar{p}_{t9}}{\bar{q}_2}$

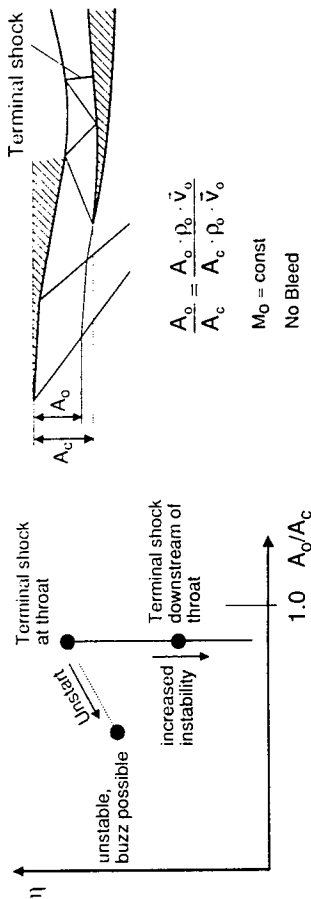
mean total pressure in the "worst" section of extent  $\Theta$

mean total and dynamic pressures at the engine interface plane

Distortion and Swirl

Fig. 2.4.2-1

NCB-VKI-96/74



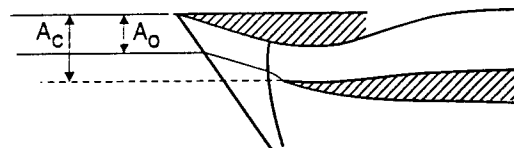
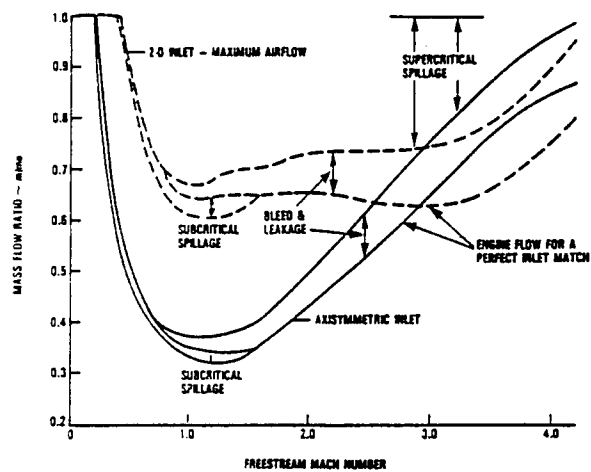
$$\frac{A_0}{A_c} = \frac{A_0 \cdot \rho_0 \cdot \vec{V}_0}{A_c \cdot \rho_c \cdot \vec{V}_c}$$

$M_0 = \text{const}$   
No Bleed

### Intake Airflow and Pressure Recovery Characteristic of Mixed Compression Intake

Fig. 2.4.3-2

NCB-VKI-96/76



Intake Sizing

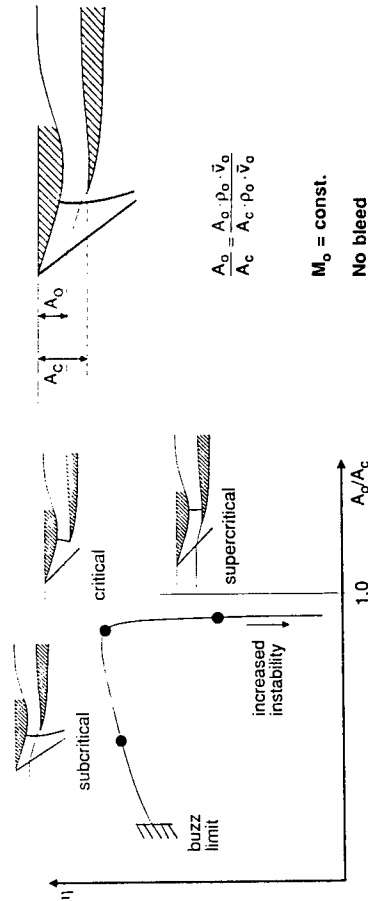
Ref. 2.11

Fig. 2.4.3-3

### Intake Airflow and Pressure Recovery Characteristic of External Compression Intake

Fig. 2.4.3-1

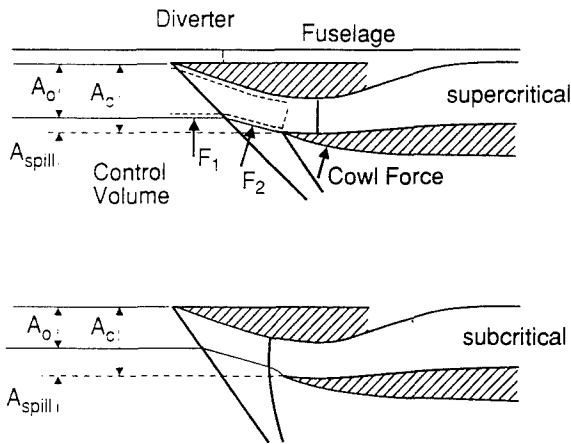
NCB-VKI-96/75



Intake Drag: drag due to flow spillage around the  
(Spillage) intake whenever  $A_0/A_c < 1.0$

Bypass/Bleed Drag: drag due to momentum losses in the flow

Diverter Drag: momentum losses, boundary layer separations and shocks



## Intake Drag

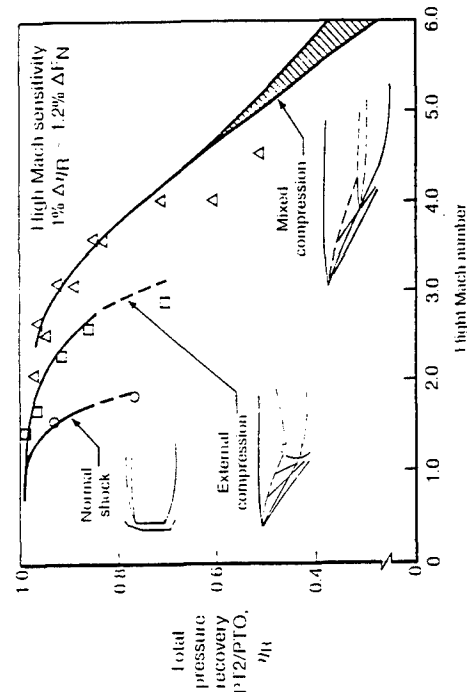
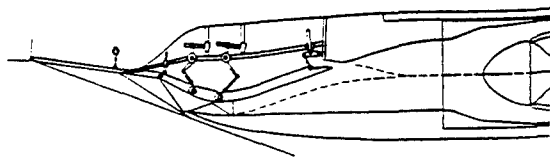


**Fig. 2.5.1-1**

### Comparison of Internal Performance of Different Types of Intakes

Ref. 2.13



1. Less outward deflection of the flow
  - smaller cowl wave drag
  - less turning back of the flow
  - less normal forces on external compression surfaces (pressure loads, pitching moments)
  - smaller frontal area
2. Longer supersonic compression section
  - increased intake weight
  - increased reflected shock/ boundary layer interactions
  - more complex bleed system
  - sophisticated control system to prevent unstart
  - effects pitching moments of vehicle (shift of engine)
  - larger cooling surfaces (no radiation)

## Effects of Increased Internal Compression in Mixed Compression Intake

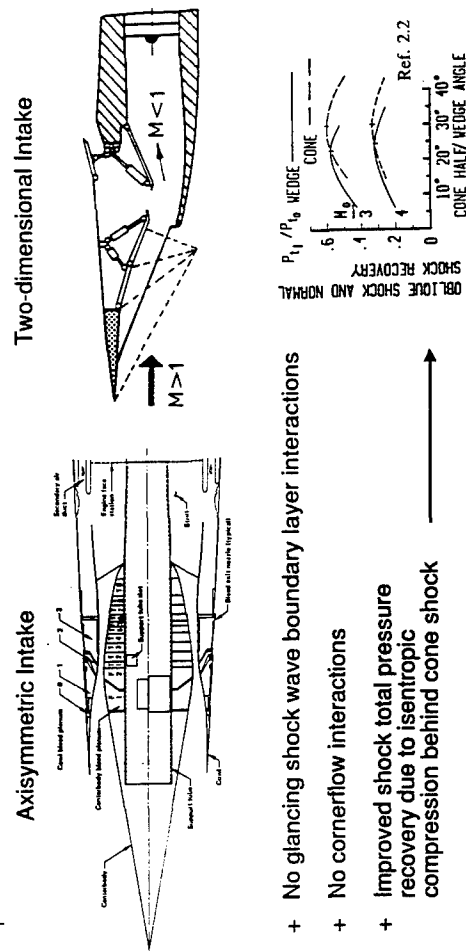
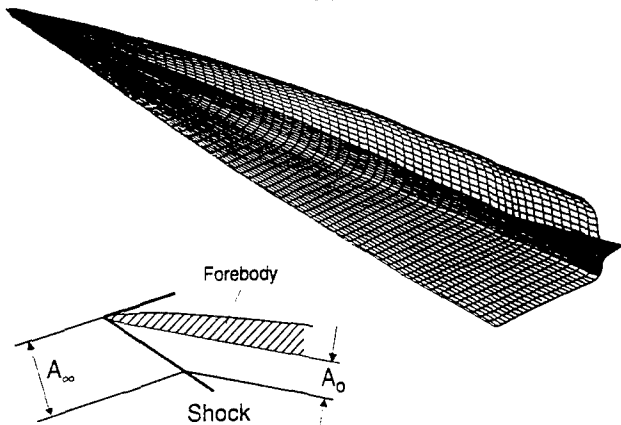
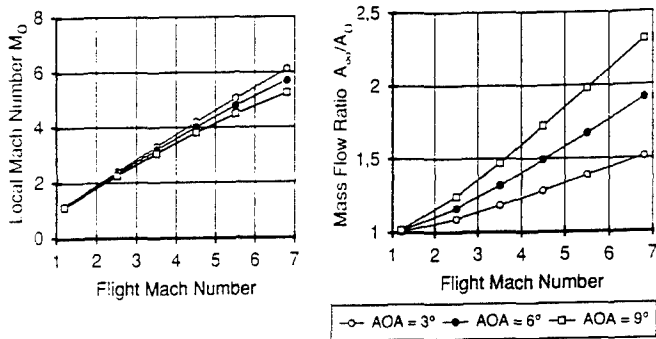


**Fig. 2.5.1-3**

# Superior Performance of Axisymmetric Mixed Compression Intakes with Extensive Boundary-Layer Bleed

**Ref. 2.15**

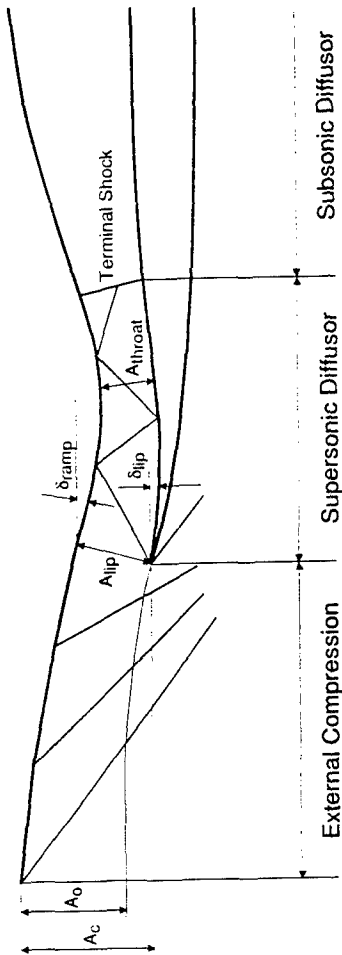




Effect of Forebody Precompression on Mass Flow Ratio and Local Mach Number

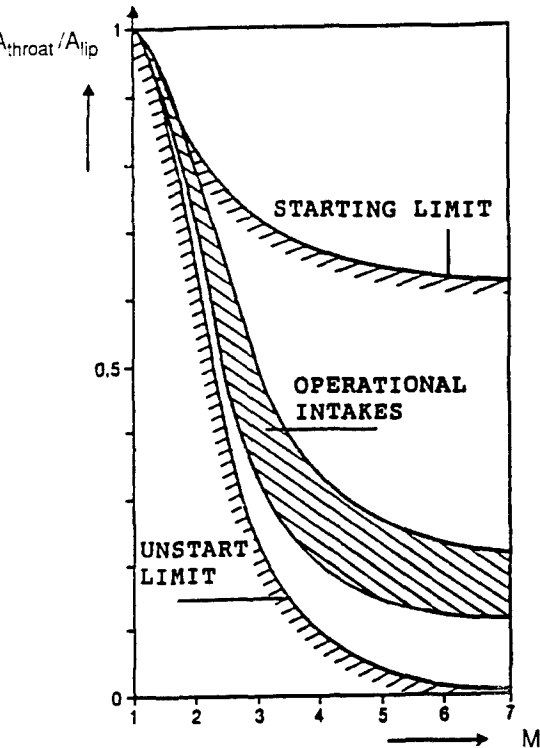
Ref. 2.20

Fig. 2.5.2-4



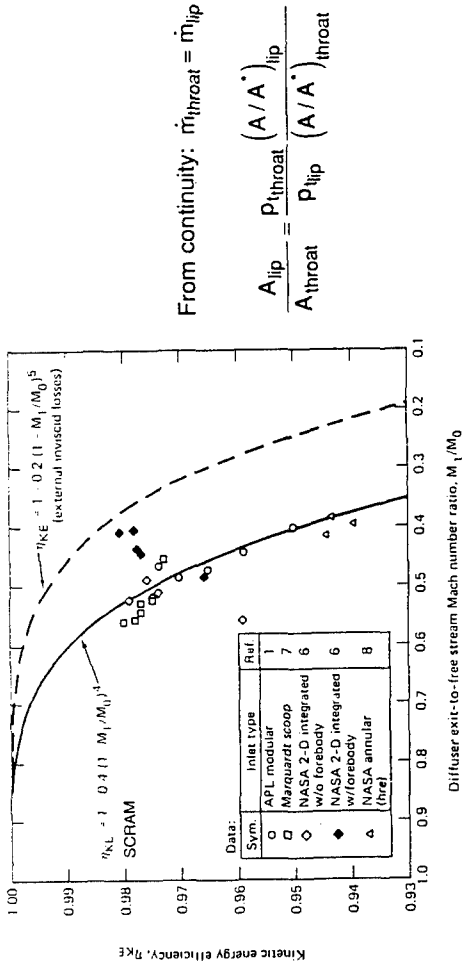
Intake Components to be Optimized During Design Process

Fig. 2.5.3-1



Throat Area Limits for Internal Compression

Fig. 2.5.3.3-1

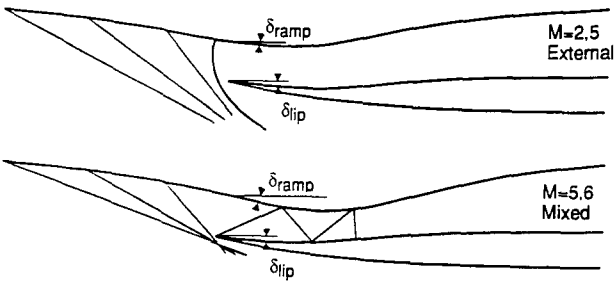


Estimation of Intake Contraction Ratio

Fig. 2.5.3.3-2

Ref. 2.23

NCB-VKI 96/90

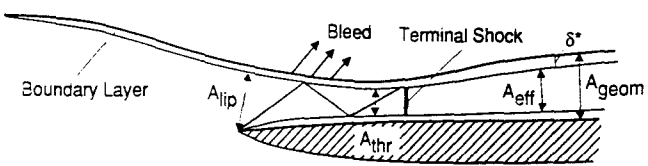


- Small frontal area and small external axial forces require small  $\delta_{lip}$
- Important is flow turning angle at lip:  $\delta_{ramp} - \delta_{lip}$
- External compression mode:  $\delta_{lip} \geq \delta_{ramp}$
- Mixed compression mode
  - a) Turbo: high  $\eta$  = equal shock strength
  - b) RAM: max  $\delta_{ramp} \triangleq$  large  $\delta_{lip}$
- Attached lip shock
- No boundary layer separation at shock reflection

Conflicting requirement:

- $\delta_{lip}$  large  $\rightarrow$  no boundary layer separation
- $\delta_{lip}$  small  $\rightarrow$  high pressure recovery

**External and Mixed Compression Modes of a Variable Hypersonic Intake**



- |                                   |   |
|-----------------------------------|---|
| Inviscid flow:                    | Method of characteristics (shocks, bleed model)   |
| Viscous flow:                     | Boundary layer finite difference code (bleed)   |
| Shock/Boundary layer interaction: | Control volume approach (Conservation of momentum and mass)   |
| <u>Aim:</u>                       | Calculate boundary layer development  |
| <u>Approach:</u>                  | <ul style="list-style-type: none"><li>- Calculate inviscid flow for <math>A_{eff}</math>, determine <math>\delta^*</math> and <math>A_{geom}</math></li><li>- Calculate inviscid flow for <math>A_{geom}</math>, determine <math>\delta^*</math> and <math>A_{eff}</math>, recalculate inviscid flow for <math>A_{eff}</math></li></ul> |

Shortcomings:

- Subsonic flow stops MOC calculation
- Man power and skill for smoothing and patching of solutions

Fig. 2.5.3.4-1

Fig. 2.5.3.5-1

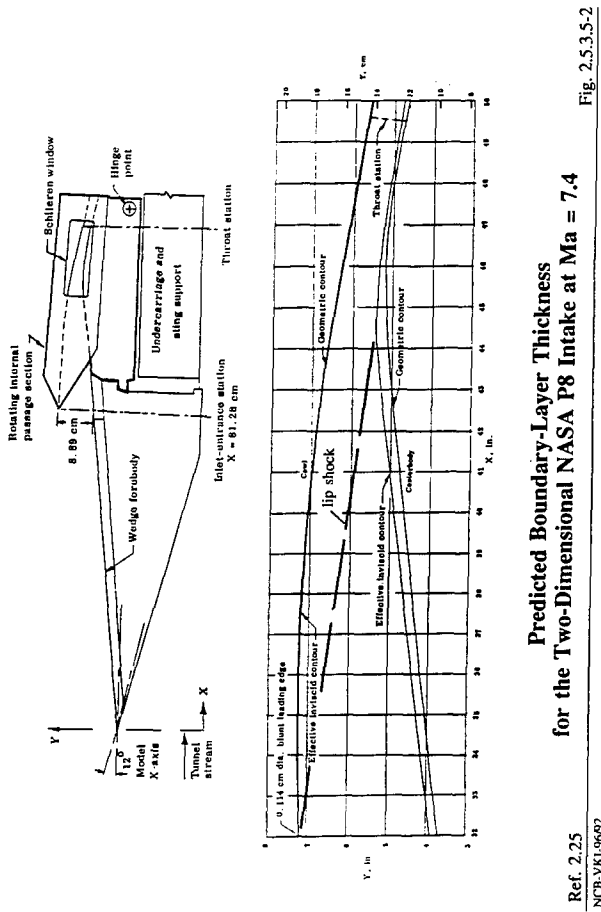
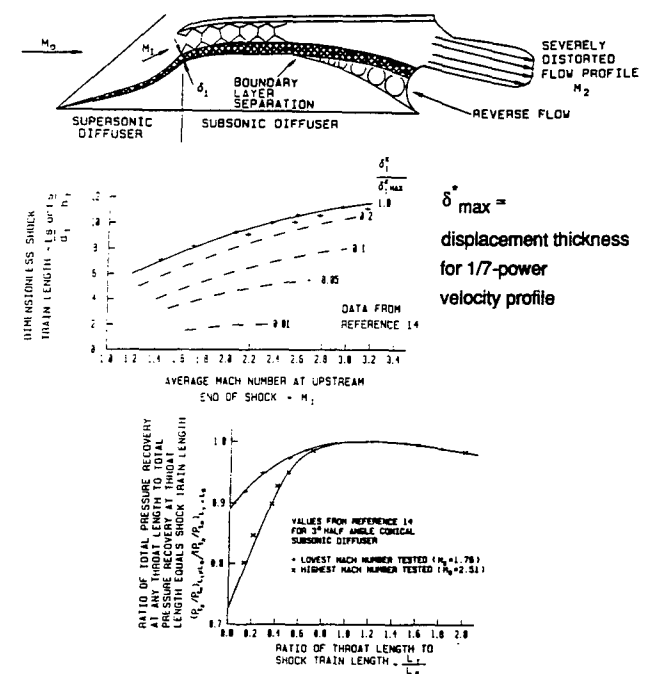


Fig. 2.5.3.5-2  
Ref. 2.25  
NCB-VKI-9692



- Subsonic diffuser: maintenance or establishment of uniform flow
- total pressure losses small (3% to 6%) if separation can be avoided

**Throat Length and Subsonic Diffuser**

Ref. 2.2

Fig. 2.5.3.6-1

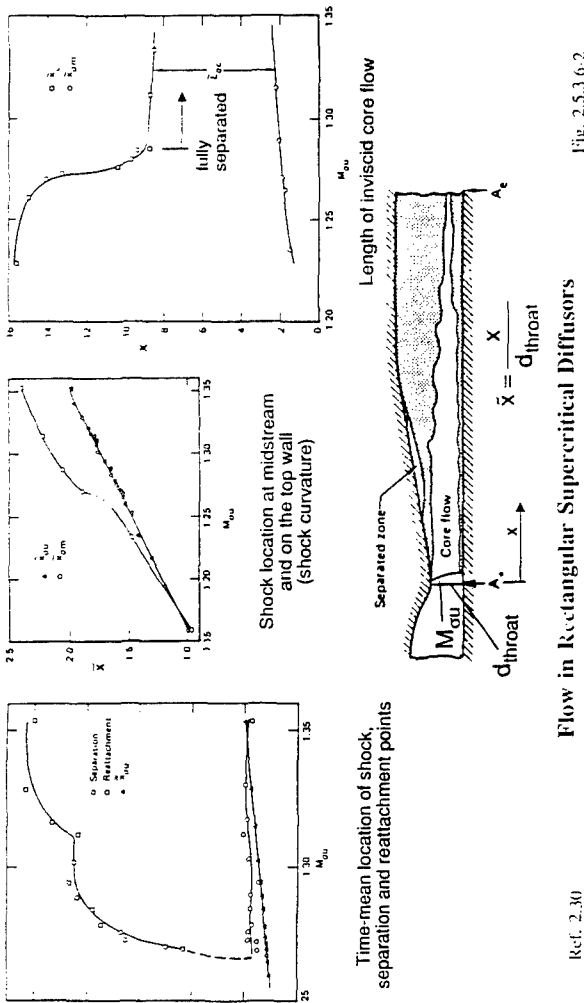
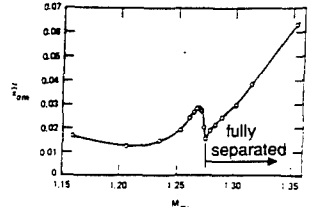
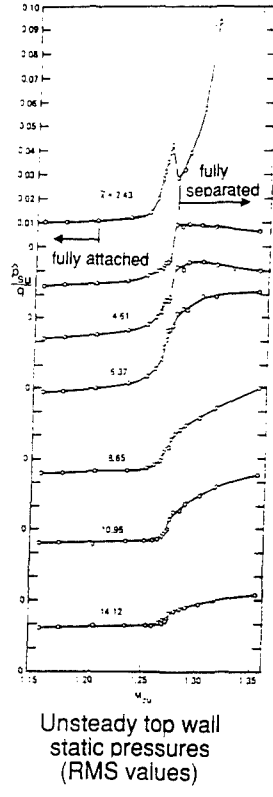


Fig. 2.5.3.6-2

Flow in Rectangular Supercritical Diffusers



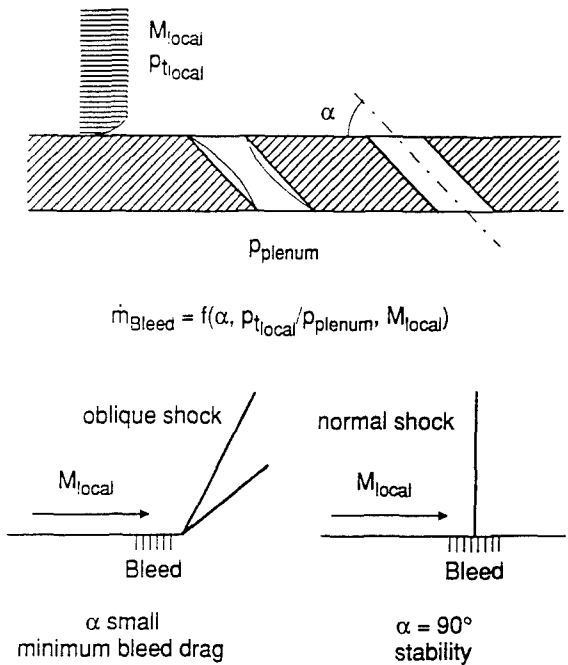
- low frequency shock motion
- independent of channel length
- highest value depends on flow situation (e.g.  $A_{exit}/A_{throat}$ , boundary layers, core speed)

(Mechanisms of separated flow oscillations not understood)

Flow in Rectangular Supercritical Diffusers

Ref. 2.30

Fig. 2.5.3.6-3



**Important:** Area available and structural strength (weight!)

Bleed

Fig. 2.5.3.7-1

- Turbo Mode:**  
(Low/Medium Ma)
- Bleed necessary for high pressure recovery and low distortion
- Limited data base ( $Ma < 2.2$ )
- Modelling problem (Wind tunnel and CFD)
- Recovery of bleed momentum (Injection in nozzle or A/C base  $\rightarrow$  weight)
- Bleed no longer possible (heat loads)
- Thrust is dominated by mass flow not pressure recovery (if pressure recovery large enough!!) (Ref. 2.14; 1962)
- To close bleed holes adds complexity and weight
- Roughness of bleed holes adds aerodynamic losses (modelling problem in experiment and CFD)
- Heat loads of closed bleed holes
- RAM Mode:**  
(High Ma)

Aspects of Intake Bleed

Fig. 2.5.3.7-2



- Control moveable ramp positions and throat height, i.e. mass flow entering intake lip plane
- Control position of terminal shock, i.e. pressure recovery and prevention of unstart
- Control start - unstart condition of intake, i.e. initiate starting procedure in case of unstart

Requirements:

- simplicity
- reliability
- accuracy
- working conditions: high temperatures  
high pressures  
high noise levels and vibrations

Necessary:

- Calibration of system (Windtunnel?, Flight Test)
- Accurate measurement of flight Mach number and vehicle attitude ( $\alpha, \beta$ ):  $\Delta Ma \sim -0.05$ ;  $\Delta \alpha \sim +0.5^\circ$  for prevention of unstart (fixed intake geometry)

**Intake Control**

Fig. 2.5.3.8-1

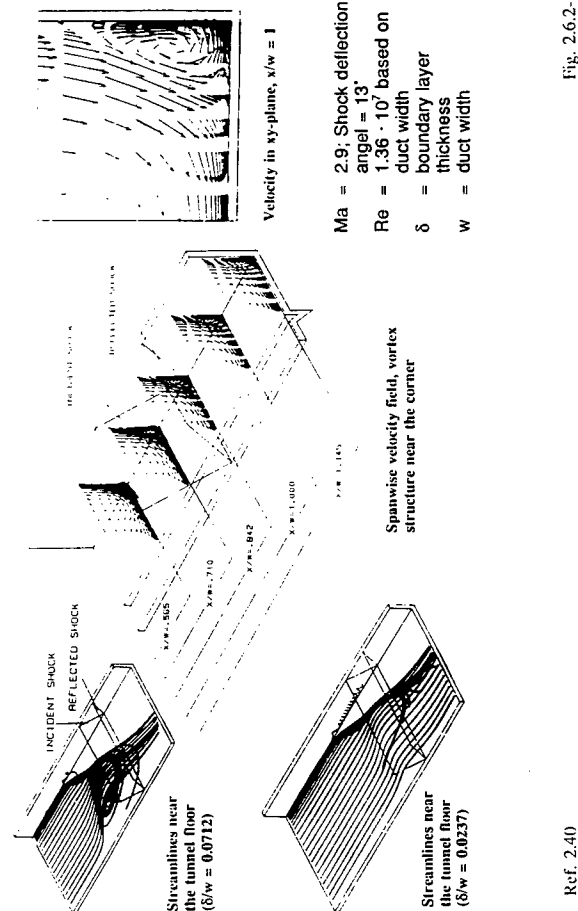


Fig. 2.6.2-1

Ref. 2.40

NCB VKI 96/127

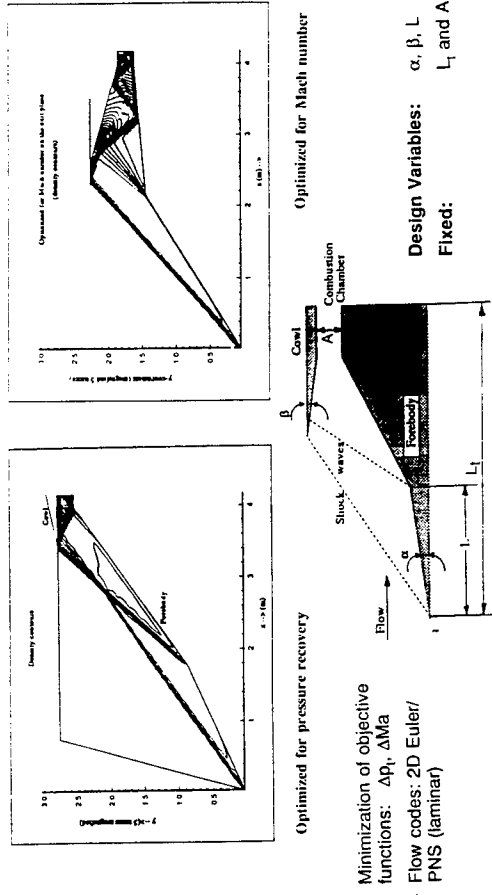


Fig. 2.6.3-1

Ref. 2.41; 2.42

NCB VKI 96/129

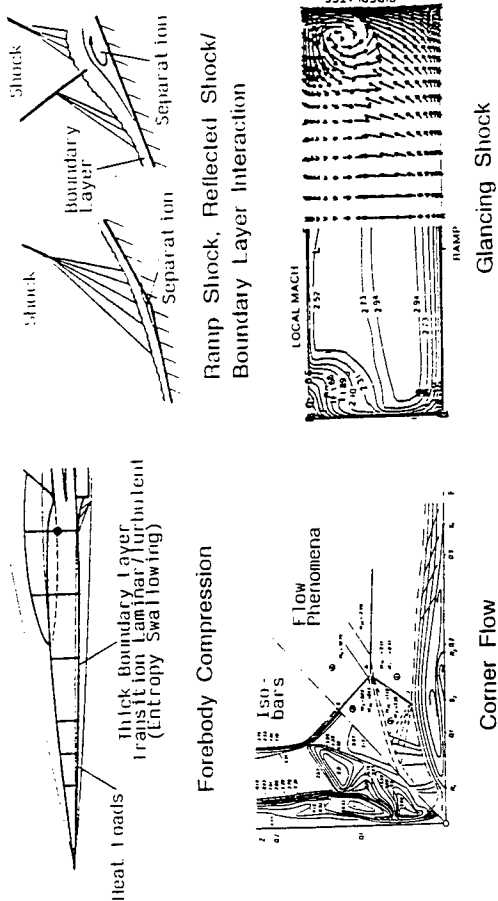
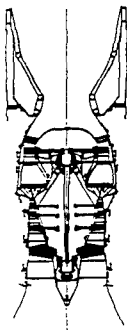


Fig. 2.6.1-1

NCB VKI 96/118

Mach 4 Dry Turbojet



Turbofan/Ramjet



Turboramjet



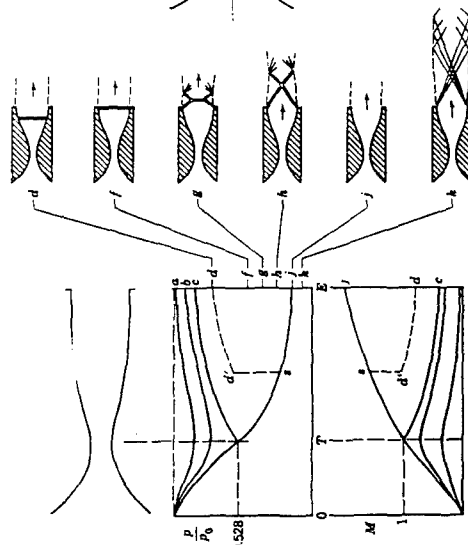
Air/Turbo/Ramjet



### Propulsion Systems for High Speed Vehicles

Ref. 3.1  
NCB-VKI-96/3

Fig. 3.1-2

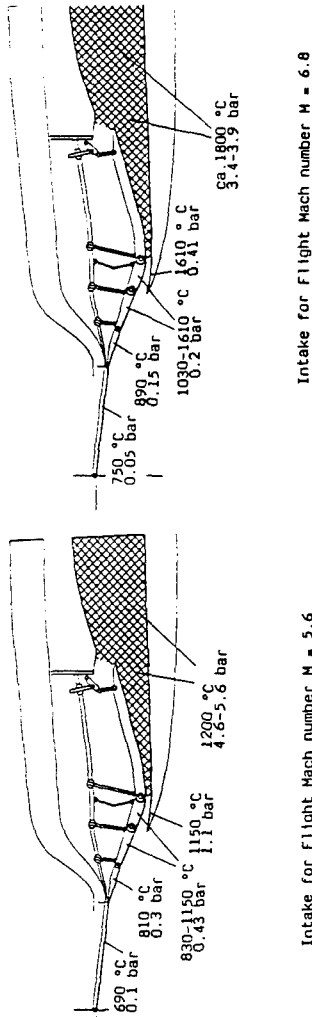


Ref. 1.1

### Axisymmetric Laval Nozzle

NCB-VKI-96/7

Fig. 3.1-1



Intake for Flight Mach number  $M = 6.8$

Intake for Flight Mach number  $M = 5.6$

HYTEX

### Pressure and Temperature Loads

Fig. 2.6.4-1

NCB-VKI-96/101

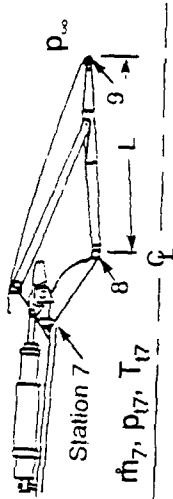
1. No strong temporal temperature gradients
  - Adiabatic/radiation-adiabatic walls
2. Local temperature gradients (leading edges, shock reflections etc.)
  - Deformations known and acceptable?
3. Deformations due to pressure loads acceptable?
  - Trade between aerodynamics and weight (capture and throat area)
4. Gaps and steps in intake skin are potentially dangerous because they produce shocks/expansions whose effects may be amplified (confined flow).
5. Effect of forebody deformation (due to pressure or heat loads) on pre-compression must be known and be considered in intake control laws.
6. Intake should be rigidly attached to fuselage to have clearly defined intake on-set flow. Possible?
7. A light-weight flight structure will not be able to sustain intake unstart loads - control problem - atmospheric disturbances.
8. Model and flight structure most likely differ.

### Structural/Acrothermodynamic Aspects for Intake

Fig. 2.6.4-2

NCB-VKI-96/106





**Nozzle gross thrust coefficient:**

$$C_{FG} = \frac{F_G}{F_i}$$

where

- $F_G$  = Nozzle gross thrust
- $F_i$  = Nozzle ideal gross thrust =  $\dot{m} \cdot V_i$
- $V_i$  = Ideal velocity at nozzle exit (isentropic expansion to  $p_\infty$ )
- $\dot{m}$  = Nozzle mass flow

**Nozzle installed thrust:**

$$F_N = F_G - D_{Ext. Nozzle} - F_R$$

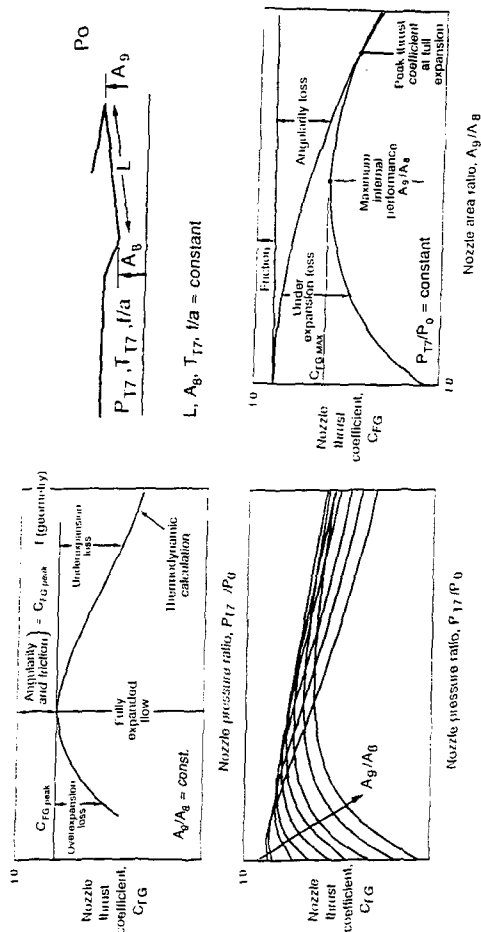
where

- $F_R$  =  $\dot{m}_0 \cdot V_\infty$  = Ram drag
- $\dot{m}_0$  = Inlet mass flow
- $V_\infty$  = Flight velocity of A/C
- $D_{Ext. Nozzle}$  = Drag on external nozzle walls (Def. according to book-keeping)

### Definition of Nozzle Gross Thrust Coefficient and Engine Installed Thrust

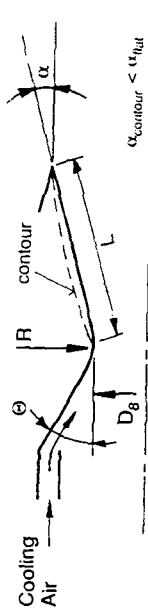
Fig. 3.2-1

NCB VKI 99/4



Internal Nozzle Performance

NCB VKI 99/4

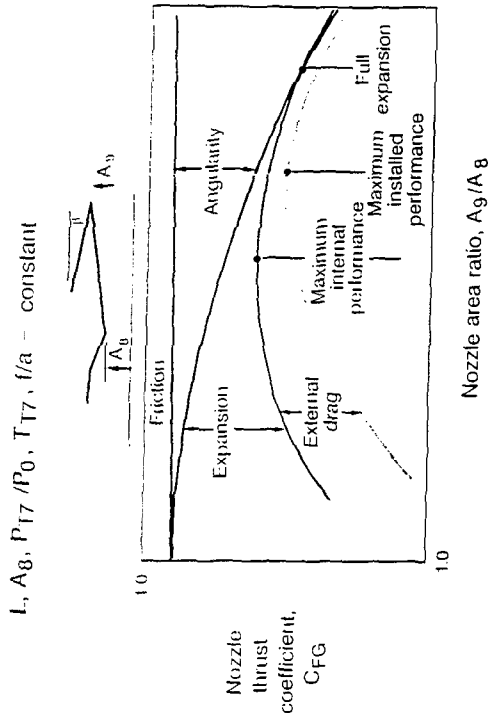


- Nozzle Flap Length (Reduced Underexpansion)
- Nozzle Flap Contouring (Reduction of Divergence Losses)
- Nozzle Throat Radius R (Effective throat area  $A_8 = f(\theta, R/D_8)$ )
- Unrealized Thrust due to Unburned Cooling Air
- Leakage

### Additional Factors Influencing Nozzle Efficiency

Fig. 3.2-3

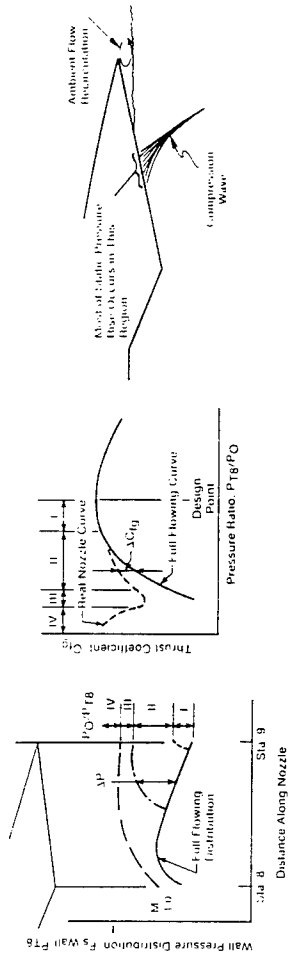
NCB VKI 99/4



Installed Nozzle Performance

Fig. 3.2-4

NCB VKI 99/4

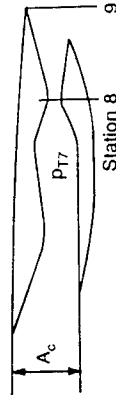


- nozzles not designed for these conditions
- little or no experience
- can be utilized for hypersonic ?
- separation predictable, unsteady ?

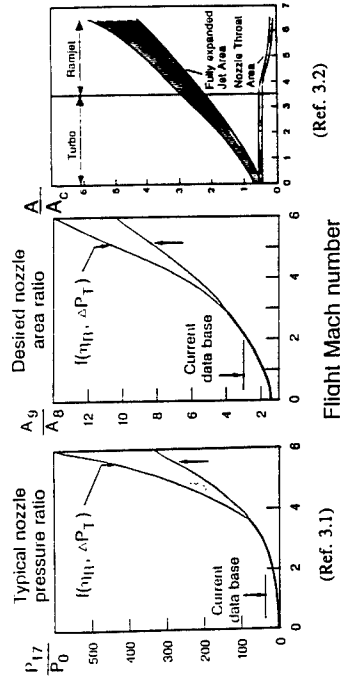
Overexpansion Effects in C-D Nozzle

Fig. 3.2-5

Ref. 1.4  
NCB-VKI-96/10



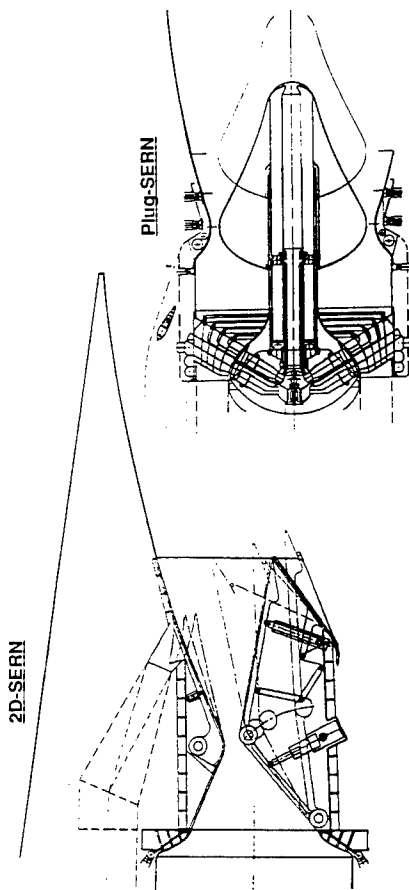
- Variable nozzle throat area
- For  $Ma > 4$  axisymmetric nozzle not possible
- For high  $Ma$  fully expanding nozzle not practical (weight, drag)



High Mach Nozzle

Fig. 3.3-1

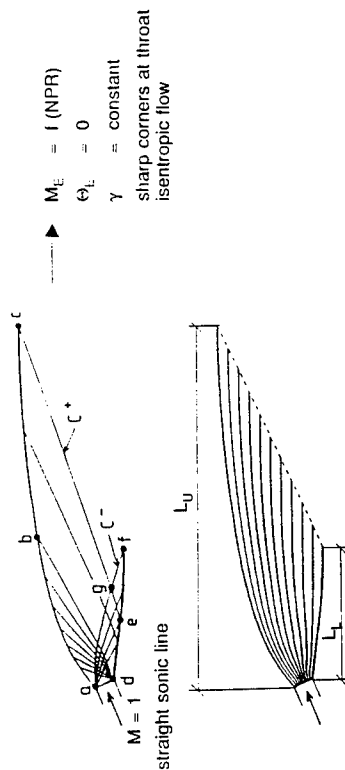
Ref. 1.4  
NCB-VKI-96/10



Nozzle Candidates for Hypersonic Vehicles

Fig. 3.4-1

Ref. 3.3  
NCB-VKI-96/11

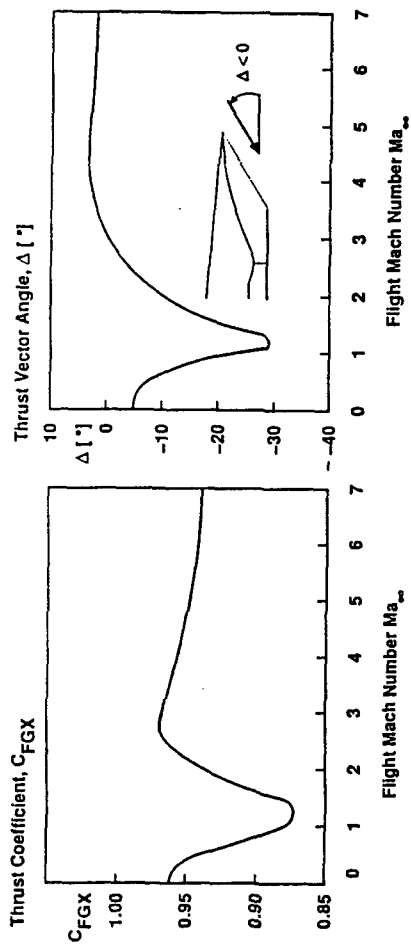


Family of Nozzles =  $f(L_u, L_v)$  expansions and flow angle at throat)

Design of Ideal SERN-Geometry with Method of Characteristics (MOC)

Fig. 3.5-1

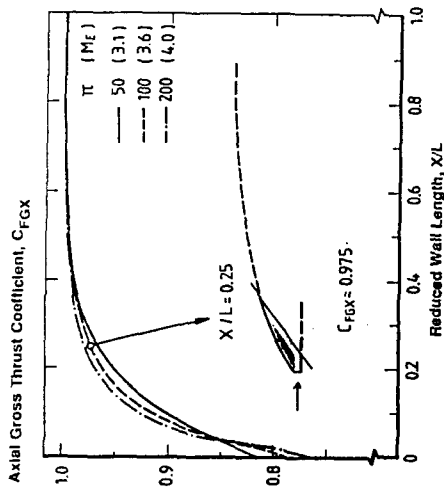
Ref. 3.3  
NCB-VKI-96/11



SERN Nozzle Performance

Ref. 3.5  
NCB-VKI 96/16

Fig. 3.6-1



Axial Thrust Coefficient  $c_{fgx}$  for Reduced Nozzle Length

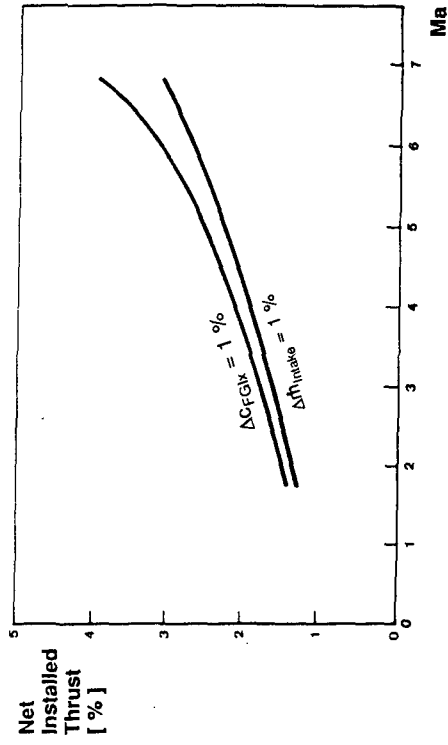
Ref. 3.3  
NCB-VKI 96/14

Fig. 3.5-2



Ref. 3.6  
NCB-VKI 96/17

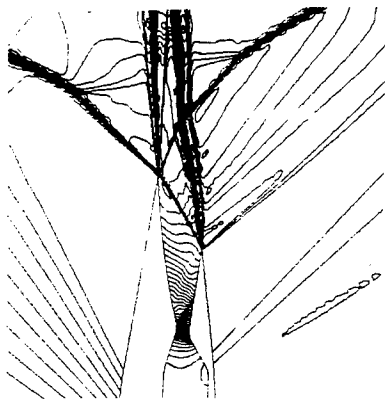
Fig. 3.6-2



Sensitivity of Net Installed Thrust to Nozzle Efficiency and Inlet Bleed Mass Flow

Ref. 3.4  
NCB-VKI 96/15

Fig. 3.5-3

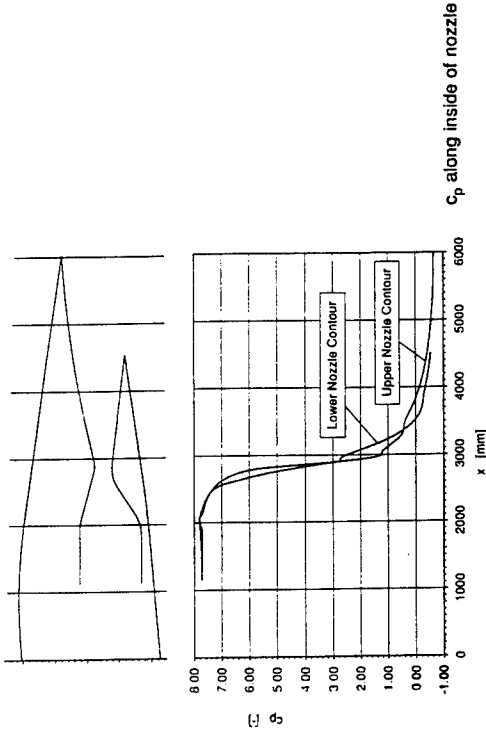


Mach Numbers

2D Euler Results for Ma = 1.2

Ref. 3.7  
NCB-VKI/96/21

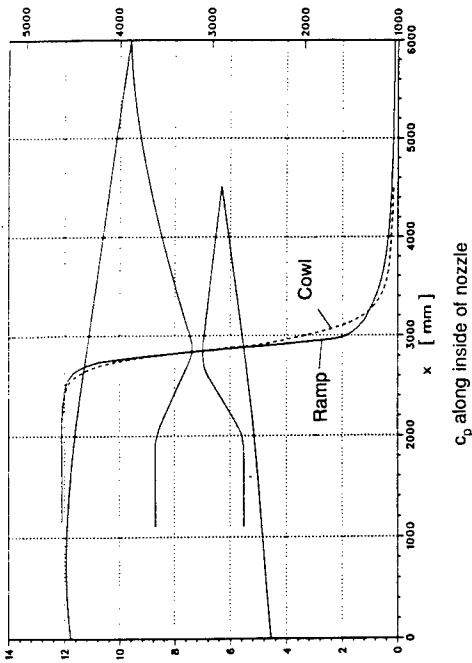
Fig. 3.6-5



2D Euler Results for Ma = 1.2

Ref. 3.7  
NCB-VKI/96/23

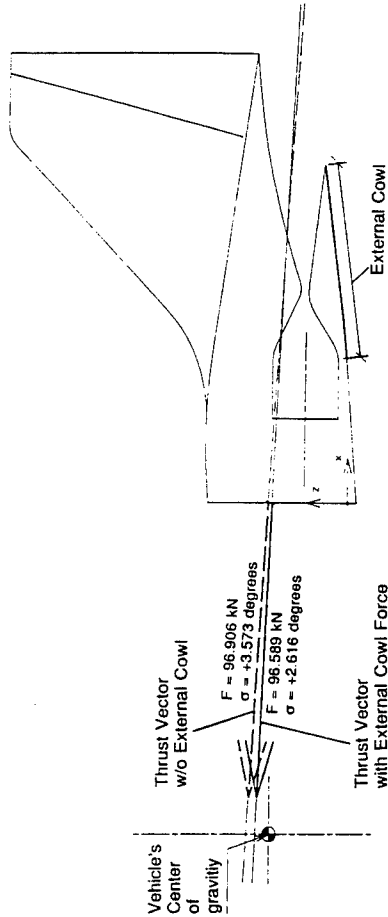
Fig. 3.6-6



2D Euler Results for Ma = 5.6

Ref. 3.6  
NCB-VKI/96/19

Fig. 3.6-3

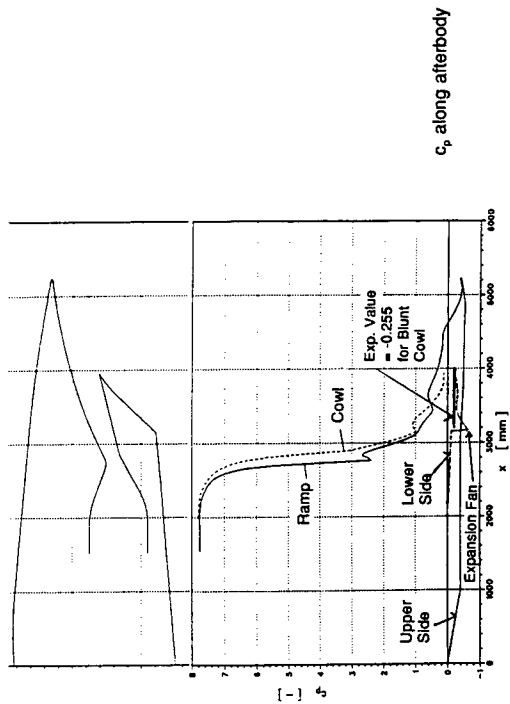


Thrust vector and thrust vector angle with and without force on external cowl

2D Euler Results for Ma = 5.6

Ref. 3.6  
NCB-VKI/96/20

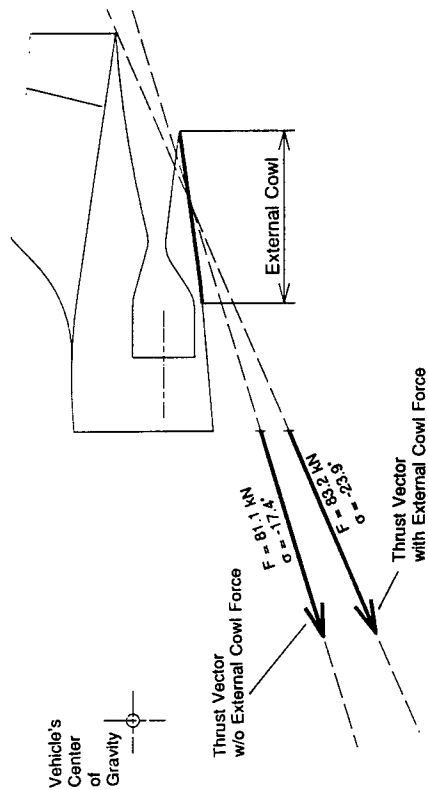
Fig. 3.6-4



2D Euler Results for  $Ma = 1.2$  (Blunt Cowl)

Ref. 3.9  
NCB-VKI-96/27

Fig. 3.6-9

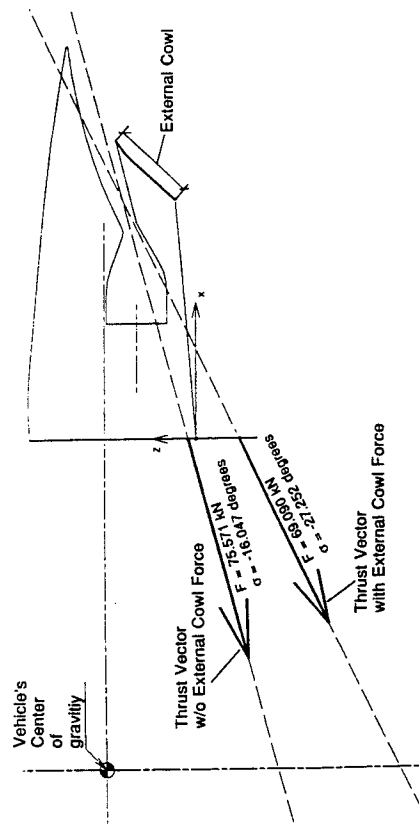


Thrust vector and thrust vector angle with and without force on external cowl

2D Euler Results for  $Ma = 1.2$

Ref. 3.7  
NCB-VKI-96/24

Fig. 3.6-7



Thrust vector and thrust vector angle with and without force on external cowl

2D Euler Results for  $Ma = 1.2$  (Blunt Cowl)

Ref. 3.9  
NCB-VKI-96/28

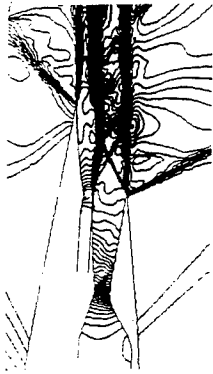
Fig. 3.6-10



2D Euler Results for  $Ma = 1.2$  (Blunt Cowl)

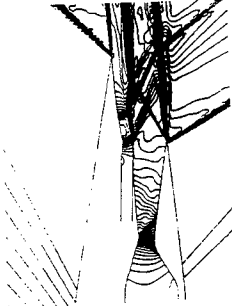
Ref. 3.9  
NCB-VKI-96/26

Fig. 3.6-8



$\sigma_{jet} = +5.94^\circ$   
 $\sigma_{total} = -0.17^\circ$

Lines of constant Mach number ( $\Delta Ma = 0.05$ )

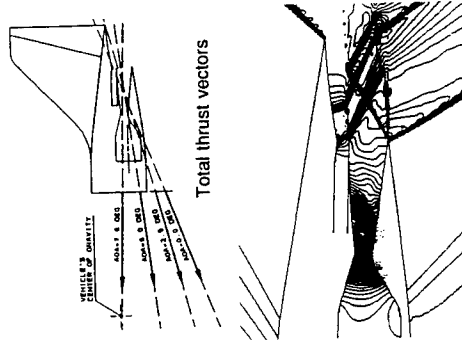


$\sigma_{jet} = -1.0^\circ$   
 $\sigma_{total} = -7.5^\circ$

Injection of secondary air (afterbody 2)  
(without injection:  $\sigma_{total} = -24^\circ$ )

2D Euler Results for  $Ma = 1.2$

Fig. 3.7-3

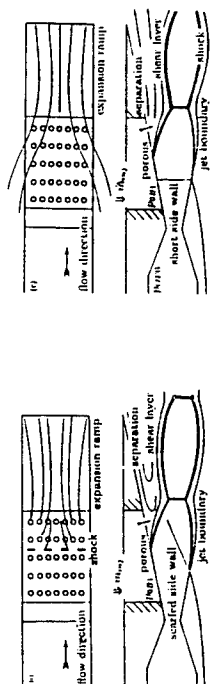


Lines of constant  $c_p$   
 $\Delta c_p = 0.05$   
 $\alpha = 5^\circ$

Influence of external flow: angle of attack variation

2D Euler Results for  $Ma = 1.2$

Fig. 3.7-4

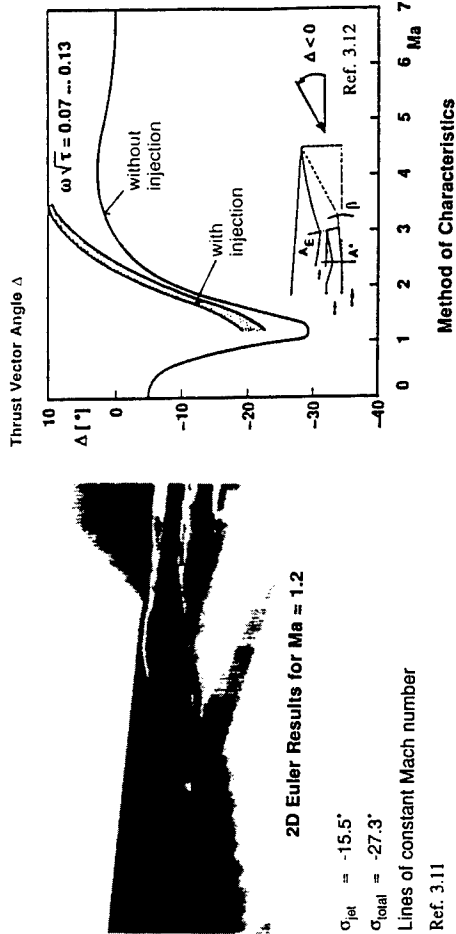


Short side wall - active control

- Active/passive Bleeding
- Turning of Nozzle Flow
- Separation leads to vortices with reduced pressures  $\rightarrow$  local heating problems?
- Strong influence of external flow depending on side wall shapes (short, scarfed)
- Increased complexity and weight

Wall Bleeding to Solve Transonic Afterbody Moment Problem

Fig. 3.7-1



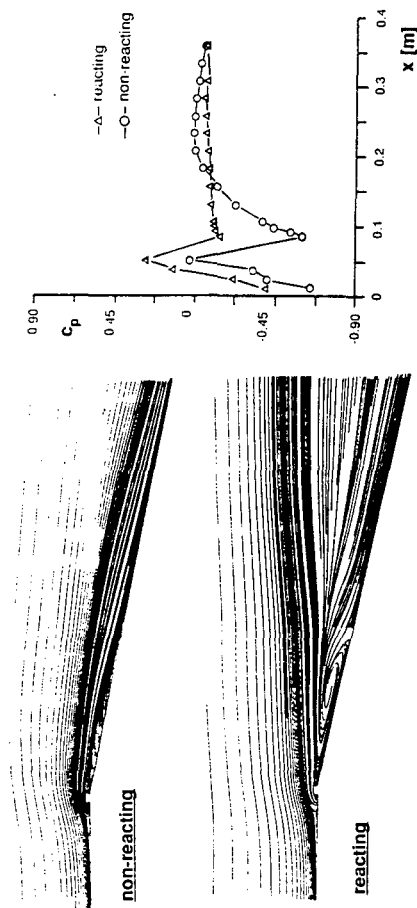
$\sigma_{jet} = -15.5^\circ$   
 $\sigma_{total} = -27.3^\circ$

Lines of constant Mach number

Ref. 3.11

Injection of secondary air (afterbody 1)

Fig. 3.7-2

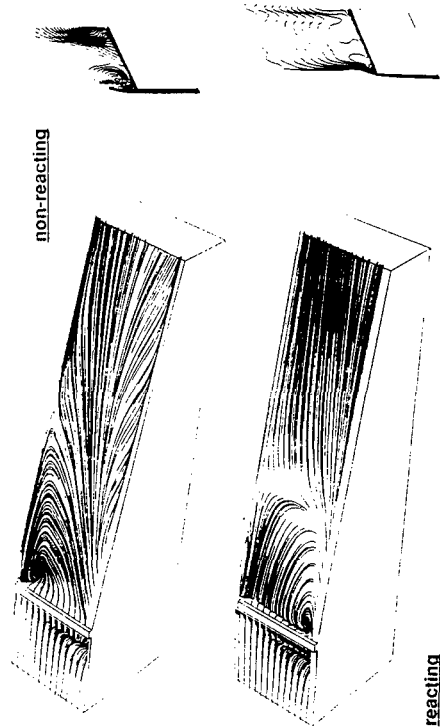


Particle traces and center-line pressure distribution

Example for External Hydrogen Burning on Nozzle/Afterbody Cowl Flap

Ref. 3.19  
NCB-VKI 96/39

Fig. 3.7-7

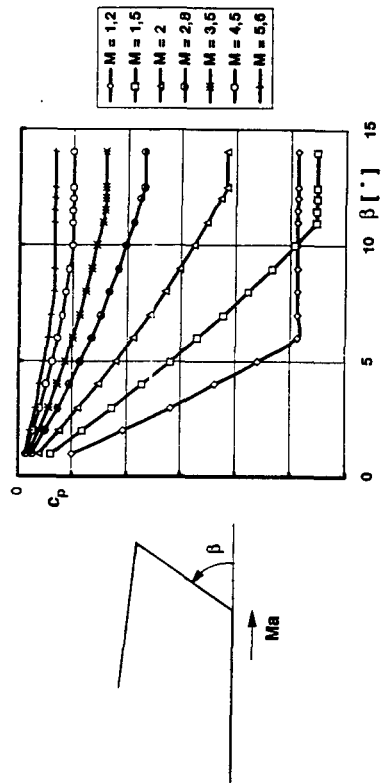


Particle traces and Mach contours

Example for External Hydrogen Burning on Nozzle/Afterbody Cowl Flap

Ref. 3.19  
NCB-VKI 96/39

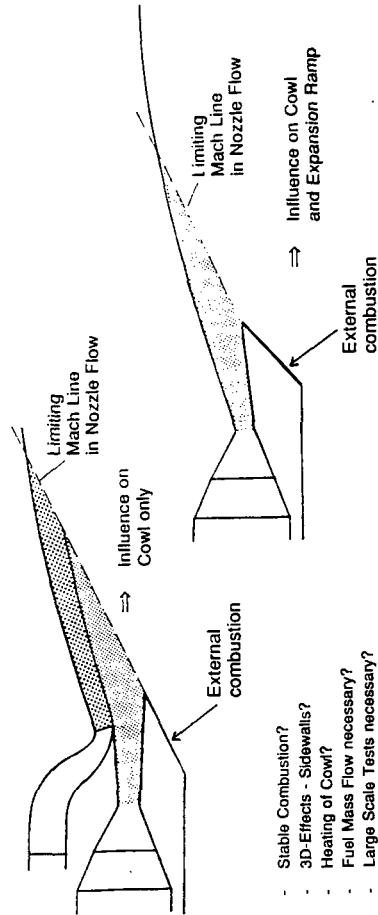
Fig. 3.7-8



$c_p$  on External Afterbody Cowl

Ref. 3.14  
NCB-VKI 96/33

Fig. 3.7-5

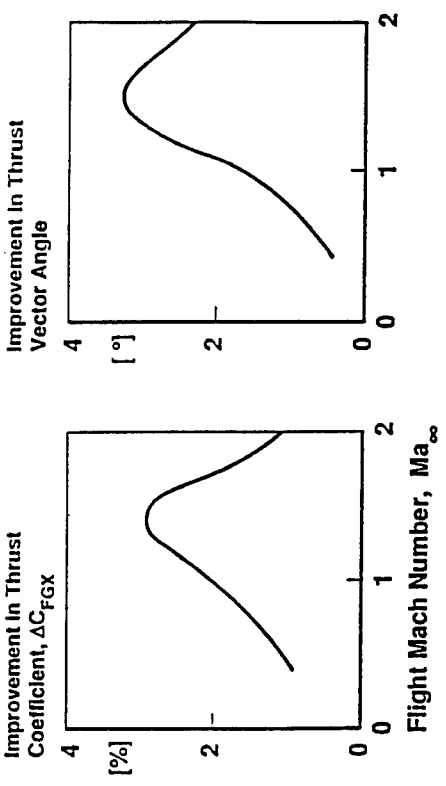


- Stable Combustion?
- 3D-Effects - Sidewalls?
- Heating of Cowl?
- Fuel Mass Flow necessary?
- Large Scale Tests necessary?

Effects of Constant Pressure External Combustion at Transonic Mach Numbers

NCB-VKI 96/34

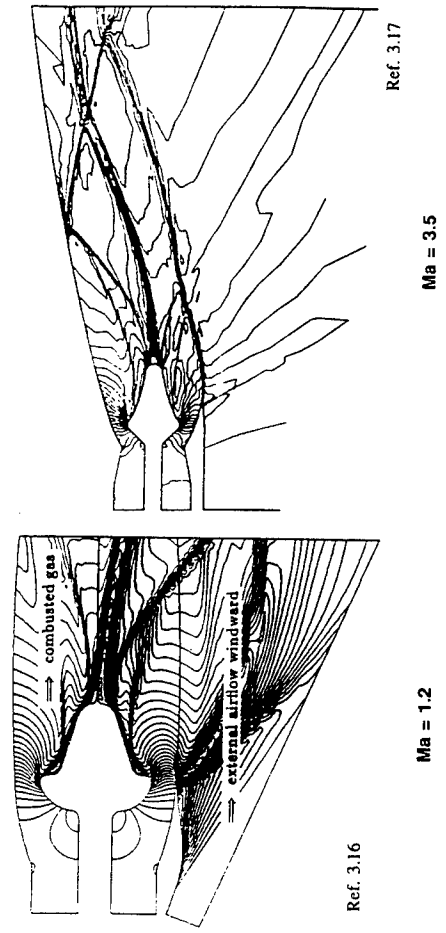
Fig. 3.7-6



Effects of External Combustion

Ref. 3.12  
NCB-VKI-96/15

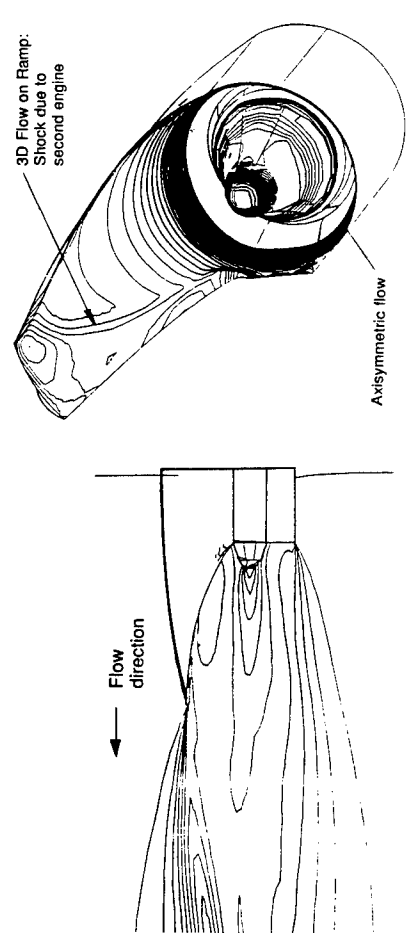
Fig. 3.7-9



Examples of 2D Euler Solutions for Different Plug Nozzles

Ref. 3.16  
NCB-VKI-96/15

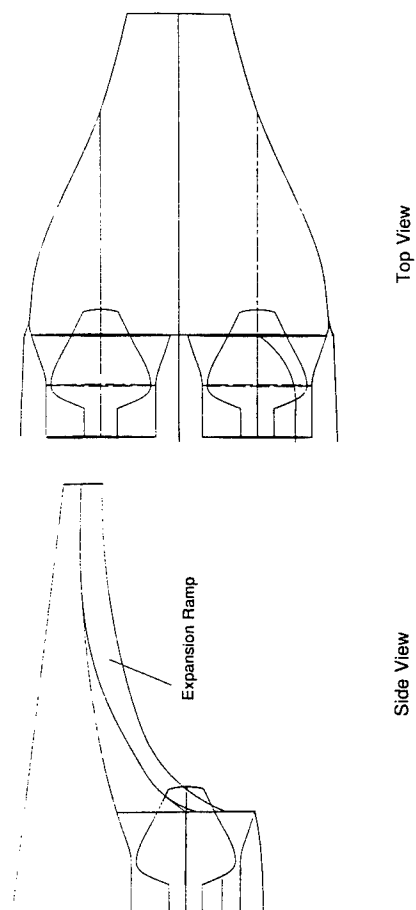
Fig. 3.8-2



Temperatures of 3D Euler Result for Plug Nozzle Afterbody,  $Ma=5.6$  (underexpanded)

Ref. 3.18  
NCB-VKI-96/17

Fig. 3.8-3



Afterbody Integration with Two Engines with Plug Nozzles

Ref. 3.19  
NCB-VKI-96/16

Fig. 3.8-1



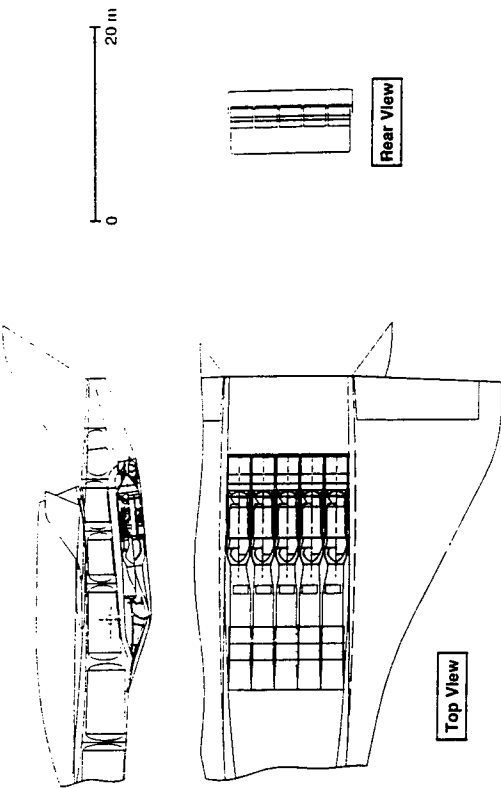
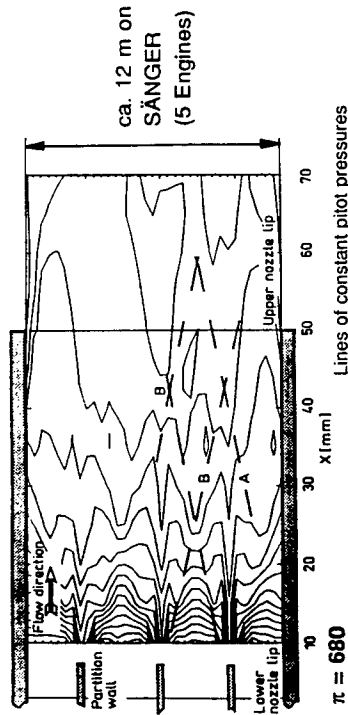


Fig. 3.9-1

### Säger Propulsion Systems

NCB-VKI 96/117



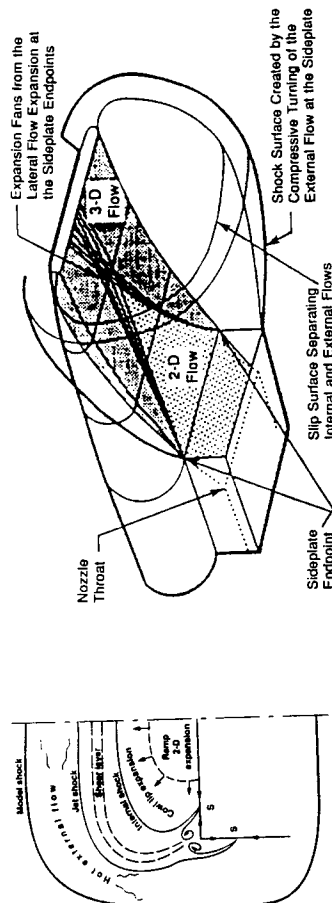
- o Additional boundary layers - wake losses - corner flows
- o Additional glancing shock losses

### Influence of Engine Partition Walls

Fig. 3.9-3

Ref. 3.15

NCB-VKI 96/114



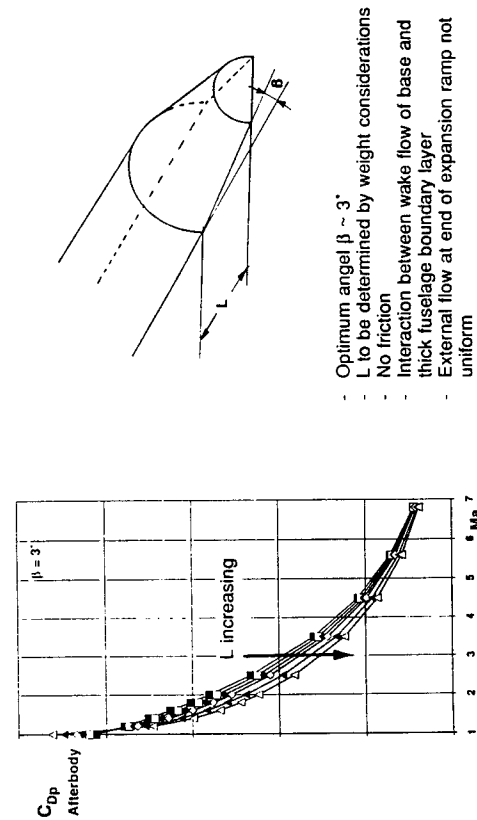
Ref. 3.28

- 2D flow area on ramp
- 3D expansion stronger than 2D → lower pressures - less thrust - lower nose - down moments
- Separation on fuselage sidewall due to jet shock → hot spots on external surface
- Internal shock → cross flow separation on ramp
- 3D vortices

### Underexpanded Afterbody Flow without Sidewalls

Fig. 3.9-4

NCB-VKI 96/119



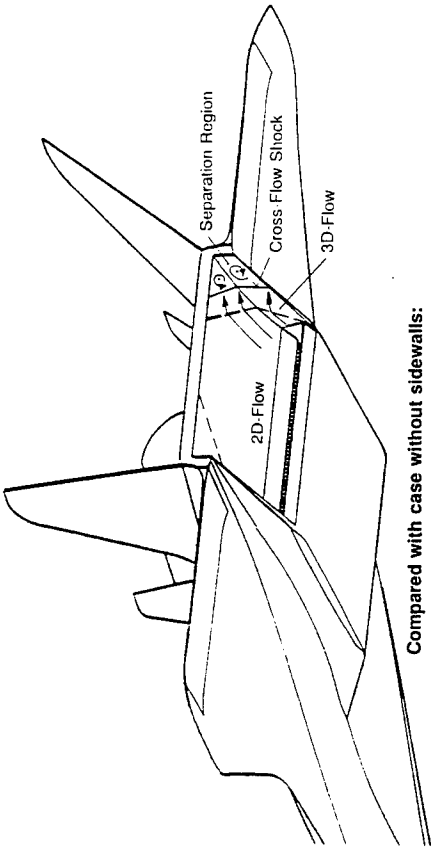
- Optimum angle  $\beta \sim 3^\circ$
- L to be determined by weight considerations
- No friction
- Interaction between wake flow of base and thick fuselage boundary layer
- External flow at end of expansion ramp not uniform

### Upper Stage Boattail Pressure Drag

Fig. 3.9-2

Ref. 3.22

NCB-VKI 96/96



Compared with case without sidewalls:

- Sidewalls delay 3D expansion → higher pressures (thrust, nose-down moments)
- 2D flow area on ramp enlarged
- Complex flow on sidewall depending on NPR and external flow
- Cross flow shock on ramp and sidewalls possible → separation

Underexpanded Afterbody Flow with Sidewalls

NCB-VKI 96/10

Fig. 3.9.7

Ref. 3.20  
NCB-VKI 96/51

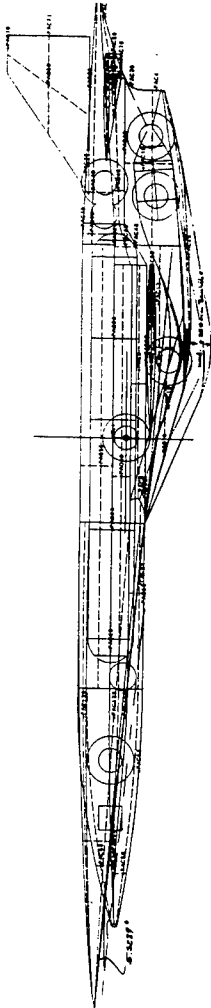
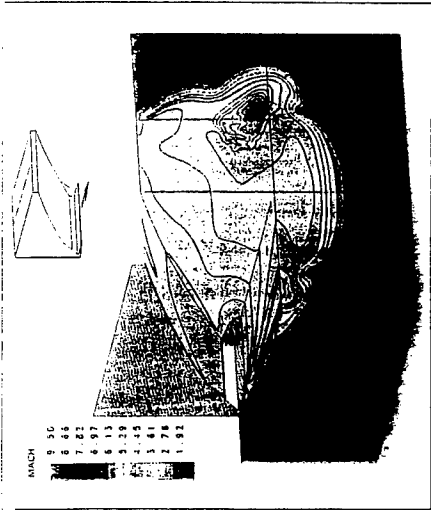


$\pi = 310$  (Baseline)

$Ma_\infty = 7.33$ ;  $p_{t_\infty} = 6895$  kPa;  $T_{t_\infty} = 828$  K;  $Re = 17 \cdot 10^6$  [1/m]; Test Medium Argon/Freon ~ Air

Ramp Surface Flow Angles

Fig. 3.9.5



Possible Changes to HYTEX R-A3 due to Forebody Modification

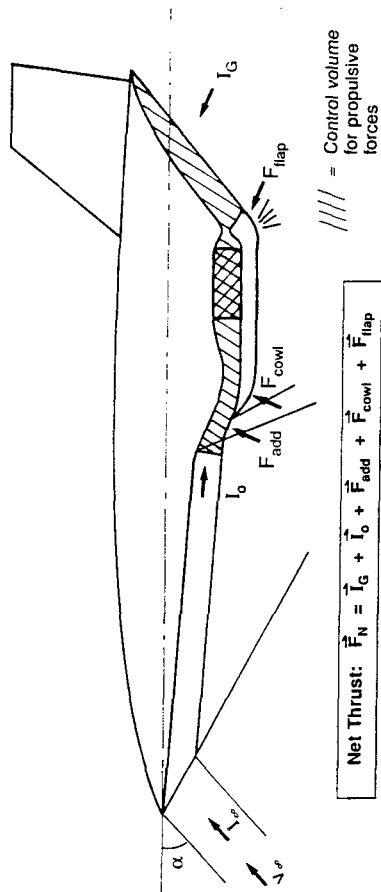
NCB-VKI 96/131

Fig. 4-1

Mach Number Distribution from Navier-Stokes Solution for SERN Afterbody

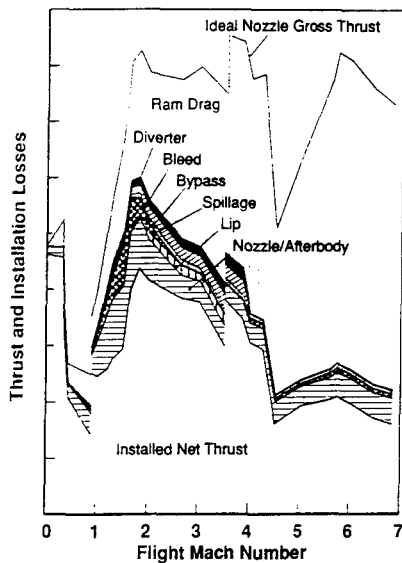
Ref. 3.25  
NCB-VKI 96/59

Fig. 3.9.6



Definition of Net Thrust and Book-Keeping

Fig. 4-2



Note: Ideal nozzle gross thrust accounts for intake total pressure losses

Thrust and Installation Losses

Ref. 4.7

Fig. 4-3

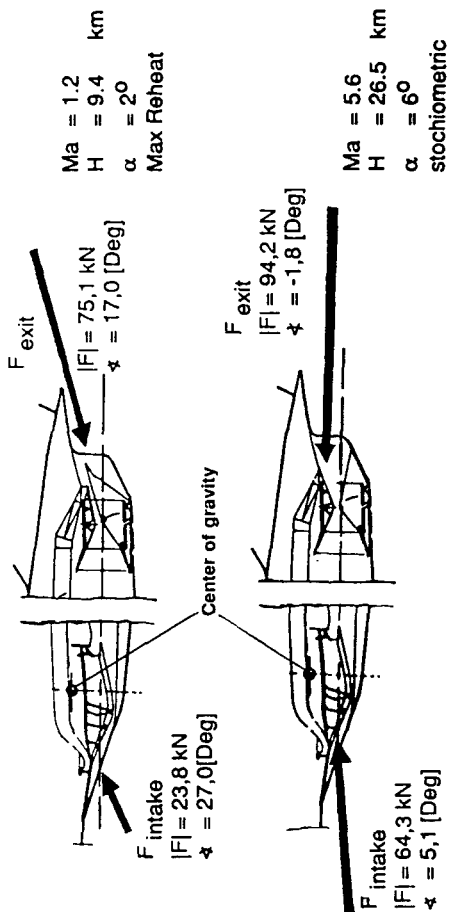
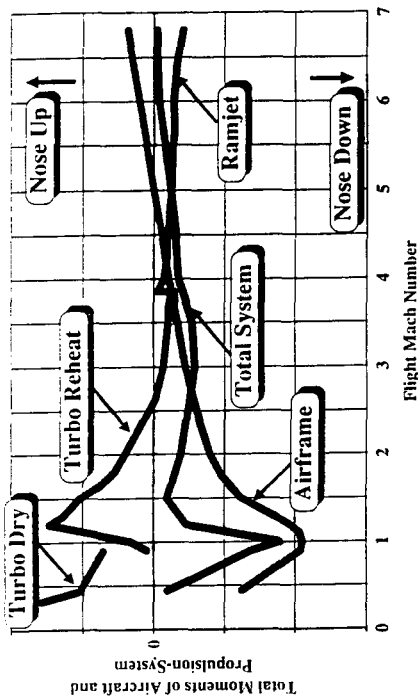


Fig. 4-4

Intake and Afterbody Forces

At higher Mach number net thrust becomes a small difference between two large forces

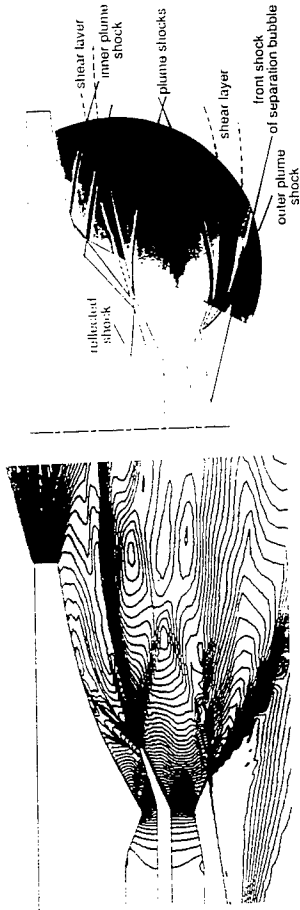
NCB-VKI 96/103



Pitching Moments of Aircraft and Propulsion System

Fig. 4-5

Ref. 4.7  
NCB-VKI 96/105



Euler Result  
 $C_{f0} = 0.966$

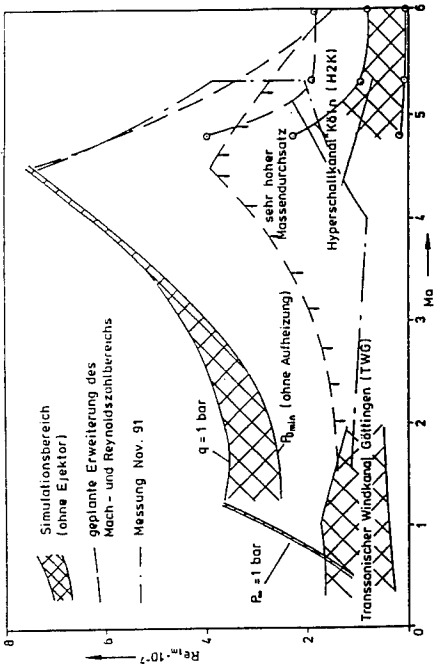
Test Result

$Ma_{\infty} = 3.5; \pi_{engine} = 38.90; \pi_{injection} = 20.75$

Generic Afterbody Model for Parallel Propulsion Concept (RAM, Turbo)

Ref. 3.23  
N°B-VK1 96/67

Fig. 5.1-3



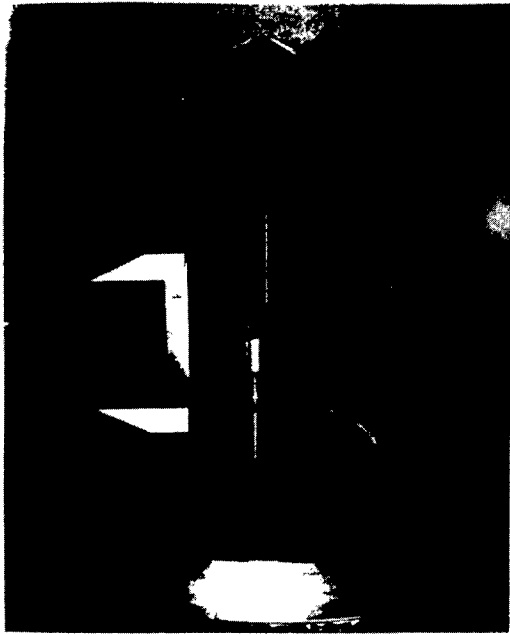
"Cold" Tunnel

- o Isolated small scale models (intake and afterbody)
- o Ma and Re nearly correct
- o Testing Times  $\approx 60$  secs

TMK, DLR Cologne; Ma and Re Range

N°B-VK1 96/108

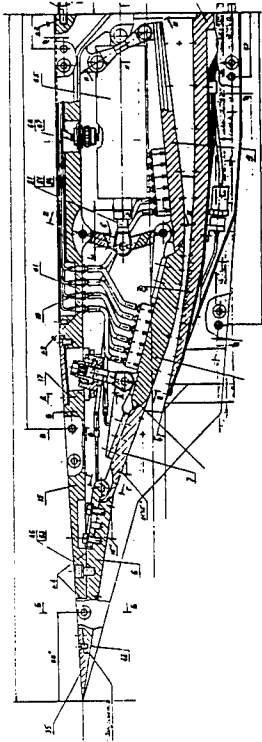
Fig. 5.1-1



Generic Afterbody Model for Parallel Propulsion Concept (RAM, Turbo)

Ref. 3.24  
N°B-VK1 96/78

Fig. 5.1-4

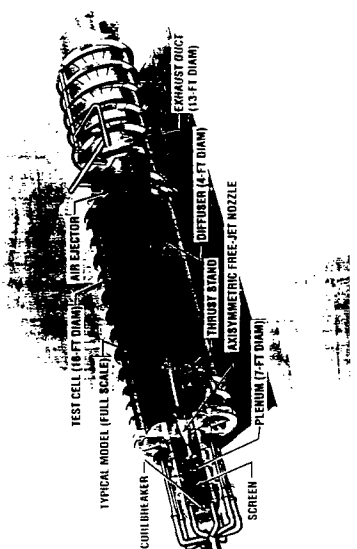


Ma = 3.5 to 6.0

Dasa-LM Intake Model ETM3M (1:4.97) Tested at TsAGI and DLR

N°B-VK1 96/112

- Combustion of butane / methane or hydrogen
- Addition of oxygen
- Free-jet testing inside evacuated test cabin
- Larger but limited model size (test rhombus)
- Water vapor of combustion may form water or ice
- $Ma \leq 8$
- $T_1 \approx 1100\text{ K}$
- isolated intake / propulsion testing



AEDC Aerodynamic and Propulsion Test Unit (APU)

### Combustion - Heated Windtunnels

Fig. 5.1-5

NCH VKI 96/109

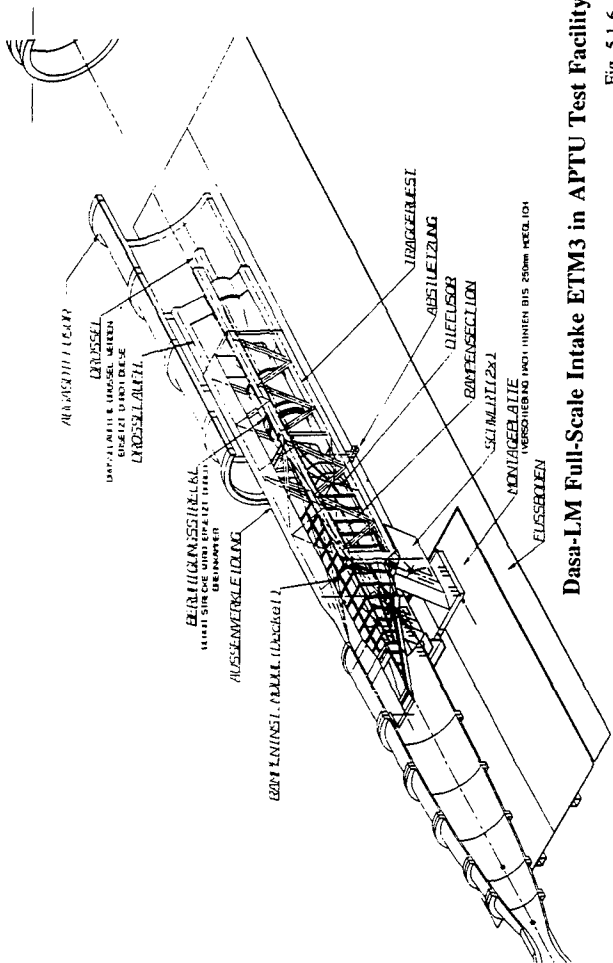
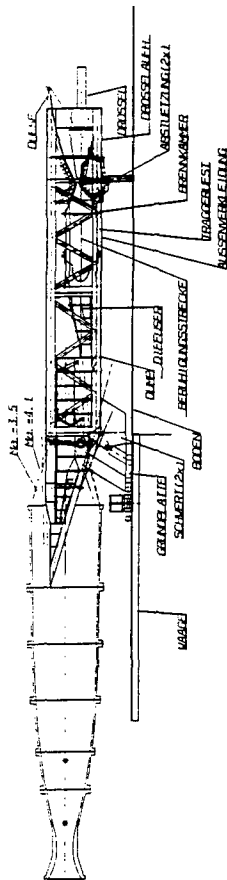


Fig. 5.1-6

NCH VKI 96/111



### Dasa/MTU RAM Propulsion Unit in APTU Test Facility

Fig. 5.1-7

NCH VKI 96/110

#### Snger

##### Intake and afterbody

- Full-scale testing with light hardware not possible
- Isolated small-scale model testing possible
- Problems: Extrapolation to light conditions
- Real-gas effects (substitute gases for jets: air, Argon, Freon)
- Heat transfer effects

##### Propulsion

- Full-scale testing not possible (isolated and integrated)

#### Experimental Vehicle

##### Intake and afterbody

- Full-scale testing of isolated models possible (Vehicle integration testing limited)
- Problems: Not flight structure
- Flight condition simulation limited ( $T_1$ ,  $p_1$ , gas composition)
- Small-scale integration testing possible
- Problems: as with Snger (see on the left side)

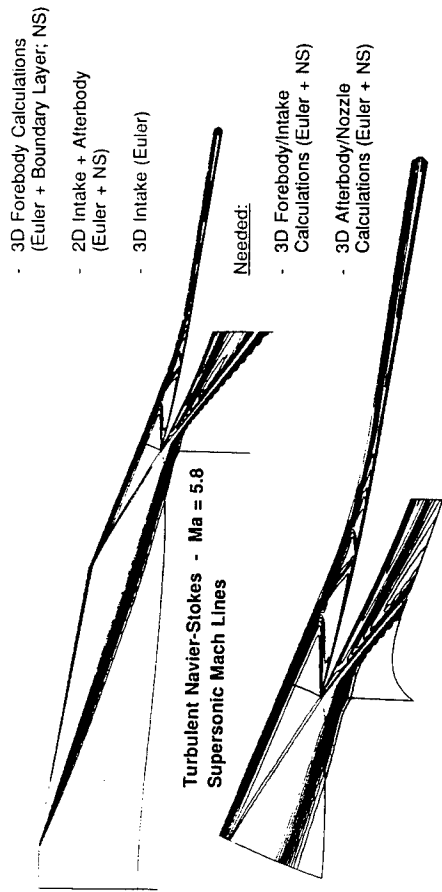
##### Propulsion

- Full-scale testing of isolated propulsion unit possible
- Problems: Use of flight hardware possible?
- Flight condition simulation limited ( $T_1$ ,  $p_1$ , gas composition)

### Wind Tunnel Testing

Fig. 5.1-8

NCH VKI 96/114



Computational Fluid Dynamics

Fig. 5.2-3

NCB-VKI-96/113

Potentials:

- 2 and 3 dimensional flows
- Isolated and integrated (tip to tail)
- Test and flight conditions

Deficits:

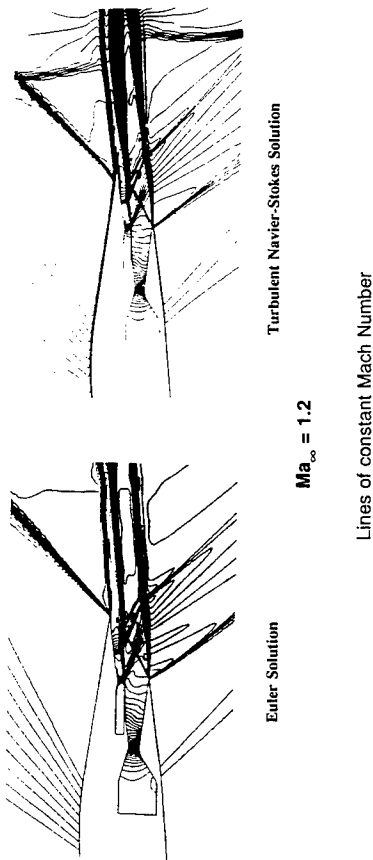
- Transition modelling
- Turbulence models
- Combustion models /chemistry
- Real gas models
- Unsteady effects (shocks, separations, combustion etc.)
- Coupling with structure (deformations, heat transfer)

⇒ **Best analysis and diagnostic tool available Needed during design**

Computational Fluid Dynamics

Fig. 5.2-4

NCB-VKI-96/115



Influence of Viscosity on Flow with Injection at  $Ma = 1.2$

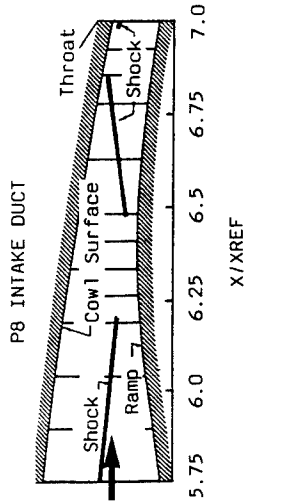
Fig. 5.2-1

Ref. 3.8

NCB-VKI-96/66

TEST CASE 6

PITOT PRESSURE DISTRIBUTION  
(  $X/X_{REF} = 5.67$  )



Ref. 2.43

NCB-VKI-96/112

Fig. 5.2-2

- Hypersonic Vehicles require a joint optimization of vehicle and propulsion
- Integration aspects are not new boundary conditions for the design of Intakes and afterbodies/nozzles - they are different
- Aerothermodynamics is one of the important design drivers
- Aerodynamic tools available have limited applicability
- Development and verification of hypersonic vehicle (Sänger) can be accomplished by the use of wind tunnels, CFD and flight testing of experimental vehicle(s).

#### Concluding Remarks

Fig. 6-1

## INLET and PROPULSION INTEGRATION OF SCRAM PROPELLED VEHICLES

by

Dr. Louis A. Povinelli\*  
NASA Lewis Research Center  
Cleveland, Ohio USA

### SUMMARY

The material to be presented in these two lectures begins with cycle considerations of the turbojet engine combined with a ramjet engine to provide thrust over the range of Mach 0 to 5. We will then examine in some detail the aerodynamic behavior that occurs in the inlet operating near the peak speed. Following that, we shall view a numerical simulation through a baseline scramjet engine, starting at the entrance to the inlet, proceeding into the combustor and through the nozzle. In the next segment, we examine a combined rocket and ramjet propulsion system. Analysis and test results will be examined with a view toward evaluation of the concept as a practical device. Two other inlets will then be reviewed; a Mach 12 inlet and a Mach 18 configuration. Finally, we close our lectures with a discussion of the Detonation Wave engine, and inspect the physical and chemical behavior obtained from numerical simulation. A few final remarks will be made regarding the application of CFD for hypersonic propulsion components.

\*Acting Chief, Internal Fluid Mechanics Division



## LECTURE 1

Conceptual Aircraft  
Turbojet/Ramjet Combined Cycle

The lecture begins with the idea of an advanced aircraft capable of operating over a flight range from takeoff to Mach 5. The proposed propulsion device is an over-under turbojet/ramjet. At takeoff and up to approximately Mach 3, the power would be provided by the turbojet. Transition to ramjet power and close-off of the turbojet duct would provide propulsion up to somewhere in the Mach 6 range. Such a concept was proposed by Watts et al (ref 1) and briefly discussed by Weir et al (ref 2). Figs 1 and 2, from ref 2, illustrate the concept. Some time later, Trefny and Benson (ref 3) have performed a rudimentary cycle analysis which showed that the integration of a turbojet with a single throat ramjet is feasible. We begin by viewing the proposed installation scheme of Trefny and Benson, shown in their fig 1. As envisioned in ref 1, a turbojet or a row of turbojets is installed in a bay above the ramjet passage. Aerodynamic isolation of the turbojet exhaust stream from the ramjet stream occurs through an ejector action. Operation at low speed relies only on the turbojet, mid-range speed relies on the ramjet with subsonic combustion, and high speed would utilize a scramjet mode. During the ramjet mode, hydrogen is burned and a thermal throat is formed. Control of the thermal choke location is required. In the scramjet mode, the spraybar is removed and wall injection of the fuel is used. Trefny and Benson chose to bias the design of the integrated system towards high efficiency so as to maximize range. The 10 to 1 contraction on the inlet is sized for approximately Mach 8. Various assumptions made in their analysis will be discussed. The final outcome of their work is shown in fig 10; where the thrust per unit mass is plotted versus free stream Mach number. The minimum thrust appears at Mach 1.3 where the spill drag is at a maximum. Only a small change is observed at Mach 3 where the turbojet inlet and nozzle flaps are closed, the inlet starts and the conversion to a hydrogen ramjet is complete. An alternate concept which attempts to eliminate the ejector total pressure losses at low speed was also investigated. Fig 11 shows the position of the ejector flap, and figs 12 through 15 show the results. It was concluded that the benefits associated with a fixed geometry would outweigh the loss in specific impulse. Control of the thermal throat turns out to be a critical factor in the operation of this combined cycle. The net specific thrust of the system is maximized when the ejector operates at its critical point. This would necessitate a prescribed variation in thermal throat location with flight Mach number. Finally, some comments on supersonic combustion requirements and turbojet weight restrictions round out this portion of the lecture.

## Inlet Testing/Analysis for Mach 5

We now proceed to a discussion of the inlet needed for this type of combined propulsion system. Our primary focus is on the aerodynamic performance at the cruise condition. A long term multi-year effort was carried out in this study, involving many participants. The effort was recently summarized in a presentation by Weir (ref 4) and the figures used herein are from that presentation. Further information related to this work can be found in references 5 through 16. One of the first three dimensional viscous computations were carried out by Benson (ref 5). His computations showed that the ramp shock waves generated on an inlet surface will interact with the sidewall boundary layers to create a region of lower pressure. The aerodynamics leading to the pressure loss were found to be caused by the movement of fluid within the boundary layer which generate intense secondary flows in the region near the cowl inlet surface. Figure 20 shows the resulting loss in total pressure near the cowl surface, as well as a separation point. Subsequent testing was carried out in a supersonic wind tunnel with a wedge generated shock. Flow tracing showed the strong three dimensional flows that can occur. The corresponding computation for the tunnel flow reveals transverse components of velocity that can cause substantial losses due to shock wave-boundary layer interactions. Anderson (ref 11) then performed a series of calculations for a candidate Mach 5 inlet designed with the method of characteristics. His computations confirmed the previous studies in that significant regions of low pressure were found at the cowl entrance corners. This result led to additional tunnel testing with a small model of a proposed Mach 5 inlet. The model was a duplicate of that to be tested at full scale. Experimental results identified regions of flow migration in the boundary layer toward the sidewall on the surface of the final ramp and up the sidewalls in the vicinity of the cowl lip as predicted by the computational analysis. A full scale Mach 5 mixed compression inlet was then fabricated to be tested over the range from Mach 2.7 to 5.0. The inlet had a series of ramps generated oblique shock waves external to the cowl. An oblique shock from the cowl leading edge reflects from the ramp surface and terminates in a normal shock downstream of the inlet throat. Operation in the wind tunnel was such that a Mach number of 4.1 occurred on the first ramp. The inlet incorporated variable geometry with a collapsible ramp and had variable bleed on the cowl, sidewalls and ramp. A bleed of 0.5 percent was removed on the ramp upstream of the shoulder. Additional bleed from the cowl and sidewalls was approximately 8.8 percent of the capture mass flow. Pressure probes and rakes were mounted throughout the inlet. A 0.5 inch (1.27 cm) strip of grit was applied near the leading edge to ensure that the boundary layer ingested by the inlet was turbulent. Viscous flow

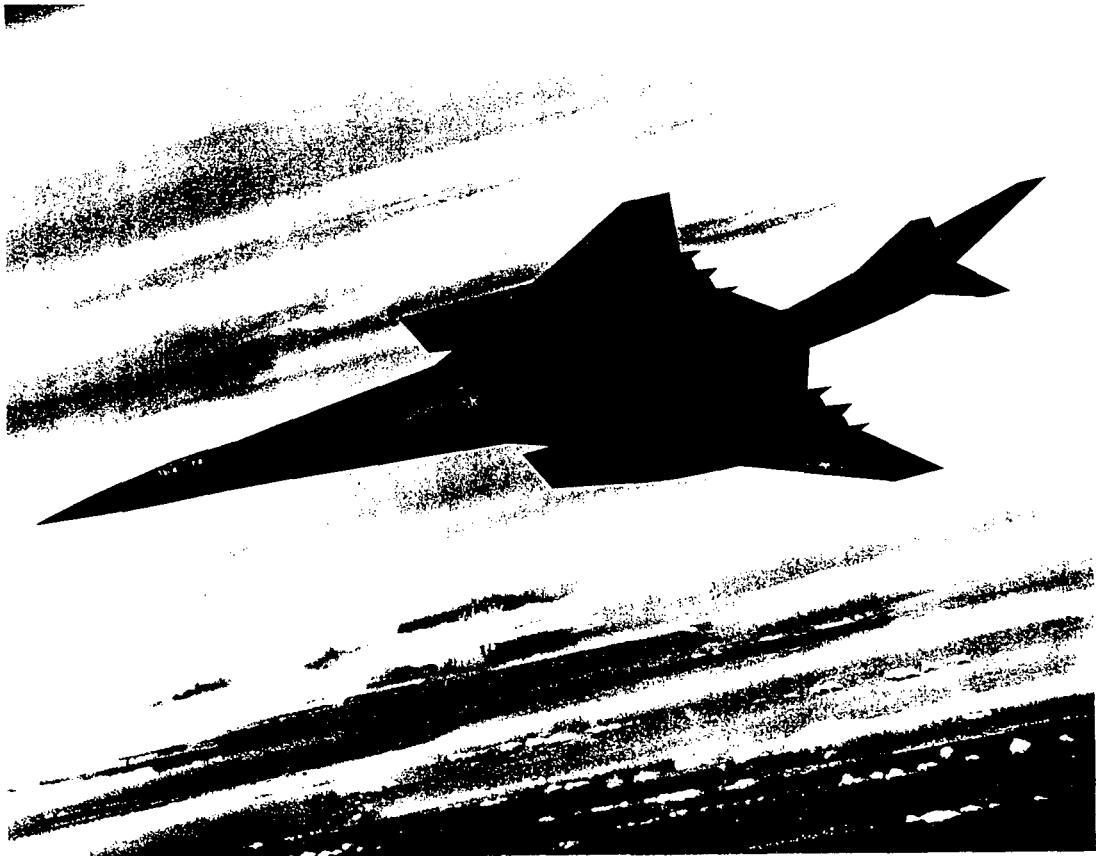
calculations were carried out using the PARC3D code. The computations show that the same low Mach regions occurred and were swept into the inlet. Particles released into the computation grid also revealed strong secondary flow regions as well as a roll-up of the flow on the sidewalls. Corner probe experimental data were compared to computed results from the SCRAM3D, PARC and PEPSI codes. Comparisons of the data and analysis were subject to question since probe orientation relative to the local flow direction was not not completely known. Laser sheet experiments were then carried out and the regions of secondary flow were verified in the large scale inlet. In an attempt to eliminate the secondary from entering the inlet, the cowl surface was cut or notched. It was found that this change eliminated the secondary flow from the inlet. Various laser sheet orientations will be shown. An alternative concept was tried utilizing a scoop at both ends of the cowl lip. As a result of this Mach 5 study, an extensive data base has been generated and calibration of CFD codes has taken place. Although bleed was not effective in relieving the secondary flows, cut backs on the cowl lip were found to be effective. The results lead to some practical ways to avoid the regions of high pressure loss.

### Numerical Simulation of a Baseline Engine

Now, we shall turn our attention to an analysis of a baseline or generic scramjet engine system. What we are interested in performing is a complete Reynold's average Navier-Stokes solution through the entire engine. To illustrate this solution, we shall view a 14 minute video. The initial computations are for the Mach 5 inlet discussed in the last section. We then examine the combustor which has 4 normal hydrogen injection ports. The nature of the reacting flow field is described using both normal injection, followed by vorticity enhancing injectors; a concept introduced by Lewis (ref 12). Finally, we examined the nozzle flow field and its three dimensional behavior as expansion takes place. The video then moves to a complete engine simulation at a flight Mach number of 3.44. The flow is followed through the entire engine flow path from the inlet to the nozzle exhaust. This video completes our first lecture.

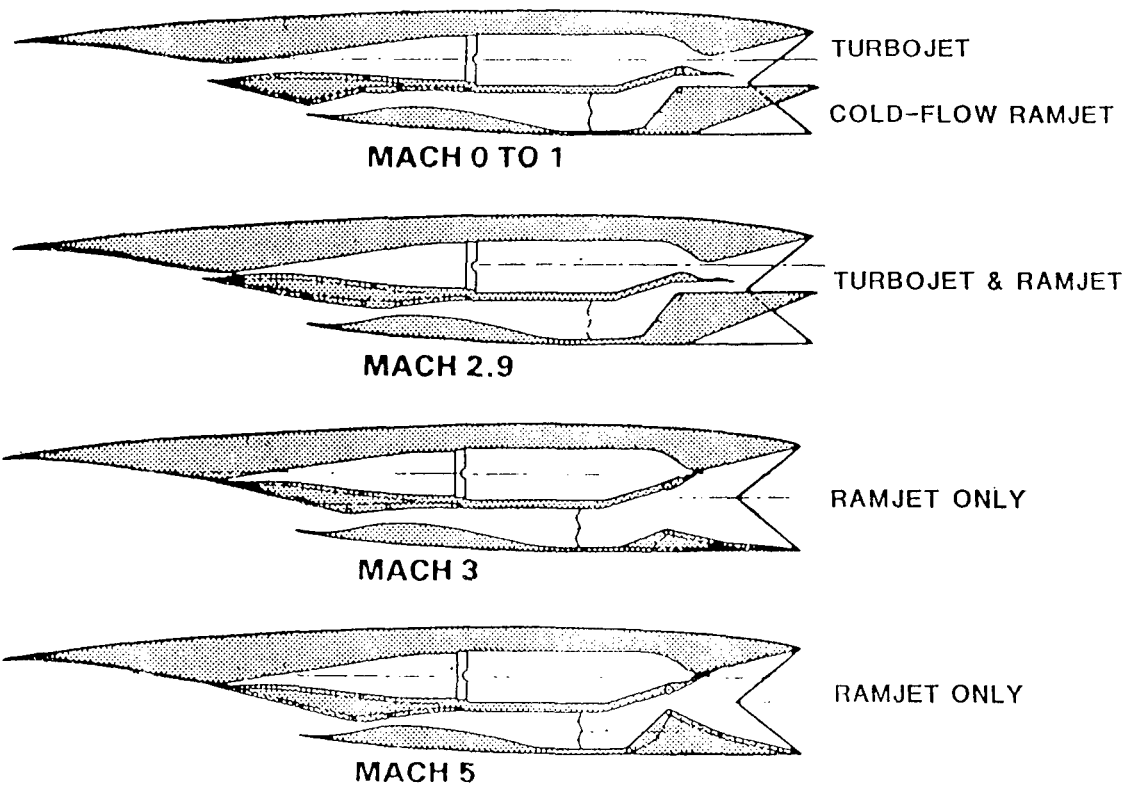
NASA  
C-86-6170

A MACH 5 INTERCEPTOR



REF 4, WEIR

OVER-UNDER TURBOJET/RAMJET



REF 4, WEIR

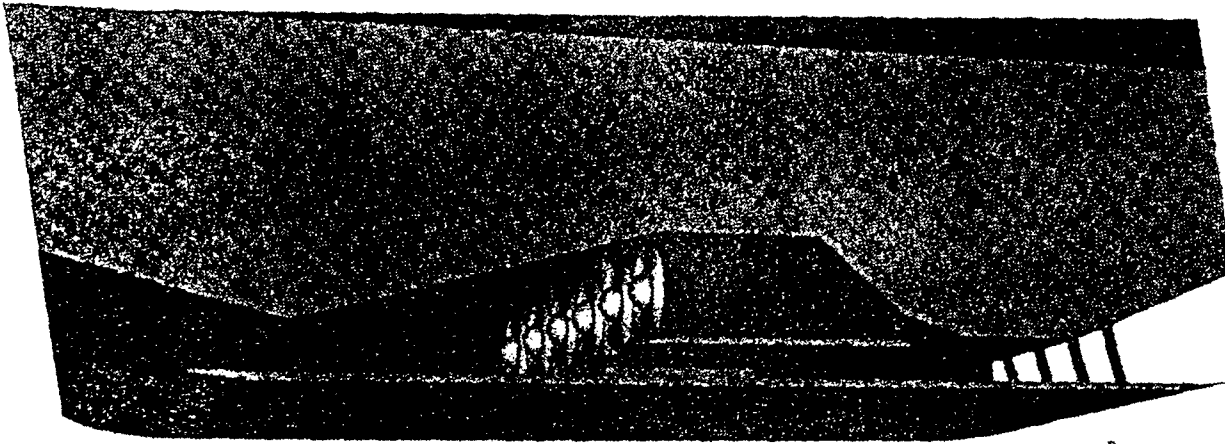


Figure 1.—Turbine-based combined-cycle (TBCC) propulsion system (sidewall removed).

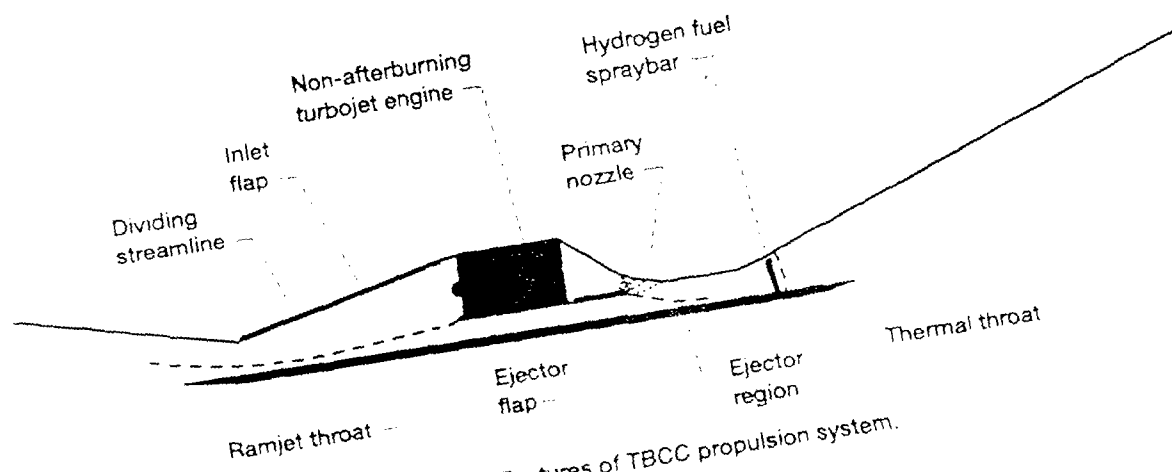


Figure 2.—Features of TBCC propulsion system.

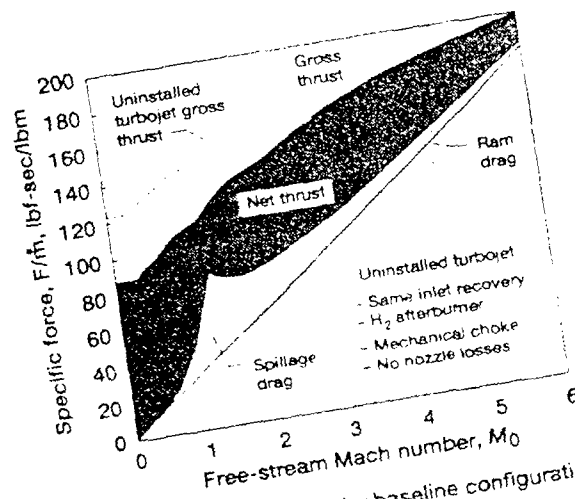


Figure 10.—Specific forces for baseline configuration.

REF 3, TREFNY AND BENSON

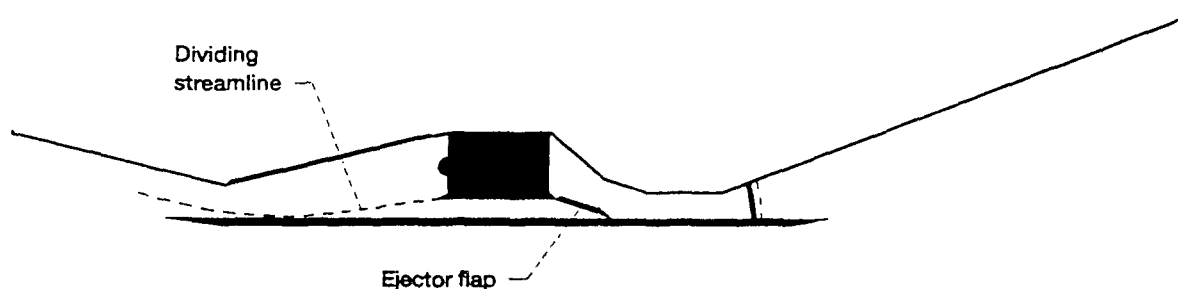


Figure 11.—Ejector flap in alternate position for takeoff and low-speed operation.

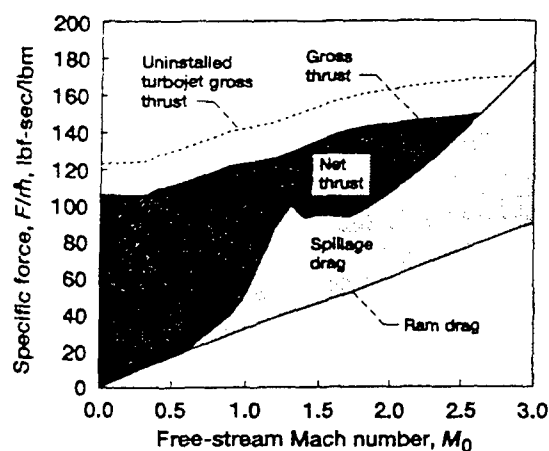


Figure 12.—Specific forces for alternate takeoff and low-speed configuration.

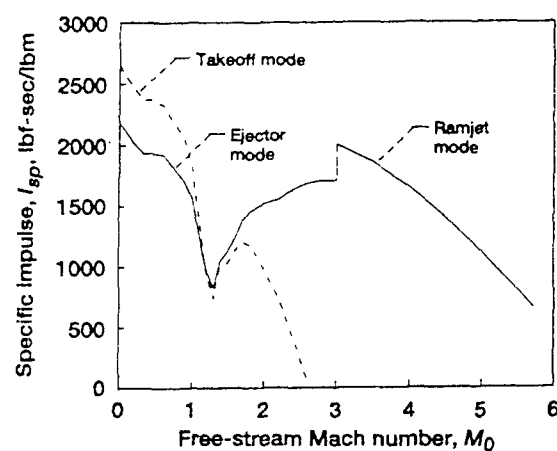


Figure 14.—TBCC system specific impulse.

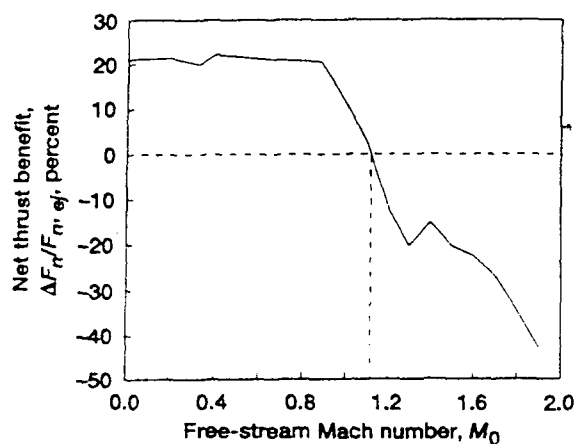


Figure 13.—Net thrust benefit for takeoff mode.

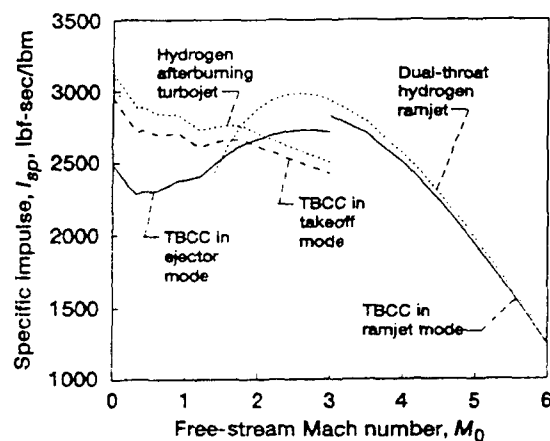


Figure 15.—Uninstalled specific impulse compared to ideal cycles (MIL-E-5007D inlet pressure recovery assumed for all).

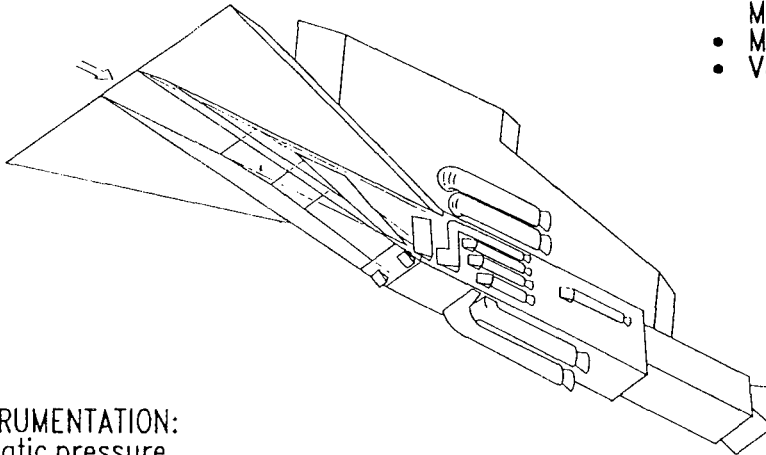
REF 3, TREFNY AND BENSON

National Aeronautics and  
Space Administration  
Lewis Research Center

## MACH 5 INLET PROGRAM



### MACH 5 INLET MODEL



#### REMOTE CONTROL:

- Variable geometry ramp  
Mach 2.7 – 5.0
- Main flow control
- Variable bleed exits (15)

#### INSTRUMENTATION:

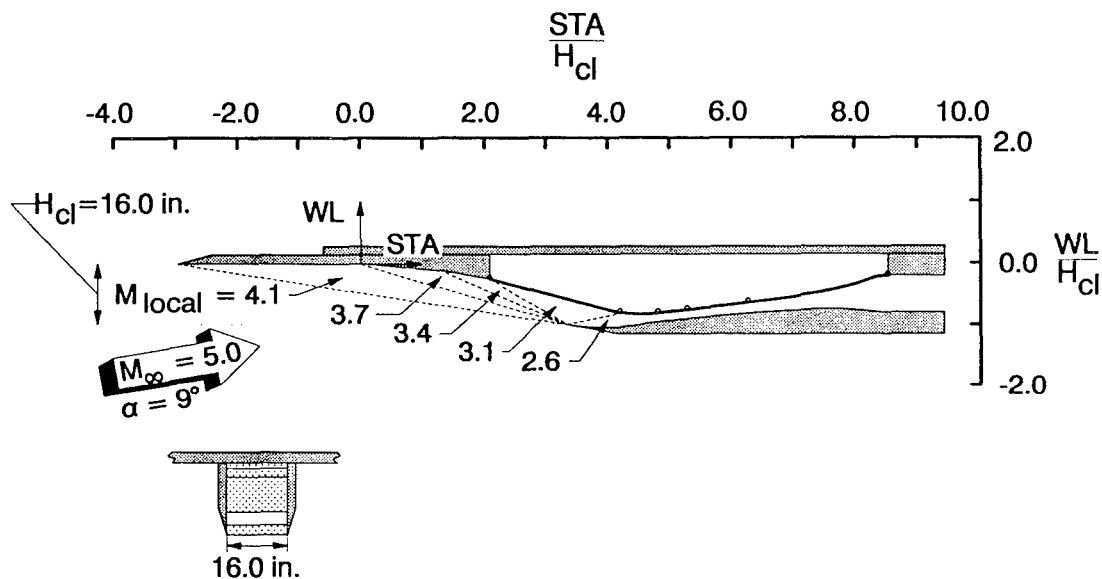
- Static pressure
- Total pressure
  - Fixed rakes
  - Translating probes
- Dynamic pressure transducers
  - Static
  - Total

#### DIMENSIONS:

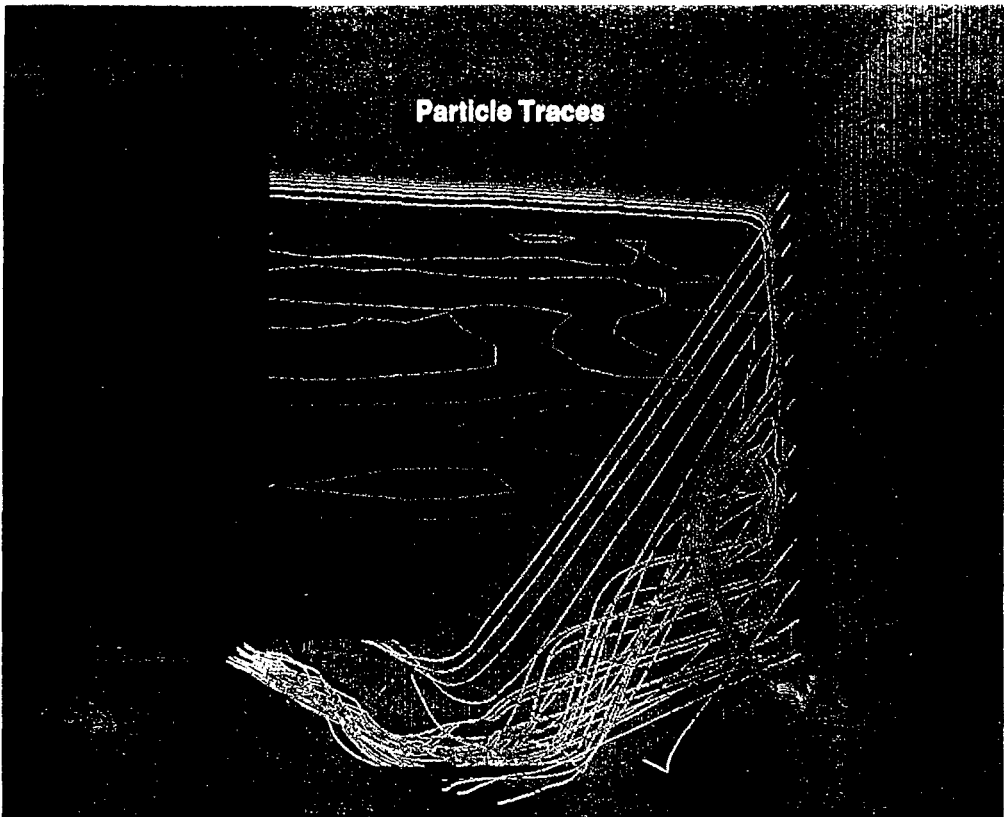
- Plate width = 100"
- Cowl lip height = 16"
- Length = 20'

REF 4, WEIR

### INLET DESIGN CONTOURS

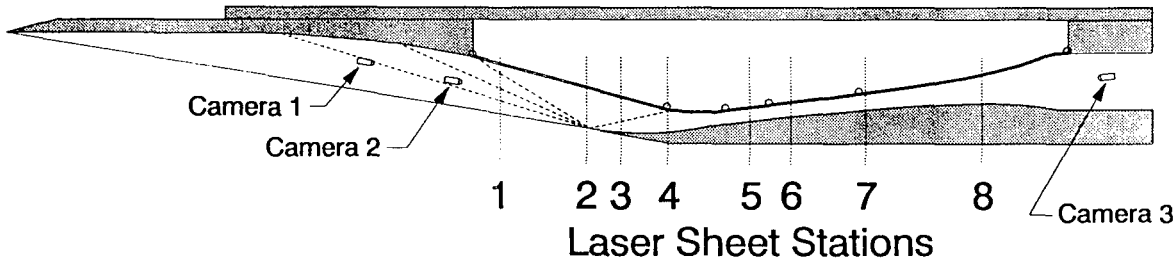


REF 4, WEIR



REF 4, WEIR

MACH 5 INLET  
LASER SHEET CONFIGURATION

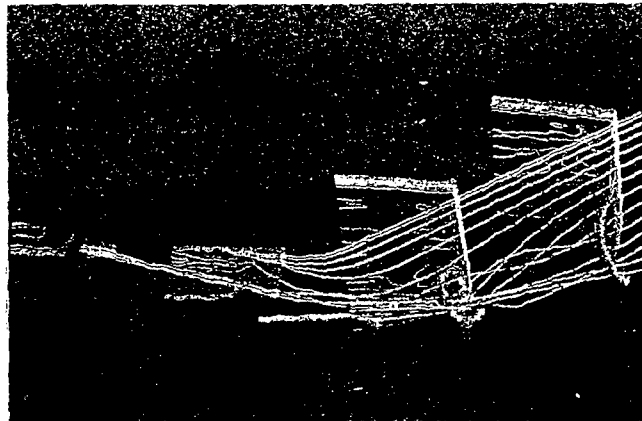


REF 4, WEIR

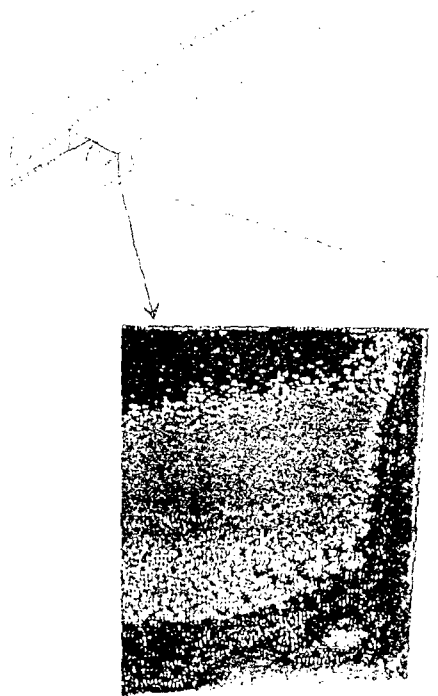


# MACH 5 INLET PROGRAM LASER SHEET FLOW VISUALIZATION

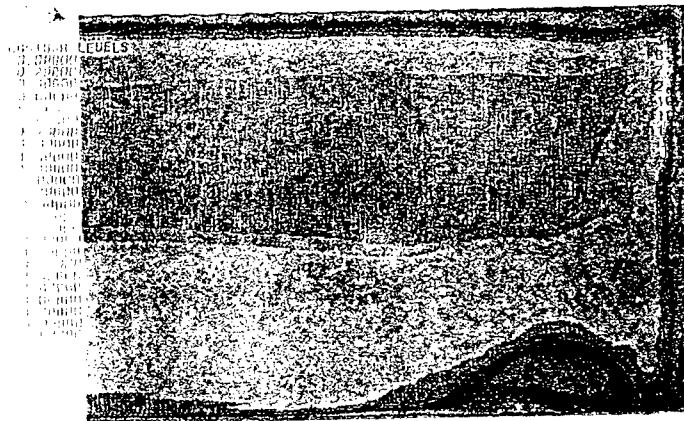
LASER SHEET STATION 3  
(6" DOWNSTREAM OF COWL LIP)



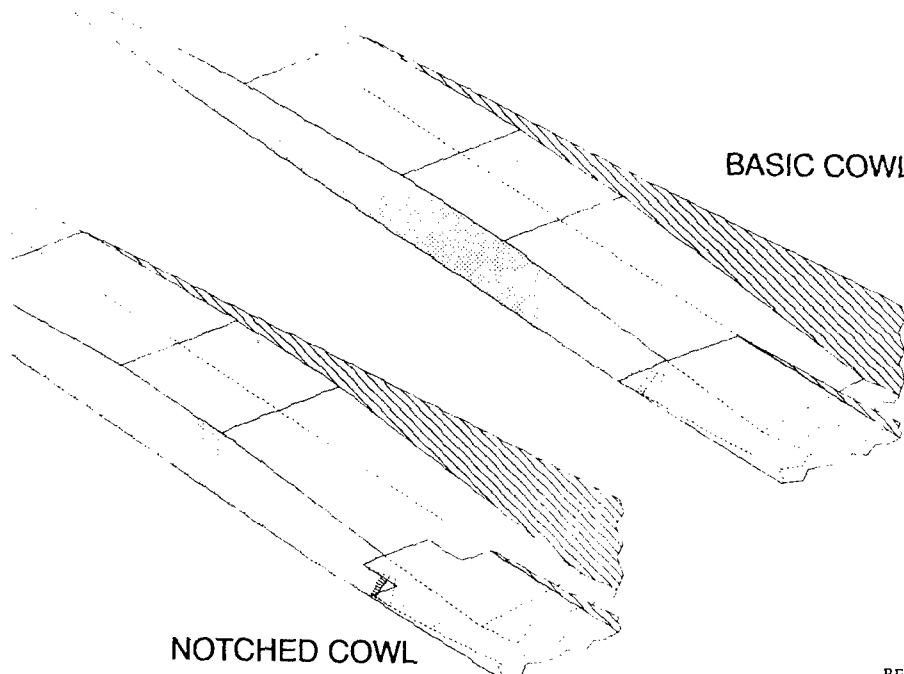
SCRAM3D ANALYSIS OF INLET FLOWFIELD  
(MACH CONTOURS AND PARTICLE TRACES)



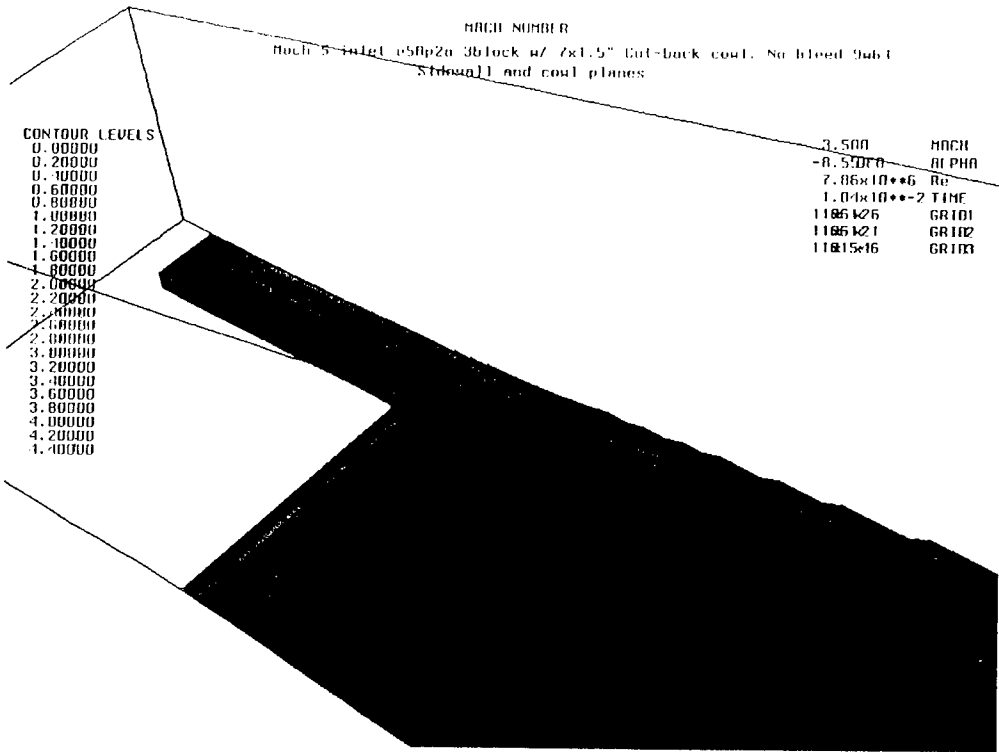
COLOR ENHANCED LASER SHEET IMAGE



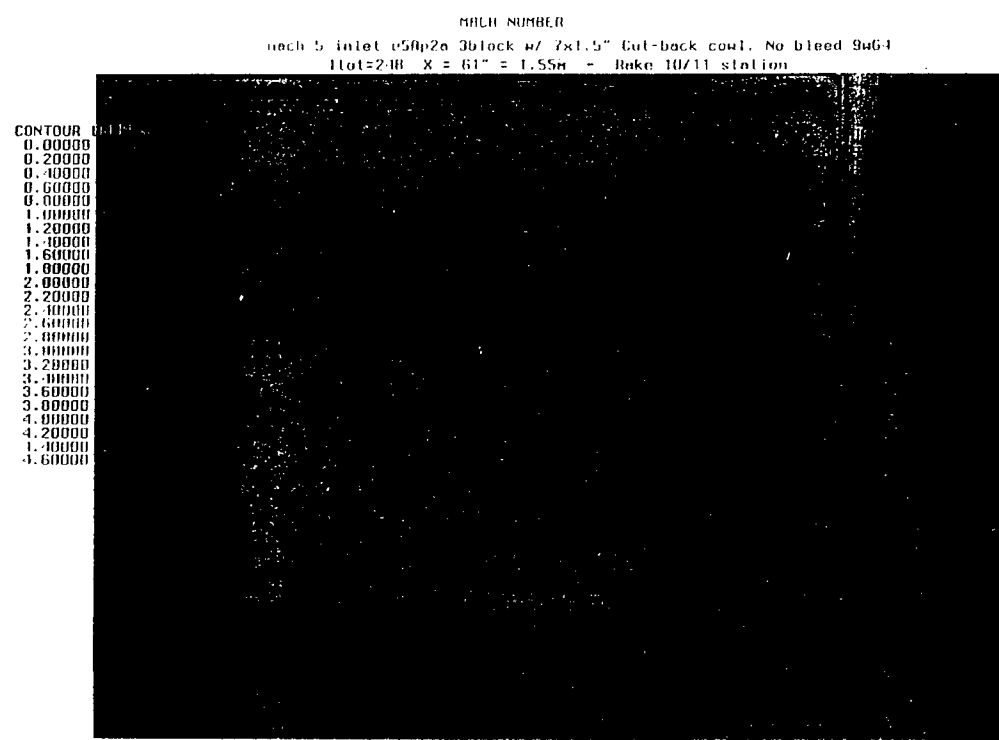
SCRAM3D ANALYSIS  
(MACH NUMBER CONTOURS) REF 4, WEIR



REF 4, WEIR

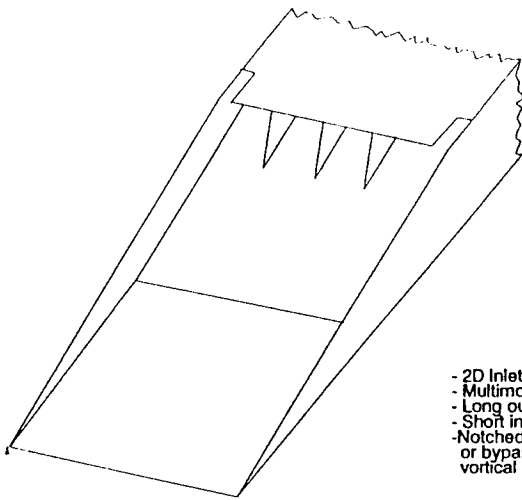


REF 4, WEIR

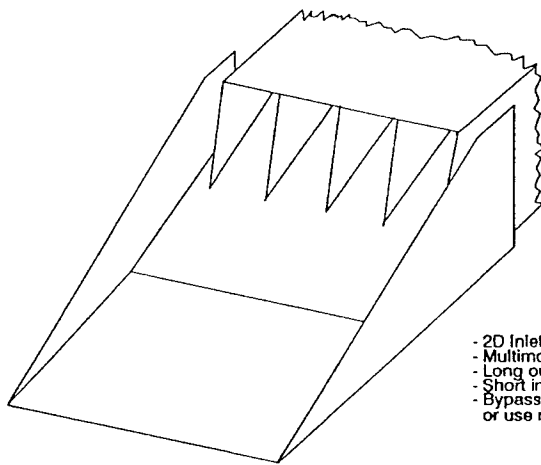


REF 4, WEIR

ARRANGEMENT FOR HYPERSONIC INLETS



- 2D Inlet
- Multimodule config.
- Long outside sidewalls
- Short inside sidewalls
- Notched cowl or bypass of vortical flow



- 2D Inlet
- Multimodule config.
- Long outside sidewalls
- Short inside sidewalls
- Bypass vortical flow or use notched cowl

REF 4, WEIP

## LECTURE 2

### Rocket/Ramjet Analysis and Test

In this portion of the lecture we shall consider a different approach to achieving hypersonic flight; namely by use of a combined rocket and ramjet cycle. This particular concept avoids the penalty associated with the turbojet/ramjet cycle wherein the turbojet is carried to orbit in a non-functioning manner. The rocket based combined cycle has the advantage of a high thrust to weight of a rocket combined with the high specific impulse of the ramjet. This system is capable of going from sea static to hypersonic speeds. Recently, Escher (ref 13) discussed the rocket based combined cycle and its benefit relative to gross vehicle mass fraction. Clearly, this integrated system outperforms an all rocket powered single stage to orbit vehicle, as displayed in the accompanying figure. A similar concept of a strut type scramjet has been explored at Lewis by Povinelli (ref 14). In that work, the drag of a number of struts arranged within a combustion module was measured at chamber Mach numbers of 2, 2.5 and 3. The effect of leading edge radius, position of maximum thickness, thickness ratio, sweep angle, and strut length was determined. Forward sweep was also studied. Fuel injection was simulated using helium and concentration measurements were made at the combustor exit. Spacing between struts was shown to optimized at 10 jet diameters (ref 14). More recently, the strutjet engine has been explored at NASA Lewis Research Center by Fernandez et al (ref 15). As shown in the figure, the engine tested at Lewis uses small rocket chambers embedded within the struts of the ramjet. Again, as we discussed in our first lecture, ramjet operation starts at about Mach 3. Prior to that, the system uses the fuel rich rocket exhaust to pump air through the engine. Additional fuel is added as required. And, again, transition to a supersonic combustion ramjet begins at Mach 6. Construction of such an engine is underway and will be tested at Mach 6 and 7. Proper conditions for simulating flight conditions and enthalpy levels will be produced in a large hypersonic tunnel facility. The same facility was used in the late 60's and early 70's to test the Hypersonic Ramjet Engine at Mach 5, 6 and 7. In the current LeRC model the rockets use MMH and RFNA, and JP-10 is used as the ramjet fuel (ref 15). Some of the engine features will be discussed from the viewpoint of inlet behavior and engine start. The system was backpressured with a moveable plug. Preliminary testing has been performed in a small tunnel facility. No combustion was present for

this phase of the testing. The primary purpose was to establish the starting characteristics as a function of Mach number for three different strut configurations. A self starting fixed geometry inlet with reasonable performance was desired. Measurements of the pitot pressure were made at the base of the struts. Mach numbers, total pressures and mass flow were determined at various Reynold numbers. In the initial phase, concern existed regarding inlet performance and operability. The subscale inlet model was run to determine optimum strut geometry, boundary layer diversion and to establish the cross-sectional area distribution at the base of the struts. The inlet was also simulated numerically using a full Navier-Stokes analysis code, NPARC (ref 16). The computations were used to to obtain a complete flow field analysis as well as the integrated inlet performance. The calculations were made for Mach 5 and 6 flight speed for both super-critical and near critical operating conditions. The analyses were also used to establish pre-test performance and operability predictions for subsequent testing in a major hypersonic facility.

The uncooled model is shown in the photograph and described in the subsequent figures. The inlet was run with the leading edge of the top surface flush with a precompression plate or, alternatively, below the surface in order to divert the boundary layer. Three different struts designs were used, and configuration was found to have the most desirable features. The captured mass flow was found to be level at M4.8 to 6. Typical static pressure and Mach contour plots for M5 will be discussed for a variety of backpressure conditions. The overall performance was also determined. It was found in the Mach 5 case, the inlet unstated before the local Mach number behind the strut became sonic. In the Mach 6 case, the inlet unstated after the strut Mach number became sonic.

Comparison of the pitot pressure contours at the strut base obtained experimentally compared reasonably with the Navier Stokes calculations. Further comparisons will be presented and discussed.

### Analysis of Mach 12 and Mach 18 Inlets

The lecture reference material for these two inlets are found in the attached reprint of an AGARD presentation by this author (ref 17)\*. See attached reprint entitled Computational Modeling and Validation for Hypersonic Inlets. In the interest of time, we shall refer to the Mach 18 results as indicative of shock structure associated with strut type inlets, and in the case of the Mach 12, we see further evidence of the strong secondary flow physics described in the first lecture. The results for both of these inlets are compared to Navier- Stokes solutions in order to establish the level of fidelity in current simulation methodology.

---

\* see Appendix A

## Detonation Wave Engine

The idea of a detonation wave engine has been described in numerous articles. Menees et al (ref 18), for example, described the operation of an oblique detonation wave engine wherein oblique shock waves are used to mix, burn and combust the air-fuel mixture in thin zones. Evaluation of the concept and a demonstration has not been unequivocally carried out. In a similar vein, Hertberg and his co-workers (ref 19) have investigated the idea of a ram accelerator. Their experiments, which have been modeled by Yungster (ref 20) have been carried out using projectiles in an expansion tube. In one such approach, an expansion tube is used for investigating ram-accelerator type phenomena. Many issues such as boundary layer growth, startup transients and operating pressures prevent the tube from duplicating the conditions in a ram accelerator. Also the short test time may be insufficient to fully establish the reacting flow field. We will discuss the results obtained by Yungster (ref 20) using a time accurate code who studied two situations. In the first one, an axisymmetric projectile, composed of two 30 degree half angle cones and a straight section is computed at a flight Mach number of 4.8 in a mixture of hydrogen with small amounts of oxygen and argon. The time accurate solution shows that the dynamic behavior of the shock front and boundary layer behavior leading up to ignition and the resulting dynamics of the combustion process. A short video will be used to illustrate this behavior. In the second case, the experiments of Hertzberg et al are closely simulated. The resulting analysis will show the rapid changes involved in the ram acceleration process and the chemistry-flow interactions occurring. These results described above will be summarized in the context of their applicability to a detonation wave engine. A long standing personal bias regarding the practicality of such an engine, which requires some pre-mixing of fuel and air (thereby assuming away the major problem in scramjet feasibility) will be examined in light of available evidence.

## Closing Remarks on Numerical Simulations

The role of computation fluid dynamics in the development of hypersonic vehicles has been accepted as a viable approach in a new flight regime for which little useable information exists. Articles highlighting the application of various computational methods abound. This lecturer, along with his colleagues from Langley and from Ames have published two general readership articles in Aerospace America (ref 21, 22). More specifically, this author has focused on the use of CFD tools for hypersonic propulsion (ref 23). In this process of applying computational methods, it is important to realize the limitations involved in the extrapolations, as well as the deficiencies that exist in numerical methods at the present time. We shall discuss current features of CFD codes that are applied to propulsion system components and identify shortcomings in the simulations with a strong emphasis on modeling. The relevant material for this portion of the lecture is found in the attached preprint entitled Advanced Computational Techniques for Hypersonic Propulsion (ref 23)\*

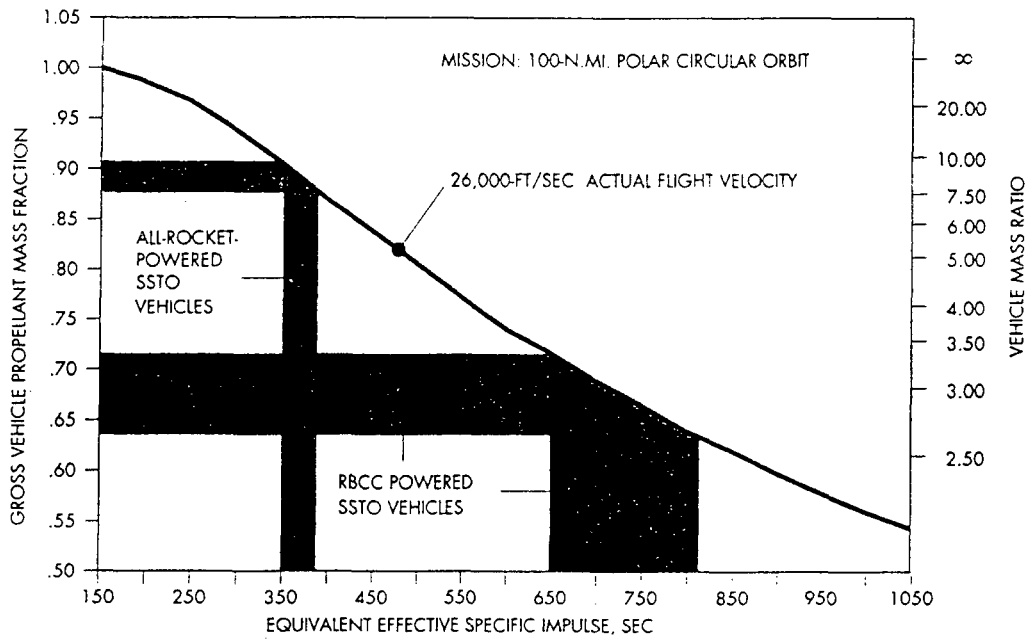
## Acknowledgements

The material presented in these lectures draws heavily on the research conducted at the NASA Lewis Research Center over the past many years and was supplied for these lectures by Lois Weir, Rene Fernandez and Shaye Yungster. The analysis group led by Bernie Anderson and Tom Benson, the experimental inlet group led by Bob Coltrin and Bobbie Sanders, the hypersonic group led by Erv Lezberg and all of the many who followed after, have been instrumental in achieving the progress we have made. Their efforts will assist in the achievement of hypersonic flight in the years to come. Thank you.

---

\* see Appendix B

**PROPELLANT MASS FRACTION OF AN RBCC-POWERED SSTD COMPARED WITH A CONVENTIONAL ALL-ROCKET-POWERED SSTD DESIGN**



REF 13, ESCHER

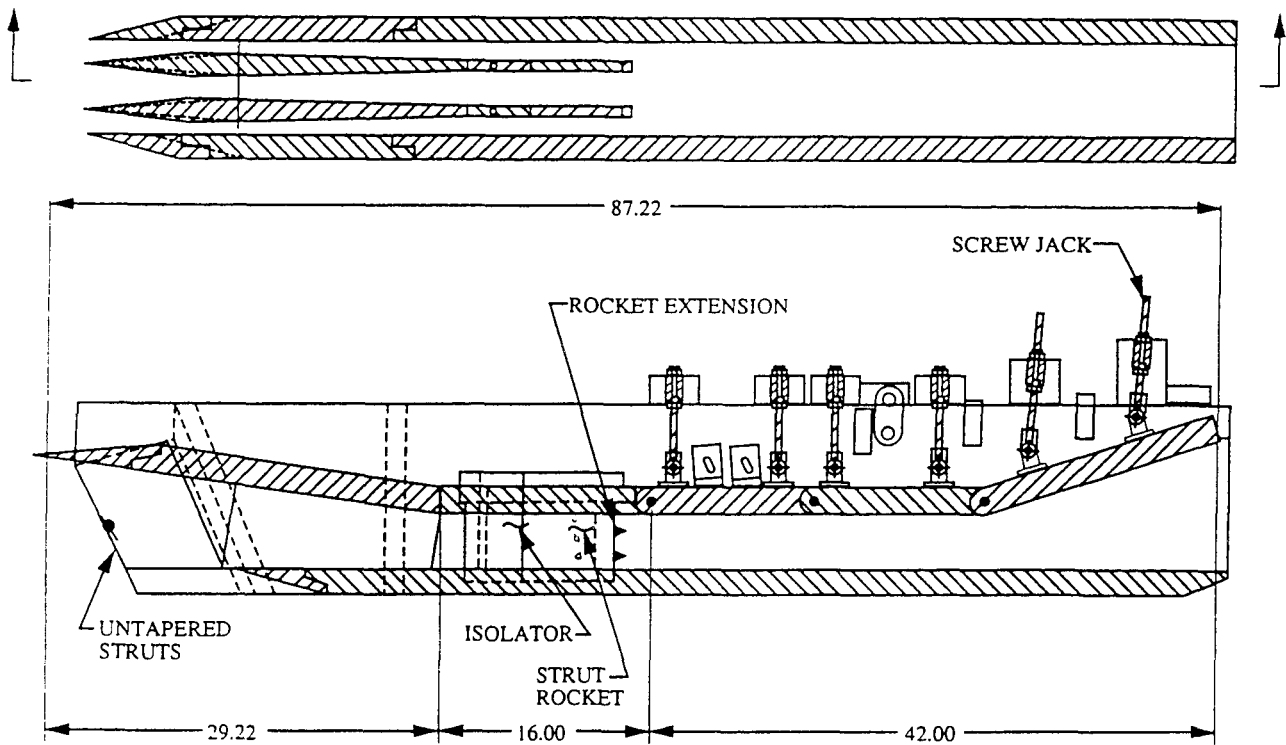


**Figure 1.— Strutjet engine test article.**

REF 15, FERNANDEZ ET AL



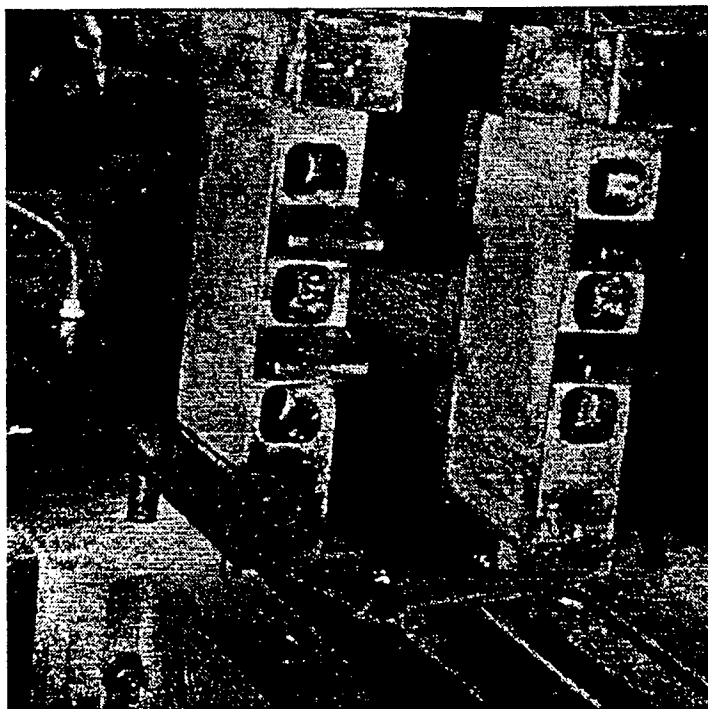


Figure 2. - Rocket chambers and injector wedges on the base region of the two struts

REF 15, FERNANDEZ ET AL

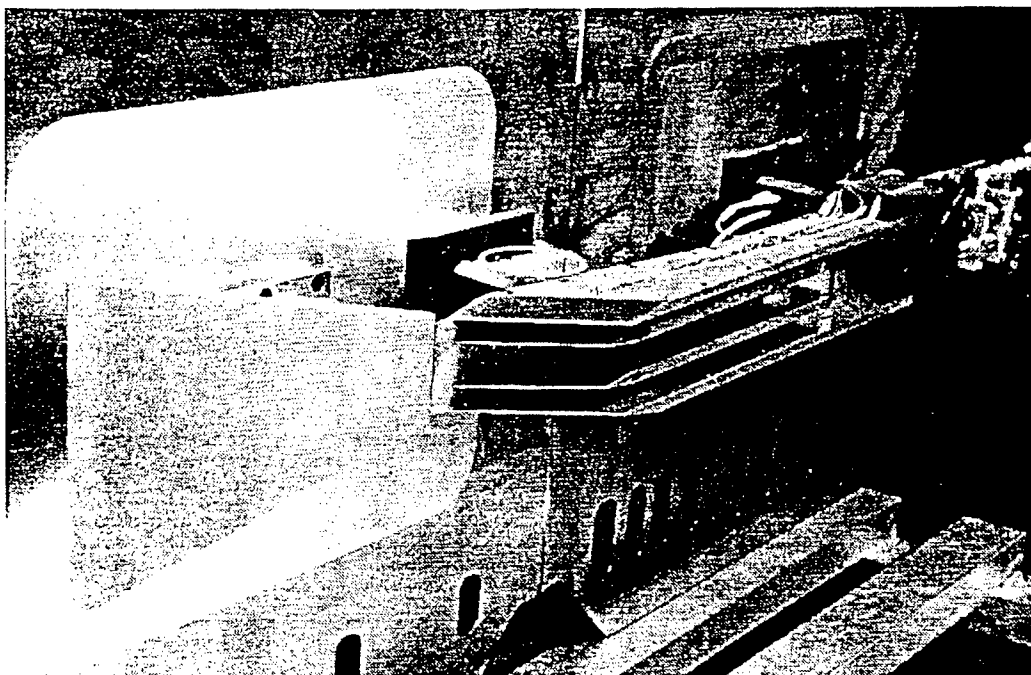


Figure 3. - 40 % RBCC inlet model mounted on tunnel sidewall

REF 15, FERNANDEZ ET AL

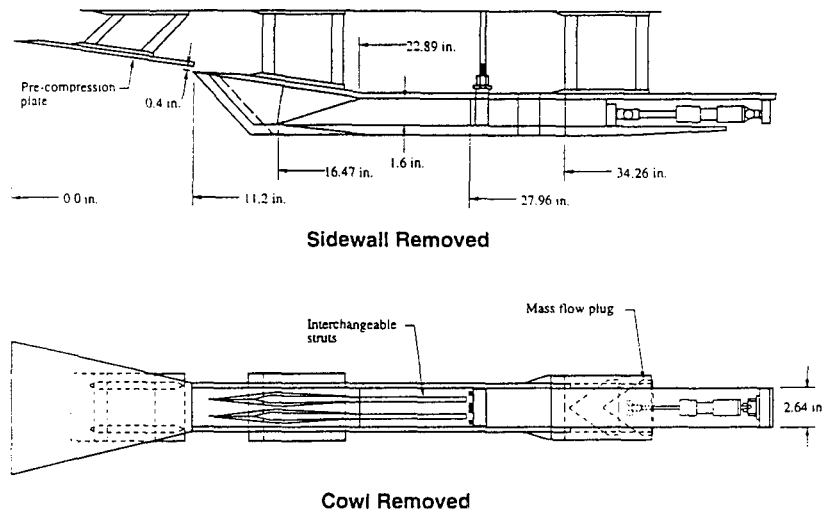


Figure 4.- Sub-scale inlet model.

REF 15, FERNANDEZ ET AL

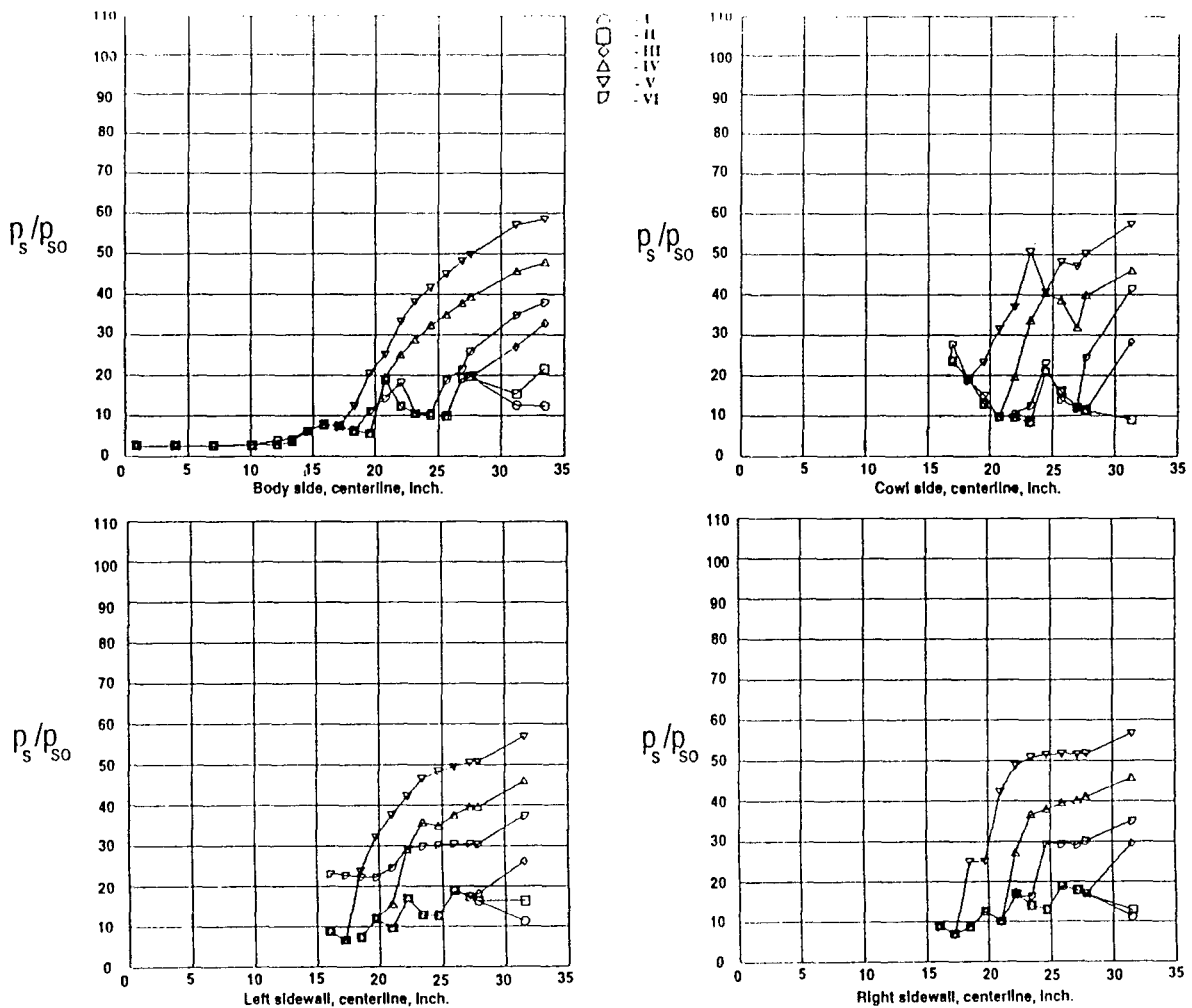


Figure 8 . - Model surface static pressure ratios for Mach 5, configuration B1

REF 15, FERNANDEZ ET AL

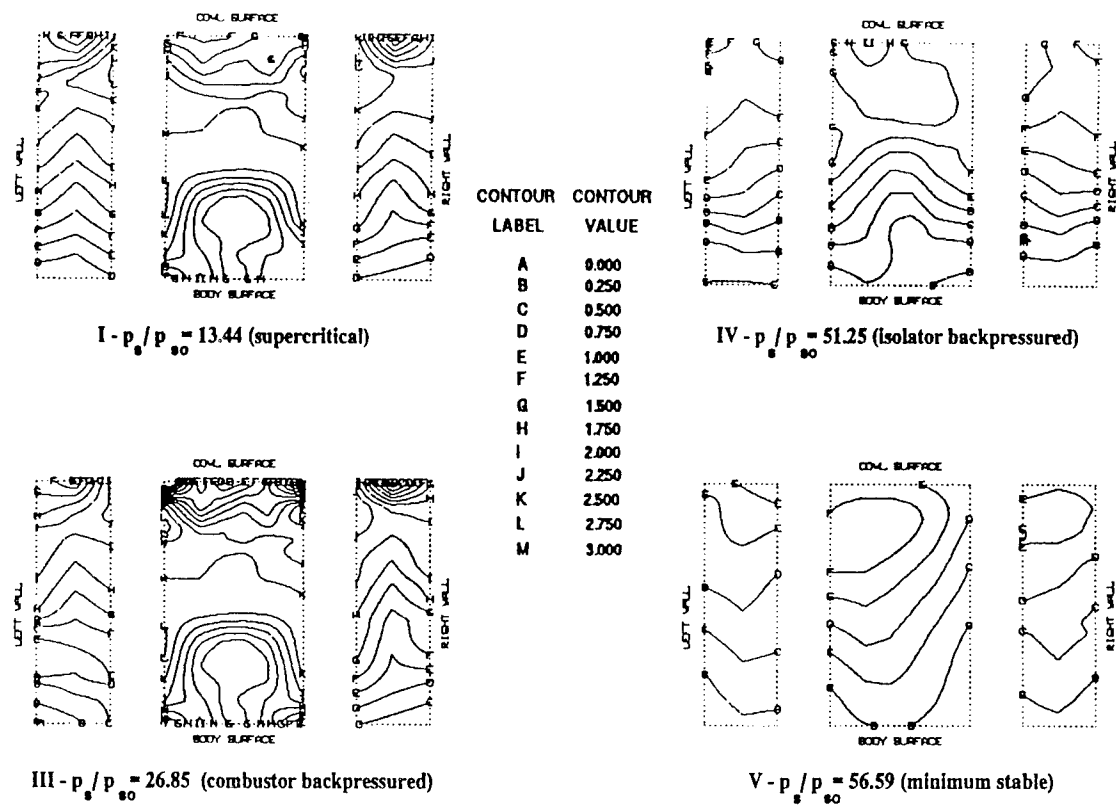


Figure 9. - Traversing rake plane Mach # contours. Mach 5 , configuration B1

REF 15, FERNANDEZ ET AL

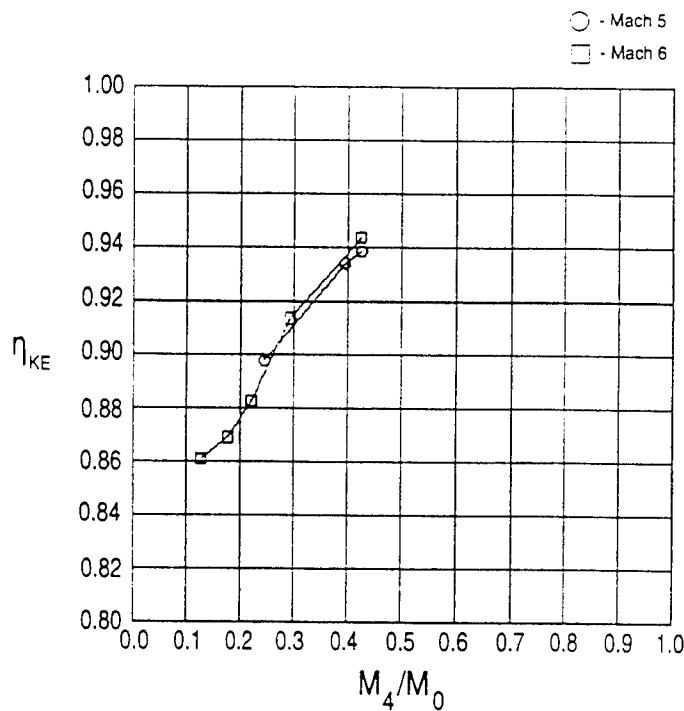


Figure 12. - RBCC inlet performance, configuration B1

REF 15, FERNANDEZ ET AL

## REFERENCES

1. Watts, J.D. et al, "Mach 5 Cruise Aircraft Research", NASA C-2398, Volume II, 1985, pp.285-304.
2. Weir, Lois J. et al, "Mach 5 Inlet CFD and Experimental Results", AIAA 89-2355, July 1989.
3. Trefny, C.J. and Benson, T.J., "An Integration of the Turbojet and Single- Throat Ramjet", NASA TM-107085, Nov. 1995.
4. Weir, Lois J. "An Experimental and Analytical Investigation of a Mach 5 Inlet", 3rd Northern Ohio Technical Symposium "Aerospace Today", Cleveland State Univ., May 16, 1994.
5. Benson, T.J., "Three dimensional Viscous Calculation of Flow in a Mach 5 Hypersonic Inlet", AIAA 86-1461, June 1986.
6. Coltrin, R.E., "High Speed Inlet Research Program and Supporting Analysis", NASA CP 10003, Nov. 1987.
7. Rose, W.C., Perkins, E.W. and Howe, G.W., "Three Dimensional heat transfer and Pressure distribution Within a Mach 5 Inlet at a Flight Condition", NASP CR 1033, Nov. 1988.
8. Reddy, D.R., Benson, T.J. and Weir, L.J., "Comparison of 3-D Viscous Flow Computations of Mach 5 Inlet With Experimental Data", AIAA 90-0600, Jan, 1990.
9. Rizzetta, D.P., "Numerical Simulation of a Supersonic Inlet", AIAA 91-0128, Jan 1991.
10. Reddy, D.R. and Weir, L.J., "Three dimensional Viscous Analysis of a Mach 5 Inlet and Comparison with Experimental Data", Jrl Propulsion and Power, vol 8, no 2, 1992, pp432-440.
11. Anderson, B.H., personal communication
12. Povinelli, L.A., Povinelli, F.P. and Hersch, M., "A Study of Helium Penetration and Spreading in a Mach 2 Airstream Using a Delta Wing Injector", NASA TN D-5322, July 1969.
13. Escher, W.J.D., "A Winning Combination for tomorrow's spaceliners", Aerospace America, Febr. 1996, pp38-43.
14. Povinelli, L.A., "Aerodynamic Drag and Fuel Spreading Measurements in a Simulated Scramjet Combustion Module", NASA TN-D 7674, May 1974.
15. Fernandez, R. et al, "Parametric Data From A Wind Tunnel Test on a Rocket Based Combined Cycle Engine Inlet",
16. DeBonis, J. and Yungster, S., "Rocket Based Combined Cycle Engine Technology Development- Inlet CFD Validation and Application", 32nd AIAA/ASME/ASEE Joint Propulsion Conference, AIAA Paper, July 1996.
17. Povinelli, Louis A., "Computational Modeling and Validation for Hypersonic Inlets". AGARD 75th Symposium on Hypersonic Combined Cycle Propulsion, PEP Panel, Madrid, Spain, May 1990.
18. Menees, G.P., Adelman, H.G. and Cambier, J.L., "Analytical and Experimental Investigations of the Oblique Detonation Wave Engine Concept", AGARD 75th Symposium on Hypersonic Combined Cycle Propulsion, PEP Panel, Madrid, Spain, May 1990.

19. Hertzberg, A. et al., "Ram Accelerator: A New Chemical Method for Accelerating Projectiles to Ultrahigh Velocities", AIAA Jrnl., vol 26, 1988, pp195-203.
20. Yungster, S. and Radhakrishnan, K., "Computational Study of Flow Establishment in Hypersonic Pulse Facilities", NASA Contractor Report 198407, ICOMP 95-19, Nov. 1995.
21. Dwoyer, D.L., Kutler, P and Povinelli, L.A., "Retooling CFD for Hypersonic Aircraft", Aerospace America, Oct 1987, pp 32-41.
22. Povinelli, Louis A., Dwoyer, Douglas I. and Green, Michael J., "CFD propels NASP propulsion progress", Aerospace America, July 1990, pp26, 86.
23. Povinelli, Louis A., "Advanced Computational Techniques for Hypersonic Propulsion", Ninth ISABE Conference Proceedings, vol. 2, 1989, pp993-1008, also NASA TM-102005.

## COMPUTATIONAL MODELING AND VALIDATION FOR HYPERSONIC INLETS

Louis A. Povinelli  
National Aeronautics and Space Administration  
Lewis Research Center  
21000 Brookpark Road  
Cleveland, Ohio 44135 U.S.A.

## SUMMARY

Hypersonic inlet research activity at NASA is reviewed. The basis for the paper is the experimental tests performed with three inlets: the NASA Lewis Research Center Mach 5, the McDonnell Douglas Mach 12, and the NASA Langley Mach 18. Both three-dimensional PNS and NS codes have been used to compute the flow within the three inlets. Modeling assumptions in the codes involve the turbulence model, the nature of the boundary layer, shock wave-boundary layer interaction, and the flow spilled to the outside of the inlet. Use of the codes in conjunction with the experimental data are helping to develop a clearer understanding of the inlet flow physics and to focus on the modeling improvements required in order to arrive at validated codes.

## INTRODUCTION

This paper presents a review of the hypersonic inlet activities at NASA. Generally, the NASA work has covered the range from Mach 5 to 18. The research has been of a computational and experimental nature with a two-fold objective: (1) to develop an improved understanding of the physics and chemistry of inlet flow fields and (2) to validate the numerical codes used for high-speed inlets. The objectives result from the basic philosophy developed for the National Aerospace Plane project; namely, that numerical codes can be validated using ground test data and extrapolated to higher velocities. Since the ground experimental data base is limited to Mach 8 and lower, extrapolation of the computational methods must be made from Mach 8 to the Mach number, approximately 16, where airbreathing propulsion terminates.

A number of codes have been used to date within NASA for inlet flows. Code development and modifications have taken place over the last several years and the emphasis today is on the application to various inlets that have been tested. Those inlets include the Mach 5 inlet at NASA Lewis Research Center, a General Dynamics Mach 12 configuration and a Mach 18 NASA Langley inlet. Only a limited amount of data is available for each configuration.

The numerical methods used have included a PNS code, the PARC NS code, the SCRAM3D and CFL3D. Generally, the codes employ a Baldwin-Lomax turbulence model. Assumptions are made regarding the state of the boundary layer and spillage has generally not been computed. Thick upstream boundary layers are computed in some cases having a forward extension surface. In this paper a comparison of the experimental and computational results will be reviewed.

## RESULTS

## Mach 12 Generic Inlet

The simple rectangular inlet configuration shown in Fig. 1 was tested at Mach 12.26. A flat plate of 30-in. length preceded the entrance to the inlet in order to simulate the boundary layer growth on the forebody of a hypersonic aircraft. Compression wedges form the top and bottom walls of the inlet and the contraction ratio was equal to 5. Swept sidewalls which connect the upper and lower walls prevent compressed flow from spilling over the inlet sides.

Computations were made with a three-dimensional PNS LBI implicit scheme (Ref. 1) with grids of 80 by 60 by 750 on a Cray X-MP. This solver includes real gas effects (Ref. 2) as well as dissociation and ionization modeling (Ref. 3). For this experiment, however, the inlet air was only heated sufficiently to avoid condensation, and the real gas modeling was not required. The issues that are of importance in this computation are the assumptions regarding the state of the boundary layer, the turbulence model, spillage of flow around the sideplates and shock boundary layer interaction. For the PNS computation it was assumed that the boundary layer was turbulent starting on the leading edge of the flat plate, the cowl leading edge and the sidewall leading edges. The turbulence model used was a Baldwin-Lomax model and spillage was not considered. Modeling of the shock boundary layer interaction involved the use of a flare approximation in order to allow the PNS to march through the region of flow separation. The results of the PNS solution are shown in Fig. 2. Contour plots of constant Mach number within the inlet are shown. The concentration of lines near the walls indicate the boundary layers, while concentrated contours in the freestream indicate shock wave locations. The flow features seen are boundary layer buildup on the flat plate followed by thickening on the sidewalls and ramp surface. Shocks generated by the compression wedges are seen as horizontal lines, and the sidewall shocks are vertical lines.

Basically, the important physics occurring are that the low energy flow in the sidewall boundary layer has been swept up the sidewall by the ramp shock, and then down the sidewall by the cowl shock. Further downstream, the shock waves cross and are distorted by interaction with the sidewall boundary layers and the expansion fan on the ramp surface. Additional complex interactions then occur as the flow moves downstream. The PNS solution fails when the ramp shock wave reflects from the cowl and strikes the ramp surface, resulting in large corner separation of the low energy flow.

An alternate view of the three-dimensional flow is obtained with sidewall particle tracing (Fig. 4). Interaction of the ramp and cowl shocks with the sidewall boundary layer causes the particles to converge near the shock interaction point. The particles are then displaced due to the vortex motion. Flow migration details are evident in this computational simulation. As a sidenote, since the vortex persists downstream, it has been proposed that enhanced fuel mixing could occur with judicious injector locations downstream (Ref. 4).

Navier-Stokes computations have also been carried out for the generic inlet at NASA Langley with CFL3D (Ref. 5). In this case, the boundary layers were assumed turbulent on all surfaces from the leading edges. The turbulence model used was a Baldwin-Lomax model and spillage over the sideplates was not considered. In the vicinity of the shock boundary no special modeling was employed. Figure 5(a) shows the pressure distributions for the ramp and centerline cowl surfaces. Figure 5(b) shows the side plane distributions. Comparison of the CFL3D results and the experimental data show good agreement, particularly along the centerline where shock locations appear to be well resolved by the code. The viscous interactions occurring along the side plane are not accurately resolved. There is a significant underprediction of the pressure on the ramp side (Fig. 5(b)). In addition, CFL3D was used to compute the heat transfer on the ramp and cowl surfaces (Figs. 6(a) and (b)). The experimental peak heat fluxes are underpredicted for the ramp centerline but well predicted for the cowl surface.

For the ramp and cowl side planes (Fig. 6(b)), the peak prediction is lower on the ramp whereas the cowl side prediction is not qualitatively correct. Again, strong viscous effects are predominating along the side walls of the inlet in agreement with the complex behavior shown in Figs. 2 to 4. Further analysis of the Mach 12 inlet is underway at the NASA Centers and industry.

#### Mach 5 Inlet

A rectangular mixed compression inlet designed for Mach 5 operation and tested at NASA Lewis is shown in Figs. 7(a) and (b) (Ref. 6). A series of ramps generate oblique shock waves external to the cowl. An oblique shock from the cowl leading edge reflects from the ramp surface and terminates in a normal shock downstream of the inlet throat. Operation in the wind tunnel was such that a Mach number of 4.1 occurred on the first ramp. The inlet incorporates variable geometry with collapsible ramp and variable bleed exits on the cowl, sidewalls and ramps. Bleed of 0.5 percent was removed on the ramp upstream of the shoulder. Additional bleed from the cowl and sidewalls was approximately 8.8 percent of the capture mass flow. Figure 8 shows the location of pressure rakes and probes in the model. A 0.5-in. strip of grit was applied near the leading edges of the ramp and sidewall to ensure that a fully turbulent boundary layer was ingested by the inlet.

Navier-Stokes computations were carried out using the PARC3D solver (Ref. 7) on the NAS Cray 2. Grid sizes of 151 by 81 by 41 were used with hyperbolic packing so that the first point was at a  $y^+$  of 2. Bleed was simulated by imposing a constant mass flux through the porous bleed surfaces based on the experimental data. The boundary layer was assumed to be turbulent throughout, and the turbulence model was that of Baldwin-Lomax. Flow spillage over the sideplates was also not computed in this case.

The computed ramp pressure results are compared with experimental data in Fig. 9. The agreement of the computations with the data is very good throughout the computed length of the inlet. Figure 10 shows the comparison for the cowl pressure distribution. The disagreement of the results at an  $x/h$  of 4.2 is believed to be due to the fact that one of the translating probe assemblies is located in the same region where the four static pressure taps are located. Because the retracting probe does not completely retract into the wall, additional shocks are generated which biased the data. Pitot pressure profiles were compared with data at various locations along the inlet. Figure 11 shows the pressure profile from rake 3 which was located on the centerline and in the region of the second ramp (Fig. 8). The agreement of data and computation is very good. Along the sidewall, however, the agreement is much poorer, as shown in Fig. 12 for rake 7. The corner effects are not being adequately simulated. An improved turbulence model may improve the comparison in these corner regions. Figure 13 shows the pitot pressure comparison for rake 10 mounted at  $45^\circ$  from the corner of the cowl and sidewall at station 59.6 from the start of the inlet. This region of the flow is dominated by low energy vortical flow as seen in Fig. 14. Large variations in the pitot pressure are seen as one moves from the corner into the stream. Measurements in these regions are also very difficult.

The Mach 5 inlet was also analyzed using the SCRAM3D Navier-Stokes code by Rose (Ref. 8). A Baldwin-Lomax turbulence was used, assuming turbulent boundary layers. These results also reveal strong glancing shock wave-boundary layer interaction leading to large regions of low momentum flow on the sidewalls. Rose carried out a number of numerical experiments to control the vortex phenomena in the corner regions. Figure 16

shows the baseline or no control case, followed by cowl cutback, cowl bleed and removal of a part of the sidewall. These modifications were made near the inlet ramp shoulder. It may be seen that these modifications were ineffective in eliminating the vortex region. Even with the cutback sidewall, the low momentum fluid exists along the entire sidewall. Some attenuation is seen along the cowl surface for that case. It is evident, however, that the shock-boundary layer physics within a rectangular shaped inlet will lead to pressure losses in the corner regions. However, if these regions can be utilized in an "integrated design approach" (Ref. 4), then combustor/nozzle design may benefit substantially. Further computations of the Mach 5 inlet with improved simulation of the bleed zones is underway, as well as further analysis of the test data.

#### Mach 18 Sidewall Compression Inlet

A sidewall compression inlet has been designed and tested at NASA Langley by Trexler. As seen in Fig. 17, the compression occurs on the sideplates. The experiments were run at an entrance Mach number of 18 to 22 with and without a flat plate upstream to simulate fuselage boundary layer buildup. The entering boundary layer was approximately one-third the cowl height. Computations were made by Rose (Ref. 9) using the SCRAM3D code. Laminar boundary layers were assumed on cowl and sidewalls, and a Baldwin-Lomax turbulence model was used.

Figure 18 shows the Mach number contours along the vertical centerplane for an entrance Mach number of 18.1. The contraction ratio was 4 and the cowl leading edge is located at the entrance to the constant area section. All of the convergence occurs along the sidewalls, which generate a pair of shock waves that intersect on the vertical centerplane. A large pressure rise is felt on the ramp surface. Further downstream, the shocks interact with the sidewall boundary layers and reflect and intersect again on the centerplane at the indicated position. A further rise in pressure causes ramp boundary layer separation.

The Mach number contours on the horizontal centerplane are shown in Fig. 19. The intersecting sidewall shocks and the intersecting reflected shocks are visible. Since the sidewall shocks strike the sidewall well upstream of the shoulder, shock cancellation is clearly not achieved. The reflected shock waves, however, are seen to cancel at the shoulder. The strong viscous interaction effects are very evident at these flow conditions.

Calculated Mach number contours are shown in Fig. 20 for both the horizontal and the vertical center planes with an entrance boundary layer. The entrance plate reduces the Mach number from the entrance value to about Mach 12. Separation of the boundary layer on the ramp, caused by the sidewall shock waves, causes a large upstream influence. As the ramp boundary layer thickens, an oblique shock occurs reducing the inlet flow to Mach 8. Sidewall shocks and their intersection are seen in the horizontal centerplane. The sidewall shock wave angle is substantially increased due to the reduced Mach number entering the inlet. The ramp shock falls outside the cowl leading edge. Figure 21 shows a comparison of the experimental and computed surface pressure distributions on the ramp centerline, for the case where the cowl is moved forward. In this particular comparison, the numerical code yields results which are higher than the measured data and also rises faster than measured. Further data analysis and comparisons are underway at the present time, which will lead to a more complete understanding of the flow in this class of inlets.

#### CONCLUSIONS

Through the use of a variety of numerical simulations and experiments, the basic flow features within rectangular hypersonic inlets are becoming better understood. Fast running PNS solvers in combination with much longer running but more sophisticated Navier-Stokes codes are providing a clearer picture of shock structure and boundary layer behavior in inlets. Clearly, the flow fields are highly three-dimensional, viscously dominated and contain significant flow separations. Shock wave-boundary layer interactions persist down to the throat and beyond. As the propulsion community moves towards the validation of these codes, a number of issues still remain which will impede the application of the methods for the design of hypersonic inlets. Perhaps the first concern is that regarding the nature of the boundary layer within the inlet. Although attempts are made to ensure the presence of turbulent layers, for example, questions still remain regarding the existence of transitional layers. Installation of hot film gauges on the walls would provide the numerical analyst with the proper information to use within his computer code; be it laminar, transitional or turbulent. An additional issue is concerned with turbulence modeling and the ability of the Baldwin-Lomax model in regions of glancing shock wave-boundary layer interaction. Current turbulence models appear to yield good qualitative flow characteristics, but may be inadequate for quantitative predictions. Alternate models are needed. A third concern deals with the necessity of including the zone outside of the inlet in order to provide proper boundary conditions for the computation. In spite of these concerns, the understanding and agreement (i.e., on centerline) are very significant. The Mach 5 inlet presents the same concerns but with the complication of bleed flow on all four surfaces. Modeling issues related to turbulence, boundary layer transition and spillage are made more complex with a distributed mass flux boundary condition. Again, it is remarkable that such good agreement, with limited data, was achieved for that inlet. A great deal more effort will be required to analyze the test data and develop the proper modeling for a bulk of the data.



The sidewall compression presents a unique approach to inlet design. Computations of the three-dimensional flow field and associated shock structure provide us with a great deal of physics. The limited data provides a basis for an improvement in current modeling. Use of the experimental data and empirically derived correlations may serve as a basis to produce improved viscous modeling. It is important to point out that in all of these inlet tests, the tunnel flow was sufficiently low to avoid real gas effects. Hence, the comparisons presented in the paper are only aerodynamic in nature. More significant modeling issues will surface as test data is acquired in high-enthalpy flows. Finally, the need to analyze variable geometry with transient disturbances will provide a significant challenge.

## REFERENCES

1. Reddy, D.R., Smith, G.E., Liou, M.-F., and Benson, T.J., "Three Dimensional Viscous Analysis of a Hypersonic Inlet," AIAA Paper 89-0004, Jan. 1989. (Also, NASA TM-101474, 1989.)
2. Liou, M.-F., "Three Dimensional PNS Solutions of Hypersonic Internal Flows With Equilibrium Chemistry," AIAA Paper 89-0002, Jan. 1989.
3. Yu, S.-T., McBride, B.J., Hsieh, K.-C., and Shuen, J.-S., "Numerical Simulation of Hypersonic Inlet Flows with Equilibrium or Finite Rate Chemistry," AIAA Paper 88-0273, Jan. 1988.
4. Povinelli, L.A., "Advanced Computational Techniques for Hypersonic Propulsion," NASA TM-102005, 1989. Presented at the Ninth International Symposium on Air Breathing Engines, Athens, Greece, Sept. 4-9, 1989.
5. Diley, A., Eppard, W., and Switzer, G., "Zonal Analysis of Two High Speed Inlets," Presented at the CFD Symposium on Aeropropulsion, NASA Lewis Research Center, Cleveland, OH, April 24-26, 1990.
6. Weir, L.J., Reddy, D.R., and Rupp, G.D., "Mach 5 Inlet CFD and Experimental Results," AIAA Paper 89-2355, July 1989.
7. Reddy, D.R., Benson, T.J., and Weir, L.J., "Comparison of 3-D Viscous Flow Computations of Mach 5 Inlet with Experimental Data," AIAA Paper 90-0600, Jan. 1990.
8. Rose, W.C., and Perkins, E.W., "Innovative Boundary Layer Control Methods in High Speed Inlet Systems-Final Report," Contract NAS3-25408, Sept. 9, 1988 (NASA CR in publication).
9. Rose, W.C., Perkins, E.W., and Benze, D.P., NASA Ames Research Review, Dec. 1989.

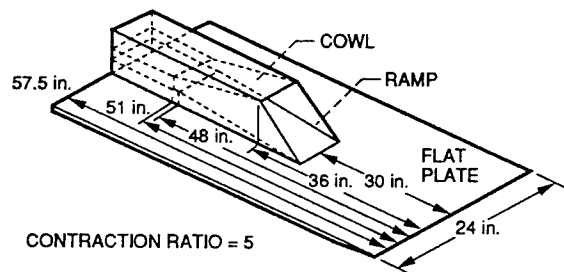
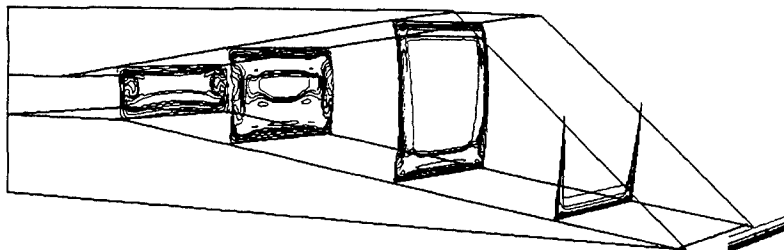


Figure 1. - Generic inlet (ref. 5).

Figure 2. - Mach number contours,  $M = 12.25$  (ref. 1).

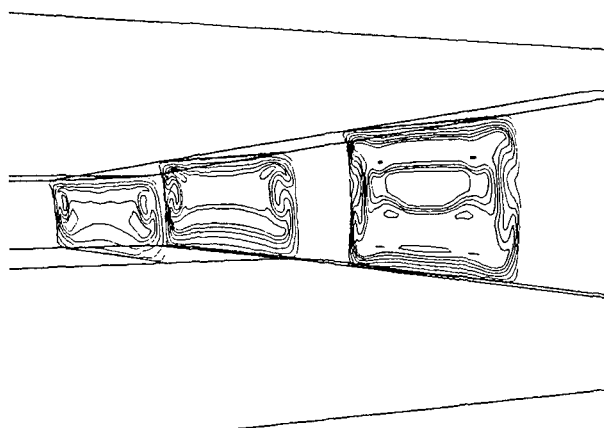


Figure 3. - Mach number contours viewed from aft (ref. 1).

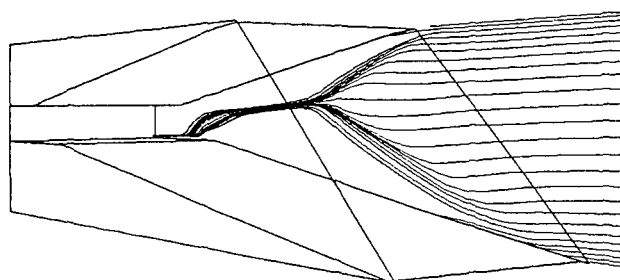
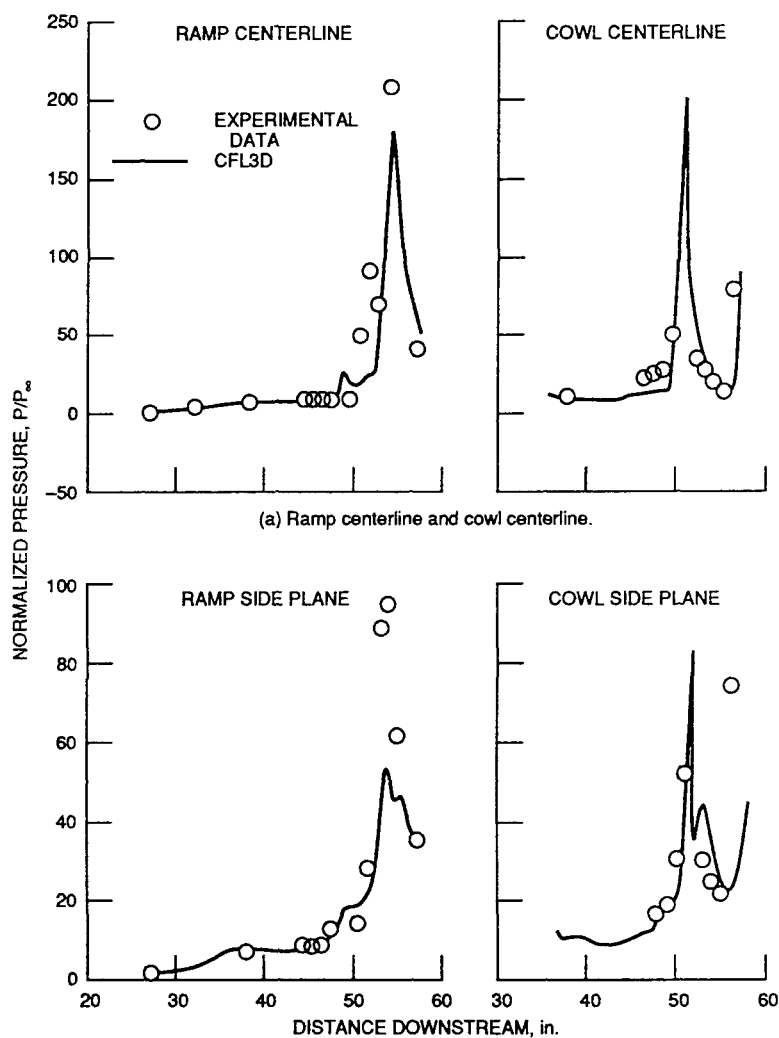
Figure 4. - Sidewall particle tracing,  $M = 12.25$  (ref. 1).

Figure 5. - Pressure comparisons (ref. 5).

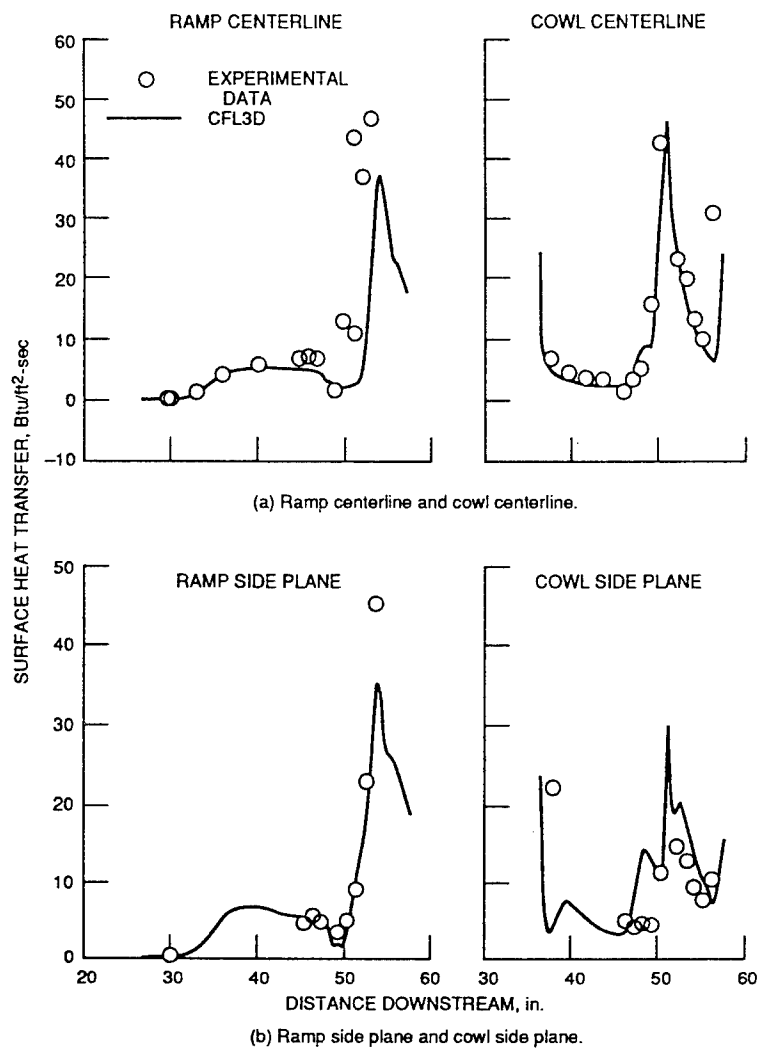


Figure 6. - Heat transfer comparisons (ref. 5).

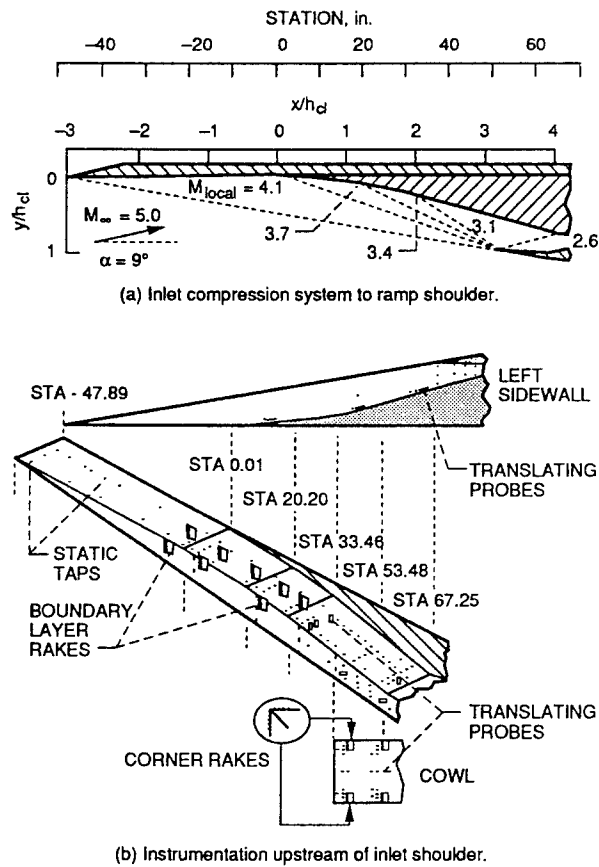


Figure 7. - (ref. 6).

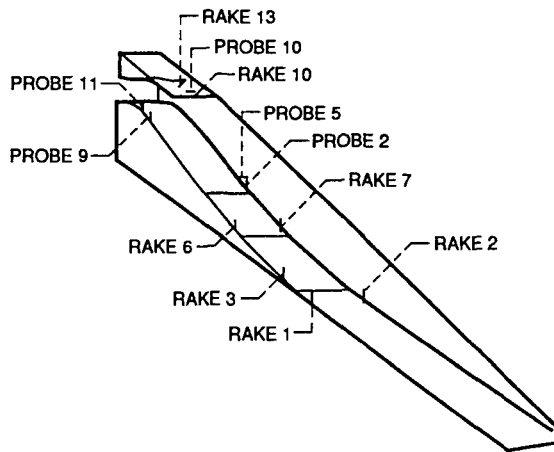


Figure 8. - Location of fixed rakes and translating probes used for pitot pressure measurement (ref. 7).

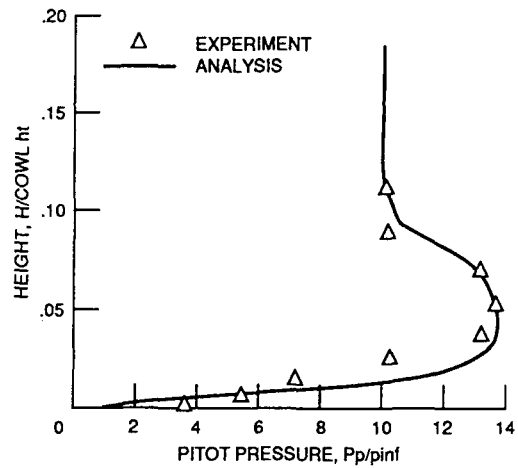


Figure 11. - Rake 3 pitot pressure profile (ref. 7).

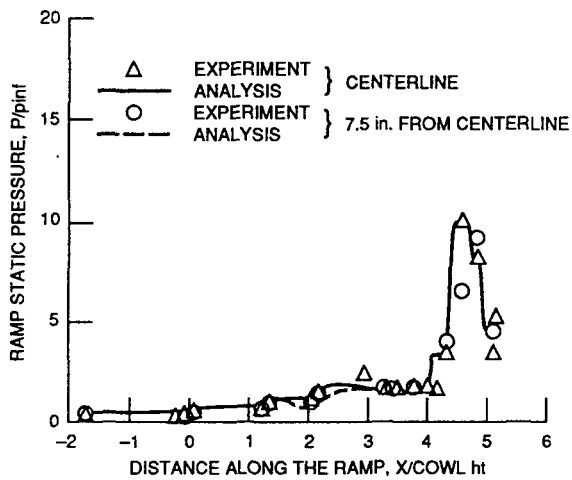


Figure 9. - Ramp static pressure distribution (ref. 7).

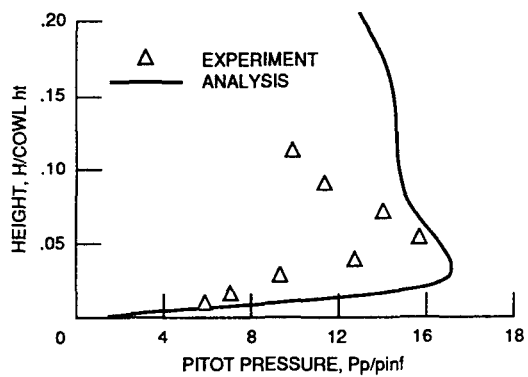


Figure 12. - Rake 7 pitot pressure profile (ref. 7).

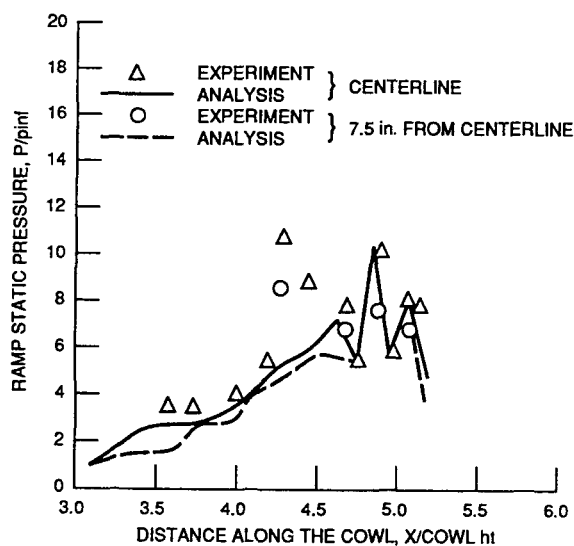


Figure 10. - Cowl static pressure distribution (ref. 7).

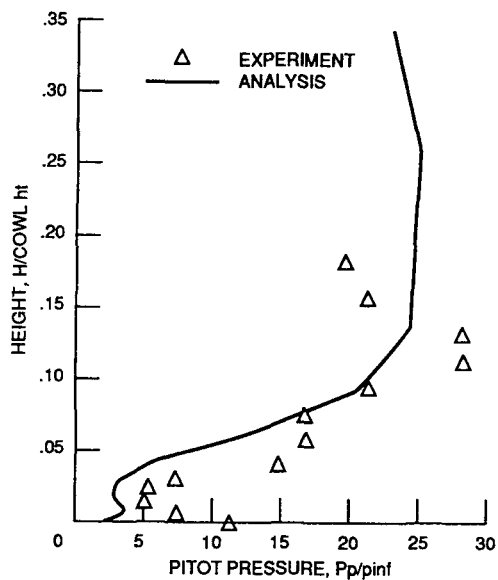


Figure 13. - Rake 10 pitot pressure profile (ref. 7).

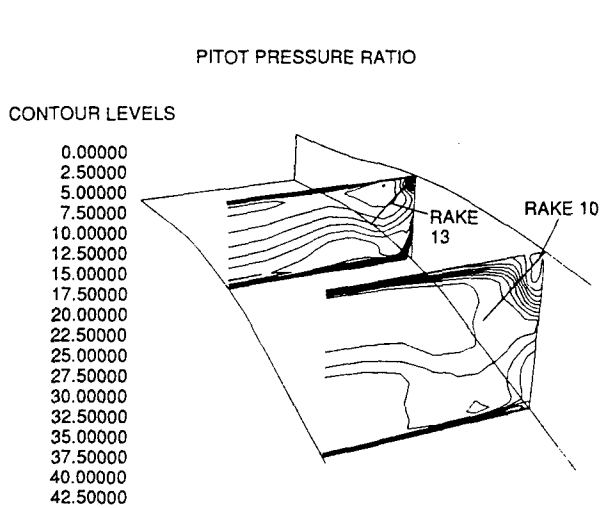


FIGURE 14. - Pitot pressure contour at rake 10 and rake 13 (ref. 7).

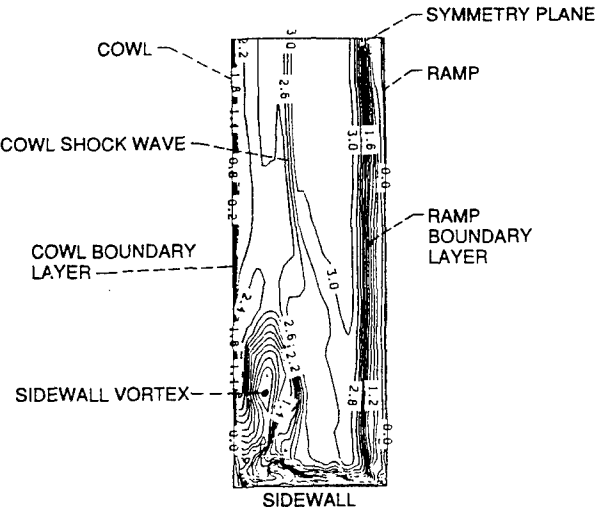


Figure 15. - Orientation of crossflow plane 150 located near the ramp shoulder showing plane of symmetry, sidewall ramp and cowl surfaces (ref. 8).

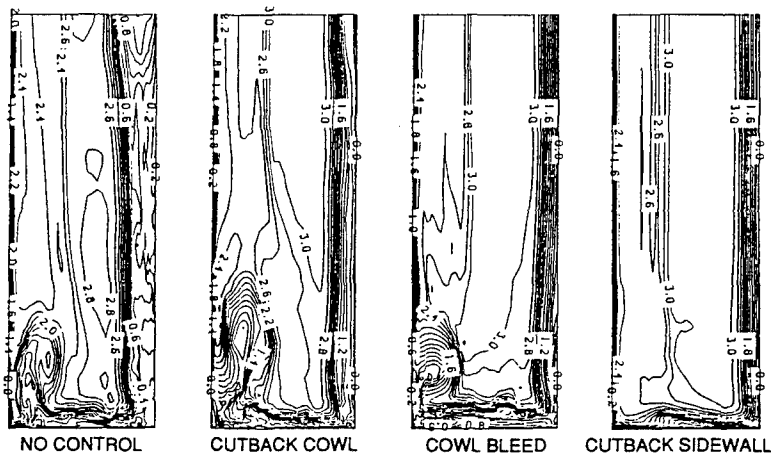


Figure 16. - Comparison of effect of various control methods on mach number contours near ramp shoulder (ref. 8).

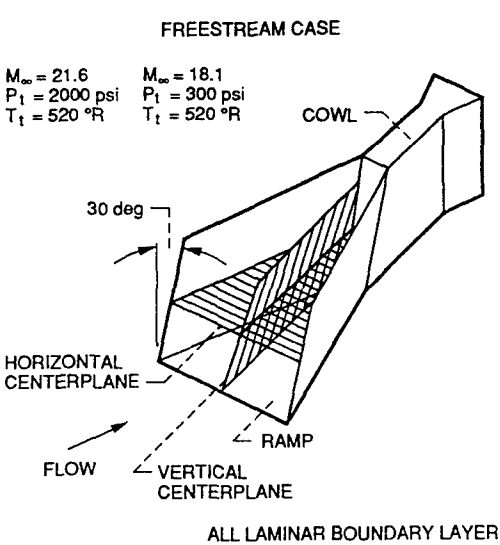


Figure 17. - Sidewall compression inlet schematic (ref. 9).

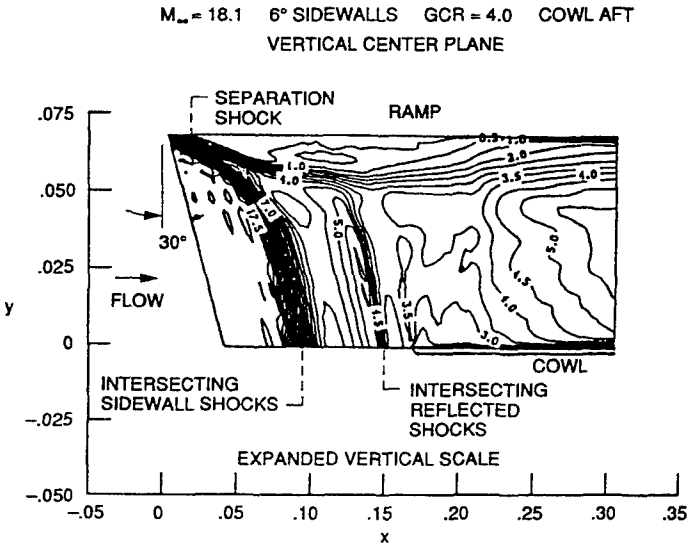


Figure 18. - Mach number contours for freestream case (ref. 9).

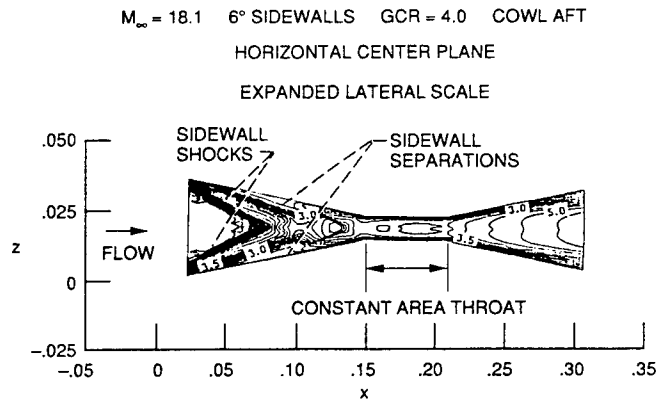


Figure 19. - Mach number contours for a representative freestream case in the horizontal center plane (ref. 9).

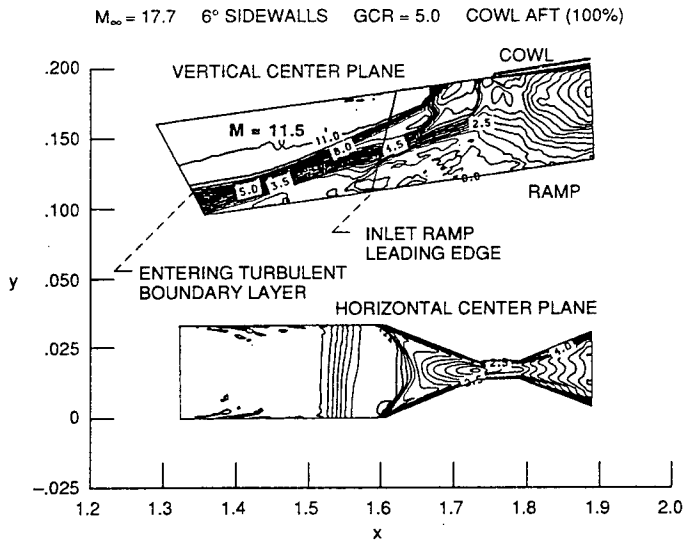


Figure 20. - Mach number contours for entering boundary layer case (ref. 9).

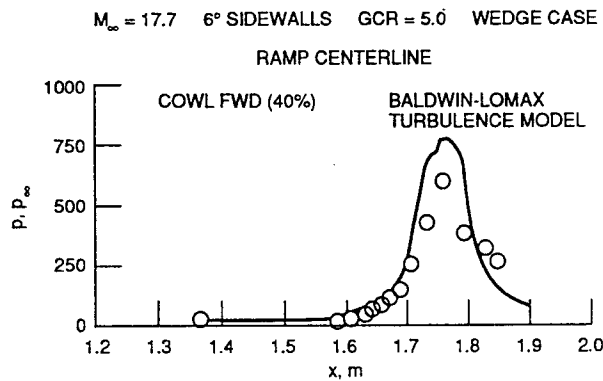


Figure 21. - Comparison of experimental and numerical surface pressure distributions (ref. 9).

## Discussion

GARNERO

1) Can you give us the CPU time for one calculation, for example for the Mach 12 Generic Inlet, with a three-dimensional PN 5 LBI implicit scheme and CRAY X-MP?

2) Do you think that a Baldwin-Lomax Turbulence Model is sufficient to compute internal aerodynamics in hypersonic inlets or do you plan to use more complex models like K-E model for example?

AUTHOR'S REPLY

1) 3-D Parabolical Navier-Stokes computations for the Mach 12 Generic Inlet on a Cray X-MP typically take 45 CPU minutes, using a linearized block implicit scheme. Navier-Stokes solutions for the same inlet take much more time, i.e. 10 Hrs of CPU time.

2) The Baldwin-Lomax turbulence has been extensively used for inlet computations. However, it has been found to have significant shortcomings. Higher order turbulence closures have been investigated and are under study. In addition, a program is in place with the objective of developing improved turbulence and transition modeling for hypersonic flows.

KORZ

The glancing sidewall shocks and the resulting separation and secondary flow would seem to have the potential for a significant input on modular scramjets configurations. Would you comment and indicate if any evaluations of this phenomenon have been carried through the entire scramjet flowfield, including the combustor and nozzle?

AUTHOR'S REPLY

Scramjet modular configurations would utilize multiple sidewalls over the span of the inlet. At each of the sidewalls, the potential for regimes of secondary flow is present. Hence a considerable fraction of the flow area can be affected by this phenomenon. At the present time, no data has been presented which tracks the secondary flow through the combustor/nozzle in a scramjet. There are measurements in a Mach 3.5 rectangular inlet, however, which does show the persistence of the vortex through inlet, through a normal shock and into a subsonic diffuser. The effect of this secondary flow on inlet performance and inlet unstart must be evaluated. It is noted that the presence of this flow feature may provide some benefit for enhanced mixing of fuel. It has been suggested previously that injection of fuel into the vortical flow region at some point within the aft portion of the inlet may lead to greater fuel spreading and additional time for chemical reaction.

Louis A. Povinelli\*  
National Aeronautics and Space Administration  
Lewis Research Center  
Cleveland, Ohio 44135

### Abstract

CFD has played a major role in the resurgence of hypersonic flight, on the premise that numerical methods will allow us to perform simulations at conditions for which no ground test capability exists. Validation of CFD methods is being established using the experimental data base available, which is below Mach 8. It is important, however, to realize the limitations involved in the extrapolation process as well as the deficiencies that exist in numerical methods at the present time. Current features of CFD codes are examined for application to propulsion system components. The shortcomings in simulation and modeling are identified and discussed.

### Introduction

An overwhelming degree of reliance has been placed on computational fluid dynamics in the achievement of hypersonic flight with a NASP-like vehicle (National Aero-Space Plane Program). This reliance covers the range of design activities; from the design of the aircraft configuration to the design of the integrated engine system. The belief that CFD can be used to predict all of the relevant flow physics and chemistry, from aircraft takeoff to orbital speeds and return, has been one of the principal reasons for the resurgence of hypersonic research. Computational methods do, in fact, provide us with the unique ability to perform ground simulations at high Mach numbers for which no ground test capability exists. Above Mach numbers of approximately 8, ground test facilities do not duplicate the relevant flight simulation parameter such as Mach number, Reynolds numbers, gas composition, and enthalpy level. Numerical analysis remains as the principal approach to the design of the aircraft and the propulsion system. It is possible that some data could be obtained from rocket test vehicles. These data would be limited, however to such items as the state of the boundary layer, boundary layer transition location, length of the transition zone and surface heat transfer. Testing of a scramjet propulsion system on a rocket vehicle would present a major problem due to the fact that scaling of the combustion process is not feasible. Therefore, a full sized propulsion module would be required as the test article on a rocket test vehicle. Such testing might be better approached through use of larger vehicles such as the Space Shuttle. However, it is currently believed that the costs associated with the flight testing described above would be extremely high. CFD, therefore, remains as a viable alternative. It must be pointed out that the philosophy regarding CFD is based on the fact that an experimental data base exists below Mach 8. Those data provide the means for assessing the accuracy of the numerical methods, as well as for calibrating the codes. Extrapolation to flight conditions, where no data

exists, can then be carried out. In theory, therefore, the procedure described would provide us with ground simulation throughout the Mach number range from takeoff to orbital velocities. It is crucial, however, to realize the capabilities and the limitations involved in the extrapolation process as well as the numerical methods at the present time. In this paper, the current features of the numerical methods available for analyzing the flow in multi-element hypersonic propulsion systems will be presented. Since this paper has as its focus the propulsion system, the aircraft configuration is only discussed relative to the propulsion flow path. Only the integration effects of the forebody and nozzle afterbody configuration will be addressed. Emphasis is placed on the inlet behavior, combustor and nozzle characteristics including ionization and dissociation effects, as well as finite rate and equilibrium chemistry effects. The critical limitations introduced by the need for turbulence, boundary layer transition and chemical modeling are discussed; and the effect of various models is illustrated for the propulsion system components. Shortcomings associated with the extrapolation to higher speeds are also presented. Current and future activities, which are directed toward improving the modeling, are discussed. These activities include elements such as direct numerical simulation, wall and shear layer turbulence modeling and probability density functions for reacting flows.

### Propulsion CFD Validation

#### Hypersonic Propulsion System

In order to demonstrate the ability of CFD codes to perform propulsion system computations and to examine their strengths and their shortcomings, a typical propulsion configuration must be chosen. In this paper, a combined ramjet/scramjet system is assumed which has a common flow path. The low speed or "accelerator" portion of the engine, which would provide sufficient speed for ramjet operation, is not considered here. The assumed flight conditions would correspond to subsonic combustion ramjet operation from flight numbers of approximately Mach 3 up to approximately Mach 5.5, where supersonic combustion operation would commence. Supersonic flow within the engine results in lower temperatures and pressures, thereby reducing heat fluxes and internal forces. The lower temperatures also allow heat to be added from the fuel without imposing high air dissociation losses. However, ignition and combustion of the fuel within the combustor remains a major challenge. The idea of an oblique detonation wave ramjet has been proposed, wherein fuel is injected upstream (inlet) for pre-mixing with air. The mixture is then ignited by a shock wave within the combustor. Detonation wave stability, completeness of combustion and pre-mixing feasibility issues must be solved to understand this concept. In this paper, the detonation engine computations are not considered. Our investigation, therefore, centers on the use of CFD for

\*Deputy Chief, Internal Fluid Mechanics Division; Associate Fellow, AIAA.

This paper is declared a work of the U.S. Government and is not subject to copyright protection in the United States.



an integrated airbreathing propulsion system operating at altitudes from near earth to the limits of the stratosphere. In the absence of specific ramjet/scramjet designs, a generic type propulsion system will be used which includes many of the features which are considered important in real systems. Those engine features which cannot be analyzed, for example, complex combustor geometries, will be discussed as limitations of CFD for hypersonic propulsion systems.

The level of sophistication required in the numerical methods varies for each of the system components. For the blunt forebody, a thin layer Navier-Stokes code is required at the nose to handle the strong viscous shock, followed by parabolized Navier-Stokes method to the inlet. Around Mach 7, the vehicle generates a high temperature, high enthalpy flow field. The elevated temperatures in the boundary layers of the vehicle dissociates the oxygen and nitrogen molecules into their respective atomic species which may also become ionized. The process can be catalyzed and enhanced further by vehicle surface contaminants. This dissociation process may lead to variations in local flow-field molecular weight, specific heat and transport properties with resultant associated changes in dynamic airflow, heat transfer and combustor kinetics. These effects cannot be accurately modeled in ground test facilities. Properties of shock heated air and combustion gases are needed for performance predictions. Three-dimensional thin layer or Navier-Stokes are required for the flow in the inlet with the presence of multiple shocks and possible flow separation and unsteadiness. The combustor requires a Navier-Stokes solution including finite rate chemistry as does the nozzle flow field. It is obvious, therefore, that real gas effects, ionization, recombination, nonequilibrium effects, and wall catalyticity must be considered at various locations through the system.

#### CFD Validation

As mentioned in the Introduction, CFD extrapolation is required for the design of the aircraft/propulsion system at the higher Mach number range ( $M > 8$ ). A critical activity, therefore, is associated with validation/calibration of the numerical techniques. To what extent or level of sophistication is validation required? Must the numerical codes duplicate all of the physics and chemistry in the flow? Before answering these questions, one must be aware of the manner in which codes will be used in the design process. In the case of the inlet, the designer is interested in certain performance parameters such as the amount of mass captured, adiabatic kinetic energy efficiency, pressure recovery, heat load, spillage drag and exit profile. Ideally, then a designer can compute, for a variety of possible inlet geometries over a range of Mach numbers, all of the parameters cited above and, eventually, arrive at a fairly efficient inlet design. At this point, however, it is necessary to ask to what extent is the designer interested in the physical and chemical phenomena occurring in the inlet, such as shock/boundary layer interactions, secondary/corner flows, mass injection, transition, bleed, equilibrium chemistry, flow separation and unsteady flows due to pressure oscillations and shock interactions? The answer is perhaps quite straightforward. The designer is interested in all of the physics and

chemistry insofar as it affects the performance parameters cited earlier. If the physical/chemical phenomena do not affect the inlet performance or loadings, it is safe to say that the designer would not be particularly upset if such features were missing in the numerical code.

The relevance of the preceding discussion to the issue of code validation/calibration is that the extent of the validation process and the number of effects to be accounted for are strongly dependent on the magnitude of the individual effects on inlet performance. Another way of stating it is to ask which of the items in the list of physical/chemical phenomena must be modeled by the CFD'er in order for the designer to have valid answers. If none of the items can be ignored, then all of them must be included as the numerical codes are exercised to develop sensitivities to the individual modeling. One must realize that in addition to the modeling required, there are also issues related to the numerics and the math modeling. These issues involve computational grid sensitivity, the ability to capture discontinuities, sensitivity to internal code parameters, the effect of numerical boundary conditions, and conservation of mass, momentum, energy and species. Therefore, one must be concerned with numerical/mathematical modeling as well as physical/chemical modeling. If these activities can be properly executed, then one may proceed to the next stage, which includes the identification of critical experiments and comparison of the numerical results with experimental results. Although the experimental methods will not be discussed, it is equally important to establish the validity and accuracy of the measured data.

The discussion regarding code validation has been somewhat general to this point. To be more specific, Table 1 shows the critical forebody design or performance parameters, the quantities that must be computed by the codes and the physics/chemistry modeling requirements. The same information is shown in Table 2 for the inlet, Table 3 for the combustor and Table 4 for the nozzle. From the viewpoint of a researcher, it is believed that a fundamental understanding of the physics and chemistry within any system must first be understood and then modeled. Its relative importance (and perhaps some eventual control) must first be understood, before a massive sensitivity study (grid, internal parameters) is carried out for every physical or chemical phenomena known to exist in the component. It is proposed, therefore, for CFD validation, that both experimental and numerical research should proceed from the basis of developing understanding first, secondly, making judgments on the importance of various phenomena, and then performing numerical sensitivity studies.

The propulsion system components will be discussed sequentially in the following sections of the paper. The items of special concern are unsteady flow behavior in the inlet, combustion-turbulence modeling in the combustor and shear layer/boundary layer characteristics in nozzle flow.

#### Numerical Methods for Inlet Flow

##### Numerical Schemes

Typical results for a high speed inlet will be presented in this section. A fairly significant

number of analyses have been carried out over the last several years at various laboratories (i.e. NASA Lewis, Langley, Rose Engr, APL/JHU). As a means of illustrating the current capability of inlet codes, we consider the results obtained by Benson and co-workers<sup>2-4</sup> using both parabolized and Reynolds averaged Navier-Stokes solvers. The PNS code solves the system of equations for hypersonic or supersonic flow by the linearized block implicit scheme of Briley and McDonald.<sup>5</sup> Since parabolized solvers have inherent limitations regarding separation regions, an approximation is used to allow the code to march through small areas of separated flow. The Reynolds averaged Navier-Stokes code (PARC3D) solves the basic equations in strong conservation form with the Beam-Warming approximate factorization algorithm.<sup>6</sup> It uses central differencing and Jameson type artificial dissipation.<sup>7</sup> Originally developed by Pulliam and Steger,<sup>8</sup> ARC was modified for propulsion analysis by Cooper<sup>9</sup> and accordingly named PARC. The simple rectangular inlet configuration shown in Fig. 1 was analyzed with the expectation that experimental data would be available. A flat plate of 30 in. length preceded the entrance to the inlet in order to simulate the boundary layer growth on the forebody of a hypersonic aircraft. Compression wedges form the top and bottom walls of the inlet and the contraction ratio was equal to 5. Swept sidewalls which connect the upper and lower walls prevent compressed flow from spilling over the inlet sides. Computations were made at an entrance Mach number of 12.25. Various turbulence models were used in the solutions, including those developed by McDonald-Camarata, Bushnell and Beckwith and Baldwin-Lomax. Two-dimensional PNS solutions were carried out using grids of 100 by 1000, and the three-dimensional cases used 80 by 60 by 750. The two-dimensional Reynolds averaged Navier-Stokes solutions used 100 by 200 grids whereas the three-dimensional solutions were carried out on grids of 150 by 81 by 41. Computations were performed on the Cray X-MP and the Cray 2. The PNS code described above has been modified by Liou<sup>10</sup> to include real gas effects. In addition, Yu et al.<sup>11</sup> have incorporated finite rate and local equilibrium approaches in the chemical reaction model for dissociation and ionization of the inlet air. The finite rate approach involves the simultaneous solution of eleven species equations coupled with the fluid dynamics equations. In the local equilibrium approach, a chemical equilibrium package has been developed and incorporated into the flow code to obtain chemical compositions directly. Gas properties for the reaction product species are calculated by methods of statistical mechanics and fit to a polynomial form for specific heat.

Rose and Perkins<sup>12</sup> have used Kumar's explicit, time-accurate implementation of MacCormack's algorithm for solving the full Navier-Stokes equations. Grid sizes used for the computations were 201 in the streamwise direction, 61 in the compression direction and 27 in the cross stream direction. Inlet surfaces were assumed to be nearly adiabatic with surface temperatures equal to stagnation temperatures.

#### Computed Inlet Results

Contour plots of constant Mach number within the inlet, obtained with the PNS analysis are shown in Fig. 2. The concentration of lines near

the walls indicates the boundary layer, while the contour concentration in the freestream indicates shock wave locations. The flow (right to left) features seen in the figure are boundary layer buildup on the flat plate followed by thickening on the side walls and ramp surface. Shocks generated by the compression wedges are seen as horizontal lines, and the sidewall shocks as vertical lines. The shocks generated by the compression surface glance across the sidewall boundary layers, producing a thickening of the boundary in the vicinity of the shock, and thinning of the layer in the corners. Strong secondary flows are developed in the shock wave/boundary layer interaction. These flows, in turn, affect the downstream inlet flow field. A more detailed view of the flow field Mach number contours is seen in Fig. 3. In this view, which looks upstream toward the inlet entrance, the ramp and cowl compression shock waves emanating from the leading edges are clearly discernible, as well as the secondary flow developed in the corners. The boundary layer growth on the wedges and sidewalls has been highly distorted by interactions with the compression shocks. Benson et al.<sup>4</sup> describe their computations in the following way, which relates to the important physical processes occurring: "The low energy flow of the sidewall boundary layer has been swept up the sidewall by the ramp shock and down the sidewall by the cowl shock. Near the sidewall where the secondary flows collide, one sees a secondary shock as a vertical line. As the flow proceeds downstream to the center plane, the shock waves cross and are distorted by interaction with the sidewall boundary layer and the expansion fan on the ramp surface. At this station, the ramp shock is reflecting from the cowl surface and the cowl shock is seen as the upper horizontal line. The lower white horizontal line corresponds to the edge of the ramp boundary layer. The vortices generated by the shock/boundary layer interactions have pulled away from the sidewall while interacting with each other. Proceeding to the last plane on the left, the expansion generated on the lower surface causes a strong pressure gradient from top to bottom. Low energy flow along the sidewall moves into the corner formed by the sidewall and the ramp surface. As the shock wave created by the ramp and reflected from the cowl strikes the ramp surface, the low energy flow in the corner separates. The PNS analysis cannot be made to proceed farther due to the magnitude of the separation in the corner. At this last station, the flow is seen to be highly distorted with separation in the lower corners, vortical flow near the sidewalls and thick boundary layers on both the ramp and cowl surfaces."

An alternate visualization of the three-dimensional flow is obtained with particle tracing, as shown in Fig. 4. Computational particles were placed along the sidewall of the inlet. Interaction of the ramp and cowl shocks with the sidewall boundary layer causes the particles to converge near the shock interaction point. The particles are then displaced due to the vortex motion described earlier. Flow migration details are clearly depicted in this computational simulation. Since this vortex phenomenon persists downstream, it is proposed that judicious fuel injector design and placement may lead to enhanced mixing of air and fuel in the combustor.

Computations performed by Rose are shown in Fig. 5 for a rectangular inlet at Mach 5. The

same features shown in the previous inlet are also seen in the Mach 5 inlet, i.e., strong viscous shock effects leading to large regions of vortex flow. Rose carried out a number of numerical experiments to control the vortex phenomena in the corner regions. Figure 6 shows the baseline or no control case, followed by cowl cutback, cowl bleed and removal of a part of the sidewall. These modifications were made near the inlet ramp shoulder. It may be seen that these modifications were ineffective in eliminating the vortex region. Even with the cutback sidewall, the low momentum fluid exits along the entire sidewall. Some attenuation is seen along the cowl surface for that case. It is evident, however, that the shock-boundary layer physics within a rectangular shaped inlet will lead to pressure losses in the corner regions. However, if these regions can be utilized in an "integrated design approach," then combustor/nozzle design may benefit substantially.

#### Improvements Required

At the present time, the design of a low drag highly efficient inlet has not been demonstrated. It must be noted here that the geometries computed are extremely simple and, to a large extent, the computations are concentrated on developing a fundamental understanding of glancing shock/boundary layer behavior within an inlet. The results obtained yield a clear picture of the physics associated with the compression process. Observations on high speed inlets verify that the secondary flow regions do in fact occur, as predicted by the numerical code. So far, therefore, the numerical results provide realistic answers. However, real inlets are more complex in shape, may have movable geometry, will spill flow over a wide Mach number range, will probably include bleed at low Mach number flight and blowing at the higher speeds. In addition, some means for shock control and elimination of buzz and unstart will be required. A design CFD code, then, would require a full three-dimensional, time accurate Navier-Stokes code capable of handling spillage and mass addition or removal. Currently, these individual effects, such as spillage, have been computed for steady inlet flows with simplified geometries.<sup>13</sup> However, incorporation of all of these features into a time accurate computer code will make efficient computations all but impossible. It is worth noting that the simple geometry shown in Fig. 1 was tested and found to exhibit unsteady flow, again stressing the need for a time accurate solver. It is further noted that the issue of dispersive and dissipative errors associated with various time accurate finite-difference numerical schemes with high grid density is only now being rigorously addressed.<sup>14</sup> Proper boundary condition treatment is also necessary to avoid degrading the accuracy of numerical solutions. Pure acoustic radiation boundary conditions do not properly account for the effects of unsteady vortex shedding, disturbance amplification caused by separation and the response due to both vorticity oscillations and entropy waves.<sup>14</sup>

Up to this point, the discussion has centered on the geometric configuration of the inlet. There are also a number of problems associated with understanding the fundamental flow physics and our ability to model them. These physics are associated with the transition of the boundary layer and the nature of the turbulence modeling. Currently, there is no way to determine where the

boundary layer begins to transition from laminar to turbulent, as well as the length of the transition zone. The state of the boundary layer at hypersonic speeds is unknown, and relaminarization may occur in an unpredictable manner. Direct numerical simulation may provide an approach for transition modeling at high speeds.

#### Reacting Flow Code

##### Numerical Schemes

A representative code for the analysis of combustor flow fields is described in Ref. 15. The three-dimensional code employs an implicit finite volume, lower-upper (LU) time marching method to solve the complete Navier-Stokes and species equations in a fully-coupled and efficient manner. The hydrogen-air chemistry model includes nine species and eighteen reaction steps. The code has been demonstrated for normal hydrogen injection into supersonic airstreams for nonreacting flow and also compared to other numerical schemes. The LU code, in its two-dimensional version, incorporates comprehensive real gas property models to account for high temperature flows, and includes finite rate or equilibrium chemistry. The code, RPLUS, is formulated based on eigenvalue upwinding. The scheme has the efficiency and robustness of an implicit scheme, with an operational count comparable to that of an explicit scheme. This feature of the code is of critical importance for three-dimensional calculations of a large system of equations for reacting flows. Vectorization of the code is performed by a reorganization of the indices of the grid points for parallel processing planes.

Now, we consider the case of a simple or crude combustor which utilizes some hydrogen injection from a single or double wall position into a Mach 4 freestream (see Fig. 7). For the purpose of performing computations, we assumed the temperature of the hydrogen was set at 700 K and the airstream at 1300 K. The boundary conditions include no-slip and adiabatic top wall, with gradients of variables in the streamwise direction assumed to be zero. Symmetry boundary conditions are assumed at both side walls and bottom wall. Grid sizes required for resolution of the jet interaction features were on the order of 60 by 40 by 40 (x,y,z) with clustering in both x and z for jet resolution and y clustering for boundary layer resolution. It should be re-emphasized that the case under consideration represents only a small portion of a realistic combustor geometry. In other words, this rather large computation is only a "unit problem" associated with one of the propulsion components. The results obtained with this numerical code and the grid discussed yield a great deal of the physics inherent in the injection process. Observations regarding jet interaction phenomena made over the last 20 years are accurately replicated by the code. It is noted that in the section entitled CFD Validation the ability to capture discontinuities was mentioned as one of the important numerics issues. In that regard, the recent work by Shuen and Liou<sup>16</sup> was directed toward a flux splitting algorithm for viscous flows with nonequilibrium chemistry. Upwind TVD differencing was used with a Roe flux splitting scheme. Nonequilibrium, frozen chemistry and ideal gas assumptions were used in a sample calculation for the single jet injection case described above.

## Computed Combustor Results

Figures 8 and 9 show a typical Mach number and temperature contour on yz planes for various x locations. Yu et al.<sup>15</sup> describe their computations in the following manner, which relates to the important physical/chemical phenomena: "Just behind the injecting orifice, the Mach number contours show a strong bow shock very close to the wall. Under the bow shock, the circular Mach number contour indicates the existence of the barrel shock structures. The jet has been bent and flows almost parallel to the primary flow. The penetration of the jet increases as the flow goes downstream. The shape of the jet also deforms as the flow goes downstream due to the presence of the streamwise vorticity in the lee of the injector. The secondary motion formed by two counter-rotating vortices gives the bent-over jet a kidney shape. In the temperature contour plots, the hottest region is along the wall because of the viscous dissipation in the high speed flow enhanced by the combustion of the H<sub>2</sub> and air. Away from the wall, by comparing the Mach number plots and the temperature plots, it is evident that the temperature increases after the bow shock. Further downstream a thin flame zone characterized by higher temperature is developed. Vigorous chemical reaction occurs in the flame zone." Mach number contours are also shown for the xy plane across the orifice for both the single (Fig. 10) and double jet (Fig. 11) injection computation. Features near the injection orifice(s) indicated the presence of a barrel shock structure. Separation and reattachment features upstream and downstream of the jets are also clearly discernible. In the dual injection case, blockage caused by the first jet allows the second jet to penetrate further into the free-stream due to stronger expansion. This behavior is consistent with the penetration correlation published by Povinelli et al.,<sup>17</sup> in that the free-stream momentum deficit approaching the jet is one of the parameters governing jet penetration.

## Improvements Required

So far, we have shown that for flush, single and dual wall injection, numerical computations provide realistic answers. The results, however, cannot be extended for lengthy downstream distances with the grid resolution obtained around the jets, due to computer limitations. Hopefully, once the jet regions are computed, one could proceed with different, coarser grids downstream. Some of the general flow field property distributions would need to be passed on to the new grid. We must further consider that wall jet penetration is limited in terms of providing fuel distribution in supersonic streams. Flush wall jet penetration is on the order of 10 orifice diameters.<sup>17</sup> For that reason, devices like struts which span the combustor completely<sup>18</sup> or partially<sup>19</sup> are required for distribution of fuel. The numerical codes must, then, be capable of multiple wall and strut injection from many points on the solid surfaces. With partial swept struts, a typical arrangement might include 20 injection ports from the ridge line and trailing edge of each of six struts,<sup>19</sup> as well as selected combustor wall locations of a comparable number. Clearly, our numerical ability to perform this task is not possible. Other approaches to combustor design may be possible. For example, the possibility of enhanced mixing by

the streamwise generation of vorticity has been suggested<sup>20</sup> and addressed in a number of ways.<sup>21,22</sup> Vorticity generation has been found successful for jet engine exhaust flows<sup>23</sup> and is currently under study at many laboratories for supersonic streams. Since most of the generation occurs through an inviscid mechanism,<sup>23</sup> the concept should work equally well in supersonic streams. Since it has been shown in the preceding section, Inlets, that a typical high speed inlet generates vortex flow, this flow phenomenon could be utilized as it passes downstream, to enhance combustor mixing. Vortex-shock interactions<sup>24</sup> and shock-shear layer interactions<sup>25</sup> have also been postulated for the purpose of enhanced mixing. However, these phenomena have so far proven of limited value for the improvement of mixing.

The various phenomena described above are all under continued investigation. Research on "explosive growth" in shear layer stability underway at NASA Lewis<sup>26,27</sup> may provide some assistance in this problem. Regardless of the understanding which will develop over the next few years, the numerical analysis will require extensive computer capabilities to handle the geometries which evolve. It is unlikely that simple combustor geometries will satisfy the requirement for this propulsion system.

So far, we have discussed the combustor geometry to a great extent. There is, however, even a greater problem associated with the fundamental phenomena of turbulent combustion and our ability to model it. Although a great deal of research has been carried out, the nature of the interaction between the fluctuating flow field and the chemical reaction steps or processes is not understood. Simple approaches related to the gross features of relatively ideal burner behavior have been made, such as flame propagation in turbulent mixtures. Those features studied have related to changes in flame speed due to increasing surface area and increasing transport but have not specifically dealt with how the flow field modifies the chemical reaction scheme. The proper modeling of turbulent flow reaction remains as a key requirement for the CFD of combustors.

For turbulent chemical reacting flows, the evaluation of the mean source (or sink) of the chemical species due to chemical reactions represents a major unsolved difficulty. The formation (or destruction) rates are nonlinear functions of temperature and species concentrations and thus knowledge of the mean-valued properties is insufficient to evaluate the mean formation rate. For example, in finite rate chemistry models, the mean formation rate calculated by using the mean-value temperature and species concentration in the Arrhenius form will lead to errors up to three orders of magnitude. Formally, the mean reaction rate could be obtained by decomposing the temperature, density, and mass fractions appearing therein into mean and fluctuating components, then taking the time (or Favre) average. The resulting equations involve many second order moments which need to be solved by extra transport equations or to be modeled. In this approach, the neglect of the correlation greater than second order terms is unsatisfactory and leads to erroneous solutions, while the retention of the higher order term renders the approach intractable.<sup>28</sup>

The most convenient way to circumvent this problem is to use probability density function (pdf) method. About the simplest and most popular approach is to specify a two-parameter form of the pdf in terms of mean and variance of the conserved scalar. The transport equations are readily obtained from the conservation of mass and chemical species. By solving these two equations, the pdf at each location for the whole flowfield can be obtained. Next, if the correlation is known between the conserved scalar and the chemical species concentration (which is usually calculated by equilibrium method), then the distribution of the chemical species concentration can be obtained by performing a straight forward integration. This method strongly couples the turbulence and chemical reactions. However, the choice of the pdf form and the usage of equilibrium assumption inevitably lead to errors in predicted results. There are more complex approaches along the same line, for example, the two-variable formalism adopted by Janicka and Kollmann<sup>29</sup> for the  $H_2$ /air flame. A single combined reaction progress variable was introduced to describe completeness of the three-body reactions while the two-body reactions are assumed to be in equilibrium. Thus the joint pdf for mixture fraction and reaction progress variable is needed to determine the thermochemical state of the flowfield.<sup>28</sup>

### Nozzle CFD Analysis

#### Numerical Schemes

In order to illustrate nozzle CFD capability, a number of numerical schemes may be chosen. Ruffin et al.<sup>30</sup> have used a Reynolds averaged Navier-Stokes solver which contains a LDU-ADI scheme with Roe averaging and MUSCL differencing. The algorithm is diagonal in structure and requires minimal CPU per iteration. Laminar nonreacting computations of a nozzle exhaust flow field were made using two patched grids to model the geometry. The first grid consisted of 20 by 99 by 35 grid points and the second grid contained 51 by 99 by 52 grid points. Baysal et al.<sup>31</sup> used two Navier-Stokes numerical schemes to compute nozzle flows. Both schemes were two-dimensional. One scheme was an implicit, upwind solution and constant  $\gamma$ , the second scheme was an explicit MacCormack and had variable  $\gamma$ . Baldwin-Lomax turbulence modeling was used, and the grid dimensions were 155 by 131. Lai and Nelson<sup>32</sup> used the three-dimensional PARC Navier-Stokes code to compute nonaxisymmetric nozzle flows. The numerical scheme in PARC employs three point central differencing uniformly throughout the flow field to approximate spatial derivatives. Second and fourth order Jameson type artificial dissipation is included. Diagonalization of the inviscid terms simplified the block pentadiagonal system of equations to a scalar pentadiagonal system. The numerical scheme employs an ADI Beam and Warming approximate factorization. In general, the boundary conditions assume mid-plane spanwise symmetry, with no slip velocity and adiabatic wall temperature. For the external far field, quiescent air at normal conditions is assumed and nozzle exit plane conditions are specified. Streamwise flux gradients at the outflow boundary are assumed negligible.

#### Nozzle Results

Three-dimensional laminar computations by Ruffin et al.<sup>30</sup> were made for a flight Mach number

of 7.3. The geometry chosen was that of a corresponding experimental configuration (Fig. 12). The grid zones chosen for the numerical study are shown in Fig. 13. The first grid is used for calculations up to the nozzle exit plane followed by interpolation of data to the second grid. The internal nozzle flow at the exit plane is modeled by specifying boundary layer profiles. The computed Mach number contours in the symmetry plane and the two cross-flow planes are shown in Fig. 14, with the forebody at 0°, afterbody ramp in the nozzle block region at 15°, and the long expansion plate at 20°. A complex interaction may be seen in the plume where the bow shock and the side edge vortex come together. Also, the ramp shock generated on the windward ramp causes high pressure flow to move to the leeward region. Figure 15 shows the predicted particle traces on the ramp expansion surface. In the words of Ruffin, the results are discussed in terms of the physical processes taking place: "Figure 15 (original in color) allows the identification of several flow features near the body surface. The turning of the oil traces corresponds to turning of the high pressure flow from the side edge of the ramp and above the nozzle block toward the low pressure expanded flow above the ramp. Other traces converge onto the separation line of a vortex near the side edge of the ramp. Additional traces correspond to a separation bubble at the location just after the ramp angle transitions from 15° to 20°. Finally, the footprint of the shear layer is shown by the particle traces near the far edge of the ramp. It should be noted that the predicted separation that occurs on the ramp may be induced by the assumption of laminar flow. This feature may not be present in the experimental flow field, which will be turbulent." It is noted here that Ruffin's computations were carried out in order to provide information relative to the design of a nozzle validation experiment. The proposed experimental model is fairly simple relative to an exhaust module of a NASP type vehicle. In spite of the simplicity of the model, the computed results very clearly point out the complexity of flow patterns that arise under these conditions.

In an effort to provide better definition of the nozzle flow field features, use of adaptive gridding has been studied by Hsu.<sup>33</sup> Figure 16 shows the Mach number contours and grid using a regular grid (Fig. 16(a) and (b)) and using an adaptive grid (Fig. 16(c) and (d)). These computations were carried out on a simple nozzle shape using a 81 by 201 regular grid. Grid adaption was carried out in the y direction only in the region above the cowl. Figure 16 shows that the use of adaptive grid yields a sharper shock and thinner boundary layer as well as diminishing the large region of shock induced boundary layer separation where the shock intersects the upper wall.

Baysal<sup>31</sup> also used adaptive gridding to compute the straight wall nozzle shown in Fig. 17. Again, the model is a fairly simple representation of scramjet nozzle and afterbody. Results with the implicit code are shown in Fig. 18, for nonreacting air from the nozzle and an external Mach number of 6. The nozzle/external pressure ratio was approximately 5. The shear layer can be seen originating at the cowl tip with an expansion, and it is deflected upwards at about 13°. Flow expansion proceeds down the ramp without separation. Computed values of the surface pressure on ramp

nonexistent modeling for reacting separated flow. Numerical prediction of the state of the boundary layer is also not feasible. In addition, accurate heat transfer computations for the nozzle wall have yet to be demonstrated over the range of operating conditions. In closing, it is important to note that real gas and thermal and chemical non-equilibrium effects must be considered in all of the propulsion system components at the appropriate flight conditions.

Advances in two other areas are required. The first advance involves the further development of accurate and efficient numerical methods required to improve solution accuracy with an attendant reduction in computing time. The second advance relates to computer technology and includes issues of speed, storage, structure and graphics.

It is not the intent of this paper to present the opinion that a realistic computer simulation for a hypersonic vehicle poses an impossible task. Rather the intent is to assess, in as realistic a fashion as possible, what is achievable with today's knowledge, numerical codes and computers. The progress in these areas has been remarkable over the last decade and will continue to be so in the future. It is with this understanding that this author is confident that a complete simulation over the entire flight range will be possible someday. However, the progression of the simulations to the point where design type information can be obtained, such as described earlier (Propulsion CFD Validation section), can only occur if the validation process is carried forward with more realistic propulsion geometries.

#### References

1. Dwyer, D.L., Kutler, P., and Povinelli, L.A., "Retooling CFD for Hypersonic Aircraft," Aerospace America, Vol. 25, Oct. 1987, pp. 32-35, 41.
2. Benson, T.J., "Three-Dimensional Viscous Calculation of Flow in a Mach 5.0 Hypersonic Inlet," AIAA Paper 86-1461, June 1986.
3. Kunik, W.G., Benson, T.J., Ng, W.-F., and Taylor, A., "Two- and Three-Dimensional Viscous Computations of a Hypersonic Inlet Flow," AIAA Paper 87-0283, Jan. 1987.
4. Reddy, D.R., Smith, G.E., Liou, M.-F., and Benson, T.J., "Three Dimensional Viscous Analysis of a Hypersonic Inlet," AIAA Paper 89-0004, Jan. 1989. (See also NASA TM-101474.)
5. Kim, Y.N., Buggeln, R.C., and McDonald H., "Numerical Analysis of Some Supersonic Viscous Flows Related to Inlet and Nozzle Systems," AIAA Paper 86-1597, June 1986.
6. Beam, R.M., and Warming, R.F., "An Implicit Factored Scheme for the Compressible Navier-Stokes Equations," AIAA Journal, Vol. 16, No. 4, April 1978, pp. 393-402.
7. Jameson, A., and Baker, T.J., "Solution of the Euler Equations for Complex Configurations," AIAA Paper 83-1929, July 1983. (See also Computational Fluid Dynamics, 6th, New York, AIAA, pp. 293-302.)
8. Pulliam, T.H., and Steger, J.L., "Implicit Finite-Difference Simulations of Three-Dimensional Compressible Flow," AIAA Journal, Vol. 18, No. 2, Feb. 1980, pp. 159-167.
9. Cooper, G.K., Jordan, J.L., and Phares, W.J., "Analysis Tool for Application to Ground Testing of Highly Underexpanded Nozzles," AIAA Paper 87-2015, July 1987.
10. Liou, M.-F., "Three Dimensional PNS Solutions of Hypersonic Internal Flows with Equilibrium Chemistry," AIAA Paper 89-0002, Jan. 1989.
11. Yu, S.-T., McBride, B.J., Hsieh, K.-C., and Shuen, J.-S., "Numerical Simulation of Hypersonic Inlet Flows with Equilibrium or Finite Rate Chemistry," AIAA Paper 88-0273, Jan. 1988.
12. Rose, W.C., and Perkins, E.W., "Innovative Boundary Layer Control Methods in High Speed Inlet Systems-Final Report," Contract NAS3-25408, Sept. 9, 1988. (NASA CR in publication.)
13. Narayan, J., and Kumar, A., "A Numerical Study of Hypersonic Propulsion/Airframe Integration Problem," AIAA Paper 89-0030, Jan. 1989.
14. Hsieh, K.-C., "An Assessment of Numerical Techniques for Unsteady Flow Calculations," AIAA CFD Conference, Buffalo, New York, June 1989.
15. Yu, S.-T., Tsai, and Shuen, J.-S., "Three-Dimensional Solution of Subsonic Reacting Flows with Finite Rate Chemistry," AIAA Paper 89-0391, Jan. 1989.
16. Shuen, J.-S. and Liou, M.-S., "Flux Splitting Algorithms for Two-Dimensional Real Gas Flows," AIAA Paper 89-0388, Jan. 1989.
17. Povinelli, F.P., and Povinelli, L.A., "Correlation of Secondary Sonic and Supersonic Gaseous Jet Penetration into Supersonic Crossflows," NASA TN-D-6370, June 1971.
18. Anderson, G.Y., and Gooderum, P.B., "Exploratory Tests of Two Strut Fuel Injectors for Supersonic Combustion," NASA TN-D-7581, Feb. 1974.
19. Povinelli, L.A., "Aerodynamic Drag and Fuel Spreading Measurements in a Simulated Scramjet Combustion Module," NASA TN-D-7674, May 1974.
20. Povinelli, L.A., Povinelli, F.P.; and Hersch, M., "A Study of Helium Penetration and Spreading in a Mach 2 Airstream Using a Delta Wing Injector," NASA TN-D-5322, July 1969.
21. Hersch, M., and Povinelli, L.A., "Effect of Interacting Vortices on Jet Penetration into a Supersonic Stream," NASA TM-X-2134, Nov. 1970.
22. Marble, F.E., Hendricks, G.J., and Zukoski, E.E., "Progress Toward Shock Enhancement of Supersonic Combustion Processes," AIAA Paper 87-1880, June 1987.
23. Povinelli, L.A., and Anderson, B.H., "Investigation of Mixing in a Turbofan Exhaust Duct, Part II: Computer Code Application and Verification," AIAA Journal, Vol. 22, No. 4, April 1984, pp. 518-525.

show good agreement with measured data, Fig. 19. The next calculation by Baysal<sup>31</sup> was carried out with the explicit code mentioned in the section Numerical Schemes, which included variable  $\gamma$ . The exhaust gas used was 50 percent F-12 and 50 percent argon; the free stream Mach number was 6. Density comparisons are shown in Fig. 20 and pressure contours in Fig. 19. The expansion process proceeds downstream and the shear layer deflects upwards at about 15°. The density is higher in the shear core, expanding back to its upstream value. Separation on the external cowl surface occurs, extending a significant distance upstream.

The computations of Lai and Nelson<sup>32</sup> were carried out for the nozzle experimental geometry of Re and Leavitt.<sup>34</sup> The geometry is shown in Fig. 21, and the nozzle exhaust grids used are shown in Fig. 22. The spanwise grid distribution is shown in Fig. 23. A three-dimensional computation was carried out matching the nozzle operating conditions which exhaust into still air. Streamwise contours for Mach number are shown at four different spanwise positions in Fig. 24. Figure 24(a) shows the contours at the nozzle mid-plane, and Figs. 24(b) to (d) move progressively outward to the nozzle sidewall. Behavior of the shear layer formed on the three-dimensional surface of the jet is clearly evident, as one scans Figs. 24 and 25 which are the cross-sectional planes in the x or downstream direction. The shear layer is observed to be highly three-dimensional in its structure with significant variations from top wall to bottom wall to side wall. Comparisons of the computed wall pressure with experimental data, Fig. 26, show good agreement for both surfaces.

#### Improvements Required

In all of the cases described so far, the nozzle entrance flow field was uniform and nonreacting. In a scramjet module, the combustor and nozzle are very closely coupled which means that nonuniformities in temperature, pressure and species concentration will be present at the nozzle entrance. The sensitivity of the nozzle configuration to these nonuniformities has been a matter of debate for some time. It has been proposed by this author that three-dimensional reacting nonuniform profiles should be used in CFD codes to determine the performance sensitivity of the nozzle. In this way, it would be possible to determine what profiles are desirable at the nozzle entrance for high performance. The knowledge of those profiles would provide combustor designers with "targets" or goals to achieve at the combustor exit plane in terms of pressure, temperature and concentrations. A start on providing an answer to this approach has been initiated by Tsai and Yu<sup>35</sup> who performed three-dimensional Navier-Stokes computations for a reacting hydrogen-air mixture as well as for frozen flow. Using a numerical scheme based on the LU approach of Yoon and Jameson,<sup>36</sup> pressure, temperature and Mach number distributions for both flow solutions have been compared as well as the OH, O and H mass fraction distributions. Calculation of the relative nozzle thrusts in a typical non axisymmetric configuration is still required in order to support the proposal made by this author. The ability to compute multi-exhaust modules integrated into a realistic aftbody with reacting flow exhaust over a wide Mach number range has not yet been demonstrated.

Flow separation at transonic speeds will cause significant drag losses. To date, no realistic simulation of the transonic regime has been performed. Separation of the external cowl boundary layer and incorporation of means to prevent the separation also have not been simulated. Prevention methods could include burning or deployment of a wall section such as in the aftbody. As in the other components, turbulence and transition modeling remain as significant unknowns. Relaminarization of the aftbody boundary layer is also a phenomenon which could occur. Heat transfer to the aftbody is also a computational issue which requires a significant amount of attention.

#### Conclusions

Based on the results presented in this paper, it is evident that there are many portions or features of a hypersonic propulsion system that have not been properly or accurately simulated by numerical analyses. The inlet behavior and its performance for both steady and unsteady operation have been computed for fairly simple geometries, and none of the computations incorporates all of the physics which are known to occur. The design of a high efficiency supersonic inlet, designed for a relatively narrow Mach number range, is not a simple design matter. High recovery, reduced heat load, proper cowl lip design and low spillage drag are all required while delivering usable exit profile conditions to the combustor. In the spirit of a totally integrated propulsion system design, the features of the inlet flow field must be considered as part of the combustor/nozzle design. Some thoughts on the utilization of inlet flow features for combustor design were presented in this paper. It is noted, finally, that unsteady inlet behavior with mass addition and flow spillage must be properly simulated by numerical methods in order to establish a reliable design.

In the combustor region, it is clear that only crude design features have been modeled and computed. Realistic geometries, incorporating struts, wedges and wall injection must be computed in order to provide any design benefits. Aside from the additional geometric complexity needed, the fundamental nature of turbulence-combustion interaction remains as a major unknown. The proper modeling of the unsteady flow field, both random and deterministic, with the combustion chemistry remains a major challenge. PDF modeling appears to be one of the promising avenues to pursue in this regard.

Nozzle flows are characterized by intricate patterns of shock waves and shear layers. The asymmetry of the nozzle, combined with the shear layer position, reflect the shocks in various directions. Shear layer bending occurs at the shock intersection locations. The shape and structure of these features vary considerably over the flight Mach number range with the attendant changes in nozzle back pressure. Much remaining work needs to be performed on the expansion of reacting gases with properly modeled entrance profiles of both flow stream aero properties and concentration profiles. It has been suggested in this paper that the efficient design of a hypersonic nozzle should proceed by exploring the best profiles for optimum nozzle performance. Those profiles then provide a goal for combustor exit conditions. Further deficiencies in the nozzle area are associated with



nonexistent modeling for reacting separated flow. Numerical prediction of the state of the boundary layer is also not feasible. In addition, accurate heat transfer computations for the nozzle wall have yet to be demonstrated over the range of operating conditions. In closing, it is important to note that real gas and thermal and chemical non-equilibrium effects must be considered in all of the propulsion system components at the appropriate flight conditions.

Advances in two other areas are required. The first advance involves the further development of accurate and efficient numerical methods required to improve solution accuracy with an attendant reduction in computing time. The second advance relates to computer technology and includes issues of speed, storage, structure and graphics.

It is not the intent of this paper to present the opinion that a realistic computer simulation for a hypersonic vehicle poses an impossible task. Rather the intent is to assess, in as realistic a fashion as possible, what is achievable with today's knowledge, numerical codes and computers. The progress in these areas has been remarkable over the last decade and will continue to be so in the future. It is with this understanding that this author is confident that a complete simulation over the entire flight range will be possible someday. However, the progression of the simulations to the point where design type information can be obtained, such as described earlier (Propulsion CFD Validation section), can only occur if the validation process is carried forward with more realistic propulsion geometries.

#### References

1. Dwyer, D.L., Kutler, P., and Povinelli, L.A., "Retooling CFD for Hypersonic Aircraft," *Aerospace America*, Vol. 25, Oct. 1987, pp. 32-35, 41.
2. Benson, T.J., "Three-Dimensional Viscous Calculation of Flow in a Mach 5.0 Hypersonic Inlet," AIAA Paper 86-1461, June 1986.
3. Kunik, W.G., Benson, T.J., Ng, W.-F., and Taylor, A., "Two- and Three-Dimensional Viscous Computations of a Hypersonic Inlet Flow," AIAA Paper 87-0283, Jan. 1987.
4. Reddy, D.R., Smith, G.E., Liou, M.-F., and Benson, T.J., "Three Dimensional Viscous Analysis of a Hypersonic Inlet," AIAA Paper 89-0004, Jan. 1989. (See also NASA TM-101474.)
5. Kim, Y.N., Buggeln, R.C., and McDonald H., "Numerical Analysis of Some Supersonic Viscous Flows Related to Inlet and Nozzle Systems," AIAA Paper 86-1597, June 1986.
6. Beam, R.M., and Warming, R.F., "An Implicit Factored Scheme for the Compressible Navier-Stokes Equations," *AIAA Journal*, Vol. 16, No. 4, April 1978, pp. 393-402.
7. Jameson, A., and Baker, T.J., "Solution of the Euler Equations for Complex Configurations," AIAA Paper 83-1929, July 1983. (See also *Computational Fluid Dynamics*, 6th, New York, AIAA, pp. 293-302.)
8. Pulliam, T.H., and Steger, J.L., "Implicit Finite-Difference Simulations of Three-Dimensional Compressible Flow," *AIAA Journal*, Vol. 18, No. 2, Feb. 1980, pp. 159-167.
9. Cooper, G.K., Jordan, J.L., and Phares, W.J., "Analysis Tool for Application to Ground Testing of Highly Underexpanded Nozzles," AIAA Paper 87-2015, July 1987.
10. Liou, M.-F., "Three Dimensional PNS Solutions of Hypersonic Internal Flows with Equilibrium Chemistry," AIAA Paper 89-0002, Jan. 1989.
11. Yu, S.-T., McBride, B.J., Hsieh, K.-C., and Shuen, J.-S., "Numerical Simulation of Hypersonic Inlet Flows with Equilibrium or Finite Rate Chemistry," AIAA Paper 88-0273, Jan. 1988.
12. Rose, M.C., and Perkins, E.H., "Innovative Boundary Layer Control Methods in High Speed Inlet Systems-Final Report," Contract NAS3-25408, Sept. 9, 1988. (NASA CR in publication.)
13. Narayan, J., and Kumar, A., "A Numerical Study of Hypersonic Propulsion/Airframe Integration Problem," AIAA Paper 89-0030, Jan. 1989.
14. Hsieh, K.-C., "An Assessment of Numerical Techniques for Unsteady Flow Calculations," AIAA CFD Conference, Buffalo, New York, June 1989.
15. Yu, S.-T., Tsai, and Shuen, J.-S., "Three-Dimensional Solution of Subsonic Reacting Flows with Finite Rate Chemistry," AIAA Paper 89-0391, Jan. 1989.
16. Shuen, J.-S. and Liou, M.-S., "Flux Splitting Algorithms for Two-Dimensional Real Gas Flows," AIAA Paper 89-0388, Jan. 1989.
17. Povinelli, F.P., and Povinelli, L.A., "Correlation of Secondary Sonic and Supersonic Gaseous Jet Penetration into Supersonic Crossflows," NASA TN-D-6370, June 1971.
18. Anderson, G.Y., and Gooderum, P.B., "Exploratory Tests of Two Strut Fuel Injectors for Supersonic Combustion," NASA TN-D-7581, Feb. 1974.
19. Povinelli, L.A., "Aerodynamic Drag and Fuel Spreading Measurements in a Simulated Scramjet Combustion Module," NASA TN-D-7674, May 1974.
20. Povinelli, L.A., Povinelli, F.P.; and Hersch, M., "A Study of Helium Penetration and Spreading in a Mach 2 Airstream Using a Delta Wing Injector," NASA TN-D-5322, July 1969.
21. Hersch, M., and Povinelli, L.A., "Effect of Interacting Vortices on Jet Penetration into a Supersonic Stream," NASA TM-X-2134, Nov. 1970.
22. Marble, F.E., Hendricks, G.J., and Zukoski, E.E., "Progress Toward Shock Enhancement of Supersonic Combustion Processes," AIAA Paper 87-1880, June 1987.
23. Povinelli, L.A., and Anderson, B.H., "Investigation of Mixing in a Turbofan Exhaust Duct, Part II: Computer Code Application and Verification," *AIAA Journal*, Vol. 22, No. 4, April 1984, pp. 518-525.



24. Povinelli, L.A., and Ehlers, R.C., "Swirling Base Injection for Supersonic Combustion Ram-jets," AIAA Journal, Vol. 10, No. 9, Sept. 1972, pp. 1243-1244.

25. Menon, S., "Shock Wave-Induced Enhanced Mixing in Scramjet Combustor," AIAA Paper 89-0104, Jan. 1989.

26. Goldstein, M.E., and Lieb, S.J., "Non-Linear Evolution of Oblique Waves on Compressible Shear Layers," Journal of Fluid Mechs., to be published in 1989.

27. Balsa, T.F., and Goldstein, M.E., "On the Instabilities of Supersonic Mixing Layers: A High Mach Number Asymptotic Theory," Journal of Fluid Mechs., to be published in 1989.

28. Yu, Sheng-Tao, personal communication, NASA Lewis Research Center, Cleveland, OH.

29. Janicka, J., and Kollmann, W., "A Prediction Model for Turbulent Diffusion Flames Including NO-Formation," Combustor Modelling--AGARD-CP-275, 1980.

30. Ruffin, S.M., Venkatopathy, E., Keener, E.R., and Nagaraj, N., "Computational Design Aspects of a NASP Nozzle/Afterbody Experiment," AIAA Paper 89-0446, Jan. 1989.

31. Baysal, O., Engelund, W.C., Eleshaky, M.E., and Pittman, J.L., "Adaptive Computations of Viscous Scramjet-Afterbody Flows With and Without Multi-species," AIAA Paper 89-0009, Jan. 1989.

32. Lai, H., and Nelson, E., "Comparison of 3D Computation and Experiment for Non-Axisymmetric Nozzles," AIAA Paper 89-0007, Jan. 1989.

33. Hsu, A.T., "The Effect of Adaptive Grid on Hypersonic Nozzle Flow Calculations," AIAA Paper 89-0006, Jan. 1989.

34. Re, R.J., and Leavitt, D.L., "Static Internal Performance of Single-Expansion-Ramp Nozzles with Various Combinations of Internal Geometric Parameters," NASA TM-86270, Dec. 1984.

35. Tsai, Y.-L.P., and Yu, S.-T., "Chemically Reacting Flow Calculations for Nozzles Using an LU Scheme in Three Dimensions," AIAA/ASME/SAE/ASEE 25th Joint Propulsion Conference, July 1989.

36. Yoon, S., and Jameson, A., "An LU-SSOR Scheme for the Euler and Navier-Stokes Equations," AIAA Paper 87-0600, Jan. 1987.

Table 1. - Forebody Requirements

Performance parameters
Lift
Drag
Heat load
Inlet profiles
Computed variables required
Pressure
Skin friction
Heat transfer
Inlet profiles (u,v,w,p,T,C <sub>i</sub> )
Integrals for performance
Physical/chemical modeling requirements
Transition
Turbulence
Shock boundary layer interactions
Vortical flow
Entropy layer swallowing
Equilibrium, nonequilibrium chemistry
Wall catalyticity
Low density flow

Table 3. - Combustor Requirements

Performance parameters
Thrust
Heat load
Combustion efficiency
Pressure losses
Structural load
Computed variables required
Wall pressure
Heat transfer
Skin friction
Exit profiles (u,v,w,T,C <sub>i</sub> )
Physical/chemical modeling requirements
Finite rate chemistry
Shock interactions
Shear layers
Vortex/shock interactions
Heat transfer
Injector interactions
Turbulence

Table 2. - Inlet Requirements

Performance parameters
Mass capture
Kinetic energy efficiency
Pressure recovery
Heat load
Exit profiles to combustor
Computed variables required
Wall pressure
Skin friction
Heat transfer
Exit profiles (u,v,w,T,C <sub>i</sub> )
Physical/chemical modeling requirements
Shock boundary layer interactions
Secondary/corner flows
Mass injection
Low Mach number bleed
Flow separation
Shock induced unsteadiness
Turbulence, transition
Equilibrium chemistry
Flow unsteadiness

Table 4. - Nozzle Requirements

Performance parameters
Thrust
Moment
Heat load
Computed variables required
Wall pressure
Heat transfer
Skin friction
Physical/chemical modeling requirements
Finite rate chemistry
Turbulence
Shock interactions
Shear layers
Secondary flows
Separation
Relaminarization

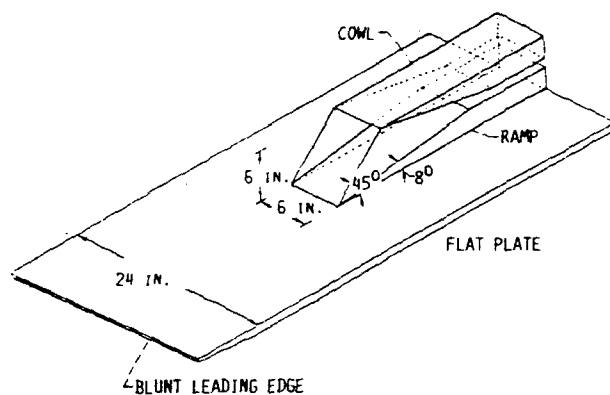


FIGURE 1. - EXPERIMENTAL MACH 12 INLET GEOMETRY (REF. 4).

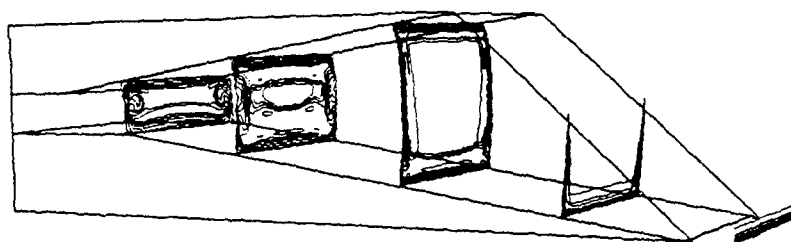
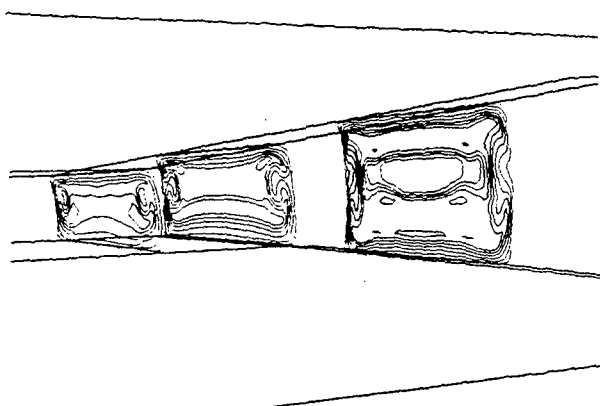
FIGURE 2. - MACH NUMBER CONTOURS,  $M = 12.25$  (REF. 4).

FIGURE 3. - MACH NUMBER CONTOURS VIEWED FROM AFT (REF. 4).

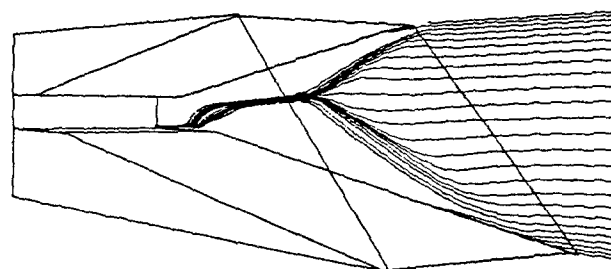
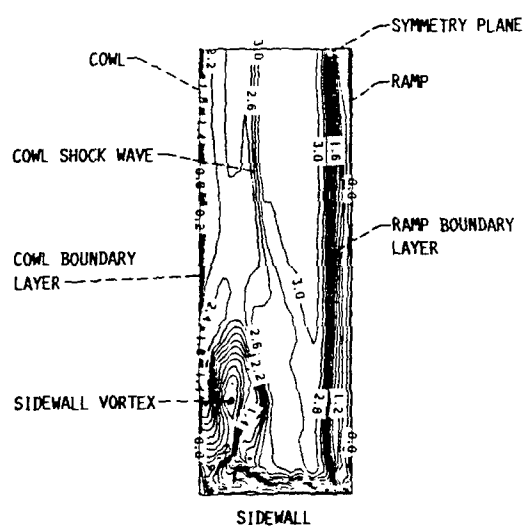
FIGURE 4. - SIDEWALL PARTICLE TRACING,  $M = 12.25$  (REF. 4).

FIGURE 5. - ORIENTATION OF CROSSFLOW PLANE 150 LOCATED NEAR THE RAMP SHOULDER SHOWING PLANE OF SYMMETRY, SIDEWALL RAMP AND COWL SURFACES (REF. 12).

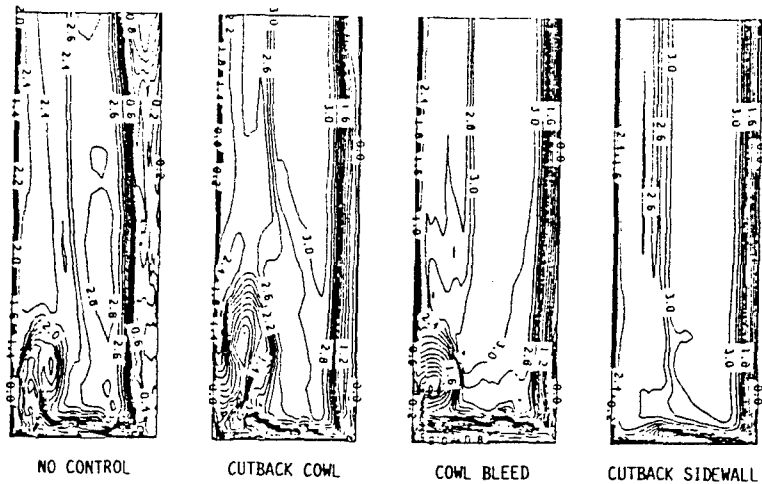


FIGURE 6. - COMPARISON OF EFFECT OF VARIOUS CONTROL METHODS ON MACH NUMBER CONTOURS NEAR RAMP SHOULDER (REF. 12).

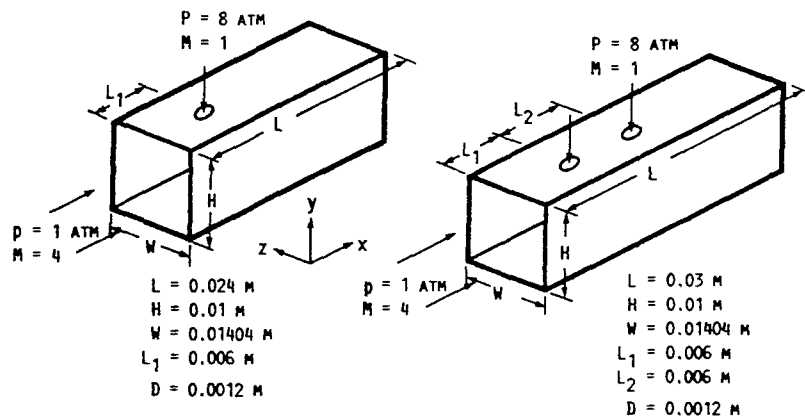


FIGURE 7. - FLOW CONFIGURATIONS (REF. 15).

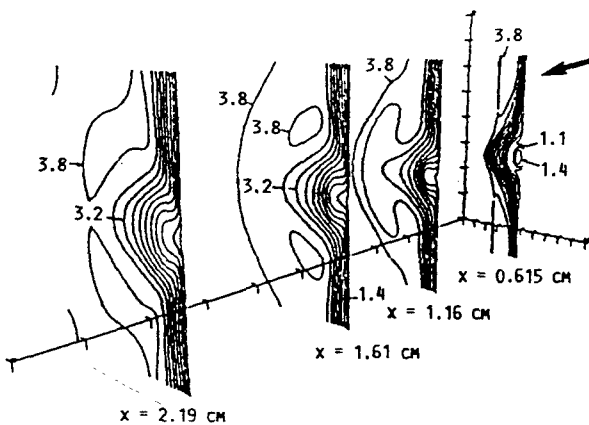


FIGURE 8. - MACH NUMBER CONTOURS ON yz PLANES AT VARIOUS x LOCATIONS FOR CASE 1 (REF. 15).

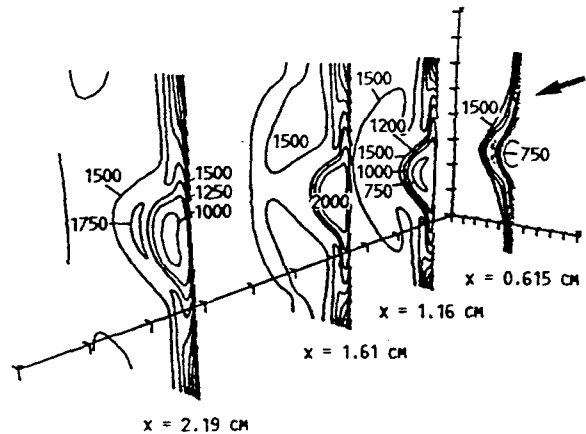


FIGURE 9. - TEMPERATURE CONTOURS ON yz PLANES AT VARIOUS x LOCATIONS FOR CASE 1 (REF. 15).

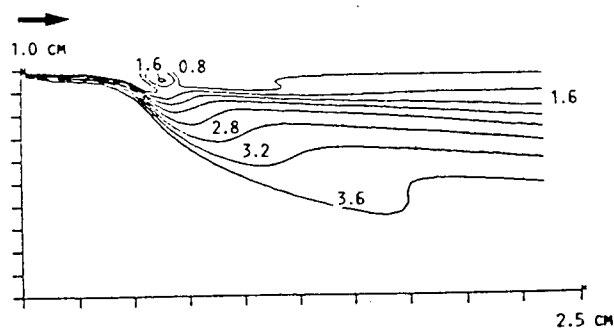


FIGURE 10. - MACH NUMBER CONTOUR ON xy PLANE AT CENTER OF INJECTION PORT FOR CASE 1 (REF. 15).

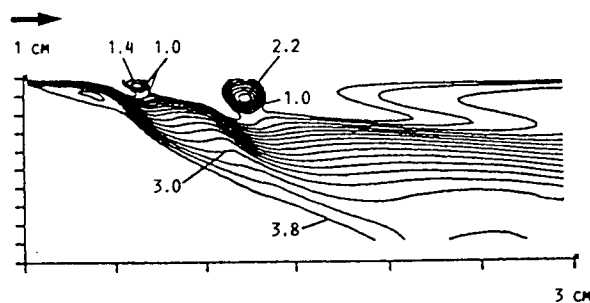


FIGURE 11. - MACH NUMBER CONTOUR ON xy PLANE AT CENTER OF INJECTION PORT FOR CASE 2 (REF. 15).

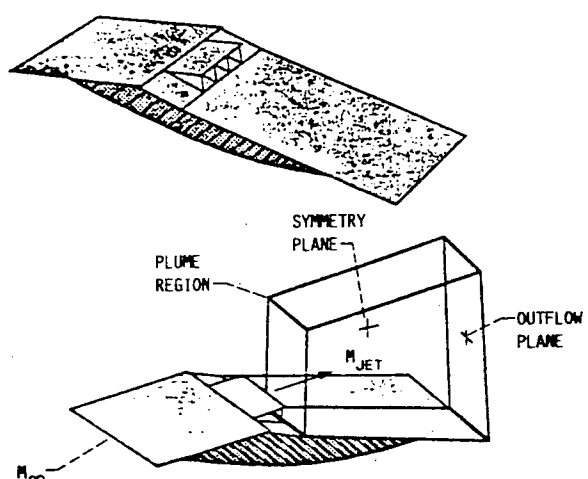


FIGURE 12. - SCHEMATIC OF EXPERIMENTAL MODEL, PERSPECTIVE VIEWS (REF. 30).

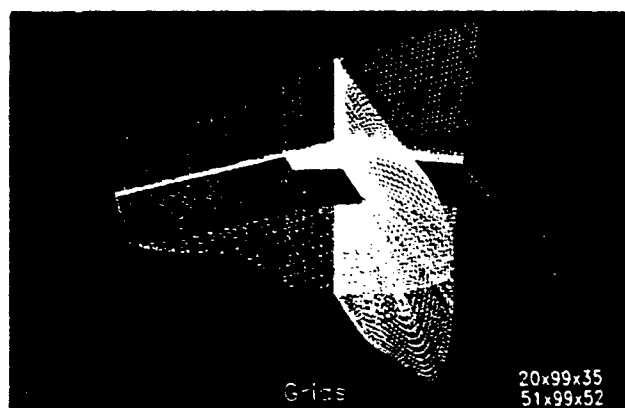


FIGURE 13. - GRID SYSTEM PERSPECTIVE VIEW FOR 3-D COMPLETE GEOMETRY CALCULATION, CASE-1,  $\alpha_f = 20^\circ$  (REF. 30).

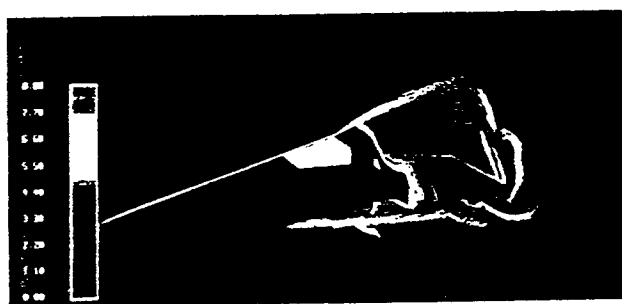


FIGURE 14. - MACH CONTOUR PERSPECTIVE VIEW FOR 3-D COMPLETE GEOMETRY CALCULATION, CASE-1,  $\alpha_f = 20^\circ$  (REF. 30).

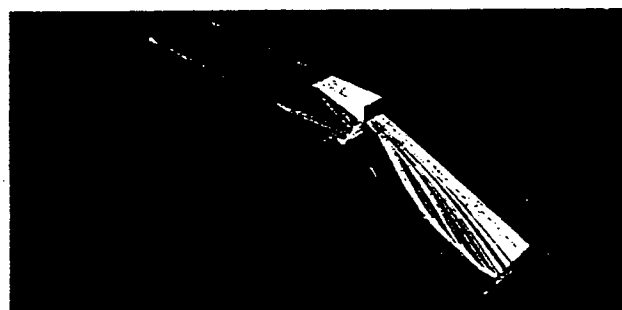


FIGURE 15. - SIMULATED SURFACE OIL FLOW FOR 3-D COMPLETE GEOMETRY CALCULATION, CASE-1,  $\alpha_f = 20^\circ$  (REF. 30).

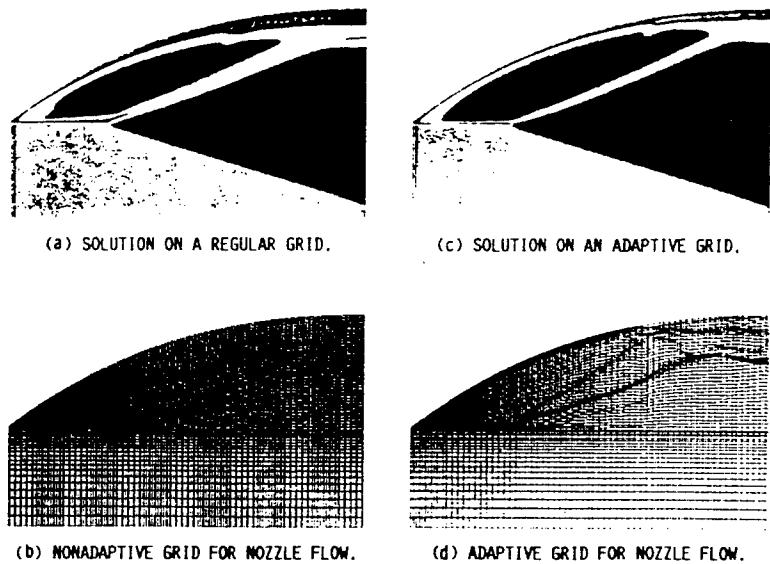


FIGURE 16. - MACH NUMBER CONTOURS AND GRIDS FOR A SCRAMJET NOZZLE (REF. 33).

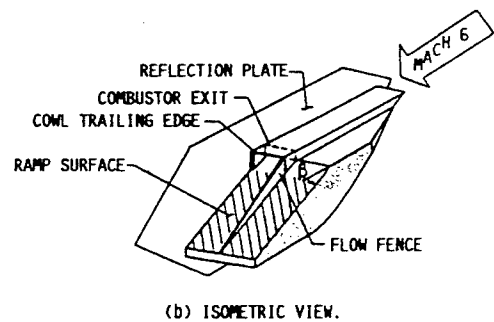
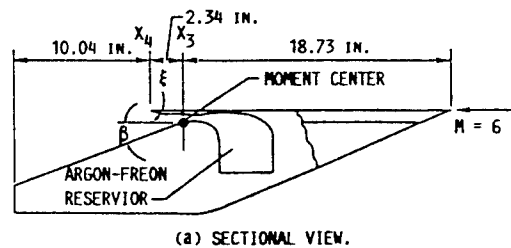


FIGURE 17. - MODEL OF AFTERBODY WITH SCRAMJET EXHAUST SIMULATION (REF. 31).

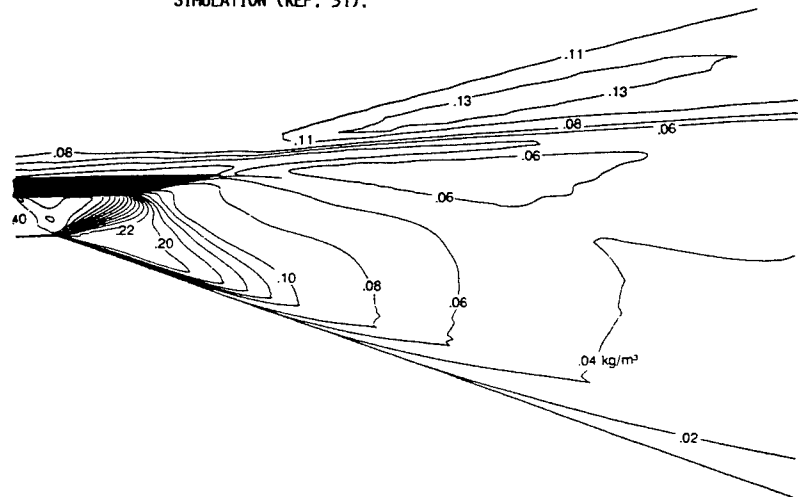


FIGURE 18. - DENSITY CONTOURS FOR CASE 2 (REF. 31).

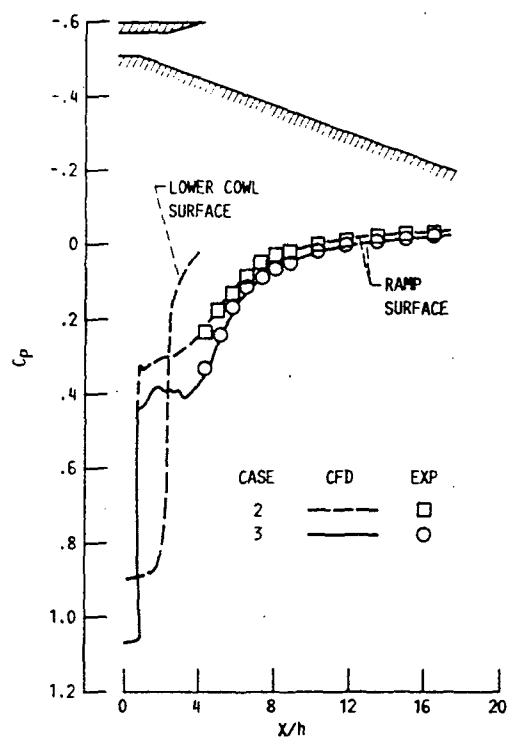


FIGURE 19. - PRESSURE COEFFICIENT DISTRIBUTIONS ON RAMP AND LOWER COWL SURFACES (REF. 31).

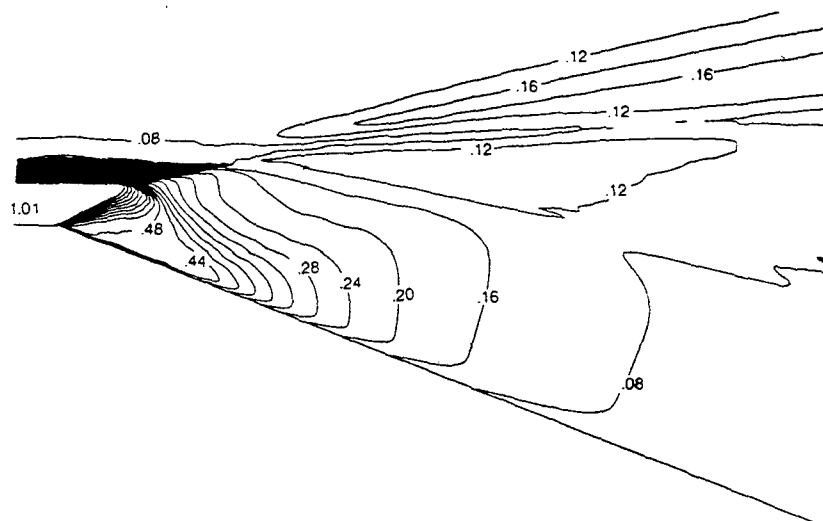


FIGURE 20. - DENSITY CONTOURS FOR CASE 3 (REF. 31).

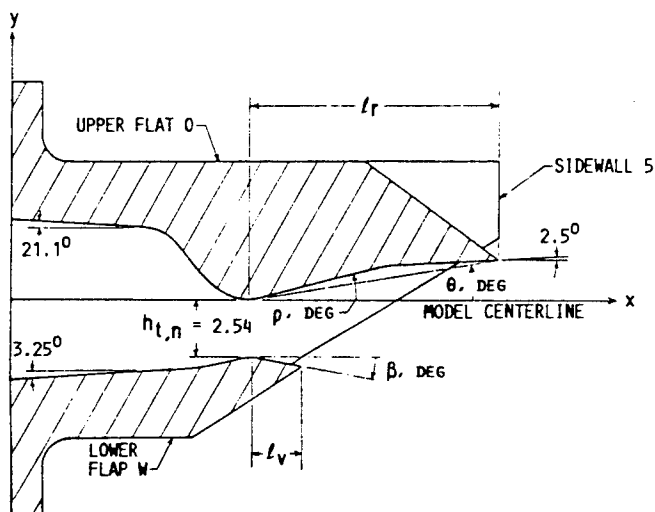
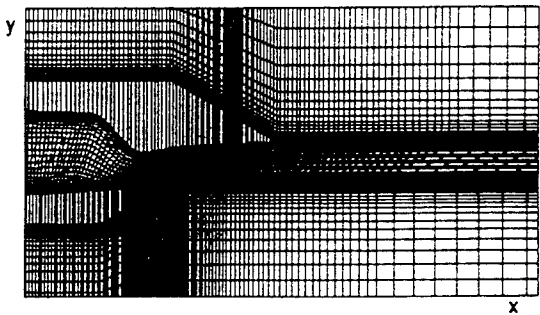
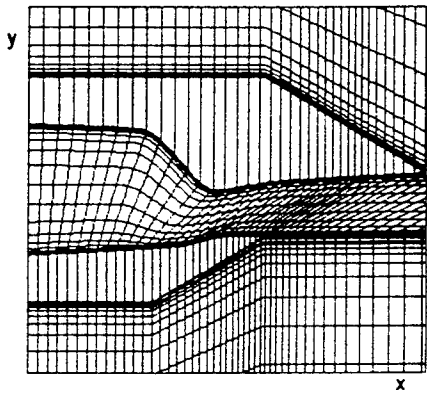


FIGURE 21. - NOZZLE GEOMETRY (REF. 32).

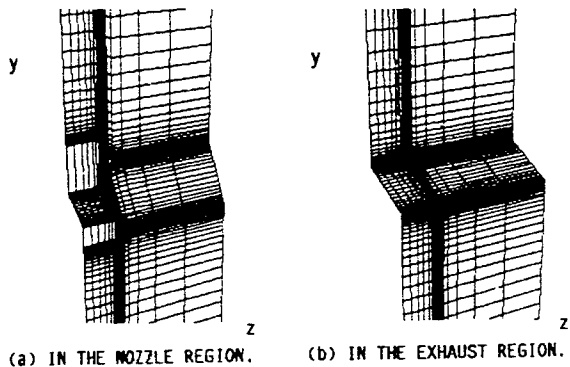


(a) NOZZLE AND EXHAUST GRID.



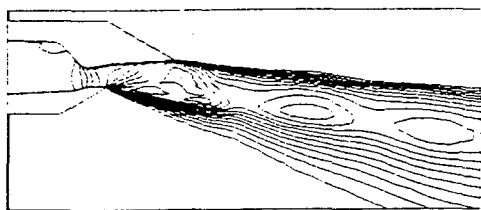
(b) NOZZLE GRID.

FIGURE 22. - STREAMWISE GRID DISTRIBUTION (REF. 32).

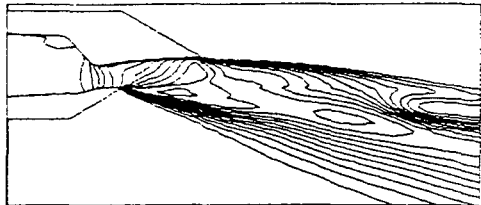


(a) IN THE NOZZLE REGION. (b) IN THE EXHAUST REGION.

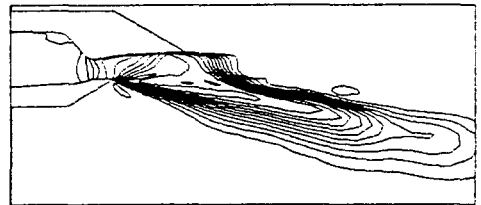
FIGURE 23. - SPANWISE GRID DISTRIBUTION (REF. 32).



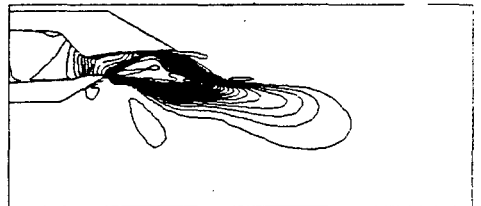
(a)  $i = 1, z = 0$ .



(b)  $i = 9, z = 1.365$ .

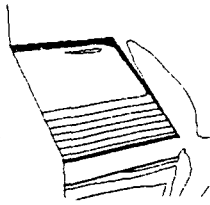


(c)  $i = 13, z = 1.7$ .

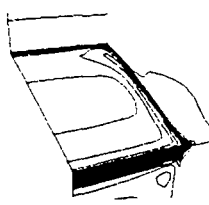


(d)  $i = 25, z = 1.982$ .

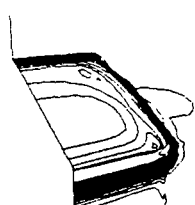
FIGURE 24. - STREAMWISE MACH NUMBER CONTOURS, CASE 1 (REF. 32).



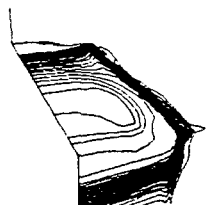
(a)  $i = 50, x = 4.485$ .



(b)  $i = 65, x = 5.372$ .

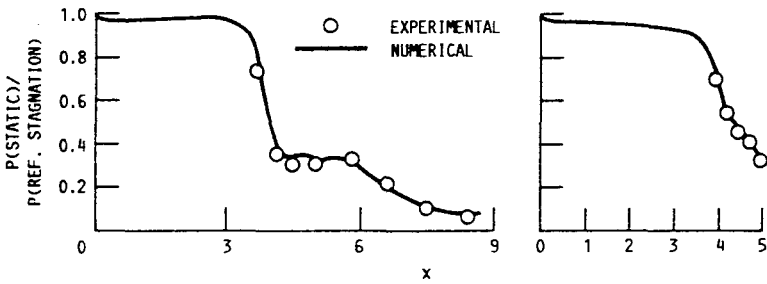


(c)  $i = 75, x = 6.221$ .



(d)  $i = 85, x = 7.513$ .

FIGURE 25. - SPANWISE MACH NUMBER CONTOURS, CASE 1 (REF. 32).



(a) UPPER WALL. (b) LOWER WALL.  
FIGURE 26. - WALL PRESSURE DISTRIBUTIONS, CASE 1 (REF. 32).



# Missile Aerothermodynamics and Propulsion Integration

D. Pagan and R.-G. Lacau

AEROSPATIALE - Missiles

2 rue Béranger, 92322 Châtillon Cedex, France

## SUMMARY

This lecture provides a general review of aerothermodynamics and propulsion integration of supersonic and hypersonic missiles. We focus on the major design problems and the simulation means with their potentials and deficits. Considered design problems are external aerothermodynamics, including the specific problem of lateral jet control, and the ramjet/scramjet propulsion integration. Simulation means cover Computational Fluid Dynamics (CFD) tools as well as ground test facilities. The last part of the lecture illustrates the feasibility to use CFD tools in the design process as a complementary approach to wind tunnels, propulsion benches and flight tests.

## 1. INTRODUCTION

Forecast studies<sup>1</sup> show that the current decline in world defence spending will bottom out in the next few years so far as missiles are concerned, and generally rise in the 1997-2002 period. There are two main reasons for that :

- world is unlikely to remain as peaceful as it was during the cold war years and regional turmoil will tend to hasten missile purchases,
- general defence budget in many regions and especially in Nato will induce a general trend towards modernisation of major platforms rather than platform replacement, and missiles offer to increase the combat capabilities of many weapons without the need for the expense of replacing the system itself.

Generally missiles are divided into mission oriented categories : air defence, air-to-air, air-to-surface, antiship, antitank and surface-to-surface missiles.

On figure 1 are plotted the geometries of some high speed missiles. The large diversity in the geometries is a difficulty for aerodynamic conception.

The aim of this lecture is to provide a review of high speed missile aerothermodynamics. We will first show high velocity interest with examples of short , medium, long range supersonic/hypersonic missiles. Then we will review the major aerothermodynamic problems encountered in high speed missile design with a special emphasis on ramjet and scramjet propulsion integration. We will also present simulation means which include computational methods and ground test facilities. Finally the feasibility to use CFD

tools for high speed missile design will be illustrated on several applications.

## 2. EMPLOYMENT OF HIGH VELOCITY

High velocity makes possible

- to considerably increase the damage inflicted to the target by direct hit,
- to successfully engage targets which have been detected late and travel very fast (e.g. missiles),
- to penetrate air-defence in combination with stealth characteristics.

These three features gave birth to three families of weapons : kinetic energy projectiles, short-range supersonic/hypersonic missiles and medium to long range supersonic/hypersonic missiles propelled by rocket or air-breathing engines.

High kinetic energy can allow penetration of main battle tank (MBT) armour. Kinetic energy (KE) projectiles have been developed in this aim.

KE projectiles acquire their high energy by very high velocity (Mach 6 and more) given by gun launch and relatively high mass. Since their velocity decreases very fast - although their diameter is kept small - their range is limited to several kilometres. Because of the gun launch they have a very small inner dead region. They consist of a long rod penetrator of heavy-weight metal and some aerodynamic appendages for drag reduction and stabilisation<sup>2</sup> (see Figure 2). In some cases, simple guidance techniques are used to increase hit probability. Nowadays, muzzle velocity for tube artillery seems to reach a maximum and these KE weapons will probably have difficulties to penetrate new MBT reactive or laminate armours.

Another way of accelerating a KE penetrator with practically no recoil and to increase their diameter to engage modern MBTs is to use rocket propulsion. In contrast to gunfired projectiles, the impact energy delivered by the whole mass of the missile increases penetrativity. This idea is at the origin of a German-French High-Velocity Missile (HVM) program<sup>3</sup>. In Germany, this program was shift to short and very-short-range air-defence (SHORAD/VSHORAD) and French interest is mainly in anti-helicopter missions.

In this case the high-velocity interest is the ability to detect late detected targets. For example, if a missile flying at Mach 2.0 is detected at 12 km, knowing that it takes about 15 s to current air-defence systems between detection and launch, engagement will begin at only 2 km of the launch site ! To extend the intercept zone outwards, it is necessary to reduce reaction time and to increase missile speed. A compromise has to be found between flight time and heating loads. Helicopter pop-up or last-ditch defence against Tactical Ballistic Missiles (TBMs) poses similar problems. In the HVM program, missile is accelerated to Mach 6 in less than 1 second. The following critical aspects have been identified :

- propulsion system (demonstrated by flight test),
- IR homing head heating,
- high dynamic pressure,
- aerokinetic heating of lifting surfaces and ogive.

An other example is the Starstreak missile (antitank and very-short-range air-defence missile) which uses exploding penetrators. Three rods are mounted atop a rocket powered missile. Separation occurs when propulsion stops. The three rods stay in close formation until they hit the target.

At medium to long range, high velocity will allow strengthened air-defence and air-defence penetrativity. To acquire very high speed, the missile would be powered by a rocket engine or by an airbreathing engine (high performance ramjet or scramjet).

An example of medium range air-defence missile is the ASTER which allows to intercept various sets of threats (aircrafts, highly supersonic manoeuvring missiles, tactical ballistic missiles...). This missile is a two-stage solid propellant vehicle launched vertically. This concept results from the necessity to have a very agile missile for interception, either because of a late target discrimination or to counter manoeuvres of the hostile and to achieve in any case a very short miss-distance. This is possible thanks to a high velocity, a very high manoeuvrability and a very short guidance time constant (agility) provided by an innovative control system (PIF-PAF) which combines aerodynamic control (PAF) and direct force control (PIF) using lateral thrusters at the centre of gravity of the missile.

An example of long range air-defence missile is the THAAD which provides a high altitude intercept capability by engaging and neutralising incoming ballistic missiles. It will be the first endo/exoatmospheric system for defence against theatre ballistic missiles. THAAD is propelled by a solid fuel rocket using thrust vector control for manoeuvring. During the terminal phase, the forecone separates from the missile body and terminal manoeuvring is provided by a divert-and-attitude-control-system (DACS). There are four divert thrusters near the top of the kill vehicle and six smaller attitude control thrusters near the base. The maximum Mach number of interception will be about 9.

For medium to long range air-defence penetration, ramjet and scramjet missiles are well adapted. In this case, missiles would have unconventional geometry for low drag and high air intake integration. Ramjet missiles can reach high altitudes (up to 35 km) and cruise at high supersonic speeds (Mach 2 to 5). Examples of such missiles are : ASMP (Air Sol Moyenne Portée, see § 3.4.2) and the new generation supersonic anti-ship missile ANNG (Anti-Navire Nouvelle

Génération). For higher cruise Mach numbers (6 to 8), from sea level to several kilometres of altitude, scramjet propulsion would be necessary. Such type of propulsion is still under development and no operational vehicle is presently equipped with it.

Higher Mach numbers and altitudes are in the domain of space launchers and are beyond the scope of this lecture.

### 3. MAJOR DESIGN PROBLEMS

#### 3.1. Hypersonic Missiles Main Characteristics

We have previously seen that the Mach number domain for hypersonic missile is between 5 and 10. These Mach numbers are low in comparison with the Mach 36 of an Apollo re-entry. So we do not have to deal with the same physical phenomenons than for space vehicles. A first particularity of hypersonic missiles is that these Mach numbers have to be reached as well as at low altitude as at high altitude. An other one is that drag reduction is fundamental to save kinetic energy or to achieve medium to long range mission. Moreover, either they are surface-launched or aircraft-launched, missiles have to be controllable at low supersonic speed (sometimes high subsonic and transonic speeds). For these reasons, hypersonic missile design is closer to supersonic aerodynamics design than to specific hypersonic design.

#### 3.2. What is Important for Hypersonic Missile Aerothermodynamics?

Anderson<sup>4</sup> sees five physical phenomena becoming more important as Mach number increases.

- *Thin shock layers* : at high Mach numbers the shock wave lies close to the surface and thin shock layer theory can be used.
- *Entropy layer* : different streamlines crossing the detached shock created by a blunt nose experience different entropy increases, creating the so-called entropy layer. Hypersonic missile design will be a compromise between drag reduction (small nose radius) and stagnation point heat flux reduction (large nose radius). For the lowest Mach numbers (5.0 - 6.0) and short flight time, sharp nose can be selected. For higher Mach number or longer flight time, a blunt nose is necessary. In this case an entropy layer is created and boundary layer outer-edge conditions have to be revised. The presence of an entropy layer increases the values of heat-fluxes<sup>5</sup> and can affect the overall air-intake performance of an hypersonic air-breathing vehicle.
- *Viscous interaction* : at high Mach numbers, boundary layer thickness increases under the combined effects of temperature increase and density decrease within the boundary layer. This can have important effects on pressure distributions (see figure 3), and lift, drag and stability are affected. Moreover, skin friction and heat fluxes are increased by viscous interactions. The parameter that governs laminar viscous interactions is  $\chi$  defined as :

$$\chi = M_{\infty}^3 Re^{-0.5} C^{0.5} \quad (1)$$

where :

$$C = \rho_w \mu_w / \rho_e \mu_e \quad (2)$$

$\chi < 3$  weak interaction

$\chi > 3$  strong interaction

Figure 4 shows a classical result of pressure distribution over a flat plate obtained from experimental data.

Stollery<sup>6</sup> identified different viscous interaction parameters for turbulent flows and drew viscous effects on lift-to-drag ratio of different classes of vehicles (see figure 5). Viscous effects are important on drag and limited on lift. Consequently, maximum lift-to-drag ratio decreases when viscous interaction increases. During the design phase of an hypersonic missile it is important to examine the values of the interaction parameters.

Among viscous effects, one of the most difficult is probably laminar-turbulent boundary layer transition on a forebody at hypersonic speed<sup>7</sup>. This transition is difficult to predict and can affect global aerodynamic coefficients, control efficiency, heat fluxes and overall air-intake total pressure recovery.

- *High-temperature flows*: in general, for this Mach range, vibrational effects are taken into account (when temperature is higher than 800 K for air) but not chemical reactions or dissociations ( $O_2$  dissociation begins at 2 000 K). A good approximation is to take into account the evolution of the specific heats with temperature.

Of course aerodynamic heating (mainly convective heating) is an important feature of hypersonic missile design. At the stagnation point, the heat flux varies inversely with the square root of the nose radius :

$$q_w \propto R^{-0.5} \quad (3)$$

thus, to reduce stagnation heat flux, it is necessary to increase nose radius, with effects on drag and entropy layer.

- *Low-density flows*: at altitudes less than 60 km, air can be considered as a continuous medium and Navier-Stokes equations with no-slip boundary conditions are valid. At higher altitudes, the test parameter is the Knudsen number which is the ratio of the mean free path of the particle at the given altitude to a characteristic scale of the vehicle. For high altitude interception of TBMs by endo-exoatmospheric interceptors different regimes are encountered during the ascent phase, first continuum regime ( $Kn \leq 0.03$ ), then transition regime ( $0.03 \leq Kn \leq 0.2$ ) where Navier-Stokes equations still holds but slip conditions have to be applied and finally, at higher altitude, the free molecular regime where Boltzmann equations have to be solved.

Keeping these phenomena in mind, we are going to look in more details at the aerothermodynamics of supersonic/hypersonic missiles.

### 3.3. Aerothermodynamics

A large number of excellent text books<sup>8,9,10</sup>, reviews<sup>11</sup> and lectures<sup>12,13</sup> already exist on this subject, the object of this

chapter is just to point out some of the most significant Mach number effects on missile aerodynamics.

#### 3.3.1. Forces and Moments

For a simple body tail configuration, the evolution of  $C_N$  with Mach number is given on figure 6. The centre of pressure varies with Mach number. Each component contributes to this variation. As Mach number increases,  $C_N$  for the body varies only slightly, and the centre of pressure, moves aft slightly.  $C_N$  for the tails decreases (nearly inversely with Mach number) and the centre of pressure varies only slightly. As a result, the centre of pressure of such a body tail configuration moves forward with increasing Mach number because of the lowered tail force coefficient. This centre of pressure movement increases instability.

At high Mach numbers, stability can be obtained by use of a conical flare as shown on figure 7. In this case, centre of pressure location is almost constant with Mach number. Of course, the flare increases drag and base pressure is modified.

Real gas effects have a slight effect on pitching moment, but only second order effect on axial and normal forces<sup>14</sup>.

If viscous effects are neglected, one can make use of the concept of hypersonic similarity<sup>16</sup> to evaluate pressure distributions on slender bodies.

If  $\tau = D / L$  is the slenderness ratio, the principle of hypersonic similarity says that :

$$C_p / \tau^2 = f(\gamma, M_\infty \tau) \quad (4)$$

for three dimensional flows we obtain :

$$C_N / \tau = F(\gamma, M_\infty \tau, \alpha / \tau) \quad (5)$$

$$C_D / \tau^2 = G(\gamma, M_\infty \tau, \alpha / \tau) \quad (6)$$

$K = M_\infty \tau$  is the hypersonic similarity parameter.

This rule extends to supersonic flows if the similarity parameter  $M_\infty \tau$  is replaced by  $\tau (M_\infty - 1)^{0.5}$ .

To illustrate the hypersonic similarity the evolution of the relative pressure distribution on ogives and cones for different slenderness ratios  $\tau = 1/E$  and constant values of the similarity parameter is given on figure 8. The three pressure distributions are almost perfectly superimposed.

Drag evolution of bodies with Mach number is given on figure 9. Generally, minimum drag coefficient decreases with Mach number until Mach 3 and stays rather constant between Mach 4 and 5. It appears that the cone-cylinder has the lowest minimum drag for a Mach number higher than 3.

Drag reduction at hypersonic speeds is at the origin of waveriders<sup>20</sup>. They result from inviscid flow inverse design. Their name comes from the fact that, for most of them, edges would ride on a shock wave as shown for the simplest one, the caret wing, in figure 10. The general idea of waveriders design is that forces generated by compression at hypersonic speed (lower side) are very large compared with suction generated by expansion. This is why

they generally present upper surfaces aligned with free stream velocity.

For the design Mach number, they present low-drag, high lift, high lift-to-drag ratio and large internal volume. Different geometries can be derived from different inviscid flow fields, an example with propulsion integrated is also given on figure 10.

Viscous effects can considerably affect waveriders lift-to-drag ratio because of their large wetted surfaces. Moreover, the necessary bluntness of the leading edges (because of heating loads) will also decrease the lift-to-drag ratio. It is why waverider design is now departing from inviscid analytic flow fields solutions.

### 3.3.2. Aerodynamic Control

High agility combined with very short missile time constants are the basic requirement for reducing target miss distance.

High manoeuvrability at high velocity and low altitude results of very high dynamic pressure and can be achieved with low angles of attack and classical control surfaces.

For conventional geometries, the equivalent angle of attack concept is still very useful in helping to predict the normal force and centre of pressure location of a fin in the presence of a body and the amount of normal force carried over onto the body<sup>21</sup>.

At moderate angle of attack, subsonic to moderate supersonic Mach numbers, the body lift interference parameter is :

$$K_B = N_{B(W)} / N_W \quad (7)$$

and the wing lift interference parameter is :

$$K_W = N_{W(B)} / N_W \quad (8)$$

where :

$N_W$  is the normal force on the wing alone,

$N_{B(W)}$  is the normal force on the body caused by the presence of the wing (at 0 deflection)

$N_{W(B)}$  is the normal force of the wing in the presence of the body (at 0 deflection).

Extensive measurements of all-movable fins normal force, root bending moment and fin hinge moment has been realised and added to the US Tri-service data base for high angle of attack and Mach numbers up to 4.5. Based on these experiments extensions have been introduced in the semi-empirical codes<sup>22</sup>.

Figure 11 shows that between free stream Mach number 2 and 4.5 compressibility effects on  $K_W$  are noticeable.

It is possible to correlate the efficiency results at different free stream Mach numbers by making use of local Mach number, dynamic pressure an upwash angle (the flow angle in a streamwise plane normal to the wing planform)<sup>11</sup>.

The evolution of the resulting lift interference parameter :

$$k_W = N_{W(B)} / N_W \quad (9)$$

where :

$N_W$  is the normal force on the wing alone,

$N_{W(B)}$  is the normal force of the deflected wing in the presence of the body (at 0 angle of attack),

is given in figure 12.

### 3.3.3. Lateral Jet Control

In some cases, aerodynamic control is not adequate :

- interception of sea-skimmers alternating 10 to 15 g of lateral acceleration at high frequency demands shorter time constants,

- high altitude (e.g. THAAD) induces low dynamic pressure and low efficiency.

The use of a propulsive force at the missile centre of gravity overrides these two disadvantages. However, jet control at the centre of gravity has certain constraints :

- used as single mean of control, its operational domain is limited in duration by its fuel consumption. In particular, with a gas generator associated to a distribution system towards the nozzles, powder consumption remains constant whichever the manoeuvre,

- need for a very slight variation of the centre of gravity,

- interferences with the external flow, near the nozzle exit (local interactions) and on the rear part of the body or on the fins located downstream (downstream interactions). These interactions can considerably reduce the lateral jet efficiency.

For these reasons, purely force control is only suitable for very short range missiles or for terminal manoeuvring. In the latter case, it has to be associated with an aerodynamic control system (ASTER).

The lateral jet can also be located at the rear part or at the forward part of the body, to create a moment control, as in the case of tail or canard control. Missile time constant is not as much reduced as in the case of force control. It only eliminates actuators bandwidth limitations. In this case, nozzles are distributed around the missile circumference. Hot gases ever come from a common gas generator, or from individual thrusters installed normally to the body axis (ERINT).

Local interactions (figure 13) are related to the jet obstacle effect which, at supersonic speed, produces upstream of the nozzle a detached shock and a separation of the boundary layer forming a shock generating an overpressure zone. The separation area dimensions depend strongly on the laminar/turbulent status of the boundary layer. For laminar boundary layer encountered at high altitudes the separation zone is much larger than in the turbulent case. Just immediately downstream of the nozzle, the external flow around the jet produces a depression zone.

Downstream interactions (figure 14) are due to the highly vortical character of the flow downstream of the jet. Far from the exit section, the jet wake takes the form of two contra-rotating vortices resulting from the curvature of the jet and its rounding by the external flow. Thus the speeds induced by these vortical structures affect the lifting

surfaces located downstream, generally producing a loss of lift and moments.

The total sum of these interactions results in :

- an interaction force which is added to the lateral propulsive force,
- disturbing pitch and roll moments.

### 3.3.4. Mechanical and Heat Loads

For a typical SHORAD mission at high velocity different constraints have been identified :

- a high rate of acceleration induces high stress on the missile's propellant mass, structural components and equipments (approx. 200 - 400 g),
- a low structural mass to achieve a large velocity increase (see eq. 14 below),
- combination of high velocity and low altitude results in high dynamic pressure and thermal stresses.

Thus, selecting the optimal speed would require very careful consideration of the cost/effectiveness ratio. For example, increasing the missile's speed from Mach 5 to Mach 6 would not reduce significantly the total flight time but would increase significantly the kinetic heating.

To reduce production costs, the objective is to make use of standard composite materials without special coatings. Only some areas would have to be protected (nose, leading edges), and a careful thermal analysis is necessary.

To illustrate heat loads and drag evolution with Mach number, flow around a typical conical nose ( $L/D = 4$ ,  $D = 150$  mm) has been computed at  $0^\circ$  angle of attack with a PNS code with perfect gas assumption (PG :  $\gamma = 1.4$ ) and equilibrium air assumption (EG) for different Mach numbers (4, 5, 6, 7 and 10). Stagnation conditions are taken at sea level, and boundary layer is supposed to be fully turbulent, wall temperature is 800 K.

On figure 15 is plotted the axial force evolution with Mach number. It appears that the axial force does not depend on the thermodynamical hypothesis : PG and EC curves are exactly matching. It is a constant result that surface pressure on cones is the same for a calorically perfect gas than for equilibrium air. Friction drag is roughly a third of total drag.

Drag coefficients (taking base area as reference area) are given in table 1 :

	Mach Number				
	4	5	6	7	10
pressure drag	0.046	0.043	0.041	0.039	0.037
friction drag	0.016	0.016	0.016	0.016	0.017
total drag	0.062	0.059	0.057	0.055	0.054

Table 1 : Drag coefficient on a  $L/D = 4$  cone at  $0^\circ$  angle of attack (equilibrium air values)

Pressure drag coefficient decreases slowly with Mach number, friction drag coefficient stays constant.

Pressure drag coefficient values can be compared to the value obtained by the Newtonian theory which gives<sup>4</sup> :

$$C_p = 2 \sin^2 \theta \quad (10)$$

where  $\theta$  is the half cone angle.

The pressure effort is normal to the wall, thus its contribution to the axial force is  $C_p \sin \theta$  :

$$C_D = C_p \cdot \sin \theta \cdot S_{\text{cone}} / S_{\text{ref}} = 2 \sin^2 \theta \quad (11)$$

In the present case, Newtonian theory gives  $C_D = 0.031$ , a value which is significantly lower than the numerical results (0.037 at Mach 10).

On figure 16 is plotted the heat flux evolution ( $x = 0.6$  m) with Mach number. Heat flux depends on the thermodynamical hypothesis. Lower fluxes are obtained for equilibrium air than for perfect gas. Heat flux is about  $1.7 \text{ MW/m}^2$  at Mach 5 and  $3.5 \text{ MW/m}^2$  at Mach 6.

Heat flux coefficient  $C_H$  defined as :

$$C_H = \phi / (\rho_\infty u_\infty C_{p\infty} (T_{i\infty} - T_w)) \quad (12)$$

is given in table 2 at  $x = 0.6$  m :

	Mach Number				
	4	5	6	7	10
perfect gas	9.23	9.58	9.65	9.76	10.1
equilibrium air	7.92	8.49	8.69	8.73	9.08

Table 2 : Heat flux coefficient  $C_H (x 10^4)$  on a  $L/D = 4$  cone at  $0^\circ$  angle of attack.  $x = 0.6$  m.  $T_w = 800$  K.

As shown on figure 17 maximum temperature within the boundary layer is about 1000 K, supporting *a posteriori* the equilibrium air hypothesis.

Similar results can be obtained on wedges representing losangic wings.

From these results, it comes out that for pressure distributions, a classical perfect gas hypothesis is generally adequate, but for heat fluxes better results are obtained with the equilibrium air hypothesis.

Time-dependant evolution of wall temperature along the trajectory is evaluated at the preliminary design phase by coupling semi-empirical formulas with a simple unsteady conduction computation within the wall. Wall representation is ever one-dimensional or two-dimensional. Body and wings are treated separately. The different structural layers are represented by their density, thermal conductivity, specific heat and when necessary emissivity. At each time step the inviscid flow is computed (if flight conditions have changed), heat fluxes are evaluated making use of the preceding time-step wall temperatures and conduction computation is advanced. Doing so, temperature evolution on and inside the whole body or wing can be evaluated all along the trajectory.

This unsteady approach is particularly important when dealing with the cone apex or the wing leading edges to avoid overestimation of wall temperature.

In a more advanced design phase, heat fluxes are determined for different wall temperatures by use of semi-empirical codes and, for some points of the flight domain, with Euler/boundary layer or PNS approaches (giving also pressure distributions). These heat fluxes and pressure distributions tables are entered in a thermostructural analysis code and a precise determination of temperature and constraints within the material can be realised.

When deterioration of certain parts of the missile (nose, fins) under ablation, abrasion, sublimation or carbonisation cannot be avoided a more complex approach has to be used.

In case of IR homing, temperature and constraints in the hemispherical IR sensor window can be determined using the same approach. Furthermore, the overall signal-to-noise ratio has to be determined taking into account the presence of a detached shock wave, a hot gas layer and a non-uniform temperature distribution within the window.

### 3.4. Propulsion Integration

#### 3.4.1. The Different Propulsion Modes

Missile propulsion is either of rocket type or of air-breathing type.

Rocket propulsion does not use the oxygen of air. It can be used at all altitudes with almost constant thrust. High specific thrust (thrust over main section ratio) can be achieved. Propellant is either solid, liquid or hybrid.

A solid rocket engine is characterised by the constructive index  $mi/mp$  (inert mass other propellant mass ratio) which can be as low as 7 %, the nature of the propellant and the powder block geometry. Details on these characteristics are beyond the scope of this lecture. Most of tactical missiles use solid rocket propulsion because of the following advantages: easy integration, high thrust, jet deviation control capability, high manoeuvrability and low price.

Specific impulse  $I_{sp}$  is rather low :

$$I_{sp} = F / (g \cdot m_f) \cong 250 \text{ s} \quad (13)$$

where  $m_f$  is the fuel mass flow. The specific impulse represents the time taken by the combustion of 1 kg of propellant for a thrust of 1 daN.

The velocity increase (drag excluded) is given by :

$$\Delta V = g I_{sp} \text{Log} (1 + mp / mi) \quad (14)$$

showing the importance of the constructive index.

Thrust regulation is difficult and gases are not stealthy. Solid rocket engines are used for all kind of missions except long range atmospheric missions.

In general, liquid or hybrid rocket propulsion is not suitable for tactical missiles, because of its complexity and the problems caused by fuel storage.

Air-breathing propulsion uses the oxygen of air. Only atmospheric missions can be achieved and thrust varies with altitude. Specific thrust is low and angle of attack is

limited. Air-breathing propulsion consists in turbojets, ramjets, scramjets or pulsed detonation engines. All these engines need air intakes and give rise to integration difficulties.

Turbojets have high specific impulse (more than 3000 s) and can achieve long range missions. Their thrust can be easily modulated. The exhaust gases can be made stealthy by dilution. Their technology is rather complex, and their global price is high. Turbojet powered missiles manoeuvrability is low and velocity is limited to low supersonic regime, they are mainly used for air-to-surface stand-off missions or antiship missions.

Ramjets have rather high specific impulse (between 1000 s and 1500 s) and can achieve medium to long range missions. They can reach high altitudes (up to 35 km) and cruise at high supersonic speed ( $2 \leq M \leq 6$ ). Their thrust can be easily regulated, and exhaust gases are rather stealthy. On the other hand, integration is made complex by the need of accelerators and air-intakes. Due to the simplicity of their components, production price is moderate. Ramjet powered missiles can be used for all medium to long range missions (air-to-air, antiship, stand-off air-to-surface, ...)

Scramjets, in which supersonic combustion takes place, are still under development and no vehicle is presently equipped with this kind of propulsion. Nevertheless, scramjet is the only propulsion mode which will allow to achieve medium to long range hypersonic missions. Advantages and drawbacks are rather the same than for ramjets. Optimal flight regime is between Mach 5 and Mach 12, and rather high specific impulse are awaited for H2-scramjets (about 2000 s at Mach 10).

Pulsed detonation engines rely on detonation waves that propagate through a premixed fuel/air mixture and produce large chamber pressure. The rapid detonation process results in constant volume combustion with high operating frequency, combustion pressure and thrust at subsonic and low supersonic regime. At present, no missile uses pulsed detonation engine.

Figure 18 shows the evolution of specific impulse with Mach number for rockets, turbojets, ramjets and scramjets. The advantage of air-breathing propulsion on rocket propulsion in terms of specific impulse is clearly seen. Furthermore, it appears that turbojets are well adapted to subsonic and low supersonic missions and that ramjets are adapted to supersonic regime for Mach numbers varying between 2 and 6. For higher Mach numbers, it appears that scramjets are more efficient.

On Figure 19 is represented the flight domain of the different air-breathing propulsion systems in the (altitude, Mach number) plane. It is shown that ramjet can cover most of the mission requirements from Mach 2 to Mach 6 and from 0 to 35 km of altitude.

#### 3.4.2. Ramjet Missiles

We can distinguish three generations of ramjet missiles.

In the first one, the ramjet engine is positioned within a nacelle outside the missile dart. Intakes are axisymmetric and have good performance (low interference with fuselage flowfield) but the missile is heavy and bulky and its drag is

high. Such missiles were developed in the 1950's : Bomarc (US), Bloodhound (UK), Sirius CT 41 (F).

In the second generation, the engine is integrated in the dart, with the intake placed in the nose and with jettisonable rocket booster located at the base. This configuration has several advantages as compactness and good intake performance, but has also some drawbacks as loss of volume for the payload and excessive length. The main missiles developed are : Talos (US), Sea Dart (UK), Vega (F), Stalartex (F), and SA4 Ganef with the particularity of having an annular intake located downstream of the payload.

On figure 20, Bomarc and Talos<sup>23</sup> are compared. Bomarc was a land-launched missile boosted by a parallel rocket engine. In this case, boost and sustain engine are independent. Bomarc is about 14 m long and weight more than 6 500 kg at launch. Engines diameter is 0.7 m, leading to a low specific thrust. These dimension were made necessary for heat release purposes, because of the unavailability of efficient thermal protection. Talos was ship launched.

In the third generation, which represents today's integration method, the air intakes are located on the sides of the fuselage and the rocket booster is integrated in the ramjet combustion chamber. This configuration avoids any loss of volume and therefore is optimum. Examples of such missiles are : ASMP (F) and ANNG (F/G) equipped with two rectangular intakes.

This third generation made ramjet-powered air-launched missiles feasible. The overall missile weight and volume requirements for a given payload size are smaller and specific thrust increases. For example ASMP length is 5.3 m. Efficient thermal protection are available, allowing long range missions with a small engine diameter. ASMP is powered by a liquid fuelled ramjet with an integrated solid propellant booster. Upon launch, the rocket accelerates the missile to ramjet ignition speed. At burn out of the booster, the nozzle is ejected, the air intakes are opened and the kerosene is pumped in the combustion chamber. This transition sequence is described on figure 21.

ASMP was completely deployed in 1986 and French MoD undertook general studies to define what could be a successor, defined as a stealth air-to-ground missile carried by Dassault Rafale fighter aircraft with several times the range of the ASMP. Within this context AEROSPATIALE with help of ONERA proposed and studied a high velocity liquid fuelled ramjet missile.

High lift-to-drag ratio configurations have also been studied by ONERA<sup>24</sup> (figure 22).

### 3.4.3. Ramjet Performance

A standard ramjet can be described by the sketch of figure 23 :

- station 0 represents free stream conditions,
- station 1 is the inlet cowl lip station,
- station 2 is the end of the inlet component
- station 3 is the end of the combustor,
- station 4 is the exit nozzle throat,
- station 5 is the end of the exit nozzle.

A detailed one dimensional analysis of a ramjet can be found in Mahoney<sup>23</sup>. Let us recall here the main results.

Using one dimensional steady analysis, the continuity equation leads to the conservation of mass flow between sections 0 and 4 :

$$m_4 = m_0 \cdot (1 + f/a) \quad (15)$$

where  $f/a$  is the fuel-to-air ratio,

Introducing the characteristic speed :

$$C^* = ((\gamma + 1) / 2)^{(\gamma + 1) / (2(\gamma - 1))} \cdot (r T_1 / \gamma)^{0.5} \quad (16)$$

the mass flow writes :

$$m = P_i A_c / C^* \quad (17)$$

and the mass flow conservation becomes :

$$P_{i4} / P_{i0} = A_0 / \Sigma (M_0) \cdot C_4^* / C_0^* \cdot (1 + f/a) / A_4 \quad (18)$$

where :

$$\Sigma (M) = A(M) / A^* \quad (19)$$

$$\Sigma (M) = 1/M \cdot ((2 + (\gamma - 1) M^2) / (\gamma + 1))^{(\gamma + 1) / (2(\gamma - 1))} \quad (20)$$

At this level, it is convenient to introduce some classical notations.

$$\text{Mass flow ratio : } \epsilon = A_0 / A_1$$

The mass flow ratio represents the mass flow entering the air-intake nondimensionalised by the mass flow that would pass through the same section if it was placed in the freestream at flight conditions ( $\epsilon \leq 1$ ).

$$\text{Air intake total pressure recovery : } \eta_{02} = P_{i2} / P_{i0}$$

The air intake total pressure recovery is a measure of the efficiency of the compression.

$$\text{Combustor total pressure recovery : } \eta_{24} = P_{i4} / P_{i2}$$

The combustor total pressure recovery represents the total pressure loss attributable to the combustor component.

We have  $\eta_{02} \leq 1$  and  $\eta_{24} \leq 1$ .

Using these notations equation 18 becomes :

$$\eta_{02} / \epsilon = F(M_0, Z) \cdot A_1 / A_4 \cdot C(T_{i0}, f/a) \quad (21)$$

where :

$$F(M_0, Z) = 1 / (\Sigma (M_0) \cdot C_0^*) \quad (22)$$

depends only on flight conditions,

$A_1 / A_4$  depends only on geometry and,

$$C(T_{i0}, f/a) = C_4^* \cdot (1 + f/a) / \eta_{24} \quad (23)$$

represents the combustion process.

So, in the  $(\eta_{02}, \epsilon)$  plane, as shown on figure 24 one can draw two families of curves. The first one is made of the characteristic curves of the air-intake (depending on flight

conditions) and the second is a family of straight lines coming from the origin (at a given  $T_{io}$ ). On each of these lines the equivalence ratio is constant. So air intake running point is at the intersection of the air intake characteristic curve and of the combustion line.

Making use of the momentum equation, thrust is :

$$F = P_5 A_5 (1 + \gamma_5 M_5^2) - P_0 A_0 \gamma_0 M_0^2 - P_0 A_5 \quad (24)$$

Thrust is nondimensionalised by dividing it by the product of the reference area and the dynamic pressure to obtained the thrust coefficient :

$$C_F = F / (q_0 A_R) \quad (25)$$

$$C_F = 2 / (\gamma_0 M_0^2) \cdot A_5 / A_R \cdot (P_5 / P_0 \cdot (1 + \gamma_5 M_5^2) - 1) - 2 A_0 / A_5 \quad (26)$$

Introducing the precedent notations, one directly obtains :

$$C_F = 2 / (\gamma_0 M_0^2) \cdot A_5 / A_R \cdot (\eta_{02} \cdot \eta_{24} \cdot \eta_N \cdot \varpi(M_5) / \varpi(M_0) \cdot (1 + \gamma_5 M_5^2) - 1) - 2 A_1 / A_5 \cdot \varepsilon \quad (27)$$

where :

$$\varpi(M) = P/P_i = (1 + (\gamma - 1)/2 \cdot M^2)^{-\gamma/(\gamma - 1)} \quad (28)$$

and where  $\eta_N$  is introduced to take into account for the nozzle efficiency.

Equations 21 and 27 describe entirely the engine performance. The thrust of a ramjet engine can be expressed nondimensionally in terms of area ratios, pressure ratios and Mach number functions.

The subsonic combustion ramjet engine is analogous to a closed channel with two throats, where the second throat, the nozzle, has a larger area than the first throat, the inlet, to accommodate increases in entropy and temperature between the two throats. Variation in flow conditions can either be accomplished by variation in fuel flow rate at constant geometry, or by variation of  $A_4/A_1$ .

Optimum values of  $A_4/A_1$  strongly depend on Mach number and thrust wanted, to reach them two approaches are possible (see figure 25) :

- using a nozzle with a variable sonic throat,
- using variable capture area inlet.

Moreover, the air-intake importance is clearly shown : thrust coefficient depends directly on air-intake total pressure recovery.

#### 3.4.4. Air Intake for Ramjet Missiles

On this subject extensive information is available in some good text books<sup>23,25</sup> and reviews<sup>26,27,28</sup>.

The primary function of high speed air-intakes is to decelerate air to subsonic conditions (or lower supersonic conditions in case of a scramjet) with the highest possible

total pressure recovery and the required engine mass flow. Another function is to provide sufficiently uniform flow in the combustion chamber for a good combustion process.

The achievement of these requirements is a very difficult task, especially when air-intakes are installed on the fuselage, and therefore in a non uniform flowfield.

The number, shape and position of air-intakes are various and their choice depend on performance requirements : internal performance (thrust), external aerodynamics (drag, lift to drag ratio), operational constraints and control (skid to turn or bank to turn).

We distinguish (figure 26) :

- single intake :

*nose intake* : e.g. Sea Dart, Talos, high pressure recovery but very bad integration,

*annular intake* : e.g. SA4 Ganef, better integration and lower performance (in particular at incidence) because intake height is small in comparison with forebody boundary layer thickness,

*chin intake* : e.g. ASALM, SLAT, well suited for bank-to-turn flight control (well adapted for long range missions), it uses the windward part of the forebody as a compression ramp, integration is difficult,

*ventral intake*

excellent solution, well suited to bank-to-turn steering, favourable incidence effect (high altitude cruise), good integration,

*top mounted intake* :

limitations in incidence, good integration, the intake is hidden from ground based radars,

- two lateral intakes : e.g. ASMP, ANNG,

a missile configuration with two lateral intakes is well adapted for a bank to turn control. The intakes are located diametrically opposed or inclined toward the bottom. The first case is better for mass flow and normal force, the second one is better for pressure recovery,

- three intakes :

they can be identical (skid-to-turn control) or composed of two identical lateral intake and one different bottom intake (bank-to-turn control),

- four intakes : e.g. KH31, ANS,

well adapted to skid-to-turn control giving high manoeuvrability. At high incidence, leeward intakes are less efficient. Lift-to-drag ratio is not optimal (two intakes give lift, and two induce drag).

The shape may be axisymmetric (full, half or quarter) or rectangular (conventional, inverted or lateral) as shown on figure 27. Figure 28 presents a comparison of the principal types of air intakes in a four intake configuration, assuming the entry areas and the diverter height to be identical.

To compress the flow, multiwedge ramps are used. They may be completely external or mixed external-internal (figure 29). For Mach numbers over about 3.0, mixed



external-internal supersonic compression is a good process. It allows to limit the turning of the external flow ahead the cowl lip and so to avoid steep cowl angle and therefore high cowl wave drag.

In order to improve supersonic air-intake efficiency external boundary layer bleed is generally used in order to evacuate as much forebody boundary layer as possible with moderate increase of external drag.

Internal boundary layer bleed at intake throats catches a small part of the intake mass flow. This bleed has two main functions :

- improve air-intake efficiency by decreasing viscous losses i.e. boundary layer height at engine entry,
- stabilise and smooth the flow at engine entry by reducing normal shock-boundary layer interaction at critical point.

Internal bleed allows higher critical efficiency by delaying subcritical running<sup>30</sup>.

Axisymmetric intakes have maximum performance at 0 incidence with medium incidence sensitivity. Rectangular intakes have favourable incidence effects (figure 30), but are highly sensitive to sideslip angle (figure 31).

The internal performance of an air intake may be described at each flight conditions (Mach number, incidence and sideslip angles) by a single curve, the *intake characteristic curve* :

$$\eta_{02} = f(\epsilon) \quad (29)$$

where  $\epsilon$  is either the total mass flow ratio or the engine mass flow ratio (in case of an internal bleed).

The point at which air intake operates on the characteristic curve is governed by conditions at the downstream end of the intake duct, that is, by the engine air flow demand. This is known as the *matched operating point*.

On the characteristic curve, we can distinguish different air-intake runnings :

- *supercritical running* : the normal shock which separates supersonic from subsonic flows in the duct is downstream the cowl lip for external supersonic compression (ESC) or downstream the throat for mixed supersonic compression (MSC) air intake,
- *critical running* : the normal shock is located at the cowl lip for ESC or at the throat for MSC,
- *subcritical running* : the normal shock is upstream the cowl lip for ESC and MSC (a normal shock located between the lip and the throat in case of MSC leads to unstable flow).

Figure 32 (resp. 33) presents the two common forms of a typical characteristic curve for an ESC (resp. MSC) intake with internal boundary layer bleed.

In addition to these performance data we need :

- internal pressure and heat fluxes distribution to ensure structural feasibility,
- flow profile at intake exit in order to verify air intake / engine compatibility.

Due to the operational constraints, air intakes are now always in the fuselage flowfield. On conventional geometries, the fuselage is circular. In case of a blunt nose, the detached bow shock generates a loss in total pressure and limits intake performance. This effect increases with flight Mach number.

The longitudinal location is a compromise between the flow field around the fuselage, the diffuser length, the aerodynamic stability of the missile and the attachment points on the fuselage.

On a circular body there are two interesting locations for intakes :

- around the ogival nose :
  - advantages* : undervelocity region, low boundary layer thickness,
  - drawbacks* : long diffuser, forward location of centre of pressure,
- 2 or 3 diameters downstream of ogive-cylinder junction :
  - advantages* : better integration
  - drawbacks* : higher external bleed, sensitivity to incidence and sideslip.

At high Mach number and altitude, it is possible to have laminar boundary layer on the fuselage just in front of side mounted intakes. In this case, the boundary layer is very sensitive to adverse pressure gradients and separation be generated and modify the flow field in front of the air intake.

At incidence (see figure 34), there are two unfavourable locations :

- *the leeward side* with thick boundary layers and vortices,
- *the lateral sides* with their overvelocities and high local incidences.

In the preliminary design phase, it is possible to evaluate the performance of a mounted intake using the following approach.

Given the fuselage flowfield, it is possible to evaluate in the intake capture area  $A_1$  the average Mach number  $\langle M_1 \rangle$ , total pressure  $\langle P_{11} \rangle$ , incidence  $\langle \alpha_1 \rangle$  and sideslip angle  $\langle \beta_1 \rangle$ . Then the mounted intake (mi) performance can be obtained from wind-tunnel tests of isolated intakes (ii) by the following formulas<sup>28</sup> :

$$\epsilon_{mi} = \epsilon_{ii} \cdot (\langle P_{11} \rangle / P_{i0}) \cdot (\Sigma(M_0) / \Sigma(\langle M_1 \rangle)) \quad (30)$$

$$\epsilon_{ii} = F(\langle M_1 \rangle, \langle \alpha_1 \rangle, \langle \beta_1 \rangle) \quad (31)$$

$$\eta_{02mi} = \eta_{02ii} \cdot (\langle P_{11} \rangle / P_{i0}) \quad (32)$$

$$\eta_{02ii} = G(\langle M_1 \rangle, \langle \alpha_1 \rangle, \langle \beta_1 \rangle) \quad (33)$$

Reasonable agreement with wind tunnel results is generally observed.

In case of multiple intake configurations, overall mass flow ratio is obtained by averaging, and overall pressure

recovery is assumed to be equal to the minimum pressure recovery of the different mounted intakes.

In a more advanced design phase, detailed numerical computations and wind tunnel testing of mounted intakes are necessary.

3.4.5. Future ramjet missiles

In the future, ramjet missile configurations will have non-circular cross sections for an optimum integration of the air intakes in the fuselage flowfield, a low drag, a high lift to drag ratio, a small radar cross-section and a good integration on carrier aircraft (figure 22). Their range can be significantly increased by use of high density fuel<sup>32</sup> :

Fuel	Kerosene	Synthetic	Boron slurry
d (density)	0.78	1.04	1.25
Isp (M = 2)	1670 s	1560 s	1700 s
d*Isp	1300 s	1620 s	2125 s
range	1	1.127	1.493

Table 3 : Range evolution with fuel density

Very long range missions require improved insulation of the combustion chamber. Two ways are possible :

- structurally reinforced thermal protections protected from the flames by ceramic composite internal layer,
- air cooling at the wall.

Long duration ground tests have already established the efficiency of the structurally reinforced protections in case of kerosene combustion.

With air cooling, there is theoretically no range limitation, but rocket integration is made more difficult.

With such ramjet missiles a cruise velocity of Mach 4.5 could be achieved.

3.4.6. Scramjet

Missiles cruising at Mach 6 to 8 from sea level to several kilometres of altitude would be well suited to penetrate strengthened air-defences for ground strikes, engage airborne warning and control systems (AWACS) and be used as reusable unmanned reconnaissance aerial vehicles (URAVs). Work on hypersonic unmanned aerial vehicles (UCAVs) is already underway in the US<sup>33</sup>.

For such missions, airbreathing vehicles are necessary.

At first sight, there it is not impossible to reach high velocities with a ramjet : on a theoretical point of view, one has always interest to burn fuel at low speed (see figure 35) and it results that subsonic combustion is always better than supersonic one.

In fact, at hypersonic speed, slowing the air flow to subsonic speed results in :

- *high total pressure loss* : a ramjet air intake pressure recovery is lower than 0.2 at Mach 7 when a scramjet

air intake pressure recovery can reach 0.5 at Mach 7 (see figure 36),

- *high temperature* : evolution of ramjet thrust coefficient with Mach number is given on figure 37. At Mach 10, temperature in a ramjet would be so high that fuel would decompose rather than burn<sup>4</sup>.

To reach high velocities, the scramjet is more adapted. In a scramjet, the hypersonic free stream is slowed to supersonic speed by an inlet compression. Fuel (usually H2) is injected in the supersonic stream where it mixes and burns downstream of the injector strut. Burned gases expand through a supersonic nozzle, producing thrust.

Furthermore, it seems accepted that scramjet combined with other propulsion means will ensure the feasibility of reusable airbreathing space launchers.

This latter argument motivated a French four year Research and Technology Program for the Advanced Hypersonic Propulsion (PREPHA), financed by DGA (Délégation Générale pour l'Armement), CNES (Centre National d'Etudes Spatiales) and MRT (Ministère de la Recherche et Technologie), in which AEROSPATIALE, DASSAULT, SEP, SNECMA and ONERA are studying and testing on ground the scramjet technology<sup>24,34</sup>.

The key point of this program is the ground test of the CHAMOIS scramjet<sup>35,36</sup>.

3.4.7. Forebody, air-intake and afterbody of a scramjet propelled vehicle

The Mach number flight range estimated for scramjet propulsion mode is from M=6 to M=12-15. The design of the propulsive streamtube is classically divided from upstream to downstream between forebody, inlet, combustor and nozzle (see figure 38). The main difference of this engine, compared to ramjet, is the way each component is integrated to the previous one. Due to high speed, compactness is necessary as it usually means drag reduction but also weight limitation. Nevertheless, at high altitude and high Mach number, the engine must be fed with high captured mass flow, thus arising the need for large structures. This mass flow is usually captured by many air inlets in parallel (for structural feasibility), which leads to rectangular (so-called two-dimensional) inlet shape. Such a shape also authorises separate ground tests of one of the inlets due to modularity of the concept.

The function of scramjet air inlet is to provide the cleanest possible flow to combustor with the highest total pressure at a prescribed Mach number. The main difference with ramjet inlet is that Mach number at combustor entrance is supersonic. But this Mach number should be low enough to allow correct injection of propellant and complete ignition before the flow has reached the end of the combustion chamber. The highest total pressure is needed to ensure the most energetic flow. This criterion of efficiency is nevertheless not unique and several other criteria exist, based on static pressure, kinetic energy. Total pressure losses are mainly due to shocks and viscous effects. In fact, due to potential thermal overheating and drag increase, there is usually no boundary layer bleed at the end of the forebody. This high forebody-inlet integration is reinforced by locating the air inlet on the windward side, so using the

whole forebody for compression of the captured flow<sup>37</sup>. This implies that :

- the bow shock on the blunt forebody influences the air inlet flow through entropy layer,
- the boundary layer developing on the forebody is entirely transmitted to the air inlet.

External compression ramp is a common feature but it is usually coupled with internal compression through the cowl (mixed compression), the struts and sometimes the lateral walls in order to ensure satisfactory slowing down without any major deviation of the flow.

Starting of the inlet is one of the major constraints in the design phase if the inlet is supposed to work for a large Mach number range : at the lower Mach number limit, starting condition leads to low contraction ratio whereas, at the upper limit, high contraction ratio is mandatory to satisfy combustor entry requirements (slowing down of the flow). Apart from variable geometry where the captured mass flow ratio is a function of the Mach number, air inlet has to get started at the slowest flight conditions. This point is very sensitive to the geometry of the internal streamtube : contraction ratio is a factor but lateral wall and cowl leading edges may also be shaped so as to favour starting<sup>37</sup>.

Depending on the propellant injection mode, contraction in a scramjet inlet may be partially due to struts obstruction. In this case, struts position is the result of a compromise between structural feasibility, injection constraints and heterogeneity of the flow captured by the air inlet. For a rectangular combustion chamber, struts may be positioned either horizontally or vertically. Apart from structural resistance (which is better in the case of vertical struts) and technological feasibility of injection and cooling (in both cases), flow stratification at combustor entry has to be taken into account for positioning the struts. Large entropy and boundary layers develop on the upper side (due to bow shock and boundary layer on the forebody) and oblique shocks reflects on the upper and lower sides (if no lateral compression is considered). So, on the one hand, each horizontal strut will be fed by a quasi-uniform flow, each flow being different from one another. On the other hand, each vertical strut will see non uniform flow and this flow will almost be the same for every strut. Different positions may also be adopted, leading to completely three-dimensional configurations (strut leading edge not perpendicular to engine axis, strut length lower than combustor width) that may favour flow mixing but also starting of the air inlet.

Air inlet-combustor coupling is not as evident as it is for ramjet engine : the flow is mainly supersonic (and one may imagine that air inlet influences combustion and not the contrary), but coupling is important because combustion chamber is next to air inlet and supersonic combustion is known to eventually induce pre-combustion shocks that may influence upstream duct flow. An isolator function may be prescribed to a portion of the duct between air inlet and combustor. Large viscous effects may also induced upstream influence of the struts through subsonic regions near the walls. More generally, coupling of the different elements in the scramjet propulsion mode is also induced by compactness requirement of the engine.

A scramjet nozzle would be asymmetric with a short interior flap (cowl side) and a longer expansion ramp (body

side). Thrust prediction depends slightly on gas modelisation (thermal equilibrium frozen gas, chemical equilibrium or reactive flow) and special attention has to be paid to it for precise evaluation of  $T - D$  (thrust minus drag) balance.

## 4. POTENTIALS AND DEFICITS OF SIMULATION MEANS

### 4.1. Computational Simulation

Two types of computational methods are available : semi-empirical methods and numerical methods.

#### 4.1.1. Semi-Empirical Methods

Semi empirical methods are the simplest and the fastest methods to predict missile aerodynamics, thermal loads and two-dimensional air-intake performances. They only need a small amount of computer time and they are well suited to calculate sets of different configurations for systematic design studies.

For external aerodynamics, most of the codes are based on component build-up technique. They consist in determining the contribution of each element of the missile (body, wing, tail) and in evaluating the interactions between these elements by introducing interference factors. These methods are based on approximate theoretical methods (slender body, shock expansion, linearised potential) and on experimental and numerical data bases.

Different reviews of these methods are already available<sup>39,40,41,42</sup>. In cases where good data bases exist and where theoretical methods can be applied, very good predictions are possible.

- *Geometries* : most of semi-empirical codes can compute conventional missiles with one or two series of cruciform fins (wing-body, wing-body-tail, canard-wing-body) or even boosted missiles with 3 sets of lifting surfaces. Just a few of them can handle unconventional geometries<sup>43</sup> (elliptic cross sections, square cross sections, air-intakes).
- *Angle of attack* : most of these codes are valid only for low to moderate angle of attack (30°). Some of them allow high angle of attack analysis (up to 90° or 180°).
- *Mach number* : in general, these codes have been developed for subsonic/supersonic use, some of them are valid up to Mach 5 or 8.

In general, standard coefficients like normal force, stability, and even drag (Fig. 39) and damping coefficients (Fig. 40) can be predicted with a precision that is sufficient for design purposes.

Difficulties arise in the prediction quality for configurations far outside the data bases and for coefficients that are small in comparison with interaction effects (control effectiveness, hinge moments, rolling moment, ...).

A very popular design tool for the investigation of unconventional hypersonic vehicles has been developed and is in wide use throughout industry since the early 1970s, the "Hypersonic Arbitrary Body Program"<sup>44</sup>. It has been extended to supersonic regime (SHABP). It make use of simplified theories like :

- Newtonian method,
- modified Newtonian method,
- Newton-Busemann method,
- tangent-wedge or tangent-cone methods,
- shock-expansion method.

If these methods are carefully selected, useful information can be obtained for preliminary design.

Some of these semi-empirical methods offer the possibility of computing heat fluxes for a given wall temperature. Tables of fluxes vs. wall temperature can then be introduced in standard thermostructural analysis codes. In general, body and wing are treated separately. Pressure distribution is provided by second order shock-expansion methods. Heat fluxes for a given wall temperature are then evaluated by making use of reference enthalpy method<sup>45</sup>.

Semi-empirical methods are also used to predict two-dimensional air-intake performance. They are based upon shock wave theory for compression calculation and experimental results for internal loss evaluation. Intake efficiency and mass flow ratio entering the combustor can be determined.

OCEAS code, developed by AEROSPATIALE, predicts supersonic and hypersonic two-dimensional air-intake performance.

As the flow is supposed to be two-dimensional and planar, the amount of flow spilled sideways<sup>46,47</sup> is not taken into account.

OCEAS computes analytically, step by step, shock waves, expansion waves, slip lines and their interactions.

The total pressure recovery can be computed for different normal shock wave location.

Internal losses at the critical point are determined by use of an empirical function obtained by ONERA from the compilation of experimental results from Mach 2.0 to 3.5 :

$$1 / \cosh((M - 1) / 3) \quad (34)$$

In supercritical regime, bleed mass flow  $\epsilon_{\text{bleed}}$  is calculated as a function of the total pressure in the bleed and the throat section of the bleed. The engine mass flow is then deduced :

$$\epsilon_{\text{engine}} = \epsilon_{\text{total}} - \epsilon_{\text{bleed}} \quad (35)$$

Boundary layer effects are taken into account by wall displacement in an iterative process. Displacement thickness is obtained by use of semi-empirical formulas<sup>45</sup>.

#### 4.1.2. Numerical Methods

Numerical methods are essential to compute unconventional configurations like air-breathing missiles, to determine load distributions for mechanical analysis, local flowfield properties (e.g. velocity profiles at an inlet entry section or shear stresses for aeroacoustic methods), thermal fluxes to provide the designer with fundamental information on the physical effects taking place in a complex flowfield (e.g. lateral jet interaction).

According to the value of the Knudsen number the flow can range from the near collision-free molecular flow ( $Kn \approx 1$ ) to the collision-dominated continuum flow ( $Kn \ll 1$ ). The governing equation for all these flow ranges is the

Boltzmann equation, an integro-partial differential equation for the molecular distribution function. The complexity of this equation is high and numerical solution are costly (Monte Carlo methods).

The Navier-Stokes equations are the most complete set of equations modelling the evolution of a Newtonian fluid in a continuum regime. Unfortunately, due to computer limitations, Direct Navier-Stokes Simulation (DNS) are still restricted to very simple geometries (flat plates or ducts) at relatively low Reynolds number. Nevertheless, these DNS computations are essential for the progress of turbulence or combustion modelling.

A first approximation is to resort to time-average rapidly fluctuating components. This yields to the Reynolds-Average Navier-Stokes equations (RANS) which require a turbulence model to provide closure for the solution (and combustion models in case of reactive flows). These equations should be used for the most complex flows including large scale separations, with possibility of unsteadiness. Such situations on a missile are :

- base flow,
- very high incidence flow (up to 90°),
- strong shock / boundary-layer interaction,
- unstating point determination.

A second step of approximation is to neglect the viscous terms in the streamwise direction, this yields to the Thin-Layer Navier-Stokes equations (TLNS). They are unsteady equations. The slenderness of a missile body make them attractive for computation of high incidence flow with unsteady separation.

Making the hypothesis of steady phenomenon yields to the Parabolized Navier-Stokes equations (PNS). These equations only apply to supersonic flows.

Neglecting viscous terms in two directions (parallel to the wall) yields to Viscous Shock Layer (VSL) approximation, often used to compute blunt noses regions.

Let us come back to the RANS equations and make the hypothesis that the viscous effects stay in a thin layer around the vehicle. We are then authorised to separate the flow in two regions :

- an outer region, where all viscous effects are neglected (Euler equations),
- a thin inner region where simplified viscous equations are derived : the boundary layer equations.

An adequate coupling technique has to be used at the limit of the two regions following the strength of the viscous/inviscid interaction. Euler/boundary layer coupling technique does not apply in case of flow separation.

At a given design phase, and subsequently for a given precision demand, it is important to use the right code for the right application, and not to overestimate the need.

In external aerodynamics, semi-empirical tools will be very efficient in determining forces and moments on a conventional geometry.

For a non-conventional supersonic missile at small to moderate angle of attack, an Euler approach can give a very accurate prediction of forces and moments. This approach is particularly attractive, because an economic "space-marching" technique can be applied. Run on the now

available cheap and fast scalar processors, computation times have been drastically decreased, making possible to compute several evolutions of aerodynamic coefficients in one single night. On the other hand, meshing bottleneck has been by-passed by powerful multiblock mesh generator and use of overlapping or Chimera meshes<sup>48</sup>. This conjunction allowed to introduce CFD in the early missile design loop, at a cost compatible with the small budgets available in this circumstances.

In a more advanced phase, Euler computations will be adjusted with a few Navier-Stokes computations. In a supersonic case without transversal separation, PNS approach will be used.

For internal aerodynamics and combustion chambers computations, 3D unsteady Navier-Stokes equations in the RANS form are needed in almost all cases. Euler equations can be used in some cases for inlet computations. In the latter case, computation costs can be reduced by judicious initialisation of the flow field and use of laws of the wall.

Some years ago these different CFD approaches were available in different numerical codes. Nowadays we observe in many countries that numerical codes take the form of large structures with common features (numerical schemes, implicit algorithm, ...) and different physical modelisations.

To illustrate these different approaches, several numerical codes are described below :

#### *Aerothermodynamics*

Two codes are presented. The first one is a general purpose code, the second one is specialised on supersonic missile aerodynamics.

- FLU3M/MUSE<sup>49,50</sup> Euler/Navier-Stokes code has been developed by ONERA in collaboration with AEROSPATIALE for 3D external/internal transonic/supersonic flows. The following potentialities are now available :
  - explicit or implicit algorithms,
  - van Leer, Osher or Roe upwind schemes,
  - second order accuracy by MUSCL technique,
  - unsteady or space-marching Euler,
  - RANS or PNS,
  - multiblock, overlapping or Chimera structured meshes<sup>48</sup>,
  - perfect gas or equilibrium air,
  - Baldwin-Lomax or Jones-Launder turbulence models.
- TORPEDO<sup>51</sup> was developed in co-operation between AEROSPATIALE-Missiles, ENSAE and ONERA/CERT. It solves 3D PNS equations by means of a non-iterative implicit Roe-Osher-Chakravarthy scheme. Upwinding is maintained in the subsonic layer. Low memory size and CPU time requirement was one of its main objectives. Advanced turbulence modelling has been introduced in order to accurately predict longitudinal separation (algebraic and two-equation models in a two-layer approach, second-moment closure models).

#### *Aerothermochemistry*

Two codes are also presented. The first one is a general purpose reactive code, the second one is specialised in nose-to-tail computations of hypersonic scramjet propelled vehicles.

- MATHILDA has been developed by ONERA<sup>52</sup> with contribution of AEROSPATIALE. It is a 3D Euler and Navier-Stokes code for multispecies reactive flows. The numerical scheme is of Roe type and the implicit algorithm is 3ADI.  $k-\epsilon$  turbulence model is available, with law of the wall or low Reynolds models. Polynomial laws of  $\mu(T)$  and  $C_p(T)$  are included. Different combustion models have been introduced for air- $H_2$  and/or air-kerosene combustion : two-step global models, Eddy Break-Up (EBU) and Coherent Flame Model<sup>53</sup> (CFM) for turbulent combustion. Structured mesh can be of multiblock, overlapping and Chimera type.
- PNS2D is being used at AEROSPATIALE-Missiles in a unified nose-to-tail strategy for scramjet two-dimensional propulsive streamtube computations. It includes :
  - fitted bow shock (forebody and cowl external flow),
  - $k-\epsilon$  turbulence model with transition capability,
  - equilibrium air chemistry,
  - Roe/TVD and central differencing non iterative implicit numerics,
  - integrated gridding,
  - 10 species/17 equations kinetic model for air- $H_2$  combustion.

## **4.2. Ground Facility Simulation**

### *4.2.1. Aerothermodynamics*

Experimental simulation is still today absolutely necessary in spite of the important progress in numerical simulation.

Classical supersonic aerodynamics (external and internal) is determined in usual wind tunnels, and we will not go further on this subject.

For hypersonic regime there are different ground test installation :

- cold hypersonic regime, with low enthalpy and perfect gas conditions wind-tunnels,
- high enthalpy and generally low Reynolds number wind tunnels.

Following are several hypersonic facilities in France and Germany :

- The R5 wind tunnel<sup>54</sup> at ONERA Meudon is a Mach 10,  $T_1 = 1100$  K low Reynolds number facility that operates in laminar flow simulating altitudes of about 60 km. There are no real gas effects and in this way this tunnel can also be useful for CFD validation experiments on viscous interaction effects.
- The F4 arc-jet wind tunnel<sup>54</sup> at ONERA Fauga-Mauzac is a real gas facility with reduce stagnation enthalpy. It has been designed to reach  $H_1 / RT_a = 200$ . The static conditions in the test section are non-

equilibrium with running time of about 80 ms, adequate for balance measurements.

- The TH 2<sup>55</sup> heated driver shock-tunnel in Aachen has test section conditions of non-equilibrium flow at Mach 6 to Mach 15.
- The HEG<sup>55</sup> free piston driven shock tunnel in Göttingen is design to obtain Mach 7 to 9.

Most of the hypersonic facilities have non-equilibrium flow in the test section.

New instrumentation technologies have been developed : measurements of temperature and concentration using Electron Beam Fluorescence (EBF), LASER Induced Fluorescence (LIF), Coherent Anti-Stokes Raman Scattering (CARS), pressure measurements using piezoelectric and piezoresistive transducers, pressure sensitive paints, holographic flow visualisation, liquid-crystal and infra-red mapping of temperatures and heat transfer rates.

Due to their limited flight domain, hypersonic missiles will generally not need to be tested in hypersonic facilities which have been designed for space vehicles.

On the other hand, production cost reduction will impose to realise hot structures with standard materials. These installation can help to test these materials in realistic conditions.

AEROSPATIALE has designed and built the SIMOUN plasma wind-tunnel for material testing. In order to provide high temperature air, an high power arc heater plasma generator is used , placed just before the nozzle. The nozzle ends into a free jet chamber where the model is mounted. Main characteristics are listed below :

power supply system	6MW
stagnation pressure	1 to 14 bar
stagnation enthalpy	3 to 11 MJ/kg
mass flow rate	0.04 to 1 kg/s
run duration	1 500 s

#### 4.2.2. Ramjet and scramjet ground testing

Ramjet and scramjet ground-testing necessitates specific facilities with performance characteristics related to those of the missiles :

- Mach 2 to 6.5,
- altitude from 0 to 35 km,
- accelerations, climbing, diving and turns,
- integrated rocket/ramjet tests.

AEROSPATIALE has built at Bourges-Subdray specific facilities (see figure 41).

These facilities are used for testing high-performance missiles :

- combustion (operating range, performance levels, ...)
- endurance (thermal protection, electronic equipment)
- adjustment of transition between rocket mode and ramjet mode,
- synthesis tests (complete missile except warhead).

Two vast cells able to fire boosters with 600 kg of fuel contain four test lines with altitude simulation equipment.

Air is provided in a blow-down mode. Pressure (0.2 to 80 bar ) and mass flow (1 to 300 kg/s) are regulated. Air is either heated at constant temperature by an accumulation heater, or by hydrogen heaters if temperature regulation is needed. In the latter case O<sub>2</sub> is injected downstream of the heater in order to regenerate the air. Maximum temperature is 1800 K. Fuel regulation (liquid or gas) is automatic.

Three test modes are possible :

- connected pipe mode to simulate complete trajectories, with known inlet characteristics,
- semi-free jet mode to simulate constant Mach number flight of a complete missile with inlets,
- free jet test for overall check and approximate measurement of T-D balance.

All the AEROSPATIALE ramjets and the CHAMOIS scramjet model have been tested in this facility.

### 4.3. In Flight Testing

The development of scramjet technology needs a large phase of flight experimentation because of the difficulties to simulate flight conditions on ground, and the extreme sensitivity of the aeropropulsive balance.

A first experiment has been carried on by the CIAM<sup>57</sup> on an axisymmetric hydrogen engine.

## 5. RESULTS OF COMPUTATIONAL AND EXPERIMENTAL STUDIES

Due to the simulation limitations of test facilities, hypersonic vehicle design depends on a strong interaction between computational fluid dynamics, wind tunnel testing and in-flight testing (see figure 42).

### 5.1. External Aerothermodynamics

#### 5.1.1. Supersonic force-type flight control surface-to-air missile (ASTER)

It is a cruciform missile with four low aspect ratio wings and four control surfaces (figure 43). Force control is achieved by means of jets emerging from the lateral sides of the wings. Global aerodynamic model is determined in two phases :

- determination of the aerodynamic model without jets,
- determination of jet interaction model.

Due to the high number of wind-tunnel tests to cover all the cases of jet interaction (Mach, incidence, roll angle, altitude), a combined wind-tunnel/CFD approach has been used for the second phase.

On this configuration, it has been demonstrated that inviscid two-species computations can give enough accurate results for forces and moment prediction<sup>56</sup>. As an illustration, a two jet configuration is presented on figure 44.

Table 4 presents at Mach 3, incidence 10° comparisons between experimental and numerically determined global

coefficients<sup>58</sup>. Results without jet are of good quality. With jets, normal and side force coefficients are well predicted, as well as pitching moment.

	without jet	with two jets
CN/CN <sub>exp.</sub> -1	0.01	0.03
CY/CY <sub>exp.</sub> -1	-	0.13
(Xcp - Xcp <sub>exp.</sub> )/D	0.12	0.2

Table 4 : Euler results on surface-to-air configuration

These results clearly set the capabilities of Euler computations for complex transverse jet applications at moderate supersonic regime. In the present case, jets are issued from wing leading edges, and local viscous interactions can be neglected, it follows that global forces and moment are correct.

The same missile without jets has been computed in a PNS approach in the same upstream conditions. Flow is assumed to be symmetric. Turbulent boundary layer was imposed in computation as well as in the experiment on the ogive apex. The Reynolds number (from wind-tunnel testing) is  $0.9 \cdot 10^6$ .

Total pressure contours in various missile sections (figure 45) demonstrate the influence of vortex development on lifting surfaces. Furthermore, body wall pressure in two sections (figure 46) evidence an improvement due to viscous modelling. One may notice that good prediction was already given by Euler computation as far as lifting surfaces are concerned (apart from leading edge).

5.1.2. Supersonic airbreathing missiles

As illustrated in figure 47 (ANS missile), supersonic airbreathing missiles have unconventional geometries. In this case, forces and moments are determined by an Euler computation, giving also local pressure distribution.

For inlet integration, Euler computation is not adequate, and a Navier-Stokes computation has to be carried out, as illustrated on figure 48. On this figure are compared space marching Euler and PNS computations on a three calibre ogive cylinder at Mach 2 and 8° angle of attack. On the bottom graph is plotted the total pressure recovery of the forebody  $\langle P_{i1} / P_{i0} \rangle$  for different roll location of a square inlet. It appears that pressure recovery is almost constant in case of the Euler computation, whereas a 6 % decrease occurs at 60° roll angle in case of PNS computation.

5.2. Ramjet Intake Flowfield Computation and Performance Prediction

Due to the complexity of intake geometries and flow fields, computations are usually split into two phases<sup>59</sup>.

In the first one, intakes are computed alone, with an uniform upstream flowfield corresponding to the averaged flowfield entering the intake. This method is well suited for the preliminary design phase. But, this simplified method is imperfect and in a second phase it becomes necessary to take into account the real non uniform flowfield entering the air intake.

5.2.1. Intake in a uniform external flowfield

After the fuselage flowfield has been computed, it is possible to determine average values in the inlet capture area (usually we consider a transverse plane located at the apex of the first compression ramp), for Mach number, total pressure, incidence and sideslip angles. Then, the intake can be considered in this uniform flowfield as an isolated intake.

In this phase, the intake is considered 2D or axisymmetric.

Computation tools used are based on semi-empirical, Euler and Navier-Stokes methods.

To demonstrate the capabilities of these tools, we will consider the two-dimensional intake presented in figure 49. This intake has two compression ramps and an internal boundary layer bleed, the free stream Mach number is 2.89. During the wind tunnel test, the ramjet operation is simulated with an obstrucater located at the end of the diffuser.

- *Semi-empirical calculation.* Figure 50 presents the predicted characteristic curve. The comparison between experiment and computational results shows a quite good agreement. However, the efficiency at the critical point is underestimated. But, if we do not take into account the internal losses through the empirical function of eq. 34, we overestimate the efficiency at this point.
- *Euler calculation.* Although Euler equations do not take into account viscous effects, they allow to analyse the flow in all the intake and to estimate mass flow ratio, total pressure recovery and wall pressures.

To build a structured grid in the intake, it is necessary to adopt multiblock strategy. The grid used contains about 30 000 points and is divided into four domains (figure 49). The first one extends from the upstream boundary to the cowl lip plane, the second one from the cowl lip plane to the outer downstream boundary, the third one from the cowl lip plane to the diffuser end boundary, and the last one represents the boundary layer bleed.

In computation, we can use two possibilities to represent obstruction :

- apply a static pressure in the downstream diffuser,
- use a variable throat to fix the mass flow.

The use of the first possibility is delicate<sup>47</sup>. To avoid divergence or unphysical solutions, one has to begin computations with a low static pressure and to increase it progressively. Furthermore, it is not possible to reach the critical regime.

Figure 51 presents the Mach number contours obtained with such a procedure. For this computation, the experimental static pressure has been applied downstream of the internal bleed. The presented solution corresponds to a critical regime. We can see the external compression shocks, the cowl shock and the downstream normal shock, near the internal boundary layer bleed entrance, which makes the separation between the supersonic part and the subsonic part of the flow.

Figure 52 presents the characteristic curve obtained with Euler computation. The comparison between experimental and computational results shows good agreement on engine mass flow and pressure recovery.

- *Navier-Stokes equations* allow to take into account viscous effects like total pressure losses near the wall, shock-boundary layer interactions, vortical flow at bleed entrance, ...

Figure 53 presents a comparison between Euler and turbulent Navier-Stokes computations. We can see that Navier-Stokes calculation provides a normal shock located slightly upstream from the one obtained with the Euler computation. It is certainly due to the boundary layer displacement thickness in the diffuser which reduces the available cross-section.

### 5.2.2. Intake with a non-uniform external flow field

The previous method is approximate as it does not take into account 3D effects due to forebody influence and also to compression ramp finite width or intake lateral wall. In this case 3D air-intake computation with the real non-uniform flow field around the fuselage is necessary. To perform these computations, two ways are possible :

- compute the intake placed in a non uniform flow field,
- compute together external and internal flow fields (global computation).

Principle of the first method is exemplified on figure 54. The advantages of this method is that only one external computation is necessary at each flight point, whatever the geometry and the running point (supercritical or close to critical conditions) of the air-intake. The drawback is that strong interactions between internal and external flows are not taken into account (subcritical running, high sideslip angle, ...). Figure 55 presents an application of such a method on the AEROSPATIALE ASMP type missile configuration.

The global computation applies to all operating conditions from the supercritical to the subcritical one. Furthermore, it allows to take into account the internal flow effects on external aerodynamics, but it demands more CPU and meshing time. An example is given on figure 56.

An intermediate method is to interpolate the external flowfield on boundaries which are located enough away from the intake. Overlapping and Chimera grid techniques make it very powerful.

## 5.3. Scramjet intake Flowfield Computation and Performance Prediction

In this section are presented the computation of an isolated scramjet inlet tested by NASA, the design of an isolated inlet with struts and a forebody-inlet analysis<sup>62</sup>.

### 5.3.1. NASA P8 inlet

P8 air inlet was tested by NASA<sup>63</sup>. It is an isolated rectangular air inlet (figure 57), on design for freestream Mach number equal to 7.4. Two-dimensional Euler and PNS equations are solved for a transitional flow with perfect gas hypothesis. Transition location was given by

experimental tests. The most important feature is the location of the reflections of the cowl shock on the centerbody and then on the upper side. PNS approaches predict with a better accuracy shock location on both upper and lower side. Flowfield visualisation shows a thick boundary layer on the lower side so that viscous effects are of primary importance for shocks location. PNS pressure levels are in qualitative agreement on the centerbody where strong viscous effects take place at shock reflection but quite good correlation with experiments is obtained on the cowl.

Three-dimensional Reynolds Averaged Navier-Stokes computations are mandatory in order to take into account three dimensional effects :

- lateral compression,
- lateral boundary layers development and corner flows (even for rectangular ducts),
- various struts positions : not only horizontal but also vertical or with swept leading edge,
- sideslip influence,
- forebody influence.

As it is shown of figure 58, 2D and 3D Navier-Stokes computations of the same inlet have been realised. In the symmetry plane, all computations are very close one to the other. In this case, the three-dimensional effects which affect the pressure distribution along the lateral walls do not modify the flow in the symmetry plane.

### 5.3.2. Scramjet inlet design

Design phase of a two-dimensional air inlet with struts is demonstrated on figure 59. Shocks and expansion waves are first computed with OCEAS and design is conducted by the following guidelines :

- starting of the inlet,
- on design Mach number,
- required conditions for injection.

The first two parameters depend on the flight envelop of the airbreathing scramjet vehicle.

The following parameters are to be defined :

- number, angle and length of compression ramps,
- cowl angle and location,
- struts number and location.

Starting of the inlet may be analysed through simple quasi-one dimensional approach<sup>64</sup> but this criterion may be very restrictive and do not account for viscous effects. In fact, starting depends on the unsteady phase before established Mach number is obtained, so it is very sensitive to initial conditions : starting may strongly depend on the testing facility and computational analysis should be done through unsteady Navier-Stokes solvers.

Struts participate to flow compression. Their number and position is a compromise between injection requirements, structural feasibility and starting of the inlet.

Various shapes are presented on figure 59. They lead to a compromise between low contraction ratio (necessary for low Mach number inlet starting) and high pressure recovery (favourable to combustion rate and thrust).



PNS computation was performed on the final version of the inlet so as to fine tune flow parameters.

Two forebody-inlet configurations are now considered. The first one is a sharp nose forebody with the following freestream conditions (figure 60) :

- Mach number = 15,
- incidence = 7°.

This test case is interesting for code validation. Many interactions may be distinguished within the internal duct.

The second case is made of a blunt forebody. Freestream conditions are (figure 61) :

- Mach number = 12,
- incidence = 4°.

The inlet is designed first with OCEAS with a sharp forebody nose. Then, coupled VSL-PNS2D approaches allow us to account for nose bluntness (2 nose radii). The resulting inlet performances (see table below) show in what proportion nose bluntness deteriorates pressure recovery at combustor entry. The same geometry has been computed at a freestream Mach number equal to 6, leading to the same conclusion.

	Mach number	Pressure recovery
R=20 mm	4.50	0.22
R=40 mm	4.25	0.18

*Table 5 Mean flow results at inlet exit section*

The above mentioned applications demonstrate the ability to design scramjet inlets through numerical approach. However, further improvements of CFD tools are necessary. Two main directions can be distinguished :

- need for more efficient three-dimensional viscous computations,
- integration of air inlet design into a coherent numerical strategy for the whole propulsive streamtube.

#### 5.4. Scramjet combustion chamber

AEROSPATIALE-Missiles has designed, build and test a steel scramjet model called "CHAMOIS" in its Bourges Subdray facility.

Its rectangular entrance area is about 0.05 m<sup>2</sup>. It is equipped with wall measurement devices (80 pressure taps, 10 heat flux sensors, 1 skin friction gage). Its objectives are to estimate combustor efficiency, to compare different injection systems, to understand real size scramjet phenomena and to validate numerical tools.

The nominal air feeding conditions correspond to a Mach 6 velocity flight at 60 kPa of dynamic pressure. Nominal values at the entrance of the combustor are Mach 3.1, stagnation pressure 3 MPa, stagnation temperature 1650 K, and an air mass flow of 30 kg/s. It is the largest scramjet combustor tested in Europe (see figures 41, 62).

Self-ignition was obtained at the first test. Optimised shape tests will be realised in 1996 and 1997. Improvements in the measurement system are planned :

- optical window in the injection box,
- thrust measurement,
- optimised location and eventual adding of heat flux sensors and pressure taps,
- use of several friction gages.

After the tests, a 1D analysis is used as a way to estimate the combustor efficiency.

As very complex physical phenomena take place inside the combustion chamber, CFD analysis is used to complement to 1D analysis. 2D and 3D reactive Navier-Stokes computations are performed. Thick boundary layer at the entrance of the injection box, air-viciation by water, as well as detailed features of the injection struts are taken into account. The aim of these computations is to give an assessment of the main flow features, in order to check design parameters, to prepare test sessions, and to explain experimental measurements, and understand self-ignition process.

Examples of 3D results are given on figures 63 and 64. In this first shape the injection struts are very simple, using a combination of both transverse and tangential injections. Ignition take place near the struts, at shock interaction locations, as low temperature levels in the incoming air do not allow instantaneous ignition. Flow is highly stratified. 3D computation is necessary to take into account wall corner effects and initiation of eventual upstream shock train at high equivalence ratio.

Parametric study is facilitated by use of Chimera meshes, as shown on figure 65. A simple combustion chamber mesh is realised without any strut, then an adapted mesh is realised around the strut with refinement in the boundary layer and near the hydrogen injection holes. Then both meshes are superimposed and a global computation is done. This method has three major advantages :

- meshes are easier to generate,
- struts can be shift without remeshing,
- local refinement do not spread.

Pressure and temperature contours are presented in figure 66.

#### 5.5. Scramjet nozzle

Nozzle flow can be studied with three types of tools : analytical codes based on characteristics method able to give a preliminary nozzle geometry in the design phase, Euler codes for the design phase with two-species flow formulation, and 3D Navier-Stokes codes with chemistry to calculate 3D viscous and recombination effects.

Figure 67 shows a 2D Euler computation of a scramjet nozzle with two species modelisation for internal/external flows confluence.

#### 5.6. Thrust Evaluation

In order to predict vehicle thrust and to evaluate specific impulse we may use two types of tools :

- 3D computational tools already mentioned, applied to the whole propulsive stream tube, component after component,
- global computational tools.

Global tools participate in the design phase of the project and can give a rough estimate. They are two types: 1D analytical codes for ramjets and scramjets, 2D PNS codes for scramjets.

One-dimensional analytical codes, devoted to scramjets, calculate the performance of a two dimensional mixed-compression scramjet inlet, a kerosene or hydrogen fuelled combustor with staged injection of liquid or gaseous fuel, and a nozzle. They take into account real gas properties, viscous effects and shock-waves interactions.

Nose-to-tail PNS2D codes compute the complete stream tube from the nose to the nozzle end section with longitudinal hydrogen injection and internal/external flows confluence.

Figure 68 shows an example of a 2D PNS nose-to-tail calculation, for an AEROSPATIALE demonstrator. This demonstrator would allow to validate the engine at speed near Mach 8, in order to combine ground tests and numerical results. The concept is based on a simple architecture to reduce the cost of the vehicle and make it reasonable in a short term. The concept uses a two-dimensional scramjet. Computational results shown are Mach number distribution for the internal and external flows.

### 5.7. Experimental facilities and CFD as complementary tools

The propulsion systems development of hypersonic airbreathing vehicles involving experimental tests and theoretical evaluation require not merely an evolution of current technology, but large technology steps. The deficiencies in hypersonic propulsion test and evaluation methodology, including ground testing, CFD, and flight testing, are known, and the need for improving the traditional approach through the use of an integrated computational/experimental evaluation methodology is real.

In the aerospace industry, CFD is recognised as a design tool, and is commonly used in an interactive process to select the best geometry among several before any model manufacturing and ground testing. Even if there are still many unsolved problems with shortcomings and if computational results are not close enough to experimental ones, this methodology based on numerical comparisons gives good results. Moreover, this predictive use of theoretical tools provides numerical results package to experimental specialists, allowing them to adjust their probes locations and test conditions in order to catch flow phenomena, then to understand experimental results immediately by flow analysis.

Furthermore, it is generally difficult to measure thrust and impossible to measure the aeropropulsive force. So CFD is used, as a data reduction tool to compute the engine thrust from available experimental results (static and pitot pressure...), then to give an aeropropulsive force estimate by nose to tail calculation before flight test.

Whereas in supersonic systems, the state of the art in ground testing, computations, and flight testing is

developed in a balanced state, hypersonic vehicle systems, in contrast, are severely lacking in ground test capabilities, particularly at high Mach numbers. Current ground test facilities are not very adequate in performance, size and run times, especially for the vehicle engineering development. So, for these hypersonic systems, an ever larger dependence must be placed upon computation and flight testing to achieve confidence in system performance. Therefore, it is important that CFD should be given continued emphasis and financial support to provide a bridge between the capabilities of the best ground test facilities, and the requirements for vehicle development and certification prior to first flight.

The evolution of hypersonic testing methodology should be based upon the synergy made possible by integrating the complementary capabilities of ground test facilities, CFD and flight tests (figure 42).

## 6. CONCLUSION

Design of supersonic/hypersonic missiles implies the study of very complex flowfields, mainly when they are controlled by lateral jets or powered by ramjet or scramjet engines.

At the present time computational tools are able to predict fairly well external and internal airbreathing missile aerothermodynamics. However progress must be made in the development of physical models to improve flow field prediction when viscous and chemical effects are predominant.

CFD tools added to wind tunnel, propulsion bench and flight test, allow to design and optimise faster and at a lower cost supersonic/hypersonic airbreathing missiles.

### Acknowledgements

We specially thanks J.-V. Hachemin, V. Le Gallo, X. Montazel, D. Sitbon for their contribution to the computations.

### References

- 1 Teal Group Corporation, "World Missiles Briefing", 1995.
- 2 Weinacht P., Sturek W.B. " Navier-Stokes Predictions of Static and Dynamic Aerodynamic Derivatives for High L/D Finned Projectiles", in " Missile Aerodynamics", AGARD CP-493, April 1990, Paper 20.
- 3 Taufer-Knöpfl I., "Hypersonic Missiles", in Military Technology, October 1995.
- 4 Anderson J. D., "Hypersonic and High Temperature Gas Dynamics", McGraw-Hill, (ISBN 0-07-001671-2), 1989.
- 5 DeJarnette F. R., Hamilton H. H., Weilmuenster K. J., Cheatwood F. M., "A Review of Some Approximate Methods Used in Aerodynamic Heating Analyses", Journal

- of Thermodynamics and Heat Transfer, vol. 1, n° 1, January 1987.
- 6 Stollery J. L., "Viscous Interaction Effects and Re-entry Aerothermodynamics : Theory and Experimental Results", in Aerodynamic Problems of Hypersonic Vehicles, vol. 1, AGARD Lecture Serie n° 42, July 1972.
- 7 Arnal D., "Laminar-Turbulent Transition" in "Computational Methods in Hypersonic Aerodynamics", Murphy T.K.S. editor, Fluid Mechanics and its Application Vol. 9, Computational Mechanics Publications and Kluwer Academic Publishers, 1991.
- 8 Nielsen J. N., "Missile Aerodynamics", Mountain View, CA, (ISBN 0-9620629-0-1), 1960.
- 9 Chin S. S., "Missile configuration Design", McGraw-Hill Book, 1961.
- 10 Hemsch M. J. (Editor), "Tactical Missile Aerodynamics : General Topics (Vol. 141) and Prediction Methodology (Vol. 142) Progress in Astronautics and Aeronautics, AIAA 1992.
- 11 Nielsen J.N., "The Present Status and the Future of Missile Aerodynamics", in "Stability and Control of Tactical Missiles Systems", AGARD CP 451, May 1988.
- 12 "Special Course on Missile Aerodynamics" AGARD Report 754, 1987.
- 13 "Special Course on Missile Aerodynamics" AGARD Report 804, 1994.
- 14 Park C. Leon S., "Calculation of Real-Gas Effects on Blunt-Body Trim Angles", AIAA Paper 89-0685.
- 15 Cronvich L. L., "Missile Aerodynamics", in Johns Hopkins APL Technical Digest, Vol. 4, n° 3, 1983.
- 16 Tsien, H. S., "Similarity Laws of Hypersonic Flows", in Journal of Mathematics and Physics, vol. 25, 1946.
- 17 Poisson-Quinton, Cérésuela, "Stabilisation d'un engin par évasement conique au culot en supersonique élevé, La Recherche Aéronautique n° 68, 1959.
- 18 Penland J. A., NACA TN 3861, 1957.
- 19 Spearman M.L., "Historical Review of Tactical Missile Airframe Developments", in Tactical Missile Aerodynamics : General Topics, Vol. 141, Progress in Astronautics and Aeronautics, AIAA 1992.
- 20 Schindel L.H., "Waveriders", in Tactical Missile Aerodynamics : General Topics, Vol. 141, Progress in Astronautics and Aeronautics, AIAA 1992.
- 21 Hemsch M. J., Nielsen J. N., "Equivalent Angle of Attack Method for Estimating Nonlinear Aerodynamics of Missile Fins", J. Spacecraft and Rockets, Vol. 20, 1983.
- 22 Lesieutre D.J., Mendenhall M. R., Nazario S.M. Hemsch M.J., "Aerodynamic Characteristics of Cruciform Missiles at High Angles of Attack", AIAA Paper 87-0212, 1987.
- 23 Mahoney J. J., "Inlets for Supersonic Flows", AIAA Education Series, (ISBN 0-930403-79-7), 1990.
- 24 Falempin F.H., "Overview of French Research Center ONERA Activities on High-Speed Airbreathing Propulsion", XII ISABE, Melbourne, 1995.
- 25 Seddon J., Goldsmith E.L., "Intake Aerodynamics", Collins Professional and Technical Books, (ISBN 0-00-383048-9), London, 1985.
- 26 Laruelle G., "Supersonic Missile Air-Intakes : Design and Development Criteria", La Recherche Aéronautique 1987-6.
- 27 Laruelle G., "Missile Intakes", VKI Lecture Serie 1988-04 on Intake Aerodynamics, 1988.
- 28 Laruelle G., Goldsmith E.L., "Intakes for Missiles with Air-Breathing Propulsion", in "Practical Intake Aerodynamic Design" Goldsmith E.L., Seddon J. editors, Blackwell Scientific Publications, (ISBN 0-632-03103-4), Oxford, 1993.
- 29 Oswatich K., "Pressure Recovery for Missiles with Reaction Propulsion at High Supersonic Speed", NASA TM 1140, 1947.
- 30 Leynaert J., "Fonctionnement du Piège à Couche Limite Interne d'une Prise d'Air à Compression Supersonique Externe", AGARDograph 103, 1965.
- 31 Richards C.S., "Supersonic Air Intakes for Missiles", Weapons Aerodynamics Symposium, Royal Aeronautical Society, 1988.
- 32 Laurent J. M., Garnéro P., "Propulsion par Statoréacteur pour Missiles dans le domaine Mach 3 à 4.5", 79th AGARD/PEP "Airbreathing Propulsion for Missiles and Projectiles", Symposium, AGARD CP 526 St Médard, 1992.
- 33 Fulghum D. A., "Pilots to Leave Cockpit in Future Air Force", in Aviation Week & Space Technology, February 5, 1996.
- 34 Chevalier A., Falempin F., "Review of New French Facilities for PREPHA Program", AIAA Paper 95-6128.
- 35 Chevalier A., Bouchez M., Bouchaud D., Auneau I., Montmayeur N., "An Industrial Point of View on Scramjet Combustor Design", IUTAM 95.
- 36 Bouchez M., Montmayeur N., Leboucher C., Souchet M., "Scramjet Combustor Design in France", AIAA Paper 95-6094.
- 37 Heindrick P., Vandenkerkhove : Precompression influence on SSTO performance. AIAA 93-5030, Munich (Germany), December 1993
- 38 Torrence M.G., "Experimental Investigation of a Mach 6 Fixed-Geometry Inlet Featuring a Swept External-Internal Compression Flowfield. Langley Research Center (USA), 1975
- 39 Lacau R. G., "An Introduction to Tactical Missile Aerodynamics", in AGARD Report n° 754.
- 40 Lacau R. G., "A Survey of Missile Aerodynamics", NEAR Conference on Missile Aerodynamics, Monterey, 1988.
- 41 Hemsch M. J., "Component Build-Up Method for Engineering Analysis of Missiles at Low-to-High Angles of Attack", in Tactical Missile Aerodynamics : Prediction

Methodology, Vol. 142, Progress in Astronautics and Aeronautics, AIAA 1992.

42 Moore F. G., "Engineering Codes for Aeroprediction : State-of-the-Art and New Methods", in AGARD Special Course on Missile Aerodynamics, AGARD REPORT 804, 1994.

43 Champigny P., Baudin D., Gonidec P., "Prévision des coefficients aérodynamiques de missiles munis de prises d'air", in AGARD CP 493, 1990.

44 Gentry A. E., "Hypersonic Arbitrary-Body Aerodynamic Computer Program (Mark III version). Vol. 1 - User's Manual", Report DAC 61552, McDonnell-Douglas, 1969.

45 Cousteix J., "Turbulence et Couche Limite", Cepadus-Editions, 1989.

46 Gregor I. Mc, "Some Theoretical Parameters Relevant to the Performance of Rectangular Air Intakes with Double Ramp Compression Surfaces at Supersonic Speeds", RAE-TR-71232, 1971.

47 Duveau P., Thépot R., "Prediction methods for supersonic inlets", Xth ISABE Symposium, 1991.

48 Gillybœuf J.G., Mansuy P., Pavsic S., "Two New Chimera Methods: Application to Missile Separation", AIAA Paper 95-0353.

49 Guillen P., Dormieux M., "Design of a 3D Multidomain Euler Code", Computational Mechanics Institute, Supercomputing in Fluid Flows, Boston 1989.

50 Dormieux M., Jouet C., Borrel M., "Simulations Numériques d'Ecoulements non Réactifs avec Jet Transversal au Moyen de Codes Euler et Navier-Stokes Laminaire", 28ème Colloque d'Aérodynamique Appliquée, 1991.

51 Lafon A., Deniau H., Maman P., Moschetta J.M., "A Fully Upwind Implicit PNS Solver for the Computation of 3D Supersonic Flows with Crossflow Separation", AIAA Paper 94-0643.

52 Dutoya D., Errera M. P., "Une Décomposition Formelle du Jacobien des Equations d'Euler. Application à des Schémas Numériques Décentrés", La Recherche Aérospatiale, vol. 1, 1992.

53 Montazel X., "Etude Expérimentale et Modélisation de la Combustion Turbulente dans les Foyers de Statoréacteur", Thèse Ecole Centrale de Paris, 1994.

54 Chanetz B., Coët M.C., Nicout D., Pot T., Broussaud P., François G., Masson A., Vennemann D. "Nouveaux Moyens d'Essais Hypersoniques Développés à l'ONERA : les Soufflerie R5 et F4", AGARD-CP 514.

55 Eitelberg G., Olivier H., "The High Enthalpy Facilities HEG and TH 2 in Germany", AGARD-CP 514.

56 Dormieux M., Marsaa-Poey R., "Numerical Assessment of Aerodynamic Interaction on Missiles with transverse Jets Controls", AGARD FDP symposium "Computational and Experimental Assessment of Jets in Cross Flow, Winchester, Apr.1993.

57 Roudakov A., Schickhman Y., Semenov V., Novelli Ph., Fourt O., "Flight Testing an Axisymmetric Scramjet - Russian Recent Advances", IAF-93, S. 4.485, Gratz, 1993.

58 Pagan D., Gaible F., Marsaa-Poey R., Dormieux M., "Application of Euler and Navier-Stokes Solvers for Predicting Lateral Jet and Vortex Structures on Missiles", AIAA Paper 94-1937, Colorado-Springs, July 1994.

59 Lacau G., Garnéro P., Gaible F., "Computation of Supersonic Intakes" in AGARD "Special Course on Missile Aerodynamics", AGARD Report 804, 1994.

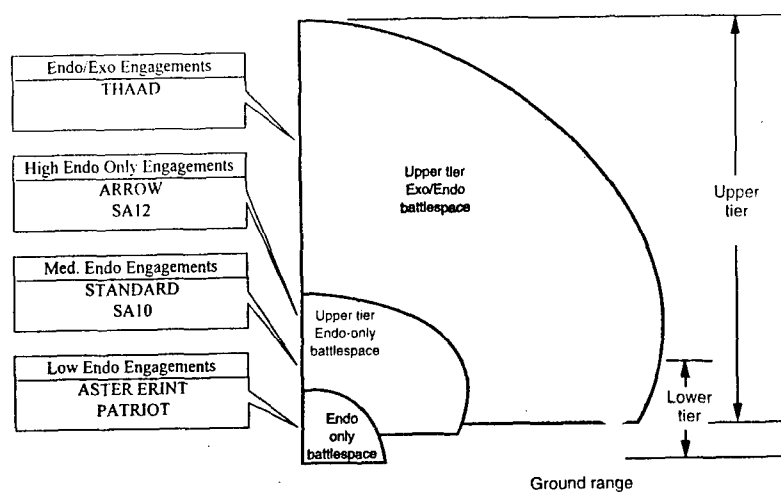
60 Garnéro P., Lacau R.G., "Etudes aérodynamiques de prises d'air supersoniques", AGARD Symposium on Aerodynamic Engine/Airframe Integration for High Performance Aircraft Missile, AGARD-CP-498, 1992.

61 AGARD Working Group 13 on Air-Intakes for high speed vehicle, AGARD-AR-270, 1991.

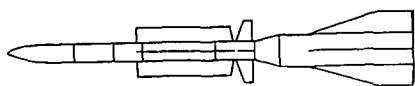
62 Gaible F., Garnéro P., Kaghian S., "CFD for Scramjet Inlets", Proc. of the Second European Symposium on Aerothermodynamics for Space Vehicles, ESTEC, 1995.

63 Seebaugh W.R., Doran R.W., De Carlo J.P., "Detailed Investigation of Flowfields within Large-Scale Hypersonic Inlet Models. NASA Ames Research Center (USA), NASA CR 114305, April 1971.

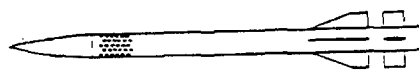
64 Carrère P.: "Air intakes", ENSAE lecture, Toulouse (France)



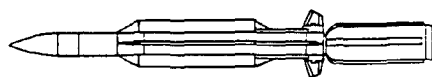
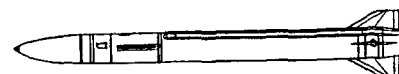
ASTER



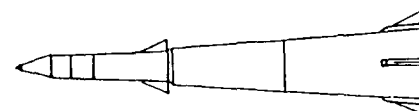
ERINT



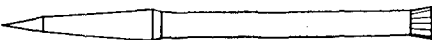
PATRIOT



STANDARD

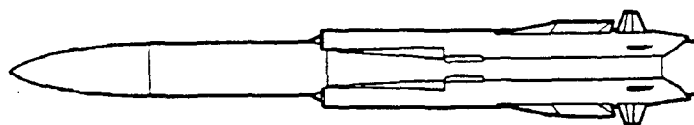


ARROW

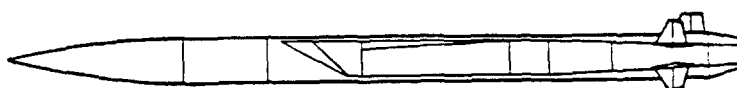


THAAD

Examples of high speed air-defence missiles



KH 31



ASMP

Examples of air-to-surface ramjet missiles

Figure 1 - Some geometries of high speed missiles.

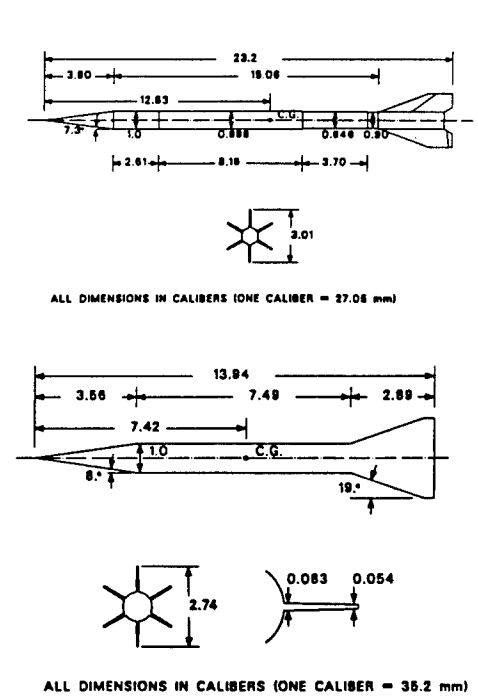


Figure 2 - Schematic sketch of a KE projectile<sup>2</sup>.

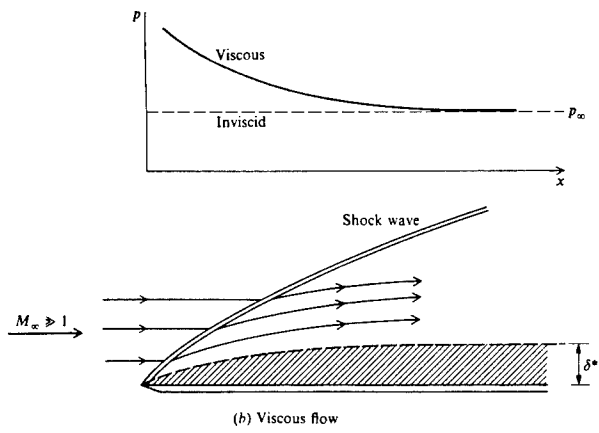


Figure 3 - Pressure distribution over a flat plate<sup>4</sup>.

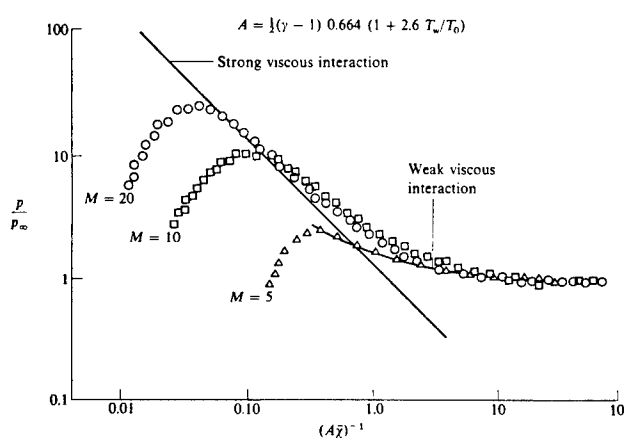


Figure 4 - Correlation of induced pressures over an insulated flat plate. Comparison with strong and weak viscous interaction theory<sup>4</sup>.

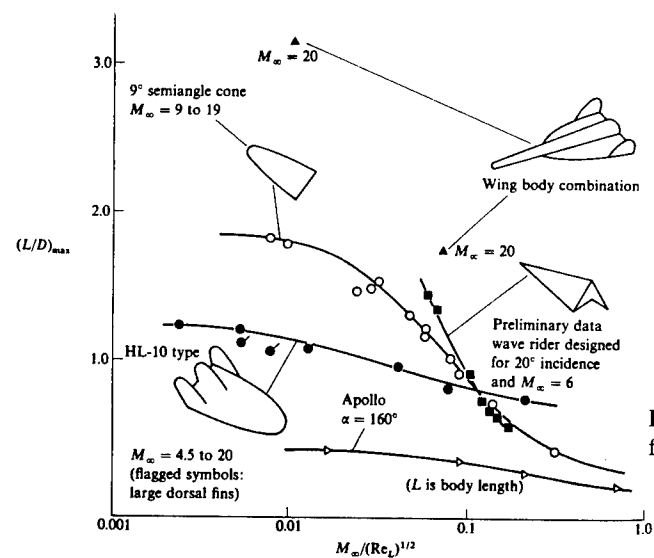


Figure 5 - Viscous effects on maximum lift-to-drag ratio for five classes of vehicles<sup>6</sup>.

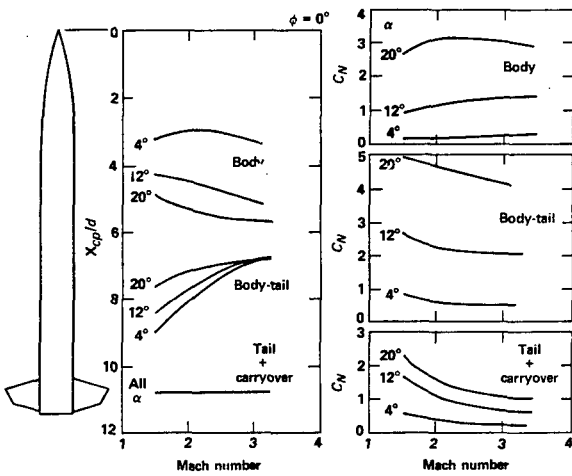


Figure 6 - Normal force coefficient and center of pressure<sup>15</sup>.

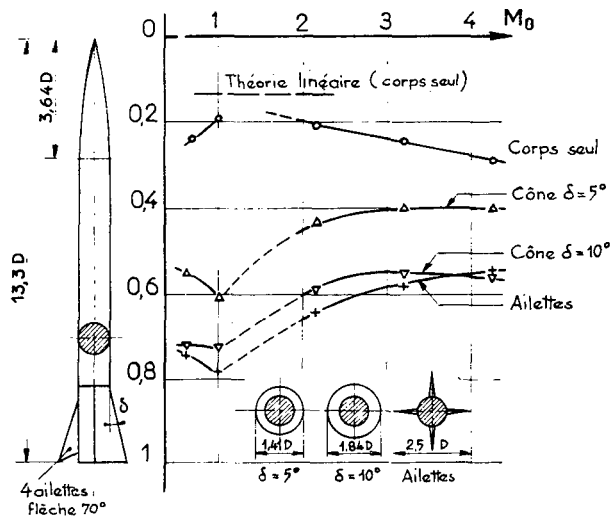


Figure 7 - Center of pressure evolution on body-tail and body-flare configuration<sup>17</sup>.

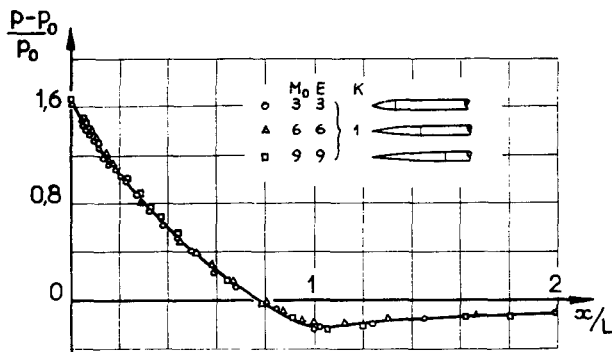


Figure 8 - Relative pressure distributions on ogives for different slenderness ratios  $\tau = 1/E$  and constant similarity parameter  $K = M_\infty / E$ <sup>18</sup>.

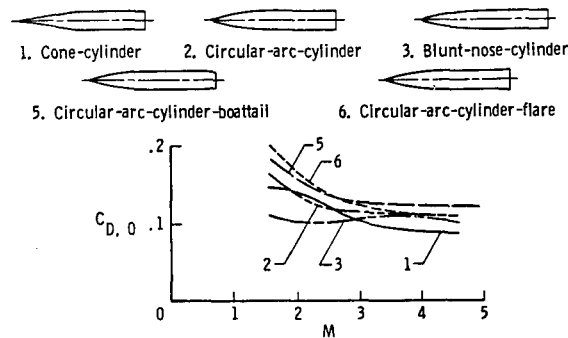


Figure 9 - Minimum drag evolution with Mach number for various forebodies and afterbodies<sup>19</sup>.

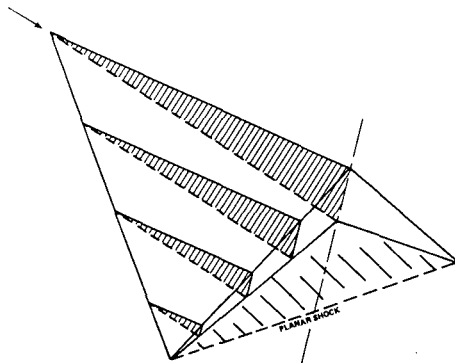


Figure 10 - The caret wing and waverider with underslung engine and plug nozzle<sup>20</sup>.

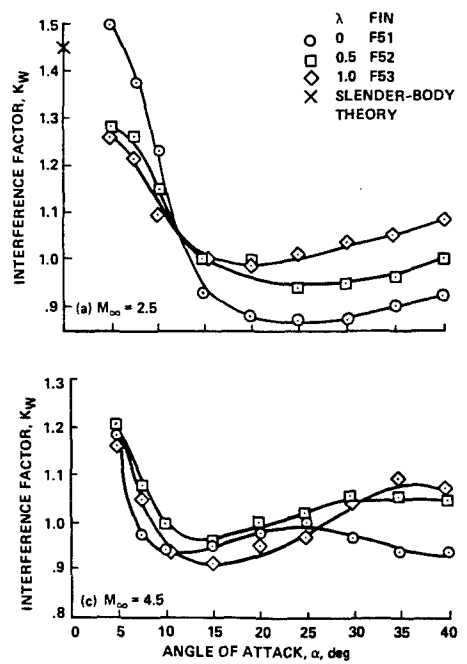


Figure 11 - Effect of taper ratio on interference factor  $K_W$  for aspect ratio 2 fins<sup>11</sup>.

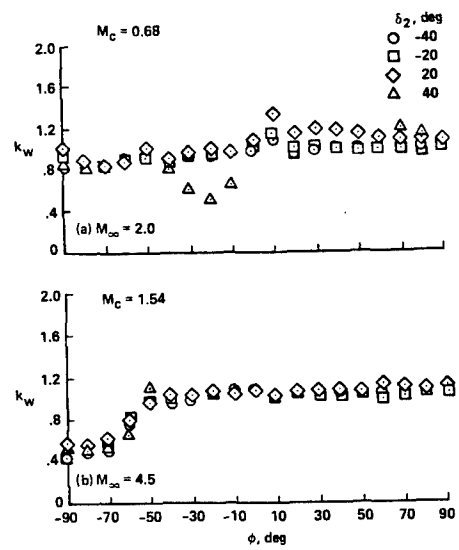


Figure 12 - Effect of roll angle and control deflection on  $k_W$  for all-movable controls<sup>11</sup>.

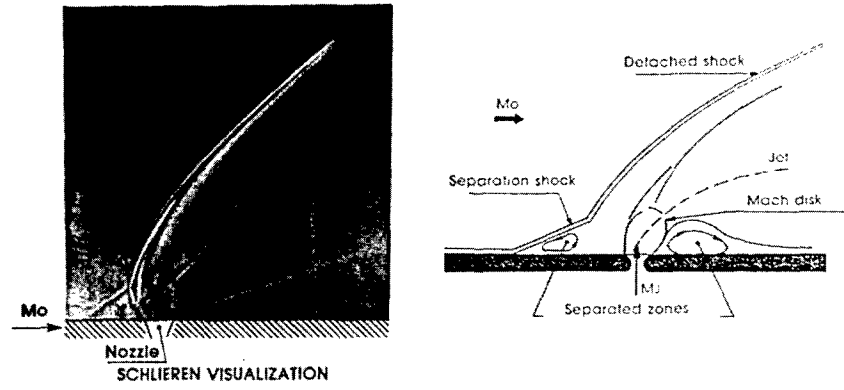


Figure 13 - Local interactions.

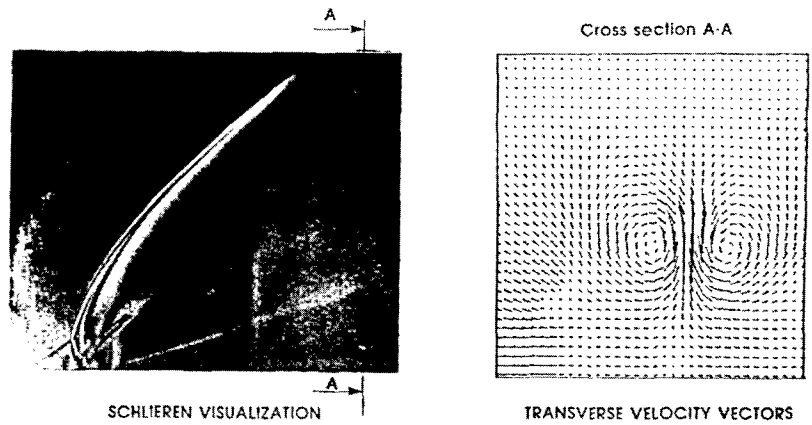


Figure 14 - Downstream interactions.



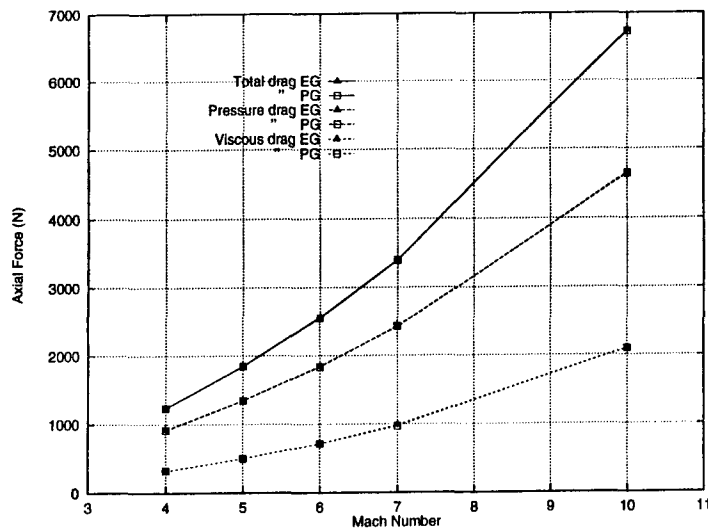


Figure 15 - Axial force evolution with Mach number on a  $L/D = 4$  cone at  $0^\circ$  angle of attack. PG : perfect gaz ( $\gamma = 1.4$ ), EG : equilibrium air.  $D = 150$  mm.

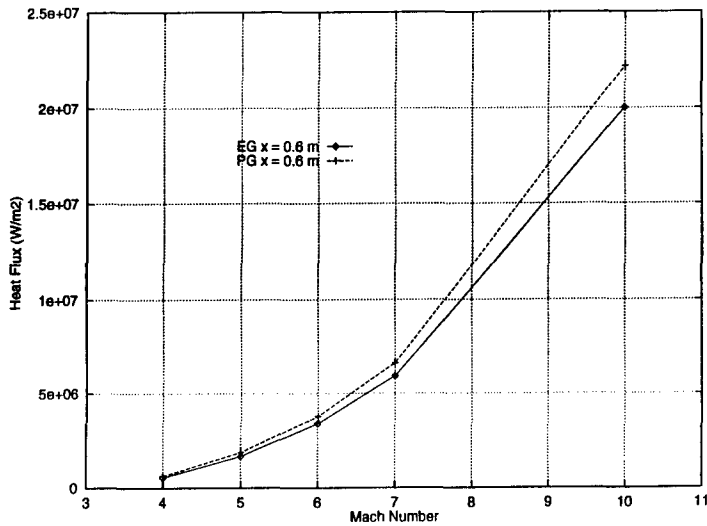


Figure 16 - Heat flux evolution with Mach number on a  $L/D = 4$  cone at  $0^\circ$  angle of attack. PG : perfect gaz ( $\gamma = 1.4$ ), EG : equilibrium air.  $D = 150$  mm.  $T_w = 800$  K.

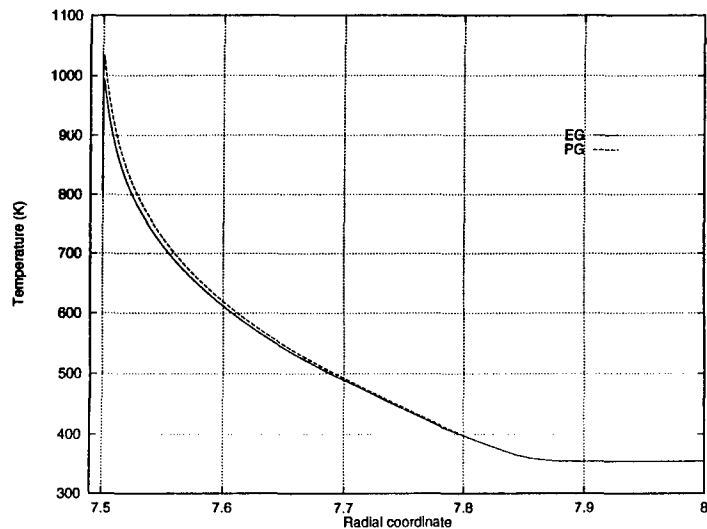


Figure 17 - Temperature evolution with radial distance on a  $L/D = 4$  cone at  $0^\circ$  angle of attack. PG : perfect gaz ( $\gamma = 1.4$ ), EG : equilibrium air.  $D = 150$  mm.  $T_w = 800$  K. Mach 6.

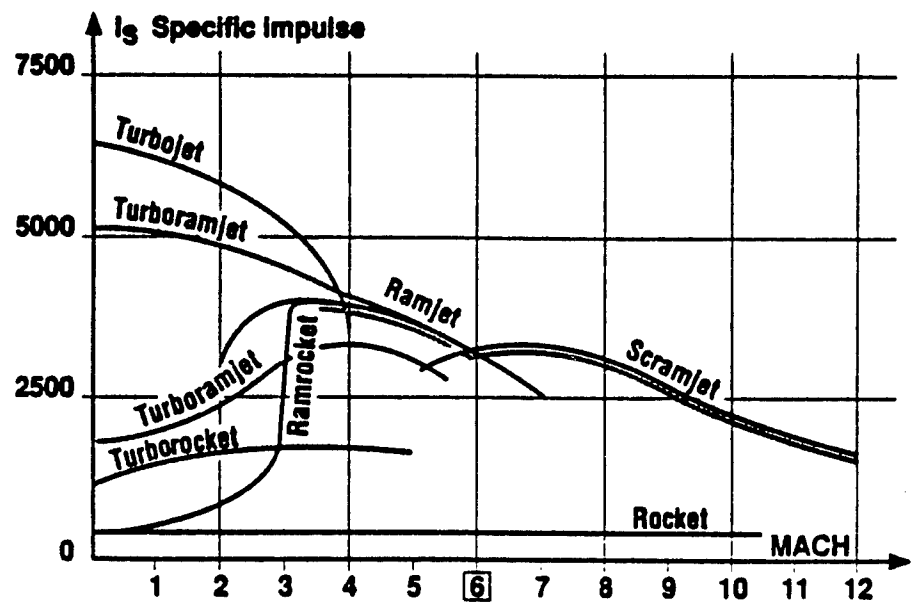


Figure 18 - Evolution of specific impulse with Mach number for rockets, turbojets, ramjets and scramjets.

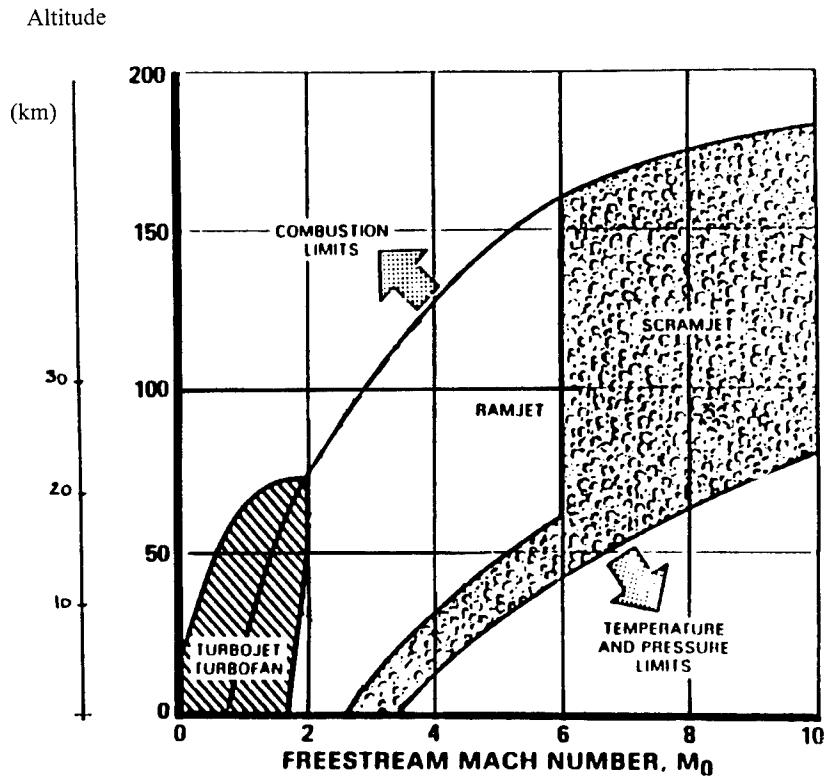


Figure 19 - Operational limits of different propulsion means.

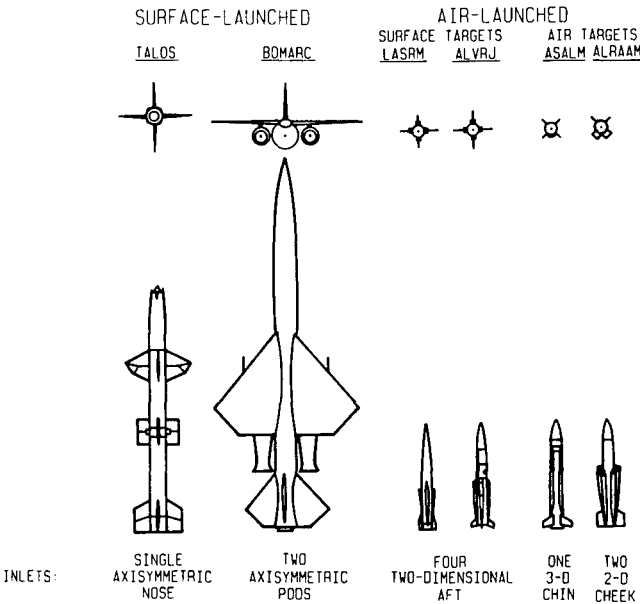


Figure 20 - U.S. missiles powered by boost rocket/sustain ramjet engines<sup>23</sup>.

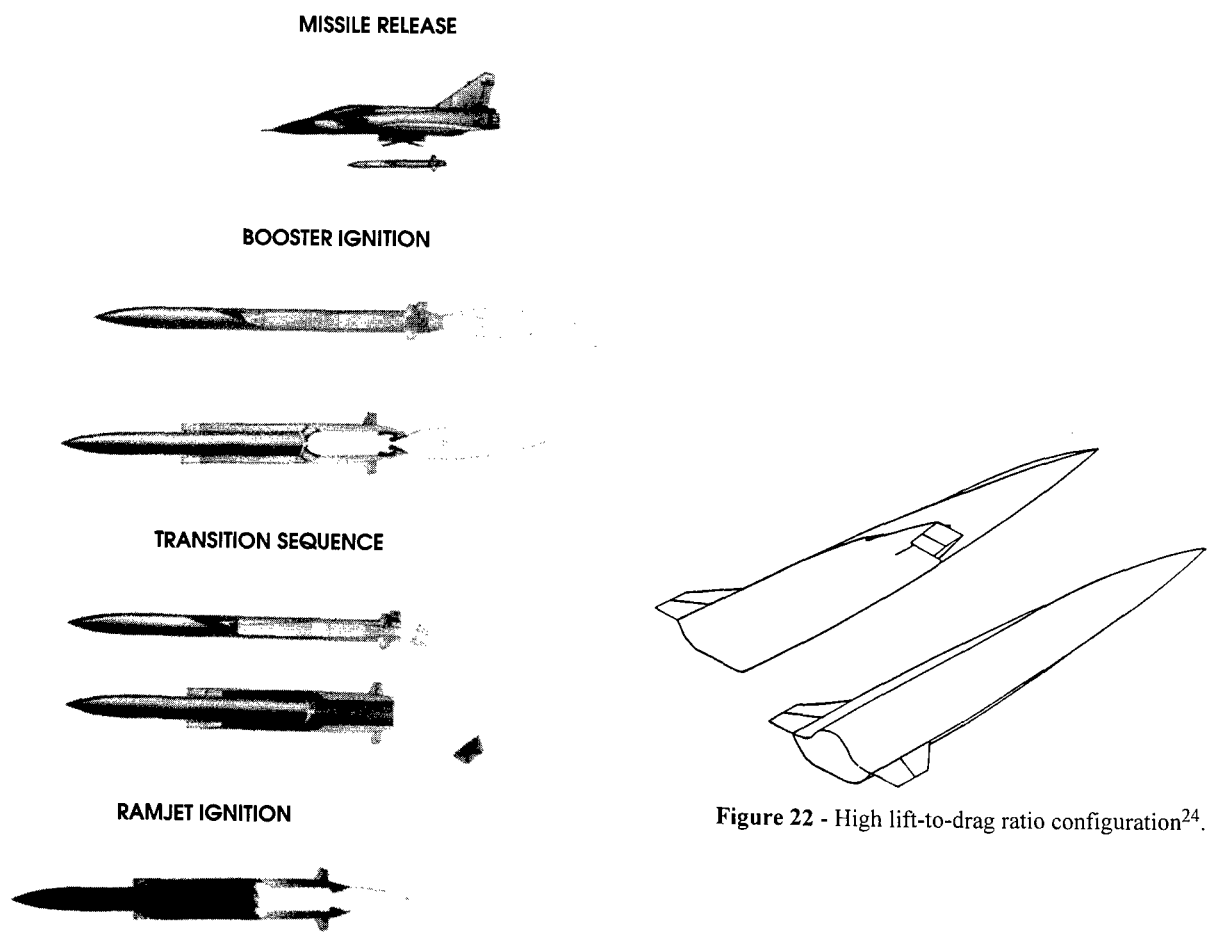


Figure 21 - French ramjet missile : ASMP transition sequence.

Figure 22 - High lift-to-drag ratio configuration<sup>24</sup>.

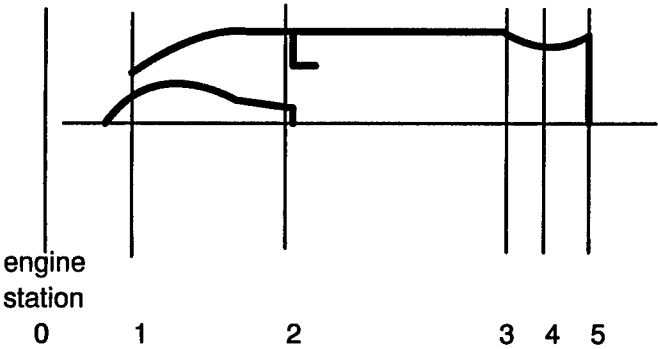


Figure 23 - Schematic ramjet engine.

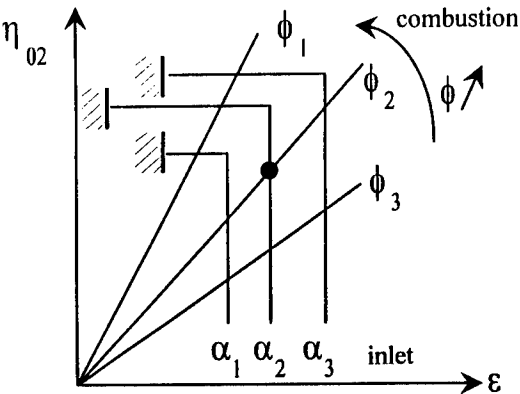


Figure 24 - Ramjet operating point.

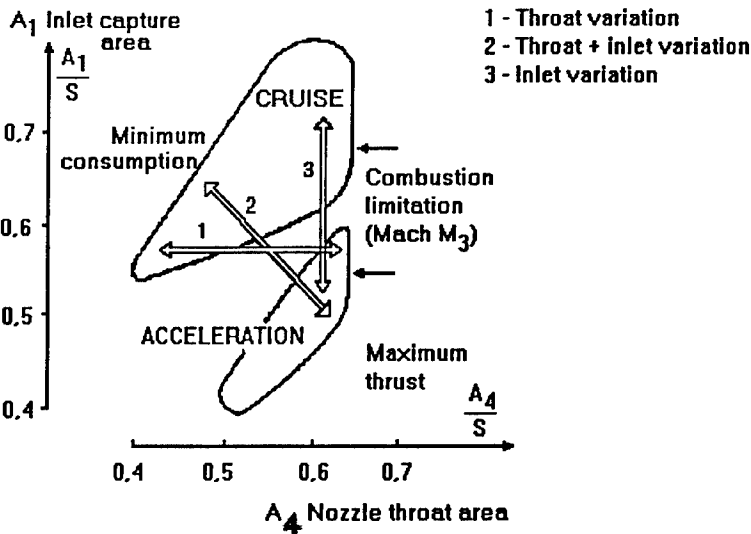


Figure 25 - Switching between cruise and acceleration regimes with variable inlet and/or nozzle.

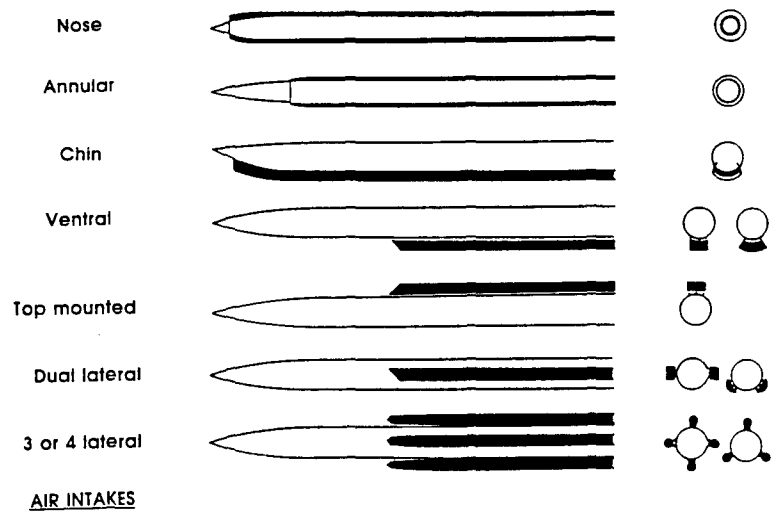


Figure 26 - Air-intake configurations.

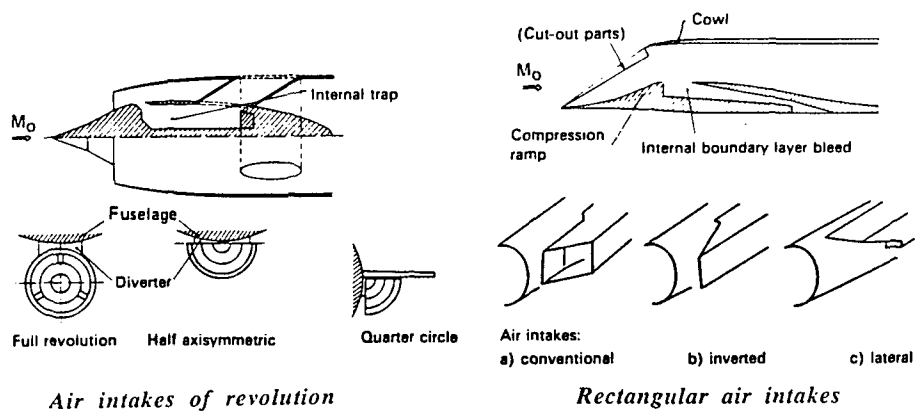


Figure 27 - Air-intake types<sup>26</sup>.

$A_1/S = 0.4$   
 $h/D = 0.063$

		AXISYMMETRIC	RECTANGULAR
		HALF	COMPLETE
		CLASSICAL	INVERTED
— SPAN :	$C_N \nearrow$	+	++
— DIVERTER :	$C_D \searrow$	+	++
— COWL , SIDEWALLS :	$C_D \searrow$	+	++
— LOCATION OF COMPRESSION PROFILE :	$P_R \nearrow \quad m_R \nearrow$	+	+++
— STRUCTURAL RIGIDITY :	$MASS_{INTAKE} \searrow$	++	+++
— DOOR WIDTH :	$MASS_{CHAMBER} \searrow$	+	++

Figure 28 - Comparison of different types of intakes in four intake configurations<sup>28</sup>.

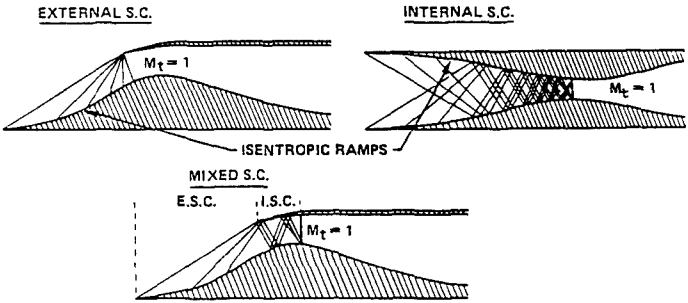


Figure 29 - External, internal and mixed supersonic compression<sup>29</sup>.

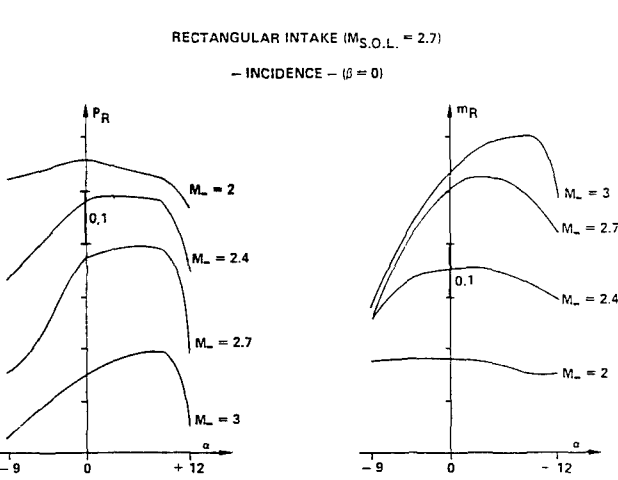


Figure 30 - Incidence effect on rectangular intakes<sup>28</sup>.

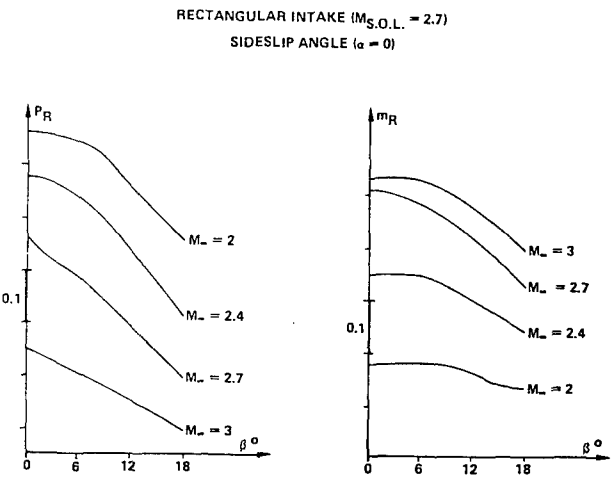


Figure 31 - Sideslip angle effect on rectangular intakes<sup>28</sup>.

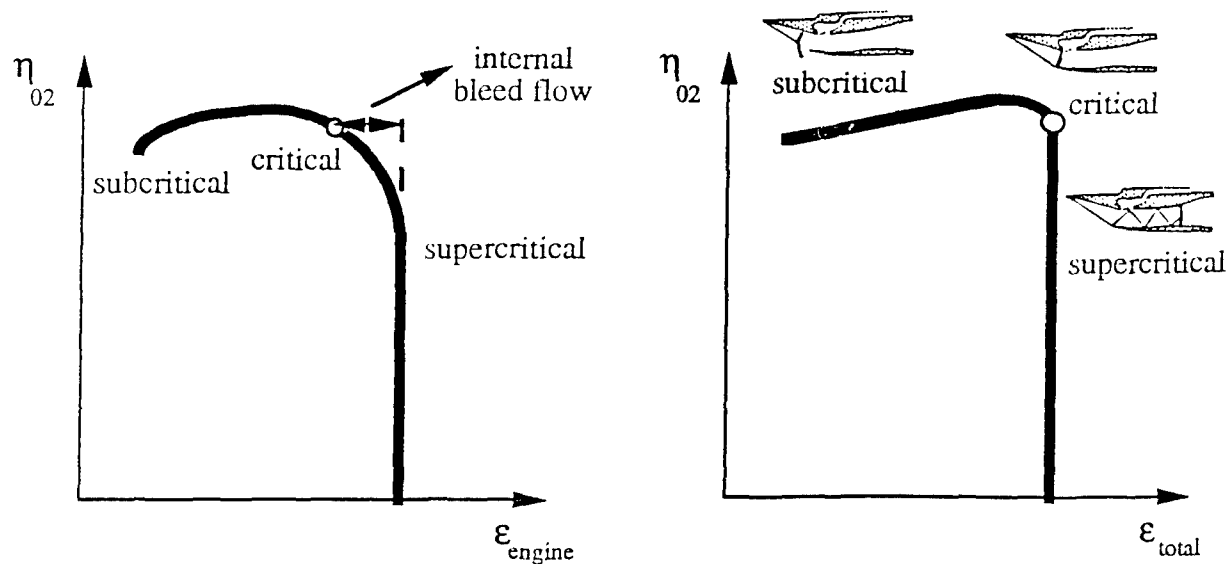


Figure 32 - Typical characteristic curves for external compression intake with internal boundary layer bleed.

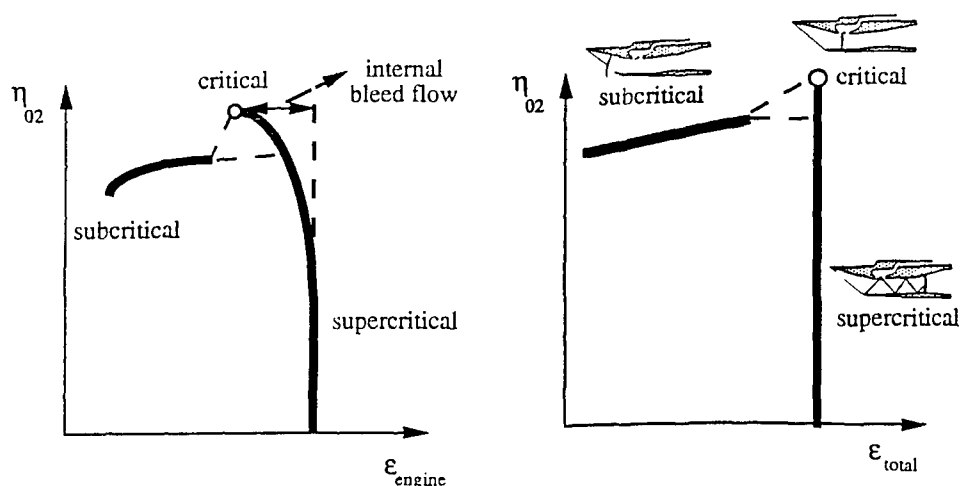


Figure 33 - Typical characteristic curves for mixed compression intake with internal boundary layer bleed.

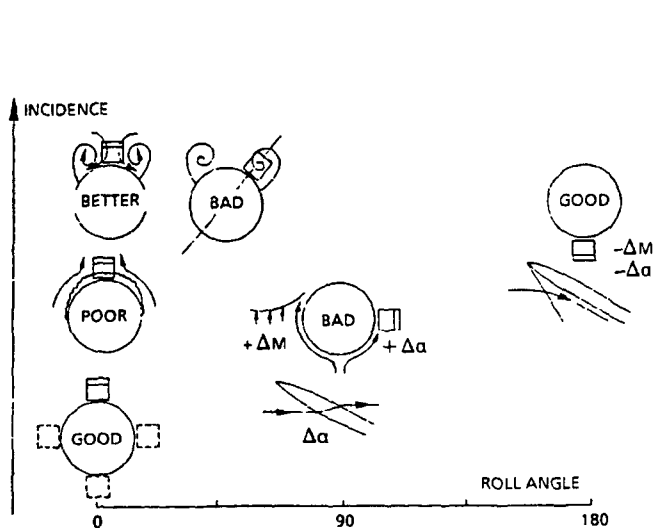


Figure 34 - Flowfield variation around missile body<sup>31</sup>.

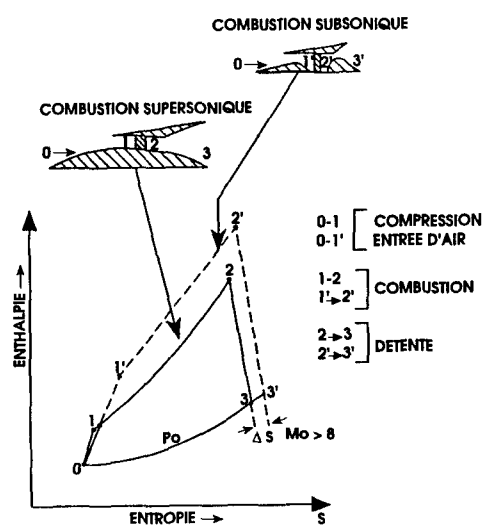


Figure 35 - Comparison of theoretical thermodynamical cycles for subsonic and supersonic combustion.

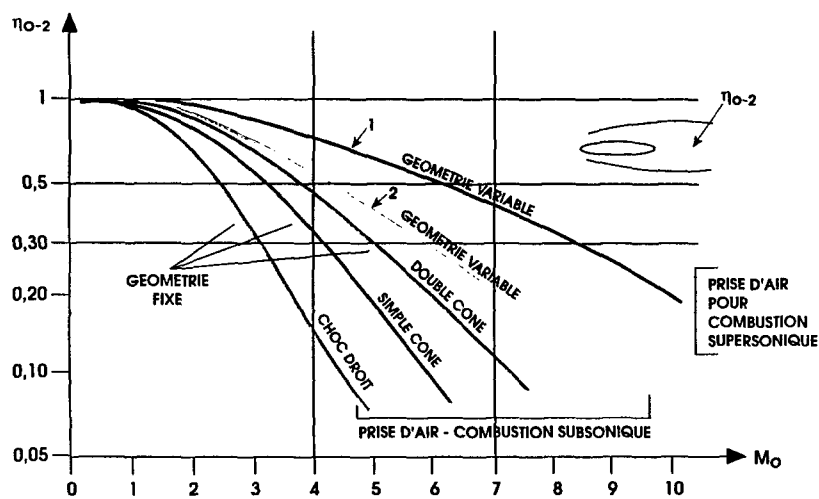


Figure 36 - Ramjet and scramjet air intakes pressure recovery.

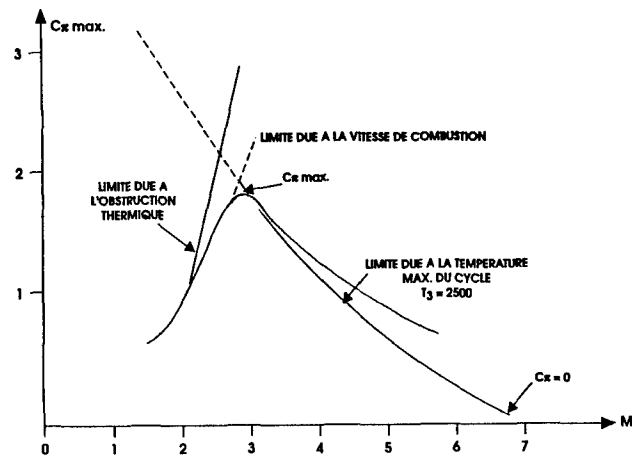


Figure 37 - Evolution of ramjet thrust coefficient with Mach number.

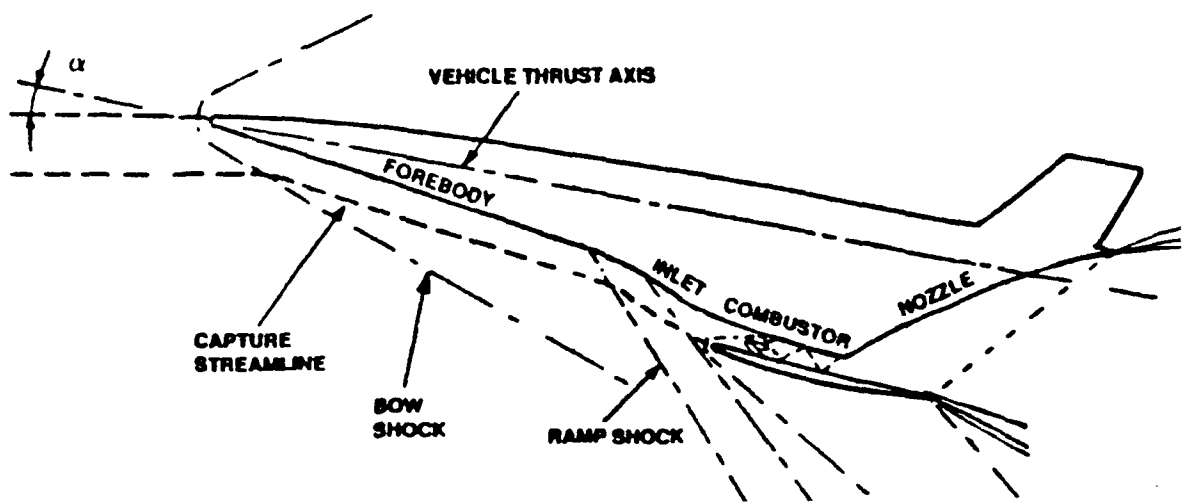


Figure 38 - Generic hypersonic airbreathing vehicle.

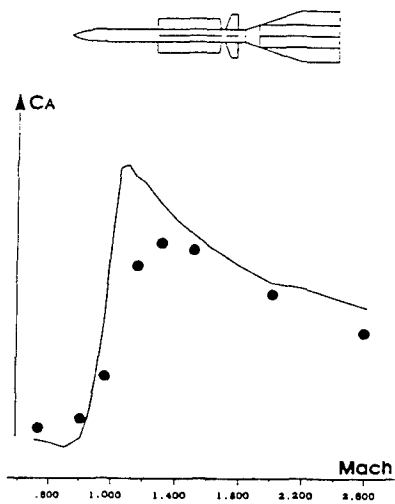


Figure 39 - Drag prediction for a geometry with 3 sets of lifting surfaces.

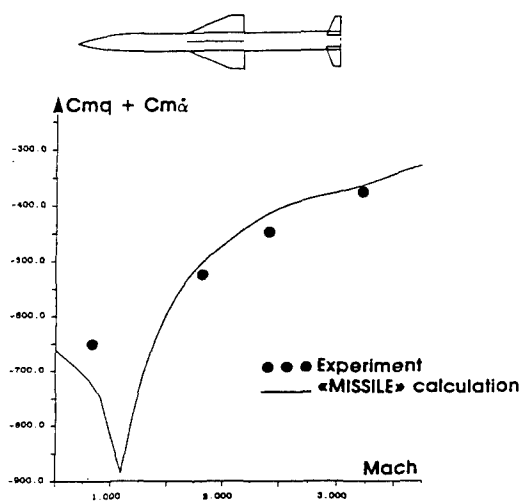


Figure 40 - Prediction of pitch damping coefficient.



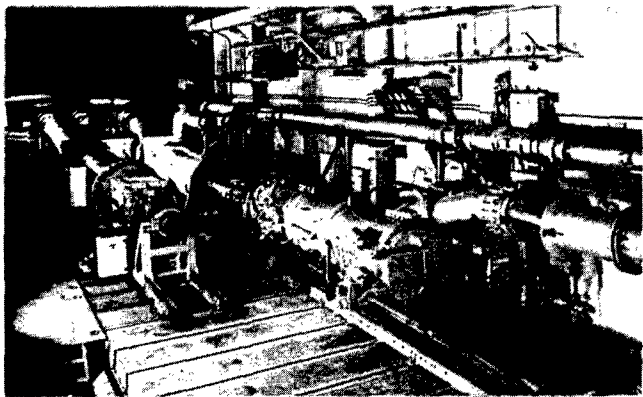


Figure 41 - Ramjet and scramjet ground-test facility at AEROSPATIALE Missiles/CELERG.

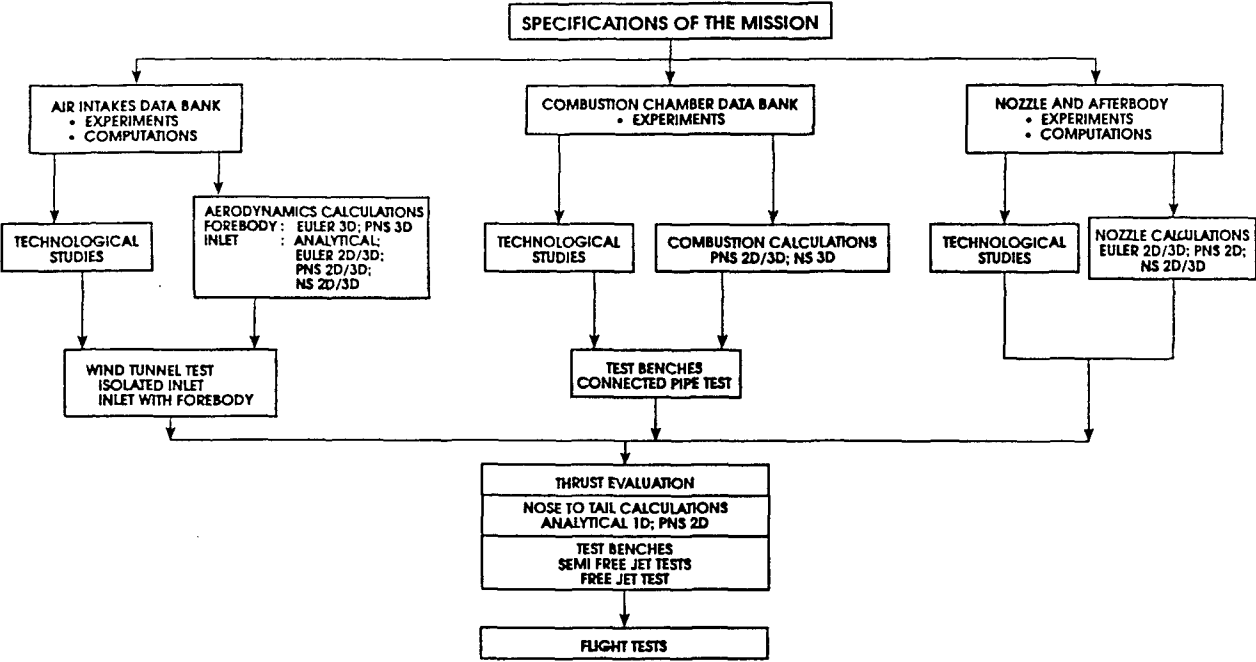


Figure 42 - Development methodology of integrated propulsion of high speed airbreathing vehicles.

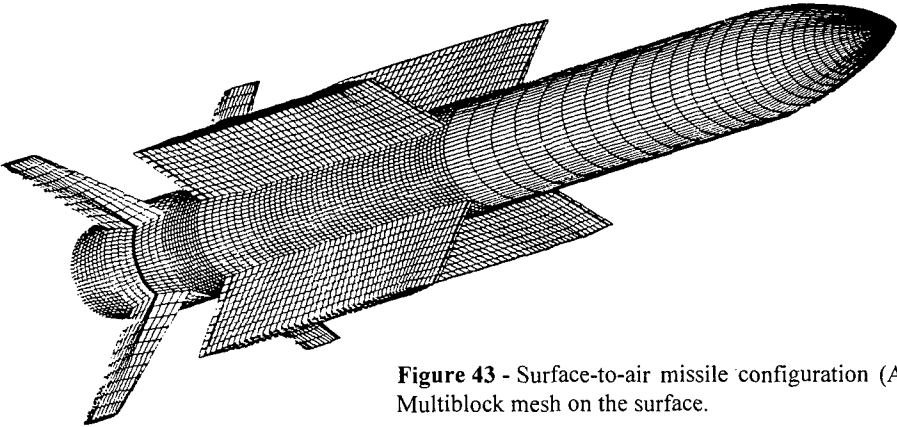


Figure 43 - Surface-to-air missile configuration (ASTER). Multiblock mesh on the surface.

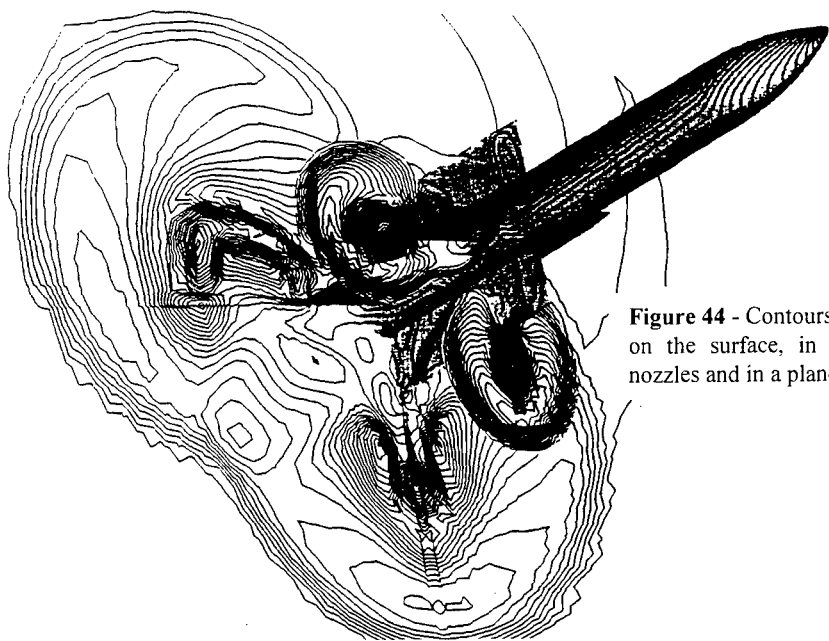


Figure 44 - Contours of Mach number.  $M = 3.0$ ,  $\alpha = 10^\circ$ , on the surface, in a plane located downstream of the nozzles and in a plane located near the wing trailing edge.

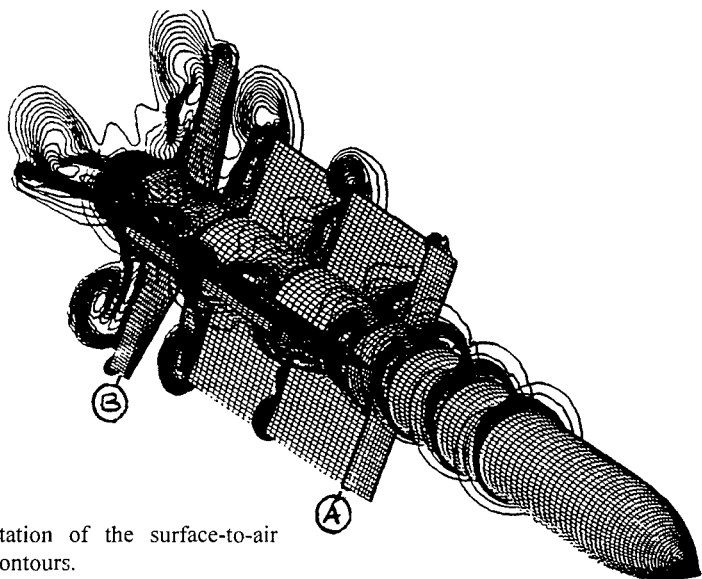


Figure 45 - Turbulent computation of the surface-to-air configuration. Total pressure contours.

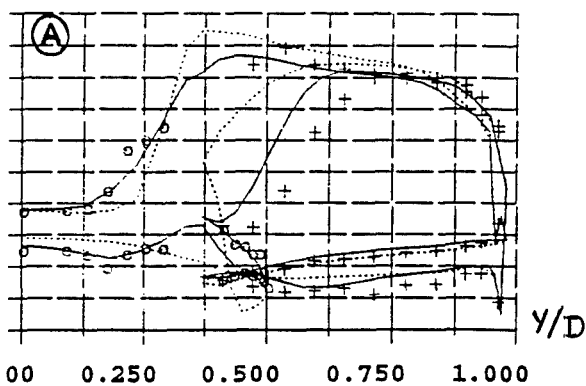
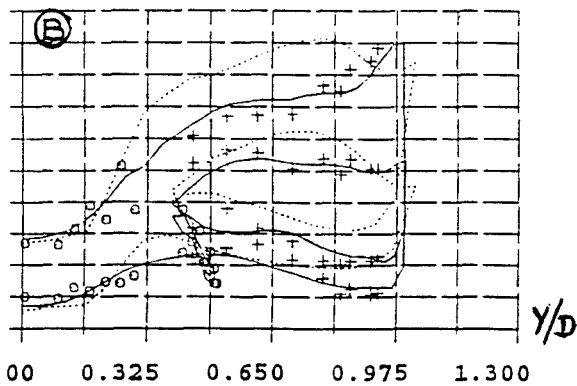


Figure 46 - Pressure distribution.  
o experiment  
... Euler  
- space marching PNS

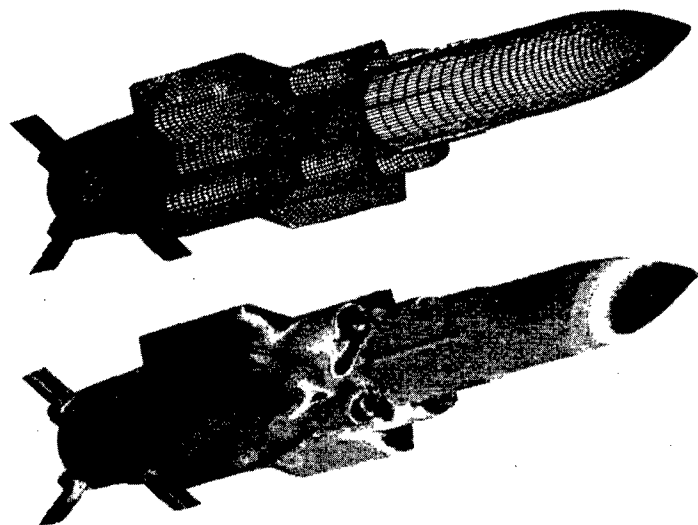


Figure 47 - ANS airbreathing missile. Euler computation for external aerodynamics.

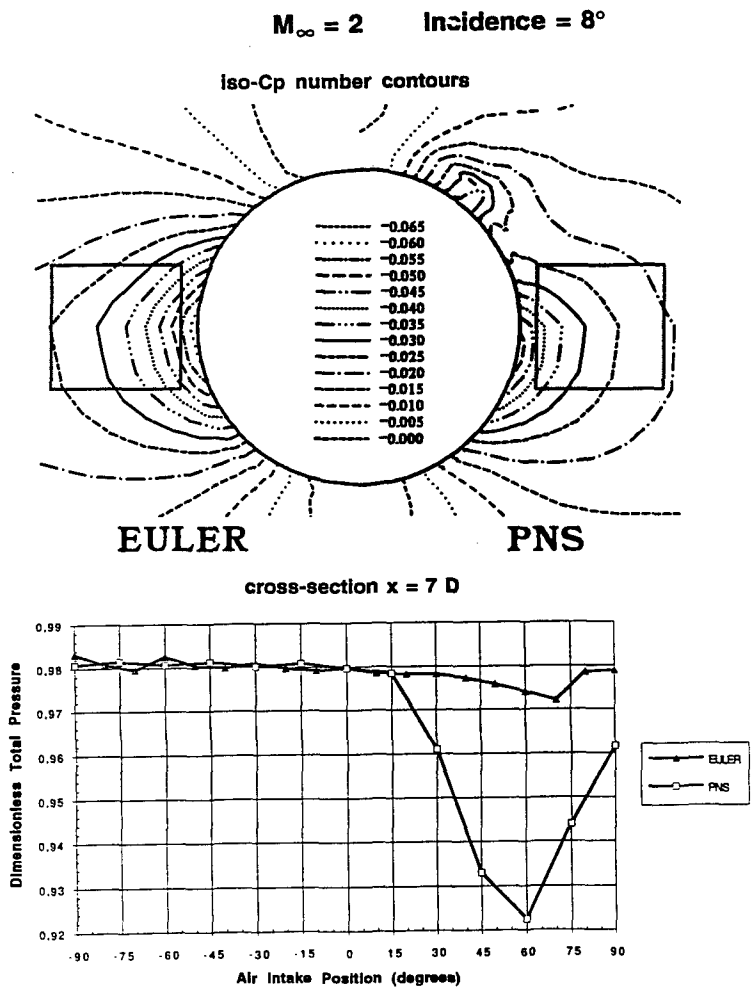


Figure 48 - Euler and PNS computation on a supersonic ogive. Influence on inlet capture area total pressure at different roll angles

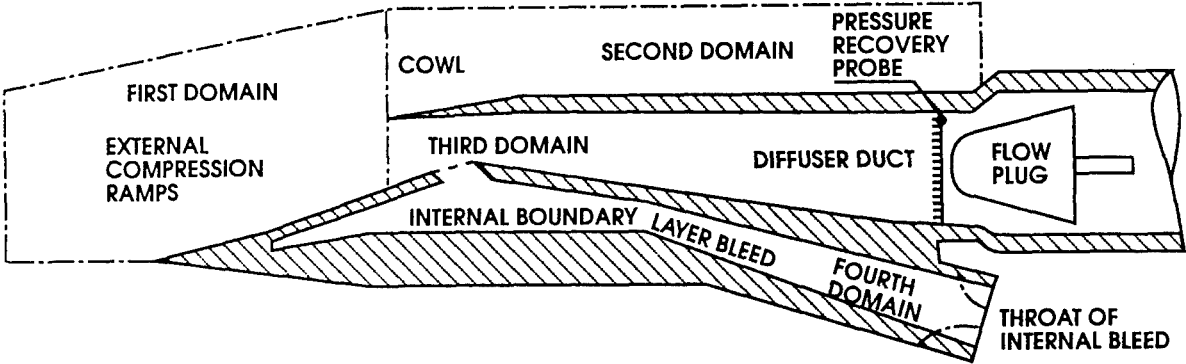


Figure 49 - Schematic drawing of the 2D air-intake. Experimental geometry and mesh topology.

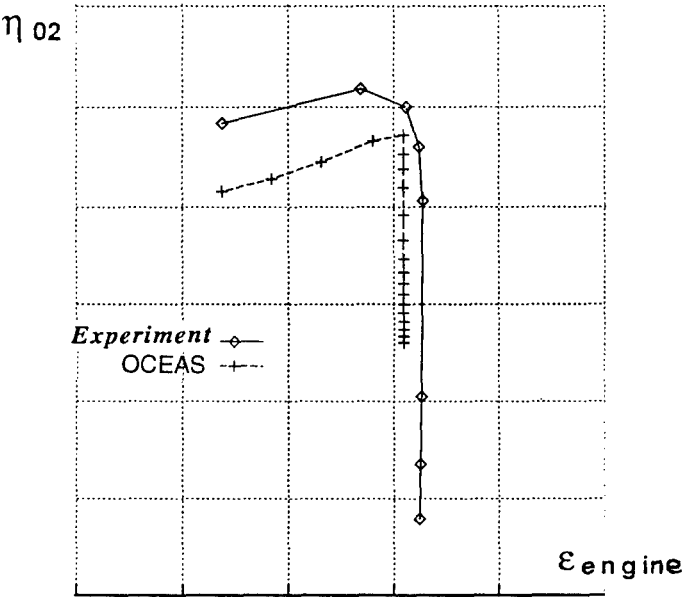


Figure 50 - 2D air-intake performance. Comparison between semi-empirical calculation (OCEAS) and experiment.

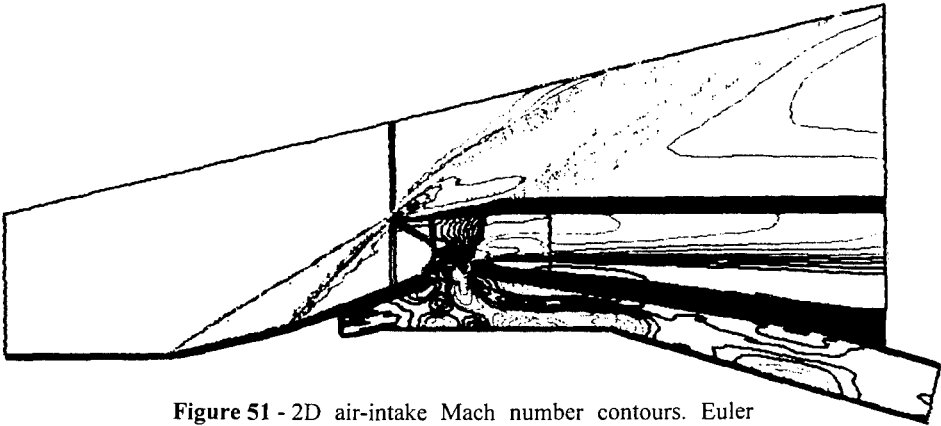


Figure 51 - 2D air-intake Mach number contours. Euler computation.

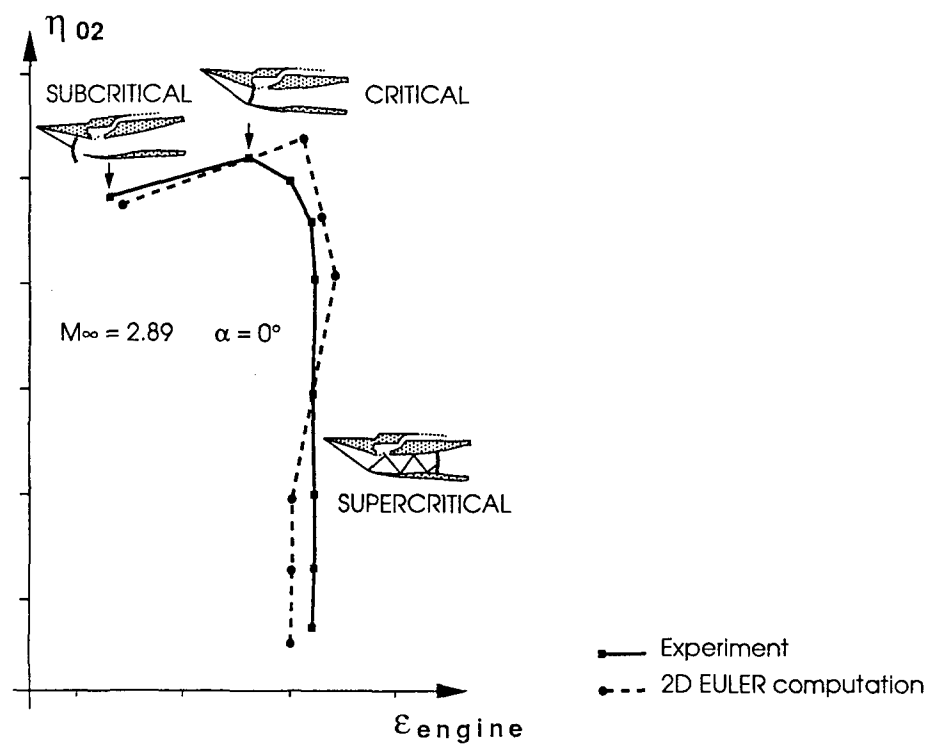


Figure 52 - 2D air-intake performance. Comparison between Euler and experiment.

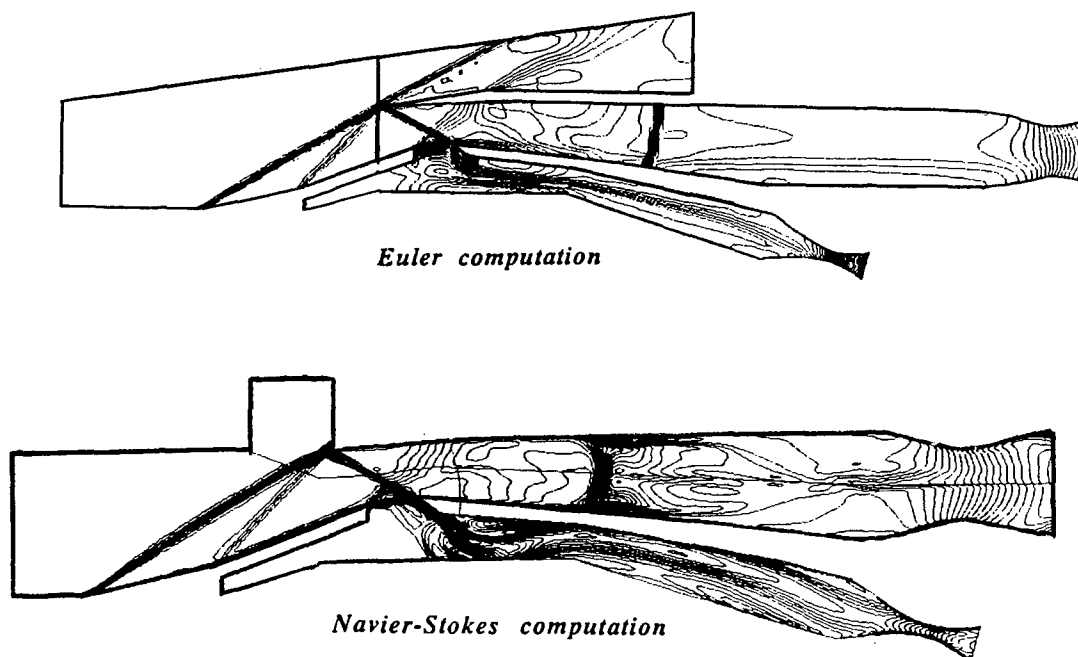


Figure 53 - 2D air-intake Mach number contours. Euler and Navier-Stokes computations.

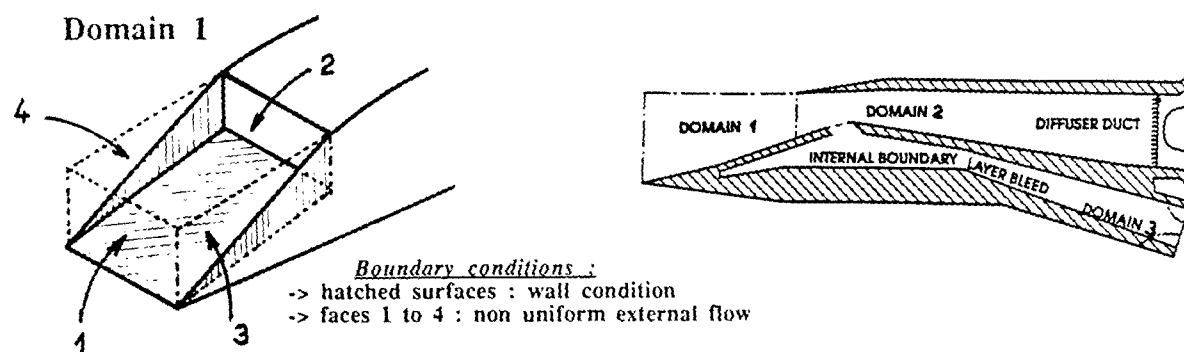


Figure 54 - Example of topology decomposition for a structured internal-external multiblock grid.

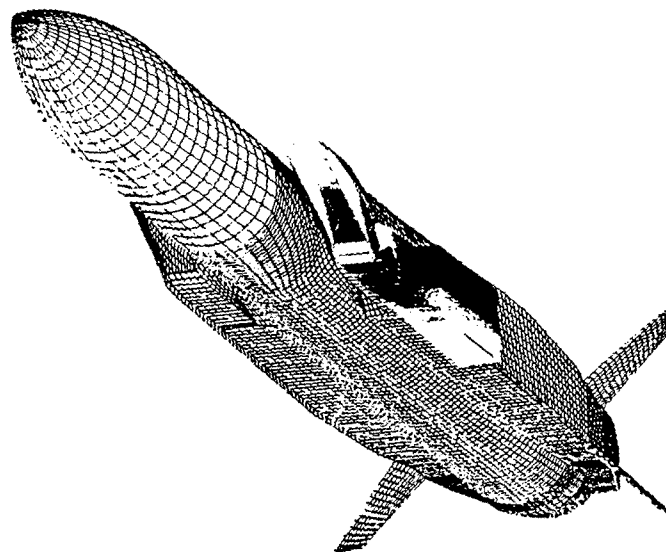


Figure 55 - ASMP type configuration. Internal flowfield computation taking into account non uniform external flowfield.

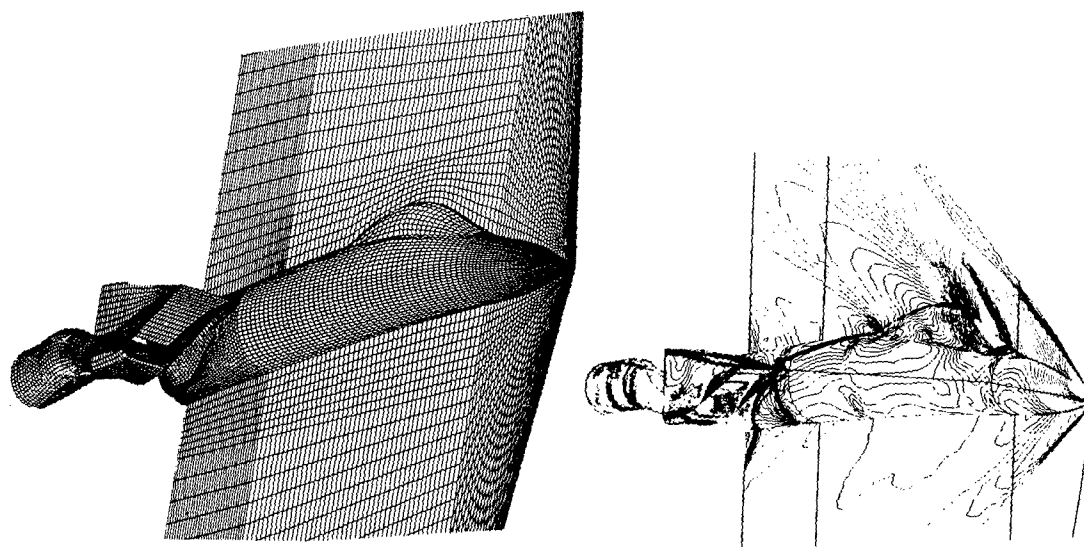
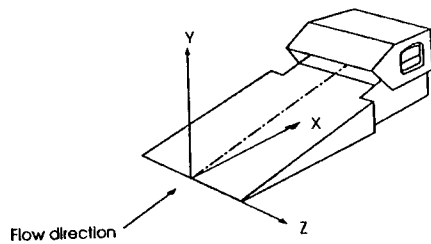


Figure 56 - 3D forebody/intake configuration<sup>60,61</sup>. Surface and symmetry plane grid. Euler static pressure contours. .



NASA P8 HIGH ASPECT-RATIO  
MIXED COMPRESSION AIR INTAKE

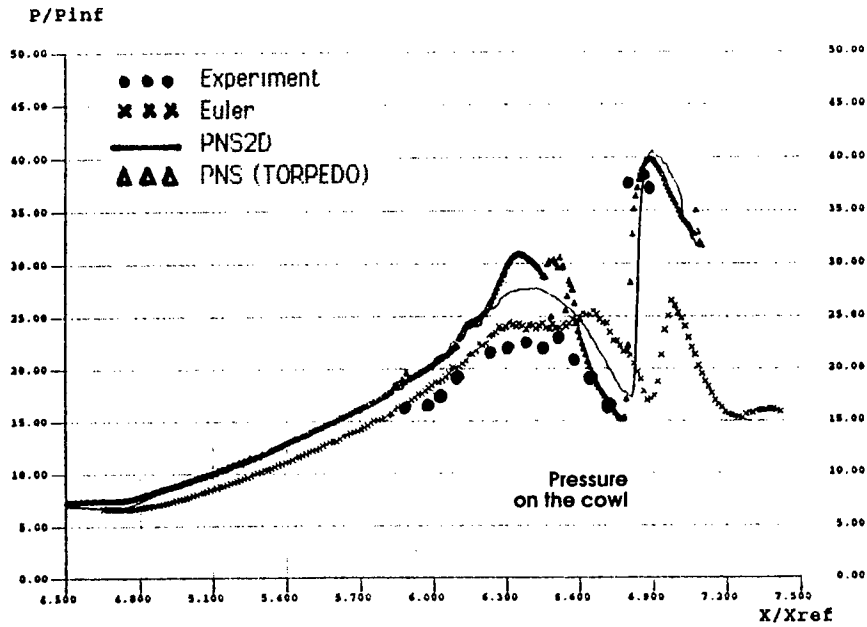


Figure 57 - 2D Euler and PNS computations of NASA P8 inlet. Upstream Mach number 7.4.

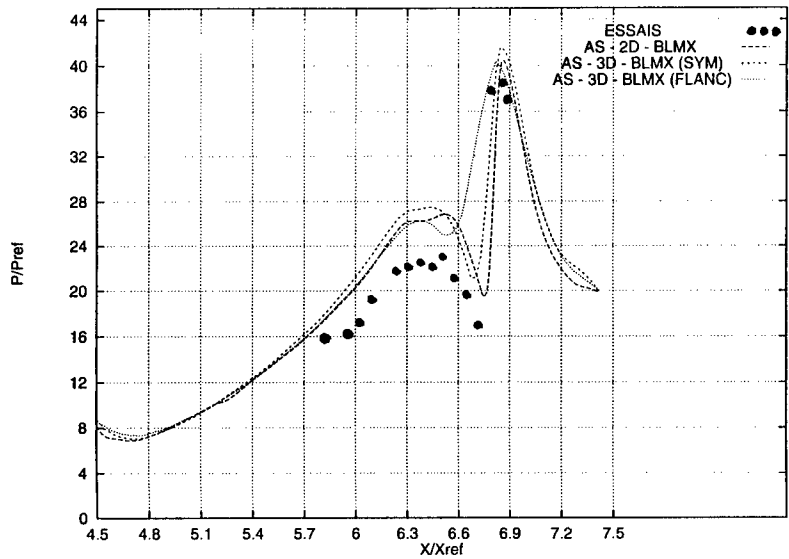


Figure 58 - 2D and 3D Navier-Stokes computations on NASA P8 inlet. Upstream Mach number 7.4.

# ISOLATED AIR-INLET WITH STRUTS

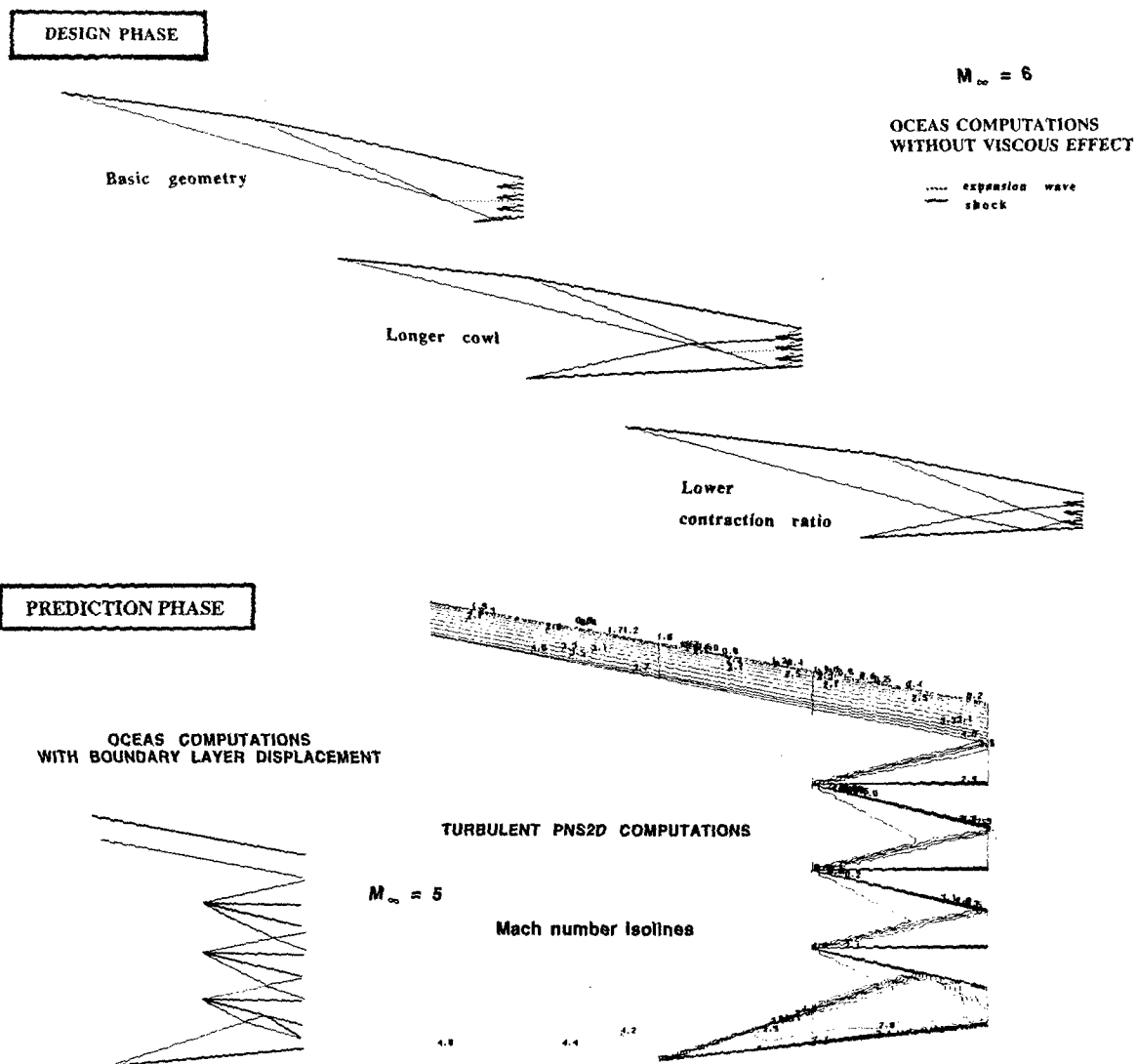


Figure 59 - Generic isolated inlet design. Mach = 5 and 7.

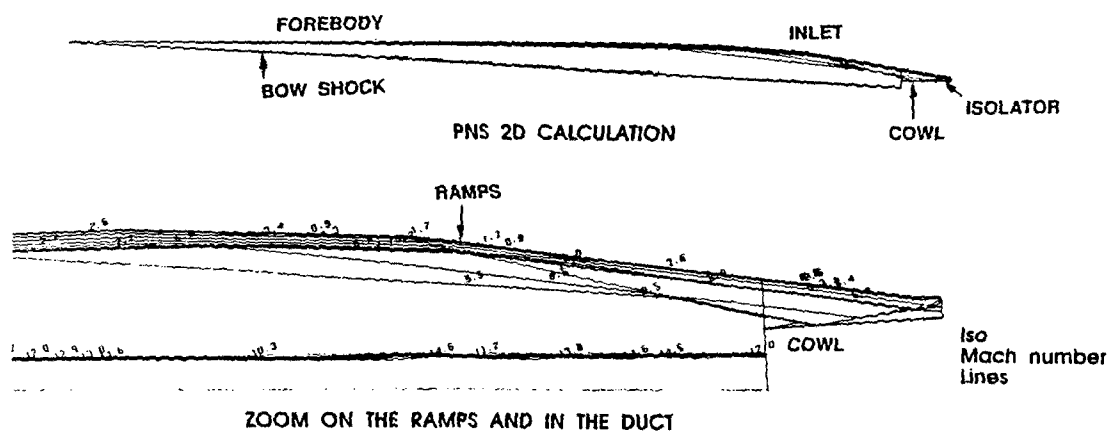


Figure 60 - Generic sharp nose forebody-inlet. Mach 15.  
Incidence 7°.



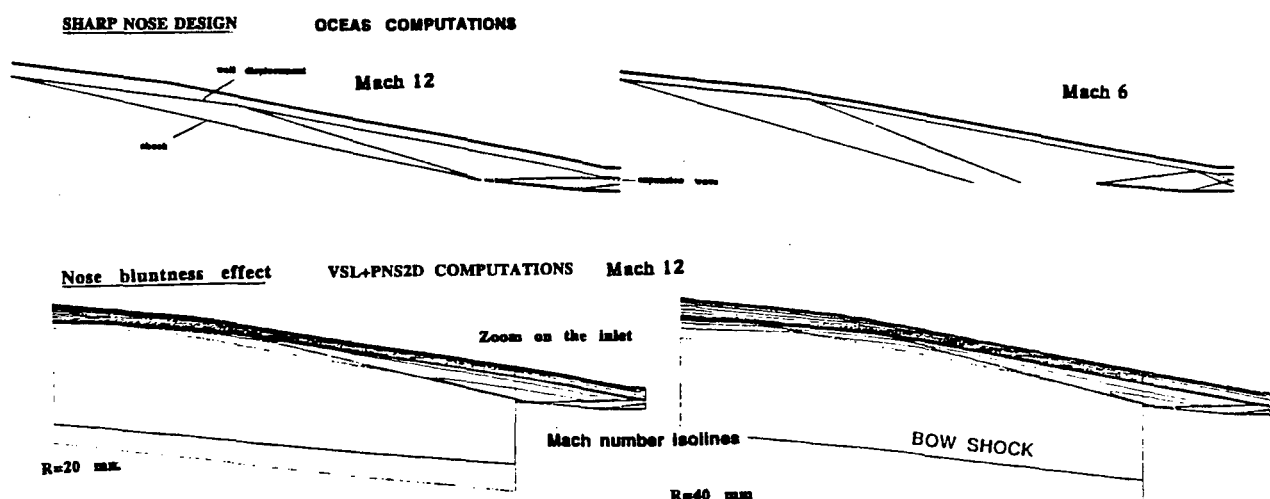


Figure 61 - Generic blunt nose forebody-inlet. Mach 12 and 6. Incidence 4°.

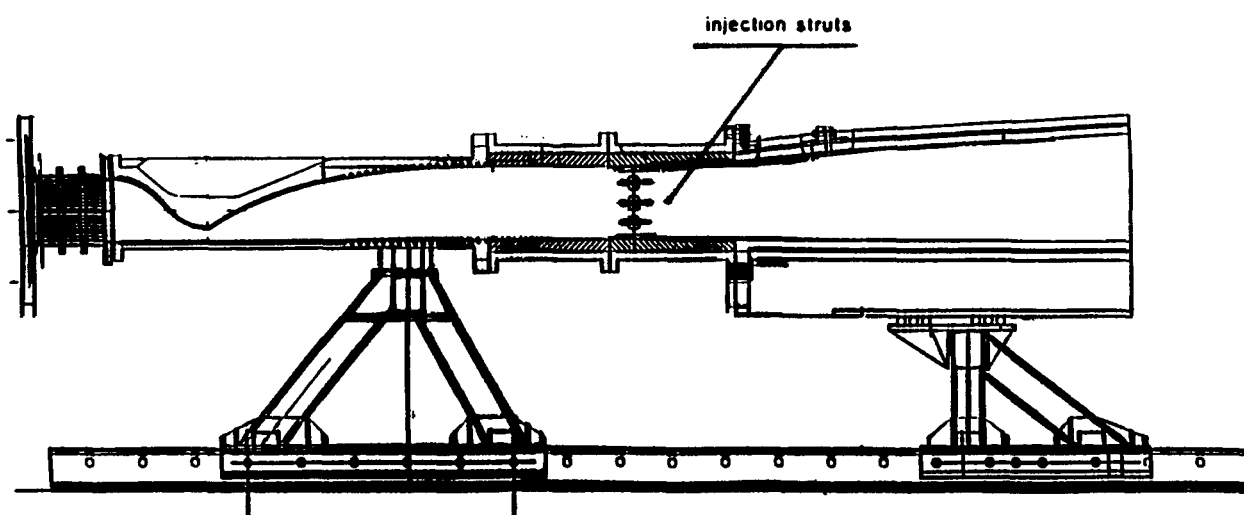
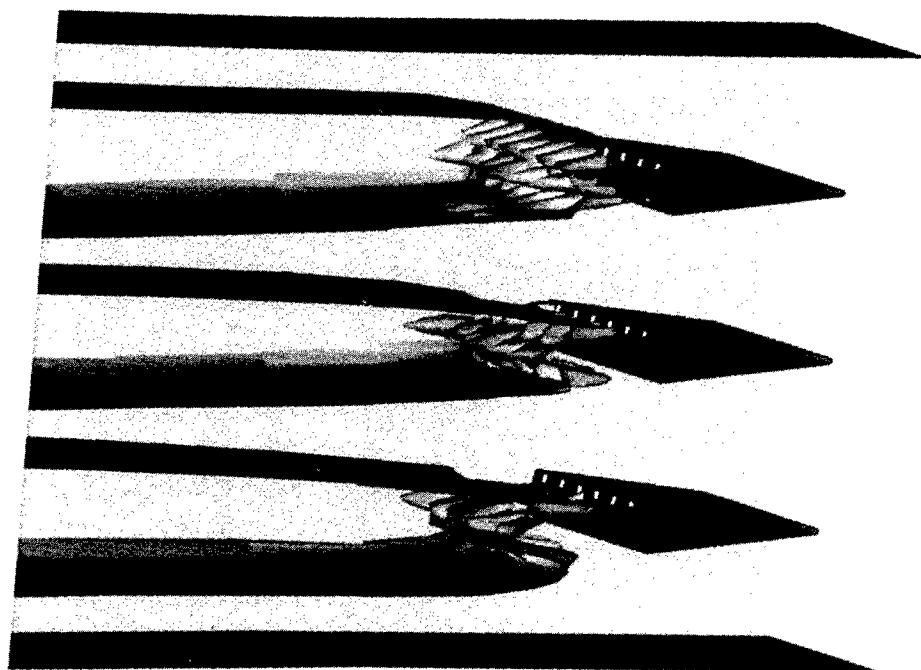
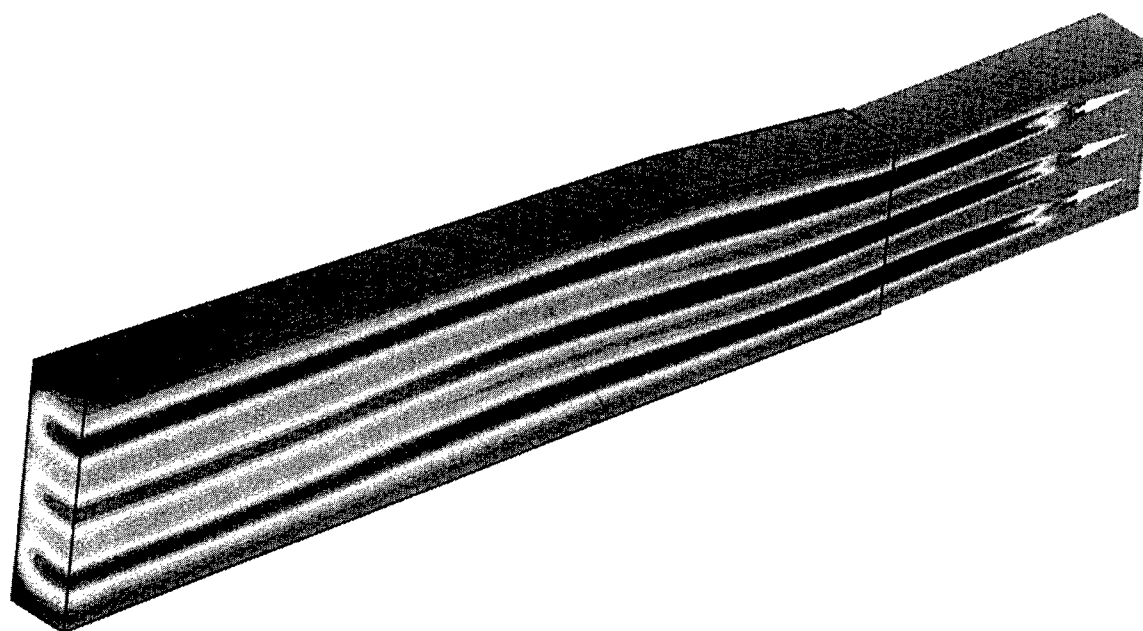


Figure 62 - CHAMOIS scramjet combustor in AEROSPATIALE test facility.

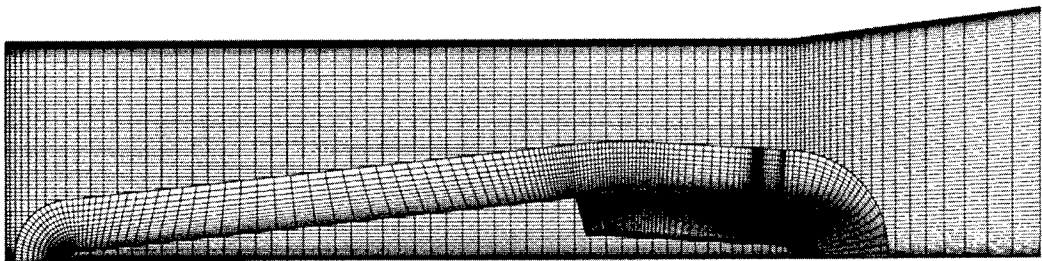


**Figure 63** 3D Navier-Stokes reactive computations : total temperature surface limiting combustion regions just after ignition (CHAMOIS combustor).



**Figure 64** - 3D Navier-Stokes reactive computations : total temperature contours (CHAMOIS combustor).

CHIMERA DOMAIN DECOMPOSITION OF A GENERIC SCRAMJET



HOLE BOUNDARY CAUSED BY THE STRUT INJECTOR

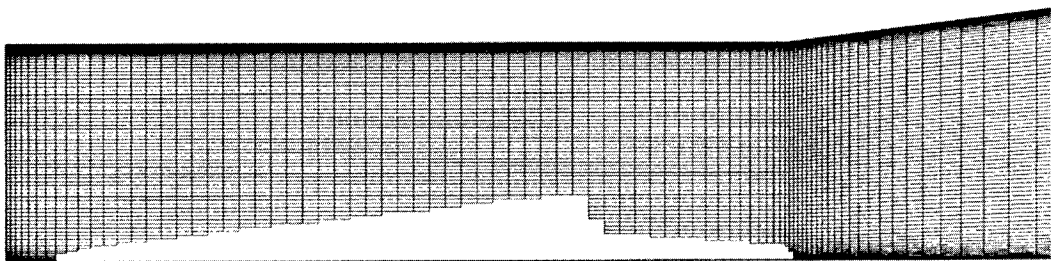
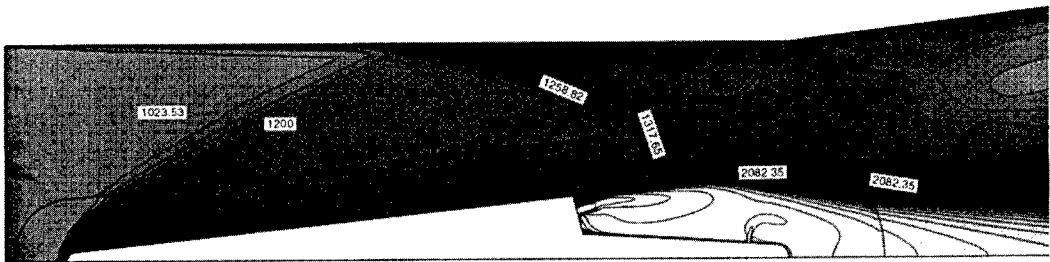


Figure 65 - 2D Navier-Stokes reactive computation of a generic scramjet : Chimera grid technique.

TEMPERATURE CONTOURS



PRESSURE CONTOURS

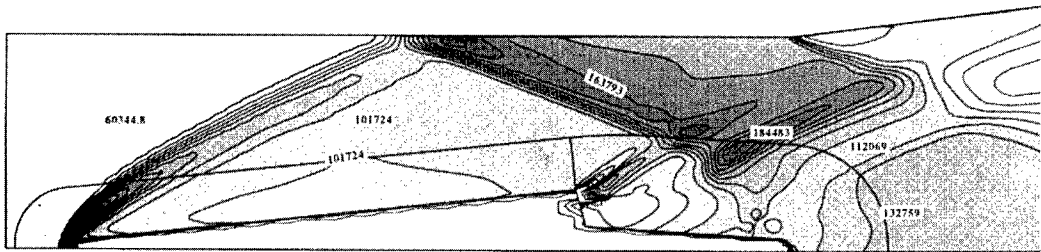


Figure 66 - 2D Navier-Stokes reactive computation of a generic scramjet : Chimera results.

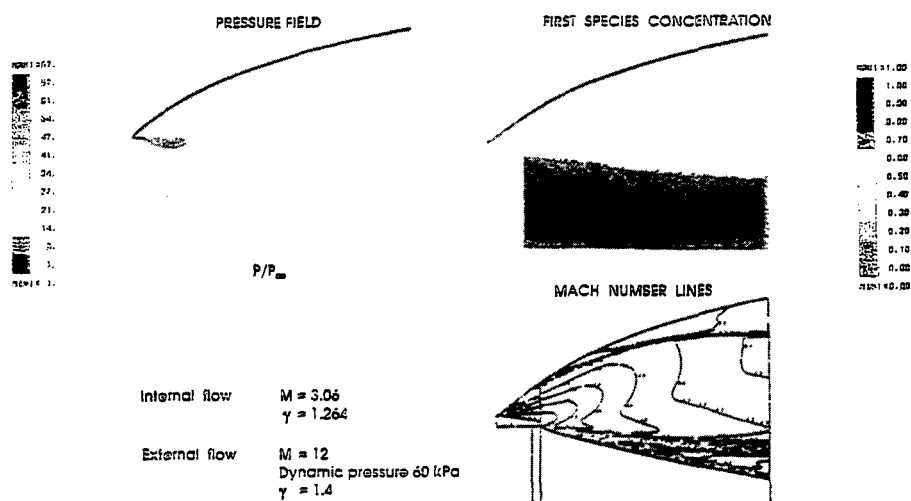


Figure 67 - 2D scramjet nozzle - Euler computation with two species modelization

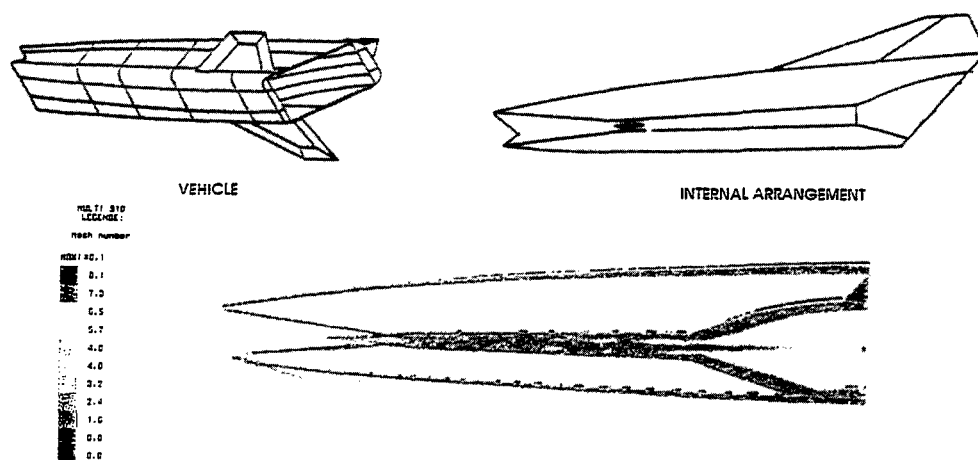


Figure 68 - AEROSPATIALE scramjet powered flight test vehicle. 2D PNS nose-to-tail computation.

# Stage Separation Aerothermodynamics

*Claus Weiland*

Daimler-Benz Aerospace AG  
Space Infrastructures, RIT49  
Postfach 80 11 69  
81663 Munich, Germany

## ABSTRACT:

Aerothermodynamic problems during the sequence of ascent flight are investigated. The flows for the pickaback configuration, the stage separation, the lower stage alone, inside of the trough of the lower stage and the fin/winglet interaction are considered. The main attention will be drawn to the stage separation process. During hypersonic flight the upper stage is separated from the lower stage which induces thereby a highly complicated flow field in the gap between the both stages, leading to aerodynamic and thermal loads. From the flight mechanical point of view the aerodynamic coefficients have to be determined, whereas for structures and thermal protection purposes the local loads are of most importance.

Several physical aspects are examined for the various kinds of flows, i.e., wall radiation, turbulence, real gases, shock / boundary layer and shock / shock interaction, flow separation and reattachment. The flowfields are analysed by employing numerical simulation methods as well as windtunnel experiments. Inviscid and viscous numerical simulations are performed applying the Euler and the Navier-Stokes equations. The influence of the grid fineness on the accuracy of the numerical results are also object of consideration. Results of the above described flow cases will be presented and discussed in very detail and the windtunnel data will be compared with the numerical results for validation reasons.

## 1. INTRODUCTION

Most of today's space transportation systems are either not or only partially reusable. Although these systems represent reliable means of space transportation, the costs of delivering payloads into LEO are still too high. Partially reusable are the vertically launched systems of the U.S. Space Shuttle, the Russian Buran, the European Hermes and the Japanese Hope, where the orbiter is reusable and the launch system expendable.

Consequently, numerous activities over the world aim to develop concepts for completely reusable space

transportation systems.

To achieve a significant cost reduction for future missions into the orbit horizontal take-off and landing capabilities with airbreathing propulsion as well as completely reusable structures seem to be indispensable. Conceptual design studies have covered single stage to orbit (SSTO) and two stage to orbit (TSTO) systems. SSTO concepts are under investigation in the U.S. with NASP (National Aerospace Plane), in Great Britain with HOTOL (Horizontal Take-Off and Landing), in Japan with the Aerospaceplane of the National Aerospace Laboratory. In Europe some national programs favour two-stage versions of horizontal take-off and landing space transportation systems (TSTO). Some of these studies make use of conventional transport aircraft as carrier for the orbiter, e.g. the AN 225 / Interim HOTOL of British Aerospace and the MAKS system of Russia. The separation of the upper and the lower stages is planned to take place at maximum flight level of the carrier aircraft at subsonic speeds.

The most advanced concepts provide a first stage belonging to a new generation of hypersonic aircrafts, with conventional take-off and landing capabilities, but with propulsion systems that enable the lower stages to operate with hypersonic speeds at flight levels high above the maximum ceiling of turbo-jet engines. Possible solutions for such propulsion systems are given by integrated turbo/ramjet or turbo/scramjet systems.

One of these above mentioned concepts is considered in the frame of Germany's Hypersonic Technology Program, based on the idea of E. Sänger. Another one is the French STAR-H concept for which is planned to use a combined turbo/scramjet propulsion system. According to Sänger's concept upper and lower stage, both designed as high lift over drag vehicles, climb up as a pickaback configuration to an altitude of about 35 km and accelerate to a speed of  $M_\infty = 6.6$ . Then, both stages separate and the upper stage continues the ascent to the orbit while the lower stage flies back to its launch site like an aircraft. After the mission of the orbiter is accomplished it returns to earth operating during re-entry and landing like the Space Shuttle.

Many interesting aerothermodynamic problems occur during this sequence of ascent flight. In this lecture we will report about the findings of flow field behaviour for four different flight situations.

- 1.) the pickaback configuration during ascent up to the altitude of stage separation maneuver
- 2.) the stage separation maneuver itself
- 3.) the lower stage configuration after the stage separation maneuver
- 4.) the flow inside the trough of the lower stage

The main attention will be drawn to the second point, the aerothermodynamics of the stage separation maneuver. In principle the stage separation maneuver will be carried out as follows. Using a strut mechanism the upper stage is lifted to a certain incidence angle and an appropriate gap width between the stages. Subsequently, the rocket propulsion system of the upper stage provides sufficient thrust to gain enough lift for the separation maneuver. The separation maneuver takes place. Thereafter the lower stage returns to the launch site for horizontal landing and the completely reusable upper stage flies into an orbit. After the mission of the orbiter is accomplished it returns to earth operating like the U.S. Shuttle.

Extensive numerical effort was spent for the investigation of the above mentioned flow cases and the numerical results were compared and validated with experimental data where ever possible.

Fig.1 gives an overview about the strategy of the investigations and the special examinations of sensitivities performed.

In the flight situation 1.) we analyse the wall radiation on the wall temperature distribution which is very important for the design of the thermal protection system (TPS).

The most challenging task was the investigation of the flight situation 2.) where a two body system has to be considered. The main objective was the revelation of the general flow structure. The influences of the physical modelling, inviscid versus viscous, perfect gas versus real gas and laminar versus turbulent flow are analyzed.

The investigation for the flight situation 3.) is devoted to the aerodynamic performance of the isolated lower stage, where in addition flow topologies on the leeward side and determination of the heat fluxes are considered.

Finally, the flight situation 4.) deals with the influence of the design of the trough, where the upper stage is located during ascent until separation, on the aerodynamic performance which is important for the trim behaviour and the static stability of the hypersonic aircraft.

## 2. MAJOR AERODYNAMIC DESIGN PROBLEMS

Generally, for the development of such a high sophisticated launch system like TSTO a lot of aerothermodynamic design problems occur. Besides the ones listed above, the integration of the propulsion system including the air inlet, the combined propulsion system itself, the free expansion nozzle and the base flow are of particular importance for the trim and stability behaviour and with that the controllability of the hypersonic aircraft in the different Mach number ranges. All these effects cannot be addressed in this paper.

Our interest is focused on the following topics.

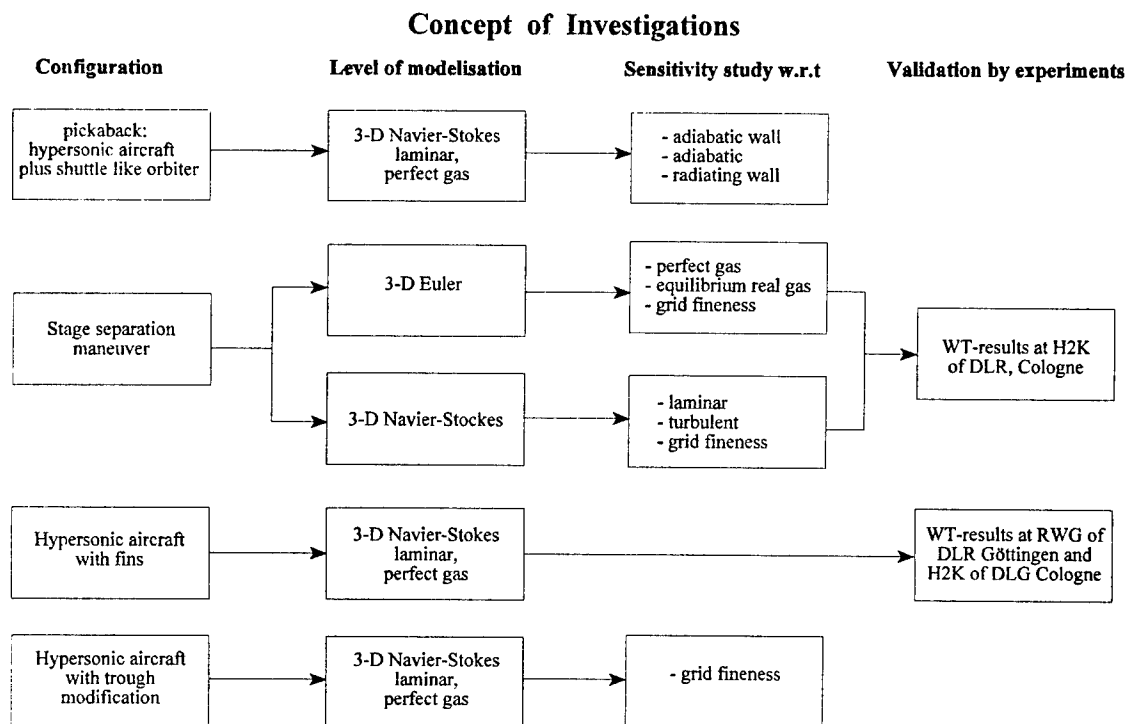


Fig.1 Concept of investigation

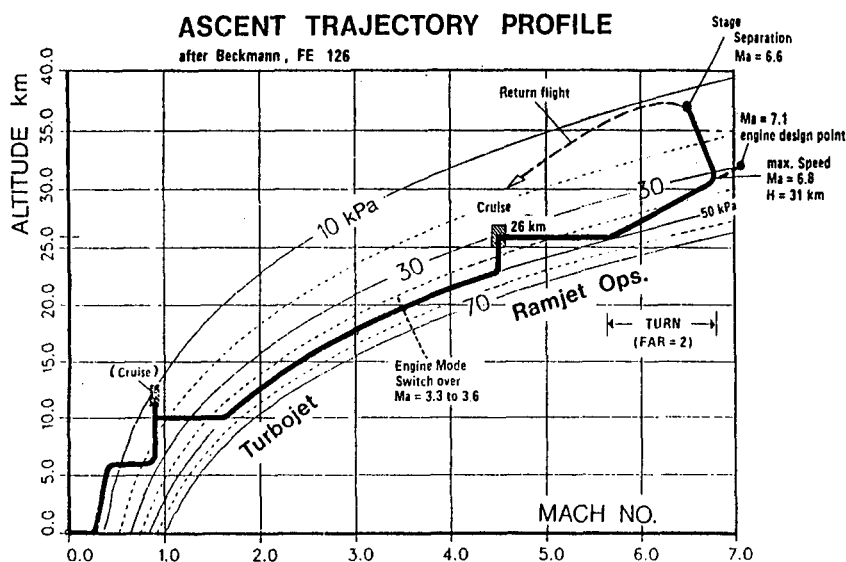


Fig.2 Typical ascent trajectory

## 2.1 Pickaback configuration

During ascent the upper stage is transported by the lower stage in a pickaback configuration, i.e. the orbiter is mounted on top of the hypersonic aircraft. A typical ascent trajectory for a TSTO is shown in Fig.2, where also the operation ranges of the propulsion modules are indicated. The pickaback configuration is delineated in Fig.3. Aerodynamic performance data along selected trajectory points were determined by employing Euler and Navier-Stokes methods. For the separation Mach number ( $M_\infty = 6.6$ ) the influence of the wall radiation on the wall temperature distribution is investigated.

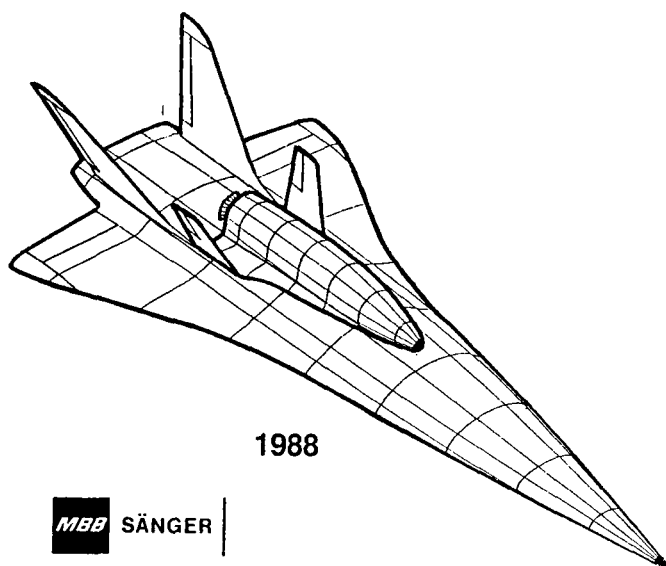


Fig.3 Pickaback configuration

## 2.2 Flow field interactions during stage separation

During the separation maneuver (Fig.4) the stages are in close proximity and the aerodynamic interaction between the vehicles may cause significant effects on the aerodynamic characteristics of each vehicle.

Unlike the standard separation of vehicles of different size in which only the flight conditions of the smaller stage are noticeably perturbed, the separation of the two vehicles of comparable size can mutually impair the aerodynamics of both stages. For this reason the analysis of the flowfields is extremely important for the flight mechanics of both stages during the separation maneuver. So far, only little work has been published on the investigation of supersonic / hypersonic separation maneuvers. In /1/ an experimental analysis of the stage separation was conducted at Mach numbers 3 and 6, where the aerodynamic data obtained are input for the system of equations of dynamic motion. A similar approach was applied in /2/ in which slender body theory provides the input data for the equation of dynamic motion. The most recent experiments /3/ were focused on the analysis of the flow behaviour at small gap widths between upper and lower stages, where the main interferences should occur.

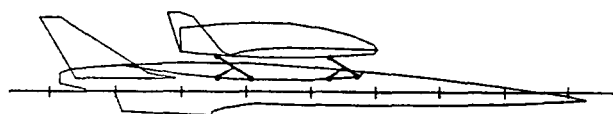


Fig.4 Separation configuration

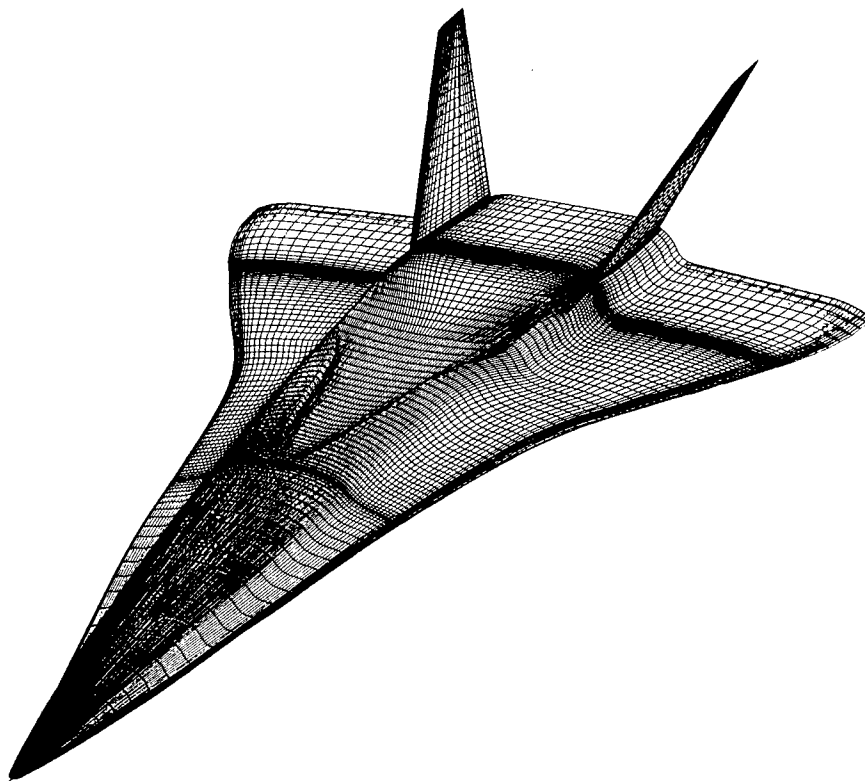


Fig.5 Lower stage configuration with trough

The aim of our simulation work was to identify the parameters of the flowfield which are sensitive with respect to the interaction between both stages. Some of these are: the gap width, the relative angle of attack, the viscous effects, the real gas effects, the shock boundary layer interactions, the shock and compression wave reflexions, etc..

### 2.3 Angle of attack sensitivity of the lower stage

After the upper stage is separated the lower stage returns to the launch site. The lower stage is a long and slender blended wing-body configuration flying at high altitudes and hypersonic speeds (Fig. 5). Therefore the flowfield around this configuration for the given flight characteristic is dominated by viscous effects. Thick boundary layers develop and influence strongly the aerodynamic coefficients and loads. For this reason, an inviscid simulation of the flowfield is only helpful to get some informations on the pressure distribution at the wall of the configuration and to understand the location and interaction of shock waves. The experience has evidenced that just the lift coefficient could be predicted with some reasonable accuracy, while the other coefficients may be spurious. For an improved determination of the aerodynamic loads and a prediction of the thermal loads a viscous analysis of the flow field is definitely necessary.

The viscous flowfield around the complete configuration including the vertical fins is calculated by

employing a Navier-Stokes method. An angle of attack investigation has been performed in order to identify the effects on the leeward side and to compare these results with windtunnel data.

### 2.4 Design of the trough

The flight mechanics during the return-flight of the lower stage to the landing site, will be effected by the flow inside the trough. The trough geometry is displayed also in Fig.5. Therefore the flow field in the surroundings of the trough was analyzed in detail and the influence of the trough geometry was examined. The outcome of this investigation was that the pitching moment is the most sensitive quantity. The simulations were done by a Navier-Stokes method where particular attention was paid to the flow topology in the vicinity of the trough.

### 2.5 Fin / winglet interaction

The integration of the upper stage on top of the lower stage should not affect the control capability given by the fin of the lower stage in an unacceptable manner (see Fig. 3). Therefore the interaction between the winglet of the upper stage and the fin of the lower stage was investigated. To do so, flow simulations were performed on an isolated fin / winglet configuration (Fig. 6) which was mounted on top of a delta wing. Different Machnumbers, angles of yaw and relative positions of the fin to the winglet were considered. Since it was expected that the main interference would occur through



the shock waves generated at the upper stage winglet and touching the lower stage fin, the investigation was performed by applying an Euler method.

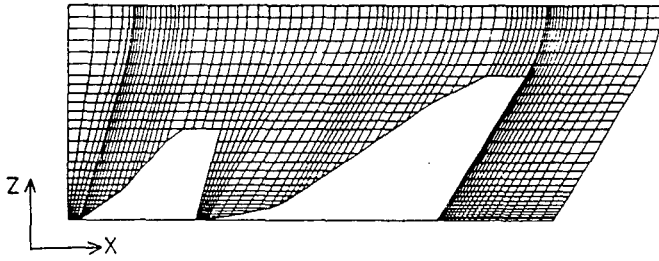


Fig.6 Fin / winglet configuration

### 3. NUMERICAL SIMULATION METHODS

The numerical simulation of the flow cases considered and discussed above are performed by applying 3D Euler and 3D Navier-Stokes methods. Some Euler calculations were done with the finite difference method published in /3,4/. The Navier-Stokes equations are integrated using the finite volume approach. Two approximations are available where one of them /5,6/ has the capability to march in space using the time operator, which is similar from the efficiency point of view to the parabolized Navier-Stokes approach. We will now concentrate on the second method since most of the computations discussed in this paper are carried out with this prediction tool /7,8,9,10,11/. The main differences of the strategy of approximation between the both methods consist in the treatment and discretisation of the left hand side and the boundary conditions.

#### 3.1 Governing equations

The non-dimensional form of the time-dependent Navier-Stokes equations in three dimensions is considered. In generalized, body-fitted coordinates these read

$$Q_t J^{-1} + E_\xi + F_\eta + G_\zeta -$$

$$Re_\infty^{-1}(E_{v,\xi} + F_{v,\eta} + G_{v,\zeta}) = 0$$

where  $Q = (\rho, \rho u, \rho v, \rho w, e)^T$  using  $e = \rho (\varepsilon + 0.5 (u^2 + v^2 + w^2))$  is the vector of the conservative variables,  $\rho$  denotes the density,  $u, v, w$  the cartesian velocity components and  $\varepsilon, p$  the specific internal energy and the pressure.  $J = \partial(\xi, \eta, \zeta) / \partial(x, y, z)$  is the Jacobian of the transformation from the cartesian frame of reference  $(x, y, z)$  to the generalized coordinate system  $(\xi, \eta, \zeta)$ , where  $\xi$  is the streamwise direction,  $\eta$  is the direction normal to the wall and  $\zeta$  corresponds to the circumferential direction. The quantities  $E, F, G$  represent the inviscid fluxes, while

the viscous fluxes are given by  $E_v, F_v, G_v$ . The viscous fluxes contain only those parts of the shear stress and the heat conduction with pure derivatives in the  $\xi, \eta, \zeta$  - direction (TLNS approach). The Reynolds number with respect to the reference values is defined by  $Re_\infty = \rho_\infty u_\infty L / \mu_\infty$ . From the thermodynamic point of view the system of equations is closed by the equations of state (for systems in thermodynamic equilibrium), where the variables  $\rho, \varepsilon$  are used as thermodynamically independent and  $p, T, c$  ( $c$  speed of sound) as dependent variables. The bulk viscosity is determined via Stokes hypothesis to formulate the simplified form of the shear stress.

When perfect gas flows are investigated, the molecular viscosity  $\mu$  is determined by applying Sutherland's law /12/. The thermal conductivity  $\kappa$  is calculated under the assumption of a constant Prandtl number  $Pr_\infty = \mu_\infty c_p / \kappa_\infty$ . In case of equilibrium real gas air flow the thermodynamic and transport properties are taken from the fitting routines reported in /13/.

The inflow and outflow boundary conditions are determined by the characteristic relations of the one-dimensional Euler equations. No-slip and adiabatic conditions are imposed on solid walls and undisturbed flow is assumed for the far field. More details can be found in /10,11,14/.

#### 3.2 Discretisation procedure

For completeness, the main ideas of the discretisation method as they were outlined in /8,9,10/ are repeated below.

The time derivative and the space derivatives are discretised separately in order to obtain a steady state independency of the time step. The numerical scheme is implicit in time and is solved by employing Newton's method for the new time step. When discretised in time and expanded in  $\Delta q$ , not in  $\Delta Q$ , one gets the following semi-discrete version of the TNLS equations. The quantity  $q$  is given by  $q = J^{-1}(\rho, u, v, w, H = (e+p)/\rho)^T$

$$Q_q \frac{\Delta q^{n+1,s}}{\Delta t} J^{-1} + \tau L^{n+1,s} =$$

$$-\left\{ \frac{Q^{n+1,s} - Q^n}{\Delta t} J^{-1} + \tau R^{n+1,s} + (1-\tau) R^n \right\}$$

$$R \equiv E_\xi + F_\eta + G_\zeta - Re_\infty^{-1}(E_{v,\xi} + F_{v,\eta} + G_{v,\zeta})$$

$$L \equiv (A \Delta q)_\xi + (B \Delta q)_\eta + (C \Delta q)_\zeta -$$

$$Re_\infty^{-1}((A_v \Delta q)_\xi + (B_v \Delta q)_\eta + (C_v \Delta q)_\zeta)$$

The indices  $n$  and  $s$  define the time and the iteration level, respectively. Setting  $r = 1$  provides an  $O(\Delta t)$  scheme, whereas for  $r = 1/2$  the TNLS equations are

approximated second order accurate in time. The quantities  $Z = A, B, C$  are the flux matrices of the convective part of the equations while the flux matrices of the viscous part are denoted by  $Z_v = A_v, B_v, C_v$ . The linearization with respect to  $q$  instead of  $Q$  is used to ensure efficiency and robustness of the scheme also in the hypersonic regime. Since the density changes dramatically in hypersonic flows due to shock waves and strong expansions the matrices become stiff owing to the reciprocal occurrence of the density in the elements. Additionally, low density values impair the robustness and the maximum possible time step which generally deteriorates the convergence of the scheme. For that reason the number of terms containing the factor  $\rho^{-1}$  should be reduced which is possible by expanding the flux matrices with respect to  $q$ . Furthermore using such an expansion the matrices  $Z_v$  are less costly to compute than  $\partial(E_v, F_v, G_v) / \partial Q$ , since  $Z_v$  contains more zero elements than the other one. The matrices  $\partial Q / \partial q, Z$  and  $Z_v$  will not be given here. They can be found in [8, 9, 10]. The TLNS equations are solved using a finite volume method, i.e., flow variables are defined at cell centers and coordinates at cell vertices. Using a general notation for the spatial discretization the discrete problem reads

$$Q_q \frac{\Delta q^{n+1,s}}{\Delta t} J^{-1} + r L_\delta^{n+1,s} =$$

$$- \left\{ \frac{Q^{n+1,s} - Q^n}{\Delta t} J^{-1} + r R_\delta^{n+1,s} + (1-r) R_\delta^n \right\}$$

$$R_\delta \equiv \delta_\xi E + \delta_\eta F + \delta_\zeta G - Re_\infty^{-1} (\delta_\xi E_v + \delta_\eta F_v + \delta_\zeta G_v)$$

$$L_\delta \equiv \delta_\xi (A \Delta q) + \delta_\eta (B \Delta q) + \delta_\zeta (C \Delta q) -$$

$$Re_\infty^{-1} (\delta_\xi (A_v \Delta q) + \delta_\eta (B_v \Delta q) + \delta_\zeta (C_v \Delta q))$$

The symbol  $\delta_\omega M$  with  $M = E, F, G$ ,  $\omega = \xi, \eta, \zeta$  and  $m = i, j, k$  is understood as  $\delta_\omega M = M_{m+1/2} - M_{m-1/2}$  where the constant subscripts along the  $\omega$ -line are dropped. The approximative solution of the TLNS equations in the steady and the unsteady case is determined only by the right hand side, that is by the  $R_\delta$  expression. Therefore the spatial approximation of the  $L_\delta$ -term on the left hand side can be chosen to develop an efficient algorithm to invert the solution matrix in every time step.

### 3.3 Spatial discretisation of the explicit operator

The spatial accuracy of the numerical scheme is determined by the formulation of the inviscid and viscous fluxes at the cell faces. The viscous terms are

expressed by central differences in which second derivatives are treated as differences across cell faces of first derivative terms. The derivatives of the inviscid fluxes are approximated by a symmetric TVD scheme in the sense of [15, 16]. At the cell face  $\Gamma_{m+1/2}$  the general flux  $M_{m+1/2}$  is formulated as

$$M_{m+1/2} =$$

$$\frac{1}{2} \{ M(Q_{m+1}, \Gamma_{m+1/2}) + M(Q_m, \Gamma_{m+1/2}) -$$

$$(\varphi^{-1} R^N \psi(\Lambda^N))_{m+1/2} (\alpha_{m+1/2}^N -$$

$$S(\alpha_{m-1/2}^N, \alpha_{m+1/2}^N, \alpha_{m+3/2}^N)) \}$$

where a four argument minmod limiter

$$S(\alpha_{m-1/2}^N, \alpha_{m+1/2}^N, \alpha_{m+3/2}^N)/2 = \minmod(\alpha_{m-1/2}^N,$$

$$\alpha_{m+1/2}^N, \alpha_{m+3/2}^N, \frac{1}{4}(\alpha_{m-1/2}^N + \alpha_{m+1/2}^N))$$

is applied to the difference in the Riemann invariants

$$\alpha_{m+1/2}^N = \phi(R_{m+1/2}^N)^{-1} (Q_{m+1} - Q_m)$$

and the entropy correction function  $\Psi(f)$

$$\psi(f) = \begin{cases} |f| & |f| \geq \varepsilon \\ (f^2 + \varepsilon^2)/2\varepsilon & |f| < \varepsilon \end{cases}$$

with a small positive parameter  $\varepsilon$  is used.

To accomplish a sensitive limiting the Riemann invariants are scaled by  $\varphi = c_R^2 / \rho$ , where the square of the speed of sound is defined by

$$c_R^2 = \frac{\partial p}{\partial \rho}|_\varepsilon + \frac{p}{\rho^2} \frac{\partial p}{\partial \varepsilon}|_\rho =$$

$$\frac{\partial p}{\partial \rho}|_\varepsilon + \Gamma(H - \varepsilon - \frac{1}{2}(u^2 + v^2 + w^2))$$

with

$$\Gamma = \frac{1}{\rho} \frac{\partial p}{\partial \varepsilon}|_\rho$$

The matrices  $R^N, (R^N)^{-1}$  are the right and left eigenvector matrices of the flux matrices  $N = \partial M / \partial Q$  and  $\Lambda_{m+1/2}^N$

represents the eigenvalue matrix

$$\Lambda_{m+1/2}^N = \text{diag}(\vartheta_\omega, \vartheta_\omega, \vartheta_\omega, \\ \vartheta_\omega + c_R |\Delta\omega|, \vartheta_\omega - c_R |\Delta\omega|)$$

$\vartheta_\omega$  is the contravariant velocity. Unless otherwise stated, the variables at cell interfaces are computed as Roe-averages [17]. This discretisation results in a second order accurate approximation of the steady state operator.

### 3.4 Spatial discretisation of the implicit operator

The implicit operator is in total first order accurate in space. Again central differences are applied to the second derivatives. As for the explicit operator the inviscid fluxes are formulated by the balance across the cell  $\delta_\omega (Z \Delta q) = (Z \Delta q)_{m+1/2} - (Z \Delta q)_{m-1/2}$  and  $(Z \Delta q)_{m+1/2}$  is given by

$$(Z \Delta q)_{m+1/2} = \frac{1}{2} \{ Z(Q_{m+1}, \Gamma_{m+1/2}) \Delta q_{m+1} + \\ Z(Q_m, \Gamma_{m+1/2}) \Delta q_m - \\ (Q_q X^P \psi(\Lambda^P)(X^P)^{-1})_{m+1/2} (\Delta q_{m+1} - \Delta q_m) \}$$

Since  $P = (\partial Q / \partial q)^{-1} Z = (\partial Q / \partial q)^{-1} \partial M / \partial q$  and  $N = \partial M / \partial Q$  are similar matrices they have the same eigenvalues with  $\Lambda^N = \Lambda^P$ . The left and right eigenvector matrices  $X^P$  and  $(X^P)^{-1}$  of the matrices  $P$  can be found in [8,9,10]. To reduce the computational costs and to strengthen the main diagonal of the solution matrix the difference  $Z(Q_m, \Gamma_{m+1/2}) - Z(Q_m, \Gamma_{m-1/2})$  is neglected that occurs when the above defined equation for  $(Z \Delta q)_{m+1/2}$  is inserted in  $\delta_\omega (Z \Delta q)$ . Further the maximum eigenvalue to determine  $\psi_{\max}^P = \psi(\Lambda_{\max}^P)$  is used which results in

$$(Z \Delta q)_{m+1/2} = \frac{1}{2} \{ Z(Q_{m+1}, \Gamma_{m+1/2}) \Delta q_{m+1} - \\ (Q_q I \psi_{\max}^P)_{m+1/2} (\Delta q_{m+1} - \Delta q_m) \}$$

where  $I$  denotes the identity matrix. Arithmetic averaging is applied to evaluate the variables at the cell interfaces.

### 3.5 Solution method

The discretisation described in the preceding subsections results in a block-heptadiagonal system of equations when three-dimensional flow problems are considered. The discrete problem is rewritten in a

compact form to admit a reasonable discussion of the solution method. Omitting the indices  $n$  and  $s$  of the equation of the discrete problem and using the notation  $(T_m + T_{m+n}) \Delta q = T_m \Delta q_m + T_{m+n} \Delta q_{m+n}$ , one has

$$(T_{ijk} + T_{i+1jk} + T_{ij+1k} + T_{ijk+1} + \\ T_{i-1jk} + T_{ij-1k} + T_{ijk-1}) \Delta q = RHS_{ijk}$$

where the matrices  $T_{ijk}$  contain all the coefficients of the cell volume  $(ijk)$  and  $RHS_{ijk}$  represents the right-hand side of the discrete problem. One of the main goals for the choice of the solution method is to attain best possible convergence and simplicity for vectorization. Therefore a symmetric point Gauss-Seidel relaxation scheme with red-black pattern is selected.

$$T_{ijk} \Delta q_{ijk} =$$

$$RHS_{ijk} - (T_{i-1jk} + T_{ij-1k} + T_{ijk-1}) \Delta q$$

$$T_{ijk} \Delta q_{ijk}^{n+1,s} = RHS_{ijk} - (T_{i-1jk} + T_{ij-1k} + \\ + T_{ijk-1}) \Delta q - (T_{i+1jk} + T_{ij+1k} + T_{ijk+1}) \Delta q^{n+1,s}$$

Subsequently, the vector of solution  $Q^{n+1,s+1}$  is updated via

$$Q^{n+1,s+1} = Q^{n+1,s} + Q_q \Delta q^{n+1,s}$$

Because only steady-state solutions are sought first order accuracy of the time discretisation is sufficient which is realized by setting  $r = 1$  in the equations of the discrete problem. Additionally, only one inner iteration step is executed to proceed from time level  $n$  to  $n+1$  which may lead to a simplification of the superscripts of the above equation by setting  $n+1, s+1 \rightarrow n+1$  and  $n+1, s \rightarrow n$ . The reciprocal value of the maximum residual, i.e., the right-hand side of the equation of the discrete problem controls the time step. At the beginning of the computation the time step is increased with decreasing maximum residual. If, however, the time step is larger than  $\Delta t_{\max} = 1$  then  $\Delta t$  is set equal to unity. Stepping from level  $n$  to  $n+1$  the boundary conditions are treated explicitly. That is, the boundary values are updated only after the values at interior points have been iterated. As a consequence the solution vector  $Q$  has all its components at the same order of accuracy only when the iterations have converged.

## 4. RESULTS

As already mentioned in chapter 2. from the aerothermodynamic point of view our interest was focused on five specific topics where experimental and

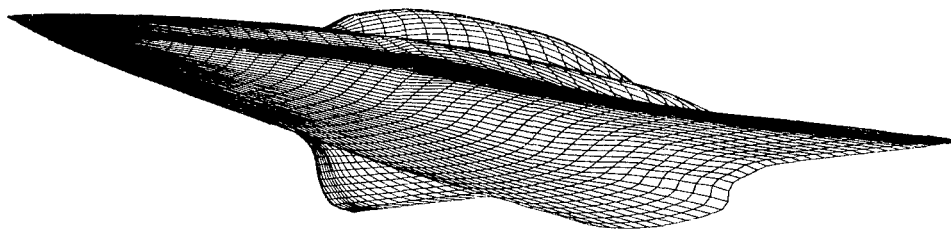


Fig.8 Grid for the Navier-Stokes computation around the pickaback configuration

numerical investigations have been carried out. We will start with the discussion of the aerothermodynamics of the pickaback configuration.

#### 4.1 Pickaback configuration

During the ascent, the upper stage is transported in a pickaback configuration on top of the lower stage to an altitude of approximately  $32\text{km}$  where then at the end of a pull up maneuver the orbiter is separated from the lower stage. The spacecraft is propelled by a combined turbo - ramjet propulsion system, where the turbojet accelerates the vehicle up to a Machnumber of roughly  $3.5$  while after that the ramjet operates until the separation process takes place ( $M_\infty = 6.8$ ). Of course, a lot of aerothermodynamic problems occur during this ascent and have to be answered, but here we will focus our interest only on the shock/boundary layer interaction in front of the upper stage, the bow shock interaction at the wing leading edge and the influence of the wall radiation on the thermal loads for the separation Machnumber  $M_\infty = 6.8$  /14/.

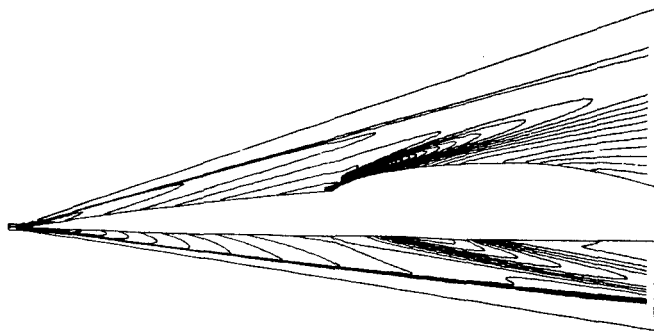


Fig. 8 Isobars in the plane of symmetry

The Navier-Stokes method proposed in /5/ with space marching capability is used to calculate the flowfield for an angle of attack  $\alpha = 6^\circ$ ,  $M_\infty = 6.8$  and a Reynolds number  $Re = 1.8 \times 10^8$  based on the vehicle length. The influence of the winglets and the fins and their interaction is for reasons of simplicity not considered here. The flowfield is resolved by  $75 \times 65$  cells in crossflow sections and 45 planes in marching direction (Fig. 7). The static pressure distribution in the plane of symmetry in Fig. 8 illustrates the canopy shock followed by an expansion on the leeward side of the upper stage. In Figs. 9a-c isobars in crossflow

planes at  $x = 59\text{m}$ ,  $71\text{m}$ ,  $83\text{m}$  for an adiabatic non - radiating wall are depicted. The bow shock touches the wing leading edge at approximately  $71\text{m}$  which carries to an increase of the aerodynamic and thermal loads in this wing area. The heating of the vehicle under adiabatic radiating wall boundary conditions with  $\epsilon = 0.85$  is displayed in Fig. 10. Non-radiating walls show much higher thermal loads than radiating (see /14/).

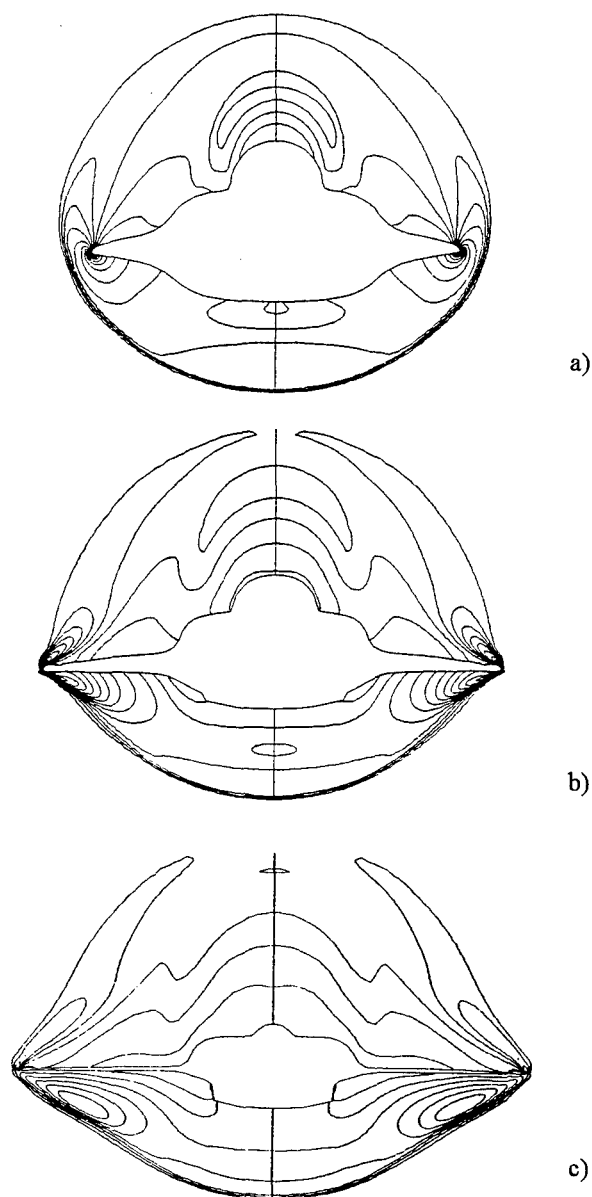


Fig. 9 Isobars in crossflow planes;  
a) =  $59\text{m}$ , b) =  $71\text{m}$ , c) =  $83\text{m}$

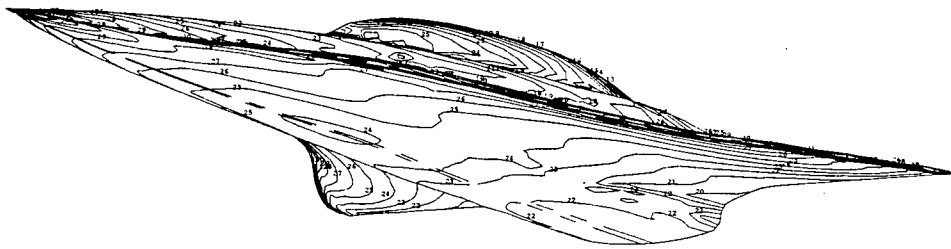


Fig. 10 Wall temperature distribution at an adiabatic radiating wall  $((T/T_{\infty})_{\min,\max,\Delta} = 1.,7.7,0.2)_{\text{radiating}}$ ;  
 $((T/T_{\infty})_{\min,\max,\Delta} = 1.,10.3,0.2)_{\text{non-radiating}}$ ; Ref. /14/

4.2 Flow field interaction during stage separation

Object of this investigation is the computation of the steady flow field whilst the upper stage has a certain distance from the lower stage during the separation process /10,14,18/. In such a case strong flow field interactions occur. The computation of the complete dynamic separation behaviour is beyond the scope of this paper. For validation reasons the flow parameters selected are exactly the ones of the experiments performed at the H2K windtunnel of the DLR in Cologne /19/, where the size of the model was 1:160. The freestream conditions are:  $M_{\infty} = 6$ ,  $Re_{\infty} = 1.13 \times 10^6$ ,  $T_{\infty} = 242K$ , angle of attack of the lower stage  $\alpha = 0^{\circ}$ , gap width between upper and lower stage at the trailing edge of the fuselage  $\Delta z = 14\text{ mm}$  (which corresponds to  $\Delta z = 2.24m$  for the real configuration). The relative angle of attack between upper and lower stage was varied within the range  $\Delta\alpha = 0^{\circ}, 2^{\circ}, 4^{\circ}$ . The following discussion addresses the influence of

- viscous effects by comparing Euler and Navier-Stokes solutions /10,14/ ,
- real gas effects by comparing perfect and real gas Euler solutions /20,21/ ,
- turbulence effects by contrasting laminar and turbulent Navier-Stokes solutions /11,18/ ,
- grid effects by comparing coarse and fine grid Euler and Navier-Stokes solutions /20/.

Further, the results obtained will be compared in very detail with the experimental data of /19/ .

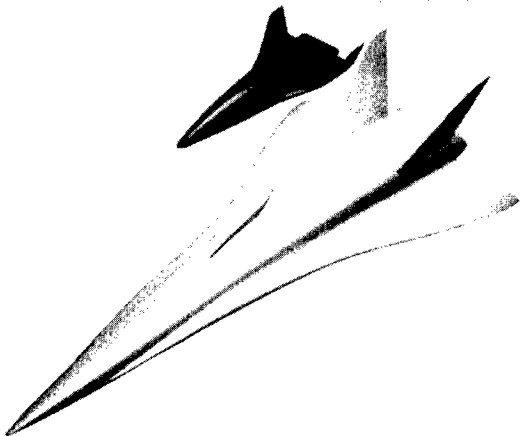


Fig.11 Windtunnel model of the two-stage system

Grid generation and boundary conditions

A CATIA imaging of the windtunnel model of the upper and the lower stage is shown in Fig.11. According to the experiments conducted no yaw angle is taken into account, i.e., the flow is considered symmetric with respect to the spanwise direction, which means that all the computations are performed just in the semi space. Since

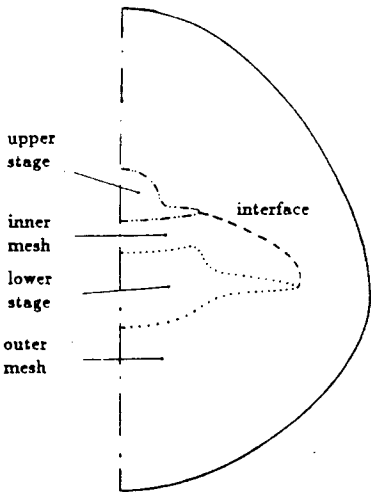


Fig. 12 Sketch of the two- block grid

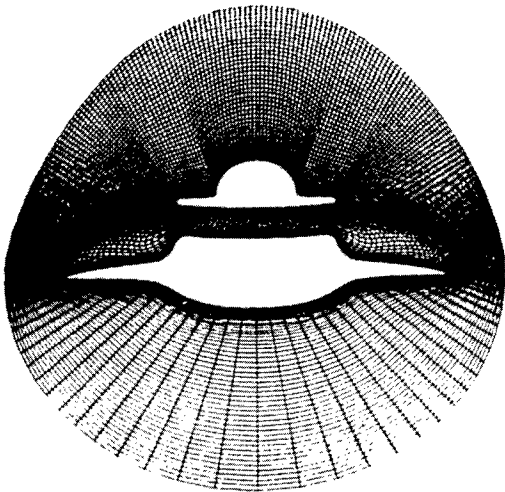


Fig.13 Two-block grid in a cross sectional view

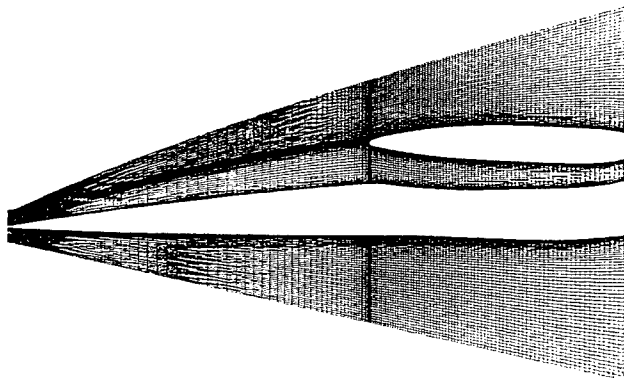


Fig. 14 Two-block grid in the plane of symmetry

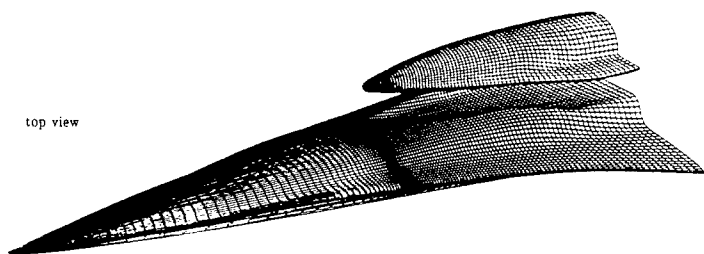


Fig.15 Surface mesh

the main interest consists in the comparison of the global aerodynamic coefficients of the windtunnel data with the numerical data of the upper stage, it is assumed that some simplifications of the shape and of the flow field will not have any evident impact on the magnitude of the global aerodynamic coefficients. First the winglets of the upper stage are not considered, which keeps the mesh structure relatively simple and second the wake flow is not calculated because the experimental quantities of the aerodynamic coefficients are evaluated on the basis of a constant state in the wake ( $p = 0$ ) due to the sting /19/. Therefore the outflow boundary of the computational domain coincides with the trailing edge of the fuselage of the upper stage.

A two- block mesh is used. The outer O-H grid covers the region between the outermost boundary, the interface of the two blocks, and the lower and upper surfaces of the lower and upper stages. The inner block resolves the gap between the upper and the lower stages (Fig.12). This structure extends over

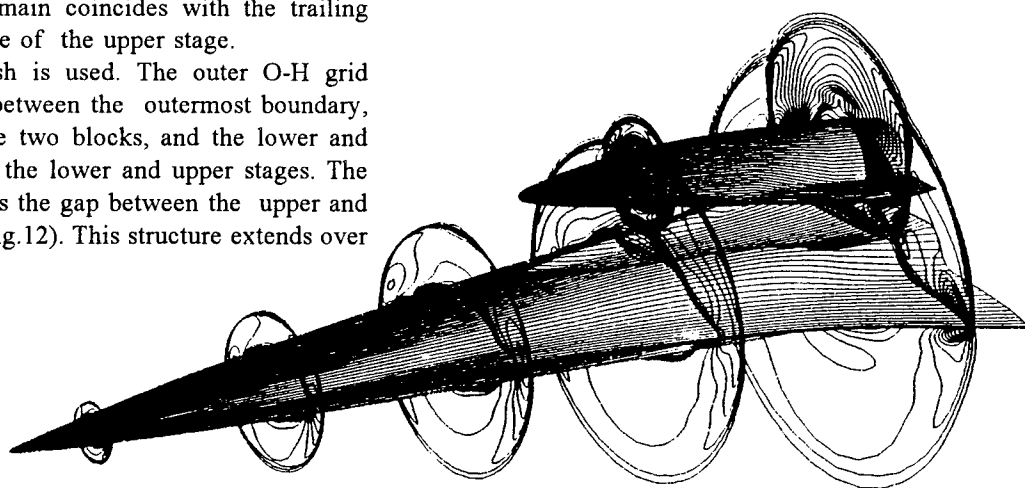
the the total length of the lower stage, even in front of the upper stage, where the surface of the upper stage degenerates to an interface. In the laminar case the outer mesh consists of  $51 \times 146 \times 95$  cells in the normal  $\times$  streamwise  $\times$  spanwise, while for the turbulent calculations  $61 \times 146 \times 110$  cells are used. The inner mesh has for the laminar case the size  $40 \times 146 \times 35$  cells and for the turbulent one  $55 \times 146 \times 35$  cells. The minimum normal stepsize in streamwise direction varies between  $10^{-3}$  and  $10^{-4}$  for laminar flow and is kept constant at  $10^{-5}$  for turbulent flows. The complete grid contains 911 770 cells for laminar flows and 1 260 710 cells for turbulent flows.

The influence of the grid is also considered by computing the flow fields with a mesh where every other cell is dropped.

The Figs. 13 - 15 give an idea about the structure of the three dimensional two block mesh. The outermost boundary is located such that the bow shocks of the lower and the upper stages are within this domain and to ensure that the number of cells in the undisturbed area is as low as possible. The cells are clustered near the walls and in the nose region of the upper stage to allow for a proper resolution of the strong gradients therein.

Most of the calculations were done for laminar and perfect gas flow since these were the most likely conditions in the windtunnel, but as already mentioned above the sensitivity to real gas and turbulent effects will also be checked.

Freestream conditions are prescribed at the inflow and the far field boundary. At the outflow all the conservative variables are computed via the one dimensional characteristics of the Euler equations /22/. Symmetry conditions are used in the plane of symmetry. For the Navier-Stokes computations adiabatic, zero normal pressure gradient and no-slip conditions at the walls are used, while for the Euler equations the normal velocity component is set to zero and the pressure at the body is determined by a locally one dimensional approach.

Fig. 16 Density contours at cross sections for  $\Delta\alpha = 4^\circ$

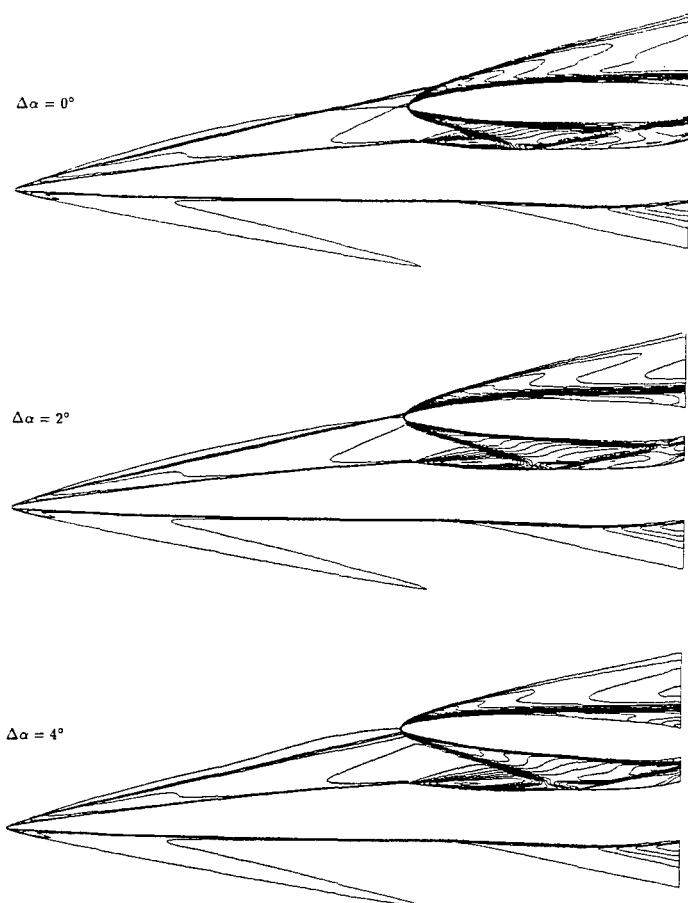


Fig. 17 Mach number contours in the plane of symmetry at  $\Delta\alpha = 0^\circ, 2^\circ, 4^\circ$  (inviscid flow)

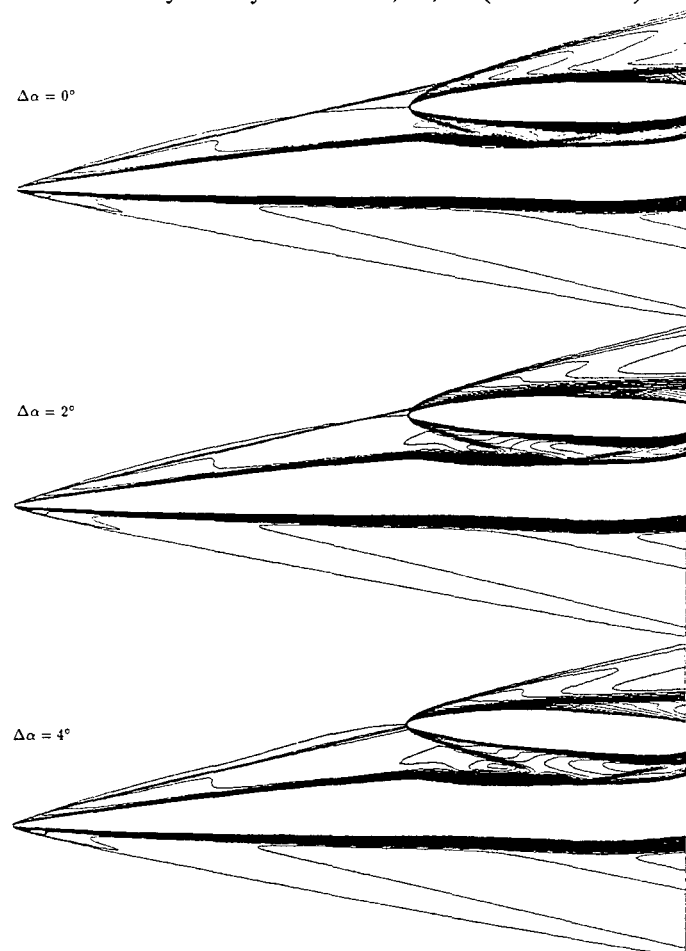


Fig. 18 Mach number contours in the plane of symmetry at  $\Delta\alpha = 0^\circ, 2^\circ, 4^\circ$  (viscous flow)

#### Discussion of inviscid and viscous flow computations

An overall impression of the flow is evidenced by the three dimensional plot of the density contours in Fig. 16 for a relative angle of attack  $\Delta\alpha = 4^\circ$  (laminar flow). The evolution of the bow shock waves, the boundary layer on the upper surfaces of the lower stage (aircraft) and the upper stage (space vehicle), and the shock / boundary layer interaction can be realized.

The results for the inviscid flow field computations for  $\Delta\alpha = 0^\circ, 2^\circ, 4^\circ$  are displayed in Fig. 17, where Mach number contours in the plane of symmetry are drawn. Downstream of the nose on the windward side of the lower stage no remarkable change of the flow variables occur due to the little deflection of the shape. The flow accelerates only in the nose and the tail region. On the upper part of the aircraft this behaviour is completely changed, because due to the larger deflection angle a shock wave is produced. This shock wave interacts with the bow shock of the space vehicle in the symmetry plane in the proximity of the nose of the upper stage (Fig. 17,  $\Delta\alpha = 0^\circ$ ). Further downstream this interaction occurs farther away from the symmetry plane (Fig. 20,  $\Delta\alpha = 0^\circ$ ), whereby the strength of the bow



Fig. 19 Schlieren photographs of the windtunnel tests in H2K /19/

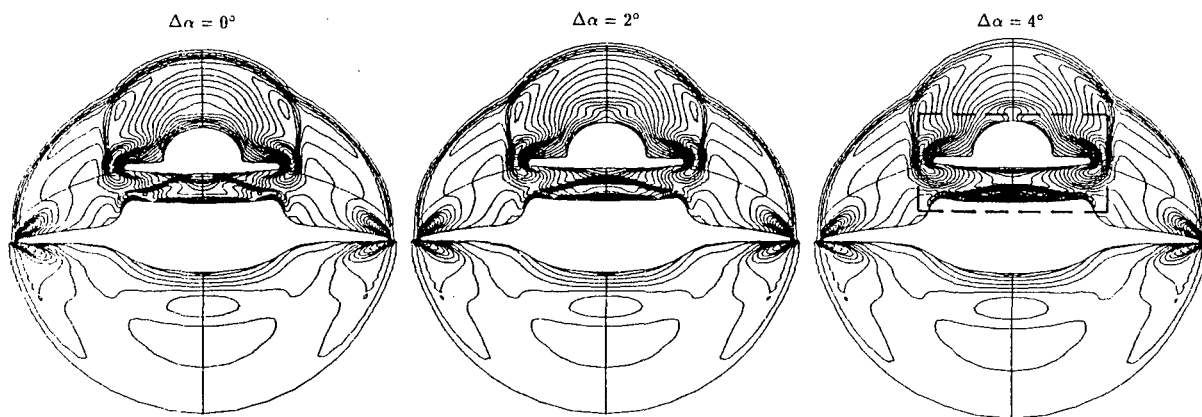


Fig. 20 Density contours in crossflow planes (inviscid flow);  $X/L = 2.55$  or  $X = 68.42\text{m}$  at  $\Delta\alpha = 0^\circ, 2^\circ, 4^\circ$

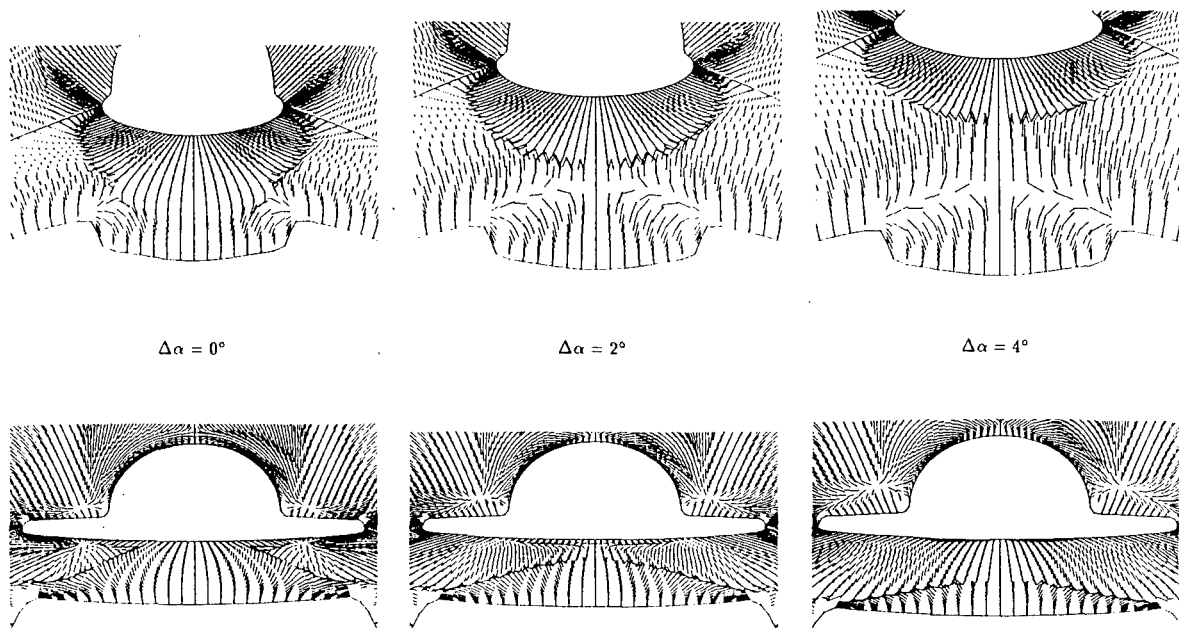


Fig. 21 Quasi- streamlines in crossflow planes (inviscid flow);  $X/L = 1.95$  or  $X = 52.3\text{m}$  (top),  $X/L = 2.55$  or  $X = 68.42\text{m}$  (bottom) at  $\Delta\alpha = 0^\circ, 2^\circ, 4^\circ$

shock wave of the lower stage is so little that no evident impact on the shape of the bow shock of the upper stage can be observed. For increased  $\Delta\alpha$  the location of the interaction point of the both bow shocks moves from leeward down to the windward side (Fig. 17,  $\Delta\alpha = 4^\circ$ ). Generally, the variation of the relative angle of attack  $\Delta\alpha$  has an impact on the flowfield of the aircraft only in the surroundings of the gap. The flow pattern within the gap is characterized by strong expansions and shock reflections. Before the bow shock of the upper stage impinges upon the leeward side of the aircraft it is weakened by the expansion waves generated by the edge of the trough. The first impingement of the compression wave on the surface of the lower stage occurs in the symmetry plane (Fig. 17,  $\Delta\alpha = 0^\circ$ ). Further downstream the shock impingement location moves in spanwise direction where the trace forms a C-like shape insight of the trough. The reflected shock interacts with the windward side of the upper stage

depending of  $\Delta\alpha$ . For increasing  $\Delta\alpha$  the shock impingement point on the upper surface of the aircraft is clearly shifted downstream because of the relatively small gap width  $\Delta z = 14\text{mm}$  (Fig. 17). For this reason the reflected shock wave impinges upon the lower surface of the space vehicle for  $\Delta\alpha = 0^\circ$ , whereas for  $\Delta\alpha = 4^\circ$  no shock - surface interaction takes place, although the shock angle of the reflected shock at  $\Delta\alpha = 4^\circ$  is larger than that at  $\Delta\alpha = 0^\circ$  (Fig. 17).

In the viscous case the development of the boundary layer along the surfaces of the lower and the upper stages is evident (Fig. 18), which leads to a slightly stronger bow shock wave of the lower stage. Furthermore the strong expansion at the edge of the trough does no longer exist. Within the gap the influence of the viscous effects compared to the inviscid ones will grow with decreasing relative angle of attack  $\Delta\alpha$ . As in the inviscid case, the location of the bow shock interaction slides from the leeward side to the windward side of the space vehicle with



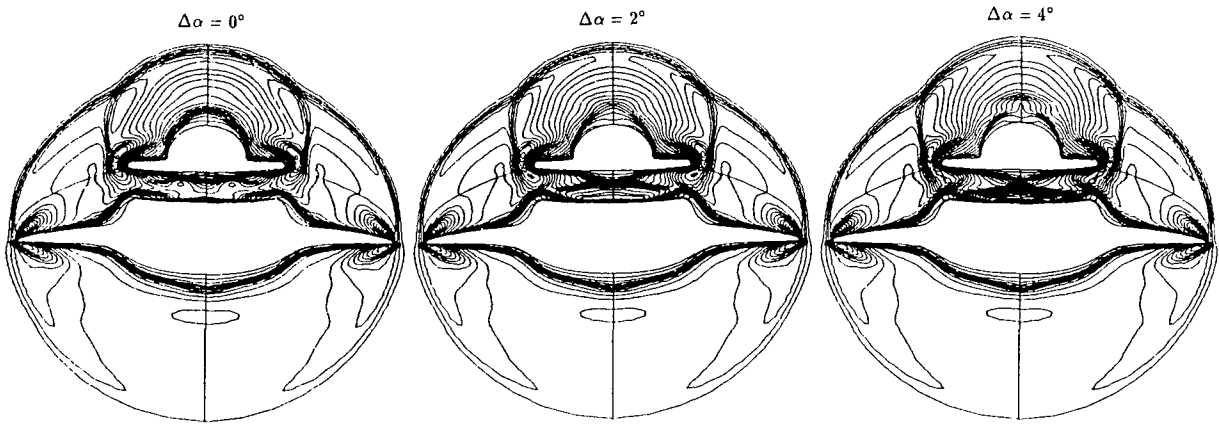


Fig.22 Density contours in crossflow planes (viscous flow);  $X/L = 2.55$  or  $X = 68.42m$  at  $\Delta\alpha = 0^\circ, 2^\circ, 4^\circ$

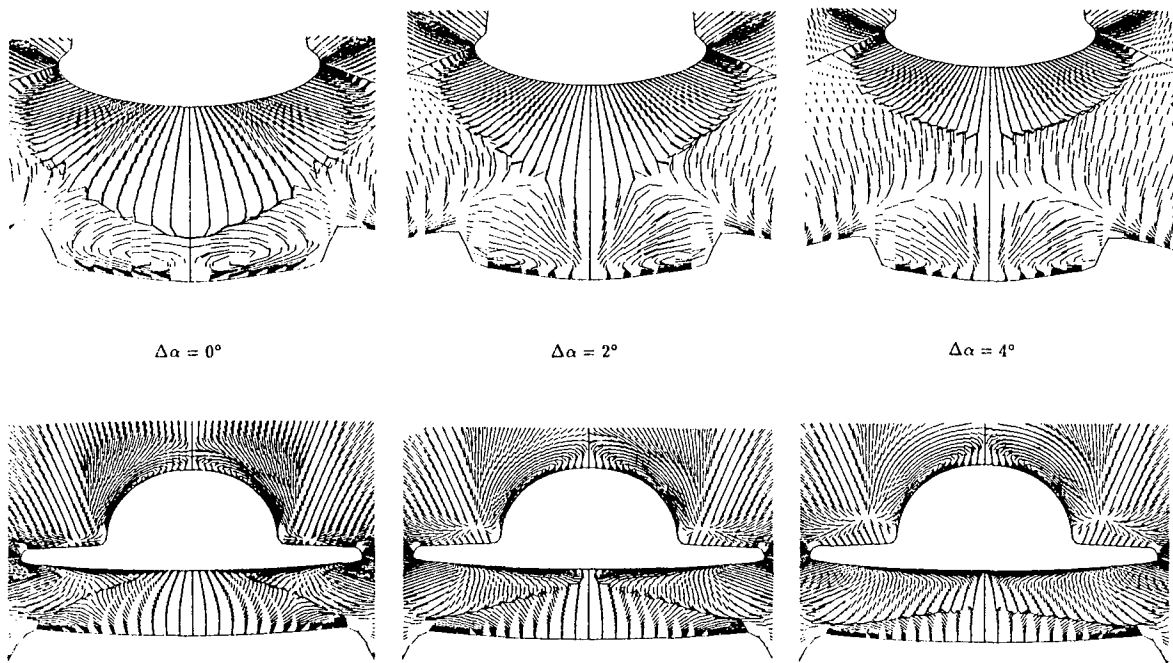


Fig. 23 Quasi- streamlines in crossflow planes (viscous flow);  $X/L = 1.95$  or  $X = 52.3m$  (top),  $X/L = 2.55$  or  $X = 68.42m$  (bottom) at  $\Delta\alpha = 0^\circ, 2^\circ, 4^\circ$

increasing  $\Delta\alpha$ . However, at  $\Delta\alpha = 4^\circ$  this interaction takes place a bit closer to the tip of the nose of the space vehicle compared to the inviscid case. The bow shock reflection of the upper stage in the trough area of the lower stage happens somewhat more upstream than in the inviscid case, which leads to the effect that still in the  $\Delta\alpha = 4^\circ$  case the lower side of the space vehicle is slightly affected (Fig. 18).

A qualitative comparison of the numerical results with experiments is presented by the Schlieren Photographs of Fig. 19 for  $\Delta\alpha = 0^\circ, 2^\circ, 4^\circ$  and the Machnumber contours for the inviscid (Fig.17) and viscous (Fig.18) flow field predictions. Note that in the photographs the shock boundary layer interaction within the trough is covered by the sidewalls, whereas the sidewalls are not shown in the numerical results. The location of the interaction of the both bow shocks are in good agreement for  $\Delta\alpha = 0^\circ, 2^\circ$ , while for  $\Delta\alpha = 4^\circ$  the Schlieren Photograph shows the nose of the space

vehicle somewhat outside of the bow shock area of the lower stage. It seems from the tendency that the numerical result is more reliable and that in the experiment the angle of attack of the lower stage  $\alpha$  was not equal to zero. As far as the flow pattern inside of the gap is concerned, the correspondence between the Navier-Stokes results and the experiments seems to be somewhat better due to the slightly smaller shock angle of the reflected shock wave than in the inviscid solution.

Fig. 20 shows for inviscid flow the dependence of the shape and the location of the reflected shock wave inside the gap on  $\Delta\alpha$  for a cross section  $X = 68.42m$ . At  $\Delta\alpha = 0^\circ$  the shock wave has already touched the space vehicle's lower surface and the impingement trace away from the symmetry plane, whereas for  $\Delta\alpha = 2^\circ$  the compression wave just approaches this lower surface. For  $\Delta\alpha = 4^\circ$  the entire shock wave is just reflected from the trough area of the lower stage. In contrast to that the viscous flow (Fig. 22) evidence

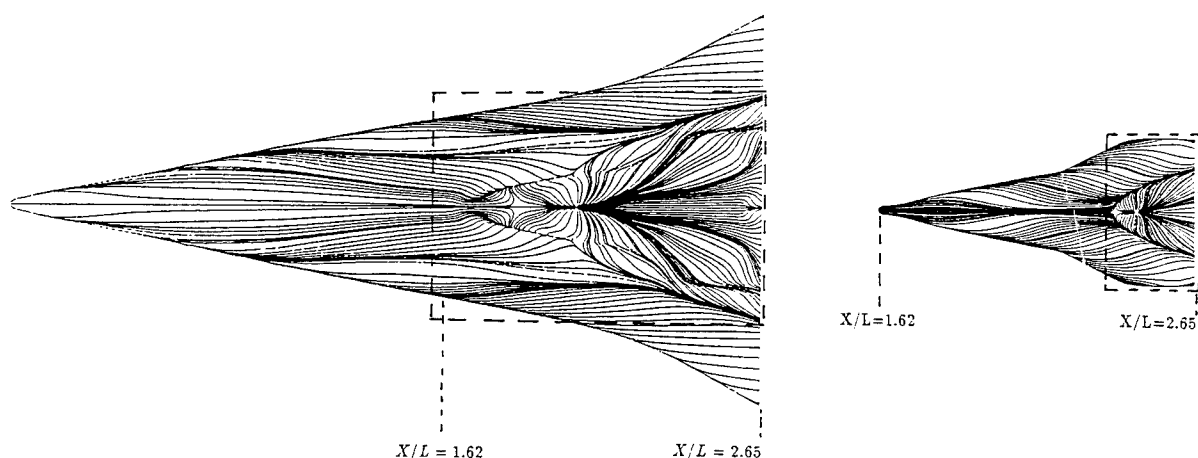


Fig. 24 Wall streamlines on the upper surface of the aircraft (left), and the lower surface of the space vehicle (right)

that for  $\Delta\alpha = 0^\circ$  the shock wave is mostly swallowed by the viscous forces. For  $\Delta\alpha = 2^\circ$  the shock is relatively close to the windward side of the space vehicle and its spanwise extension is confined by the boundary layer.

To get a deeper insight into the complex gap flow between upper and lower stage quasi-streamline plots in crossflow planes are considered. For the cross flow planes  $X = 52.3m$  and  $X = 68.42m$  Fig. 21 shows the inviscid results, while in Fig. 23 the viscous results are displayed. Note that the quasi-streamlines evidence only the flow direction, they do not give any information about the magnitude of the velocity. In the inviscid prediction no vortex pair can be observed within the trough. For  $\Delta\alpha = 0^\circ$  the bow shock of the space vehicle and the expansion at the edge of the trough already interact, for higher  $\Delta\alpha$ , however, the interference sets in further downstream (Fig. 21 top). The difference in the reflected shock positions as a function of  $\Delta\alpha$  can clearly be identified in the cross section  $X = 68.42m$  (Fig. 21 bottom), where for  $\Delta\alpha = 2^\circ$  and  $4^\circ$  the reflected shock waves still approach the windward side of the space vehicle, while for  $\Delta\alpha = 0^\circ$  the shock has already impinged the space vehicle's lower side.

Turning now to the viscous flow a vortex pair that lies inside the trough can be identified at  $X = 52.3m$  (Fig. 23 top) in contrast to the inviscid results. At  $\Delta\alpha = 0^\circ$  and  $2^\circ$  the bow shock of the space vehicle and the vortices interfere with each other. For the higher relative angle of attack  $\Delta\alpha = 4^\circ$  the interaction has not yet started. For the cross sections  $X = 68.42m$  (Fig. 23 bottom) no remarkable differences occur compared to the inviscid results. Again no shock boundary layer interaction at the windward side of the space vehicle can be observed for  $\Delta\alpha = 4^\circ$ , whereas at  $\Delta\alpha = 2^\circ$  there is an incipient interference between the shock and the boundary layer leading to the production of two small vortices at the space vehicle's lower surface.

For further analysis of the gap flow wall streamlines are plotted on the upper surface of the aircraft and the

lower surface of the space vehicle (Fig. 24). In Fig. 25 a partial view of the wall streamlines in the trough regime of the aircraft for  $\Delta\alpha = 0^\circ, 2^\circ, 4^\circ$  is given.

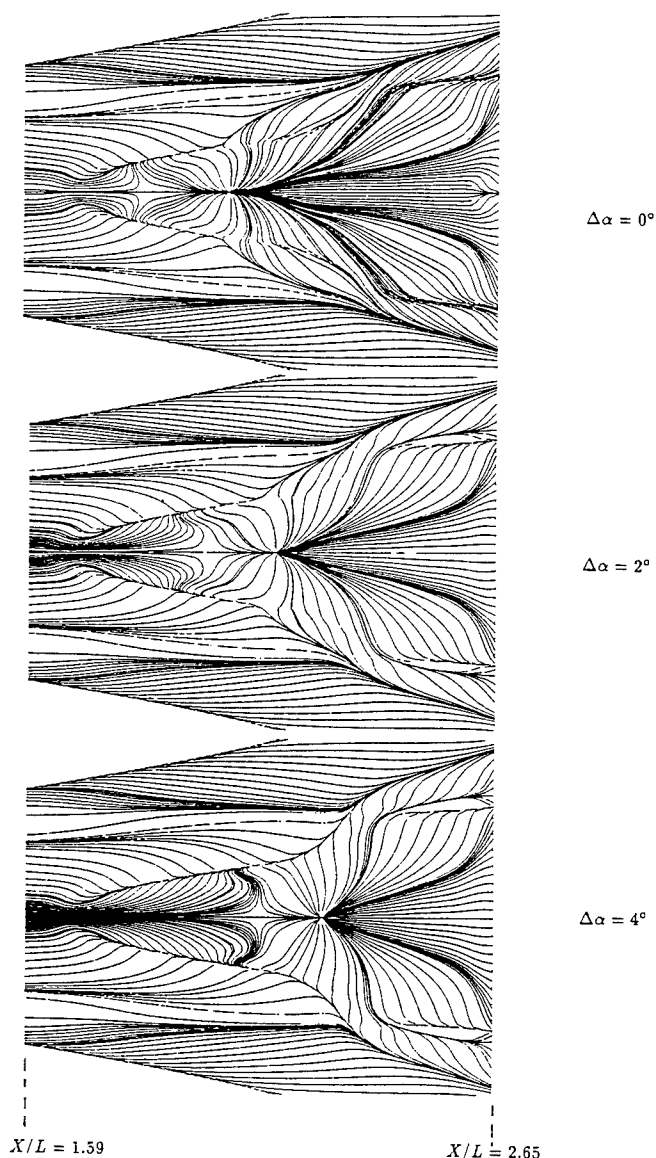


Fig. 25 Wall streamlines on the upper surface of the aircraft at  $\Delta\alpha = 0^\circ, 2^\circ, 4^\circ$

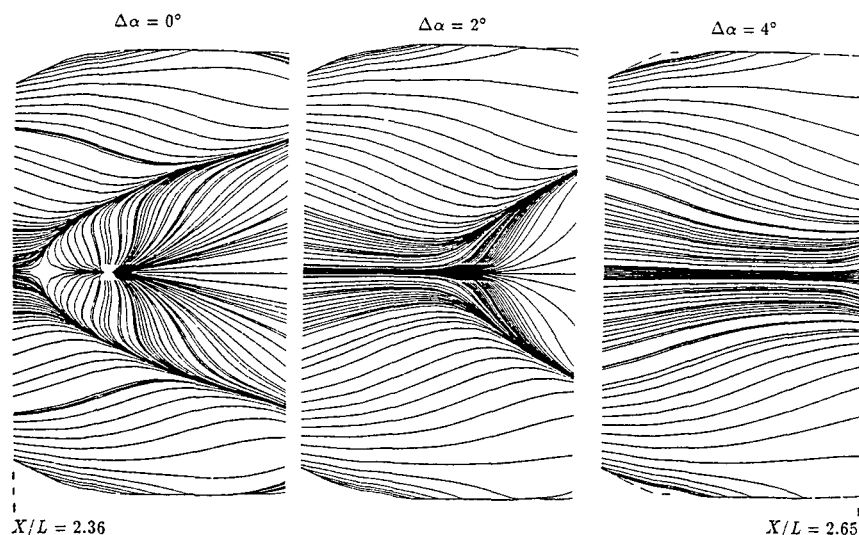


Fig. 26 Wall streamlines on the lower surface of the space vehicle at  $\Delta\alpha = 0^\circ, 2^\circ, 4^\circ$

The downstream shift of the separation region at higher  $\Delta\alpha$  values caused by the x-shift of the shock-boundary layer interaction can clearly be realized. The wall streamlines demonstrate that for varying  $\Delta\alpha$  values the separation and reattachment locations are functions of span. This means, when considered in streamwise direction, the reverse flow is smallest in the symmetry plane. In spanwise direction the separation region is generally confined by the edge of the trough. This is also true for the vortex pair upstream of the separation regime. Further downstream these vortices overflow the edges of the trough caused by the interaction of the bow shock of the space vehicle with the boundary layer of the aircraft.

As mentioned above, the reflected bow shock of the

space vehicle at the upper surface of the aircraft affects the windward side of the space vehicle only for low  $\Delta\alpha$  and  $\Delta z$  values. This is illustrated by the wall streamlines on the windward side of the space vehicle shown in Fig. 26. At  $\Delta\alpha = 0^\circ$  the reverse flow region in streamwise direction and the spanwise vortices are encompassed by the C-like shape separation line. The separation bubble is vanished for  $\Delta\alpha = 2^\circ$  and only the vortex pair is retained, and for  $\Delta\alpha = 4^\circ$  the wall streamlines indicate that barely any interference occurs. For the considered gap with of  $\Delta z = 14$  mm it is concluded that the larger the relative angle of attack the less the the impact of the lower stage on the aerodynamic characteristics of the upper stage.

Since a strong interest exists in the aerodynamic coefficients of the space vehicle, the measured /19/ and predicted data are compared in Fig. 27. At all relative angles of attack the lift and pitching moment coefficients of the experiments and inviscid as well as viscous calculations agree quite well. Of course, the drag coefficient  $c_{d(fb)}$  ( i.e., (fb) means forebody with base pressure  $p=0$  ) is not well predicted by the inviscid approach. For that the Navier-Stokes results have to be considered. Generally, the discrepancy between the experimental and theoretical values is less than 5%. This means that lift and even pitching moment can be sufficiently accurately predicted by solving the Euler equations, while the Navier-Stokes equations are mandatory for the determination of the drag. Especially with respect to the pitching moment this result might completely change when the gap width is reduced, since then the viscous forces became more dominant for the shock pattern.

#### Real gas effects

To investigate the influence of the real gas effects on the solution an inviscid flow field calculation at  $\Delta\alpha = 2^\circ$  was performed. If, on the whole, real gas effects appear, they occur in the nose regions of the upper

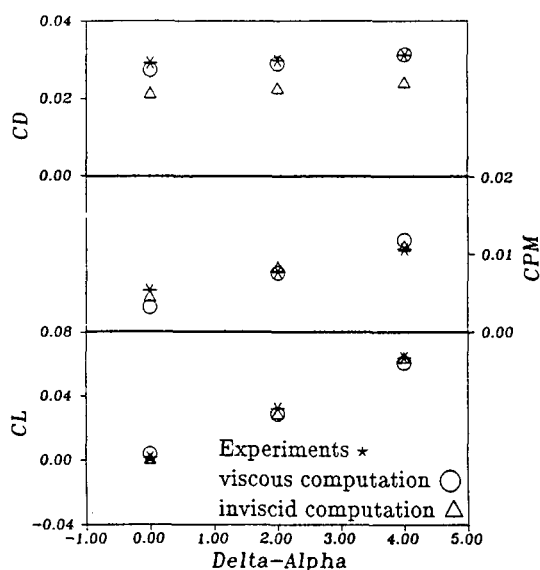


Fig. 27 Aerodynamic coefficients of the upper stage; comparison of experiment and numerical simulation

Equations	Grid size	State of the gas	$C_{d(fb)}$	$C_l$	$C_m$
Euler	coarse	perfect	0.02204	0.02790	0.00781
Euler	fine	perfect	0.02232	0.02814	0.00805
Euler	fine	real	0.02235	0.02838	0.00803
Navier-Stokes	coarse	perfect	0.02800	0.03198	0.00758
Navier-Stokes	fine	perfect	0.02903	0.02873	0.00750

Table 1: Aerodynamic coefficients of the space vehicle at  $\Delta\alpha = 2^\circ$

and the lower stages and along the surface of the upper stage. Using a perfect gas the stagnation point temperature at a freestream Mach number  $M_\infty = 6$  is  $T_{o,perf} = 1984\text{ K}$  and for an equilibrium real gas assumption  $T_{o,real} = 1888\text{ K}$ . This little difference indicates that a perceptible influence of the real gas effects on the flow field is unlikely. Plots of density distributions on the surface of the space vehicle for perfect and equilibrium real gas coincide completely (see /21/). In Tab. 1 the aerodynamic coefficients for the upper stage of a fine grid Euler solution for perfect and equilibrium real gas is compared. The differences between the numbers are so small that it is concluded that for this freestream conditions no noticeable real gas effects occur.

Influence of grid fineness

Besides the standard fine grid solutions (inviscid and laminar case: 911 770 cells), coarse grid solutions (inviscid and laminar case: 179 250 cells) of the Euler and Navier-Stokes equations at  $\Delta\alpha = 2^\circ$  are established in order to reveal the influence of the grid fineness on the results. In Tab.1 the aerodynamic coefficients are listed. Obviously, the Navier-Stokes solutions are more susceptible to such a drastic mesh reduction than the Euler solution. But nevertheless the overall agreement of these integrated values is quite good, except the value for the lift coefficient in the Navier-Stokes solution.

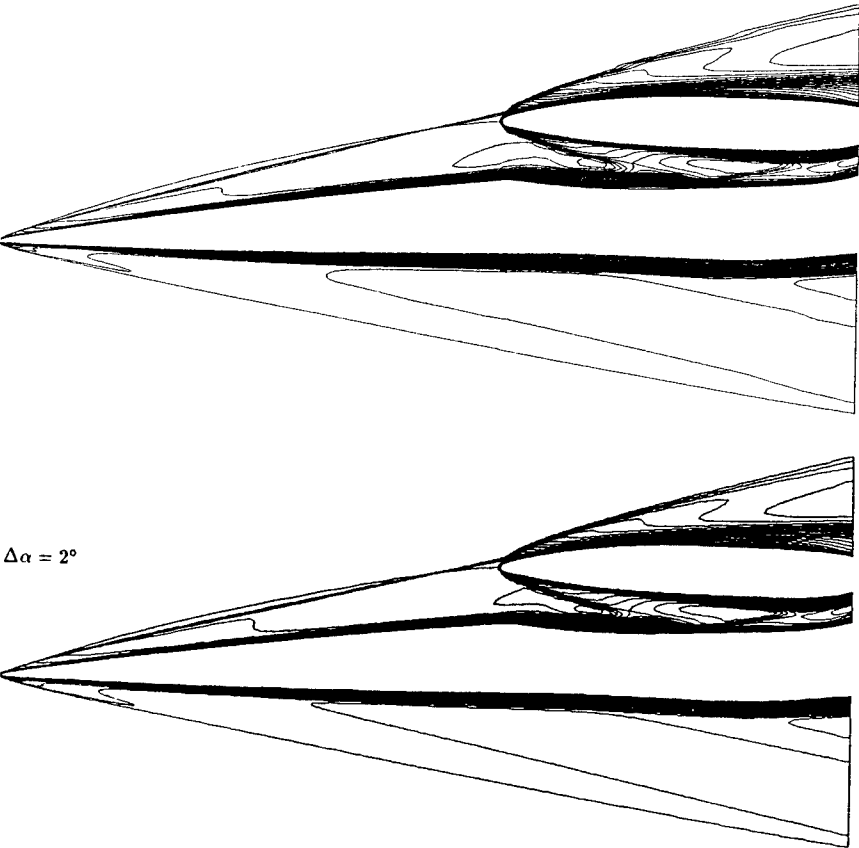


Fig. 28 Mach number contours in the plane of symmetry at  $\Delta\alpha = 2^\circ$  (turbulent flow, top; laminar flow, bottom)

Flow	$C_{d(fb)}$	$C_l$	$C_m$
laminar	0.02903	0.02873	0.00750
turbulent	0.04830	0.02967	0.00810

Table 2: Aerodynamic coefficients for the space vehicle at  $\Delta\alpha = 2^\circ$

Turbulence effects

Since it was not a priori known if the flow fields in the windtunnel tests /19/ were entirely laminar or partially turbulent a fully turbulent Navier-Stokes solution was established /11/ by applying the two equation  $k-\omega$  model of Wilcox /23/. For this comparison the  $\Delta\alpha = 2^\circ$  case was chosen. Fig. 28 (top) shows the Mach number contours in the plane of symmetry for the turbulent case and Fig. 28 (bottom)

the Machnumber contours for the laminar case. The flow upstream of the space vehicle, the flow pattern inside the gap, the interaction of the bow shocks in front of the nose of the space vehicle remain obviously almost unaltered. In /11/ there is an additional discussion given for the behaviour of the wall streamlines on the upper surface of the aircraft (mainly in the trough regime) and on the windward surface of the space vehicle. The overall outcome of this analysis is that under the flow parameter considered, comparable flow phenomena occur in the laminar and turbulent flows. However, as can be seen from Tab. 2 there is quite a drastic difference in the drag coefficient that, of course, evolves from higher shear stresses in the turbulent flow field. By comparing the computed (for turbulent flow) and measured results, it can be seen that the predicted drag coefficient is far too high related to the experimental value, whereas the laminar drag

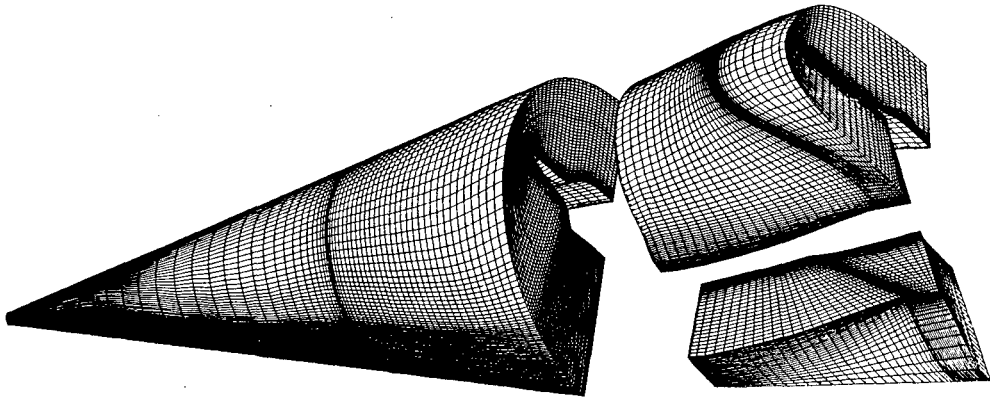


Fig. 29 Three-block grid for the aircraft with fins

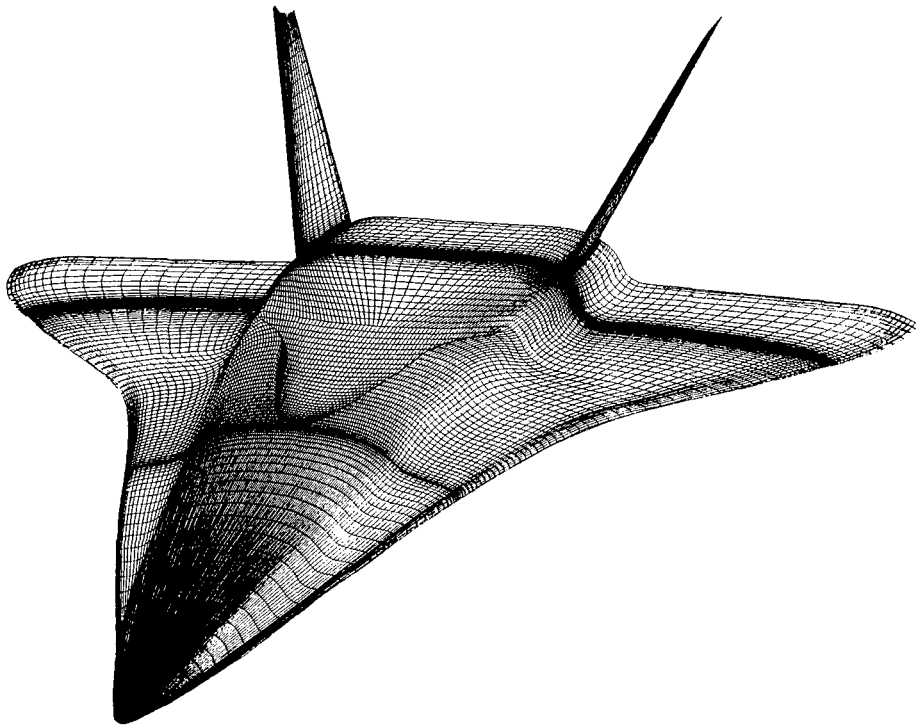


Fig. 30 Surface grid for the aircraft with fins

coefficient agrees quite well. Thus, one can conclude that the physics of the flow is better represented by assuming laminar instead of fully turbulent flow.

4.3 Angle of attack sensitivity of the lower stage

In this chapter the viscous flow field about the lower stage alone is considered, that is after the upper stage has been released. The freestream conditions used are the one of the windtunnel experiments performed in the RWG windtunnel at the DLR in Göttingen [24] :  $M_\infty = 6.83$ ,  $Re_\infty = 1.7 \times 10^6$ ,  $T_\infty = 59\text{ K}$ , wall temperature  $T_w = 330\text{ K}$ . The model scale was 1:330. Perfect gas is assumed and the flow is considered to be laminar which corresponds with the conditions known from the windtunnel. In the experimental campaign only the angle of attack was varied, but no yaw angle variations has been considered. Therefore the flow was symmetric with respect to the spanwise

direction and as such all calculations are conducted for the configuration in the half space.

Since we reflect hypersonic flows, at all inflow boundaries freestream values are prescribed, at outflow boundaries the flow variables are determined by extrapolation, at the wall no slip condition, zero pressure gradient and isothermal wall condition are implemented.

A more complex grid structure has necessarily to be generated for the configuration including the fins. A global view of the grid used for this shape is shown in Fig. 29. The front part of the configuration is embedded into a mono-block H-O type mesh. At the rear of the vehicle, beginning somewhat upstream of the leading edge of the fin, the mesh is split into two blocks. One covers the domain located between the leeward symmetry plane and the fin and the other block encompasses the remaining spanwise region between the fin and the windward symmetry plane.

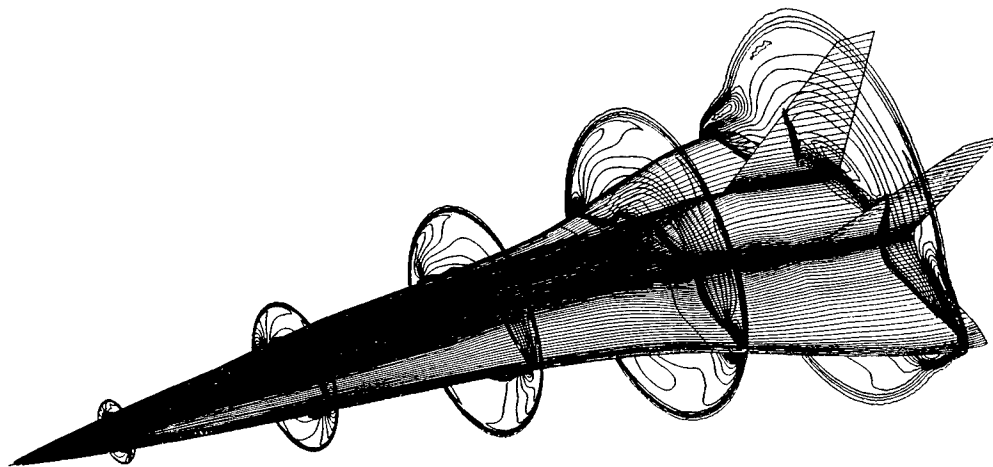


Fig. 31 Density contours in several cross section at the aircraft

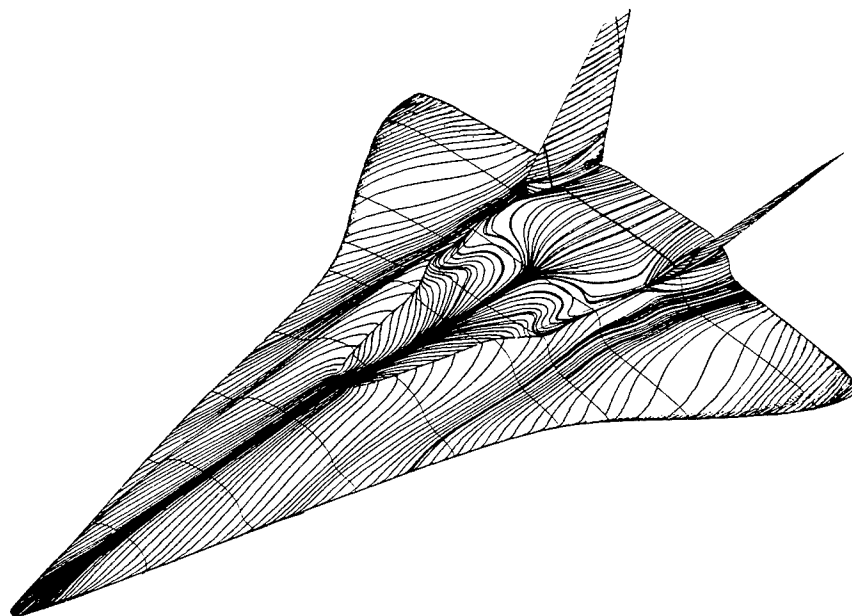


Fig. 32 Wall streamlines for the aircraft at  $\Delta\alpha = 3^\circ$

The outermost boundary was chosen such that the bow shock, taken from the Schlieren Photographs of the windtunnel experiments /24/ was entirely encompassed by the grid. The total number of grid points for all the three blocks amounts to roughly 600 000. The corresponding surface grid for the complete aircraft is displayed in Fig.30.

For more detailed investigations like angle of attack dependence, flow inside the trough and trough design modifications a simplified shape is considered. First the fins at the rear are dropped and the configuration is cut off at the maximum wingspan /21/. This simplified shape enables one to perform a larger amount of computations in an efficient way and at comparatively low costs. The detailed investigations of the trough flow which are discussed in the next chapter are also carried out using this reduced configuration. The grid consists of  $51 \times 83 \times 71$  cells in normal  $\times$  streamwise  $\times$  spanwise direction which amounts to about 300 000 cells.

An overview about the hypersonic viscous flow about the aircraft is given in Fig.31. In this case the angle of attack was  $\alpha = 3^\circ$ . Density contours in several cross sections and streamwise grid lines on the vehicle surface are plotted. The bow shock produced at the nose of the vehicle exhibits in all planes upstream of the fins an almost circular shape. Downstream of the last but one cross sectional plane an interaction between the bow shock and the leading edge of the wing occurs. Despite the fact that the mesh used is too coarse for a detailed analysis of this impingement problem the streamwise location where the bow shock touches the wing leading edge can be determined from the numerical result to  $X/L \approx 0.73$  ( $L \div$  length of the aircraft). This location is in an acceptable agreement with the outcome of the Schlieren pictures of Ref. /24/, where a value of  $X/L \approx 0.75$  is found. At the surface of the vehicle steep density gradients are encountered that indicate the extension of the boundary layer. The wall streamlines delineated in Fig. 32 provide supplementary information on the flow characteristics at the lower stage. The streamline pattern is strongly affected by the geometry of the trough. A clear spanwise separation line can be detected along the edge of the trough. At the rear end of the trough a region of reversed flow is indicated. A series of computations were performed with varying angles of attack applying the above defined simplified shape. For the three angles of attack  $\alpha = 3^\circ, 6^\circ, 9^\circ$  the wall streamlines on the upper surface of the aircraft are displayed in Fig. 33. These figures evidence that the extension of the region of reversed flow decreases with increasing  $\alpha$ . At an incidence angle of  $\alpha = 9^\circ$  a reversed flow can no longer be detected. This behaviour can be explained by the pressure evolution due to the contour of the fuselage at the aft end of the trough.

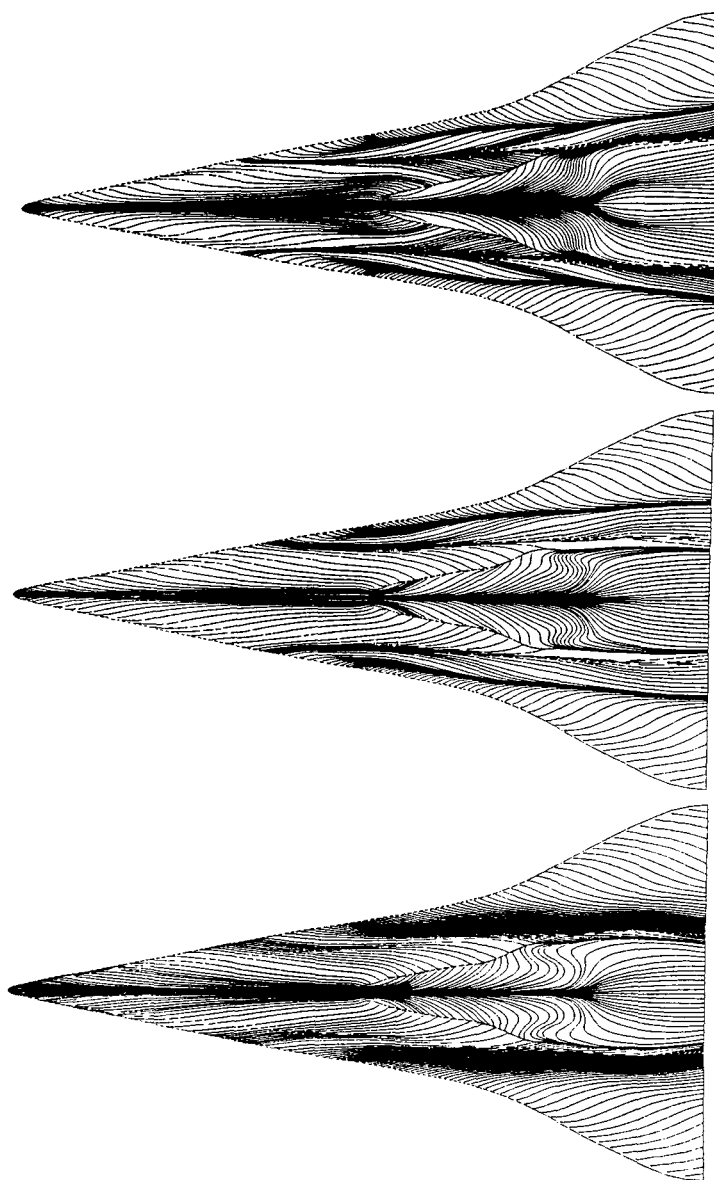


Fig. 33 Wall streamlines on the upper surface of the aircraft at  $\alpha = 3^\circ$  (bottom),  $\alpha = 6^\circ$  (middle),  $\alpha = 9^\circ$  (top)

At the wing surface the streamline pattern exhibits for  $\alpha = 6^\circ$  and  $9^\circ$  a separation and a reattachment line, while for  $\alpha = 3^\circ$  these phenomena do not occur. It should be mentioned that in all these cases no leading edge vortices could be detected in the flowfield, as it is known from slender delta wings.

Aerodynamic coefficients for the aircraft are measured in the H2K windtunnel at DLR in Cologne and the results are reported in /19/. Although the freestream Mach number has been  $M_\infty = 6$  the comparison is justified due to the little dependence of the aerodynamic coefficients on such high Mach numbers. From Fig. 34, where the measured and computed data are displayed, one can conclude that the agreement between the values is quite good.

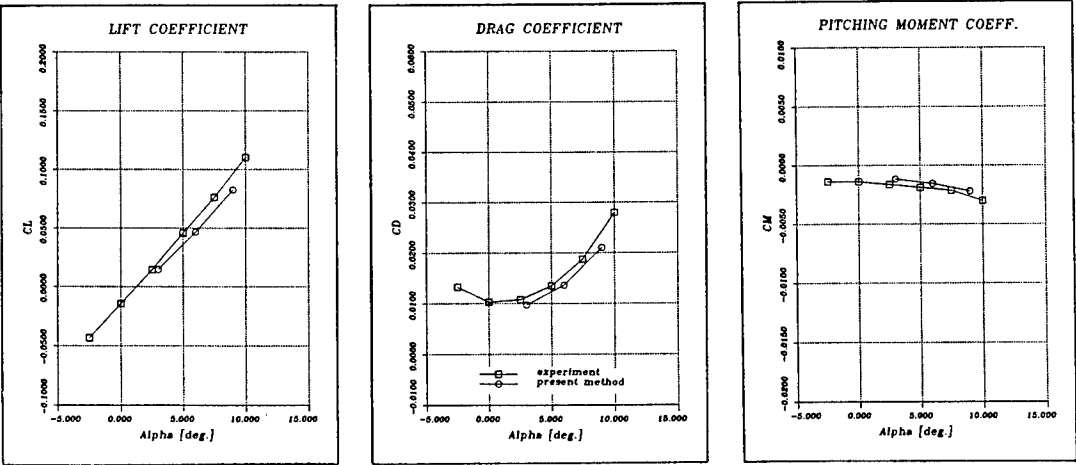


Fig. 34 Aerodynamic coefficients of the aircraft as function of angle of attack  $\alpha$ . Experiments /19/

4.4 Design of the trough

A more detailed discussion of the flow inside the trough will be given in this chapter. Special flow phenomena will be revealed and their effects on the aerodynamic loads will be pointed out. The simplified shape as defined in the previous chapter is used as well as the formulation of the boundary conditions and the computational grid, except for some grid refinement within the trough. There, the usual grid of  $51 \times 83 \times 71$  cells is replaced in a first step by  $51 \times 83 \times 101$  cells and in a second step by  $51 \times 124 \times 101$ , where all the 30 additional cells in spanwise direction and the 41 cells in streamwise direction are distributed in the trough area. In Fig. 35 a-c, where the Mach number contours in the plane of symmetry are plotted, the overall flow fields of the configuration with and without trough, and for the spanwise refined grid in the trough regime will be compared. As expected, the location and the characteristics of the bow shock emanating from the nose of the configuration are not affected by the presence of the trough (Fig. 35a, b). Due to the slender forebody of the fuselage and the small angle of attack ( $\alpha = 3^\circ$ ) the curvature of the bow shock in the vicinity of the nose region is extremely high and therefore, the shock wave further downstream is relatively weak, whereby the flow deflection is small. A further comparison of the Mach number contours shows that the flowfield in all the three cases ( Fig. 35 a - c) on the upper side of the vehicle upstream of the trough is nearly identical. The Fig. 36 and 37 give a three-dimensional impression of the flow field with and without trough, where the density contours in several cross flow planes are displayed. From the Figs. 35 -37 the extension of the influence caused by variations of the trough contour can be estimated. To focus on the trough regime itself one can realize that the flowfield in close proximity to the surface is affected by the contraction of the contour at the

beginning of the trough. Compared with the fuselage without trough the pressure decreases as long as the depth of the trough grows and increases again when

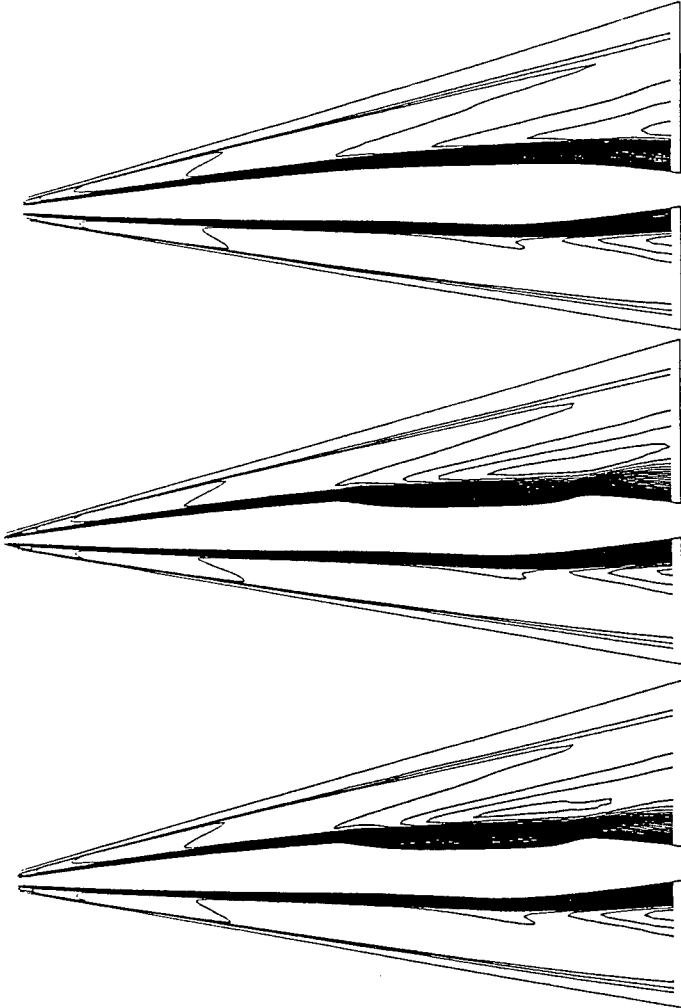


Fig.35 a-c Mach number contours in the plane of symmetry;  
(a; top) shape without trough, coarse grid  
(b; middle) shape with trough, coarse grid  
(c; bottom) shape with trough, fine grid



the aft end of the trough is approached (Fig. 38). Between the rear end of the trough and the outflow boundary the Mach number contours are quite different. Therefore, the flow region influenced by the modification of the trough extends from the beginning of the trough up to the outflow boundary.

Another evaluation tool to analyze flowfields is give by the wall streamlines. In this case these wall streamlines give an even clearer picture of the changes in the flowfield caused by contour variations of the trough regime. In Figs. 39a and b the wall streamlines for the cases without (a) and with trough (b) are contrasted. Again, also by these plots we can see that the flow pattern outside of the trough region, which is extended to the outflow boundary, is not affected

by the contour variations. Those streamlines that encounter the trough in close proximity of the symmetry plane spread over the bottom of the trough turning outward to the edge of the trough. Coming to the rear end of the trough the concave contour of the fuselage causes a positive pressure gradient, which leads to a spanwise deflection of the wall streamlines and even to a small reverse flow region (Fig. 39b). In opposition to this, the wall streamlines of the contour without trough evidence a smooth flow over the whole upper surface of the vehicle (Fig. 39a).

The oilflow picture taken from /24/ (Fig.40) shows qualitatively similar flow directions than the plots of the wall streamlines of the flow field simulations.

A further analysis of the properties of the trough flow

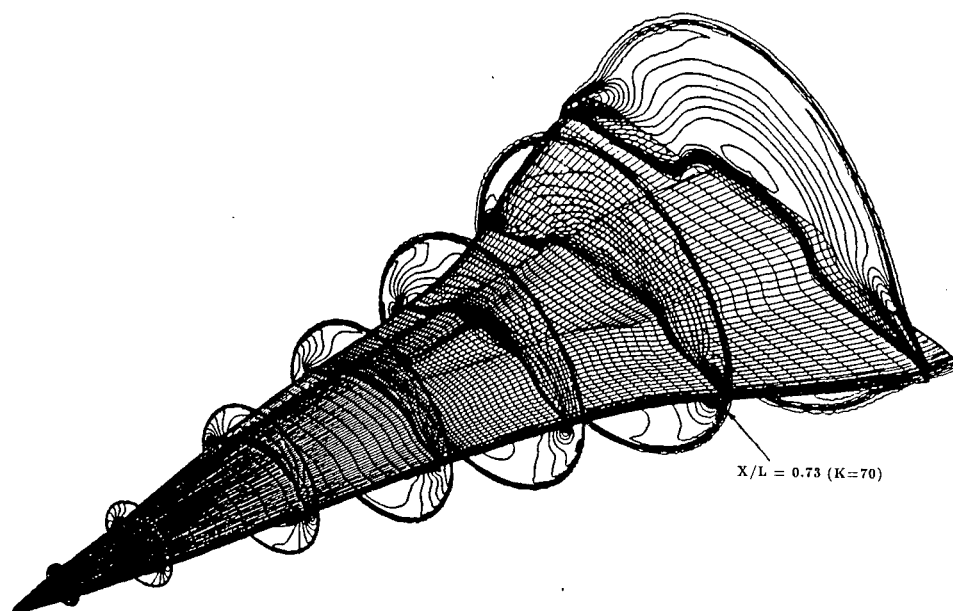


Fig.36 Density contours in cross flow planes plotted at several  $X/L$  locations; shape with trough  $\alpha = 3^\circ$

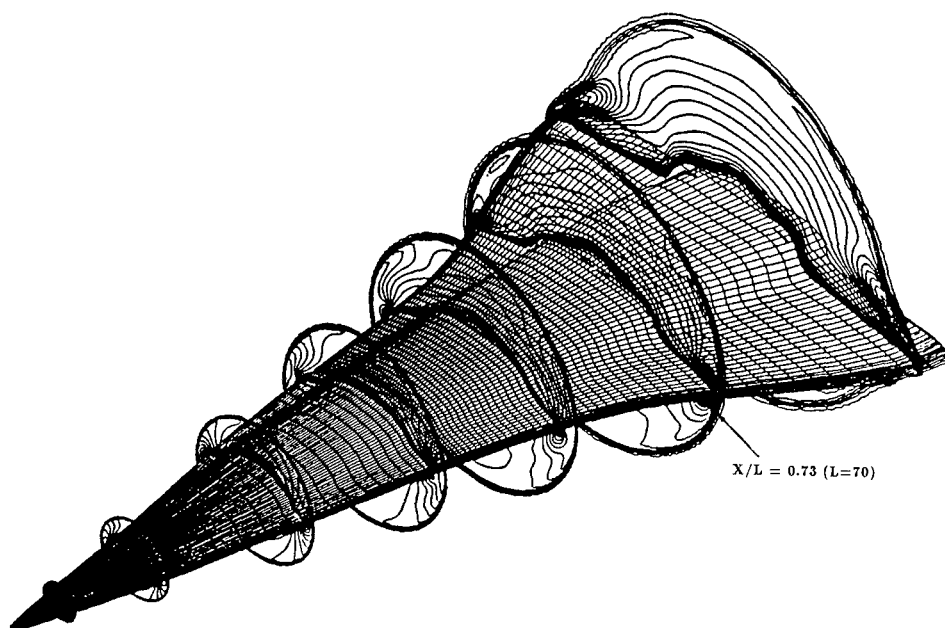


Fig.37 Density contours in cross flow planes plotted at several  $X/L$  locations; shape without trough  $\alpha = 3^\circ$

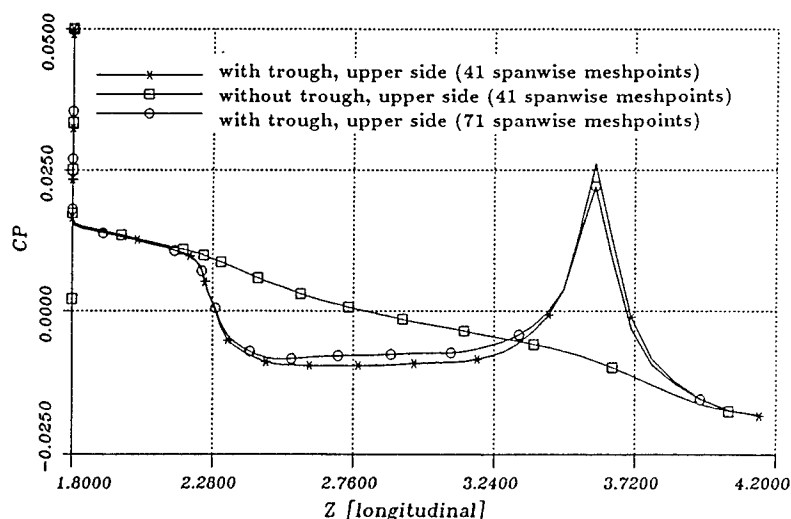


Fig. 38 Pressure coefficients in the plane of symmetry versus streamwise coordinate;  $\alpha = 3^\circ$

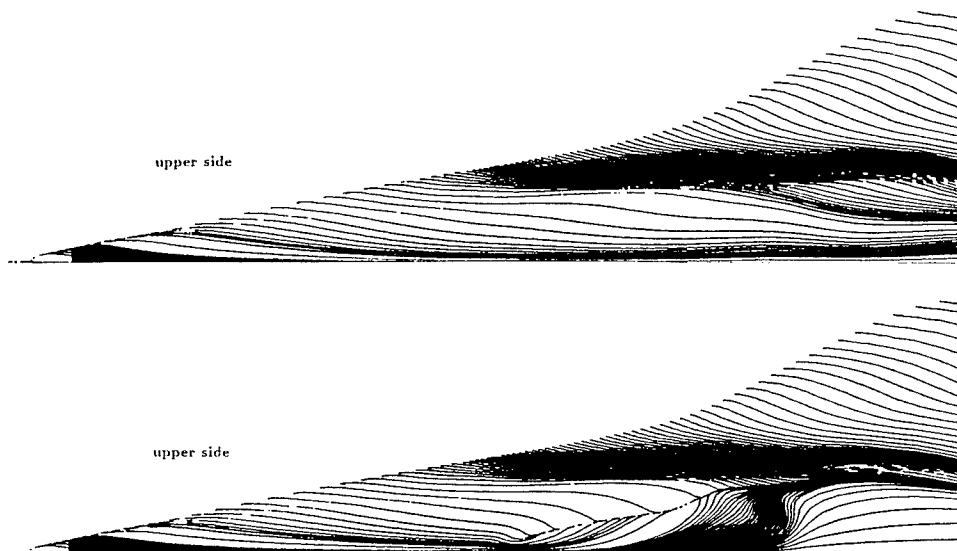


Fig. 39 Wall streamlines on the upper surface of the aircraft;  $\alpha = 3^\circ$ ; (without trough, top; with trough, bottom)

can be attained by evaluating the quasi-streamline pattern in selected cross flow planes. In Fig. 41 those quasi-streamlines are drawn in several cross flow planes, where also the sensitivity of the solution with respect to the grid refinement is addressed. The coarse grid includes 21 cells in spanwise direction within the trough while the fine grid uses 51 cells. At  $X/L = 0.5$  the quasi-streamlines demonstrates the deflection of the flow towards the symmetry plane. In addition, the fine grid solution has a small vortex resolved close to the edge of the trough. Further downstream the cross flow planes show the generation of two streamwise vortices, where their center moves from the edge of the trough ( $X/L = 0.53$ ) to the plane of symmetry ( $X/L = 0.67$ ). The presence of the vortex causes the flow at the bottom of the trough to turn outward as was already exhibited in Fig. 39b. Generally, the center of the vortex predicted by the coarse grid is located closer to the edge of the trough than the one of the fine grid prediction. The vortex itself has in the

coarse grid approach a more oblate shape than in the fine grid approach. For both meshes the last cross section ( $X/L = 0.72$ ) looks quite similar. Although the vorticity produced by the flow separation is still present it does not form in this cross section a visible vortex.

Fig. 42 gives a direct comparison of the wall streamlines at the trough region for the coarse grid, the spanwise refined grid, and the spanwise and streamwise refined grid. The basic flow characteristics, also known from the experiments /24/ are reproduced in all three cases, but with different accentuation. One remarkable difference between the solutions exists and that is the extension of the reverse flow region. The influence of the positive pressure gradient at the rear end of the trough travels upstream leading to a deflection of the wall streamlines and creating a reverse flow region. This pressure impact is much better resolved in the fine grid solutions. At last, the question has to be answered, in which way

the modification of the trough shape influences the global aerodynamic coefficients. These aerodynamic coefficients are established by assuming that the pressure at the base is set to zero and that the reference area and the reference length are taken from the simplified shape. In Table 3 the lift  $c_l$ , drag  $c_d$  and pitching moment  $c_m$  as well as the lift over drag ratio  $L/D$  for the different trough geometries and resolutions are compiled. The lift produced by the configuration with trough is barely increased

compared to the modified version without trough. The drag is a bit stronger increased than the lift leading to a slight decrease of the  $L/D$  value. On the contrary the pitching moment is reduced by the trough shape. Considering the pressure distribution displayed in Fig. 38 this behaviour is apparent. At the beginning of the trough the pressure diminishes and at the rear part it rises. Both effects lead to the reduction of the absolute value of the pitching moment. Also, the small deviation of the lift can be explained with the

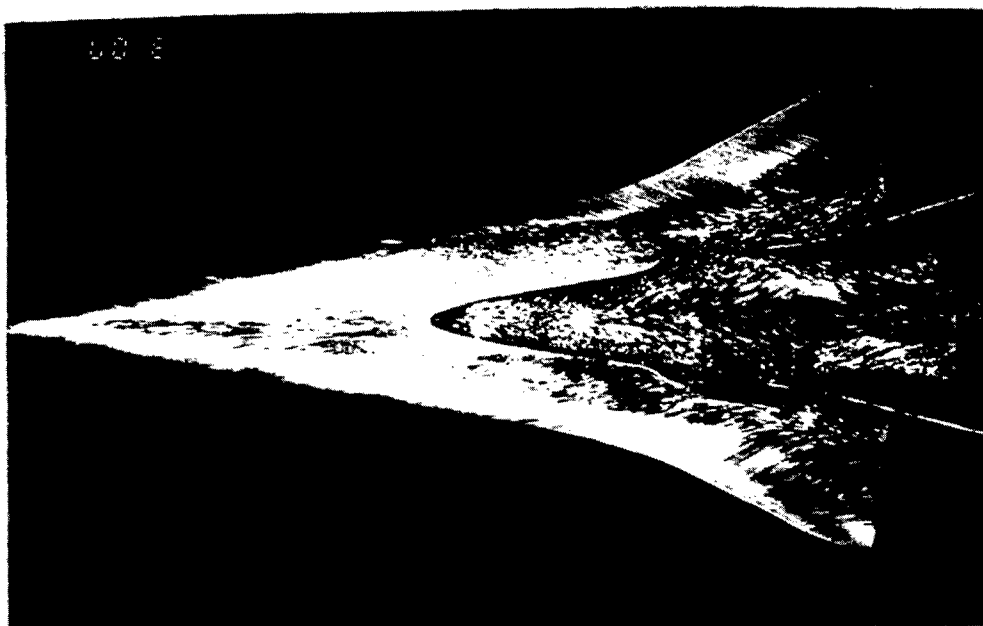


Fig. 40 Oil flow picture at the upper side of the aircraft, taken from /24/ with  $\alpha = 3^\circ$

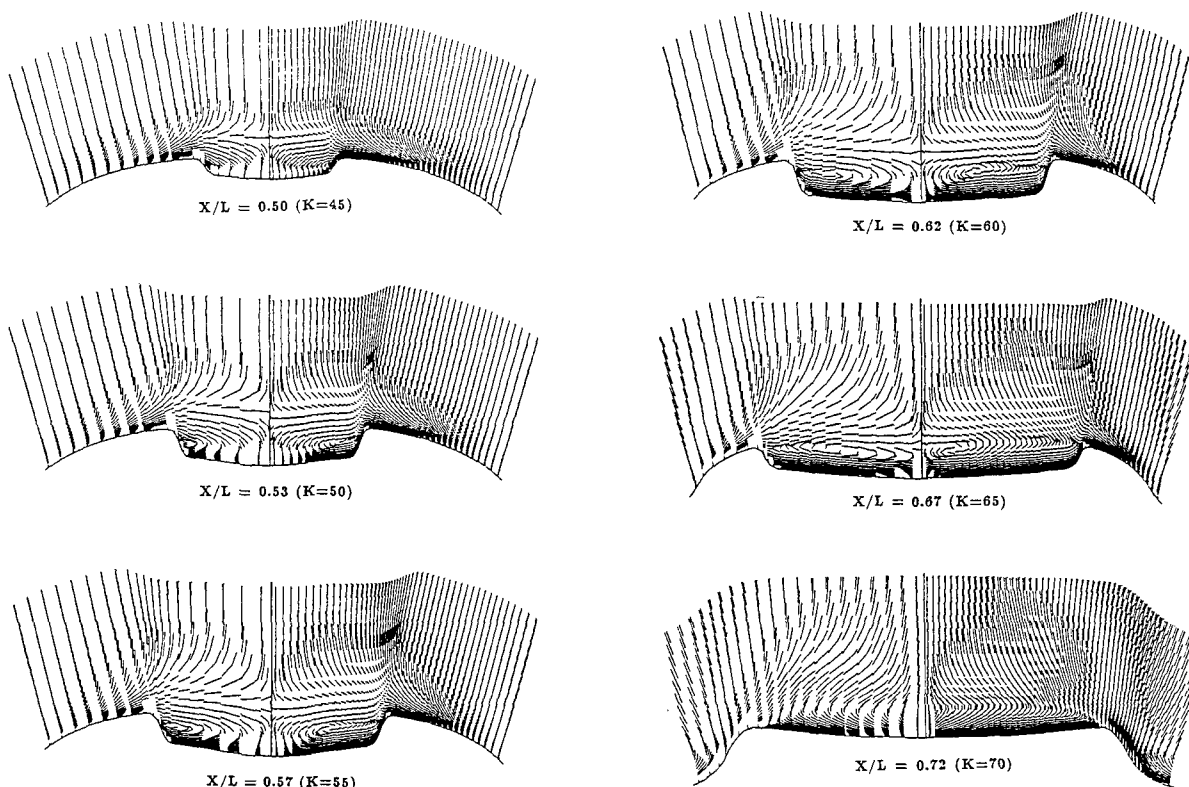


Fig. 41 Quasi-streamlines in cross flow planes at the trough area (left: coarse grid; right: fine grid)

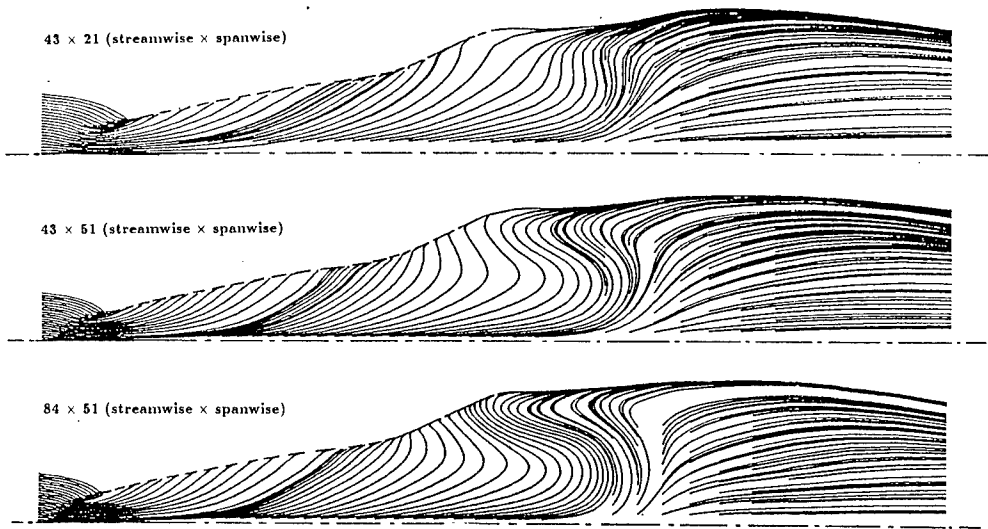


Fig. 42 Wall streamlines in the trough area;  $\alpha = 3^\circ$  ; ( coarse grid, top; spanwise fine grid, middle; spanwise and streamwise fine grid, bottom )

Configuration	number of cells	$C_l$	$C_d$	$C_m$	L/D
no trough	51 x 83 x 71	0.01455	0.00944	-0.00135	1.5413
trough	51 x 83 x 71	0.01484	0.00991	-0.00119	1.4975
trough	51 x 83 x 101	0.01463	0.00966	-0.00116	1.5145

Table 3 Aerodynamic coefficients versus trough modifications and grid refinement

pressure distribution along the trough surface. The additional lift generated at the front part of the trough is not completely compensated by the pressure increase at the rear end of the trough. The rise of the drag coefficients can be seen as a consequence of all the shear stress effects inside the trough, in particular the generation of the vortices according to the flow separation at the edge of the trough.

4.5 Fin / winglet interaction

An important question for the controllability and maneuverability of a two-stage system is the interaction between the vertical fin of the lower stage and the winglets of the upper stage during ascent ( see Fig. 3 ). To allow parametrical investigations a model problem has been defined, where a simplified fin / winglet configuration is placed on a flat plate (Fig. 43) /25/. The parameters Mach number  $M_\infty$ , relative  $y$ - position between fin and winglet  $\Delta y$  and angle of yaw  $\beta$  are varied. Inviscid flowfields are computed using the finite volume approach of the three-dimensional Euler equations reported in /26/. At the wall boundaries the kinematic boundary condition together with the locally one-dimensional characteristic relations are used, at inflow boundary the freestream conditions are prescribed, at outflow boundary the variables are extrapolated, in the

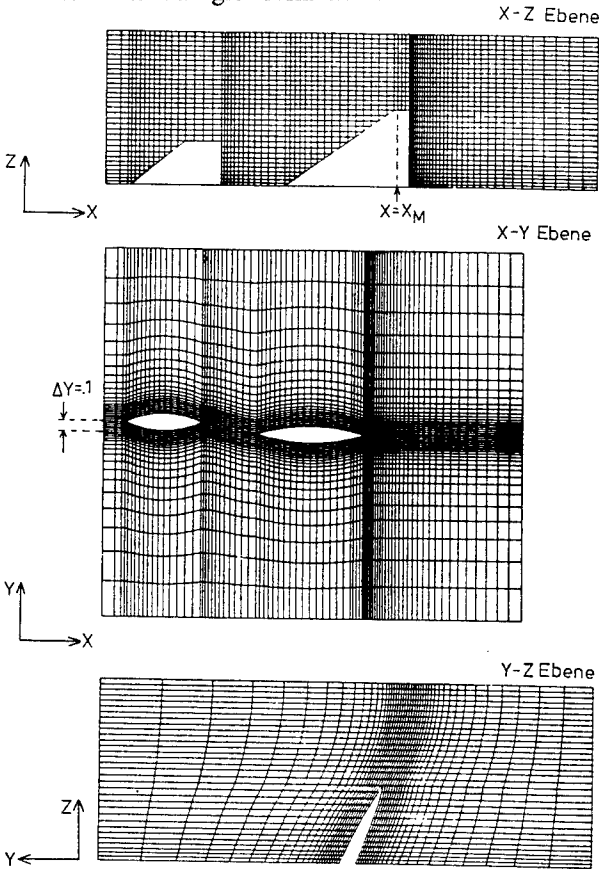


Fig. 43 Grid structure of the simplified winglet/fin configuration



Fig. 44 a,b Mach number contours in  $z = 0$  plane  
 $M_\infty = 2.0$ ;  $\beta = 6^\circ$  case a; top  
 $M_\infty = 4.5$ ;  $\beta = 6^\circ$  case b; bottom

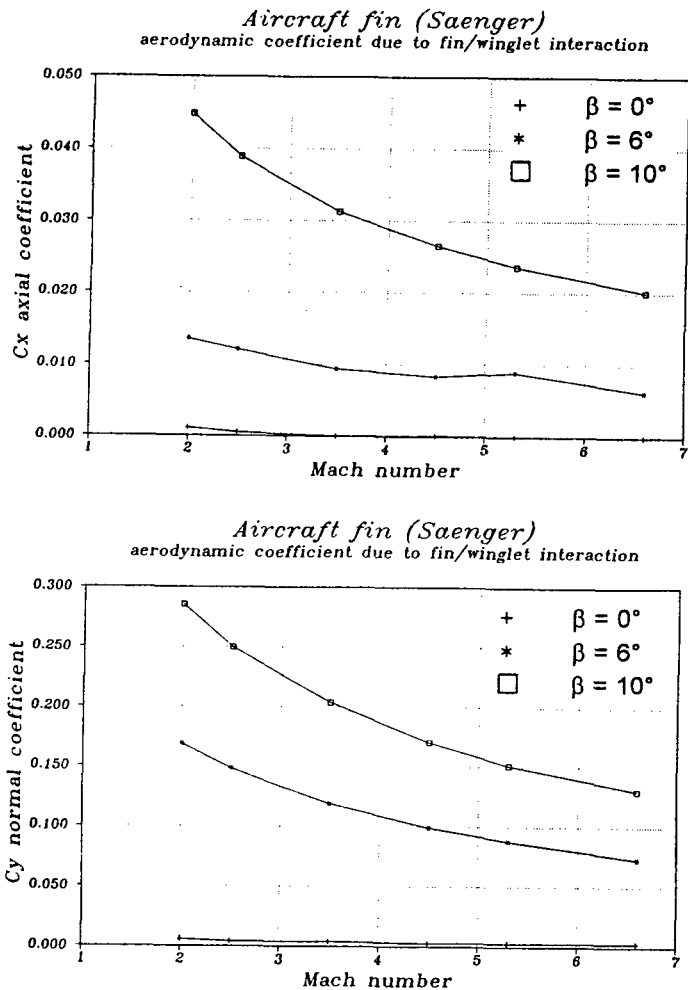


Fig. 45 a,b Aerodynamic coefficients of aircraft fin

symmetry plane symmetry conditions are applied and at the upper plane as well as at the streamwise vertical plane the variables are extrapolated. Solutions are computed for six Mach numbers, three angles of yaw and three relative  $y$  - positions. Generally, increasing the yaw angle and the freestream Machnumber leads to a reinforcement of the tip shock at the windward side and of the recompression shock at the rear end of the leeward side of the winglet, which means that the shock angles decrease. Due to this behaviour, beyond specific angle of yaw and Mach number combinations, the recompression shock of the winglet will impact on the leeward side of the fin of the aircraft. Fig. 44a shows the Mach number contours in the  $(x, y, z = 0)$  - plane for  $\Delta y = 0.1$  with  $M_\infty = 2.0$  and  $\beta = 6^\circ$ . In that case the recompression shock has no influence on the surface of the fin. But in the case of  $M_\infty = 4.5$  and  $\beta = 6^\circ$  the recompression shock impinges upon the leeward side of the fin (Fig. 44b). Nevertheless, these flowfield perturbations have only little influence on the aerodynamic coefficients as can be seen in the Figs. 45a and 45b, where the axial and the normal aerodynamic coefficients are drawn. Neither the smooth contour of the axial coefficient function nor the one of the normal coefficient function are disturbed perceptibly.

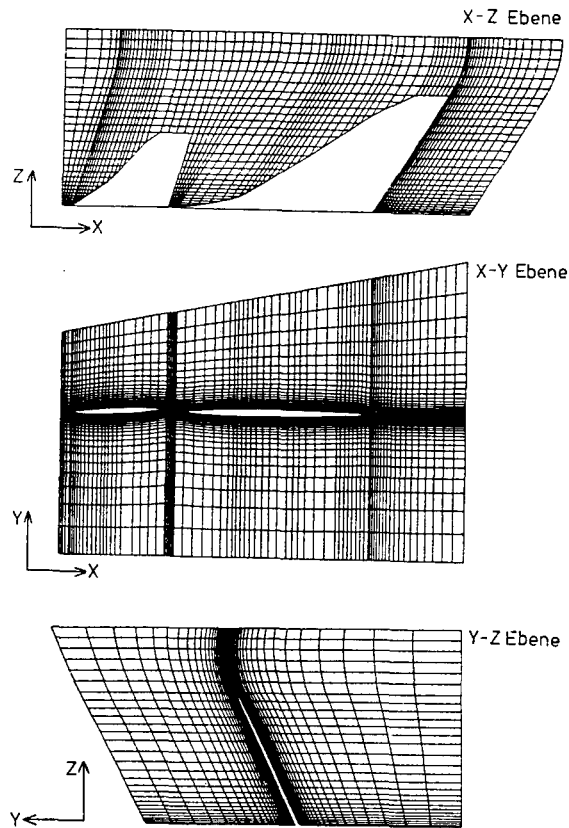


Fig. 46 Grid structure for the real winglet/fin configuration

A more realistic situation was generated by putting the fin / winglet configuration on the leeward side of a delta wing. Now the design of the fin / winglet configuration was taken from the real Sanger design as is shown in Fig. 46 together with the computational grid. A sketch of the delta wing, which has the same aspect ratio than the Sanger configuration is shown in Fig. 47. There, the block, where the fin /winglet configuration is positioned, is marked by a dashed line. The calculation of the flowfield was performed in two steps. First, the flowfield around the delta-wing was computed using the marching procedures of /27,28/. In a second step, the solution in a block containing the fin/winglet configuration is computed by using the flow variables of the first computation at the block boundaries, in particular in the crossflow plane nearby the onset of the winglet contour (inflow conditions) and at upper and vertical streamwise planes, which are defined such that no influence from the fin/winglet configuration is disturbing this boundaries.

Flow field computations were performed for four different points of the ascent trajectory /25/ (see Fig. 2) , which are

- 1.)  $M_\infty = 3.5 \quad \alpha_\infty = 4.5^\circ$
- 2.)  $M_\infty = 4.5 \quad \alpha_\infty = 6.0^\circ$
- 3.)  $M_\infty = 5.3 \quad \alpha_\infty = 5.1^\circ$
- 4.)  $M_\infty = 6.6 \quad \alpha_\infty = 7.2^\circ$  .

A result for the 3.) trajectory point is shown in Fig. 48. The figure on top evidence the Mach number contours in the crossflow plane, from which the inflow conditions for the block containing the fin/winglet configuration are taken. The figure on bottom exhibits the development of the front and the tail shocks of the winglet. Since no tail shock of the winglet impinges the surface of the fin, the influence of the winglet flow on the fin characteristic remains small. In Tab. 4 the aerodynamic coefficients of the winglet and the fin are compiled. These data agree well with the ones of the simplified configuration with  $\Delta y = 0$  and  $\beta = 0^\circ$  (Fig. 45).

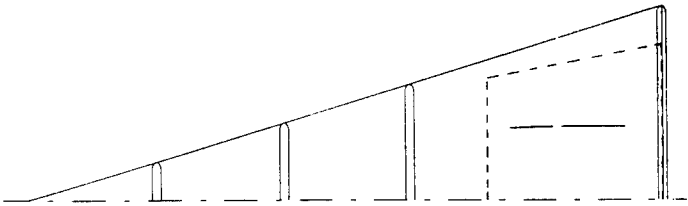


Fig. 47 Sketch of the halfspace of the delta wing

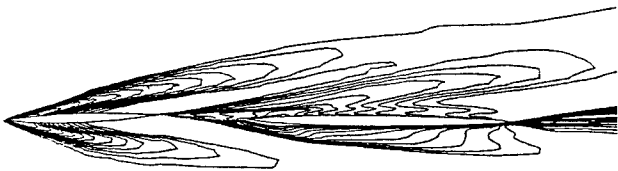
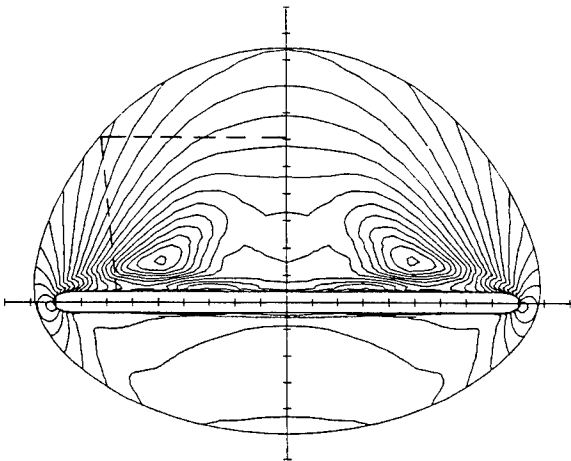


Fig. 48 Mach number contours in a cross flow plane (top) of the delta wing and in a x,y-plane of the winglet/fin configuration(bottom)

Machnumber	angle of attack	C <sub>x</sub>	C <sub>y</sub>	C <sub>z</sub>	shape
3.5	4.5°	0.001502 0.000076	-0.014420 -0.001554	-0.000187 0.004032	winglet fin
4.5	6.0°	0.001275 0.000124	-0.014580 -0.003746	-0.003969 0.000245	winglet fin
5.3	5.1°	0.000873 0.000121	-0.013730 -0.004755	-0.004313 -0.000799	winglet fin
6.6	7.2°	0.000936 0.000087	-0.006816 -0.003599	-0.002402 -0.001156	winglet fin

Table 4 Aerodynamic coefficients of the winglet and the fin mounted on the leeward side of a delta wing

## 5. CONCLUSIONS

Several flight situations during the mission of a Two-Stage-To-Orbit System are investigated. During ascent the hypersonic aircraft transports in a pickaback configuration the space vehicle up to an altitude of about 35 km. This flight phase has been considered, where special attention has been drawn on the wall radiation effects lowering the thermal loads and the interaction of the winglet / fin configuration, which affects the controllability and maneuverability of the flight system. Hereafter the space vehicle is released from the hypersonic aircraft it continues the ascent to the orbit propelled by a rocket system. The separation process has been analyzed in very detail including possible real gas effects and turbulent aspects of the windtunnel tests. After separation the hypersonic aircraft has to fly back to the landing site. The aerodynamics during this flight phase is effected by the flow behaviour within the trough where the space vehicle was located during ascent. The influence of the trough flow on the aerodynamic coefficient was evidenced. All these above mentioned flow situations and flow phenomena were investigated by numerical simulation methods and were compared with experimental results when available.

Generally, the numerical simulation methods, here applied, have the capability to predict such complicated flow fields with a satisfactory to good reliability as was demonstrated by the comparison with the experimental data.

Of course, nevertheless there is still a necessity for further development work of numerical methods, since the convergence behaviour, the accuracy and some aerodynamic (transition and turbulence modelling) and thermodynamic (real gas effects, transport coefficients) properties have to be improved.

## REFERENCES

- /1/ Decker, J.P. and Gera, J.: *An Exploratory Study of Parallel-Stage Separation of Reusable Launch Vehicles*, NASA TN D-4765, 1968
- /2/ Naftel, J.C., Wilhite, A.W. and Cruz, C.I.: *Analysis of Separation of a Two-Stage Winged Launch Vehicle*, AIAA Paper 86-0195, 1986
- /3/ Weiland, C.: *A Split-Matrix Runge Kutta Type Space Marching Method*, J. of Comp. Phys., Vol.102, 1992, pp. 319-335
- /4/ Pfitzner, M. and Weiland, C.: *3-D Euler Solutions for Hypersonic Freestream Mach numbers*, AGARD - CP - 428, Paper No. 2 2 Bristol, 1987
- /5/ Menne, S. and Weiland, C.: *Calculation of Three-Dimensional Viscous and Inviscid Hypersonic Flows Using Split-Matrix Marching Methods*, AIAA Paper 90-3070, 1990
- /6/ Menne, S.: *Efficient Solution of the Three-Dimensional Viscous Hypersonic Flows*, Proc. of First European Symp. on Aerodynamics for Space Vehicles, ESA SP-318, 1991, pp. 267-272
- /7/ Schröder, W. and Hartmann G.: *Implicit Solution of Three-Dimensional Viscous Hypersonic Flows*, Computer and Fluids Vol.21, 1992 pp. 109-132.
- /8/ Schröder W. and Hartmann G.: *Detailed Numerical Analysis of Hypersonic Flows over a Two-Stage Spacecraft*, Comp. Fluid Dynamics J., Vol. 1, 1993, pp.375-404.
- /9/ Schröder W. and Hartmann G.: *Robust Computation of 3D Viscous Hypersonic Flow Problems*, Notes on Numerical Fluid Mechanics, Vol. 35, 1992, pp.128-137
- /10/ Schröder W. and Behr R.: *3D Hypersonic Flow over a Two-Stage Spacecraft*, SPACE COURSE Paper 14, Munich, Oct. 1993
- /11/ Schröder W. and Mergler F.: *Investigation of the Flowfield over Parallel-Arranged Launch Vehicles*, AIAA Paper 93-3060, 1993
- /12/ Schlichting H.: *Grenzschicht - Theorie*, Verlag G. Braun, Karlsruhe, 1982
- /13/ Fischer, J.: *Entwicklung verbesserter Approximationen der Zustandsfunktionen für atmosphärische Luft im thermochemischen Gleichgewicht*, Diploma thesis, TU München, 1989
- /14/ Schröder W., Behr R. Menne S.: *Analysis of Hypersonic Flows Around Space Transportation Systems via CFD Methods*, AIAA Paper No 93-5067, Munich, 1993
- /15/ Yee H.C.: *Upwind and Symmetric Shock Capturing Schemes*, NASA TM 89464, 1987
- /16/ Davis S.F.: *TVD Finite Difference Schemes and Artificial Viscosity*, ICASE Report No. 84-20, NASA Langley Report, 1984
- /17/ Roe P.L.: *Approximate Riemann Solvers, Parameter Vectors and Difference Schemes*, J. of Comp. Phys. Vol. 43, 1981, pp.357-372
- /18/ Schröder W., Behr R., Mergler F.: *Computational Investigation of 3D Hypersonic Flows Over a Two-Stage-To-Orbit Transportation System*, MBB Technical Note-RTT32-92-0099, Dez 1992
- /19/ Esch H.: *Kraftmessungen zur Stufentrennung am MBB-Sängerkonzept bei M = 6 im Hyperschallkanal H2K*, DLR Report IB-39113-90C18, 1990
- /20/ Schröder W. and Hartmann G.: *Analysis of Inviscid and Viscous Hypersonic Flows past a Two-Stage Spacecraft*, J. of Spacecraft and Rockets, Vol. 30, 1993, pp. 8-13
- /21/ Schröder W. and Behr R.: *Numerical Analysis of Hypersonic Flows Over a Two-Stage-To-Orbit Transport System*, MBB Technical Note - RTT32-92-0056, July 1992
- /22/ Whitfield D. L. and Janus J. M.: *Three-Dimensional Unsteady Euler Equations Solution Using Flux Vector Splitting*, AIAA Paper 84-1552, 1984
- /23/ Wilcox D. C.: *Progress in Hypersonic Turbulence Modelling*, AIAA Paper 88-2829, 1988
- /24/ Krogmann P. and Schöler H.: *Windkanalversuche zur Sichtbarmachung des Strömungsfeldes und der Wärmeflussverteilung an der Sänger Konfiguration bei Mach 6.8*, DLR Report IB-222-88C18, 1988
- /25/ Schröder W.: *Hyperschall- Technologie Programm: "Aerothermodynamik"*, MBB Technical Note- KT22-28/ 90, 1990
- /26/ Pfitzner M., Schröder W., Menne S., Weiland C.: *Three-Dimensional Simulations of Hypersonic Flows*, Proceedings: Int. Conf. on Hypersonic Aerodynamics, Manchester, U.K., Sept. 1989
- /27/ Weiland C.: *A split Matrix Method for the Integration of the Quasi-Conservative Euler Equations*, Notes on Numerical Fluid Mechanics, Vol.13, Vieweg, 1986
- /28/ Weiland C.: *A Split-Matrix Runge-Kutta Type Space Marching Method*, J. of Comp. Phys., Vol.102, 1992, pp. 319-335



# The Technology Development and Verification Concept of the German Hypersonics Technology Programme

E.H. Hirschel  
Daimler-Benz Aerospace AG  
Militärflugzeuge  
Postfach 80 11 60  
81633 München  
Germany

## SUMMARY

In the German Hypersonics Technology Programme a Technology Development and Verification study was performed in order to structure the at that time planned European Technology Maturation and Verification Phase. Elements of this study are discussed in this contribution. After an introduction to the topic a classification of hypersonic vehicles is given and the general design process is sketched. The structure of the German Technology and Verification Study is shown, the reference concept and the major flight parameters are presented. It follows an assessment of aerothermodynamics simulation means, a consideration of some selected results of sensitivity studies and an explanation of the Transfer Model approach, which was developed in the study. Some remarks on flight testing with experimental vehicles lead over to a summary of the results of the study.

## 1. INTRODUCTION

Advanced space transportation systems, especially winged airbreathing vehicles pose very large technological challenges. The demand to reduce substantially transportation costs on the one hand and the attempt to achieve large technology steps on the other hand makes large and well planned and directed efforts necessary. Hypersonic aerodynamics, also called aerothermodynamics, is a key technology for the design of such vehicles. Compared to ordinary aircraft a very strong coupling of aerothermodynamics, propulsion, structures and materials, and flight dynamics exists with winged airbreathing hypersonic vehicles. This complicates the design and development of such vehicles to a very large degree, especially in view of the fact that almost no experience from earlier projects is available.

In the aerothermodynamics area, but also in the propulsion, and in the structures and materials areas major deficiencies and shortcomings exist in the two main classes of simulation means

- ground-facilities simulation
- computational simulation.

This is a large problem in the vehicle design and development processes, because the simulation means are the prerequisite for effective design work. Even more important is that this also holds for the verification processes, which are indispensable with high-risks and high-costs products like aircraft and especially spacecraft.

Hence new ways must be found to overcome this problem. A possible way out is the Transfer Model concept, which combines and structures the triad ground facility simulation, computational simulation and in-flight simulation.

In the following the role of aerothermodynamics is discussed in the frame of the vehicle design process, major problem areas

are identified, and the Technology Development and Verification Concept of the German Hypersonics Technology Programme is sketched.

## 2. CLASSIFICATION OF HYPERSONIC VEHICLES

When discussing aerothermodynamics it is necessary to specify the class of hypersonic vehicle, which is in the background of the discussion. The term "hypersonic vehicle" is here used in the widest sense, not only for hypersonic airbreathing vehicles, as it recently became customary in some places. The reason to distinguish classes of vehicles is, that very different key technology demands exist for the different classes, although, of course, also a large number of common features is present.

In general it is sufficient to distinguish the following major classes of hypersonic vehicles, which are shown in Fig.1 (Ref.1):

- o winged reentry vehicles (RV), like the USA Space Shuttle, BURAN, HERMES,
- o cruise and acceleration vehicles with airbreathing propulsion (CAV), like the SÄNGER lower stage, HYTEX, STAR-H, RADIANCE,
- o ascent and reentry vehicles with airbreathing and/or rocket propulsion (ARV), like the X30, ORIFLAMME and HOTOL as SSTO-systems, and the rocket propelled upper stages of the TSTO-systems SÄNGER, STAR-H, RADIANCE,
- o aero-assisted orbital transfer vehicles(AOTV).

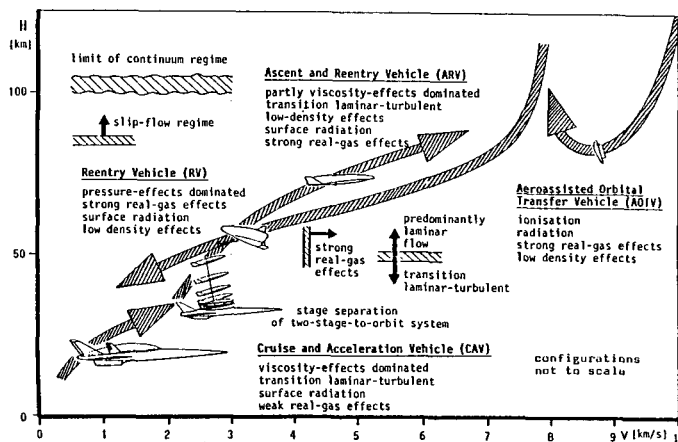


Fig. 1 Four major classes of hypersonic vehicles and major aerothermodynamic features, Ref. 1

Each of these four classes has special aerothermodynamic

features, which must be regarded in design work, and which lead to different research and development needs, Table 1 (Ref.1). It is evident, even without a quantification of features and effects in Table 1, with CAVs

Table 1 Comparative consideration of the aerothermodynamic features of the major classes of hypersonic vehicles, Ref. 1

	RV	CAV	ARV ascent/reentry	AOTV
Mach number range	28 - 0	0 - 7 (12)	0 (7) - 28	20 - 35
configuration	blunt	slender	opposite demands at ascent and reentry	blunt
flight time	short	long	short	short
angle of attack	large	small	small/large	head on
drag	large	small	small/large	large
lift/drag	small	large	opposite situations	small
thermal problem	loads	household	household/loads	loads
flow field	pressure-field dominated	viscosity-effects dominated	viscosity-effects dominated / pressure-field dominated	pressure-field dominated
rarefaction effects	initially strong	weak	weak / initially strong	strong
thermodynamic effects	strong	weak, except for nozzle/base	medium/strong	strong
critical components	control surfaces	inlet, nozzle/base, control surfaces	inlet, nozzle/base, control surfaces	control devices
special problems	large Mach number span	propulsion integration	propulsion integration, opposite demands	plasma effects

and ARVs viscosity effects, notably transition laminar-turbulent and turbulence play a major role, while thermochemical effects are very important with RVs, ARVs and AOTVs, and with the latter especially plasma effects (ionization, radiation emission and absorption). It should be mentioned that future RVs will have demand of larger down and cross range capabilities. Then L/D "small" actually should read "small to medium". Heat loads always must be considered together with the materials and structures concept of the respective vehicle, and its cooling concept. The thermal household of an CAV or ARV must take into account all heat loads (sources), cooling needs and cooling potentials of airframe, propulsion system, sub-systems and cryogenic fuel system.

Table 1 does not include explicitly the new concepts under discussion, like rocket-propelled aeroassisted and non-aeroassisted SSTD systems. The main purpose of this discussion is to sharpen the perception, that a TSTD airbreathing, aeroassisted system, like the reference concept SÄNGER, Ref.2, (actually the lower stage of that system was the reference concept) of the German Hypersonics Technology Programme definitely poses a design problem, that is different from that of a pure reentry vehicle, which is more or less "only" a deceleration system.

3. AEROTHERMODYNAMICS IN THE DESIGN PROCESS OF HYPERSONIC VEHICLES

The aerothermodynamics design process is embedded in the vehicle design process. Aerothermodynamics has, in concert with the other disciplines, the following objectives:

- o Definition of the outer "aerodynamic" shape of the vehicle in order to ensure its aerodynamic performance, flyability and controllability. This objective, which is the classical objective of aerodynamics in aircraft design, holds for all

of the four vehicle classes mentioned in Chapter 2. For TSTD systems like SÄNGER the aerodynamic upper stage integration and separation is to be added.

- o Integration, where it applies (CAV, ARV), of the airframe and the propulsion system (forebody shape definition, inlet design, external nozzle (SERN)/afterbody design and overall integration of these components with the airframe).
- o Determination of the mechanical (surface pressure and skin friction) loads and the heat loads for the layout of the structures and materials concept, the sizing of the structure and the external or internal thermal protection system, including possible active cooling systems of the airframe. This also holds for all four classes.
- o Definition of the surface properties (necessary radiation emissivity, permissible surface catalyticity, permissible surface roughness and waviness, etc.). The first two items between the brackets are important with regard to the heat loads (surface radiation cooling, heat loads increments due to catalytic surface recombination) and the second two with regard to heat loads and viscous drag increments, but also, very importantly, with regard to the manufacturing tolerances, which drive manufacturing costs strongly, if they are very small.

These objectives on purpose have been detailed somewhat in order to show the strong couplings of aerothermodynamics with the other major disciplines of hypersonic vehicle design, to which vehicle control should explicitly be added. These couplings are extraordinary large for airbreathing vehicles, which are drag sensitive, and where the effective integration of the (elastic) airframe with the propulsion system is of utmost importance in order to achieve positive "thrust minus drag".

Of course the performance demands on the vehicle must be met on all trajectory segments, including take-off, landing and also on abort trajectories. Structural heat loads pose a special problem, because they are cumulative on the trajectory, with positive and negative increments. Another problem typical for hypersonic flight are strong interaction phenomena, including gap and sneak flow phenomena, which can lead to very large heat loads and mechanical (pressure) loads increments. Their locations and their strengths vary with vehicle attitude, speed and altitude, which is difficult to predict with the presently available simulation means. In the structure layout this can lead to special risks or to weight increments out of safety considerations.

The objectives of aerothermodynamics are discussed here without special regard to the particular design problems, which are connected to the vehicle classes discussed in Chapter 2. The demands on the design strategies, the tools and the interdisciplinary couplings are very different, although commonalities exist. The similarities of, for instance, the vehicle planforms, Fig.2 (Ref.3), would be misleading in this respect. None of the vehicle classes can be considered as to be established like in aircraft design the classes "wide body transport aircraft", or "slender fighter aircraft". The design experience, if available at all, is very limited in each of the classes.

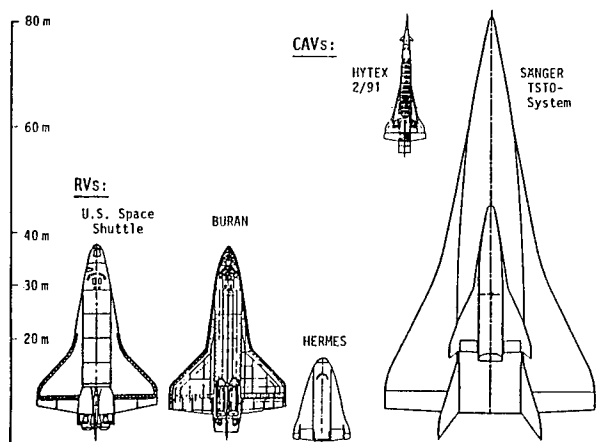


Fig. 2 Comparison of size and shape(planform) of the RVs USA Space Shuttle, BURAN, HERMES and the CAVs SÄNGER and HYTEX of the German Hypersonics Technology Programme, Ref.1

Table 2, Ref. 3, finally shows in a summarizing manner the major roles/activities of aerothermodynamics in the different design and development processes of flight vehicle design.

Table 2 Schematic of aerodynamic design processes and the use of simulation tools ( → : current change in tool use), Ref. 3.

phase	major tools	results	objective in vehicle design
• pre-design	hand book methods approximate methods	approximate aerodynamic performance data, loads	configuration definition, trades, preliminary vehicle feasibility: performance, sensitivities, flight dynamics, propulsion, materials and structure
• design ↓ cycle ↑	approximate methods → numerical methods	aerodynamic data base	vehicle feasibility, configuration finalization, input for other disciplines: propulsion, flight dynamics, performance
• verification	wind tunnel		
• development	wind tunnel → numerical methods	mechanical and thermal loads, "elastified" aerodynamic data base	input for structural design of vehicle and components, aero-elastic increments

4. THE TECHNOLOGY DEVELOPMENT AND VERIFICATION CONCEPT OF THE GERMAN HYPERSONICS TECHNOLOGY PROGRAMME

The perceived large technological risks of the reference concept SÄNGER, the apparent shortcomings of simulation means, and the large costs of an as necessary considered experimental vehicle, Ref. 4, led early in the Technology Programme to plans to develop a Technology Development and Verification Concept, Ref. 5.

The objectives of this concept for Phase II (technology maturation and verification) of the Technology Programme, which at that time was seen as a continuation of Phase I in a European frame, are:

- structuring of the technology development (maturation) and verification process,
- identification of interdependencies between the four technology areas propulsion, aerothermodynamics, structures and materials, guidance and control, subsystems,
- identification of simulation needs (ground-facility simulation, computational simulation) and of shortcomings and deficiencies of simulation means,

- identification of necessary Transfer Models,
- definition of technology development and verification strategies for the technology areas and of the overall strategy,
- identification of long-term basic research and development work,
- development of a simulation-hardware master plan (ground-simulation facilities, super computers, experimental vehicles), with time schedules and costs estimations.

The approach to develop this concept is sketched in Fig.3, Ref.6. With the results and knowledge obtained in the Technology Programme, including the reference concept studies, the requirements on the key

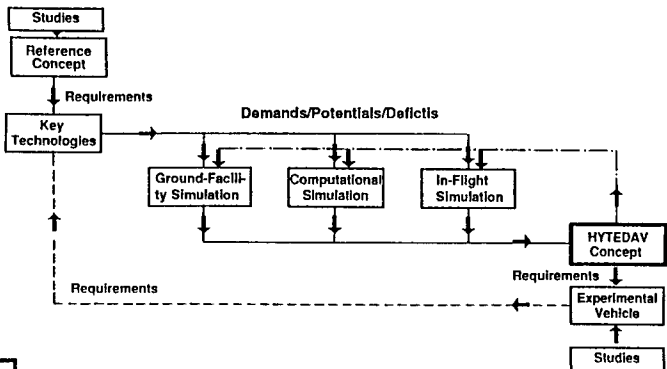


Fig. 3 Schematic of the approach in the Hypersonics Technology and Verification Concept study, Ref. 6

technologies are assessed. Then the demands on the simulation means are compared with their potentials. Deficits are identified, also necessary Transfer Models. Technology development and verification strategies are formulated. These in turn have demands on the simulation means, for instance, new ground-simulation facilities and techniques for basic R&D work can become necessary. They may also have demands for one or more experimental vehicles, which must allow to obtain data (e.g. flow-physics data for Transfer Modells, which cannot be obtained in wind tunnels), to test component technologies, and to verify the design strategy, Transfer Models, etc. (see Chapter 10). The experimental vehicles themselves must be designed and developed, and may have their own requirements on key technologies. Hence the doubly recursive structure in Fig. 3.

The major topics treated in the study were, Ref. 6,

- o the reference concept (flight parameters, configuration/component structuring, beyond the reference concept, potential experimental vehicles),
- o the design problem (design strategy, airframe/propulsion integration with regard to the flow path from tip to tail, airframe/propulsion integration with regard to flyability and controllability, heat-loaded structure, component technologies, simulation means, sensitivities and the implications, the Transfer Model concept),

for each of the four technology areas propulsion, aerothermodynamics, structures and materials, guidance and control, subsystems

- o technology demands of the reference concept and of po-

tential experimental vehicles,

- o potentials and deficits of simulation means,
- o technology development and verification strategies

and finally

- o certification issues and the general technology development and verification concept (problem summary, the general concept, implementation issues, cost estimation, risks consideration, alternatives).

5. THE REFERENCE CONCEPT OF THE GERMAN HYPERSONICS TECHNOLOGIES PROGRAMME

The reference concept of the German Hypersonics Technology Programme was the lower stage of the space-transportation system SÄNGER. It was documented in several publications, see e.g. Refs. 2 and 7. In the following a short description of it is given.

The space-transportation system SÄNGER is a fully reusable two-stage-to-orbit system with an airbreathing first stage and a rocket-propelled upper stage. The stage- separation process is initiated at  $M \approx 6.8$  at an altitude of about 32 km. The only fuel is liquid hydrogen, burned by air in the lower stage, and by onboard liquid oxygen in the upper stage. Both stages take off - the upper stage on top of the lower stage - and land horizontally like airplanes, making use of aerodynamic lift. Fig. 4 shows a three-sides view of the space-transportation system.

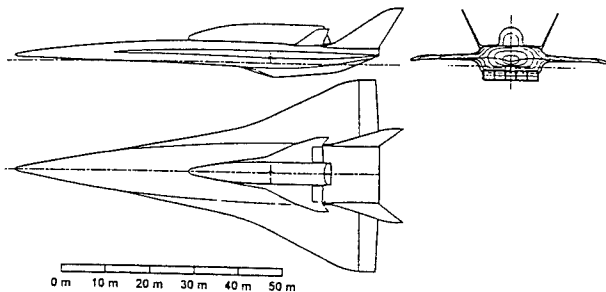


Fig . 4 The SÄNGER configuration, Ref. 7

The payload is 7 Mg for the unmanned version, and 3.3 Mg plus up to 5 astronauts for the manned version, which is taken into the Space Station orbit. The launch and landing site requirements - launch from and landing in Europe - are met by a cruise capability of 3100 km for the lower stage, and a cross-range capability of 2500 km for the upper stage. The major data of the SÄNGER system are given in Table 3.

Table 3 Major data of the SÄNGER system, Ref. 7

	lower stage	upper stage
fuselage length	82,5 m	32,45 m
fuselage height	4,5 m	5,40 m
fuselage width	14,4 m	5,20 m
span width	45,1 m	17,7 m
engines	Turbo/RAM (LH2)	Rocket (LH2/LOX)
number	5	1
thrust	500 kNmax each	1500 kN
payload	115 to	unmanned: 7 to
gross take-off weight	410 to (with upper stage)	115 to

The aerodynamic shape of the lower stage represents a blended body configuration with a double delta wing, Fig. 4. The long and slender forebody is flat on the lower side in order to achieve so much pre-compression, that the capture area of the inlets is reduced to a sufficient degree. The propulsion system, including the inlet and the nozzle, is located at the lower side between 60 and 90 per cent of the fuselage length. The last 10 percent are the outer expansion ramp of the nozzle. Control surfaces at the trailing edge of the second delta of the wing, together with the thrust vector, control the longitudinal movement. The lateral movement is controlled by two fins at the end of the configuration. The upper stage sits in a trough on the upper side between 50 and 90 per cent.

At hypersonic flight, the lower side of the vehicle is a highly integrated lift, propulsion and control system, Ref. 8. The upper side does not contribute much to the lift at hypersonic speed. The lower stage is viscous-effects dominated, in contrast to the upper stage, which is pressure-field dominated. The airbreathing propulsion system consists of five turbo/RAM-jet engines. The RAM duct surrounds the turbo engine and is completely closed during turbo-mode operation, Fig. 5. The transition from turbo to RAM-jet mode occurs between  $M = 3.3$  and  $M = 3.8$ . The RAM-combustion chamber and fuel injection devices

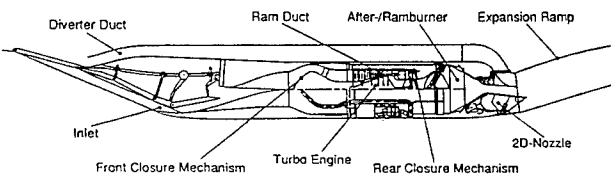


Fig. 5 Lower stage airbreathing propulsion system, Ref. 7

serve also as the afterburner devices during turbo operation. In order to adapt the engine to the actual flight Mach number, the air inlet and the two-dimensional nozzle need to have variable geometry.

For the lower stage airframe two structural concepts are possible in principle:

- a hot thin-sheet load carrying (primary) structure without heat protection system,
- a cold load-carrying (primary) structure with a heat protection system.

Due to the maximum Mach number of  $M \approx 7$  there is no need of active cooling of the structure, or parts of it, which holds for both concepts. Surface-radiation cooling is so effective, that the actual structure, the concept of which is a combination of the two extremes mentioned above, predominantly has a hot primary structure made from advanced titanium alloy, Fig. 6.

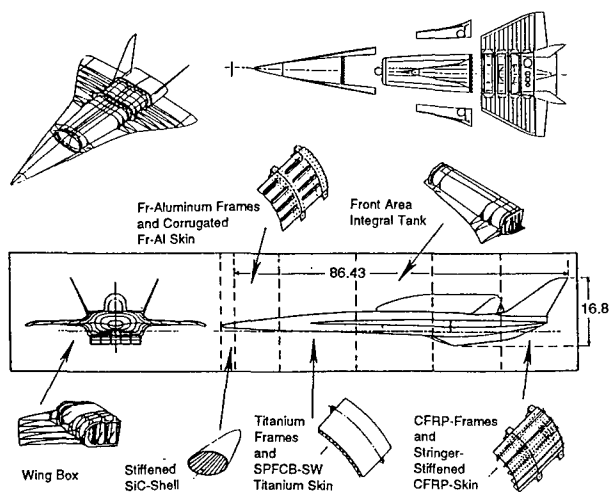


Fig. 6 Lower stage reference structural concept, Ref. 7

There is certainly no doubt, that a Mach 6 to 7 airbreathing hypersonic aircraft can be developed and flown today. However, the technological challenge is enormous, Fig. 7, if a space transportation system of SÄNGER size is to be developed, which is supposed to reduce orbit transportation costs by one order of magnitude compared to the costs of the presentday rocket technology.

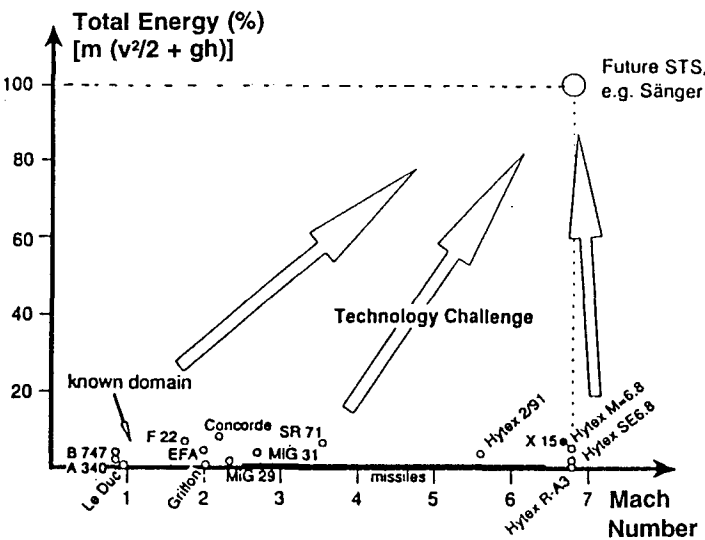


Fig. 7 Comparison of the total energy of airbreathing aircraft and the X15 to that of the reference concept SÄNGER, Ref. 5

6. FLIGHT PARAMETERS OF THE REFERENCE CONCEPT

The technology demands, and hence also the demands on the technology means for the development of any flight vehicle are directly depending on the physical parameters, which are present on the trajectory. In the following some of the flight parameters of the lower stage of the reference concept SÄNGER are given, Figs. 8 to 15, Ref. 6. In Figs. 11 to 15 data are included from the "beyond- the- reference-concept" considerations in Ref. 6 ( $v = 3 \text{ km/s}$  and  $v = 4 \text{ km/s}$ , with the same reference length,  $L = 82.5 \text{ m}$ , where it applies, as that for the reference concept).

Fig. 8 shows the flight Mach number over the flight altitude. The largest Mach number  $M = 6.8$  occurs shortly before the staging manoeuvre. The descent trajectory lies higher than the ascent trajectory. The flight time, Fig. 9, is about 45 min for the ascent, and about 40 min for the descent. The angles of attack and yaw ranges are given in Fig. 10.

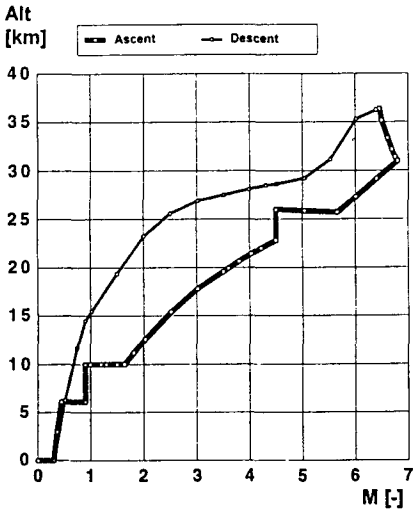


Fig. 8 Mach number  $M$  of SÄNGER lower stage vs. altitude Alt, Ref. 6

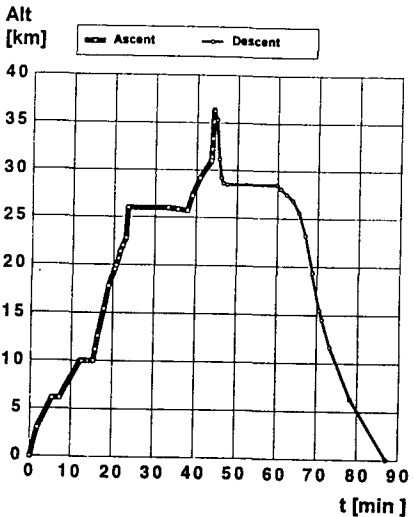


Fig. 9 Time history of lower stage flight, Ref. 6

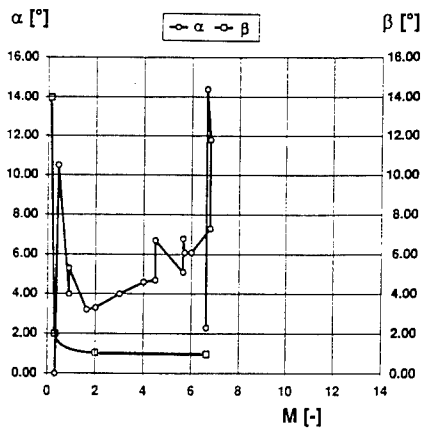


Fig. 10 Angle of attack  $\alpha$ , and limiting yaw angle  $\beta$  for the SÄNGER lower stage as functions of the Mach number  $M$ , Ref. 6

Because the ascent trajectory lies at a lower altitude, where the loads are larger, the flight parameters in the following are given only for this trajectory. The flight velocity follows almost linearly the Mach number, Fig. 11, because the static temperature does not vary very much along the trajectory, Fig. 12. Although the static pressure, and hence the density, soon becomes very low, Fig. 12, the Reynolds number, which is based on the vehicle length,  $L = 82.5$  m, is so large, Fig. 11, that the flow on the configuration becomes turbulent.

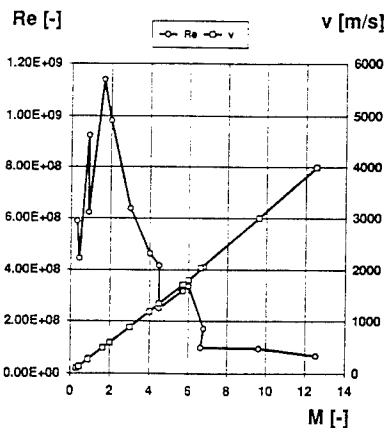


Fig. 11 Reynolds number  $Re$  and velocity  $v$  as functions of the Mach number  $M$ , Ref. 6

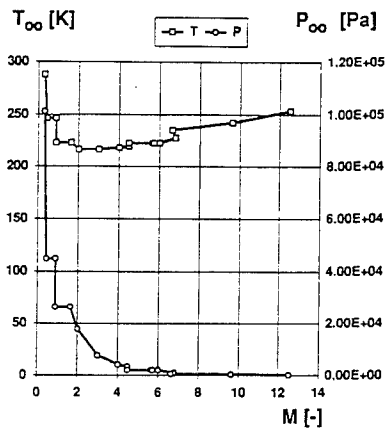


Fig. 12 Static temperature  $T_\infty$  and static pressure  $p_\infty$  as function of the Mach number  $M$ , Ref. 6

The total enthalpy, the total temperature for both perfect and equilibrium real gas (forebody nose tip, Euler calculation) are given in Fig. 13. At  $M = 6.8$  the real gas effects are not yet strong ( $\Delta T_o \approx 200$  K), but appreciable. Beyond the reference concept they become overwhelming, and certainly non-equilibrium effects, Refs. 9, 10, will have to be regarded in the flow past and through (propulsion system) the vehicle. Note, that the total temperature (more exactly the total enthalpy) at a given Mach number and altitude is constant everywhere on the airframe and in the propulsion system, except where energy is added or subtracted. With regard to structural heat loads, however, it must be remembered, that external configuration surfaces are radiation cooled. Therefore the total temperature, or, respectively, the recovery temperature, actually is only an independent variable in the radiation-adiabatic temperature relation, Ref. 11.

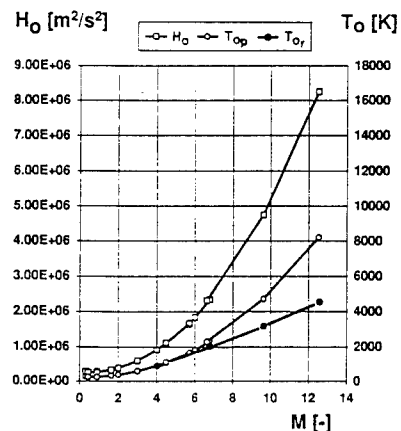


Fig. 13 Total enthalpy  $H_0$ , total temperature perfect gas  $T_{0p}$  and equilibrium real gas  $T_{0r}$  as function of the Mach number  $M$ , Ref. 6

An important parameter is the Knudsen number, Refs. 9,10. For values above approximately 0.01 rarefaction effects must be regarded in the aerothermodynamic design of the vehicle and its components. The Knudsen numbers given in Fig. 14 are based on the free-stream mean-free path and different characteristic lengths. Up to the highest Mach numbers considered the Knudsen number for the whole vehicle is not critical. For the two smallest length scales  $L_{ref} = 1$  cm and 1 mm, which may represent inlet-lip diameters, measurement orifices and the like, however, rarefaction effects must be regarded for Mach numbers larger than  $M = 6$ .

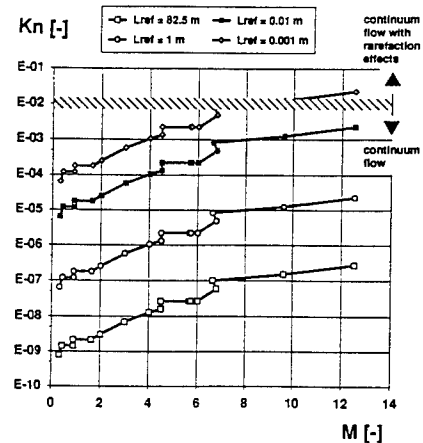


Fig. 14 Knudsen number  $Kn$  for different characteristic lengths  $L_{ref}$  as functions of the Mach number  $M$ , Ref. 6

Similarly, hypersonic viscous interaction effects, Refs. 9,10, which locally can lead to large pressure rises, which will also affect global forces and moments, must be regarded at Mach numbers  $M > 7$ , especially in the region beyond the reference concept, Fig. 15. Note, that the viscous interaction parameter  $v'2$  takes into account the hot vehicle surface via the Chapman-Rubesin factor  $c'$ , Ref. 9. This, of course, is the more critical parameter.

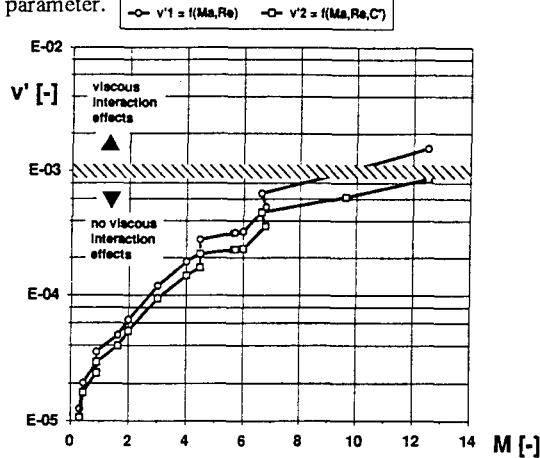


Fig. 15 Viscous interaction parameters  $v'1$  and  $v'2$  as functions of the Mach number  $M$ , Ref. 6

## 7. GENERAL ASSESSMENT OF AEROTHERMODYNAMICS SIMULATION MEANS

Two major classes of simulation means are distinguished in aerothermodynamics:

- computational simulation, which encompasses approximate and numerical methods, notably transfer models,
- ground-facility simulation, which encompasses wind tunnels, shock tubes, etc., with appropriate sub-scale models of vehicle configurations and configuration components like the inlet and the nozzle/afterbody.

In this chapter an overview is given over their abilities to simulate aerothermodynamic phenomena, which appear on the respective vehicle configurations and their components. These abilities are partly very restricted. Considered are phenomena, Table 4, which come on top of the phenomena, which are dealt with in aerodynamic design work for aircraft with a speed up to  $M \approx 3$ .

Table 4 Assessment of simulation means for potentially critical aerothermodynamic phenomena, Ref.1 (RV: reentry vehicle, CAV: cruise and acceleration vehicle, ARV: ascent and reentry vehicle, AOTV: aeroassisted orbital transfer vehicle)

No.	Phenomena	Vehicle class	Simulation means	
			computational	ground facilities
1	transition laminar-turbulent	CAV, ARV (RV)	poor	poor
2	attached turbulent flow	CAV, ARV (RV)	fair	fair (?) --> Re, tripping
3	laminar strong interaction (boundary layer / shock / vortex)	RV, AOTV	good	good
4	turbulent strong interaction (boundary layer / shock / vortex)	CAV, ARV (RV)	poor	fair (?) --> Re, tripping
5	laminar separation	RV, AOTV	good	good
6	turbulent separation	CAV, ARV (RV)	poor	fair (?) --> Re, tripping
7	hypersonic viscous interaction / low-density effects (slip, temperature jump)	RV, ARV, AOTV	good	fair (?)

No.	Phenomena	Vehicle class	Simulation means	
			computational	ground facilities
8	equilibrium real-gas effects	CAV, ARV (RV)	good	poor
9	non-equilibrium real-gas effects	RV, ARV, AOTV (CAV)	good (range?)	poor
10	turbulent heat transfer	CAV, ARV (RV)	poor	fair (?) --> Re, tripping
11	turbulent mass transfer/turbulent mixing	CAV, ARV	poor	fair (?) --> Re, tripping
12	general hot-surface effects	RV, CAV, ARV, AOTV	good	poor
13	surface radiation cooling	RV, CAV, ARV, AOTV	good	presently not
14	catalytic surface recombination	RV, ARV, AOTV (CAV)	poor	poor
15	surface accommodation	RV, ARV, AOTV	good	good
16	plasma effects	AOTV	fair	fair (?)

Table 4 shows the big problems with present-day aerothermodynamic simulation means. Especially viscosity-effects dominated vehicles with turbulent flows (CAV, ARV, partly also RV, if they are to have large down range and cross range capabilities) are most affected. In the design process especially the verification step in ground facilities has the biggest shortcomings.

The reason why viscosity-effects dominated vehicles with turbulent flow are affected, are the ground-facility shortcomings to simulate properly transition laminar-turbulent and turbulent flow, and in computation methods the shortcomings of transition models, of turbulence models for separated and strongly interacting flows, and of uncertain models for turbulent heat and mass transport, especially if thermochemical effects play a role. This affects both viscosity-dominated phenomena (items No. 4 and 6 in Table 4), and heat and mass transfer (items No. 10,11). Of course, depending on the flight domain, the shortcomings can be more or less important, and the predictability might even be fair to good. Surface catalytic recombination (item No. 14) can be described well only in the limiting cases of fully catalytic or non-catalytic surfaces. Finite catalyticity causes major modelling problems. Surface accommodation (item No. 15) refers to slip and temperature jump (item No. 7). The dependency of these phenomena on the respective accommodation coefficients is not very strong, as experience so far indicates.

However, the message of Table 4 demands a very differentiated consideration. A major rule is, that not each of the considered phenomena necessarily needs a simulation of high accuracy in the design process of a hypersonic vehicle (this is a general rule, which holds for every design problem). The accuracy demand is a function of the sensitivity of the vehicle/component performance, property etc. on the respective phenomenon. For the recovery temperature, for instance, it does not matter much, whether the flow is laminar or turbulent. This is in contrast to the radiation-adiabatic temperature, which is very strongly affected by the state of the boundary layer, Ref. 11. Hence, if only the recovery temperature is of interest, and the structure and materials concept chosen permits small uncertainties, the location of transition laminar-turbulent does not play a deciding role. It could be assumed in numerical simulations that the flow is completely turbulent, and, if possible at all for other reasons, in wind-tunnel simulation boundary-layer tripping near the tip of the configuration would suffice.

On the other hand the radiation-adiabatic temperature, for instance at the radiation-cooled lower side of a  $M = 7$  CAV - type configuration, not only affects the structure and materials

concept, but also the viscous drag of a large part of the vehicle, and the onset-flow to the inlet. Even this would not make an accurate determination of the transition location necessary in the begin. Instead first it would be studied parametrically with numerical simulation tools, how the transition location affects the structure and materials concept, drag and the inlet-onset flow. If all these are insensitive to the parametrical changes, and the whole design is not affected, the flow could be considered as completely turbulent as in the recovery-temperature case. Only if one or more of the above would emerge as sensitive to the laminar-turbulent transition location, the designer has a simulation problem. This concerns then not only transition (item No.1), but also items No. 2, 10, 12 and 13 of Table 4 (unfortunately the prediction of the location of transition laminar-turbulent is a major problem with CAV- and ARV-type configurations, very large with a SÄNGER-type vehicle ( $M \approx 7$ ), and extremely large with a X30-type vehicle ( $M \approx 12 - 16$ )).

This short discussion reveals why a technology programme needs a reference concept, which must be studied to a sufficient depth in order to identify sensitivities, technology gaps, etc.. Actually it must go through the pre-design phase (Table 2), in order to insure the vehicle feasibility, although this feasibility is only a preliminary one, because the key technologies are not available by definition. Once the technology base has been improved, the reference concept must be reconsidered. It may happen then, that sensitivities have shifted, and that other problems, phenomena etc. become more important. In the best case, the reference-concept work focusses and shapes the technology programme in an optimum way with regard to funding and time. However, the larger the technology steps, the larger are the risks. Therefore a technology programme must not be defined too narrow, in order to cover key-technology demands, which might be hidden initially, and surface only if the reference concept and/or the technology programme has evolved sufficiently.

Table 4, however, also shows that large concerted efforts of research in flow-physics and in thermochemical modelling are necessary (this also holds for structure physics). Necessary are also new types of ground-simulation facilities, for instance with regard to hot-surface effects (radiation cooling, catalytic surface recombination, strong interaction effects), Ref. 11.

Finally, Table 4 gives the motivation to develop the Transfer-Model approach sketched in Chapter 9. The major reasons for it are several principle shortcomings of ground-facility simulation, see also Refs. 12 and 13, which cannot be overcome to a sufficient degree by improvements. It gives also the motivation for experimental vehicles, which are needed because of the ground-facility simulation shortcomings, to acquire the data base to check the design strategy, the design tools, and to give the final input into flow-physics and thermochemical models for the computational simulation tools and transfer models.

## 8. SENSITIVITIES OF THE REFERENCE CONCEPT

Sensitivity studies reveal critical items, performance and systems risks, technology risks, and in the extreme, non-feasibility of a technical product. The results of a sensitivity study must be considered very cautiously, because of the assumptions made, the general description level of the product, and because they are just a snapshot of the present status of the design.

In the following a few selected results from sensitivity studies of the reference concept SÄNGER (11/91-configuration, Ref. 7) and its propulsion system are discussed. These results must be considered with care, because the underlying assumptions and the investigation logic are not obvious. In the frame of this presentation they are used only to illustrate and quantify to a certain degree the technology demands of the reference system, which must be perceived as "frozen" during the discussion.

In Fig. 16 the sensitivity of the take-off gross-weight of SÄNGER is given as function of the increments of the net thrust, the specific fuel consumption, the total drag, and the structural weight, Refs. 14, 15. Engine weight and size are fixed. The largest sensitivities exist for the thrust, where a decrease of about 3.5 per cent already causes the divergence of the design. The same happens, if the total drag is only about 6 per cent larger than the nominal one. The other sensitivities are not so large.

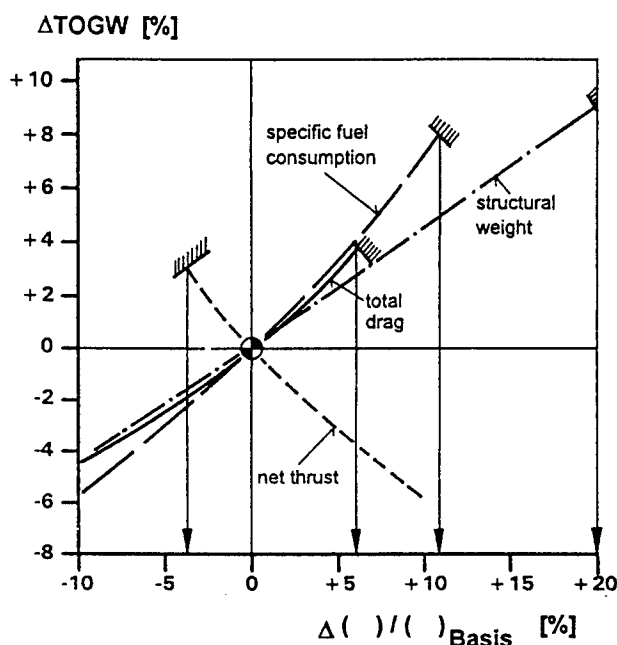


Fig. 16 Sensitivity of the take-off gross-weight of the reference concept (engine size and weight are fixed) (after Refs. 14,15)

At the high Mach number end the viscous drag accounts roughly for about one third of the total drag. Fig. 17 shows the skin friction at the lower symmetry line of the lower stage of the reference concept, Ref. 16. The flow is assumed to become turbulent at  $x/L = 0.1$ , where  $L$  is the length of the forebody. Apart from the fact, that today the location of transition cannot be estimated to a reasonable degree of accuracy, the different assumptions with regard to perfect gas/real gas, and cold surface/radiation-adiabatic surface/adiabatic surface result in a prediction uncertainty of the viscous drag alone, which by far exceeds the permissible uncertainty of the total drag in Fig. 16. Note the curve representing a (computed) typical wind-tunnel result (H2K, DLR Köln-Porz,  $Re = 3 \cdot 10^6$ ,  $T_\infty = 61$  K,  $T_w = 300$  K), Ref 17, which apparently is far away from reality, and note in addition the fact, that it is not known how good the turbulence models are, which were employed for the computation of the different cases in Fig. 17.



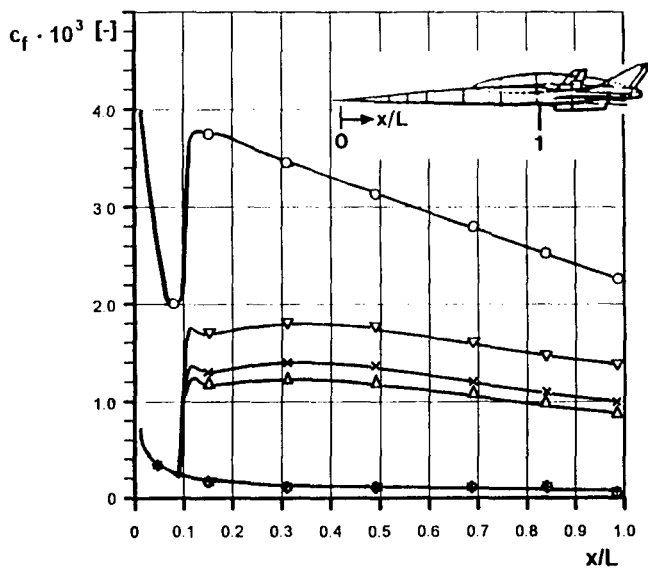


Fig. 17 Skin friction at the lower symmetry line of the SÄNGER lower stage computed with different assumptions (Refs. 16,17), legend see Fig. 18 ( $M = 6.8$ ,  $Re_L = 1.22 \cdot 10^8$  ( $L=55m$ ),  $\alpha = 6^\circ$ ,  $(x/L)_r = 0.1$ )

With regard to the uncertainty of the location of the laminar-turbulent transition region, it has been reported on the X-30, that there this uncertainty had affected (in the design studies) the gross take-off weight by a factor of two and more, Ref. 18.

The skin friction exerted by the turbulent boundary layer depends strongly on the wall temperature. In the radiation-adiabatic situation (nominal design situation) the wall temperature depends much more on the state of the boundary layer - laminar or turbulent - than in the adiabatic-wall situation, Fig. 18.

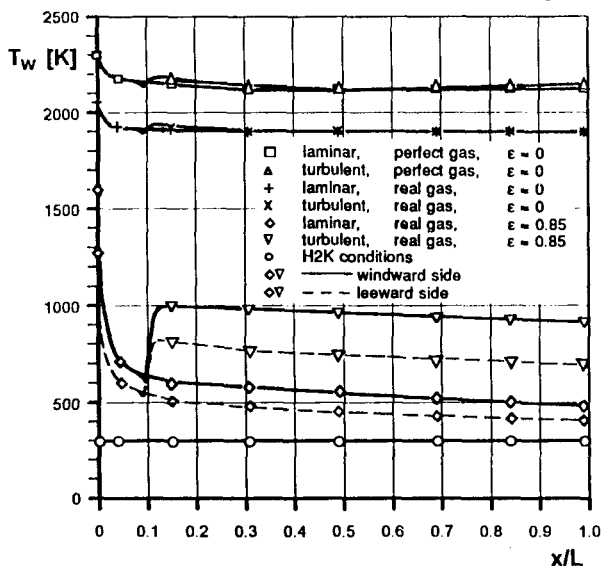


Fig. 18 Wall temperature at the lower symmetry line of the SÄNGER lower stage computed with different assumptions (flight parameters see Fig. 17), Ref. 16

Accordingly, the heat loads on the airframe structure are not known very accurately, because of the uncertainties in turbulence modelling, and because of the present impossibility of an experimental simulation of the flow and the actual heat loads, Ref. 11. Of very large concern is the fact, that in the transition

region the radiation-adiabatic wall temperature rises by about 400 K. In Fig. 18 this rise occurs over about 1 m due to the fact that the turbulence model simply was switched on. In reality this distance might be larger. It is, however, very likely that the transition region does not simply wrap around the forebody like a band, but that narrow tongues might develop with resulting large temperature gradients not only in longitudinal but also in transversal direction. As a result, these uncertainties will lead to excessive weight, but also to uncertainties with regard to the static and dynamic aeroelastic properties of the airframe.

Fig. 19, Refs. 14, 15, illustrates the static deformation of the SÄNGER forebody at flight condition ( $M = 6.8$ ) with the cold forebody as reference. A hot primary structure was assumed with such a structural design, that the heating results rather in deformations than in additional stresses. Because at the flight condition considered ( $M = 6.8$ ) the (nominal) radiation-adiabatic temperature is about 250 K (turbulent flow) lower on the upper side of the forebody than on the lower side, Fig. 18, a "bananization", Ref. 15, with a nose-up displacement of about 2 m occurs. Secondary effects reduce this displacement somewhat. And, of course a proper insulation, or even a cold primary structure concept with a thermal protection system could reduce it almost completely. Much more effective would be a tailoring (reduction) of the surface-radiation emission coefficient on the upper side of the forebody in order to avoid the temperature differences. This would in addition reduce the turbulent viscous drag on the upper side.

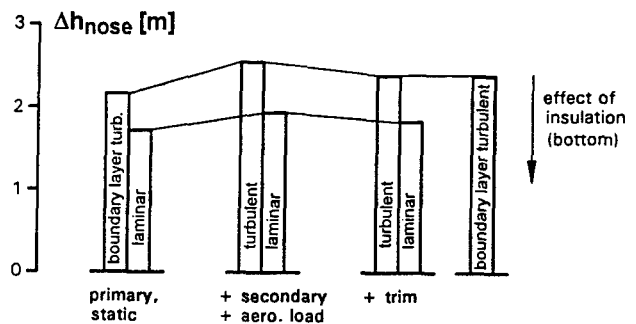


Fig. 19 Idealized effect of the temperature difference between the lower and the upper side of the forebody ( $L=55$  m) of the SÄNGER lower stage on its static aeroelastic behaviour, Ref. 15 ( $M = 6.8$  at 31 km altitude,  $\alpha = 6^\circ$ ,  $\Delta h_{Nose}$ : nose-up displacement)

Remains the dynamic deformation of the forebody in flight. Preliminary estimations of the amplitude range for the present structure concept from  $1^\circ$  to  $3^\circ$ , with complicated eigenmodes, with frequencies from 1 to 3 Hz, Ref. 6. Such dynamic properties of the forebody structure certainly are not acceptable. A solution would be to make the structure stiffer, however, this would be possible only with severe weight penalties. Considering the fact that the ratio payload/"dry-mass empty" of SÄNGER is only 4.4 percent, Ref. 6 (it is one order of magnitude smaller than that of modern passenger aircraft), structural weight is a problem, even if the overall take-off gross-weight sensitivity is relatively small, Fig. 16. In the design of modern fighter aircraft a contingency of about 7 to 8 percent for the "dry-mass empty" is worked with today (e.g. Ref. 19). From first flight to full mission employment another 2.5 to 3 percent mass growth is the rule. These numbers and the very small payload/"dry-mass empty" ratio illustrate the very large chal-

allenges in the structures and materials field. The "dry-mass empty" must be exactly the nominal one with the first copy of the STS.

These results must be seen in connection with the sensitivities of the propulsion system. Fig. 20, taken from Ref. 20, demonstrates a very large sensitivity of the net installed thrust on changes of the angle of attack. The net installed thrust is the actual thrust produced by the nozzle minus the flow momentum entering the inlet, the drag due to forebody boundary-layer diverting, spill drag, bypass drag and bleed drag, Ref. 20.

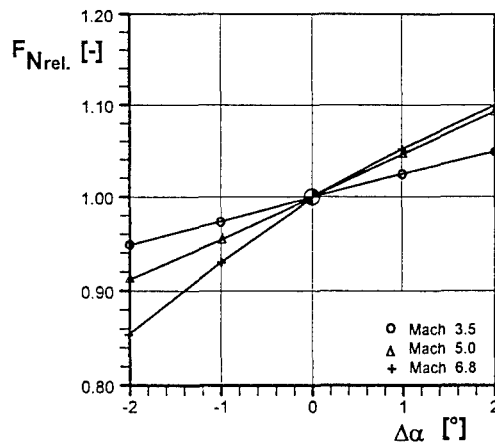


Fig. 20 Influence of (effective) angle of attack changes  $\Delta\alpha$  of the lower side of the SÄNGER forebody on the net installed thrust  $F_{Nrel}$ , Ref. 20

The main mechanism of this sensitivity is to be seen in the influence of the amount of pre-compression on the propulsion system. At  $M = 6.8$  only one degree less than the nominal angle of attack (of the lower side of the forebody) reduces the net installed thrust by about seven percent. One degree more would give four percent more thrust. Both numbers, however, must be connected to the wave-drag changes, associated with the angle of attack changes, which is not done here. The important result is, that the effective angle of attack of the lower side of the forebody must be controlled very delicately. The real static and dynamic deformations of the forebody must be known very early in the design process in order to design the necessary control means (sensors, flight/propulsion-control system, aerodynamic control surfaces). If this structure system cannot be controlled, the discussed sensitivity must be reduced by structural changes, or, for instance, by an adaptation of the inlet/propulsion control system to this situation.

As was said initially, all these results must be considered very carefully. They represent a snapshot picture of the system at a given moment in the design process. The designer must try to find means and ways to reduce the sensitivities to acceptable ones. Acceptable are those risks, which can be met. This is the case, when the functional properties of the whole system and its components meet the performance needs. This, however, can only be determined with adequate simulation means. This implies, that the sensitivities govern to a large extent the demands on the simulation means.

## 9. THE TRANSFER MODEL CONCEPT

The very large design (technical, financial) and operation (personal, performance) risks make it necessary to find alternatives to the classical design process in all technology fields

considered here, because of the many serious simulation problems and shortcomings encountered in hypersonic vehicle design. Examples are the propulsion system, airframe/propulsion integration, upper-stage separation etc. Fig. 7 illustrates the very large technology challenge by comparing the nominal total energy of airbreathing aircraft and the X15 to that of the reference concept of the German Hypersonics Technology Programme.

While the design objectives of the classical design process remain valid, kind and role of the design tools must be redefined. In the frame of the German Hypersonics Technology Programme the Transfer-Model philosophy, Ref. 5, was developed, which is valid for all involved technology areas. The main reason is always the shortcomings of ground simulation in the verification step to cope with the parameter demands, and partly with the sheer size of the vehicles and their components.

Transfer models are disciplinary and especially interdisciplinary steady and unsteady

- numerical simulation methods of highest complexity

and partly very sophisticated

- scaling methods

of such power and accuracy that the demands of all design steps including the verification step are covered. Essentially they must allow to transfer knowledge and data found with ground simulation (sub-scale tests) and computational simulation to the full-size design problem without the classical ground-facility verification step.

The term "Transfer Model" has been introduced deliberately, because not simply computation methods are meant like those of computational fluid dynamics (CFD), or computational structural mechanics (CSM), etc. It must be clearly understood, that Transfer Models are numerical simulation methods (and scaling methods), which describe real life processes, which are characterized in the present context by severe flow/structure interactions, and by dynamic phenomena due to these interactions, but also due to flow separation (the Reynolds or Favre averaged Navier-Stokes equations by definition do not describe the real "granularity" of turbulent flow, Ref. 21), acoustic phenomena, and combustion instabilities. On the other hand the true dynamic behaviour and responses of extreme light-weight structures presently are not known before fully representative samples have been built and tested.

Transfer Models on the other hand are nothing new. They are used in many fields, also in aerodynamics, however, not in such an interdisciplinary environment. In the present context they pose an enormous challenge, because the very fact, that the design verification in ground-simulation facilities is not possible to a sufficient degree, hampers also the development of such models. The development of such models solely from first principles would be utopian. Instead a pragmatical approach with much engineering judgement and a systematic use of all simulation means including experimental vehicles is necessary.

Several basic requirements exist for the successful development of transfer models:

- high performance interdisciplinary computation methods,

- computer architectures with true teraflops and even higher performance at very low cost levels,
- flow-physics and thermochemical models of sufficient accuracy,
- dynamic structural models with sufficient accuracy of material properties and the modelling of joints (structure-physics models),
- novel special ground-simulation facilities and test techniques for the creation of appropriate experimental data bases,
- appropriate hypersonic experimental vehicles for the gathering of experimental data, which cannot be obtained in ground-simulation facilities, for the validation of flow-physics, thermochemical and structure-physics models and finally for the validation of Transfer Models, other design tools and the overall design strategy.

The development and the application process of Transfer Models in general is shown in Fig. 21 in a very schematic way. Basically the classical simulation means are employed. In Step 1 a generic configuration or component is designed with the available methodology and computational tools. A model is tested in a suitable ground facility. With the knowledge and data gained the Transfer Model, which in general will be a (interdisciplinary) computation method, or a combination of (interdisciplinary) computation methods, is improved. A pre-operational design is made in Step 2 with the improved Transfer Model, and a model is tested in a preferably larger ground facility. Methodology, simulation tools and the Transfer Model have reached the first validation level at the end of Step 2. Note that not only the computational tools, and the Transfer Model must be validated, but also design methodology and ground-facility simulation. All is put in Step 3 to the first decisive test. An operational experimental vehicle is designed. Preferably models of the configuration and its major components should be tested, if ground facilities are available (size, parameter range). The flight tests and experiments then show whether the design methodology and the design tools (computational simulation, ground-facility simulation) have reached a sufficient validation level (level 2). In addition the information, which cannot be gained in ground facilities (flight data as final input into flow-physics and thermodynamic models, notably laminar-turbulent transition and turbulence data) is obtained. Level 2-validation by definition means that the enabling technology is available, and especially the Transfer Models, to design a space-transportation system of the reference-concept type.

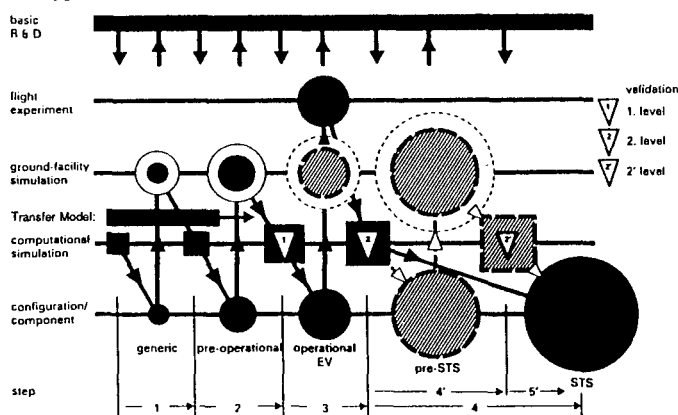


Fig. 21 Schematic of the development, verification and application process of transfer models (EV: experimental vehicle, TST: space transportation system), Ref. 5

However, the flight tests may reveal, that level 2-validation of a particular Transfer Model cannot be reached, and that, for instance, a pre-STs configuration or component must be designed, which is then to be tested in a very large and costly, newly to be created, dedicated ground facility (Step 4'). The data and knowledge then gained could lead to the necessary level 2'-validation of the respective Transfer Model. In the worst case the result of Step 4' could be, that the necessary enabling technology cannot be provided. History has seen such situations.

Basic research in flow-physics and thermodynamic modelling plays a major role, and must combine all kinds of research efforts and tools in continuous long-year Unified Approaches, Ref. 21, which also holds for structure-physics modelling. It will give input into the Transfer Models, will get data from ground-facility simulation, and very important, from the flight experiments. Dedicated ground facilities, computational tools etc. will be developed and employed.

## 10. FLIGHT TESTING WITH EXPERIMENTAL VEHICLES

In Chapter 4 it was explained that potential experimental vehicles, as well as all simulation means, must be considered for the Technology Development and Verification Concept, too, Fig. 3. This is necessary because they can pose technology demands different from that of the reference concept. The design risk and the operational risk of such vehicles are of concern, too, even if low-cost approaches are chosen.

Hypersonics technology development in the USA has relied on many experimental vehicles, Ref. 22, especially for reentry purposes (X-23, X-24). In Russia the BOR I to IV vehicles were flown to prepare the technology needed for BURAN. In the frame of the NASP-programme originally the X-30 was conceived as an experimental vehicle. For the European HERMES project the experimental vehicle MAIA was envisaged, Refs. 12,23. An overview over the known hypersonics experimental vehicle programmes, especially the programmes to explore reentry and lifting-body technology at both high and low-speed in the USA, is given in Ref. 23.

The primary objectives of experimental vehicles are, Refs.5,23:

- validation of overall system design,
- validation of overall design methodology,
- validation of design tools and simulation means (Transfer Models),
- validation of the aerothermodynamic design methodology,
- in-flight testing of propulsion system,
- in-flight testing of propulsion integration,
- proof of flight-vehicle stability and control properties,
- gathering of flow-physics and thermochemical data, which cannot be obtained in ground facilities (Transfer Model aspects).

The following demands must be put on experimental vehicles:

- they must be cheap, low-risk vehicles,
- they must be reusable in order to perform a "step by step" programme,
- they must be large enough and fly an envelope such that

the needed information can be obtained (functions and phenomena must be present, and not unduely mixed or masked),

- they must be in time in the whole technology programme schedule.

The problems then encountered are

- experimental vehicles themselves must be designed with all their own problems and risks, which however can be reduced by a stepwise approach with several vehicles from smaller to larger ones (cost? time?),
- in-flight measurements of data with sufficient accuracy, data rates and repeatability,
- air data measurements ( $v_\infty$ ,  $\rho_\infty$ ,  $T_\infty$ ) and data rates (speed and atmospheric inhomogenities as driver),
- weight, volume, energy demand, cooling demand, flight qualification, availability and cost of measurement systems,
- vehicle system behaviour (stability and control, flight quality, transient states, aerothermoclastic effects),
- numerical analysis methods for the investigation and correlation of the measured data, and the isolation of the functions and phenomena in question and their parameters.

In the frame of the German Hypersonics Technology Programme, experimental vehicle studies were performed continuously in parallel to the technology development work. The technological demands of the reference concept led to a first concept of an "aircraft-like" experimental vehicle, HYTEX 5.6, Refs. 24,25. The abbreviation "HYTEX" stands for Hypersonics Technology Experimental vehicle. Fig. 22 shows this manned vehicle with two turbo-RAM combined cycle engines, which could meet nearly all requirements with regard to the propulsion system, aerothermodynamics, materials, structures and subsystems resulting from the flight path of the SÄNGER lower stage including horizontal take-off and landing.

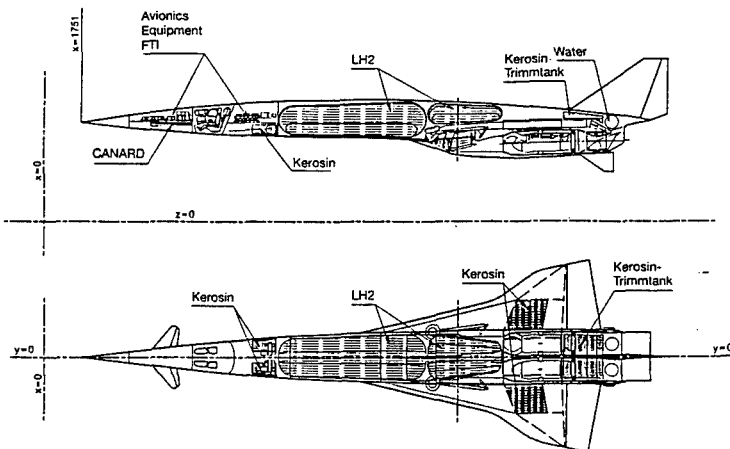


Fig. 22 HYTEX 5.6 ( $M = 5.6$ ) - baseline configuration 2/91, Ref. 24

A first assessment of costs for the development and procurement of this vehicle resulted in the recommendation to investigate less costly demonstrator vehicle concepts. Several studies have been performed since, see e.g. Refs. 4, 26, 6.

The last one finally led to an alternative concept, which had its emphasis on RAM-engine testing. HYTEX D2 (R-A3), shown in Fig. 23, is based on an existing drone produced by RADUGA in Dubna, Russia. This drone has been launched successfully several hundred times from a Tupolev Tu-22M3 aircraft at  $M = 1.6$ . The rocket-propelled vehicle can reach Mach numbers up to 6<sup>+</sup> and maintain constant speed during its flight envelope for a short time. It has originally been developed to be used as a target vehicle. The basic idea was to attach the RAM-engine to be tested on the lower side of the vehicle (passenger test) and to ignite it during flight at constant speed. The feasibility of the RADUGA drone D2 to carry the test engine has been investigated and proven by the latest study work together with Russian partners, Ref. 26. This demonstrator vehicle concept seems to be the easiest and cheapest means to demonstrate the RAM-engine operating in real flight environment within a short time schedule. It is based to a large extent on already existing and available flight hardware (RADUGA Drone D2 and Tupolev TU-22M3), flight testing experience and infrastructure available at the Russian Flight Testing Institute (LEE) at Zhukowsky. Only the development and manufacturing of the RAM-engine to be tested in flight-rated hardware would have been required.

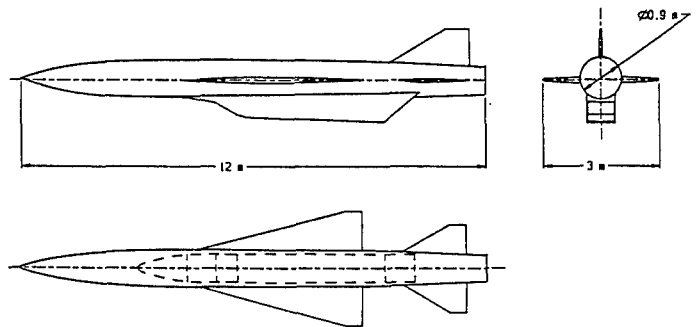


Fig. 23 HYTEX D2 (R-A3), based on the TsAGI/RADUGA drone D2, Ref. 26

Finally it is remarked, that experimental vehicles must strictly be seen as an integral part of a technology development effort. They are to be the "capstone" in the "vault" of the technology programme. Actually they must play the role of a precursor reference concept, which is in parallel of the actual reference concept, but must not be just a down-scaled vehicle. This anyway in general is not possible because of, at least, heat loads issues, Ref. 11.

## 11. TECHNOLOGY DEVELOPMENT AND VERIFICATION: GENERAL RESULTS

System studies, including sensitivity studies, and technology work have identified the critical technology issues of future airbreathing space transportation systems, i.e. the lower stage of the two-stage-to-orbit reference system SÄNGER of the German Hypersonics Technology Programme. This regards all four technology areas. The critical topics are mainly connected with simulation problems (computational simulation, ground-facility simulation, in-flight simulation) of structure and functions of the lower stage and its components.

In view of the technology development processes and finally the system definition, development and verification processes of an space transportation system and its components, four most critical items were identified in the study, Ref. 6. In a sense, they encompass almost all key-technology items, and aerothermodynamics is always involved directly or indirectly.

These four items are:

- o The determination and verification of the viscous drag of the lower stage, the viscous forebody (inlet-onset) flow, and the (especially) forebody mechanical and heat loads in view of the identified sensitivities of the system (drag, airframe/propulsion integration/coupling, structures and materials concept). Viscous flow in presence of the nose-tip entropy layer, a radiation cooled surface, low to medium real-gas effects, multi-mechanisms laminar-turbulent transition and turbulence make these issues very hard to simulate computationally, and impossible to simulate fully in any ground facility (wind tunnel).
- o The design and especially the ground-facility verification of a  $M = 3$  to 7 RAM propulsion inlet in a realistic environment with real-gas effects, hot (although partially cooled) elastic surfaces, laminar-turbulent transition, turbulent strong interaction effects, and realistic viscous inlet-onset flow, with and without forebody boundary-layer diverter effects. A full ground test, which allows to answer all technology, performance and sensitivity issues is considered as not possible.
- o The ground-facility verification (free-jet test) of the lower stage propulsion system, i.e. the system inlet/RAM burner/nozzle for the  $M = 3$  to 7 regime under real flight conditions. With 2 meter diameter of the RAM burner, and an overall length of the propulsion system of about 30 m, such testing is not possible in view of the necessary facility size and the power demands. Costs would be prohibitive and the simulation fidelity not assured.
- o The ground-facility verification of the static, but especially the dynamic properties of the lower stage airframe (hot primary structure at a maximum temperature level of about 1000 K, mechanical and heat loads of  $M = 3$  to 7 flight (problem of laminar-turbulent transition zone shape, strong-interaction zone loads)). In view of the sensitivities (airframe/propulsion coupling) and the sheer size of the airframe static tests appear feasible at that temperature level, but not the dynamic tests, because again of prohibitive costs, power demands, and not assured simulation fidelity.

No attempt was made in the study to classify all technology items according to, for instance, the NASA technology readiness levels, Ref. 27. Although such an exercise would be highly useful, and should perhaps be done at a later stage, it would not have suited the present study, which looked at the overall system issues, and the related component and component-integration issues. Important is the understanding of the systems and components sensitivities and their implications for the simulation means, if they cannot be eliminated or defused during the definition and development processes by alternative technical solutions.

Finally a note on the sensitivities discussed in Chapter 8. As was already stated above, alternative technical solutions must be found, if the sensitivities lead to unacceptable design and operation risks, and/or to unacceptable or not realizable simulation demands. With regard to the mass-flow sensitivity of the propulsion system, this could, for instance, be an inlet ramp control system with much higher complexity than considered now, in order to adjust to mass-flow fluctuations due to the

dynamic deformation behaviour of the forebody. It could also be a stiffer cold primary structure of the airframe with a thermal protection system. Such a concept could be tested statically and especially dynamically, because the heat-loading would be a secondary problem. However, both of these possible solution examples imply other and new problems, which need a full understanding, before they could be adopted. No easy solution can be guaranteed, if new and very demanding technologies are to be developed, which has led to the cancelling of many projects in the past. A noteworthy study in this respect, but also with regard to the whole subject of the present study is the report Ref.28 on the design evolution of a supersonic transport aircraft.

The above concentration on the four most critical items must not distract the reader from the fact, that in all technology areas dedicated long and continuous development work would have been necessary in order to reach the goal of Phase II, the readiness of the enabling technologies for the development of a new advanced space-transportation system.

The simulation means and the design and verification processes, especially with regard to aerothermodynamics can be rated, according to the results of the study, Ref.6, as follows:

- o **Ground-simulation facilities:** in general available, assessment and re-calibration with numerical methods necessary, Hot Experimental Technique with hot, quiet hypersonic tunnel needed, principal restrictions of facilities to be overcome with Transfer-Model concept.
- o **Computational simulation:** in general available, very large growth potential with massively parallel processor (MPP) computer architectures, urgent need of interdisciplinary computation tools, flow-physics, thermochemical, structure-physics etc. models and general validation shortcomings to be overcome with the Transfer-Model concept.
- o **General verification work:** wherever possible with classical ground-facility simulation, otherwise with the Transfer-Model concept.
- o **Formalized and computer-based definition and development processes:** urgent need of a holistic description of the highly integrated and sensitive vehicle system in view of the very large development and operation risks. The objectives are:
  - highly reliable feasibility assessments in any stage of the processes,
  - initiation of alternative studies and approaches in due time,
  - identification and assessment of technology issues,
  - focussing of technology development efforts.

The final recommendation given in Ref. 6 for the technology development and verification in Phase II is a fully integrated and highly interdisciplinary approach, which combines work on technologies, experimental vehicles, and transfer-model development with extended reference concept studies in the following five elements, Fig. 24:

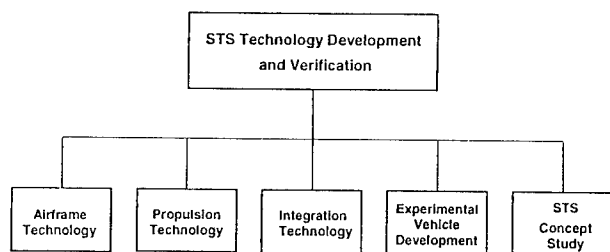


Fig. 24 The five elements of the general Technology Development and Verification Concept of Phase II of the German Hypersonics Technology Programme, Ref. 6

### 1. Development of Airframe Technology

In this element the development work of the three classical technology areas Aerothermodynamics, Structures and Materials, and Guidance and Control, Subsystems is combined into one entirety, in order to reach highest efficiency, because of the partly very strong coupling of the three areas. Consequently the related transfer models are combined to the transfer model "outer flow path", which contains appropriate subsets.

### 2. Development of Propulsion Technology

This element so far was rather self-contained, compared to the airframe technologies, and remains so. To it belongs the "inner flow path" transfer model, with appropriate subsets.

### 3. Development of Integration Technology

This is a new element, which makes use of the presently emerging formalized computer-based product definition and development processes. This element is to combine in the sense of the Virtual Product, Ref. 29, formalized processes, the transfer models as multidisciplinary super modules, multidisciplinary numerical optimization methods, cost models, mass budgeting, "ilities" models (see element No. 5), etc. into a tool of concurrent engineering. This element is proposed in order to permit to describe the physical properties of the to the highest degree integrated flight vehicles (the space transportation system and the proposed experimental vehicles), to determine their performances, sensitivities, critical elements, etc., and in order to perform trade-offs, study alternatives, etc.. The integration technology development work culminates in formalized and computerized definition and development processes, which describe the future space transportation system and the experimental vehicles as virtual products.

### 4. Development of Experimental Vehicles

In this element the proposed experimental vehicles and their variants are developed or modified, respectively, by employing the transfer models emerging from elements 1 and 2 and the integration technology (element 3), while the experimental vehicles themselves are elements of the transfer-model concept.

### 5. Space Transportation System Concept Study

This element iterates permanently the reference concept by applying the emerging and maturing technologies, the transfer models, the integration technology. It is structured and works to a degree, as if the actual development (Pha-

se III) would already happen. Depending on discovered sensitivities, critical elements, etc., the reference concept is evolving, new technological solutions are identified, if necessary, and the overall direction of the work especially in the elements 1 to 3 is checked and adapted, if necessary. The emerging overall simulation needs must be monitored, because they lead to high costs, when experimental vehicles become evolved. This element must also look at the "ilities" of the Space Transportation System. These are "reliability", "maintainability", and "testability" of any hardware component of the STS. The "ilities" are potential operation cost drivers. They must constantly be considered in the concept study and must be regarded in the technology work already in the early phases.

Details of the Technology Development and Verification Concept, which assumed a begin of the STS development in the year 2006, the first flight in the year 2016, and the full operability in the year 2021, can be found in Ref. 6.

## 12. CONCLUSION

The technological challenges of airbreathing space-transportation systems are extraordinarily large. Ground-facility simulation is restricted in all technology areas, also in aerothermodynamics. The classical design and verification approach therefore is partly no more feasible. The Transfer-Model approach, based on ground-facility simulation, computational simulation and in-flight simulation, which addresses especially the strong interdisciplinary couplings between the technology areas, appears to be the only possible way out of the problem. The Hypersonics Technology Development and Verification Concept was to structure the maturation and verification paths of the enabling technologies in the European Phase II of the Technology Programme. The basic results, insights and conclusions are valid for the technology development of any new advanced space transportation system or hypersonic vehicle.

## 14. REFERENCES

1. Hirschel, E.H., "Hypersonic Aerodynamics", in: Space Course 1993, Vol.1, München, 1993, pp 2-1 to 2-17.
2. Weingartner, S., "SÄNGER - The Reference Concept of the German Hypersonics Technology Programme", AIAA-Paper 93-5161, 1993.
3. Hirschel, E.H., Heindl, H.A., "Aerothermodynamics Analysis Tools and Strategy for the Design of Reusable Launch Vehicles", FESTIP study, Dasa/LME12/S/STY/188/B, 1996.
4. Sacher, P.W., "Hypersonic Flight Test Issues", AIAA-Paper 93-5078, 1993.
5. Hirschel, E.H., "The Hypersonics Technology Development and Verification Strategy of the German Hypersonics Technology Programme", AIAA-Paper 93-5072, 1993.
6. Hirschel, E.H., "The Technology Development and Verification Concept of the German Hypersonics Technology Programme", Dasa/LME12/Hypac/STY/0017/A, 1995.
7. Hauck, H., "Leitkonzept SÄNGER, Referenz-Daten Buch", Ausgabe 1, Revision 2, March 1993.

8. Hirschel, E.H., "Aerothermodynamic Phenomena and the Design of Atmospheric Hypersonic Airplanes", in: *Advances of Hypersonics II*, Vol. I, Defining the Hypersonic Environment, J.Bertin, J.Periaux, J.Ballmann, eds., Birkhäuser, Boston, 1993, pp 1 - 39.
9. Bertin, J.J., "Hypersonic Aerothermodynamics", AIAA, New York, 1993.
10. Anderson, J.D., "Hypersonic and High Temperature Gasdynamics", McGraw-Hill Book Co., New York, 1989.
11. Hirschel, E.H., "Heat Loads as Key Problem of Hypersonic Flight", *Zeitschrift für Flugwissenschaften und Weltraumforschung*(ZFW), Vol.16, Nr.6, 1992, pp 349 - 356.
12. N.N., "Complementary Study on Hypersonic Test Vehicle", Final Report No. H-ST-13-01-AS, Avion Marcel Dassault and MBB under ESA contract, 1987.
13. Neyland, V.Ya., "Scientific and Engineering Problems and Methods of Preflight Development of Orbiter", TsAGI Central Aerohydrodynamic Institute, Moskow, 1992.
14. Wimbauer, J., "Sensitivitäten und Trade-offs am SÄNGER 4/92 Unterstufe", DASA-TN-LME112-HYPAC-TN-287, 1992.
15. Staudacher, W., Wimbauer, J., "Design Sensitivities of Airbreathing Hypersonic Vehicles", AIAA-Paper 93-5099, 1993.
16. Schmatz, M.A., Höld, R.K., Monnoyer, F., Mundt, Ch., Rieger, H., Wanie, K.M., "Numerical Methods for Aerodynamic Design II", Space Course Aachen, 1991, Paper No. 62, also MBB/FE211/S/PUB/442, 1991.
17. Radespiel, R., personal communication, 1994.
18. Shea, J.F., (ed.): "Report on the Defense Science Board Task Force on the National Air Space Plane (NASP)". Office of the Under-Secretary of Defense for Acquisition, Washington, D.C., 1988.
19. Platt, J.T., "Sensitivity of Combat Aircraft Mass to Changes in Structural Design Safety Factors", SAWE (Society of Allied Weight Engineers, Inc.), Paper 1202, 1978.
20. Schaber, R., "Einfluß entscheidender Triebwerksparameter auf das Leistungsverhalten eines Hyperschall-Antriebs", MTU-N94-EP-0001, 1994.
21. Hirschel, E.H., Stock, H.W., Cousteix, J., "Current Turbulence Modelling in Aircraft Design", In: *Engineering Turbulence, Modelling and Measurements 2* (W.Rodi, F.Martelli, eds.), Elsevier Science Publishers, Amsterdam, 1993, pp 665 - 690.
22. Miller, J., "The X-Planes X-1 to X-29", Speciality Press Publishers and Wholesalers, Inc., Marine on St. Croix, Maine, USA, 1983.
23. Hirschel, E.H., Grallert, H., Lafon, J., Rapuc, M., "Acquisition of an Aerothermodynamic Data Base by Means of a Winged Experimental Reentry Vehicle", *Z. Flugwiss. Weltraumforsch.*, Vol. 16, No.1, 1992, pp 15-27.
24. Sacher, P.W., "Feasibility Investigations of a Hypersonic Flight Demonstrator", MBB-FE13-HYPAC-STY-4A, 1991.
25. Sacher, P.W., Kraus, M., Zellner, B., "Untersuchungen zu Flugerprobungsträger-Alternativen", MBB-FE13-HYPAC-STY-14A, 1992.
26. Sacher, P.W., Zellner, B., "Investigations of Alternative Concepts of Hypersonic Flight Test Vehicles", Dasa-LME13-HYPAC-STY-XX, 1995.
27. Stanley, D.O., Piland, W.M., "Technology Requirements for Affordable Single-Stage Rocket Launch Vehicles", IAF-Paper 93-V.4.627, 1993.
28. Swan, W.C., "Design Evolution of the BOEING 2707-300 Supersonic Transport, Part I: Configuration Development, Aerodynamics, Propulsion, and Structures", AGARD CP147-Vol. 1-9, 1973, pp 9-1 to 9-18.
29. Hirschel, E.H., "Potential and Implications of New Information Technologies for the Product Definition and Development Processes of Aircraft", In preparation.

AGARD-R-813, 1996

(AGARD-FDP-VKI Special Course on Aerothermodynamics and Propulsion Integration, Rhode-Saint-Genèse, April 15-19, 1996)

## REPORT DOCUMENTATION PAGE

<b>1. Recipient's Reference</b>	<b>2. Originator's Reference</b>  AGARD-R-813	<b>3. Further Reference</b>  ISBN 92-836-1041-5	<b>4. Security Classification of Document</b>  UNCLASSIFIED/ UNLIMITED												
<b>5. Originator</b> Advisory Group for Aerospace Research and Development North Atlantic Treaty Organization 7 rue Ancelle, 92200 Neuilly-sur-Seine, France															
<b>6. Title</b>  Aerothermodynamics and Propulsion Integration for Hypersonic Vehicles															
<b>7. Presented at/sponsored by</b>  The Special Course held at the von Kármán Institute for Fluid Dynamics (VKI) in Rhode-Saint-Genèse, Belgium, 15-19 April 1996.															
<b>8. Author(s)/Editor(s)</b>  Multiple			<b>9. Date</b>  October 1996												
<b>10. Author's/Editor's Address</b>  Multiple			<b>11. Pages</b>  448												
<b>12. Distribution Statement</b> There are no restrictions on the distribution of this document. Information about the availability of this and other AGARD unclassified publications is given on the back cover.															
<b>13. Keywords/Descriptors</b> <table style="width: 100%; margin-top: 10px;"> <tr> <td style="width: 50%;">Aerothermodynamics</td> <td style="width: 50%;">Hypersonic vehicles</td> </tr> <tr> <td>Hypersonic flow</td> <td>Turbulent boundary layer</td> </tr> <tr> <td>Missile propulsion</td> <td>Reentry vehicles</td> </tr> <tr> <td>Ramjet engines</td> <td>Supersonic combustion ramjet engines</td> </tr> <tr> <td>Rocket propulsion</td> <td>Stage separation</td> </tr> <tr> <td>Turbulence</td> <td>Navier-Stokes equations</td> </tr> </table>				Aerothermodynamics	Hypersonic vehicles	Hypersonic flow	Turbulent boundary layer	Missile propulsion	Reentry vehicles	Ramjet engines	Supersonic combustion ramjet engines	Rocket propulsion	Stage separation	Turbulence	Navier-Stokes equations
Aerothermodynamics	Hypersonic vehicles														
Hypersonic flow	Turbulent boundary layer														
Missile propulsion	Reentry vehicles														
Ramjet engines	Supersonic combustion ramjet engines														
Rocket propulsion	Stage separation														
Turbulence	Navier-Stokes equations														
<b>14. Abstract</b> <p>Lecture notes for the AGARD Fluid Dynamics Panel (FDP) Special Course on "Aerothermodynamics and Propulsion Integration for Hypersonic Vehicles" have been assembled in this report. The following topics were covered:</p> <ul style="list-style-type: none"> <li>• Aerothermodynamics of radiation-cooled surfaces;</li> <li>• Real-gas and strong interaction phenomena;</li> <li>• Hypersonic laminar turbulent transition and turbulence modeling;</li> <li>• Configurational aerothermodynamics of reentry vehicles (winged and capsule) as well as RAM and SCRAM propelled vehicles;</li> <li>• RAM and SCRAM inlet and propulsion integration;</li> <li>• Hypersonic missile aerothermodynamics and stage separation for two-stage launch configurations.</li> </ul> <p>In addition, the Hypersonic Aerothermodynamic Program at VKI was presented as well as a Navier Stokes-solver for Hypersonic applications.</p> <p>The material assembled in this report was prepared under the combined sponsorship of the AGARD Fluid Dynamics Panel, the Consultant and Exchange Program of AGARD, and the von Kármán Institute (VKI) for Fluid Dynamics.</p>															



Aucun stock de publications n'a existé à AGARD. A partir de 1993, AGARD détiendra un stock limité des publications associées aux cycles de conférences et cours spéciaux ainsi que les AGARDographies et les rapports des groupes de travail, organisés et publiés à partir de 1993 inclus. Les demandes de renseignements doivent être adressées à AGARD par lettre ou par fax à l'adresse indiquée ci-dessus. *Veuillez ne pas téléphoner.* La diffusion initiale de toutes les publications de l'AGARD est effectuée auprès des pays membres de l'OTAN par l'intermédiaire des centres de distribution nationaux indiqués ci-dessous. Des exemplaires supplémentaires peuvent parfois être obtenus auprès de ces centres (à l'exception des Etats-Unis). Si vous souhaitez recevoir toutes les publications de l'AGARD, ou simplement celles qui concernent certains Panels, vous pouvez demander à être inclu sur la liste d'envoi de l'un de ces centres. Les publications de l'AGARD sont en vente auprès des agences indiquées ci-dessous, sous forme de photocopie ou de microfiche.

CENTRES DE DIFFUSION NATIONAUX

## ALLEMAGNE

Fachinformationszentrum Karlsruhe  
D-76344 Eggenstein-Leopoldshafen 2

## BELGIQUE

Coordonnateur AGARD-VSL  
Etat-major de la Force aérienne  
Quartier Reine Elisabeth  
Rue d'Evere, 1140 Bruxelles

## CANADA

Directeur, Services d'information scientifique  
Ministère de la Défense nationale  
Ottawa, Ontario K1A 0K2

## DANEMARK

Danish Defence Research Establishment  
Ryvangs Allé 1  
P.O. Box 2715  
DK-2100 Copenhagen Ø

## ESPAGNE

INTA (AGARD Publications)  
Carretera de Torrejón a Ajalvir, Pk.4  
28850 Torrejón de Ardoz - Madrid

## ETATS-UNIS

NASA Goddard Space Flight Center  
Code 230  
Greenbelt, Maryland 20771

## FRANCE

O.N.E.R.A. (Direction)  
29, Avenue de la Division Leclerc  
92322 Châtillon Cedex

## GRECE

Hellenic Air Force  
Air War College  
Scientific and Technical Library  
Dekelia Air Force Base  
Dekelia, Athens TGA 1010

## ISLANDE

Director of Aviation  
c/o Flugrad  
Reykjavik

## ITALIE

Aeronautica Militare  
Ufficio del Delegato Nazionale all'AGARD  
Aeroporto Pratica di Mare  
00040 Pomezia (Roma)

## LUXEMBOURG

Voir Belgique

## NORVEGE

Norwegian Defence Research Establishment  
Attn: Biblioteket  
P.O. Box 25  
N-2007 Kjeller

## PAYS-BAS

Netherlands Delegation to AGARD  
National Aerospace Laboratory NLR  
P.O. Box 90502  
1006 BM Amsterdam

## PORTUGAL

Estado Maior da Força Aérea  
SDFA - Centro de Documentação  
Alfragide  
2700 Amadora

## ROYAUME-UNI

Defence Research Information Centre  
Kentigern House  
65 Brown Street  
Glasgow G2 8EX

## TURQUIE

Millî Savunma Başkanlığı (MSB)  
ARGE Dairesi Başkanlığı (MSB)  
06650 Bakanlıklar-Ankara

**Le centre de distribution national des Etats-Unis ne détient PAS de stocks des publications de l'AGARD.**

D'éventuelles demandes de photocopies doivent être formulées directement auprès du NASA Center for AeroSpace Information (CASI) à l'adresse ci-dessous. Toute notification de changement d'adresse doit être fait également auprès de CASI.

AGENCES DE VENTE

NASA Center for AeroSpace Information  
(CASI)  
800 Elkridge Landing Road  
Linthicum Heights, MD 21090-2934  
Etats-Unis

The British Library  
Document Supply Division  
Boston Spa, Wetherby  
West Yorkshire LS23 7BQ  
Royaume-Uni

Les demandes de microfiches ou de photocopies de documents AGARD (y compris les demandes faites auprès du CASI) doivent comporter la dénomination AGARD, ainsi que le numéro de série d'AGARD (par exemple AGARD-AG-315). Des informations analogues, telles que le titre et la date de publication sont souhaitables. Veuillez noter qu'il y a lieu de spécifier AGARD-R-nnn et AGARD-AR-nnn lors de la commande des rapports AGARD et des rapports consultatifs AGARD respectivement. Des références bibliographiques complètes ainsi que des résumés des publications AGARD figurent dans les journaux suivants:

Scientific and Technical Aerospace Reports (STAR)  
publié par la NASA Scientific and Technical  
Information Division  
NASA Langley Research Center  
Hampton, Virginia 23681-0001  
Etats-Unis

Government Reports Announcements and Index (GRA&I)  
publié par le National Technical Information Service  
Springfield  
Virginia 22161  
Etats-Unis  
(accessible également en mode interactif dans la base de  
données bibliographiques en ligne du NTIS, et sur CD-  
ROM)

